

WCAP-16996-NP  
Revision 0

November 2010

**Realistic LOCA Evaluation  
Methodology Applied to the  
Full Spectrum of Break Sizes  
(FULL SPECTRUM LOCA  
Methodology)**

**Volume II, Part 2  
WCOBRA/TRAC-TF2  
Assessment**



## 15 ASSESSMENT OF THE VESSEL POST-CHF HEAT TRANSFER

### 15.1 INTRODUCTION

Section 7 describes the VESSEL component heat transfer package. This package consists of a set of heat transfer correlations and selection logic to determine the appropriate correlation based on the local thermal-hydraulic conditions. The heat transfer package in WCOBRA/TRAC-TF2 produces a continuous boiling curve as a function of wall temperature and local fluid conditions. Figure 15.1-1 shows the heat transfer regime map used by the WCOBRA/TRAC-TF2 vessel component.

Heat transfer is modeled in WCOBRA/TRAC-TF2 as a regime dependent, three step process. Specific models and correlations are used for heat transfer from the wall to vapor field, heat transfer from the wall to the liquid fields (continuous and entrained liquid), and interfacial heat transfer between the phases. Each of these processes is flow regime dependent and is based on the local hydrodynamic conditions in the computational cell. Section 7 described the wall to fluid heat transfer models, and Section 6 described those for interfacial heat transfer.

The same heat transfer package in WCOBRA/TRAC-TF2 is used for small, intermediate and large break phenomena. No specific logic is included that would result in a difference in small, intermediate and large break heat transfer models.

Section 14 described the tests chosen to assess the WCOBRA/TRAC-TF2 heat transfer models. This section presents a summary of comparisons between test data and predictions of these tests based on the WCOBRA/TRAC-TF2 heat transfer package. Specific aspects of the heat transfer models and calculations will be compared to data where available, and specific calculated parameters are presented to show self-consistency of the WCOBRA/TRAC-TF2 heat transfer package.

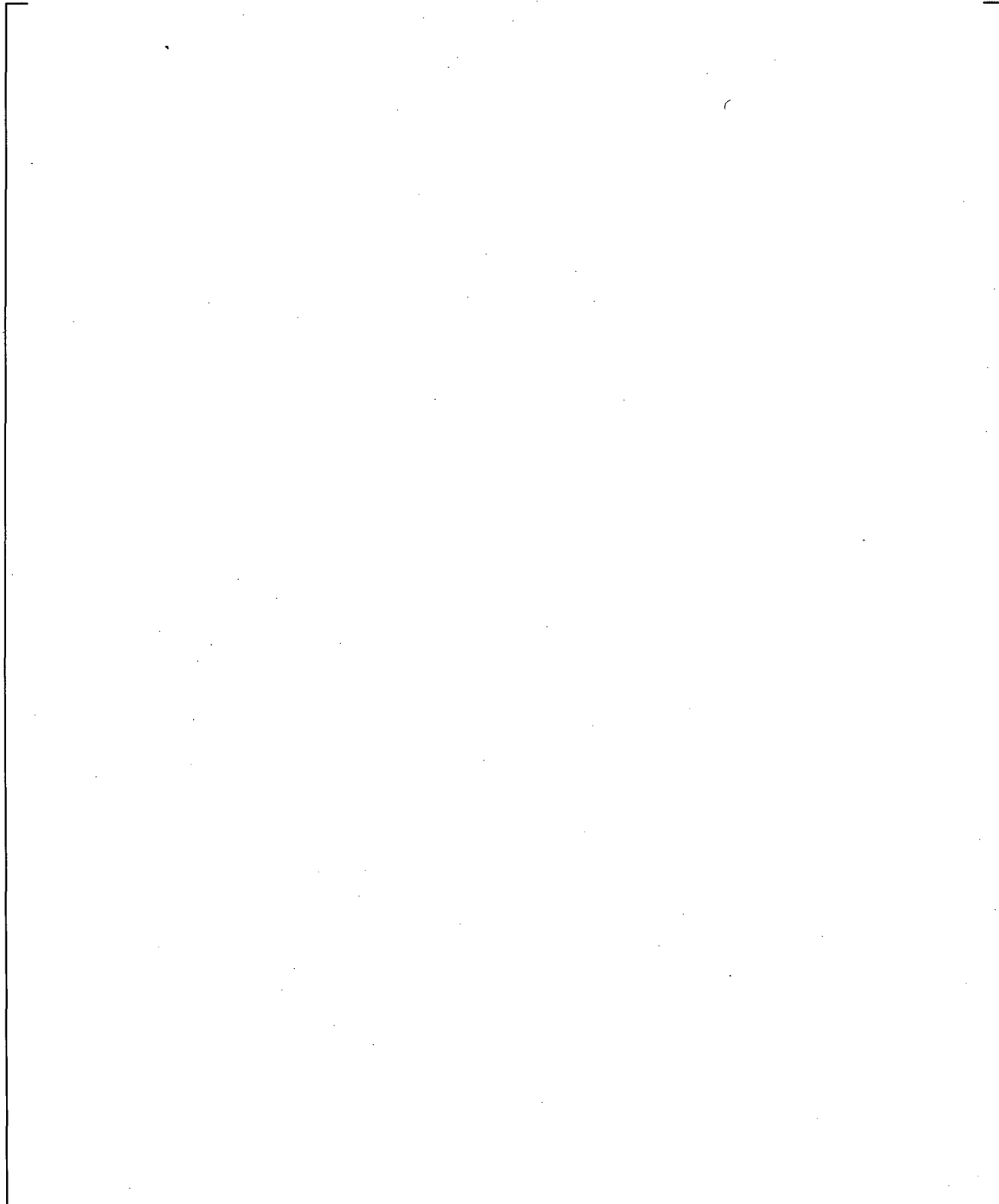


**Figure 15.1-1**      **WCOBRA/TRAC-TF2 Vessel Component Heat Transfer Regime Map (from Figure 7.2-3)**

## 15.2 ROADMAP TO THE ASSESSMENT

The core heat transfer assessment is split into three main areas: single phase vapor (SPV), dispersed flow film boiling (DFFB), and reflood. Heat transfer to SPV is important for predicting clad temperatures during the refill phase of a large break and the boiloff and recovery phases of a small break. Heat transfer in DFFB is important for predicting clad temperatures during the blowdown phase of a large break and during the safety injection and accumulator injection phases of an intermediate break. Because of the complicated nature of the reflood phase of a large break which may involve all heat transfer regimes, it will be assessed separately.

One of the issues in quantifying the accuracy of heat transfer relations in a large thermal-hydraulic systems code such as WCOBRA/TRAC-TF2 is that few experimental tests provide a sufficient amount of simultaneous local information on void fraction, phasic flow rates, and phase temperatures. While modeling an entire separate effects test facility and simulating experiments can provide useful information on overall code performance, the predicted results are subject to compensating errors. That is, inaccuracies in one model package can compensate for the inaccuracies in another package producing a fortuitously correct result. An example is an accurate prediction of wall heat flux when heat transfer coefficients are under-predicted, while  $(T_w - T_v)$  was over-predicted because of errors in the hydraulics package. If sufficient local information is available, it is possible to separate the calculation of the heat transfer coefficients from the calculation of the fluid conditions and provide an assessment of the heat transfer prediction alone.

Two types of calculations were used to assess the WCOBRA/TRAC-TF2 heat transfer package. [

] <sup>a,c</sup>

[

]a,c

a,c



(15-1)

[

]a,c



**Figure 15.2-1 COBRAHT-TF2 Calculation Procedure**

### 15.3 ASSESSMENT OF CHF

Section 13 presents the level swell assessment with which predicting the dryout point is important for determining the location of the mixture level. Section 13.4.2 discusses the level swell assessment for the ORNL-THTF uncovered bundle heat transfer test simulations. These tests are assessed for heat transfer in Section 15.4.1. From the vapor temperature figures presented in Section 15.4.1 (Figures 15.4.1-9 to 15.4.1-14), the dryout point for the test simulations [

] <sup>a,c</sup>

Section 13.4.5 presents an assessment of the critical heat flux (dryout point) for JAERI-TPTF tests, and it was concluded that [

] <sup>a,c</sup>

Tables 22-6 through 22-9 in Section 22.5.3 provides a comparison of measured vs. predicted CHF timing for the LOFT experiments and simulations, and concluded that [

] <sup>a,c</sup>

WCOBRA/TRAC-TF2 models and correlations provide [ <sup>a,c</sup> of the ORNL dispersed flow film boiling tests (Section 15.5.2). There is a [

] <sup>a,c</sup>

Based on the above, WCOBRA/TRAC-TF2 [

] <sup>a,c</sup>

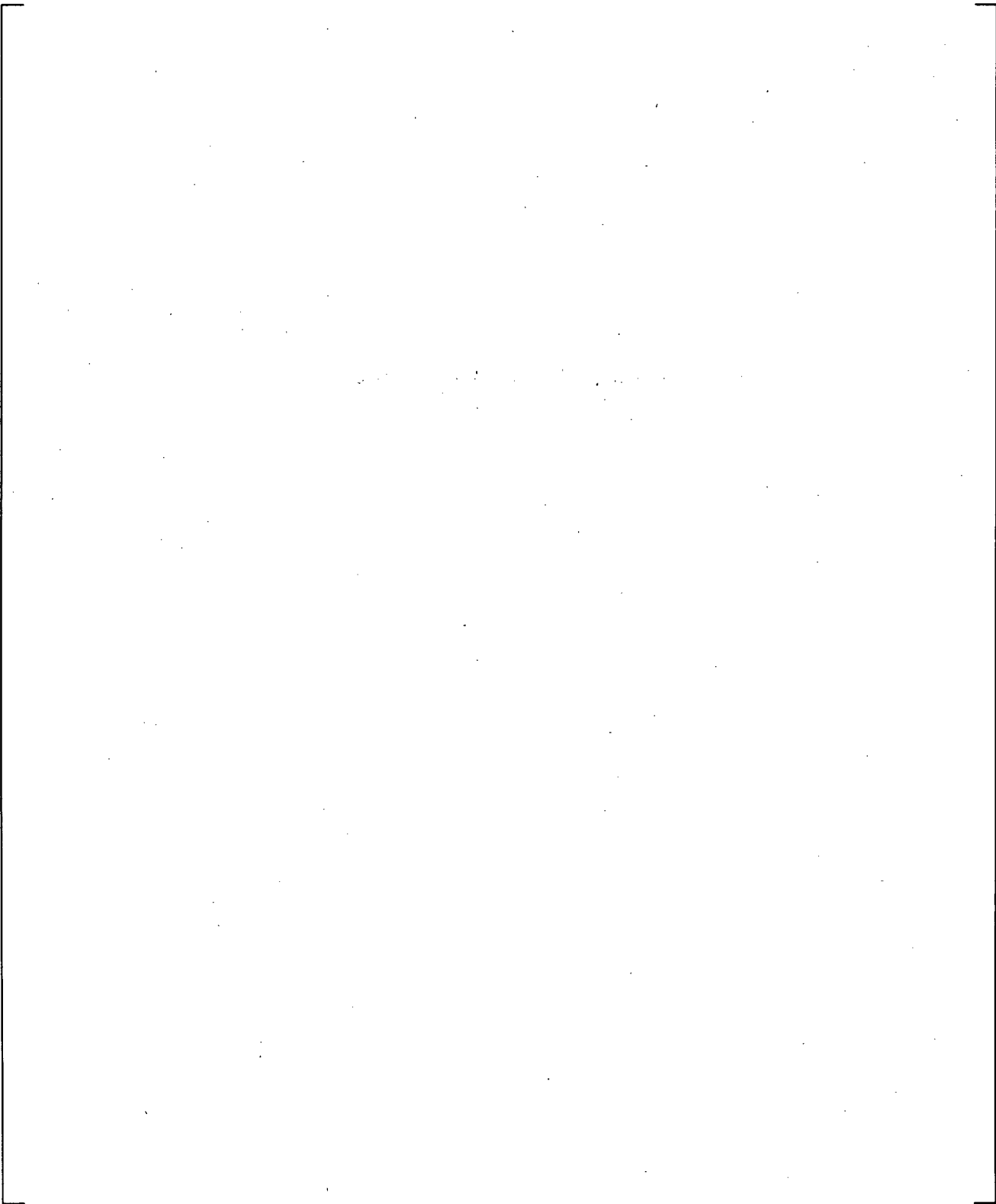


**Figure 15.3-1 Predicted Versus Measured Critical Heat Flux Elevation from JAERI-TPTF Tests (from Figure 13.4.5-6)**

## 15.4 SINGLE PHASE VAPOR (SPV) HEAT TRANSFER ASSESSMENT

### 15.4.1 ORNL-THTF Uncovered Bundle Heat Transfer Test Simulations

The measured local heat flux and wall surface temperature were reported as a cross-sectional average value of all thermocouples at each level in (Anklam et al., 1982). In this validation, [

] <sup>a,c</sup> Figure 15.4.1-1a shows a comparison of the predicted versus measured heat transfer coefficients for the ORNL-THTF uncovered bundle heat transfer tests. On average, the experimental heat transfer coefficients are [

] <sup>a,c</sup> Figure 15.4.1-1b further shows this by comparing the ratio of the measured to the predicted heat transfer coefficients [

] <sup>a,c</sup> versus vapor film Reynolds number. Figure 15.4.1-1b also shows that [ ] <sup>a,c</sup>

Section 13.4.2 describes the ORNL-THTF test facility and conditions as well as the WCOBRA/TRAC-TF2 simulations. In addition to void fraction, cladding temperature measurements were taken. Figures 15.4.1-2 through 15.4.1-7 provide a comparison of the measured cladding temperature profiles to the predicted temperature profiles from WCOBRA/TRAC-TF2.

In general, [

] <sup>a,c</sup> This is further exemplified in Figure 15.4.1-8, which shows the predicted vs. measured cladding temperatures.

Figures 15.4.1-9 through 15.4.1-14 provide a comparison of the measured and predicted vapor temperatures profiles. As shown by the figures, [

] <sup>a,c</sup>

a,c

**Figure 15.4.1-1a Heat Transfer Coefficient Comparison for ORNL-THTF Uncovered Bundle Tests (from COBRAHT-TF2)**

a,c

**Figure 15.4.1-1b Ratio of Measured to Predicted Heat Transfer Coefficient vs. Vapor Film Reynolds Number for ORNL-THTF Uncovered Bundle Tests (from COBRAHT-TF2)**

a,c



**Figure 15.4.1-2 Cladding Temperature Profile Comparison for ORNL-THTF Uncovered Bundle Test I**

a,c



**Figure 15.4.1-3 Cladding Temperature Profile Comparison for ORNL-THTF Uncovered Bundle Test J**

a,c

**Figure 15.4.1-4 Cladding Temperature Profile Comparison for ORNL-THTF Uncovered Bundle Test K**

a,c

**Figure 15.4.1-5 Cladding Temperature Profile Comparison for ORNL-THTF Uncovered Bundle Test L**

a,c

**Figure 15.4.1-6 Cladding Temperature Profile Comparison for ORNL-THTF Uncovered Bundle Test M**

a,c

**Figure 15.4.1-7 Cladding Temperature Profile Comparison for ORNL-THTF Uncovered Bundle Test N**

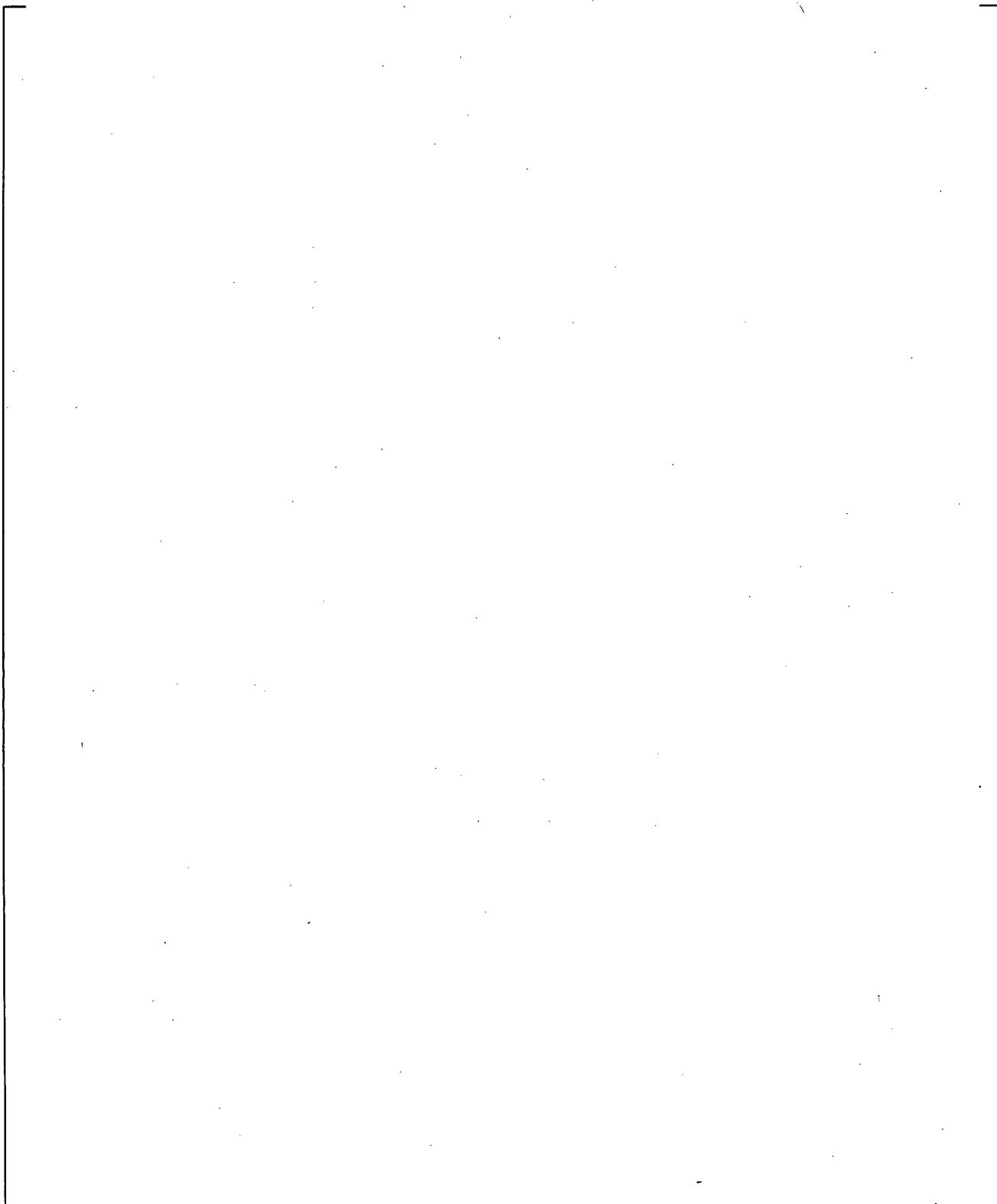


**Figure 15.4.1-8 Comparison of Predicted vs. Measured Cladding Temperatures for ORNL-THTF Uncovered Bundle Tests**

a,c

**Figure 15.4.1-9 Vapor Temperature Profile Comparison for ORNL-THTF Uncovered Bundle Test I**

a,c

**Figure 15.4.1-10 Vapor Temperature Profile Comparison for ORNL-THTF Uncovered Bundle Test J**

a,c

**Figure 15.4.1-11 Vapor Temperature Profile Comparison for ORNL-THTF Uncovered Bundle Test K**

a,c

**Figure 15.4.1-12 Vapor Temperature Profile Comparison for ORNL-THTF Uncovered Bundle Test L**

a,c

**Figure 15.4.1-13 Vapor Temperature Profile Comparison for ORNL-THTF Uncovered Bundle Test M**

a,c

**Figure 15.4.1-14 Vapor Temperature Profile Comparison for ORNL-THTF Uncovered Bundle Test N**

**Figure 15.4.1-15**      **Conduction Node and Cell Vapor Temperature Profile Comparison for ORNL-THTF Uncovered Bundle Test I**

## 15.4.2 FLECHT SEASET Single Phase Vapor Heat Transfer Test Simulations

The measured local heat flux and wall surface temperature were reported for individual thermocouples at various elevations in Wong, S and Hochreiter, L. E., 1981. In this validation, [

] <sup>a,c</sup> Figure 15.4.2-1 shows a comparison of the predicted versus measured heat transfer coefficients for the FLECHT SPV heat transfer tests. On average, [

] <sup>a,c</sup> Figure 15.4.2-2 shows a comparison of the ratio of the measured to the predicted heat transfer coefficients [

] <sup>a,c</sup> versus vapor film Reynolds number. As the figure shows, [

] <sup>a,c</sup>

a,c

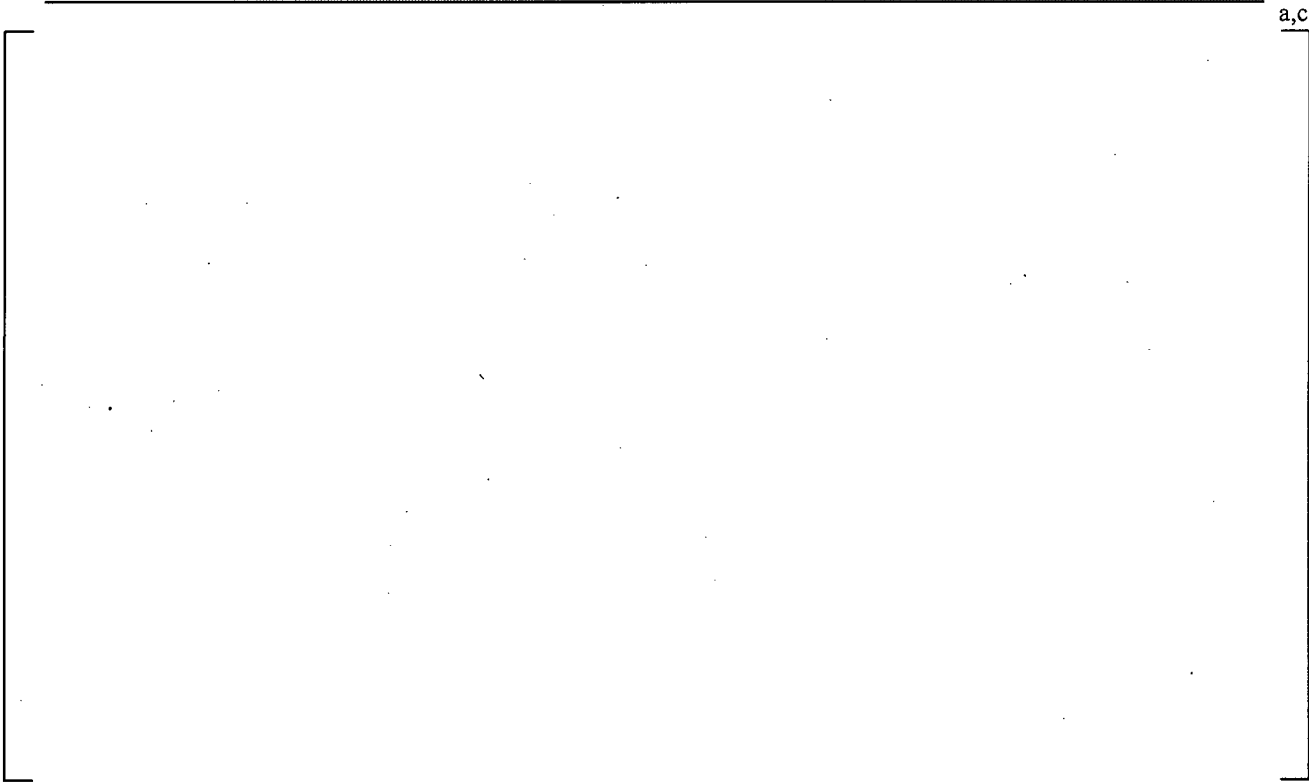


**Figure 15.4.2-1 Heat Transfer Coefficient Comparison for FLECHT SPV Tests (from COBRAHT-TF2)**

a,c



**Figure 15.4.2-2 Ratio of Predicted to Measured Heat Transfer Coefficient vs. Vapor Film Reynolds Number for FLECHT SPV Tests (from COBRAHT-TF2)**

### 15.4.3 Single Phase Vapor Heat Transfer Summary and Conclusion

The heat transfer package in WCOBRA/TRAC-TF2 was “driven” with known local conditions from single-phase vapor experiments. The code predicted the heat transfer coefficient [ ]<sup>a,c</sup> for both data sets. The [ ]<sup>a,c</sup>

## 15.5 DISPERSED FLOW FILM BOILING (DFFB)

Dispersed flow film boiling (DFFB) was assessed using two methods. The first method [ ]<sup>a,c</sup>

The second method [ ]<sup>a,c</sup>

### 15.5.1 Assessment Using COBRAHT-TF2

#### 15.5.1.1 ORNL-THTF Steady-State Film Boiling Tests

In Yoder et al., (1982), the measured local heat flux and wall surface temperature were reported for each thermocouple at different levels for individual rods and as a cross-sectional average value of all thermocouples at each level. In this validation, the heat transfer coefficient data at [ ]<sup>a,c</sup>

Figure 15.5.1-1 compares the predicted and measured HTC's, with [ ]<sup>a,c</sup>. On average, the experimental heat transfer coefficients are [ ]<sup>a,c</sup>. This is further exemplified with Figure 15.5.1-2, which also shows that [ ]<sup>a,c</sup>.

a,c

Figure 15.5.1-1

Heat Transfer Coefficient Comparison for all Thermocouples at [ ]<sup>a,c</sup> in ORNL Steady-State Film Boiling Tests (from COBRAHT-TF2)

]a,c in

a,c

Figure 15.5.1-2

Ratio of Measured to Predicted Heat Transfer Coefficient vs. Vapor Film Reynolds Number for all Thermocouples at [ ]<sup>a,c</sup> in ORNL Steady-State Film Boiling Tests (from COBRAHT-TF2)

## 15.5.2 Assessment Using Test Simulations

### 15.5.2.1 ORNL-THTF Test Simulations

The WCOBRA/TRAC-TF2 model of the ORNL-THTF is shown in Figure 15.5.2.1-1. The test section is modeled using the vessel component of WCOBRA/TRAC-TF2. Section 1 of the vessel models the lower plenum of the test section. Section 2 models the heated length of the test section with two channels:

[ ]<sup>a,c</sup>. In this model, the bottom of the heated test section begins 13.5 inches above the bottom of the test section. The measured outlet pressure is applied to the top of the vessel as a pressure and enthalpy boundary condition. Two other boundary conditions representing inlet mass flowrate and inlet flow enthalpy are applied to the bottom of the vessel. These boundary conditions are also derived from measured test data. Figures 14.2.2.1-1 to 14.2.2.1-6 provide the boundary conditions used for the transient tests, and Table 14.2.2.1-2 provides the boundary conditions for the steady-state test.

Two heater rod models are used to represent the 59 heater rods in the test section (one of the 60 heater rods failed during the test; therefore, only 59 heater rods are simulated). Two unheated structures are also used to simulate the shroud box of the test section. This is necessary since the stored energy in these structures is important in the transient experiments. The six grids of the assembly are explicitly modeled in the inner and outer portions of the rod bundle.

Two one-dimensional components are included in the model to satisfy WCOBRA/TRAC-TF2 input requirements. A PIPE component is attached to the last cell of Channel 4 of the VESSEL component. The volume of the pipe is set to a very small value ( $1.0 \times 10^{-4} \text{ ft}^3$ ) such that negligible mass is contained in the pipe. A FILL component is attached to the other end of the PIPE to supply a zero velocity boundary condition. Such an arrangement ensures that the vessel component will not lose any fluid through the one-dimensional components.

#### 15.5.2.1.1 Test 3.07.9B Simulation

The comparison of the axial heater rod surface temperature profile between the WCOBRA/TRAC-TF2 predictions and experimental data is shown in Figure 15.5.2.1-2. The experimental data are level averaged values as reported by Yoder et al. (1982). The local grid spacer effect on the rod temperature profile is clearly evident from the sharp temperature drop around the spacer grid locations. It can also be seen that the overall trend is a decrease in surface temperature with increasing distance above the dryout point. For this test, mass velocities remain high in the bundle, and the increased mixture velocity which results from increased steam quality, provides improved cooling.

The WCOBRA/TRAC-TF2 predictions are indicated by a solid line in the same figure. The dryout point is predicted between [ ]<sup>a,c</sup> from the bottom of the heated section. From the available data in the ORNL report, the actual dryout point is approximately 62 inches. Above the dryout point, the heater rod temperature increases during the test because the rod surface is in the transition and film boiling regime. The PCT predicted by WCOBRA/TRAC-TF2 is [ ]<sup>a,c</sup> above the bottom of the heated test section. The experimental data indicates an averaged PCT of 1374°F at 62 inches (Level H).

Calculated fluid conditions at the inner channel PCT location and time are presented in Table 15.5.2.1-1.  
[

] <sup>a,c</sup>

#### 15.5.2.1.2 Test 3.03.6AR Simulation

In Test 3.03.6AR, the axial temperature profile increases with increasing distance above the dryout point. In this test, low flowrates, increasing void fraction, and superheating of vapor decreases heat transfer, despite increased mixture velocity. The WCOBRA/TRAC-TF2 predictions and experimental data at the time the PCT occurred (11 seconds and 10 seconds from experimental data and WCOBRA/TRAC-TF2 predictions, respectively) are shown in Figure 15.5.2.1-3. The average PCT predicted by WCOBRA/TRAC-TF2 is [ ] <sup>a,c</sup> above the bottom of the heated test section, while the experimental data indicates a PCT of 1194°F at 143 inches (near the top of the heated test section).

The WCOBRA/TRAC-TF2 prediction of the transient response of the ORNL-THTF bundle is compared to data at several locations (Figures 15.5.2.1-4 to 15.5.2.1-6). In these figures, averaged data and average predicted rod results are shown. These comparisons indicate that WCOBRA/TRAC-TF2 is [

] <sup>a,c</sup> This test was characterized by relatively large uncertainties in measured inlet flow, as reported by Mullins et al. (1982).

Calculated fluid conditions at the inner channel PCT location and time are presented in Table 15.5.2.1-1.  
[

] <sup>a,c</sup>

#### 15.5.2.1.3 Test 3.08.6C Simulation

The axial rod surface temperature profile, at the time (20 seconds) when the PCT is predicted is shown in Figure 15.5.2.1-7. Because of the high inlet mass flowrate maintained during the first 20 seconds of this test, the temperature decreases with increasing distance above the dryout point. The average PCT predicted by WCOBRA/TRAC-TF2 is [ ] <sup>a,c</sup>, while the available experimental data indicates a PCT of 1483°F at 107 inches. Transient heater rod temperatures predicted by WCOBRA/TRAC-TF2 are compared to averaged data at three axial elevations in Figures 15.5.2.1-8 to 15.5.2.1-10. The predicted average cladding temperatures are [ ] <sup>a,c</sup>.

Calculated fluid conditions at the inner channel PCT location and time are presented in Table 15.5.2.1-1.  
[

] <sup>a,c</sup>

#### 15.5.2.1.4 Summary and Conclusions

The measured and predicted PCTs for all three ORNL tests are shown in Table 15.5.2.1-2 and in Figure 15.5.2.1-11. These results, along with the COBRAHT-TF2 results, indicate that:

[

] <sup>a,c</sup>

Table 15.5.2.1-1 WCOBRA/TRAC-TF2 Calculated Fluid Conditions at Rod 1 PCT Time and Locations

Test Number	Time (s)	Location (in)	Fractions			Vapor Velocity (ft/s)	Entrained Liquid Velocity (ft/s)	Vapor Temperature (°F)	Droplet Size (ft)
			Liquid	Vapor	Entrained				

a,c

**Table 15.5.2.1-2 WCOBRA/TRAC-TF2 PCT Comparisons**

Test Number	Experimental Data PCT, (°F)	WCOBRA/TRAC-TF2 Prediction PCT, (°F)

a,c

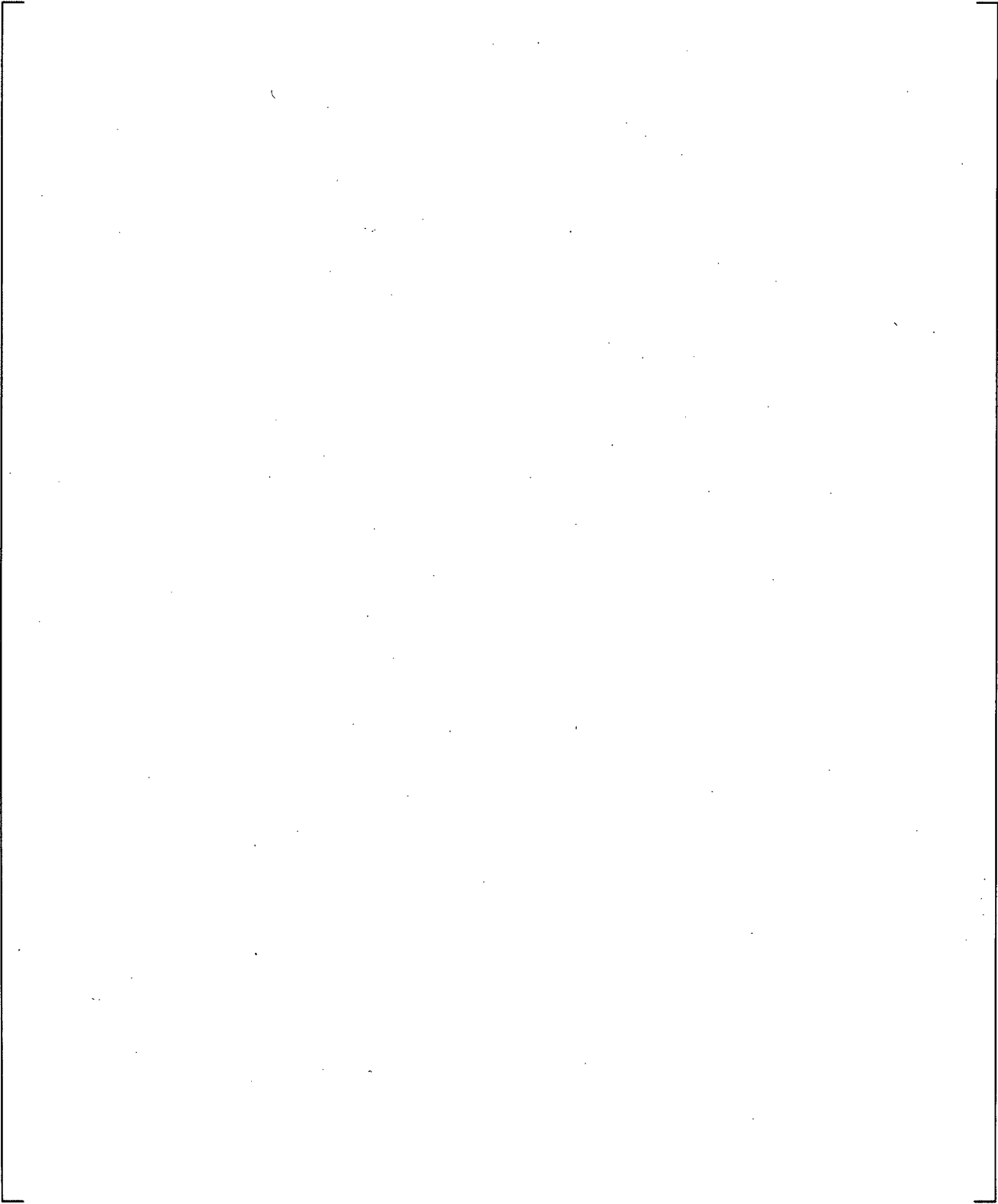


**Figure 15.5.2.1-1 WCOBRA/TRAC-TF2 Model for the ORNL-THTF Simulations**

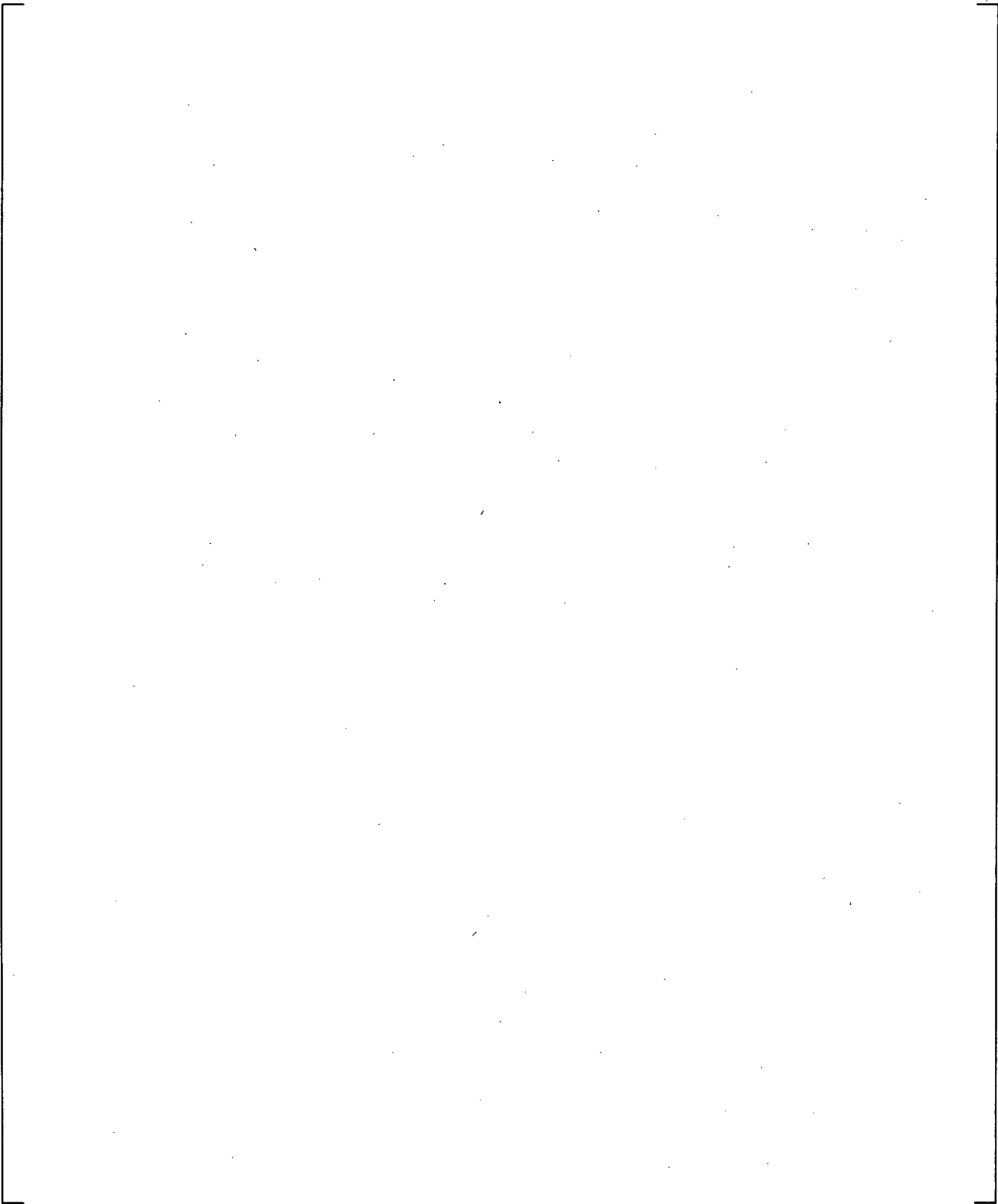


**Figure 15.5.2.1-2 ORNL-THTF 3.07.9B Axial Heater Rod Temperature Profile at 20 s of Transient**

a,c

**Figure 15.5.2.1-3 ORNL-THTF 3.03.6AR Axial Heater Rod Temperature Profile at 10 s of Transient**

a,c

**Figure 15.5.2.1-4 ORNL-THTF 3.03.6AR Transient Heater Rod Temperature at 96 in**

a,c

**Figure 15.5.2.1-5 ORNL-THTF 3.03.6AR Transient Heater Rod Temperature at 118 in**

a,c

**Figure 15.5.2.1-6 ORNL-THTF 3.03.6AR Transient Heater Rod Temperature at 143 in**

a,c

**Figure 15.5.2.1-7 ORNL-THTF 3.08.6C Axial Heater Rod Temperature Profile at 21 s of Transient**

a,c

**Figure 15.5.2.1-8 ORNL-THTF 3.08.6C Transient Heater Rod Temperature at 95 in**

a,c

**Figure 15.5.2.1-9 ORNL-THTF 3.08.6C Transient Heater Rod Temperature at 118 in**

a,c

**Figure 15.5.2.1-10 ORNL-THTF 3.08.6C Transient Heater Rod Temperature at 143 in**

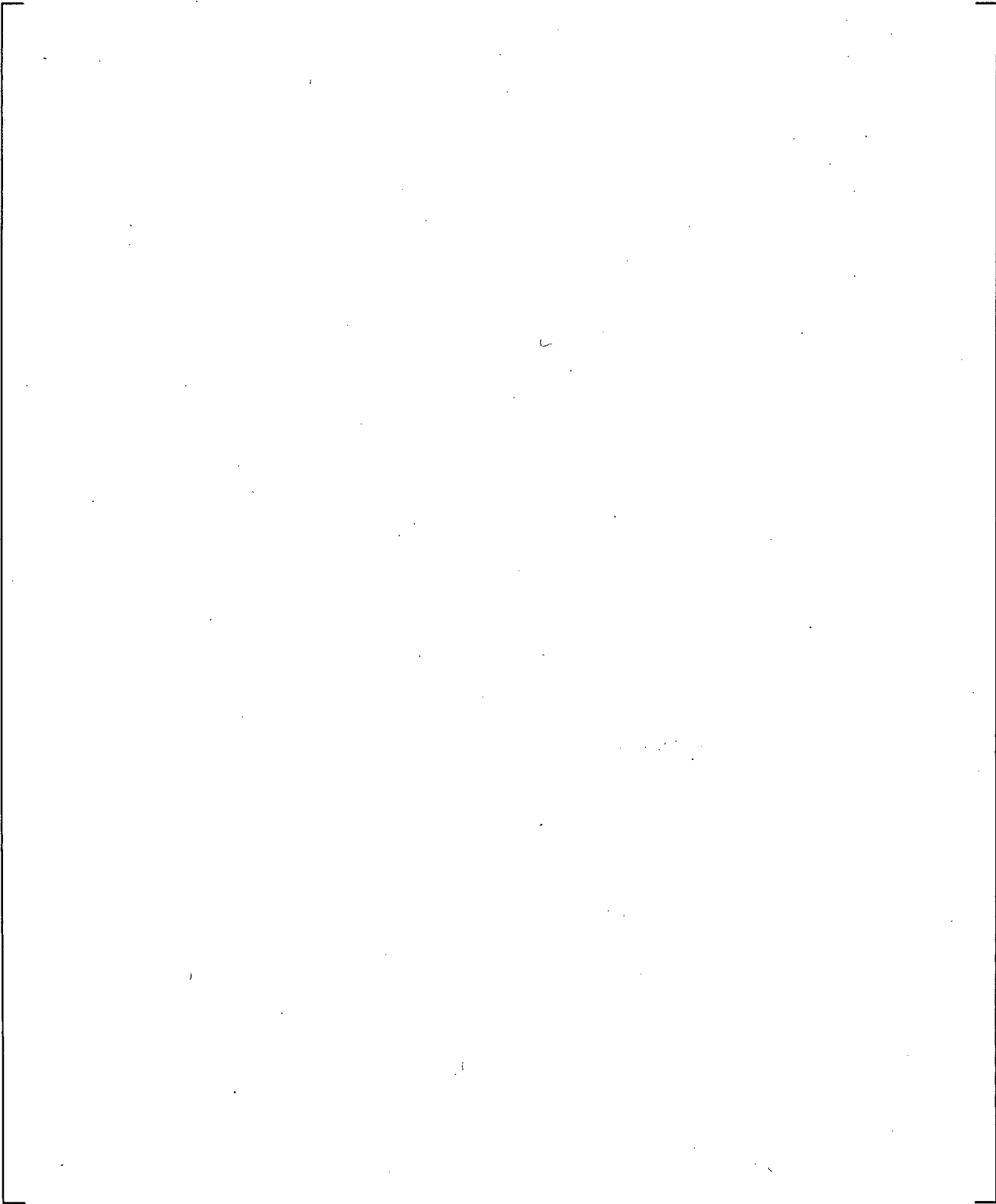


**Figure 15.5.2.1-11 ORNL-THTF Predicted versus Measured Peak Cladding Temperature**

**15.5.2.2 G-1 Blowdown Test Simulations**

The WCOBRA/TRAC-TF2 model of the G-1 bundle is comparable to the PWR core modeling, with similar core node heights. The G-1 model consists of three components: a vessel, a hot leg pipe, and a hot leg break. The vessel contains [ ]<sup>a,c</sup> in twelve channels. A schematic diagram of the model is shown in Figure 15.5.2.2-1.

Sections 1 and 2 of the vessel model the lower plenum of the vessel. Section 3 models the heated length of the test section with two channels: [

] <sup>a,c</sup>. The fluid nodes are thermally connected to rods simulating the heater rods. Grids were explicitly modeled to simulate their effect on heat transfer. The inner channel represents the region [ ]<sup>a,c</sup> from the test section wall, as illustrated in Figure 14.2.2.2-5. Section 4 models the ground plate, which also has a loss coefficient. Section 5 of the vessel models the upper plenum. At the bottom of the vessel, a pressure and enthalpy boundary condition is used to model the pressure boundary condition imposed on the test section by the cold leg and downcomer. Section 6 models the elevation of the hot leg, and Section 7 models the upper plenum above the hot leg region. A flow and enthalpy boundary condition is used to model the flash chamber flow introduced into the test section through the hot leg (Channel 11). UHI flow (if specified) into the upper plenum (Channel 7) is also provided by a flow and enthalpy boundary condition.

**15.5.2.2.1 Test 143 Simulation**

Test 143 was designated the reference test. It was performed without UHI flow. Other initial conditions for this test are listed in Table 14.2.2.2-2 and repeated below.


a,c

[

] <sup>a,c</sup>

[

] <sup>a,c</sup>

[

] <sup>a,c</sup>

**15.5.2.2.2 Test 148 Simulation**

[

] <sup>a,c</sup>

**15.5.2.2.3 Test 152 Simulation**

[

] <sup>a,c</sup>

**15.5.2.2.4 Test 146 Simulation**

[

] <sup>a,c</sup>

**15.5.2.2.5 Test 153 Simulation**

[

] <sup>a,c</sup>

**15.5.2.2.6 Test 154 Simulation**

[

] <sup>a,c</sup>

### 15.5.2.2.7 Summary and Conclusions

Overall, WCOBRA/TRAC-TF2 had a tendency to [

] <sup>a,c</sup>.

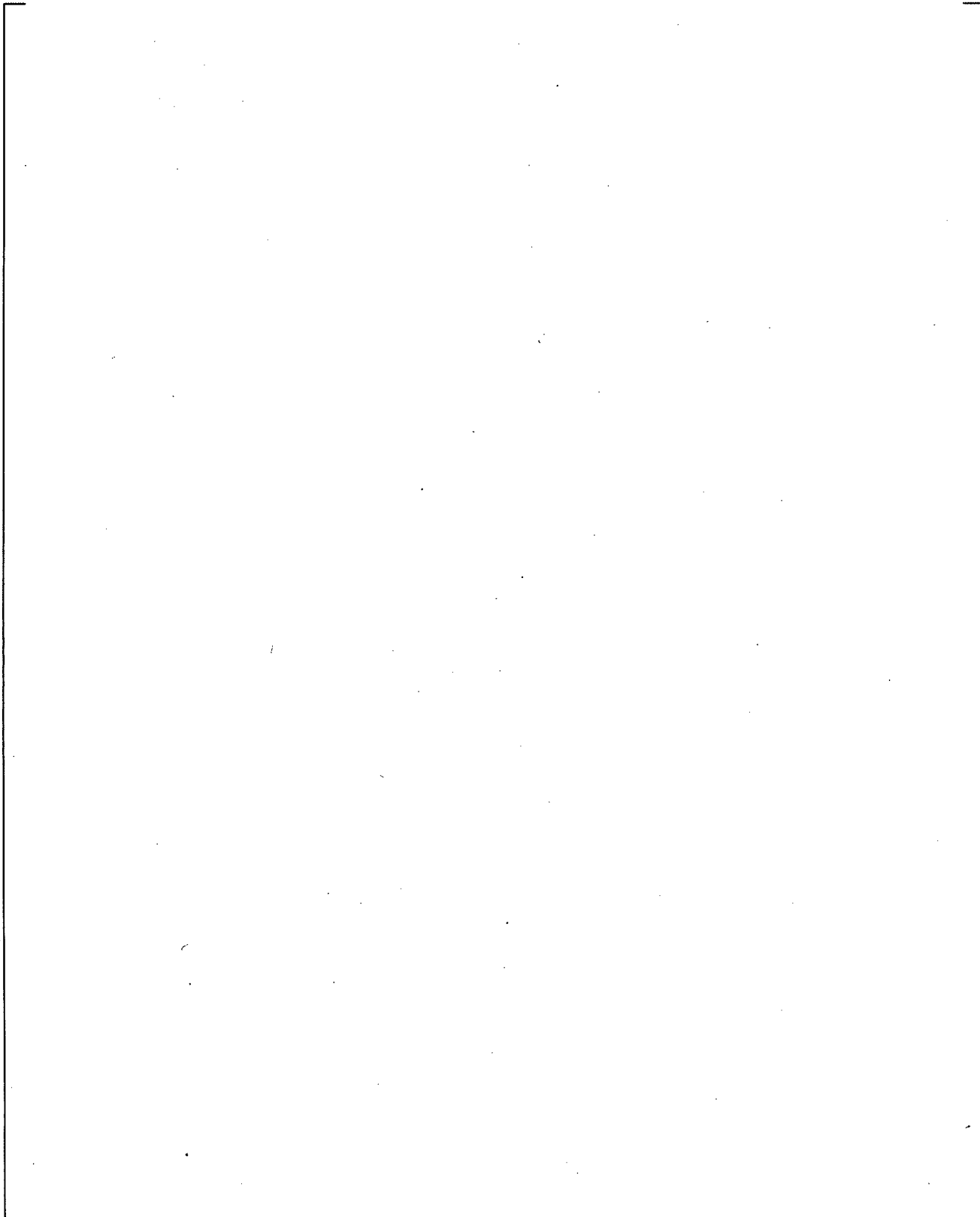


**Figure 15.5.2.2-1 WCOBRA/TRAC-TF2 Model of the G-1 Blowdown Test Simulations**

a,c



**Figure 15.5.2.2-2 G-1 Blowdown Test 143 Cladding Temperature Time History Comparison (24-inch Elevation)**

a,c



**Figure 15.5.2.2-3 G-1 Blowdown Test 143 Cladding Temperature Time History Comparison (48-inch Elevation)**

a,c

**Figure 15.5.2.2-4 G-1 Blowdown Test 143 Cladding Temperature Time History Comparison (72-inch Elevation)**

a,c

**Figure 15.5.2.2-5 G-1 Blowdown Test 143 Cladding Temperature Time History Comparison (96-inch Elevation)**

a,c



**Figure 15.5.2.2-6 G-1 Blowdown Test 143 Cladding Temperature Time History Comparison (120-inch Elevation)**

a,c



**Figure 15.5.2.2-7 G-1 Blowdown Test 143 Axial Cladding Temperature Comparison (Time = 6 Seconds)**



**Figure 15.5.2.2-8 G-1 Blowdown Test 143 Axial Cladding Temperature Comparison  
(Time = 10 Seconds, PCT Time)**



**Figure 15.5.2.2-9 G-1 Blowdown Test 143 Axial Cladding Temperature Comparison  
(Time = 15 Seconds)**

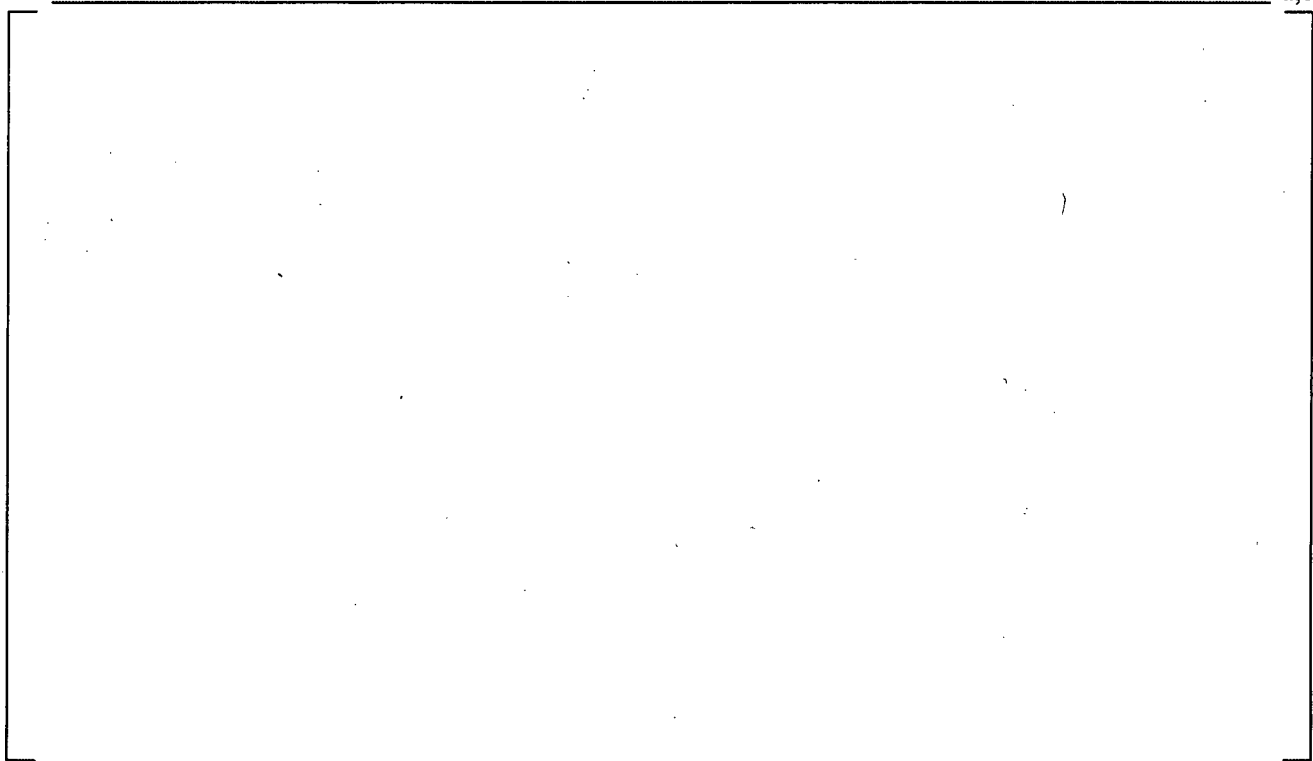


**Figure 15.5.2.2-10 G-1 Blowdown Test 143 Axial Cladding Temperature Comparison (Time = 20 Seconds)**

a,c

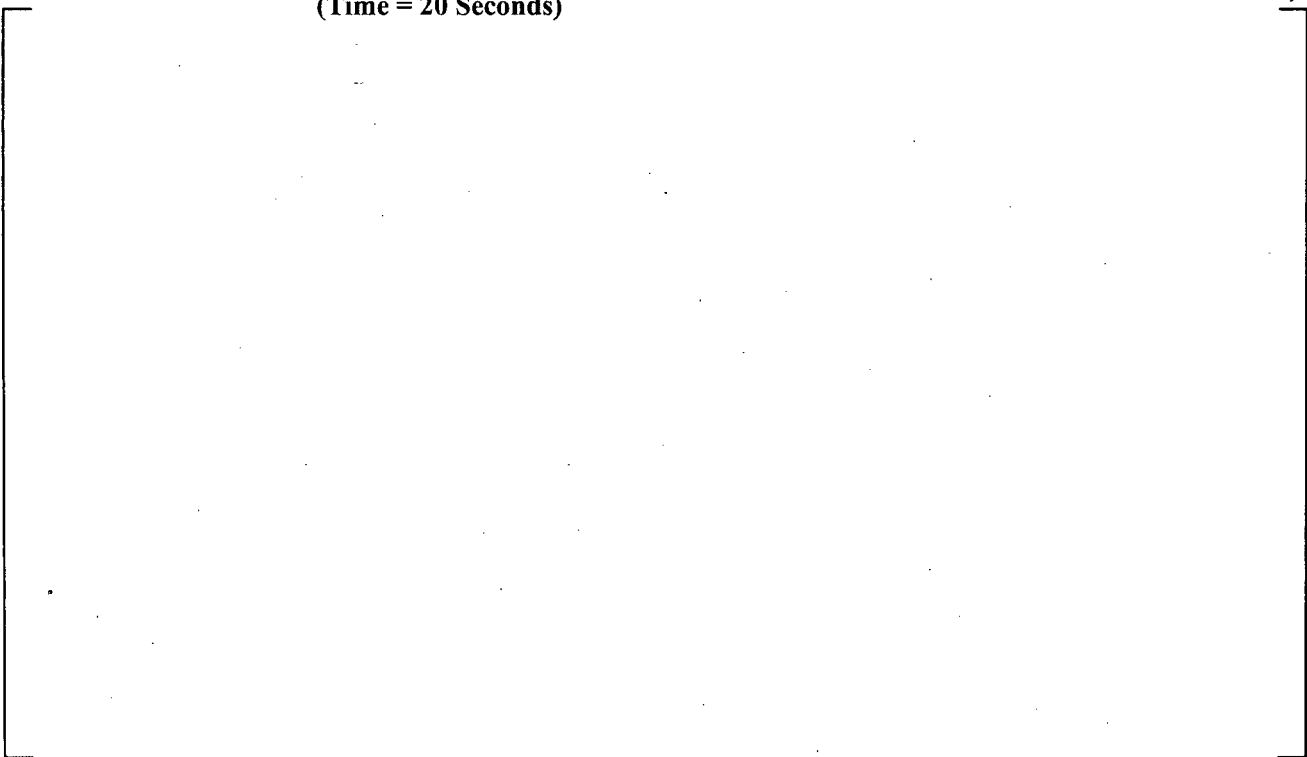


**Figure 15.5.2.2-11 G-1 Blowdown Test 143 Axial Cladding Temperature Comparison (Time = 30 Seconds)**

a,c



**Figure 15.5.2.2-12 G-1 Blowdown Test 148 Cladding Temperature Time History Comparison (24-inch Elevation)**

a,c



**Figure 15.5.2.2-13 G-1 Blowdown Test 148 Cladding Temperature Time History Comparison (48-inch Elevation)**

a,c



**Figure 15.5.2.2-14 G-1 Blowdown Test 148 Cladding Temperature Time History Comparison (72-inch Elevation)**

a,c



**Figure 15.5.2.2-15 G-1 Blowdown Test 148 Cladding Temperature Time History Comparison (96-inch Elevation)**

a,c



**Figure 15.5.2.2-16 G-1 Blowdown Test 148 Cladding Temperature Time History Comparison (120-inch Elevation)**

a,c



**Figure 15.5.2.2-17 G-1 Blowdown Test 148 Axial Cladding Temperature Comparison (Time = 6 Seconds)**



**Figure 15.5.2.2-18 G-1 Blowdown Test 148 Axial Cladding Temperature Comparison (Time = 10 Seconds, PCT Time)**

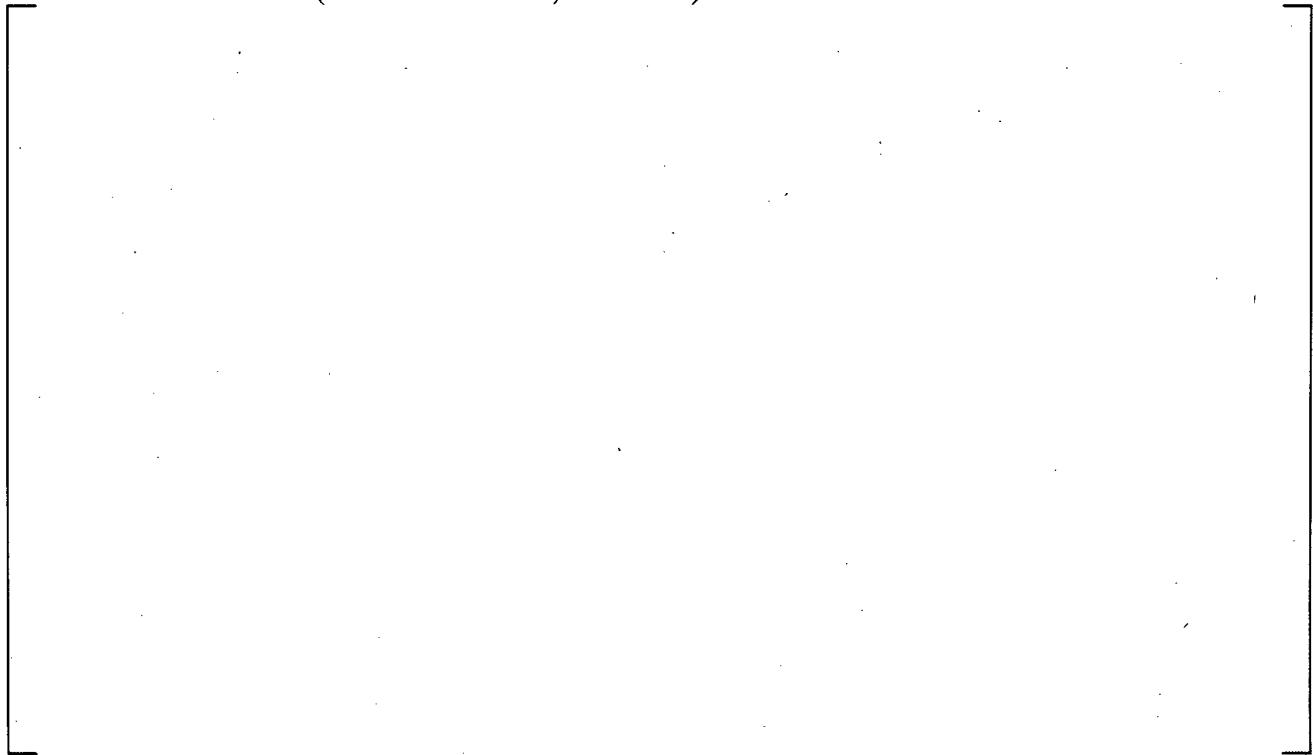


**Figure 15.5.2.2-19 G-1 Blowdown Test 148 Axial Cladding Temperature Comparison (Time = 15 Seconds)**

a,c

**Figure 15.5.2.2-20 G-1 Blowdown Test 148 Axial Cladding Temperature Comparison  
(Time = 20 Seconds)**

a,c

**Figure 15.5.2.2-21 G-1 Blowdown Test 148 Axial Cladding Temperature Comparison  
(Time = 30 Seconds)**

a,c

**Figure 15.5.2.2-22 G-1 Blowdown Test 152 Cladding Temperature Time History Comparison (24-inch Elevation)**

a,c

**Figure 15.5.2.2-23 G-1 Blowdown Test 152 Cladding Temperature Time History Comparison (48-inch Elevation)**

a,c



**Figure 15.5.2.2-24 G-1 Blowdown Test 152 Cladding Temperature Time History Comparison (72-inch Elevation)**

a,c



**Figure 15.5.2.2-25 G-1 Blowdown Test 152 Cladding Temperature Time History Comparison (96-inch Elevation)**

a,c

**Figure 15.5.2.2-26 G-1 Blowdown Test 152 Cladding Temperature Time History Comparison (120-inch Elevation)**

a,c

**Figure 15.5.2.2-27 G-1 Blowdown Test 152 Axial Cladding Temperature Comparison (Time = 6 Seconds)**

a,c



**Figure 15.5.2.2-28 G-1 Blowdown Test 152 Axial Cladding Temperature Comparison  
(Time = 10 Seconds, PCT Time)**

a,c

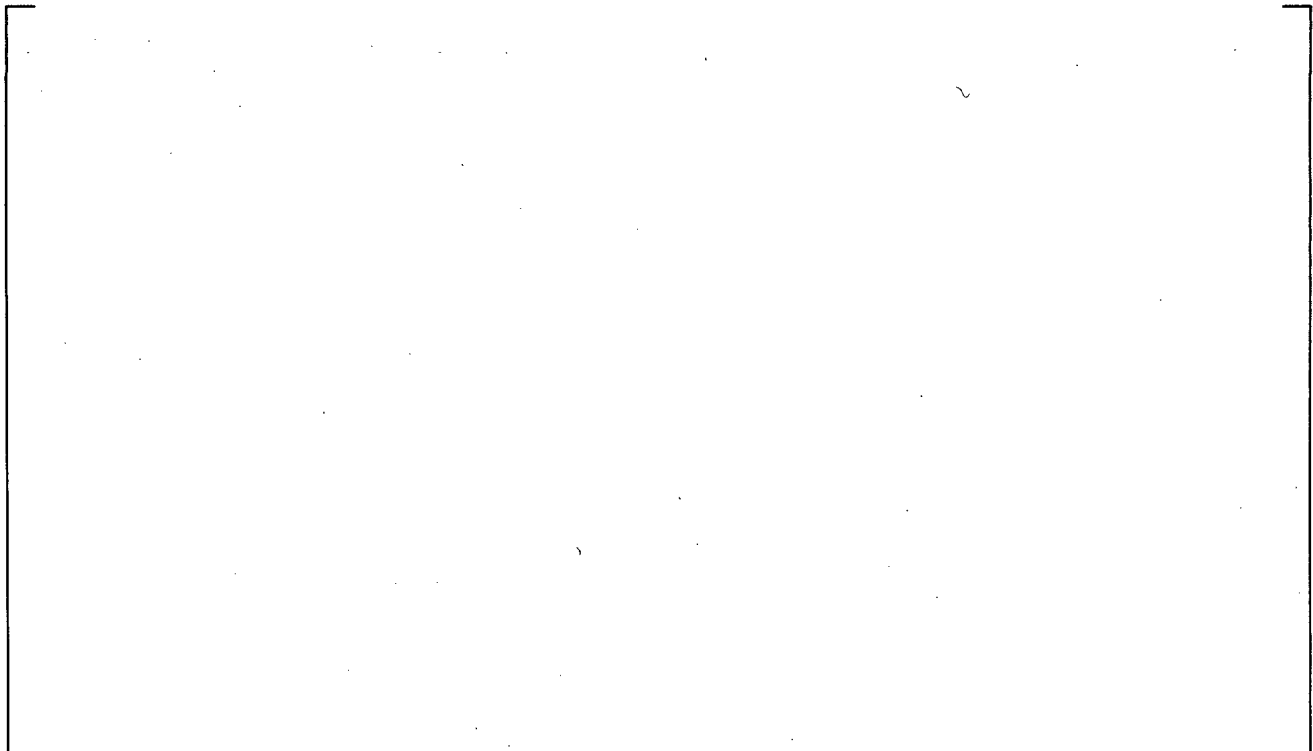


**Figure 15.5.2.2-29 G-1 Blowdown Test 152 Axial Cladding Temperature Comparison  
(Time = 15 Seconds)**

a,c



**Figure 15.5.2.2-30 G-1 Blowdown Test 152 Axial Cladding Temperature Comparison  
(Time = 20 Seconds)**

a,c



**Figure 15.5.2.2-31 G-1 Blowdown Test 152 Axial Cladding Temperature Comparison  
(Time = 30 Seconds)**

a,c



**Figure 15.5.2.2-32 G-1 Blowdown Test 146 Cladding Temperature Time History Comparison (24-inch Elevation)**

a,c



**Figure 15.5.2.2-33 G-1 Blowdown Test 146 Cladding Temperature Time History Comparison (48-inch Elevation)**

a,c

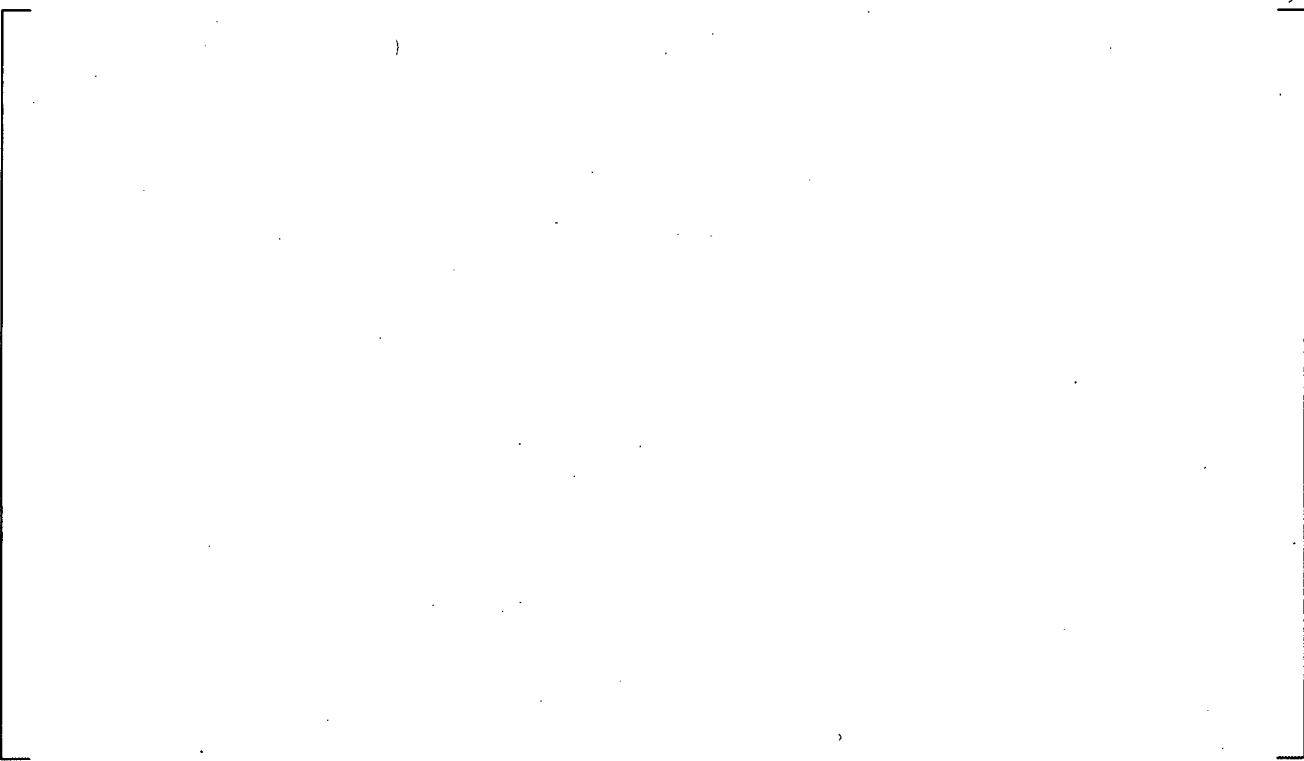


**Figure 15.5.2.2-34 G-1 Blowdown Test 146 Cladding Temperature Time History Comparison (72-inch Elevation)**

a,c



**Figure 15.5.2.2-35 Blowdown Test 146 Cladding Temperature Time History Comparison (96-inch Elevation)**

a,c

**Figure 15.5.2.2-36 G-1 Blowdown Test 146 Cladding Temperature Time History Comparison (120-inch Elevation)**

a,c

**Figure 15.5.2.2-37 G-1 Blowdown Test 146 Axial Cladding Temperature Comparison (Time = 6 Seconds)**

a,c



**Figure 15.5.2.2-38 G-1 Blowdown Test 146 Axial Cladding Temperature Comparison (Time = 10 Seconds, PCT Time)**

a,c



**Figure 15.5.2.2-39 G-1 Blowdown Test 146 Axial Cladding Temperature Comparison (Time = 15 Seconds)**

a,c

**Figure 15.5.2.2-40 G-1 Blowdown Test 146 Axial Cladding Temperature Comparison  
(Time = 20 Seconds)**

a,c

**Figure 15.5.2.2-41 G-1 Blowdown Test 146 Axial Cladding Temperature Comparison  
(Time = 30 Seconds)**

a,c

**Figure 15.5.2.2-42 G-1 Blowdown Test 153 Cladding Temperature Time History Comparison (24-inch Elevation)**

a,c

**Figure 15.5.2.2-43 G-1 Blowdown Test 153 Cladding Temperature Time History Comparison (48-inch Elevation)**

a,c



**Figure 15.5.2.2-44 G-1 Blowdown Test 153 Cladding Temperature Time History Comparison (72-inch Elevation)**

a,c



**Figure 15.5.2.2-45 G-1 Blowdown Test 153 Cladding Temperature Time History Comparison (96-inch Elevation)**

a,c



**Figure 15.5.2.2-46 G-1 Blowdown Test 153 Cladding Temperature Time History Comparison (120-inch Elevation)**

a,c



**Figure 15.5.2.2-47 G-1 Blowdown Test 153 Axial Cladding Temperature Comparison (Time = 6 Seconds)**

a,c

**Figure 15.5.2.2-48 G-1 Blowdown Test 153 Axial Cladding Temperature Comparison  
(Time = 10 Seconds, PCT Time)**

a,c

**Figure 15.5.2.2-49 G-1 Blowdown Test 153 Axial Cladding Temperature Comparison  
(Time = 15 Seconds)**

a,c



**Figure 15.5.2.2-50 G-1 Blowdown Test 153 Axial Cladding Temperature Comparison (Time = 20 Seconds)**

a,c

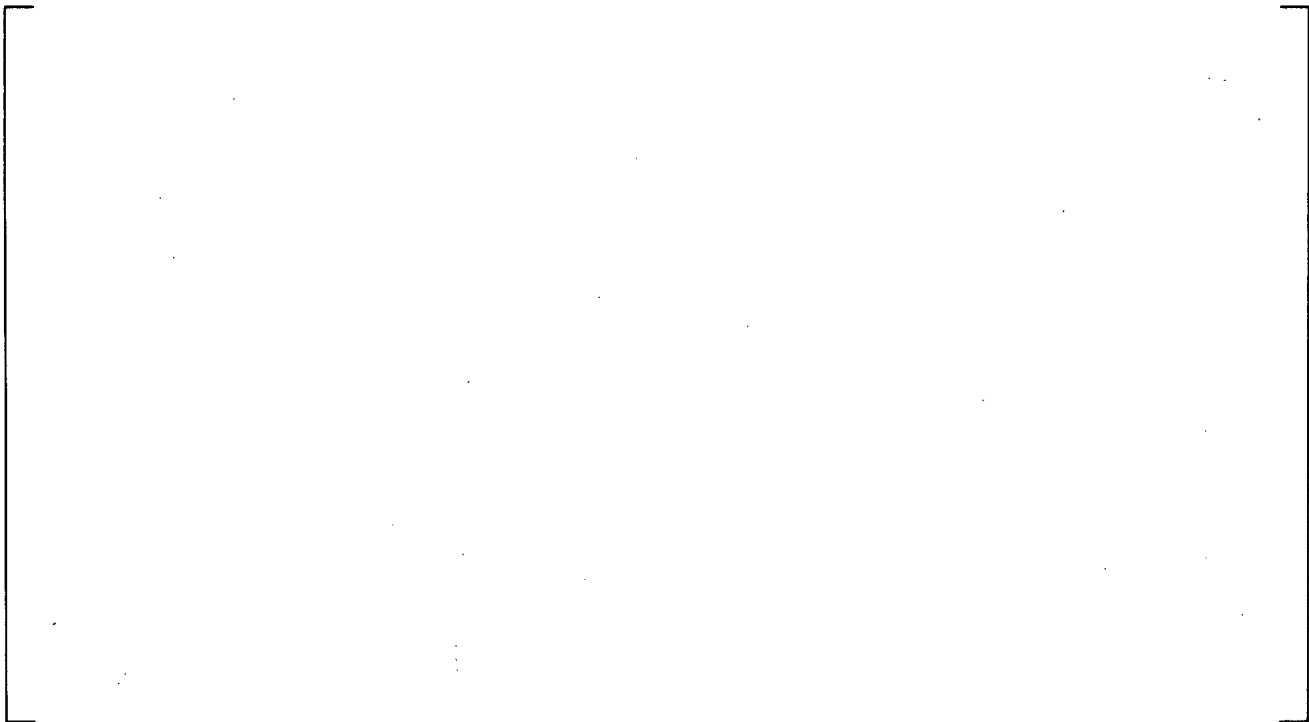


**Figure 15.5.2.2-51 G-1 Blowdown Test 153 Axial Cladding Temperature Comparison (Time = 30 Seconds)**

a,c



**Figure 15.5.2.2-52 G-1 Blowdown Test 154 Cladding Temperature Time History Comparison (24-inch Elevation)**

a,c



**Figure 15.5.2.2-53 G-1 Blowdown Test 154 Cladding Temperature Time History Comparison (48-inch Elevation)**

a,c



**Figure 15.5.2.2-54 G-1 Blowdown Test 154 Cladding Temperature Time History Comparison (72-inch Elevation)**

a,c



**Figure 15.5.2.2-55 G-1 Blowdown Test 154 Cladding Temperature Time History Comparison (96-inch Elevation)**

a,c



**Figure 15.5.2.2-56 G-1 Blowdown Test 154 Cladding Temperature Time History Comparison (120-inch Elevation)**

a,c



**Figure 15.5.2.2-57 G-1 Blowdown Test 154 Axial Cladding Temperature Comparison (Time = 6 Seconds)**

a,c

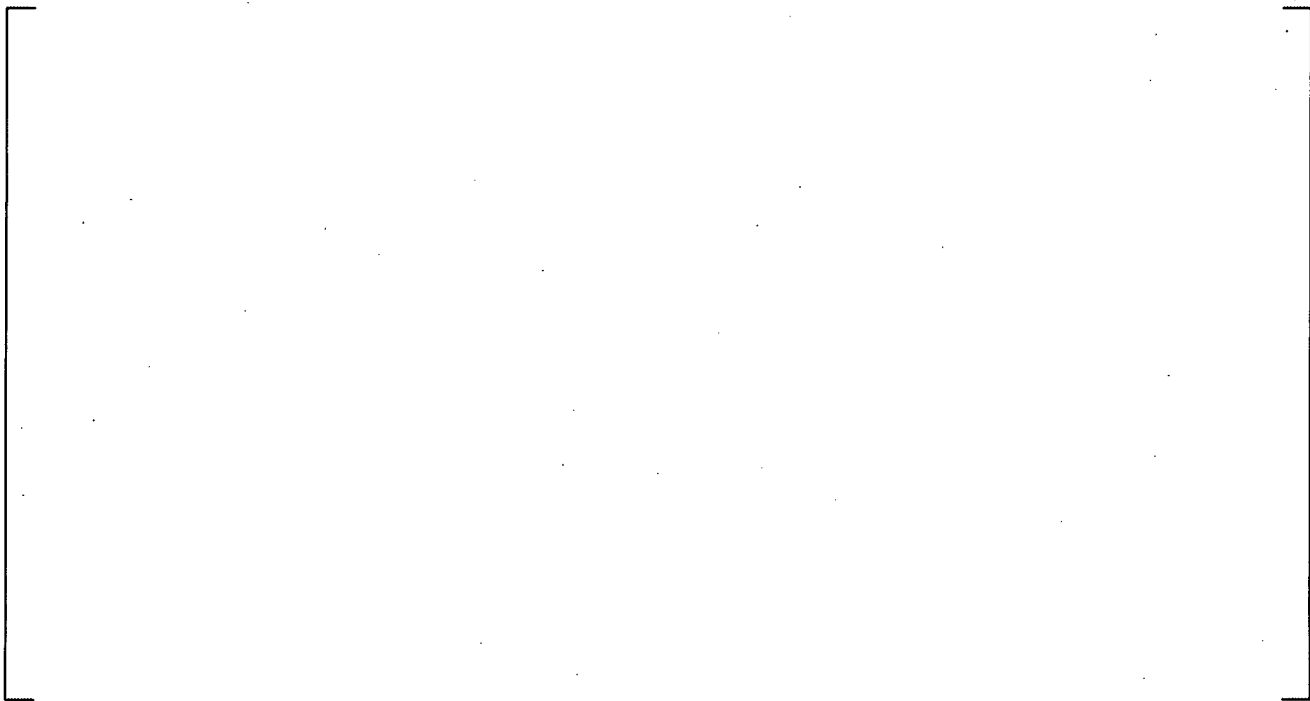


**Figure 15.5.2.2-58 G-1 Blowdown Test 154 Axial Cladding Temperature Comparison (Time = 10 Seconds, PCT Time)**

a,c

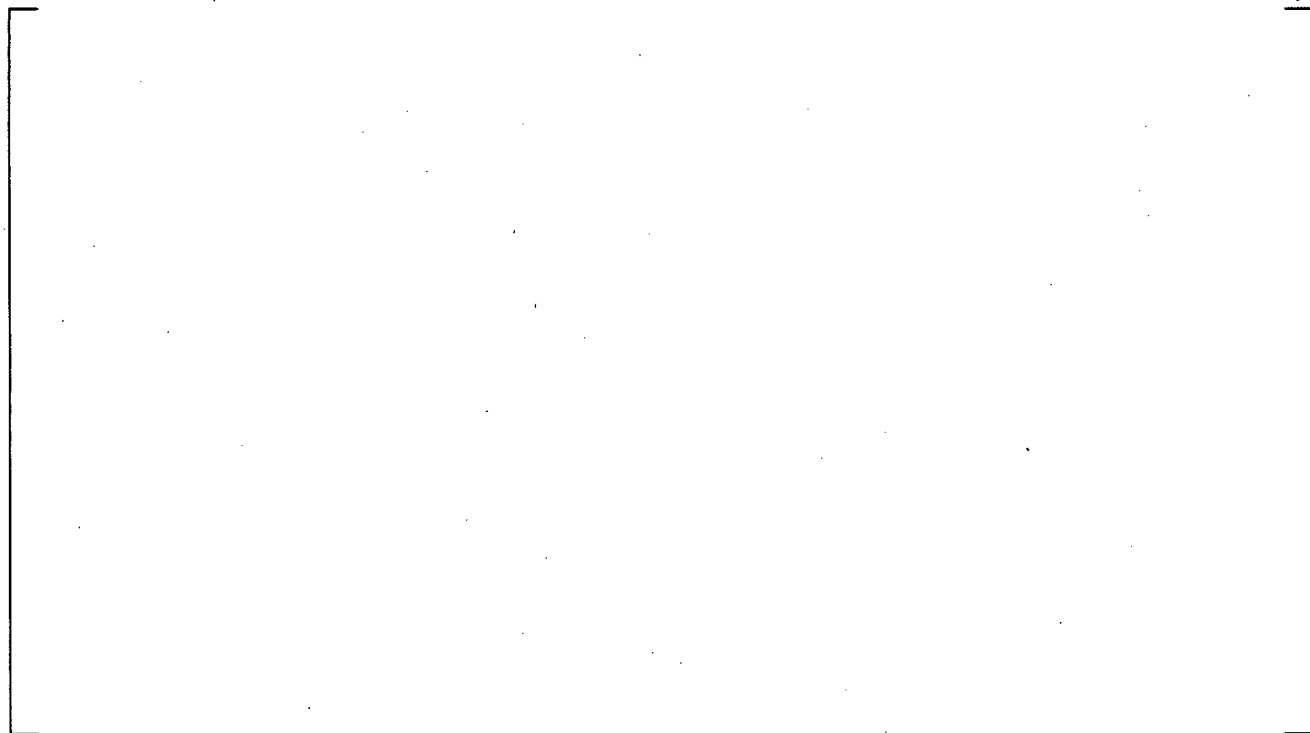


**Figure 15.5.2.2-59 G-1 Blowdown Test 154 Axial Cladding Temperature Comparison (Time = 15 Seconds)**



**Figure 15.5.2.2-60 G-1 Blowdown Test 154 Axial Cladding Temperature Comparison (Time = 20 Seconds)**



**Figure 15.5.2.2-61 G-1 Blowdown Test 154 Axial Cladding Temperature Comparison (Time = 30 Seconds)**

a,b,c

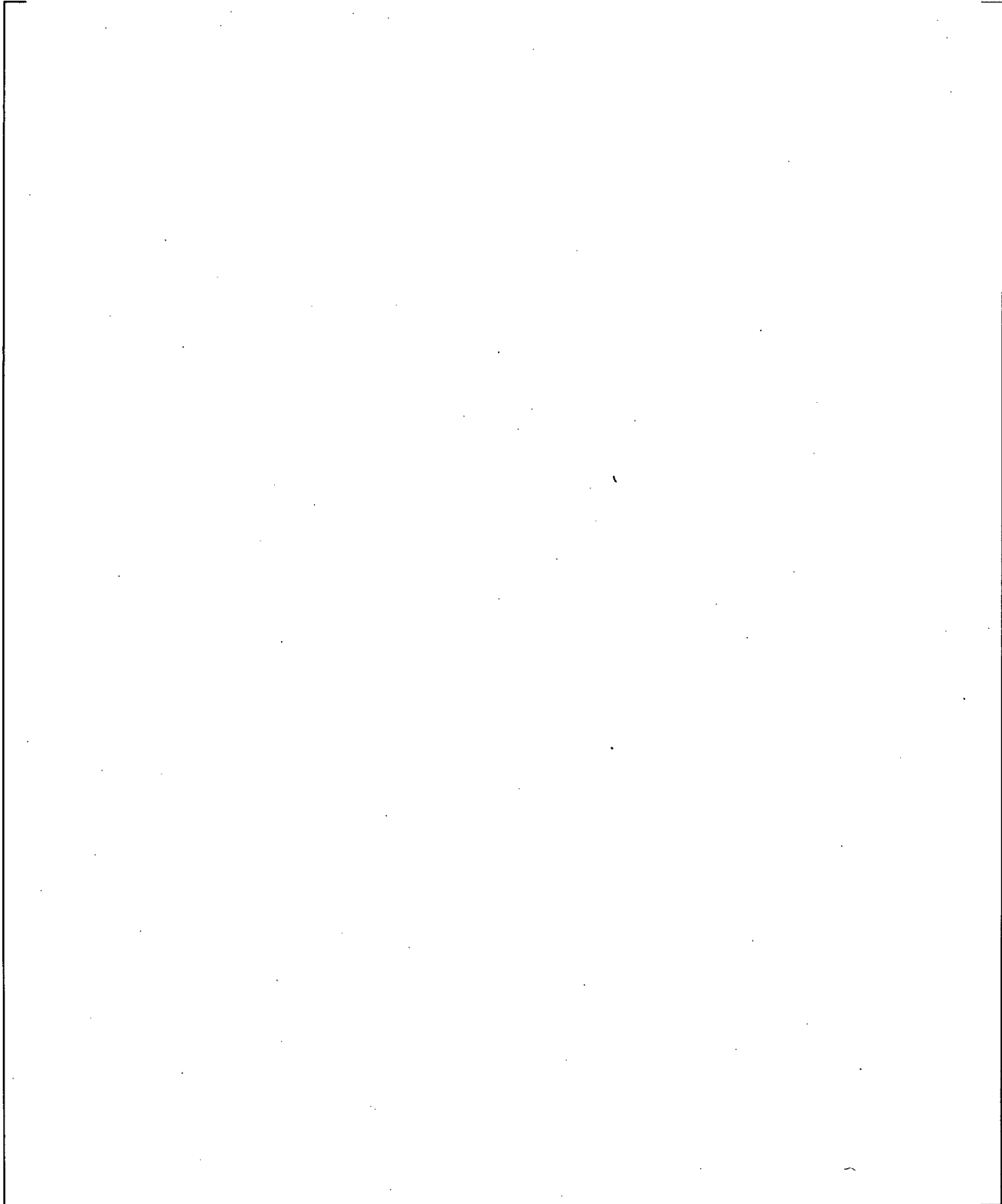


**Figure 15.5.2.2-62 Measured Thermocouple Data from (Cunningham, J. P., 1974)**

### 15.5.2.3 G-2 Refill Test Simulations

The WCOBRA/TRAC-TF2 model of the G-2 facility consisted of a vessel component, a pipe component, and a fill component. The vessel contained [ ]<sup>a,c</sup> in six channels. A schematic diagram of the model is shown in Figure 15.5.2.3-1.

Sections 1 and 2 of the vessel model the lower plenum of the vessel. Section 3 models the heated length of the test section with two channels: [

] <sup>a,c</sup>. The fluid nodes are thermally connected to rods simulating the heater rods. Loss coefficients are used to model the nine grids of the fuel assembly in the inner and outer portions of the rod bundle. Section 4 models the ground plate region, and Section 5 of the vessel models the upper plenum. UHI flow into the upper plenum is provided by a vessel boundary condition. The boundary condition specifies the enthalpy and mass flow rate of water into the top of the vessel. At the bottom of the vessel, a pressure and enthalpy boundary condition is used to model the pressure boundary condition imposed on the test section by the cold leg and downcomer. Table 14.2.2.3-2 provides the initial conditions for these tests and is included here.

a,c


#### 15.5.2.3.1 Test 743 Simulation

[

] <sup>a,c</sup>

#### 15.5.2.3.2 Test 750 Simulation

[

] <sup>a,c</sup>

[

] <sup>a,c</sup>

**15.5.2.3.3 Test 760 Simulation**

[

] <sup>a,c</sup>

**15.5.2.3.4 Test 761 Simulation**

[

] <sup>a,c</sup>

**15.5.2.3.5 Test 762 Simulation**

[

] <sup>a,c</sup>

**15.5.2.3.6 Test 767 Simulation**

[

] <sup>a,c</sup>

[

] <sup>a,c</sup>

### 15.5.2.3.7 Summary and Conclusions

The capability of WCOBRA/TRAC-TF2 to accurately predict film boiling and rewet phenomena in the simulation of G-2 refill tests can be evaluated by comparisons with data of axial temperature profiles, cladding temperature transient histories at specific elevations, and the maximum cladding temperatures for the entire fuel assembly. [

] <sup>a,c</sup>

Table 15.5.2.3-1 compares measured and predicted  $\Delta T_{CLAD_z}$  ( $= T_{CLAD_z}(t_{end}) - T_{CLAD_z}(0)$ ) at either 50 or 60 seconds (Data for some test is not available at 60 s) at several elevations Z. Table 15.5.2.3-2 compares measured and predicted  $\Delta PCT$  ( $= PCT(t_{end}) - PCT(0)$ ) at either 50 or 60 seconds (Data for some test is not available at 60 s). The average difference and standard deviations are also given in both tables.

[

] <sup>a,c</sup>

**Table 15.5.2.3-1 WCOBRA/TRAC-TF2 Cladding Temperature Comparison with the Means of the G-2 Refill Experimental Data**

a,c

**Table 15.5.2.3-1 WCOBRA/TRAC-TF2 Cladding Temperature Comparison with the Means of the G-2 (cont.) Refill Experimental Data**

a,c




a,c

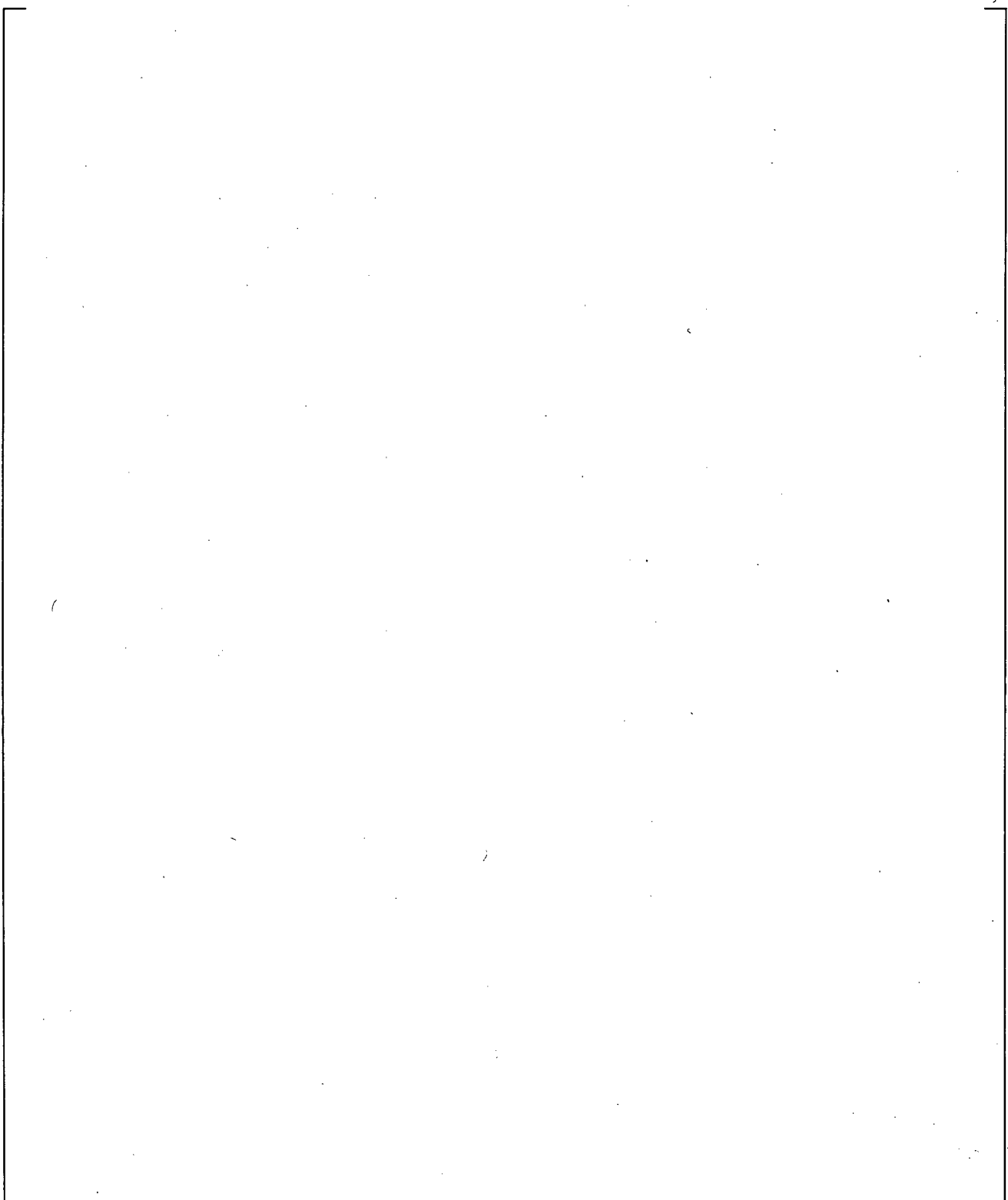


**Figure 15.5.2.3-1 WCOBRA/TRAC-TF2 Model for the G-2 Refill Test Simulations**

a,c



**Figure 15.5.2.3-2 G-2 Refill Test 743 Cladding Temperature Time History Comparison (12.3-inch Elevation)**

a,c



**Figure 15.5.2.3-3 G-2 Refill Test 743 Cladding Temperature Time History Comparison (28.7-inch Elevation)**



**Figure 15.5.2.3-4 G-2 Refill Test 743 Cladding Temperature Time History Comparison (45.1-inch Elevation)**



**Figure 15.5.2.3-5 G-2 Refill Test 743 Cladding Temperature Time History Comparison (82.0-inch Elevation)**



**Figure 15.5.2.3-6 G-2 Refill Test 743 Cladding Temperature Time History Comparison (118.9-inch Elevation)**



**Figure 15.5.2.3-7 G-2 Refill Test 743 Axial Cladding Temperature at 60 s**

a,c



**Figure 15.5.2.3-8 G-2 Refill Test 750 Cladding Temperature Time History Comparison (12.3-inch Elevation)**

a,c



**Figure 15.5.2.3-9 G-2 Refill Test 750 Cladding Temperature Time History Comparison (28.7-inch Elevation)**

a,c



**Figure 15.5.2.3-10 G-2 Refill Test 750 Cladding Temperature Time History Comparison (45.1-inch Elevation)**

a,c



**Figure 15.5.2.3-11 G-2 Refill Test 750 Cladding Temperature Time History Comparison (82.0-inch Elevation)**



**Figure 15.5.2.3-12 G-2 Refill Test 750 Cladding Temperature Time History Comparison (118.9-inch Elevation)**



**Figure 15.5.2.3-13 G-2 Refill Test 750 Axial Cladding Temperature at 60 s**

a,c



**Figure 15.5.2.3-14 G-2 Refill Test 760 Cladding Temperature Time History Comparison (12.3-inch Elevation)**

a,c



**Figure 15.5.2.3-15 G-2 Refill Test 760 Cladding Temperature Time History Comparison (28.7-inch Elevation)**

a,c



**Figure 15.5.2.3-16 G-2 Refill Test 760 Cladding Temperature Time History Comparison (45.1-inch Elevation)**

a,c



**Figure 15.5.2.3-17 G-2 Refill Test 760 Cladding Temperature Time History Comparison (82.0-inch Elevation)**

a,c

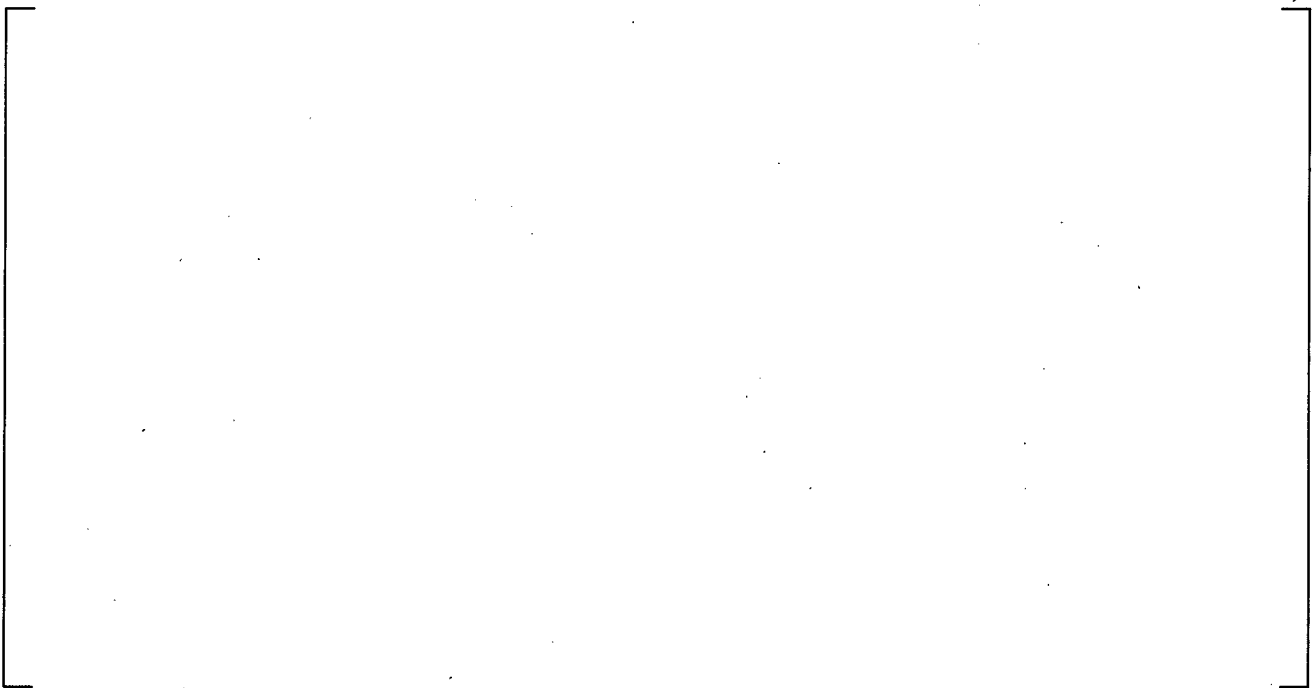


**Figure 15.5.2.3-18 G-2 Refill Test 760 Cladding Temperature Time History Comparison (118.9-inch Elevation)**

a,c



**Figure 15.5.2.3-19 G-2 Refill Test 760 Axial Cladding Temperature at 50 s**

a,c



**Figure 15.5.2.3-20 G-2 Refill Test 761 Cladding Temperature Time History Comparison (12.3-inch Elevation)**

a,c



**Figure 15.5.2.3-21 G-2 Refill Test 761 Cladding Temperature Time History Comparison (28.7-inch Elevation)**

a,c



**Figure 15.5.2.3-22 G-2 Refill Test 761 Cladding Temperature Time History Comparison (45.1-inch Elevation)**

a,c



**Figure 15.5.2.3-23 G-2 Refill Test 761 Cladding Temperature Time History Comparison (82.0-inch Elevation)**

a,c



**Figure 15.5.2.3-24 G-2 Refill Test 761 Cladding Temperature Time History Comparison (118.9-inch Elevation)**

a,c



**Figure 15.5.2.3-25 G-2 Refill Test 761 Axial Cladding Temperature at 50 s**

a,c



**Figure 15.5.2.3-26 G-2 Refill Test 762 Cladding Temperature Time History Comparison (12.3-inch Elevation)**

a,c



**Figure 15.5.2.3-27 G-2 Refill Test 762 Cladding Temperature Time History Comparison (28.7-inch Elevation)**

a,c



**Figure 15.5.2.3-28 G-2 Refill Test 762 Cladding Temperature Time History Comparison (45.1-inch Elevation)**

a,c



**Figure 15.5.2.3-29 G-2 Refill Test 762 Cladding Temperature Time History Comparison (82.0-inch Elevation)**

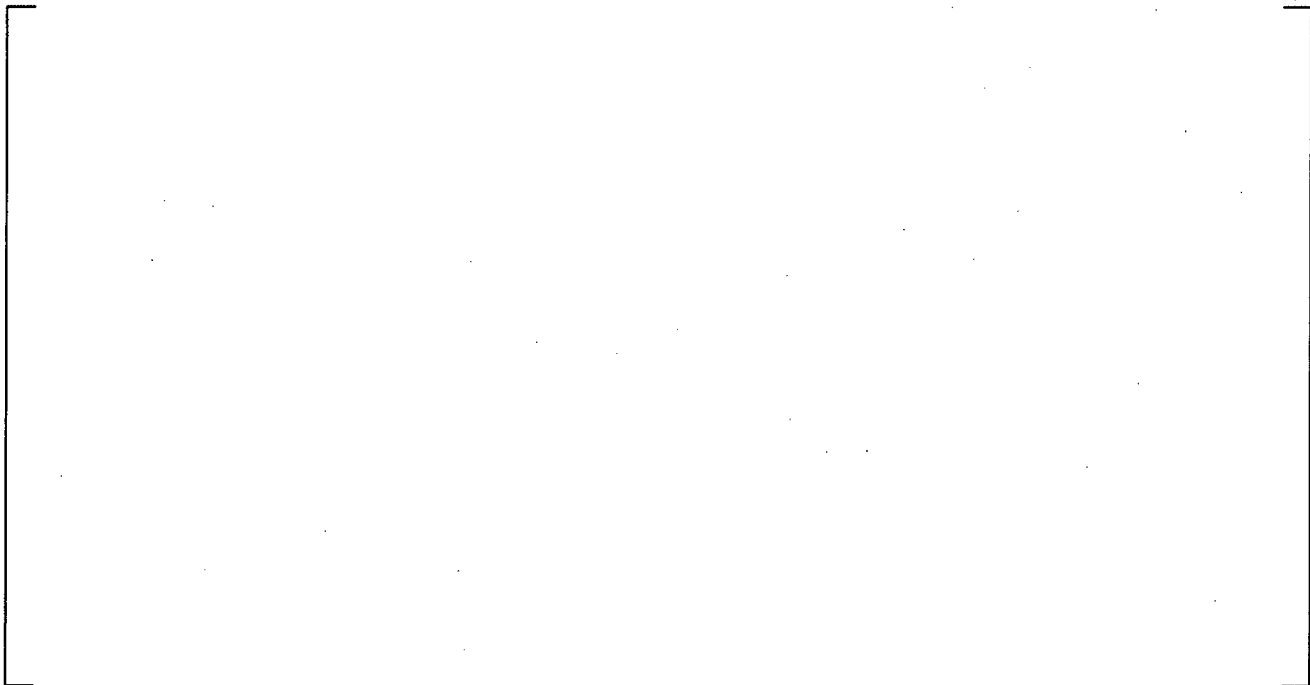


**Figure 15.5.2.3-30 G-2 Refill Test 762 Cladding Temperature Time History Comparison (118.9-inch Elevation)**



**Figure 15.5.2.3-31 G-2 Refill Test 762 Axial Cladding Temperature at 50 s**



**Figure 15.5.2.3-32 G-2 Refill Test 767 Cladding Temperature Time History Comparison (12.3-inch Elevation)**



**Figure 15.5.2.3-33 G-2 Refill Test 767 Cladding Temperature Time History Comparison (28.7-inch Elevation)**

a,c



**Figure 15.5.2.3-34 G-2 Refill Test 767 Cladding Temperature Time History Comparison (45.1-inch Elevation)**

a,c

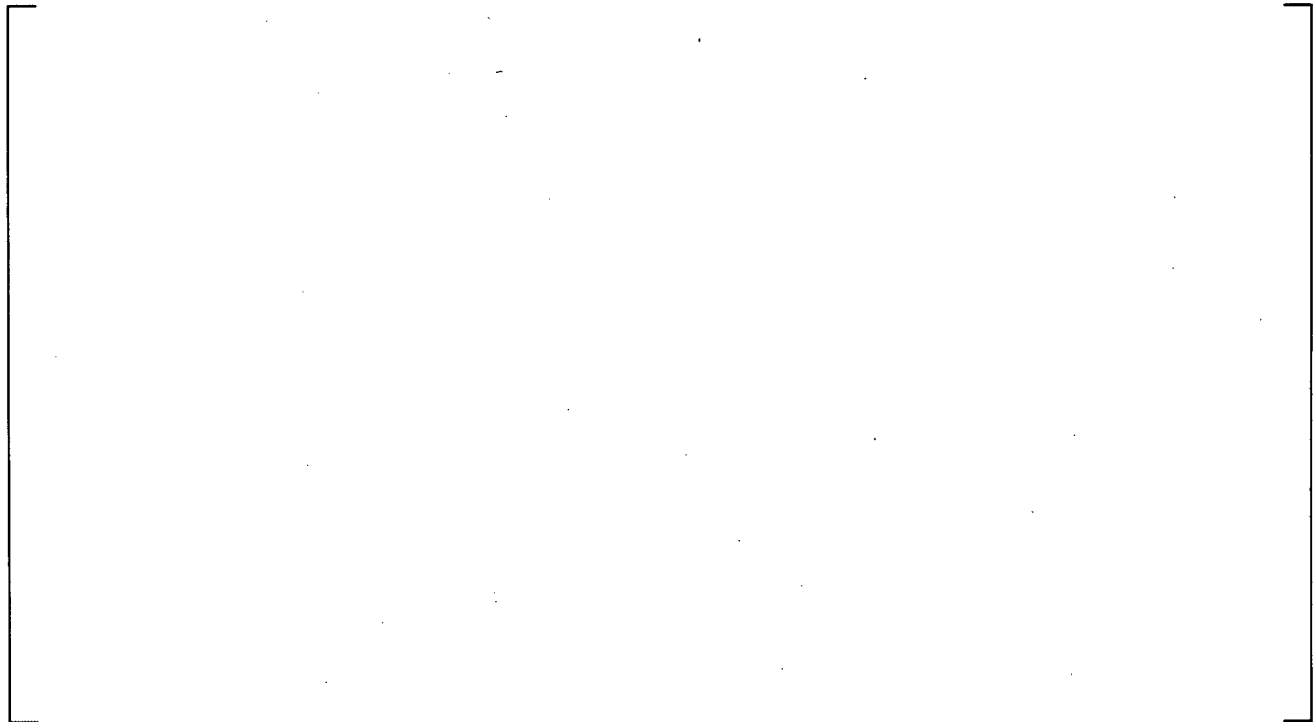


**Figure 15.5.2.3-35 G-2 Refill Test 767 Cladding Temperature Time History Comparison (82.0-inch Elevation)**

a,c



**Figure 15.5.2.3-36 G-2 Refill Test 767 Cladding Temperature Time History Comparison (118.9-inch Elevation)**

a,c



**Figure 15.5.2.3-37 G-2 Refill Test 767 Axial Cladding Temperature at 60 s**

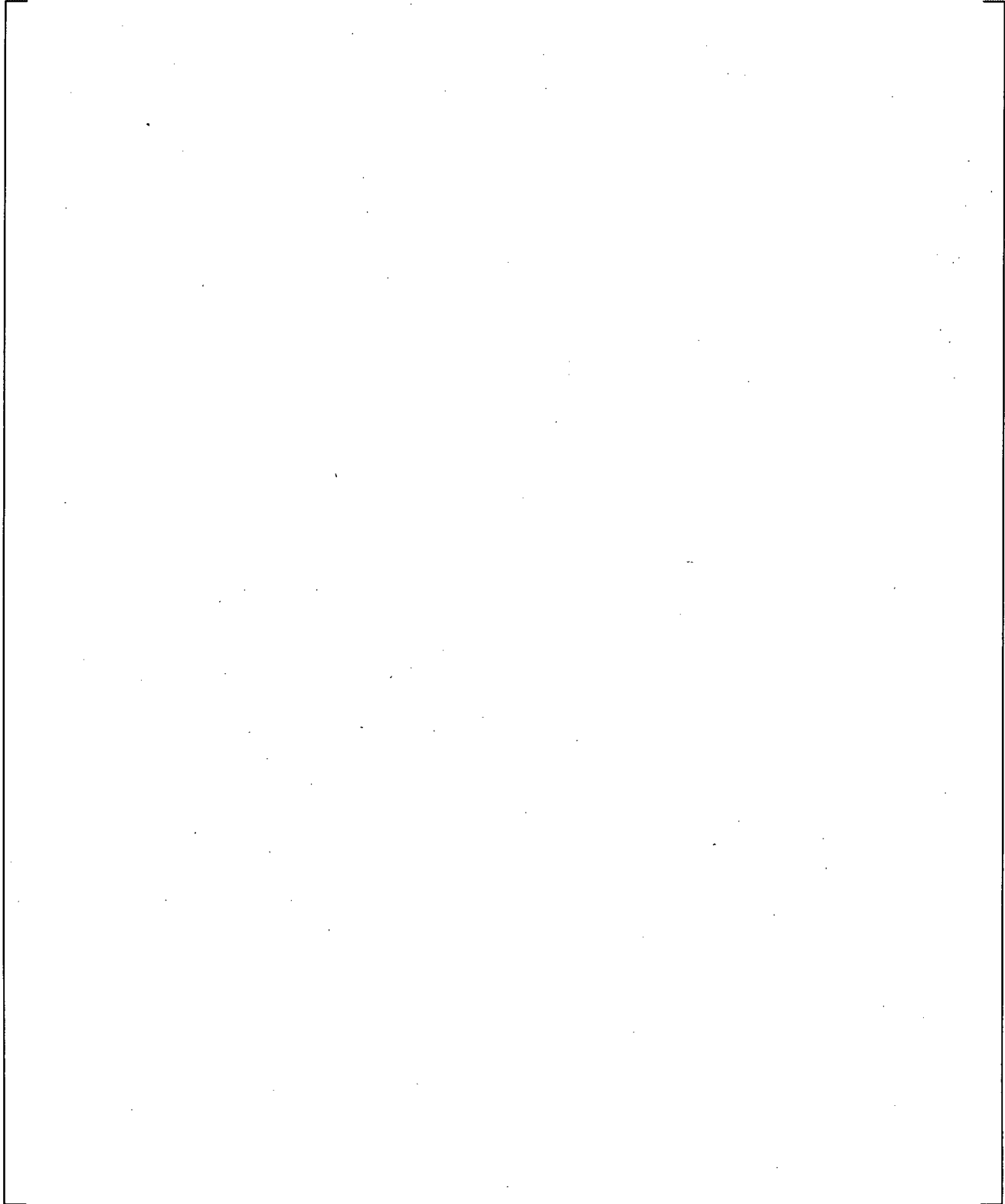


**Figure 15.5.2.3-38 Comparison of G-2 Refill Test Predicted vs. Measured Peak Cladding Temperature**

### 15.5.3 DFFB Heat Transfer Summary and Conclusions

WCOBRA/TRAC-TF2 simulations were performed for blowdown and refill DFFB heat transfer tests conducted in three different experimental programs using three different facilities. The heat transfer was assessed in two ways: 1) [

] <sup>a,c</sup>, as discussed in Section 15.5.1, and, 2) [

] <sup>a,c</sup>, as discussed in Section 15.5.2.

Using [

] <sup>a,c</sup>

Using [

] <sup>a,c</sup>

Six G-1 Blowdown test simulations were performed using WCOBRA/TRAC-TF2. In all six cases, the code [

] <sup>a,c</sup>.

Using WCOBRA/TRAC-TF2, simulations were performed for six G-2 Refill tests. In all six cases, the code [

] <sup>a,c</sup>.

It is concluded that WCOBRA/TRAC-TF2 [

] <sup>a,c</sup>.

Additional assessments for blowdown cooling rates, quench times and entrained droplets are performed in Section 15.9.

## 15.6 REFLOOD

### 15.6.1 WCOBRA/TRAC-TF2 Simulations of FLECHT-SEASET Test Series

The FLECHT-SEASET test assembly is modeled with three WCOBRA/TRAC-TF2 components. A vessel component is used to model the heated bundle, the upper plenum, and the top six inches of the lower plenum. Boundary conditions based on measured values were imposed on the top and the bottom of the VESSEL component. A PIPE component is attached at the top of the VESSEL, while a zero velocity FILL component is attached to the PIPE only to satisfy the WCOBRA/TRAC-TF2 requirement of at least one one-dimensional component.

The VESSEL component is composed of four channels. Two channels are used to model the test section, one for the inner region of the bundle and one for the outer region that includes the bundle housing. The transverse noding is shown in Figure 15.6.1-1. [

] <sup>a,c</sup> (The two rods that failed before testing were neglected.) These rods are each modeled with a single rod model having the dimensions of the actual heater rods. The heat flux from the rod to the fluid is multiplied by the

number of heater rods in the region represented by the channel to obtain the correct heat flux to the fluid. The test section housing is modeled with an unheated structure having a TUBE geometry, thermally connected to the outer channel on the inside surface and insulated on the outer surface. The WCOBRA/TRAC-TF2 vertical cell lengths for the vessel are shown in Figure 15.6.1-2.

The WCOBRA/TRAC-TF2 heater rods are initialized with axial temperature profiles determined by measured temperatures at the start of reflood for each individual test. The initial temperatures for all axial levels were computed by averaging the thermocouple temperatures within a radial boundary at a given elevation. Two heater rods were inoperative during the entire transient, therefore the rod temperatures in the immediate vicinity of the unpowered rods were eliminated from the initial temperature averaging. The housing is initialized with an axial temperature profile determined from thermocouples that were attached to the facility housing.

Both of the WCOBRA/TRAC-TF2 rods used the axial power profile shown in Figure 15.6.1-3. The housing had zero power generation.

The reflood transient was simulated using measured values of the injected flow as a boundary condition imposed on the bottom of the VESSEL component. A constant pressure and enthalpy boundary condition is imposed on the top node of the VESSEL. During the experiment, the heater rod power was decreased according to the ANS 1971 + 20 percent power decay curve, assuming a bottom of core recovery time of 30 seconds. The bundle power measurements were used as input for the simulated rods. The simulation was continued until quench was predicted at all elevations.

Additional initial conditions are provided in Table 14.1-6 for each test and are repeated here.

Test Series	Test Number	Pressure psia	Flooding Rate in/s	Inlet Subcooling °F	Peak Power kW/ft	Comment
FLECHT	31805	40	0.81	143	0.7	COSINE POWER
SEASET	31203	40	1.51	141	0.7	SHAPE
	31701	40	6.1	140	0.7	17x17 ROD
	31504	40	0.97	144	0.7	ARRAY
	32013	60	1.04	143	0.7	

### 15.6.1.1 FLECHT-SEASET Results

#### 15.6.1.1.1 FLECHT-SEASET Test 31805

The reflood rate for Test 31805 was 0.81 in/sec. The test pressure was maintained at 40 psia and the injected coolant temperature was 124°F. The WCOBRA/TRAC-TF2 simulation of Test 31805 was run for the first 800 seconds of the experiment, by which time all heater rod elevations had quenched in both the prediction and the test. Figures 15.6.1-4 through 15.6.1-10 show the comparison of predicted and measured temperatures at elevations 24, 48, 72, 78, 84, 96, and 120 inches from the bottom of the heated length. The code prediction (the solid curve) is for simulated rod temperatures in the inner channel (rod no. 1 located in Channel 2 of Figure 15.6.1-2). The curves in these figures representing the data show individual thermocouples located within the boundary of the WCOBRA/TRAC-TF2 inner channel. Figure 15.6.1-11 shows the prediction of the quench front elevation compared to the quench elevations

deduced from temperature measurements. The code prediction shows [

] <sup>a,c</sup>

Comparisons of the axial temperature profiles are shown in Figure 15.6.1-12 at 100 seconds, and in Figure 15.6.1-13 at 200 seconds. [

] <sup>a,c</sup>

Figure 15.6.1-14 summarizes the comparisons of the maximum predicted cladding temperatures at elevations where thermocouples were located. The predicted and measured turn-around times for this test are compared in Figure 15.6.1-15. The code predicts [

] <sup>a,c</sup>

Figures 15.6.1-16 through 15.6.1-18 provide comparisons of the predicted and measured axial pressure differentials in the bundle, which shows the distribution of liquid in the bundle. Figure 15.6.1-16 shows a comparison of the pressure differentials in the lower half (0 to 72 inches) of the bundle. The WCOBRA/TRAC-TF2 prediction is [

] <sup>a,c</sup>

The FLECHT-SEASET facility included steam temperature probes located in the thimble tubes. Figures 15.6.1-19 through 15.6.1-23 show comparisons of the measured and predicted vapor temperatures at several locations in the bundle. Figure 15.6.1-19 shows a comparison low in the bundle, at the 48-inch elevation. Figure 15.6.1-20 shows the comparison near the bundle mid-height, just upstream of the peak temperature elevations, while Figure 15.6.1-21 shows the comparison just downstream of the peak temperatures. Figure 15.6.1-22 shows the comparison at the 120-inch elevation, and Figure 15.6.1-23 the comparison near the bundle exit. [

] <sup>a,c</sup>

#### 15.6.1.1.2 FLECHT-SEASET Test 31504

The reflood rate for Test 31504 was 0.97 in/sec. The test pressure was maintained at 40 psia and the injected coolant temperature was 123°F. The WCOBRA/TRAC-TF2 simulation of Test 31504 was run for the first 800 seconds of the experiment, by which time all heater rod elevations had reached their peak temperature and had started to decline. Figures 15.6.1-24 through 15.6.1-30 show the comparison of predicted and measured temperatures at elevations 24, 48, 72, 78, 84, 96, and 120 inches from the bottom of the heated length. The code prediction is for simulated rod temperatures in the inner channel (rod no. 1 located in Channel 2 of Figure 15.6.1-2). The curves in these figures that represent the data show the individual thermocouples located within the boundary of the WCOBRA/TRAC-TF2 inner channel. Figure 15.6.1-31 shows the prediction of the quench front elevation compared to the quench elevations deduced from temperature measurements. The code prediction shows [

] <sup>a,c</sup>

[

] <sup>a,c</sup>

Comparisons of the axial temperature profiles are shown in Figure 15.6.1-32 at 50 seconds, and in Figure 15.6.1-33 at 100 seconds. The predicted temperature profiles are [

] <sup>a,c</sup>.

Figure 15.6.1-34 summarizes the comparisons of the maximum predicted cladding temperatures at each elevation where thermocouples were located. For this test, the WCOBRA/TRAC-TF2 predictions of the maximum cladding temperatures are [ ] <sup>a,c</sup>. The predicted and measured turn-around times are compared in Figure 15.6.1-35. This figure shows that for this test, [

] <sup>a,c</sup>.

Figures 15.6.1-36 through 15.6.1-38 show comparisons of the predicted and measured axial pressure differentials in the bundle. Figure 15.6.1-36 shows a comparison of the pressure differentials in the lower half (0 to 72 inches) of the bundle. The WCOBRA/TRAC-TF2 prediction is [

] <sup>a,c</sup> The overall pressure differential comparison is shown in Figure 15.6.1-38.

The FLECHT-SEASET facility included steam temperature probes located in the thimble tubes. Figures 15.6.1-39 through 15.6.1-43 show comparisons of the measured and predicted vapor temperatures at several locations in the bundle. Figure 15.6.1-39 shows a comparison low in the bundle, at the 48-inch elevation. Figure 15.6.1-40 shows the comparison near the bundle mid-height, just upstream of the peak temperature elevations, while Figure 15.6.1-41 shows the comparison just downstream of the peak temperatures. Figure 15.6.1-42 shows the comparison at the 120-inch elevation, and Figure 15.6.1-43 the comparison near the bundle exit. [

] <sup>a,c</sup>

### 15.6.1.1.3 FLECHT-SEASET Test 32013

The reflood rate for Test 32013 was 1.04 in/sec. The test pressure was maintained at 60 psia and the injected coolant temperature was 150°F which is approximately 143°F of sub-cooling, similar to the other tests in this series. The WCOBRA/TRAC-TF2 simulation of Test 32013 was run for 800 seconds, by which time all heater rod elevations had reached their maximum temperature and had quenched.

Figures 15.6.1-44 through 15.6.1-50 show the comparison of predicted and measured temperatures at elevations 24, 48, 72, 78, 84, 96, and 120 inches from the bottom of the heated length. The code prediction is for simulated rod temperatures in the inner channel (rod no. 1 located in Channel 2 of Figure 15.6.1-2). The curves in these figures that represent the data show the individual thermocouples located within the boundary of the WCOBRA/TRAC-TF2 inner channel. Figure 15.6.1-51 shows the prediction of the quench front elevation compared to the quench elevations deduced from temperature measurements. [ ] <sup>a,c</sup>

[ ]<sup>a,c</sup>

Comparisons of the axial temperature profiles are shown in Figure 15.6.1-52 at 50 seconds, and in Figure 15.6.1-53 at 100 seconds. The predicted temperature profiles are shown to be [ ]<sup>a,c</sup>.

Figure 15.6.1-54 summarizes the comparisons of the maximum predicted peak cladding temperatures at each elevation where thermocouples were located. [ ]<sup>a,c</sup> The predicted and measured turn-around times are shown in Figure 15.6.1-55. For this test, [ ]<sup>a,c</sup>

Figures 15.6.1-56 through 15.6.1-58 show comparisons of the predicted and measured axial pressure differentials in the bundle. Figure 15.6.1-56 shows a comparison of the pressure differentials in the lower half (0 to 72 inches) of the bundle. [ ]<sup>a,c</sup>

[ ]<sup>a,c</sup> Figure 15.6.1-57 shows the comparison for the upper half (72 to 144 inches) of the bundle, with [ ]<sup>a,c</sup>. The overall pressure differential comparison is shown in Figure 15.6.1-58, and shows [ ]<sup>a,c</sup>.

The FLECHT-SEASET facility included steam temperature probes located in the thimble tubes. Figures 15.6.1-59 through 15.6.1-63 show comparisons of the measured and predicted vapor temperatures at several locations in the bundle. Figure 15.6.1-59 shows a comparison low in the bundle, at the 48-inch elevation. Figure 15.6.1-60 shows the comparison near the bundle mid-height, just upstream of the peak temperature elevations, while Figure 15.6.1-61 shows the comparison just downstream of the peak temperatures. Figure 15.6.1-62 shows the comparison at the 120-inch elevation, and Figure 15.6.1-63 the comparison near the bundle exit. Each elevation was found to [ ]<sup>a,c</sup>.

#### 15.6.1.1.4 FLECHT-SEASET Test 31203

The reflood rate for Test 31203 was 1.51 in/sec. The test pressure was maintained at 40 psia and the injected coolant temperature was 126°F (approximately 143°F of sub-cooling). The WCOBRA/TRAC-TF2 simulation of Test 31203 was run beyond the first 450 seconds of the experiment, by which time all heater rod elevations had reached their peak temperature and had quenched. Figures 15.6.1-64 through 15.6.1-70 show the comparison of predicted and measured temperatures at elevations 24, 48, 72, 78, 84, 96, and 120 inches from the bottom of the heated length. The code prediction is for simulated rod temperatures in the inner channel (rod no. 1 located in Channel 2 of Figure 15.6.1-2). The curves in these figures that represent the data show the individual thermocouples located within the boundary of the WCOBRA/TRAC-TF2 inner channel. Figure 15.6.1-71 shows the prediction of the quench front elevation compared to the quench elevations deduced from temperature measurements. [ ]<sup>a,c</sup>

[ ]<sup>a,c</sup>

Comparisons of the axial temperature profiles are shown in Figure 15.6.1-72 at 50 seconds, and in Figure 15.6.1-73 at 100 seconds. [ ]<sup>a,c</sup>

Figure 15.6.1-74 summarizes the comparisons of the maximum predicted peak cladding temperatures at each elevation where thermocouples were located. For this test, the predicted maximum temperatures [ ]<sup>a,c</sup>. The predicted and measured turn-around times are shown in Figure 15.6.1-75. The temperatures at most elevations are predicted to [ ]<sup>a,c</sup> the data.

Figures 15.6.1-76 through 15.6.1-78 show comparisons of the predicted and measured axial pressure differentials in the bundle. Figure 15.6.1-76 shows a comparison of the pressure differentials in the lower half (0 to 72 inches) of the bundle. [ ]<sup>a,c</sup>

] <sup>a,c</sup>

The FLECHT-SEASET facility included steam temperature probes located in the thimble tubes. Figures 15.6.1-79 through 15.6.1-83 show comparisons of the measured and predicted vapor temperatures at several locations in the bundle. Figure 15.6.1-79 shows a comparison low in the bundle, at the 48-inch elevation. Figure 15.6.1-80 shows the comparison near the bundle mid-height, just upstream of the peak temperature elevations, while Figure 15.6.1-81 shows the comparison just downstream of the peak temperatures. Figure 15.6.1-82 shows the comparison at the 120-inch elevation, and Figure 15.6.1-83 the comparison near the bundle exit. [ ]<sup>a,c</sup>

] <sup>a,c</sup>

#### 15.6.1.1.5 FLECHT-SEASET Test 31701

The reflood rate for Test 31701 was 6.1 in/sec. The test pressure was maintained at 40 psia and the injected coolant temperature was 127°F. The WCOBRA/TRAC-TF2 simulation of Test 31701 was run for the first 100 seconds of the experiment, by which time all heater rod elevations had reached their peak temperature and had quenched. Figures 15.6.1-84 through 15.6.1-90 show the comparison of predicted and measured temperatures at elevations 24, 48, 72, 78, 84, 96, and 120 inches from the bottom of the heated length. The code prediction is for simulated rod temperatures in the inner channel (rod no. 1 located in Channel 2 of Figure 15.6.1-2). The curves in these figures that represent the data show the individual thermocouples located within the boundary of the WCOBRA/TRAC-TF2 inner channel. Figure 15.6.1-91 shows the prediction of the quench front elevation compared to the quench elevations deduced from temperature measurements. [ ]<sup>a,c</sup>

] <sup>a,c</sup>

Comparisons of the axial temperature profiles are shown in Figure 15.6.1-92 at 10 seconds, and in Figure 15.6.1-93 at 30 seconds. The predicted temperature profiles are shown to [

] <sup>a,c</sup>

Figure 15.6.1-94 summarizes the comparisons of the maximum predicted peak cladding temperatures at each elevation where thermocouples were located. [

] <sup>a,c</sup> The predicted and measured turn-around times for this test are summarized in Figure 15.6.1-95 and shows [

] <sup>a,c</sup>.

Figures 15.6.1-96 through 15.6.1-98 show comparisons of the predicted and measured axial pressure differentials in the bundle. Figure 15.6.1-96 shows a comparison of the pressure differentials in the lower half (0 to 72 inches) of the bundle. Figure 15.6.1-97 shows the comparison for the upper half (72 to 144 inches) of the bundle, and the overall pressure differential comparison is shown in Figure 15.6.1-98.

[

] <sup>a,c</sup>

The FLECHT-SEASET facility included steam temperature probes located in the thimble tubes. Figures 15.6.1-99 through 15.6.1-103 show comparisons of the measured and predicted vapor temperatures at several locations in the bundle. Figure 15.6.1-99 shows a comparison low in the bundle, at the 48-inch elevation. Figure 15.6.1-100 shows the comparison near the bundle mid-height, just upstream of the peak temperature elevations, while Figure 15.6.1-101 shows the comparison just downstream of the peak temperatures. Figure 15.6.1-102 shows the comparison at the 120-inch elevation, and Figure 15.6.1-103 the comparison near the bundle exit. [

] <sup>a,c</sup>

### 15.6.1.2 FLECHT-SEASET Summary and Conclusions

The five FLECHT-SEASET tests simulated by WCOBRA/TRAC-TF2 cover a wide range of flooding rates. Test 31805 had a low flooding rate (0.81 in/sec) while Test 31701 had a very rapid flooding rate (6.1 inch/sec). Tests at 40 psia (31805, 31203, 31701, 31504) and 60 psia (32013) were simulated.

[

] <sup>a,c</sup>

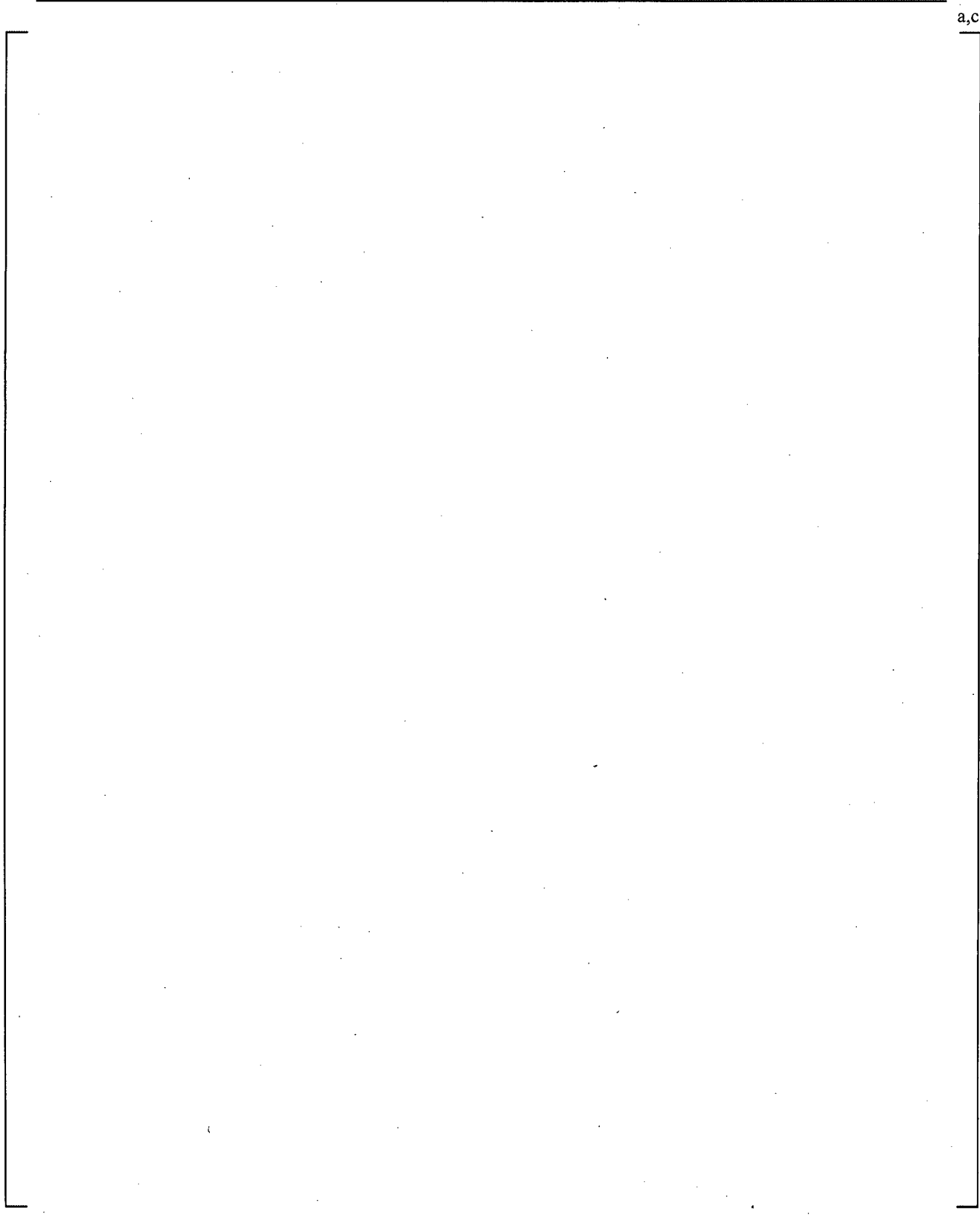


**Figure 15.6.1-1 WCOBRA/TRAC-TF2 Transverse Noding for FLECHT-SEASET**

a,c

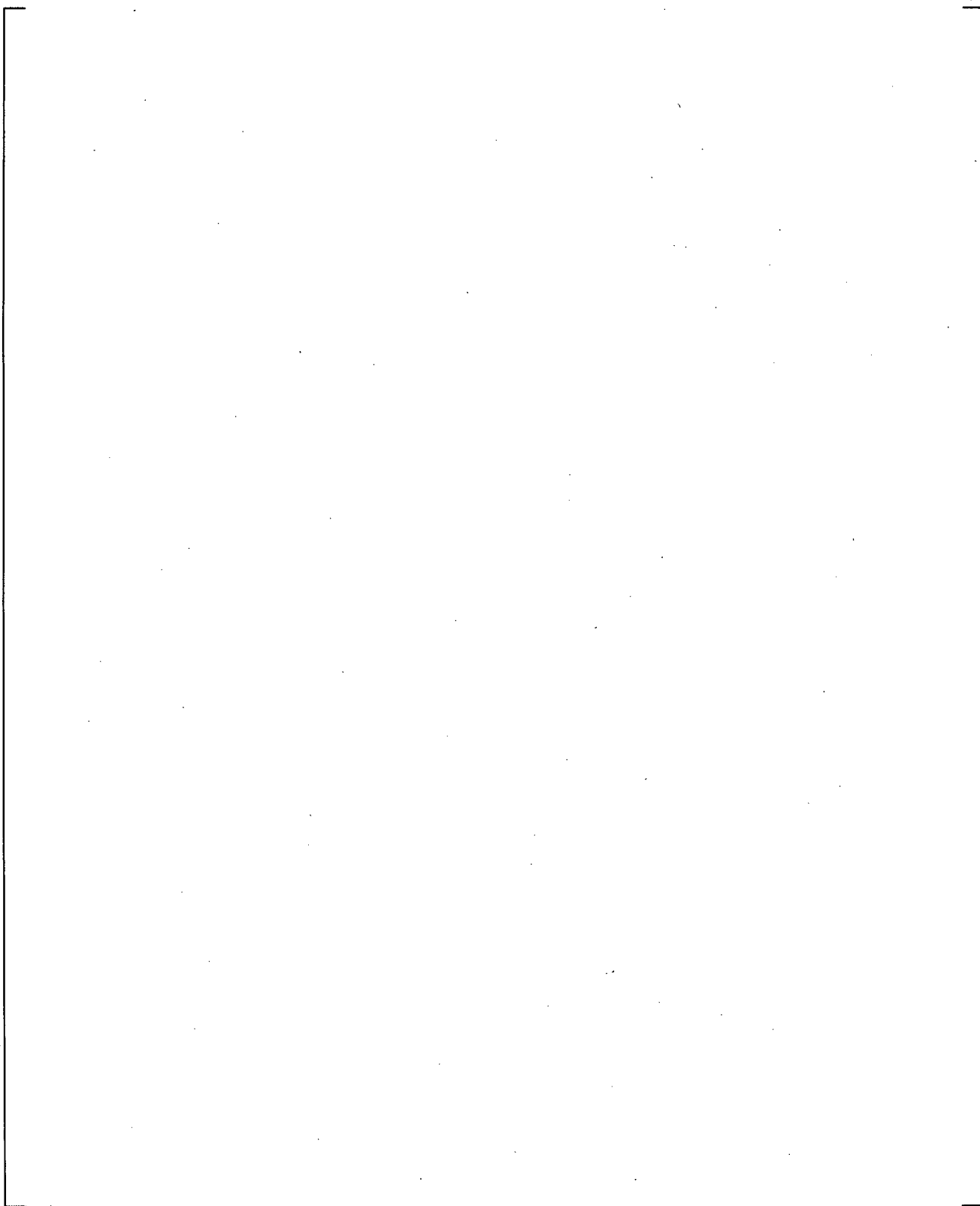
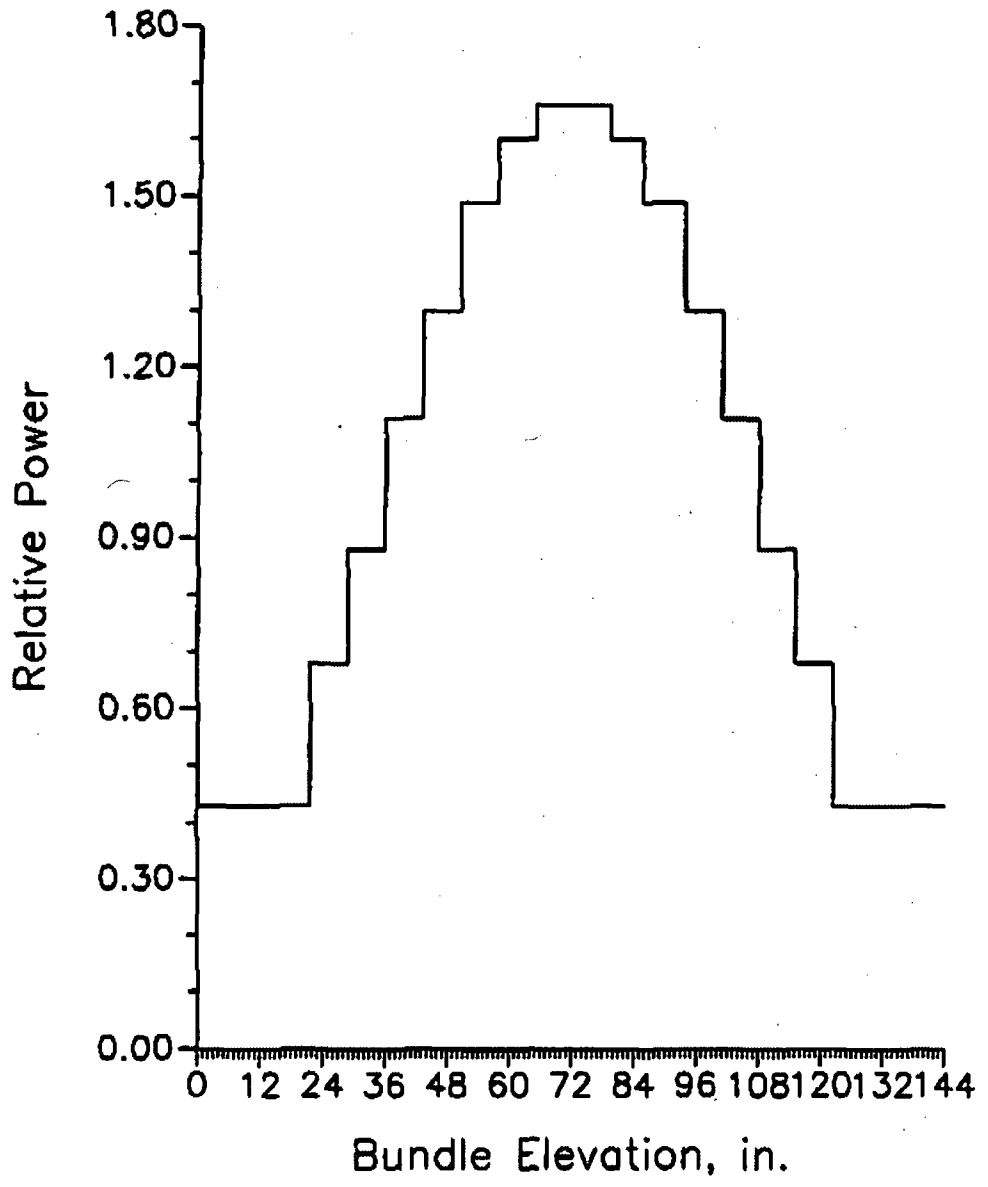


**Figure 15.6.1-2 WCOBRA/TRAC-TF2 Axial Noding for FLECHT-SEASET**

SPACER GRIDS:        G    G    G    G    G    G  
THERMOCOUPLES:    x   x    x   x    x   x   x   x   x   x   x   x   x   x



FLECHT-SEASET AXIAL POWER SHAPE,  
THERMOCOUPLE AND GRID LOCATIONS

Figure 15.6.1-3 FLECHT-SEASET Axial Power Shape Profile

a,c



**Figure 15.6.1-4 FLECHT-SEASET 31805 Rod Temperatures at 24-inch Elevation**

a,c



**Figure 15.6.1-5 FLECHT-SEASET 31805 Rod Temperatures at 48-inch Elevation**

a,c



**Figure 15.6.1-6 FLECHT-SEASET 31805 Rod Temperatures at 72-inch Elevation**

a,c

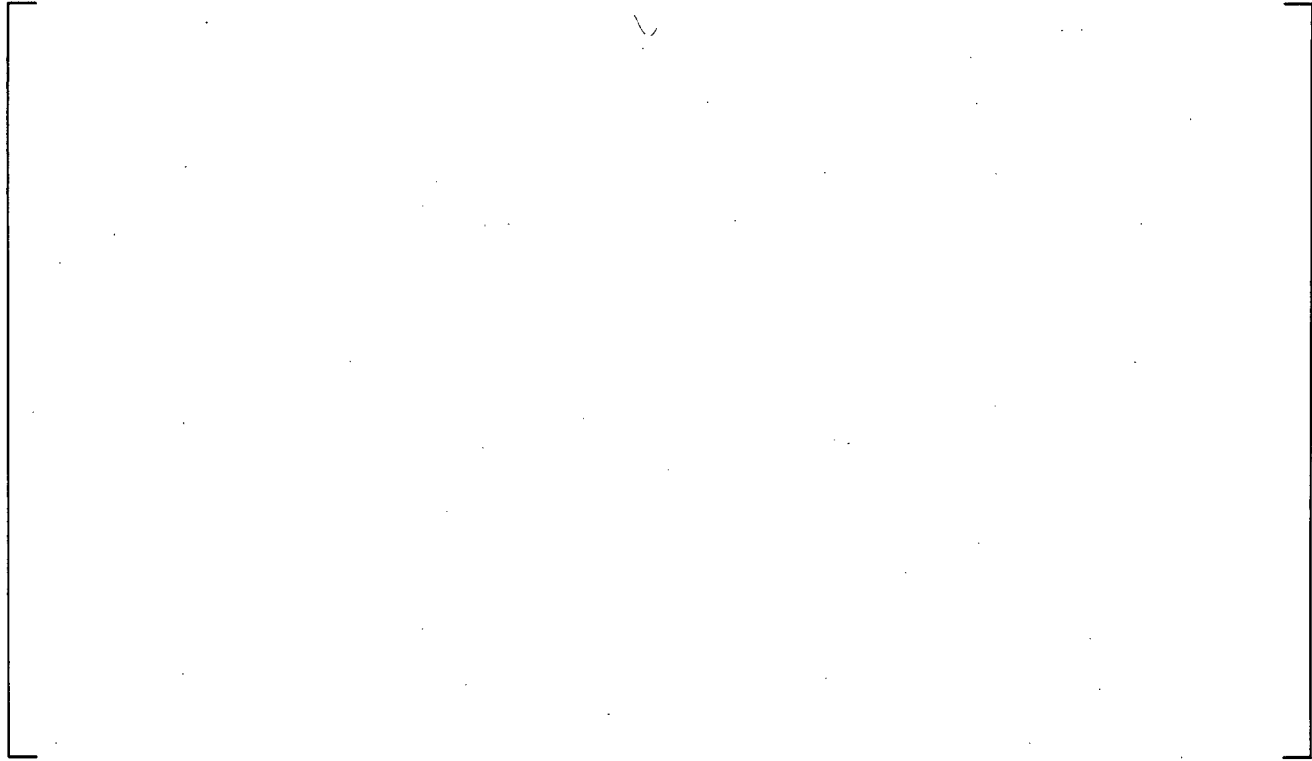


**Figure 15.6.1-7 FLECHT-SEASET 31805 Rod Temperatures at 78-inch Elevation**

a,c



**Figure 15.6.1-8 FLECHT-SEASET 31805 Rod Temperatures at 84-inch Elevation**

a,c

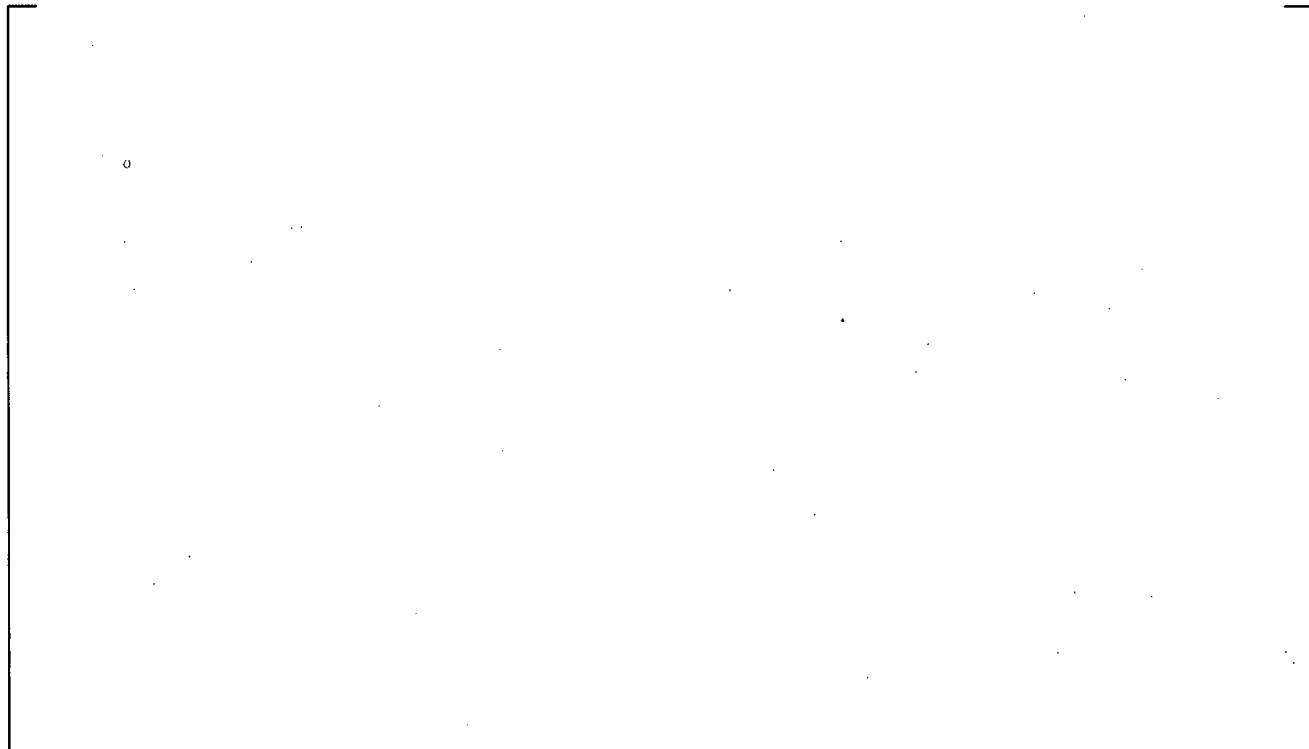


**Figure 15.6.1-9 FLECHT-SEASET 31805 Rod Temperatures at 96-inch Elevation**



**Figure 15.6.1-10 FLECHT-SEASET 31805 Rod Temperatures at 120-inch Elevation**



**Figure 15.6.1-11 Comparison of Predicted and Estimated Quench Front Elevations for FLECHT-SEASET 31805**

a,c



**Figure 15.6.1-12 Comparison of Predicted and Measured Axial Temperature Profile for FLECHT-SEASET 31805 at 100 Seconds**

a,c



**Figure 15.6.1-13 Comparison of Predicted and Measured Axial Temperature Profile for FLECHT-SEASET 31805 at 200 Seconds**

a,c



**Figure 15.6.1-14 Comparison of Predicted and Measured Maximum Cladding Temperatures at all Thermocouple Elevations for FLECHT-SEASET 31805**

a,c



**Figure 15.6.1-15 Comparison of Predicted and Measured Turn-Around Times for FLECHT-SEASET 31805**

a,c

**Figure 15.6.1-16 FLECHT-SEASET 31805 Bundle Lower Half  $\Delta P$**

a,c

**Figure 15.6.1-17 FLECHT-SEASET 31805 Bundle Upper Half  $\Delta P$**

a,c

**Figure 15.6.1-18 FLECHT-SEASET 31805 Overall  $\Delta P$**

a,c

**Figure 15.6.1-19 FLECHT-SEASET 31805 Vapor Temperatures at 48-inch Elevation**

**Figure 15.6.1-20 FLECHT-SEASET 31805 Vapor Temperatures near 72-inch Elevation**

**Figure 15.6.1-21 FLECHT-SEASET 31805 Vapor Temperatures near 90-inch Elevation**

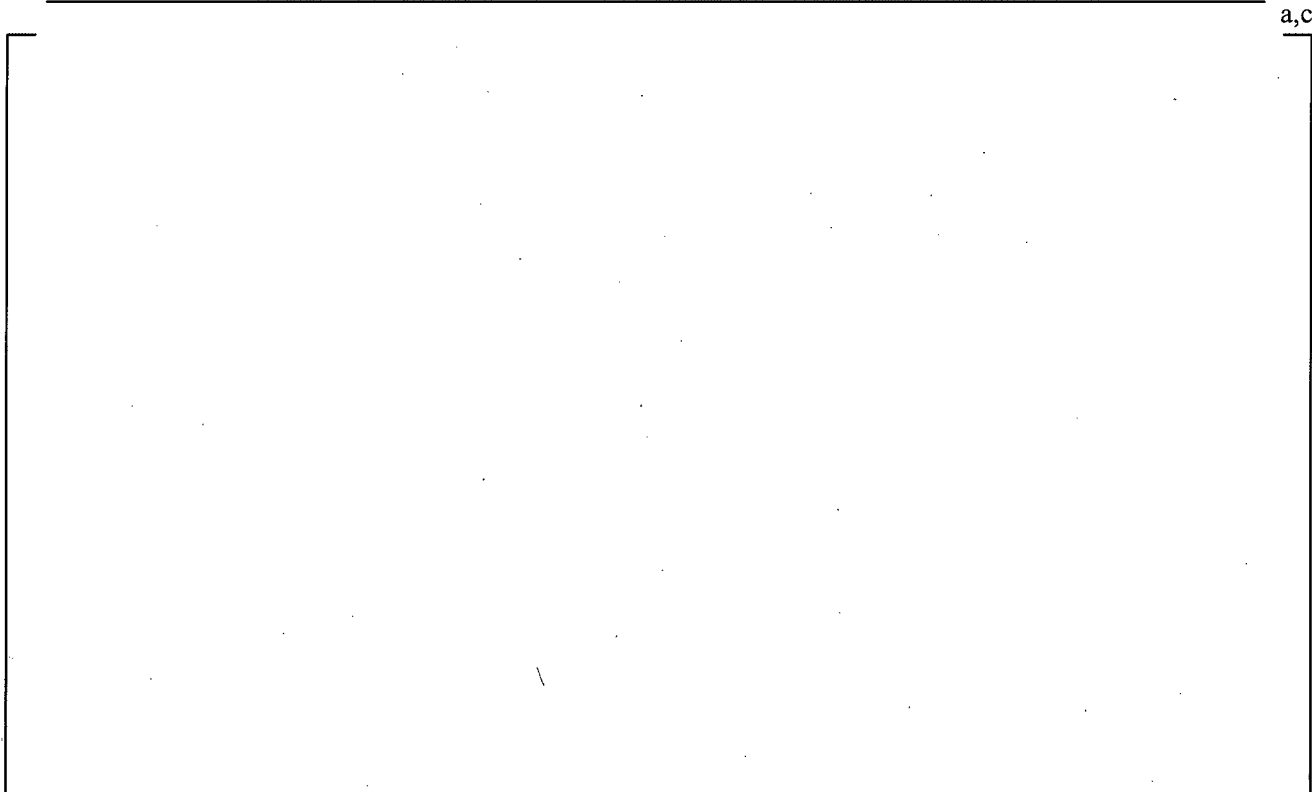


**Figure 15.6.1-22 FLECHT-SEASET 31805 Vapor Temperatures near 120-inch Elevation**



**Figure 15.6.1-23 FLECHT-SEASET 31805 Vapor Temperatures near 138-inch Elevation**

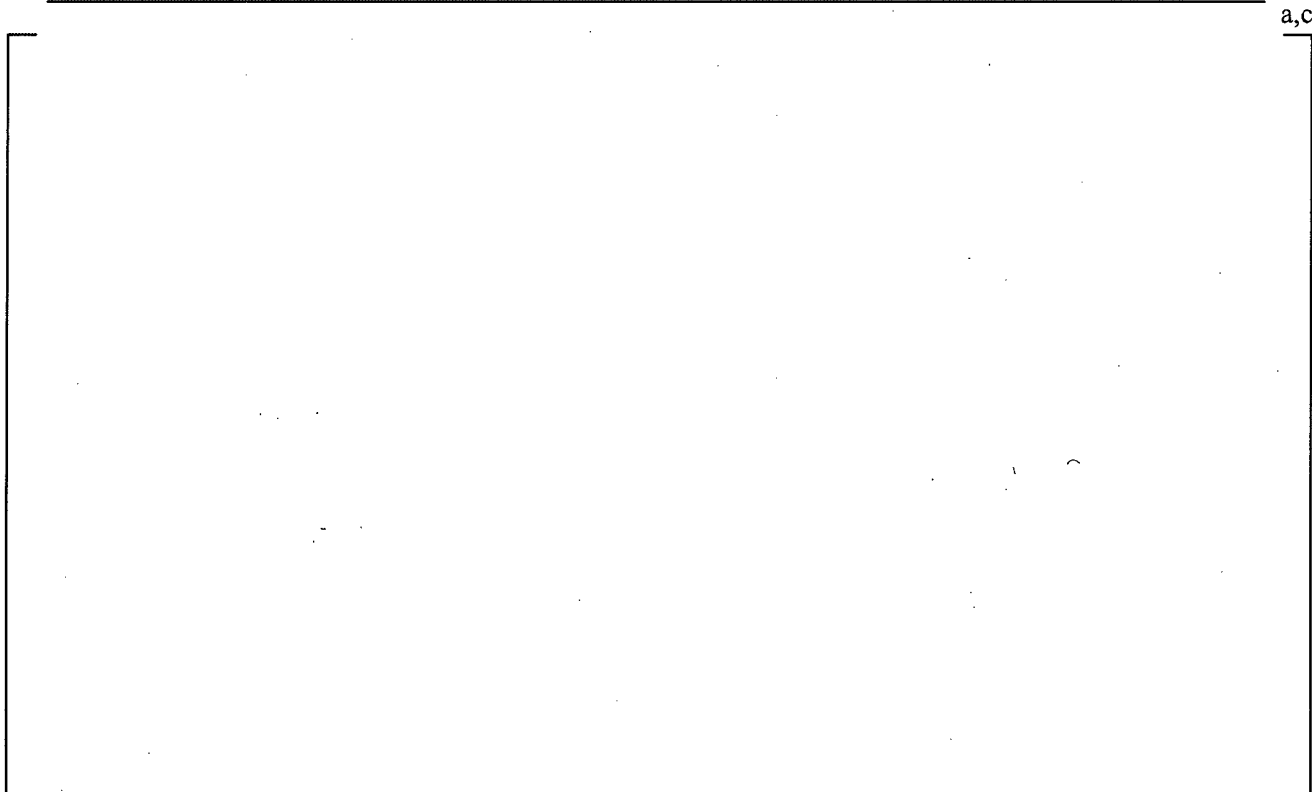


**Figure 15.6.1-24 FLECHT-SEASET 31504 Rod Temperatures at 24-inch Elevation**



**Figure 15.6.1-25 FLECHT-SEASET 31504 Rod Temperatures at 48-inch Elevation**

a,c

**Figure 15.6.1-26 FLECHT-SEASET 31504 Rod Temperatures at 72-inch Elevation**

a,c

**Figure 15.6.1-27 FLECHT-SEASET 31504 Rod Temperatures at 78-inch Elevation**

a,c



**Figure 15.6.1-28 FLECHT-SEASET 31504 Rod Temperatures at 84-inch Elevation**

a,c

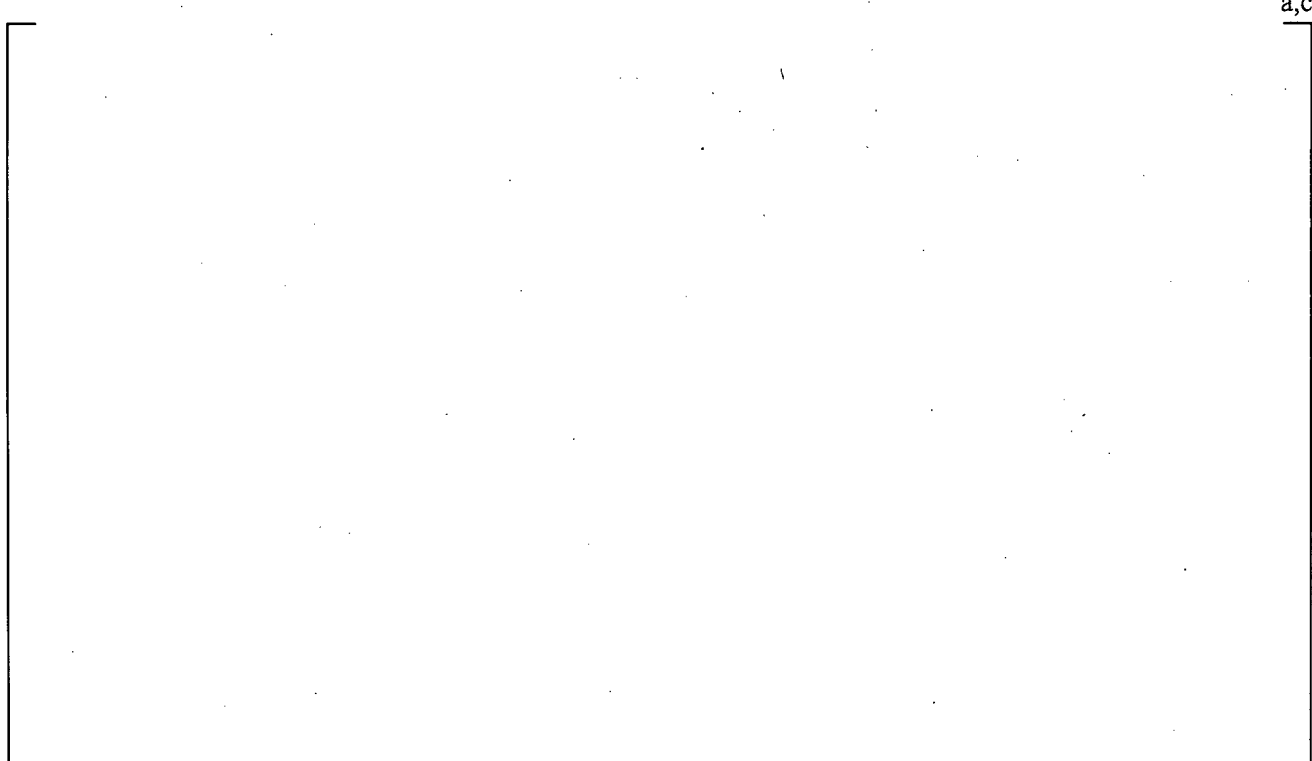


**Figure 15.6.1-29 FLECHT-SEASET 31504 Rod Temperatures at 96-inch Elevation**



**Figure 15.6.1-30 FLECHT-SEASET 31504 Rod Temperatures at 120-inch Elevation**



**Figure 15.6.1-31 Comparison of Predicted and Estimated Quench Front Elevations for FLECHT-SEASET 31504**

a,c



**Figure 15.6.1-32 Comparison of Predicted and Measured Axial Temperature Profile for FLECHT-SEASET 31504 at 50 Seconds**

a,c



**Figure 15.6.1-33 Comparison of Predicted and Measured Axial Temperature Profile for FLECHT-SEASET 31504 at 100 Seconds**



**Figure 15.6.1-34 Comparison of Predicted and Measured Maximum Cladding Temperatures at all Thermocouple Elevations for FLECHT-SEASET 31504**



**Figure 15.6.1-35 Comparison of Predicted and Measured Turn-Around Times for FLECHT-SEASET 31504**

a,c



**Figure 15.6.1-36 FLECHT-SEASET 31504 Bundle Lower Half  $\Delta P$**

a,c



**Figure 15.6.1-37 FLECHT-SEASET 31504 Bundle Upper Half  $\Delta P$**

a,c



**Figure 15.6.1-38 FLECHT-SEASET 31504 Overall  $\Delta P$**

a,c



**Figure 15.6.1-39 FLECHT-SEASET 31504 Vapor Temperatures at 48-inch Elevation**

a,c



**Figure 15.6.1-40 FLECHT-SEASET 31504 Vapor Temperatures near 72-inch Elevation**

a,c



**Figure 15.6.1-41 FLECHT-SEASET 31504 Vapor Temperatures near 90-inch Elevation**

**Figure 15.6.1-42 FLECHT-SEASET 31504 Vapor Temperatures at 120-inch Elevation**

**Figure 15.6.1-43 FLECHT-SEASET 31504 Vapor Temperatures at 138-inch Elevation**

a,c

**Figure 15.6.1-44 FLECHT-SEASET 32013 Rod Temperatures at 24-inch Elevation**

a,c

**Figure 15.6.1-45 FLECHT-SEASET 32013 Rod Temperatures at 48-inch Elevation**

a,c

**Figure 15.6.1-46 FLECHT-SEASET 32013 Rod Temperatures at 72-inch Elevation**

a,c

**Figure 15.6.1-47 FLECHT-SEASET 32013 Rod Temperatures at 78-inch Elevation**

a,c

**Figure 15.6.1-48 FLECHT-SEASET 32013 Rod Temperatures at 84-inch Elevation**

a,c

**Figure 15.6.1-49 FLECHT-SEASET 32013 Rod Temperatures at 96-inch Elevation**

a,c

**Figure 15.6.1-50 FLECHT-SEASET 32013 Rod Temperatures at 120-inch Elevation**

a,c

**Figure 15.6.1-51 Comparison of Predicted and Estimated Quench Front Elevations for FLECHT-SEASET 32013**

a,c

**Figure 15.6.1-52**

**Comparison of Predicted and Measured Axial Temperature Profile for FLECHT-SEASET 32013 at 50 Seconds**

a,c

**Figure 15.6.1-53**

**Comparison of Predicted and Measured Axial Temperature Profile for FLECHT-SEASET 32013 at 100 Seconds**

a,c



**Figure 15.6.1-54 Comparison of Predicted and Measured Maximum Cladding Temperatures at all Thermocouple Elevations for FLECHT-SEASET 32013**

a,c



**Figure 15.6.1-55 Comparison of Predicted and Measured Turn-Around Times for FLECHT-SEASET 32013**

a,c

**Figure 15.6.1-56 FLECHT-SEASET 32013 Bundle Lower Half  $\Delta P$**

a,c

**Figure 15.6.1-57 FLECHT-SEASET 32013 Bundle Upper Half  $\Delta P$**

a,c

**Figure 15.6.1-58 FLECHT-SEASET 32013 Overall  $\Delta P$**

a,c

**Figure 15.6.1-59 FLECHT-SEASET 32013 Vapor Temperatures at 48-inch Elevation**

a,c



**Figure 15.6.1-60 FLECHT-SEASET 32013 Vapor Temperatures near 72-inch Elevation**

a,c



**Figure 15.6.1-61 FLECHT-SEASET 32013 Vapor Temperatures near 90-inch Elevation**

a,c



**Figure 15.6.1-62 FLECHT-SEASET 32013 Vapor Temperatures at 120-inch Elevation**

a,c



**Figure 15.6.1-63 FLECHT-SEASET 32013 Vapor Temperatures at 138-inch Elevation**

a,c



**Figure 15.6.1-64 FLECHT-SEASET 31203 Rod Temperatures at 24-inch Elevation**

a,c



**Figure 15.6.1-65 FLECHT-SEASET 31203 Rod Temperatures at 48-inch Elevation**

a,c



**Figure 15.6.1-66 FLECHT-SEASET 31203 Rod Temperatures at 72-inch Elevation**

a,c



**Figure 15.6.1-67 FLECHT-SEASET 31203 Rod Temperatures at 78-inch Elevation**

a,c

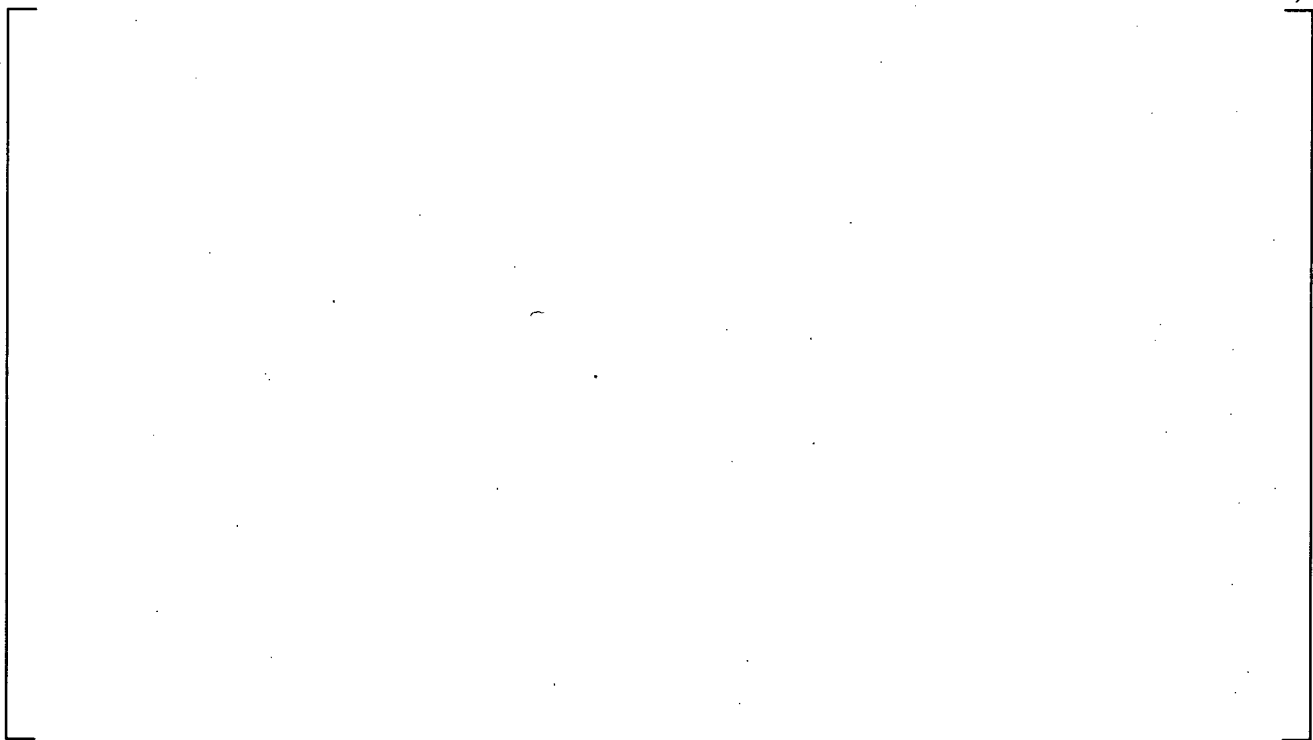


**Figure 15.6.1-68 FLECHT-SEASET 31203 Rod Temperatures at 84-inch Elevation**

a,c



**Figure 15.6.1-69 FLECHT-SEASET 31203 Rod Temperatures at 96-inch Elevation**

a,c

**Figure 15.6.1-70 FLECHT-SEASET 31203 Rod Temperatures at 120-inch Elevation**

a,c

**Figure 15.6.1-71 Comparison of Predicted and Estimated Quench Front Elevations for FLECHT-SEASET 31203**

a,c

**Figure 15.6.1-72 Comparison of Predicted and Measured Axial Temperature Profile for FLECHT-SEASET 31203 at 50 Seconds**

a,c

**Figure 15.6.1-73 Comparison of Predicted and Measured Axial Temperature Profile for FLECHT-SEASET 31203 at 100 Seconds**

a,c



**Figure 15.6.1-74 Comparison of Predicted and Measured Maximum Cladding Temperatures at all Thermocouple Elevations for FLECHT-SEASET 31203**

a,c



**Figure 15.6.1-75 Comparison of Predicted and Measured Turn-Around Times for FLECHT-SEASET 31203**

a,c

**Figure 15.6.1-76 FLECHT-SEASET 31203 Bundle Lower Half ΔP**

a,c

**Figure 15.6.1-77 FLECHT-SEASET 31203 Bundle Upper Half ΔP**

a,c

**Figure 15.6.1-78 FLECHT-SEASET 31203 Overall  $\Delta P$**

a,c

**Figure 15.6.1-79 FLECHT-SEASET 31203 Vapor Temperatures at 48-inch Elevation**

a,c



**Figure 15.6.1-80 FLECHT-SEASET 31203 Vapor Temperatures near 72-inch Elevation**

a,c



**Figure 15.6.1-81 FLECHT-SEASET 31203 Vapor Temperatures near 90-inch Elevation**

a,c

**Figure 15.6.1-82 FLECHT-SEASET 31203 Vapor Temperatures at 120-inch Elevation**

a,c

**Figure 15.6.1-83 FLECHT-SEASET 31203 Vapor Temperatures at 138-inch Elevation**

a,c



**Figure 15.6.1-84 FLECHT-SEASET 31701 Rod Temperatures at 24-inch Elevation**

a,c



**Figure 15.6.1-85 FLECHT-SEASET 31701 Rod Temperatures at 48-inch Elevation**



**Figure 15.6.1-86 FLECHT-SEASET 31701 Rod Temperatures at 72-inch Elevation**

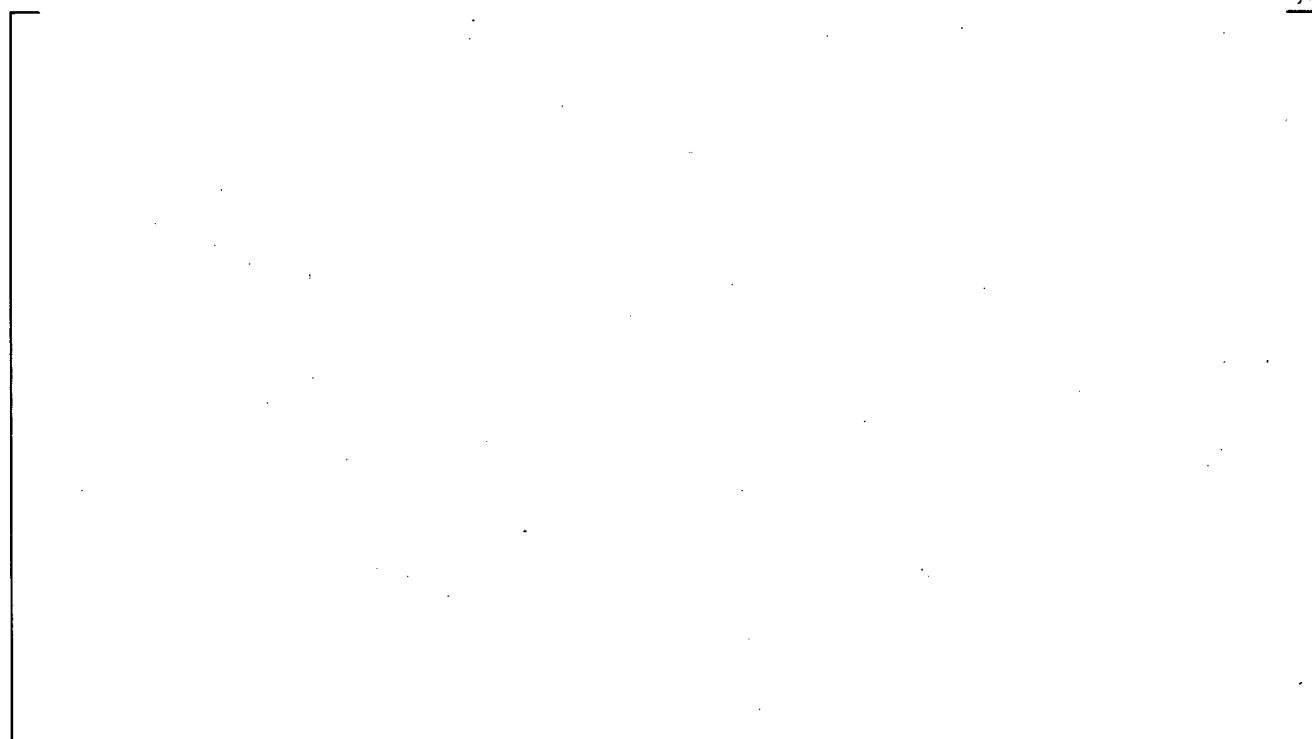


**Figure 15.6.1-87 FLECHT-SEASET 31701 Rod Temperatures at 78-inch Elevation**

a,c

**Figure 15.6.1-88 FLECHT-SEASET 31701 Rod Temperatures at 84-inch Elevation**

a,c

**Figure 15.6.1-89 FLECHT-SEASET 31701 Rod Temperatures at 96-inch Elevation**

a,c



**Figure 15.6.1-90 FLECHT-SEASET 31701 Rod Temperatures at 120-inch Elevation**

a,c



**Figure 15.6.1-91 Comparison of Predicted and Estimated Quench Front Elevations for FLECHT-SEASET 31701**

a,c

**Figure 15.6.1-92 Comparison of Predicted and Measured Axial Temperature Profile for FLECHT-SEASET 31701 at 10 Seconds**

a,c

**Figure 15.6.1-93 Comparison of Predicted and Measured Axial Temperature Profile for FLECHT-SEASET 31701 at 30 Seconds**

a,c



**Figure 15.6.1-94 Comparison of Predicted and Measured Maximum Cladding Temperatures at all Thermocouple Elevations for FLECHT-SEASET 31701**

a,c



**Figure 15.6.1-95 Comparison of Predicted and Measured Turn-Around Times for FLECHT-SEASET 31701**

a,c



**Figure 15.6.1-96 FLECHT-SEASET 31701 Bundle Lower Half  $\Delta P$**

a,c



**Figure 15.6.1-97 FLECHT-SEASET 31701 Bundle Upper Half  $\Delta P$**

a,c

**Figure 15.6.1-98 FLECHT-SEASET 31701 Overall  $\Delta P$**

a,c

**Figure 15.6.1-99 FLECHT-SEASET 31701 Vapor Temperatures at 48-inch Elevation**

a,c

**Figure 15.6.1-100 FLECHT-SEASET 31701 Vapor Temperatures near 72-inch Elevation**

a,c

**Figure 15.6.1-101 FLECHT-SEASET 31701 Vapor Temperatures near 90-inch Elevation**



**Figure 15.6.1-102 FLECHT-SEASET 31701 Vapor Temperatures at 120-inch Elevation**



**Figure 15.6.1-103 FLECHT-SEASET 31701 Vapor Temperatures at 138-inch Elevation**

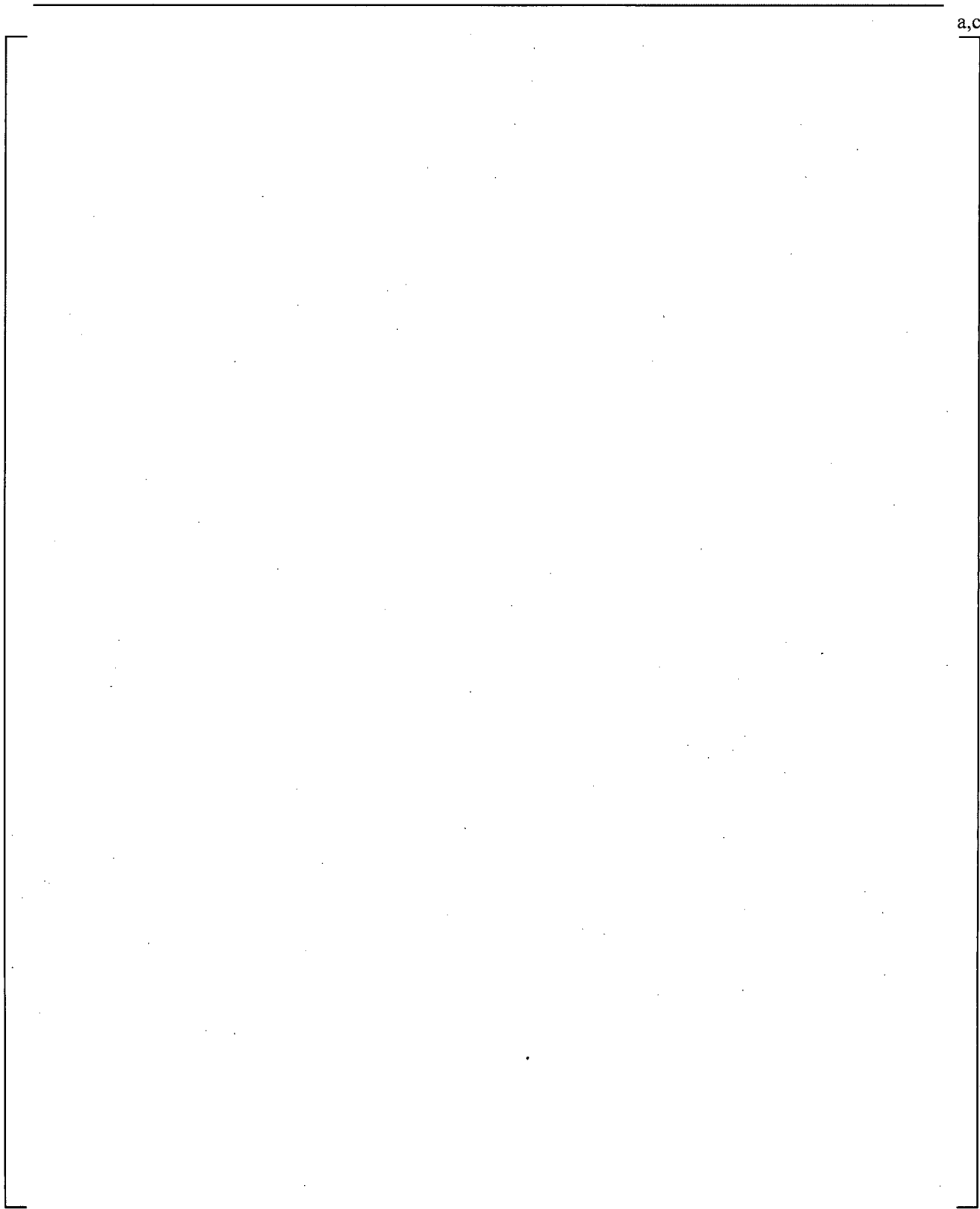


**Figure 15.6.1-104 Comparison of Predicted and Measured Maximum Temperatures for FLECHT-SEASET Simulations**

## 15.6.2 WCOBRA/TRAC-TF2 Simulations of FLECHT Low Flooding Rate (LFR) Test Series and One Supplemental Test

The FLECHT test assembly is modeled with three WCOBRA/TRAC-TF2 components. A VESSEL component is used to model the heated bundle, the upper plenum, and the top 6 inches of the lower plenum. Boundary conditions based on measured values were imposed on the top and the bottom of the VESSEL component. A PIPE component is attached to the top of the VESSEL, and a zero velocity FILL component is attached to the PIPE to satisfy the WCOBRA/TRAC-TF2 requirement of at least one one-dimensional component.

The VESSEL component is composed of four channels. Two channels are used to model the test section, one for the inner region of the bundle and one for the outer region that includes the bundle housing. The radial noding is shown in Figure 15.6.2-1. Channel 2 represents the inner channel. The remainder of the bundle is in the outer channel. [

]<sup>a,c</sup> These rods are each modeled with a single rod model having the dimensions of the actual heater rods. The heat flux from the rod to the fluid is multiplied by the number of heater rods in the region represented by the channel to obtain the correct heat flux to the fluid. The test section housing is modeled with a wall geometry non-heated conductor that is thermally connected to the outer channel on the inside surface and is insulated on the outer surface. The WCOBRA/TRAC-TF2 vertical mesh lengths for the vessel are shown in Figure 15.6.2-2.

The WCOBRA/TRAC-TF2 heater rods are initialized with axial temperature profiles determined by measured temperature at the start of reflood for each individual test. The initial temperatures for all axial levels were computed by averaging the thermocouple temperature within a radial boundary at a given elevation. One heater rod was inoperative during the entire transient, therefore the thermocouples in the immediate vicinity of the unpowered rod were eliminated from the initial temperature averaging.

The housing is initialized with an axial temperature profile determined from thermocouples that were attached to the facility housing.

Both of the WCOBRA/TRAC-TF2 rods used the axial power profile shown in Figure 15.6.2-3. The housing had zero power generation.

The reflood transient is run by using measured values of the injected flow as a boundary condition imposed on the bottom of the VESSEL component. A constant pressure and enthalpy boundary condition is imposed on the top node of the VESSEL. During the transient, the heater rod power is decreased according to the ANS 1971 + 20 percent power decay curve. The simulations were continued until the entire bundle had quenched.

Additional initial conditions are provided in Table 14.1-6 for each test and are repeated here.

Test Series	Test Number	Pressure psia	Flooding Rate in/s	Inlet Subcooling °F	Peak Power kW/ft	Comment
FLECHT LOW FLOODING RATE	05029 05132 04641	40 40 20	0.85 1.0 1.0	141 140 139	0.73 0.95 0.95	COSINE POWER SHAPE 15x15 ROD ARRAY
FLECHT SUPPLEMENTAL	0791	15	0.4	25	0.7	COSINE POWER SHAPE

### 15.6.2.1 FLECHT LFR Results

#### 15.6.2.1.1 FLECHT Test 05029

The reflood rate for Test 05029 was 0.85 in/sec. The test pressure was maintained at 40 psia and the injected coolant temperature was 126°F. Conditions for this test are very similar to those for FLECHT-SEASET Test 31805. The WCOBRA/TRAC-TF2 simulation of Test 05029 was run past 500 seconds, by which time all heater rod elevations had reached their peak temperature and had started to decline. Figures 15.6.2-4 through 15.6.2-10 show the comparison of predicted and measured temperatures at elevations 24, 48, 72, 78, 84, 96, and 120 inches from the bottom of the heated length. The code prediction is for simulated rod temperatures in the inner channel (rod no. 1 located in Channel 2 of Figure 15.6.2-2). The curves in these figures that represent the data show the individual thermocouples located within the boundary of the WCOBRA/TRAC-TF2 inner channel. Figure 15.6.2-11 shows the prediction of the quench front elevation compared to the quench elevations deduced from temperature measurements. [

] <sup>a,c</sup>

Comparisons of the axial temperature profiles are shown in Figure 15.6.2-12 at 50 seconds, and in Figure 15.6.2-13 at 100 seconds. The predicted temperature profiles are shown to [

] <sup>a,c</sup>.

Figure 15.6.2-14 summarizes the comparisons of the maximum predicted peak cladding temperatures at several thermocouple elevations. [

] <sup>a,c</sup>

Figures 15.6.2-15 through 15.6.2-17 show comparisons of the predicted and measured axial pressure differentials in the bundle. Figure 15.6.2-15 shows a comparison of the pressure differentials in the lower half (0 to 72 inches) of the bundle. [

] <sup>a,c</sup> Figure 15.6.2-16 shows the comparison for the upper half (72 to 144 inches) of the bundle, [ ] <sup>a,c</sup>. The overall pressure differential comparison is shown in Figure 15.6.2-17.

The FLECHT facility included steam temperature probes located in the thimble tubes. Figure 15.6.2-18 shows the comparison at the 84-inch elevation, just downstream of the peak temperature location. Figure 15.6.2-19 shows the comparison at the 120-inch elevation, and Figure 15.6.2-20 the comparison near the bundle exit. [

] <sup>a,c</sup>

### 15.6.2.1.2 FLECHT Test 05132

The reflood rate for Test 05132 was 1.0 in/sec. The test pressure was maintained at 40 psia and the injected coolant temperature was 127°F. The initial peak rod power for this test was 0.95 kW/ft. The WCOBRA/TRAC-TF2 simulation of Test 05132 was run past the 500 seconds of the experiment, by which time all heater rod elevations had reached their peak temperature and had quenched.

Figures 15.6.2-21 through 15.6.2-27 show the comparison of predicted and measured temperatures at elevations 24, 48, 72, 78, 84, 96, and 120 inches from the bottom of the heated length. The code prediction is for simulated rod temperatures in the inner channel (rod no. 1 located in Channel 2 of Figure 15.6.2-2). The curves in these figures that represent the data show the individual thermocouples located within the boundary of the WCOBRA/TRAC-TF2 inner channel. Figure 15.6.2-28 shows the prediction of the quench front elevation compared to the quench elevations deduced from temperature measurements. [

] <sup>a,c</sup>

Comparisons of the axial temperature profiles are shown in Figure 15.6.2-29 at 50 seconds, and in Figure 15.6.2-30 at 100 seconds. The predicted temperature profiles are shown to [

] <sup>a,c</sup>.

Figure 15.6.2-31 summarizes the comparisons of the maximum predicted peak cladding temperatures at several thermocouple elevations. [

] <sup>a,c</sup>

Figures 15.6.2-32 through 15.6.2-34 show comparisons of the predicted and measured axial pressure differentials in the bundle. Figure 15.6.2-32 shows a comparison of the pressure differentials in the lower half (0 to 72 inches) of the bundle. The WCOBRA/TRAC-TF2 prediction is [

] <sup>a,c</sup>.

Figure 15.6.2-33 shows the comparison for the upper half (72 to 144 inches) of the bundle, where the code is [ ] <sup>a,c</sup>. The overall pressure differential comparison is shown in Figure 15.6.2-34.

The FLECHT facility included steam temperature probes located in the thimble tubes. Figure 15.6.2-35 shows the comparison at the 84-inch elevation, just downstream of the peak temperature location. Figure 15.6.2-36 shows the comparison at the 120-inch elevation, and Figure 15.6.2-37 the comparison near the bundle exit. [

] <sup>a,c</sup>

### 15.6.2.1.3 FLECHT Test 04641

The reflood rate for Test 04641 was 1.0 in/sec. The test pressure was maintained at 20 psia and the injected coolant temperature was 89°F (139°F of sub-cooling). The initial peak rod power for this test was 0.95 kW/ft. The WCOBRA/TRAC-TF2 simulation of Test 04641 was run past 800 seconds, by which time all heater rod elevations had reached their peak temperature and had quenched. Figures 15.6.2-38 through 15.6.2-44 show the comparison of predicted and measured temperatures at elevations 24, 48, 72, 78, 84, 96, and 120 inches from the bottom of the heated length. The code prediction is for simulated rod temperatures in the inner channel (rod no. 1 located in Channel 2 of Figure 15.6.2-2). The curves in these figures that represent the data show the individual thermocouples located within the boundary of the WCOBRA/TRAC-TF2 inner channel. Figure 15.6.2-45 shows the prediction of the quench front elevation compared to the quench elevations deduced from temperature measurements. [

] <sup>a,c</sup>

Comparisons of the axial temperature profiles are shown in Figure 15.6.2-46 at 50 seconds, and in Figure 15.6.2-47 at 100 seconds. The predicted temperature profiles are shown to [

] <sup>a,c</sup>.

Figure 15.6.2-48 summarizes the comparisons of the maximum predicted peak cladding temperatures at several thermocouple elevations. The code tends to [

] <sup>a,c</sup>.

Figures 15.6.2-49 through 15.6.2-51 show comparisons of the predicted and measured axial pressure differentials in the bundle. Figure 15.6.2-49 shows a comparison of the pressure differentials in the lower half (0 to 72 inches) of the bundle. [

in Figure 15.6.2-51. <sup>a,c</sup> The overall pressure differential comparison is shown

The FLECHT facility included steam temperature probes located in the thimble tubes. Figure 15.6.2-52 shows the comparison at the 84-inch elevation, just downstream of the peak temperature location. Figure 15.6.2-53 shows the comparison at the 120-inch elevation, and Figure 15.6.2-54 the comparison near the bundle exit. [

] <sup>a,c</sup>

## 15.6.2.2 FLECHT Supplemental Results

### 15.6.2.2.1 FLECHT Test 0791

The reflood rate for Test 0791 was nominally set at 0.4 in/sec. The test pressure was maintained at 15 psia and the injected coolant temperature was 188°F (25°F of sub-cooling). The WCOBRA/TRAC-TF2 simulation of Test 0791 was run past 1000 seconds, by which time all of the heater rod elevations had reached their peak temperature and had started to decline. Figures 15.6.2-55 through 15.6.2-59 show the

comparison of predicted and measured temperatures at elevations 24, 48, 72, 96 and 120 inches from the bottom of the heated length. The code prediction is for simulated rod temperatures in the inner channel (rod no. 1 located in Channel 2 of Figure 15.6.2-2). The curves in these figures that represent the data show the individual thermocouples located within the boundary of the WCOBRA/TRAC-TF2 inner channel. Figure 15.6.2-60 shows the prediction of the quench front elevation compared to the quench elevations deduced from temperature measurements. [

] <sup>a,c</sup>

Figure 15.6.2-61 summarizes the comparisons of the maximum predicted peak cladding temperatures at several thermocouple elevations. [

] <sup>a,c</sup>

Figures 15.6.2-62 through 15.6.2-65 show comparisons of the predicted and measured axial pressure differentials in the bundle. Figure 15.6.2-62 compares the pressure differentials at 0-2 ft and shows the code [ ] <sup>a,c</sup> in this region. Figures 15.6.2-63 and 15.6.2-64 compare the pressure differentials at 0-4 ft and 0-6 ft, respectively, and shows the code [ ] <sup>a,c</sup> in these regions. Figure 15.6.2-65 compares the pressure differentials at 0-8 ft, and shows [ ] <sup>a,c</sup>.

### 15.6.2.3 FLECHT Cosine LFR and Supplemental Summary and Conclusions

Three FLECHT Low Flooding Rate Tests were simulated using WCOBRA/TRAC-TF2. These tests had a more limited range of flooding rates (0.4 to 1.00 in/sec), but included a test of low pressure (Test 04641 at 20 psia and Test 0791 at 15 psia) and two tests with a high initial rod peak power (Tests 04641 and 05132 at 0.95 kW/ft). In addition, the degree of sub-cooling ranged from 25°F to 140°F. Figure 15.6.2-66 presents a comparison of the predicted maximum clad temperatures to the measured maximum clad temperatures for all four test simulations. [

] <sup>a,c</sup>

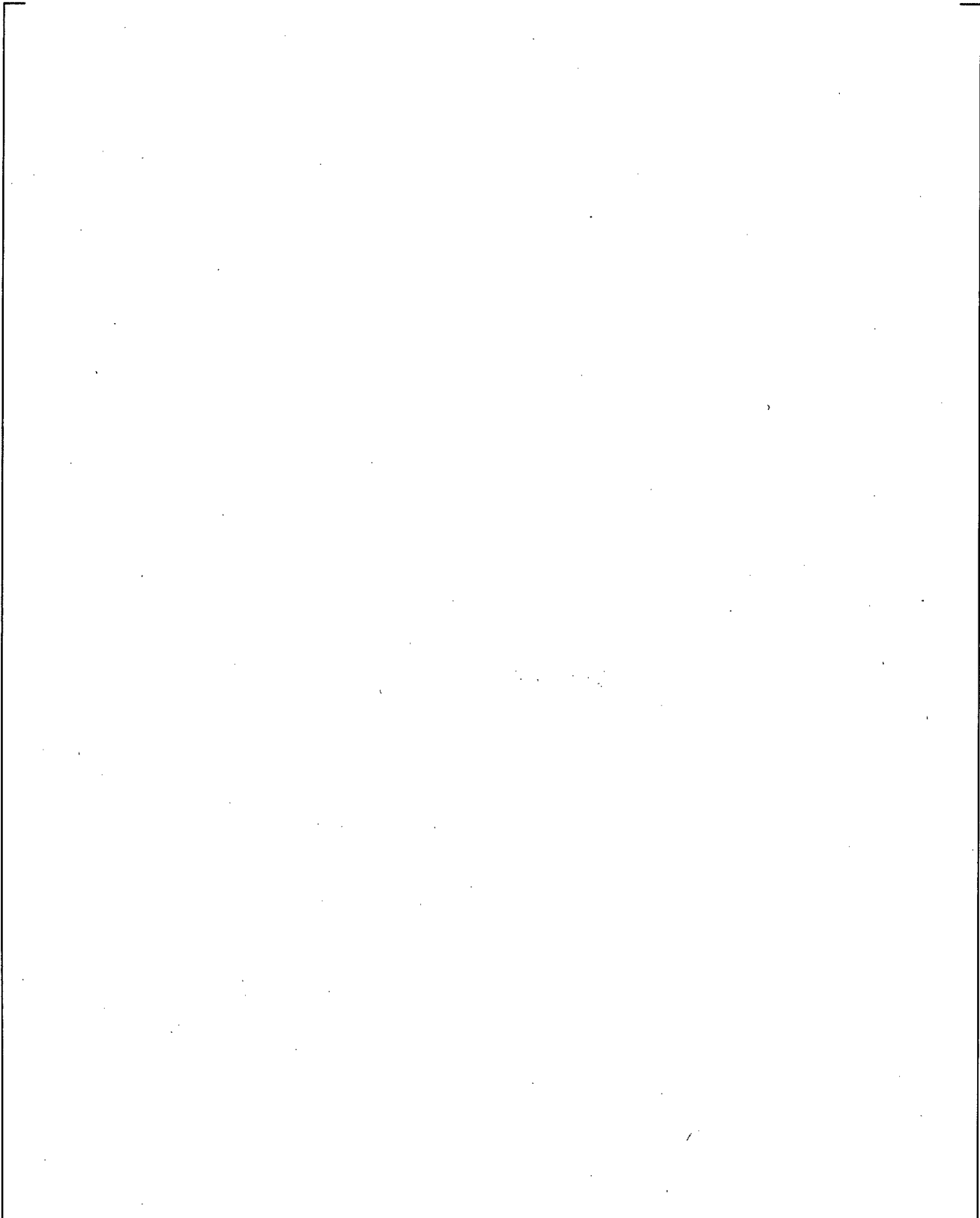


**Figure 15.6.2-1 WCOBRA/TRAC-TF2 Transverse Noding for FLECHT-LFR**

a,c

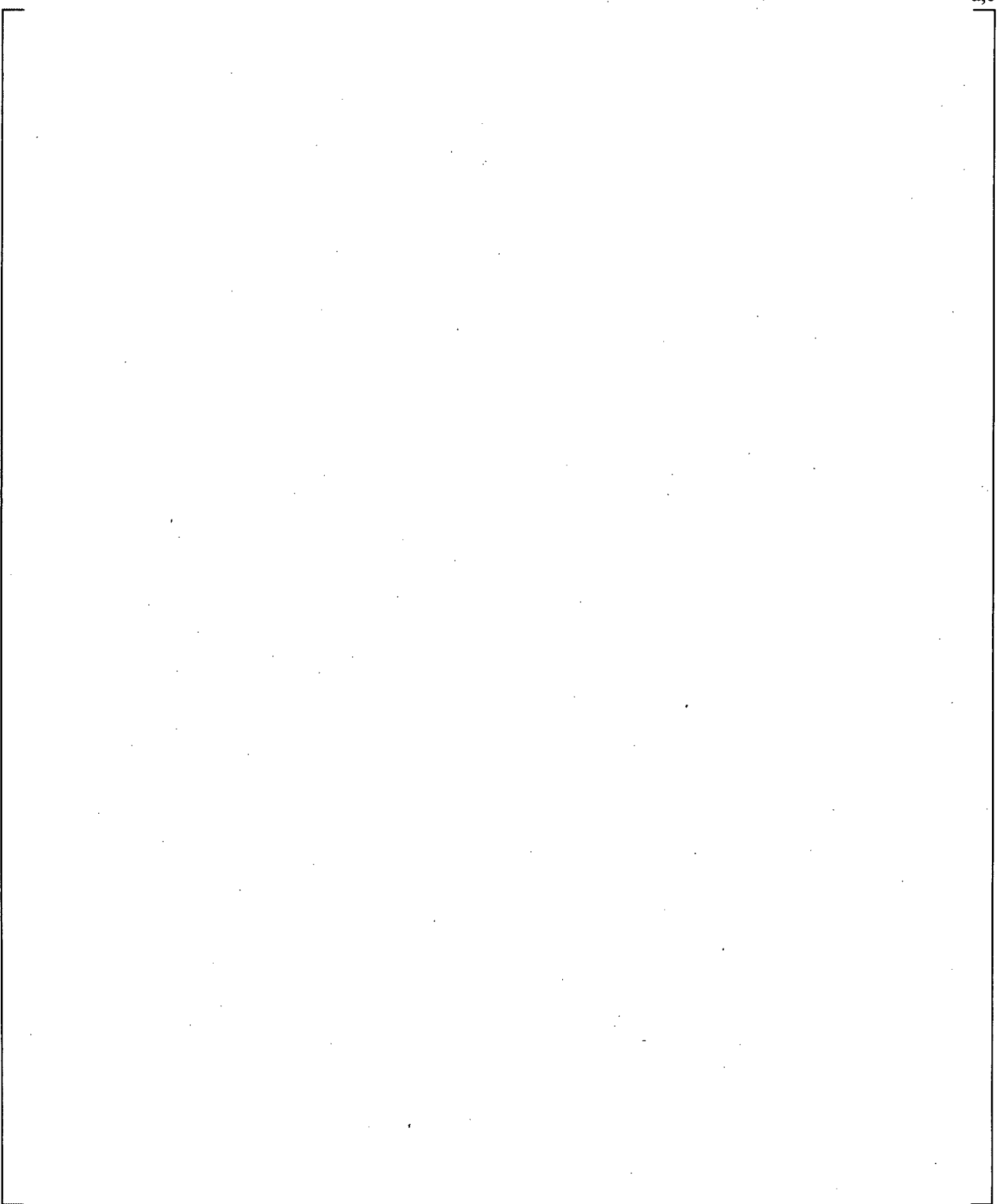
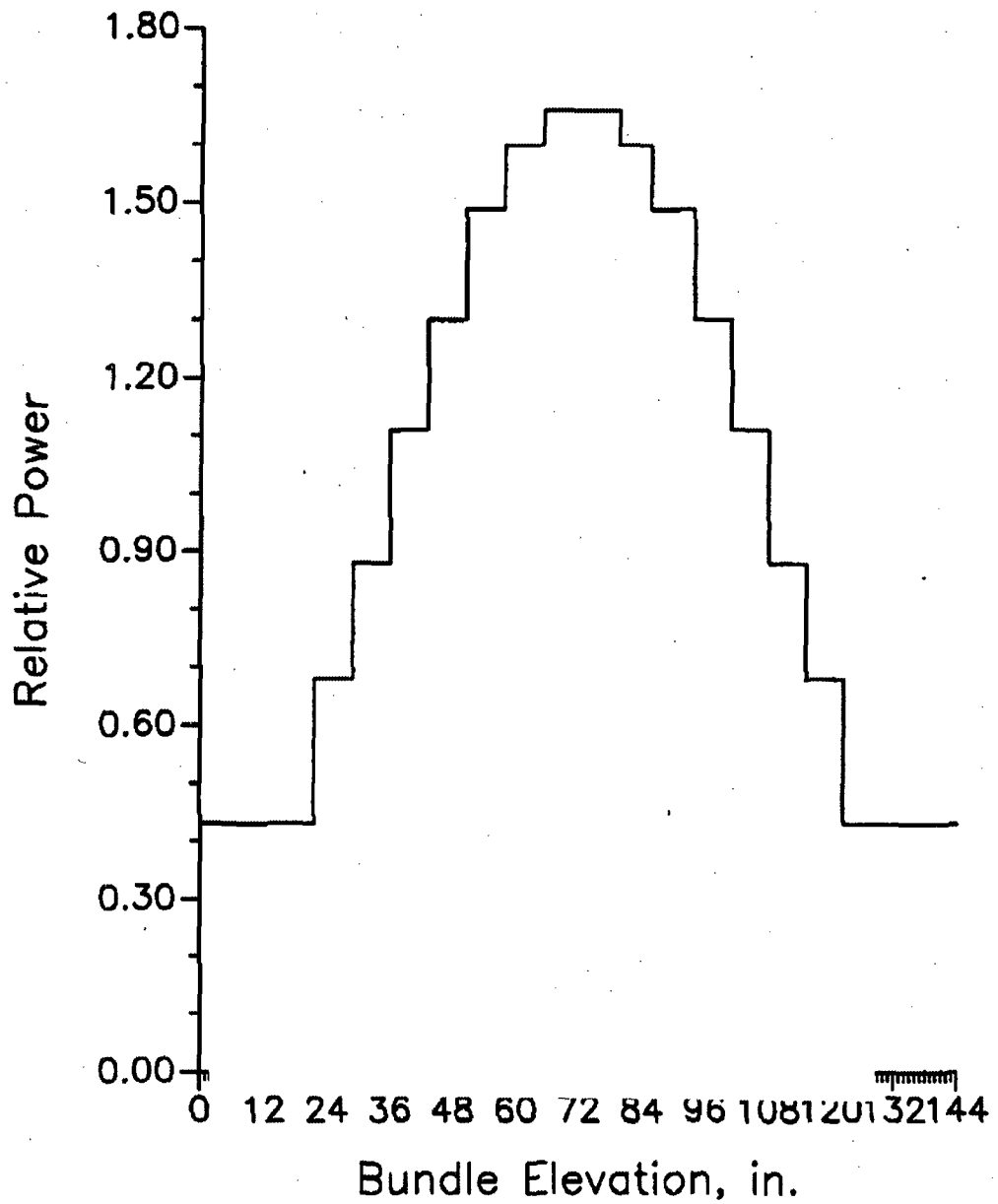


Figure 15.6.2-2 WCOBRA/TRAC-TF2 Axial Noding for FLECHT-LFR

SPACER GRIDS:        G    G    G    G    G    G

THERMOCOUPLES: x x    x    x    x            x x x    x    x    x    x



FLECHT COSINE AXIAL POWER SHAPE,  
THERMOCOUPLE AND GRID LOCATIONS

Figure 15.6.2-3 WCOBRA/TRAC-TF2 Axial Power Shape for FLECHT-LFR

a,c

**Figure 15.6.2-4 FLECHT 05029 Rod Temperatures at 24-inch Elevation**

a,c

**Figure 15.6.2-5 FLECHT 05029 Rod Temperatures at 48-inch Elevation**

a,c

**Figure 15.6.2-6 FLECHT 05029 Rod Temperatures at 72-inch Elevation**

a,c

**Figure 15.6.2-7 FLECHT 05029 Rod Temperatures at 78-inch Elevation**

a,c

**Figure 15.6.2-8 FLECHT 05029 Rod Temperatures at 84-inch Elevation**

a,c

**Figure 15.6.2-9 FLECHT 05029 Rod Temperatures at 96-inch Elevation**

a,c

**Figure 15.6.2-10 FLECHT 05029 Rod Temperatures at 120-inch Elevation**

a,c

**Figure 15.6.2-11 Comparison of Predicted and Estimated Quench Front Elevations for FLECHT 05029**

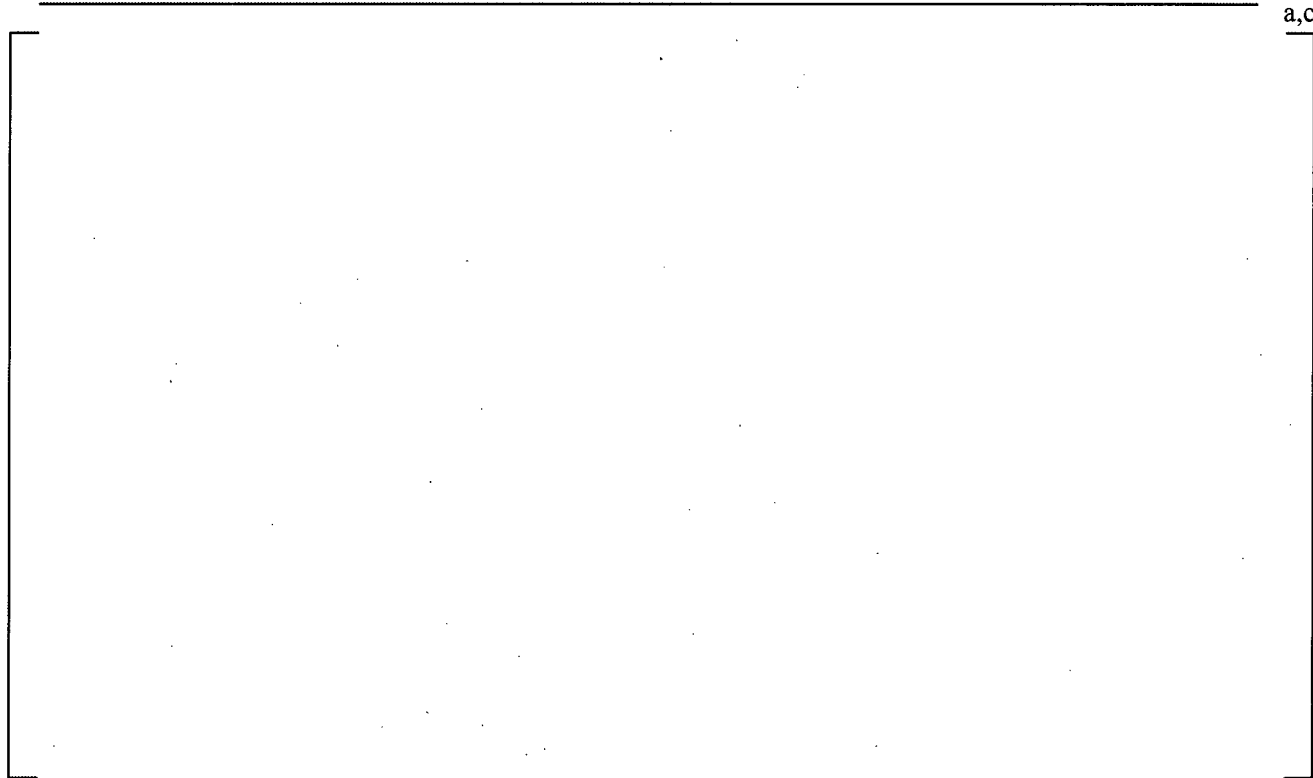


**Figure 15.6.2-12 Comparison of Predicted and Measured Axial Temperature Profile for FLECHT 05029 at 50 Seconds**



**Figure 15.6.2-13 Comparison of Predicted and Measured Axial Temperature Profile for FLECHT 05029 at 100 Seconds**

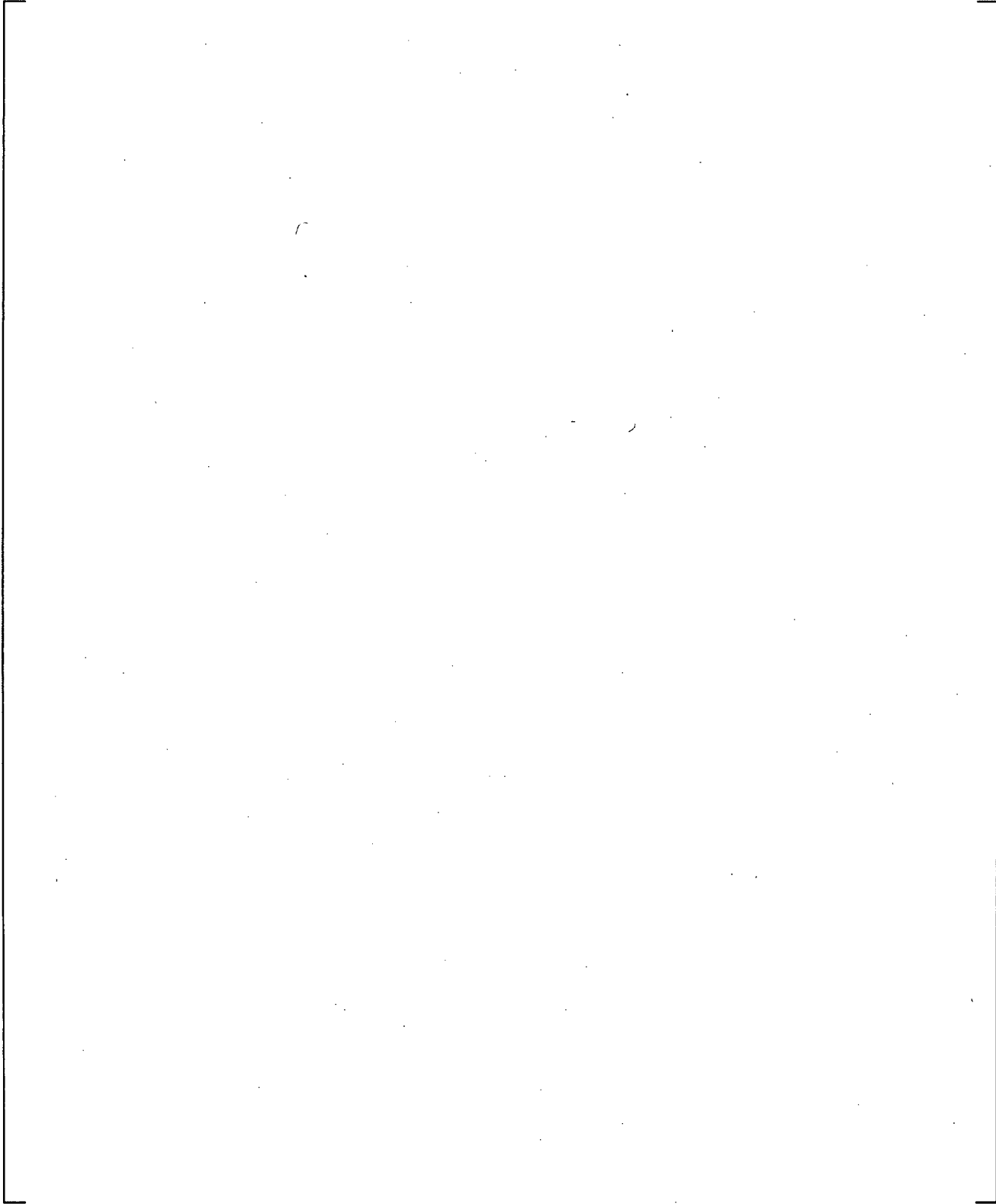


**Figure 15.6.2-14 Comparison of Predicted and Measured Maximum Cladding Temperatures at all Code Uncertainty Elevations for FLECHT 05029**



**Figure 15.6.2-15 FLECHT 05029 Bundle Lower Half  $\Delta P$**



**Figure 15.6.2-16 FLECHT 05029 Bundle Upper Half  $\Delta P$**



**Figure 15.6.2-17 FLECHT 05029 Overall  $\Delta P$**



**Figure 15.6.2-18 FLECHT 05029 Vapor Temperatures at 84-inch Elevation**



**Figure 15.6.2-19 FLECHT 05029 Vapor Temperatures near 120-inch Elevation**



**Figure 15.6.2-20 FLECHT 05029 Vapor Temperatures near Bundle Exit**



**Figure 15.6.2-21 FLECHT 05132 Rod Temperatures at 24-inch Elevation**

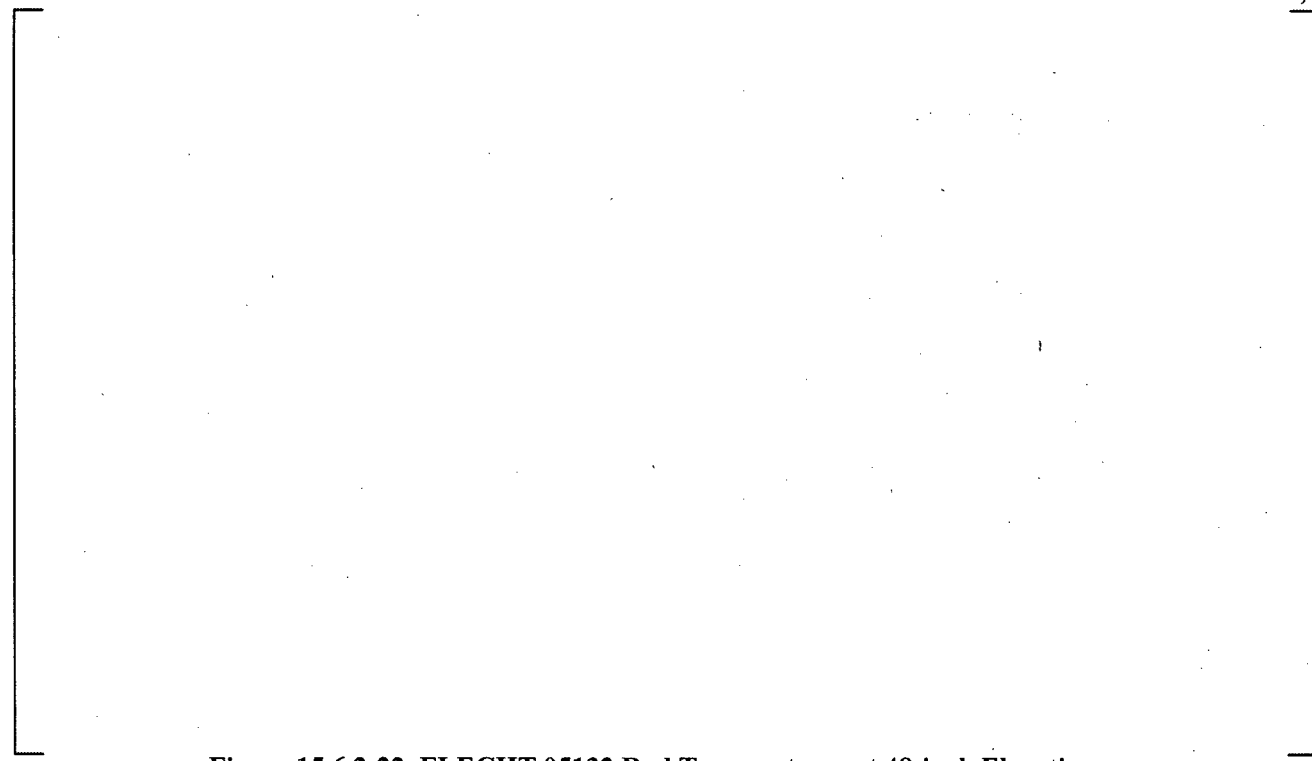


**Figure 15.6.2-22 FLECHT 05132 Rod Temperatures at 48-inch Elevation**



**Figure 15.6.2-23 FLECHT 05132 Rod Temperatures at 72-inch Elevation**



**Figure 15.6.2-24 FLECHT 05132 Rod Temperatures at 78-inch Elevation**



**Figure 15.6.2-25 FLECHT 05132 Rod Temperatures at 84-inch Elevation**

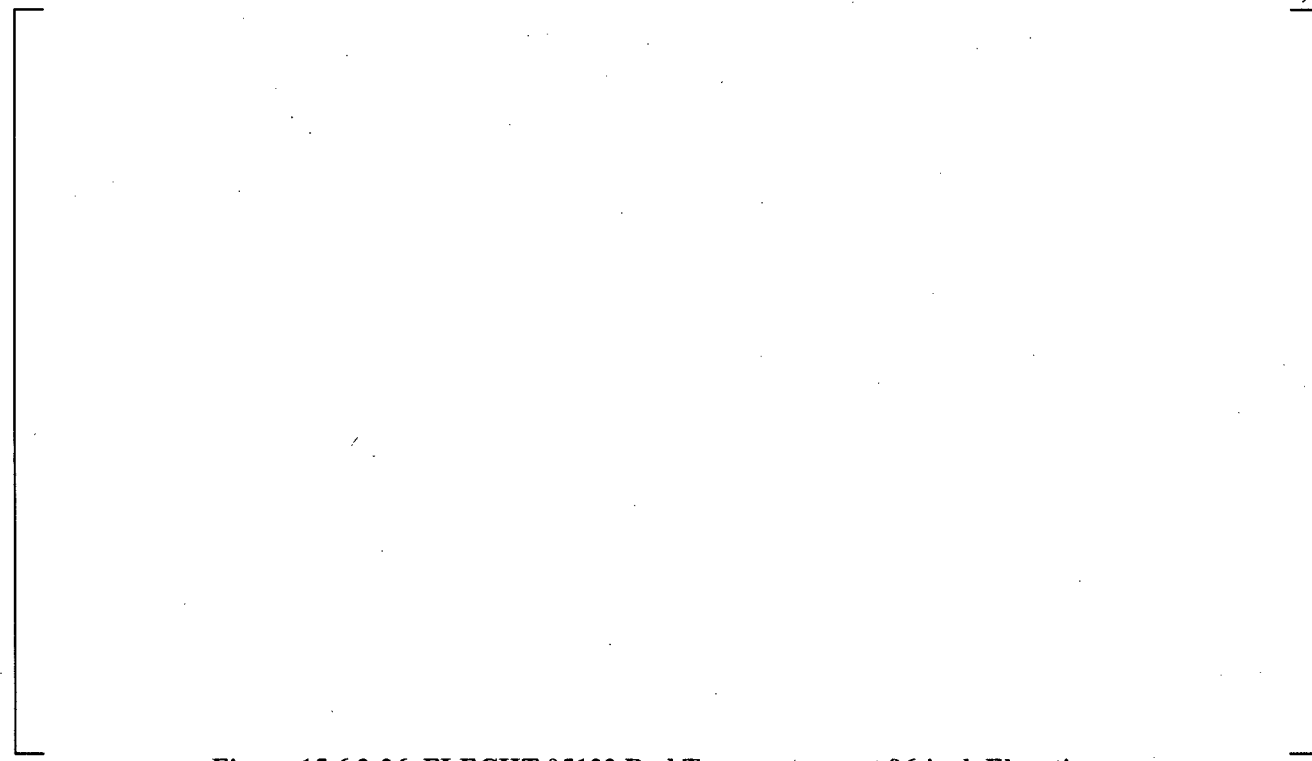


**Figure 15.6.2-26 FLECHT 05132 Rod Temperatures at 96-inch Elevation**

a,c

**Figure 15.6.2-27 FLECHT 05132 Rod Temperatures at 120-inch Elevation**

a,c

**Figure 15.6.2-28 Comparison of Predicted and Estimated Quench Front Elevations for FLECHT 05132**

a,c

**Figure 15.6.2-29 Comparison of Predicted and Measured Axial Temperature Profile for FLECHT 05132 at 50 Seconds**

a,c

**Figure 15.6.2-30 Comparison of Predicted and Measured Axial Temperature Profile for FLECHT 05132 at 100 Seconds**

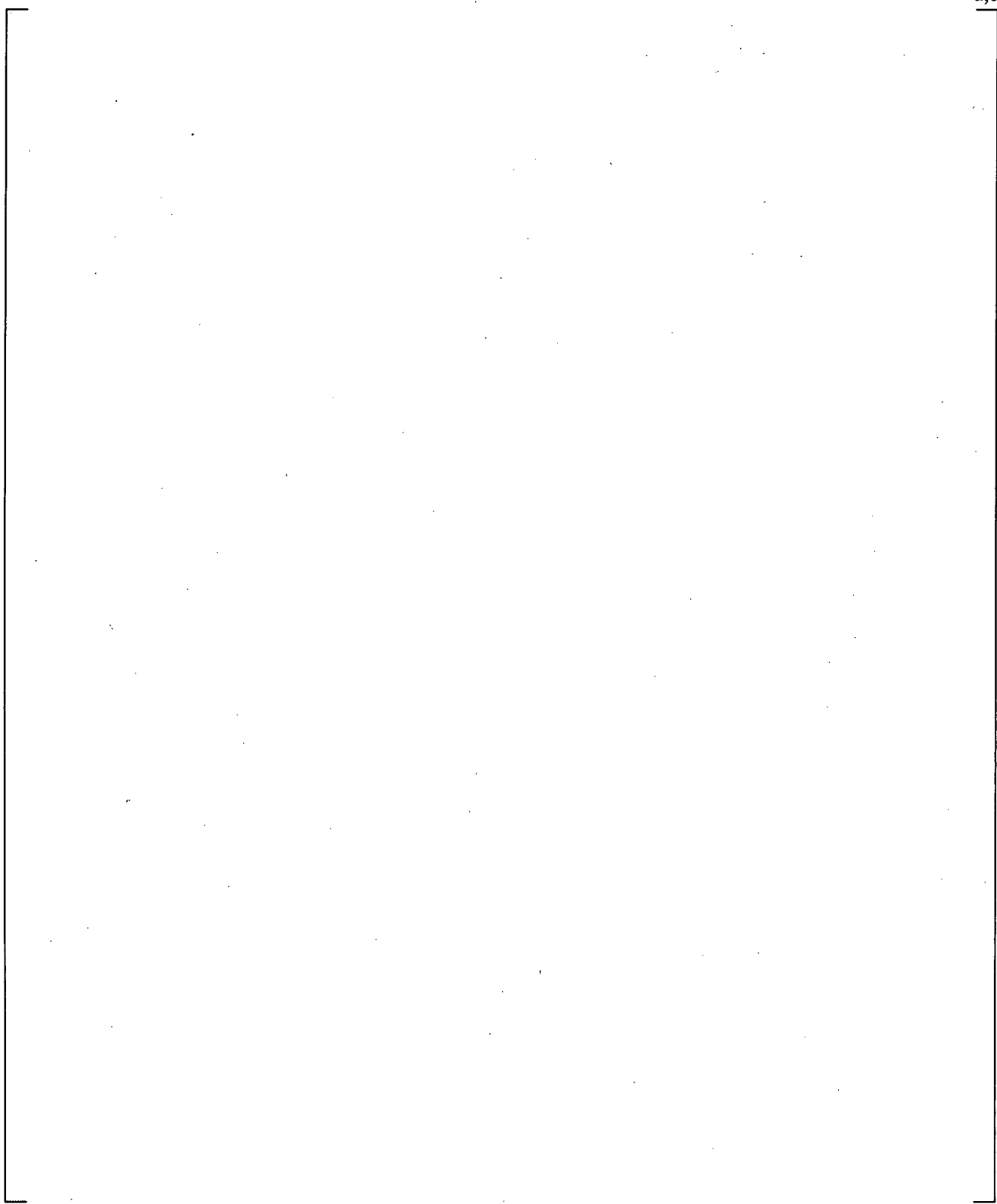


**Figure 15.6.2-31 Comparison of Predicted and Measured Maximum Cladding Temperatures at all Code Uncertainty Elevations for FLECHT 05132**

a,c



**Figure 15.6.2-32 FLECHT 05132 Bundle Lower Half ΔP**

a,c



**Figure 15.6.2-33 FLECHT 05132 Bundle Upper Half ΔP**

a,c

**Figure 15.6.2-34 FLECHT 05132 Overall  $\Delta P$**

a,c

**Figure 15.6.2-35 FLECHT 05132 Vapor Temperatures at 84-inch Elevation**

a,c



**Figure 15.6.2-36 FLECHT 05132 Vapor Temperatures near 120-inch Elevation<sup>(5)</sup>**

a,c



**Figure 15.6.2-37 FLECHT 05132 Vapor Temperatures near Bundle Exit**

a,c

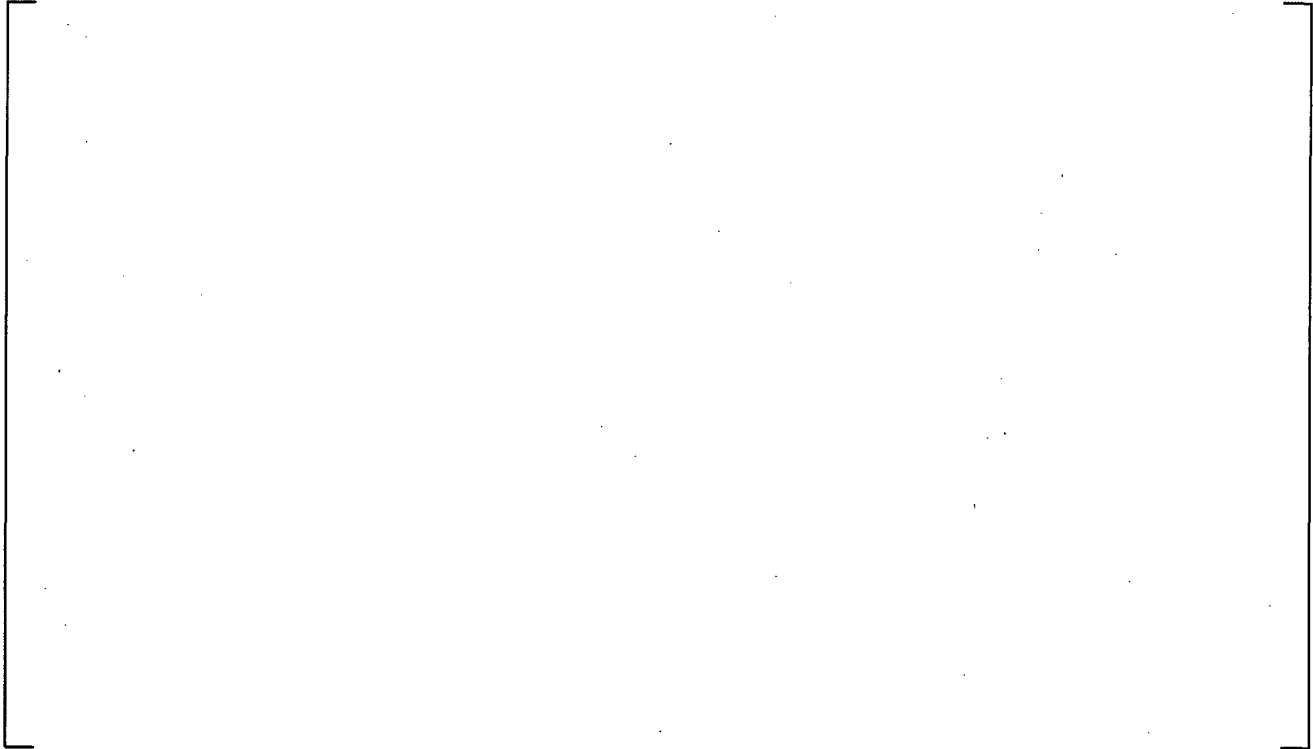


**Figure 15.6.2-38 FLECHT 04641 Rod Temperatures at 24-inch Elevation**

a,c



**Figure 15.6.2-39 FLECHT 04641 Rod Temperatures at 48-inch Elevation**

a,c

**Figure 15.6.2-40 FLECHT 04641 Rod Temperatures at 72-inch Elevation**

a,c

**Figure 15.6.2-41 FLECHT 04641 Rod Temperatures at 78-inch Elevation**

a,c



**Figure 15.6.2-42 FLECHT 04641 Rod Temperatures at 84-inch Elevation**

a,c



**Figure 15.6.2-43 FLECHT 04641 Rod Temperatures at 96-inch Elevation**



**Figure 15.6.2-44 FLECHT 04641 Rod Temperatures at 120-inch Elevation**



**Figure 15.6.2-45 Comparison of Predicted and Estimated Quench Front Elevations for FLECHT 04641**

**Figure 15.6.2-46 Comparison of Predicted and Measured Axial Temperature Profile for FLECHT 04641 at 50 Seconds**

**Figure 15.6.2-47 Comparison of Predicted and Measured Axial Temperature Profile for FLECHT 04641 at 100 Seconds**

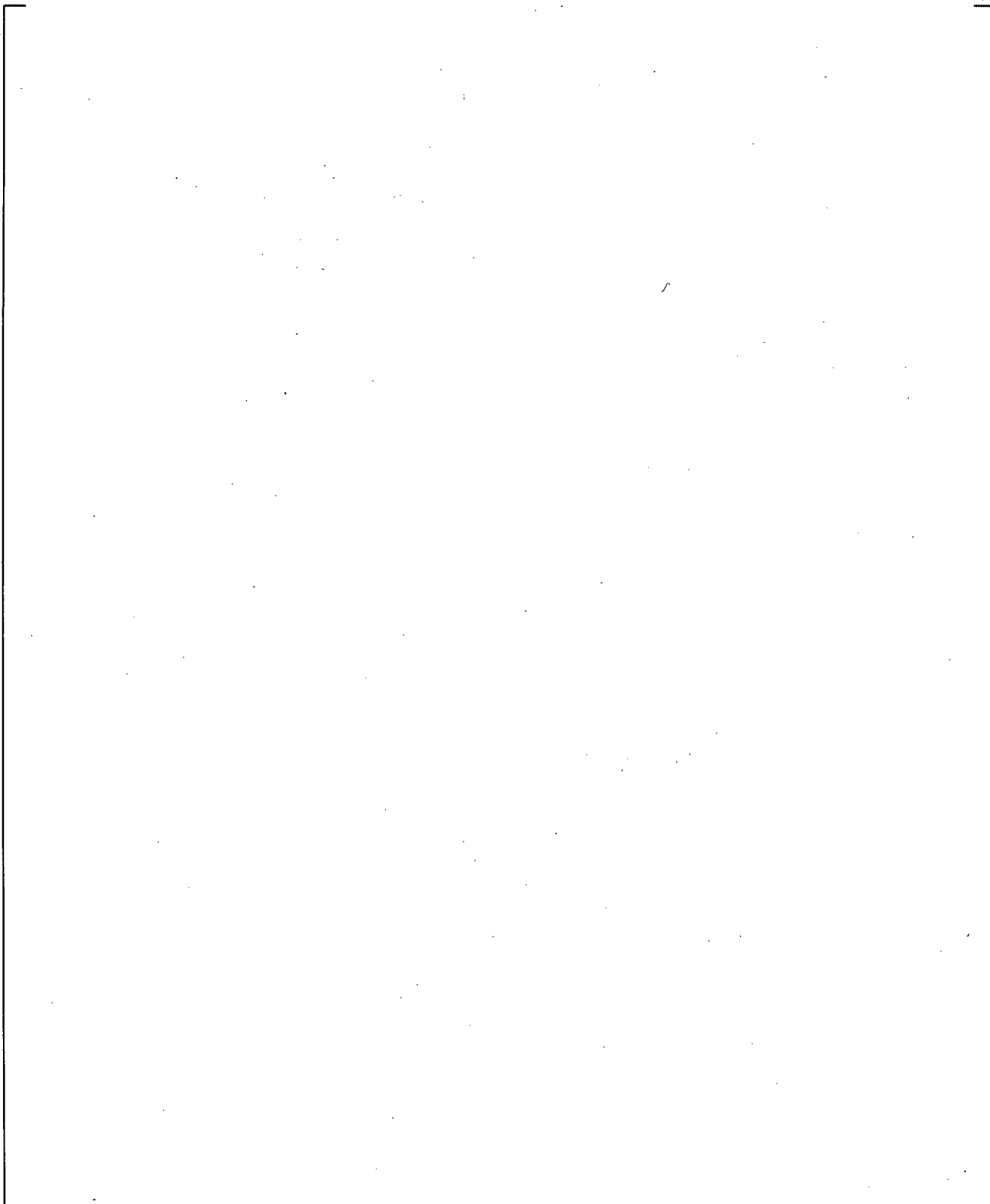


**Figure 15.6.2-48 Comparison of Predicted and Measured Maximum Cladding Temperatures at all Code Uncertainty Elevations for FLECHT 04641**

a,c



**Figure 15.6.2-49 FLECHT 04641 Bundle Lower Half  $\Delta P$**

a,c



**Figure 15.6.2-50 FLECHT 04641 Bundle Upper Half  $\Delta P$**

a,c



**Figure 15.6.2-51 FLECHT 04641 Overall  $\Delta P$**

a,c



**Figure 15.6.2-52 FLECHT 04641 Vapor Temperatures at 84-inch Elevation**

a,c



**Figure 15.6.2-53 FLECHT 04641 Vapor Temperatures near 120-inch Elevation**

a,c

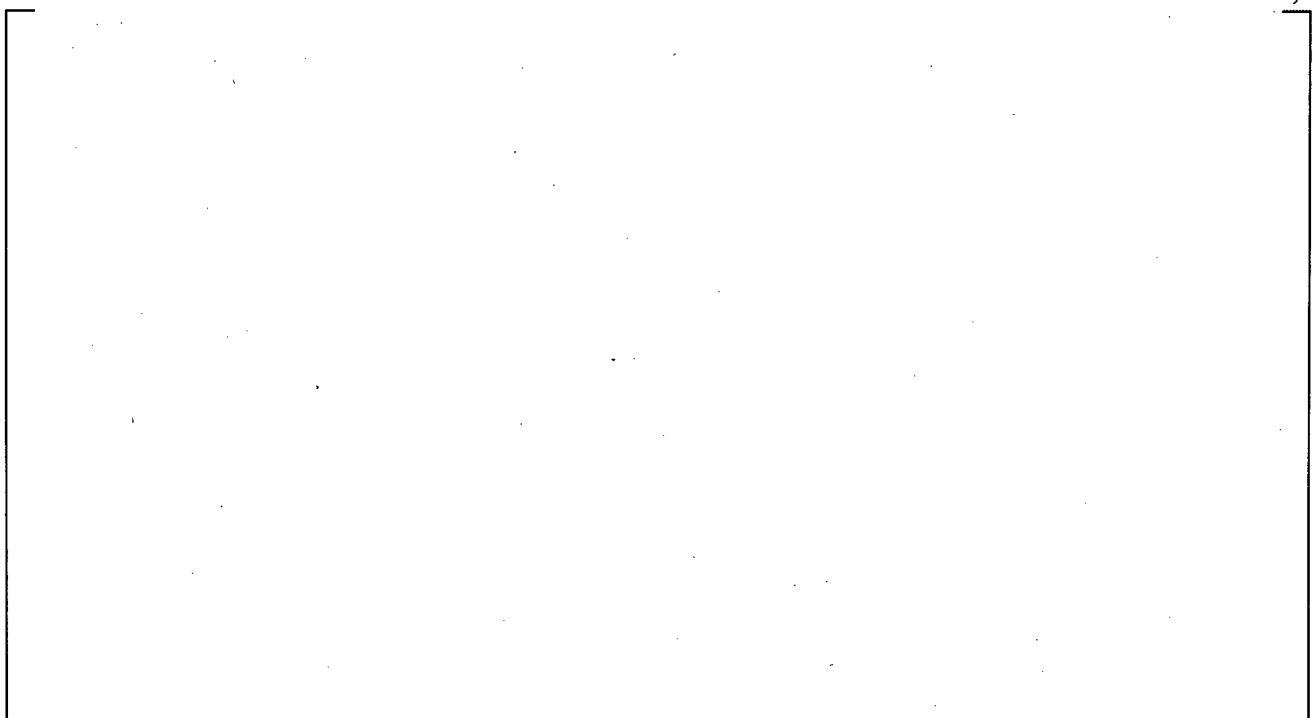


**Figure 15.6.2-54 FLECHT 04641 Vapor Temperatures near Bundle Exit**

a,c



**Figure 15.6.2-55 FLECHT 0791 Cladding Temperature at 24 inches**

a,c



**Figure 15.6.2-56 FLECHT 0791 Cladding Temperature at 48 inches**

a,c



**Figure 15.6.2-57 FLECHT 0791 Cladding Temperature at 72 inches**

a,c



**Figure 15.6.2-58 FLECHT 0791 Cladding Temperature at 96 inches**

a,c



**Figure 15.6.2-59 FLECHT 0791 Cladding Temperature at 120 inches**

a,c



**Figure 15.6.2-60 FLECHT 0791 Quench Front Progression**

a,c



**Figure 15.6.2-61 Maximum Cladding Temperature Comparison**

a,c



**Figure 15.6.2-62 FLECHT 0791 Differential Pressure 0-2 ft**



**Figure 15.6.2-63 FLECHT 0791 Differential Pressure 0-4 ft**

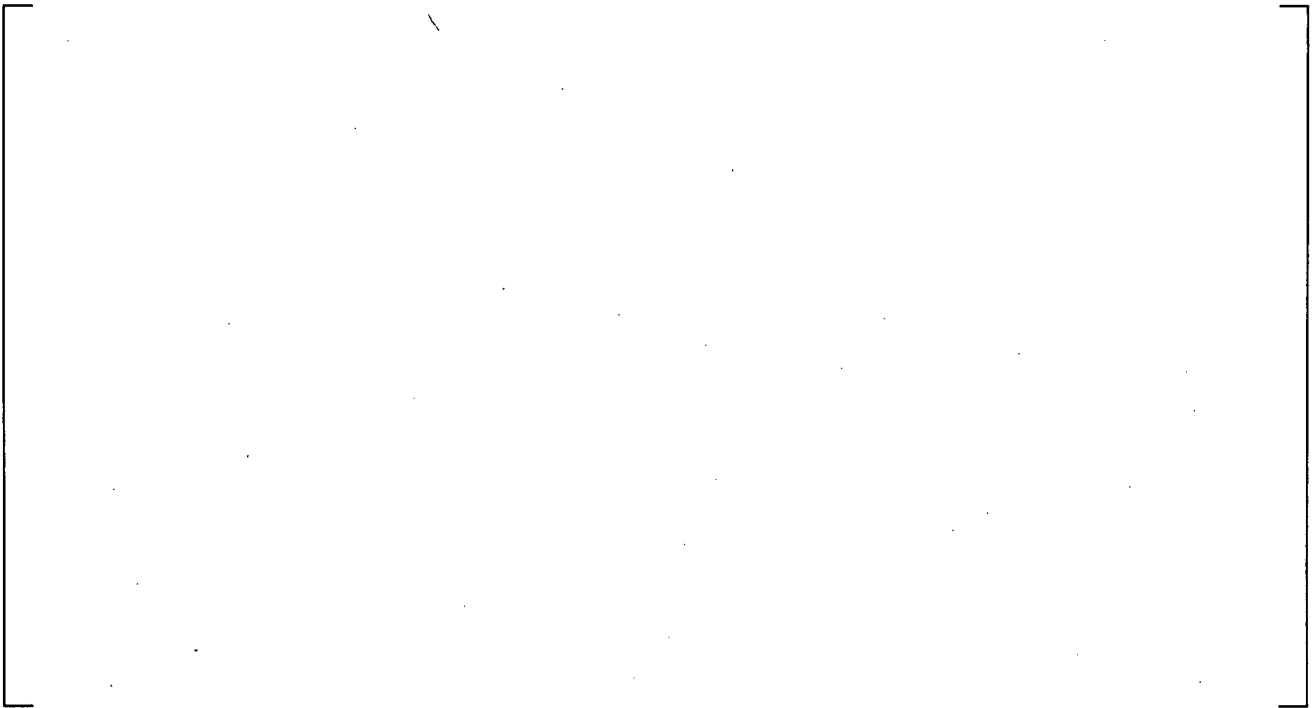


**Figure 15.6.2-64 FLECHT 0791 Differential Pressure 0-6 ft**

a,c



**Figure 15.6.2-65 FLECHT 0791 Differential Pressure 0-8 ft**

a,c



**Figure 15.6.2-66 Comparison of Predicted and Measured Clad Temperatures for FLECHT Low Flooding Rate Simulations**

### 15.6.3 WCOBRA/TRAC-TF2 Simulations of FLECHT Skewed Power Test Bundle

The FLECHT skewed power test assembly is modeled with three WCOBRA/TRAC-TF2 components. A vessel component is used to model the heated bundle, the upper plenum, and the top 6 inches of the lower plenum. Boundary conditions based on measured values were imposed on the top and the bottom of the VESSEL component. A PIPE component is attached to the top of the VESSEL, and a zero velocity FILL component is attached to the PIPE to satisfy the WCOBRA/TRAC-TF2 requirement of at least one one-dimensional component.

The VESSEL component is composed of four channels. Two channels are used to model the test section, one for the inner region (Channel 2) of the bundle and one for the outer region (Channel 3) that includes the bundle housing. The transverse noding is shown in Figure 15.6.3-1. Channel 2 is connected to Channel 3 by Gap 1. [

]<sup>a,c</sup> These rods are each modeled with a single rod model having the dimensions of the actual heater rods. The heat flux from the rod to the fluid is multiplied by the number of heater rods in the region represented by the channel to obtain the correct heat flux to the fluid. The test section housing is modeled with a tube geometry non-heated conductor that is thermally connected to the outer channel on the inside surface and is insulated on the outer surface. The WCOBRA/TRAC-TF2 axial cell lengths for the vessel are shown in Figure 15.6.3-2.

The WCOBRA/TRAC-TF2 heater rods are initialized with axial temperature profiles determined by measured temperatures at the start of reflood for each individual test. The initial temperatures for all axial levels were computed by averaging the thermocouple temperatures within a radial boundary at a given elevation. Two heater rods were inoperative during the entire transient, therefore the rod temperatures in the immediate vicinity of the unpowered rods were eliminated from the initial temperature averaging.

The housing is initialized with an axial temperature profile determined from thermocouples that were attached to the facility housing.

Both of the WCOBRA/TRAC-TF2 rods used the axial power profile shown in Figure 15.6.3-3. The housing had zero power generation.

The reflood transient is run by using measured values of the injected flow as a boundary condition imposed on the bottom of the VESSEL component. A constant pressure and enthalpy boundary condition is imposed on the top node of the VESSEL. During the transient, the heater rod power is decreased according to the ANS 1971 + 20 percent power decay curve. The simulation is continued until the cladding temperatures have peaked and begin to decrease.

Additional initial conditions are provided in Table 14.1-6 for each test and are repeated here.

Test Series	Test Number	Pressure psia	Flooding Rate in/s	Inlet Subcooling °F	Peak Power kW/ft	Comment
FLECHT SKEWED	15305	40	0.8	140	0.7	TOP SKEWED POWER SHAPE 15x15 ROD ARRAY
	13812	41	1.0	83	0.7	
	15713	40	1.0	2	0.7	
	13914	21	1.0	5	0.7	
	13609	21	1.0	141	0.7	

### 15.6.3.1 FLECHT Top-Skewed Power Results

#### 15.6.3.1.1 FLECHT Top-Skewed Power Test 15305

The reflood rate for Test 15305 was 0.8 in/sec. The test pressure was maintained at 40 psia and the injected coolant temperature was 127°F (140°F of sub-cooling). The fluid conditions for this test are very similar to those for FLECHT-SEASET Test 31805, with the main difference being the power shape. The WCOBRA/TRAC-TF2 simulation of Test 15305 was run for 800 seconds, by which time all predicted heater rod elevations had reached their peak temperature and had quenched. Figures 15.6.3-4 through 15.6.3-10 show the comparison of predicted and measured temperatures at elevations 24, 48, 72, 96, 120, 126, and 132 inches from the bottom of the heated length. The code prediction is for simulated rod temperatures in the inner channel (rod no. 1 located in Channel 2 of Figure 15.6.3-2). The curves in these figures that represent the data show the individual thermocouples located within the boundary of the WCOBRA/TRAC-TF2 inner channel. Figure 15.6.3-11 shows the prediction of the quench front elevation compared to the quench elevations deduced from temperature measurements. [

] <sup>a,c</sup>

Comparisons of the axial temperature profiles are shown in Figure 15.6.3-12 at 100 seconds, and in Figure 15.6.3-13 at 300 seconds. [

] <sup>a,c</sup>

Figures 15.6.3-15 through 15.6.3-17 show comparisons of the predicted and measured axial pressure differentials in the bundle. Figure 15.6.3-15 shows a comparison of the pressure differentials in the lower half (0 to 72 inches) of the bundle. WCOBRA/TRAC-TF2 tends to [ ] <sup>a,c</sup>. Figure 15.6.3-16 shows the comparison for the upper half (72 to 144 inches) of the bundle. As observed with the FLECHT-SEASET simulations, WCOBRA/TRAC-TF2 tends to [ ] <sup>a,c</sup>. The overall pressure differential comparison is shown in Figure 15.6.3-17.

The FLECHT facility included steam temperature probes located in the thimble tubes. Figure 15.6.3-18 shows the comparison at the 84-inch elevation, just upstream of the peak temperature location. Figure 15.6.3-19 shows the comparison at the 120-inch elevation and Figure 15.6.3-20 the comparison at

132 inches, which is near the bundle exit. [

] <sup>a,c</sup>

### 15.6.3.1.2 FLECHT Top-Skewed Power Test 13812

The reflood rate for Test 13812 was 1.0 in/sec. The test pressure was maintained at 41 psia and the injected coolant temperature was 184°F (83°F of sub-cooling). The WCOBRA/TRAC-TF2 simulation of Test 13812 was run for 800 seconds of the experiment, by which time all predicted heater rod elevations had reached their peak temperature and had quenched. Figures 15.6.3-21 through 15.6.3-27 show the comparison of predicted and measured temperatures at elevations 24, 48, 72, 96, 120, 126, and 132 inches from the bottom of the heated length. The code prediction is for simulated rod temperatures in the inner channel (rod no. 1 located in Channel 2 of Figure 15.6.3-2). The curves in these figures that represent the data show the individual thermocouples located within the boundary of the WCOBRA/TRAC-TF2 inner channel. Figure 15.6.3-28 shows the prediction of the quench front elevation compared to the quench elevations deduced from temperature measurements. [

] <sup>a,c</sup>

Comparisons of the axial temperature profiles are shown in Figure 15.6.3-29 at 100 seconds, and in Figure 15.6.3-30 at 300 seconds. [

] <sup>a,c</sup>

Figure 15.6.3-31 summarizes the comparisons of the maximum predicted peak cladding temperatures at several elevations where thermocouples were located. [

] <sup>a,c</sup>

Figures 15.6.3-32 through 15.6.3-34 show comparisons of the predicted and measured axial pressure differentials in the bundle. Figure 15.6.3-32 shows a comparison of the pressure differentials in the lower half (0 to 72 inches) of the bundle. The WCOBRA/TRAC-TF2 prediction is [

] <sup>a,c</sup>. Figure 15.6.3-33 shows the

comparison for the upper half (72 to 144 inches) of the bundle. The figure shows [

] <sup>a,c</sup>. The overall pressure differential comparison

(Figure 15.6.3-34) is seen to [

] <sup>a,c</sup>

The FLECHT top-skewed facility included steam temperature probes located in the thimble tubes.

Figure 15.6.3-35 shows the comparison at the 84-inch elevation, just upstream of the peak temperature location. Figure 15.6.3-36 shows the comparison at the 120-inch elevation, and Figure 15.6.3-37 shows the comparison at 132 inches, which is near the bundle exit. [

] <sup>a,c</sup>

### 15.6.3.1.3 FLECHT Top-Skewed Power Test 15713

The reflood rate for Test 15713 was 1.0 in/sec. The test pressure was maintained at 40 psia and the injected coolant temperature was 265°F (2°F of sub-cooling). The WCOBRA/TRAC-TF2 simulation of Test 15713 was run for 800 seconds of the experiment, by which time all heater rod elevations had reached their peak temperature and had quenched. Figures 15.6.3-38 through 15.6.3-44 show the comparison of predicted and measured temperatures at elevations 24, 48, 72, 96, 120, 126, and 132 inches from the bottom of the heated length. The code prediction is for simulated rod temperatures in the inner channel (rod no. 1 located in Channel 2 of Figure 15.6.3-2). The curves in these figures that represent the data show the individual thermocouples located within the boundary of the WCOBRA/TRAC-TF2 inner channel. Figure 15.6.3-45 shows the prediction of the quench front elevation compared to the quench elevations deduced from temperature measurements. [

] <sup>a,c</sup>

Comparisons of the axial temperature profiles are shown in Figure 15.6.3-46 at 100 seconds, and in Figure 15.6.3-47 at 300 seconds. [

] <sup>a,c</sup>

Figures 15.6.3-49 through 15.6.3-51 show comparisons of the predicted and measured axial pressure differentials in the bundle. Figure 15.6.3-49 shows a comparison of the pressure differentials in the lower half (0 to 72 inches) of the bundle. Figure 15.6.3-50 shows the comparison for the upper half (72 to 144 inches) of the bundle. [

] <sup>a,c</sup> The overall pressure differential

comparison is shown in Figure 15.6.3-51.

The FLECHT top-skewed facility included steam temperature probes located in the thimble tubes. Figure 15.6.3-52 shows the comparison at the 84-inch elevation, just upstream of the peak temperature location. Figure 15.6.3-53 shows the comparison at the 120-inch elevation, and Figure 15.6.3-54 the comparison at 132 inches, which is near the bundle exit. [

] <sup>a,c</sup>

### 15.6.3.1.4 FLECHT Top-Skewed Power Test 13914

The reflood rate for Test 13914 was 1.0 in/sec. The test pressure was maintained at 21 psia and the injected coolant temperature was 223°F (5°F of sub-cooling). The WCOBRA/TRAC simulation of Test 13914 was run past 1000 seconds, by which time all predicted heater rod elevations had reached their peak temperature and quenched. Figures 15.6.3-55 through 15.6.3-61 show the comparison of predicted and measured temperatures at elevations 24, 48, 72, 96, 120, 126, and 132 inches from the bottom of the

heated length. The code prediction is for simulated rod temperatures in the inner channel (rod no. 1 located in Channel 2 of Figure 15.6.3-2). The curves in these figures that represent the data show the individual thermocouples located within the boundary of the WCOBRA/TRAC-TF2 inner channel. Figure 15.6.3-62 shows the prediction of the quench front elevation compared to the quench elevations deduced from temperature measurements. [

] <sup>a,c</sup>

Comparisons of the axial temperature profiles are shown in Figure 15.6.3-63 at 100 seconds, and in Figure 15.6.3-64 at 300 seconds. [

] <sup>a,c</sup>

Figures 15.6.3-66 through 15.6.3-68 show comparisons of the predicted and measured axial pressure differentials in the bundle. Figure 15.6.3-66 shows a comparison of the pressure differentials in the lower half (0 to 72 inches) of the bundle. [

Figure 15.6.3-67 shows the comparison for the upper half (72 to 144 inches) of the bundle and shows [ The overall pressure differential comparison is shown in Figure 15.6.3-68. There are large oscillations in the code prediction.

The FLECHT top-skewed facility included steam temperature probes located in the thimble tubes. Figure 15.6.3-69 shows the comparison at the 84-inch elevation, just upstream of the peak temperature location. Figure 15.6.3-70 shows the comparison at the 120-inch elevation, and Figure 15.6.3-71 shows the comparison at the 132-inch elevation, which is near the bundle exit. [

] <sup>a,c</sup>

#### 15.6.3.1.5 FLECHT Top-Skewed Power Test 13609

The reflood rate for Test 13609 was 1.0 in/sec. The test pressure was maintained at 21 psia and the injected coolant temperature was 87°F (141°F of sub-cooling). The WCOBRA/TRAC-TF2 simulation of Test 13609 was run past 800 seconds, by which time all heater rod elevations had reached their peak temperature and approaching quench. Figures 15.6.3-72 through 15.6.3-78 show the comparison of predicted and measured temperatures at elevations 24, 48, 72, 96, 120, 126, and 132 inches from the bottom of the heated length. The code prediction is for simulated rod temperatures in the inner channel (rod no. 1 located in Channel 2 of Figure 15.6.3-2). The curves in these figures that represent the data show the individual thermocouples located within the boundary of the WCOBRA/TRAC-TF2 inner channel. Figure 15.6.3-79 shows the prediction of the quench front elevation compared to the quench elevations deduced from temperature measurements. [

] <sup>a,c</sup>

Comparisons of the axial temperature profiles are shown in Figure 15.6.3-80 at 100 seconds and in Figure 15.6.3-81 at 300 seconds. [

] <sup>a,c</sup>

Figure 15.6.3-82 summarizes the comparisons of the maximum predicted peak cladding temperatures at several elevations where thermocouples were located. [

] <sup>a,c</sup>

Figures 15.6.3-83 through 15.6.3-85 show comparisons of the predicted and measured axial pressure differentials in the bundle. Figure 15.6.3-83 shows a comparison of the pressure differentials in the lower half (0 to 72 inches) of the bundle. [

] <sup>a,c</sup> The overall

pressure differential comparison is shown in Figure 15.6.3-85, with [

] <sup>a,c</sup>

The FLECHT top-skewed facility included steam temperature probes located in the thimble tubes.

Figure 15.6.3-86 shows the comparison at the 84-inch elevation, just upstream of the peak temperature location. Figure 15.6.3-87 shows the comparison at the 120-inch elevation, and Figure 15.6.3-88 shows the comparison at the 132-inch elevation, which is near the bundle exit. [

] <sup>a,c</sup>

### 15.6.3.2 FLECHT Skewed Power Summary and Conclusions

Five FLECHT Top-Skewed Power Shape Tests were simulated using WCOBRA/TRAC-TF2. These tests had a power shape that was nearly 10 feet from the bottom of the heated length. This power shape is peaked at a higher elevation than most probable power shapes in an actual PWR. Thus, these tests are effectively an upper bound on the range of power shapes for full spectrum LOCA analyses. In addition, the tests had a range of inlet sub-cooling from 2°F to 141°F, a range of pressure from 20 to 40 psia, and a range of flooding rates from 0.8 in/s to 1.0 in/s.

[

] <sup>a,c</sup>

a,c

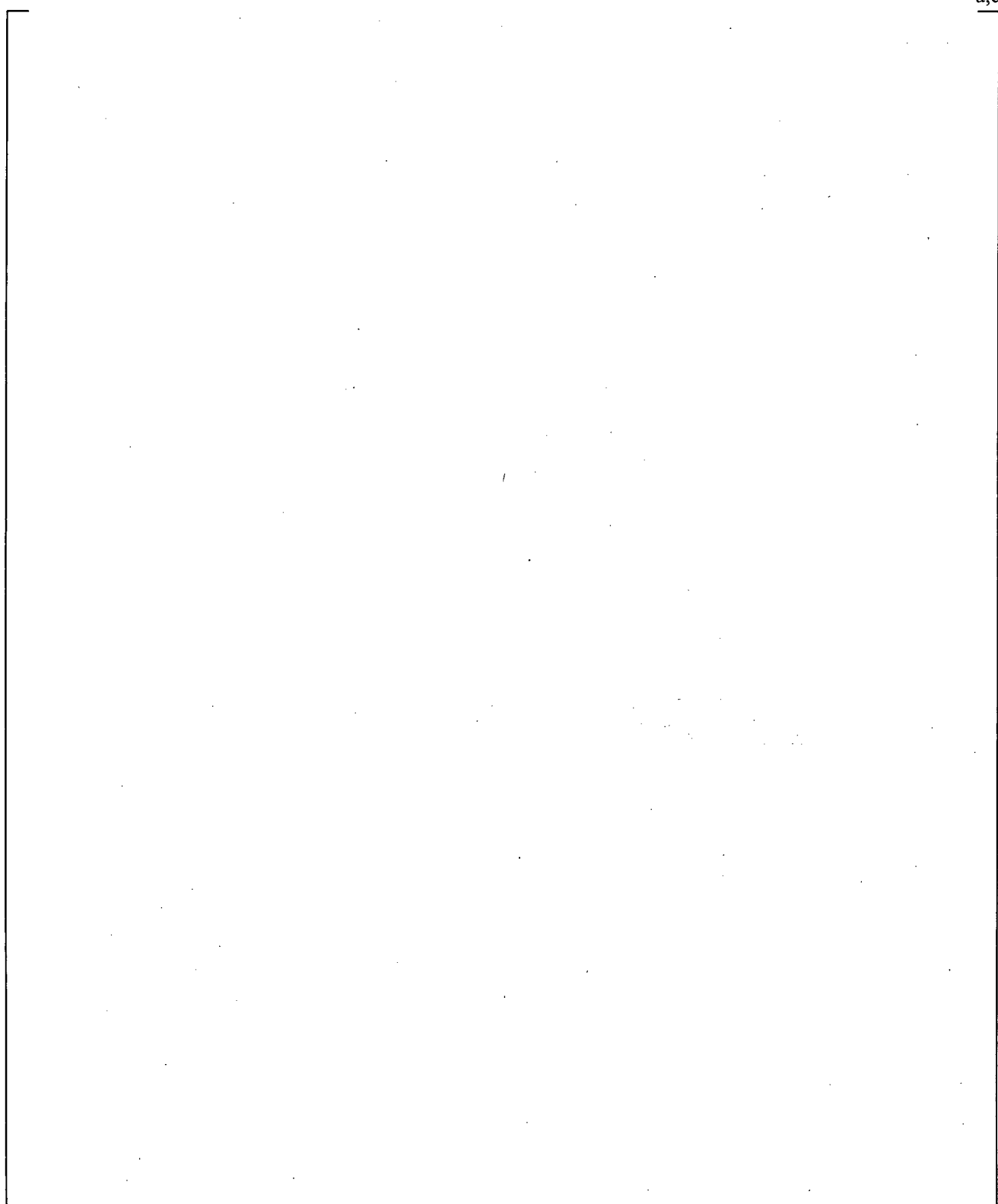


**Figure 15.6.3-1 WCOBRA/TRAC-TF2 Transverse Noding for FLECHT Top-Skewed Test Bundle**

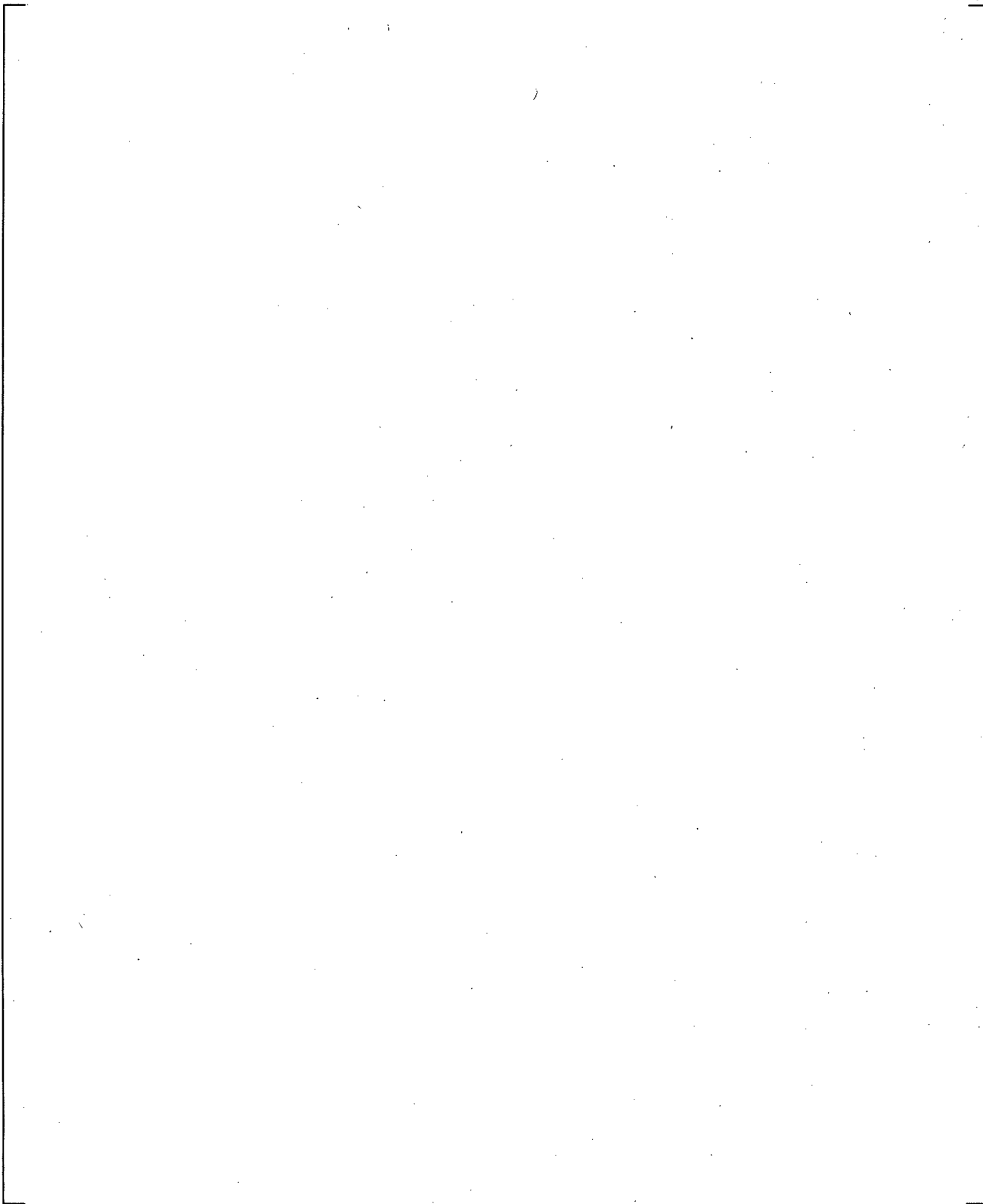
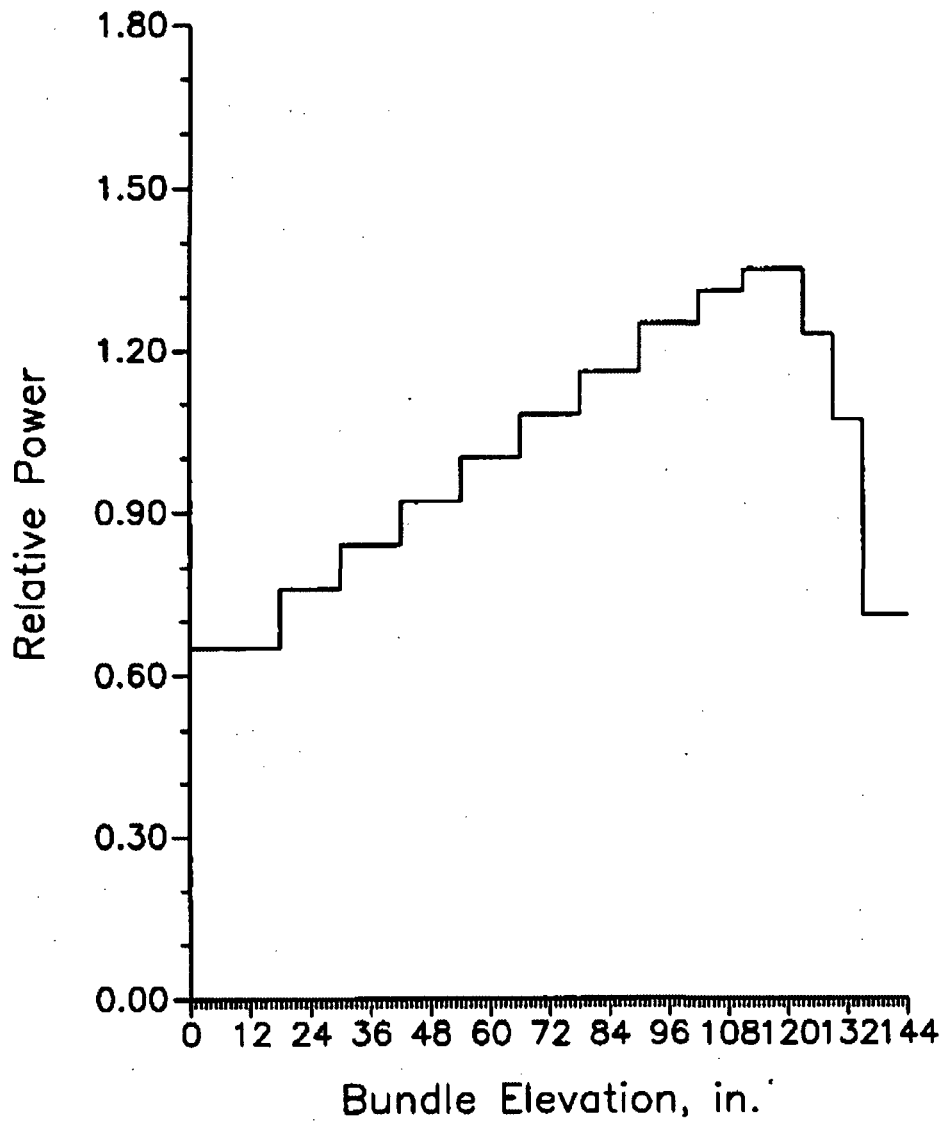


**Figure 15.6.3-2 WCOBRA/TRAC-TF2 Axial Noding for FLECHT Top-Skewed Test Bundle**

SPACER GRIDS:        G    G    G    G    G    G  
 THERMOCOUPLES:    x    x    x    x    x    x    x    x    x    x    x    x    x



**SKewed POWER AXIAL POWER SHAPE,  
 THERMOCOUPLE AND GRID LOCATIONS**

**Figure 15.6.3-3 WCOBRA/TRAC-TF2 Axial Power Shape for FLECHT Top-Skewed Test Bundle**

a,c



**Figure 15.6.3-4 FLECHT 15305 Rod Temperatures at 24-inch Elevation**

a,c



**Figure 15.6.3-5 FLECHT 15305 Rod Temperatures at 48-inch Elevation**

a,c



**Figure 15.6.3-6 FLECHT 15305 Rod Temperatures at 72-inch Elevation**

a,c



**Figure 15.6.3-7 FLECHT 15305 Rod Temperatures at 96-inch Elevation**

a,c



**Figure 15.6.3-8 FLECHT 15305 Rod Temperatures at 120-inch Elevation**

a,c



**Figure 15.6.3-9 FLECHT 15305 Rod Temperatures at 126-inch Elevation**

a,c



**Figure 15.6.3-10 FLECHT 15305 Rod Temperatures at 132-inch Elevation**

a,c

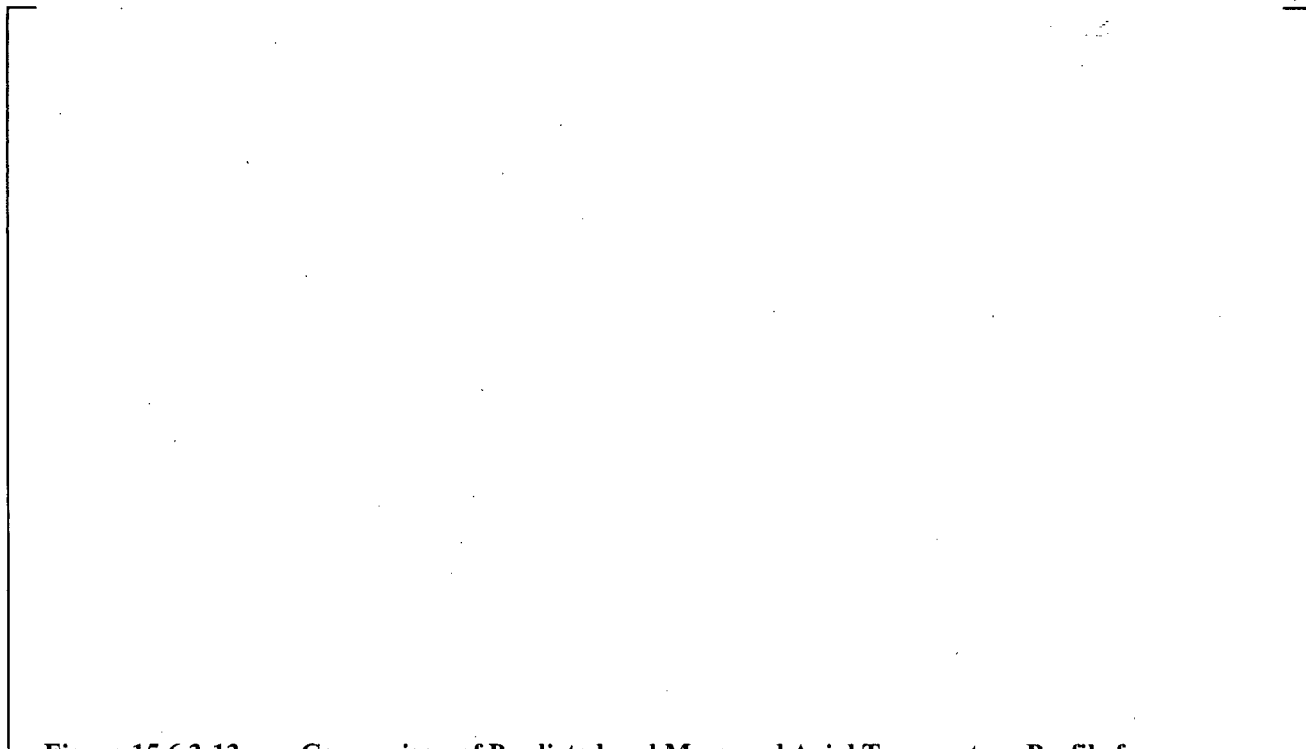


**Figure 15.6.3-11 Comparison of Predicted and Estimated Quench Front Elevations for FLECHT 15305**



a,c

**Figure 15.6.3-12 Comparison of Predicted and Measured Axial Temperature Profile for FLECHT 15305 at 100 Seconds**



a,c

**Figure 15.6.3-13 Comparison of Predicted and Measured Axial Temperature Profile for FLECHT 15305 at 300 Seconds**

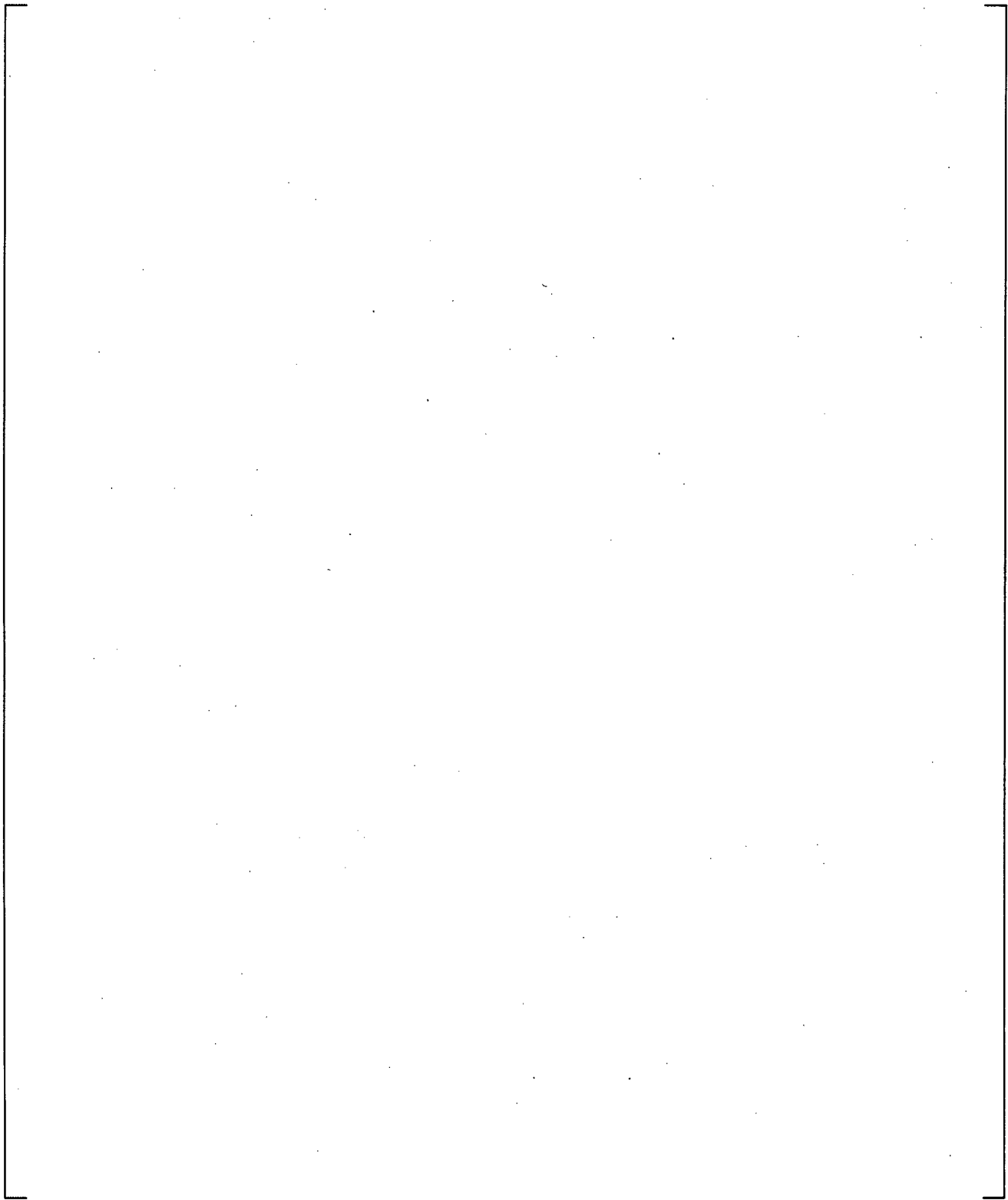


**Figure 15.6.3-14 Comparison of Predicted and Measured Maximum Cladding Temperatures at all Code Uncertainty Elevations for FLECHT 15305**

a,c



**Figure 15.6.3-15 FLECHT 15305 Bundle Lower Half  $\Delta P$**

a,c



**Figure 15.6.3-16 FLECHT 15305 Bundle Upper Half  $\Delta P$**

a,c



**Figure 15.6.3-17 FLECHT 15305 Overall  $\Delta P$**

a,c

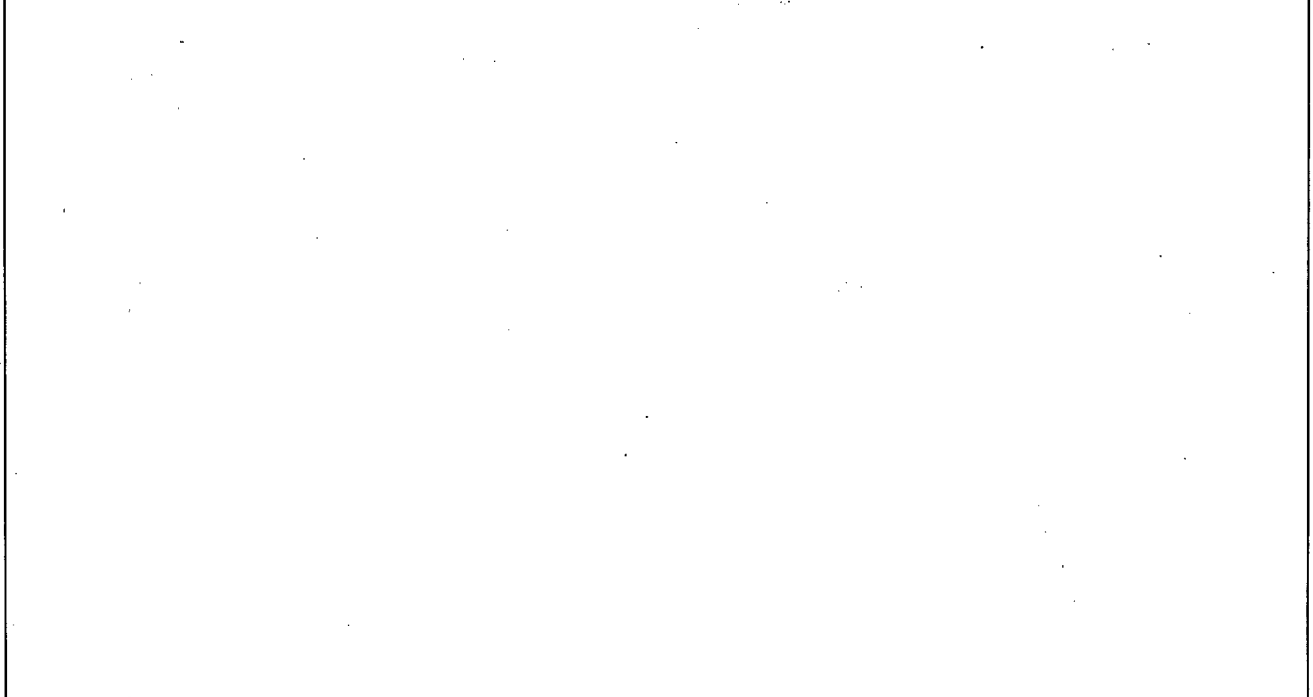


**Figure 15.6.3-18 FLECHT 15305 Vapor Temperatures at 84-inch Elevation**

a,c

**Figure 15.6.3-19 FLECHT 15305 Vapor Temperatures at 120-inch Elevation**

a,c

**Figure 15.6.3-20 FLECHT 15305 Vapor Temperatures at 132-inch Elevation**

a,c



**Figure 15.6.3-21 FLECHT 13812 Rod Temperatures at 24-inch Elevation**

a,c



**Figure 15.6.3-22 FLECHT 13812 Rod Temperatures at 48-inch Elevation**

a,c



**Figure 15.6.3-23 FLECHT 13812 Rod Temperatures at 72-inch Elevation**

a,c



**Figure 15.6.3-24 FLECHT 13812 Rod Temperatures at 96-inch Elevation**

a,c

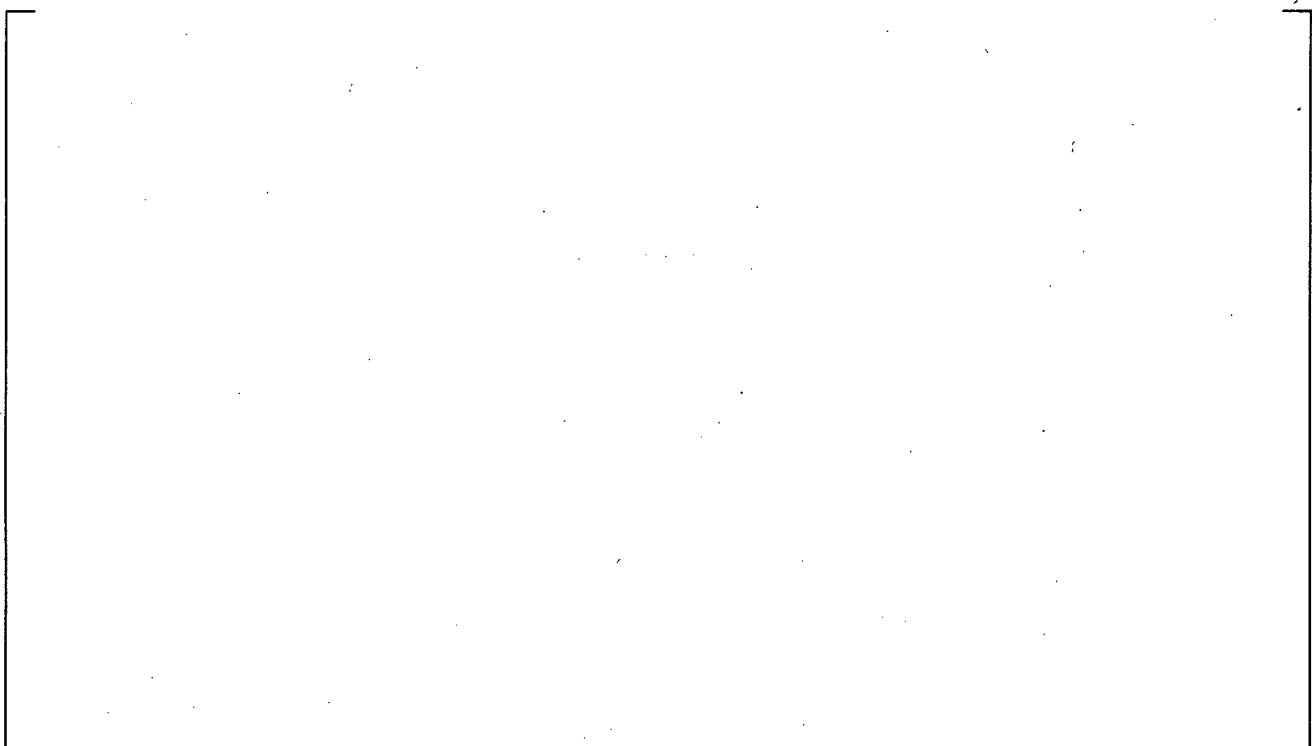


**Figure 15.6.3-25 FLECHT 13812 Rod Temperatures at 120-inch Elevation**

a,c



**Figure 15.6.3-26 FLECHT 13812 Rod Temperatures at 126-inch Elevation**

a,c



**Figure 15.6.3-27 FLECHT 13812 Rod Temperatures at 132-inch Elevation**

a,c



**Figure 15.6.3-28 Comparison of Predicted and Estimated Quench Front Elevations for FLECHT 13812**

a,c

**Figure 15.6.3-29 Comparison of Predicted and Measured Axial Temperature Profile for FLECHT 13812 at 100 Seconds**

a,c

**Figure 15.6.3-30 Comparison of Predicted and Measured Axial Temperature Profile for FLECHT 13812 at 300 Seconds**

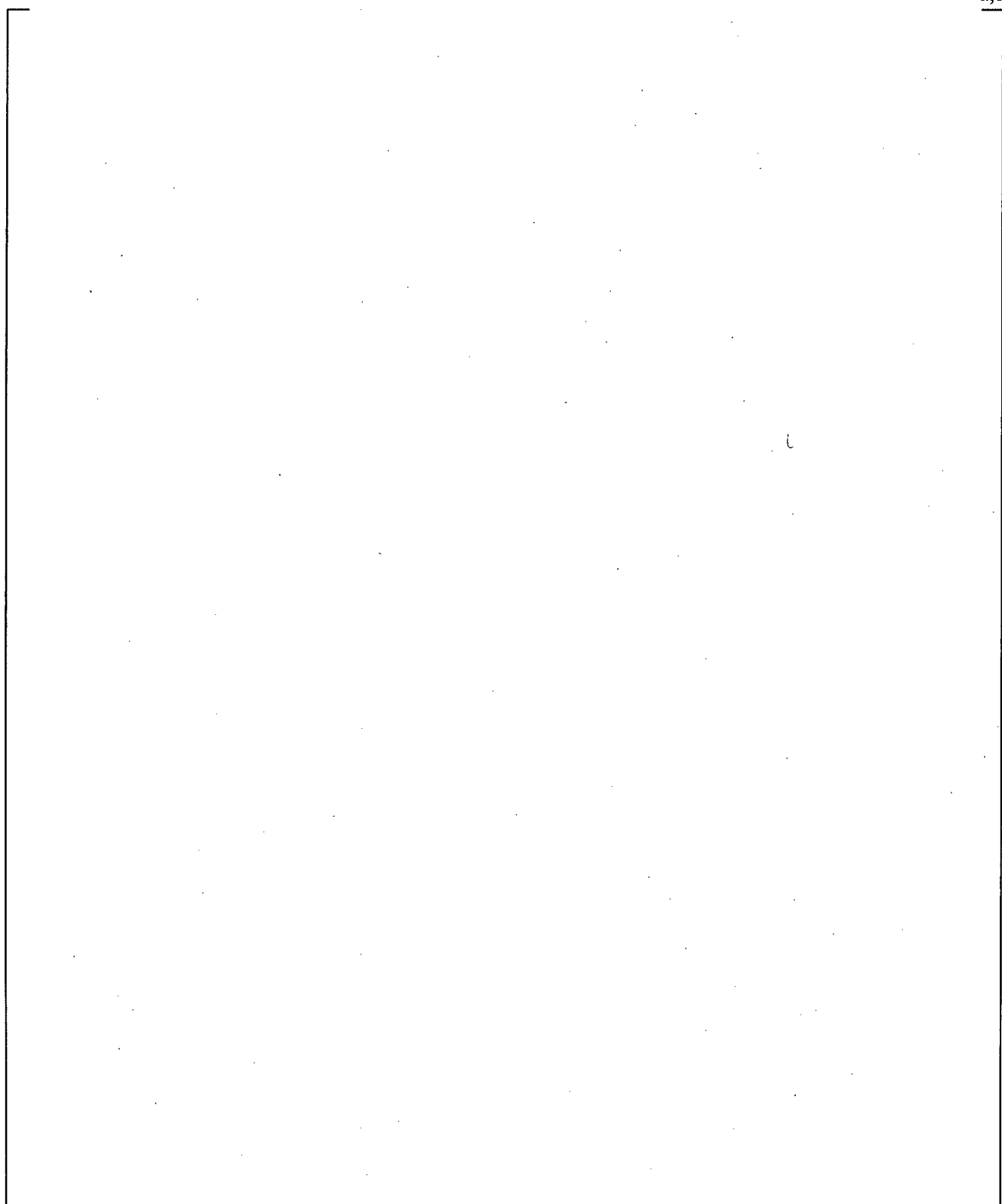


**Figure 15.6.3-31 Comparison of Predicted and Measured Maximum Cladding Temperatures at all Code Uncertainty Elevations for FLECHT 13812**

a,c



**Figure 15.6.3-32 FLECHT 13812 Bundle Lower Half  $\Delta P$**

a,c



**Figure 15.6.3-33 FLECHT 13812 Bundle Upper Half  $\Delta P$**

a,c



**Figure 15.6.3-34 FLECHT 13812 Overall  $\Delta P$**

a,c



**Figure 15.6.3-35 FLECHT 13812 Vapor Temperatures at 84-inch Elevation**



**Figure 15.6.3-36 FLECHT 13812 Vapor Temperatures near 120-inch Elevation**



**Figure 15.6.3-37 FLECHT 13812 Vapor Temperatures at 132-inch Elevation**

a,c

**Figure 15.6.3-38 FLECHT 15713 Rod Temperatures at 24-inch Elevation**

a,c

**Figure 15.6.3-39 FLECHT 15713 Rod Temperatures at 48-inch Elevation**

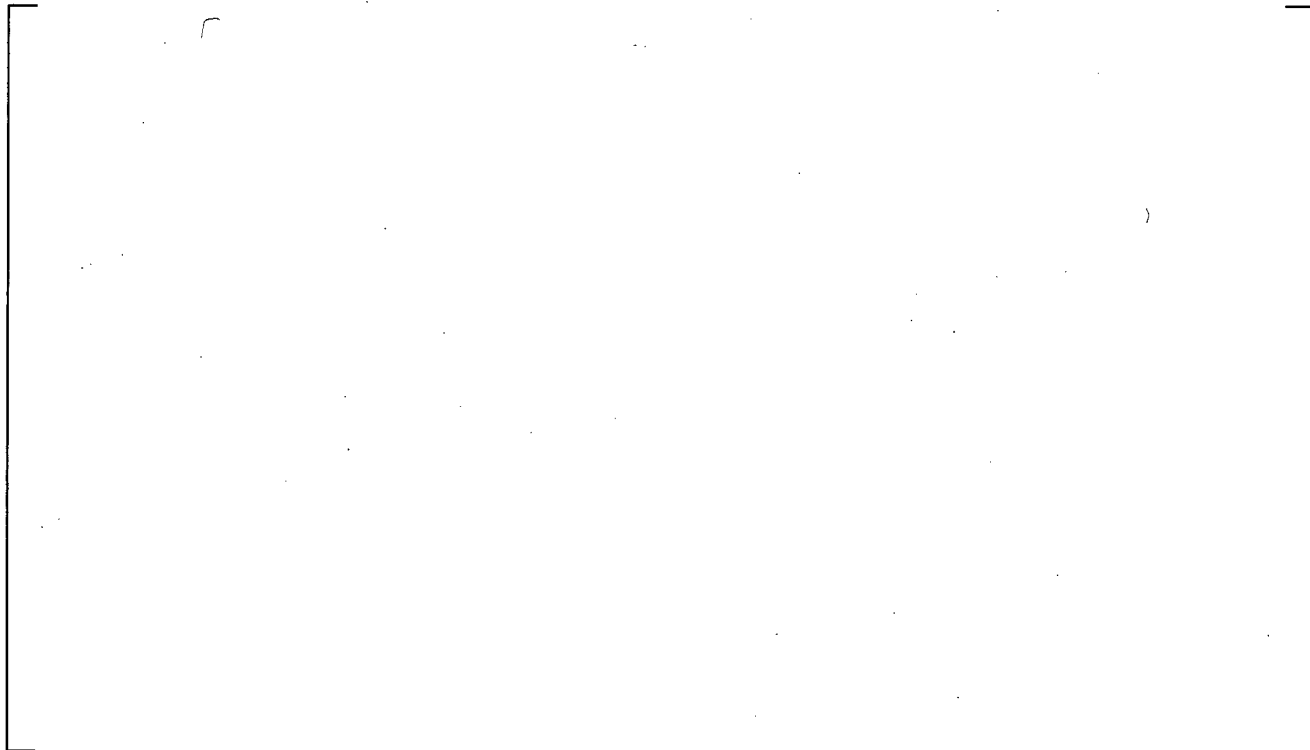


**Figure 15.6.3-40 FLECHT 15713 Rod Temperatures at 72-inch Elevation**



**Figure 15.6.3-41 FLECHT 15713 Rod Temperatures at 96-inch Elevation**

a,c



**Figure 15.6.3-42 FLECHT 15713 Rod Temperatures at 120-inch Elevation**

a,c



**Figure 15.6.3-43 FLECHT 15713 Rod Temperatures at 126-inch Elevation**

a,c

**Figure 15.6.3-44 FLECHT 15713 Rod Temperatures at 132-inch Elevation**

a,c

**Figure 15.6.3-45 Comparison of Predicted and Estimated Quench Front Elevations for FLECHT 15713**

a,c



**Figure 15.6.3-46 Comparison of Predicted and Measured Axial Temperature Profile for FLECHT 15713 at 100 Seconds**

a,c



**Figure 15.6.3-47 Comparison of Predicted and Measured Axial Temperature Profile for FLECHT 15713 at 300 Seconds**

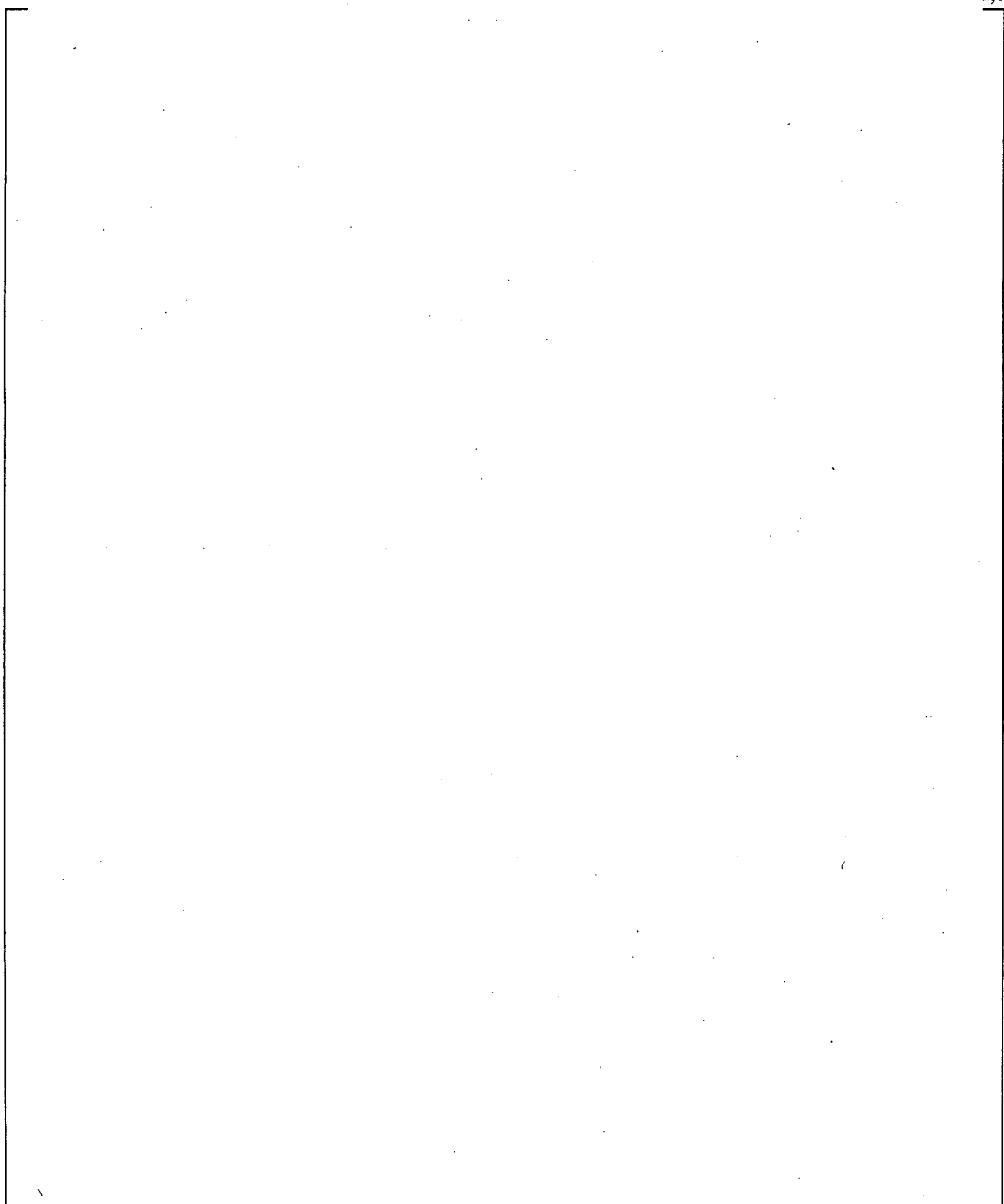


**Figure 15.6.3-48 Comparison of Predicted and Measured Maximum Cladding Temperatures at all Code Uncertainty Elevations for FLECHT 15713**

a,c

**Figure 15.6.3-49 FLECHT 15713 Bundle Lower Half  $\Delta P$**

a,c

**Figure 15.6.3-50 FLECHT 15713 Bundle Upper Half  $\Delta P$**

a,c



**Figure 15.6.3-51 FLECHT 15713 Overall  $\Delta P$**

a,c

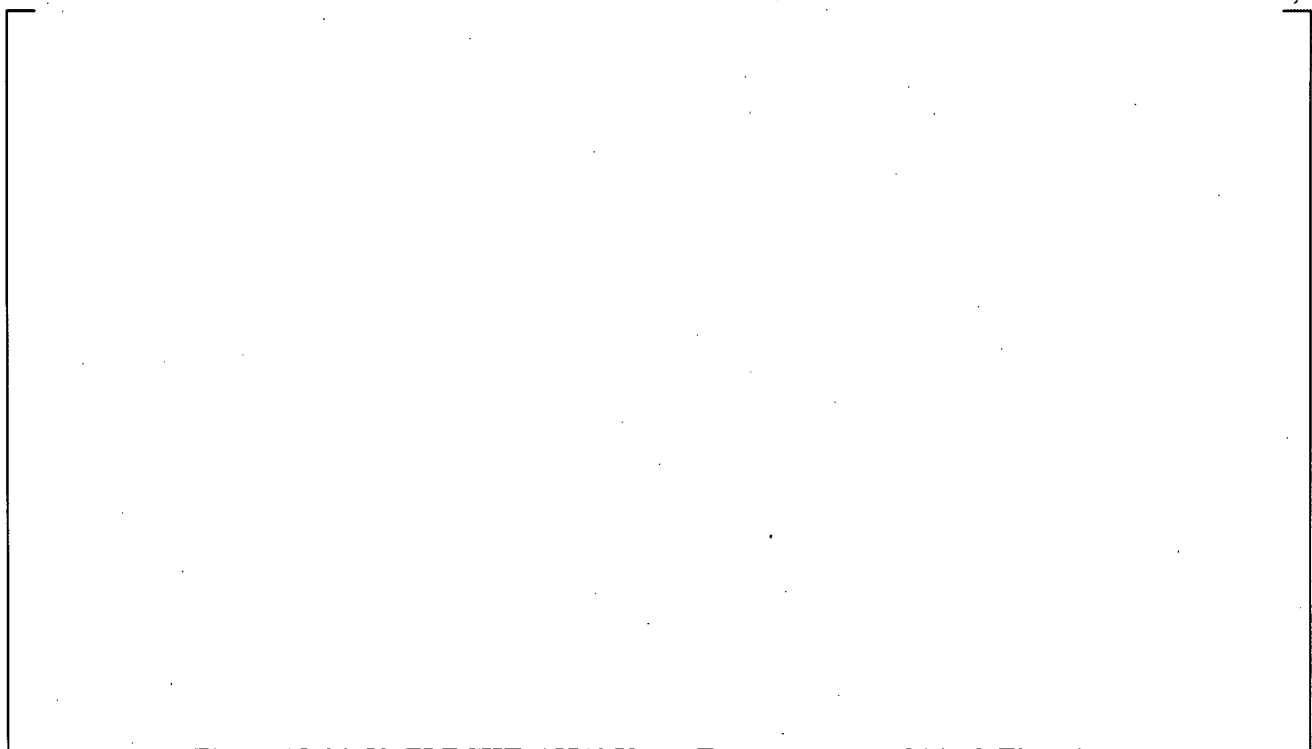


**Figure 15.6.3-52 FLECHT: 15713 Vapor Temperatures at 84-inch Elevation**

a,c



**Figure 15.6.3-53 FLECHT 15713 Vapor Temperatures near 120-inch Elevation**

a,c



**Figure 15.6.3-54 FLECHT 15713 Vapor Temperatures at 132-inch Elevation**

a,c

**Figure 15.6.3-55 FLECHT 13914 Rod Temperatures at 24-inch Elevation**

a,c

**Figure 15.6.3-56 FLECHT 13914 Rod Temperatures at 48-inch Elevation**

a,c



**Figure 15.6.3-57 FLECHT 13914 Rod Temperatures at 72-inch Elevation**

a,c



**Figure 15.6.3-58 FLECHT 13914 Rod Temperatures at 96-inch Elevation**

a,c

**Figure 15.6.3-59 FLECHT 13914 Rod Temperatures at 120-inch Elevation**

a,c

**Figure 15.6.3-60 FLECHT 13914 Rod Temperatures at 126-inch Elevation**

a,c

**Figure 15.6.3-61 FLECHT 13914 Rod Temperatures at 132-inch Elevation**

a,c

**Figure 15.6.3-62 Comparison of Predicted and Estimated Quench Front Elevations for FLECHT 13914**

a,c



**Figure 15.6.3-63 Comparison of Predicted and Measured Axial Temperature Profile for FLECHT 13914 at 100 Seconds**

a,c



**Figure 15.6.3-64 Comparison of Predicted and Measured Axial Temperature Profile for FLECHT 13914 at 300 Seconds**

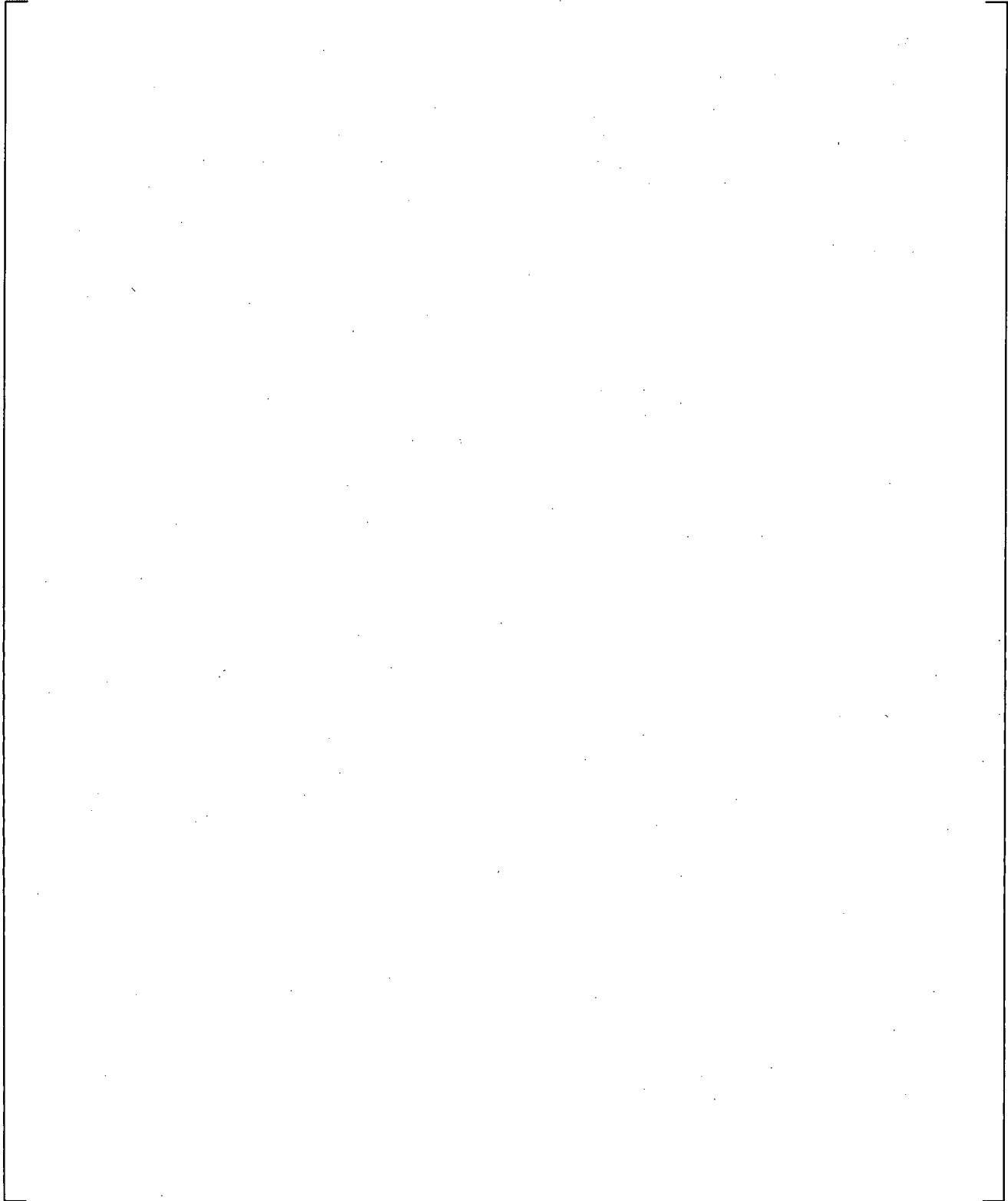


**Figure 15.6.3-65 Comparison of Predicted and Measured Maximum Cladding Temperatures at all Code Uncertainty Elevations for FLECHT 13914**

a,c



**Figure 15.6.3-66 FLECHT 13914 Bundle Lower Half  $\Delta P$**

a,c



**Figure 15.6.3-67 FLECHT 13914 Bundle Upper Half  $\Delta P$**

a,c



**Figure 15.6.3-68 FLECHT 13914 Overall  $\Delta P$**

a,c



**Figure 15.6.3-69 FLECHT 13914 Vapor Temperatures at 84-inch Elevation**

a,c

**Figure 15.6.3-70 FLECHT 13914 Vapor Temperatures at 120-inch Elevation**

a,c

**Figure 15.6.3-71 FLECHT 13914 Vapor Temperatures at 132-inch Elevation**

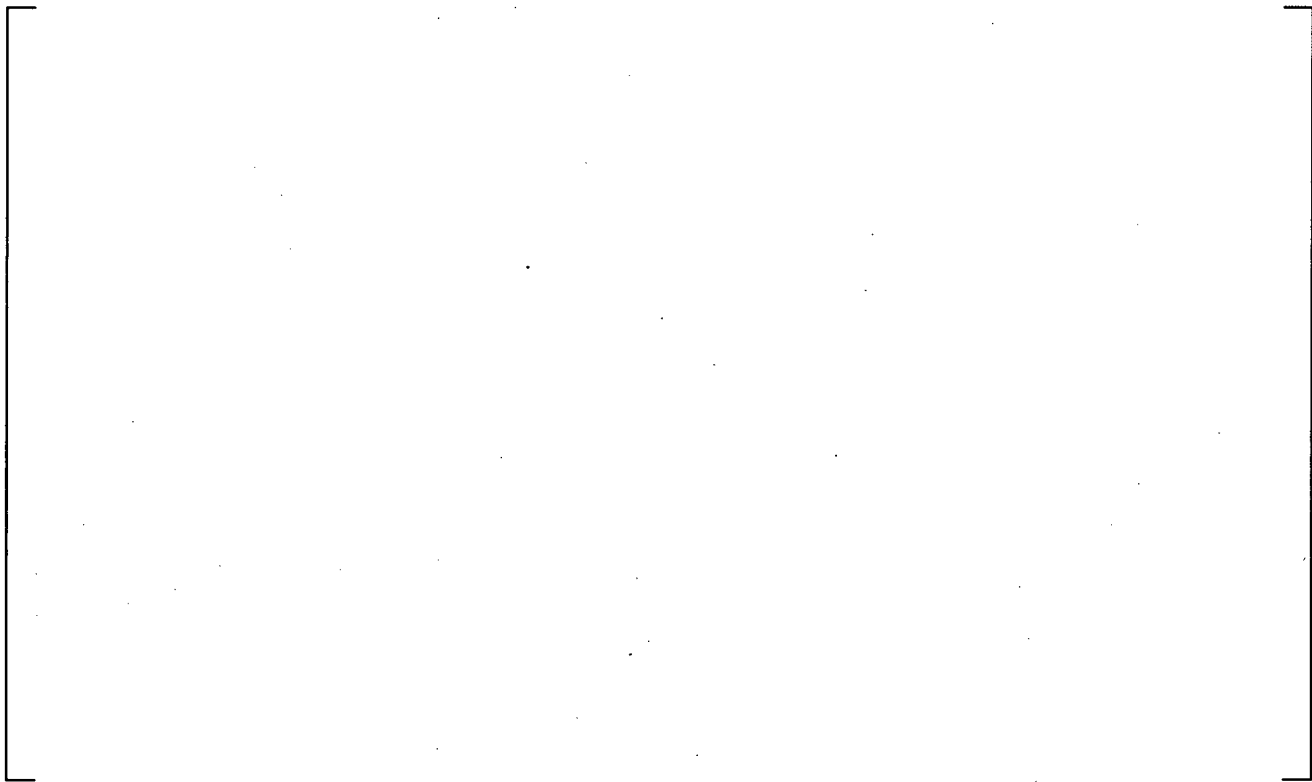


**Figure 15.6.3-72 FLECHT 13609 Rod Temperatures at 24-inch Elevation**



**Figure 15.6.3-73 FLECHT 13609 Rod Temperatures at 48-inch Elevation**

a,c

**Figure 15.6.3-74 FLECHT 13609 Rod Temperatures at 72-inch Elevation**

a,c

**Figure 15.6.3-75 FLECHT 13609 Rod Temperatures at 96-inch Elevation**

a,c

**Figure 15.6.3-76 FLECHT 13609 Rod Temperatures at 120-inch Elevation**

a,c

**Figure 15.6.3-77 FLECHT 13609 Rod Temperatures at 126-inch Elevation**

a,c



**Figure 15.6.3-78 FLECHT 13609 Rod Temperatures at 132-inch Elevation**

a,c



**Figure 15.6.3-79 Comparison of Predicted and Estimated Quench Front Elevations for FLECHT 13609**

a,c



**Figure 15.6.3-80 Comparison of Predicted and Measured Axial Temperature Profile for FLECHT 13609 at 100 Seconds**

a,c

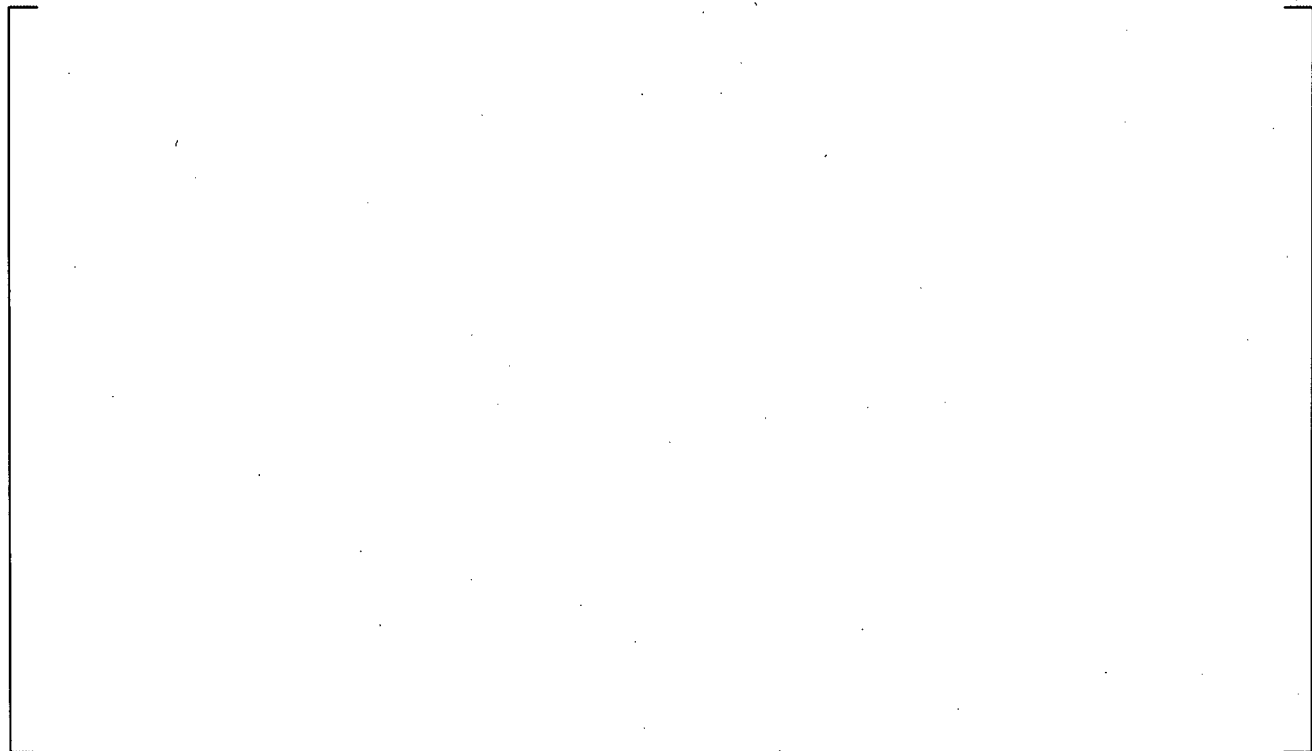


**Figure 15.6.3-81 Comparison of Predicted and Measured Axial Temperature Profile for FLECHT 13609 at 300 Seconds**

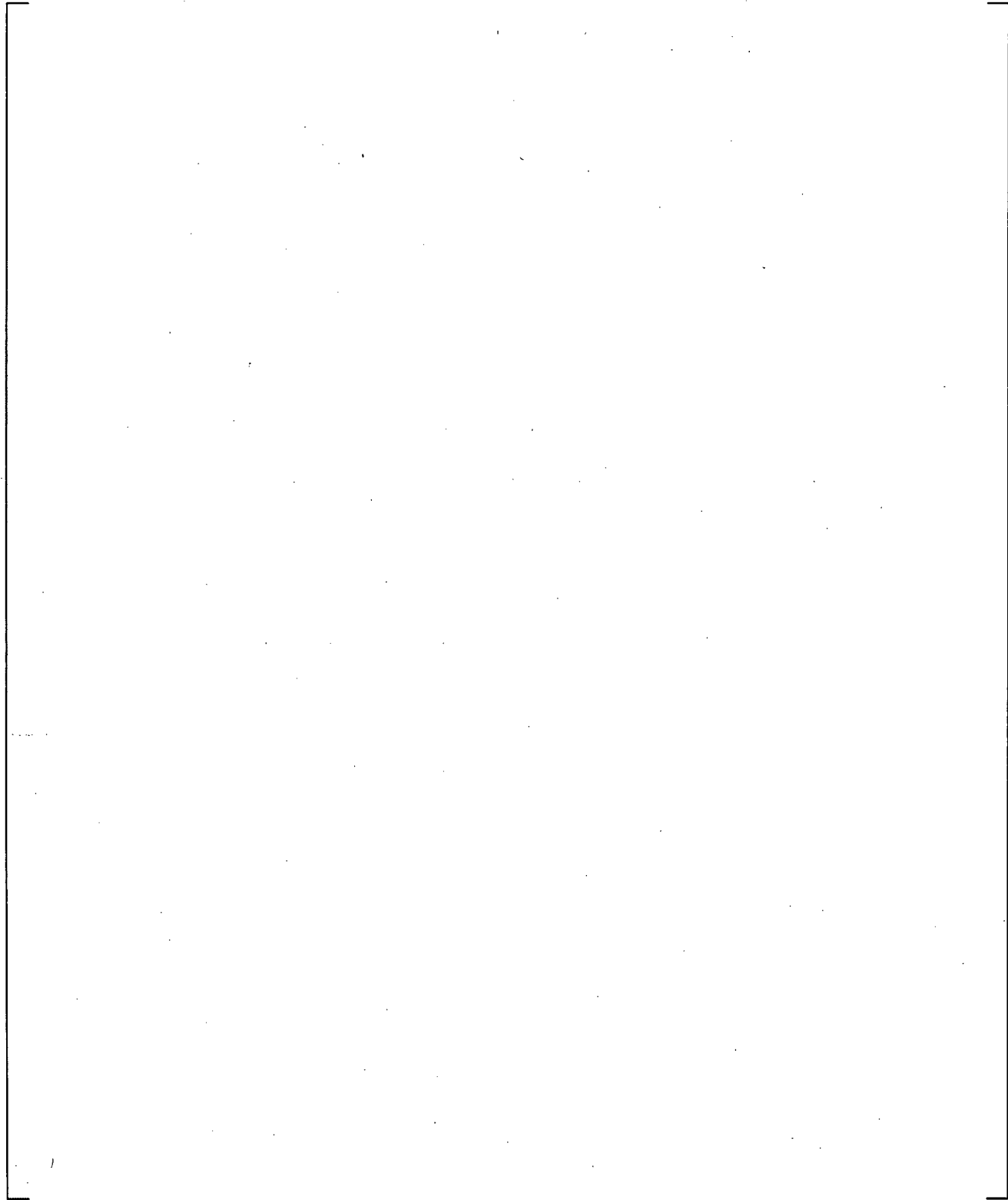


**Figure 15.6.3-82 Comparison of Predicted and Measured Maximum Cladding Temperatures at all Code Uncertainty Elevations for FLECHT 13609**

a,c

**Figure 15.6.3-83 FLECHT 13609 Bundle Lower Half  $\Delta P$**

a,c

**Figure 15.6.3-84 FLECHT 13609 Bundle Upper Half  $\Delta P$**

a,c



**Figure 15.6.3-85 FLECHT 13609 Overall  $\Delta P$**

a,c



**Figure 15.6.3-86 FLECHT 13609 Vapor Temperatures at 84-inch Elevation**

a,c

**Figure 15.6.3-87 FLECHT 13609 Vapor Temperatures at 120-inch Elevation**

a,c

**Figure 15.6.3-88 FLECHT 13609 Vapor Temperatures at 132-inch Elevation**

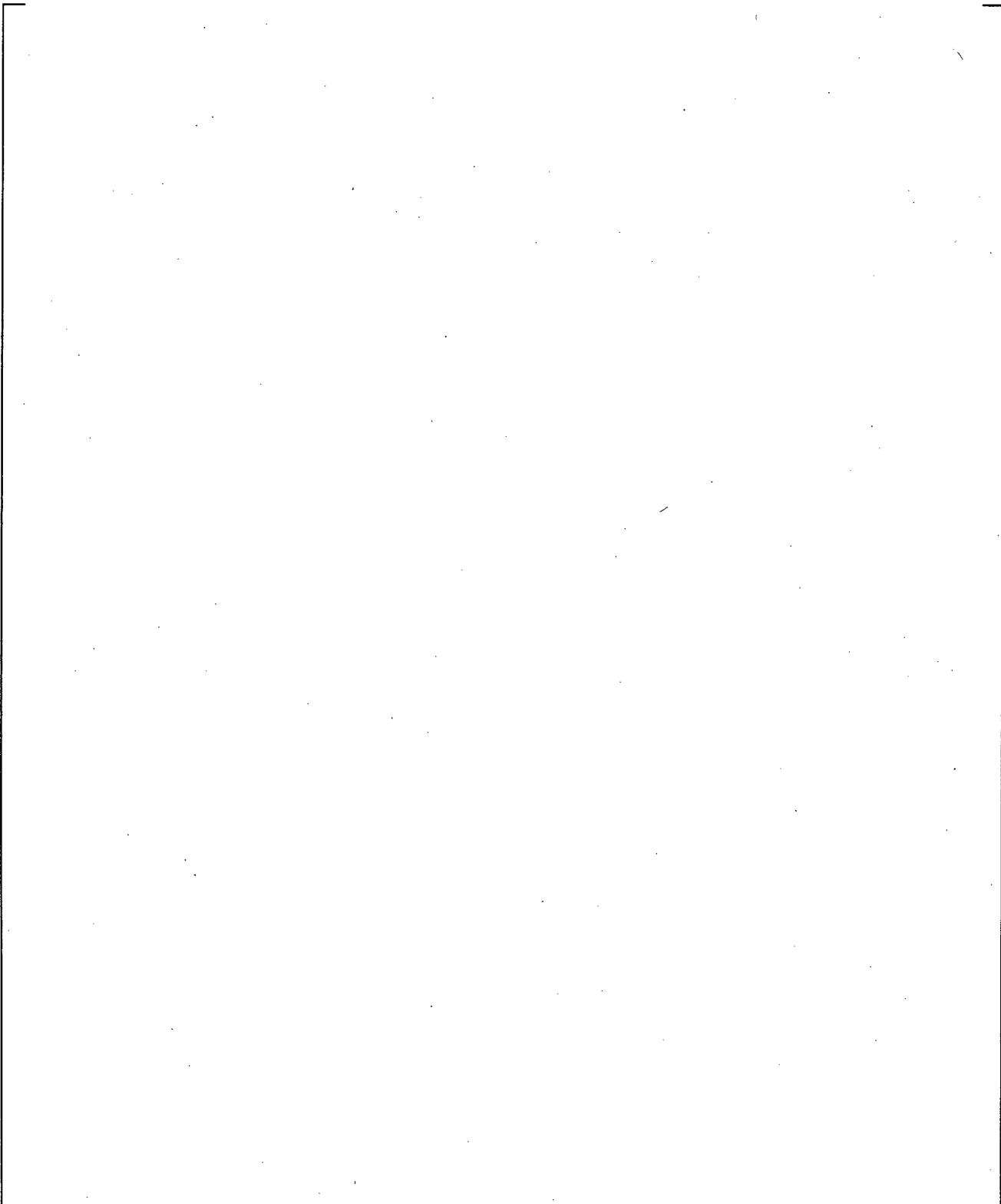


**Figure 15.6.3-89 Comparison of Predicted and Measured Maximum Clad Temperatures for FLECHT Top-Skewed Power Test Simulations**

### 15.6.4 WCOBRA/TRAC-TF2 Simulations of G-2 Reflood Test Bundle

The WCOBRA/TRAC-TF2 model of the G-2 reflood test bundle used the same level of detail as was used for other separate effects test simulations. This model consisted of three components: a VESSEL, a PIPE component, and a zero velocity FILL component. A schematic diagram of the model is shown in Figures 15.6.4-1 and 15.6.4-2.

The reflood flow into the lower plenum is provided as a vessel boundary condition in Section 1 of the VESSEL component. Section 3, shown in Figure 15.6.4-1, models the heated length of the test section with two channels: Channel 4 represents the flow around the outer heater rods and Channel 3 represents the flow in the central portion of the rod bundle. (The bundle is representative of a 14-ft, 17x17 assembly in a PWR.) The G-2 reflood tests had a radial power distribution for these experiments. The outer channel grouped together the outer, lower power rods, while the region containing the higher power rods in the bundle center was modeled as the inner channel. Figure 15.6.4-3 shows the radial power zones for the bundle and the grouping of the heater rods for the two channels in WCOBRA/TRAC-TF2. The fluid nodes are thermally connected to rods simulating the heater rods. Loss coefficients are used to model the seven mixing vane grids of the fuel assembly in the inner and outer portions of the rod bundle which are representative of Westinghouse mixing vane grids. Section 4 (Channel 5) models the ground plate, which also has a loss coefficient. Section 5 (Channel 6) represented the upper plenum.

[

] <sup>a,c</sup>

Additional initial conditions are provided in Table 14.1-6 for each test and are repeated here.

Test Series	Test Number	Pressure psia	Flooding Rate in/s	Inlet Subcooling °F	Peak Power kW/ft	Comment

] <sup>a,c</sup>

#### 15.6.4.1 G-2 Reflood Results

##### 15.6.4.1.1 G-2 Reflood Test 550

The reflood rate for Test 550 was 1.0 in/sec. The test pressure was maintained at 40 psia and the injected coolant temperature was 150°F (116°F of sub-cooling). The WCOBRA/TRAC-TF2 simulation of Test 550 was run for the first 500 seconds of the experiment, by which time all heater rod elevations had reached their maximum temperatures and had started to decline.

Figures 15.6.4-4 through 15.6.4-10 show the comparison of predicted and measured temperature histories at elevations 29, 45, 70, 82, 94, 111, and 135 inches from the bottom of the heated length. The time is after the start of reflood and start of decrease of bundle power. The code prediction is for simulated cladding temperatures in the inner channel (rod no. 1 located in Channel 3 of Figure 15.6.4-1). The data curves in these figures are all of the valid thermocouples located within the boundary of the

WCOBRA/TRAC-TF2 inner channel. [ ]<sup>a,c</sup>

Comparison of the axial temperature profiles are shown in Figures 15.6.4-11 through 15.6.4-13 at the [

] <sup>a,c</sup>

Figures 15.6.4-14 through 15.6.4-16 show comparisons of the predicted and measured axial pressure differentials in the bundle. Figure 15.6.4-14 shows a comparison of the pressure differential in the lower half of the bundle (27.3 to 82 inches). [

] <sup>a,c</sup> The overall bundle pressure differential comparison (27.3 to 136.7 inches) is shown in Figure 15.6.4-16.

The G-2 facility included steam temperature probes in the thimble tubes located at several elevations in the bundle. Figure 15.6.4-17 shows a comparison of predicted and measured steam temperatures at the 109-inch elevation. Figure 15.6.4-18 shows the comparison at the 136.7-inch elevation. [

] <sup>a,c</sup>

Figure 15.6.4-19 shows a comparison of predicted and measured maximum clad temperatures reached at all of the 12 elevations measured. The measured values are the maximum of all valid thermocouple temperatures in the inner region. [

] <sup>a,c</sup>

#### 15.6.4.1.2 G-2 Reflood Test 562

The reflood rate for Test 562 was 1.0 in/sec. The test pressure was maintained at 20 psia and the injected coolant temperature was 117°F (110°F of sub-cooling). The WCOBRA/TRAC-TF2 simulation of Test 562 was run for the first 500 seconds of the experiment, by which time all heater rod elevations had reached their peak and had started to decline.

Figures 15.6.4-20 through 15.6.4-26 show the comparison of predicted and measured temperature histories at elevations 29, 45, 70, 82, 94, 111, and 135 inches from the bottom of the heated length. The code prediction is for heater rods within the inner channel (rod no. 1 located in Channel 3 of Figure 15.6.4-1). The data curves in these figures are all valid thermocouples located within the boundary of the WCOBRA/TRAC-TF2 inner channel. [

] <sup>a,c</sup>

Comparison of the axial temperature profiles are shown in Figures 15.6.4-27 through 15.6.4-29 at times before, near, and after the occurrence of the peak average clad temperature, respectively. [

] <sup>a,c</sup>

Figures 15.6.4-30 through 15.6.4-32 show comparisons of the predicted and measured axial pressure differentials in the bundle. Figure 15.6.4-30 shows a comparison of the pressure differential in the lower half of the bundle (27.3 to 82 inches), where [

] <sup>a,c</sup>

Figure 15.6.4-31 shows the comparison for the upper half of the bundle (82 to 136.7 inches), which [ <sup>a,c</sup> The overall bundle pressure differential comparison (27.3 to 136.7 inches) is shown in Figure 15.6.4-32.

The G-2 facility included steam temperature probes in the thimble tubes located at several locations in the bundle. Figure 15.6.4-33 shows a comparison of predicted and measured steam temperatures at the 109-inch elevation. Figure 15.6.4-34 shows the comparison at the 136.7-inch elevation. [

] <sup>a,c</sup>

Figure 15.6.4-35 shows a comparison of predicted and measured maximum clad temperatures reached at all of the 12 elevations measured. The measured values are the maximum of all valid thermocouple temperatures in the inner region. [

] <sup>a,c</sup>

### 15.6.4.1.3 G-2 Reflood Test 568

The reflood rate for Test 568 was 1.00 in/sec. The test pressure was maintained at 40 psia and the injected coolant temperature was 150°F (117°F of sub-cooling). The WCOBRA/TRAC-TF2 simulation of Test 568 was run for the first 500 seconds of the experiment, by which time all heater rod elevations had reached their peak and had started to decline.

Figures 15.6.4-36 through 15.6.4-42 show the comparison of predicted and measured temperature histories at elevations 29, 45, 70, 82, 94, 111, and 135 inches from the bottom of the heated length. The code prediction is for heater rods within the inner channel (rod no. 1 located in Channel 3 of Figure 15.6.4-43). The data curves in these figures are all of the valid thermocouples located within the boundary of the WCOBRA/TRAC-TF2 inner channel. [

] <sup>a,c</sup>

Comparison of the axial temperature profiles are shown in Figures 15.6.4-43 through 15.6.4-45 at times before, near, and after the occurrence of the peak average clad temperature, respectively. [

] <sup>a,c</sup>

Figures 15.6.4-46 through 15.6.4-48 show comparisons of the predicted and measured axial pressure differentials in the bundle. Figure 15.6.4-46 shows a comparison of the pressure differential in the lower half of the bundle (27.3 to 82 inches) where [ ]<sup>a,c</sup>  
 Figure 15.6.4-47 shows the comparison for the upper half of the bundle (82 to 136.7 inches), which [ ]<sup>a,c</sup>  
 The overall bundle pressure differential comparison (27.3 to 136.7 inches) is shown in Figure 15.6.4-48.

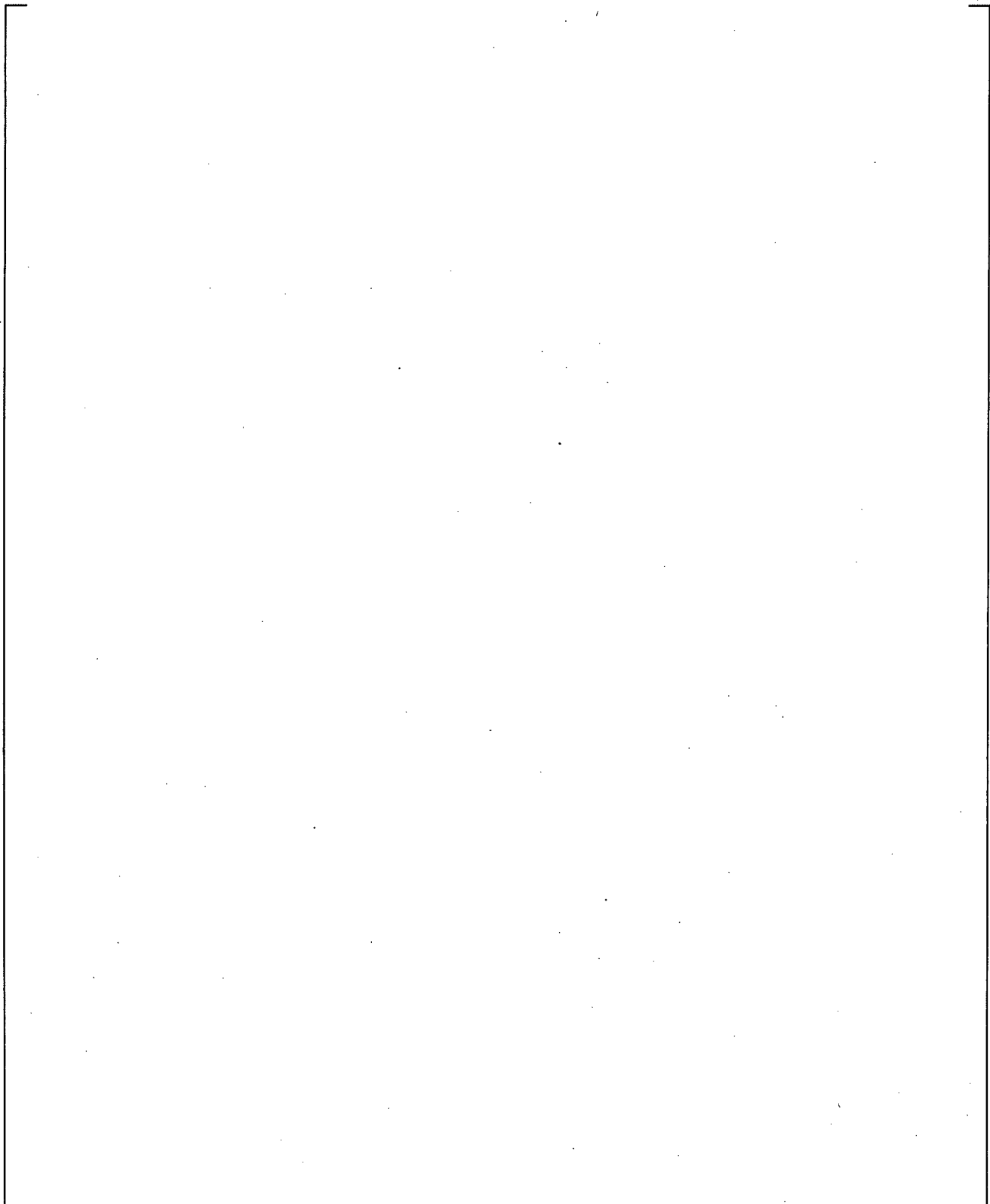
The G-2 facility included steam temperature probes in the thimble tubes located at several locations in the bundle. Figure 15.6.4-49 shows a comparison of predicted and measured steam temperatures at the 109-inch elevation. Figure 15.6.4-50 shows the comparison at the 136.7-inch elevation. [ ]<sup>a,c</sup>

Figure 15.6.4-51 shows a comparison of predicted and measured maximum clad temperatures reached at all of the 12 elevations measured. The measured values are the maximum of all valid thermocouple temperatures in the inner region. [ ]<sup>a,c</sup>

#### 15.6.4.2 G-2 Reflood Tests Simulation Summary and Conclusions

Three G-2 reflood tests were simulated with WCOBRA/TRAC-TF2. [ ]<sup>a,c</sup>

The predicted maximum clad temperatures were [ ]<sup>a,c</sup>  
 Figure 15.6.4-52 shows the comparison of predicted and measured maximum temperatures for all three G-2 test simulations. [ ]<sup>a,c</sup>



**Figure 15.6.4-1 WCOBRA/TRAC-TF2 Axial Noding for G-2 Reflood Simulations**

a,c

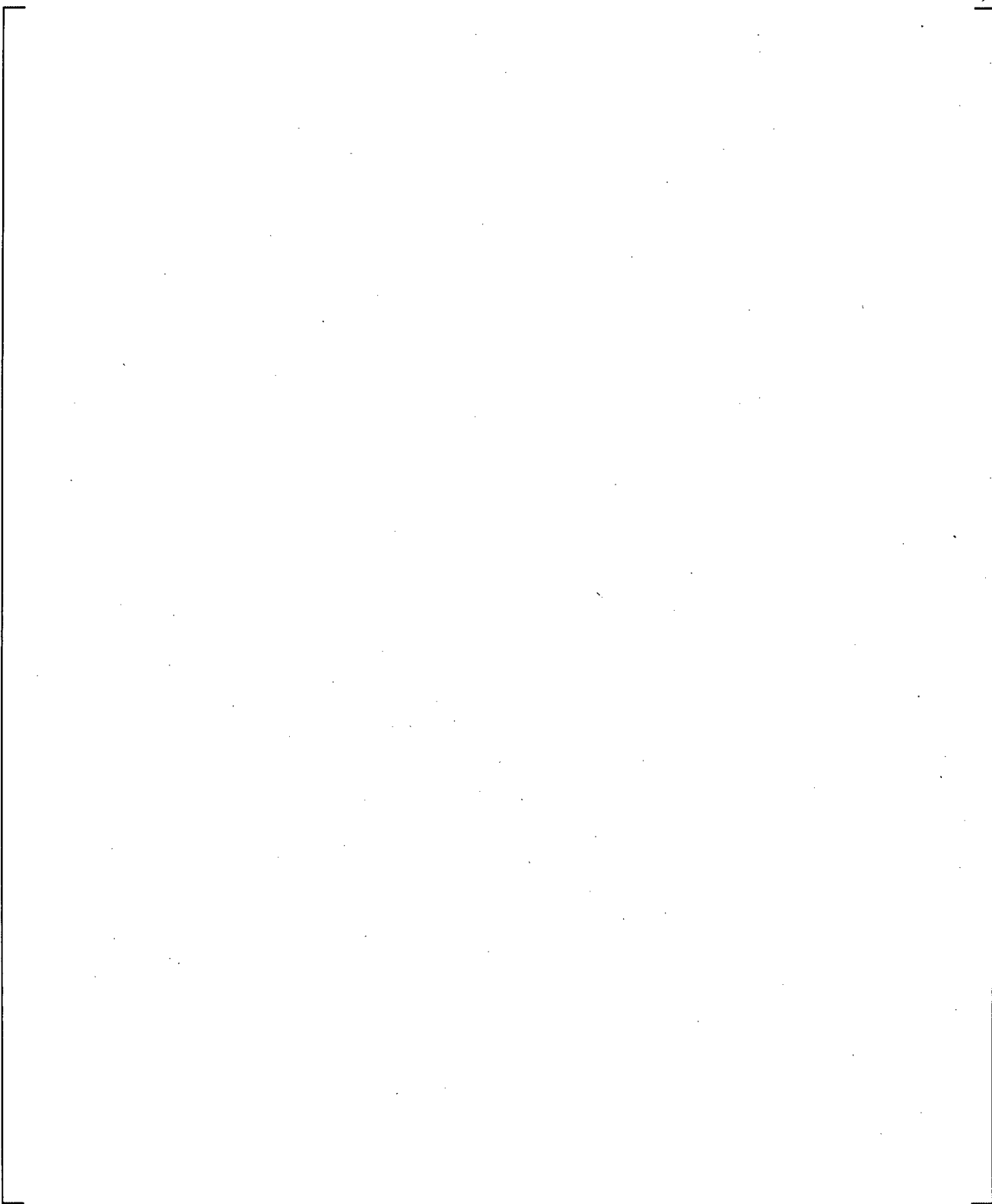


**Figure 15.6.4-2 WCOBRA/TRAC-TF2 Transverse Noding for G-2 Reflood Simulations**

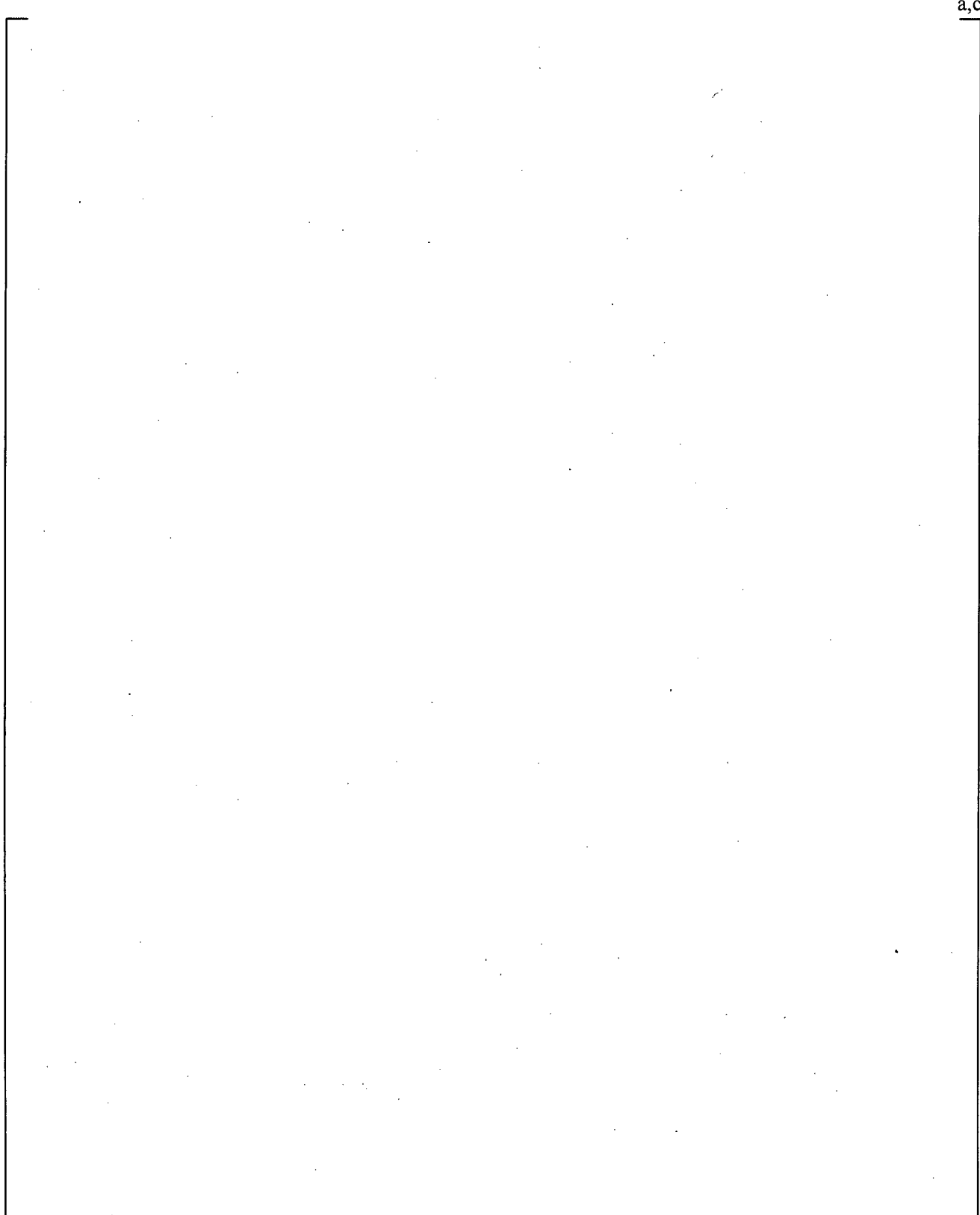


**Figure 15.6.4-3 G-2 Bundle Cross Section**

a,c

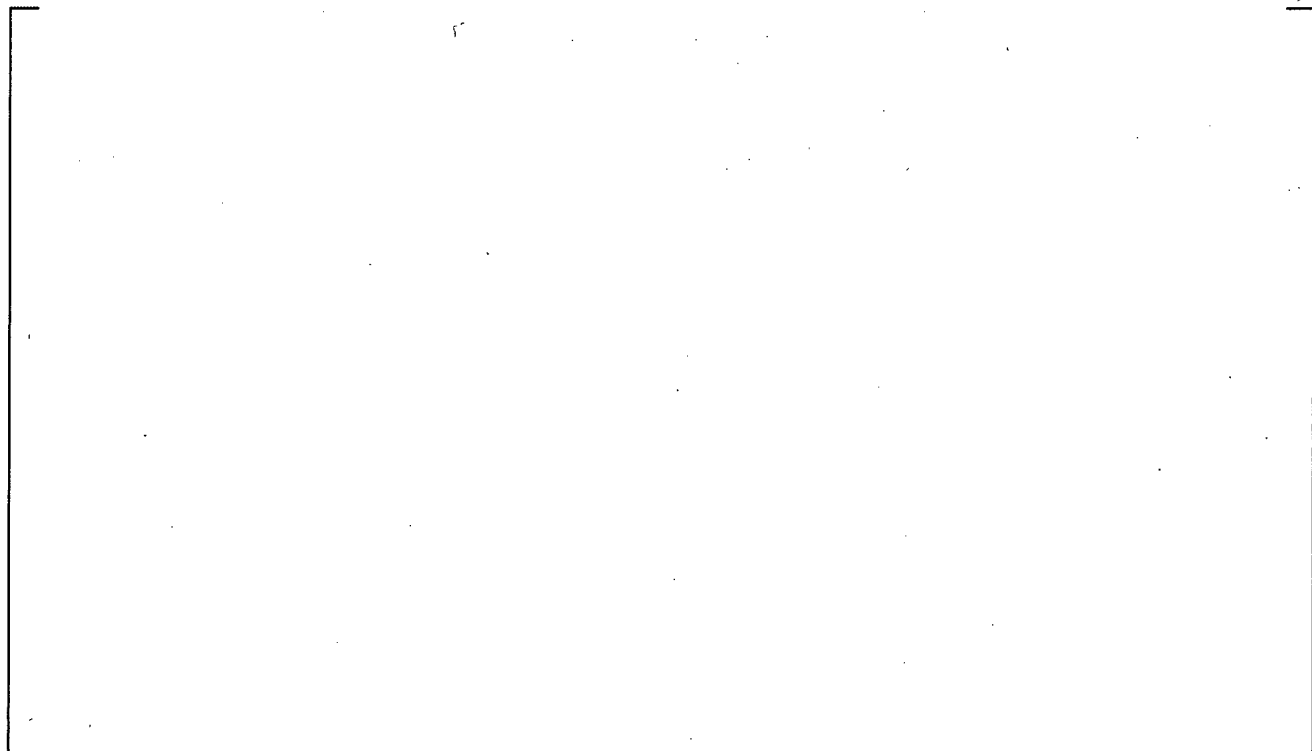


**Figure 15.6.4-4 G-2 Reflood Test 550 Rod Temperatures at 29-inch Elevation**

a,c

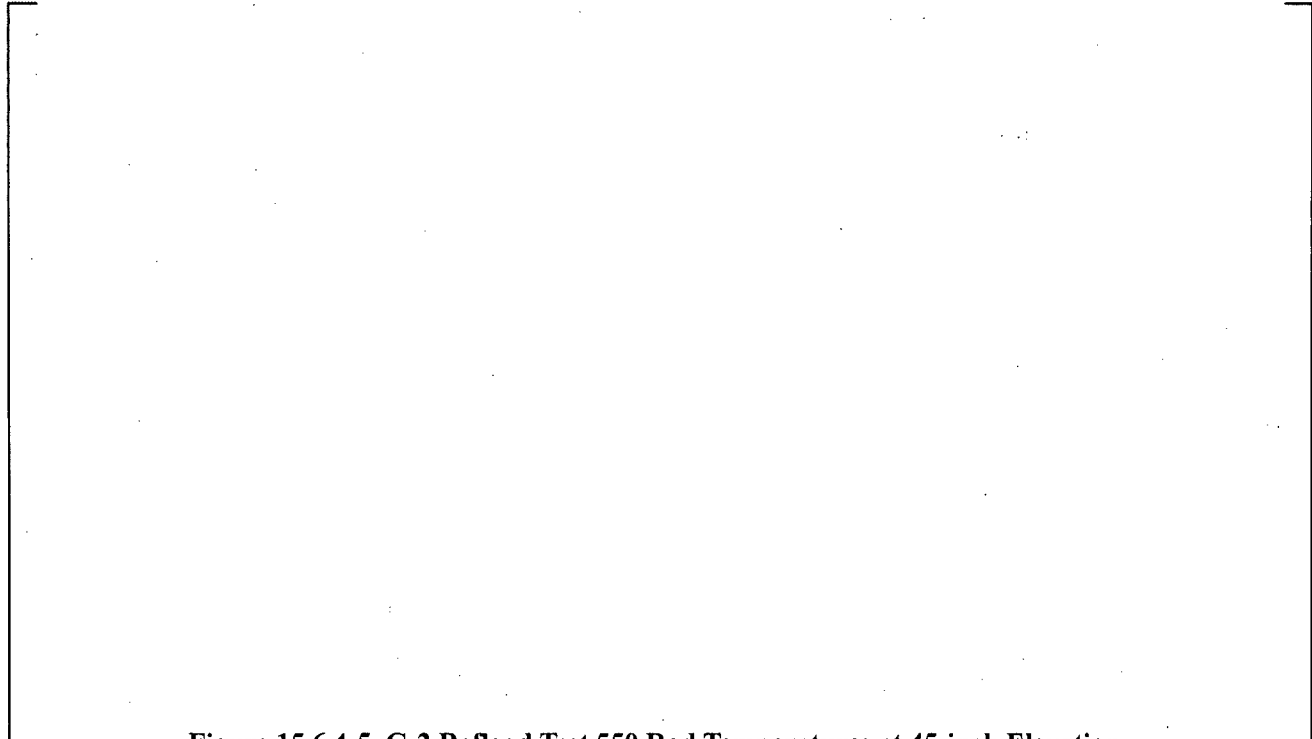


**Figure 15.6.4-5 G-2 Reflood Test 550 Rod Temperatures at 45-inch Elevation**



**Figure 15.6.4-6 G-2 Reflood Test 550 Rod Temperatures at 70-inch Elevation**



**Figure 15.6.4-7 G-2 Reflood Test 550 Rod Temperatures at 82-inch Elevation**



**Figure 15.6.4-8 G-2 Reflood Test 550 Rod Temperatures at 94-inch Elevation**

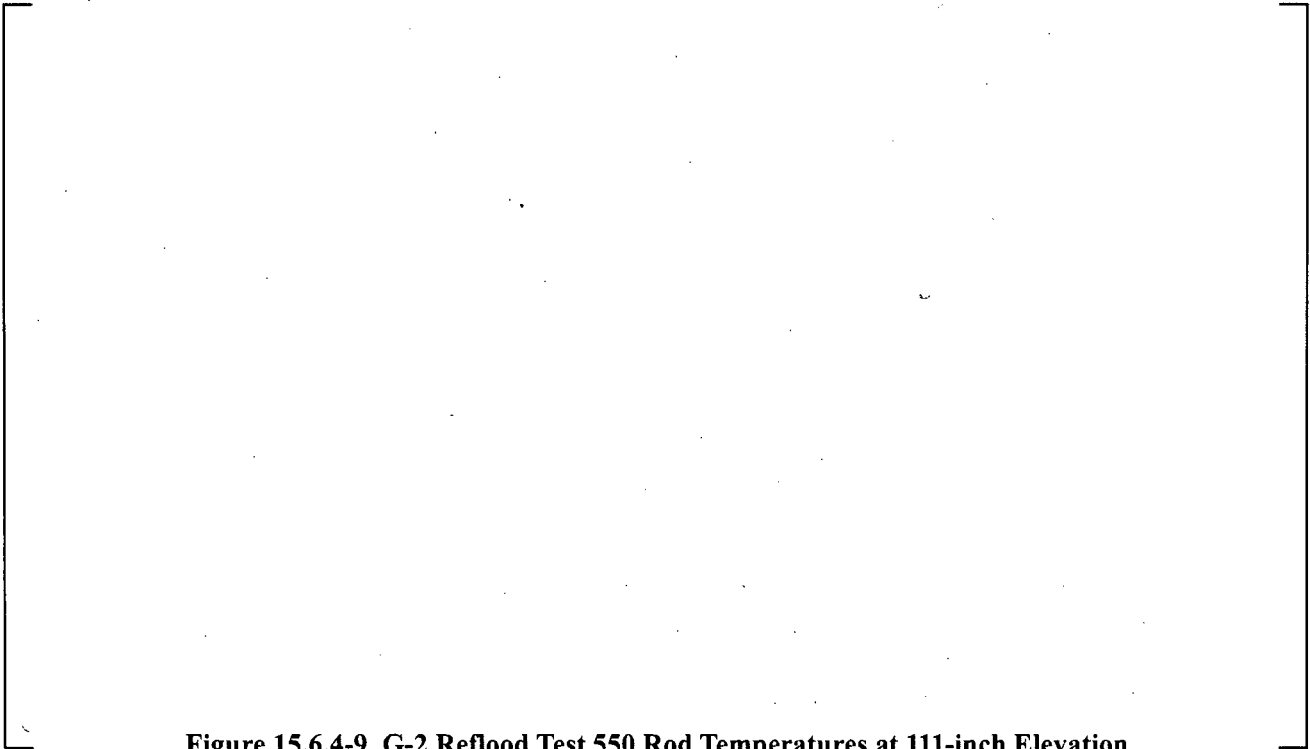


**Figure 15.6.4-9 G-2 Reflood Test 550 Rod Temperatures at 111-inch Elevation**

a,c

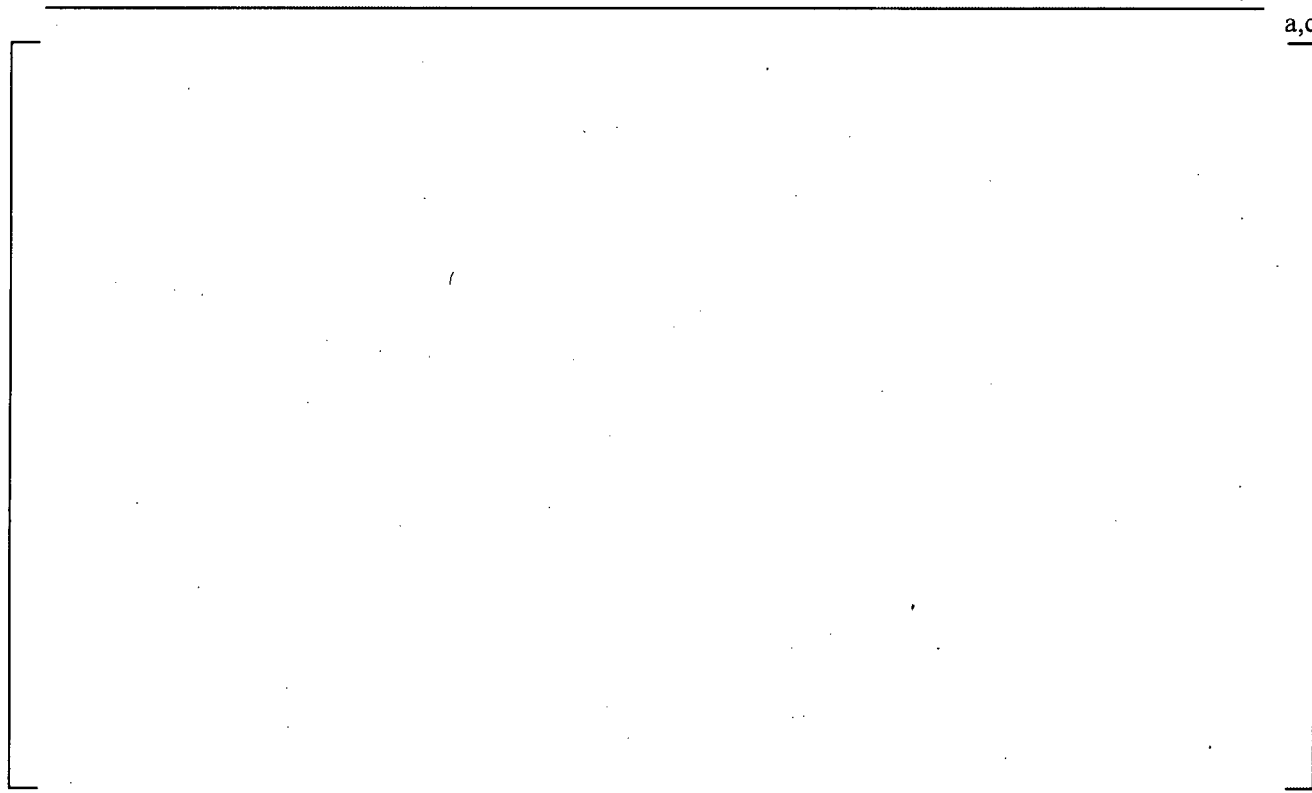


**Figure 15.6.4-10 G-2 Reflood Test 550 Rod Temperatures at 135-inch Elevation**

a,c

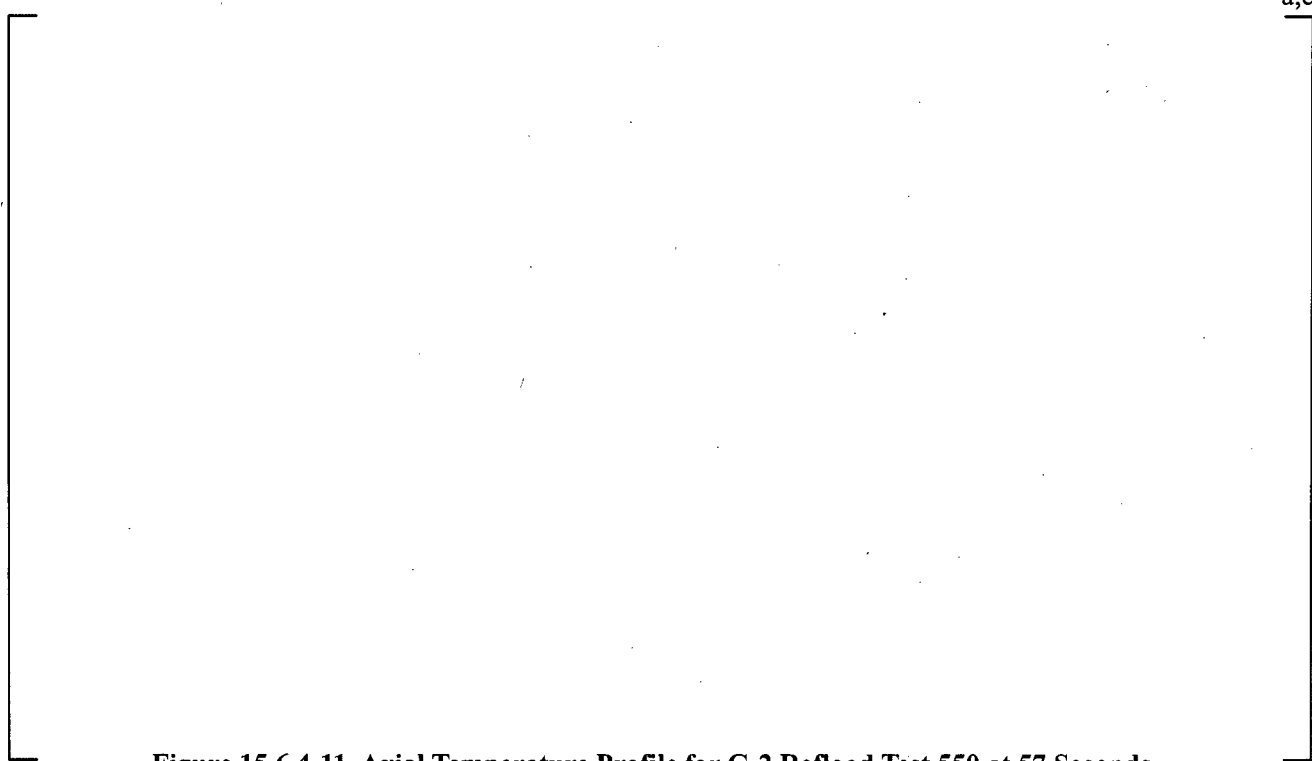


**Figure 15.6.4-11 Axial Temperature Profile for G-2 Reflood Test 550 at 57 Seconds**

a,c

**Figure 15.6.4-12 Axial Temperature Profile for G-2 Reflood Test 550 at 87 Seconds**

a,c

**Figure 15.6.4-13 Axial Temperature Profile for G-2 Reflood Test 550 at 137 Seconds**

a,c



**Figure 15.6.4-14 G-2 Reflood Test 550 Bundle Lower Half  $\Delta P$**

a,c



**Figure 15.6.4-15 G-2 Reflood Test 550 Bundle Upper Half  $\Delta P$**



**Figure 15.6.4-16 G-2 Reflood Test 550 Overall  $\Delta P$**



**Figure 15.6.4-17 G-2 Reflood Test 550 Vapor Temperatures near 109-inch Elevation**

a,c



**Figure 15.6.4-18 G-2 Reflood Test 550 Vapor Temperatures at 137-inch Elevation**

a,c

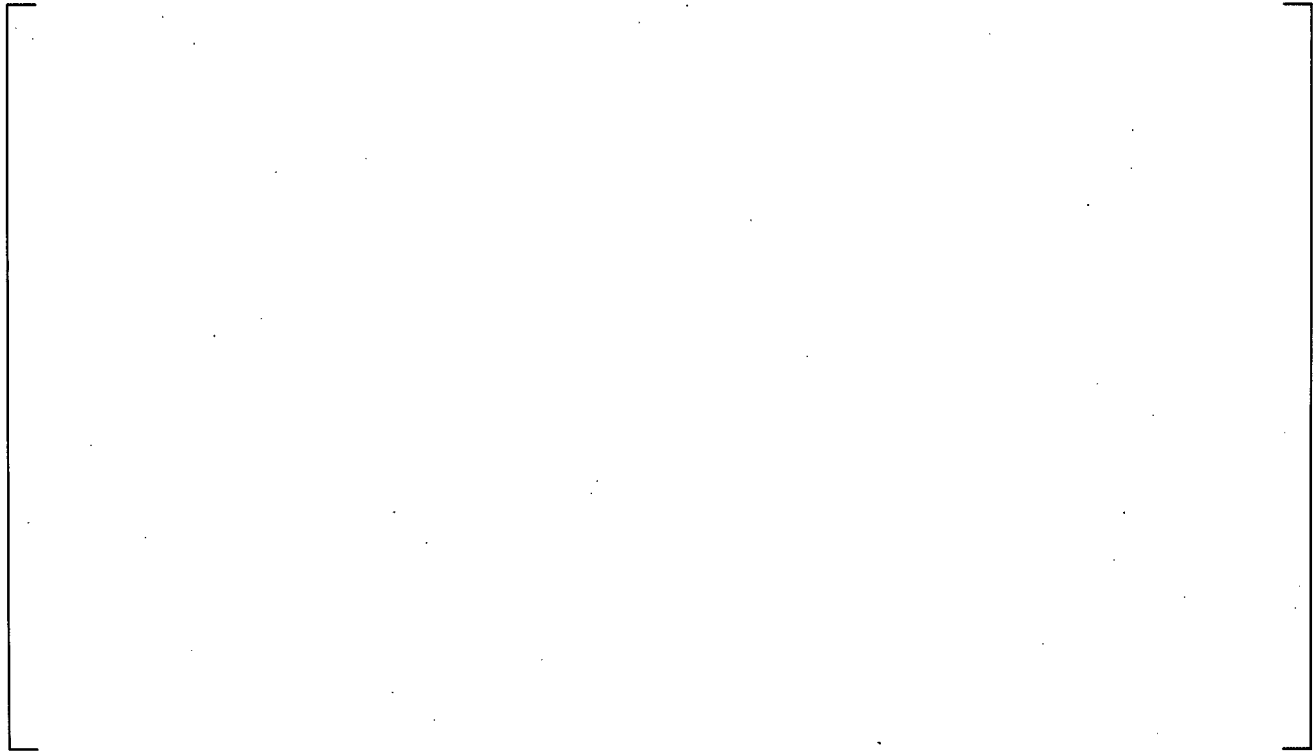


**Figure 15.6.4-19 Maximum Cladding Temperatures for G-2 Reflood Test 550**

a,c



**Figure 15.6.4-20 G-2 Reflood Test 562 Rod Temperatures at 29-inch Elevation**

a,c

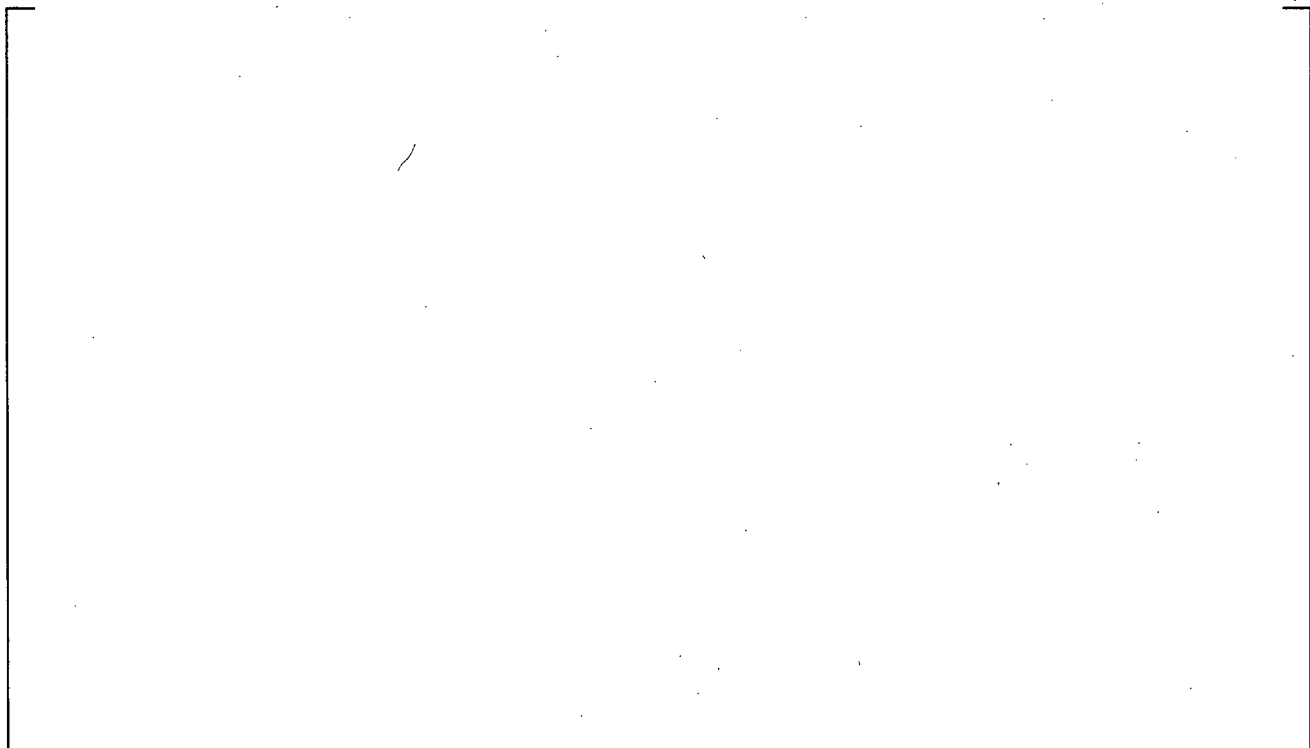


**Figure 15.6.4-21 G-2 Reflood Test 562 Rod Temperatures at 45-inch Elevation**

a,c

**Figure 15.6.4-22 G-2 Reflood Test 562 Rod Temperatures at 70-inch Elevation**

a,c

**Figure 15.6.4-23 G-2 Reflood Test 562 Rod Temperatures at 82-inch Elevation**

a,c



**Figure 15.6.4-24 G-2 Reflood Test 562 Rod Temperatures at 94-inch Elevation**

a,c



**Figure 15.6.4-25 G-2 Reflood Test 562 Rod Temperatures at 111-inch Elevation**



**Figure 15.6.4-26 G-2 Reflood Test 562 Rod Temperatures at 135-inch Elevation**



**Figure 15.6.4-27 Axial Temperature Profile for G-2 Reflood Test 562 at 34 Seconds**



**Figure 15.6.4-28 Axial Temperature Profile for G-2 Reflood Test 562 at 64 Seconds**

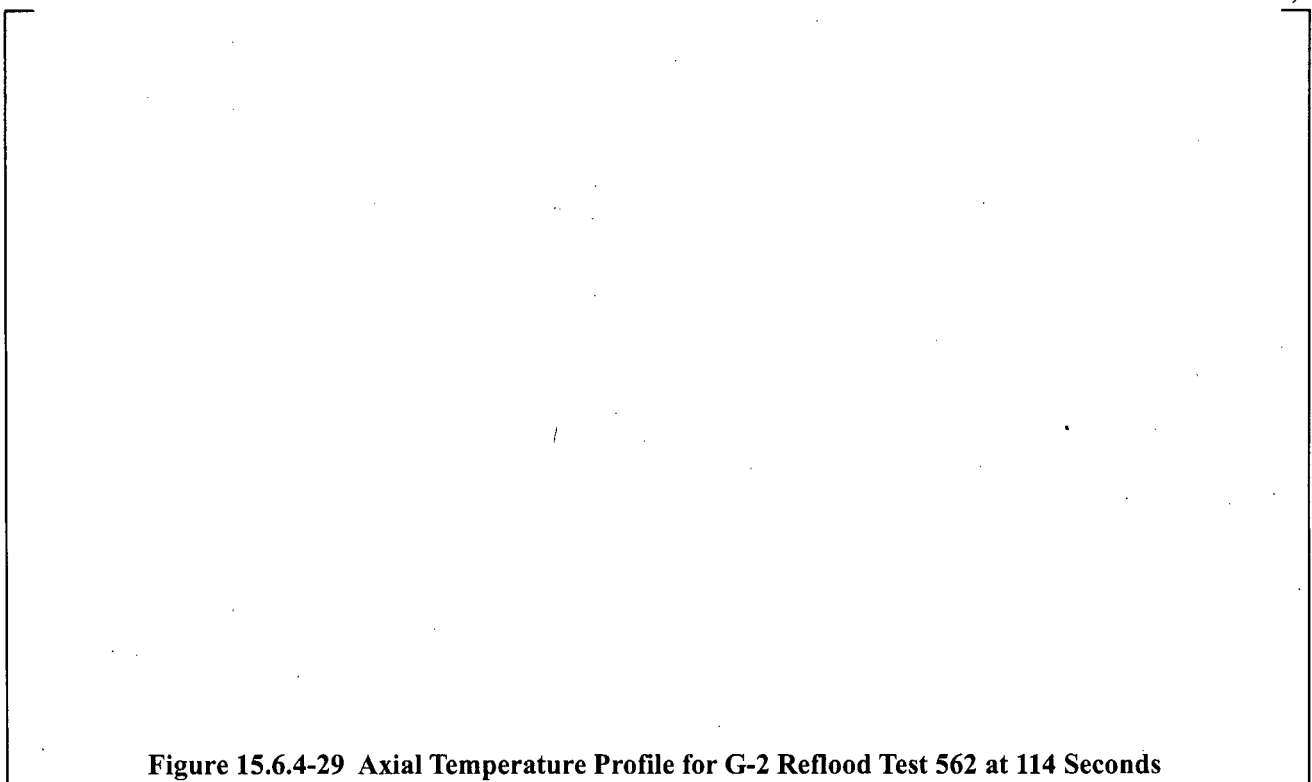


**Figure 15.6.4-29 Axial Temperature Profile for G-2 Reflood Test 562 at 114 Seconds**



**Figure 15.6.4-30 G-2 Reflood Test 562 Bundle Lower Half  $\Delta P$**

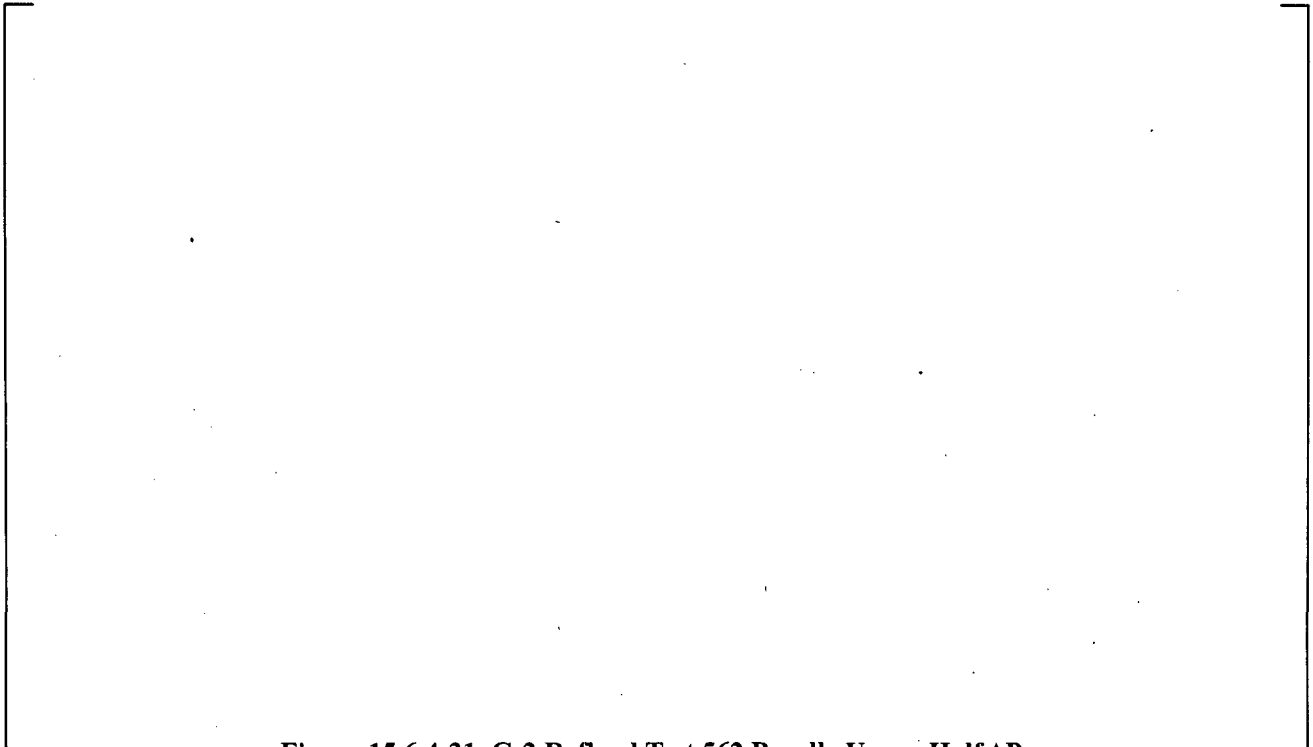


**Figure 15.6.4-31 G-2 Reflood Test 562 Bundle Upper Half  $\Delta P$**

a,c

**Figure 15.6.4-32 G-2 Reflood Test 562 Overall  $\Delta P$**

a,c

**Figure 15.6.4-33 G-2 Reflood Test 562 Vapor Temperatures near 109-inch Elevation**



**Figure 15.6.4-34 G-2 Reflood Test 562 Vapor Temperatures at 137-inch Elevation**



**Figure 15.6.4-35 Maximum Cladding Temperatures for G-2 Reflood Test 562**

**Figure 15.6.4-36 G-2 Reflood Test 568 Rod Temperatures at 29-inch Elevation**

**Figure 15.6.4-37 G-2 Reflood Test 568 Rod Temperatures at 45-inch Elevation**



**Figure 15.6.4-38 G-2 Reflood Test 568 Rod Temperatures at 70-inch Elevation**



**Figure 15.6.4-39 G-2 Reflood Test 568 Rod Temperatures at 82-inch Elevation**



**Figure 15.6.4-40 G-2 Reflood Test 568 Rod Temperatures at 94-inch Elevation**



**Figure 15.6.4-41 G-2 Reflood Test 568 Rod Temperatures at 111-inch Elevation**

a,c



**Figure 15.6.4-42 G-2 Reflood Test 568 Rod Temperatures at 135-inch Elevation**

a,c

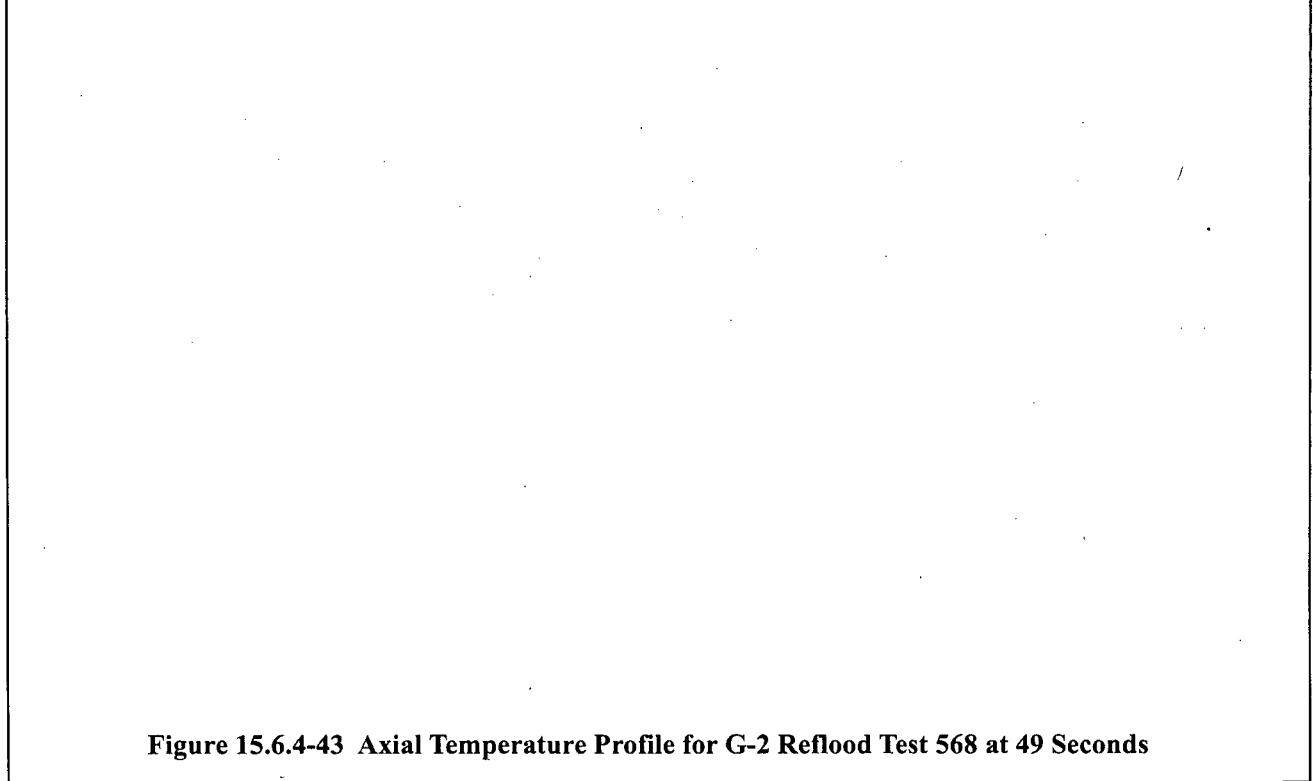


**Figure 15.6.4-43 Axial Temperature Profile for G-2 Reflood Test 568 at 49 Seconds**

a,c



**Figure 15.6.4-44 Axial Temperature Profile for G-2 Reflood Test 568 at 79 Seconds**

a,c

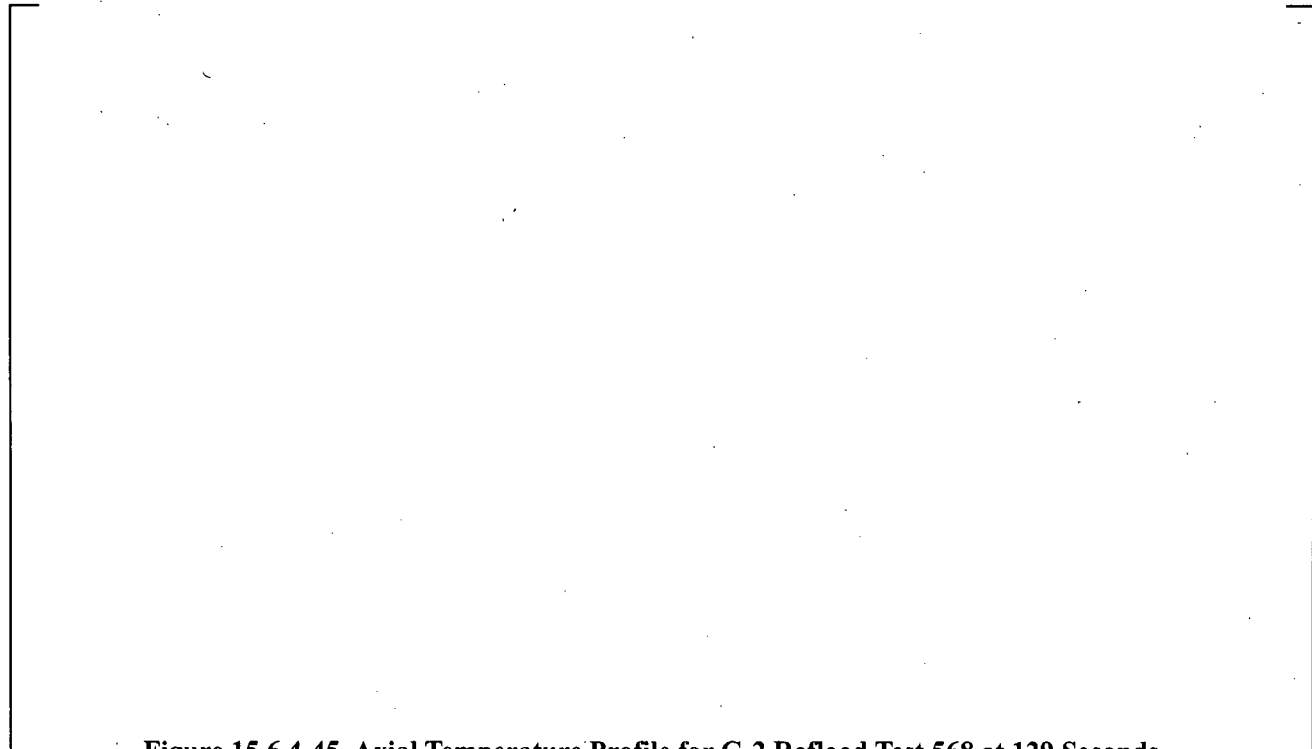


**Figure 15.6.4-45 Axial Temperature Profile for G-2 Reflood Test 568 at 129 Seconds**

a,c

**Figure 15.6.4-46 G-2 Reflood Test 568 Bundle Lower Half  $\Delta P$**

a,c

**Figure 15.6.4-47 G-2 Reflood Test 568 Bundle Upper Half  $\Delta P$**

a,c

**Figure 15.6.4-48 G-2 Reflood Test 568 Overall  $\Delta P$**

a,c

**Figure 15.6.4-49 G-2 Reflood Test 568 Vapor Temperatures near 109-inch Elevation**

a,c



**Figure 15.6.4-50 G-2 Reflood Test 568 Vapor Temperatures at 137-inch Elevation**

a,c



**Figure 15.6.4-51 Maximum Cladding Temperatures for G-2 Reflood Test 568**

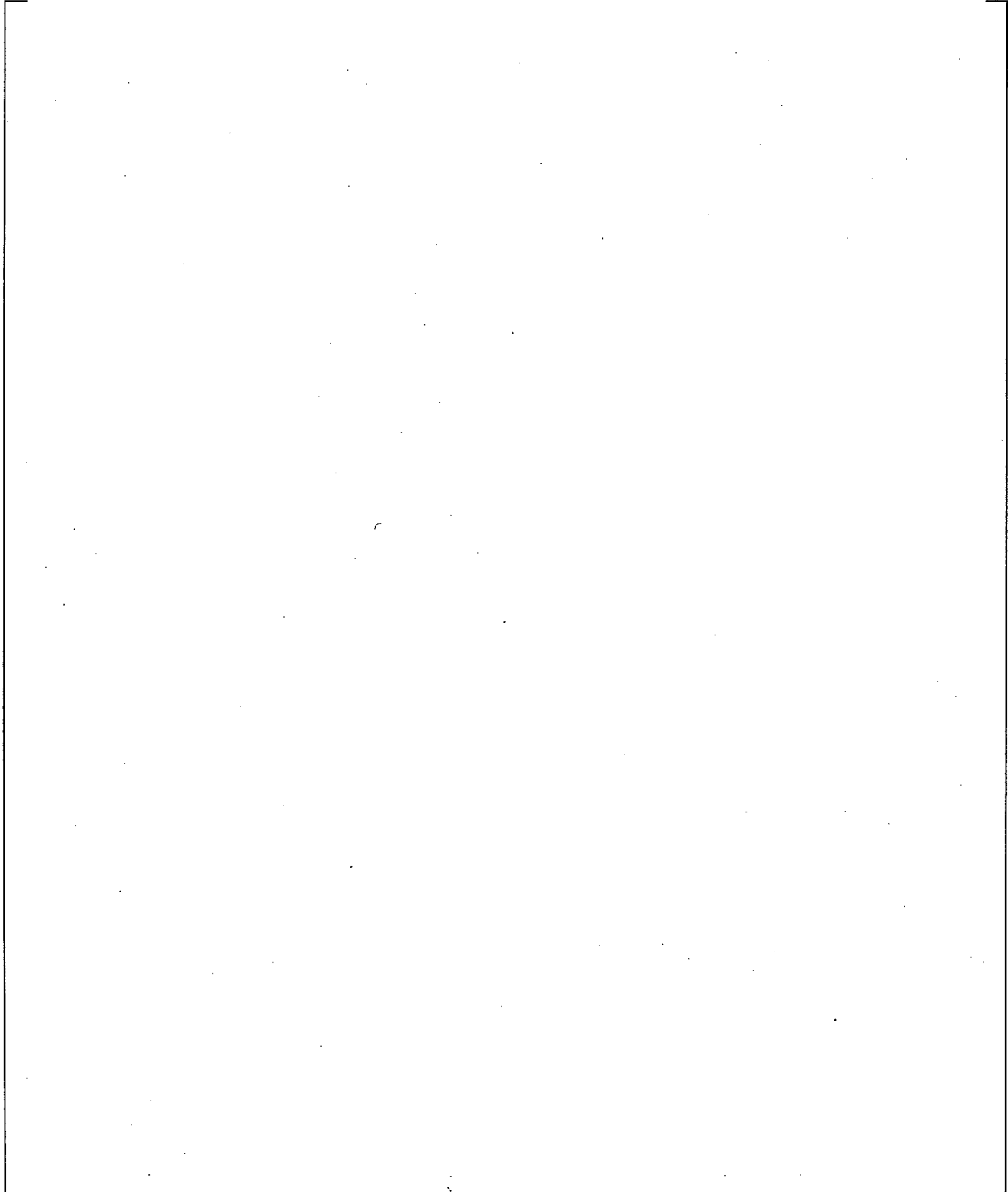


**Figure 15.6.4-52 Predicted and Measured Maximum Cladding Temperatures for G-2 Reflood Test Simulations**

### 15.6.5 WCOBRA/TRAC-TF2 Simulations of FEBA

Figures 15.6.5-1 and 15.6.5-2 presents the noding scheme used to model the FEBA test facility. A WCOBRA/TRAC-TF2 VESSEL component was used to represent the test bundle, and upper and lower plenums to the test bundle so that boundary conditions could be applied. The first section represents a lower plenum, where the flow boundary condition is applied to the bottom of Channel 1. The second section models the test bundle with two channels. [

] <sup>a,c</sup> An unheated conductor was used to model the thick FEBA housing, since metal heat release to the fluid was expected to be significant. The third section contains a single channel (Channel 4) and serves as the upper plenum. A pressure and enthalpy boundary condition is applied to the top of Channel 4. A PIPE component with a zero velocity FILL is attached to Channel 4 which serves to satisfy the WCOBRA/TRAC-TF2 requirement of at least one one-dimensional component. The zero velocity FILL prevents flow through the PIPE.

The axial noding in the section modeling the test bundle is [

] <sup>a,c</sup>

Measured values of heater rod temperature, housing temperature, injection flowrate, and bundle power were used to determine the initial temperatures and the time-dependent rod heat source in the simulation.

#### 15.6.5.1 FEBA Results

##### 15.6.5.1.1 Simulation of FEBA Test 223

Test 223 included the mid-plane spacer grid. The flooding rate was 1.5 in/sec, and the bundle pressure was maintained at 32 psia. The WCOBRA/TRAC-TF2 simulation was run for 500 transient seconds. Figures 15.6.5-3 through 15.6.5-9 compare the predicted cladding temperature with the average of the measured values at several elevations in the test bundle for [

] <sup>a,c</sup>

Figures 15.6.5-10 and 15.6.5-11 show the predicted and measured axial temperature profiles at 75 and 150 seconds, respectively. The locations of the spacer grids are apparent in the axial profiles where there is a sharp "dip" in temperature.

##### 15.6.5.1.2 Simulation of FEBA Test 234

Test 234 is similar to Test 223, except it did not include the mid-plane spacer grid. The flooding rate was 1.5 in/sec, and the bundle pressure was maintained at 29 psia. The WCOBRA/TRAC-TF2 simulation was

run for 500 seconds. Figures 15.6.5-12 through 15.6.5-18 compare the predicted cladding temperature with the average of the measured values at several elevations in the test bundle for [

] <sup>a,c</sup>

Figures 15.6.5-19 and 15.6.5-20 show the predicted and measured axial temperature profiles at 75 and 150 seconds, respectively. As can be observed, the dip at 86 inches in Figures 15.6.5-10 and 15.6.5-11 are not observed in Figures 15.6.5-19 and 15.6.5-20 due to the absence of the spacer grid.

#### 15.6.5.1.3 Simulation of FEBA Test 216

Test 216 included the mid-plane spacer grid. The flooding rate was 1.5 in/sec, and the bundle pressure was maintained at 60 psia. The WCOBRA/TRAC-TF2 simulation was run for 500 seconds.

Figures 15.6.5-21 through 15.6.5-27 compare the predicted cladding temperature with the average of the measured values at several elevations in the test bundle for [

] <sup>a,c</sup>

Figures 15.6.5-28 and 15.6.5-29 show the predicted and measured axial temperature profiles at 75 and 150 seconds, respectively.

#### 15.6.5.1.4 Simulation of FEBA Test 229

Test 229 is similar to Test 216, except it did not include the mid-plane spacer grid. The flooding rate was 1.5 in/sec, and the bundle pressure was maintained at 61 psia. The WCOBRA/TRAC-TF2 simulation was run for the first 500 seconds of the experiment. Figures 15.6.5-30 through 15.6.5-36 compare the predicted cladding temperature with the average of the measured values at several elevations in the test bundle for [

] <sup>a,c</sup>

Figures 12.5-39 and 12.5-40 show the predicted and measured axial temperature profiles at 75 and 150 seconds, respectively. As can be observed, the dip at 86 inches in Figures 15.6.5-28 and 15.6.5-29 are not observed in Figures 15.6.5-39 and 15.6.5-40 due to the absence of the spacer grid.

#### 15.6.5.2 Summary and Conclusions

Four FEBA tests were simulated using WCOBRA/TRAC-TF2. Two low pressure tests (Tests 223 and 234) were simulated as well as two at a higher pressure (Tests 216 and 229). Each pair of tests were run with similar thermal-hydraulic conditions, but in one of the two tests the mid-plane grid was removed.

[

] <sup>a,c</sup>

[

]a,c

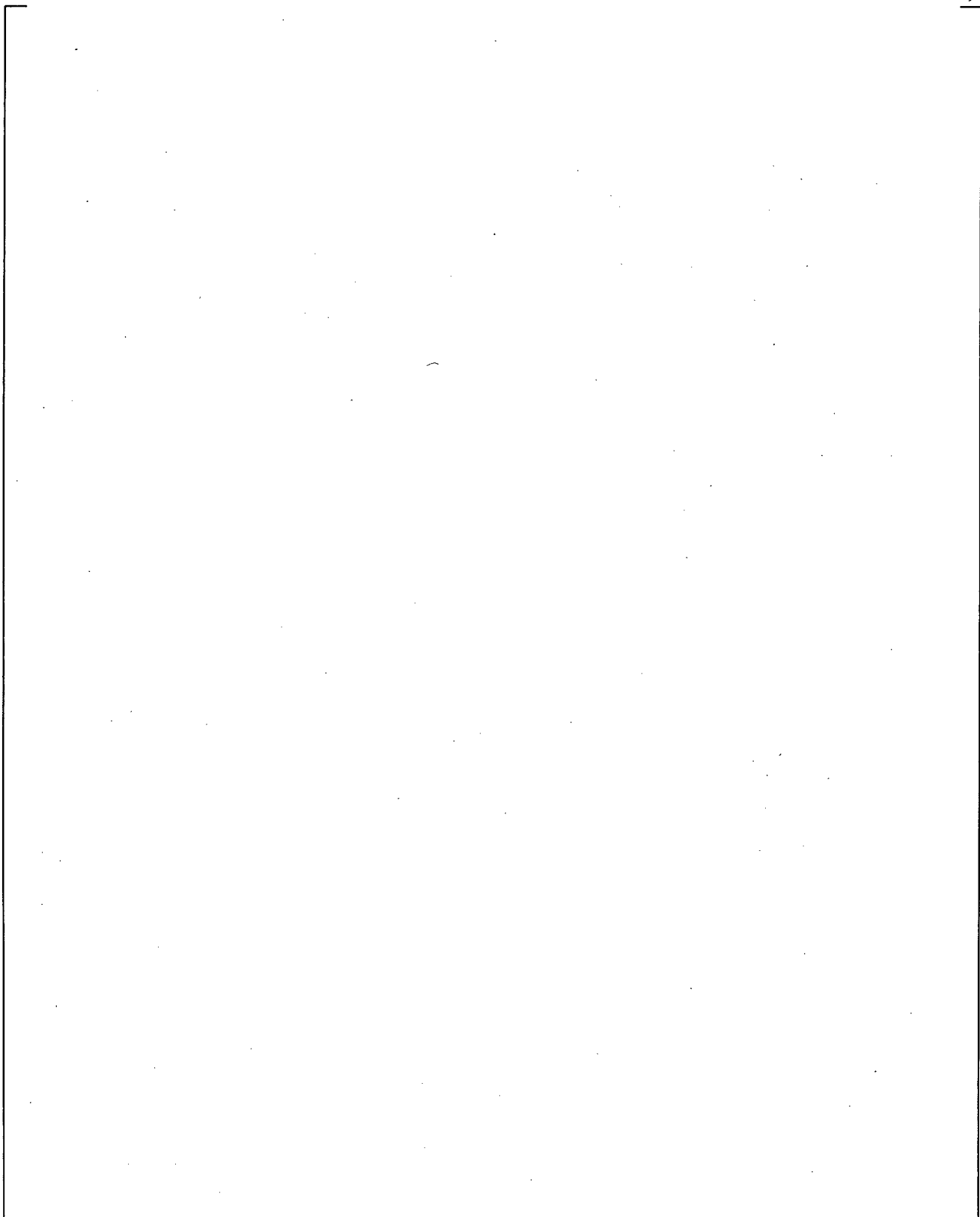


**Figure 15.6.5-1 WCOBRA/TRAC-TF2 Transverse Noding for FEBA**

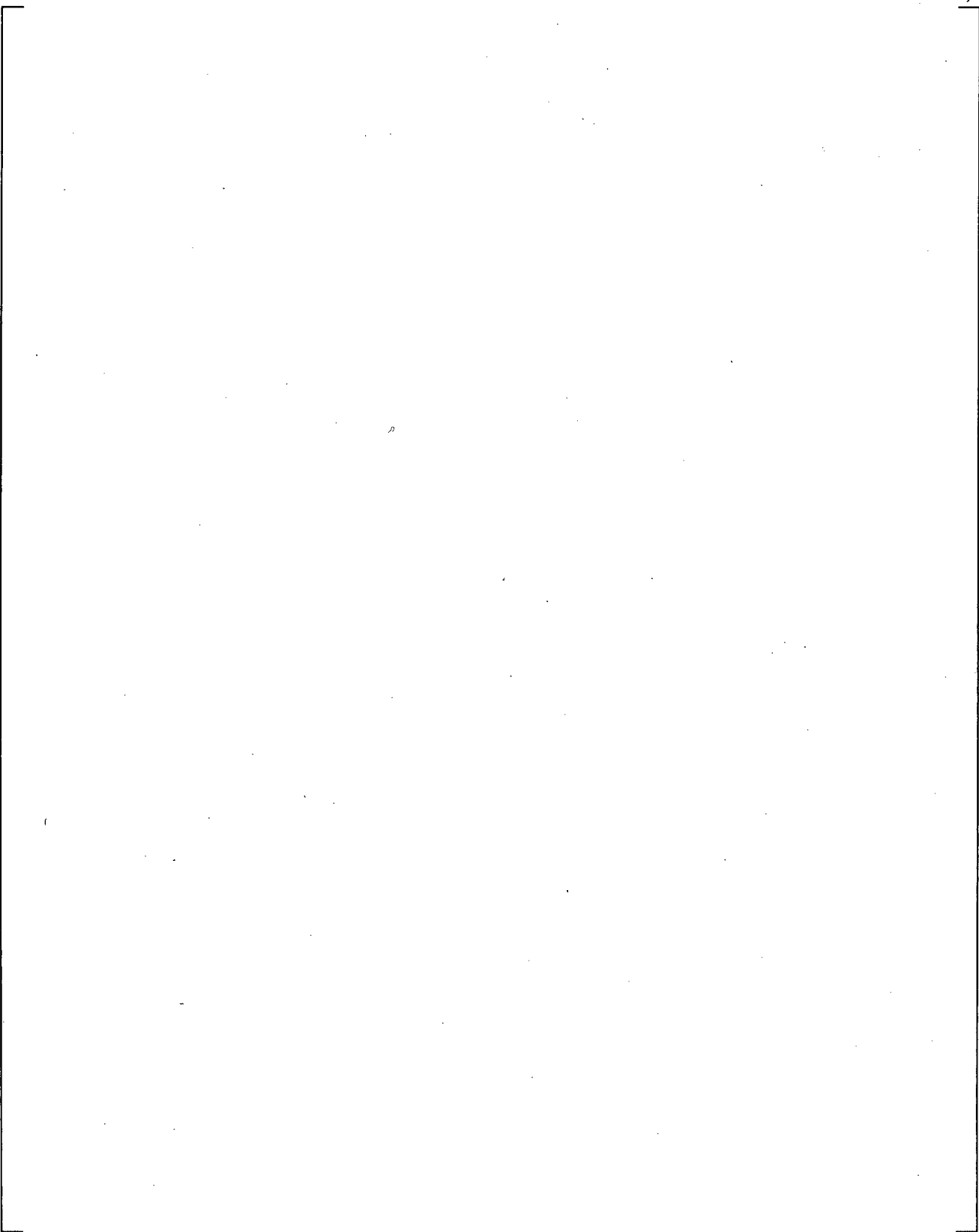


**Figure 15.6.5-2 WCOBRA/TRAC-TF2 Axial Noding for FEBA**

a,c



**Figure 15.6.5-3 Rod Temperatures for FEBA Test 223 at 2770 mm Reference Elevation**

a,c



**Figure 15.6.5-4 Rod Temperatures for FEBA Test 223 at 2225 mm Reference Elevation**



**Figure 15.6.5-5 Rod Temperatures for FEBA Test 223 at 2125 mm Reference Elevation**



**Figure 15.6.5-6 Rod Temperatures for FEBA Test 223 at 2025 mm Reference Elevation**



**Figure 15.6.5-7 Rod Temperatures for FEBA Test 223 at 1925 mm Reference Elevation**

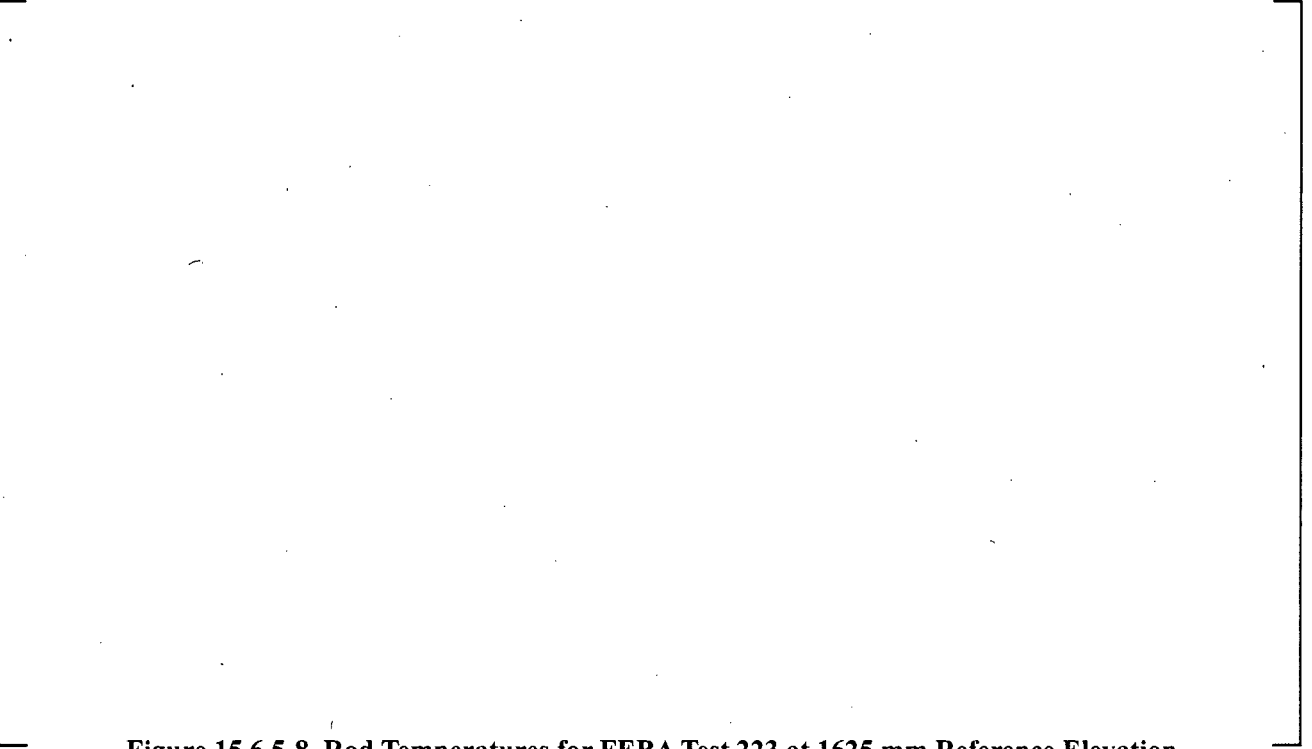


**Figure 15.6.5-8 Rod Temperatures for FEBA Test 223 at 1625 mm Reference Elevation**



**Figure 15.6.5-9 Rod Temperatures for FEBA Test 223 at 1135 mm Reference Elevation**



**Figure 15.6.5-10 Comparison of Predicted and Measured Axial Temperature Profiles for FEBA Test 223 at 75 Seconds**

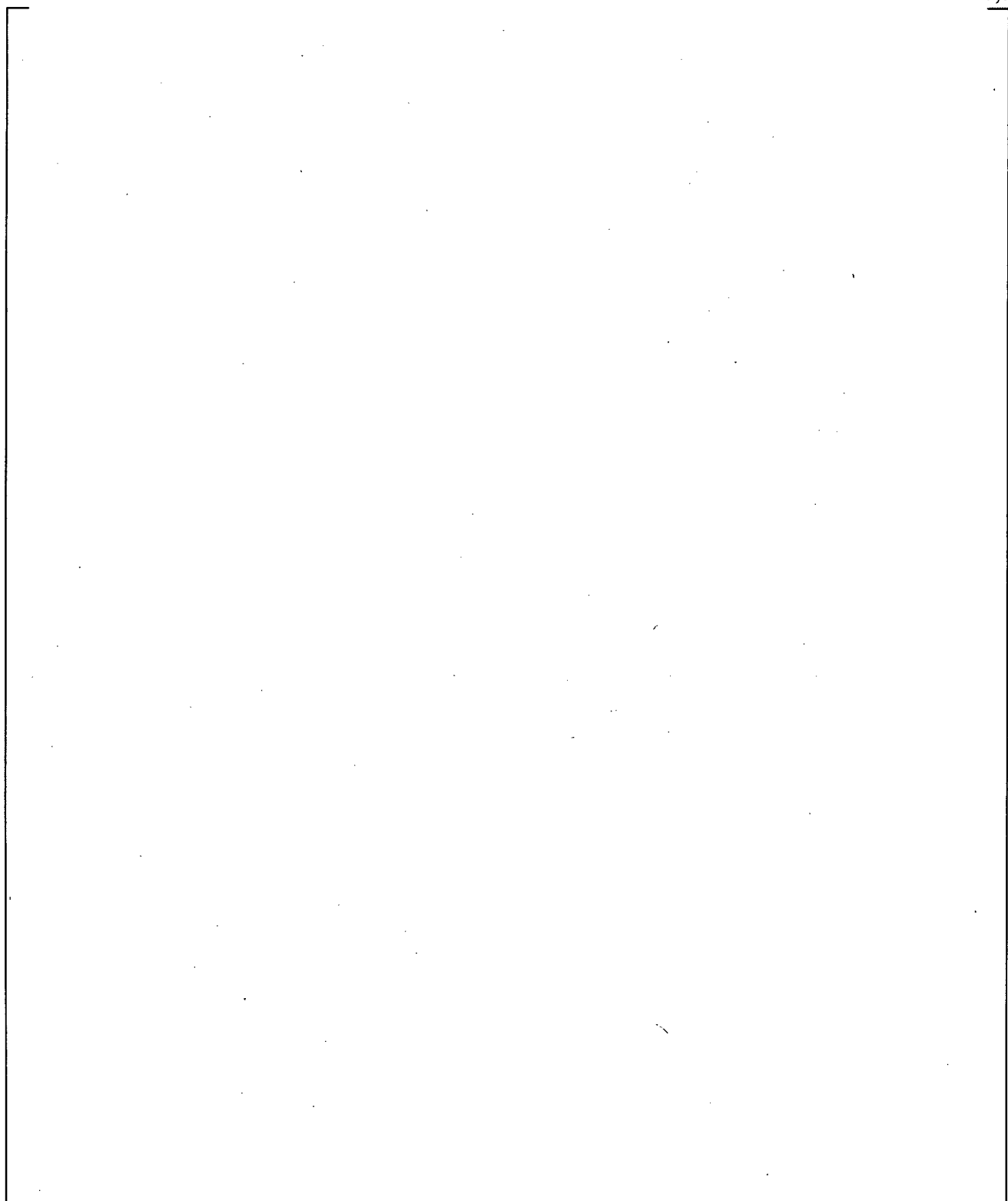


**Figure 15.6.5-11 Comparison of Predicted and Measured Axial Temperature Profiles for FEBA Test 223 at 150 Seconds**

a,c



**Figure 15.6.5-12 Rod Temperatures for FEBA Test 234 at 2770 mm Reference Elevation**

a,c



**Figure 15.6.5-13 Rod Temperatures for FEBA Test 234 at 2225 mm Reference Elevation**



**Figure 15.6.5-14 Rod Temperatures for FEBA Test 234 at 2125 mm Reference Elevation**



**Figure 15.6.5-15 Rod Temperatures for FEBA Test 234 at 2025 mm Reference Elevation**

a,c



**Figure 15.6.5-16 Rod Temperatures for FEBA Test 234 at 1925 mm Reference Elevation**

a,c



**Figure 15.6.5-17 Rod Temperatures for FEBA Test 234 at 1625 mm Reference Elevation**

a,c

**Figure 15.6.5-18 Rod Temperatures for FEBA Test 234 at 1135 mm Reference Elevation**

a,c

**Figure 15.6.5-19 Comparison of Predicted and Measured Axial Temperature Profiles for FEBA Test 234 at 75 Seconds**

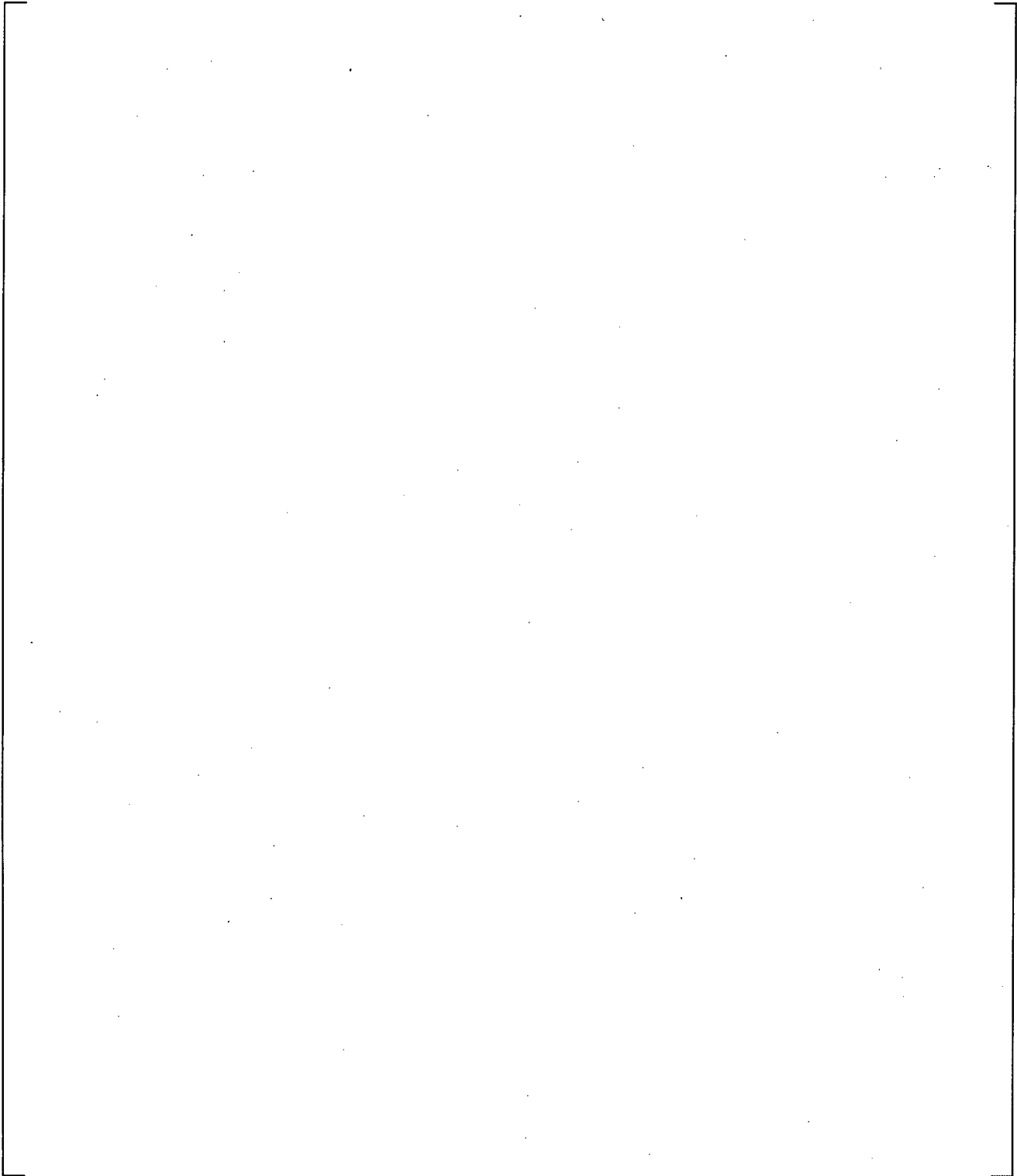


**Figure 15.6.5-20 Comparison of Predicted and Measured Axial Temperature Profiles for FEBA Test 234 at 150 Seconds**

a,c

**Figure 15.6.5-21 Rod Temperatures for FEBA Test 216 at 2770 mm Reference Elevation**

a,c

**Figure 15.6.5-22 Rod Temperatures for FEBA Test 216 at 2225 mm Reference Elevation**

a,c

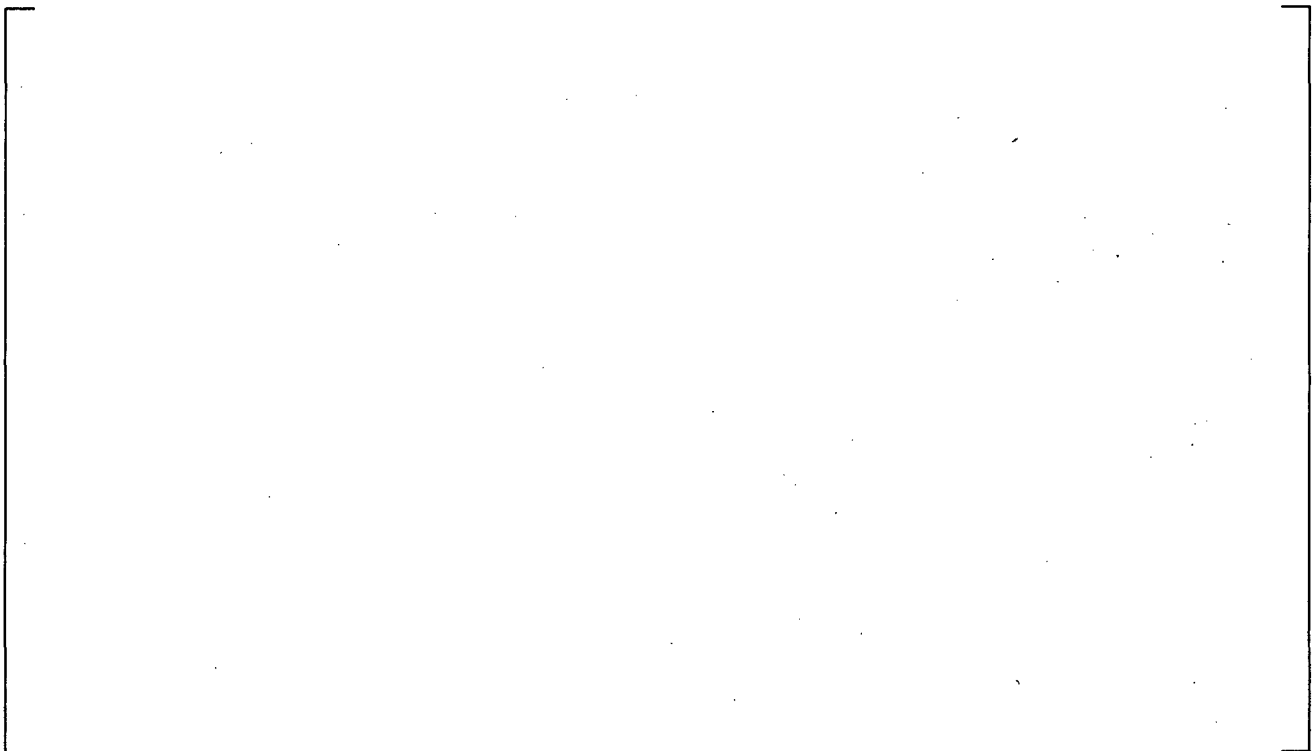


**Figure 15.6.5-23 Rod Temperatures for FEBA Test 216 at 2125 mm Reference Elevation**

a,c



**Figure 15.6.5-24 Rod Temperatures for FEBA Test 216 at 2025 mm Reference Elevation**

a,c



**Figure 15.6.5-25 Rod Temperatures for FEBA Test 216 at 1925 mm Reference Elevation**

a,c

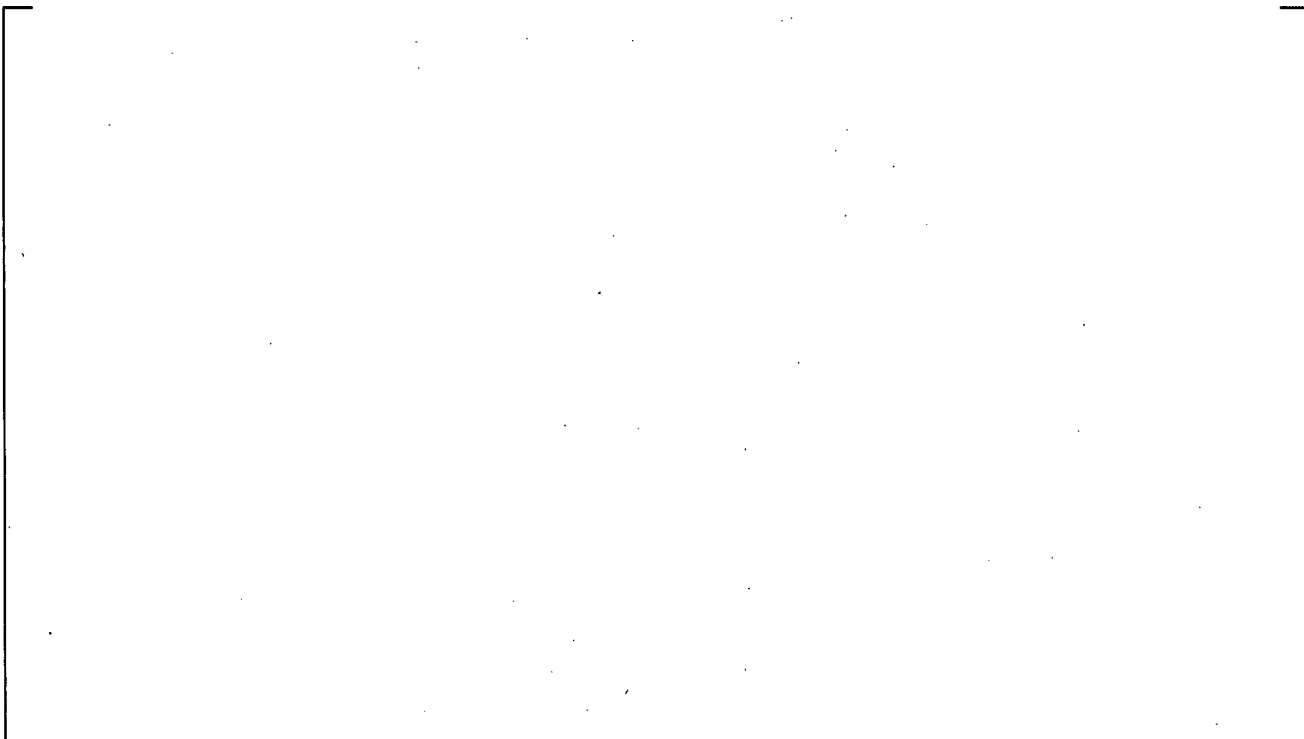


**Figure 15.6.5-26 Rod Temperatures for FEBA Test 216 at 1625 mm Reference Elevation**

a,c

**Figure 15.6.5-27 Rod Temperatures for FEBA Test 216 at 1135 mm Reference Elevation**

a,c

**Figure 15.6.5-28 Comparison of Predicted and Measured Axial Temperature Profiles for FEBA Test 216 at 75 Seconds**

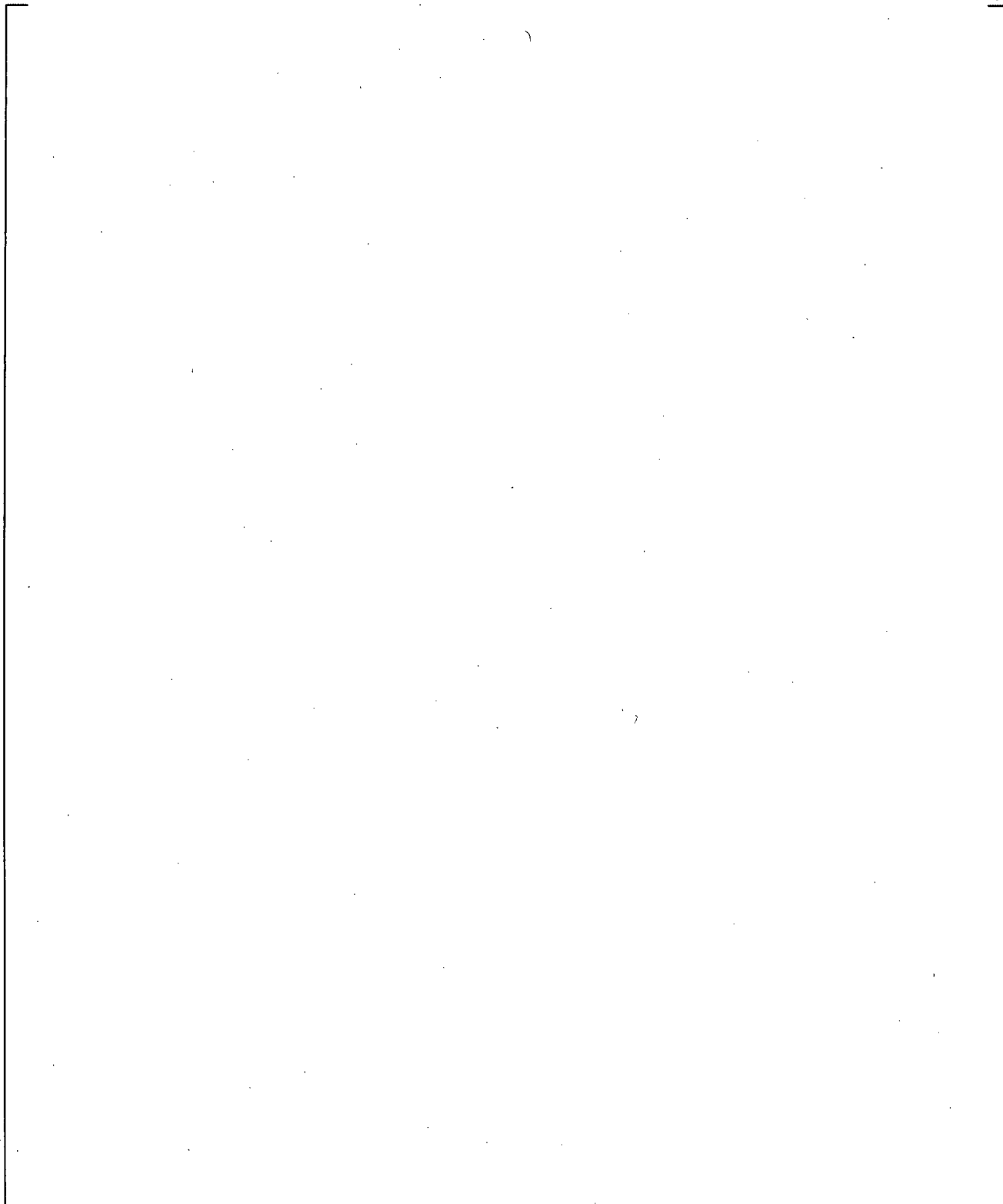


**Figure 15.6.5-29 Comparison of Predicted and Measured Axial Temperature Profiles for FEBA Test 216 at 150 Seconds**

a,c

**Figure 15.6.5-30 Rod Temperatures for FEBA Test 229 at 2770 mm Reference Elevation**

a,c

**Figure 15.6.5-31 Rod Temperatures for FEBA Test 229 at 2225 mm Reference Elevation**

a,c



**Figure 15.6.5-32 Rod Temperatures for FEBA Test 229 at 2125 mm Reference Elevation**

a,c

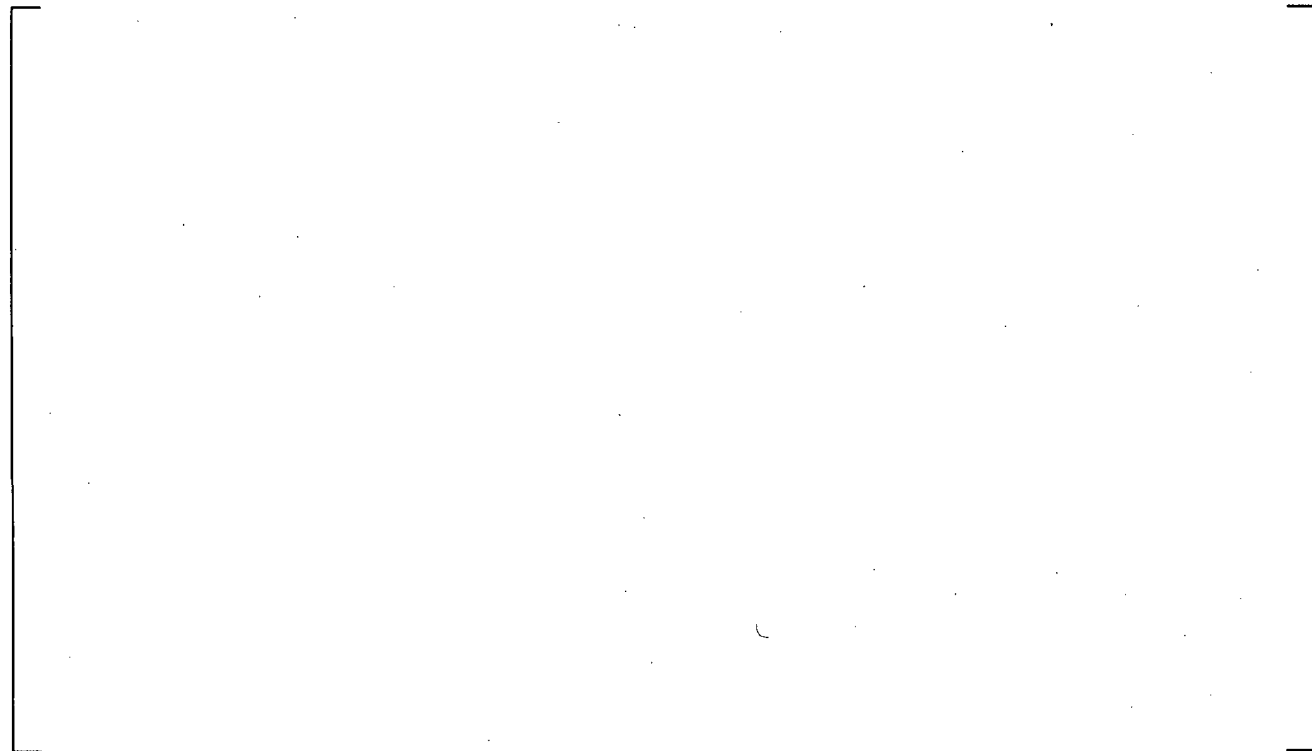


**Figure 15.6.5-33 Rod Temperatures for FEBA Test 229 at 2025 mm Reference Elevation**

a,c



**Figure 15.6.5-34 Rod Temperatures for FEBA Test 229 at 1925 mm Reference Elevation**

a,c



**Figure 15.6.5-35 Rod Temperatures for FEBA Test 229 at 1625 mm Reference Elevation**

a,c

**Figure 15.6.5-36 Rod Temperatures for FEBA Test 229 at 1135 mm Reference Elevation**

a,c

**Figure 15.6.5-37 Comparison of Predicted and Measured Axial Temperature Profiles for FEBA Test 229 at 75 Seconds**

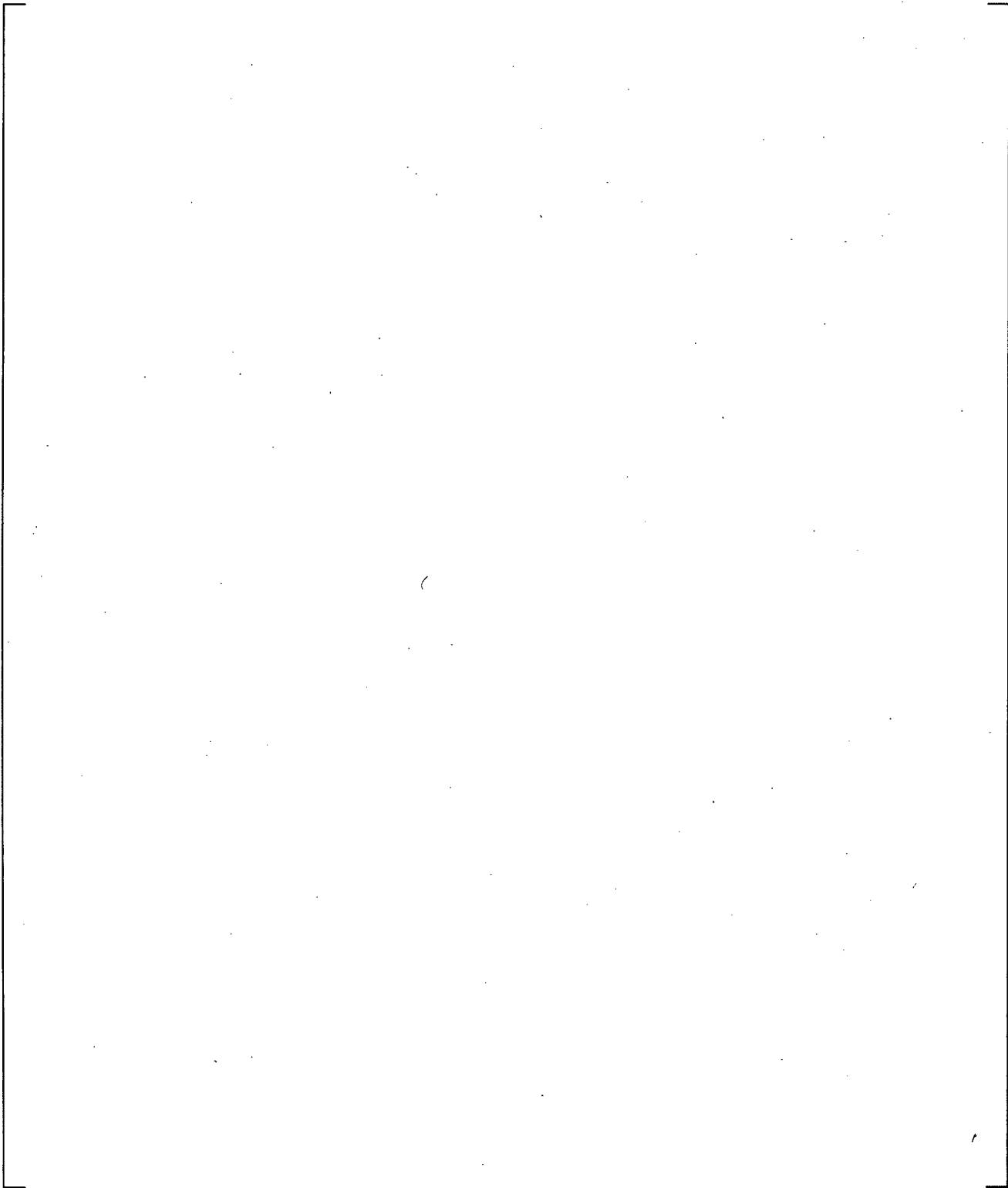


**Figure 15.6.5-38 Comparison of Predicted and Measured Axial Temperature Profiles for FEBA Test 229 at 150 Seconds**

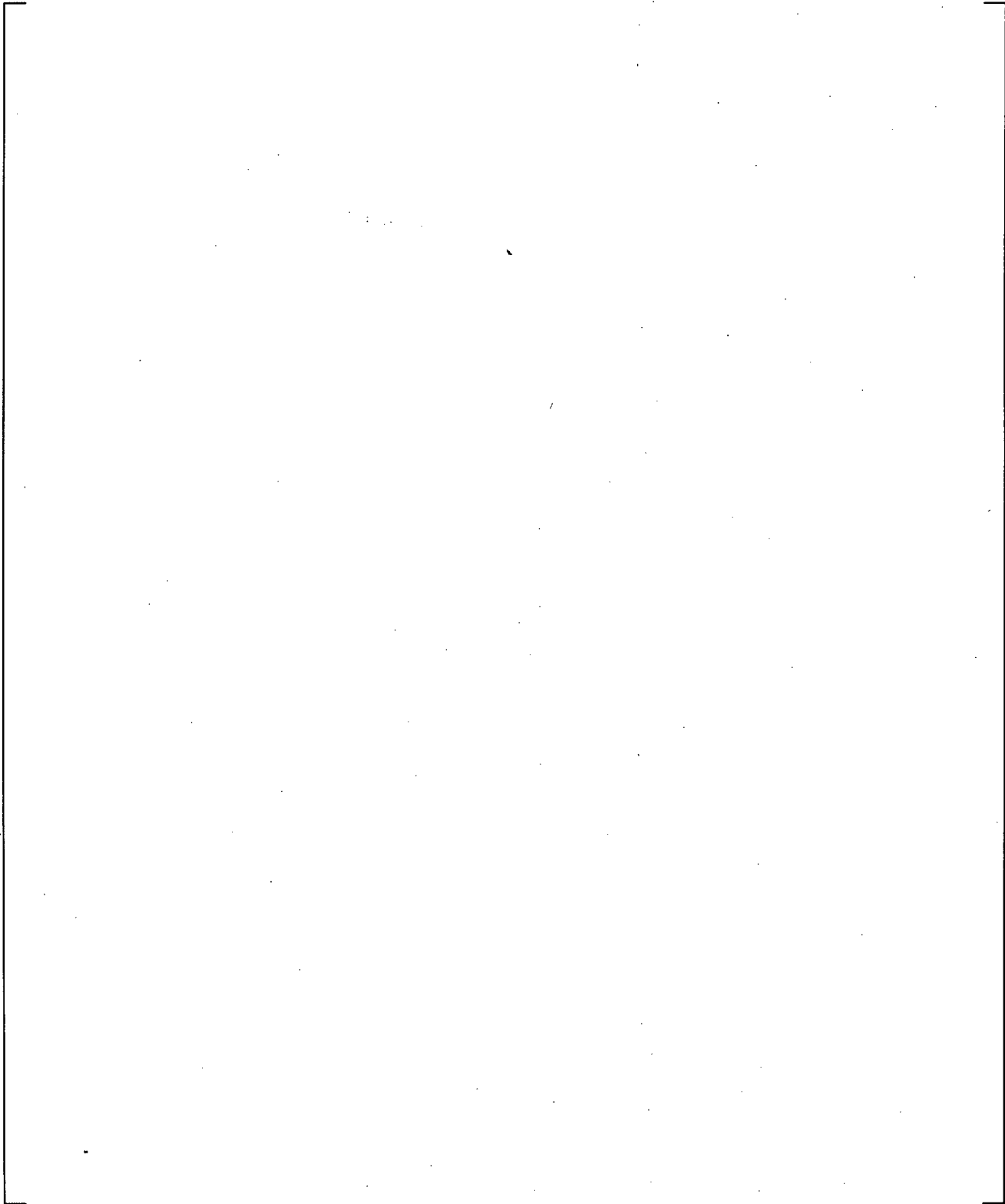


**Figure 15.6.5-39 Comparison of Predicted and Measured Maximum Clad Temperatures for FEBA Simulations**

### 15.6.6 Reflood Heat Transfer Assessment Summary and Conclusions

Table 15.6.6-1 provides a summary of the test conditions from the 21 different reflood separate effects tests simulated using WCOBRA/TRAC-TF2 and presented in Sections 15.6.1 through 15.6.5. For the FLECHT SEASET tests, the peak cladding temperatures were [

] <sup>a,c</sup>.

In general, the peak cladding temperatures are [

] <sup>a,c</sup>.

Additional assessments for pressure effects, inlet sub-cooling, inlet flow rate, grid effects and entrained droplets are performed in Section 15.9.

Parameter	Range of Conditions

<sup>a,c</sup>

## 15.7 GRID HEAT TRANSFER MODELS

Grid spacers are an integral part of all rod bundle designs, and have important effects on the local heat transfer. At a spacer grid, the assembly flow area is reduced. Flow approaching the grid first contracts, and then expands downstream of the grid. As the flow passes through the grid, the fluid and thermal boundary layers are disrupted resulting in a local increase in the rod to fluid heat transfer coefficient. In addition, the grids shatter incoming droplets, increasing the interfacial area and evaporation rate. Since the grids are unpowered, they can rewet before the local heater rod surface. Section 7 describes the WCOBRA/TRAC-TF2 models for heat transfer enhancement, grid droplet breakup and grid rewet. This section provides additional information on the calculated results near a grid spacer.

The effect of the grids on the results can be seen in nearly all of the SPV, DFFB and reflood test simulations presented in Sections 15.4 through 15.6. Figures showing the axial temperature profile of the heater rods typically indicate a sharp decrease in temperature at and immediately downstream of a spacer grid. In Figure 15.6.1-73 for example, decrease in the rod temperature at the 83-inch elevation is due to the presence of the spacer grids. [

] <sup>a,c</sup>

Most rod bundle tests did not include a sufficient number of thermocouples at grid locations to quantify the grid effect. The FEBA tests (Section 15.6.5) included a large number of thermocouples around the mid-plane grid, and the ORNL uncovered bundle tests (Section 15.4.1) included a large number of thermocouples around the upper grid. For FEBA, the mid-plane grid was at an elevation 76.77 inches from the bottom of the heated length. WCOBRA/TRAC-TF2 simulations of FEBA Tests 223 and 216, calculated a decrease in rod temperature downstream of the grid. In simulations of FEBA Tests 234 and 229, in which the mid-plane grid had been removed from the bundle, no decrease at the 76.77-inch elevation was predicted. For ORNL, the upper grid was at an elevation 131.25 inches from the bottom of the heated length. WCOBRA/TRAC-TF2 simulations of ORNL Test M calculated a decrease in rod temperature downstream of the grid. For ORNL Test N, which had a very low flow rate, the decrease in rod temperature downstream of the grid exists, but to a much lower extent.

Figure 15.7-1 shows the calculated rod temperature profile and thermocouple measurements for FEBA Test 223 at 75 seconds near the mid-plane grid. The measurements shown in this figure represent an average of all thermocouples at a given elevation. The maximum temperatures in both the measurements and the code predictions occur slightly upstream of the grid. The rod cladding between the leading and trailing edges of the grid receives good heat transfer and the clad temperature drops significantly in the test data and to a lesser extent in the simulation. The measurements show a [

] <sup>a,c</sup> in the test data. The simulation predicted a [

] <sup>a,c</sup>. Downstream of the grid, the rod

temperatures increase in both the predicted and measured results. The predicted increase in rod temperature downstream of the grid is [ ]<sup>a,c</sup>.

Figure 15.7-2 shows the calculated rod temperature profile and thermocouple measurements for ORNL Test M at 1500 s near the upper grid. Like the FEBA test, the measurements shown in this figure represent an average of all thermocouples at a given elevation. The maximum temperatures in both the measurements and the code predictions occur upstream of the grid. The rod cladding between the leading and trailing edges of the grid receives good heat transfer and the clad temperature drops significantly in both the test data and simulation. The measurements show a [ ]<sup>a,c</sup> in the test data. The simulation predicted a [ ]<sup>a,c</sup>. Downstream of the grid, the rod temperatures increase in both the predicted and measured results. The predicted increase in rod temperature downstream of the grid is [ ]<sup>a,c</sup>.

Figure 15.7-3 shows the calculated rod temperature profile and thermocouple measurements for ORNL Test N at 1500 s near the upper grid. Test N had a much lower flow rate, and shows the effect of flow rate on the grid enhancement. The measurements shown in this figure represent an average of all thermocouples at a given elevation. The maximum temperatures in both the measurements and the code predictions occur upstream of the grid. Due to the reduced flow, the rod cladding between the leading and trailing edges of the grid receives less heat transfer enhancement than the other cases presented, and the clad temperature drops slightly in both the test data and simulation. The measurements show a [ ]<sup>a,c</sup> in the test data. The simulation predicted a [ ]<sup>a,c</sup>. Downstream of the grid, the rod temperatures increase in both the predicted and measured results. The predicted increase in rod temperature downstream of the grid is [ ]<sup>a,c</sup>.

The WCOBRA/TRAC-TF2 simulations indicate that the grids have an important effect on the local clad temperatures. The predictions are [ ]<sup>a,c</sup> with available experimental results. Therefore, the grid heat transfer models in WCOBRA/TRAC-TF2 can be expected to provide reasonable estimates of the grid effect in a LOCA transient.

a,c

**Figure 15.7-1 Temperature Profile Near a Spacer Grid from FEBA 223**

a,c

**Figure 15.7-2 Temperature Profile Near a Spacer Grid from ORNL Test M**

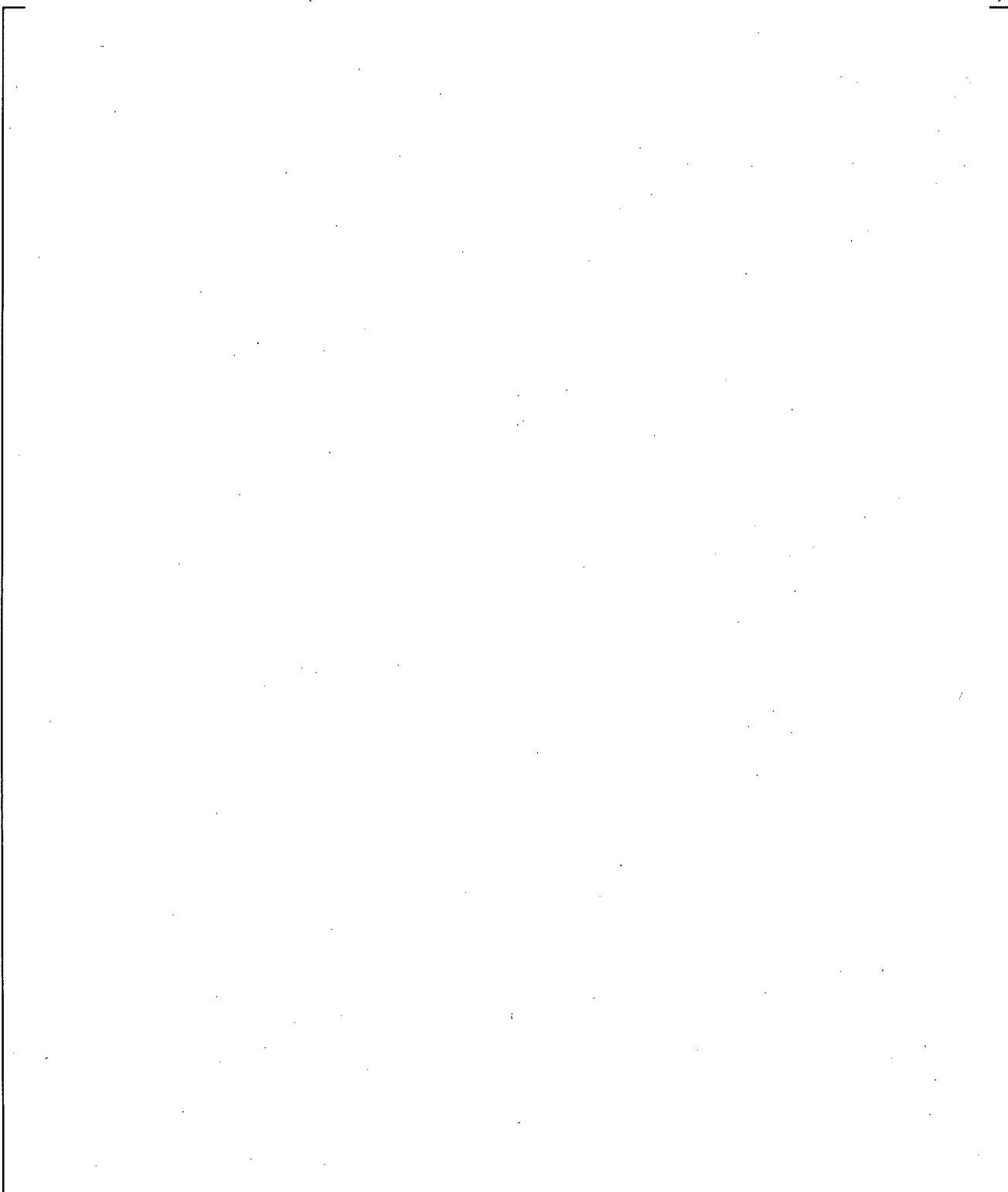


**Figure 15.7-3 Temperature Profile Near a Spacer Grid from ORNL Test N**

## 15.8 TIME STEP STUDY

Section 7 describes the WCOBRA/TRAC-TF2 models for the application of numerical damping to avoid rapid changes with time in the heat transfer models. To determine the impact of time-step size on the reflood heat transfer and numerical damping, the highest and lowest flooding rate cases from the FLECHT SEASET series (Tests 31701 and 31805, respectively) are exercised with the following maximum time-step sizes (DTMAX):

[

] <sup>a,c</sup>

Figure 15.8-1 compares the overall peak cladding temperatures for the Test 31701 transients, and Figure 15.8-2 compares the quench progression. As seen from the figures, the time-step sizes chosen here have [

] <sup>a,c</sup>.

Figure 15.8-3 compares the overall peak cladding temperatures for the Test 31805 transients, and Figure 15.8-4 compares the quench progression. As seen from the figures, the time-step sizes chosen here have [

] <sup>a,c</sup>.

Based on the above study, the changes in time step size has [

] <sup>a,c</sup> on the reflood portion of the transient, and can be executed at time steps up-to [ ] <sup>a,c</sup>.

a,c



**Figure 15.8-1 Peak Cladding Temperature Comparison for FLECHT Test 31701**

a,c



**Figure 15.8-2 Quench Front Progression Comparison for FLECHT Test 31701**

a,c



**Figure 15.8-3 Peak Cladding Temperature Comparison for FLECHT Test 31805**

a,c



**Figure 15.8-4 Quench Front Progression Comparison for FLECHT Test 31805**

## 15.9 HEAT TRANSFER COMPOSITE RESULTS

The simulations of separate effects tests which experienced single-phase vapor were described in Section 15.4; the dispersed-flow film boiling separate effects tests were described in Section 15.5; and, the reflood heat transfer separate effects tests were described in Section 15.6. Table 15.9-1 lists the major design features in these facilities that were modeled and simulated using WCOBRA/TRAC-TF2. Each of the test facilities was modeled in a consistent nodding scheme. [

] <sup>a,c</sup> Predicted and measured heater rod temperatures at several elevations in the test bundle were compared to demonstrate the ability of WCOBRA/TRAC-TF2 to simulate each transient.

This section summarizes additional comparisons to data for the core heat transfer separate effects tests. By using a consistent nodding methodology, the models and correlations cannot be "tuned" to match any one particular test or test series, and the user effects are minimized. Thus, the composite summary of the results presented in this section provides evidence that the WCOBRA/TRAC-TF2 heat transfer package is sufficiently general and accurate so that it can be used for a best-estimate PWR FULL SPECTRUM LOCA analysis.

**Table 15.9-1 Reflood Facilities Major Design Features**

a,c


## 15.9.1 Prediction of Cladding Temperatures and Quench Times

### Blowdown Cooling Rates

The simulations of the G-1 Blowdown heat transfer tests were described in Section 15.5.2.2. In these tests, the maximum cladding temperatures at all elevations occurred at or very near the beginning of the test. To assess the WCOBRA/TRAC-TF2 heat transfer package with these tests, three parameters can be compared; the cooling rate prior to quench, the time of quench, and the average heat transfer coefficient during the blowdown cooling period. The cooling rate prior to quench, referred to as the blowdown cooling rate, provides information on the models and correlations for dispersed droplet heat transfer, as well as convective heat transfer to single-phase vapor. The average blowdown cooling heat transfer coefficient also provides a means of assessing the WCOBRA/TRAC-TF2 models and correlations used in dispersed flow heat transfer. Comparisons of the time of quench provide information on the cumulative effects of the code's calculation of post-CHF heat transfer and the minimum film boiling temperature.

Figure 15.9.1-1 shows the comparison of blowdown cooling rates for the G-1 Blowdown tests. The blowdown cooling rates were calculated by subtracting the average bundle cladding temperature at a time  $t_1$  from an initial temperature at time  $t_0$ . The times were chosen [

]<sup>a,c</sup>. For some tests, at several locations, the cladding temperatures remained nearly constant before quenching. Both positive and negative axes are shown in the figure to identify elevations where the predicted and measured rates of temperature change were in opposite directions. In G-1 Blowdown Test 148, for example, the elevation 24 inches from the bottom of the heated length [

]<sup>a,c</sup>.

The predicted and estimated quench times for the G-1 Blowdown test are compared in Figure 15.9.1-2. At the upper- and lower-most elevations, WCOBRA/TRAC-TF2 is seen to [

]<sup>a,c</sup>.

### Refill Heat Transfer

The simulations of the G-2 Refill heat transfer tests also provide a means of assessing the overall capability of the WCOBRA/TRAC-TF2 heat transfer package. The simulation of the G-2 Refill tests was described in Section 15.5.2.3. In the G-2 Refill experiments, the cladding temperatures at most elevations in the bundle did not quench. Clad temperatures near the bundle mid-height increased steadily until termination of the test. These locations remained in post-CHF, two-phase flow throughout the test and simulations. Figure 15.9.1-3 compares the predicted and measured heater rod cladding temperatures at the end of the G-2 Refill tests. The figure shows that WCOBRA/TRAC-TF2 [

]<sup>a,c</sup>.

## Reflood Heat Transfer

The simulations of the reflood separate effects tests were found to predict the peak temperatures in most tests [ ]<sup>a,c</sup>. Figure 15.9.1-4 shows the comparison of the predicted maximum clad temperatures at several thermocouple elevations with the data for all of the simulated reflood separate effects tests. WCOBRA/TRAC-TF2 shows [ ]<sup>a,c</sup>.

Figures 15.9.1-5 through 15.9.1-7 show a comparison of predicted versus measured quench times for the FLECHT forced reflood tests. The elevations are the same as those used in the PCT comparisons. WCOBRA/TRAC-TF2 is seen to [ ]<sup>a,c</sup>. Figure 15.9.1-8 compares the predicted and measured turn-around times for the several locations in the forced reflood separate effects tests. There is a large scatter in the figure due to elevations in many of the tests that remained quasi-steady for a long period of time. This often occurs at upper elevations. Overall, the code [ ]<sup>a,c</sup>. Figure 15.9.1-9 compares the time the cladding temperature at the peak power elevation is greater than 1600°F for the FLECHT forced reflood tests. This is the temperature at which the oxidation kinetic is significant enough to result in appreciable transient oxidation. As the figure shows, the code [ ]<sup>a,c</sup>.

a,c



**Figure 15.9.1-1 Blowdown Cooling Rates for the G-1 Blowdown Heat Transfer Tests**

a,c



**Figure 15.9.1-2 Comparison of Predicted and Measured Quench Times in the G-1 Blowdown Heat Transfer Tests**

a,c

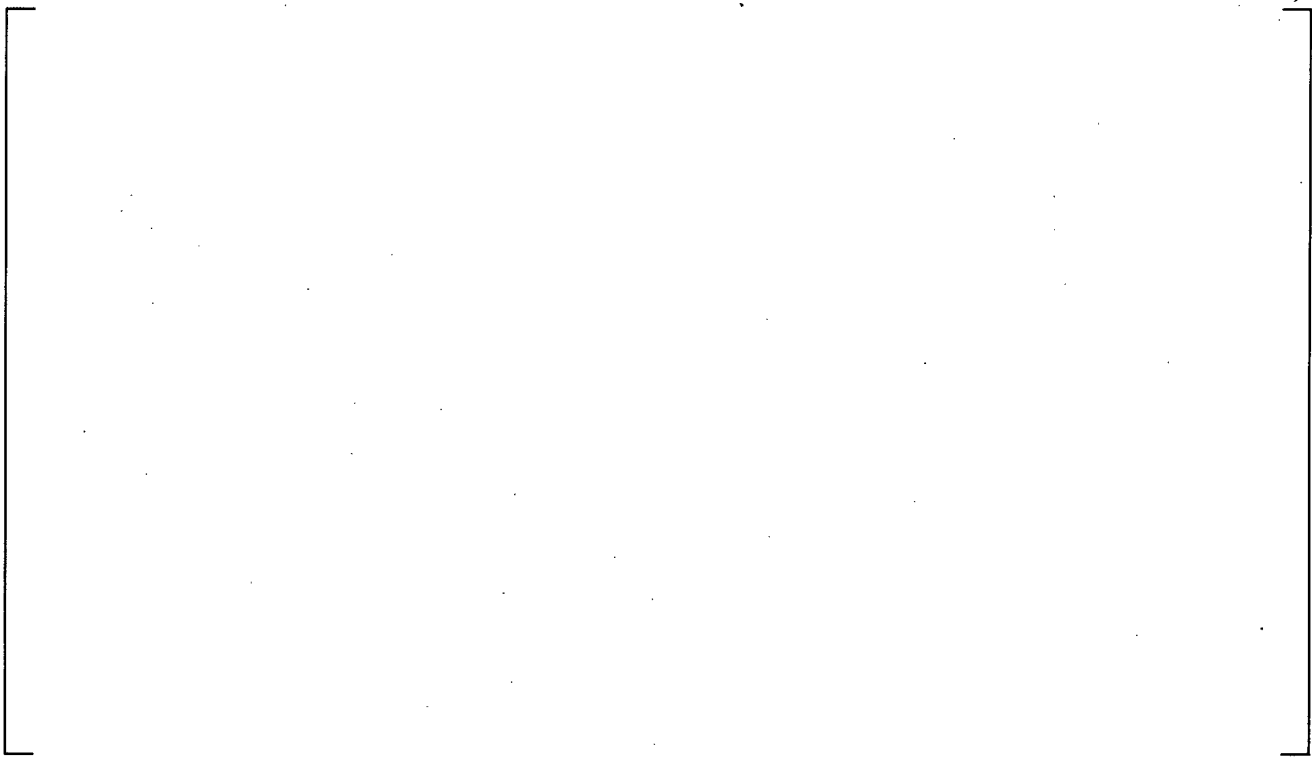


**Figure 15.9.1-3 Comparison of Predicted and Measured Clad Temperatures for the G-2 Refill Tests**

a,c



**Figure 15.9.1-4 Comparison of Predicted and Measured Maximum Clad Temperatures for all Reflood Separate Effects Tests Simulated**

a,c



**Figure 15.9.1-5 Comparison of Predicted and Measured Quench Times for the FLECHT SEASET Reflood Separate Effects Tests Simulated**

a,c



**Figure 15.9.1-6 Comparison of Predicted and Measured Quench Times for the FLECHT Low Flooding Rate Reflood Separate Effects Tests Simulated**

a,c

**Figure 15.9.1-7 Comparison of Predicted and Measured Quench Times for the FLECHT Skewed Reflood Separate Effects Tests Simulated**

a,c

**Figure 15.9.1-8 Comparison of Predicted and Measured Turn-Around Times for Each Reflood Separate Effects Tests Simulated**

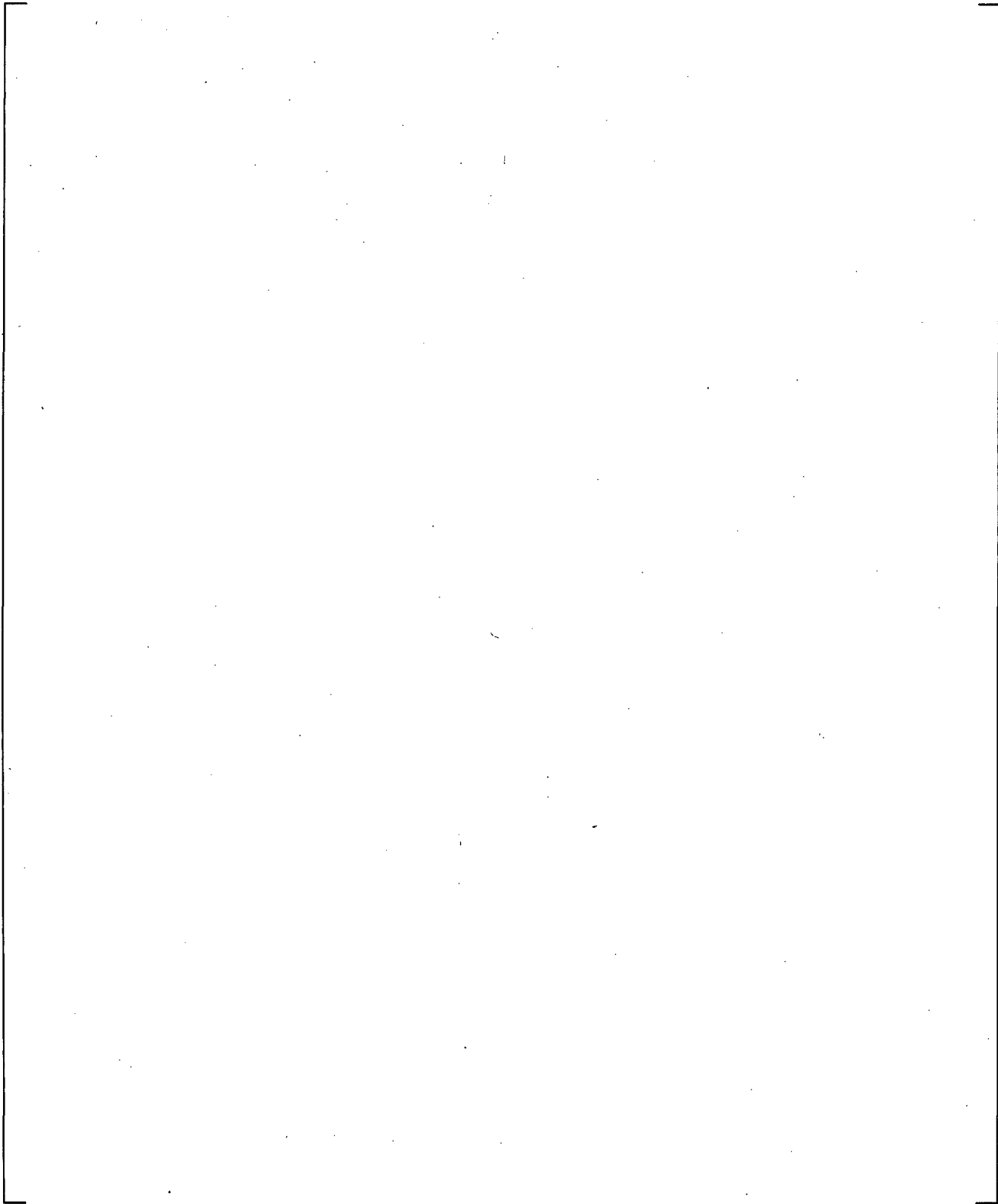


**Figure 15.9.1-9 Comparison of Predicted and Measured Time above 1600°F for the FLECHT Reflood Separate Effects Tests Simulated**

## 15.9.2 Droplet Assessment

### Dispersed Flow Film Boiling

In Section 15.5 of this report, WCOBRA/TRAC-TF2 was used to simulate a range of blowdown film boiling heat transfer experiments. In this section, the calculations will be examined in more detail to assess whether variables such as droplet phase velocity and droplet size are predicted correctly. While data will usually not be available to assess these quantities directly, judgments can be made whether the magnitude of these variables are reasonable, based on evidence from and experience in two-phase flow experiments and analyses.

The details of the film boiling heat transfer models have been given in Section 7 and are summarized in Figure 15.9.2-1. The film boiling package consists of the Bromley correlation for film boiling at low void fractions, and a detailed dispersed flow film boiling model at high void fractions. The figure indicates that as the void fraction increases, the Bromley correlation contribution to the total film boiling heat flux decreases, and the dispersed flow film boiling models become dominant. The wall-to-vapor convective heat transfer component increases as the wall-to-vapor temperature difference increases. Thermal radiation from the wall-to-vapor and from the wall-to-droplets is also calculated.

Two blowdown heat transfer experiments are examined in detail in this section to examine the WCOBRA/TRAC-TF2 calculations. The first test examined is G-1 Blowdown Test 154, and the second test is ORNL 3.08.6C.

#### G-1 Blowdown Test 154

[

] <sup>a,c</sup>

For a downflow situation, the entrained drop size is determined by the models described in Section 4. The G-1 bundle included [

] <sup>a,c</sup>

[

] <sup>a,c</sup>

The calculated axial temperature distribution is shown in Figure 15.9.2-7 along with the calculated vapor temperature. As this figure indicates, [

Figure 15.9.2-8 for this case, [

] <sup>a,c</sup> The resulting heat flux, shown in] <sup>a,c</sup>

Examining Figures 15.9.2-3 to 15.9.2-8 indicates what WCOBRA/TRAC-TF2 [

] <sup>a,c</sup>

#### ORNL Test 3.08.6C

ORNL Test 3.08.6C was an upflow film boiling experiment in which the bundle was initially in single-phase liquid flow at high pressure. A break was initiated at the test section outlet. The inlet mass flux and pressure in this test are higher than in G-1 Test 154 such that lower void fractions are calculated, as well as less non-equilibrium in the vapor phase. Figure 15.9.2-9 shows the calculated mass flows along the test section and shows [

] <sup>a,c</sup>

The calculated droplet diameter for the center channel is given in Figure 15.9.2-12 and shows that the calculated drop sizes which are [

] <sup>a,c</sup>

The entrained drops are being shattered by the spacer grids as described in Section 5. [

] <sup>a,c</sup>

Figure 15.9.2-13 shows the calculated droplet interfacial area/volume which shows [

] <sup>a,c</sup>

Figure 15.9.2-14 presents the calculated rod surface temperature, the calculated vapor temperature, and indicates where CHF occurs. Because of the high flowrate and significant amount of entrained liquid, the vapor does not become greatly superheated.

The rod heat flux is presented in Figure 15.9.2-15 and shows the different heat transfer regimes calculated for these conditions. The spacer grid locations are shown at the bottom of Figures 15.9.2-12 to 15.9.2-15. The calculated heater rod surface temperatures and the vapor temperature show the heat transfer improvement caused by the grids. This improvement is also reflected in the calculated heater rod surface heat flux. The calculated grid temperatures are also shown in Figure 15.9.2-14. All grids rewet in this calculation due to the low heater rod temperatures and the high flows.

A review of Figures 15.9.2-10 to 15.9.2-15 indicates that for this high flow, high pressure test, WCOBRA/TRAC-TF2 calculates the two-phase heat transfer behavior in a self consistent manner.

### **Reflood Assessment**

Sections 15.6.1 through 15.6.5 described the simulations of 21 different reflood separate effects tests using WCOBRA/TRAC-TF2. This section presents additional details of the code calculations for two of these reflood tests. The two tests which are examined are FLECHT SEASET Test 31701 and Test 31805, which bracket the range of flooding rates and clad temperatures expected in a best-estimate large break LOCA reflood transient. These two tests were also designated as US Standard Problem 9 and were originally used as part of the COBRA/TRAC validations by Thurgood et al. (1983).

#### FLECHT Test 31701

Test 31701 is a 40 psia, 6.1 in/sec constant forced flooding rate test. The high inlet flow results in a low quality flow with little thermal non-equilibrium and higher heat transfer rates than in tests with lower flood rates. This test is initiated with the bundle heated in steam to 1600°F. When this temperature is reached, the flow into the bundle is initiated and the rod bundle power is decayed following the ANS 1971 plus 20 percent decay curve starting at 40 seconds after the accident.

Because of the large flooding rates, the heater rod temperatures in Test 31701 turn around quickly and quench as described in Section 15.6.1.1.5. For a detailed evaluation, a time of 10 seconds into the transient was chosen since high speed films of the flow patterns were available from the test and analysis reports given by Lee et al. (1982).

The mass flows of each phase at 10 seconds are shown in Figure 15.9.2-16 and indicate [

] <sup>a,c</sup>

As Figure 15.9.2-20 indicates, [

] <sup>a,c</sup>

The calculated heater rod, spacer grid, and vapor temperatures are shown in Figure 15.9.2-19. The predicted heater rod temperatures have been compared to the test data in Section 15.6.1.1.5. The calculated spacer grid temperatures follow the calculated vapor temperatures for this test since the flows are high and the rod temperatures are relatively low. The center region of the bundle has [

] <sup>a,c</sup>.

For Test 31701, high speed movies taken through the windows of the housing of the FLECHT SEASET test facility. The movie data was reduced to obtain drop sizes and velocities for discrete times during the test. The movies were taken at the three-foot and nine-foot elevations (relative to the heated length) and drop velocities and sizes were estimated from the high speed movies (Lee et al., 1982). Figures 15.9.2-22 and 15.9.2-23 show the measured droplet data along with the drop sizes and velocities calculated by WCOBRA/TRAC-TF2 for the time period observed in the movies. [

] <sup>a,c</sup>

Figure 15.9.2-24 shows the calculated droplet diameter plotted as a function of elevation at 10 seconds into the transient. As the drops progress up the bundle, they are shattered by the spacer grids and the resulting drop sizes decrease. Most of the droplet shattering occurs low in the bundle where the droplet Weber number is large due to the large drop size and droplet velocities. Further up the bundle, the drop size is reduced and velocities are lower, resulting in a lower droplet Weber number such that less drop shattering is calculated, and the resulting change in drop size is smaller as seen in Figure 15.9.2-24.

The calculated interfacial area for droplet-to-vapor heat transfer is shown in Figure 15.9.2-25 for Test 31701. As the figure indicates, the interfacial area significantly increases in the lower regions of the bundle where the spacer grids are shattering drops and decreases at the top of the bundle due to droplet evaporation. Figure 15.9.2-26 is a histogram indicating the percent of drops that are of a given size. WCOBRA/TRAC-TF2 predicts a single average drop size, which changed over the time periods sampled

over the first 10 seconds. The predicted distribution [ ]<sup>a,c</sup>.

### FLECHT Test 31805

The second FLECHT SEASET experiment examined in detail is Test 31805. This is a constant pressure, low flooding rate test with poor overall rod heat transfer compared to Test 31701. The nominal inlet flooding rate was 0.81 in/sec and the initial temperature was 1600°F. This test attained peak temperatures near 2200°F. The WCOBRA/TRAC-TF2 results at 100 seconds are examined to show the self-consistency in the heat transfer models. Figure 15.9.2-27 shows the mass flows for each phase along the bundle and indicates that continuous liquid flow is evaporated or entrained as droplets form at the quench front. The phase velocities are shown in Figure 15.9.2-28, the void fractions for each phase are given in Figure 15.9.2-29 and the net vapor generation is given in Figure 15.9.2-30. Unlike Test 31701, there is very little liquid sub-cooling at the quench front, so that the quench front energy release results primarily in steam generation.

The quench front heat release and subsequent steam generation result in a large vapor fraction change just above the quench front, as the flow regime transitions from a bubbly flow to a dispersed flow. The high heat release at the quench front and the low vapor void fraction gives rise to large local vapor velocities.

The calculated heater rod surface, spacer grid, and vapor temperatures along the bundle length for the inner channel are shown in Figure 15.9.2-31. Only the spacer grids [

] <sup>a,c</sup>

The improvement in heat transfer downstream of a spacer grid can be seen in the calculated surface temperature at the grid locations in Figure 15.9.2-31. The rod surface heat flux is shown in Figure 15.9.2-32 and indicates the different heat transfer regimes along the rod surface. The majority of the heater rod is in DFFB.

Figure 15.9.2-33 shows the droplet diameter size along the test bundle at 100 seconds into the test. [

] <sup>a,c</sup> The calculated interfacial area per unit volume for droplet-to-vapor heat transfer is presented in Figure 15.9.2.34 showing [ ] <sup>a,c</sup>. The interfacial area/volume is largest in [ ] <sup>a,c</sup>. Above this elevation the droplet Weber number becomes smaller, such that there is less breakup and the drops evaporate in the presence of the highly superheated vapor, resulting in a decreased drop diameter along the length of the bundle.

There was high speed movie data taken for Test 31805 at the bundle mid-plane (six-foot elevation) for an extended period of time. Although the precise time of the filming was not recorded, Test 31805 is a long quasi-steady-state test where the flow conditions change very slowly and the bundle is in dispersed flow film boiling for several minutes. Calculated drop sizes and velocities at the bundle mid-plane (six-foot elevation) at several time periods just before and after 100 seconds were used to compare to the test data.

Figure 15.9.2.35 shows the comparisons of the calculated droplet velocities and sizes with respect to the test data. The drop velocities are [

]<sup>a,c</sup>.

The WCOBRA/TRAC-TF2 droplet size model for bottom reflood is described in Section 5.6.3, and was based on earlier FLECHT reflood data. Therefore, it is not surprising that good agreement is achieved with the FLECHT SEASET movie data.

As with the blowdown analysis described in previously, the WCOBRA/TRAC-TF2 heat transfer package provides a self-consistent model which captures the complex non-equilibrium two-phase flow phenomena found in the reflood experiments.

a,c

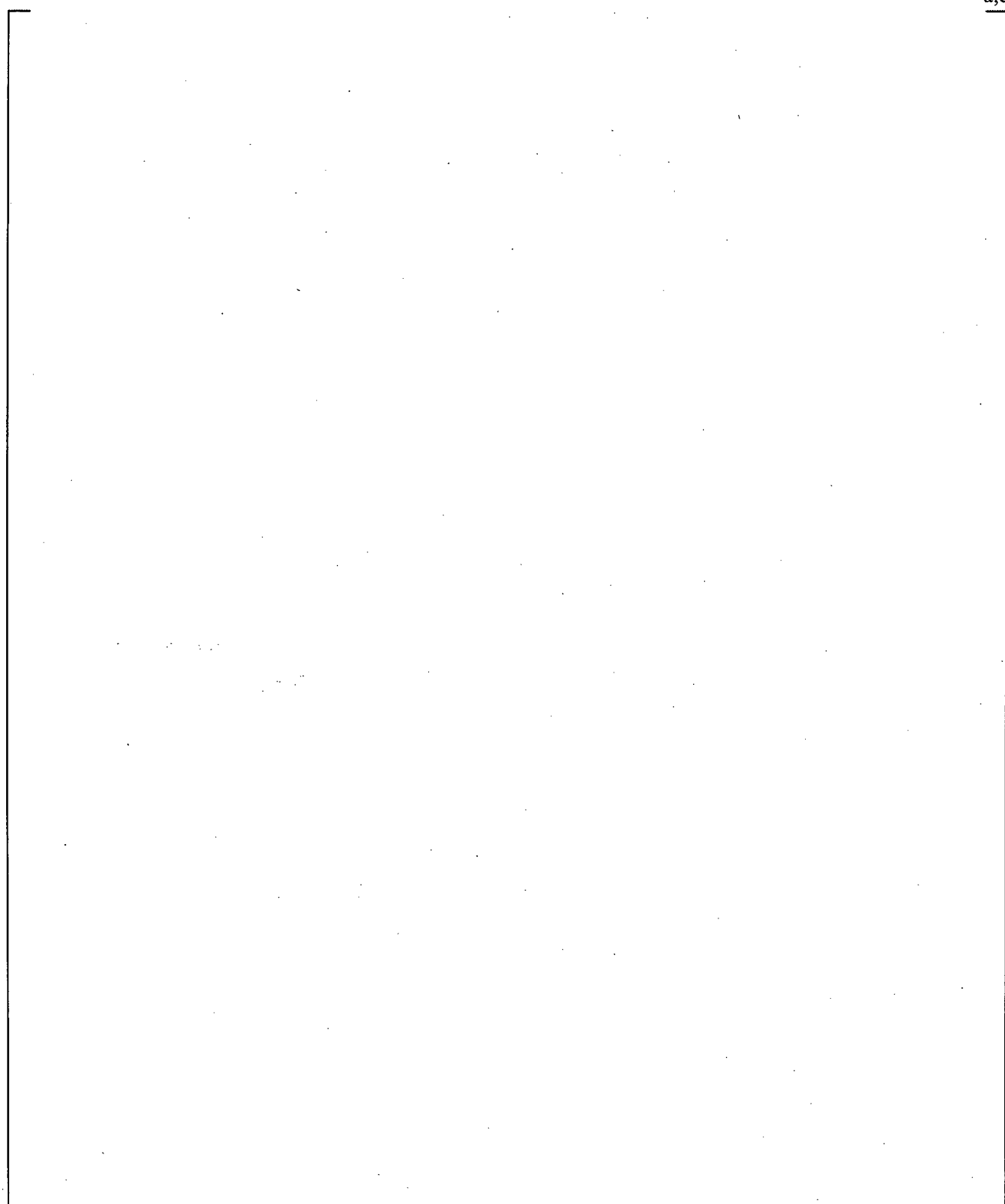


Figure 15.9.2-1 WCOBRA/TRAC-TF2 Film Boiling Model Components

a,c

**Figure 15.9.2-2**

**Calculated Mass Flows as a Function of Elevation for G-1 Test 154 at 10 Seconds into the Test**

a,c

**Figure 15.9.2-3**

**Calculated Phase Velocities as a Function of Elevation for G-1 Test 154 at 10 Seconds into the Test**

a,c



**Figure 15.9.2-4**      **Calculated Volume Fraction as a Function of Elevation for G-1 Test 154 at 10 Seconds into the Test**

a,c



**Figure 15.9.2-5**      **Calculated Droplet Size as a Function of Elevation for G-1 Test 154 at 10 Seconds into the Test**

a,c



**Figure 15.9.2-6**      **Calculated Droplet (Entrained Phase) Interfacial Surface Area as a Function of Elevation for G-1 Test 154 at 10 Seconds into the Test**

a,c



**Figure 15.9.2-7**      **Calculated Heater Rod Surface Temperature, Spacer Grid Temperature, and Vapor Temperature as a Function of Elevation for G-1 Test 154 at 10 Seconds into the Test**

a,c

**Figure 15.9.2-8**      **Calculated Heater Rod Surface Heat Flux and Heat Transfer Mode as a Function of Elevation for G-1 Test 154 at 10 Seconds into the Test**

a,c

**Figure 15.9.2-9**      **Calculated Mass Flowrates as a Function of Elevation for ORNL Test 3.08.6C at 59.5 Seconds into the Test**

a,c



**Figure 15.9.2-10**      **Calculated Phase Velocities as a Function of Elevation for ORNL Test 3.08.6C at 59.5 Seconds into the Test**

a,c



**Figure 15.9.2-11**      **Calculated Phase Volume Fraction as a Function of Elevation for ORNL Test 3.08.6C at 59.5 Seconds into the Test**

a,c

**Figure 15.9.2-12**

**Calculated Droplet Diameter as a Function of Elevation for ORNL  
Test 3.08.6C at 59.5 Seconds into the Test**

a,c

**Figure 15.9.2-13**

**Calculated Droplet Interfacial Area as a Function of Elevation for ORNL  
Test 3.08.6C at 59.5 Seconds into the Test**

a,c



**Figure 15.9.2-14**      **Calculated Heater Rod Surface Temperature, Spacer Grid Temperature, and Vapor Temperature as a Function of Elevation for ORNL Test 3.08.6C at 59.5 Seconds into the Test**

a,c



**Figure 15.9.2-15**      **Calculated Heater Rod Surface Heat Flux and Heat Transfer Mode as a Function of Elevation for ORNL Test 3.08.6C at 59.5 Seconds into the Test**

a,c

**Figure 15.9.2-16**      **Calculated Mass Flowrate of Each Phase as a Function of Elevation for FLECHT SEASET Test 31701 at 10 Seconds into the Test**

a,c

**Figure 15.9.2-17**      **Calculated Vapor and Entrained (Droplet) Velocities as a Function of Elevation for FLECHT SEASET Test 31701 at 10 Seconds into the Test**



**Figure 15.9.2-18**      **Calculated Phase Volume Fractions as a Function of Elevation for FLECHT SEASET Test 31701 at 10 Seconds into the Test**



**Figure 15.9.2-19**      **Calculated Heater Rod Surface Temperature, Spacer Grid Temperature, and Vapor Temperature as a Function of Elevation for FLECHT SEASET Test 31701 at 10 Seconds into the Test**



**Figure 15.9.2-20**      **Calculated Heater Rod Heat Flux as a Function of Elevation for FLECHT SEASET Test 31701 at 10 Seconds into the Test**



**Figure 15.9.2-21**      **Calculated Net Vapor Generation Rate as a Function of Elevation for FLECHT SEASET Test 31701 at 10 Seconds into the Test**

a,c

**Figure 15.9.2-22**

**Comparison of Calculated Droplet Size and Drop Velocity at the Three-Foot Elevation with FLECHT SEASET Test Data for Test 31701 (1 – 10 s)**

a,c

**Figure 15.9.2-23**

**Comparison of Calculated Droplet Size and Drop Velocity at the Nine-Foot Elevation with FLECHT SEASET Test Data for Test 31701 (1 – 10 s)**

a,c



**Figure 15.9.2-24**      **Calculated Droplet Diameter as a Function of Elevation for FLECHT SEASET Test 31701 at 10 Seconds into the Transient**

a,c



**Figure 15.9.2-25**      **Calculated Droplet Interfacial Area/Volume as a Function of Elevation for FLECHT SEASET Test 31701 at 10 Seconds into the Test**



**Figure 15.9.2-26 Comparison of Calculated Droplet Size Frequency for FLECHT SEASET Test 31701 (Results are from the 9-foot Elevation for 1 to 8 Seconds)**

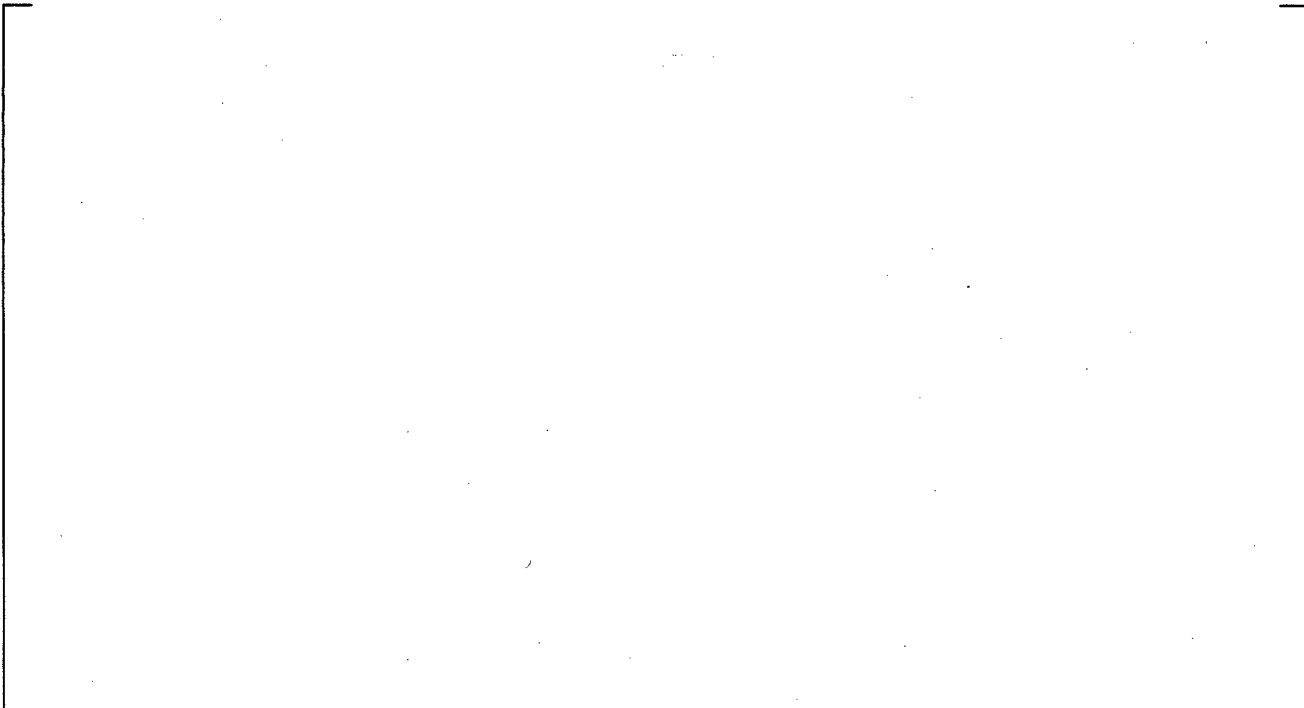


**Figure 15.9.2-27 Calculated Mass Flow for Each Phase as a Function of Elevation for FLECHT SEASET Test 31805 at 100 Seconds into the Test**



**Figure 15.9.2-28**

**Calculated Phase Velocities as a Function of Elevation for FLECHT SEASET Test 31805 at 100 Seconds into the Test**

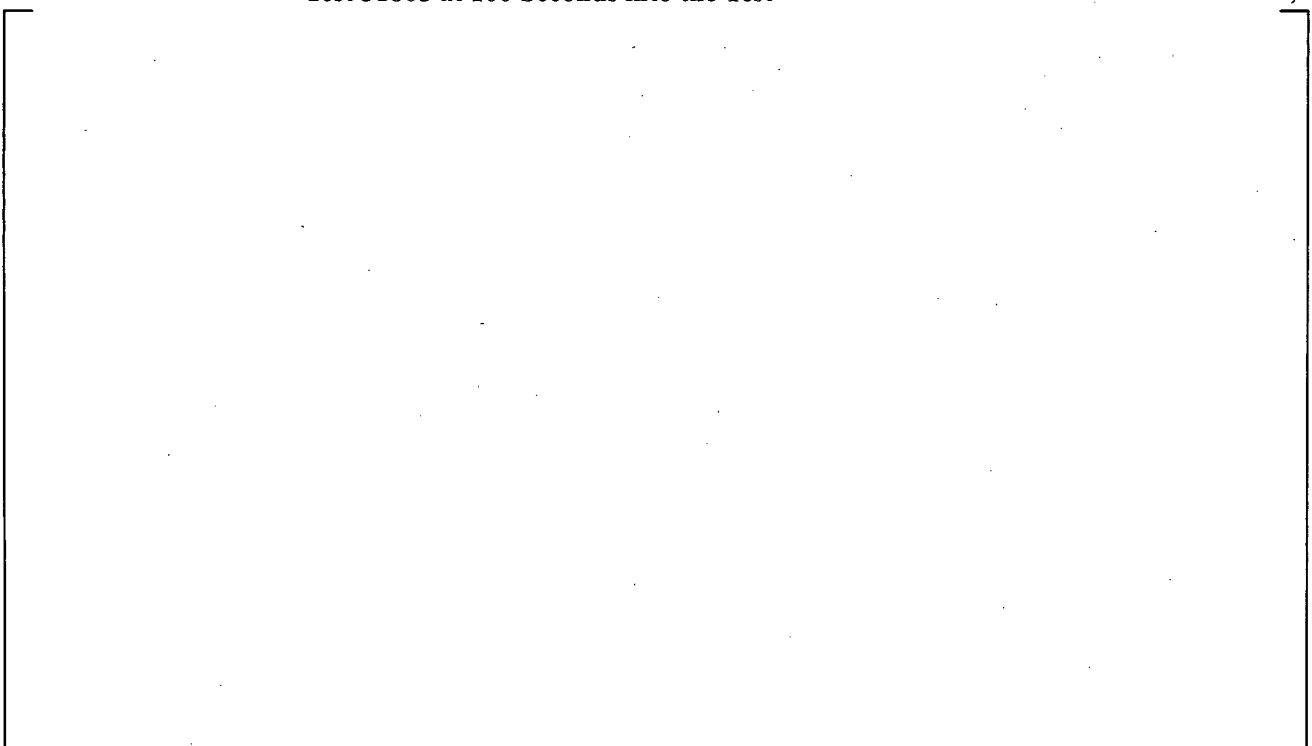


**Figure 15.9.2-29**

**Calculated Phase Void Fractions for Each Phase as a Function of Elevation for FLECHT SEASET Test 31805 at 100 Seconds into the Transient**

a,c

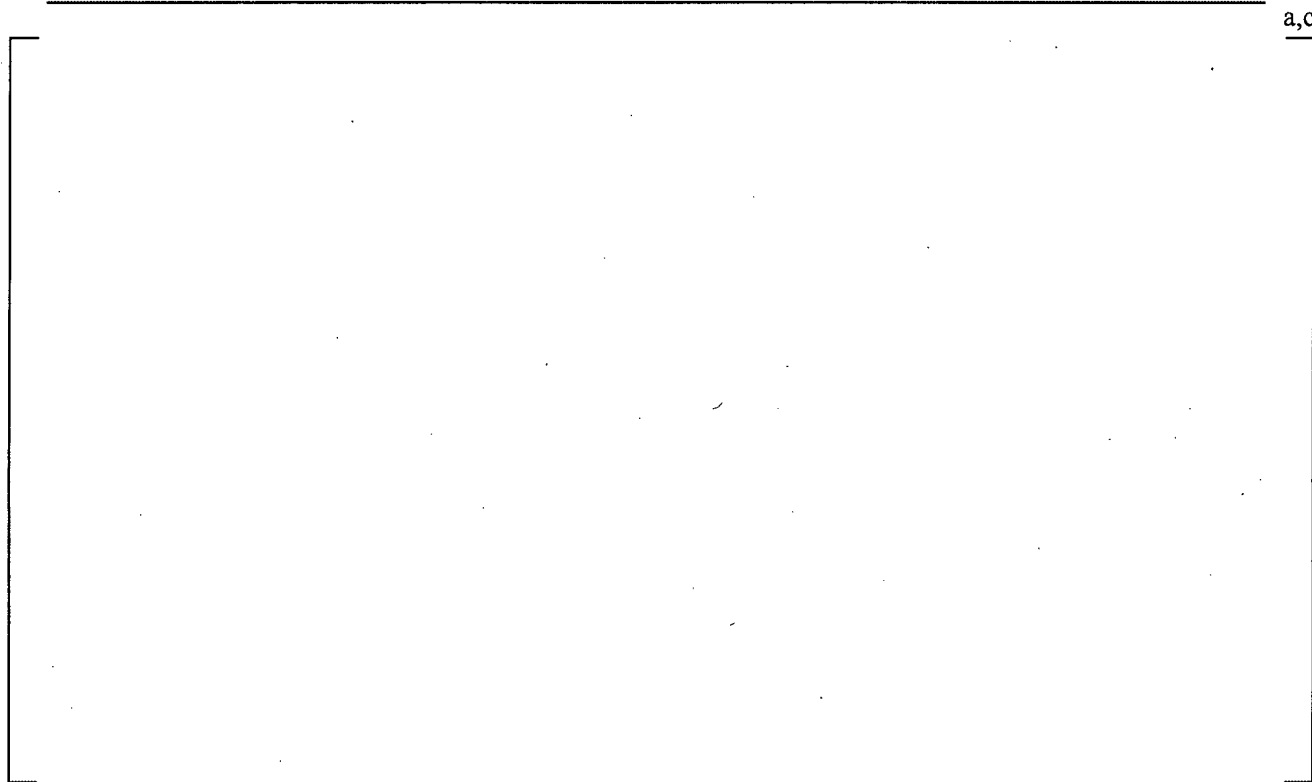


**Figure 15.9.2-30**      **Calculated Net Vapor Generation as a Function of Elevation for FLECHT SEASET Test 31805 at 100 Seconds into the Transient**

a,c



**Figure 15.9.2-31**      **Calculated Heater Rod Surface Temperature, Spacer Grid Temperature, and Vapor Temperature as a Function of Elevation for FLECHT SEASET Test 31805 at 100 Seconds into the Test**

a,c



**Figure 15.9.2-32**      **Calculated Heater Rod Surface Heat Flux as a Function of Elevation for FLECHT SEASET Test 31805 at 100 Seconds into the Test**

a,c



**Figure 15.9.2-33**      **Calculated Droplet Diameter as a Function of Elevation for FLECHT SEASET Test 31805 at 100 Seconds into the Test**

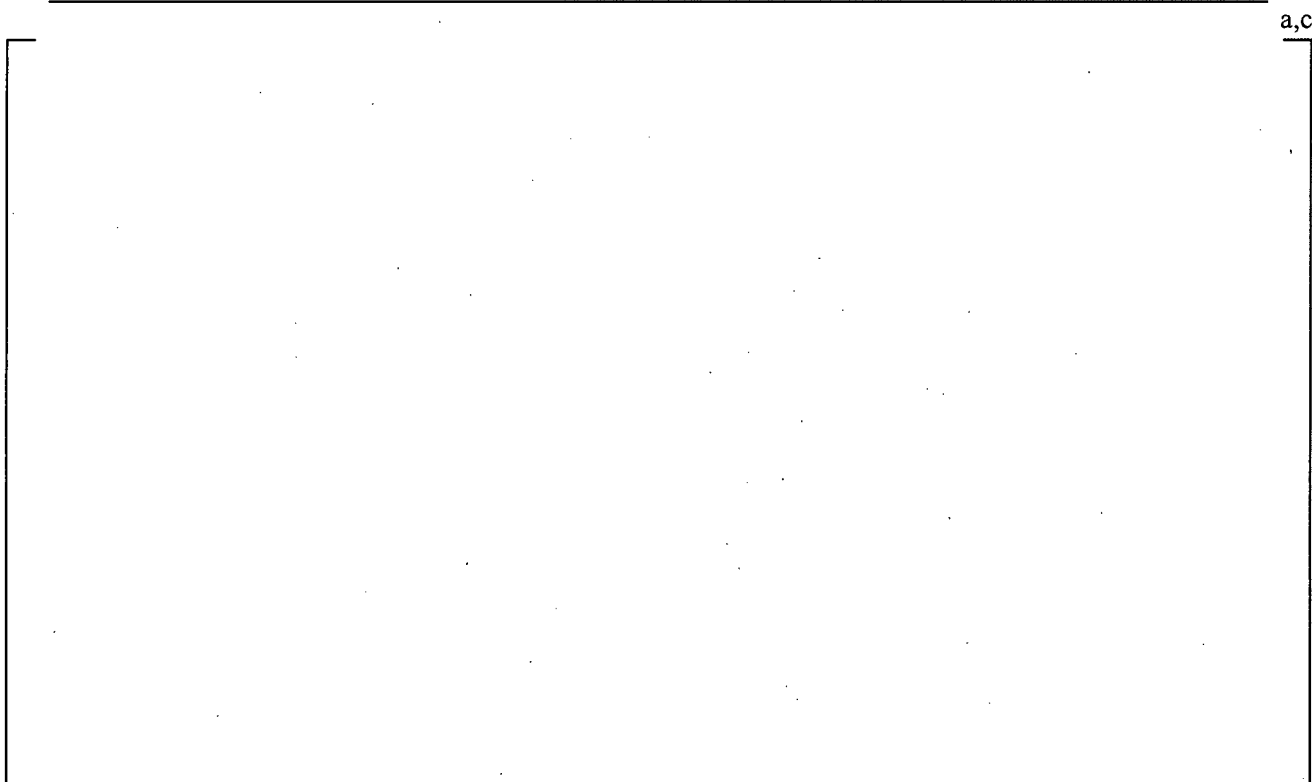


**Figure 15.9.2-34**      **Calculated Droplet Interfacial Surface Area/Volume as a Function of Elevation for FLECHT SEASET Test 31805 at 100 Seconds into the Test**



**Figure 15.9.2-35**      **Comparison of Calculated Drop Size and Velocities with FLECHT SEASET Test Data for Test 31805 at 6 ft (30 – 40 s)**

### 15.9.3 SIMULATION OF PARAMETRIC TRENDS

This section provides a description of the effects of principle test parameters and demonstrates the ability of WCOBRA/TRAC-TF2 to simulate variations in those parameters. The test simulation matrix for WCOBRA/TRAC-TF2 validation includes a number of tests that varied only one parameter at a time. The parametric effects examined are flooding rate, pressure, and subcooling.

#### Flooding Rate Effect

The FLECHT SEASET Tests 31805 (0.8 in/sec), 31504 (1.0 in/sec), 31203 (1.5 in/sec), and 31701 (6.1 in/sec) constitute a set of tests with the same test conditions except for the flooding rate. Figure 15.9.3-1 shows the experimental effect of flooding rate on heat transfer coefficient reported by Lee et al. (1982) for several FLECHT SEASET tests. The WCOBRA/TRAC-TF2 prediction of this same trend is shown in Figure 15.9.3-2. A comparison of these two figures shows that WCOBRA/TRAC-TF2 [ ]<sup>a,c</sup>.

The flooding rate effect on cladding temperature as determined experimentally is shown in Figure 15.9.3-3, and the WCOBRA/TRAC-TF2 predicted trend is shown in Figure 15.9.3-4. The code [ ]<sup>a,c</sup>.

The quench front advance as a function of flooding rate is shown in Figure 15.9.3-5 for the data and in Figure 15.9.3-6 for the WCOBRA/TRAC-TF2 predictions. [ ]<sup>a,c</sup>

#### Pressure Effect

Several experimental reflood tests have shown that heat transfer improves at higher pressure. Figure 15.9.3-7 shows the observed experimental effect on the measured heat transfer coefficient for three FLECHT SEASET tests. WCOBRA/TRAC-TF2 simulations for FLECHT SEASET Tests 31504 (40 psia) and 32013 (60 psia) were run to evaluate the ability of the code to predict the pressure effect. Figure 15.9.3-8 shows the predicted heat transfer coefficients at the 72-inch elevation for Tests 31504 and 32013. [ ]<sup>a,c</sup>

Simulations of FLECHT Low Flooding Rate Tests 04641 (20 psia) and 05132 (40 psia) also test the ability of the code to predict the pressure effect. Heat transfer coefficients from these two simulations are compared in Figure 15.9.3-9. In this comparison, [ ]<sup>a,c</sup>.

The experimental effect of pressure on cladding temperature is shown in Figure 15.9.3-10. The simulated effect for FLECHT SEASET Tests 31504 and 32013 is shown in Figure 15.9.3-11 and for FLECHT Tests 05132 and 04641 in Figure 15.9.3-12. Figure 15.9.3-13 shows the effect of pressure on the quench front advance from the experiments, and Figures 15.9.3-14 and 15.9.3-15 show the code predicted effect.

The experimental results show similar maximum cladding temperatures with an earlier quench within increasing pressure. The predictions [ ]<sup>a,c</sup>.

### Subcooling Effect

The effect of subcooling on cladding temperature has been investigated in the FLECHT SEASET, FLECHT (Cosine) Low Flooding Rate, and the FLECHT Skewed Power test series with the results shown in Figure 15.9.3-16. Tests in each of these series demonstrated that subcooling has a fairly weak effect on the cladding temperature rise. Two of the test series showed that cladding temperature rise decreased with higher subcooling, while the skewed power tests indicated a slight increase in temperature rise with subcooling.

### FLECHT SEASET

To determine the code sensitivity to inlet subcooling for forced reflood tests, a series of calculations was performed using FLECHT SEASET Test 31504 as a base case. This test was a 40 psia test, with a nominal inlet flooding rate of 1.0 in/sec and an initial peak rod power of 0.7 kW/ft. The inlet subcooling for Test 31504 was 144°F. This test matched conditions from the FLECHT SEASET tests that composed the "SUBCOOLING" tests listed on page 2-15 of Lee et al. (1982).

The main parameters of interest of the subcooling tests are listed in Table 15.9.3-1. Test 31504 is included for comparison.

Lee et al. (1982) concluded that the subcooling effect was very weak and that temperature rise decreased slightly with higher inlet subcooling based on experimental results from Tests 35114 and 31504.

Figure 15.9.3-16 shows the trends in clad temperature rise and quench time with inlet subcooling for FLECHT SEASET, FLECHT Cosine, and Skewed Power Tests as reported by Lee et al. (1982). The FLECHT SEASET points in the figure refer to Test 35114 ( $\Delta T_{sub} = 7.9^{\circ}\text{C} = 14.2^{\circ}\text{F}$ ) and Test 31504 ( $\Delta T_{sub} = 80^{\circ}\text{C} = 144^{\circ}\text{F}$ ). [ ]<sup>a,c</sup>

A WCOBRA/TRAC-TF2 sensitivity to inlet subcooling was obtained by making several calculations in which the inlet subcooling was the only boundary condition that was varied. The input deck for Test 31504 was used, and the calculations are summarized in Table 15.9.3-2. The column  $PCT_{1,6}$  represents the Rod 1 peak clad temperature (PCT) at the 6.08-foot elevation, and  $TQ_{1,6}$  is the quench time for that elevation.

[ ]<sup>a,c</sup>

[

] <sup>a,c</sup>

Figure 15.9.3-18 shows the predicted and measured trends with inlet subcooling on quench time at the 6-foot elevation. The data indicates a trend toward an earlier quench time as the inlet subcooling increases, [ ] <sup>a,c</sup>. Both show the effect to be weak. This is the same conclusion drawn by (Lee, et al., 1982) which reported that the effect of subcooling for these tests is very weak, as supported by Figure 3-18 in that report (Figure 15.9.3-16 here).

#### FLECHT LFR

In the FLECHT series of tests, two experiments were reported as being part of the "Subcooling" test series. Those tests were Tests 05342 and 05543. The conditions for these tests are listed in Table 15.9.3-4. Test 05132 data is listed for reference.

A similar sensitivity study was run for the FLECHT facility using Test 05132 as a base case. (This test was selected because it matched the rod power. The inlet flooding rate, however, is higher than that of the experimental tests composing the subcooling sensitivity study.) Table 15.9.3-5 lists results of that sensitivity study using WCOBRA/TRAC-TF2.

[

] <sup>a,c</sup>

#### FLECHT Top Skewed Power

In the FLECHT Top Skewed Power Test series three tests are listed in the data report as being part of the subcooling effect tests. Tests 13812 and 15713 were both conducted at 40 psia. The third test (Test 13914) was run at 21 psia. All three of these tests were simulated as part of the WCOBRA/TRAC-TF2 assessment matrix. Figures 15.9.3-21 and 15.9.3-22 show comparisons of the effects of subcooling on skewed power facility results. Consistent with the other experimental results in the other facilities, the data peak temperatures increase with higher inlet subcooling. [

] <sup>a,c</sup>

#### **Conclusions**

Sensitivity studies for the FLECHT SEASET, FLECHT LFR, and FLECHT Top Skewed facility bundles using WCOBRA/TRAC-TF2 indicate that the code [

] <sup>a,c</sup>

[

] <sup>a,c</sup>

**Table 15.9.3-1 FLECHT SEASET Sub-cooling Test Series – Test Data**

Test No.	Pressure (psia)	Rod Peak Power (kW/ft)	Flooding Rate (in/sec)	Coolant Temp (°F)	$\Delta T_{sub}$ (°F)	Max Temp (°F)	Temp Rise (°F)
32114	40	0.70	1.0-1.22	257	10	2172	628
35114	40	0.74	0.98	253	14	2178	550
34815	20	0.74	0.98	221	7	2152	555
34316	40	0.74	0.97	124-246	143-21	2206	646
31504	40	0.70	0.97	123	144	2101	593

**Table 15.9.3-2 FLECHT SEASET Predicted Sub-cooling Sensitivity Study Results**


a,c

**Table 15.9.3-3 Average PCT – Based on Data for Six-foot Thermocouples**

Pressure (psia)	$\Delta T_{sub}$ (°F)	Ave PCT (°F)	Ave TQ (°F)
40	10	1970	270
40	14	1947	356
20	7	1915	502
40	143-21	2041	302
40	144	1970	270

**Table 15.9.3-4 FLECHT Low Flooding Rate Sub-cooling Test Series – Test Data**

Test	Rod Peak Power (kW/ft)	Flooding Rate (in/sec)	Coolant Temp (°F)	$\Delta T_{sub}$ (°F)
05342	0.95	0.80	248	19
05543	0.95	0.81	188	79
05132	0.95	0.99	127	140

**Table 15.9.3-5 FLECHT Low Flooding Rate Inlet Sub-cooling Sensitivity Using WCOBRA/TRAC-TF2**


a,c

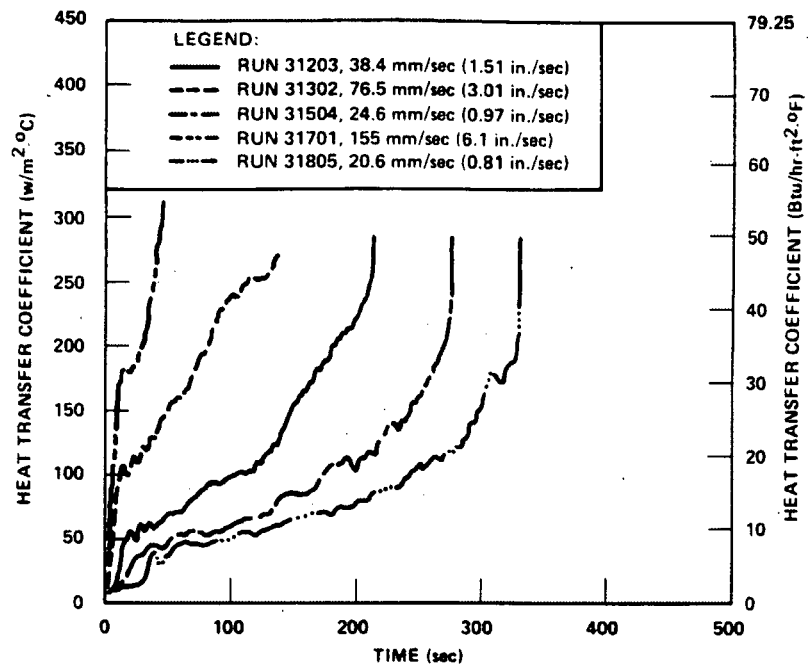
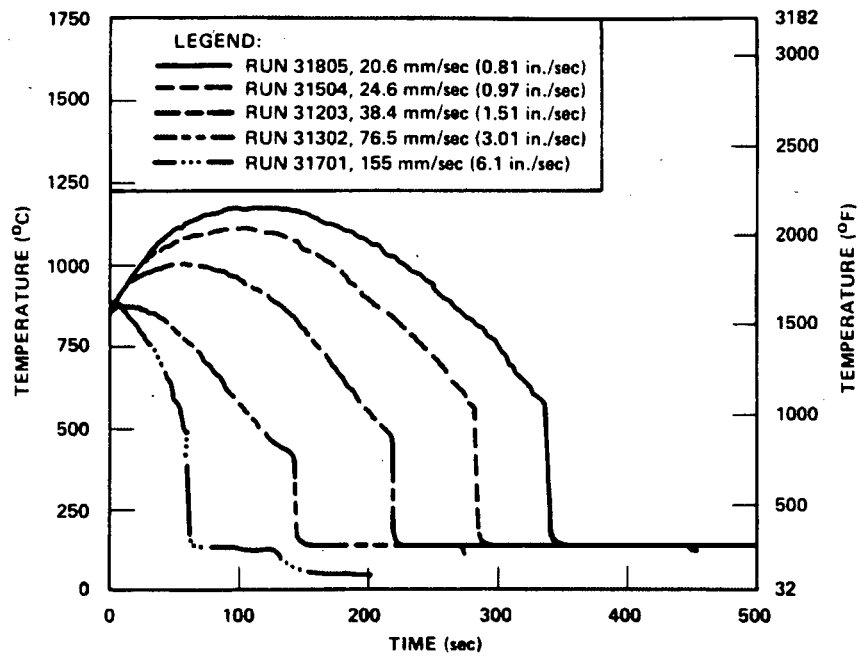


Figure 15.9.3-1 Effect of Flooding Rate on Heat Transfer Coefficient as Determined from Experimental Data (Lee et al., 1982)

a,c

Figure 15.9.3-2 Predicted Effect of Flooding Rate on Heat Transfer Coefficient



**Figure 15.9.3-3 Effect of Flooding Rate on Clad Temperature at the 72-inch Elevation as Determined from Experimental Data (Lee et al., 1982)**



**Figure 15.9.3-4 Predicted Effect of Flooding Rate on Clad Temperature at the 72-inch Elevation**

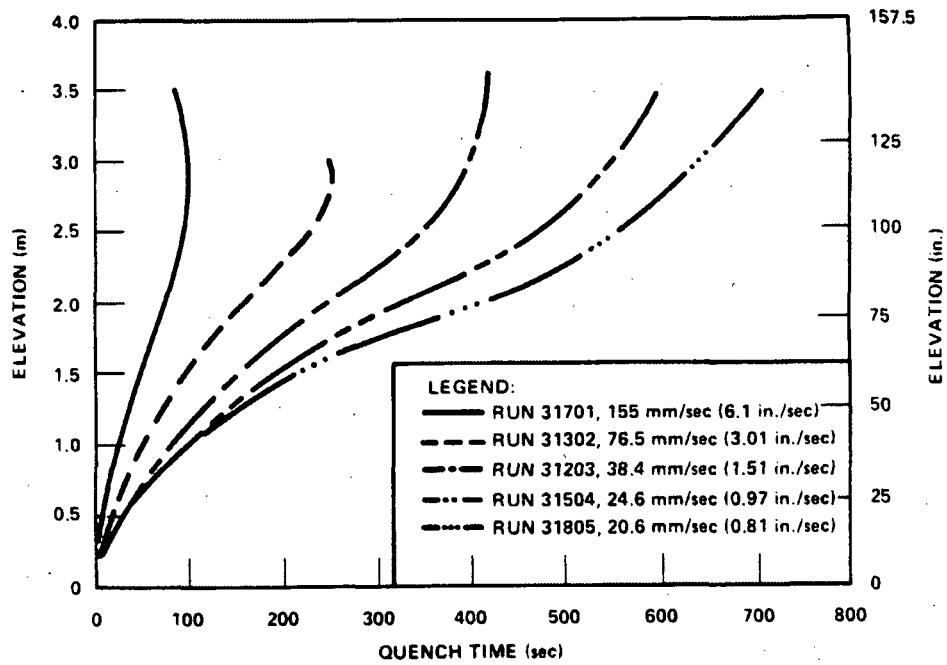


**Figure 15.9.3-5 Effect of Flooding Rate on Quench Front Advance as Determined from Experimental Data (Lee et al., 1982)**



**Figure 15.9.3-6 Predicted Effect of Flooding Rate on Quench Front Advance**

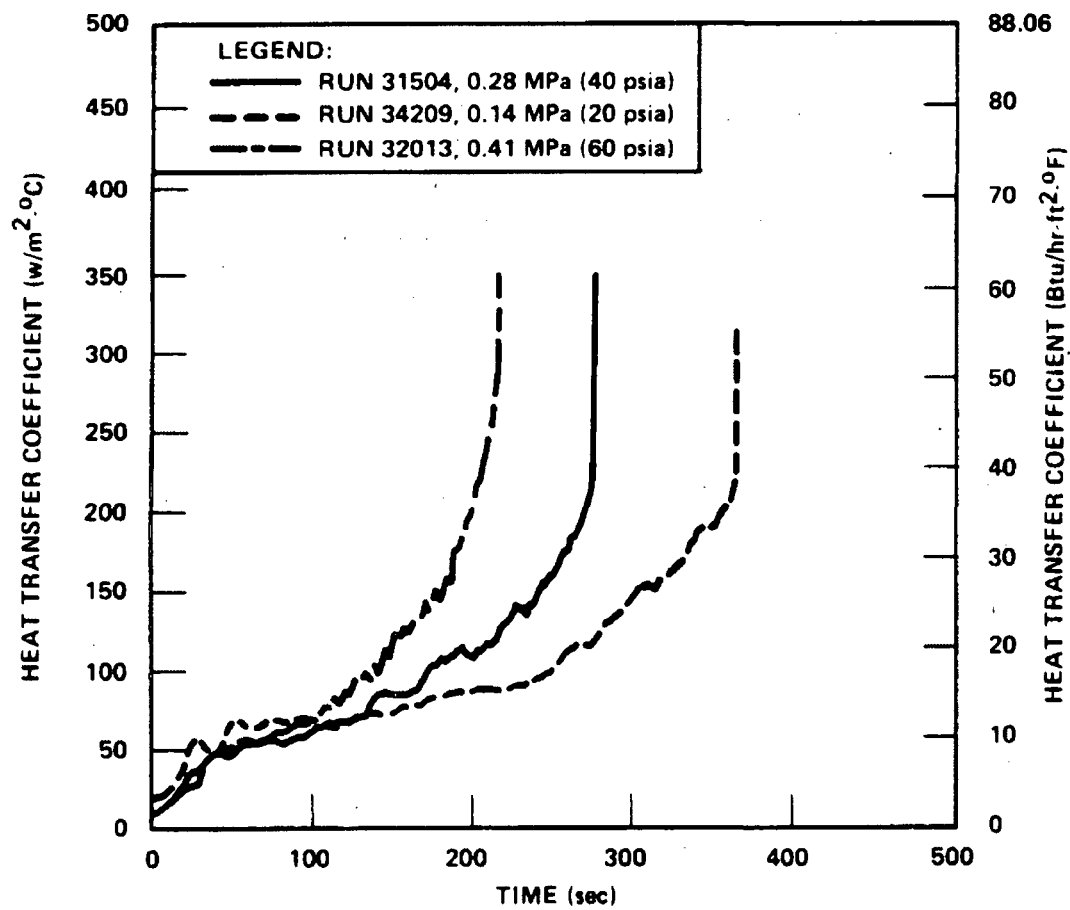
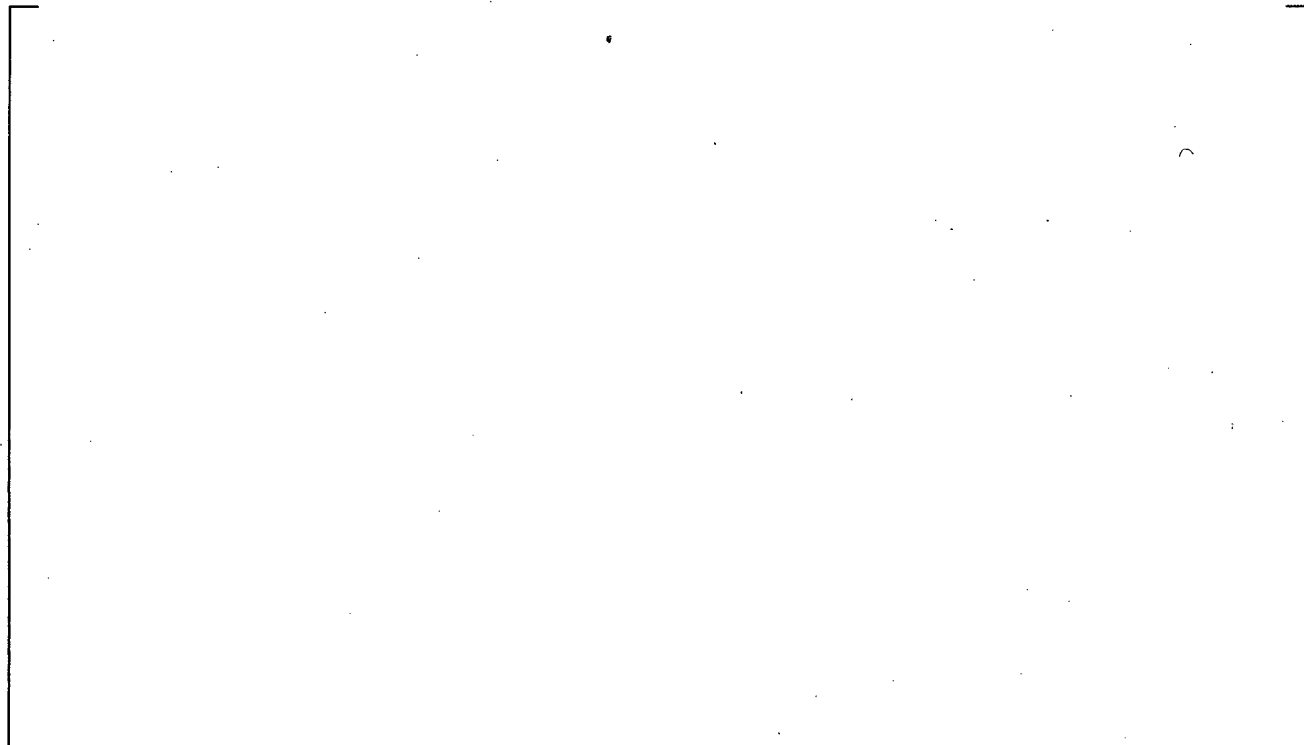


Figure 15.9.3-7 Effect of Pressure on Heat Transfer Coefficient as Determined from Experimental Data (Lee et al., 1982)

a,c



**Figure 15.9.3-8 Predicted Effect of Pressure on Heat Transfer Coefficient**

a,c



**Figure 15.9.3-9 Predicted Effect of Pressure on Heat Transfer Coefficient (FLECHT Low Flooding Rate)**

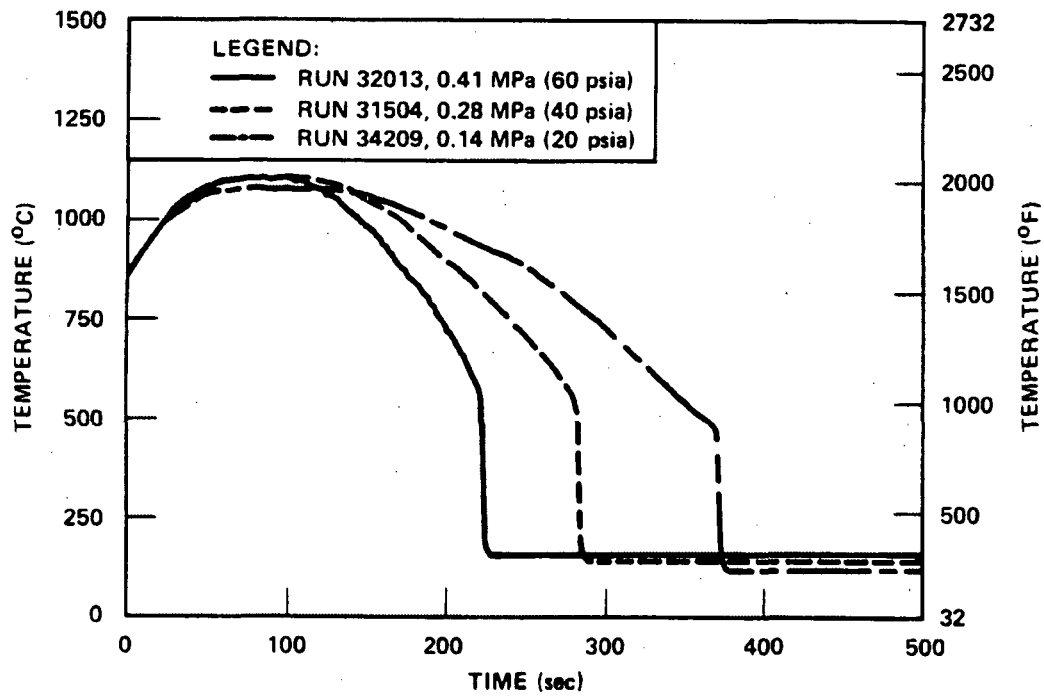


Figure 15.9.3-10 Effect of Pressure on Clad Temperature at the 72-inch Elevation as Determined from Experimental Data (Lee et al., 1982)

a,c



**Figure 15.9.3-11 Predicted Effect of Pressure on Clad Temperature at the 72-inch Elevation (FLECHT SEASET)**

a,c



**Figure 15.9.3-12 Predicted Effect of Pressure on Clad Temperature at the 72-inch Elevation (FLECHT Low Flooding Rate)**

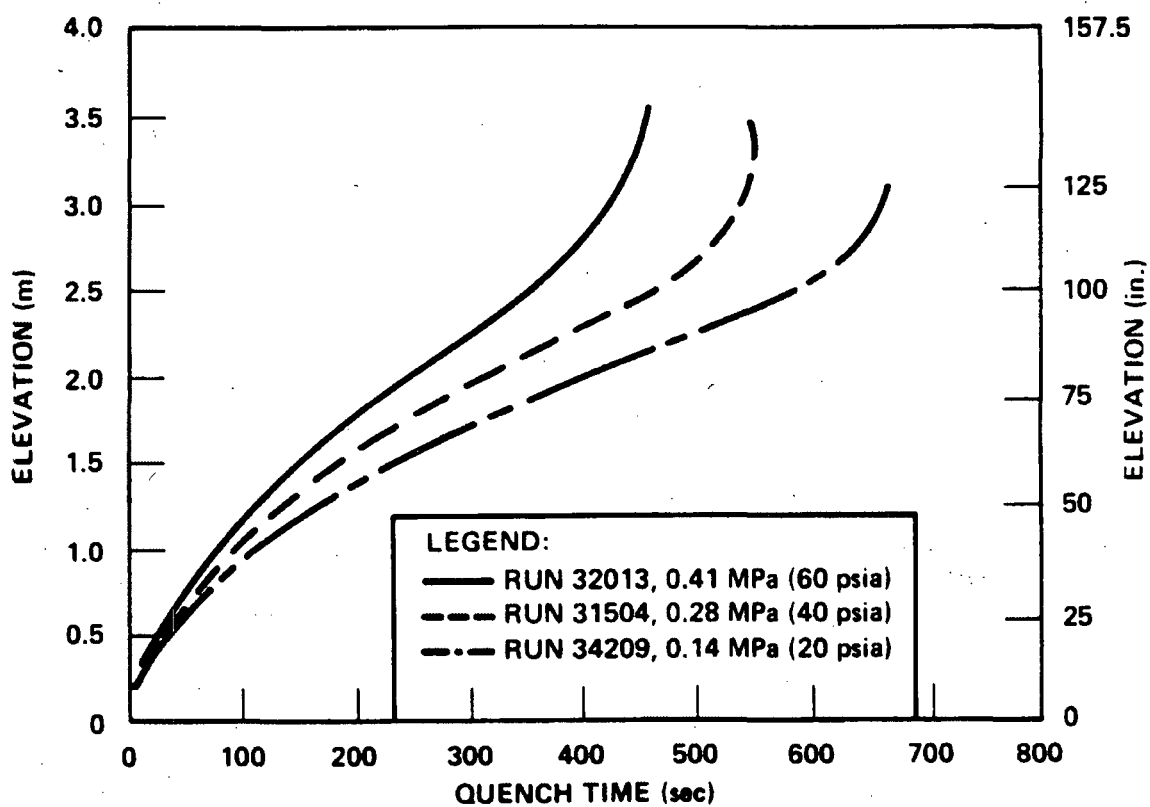


Figure 15.9.3-13 Effect of Pressure on Quench Front Advance as Determined from Experimental Data (Lee et al., 1982)

a,c



**Figure 15.9.3-14 Predicted Effect of Pressure on Quench Front Advance (FLECHT SEASET)**

a,c



**Figure 15.9.3-15 Effect of Pressure on Quench Front Advance (FLECHT Low Flooding Rate)**

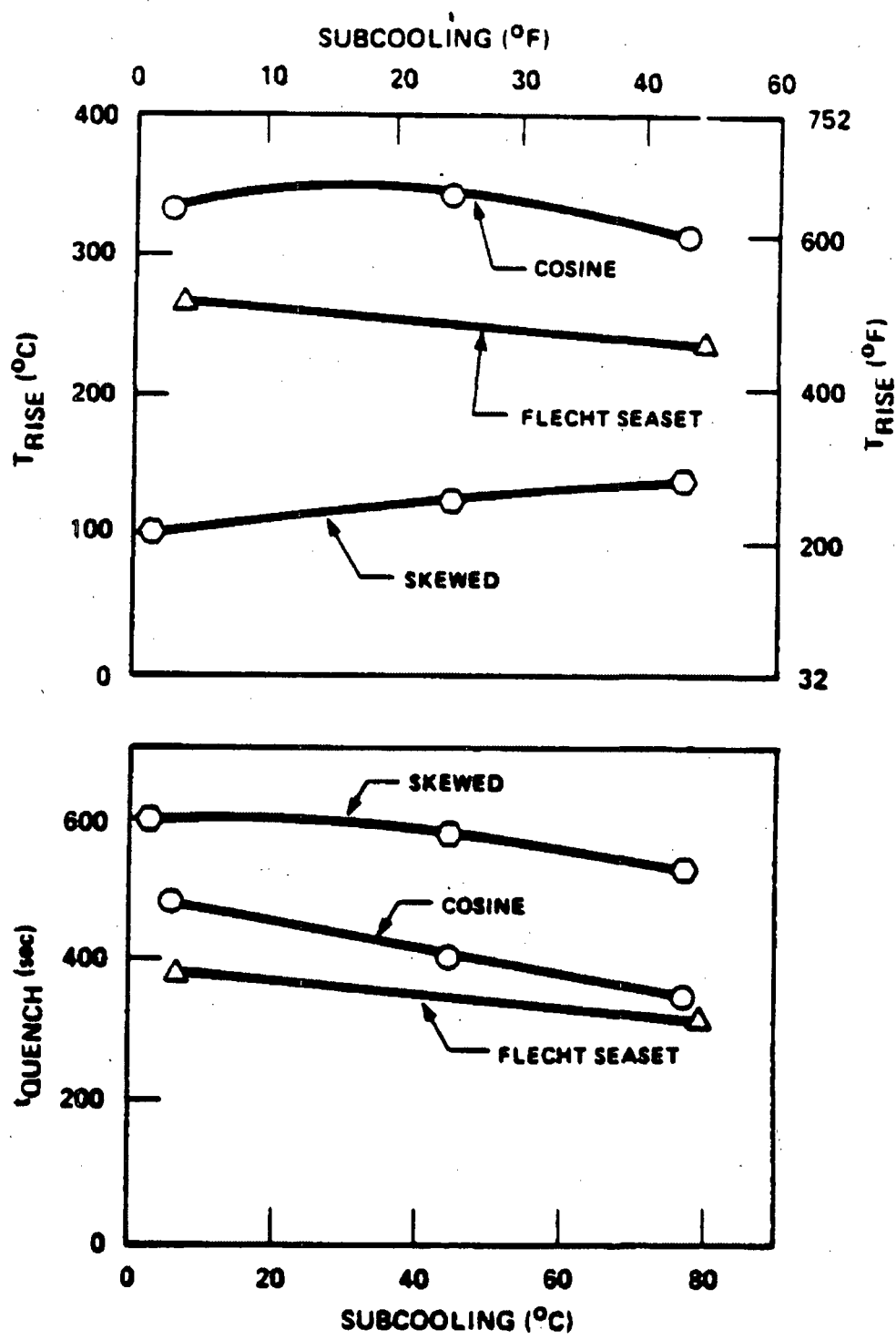


Figure 15.9.3-16 Effect of Subcooling on Temperature Rise and Quench Time as Determined from Experimental Data (Lee et al., 1982)

a,c

**Figure 15.9.3-17**

**Comparison of Clad Temperatures at 6-ft. and WCOBRA/TRAC-TF2 Prediction of Sensitivity to Inlet Subcooling in FLECHT SEASET**

a,c

**Figure 15.9.3-18**

**Comparison of Quench Times at 6-ft. and WCOBRA/TRAC-TF2 Prediction of Sensitivity to Inlet Subcooling in FLECHT SEASET**

a,c



**Figure 15.9.3-19 Comparison of Clad Temperatures at 6-ft. and WCOBRA/TRAC-TF2 Prediction of Sensitivity to Inlet Subcooling in FLECHT LFR Facility**

a,c

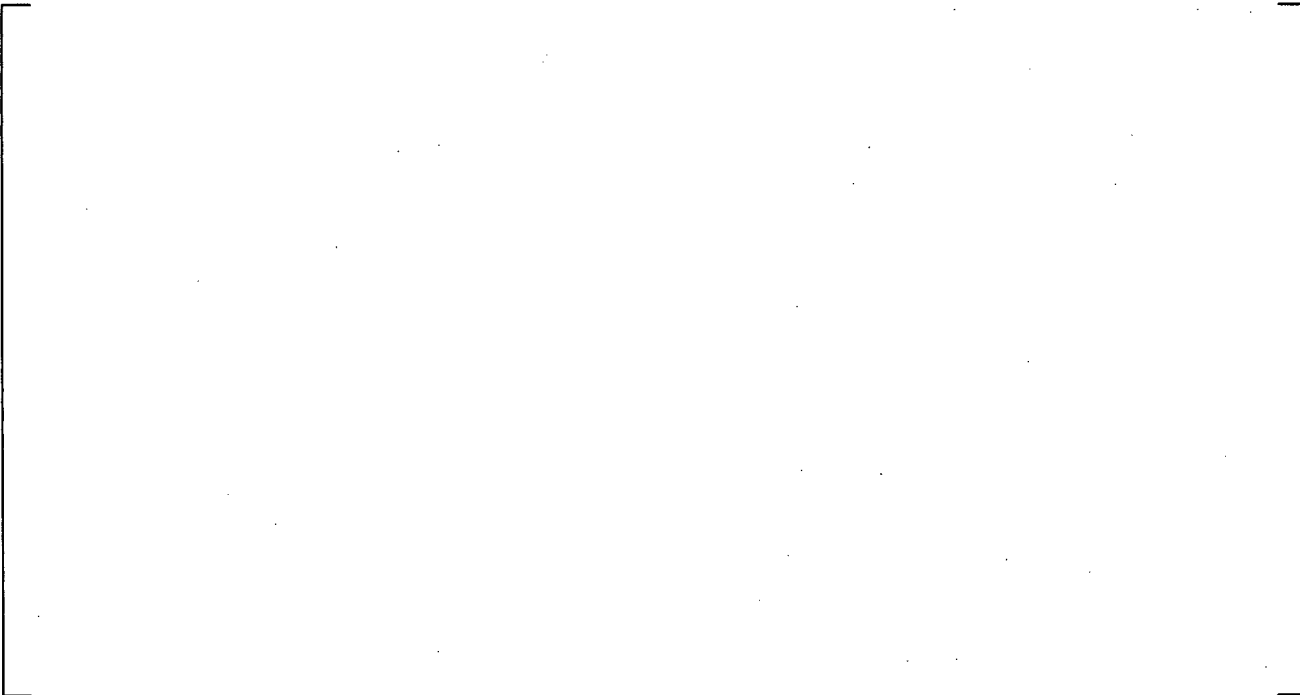


**Figure 15.9.3-20 Comparison of Quench Times at 6-ft. and WCOBRA/TRAC-TF2 Prediction of Sensitivity to Inlet Subcooling in FLECHT LFR Facility**

a,c

**Figure 15.9.3-21**

**Comparison of Clad Temperatures at 10-ft. and WCOBRA/TRAC-TF2 Prediction of Sensitivity to Inlet Subcooling in FLECHT Skewed Power Facility**

a,c

**Figure 15.9.3-22**

**Comparison of Quench Times at 10-ft. and WCOBRA/TRAC-TF2 Prediction of Sensitivity to Inlet Subcooling in FLECHT Skewed Power Facility**

## 15.10 SUMMARY AND CONCLUSIONS

The heat transfer models in WCOBRA/TRAC-TF2 have been compared to a wide range of different rod bundle heat transfer experiments which include:

- A range of fluid conditions and bundle powers expected to occur during a LOCA.
- Different rod bundle arrays and geometries characteristic of different fuel assembly designs.
- A range of axial power shapes.
- Different spacer grid geometries which can cause different subchannel blockages within the rod bundle.

Experiments were also specifically modeled which tested the WCOBRA/TRAC-TF2 calculations for upflow film boiling, downflow film boiling, and counterflow film boiling, all of which occur for a postulated LOCA.

The philosophy used in the WCOBRA/TRAC-TF2 validation was to select series from several facilities, and simulate tests over a wide range of conditions. The individual tests were selected to cover the range of thermal-fluid conditions expected in a LOCA, and to challenge particular models in the code. By analyzing different facilities with the same code, the possibility of successful comparisons by “tuning” to a particular test facility or set of experiments is reduced. By using this approach, the code has been demonstrated to be applicable to a wide range of PWR conditions and geometries.

The heat transfer and fluid flow package which has been described in Sections 5 to 7 is a complex two-phase flow, non-equilibrium, flow regime dependent model. Experiments were chosen which provide data that can test several predicted quantities, thereby reducing the possibility of compensating error. The FLECHT SEASET tests were used because they have reliable non-equilibrium vapor temperature data, axial void fraction or pressure drop data, as well as droplet diameter, velocity data, and heater rod temperature data. The FEBA reflood experiments had a different axial power shape as well as matching tests with and without the mid-plane spacer grid. The G-2 reflood experiments had prototypical spacer grid geometry.

For the DFFB assessment, downflow and upflow tests were examined. In the WCOBRA/TRAC-TF2 heat transfer logic there are differences in the entrained droplet size depending upon whether the flow is up or down since the entrainment mechanisms are different. This difference is observed in the tests, and represented in WCOBRA/TRAC-TF2. In addition, [

] <sup>a,c</sup>.

For the SPV assessment, high and low pressures and flows were examined, mainly [

] <sup>a,c</sup>.

Examining the composite blowdown and reflood results in Section 15.9, WCOBRA/TRAC-TF2-TF2 tends to [

] <sup>a,c</sup>.

[

] <sup>a,c</sup>

The data validation contained herein has examined the various aspects of a complex two-phase flow, non-equilibrium heat transfer model. The simulations presented in this volume are intended to demonstrate that the models in WCOBRA/TRAC-TF2 are reasonable. The level of detail employed by this type of model is needed to insure that the models used in analysis are proper and will correctly represent the LOCA process.

### 15.11 REFERENCES

1. Anklaam, T. M., et al., 1982, "Experimental Investigations of Uncovered Bundle Heat Transfer and Two-Phase Mixture Level Swell Under High Pressure Low Heat Flux Conditions," NUREG/CR-2456.
2. Bajorek et al., 1998, "Code Qualification Document For Best Estimate LOCA Analysis," WCAP-12945-P-A.
3. Lee, N., Wong, S., Yeh, H. C., and Hochreiter, L. E., 1982, "PWR FLECHT SEASET Unblocked Bundle, Forced and Gravity Reflood Task Data Evaluation and Analysis Report," NUREG/CR-2256, WCAP-9891.
4. Loftus, M. J. et al., 1981, "PWR FLECHT-SEASET Unblocked Bundle, Forced and Gravity Reflood Task Data Report," Volumes 1 and 2, NUREG/CR-1532, (WCAP-9699).
5. Mullins, C. B., et al., 1982, "Thermal-Hydraulic Test Facility Experimental Data Report for Test 3.03.6AR and Test 308.6C – Transient Film Boiling in Upflow," NUREG/CR-2525, Volumes 2 and 5.
6. Thurgood, M. J., et al., 1983, "COBRA/TRAC – A Thermal-Hydraulics Code for Transient Analysis of Nuclear Reactor Vessels and Primary Coolant Systems," Volume 1, PNL-4385, NUREG/CR-3046.
7. Wong, S. and Hochreiter, L. E., 1981, "Analysis of the FLECHT SEASET Unblocked Bundle Steam Cooling and Boiloff Tests," WCAP-9729.
8. Yoder, et al., 1982, "Dispersed Flow Film Boiling in Rod Bundle Geometry-Steady State Heat Transfer Data and Correlation Comparisons," NUREG/CR-2435, ORNL-5822.

## 16 HORIZONTAL STRATIFIED FLOW AND WAVY-DISPERSED FLOW

### 16.1 INTRODUCTION

[

] <sup>a,c</sup>

In general, the predicted performance of a PWR during a small break LOCA transient is, to some extent, determined by the two-phase flow regime present in the horizontal pipes of the RCS. The duration of the [ consequence of the flow regime(s) in the [ ] <sup>a,c</sup> are a ] <sup>a,c</sup> respectively.

In the WCOBRA/TRAC-TF2 computer code, a hybrid transition criterion combining [

] <sup>a,c</sup> is utilized to define the horizontal stratified flow regime. At the relatively low flow rates associated with the break size range of small break LOCA, the horizontal two-phase flow is expected to be in the horizontal stratified or wavy-dispersed flow regimes most of the time. Once flow regime is identified to be horizontal stratified or wavy-dispersed, the appropriate closure relations are selected for the interfacial area, the interfacial drag and the interfacial heat transfer. The interfacial drag and interfacial heat transfer, particularly condensation in the cold leg (Section 6), for the horizontal stratified and wavy-dispersed flow are the basic processes that are directly related to the high-ranked items in the LOCA PIRT. In addition, the offtake phenomenon (Section 5) affects the inlet boundary conditions (quality) at the inlet of the break flow. The offtake model in Section 5 is considered when the cold leg node connected to the break is calculated to be in the horizontal stratified flow regime or wavy-dispersed flow regime.

The selection criterion for either the horizontal stratified or wavy-dispersed flow regimes is discussed in Section 4, while Sections 5 (interfacial and wall drag) and 6 (interfacial heat transfer) provide the closure relationships associated with these flow regimes. Scaling and applicability of those models were also discussed in these sections.

The objective of this section is to compare the void fraction prediction for horizontal stratified flow with relevant test data to assess the stratified flow interfacial drag model, wall drag model, and influence of inlet and outlet boundaries.

### 16.2 KEY PHYSICAL PROCESSES

The capability of the code in predicting the transition from the horizontal stratified or wavy-dispersed regimes to other intermittent flow regimes (bubbly slug, churn, and annular-mist) or interpolation region

is very important because interface characteristics (interfacial drag and interfacial heat transfer) change by several orders of magnitude. This is an important mechanism because it affects the venting capability of the vessel from the upper plenum to the cold legs and finally to the break.

The transition criterion from stratified to non-stratified regimes in Section 4 is affected by the predicted void fraction, or water level, in a stratified pipe with the given liquid and gas superficial velocities. From the mass and momentum equations for the stratified flow in Section 5, the void fraction is determined by the interfacial drag, wall drag, and boundary condition (via gravitational water head term) for a horizontal pipe. [

] <sup>a,c</sup>

The wavy-dispersed flow regime is a special horizontal stratified flow regime, which prevents intermittent flow in high pressure of SBLOCA scenario. The relevance of the wavy-dispersed flow regime was discussed in Section 4. The wavy-dispersed regime is established [

] <sup>a,c</sup>. Under these circumstances, [

] <sup>a,c</sup>.

The wavy-dispersed flow regime will prevent the formation of slug flow and departure from the separated flow regimes.

The four other processes in LOCA which are affected by the horizontal stratified flow regime are:

[

] <sup>a,c</sup>

[

] <sup>a,c</sup>

In WCOBRA/TRAC-TF2 the transition criterion for stratification is a hybrid model based on [

]<sup>a,c</sup> The accuracy of the hybrid transition criterion was assessed against experimental data at various pressures, pipe diameters, and void fractions and an uncertainty range for the transition criterion was quantified. The adoption of a transition criterion as a function of [

]<sup>a,c</sup>. In this section, the assessment focuses on the accuracy of void fraction prediction by WCOBRA/TRAC-TF2.

The prediction of void fraction is controlled by the wall drag, the interfacial drag and the gravitational water head. The applicability of the wall drag model for stratified flow was addressed in Section 5. The gravitational water head term was implemented in the momentum equations as discussed in Section 3. Therefore, the assessment of this section focuses on the interfacial drag model together with the influence of the inlet and outlet boundaries.

The assessment is made against Two-Phase Flow Test Facility (TPTF) stratified flow data. TPTF is a Japan Atomic Energy Research Institute (JAERI) steam-water stratified flow test with a large scale pipe diameter, high pressure, and broad range of flow rates and void fractions. These characteristics render TPTF tests to be excellent benchmark tests for the stratification in small break LOCA. The interfacial and wall drag models for the stratified flow in WCOBRA/TRAC-TF2 are assessed via comparison between the measured void fraction and the predicted void fraction.

The wavy-dispersed flow regime was first reported by TPTF researchers as a relevant flow regime for SBLOCA (see Section 4). [

] <sup>a,c</sup>

### 16.3 TEST FACILITY DESCRIPTION

TPTF (Nakamura et al., 1983) was designed and built by JAERI to study the nature of SBLOCA. This facility was designed to perform various steam/water two-phase flow and heat transfer experiments at steady state and at pressures up to 12.8 MPa. These experiments were characterized by a high system pressure (3~12 MPa), a large test section diameter (0.18 m) and a wide range of mass flux (40 to 1000 kg/m<sup>2</sup>-s) obtained in the test section for concurrent saturated two-phase flow. The test also simulated

the pump effect at inlet, and the water level effect at outlet. These characteristics render TPTF to be an ideal test to assess SBLOCA safety evaluation codes.

Figure 16-1 shows the flow loop used in the TPTF, which consisted of an electrically heated boiler, separate pumps for steam and water lines, a mixer and a 10 m long, 180 mm inner diameter (ID) horizontal test section. The demineralized water was heated in the boiler to saturation conditions at a desired system pressure. Saturated steam was pumped from the top of the boiler through an orifice meter and into the mixer located at the entrance of the test section. The steam pump was a blower-type pump that was specially designed and manufactured for use at high pressure. The steam flowed through a demister located at the top of the boiler and became slightly superheated at the exit of the pump. Saturated liquid was drawn from the bottom of the boiler and similarly pumped through an orifice meter into the mixer. The piping for both the steam and liquid lines was well-insulated to minimize heat loss and prevented steam condensation or liquid subcooling.

The mixer was T-shaped and was connected to the steam and water lines such that steam was introduced horizontally and liquid from the bottom of the tee. There were two types of T shaped mixers used in TPTF experiments as schematically shown in Figure 16-2. Early series of tests used “bubbly flow” type of mixer. The steam was introduced horizontally into a bundle of tubes and was forced out through numerous holes drilled along the side of each tube. Liquid introduced from the bottom of the tee flowed on the outside of the tube bundle, where the steam and liquid mixed with each other. A nearly homogeneous mixture of liquid and vapor was expected to enter the test section. This homogeneous mixture is similar to the two-phase flow condition in cold leg after a rotating reactor coolant pump (RCP). The data of Kawaji et al. (1987) came from this “bubbly flow” type mixer. However, because of the homogeneous flow type inlet, the flow was far away from the equilibrium state horizontal stratified flow. The void fraction tended to be larger than the equilibrium state flow and the relative gas-liquid speed was lower than the relative speed in equilibrium state stratified flow. Thus, the non-equilibrium stratified flow due to the homogeneous flow inlet tended to be stable according to horizontal stratification model. The length of cold leg pipe ( $L/D=56$ ) was not long enough to allow flow reach equilibrium state from the homogeneous mixture. Another problem associated with “bubbly flow” mixer is that the entrained bubbles cannot be released rapidly from liquid if the speed of liquid is large. Those factors led to the observation that the separated to slug flow transition never appeared in the tests with “bubbly-flow” mixer.

The later TPTF tests used a “separated-flow” type mixer, which contained a horizontal flat plate. Due to this flat plate, the two phases entered the test section as a separated two-phase flow. The height of the separator plate was either 0.3 or 0.7 in height-to-diameter ratio. Thus, there was essentially no bubble entrainment and the flow was not far away from the equilibrium state horizontal stratified flow. All the TPTF flow regime transition data by JAERI were obtained with a “separated flow” type mixer (Anoda et al., 1989). The TPTF data from the “separated-flow” mixer was utilized to verify the stratification transition criteria in Section 4. In this section, the data from the “bubbly-flow” mixer are applied to assess the interfacial drag and the prediction of void fraction.

The water level at the exit of the test section was controlled by the water level in the boiler. There were two water levels in the TPTF tests. In the case of high water level, the water level in the boiler was 0.4 m higher than the center of the test section pipe. In the case of low water level, the water level in the

boiler was 0.4 m lower than the center of the test section pipe. The purpose of high or low water level was to simulate the effect of downcomer. The effect of full or empty downcomer was simulated in TPTF test.

The test section consisted of five sections of 180 mm inner diameter (ID) stainless-steel piping, each 2 m long and joined by Grayloc connectors. The overall length was 10.0 m and the length-to-diameter ratio ( $L/D$ ) was 56. The volumetric flow rates of vapor and liquid entering the test section were changed independently by adjusting the flow control valves and the pump speed. The maximum volumetric flow rates were  $0.194 \text{ m}^3/\text{s}$  for steam and  $0.047 \text{ m}^3/\text{s}$  for liquid. For the 180 mm ID test section, the maximum superficial liquid and vapor velocities were 1.9 and 7.6 m/s, respectively.

The horizontal test section was equipped with various two-phase flow instruments (Figure 16-3). In order to obtain detailed information about the flow structure, several of the instruments were attached to traversing devices which enabled measurement of mass and momentum distributions across the pipe cross section. To measure density (or void) distribution, two of the  $\gamma$ -densitometers with vertically-shot  $\gamma$ -ray beams were traversed across the pipe cross section horizontally, yielding a horizontal distribution of vertical chord-average void fractions at locations near the inlet ( $L/D=17$ ) and outlet ( $L/D=48$ ) of the test section. The third densitometer with a horizontal beam was traversed vertically across the pipe cross section at  $L/D=21$ , yielding a vertical distribution of horizontal chord-average void fractions. The fourth was a three-beam densitometer fixed to the pipe. To measure momentum flux, a water-purged Pitot tube was used. The Pitot tube was attached to a driving mechanism which moved the probe vertically along the centerline of the pipe at a speed of 0.22 mm/s to measure the momentum flux distribution. To further aid in flow pattern identification, five conductivity probes specially developed for use in high-temperature and high-pressure steam/water environments were attached to a rod which was situated along the vertical centerline of the test section.

A large matrix of tests was conducted by JAERI during 1980s. Part of the data is available in public literature (Kawaji et al., 1987). That data were digitized and provides the applicability for the validation of the flow regime and interfacial drag closure relation in WCOBRA/TRAC-TF2.

In summary, TPTF data are selected as the primary data source for the assessment because of the following reasons:

[

] <sup>a,c</sup>

[

] <sup>a,c</sup>

### 16.3.1 Test Selection and Basis

A large matrix of tests was conducted by JAERI during the 1980s. Part of data is available in the public literatures (Kawaji et al., 1987). TPTF experiment data are listed in Tables 2, 3, 4, and 5 in Kawaji et al. (1987). The void fraction information of the data in Table 2 (Kawaji et al., 1987) is missing, and thus could not be used here. The void fraction data in Table 5 (Kawaji et al., 1987) are in contradiction with Figure 11 in Kawaji et al. (1987). There is no other resource to verify those data, so data in Table 5 (Kawaji et al., 1987) are also excluded from the assessment. The remaining data in Tables 3 and 4 (Kawaji et al., 1987) are selected for the assessment. The data are reproduced in Table 16-1 for convenience. According to Kawaji et al. (1987), those data all were in the stratified flow regime based on visual inspections during experiments. The data points are also presented in the WCOBRA/TRAC-TF2 flow regime map in Figure 16-4. There is a substantial amount of data points beyond the horizontal stratification transition boundary of WCOBRA/TRAC-TF2. The discrepancy between the WCOBRA/TRAC-TF2 flow regime map and the observed stratified flow regime in the experiment is likely attributed to [

] <sup>a,c</sup>.

Nevertheless, the data with the homogenous inlet mixer are still applicable to assess the interfacial drag and the prediction of void fraction.

It is noted that the selected data are limited to the pressure range from 7.4 MPa to 8.0 MPa. [

] <sup>a,c</sup>

There are two main aspects that are critical for an accurate prediction of the flow regime: a) the transition from stratified to non-stratified flow regimes; and b) the predicted void fraction in the stratified flow regime.

The adequacy of the transition criterion was discussed in Section 4. Here the focus is on the accuracy of the prediction of void fraction (level) in the pipe. The main objectives of the assessment are the following:

1. Confirm the capability of the code in predicting the transition from stratified flow to non-stratified flow.
2. Assess the interfacial drag model together with the effect of boundary conditions.
3. Identify the controlling parameters and associated biases and uncertainties.

## 16.4 WCOBRA/TRAC-TF2 MODEL DESCRIPTION

The WCOBRA/TRAC-TF2 model includes the TPTF pipe from the location of first void fraction measurement point ( $L/D=17$ ) to the exit to the water tank. The pipe from the homogeneous mixer to the first void fraction measurement point at  $L/D=17$  is neglected. The influence of the homogeneous inlet mixer is removed to better assess the interfacial drag model and wall drag model for horizontal stratified flow. The inlet of the pipe is modeled with flow boundary conditions (FILL component) by providing the specific  $j_g$  and  $j_l$  for each test run. The [ ]<sup>a,c</sup> is used to evaluate the gas phase velocity and the liquid phase velocity for the FILL component. The water level in the tank is simulated by [ ]

]<sup>a,c</sup>

The noding diagram is shown in Figure 16-5. The cold leg in the TPTF test section is intended to represent the PWR's cold leg. However, the  $L/D$  of the TPTF pipe is longer than the  $L/D$  of the PWR's cold leg, but not long enough to develop an equilibrium state stratified flow. The boundary conditions of the TPTF tests have been incorporated into the input model. Thus, the non-equilibrium state stratified flow, as well as the influence from the boundary condition, is part of the simulation.

The diameter of the TPTF pipe is similar to that of the ROSA Integral Effects Test (Section 21) cold leg, but the  $L/D$  is much larger than that of ROSA. To preserve the [ ]<sup>a,c</sup> is adopted. The node length ( $DX$ ) and the hydraulic diameter (HD) of the cold leg node in the ROSA IET are [ ]<sup>a,c</sup>, respectively. The HD of the pipe in TPTF is 0.18 m (Figure 16-3). [ ]

]<sup>a,c</sup>

## 16.5 ASSESSMENT RESULTS

The simulation is carried out until a steady-state condition is reached. A typical void fraction profile in the pipe is shown in Figure 16-6 together with the flow regime numbers for TPTF Test 722. Per Table 16-1, Run 722 was a low mass flux case with a high water level in the boiler. The weighting factors

$W_{st}$  of the two measurement points in Run 722 were calculated as 1.0 and 0.95 using Equation 4-117 in Section 4.4.5. The parameters  $C_{stfru}$  and  $C_{hs\_slug}$  default to [ ]<sup>a,c</sup>, respectively. The weighting factors  $W_{st}=1$  indicates stratified flow, while  $W_{st}=0$  indicates a non-stratified flow in the basic flow regime map. In the interpolation region,  $0 < W_{st} < 1$ . The weighting factors indicate the flow in TPTF Test 722 is [ ]<sup>a,c</sup> per the WCOBRA/TRAC-TF2 flow regime map.

The code-predicted flow regime number of each node is marked with "N". A summary of flow regime numbers in a 1D component is given in Table 4.4-1. It is seen that the flow regime numbers are [ ]<sup>a,c</sup> in the nodes of the PIPE component, except [ ]<sup>a,c</sup>

The WCOBRA/TRAC-TF2 predicted void profile is shown with the solid line in Figure 16-6. The squares represent the measured void fractions at  $L/D=17$  and  $L/D=48$ . [ ]<sup>a,c</sup> The dashed line represents the theoretical void fraction that would be obtained assuming the steady-state equilibrium in an infinitely long pipe [ ]<sup>a,c</sup>. Obviously in this case, [ ]<sup>a,c</sup>

Figure 16-7 presents the void fraction distribution and the flow regime numbers for TPTF Test 845, which was a high mass flux case with a low water level in the boiler. The flow is [ ]<sup>a,c</sup>

The measured void fractions and weighting factors at  $L/D=17$  and  $L/D=48$ , together with the predicted void fractions and flow regime numbers at node 1 ( $L/D=18$ ) and node 13 ( $L/D=48$ ) are collected in Table 16-2. It is noted that the FILL component is a boundary node, so the flow regime is not evaluated by the code. Instead, [ ]<sup>a,c</sup>.

The weighting factors in Table 16-2 confirm that [ ]<sup>a,c</sup>.

Figure 16-8 compares the predicted void fraction at node 13 ( $L/D=48$ ) with the measured void fraction at  $L/D=48$  for the runs [ ]<sup>a,c</sup>

[  
] <sup>a,c</sup>

## 16.6 CONCLUSIONS

An improved horizontal flow regime map is included in the 1D module of WCOBRA/TRAC-TF2 to expand the applicability of the code to small break LOCA scenarios. The 1D module is based on the TRAC-PF1 formulation. TRAC-PF1 shortcomings are identified and corrected with a revised model which better describes the conditions expected in a PWR during postulated LOCA scenarios.

The improved model includes a hybrid transition criterion for the transition from horizontal stratified flow to non-horizontal stratified flow, [  
] <sup>a,c</sup>. A wavy-dispersed model, [  
] <sup>a,c</sup> which in

TRAC-PF1/MOD2 is applied generically regardless the orientation of the pipe. A detailed discussion on the flow regime, transition criteria and applicability can be found in Section 4.

The purpose of this section is to assess the void fraction prediction for the horizontal stratified flow against relevant test data. [  
] <sup>a,c</sup>

## 16.7 REFERENCES

1. Anoda, Y., Kukita, Y., Nakamura, N., and Tasaka, K., 1989, "Flow Regime Transition in High-Pressure Large-Diameter Horizontal Two-Phase Flow," Proc. of 26th ASME/AICHE/ANS National Heat Transfer Conference, pp. 61-68, Philadelphia.
2. Barnea, D., and Taitel, Y., 1993, "Stability criteria for stratified flow: viscous versus non-viscous (Inviscid) approaches," Int. J. Multiphase Flow, Vol. 19, No. 4, pp. 639-649.
3. Asaka, H., Kukita, Y., Anoda, Y., Nakamura, H., and Tasaka, K., 1991, "Improvement of TRAC-PF1 Interfacial Drag Model for Analysis of High-Pressure Horizontally – Stratified Two-Phase Flow," Journal of Nuclear Science and Technology, Vol. 28, No. 1, pp. 33-44.
4. Crowley, C. J., Wallis, G. B., and Barry, J. J., 1992, "Validation of one-dimensional wave model for the stratified to slug flow regime transition with consequences for wave growth and slug frequency," Int. J. Multiphase Flow, Vol. 18, No. 2, pp. 249-271.
5. Kawaji, K., Anoda, Y., Nakamura, H., and Tasaka, T., 1987, "Phase and Velocity Distributions and Holdup in High-Pressure Steam/Water Stratified Flow in a Large Diameter Horizontal Pipe," Int. J. Multiphase Flow, Vol. 13, No. 2, pp. 145-159.

6. Kukita, Y., Asaka, H., Mimura, Y., Anoda, Y., Ishiguro, M., Nemoto, T., Tasaka, K., 1990, Developmental Assessment of RELAP5/MOD3 Code Against ROSA-IV TPTF Horizontal Two-Phase Experiments, JAERI-M-90-053.
7. Nakamura, H., Tanaka, M., Tasaka, T., Koizumi, Y., and Murata, H., 1983, System Description for ROSA IV Two Phase Flow Test Facility (TPTF), JAERI-M-83-042.
8. Taitel, Y., and Dukler, A.E., 1976, "A Model for Predicting Flow Regime Transitions in Horizontal and Near Horizontal Gas-Liquid Flow," AIChE Journal, Vol. 22, No. 1, pp. 47-55.
9. Wallis, G. B., and Dobson, J.E., 1973, "The Onset of Slugging in Horizontal Stratified Air-Water Flow," Int. J. Multiphase Flow, Vol. 1, pp. 173-193.

Run	P(MPa)	Water Level <sup>(1)</sup>	G (kg/m <sup>2</sup> s)	x (-); quality	j <sub>l</sub> (m/s)	j <sub>g</sub> (m/s)	Void Fraction	
							L/D=17	L/D=48
857	7.4	Low	1016	0.2	1.12	5.15	0.67	0.64
855	7.4	Low	1020	0.104	1.26	2.69	0.51	0.47
853	7.4	Low	1025	0.06	1.33	1.55	0.35	0.33
851	7.4	Low	1015	0.02	1.37	0.52	0.17	0.17
849	7.4	Low	1015	0.011	1.38	0.28	0.08	0.10
845	7.4	Low	440	0.374	0.38	4.17	0.76	0.77
843	7.4	Low	442	0.122	0.54	1.37	0.42	0.42
847	7.4	Low	426	0.022	0.57	0.23	0.16	0.22
836	7.5	Low	114	0.81	0.03	2.33	0.89	0.91
838	7.4	Low	112	0.634	0.056	1.79	0.83	0.87
1561	7.6	Low	116	0.153	0.14	0.45	0.67	0.68
1563	7.6	Low	114	0.093	0.14	0.27	0.65	0.66
1565	7.6	Low	115	0.052	0.15	0.15	0.64	0.65
1567	7.7	Low	116	0.038	0.16	0.11	0.64	0.67
834	7.5	Low	42.6	0.575	0.025	0.62	0.82	0.88
1555	8	Low	45.2	0.378	0.041	0.42	0.87	0.83
1557	7.8	Low	43.5	0.209	0.049	0.23	0.83	0.79
1559	7.7	Low	42.8	0.122	0.053	0.13	0.79	0.82
779	7.3	High	1011	0.003	1.38	0.085	0.06	0.09
781	7.3	High	1013	0.005	1.37	0.13	0.09	0.13
775	7.3	High	1010	0.01	1.37	0.26	0.13	0.15
751	7.4	High	1007	0.019	1.35	0.51	0.19	0.15
749	7.4	High	1004	0.048	1.31	1.28	0.38	0.29
747	7.4	High	1001	0.077	1.27	2.02	0.48	0.41
773	7.3	High	1010	0.101	1.24	2.58	0.57	0.50
743	7.4	High	1000	0.195	1.1	5.1	0.73	0.69
732	7.4	High	400	0.391	0.33	4.1	0.84	0.81
730	7.3	High	402	0.196	0.44	2.06	0.66	0.64
783	7.3	High	414	0.106	0.51	1.11	0.43	0.47

**Table 16-1 Selected TPTF Test Data from Kawaji et al. (1987)**  
(cont.)

Run	P(MPa)	Water Level <sup>(1)</sup>	G (kg/m <sup>2</sup> s)	x (-); quality	j <sub>l</sub> (m/s)	j <sub>g</sub> (m/s)	Void Fraction	
							L/D=17	L/D=48
785	7.3	High	410	0.039	0.54	0.41	0.26	0.27
755	7.4	High	407	0.019	0.55	0.21	0.13	0.13
757	7.4	High	383	0.01	0.52	0.1	0.16	0.12
759	7.4	High	381	0.005	0.52	0.05	0.08	0.06
761	7.4	High	380	0.003	0.52	0.031	0.06	0.04
726	7.4	High	99.1	0.794	0.028	2.06	0.97	0.83
728	7.3	High	100	0.596	0.055	1.57	0.91	0.69
708	7.3	High	99.4	0.293	0.1	0.76	0.65	0.53
710	7.3	High	99.5	0.391	0.083	1.02	0.76	0.61
1545	7.4	High	106	0.164	0.12	0.44	0.32	0.31
1547	7.4	High	103	0.098	0.13	0.26	0.2	0.20
1549	7.4	High	105	0.05	0.14	0.13	0.12	0.11
763	7.4	High	102	0.01	0.14	0.027	0.05	0.04
720	7.3	High	39.6	0.691	0.017	0.72	0.63	0.48
722	7.3	High	39.7	0.59	0.022	0.61	0.57	0.44
712	7.3	High	39.9	0.392	0.033	0.41	0.48	0.38
714	7.3	High	40.2	0.196	0.044	0.21	0.31	0.24

**Note:**  
1. High water level: water level in boiler is about 0.4 m above center of test section pipe. Low water level: water level in boiler is below center of test section pipe.





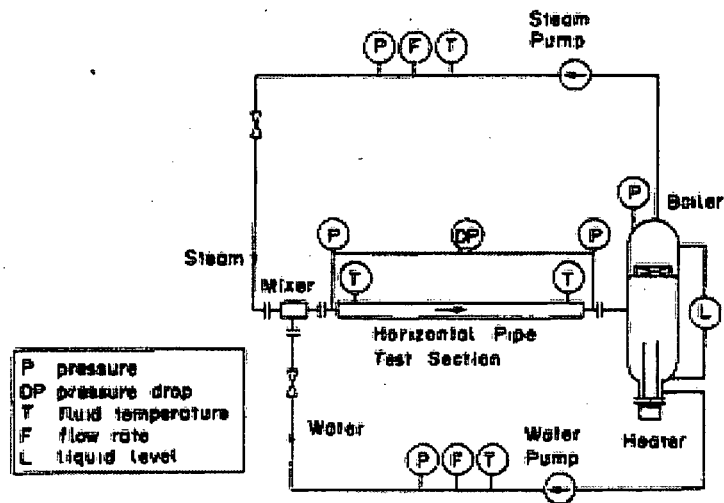
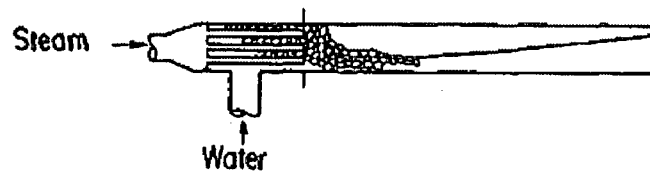
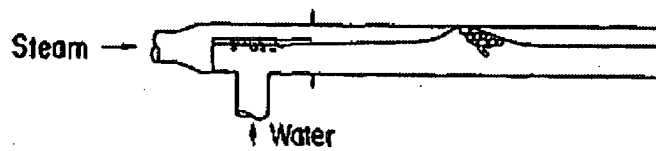


Figure 16-1 The Schematic Plot of the TPTF Facility (Nakamura et al., 1983)



(a) "Bubbly-flow" type mixer



(b) "Separated-flow" type mixer

Figure 16-2 T Shaped Mixers used in TPTF (Anoda et al., 1989)

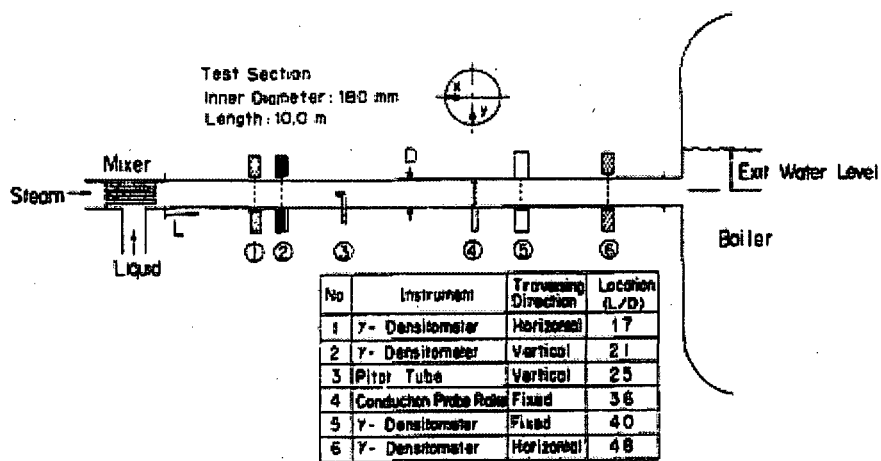
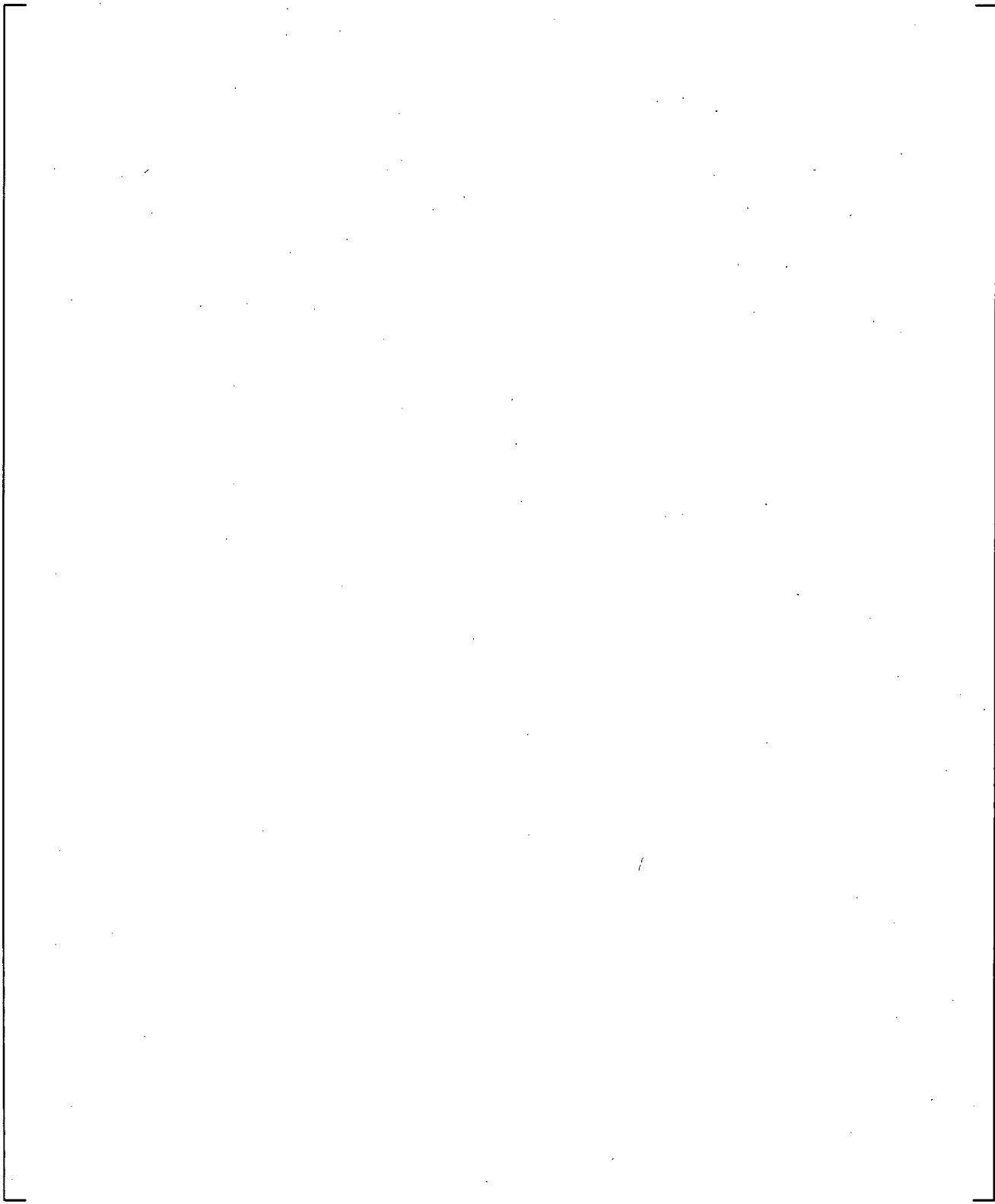


Figure 16-3 Test Section and Measurement Instruments (Kawaji et al., 1987)

a,c



**Figure 16-4 TPTF Test Data on WCOBRA/TRAC-TF2 Flow Regime Map**

a,c

**Figure 16-5** WCOBRA/TRAC-TF2 Input Models for TPTF. The Fill Component Corresponds to the Location of L/D=17 in the TPTF Facility

a,c

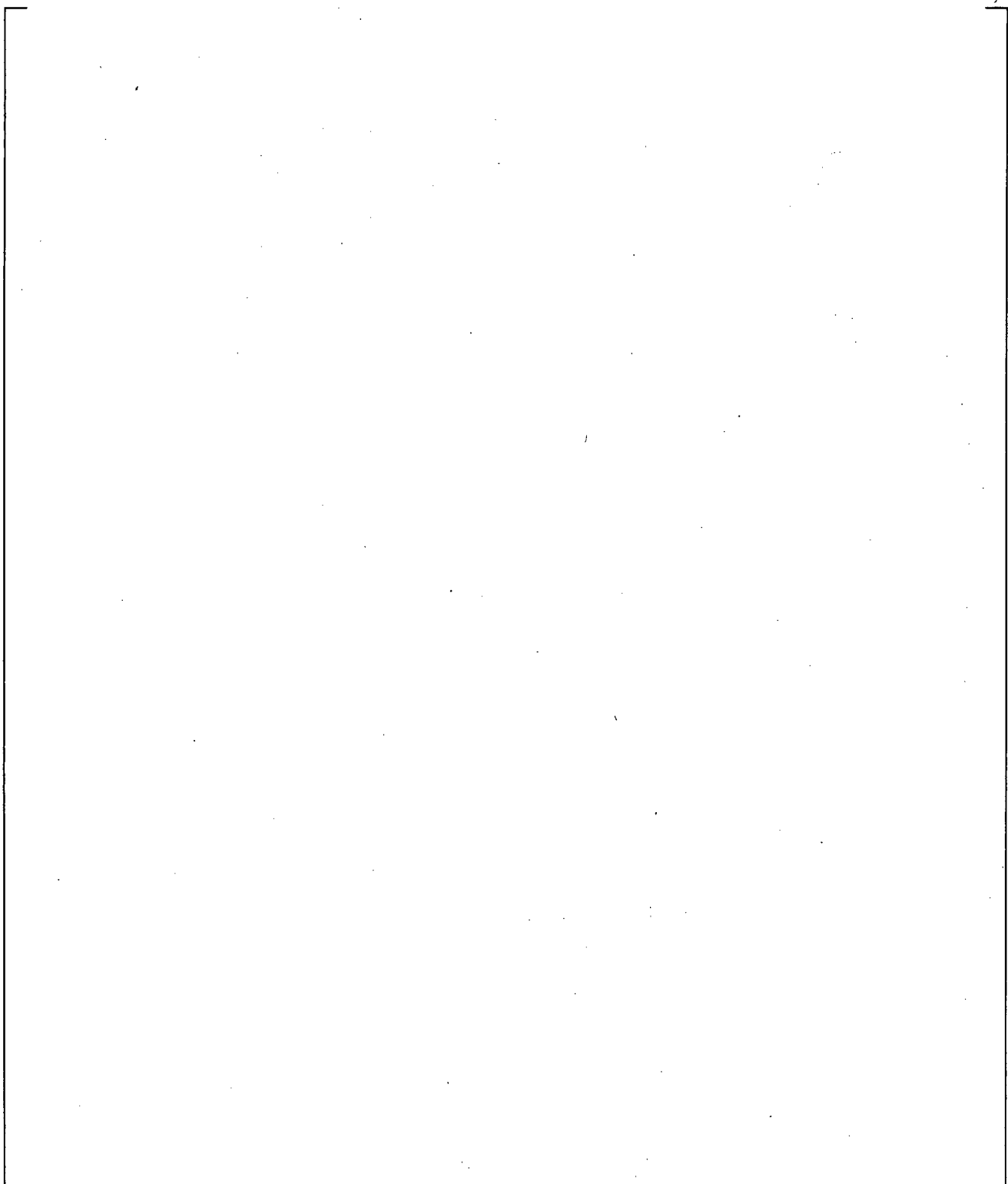


**Figure 16-6 Comparison Between Measured Void Fraction in TPTF Run 722 and Predicted Void Fraction**

a,c

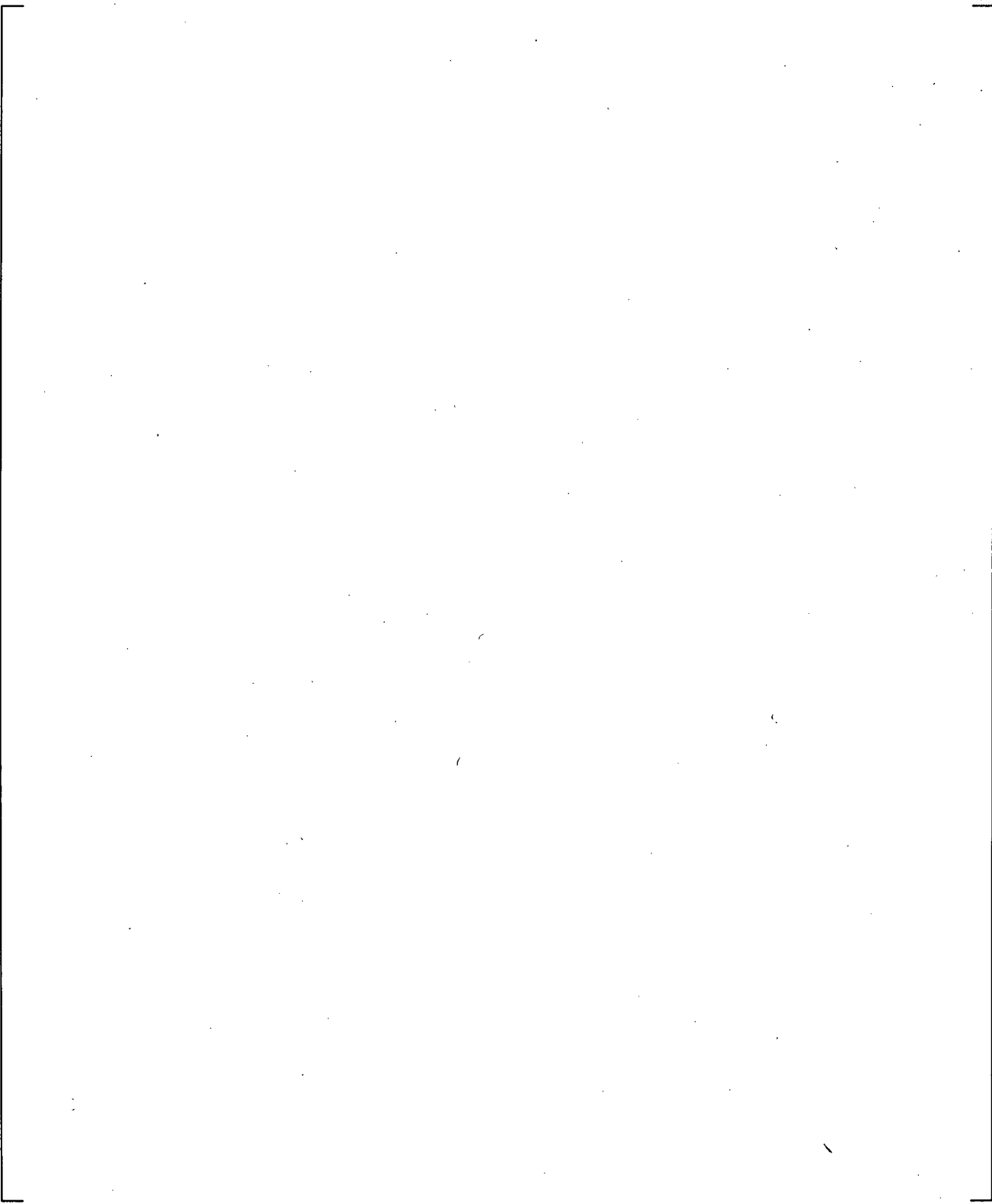


**Figure 16-7 Comparison Between Measured Void Fraction in TPTF Run 845 and Predicted Void Fraction**

a,c

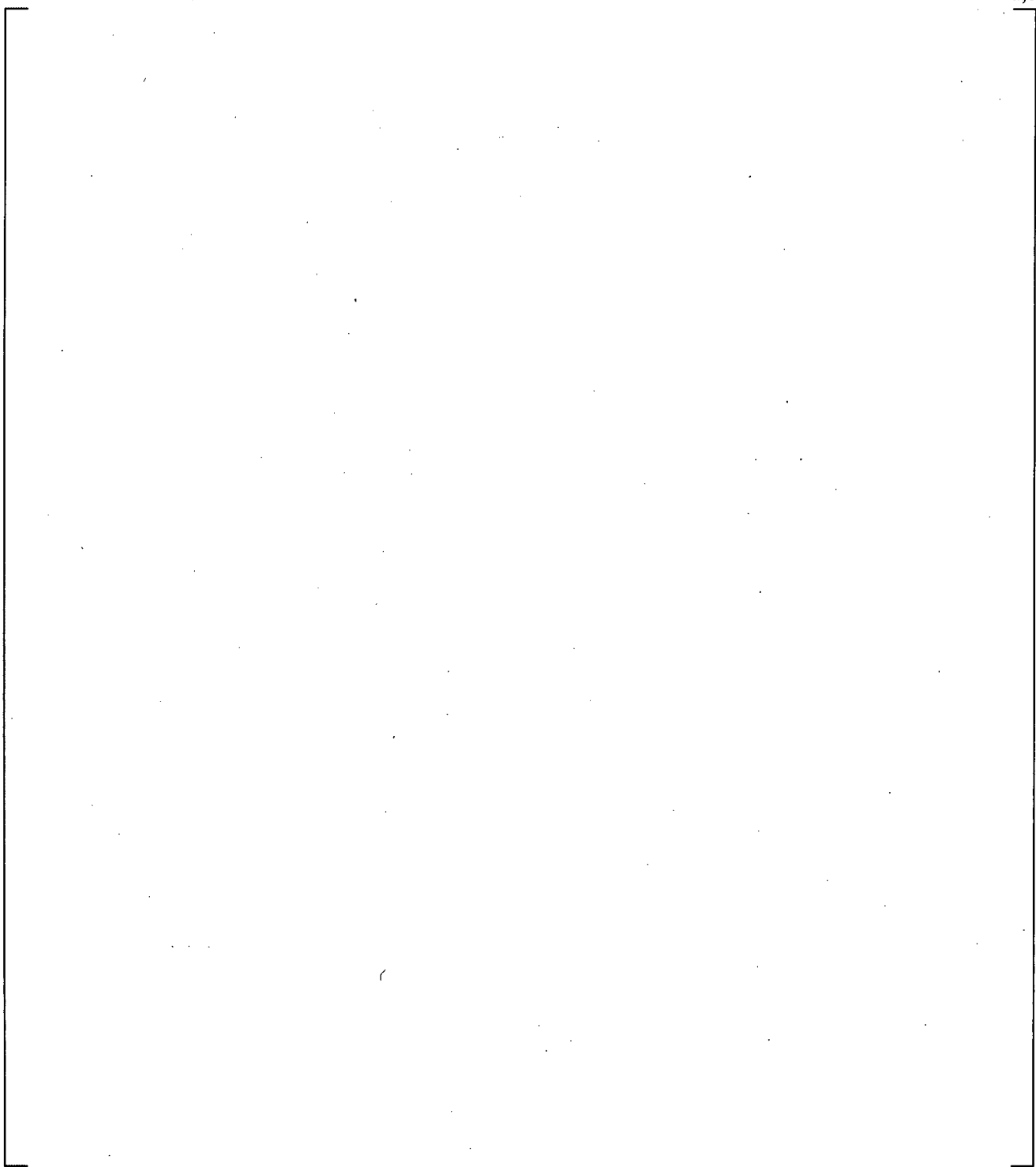


Figure 16-8 [

]a,c

## 17 COLD LEG CONDENSATION: COSI EXPERIMENTS, ROSA IV SB-CL-05 EXPERIMENT, AND UPTF-8A EXPERIMENT

### 17.1 INTRODUCTION

The condensation of steam by the cold liquid injected from the ECCS by sources such as the accumulator (ACC), safety injection (SI), and residual heat removal (RHR) injection (also called low head safety injection (LHSI)) into the cold leg is an important phenomenon during both small and large break LOCAs (see PIRT in Section 2). Cold leg condensation is ranked high (H) during the boiloff period and the recovery period of a small break LOCA. During these periods, the flow in the cold leg is stratified flow which would lead to negligible condensation due to low interfacial heat transfer. However, the impingement of the SI jet into the layer of liquid in the cold leg enhances condensation greatly. As the break size increases, the effect of the accumulator injection and of the higher pumped SI flow rates leads to an increased importance of condensation in the jet region. For a large break LOCA, the cold leg condensation is the highest (H) ranked phenomenon during the refill period when the condensation process in the cold leg helps to reduce bypass flow at the top of downcomer, promoting ECC penetration. The condensation effects are reduced during the reflood period as the accumulators end their injection and the low head safety injection continues, but condensation still impacts the break flow rate, the downcomer and core water inventory, and the liquid subcooling in the downcomer. Thus, a ranking of medium (M) was assigned for the cold leg condensation in the reflood stage of a LBLOCA. For intermediate breaks, the cold leg condensation is ranked high (H) for both the accumulator injection period and (low head) safety injection period. More details on the cold leg direct contact condensation processes were also discussed in Section 6.3.6.

As discussed in Section 6.3.6, a special cold leg condensation model was developed and implemented in WCOBRA/TRAC-TF2 to calculate the condensation heat transfer rate from cold water injection into the cold leg when the cold leg is expected to be in the horizontal stratified flow regime, wavy-dispersed flow regime, or annular-mist flow regime. The model basis, development and applicability are discussed in Section 6.3.6. The purpose of this section is to describe the assessment of the model against an independent dataset. The model is applied whenever the flow regime in the cold leg is predicted to be horizontal stratified, wavy-dispersed, or annular-mist, regardless of the break size or pressure. Therefore, it is important to assess the model performance, not only under conditions for which the model was developed (COSI experiments), but also under conditions at lower pressures and higher flow rates, more typical of intermediate and large break LOCA.

The assessments of small break LOCA and large break LOCA are given in Section 17.2 and Section 17.3, respectively. Section 17.2 covers condensation experiments designed for small break LOCA, such as COSI and ROSA IV SB-CL-05, which are high pressure and medium scale experiments, while Section 17.3 gives an assessment of the condensation in UPTF-8A experiments designed for large break LOCA (low pressure, full-scale experiments).

The focus of this section is to assess the WCOBRA/TRAC-TF2 performance in the analysis of condensation in the cold leg. Additional assessment of the condensation process, especially relative to condensation in the downcomer during the ECC bypass period of larger breaks, is provided in Section 19.

The cold leg condensation model uncertainty will be addressed in Section 29.1.6.

## 17.2 SMALL BREAK LOCA EXPERIMENTS – COSI AND ROSA SB-CL-05

To investigate the ability of the WCOBRA/TRAC-TF2 code to correctly predict condensation phenomena under conditions representative of small break scenarios, three different test facilities have been considered.

The Westinghouse Condensation On Safety Injection (COSI) facility (Shimeck, 1988) is an approximately 1:100 scale model of the cold leg and safety injection lines of a Westinghouse-type pressurized water reactor (PWR), constructed specifically for investigating the interaction of steam and cold SI water in a prototypical PWR configuration and at typical PWR fluid conditions encountered during a small break LOCA.

The cold leg condensation correlation used in WCOBRA/TRAC-TF2 was fitted against a subset of Westinghouse COSI data. Therefore, an independent dataset is needed for the code assessment. The following tests were selected for this purpose.

1. The Westinghouse horizontal injection COSI experiment [ ]<sup>a,c</sup>  
 The diameter of [ ]  
 ]<sup>a,c</sup> The assessment of the Westinghouse horizontal injection COSI tests provides information on the capability of the WCOBRA/TRAC-TF2 code with the SI pipe running partially full.
2. The Framatome COSI experiments, which compared with the Westinghouse COSI experiments were performed at a lower pressure [ ]<sup>a,c</sup>, higher SI water temperature [ ]<sup>a,c</sup>, and with a [ ]<sup>a,c</sup> condition.
3. ROSA is an integral effects test (IET). The facility had volumes scaled at 1/48 of a typical Westinghouse 4-loop plant. Its layout was a 2-loop test facility. The diameter of the cold leg was 0.207 m. An extensive assessment of the ROSA integral effects test results is provided in Section 21. In this section, we are interested in the analysis of ROSA SB-CL-05, a 5% side break in the cold leg with high head safety injection, with respect to the assessment of the condensation process in the cold leg. In the assessment, only the [ ]<sup>a,c</sup> were modeled in the WCOBRA/TRAC-TF2 input decks. This makes it a type of [ ]<sup>a,c</sup> and this ROSA SB-CL-05 SET provides a SI condensation experiment in a cold leg larger than the COSI experiment. The effect of superheated steam on the cold leg condensation model is also assessed by the ROSA SB-CL-05 cases.

### 17.2.1 Test Facilities and Tests Description

As discussed above, there are three test facilities serving as the basis for the assessment plan for small break LOCA. Those are the Westinghouse COSI facility, Framatome COSI facility, and ROSA IV SB-CL-05 test facility. Both the Westinghouse COSI and Framatome COSI tests are separate

effects tests. ROSA IV SB-CL-05 is an integral effects test, however separate effects test data was extracted for the purpose of the assessment of the condensation rate in the cold leg. The facilities are introduced separately in the following sections.

### Westinghouse COSI Facility

In the 1980's, the Condensation on Safety Injection (COSI) experiments were performed as a four party venture between Westinghouse, Framatome, the French Atomic Energy Commission (CEA), and Electricité de France (EDF). The objective of these experiments was to characterize the condensation phenomenon and develop an accurate condensation model which could be used to evaluate the condensation heat transfer in a PWR during a LOCA.

The Westinghouse COSI facility is a 1:100 scale model of the cold leg and safety injection ports of a Westinghouse-type PWR. It is capable of operating at pressures [ ]<sup>a,c</sup> and at appropriately scaled flow rates to cover nearly the entire range of injection conditions expected in an PWR small break transient, during which condensation on the safety injection water phenomenon was judged important. The main scaling philosophy followed in designing the system was to maintain similar [ ]<sup>a,c</sup> in the cold leg as would be encountered in a small break LOCA.

The main loop of the test facility [

] <sup>a,c</sup>

A removable weir with a height [ ]<sup>a,c</sup> was incorporated into a spool piece at the outlet end of the main pipe to allow for varying of the water level retained within the cold leg pipe. Measurements were available for the steam and liquid flow rates in and out of the test assembly, the temperature of fluid entering and exiting the test section, and the system pressure and differential pressures. Within the test section, a series of thermocouple rakes provided the temperature profile and the information concerning stratification of the liquid. Significant amounts of temperature stratification were observed and combined with examination of the actual temperatures the conclusion was that the overall behavior depicted in Figure 17-3 was taking place. Fluid temperatures upstream and downstream of the

injection point were stable and indicated that a counter-current flow pattern was in place on the upstream side. On the downstream side, the flow pattern was co-current or counter-current depending on the steam flow configuration, but again stratification was noted. In the immediate vicinity of the injection port, the thermocouple measurements exhibited significant temperature oscillations, indicating turbulent conditions. The downward impingement of the safety injection jet, combined with the significant influx of steam to this point, supported a turbulent jet mixing zone, with rather complex flow and heat transfer patterns. The conclusion from analysis of the data was that most of the condensation mechanism occurs in the proximity of the jet mixing zone. The Westinghouse cold leg condensation model in Section 6.3.6 was developed based on the assumption that the majority of condensation occurs near the safety injection point.

A large matrix of tests was conducted over the course of the program by both Westinghouse and Framatome (Gros d'Aillon, 1987), and some reconfigurations of the facility test section were performed with regard to the length of the main pipe in the test assembly and the angle and size of the injection piping. A core series of 15 tests, with 75 individual data, from Westinghouse configuration was conducted.

The COSI experimental data report only gives boiler power and heat loss for the entire test loop. The net condensation heat transfer rate  $Q_{cond}$  in the cold leg is calculated [

$$[ \dots ]^{a,c} \tag{17-1}$$

The condensation heat transfer rate in the downcomer  $Q_{DC}$  is estimated by [

$$[ \dots ]^{a,c} \tag{17-2}$$

$]^{a,c}$  It is also expected that the heat loss is mainly a

function of the [ ]<sup>a,c</sup>. The estimated average heat loss and its uncertainty at [ ]<sup>a,c</sup> are shown in Table 17-1.

During the COSI test, the steam entering the test section was condensed and mixed with the subcooled safety injection water. The subcooled water flowed into the downcomer and was mixed with the heated SI water (Figure 17-3).

From Equation 17-1, the  $Q_{cond}$  can be evaluated by:

$$[ ]^{a,c} \tag{17-3}$$

$$[ ]^{a,c} \tag{17-4}$$

$$[ ]^{a,c} \tag{17-5}$$

There were two types of Westinghouse COSI tests based on their SI angle relative to the direction of the cold leg. The tests with [ ]<sup>a,c</sup> are called “vertical” COSI test, and the tests with [ ]<sup>a,c</sup> injection angle are called “horizontal” COSI test. Section 6.3.6 in Volume 1 describes in detail how the vertical injection tests have been used to define the cold leg condensation model implemented in WCOBRA/TRAC-TF2. The vertical injection COSI tests also serve as a part of the assessment documented in this section because the data will be used to validate the WCOBRA/TRAC-TF2 code with the cold leg condensation model, not only the cold leg condensation correlation itself. The Westinghouse vertical COSI data, which were utilized to define the safety injection condensation correlation, are listed in Table 17-2.

Compared with the vertical COSI tests, the horizontal COSI tests have a [ ]

[ ]<sup>a,c</sup> Test data from the Westinghouse horizontal COSI tests are shown in Table 17-3.

**Framatome COSI Facility**

The Framatome COSI facility is similar to the Westinghouse COSI facility. The loop structure shown in Figure 17-1 is the same for the Framatome COSI facility, but the Westinghouse test section in Figure 17-2 was replaced with the Framatome test section, which is shown in Figure 17-5. The cold leg diameter of both test sections is 0.118 m, but the length of the Framatome test section (cold leg) is only [ ]<sup>a,c</sup> in the Westinghouse test section. Compared to the Westinghouse setup, this shorter test section is more appropriate from a scaling standpoint.

The Framatome test section had two injection points (Boileau, 1988). One injection was [ ]<sup>a,c</sup>. The diameter of this injection port

was [ ]<sup>a,c</sup>. Another injection port was located in the horizontal plane with a diameter of [ ]<sup>a,c</sup>. Since there is no data reported for the larger horizontal pipe, that flow configuration is not considered in this report.

Another difference between the Westinghouse test section and the Framatome test section is steam flow. [ ]

] <sup>a,c</sup>

The Framatome test section had two weir heights, [ ]<sup>a,c</sup> cold leg diameters, and a case without a weir. In contrast to the two downcomer water levels [ ]<sup>a,c</sup> used in the Westinghouse COSI tests, the water level in the downcomer was consistently set to [ ]<sup>a,c</sup> relative to the cold leg. In the Framatome test, the water level in downcomer was always in the high position [ ]<sup>a,c</sup>

The system pressure in the Framatome COSI tests was either [ ]<sup>a,c</sup>. The pressure of [ ]<sup>a,c</sup> is lower than the lowest system pressure [ ]<sup>a,c</sup> in the Westinghouse COSI tests.

The range of SI water temperature in the Framatome COSI tests was [ ]<sup>a,c</sup>, while the SI water temperature in the Westinghouse COSI tests was almost constant [ ]<sup>a,c</sup>. High SI water temperature is possible during the later stages of a SBLOCA in some PWRs, when the SI water comes from the sump instead of the RWST and is not cooled by the component cooling water.

The calculation for the heat loss, downcomer condensation, and upper and lower bound of the  $Q_{cond}$  follows the same procedure used for the Westinghouse COSI data reduction. There are 27 samples of heat loss in the Framatome COSI tests at a pressure of [ ]<sup>a,c</sup>. It is noted that all the Framatome COSI tests at this pressure are accounted for in the evaluation of heat loss, which include the tests excluded from the validation plan. The reason is that there is not significant steam movement during the heat loss test (the first one in the test series). The heat losses at pressures of [ ]<sup>a,c</sup> are given in Table 17-4.

The condensation in the downcomer is a function of the downcomer water level and the SI water mass flow rate. Both the Westinghouse and Framatome COSI experiments used the same downcomer (a structural difference only exists at the cold leg). The downcomer water level in the Framatome COSI tests was [ ]<sup>a,c</sup>. Therefore, the downcomer condensation can be evaluated using the same equation for the Westinghouse COSI test with a downcomer water level of [ ]<sup>a,c</sup>.

The Framatome COSI experiments include both [ ]<sup>a,c</sup>. It is noted that the cold leg condensation model does not depend on the [ ]<sup>a,c</sup> flow configuration. The cold leg condensation model predicts the same condensation heat transfer rate if all the parameters in the correlation are the same. To validate the cold leg condensation model against the possible [ ]<sup>a,c</sup> in the broken cold leg, the Framatome inverse COSI tests are included in the assessment plan.

[

] <sup>a,c</sup>

The qualified Framatome COSI test data with zero break flow are shown in the Table 17-5.

### **JAERI ROSA IV/LSTF Facility**

The ROSA IV Large Scale Test Facility a 1/48 volumetrically scaled facility is discussed in Section 21. In this section, only the ROSA IV SB-CL-05 test is considered. [

] <sup>a,c</sup>

Table 17-6 provides the major dimensions and scaling factors of the ROSA facility in comparison to the COSI facility and typical PWR dimensions. While the detailed LSTF system description is discussed in Section 21, some key features, specifically relative to the cold leg and SI injection, are reviewed here.

[

] <sup>a,c</sup>

The test facility was very well instrumented and this allowed for the extraction of separate effects test data. The test SB-CL-05 was considered for the purpose of analyzing the cold leg condensation in detail. The cold leg condensation in the cold leg was in a slow transient state. However an accurate evaluation of the cold leg condensation was possible by assuming a quasi-steady state progression of the transient.

[

] <sup>a,c</sup>

[

simulated in the separate effects test. ]<sup>a,c</sup> in ROSA is modeled and

[

] <sup>a,c</sup>

To set up the steady state separate effects test, several instantaneous flow conditions in the cold leg are captured. [

] <sup>a,c</sup> The flow conditions are given in Table 17-7.

In summary, the following key considerations are applied to select the tests for the assessment:

- The Westinghouse vertical injection COSI experiment (i.e., with injection angle of 90°) has been used, as documented in detail in Volume 1, Section 6.3.6, to define the cold leg condensation model implemented in WCOBRA/TRAC-TF2. The assessment of the vertical injection COSI tests is provided here to **verify** the WCOBRA/TRAC-TF2 code with the cold leg condensation model described in Section 6.3.6, thus to confirm the correct code implementation of the model documented in Section 6.3.6.
- The Westinghouse horizontal injection COSI experiment had a [ ] <sup>a,c</sup> injection angle in the flow direction, different than the vertical injection experiments. The diameter of the horizontal injection port was larger than the diameters in vertical experiment. This larger diameter and the 45° injection angle cause the water to [ ] <sup>a,c</sup>. The assessment of

WCOBRA/TRAC-TF2 against the Westinghouse horizontal injection serves the purpose of **validating** the cold leg condensation model.

- The Framatome COSI experiment provides the assessment of the code at lower pressure [ ]<sup>a,c</sup> and at higher SI water temperature [ ]<sup>a,c</sup> than the Westinghouse experiments.
- The ROSA SB-CL-05 separate effects test provides an SI condensation experiment with a larger diameter cold leg. The effect of superheated steam on the cold leg condensation model is also assessed by simulating ROSA SB-CL-05 cases.

### 17.2.2 DESCRIPTION OF WCOBRA/TRAC-TF2 MODELS

Figure 17-9 shows the component layout of the WCOBRA/TRAC-TF2 model of the Westinghouse vertical COSI facility. [

] <sup>a,c</sup>

The cold leg condensation model is applied only [ ]<sup>a,c</sup>. As discussed in Section 6.3.6, [

] <sup>a,c</sup> The condensed water flows to the BREAK component. It is noted that the physical location of the vertical SI injection is not at the center of the cold leg in the Westinghouse COSI test facility. Only the scaled part of the cold leg (Figure 17-2) is simulated. The injection port is at the junction of the TEE component. This logic is applied to both the Westinghouse horizontal COSI and Framatome COSI test facilities.

The layouts of the Westinghouse horizontal COSI and Framatome COSI test facilities are similar to that of the Westinghouse vertical COSI facility. The major differences are the diameter of SI line and the angle of the SI line, which is [ ] <sup>a,c</sup> for the horizontal COSI.

The noding diagram for the ROSA SB-CL-05 safety injection tests is similar to that of the Westinghouse vertical COSI facility, which is given in Figure 17-9. However, the diameters and lengths of the cold leg and SI line are different, as are the system pressure, steam flow rate, and SI flow rate. The [ ] <sup>a,c</sup> of the ROSA facility is also simulated.

The noding diagram for the Framatome counter-current (Inverse) COSI tests is shown in Figure 17-10. [

] <sup>a,c</sup>

[

] <sup>a,c</sup>

### 17.2.3 WCOBRA/TRAC-TF2 Results

The condensation heat transfer rate is calculated from the heat transfer rate of the liquid, which is given as:

$$q_{il} = h_{il}A_i(T_{sat} - T_l) \quad (17-6)$$

where  $q_{il}$  is the heat transfer rate from the liquid to the gas-liquid interface,  $h_{il}$  is the heat transfer coefficient from the liquid to the interface, and  $A_i$  is the gas-liquid interfacial area. Because the cold leg condensation model is only applied to the junction cell of the TEE component, the heat transfer comparison is only on the junction cell. [

] <sup>a,c</sup>

The comparison between the calculated condensation heat transfer rate and the measured heat transfer rate for the Westinghouse COSI tests is shown in Figure 17-11a. [

] <sup>a,c</sup>

There are differences between the vertical COSI and horizontal COSI. [

] <sup>a,c</sup>

The comparison between the calculated condensation heat transfer rate and the measured heat transfer rate for Framatome COSI tests is shown in Figure 17-12. The test series at [

] <sup>a,c</sup>

[

] <sup>a,c</sup>

The comparison between the calculated condensation heat transfer rate and the measured heat transfer rate for the ROSA SB-CL-05 cold leg condensation tests is shown in Figure 17-13. [

] <sup>a,c</sup>

The steam temperatures in the cold leg for ROSA SB-CL-05 are shown in Figures 17-14 to 17-17. Steam superheating is constant upstream of the safety injection. The steam superheating gradually decreases downstream of the safety injection. [

] <sup>a,c</sup>

#### 17.2.4 Small Break LOCA Experiments Conclusions

WCOBRA/TRAC-TF2 models for three test facilities (Westinghouse COSI, Framatome COSI, and ROSA SB-CL-05) are developed to assess the cold leg condensation model with focus on the small break LOCA scenario.

The overall assessment of code predictions against data from Westinghouse COSI, Framatome COSI, and ROSA IV SB-CL-05 is summarized in Figure 17-18. [

] <sup>a,c</sup>

[

] <sup>a,c</sup>

The uncertainty range of the cold leg condensation model will be assessed in Section 29.

## 17.3 LARGE BREAK LOCA EXPERIMENTS: UPTF TEST 8A

### 17.3.1 Introduction

In Section 17.2, the assessment of the condensation process in the cold leg was focused on the small break LOCA scenario. For the large breaks, condensation is of the highest relative importance during the refill period. When the ECC water is no longer bypassed in the refill period, the condensation process at the top of the downcomer helps to induce downflow through the core, promoting cooling. In this scenario, the thermal hydraulic conditions are different from those analyzed in the previous sections, and the effect of the accumulator injection and the low head safety injection flow rates needs to be assessed. [

] <sup>a,c</sup>

As part of the UPTF test matrix, two cold leg flow regime separate effects tests, Tests 8 and 25, were run to investigate steam/water flow phenomena in the cold legs during the refill/reflood phase of a large break LOCA. These phenomena include steam condensation on subcooled emergency core coolant (ECC) at different flow regimes (e.g., plug flow, stratified flow) in the cold leg. Test 8A (2D/3D Program Report, 1988) focused on the effect of ECC flow rate on cold leg flow phenomena. Test 25A (2D/3D Program Report, 1990) investigated the effects of steam flow rate and steam superheating. UPTF Test 25A provides the assessment basis for different hydrodynamic phenomena and is discussed in Section 19, but the implication to the cold leg condensation model will be addressed in this section. The integral UPTF Test 8A model with the VESSEL and the loop structure is developed and assessed in Section 19. In this section, the UPTF Test 8A is modeled as a single TEE as discussed in Section 17.3.2.

UPTF Test 8A was performed to investigate the flow regimes that might arise in the intact cold legs of a PWR during a postulated Large Break Loss of Coolant Accident (LBLOCA), when subcooled ECC liquid mixes with superheated steam. During the blowdown and refill phases, the flow of accumulator water is of sufficient magnitude to theoretically condense all the steam flowing into the cold leg. During reflood the low head safety injection flow (LHSI/RHR), at its minimum levels, is typically insufficient to condense all the steam flowing into the cold leg.

Cold leg liquid slug formation and oscillations may occur when the subcooled injected ECC liquid causes condensation of the steam flowing in the cold leg. A liquid slug is a region in which the cold leg is completely filled with liquid. Steam flowing through the cold leg from the pump towards the downcomer condenses when in contact with subcooled injected ECC liquid. A liquid slug in the region between the injection point and the downcomer can form when the liquid subcooling and the interfacial heat transfer are sufficient to completely condense the flow of steam.

Once the liquid slug forms, further condensation of steam results in a reduction of pressure upstream of the liquid slug. A local reduction in pressure at the condensation point causes the slug to move back towards the ECC injection point. The movement may be expected to continue until the liquid slug completely covers the injection point.

Eventually, the pressure increase, due to the steam entering the cold leg, is sufficient to move the liquid slug towards the downcomer again. These conditions were experienced in UPTF Test 8.

### 17.3.2 WCOBRA/TRAC-TF2 Model Description

The WCOBRA/TRAC-TF2 model of UPTF Test 8A is documented in Section 19.3.7 with the full structure of the loop and the vessel. The single TEE model in this section serves as the base model for validating the cold leg condensation model and performing sensitivity studies. Unlike the integral UPTF Test 8A model in Section 19.3.7, which represents the entire facility, the TEE model only represents [ ]<sup>a,c</sup>. The advantage of the single TEE model is that [ ]<sup>a,c</sup>.

The single TEE model development includes the following cases:

1. Base Model – [ ]<sup>a,c</sup>
2. Sensitivity Study on ECC Injection Angle – [ ]<sup>a,c</sup>
3. Sensitivity Study on Cold Leg Noding – [ ]<sup>a,c</sup>
4. Sensitivity Study on ECC Injection Node – [ ]<sup>a,c</sup>
5. Sensitivity Study on Ranging Cold Leg Condensation Rate Multiplier (KCOSI) – [ ]<sup>a,c</sup>
6. Sensitivity Study on Ranging Horizontal Stratification Criteria (HS\_SLUG) – [ ]<sup>a,c</sup>

The noding diagram is shown in Figure 17-20. [ ]<sup>a,c</sup>

[ ]<sup>a,c</sup>

### 17.3.3 WCOBRA/TRAC-TF2 Results: Base Model

The WCOBRA/TRAC-TF2 simulation of UPTF Test 8A was run for the first 200 seconds of the test, which covered the period where flow was injected into the Loop 2 intact cold leg. The as-measured injection steam and ECC flow rates were used as boundary conditions in the WCOBRA/TRAC-TF2 model. The BREAK component was maintained at a constant pressure of 390 kPa (57 psia).

In Section 19, it is demonstrated that the WCOBRA/TRAC-TF2 simulation of UPTF Test 8A with the full vessel model and loop structure shows [

] <sup>a,c</sup>. The TEE model for UPTF Test 8A provides additional validation on the cold leg condensation model with a fixed boundary condition. [

] <sup>a,c</sup>

The measured and predicted temperatures in the Loop 2 cold leg are compared in Figures 17-21 through 17-24. At the pump exit (Figure 17-21), the single TEE model predicts a higher degree of oscillation with a shorter time period at the beginning of stage 1 than the integral model does (Figure 19.3-156). [

] <sup>a,c</sup>

The single TEE model predicted the water temperature near the injection point is shown in Figure 17-22. [

] <sup>a,c</sup>

Figure 17-23 shows the comparison between the measured temperature and the WCOBRA/TRAC-TF2 predicted water temperature at the downstream injection point. [

] <sup>a,c</sup>

Figure 17-24 shows the comparison between the measured temperature and the WCOBRA/TRAC-TF2 predicted water temperature at the cold leg near the vessel inlet. The overall effect of the cold leg condensation is shown in this figure. [

] <sup>a,c</sup>

[ ]<sup>a,c</sup>

In general, [ ]<sup>a,c</sup>

### 17.3.4 WCOBRA/TRAC-TF2 Results: Sensitivity Studies

#### Sensitivity Study on ECC Injection Angle

This case studies the impact of the ECC injection angle on the cold leg condensation. [ ]

] <sup>a,c</sup>

#### Sensitivity Study on Cold Leg Noding

Figure 17-28 shows the noding size sensitivity on the predicted water temperatures at the injection cell of the cold leg. The predicted temperatures are different from stage 3 to stage 6. Figures 17-29 and 17-30 show the same comparison downstream of the injection cell and at the outlet of the cold leg, respectively.

[ ]

] <sup>a,c</sup>

[ ]<sup>a,c</sup>

### **Sensitivity Study on ECC Injection Node**

This is a sensitivity study on the junction node to which ECC water is injected. [

] <sup>a,c</sup>

### **Sensitivity Study on Cold Leg Condensation Rate Multiplier (KCOSI)**

The uncertainty of the cold leg condensation model is ranged using the cold leg condensation rate multiplier, KCOSI. [

] <sup>a,c</sup>

[

] <sup>a,c</sup>

### **Sensitivity Study on Horizontal Stratification Criteria**

The cold leg condensation model requires the flow regime to be horizontal stratified flow, wavy-dispersed flow, or annular-mist flow. The transition from horizontal stratified flow to non-stratified flow is ranged by the multiplier HS\_SLUG. [

] <sup>a,c</sup>

### **17.3.5 Large Break LOCA Experiments Conclusions**

UPTF Test 8A is utilized to assess the applicability of the cold leg condensation model in a large break LOCA. The simulation of UPTF Test 8A with the full vessel and loop structure in Section 19 shows

[ ]<sup>a,c</sup>. The single  
TEE models for the UPTF Test 8A experiment were assessed in this section. [  
] <sup>a,c</sup>

The sensitivity studies give the following conclusions:

[

] <sup>a,c</sup>

UPTF Test 25A is another cold leg condensation test for the reflood stage of LBLOCA characterized with a variable steam flow rate and a substantial steam superheating. The simulation and results of UPTF Test 25A are discussed in Section 19.3.

#### 17.4 OVERALL CONCLUSIONS

WCOBRA/TRAC-TF2 models for four test facilities (Westinghouse COSI, Framatome-COSI, ROSA SB-CL-05, and UPTF Test 8A) are developed to assess the cold leg condensation model over conditions representative of both small and large break LOCA scenarios.

The overall assessment documented in Sections 17.2 and 17.3, together with the LBLOCA assessment in Section 19, is summarized in Sections 17.2.4 and 17.3.5 for small and large break LOCA conditions, respectively. The comparison with experimental results shows that the WCOBRA/TRAC-TF2 code is able to predict condensation within a reasonable range of uncertainty. The WCOBRA/TRAC-TF2 predictions are judged to be acceptable for the purpose of analyzing a full spectrum of break sizes in a PWR LOCA.

Sensitivity analyses to key parameters using a single TEE model of UPTF Test 8A cold leg and ECC lines are also performed. The sensitivities considers the ECC branch line orientation relative to the cold leg, the noding size selected for modeling the cold leg, the condensation rate multiplier (KCOSI) and the

horizontal stratified flow regime transition criterion (HS\_SLUG). Results of the sensitivity studies are summarized in Section 17.3.5 to support methodology decisions for the purpose of modeling a PWR.

Additional validation of the cold leg condensation model is provided by the simulation of UPTF Test 25A in Section 19.3.

## 17.5 REFERENCES

1. 2D/3D Program Upper Plenum Test Facility Experimental Data Report, 1990, "Test No. 25, Downcomer/Cold Leg Steam/Water Interaction Test," E314/90/11, KWU.
2. 2D/3D Program Upper Plenum Test Facility Experimental Data Report, 1988, "Test No. 8, Cold/Hot Leg Flow Pattern Test," U9 316/88/12, KWU.
3. Boileau, H., 1988 "Condensation on Safety Injection, FRAMATOME Analysis Report," EP/TA/DC.0771.
4. Emmerling, R., Hertlein, R., Jakob, G., Strobel, R., and Winkler, F., 1988, "UPTF: Program and System Description," Siemens U9 414/88/023.
5. Gros d'Aillon, M., 1987, "Essais De Condensation En Regime Permanent (COSI Report)," SETH/LETC/87-45.
6. JAERI-memo 84-237, ROSA-IV Large Scale Test Facility (LSFT) System Description, January 1985.
7. JAERI-memo 61-056, ROSA-IV/LSTF 5% Cold Leg Break LOCA Experiment Data Report: Run SB-CL-05, March 20, 1986
8. Jonicot, A. and Bestion, D., 1993, "Condensation Modeling for ECC Injection," Nuclear Engineering and Design, 145, pp. 37-45.
9. MPR Associates, 1992. Summary of Results from the UPTF Cold Leg Flow Regime Separate Effects Tests, Comparison to Previous Scaled Tests, and Application to U.S. Pressurized Water Reactors, MPR-1208.
10. Shimeck, D. J., 1988, "COSI SI/Steam Condensation Experiment Analysis," WCAP-11767, Proprietary.

**Table 17-1 Westinghouse COSI Test Data Average Heat Loss and Uncertainty**



a,c







**Table 17-4 Framatome Test Data Average Heat Loss and Uncertainty**



a,c



**Table 17-6 Comparison of Facilities for Cold Leg Condensation Assessment**

a,c


**Table 17-7 ROSA SB-CL-05 SI Condensation Test Data for SETs**


a,c

a,c

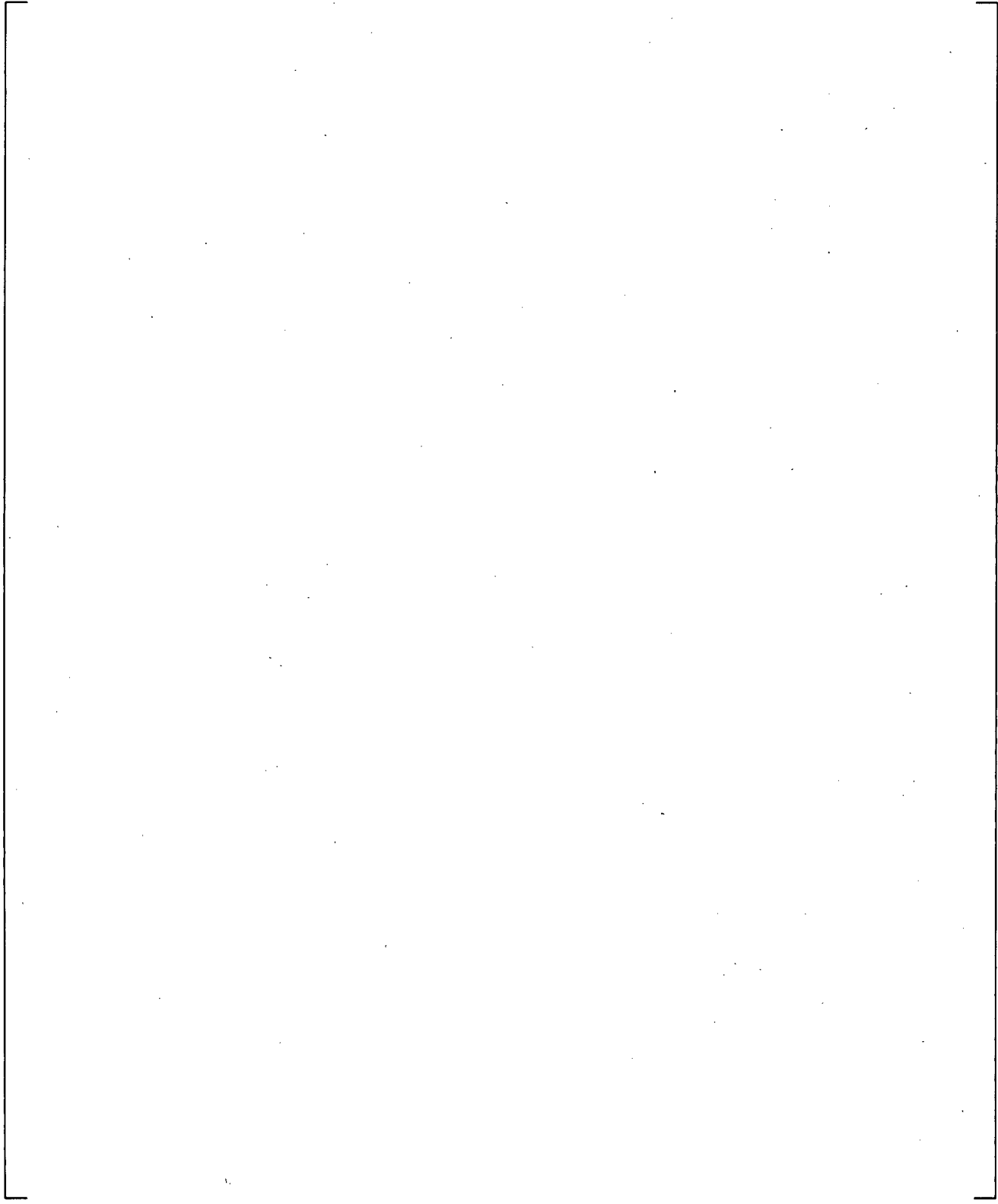


**Figure 17-1 COSI Facility Arrangement**

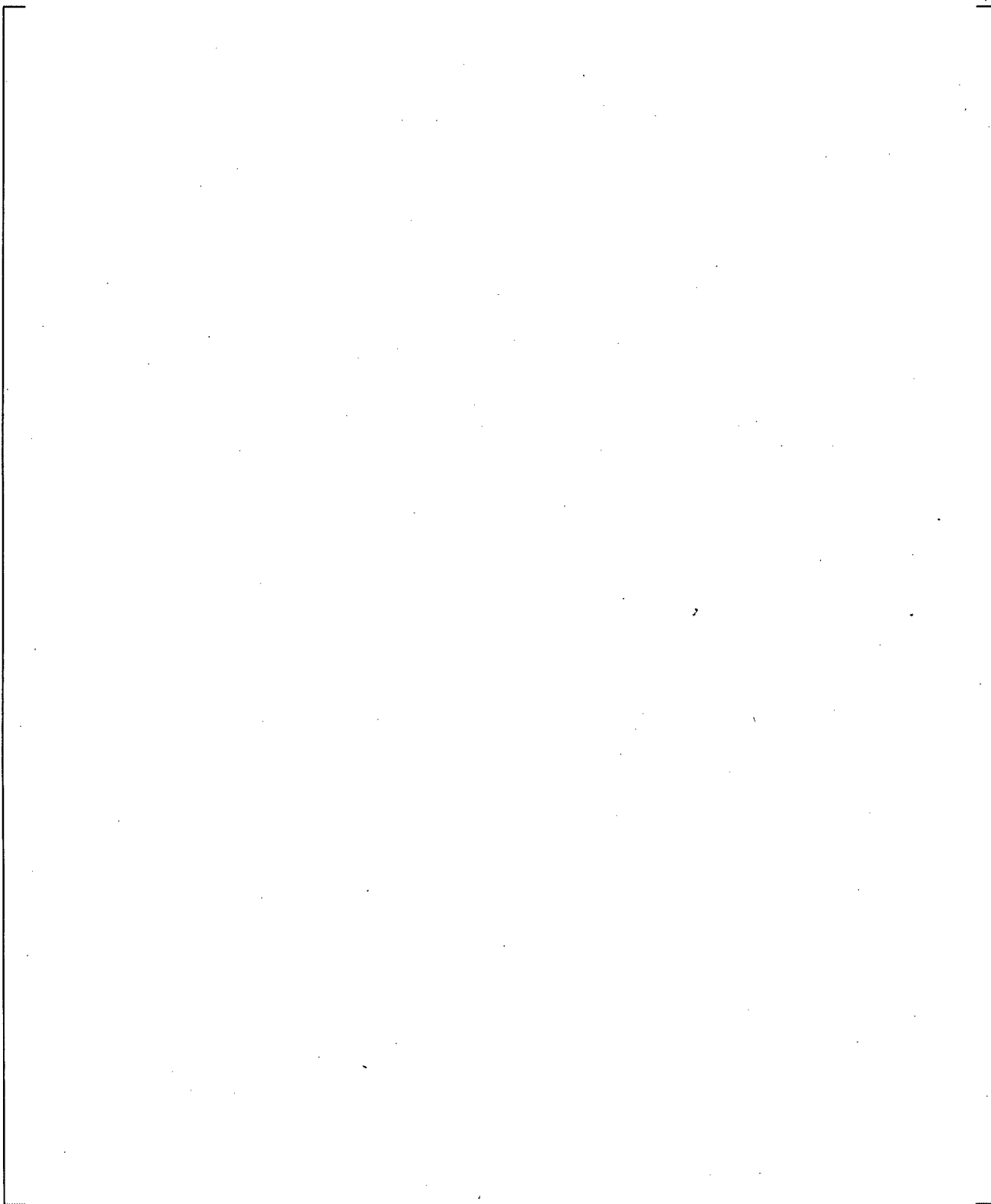


**Figure 17-2 Westinghouse COSI Test Section Arrangement**

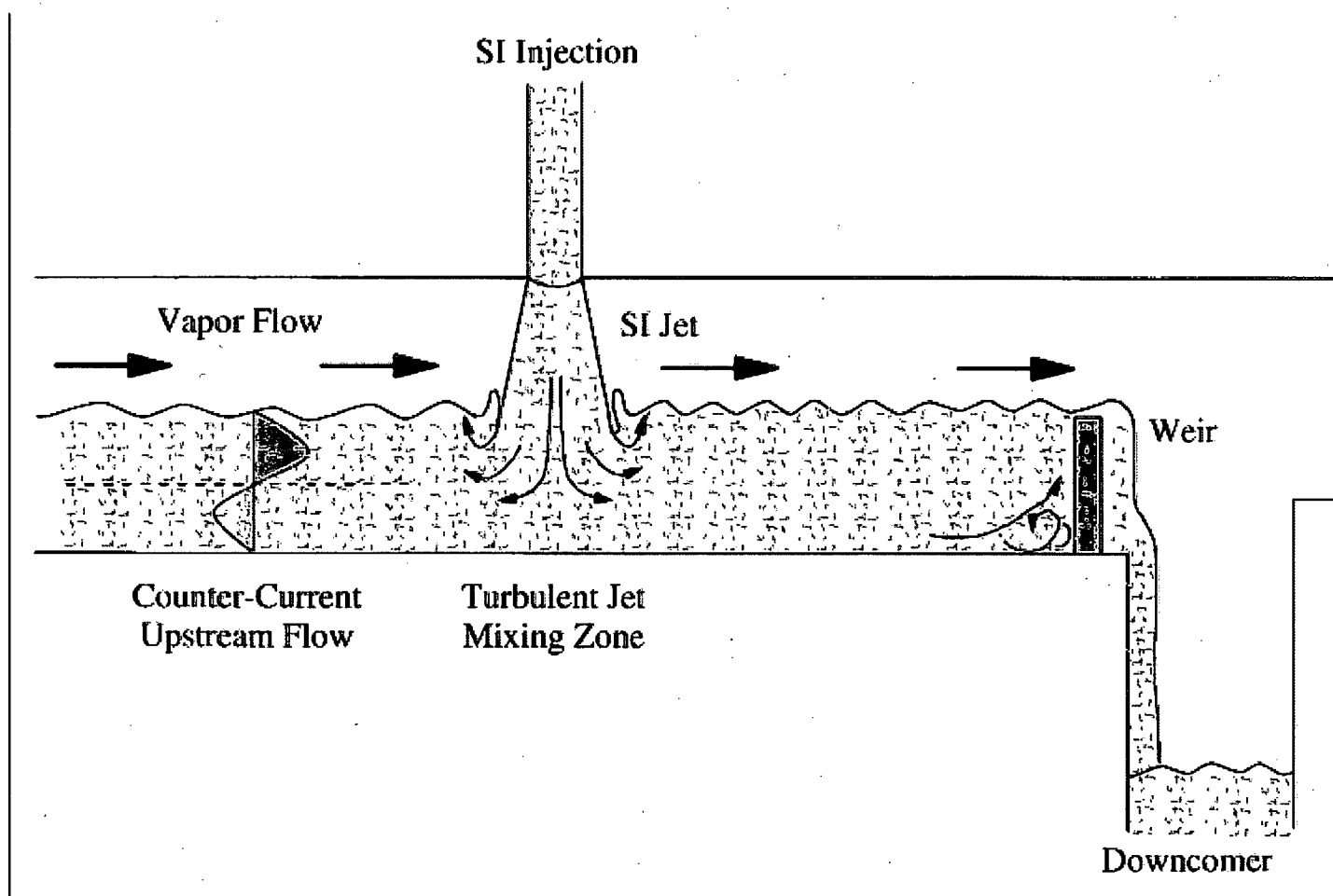


Figure 17-3 Depiction of Flow Patterns in the Test Section as Deduced from Data

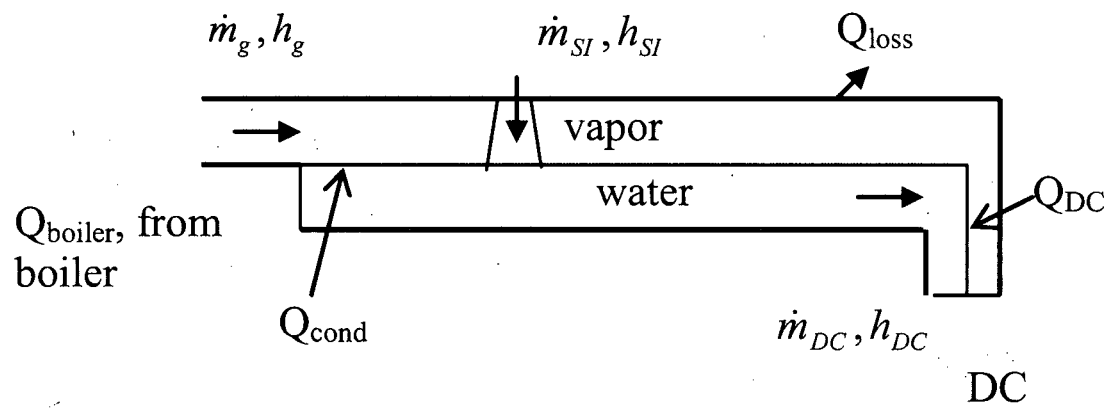


Figure 17-4 Illustration of Condensation in COSI Test Section

a,c

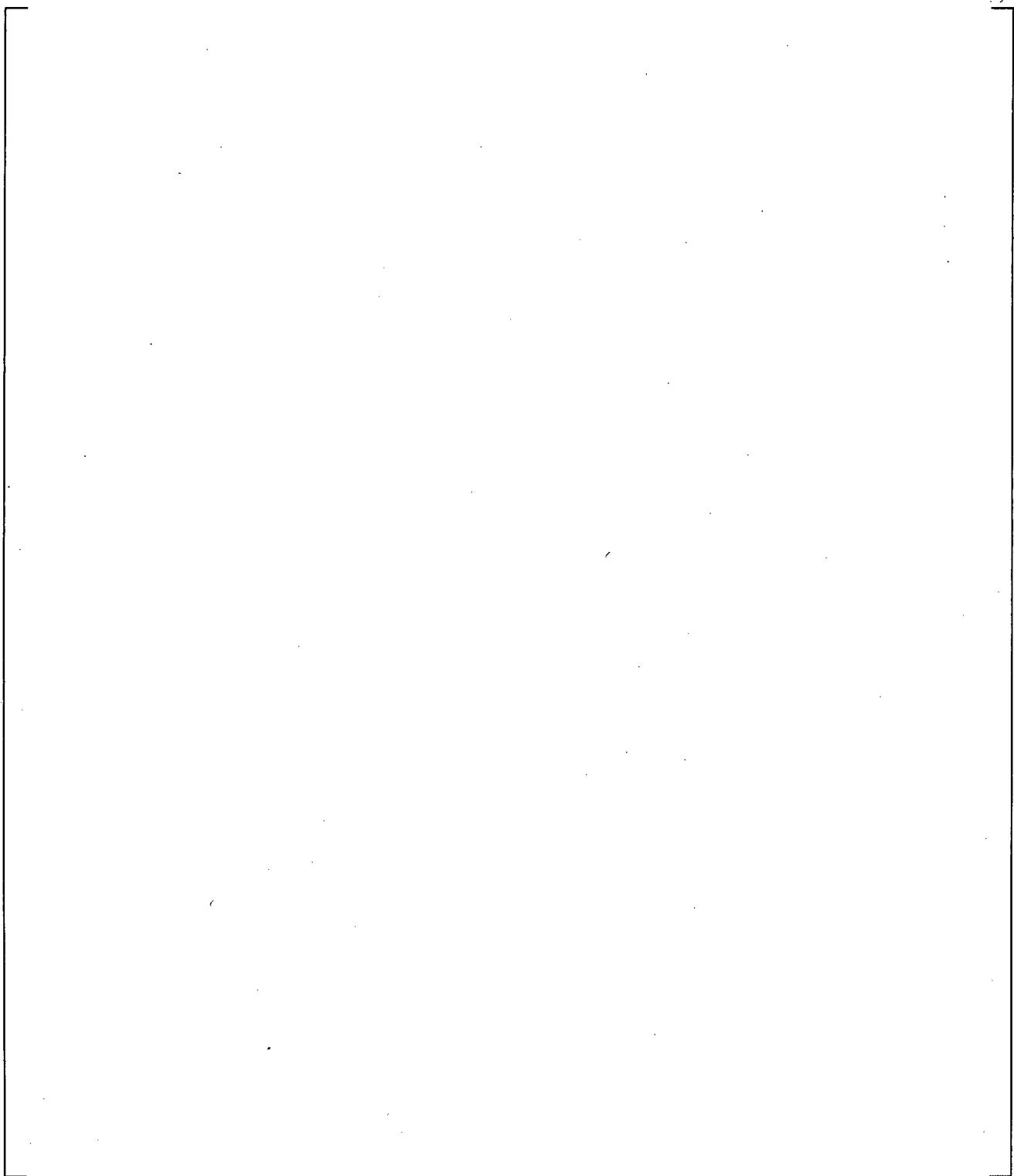
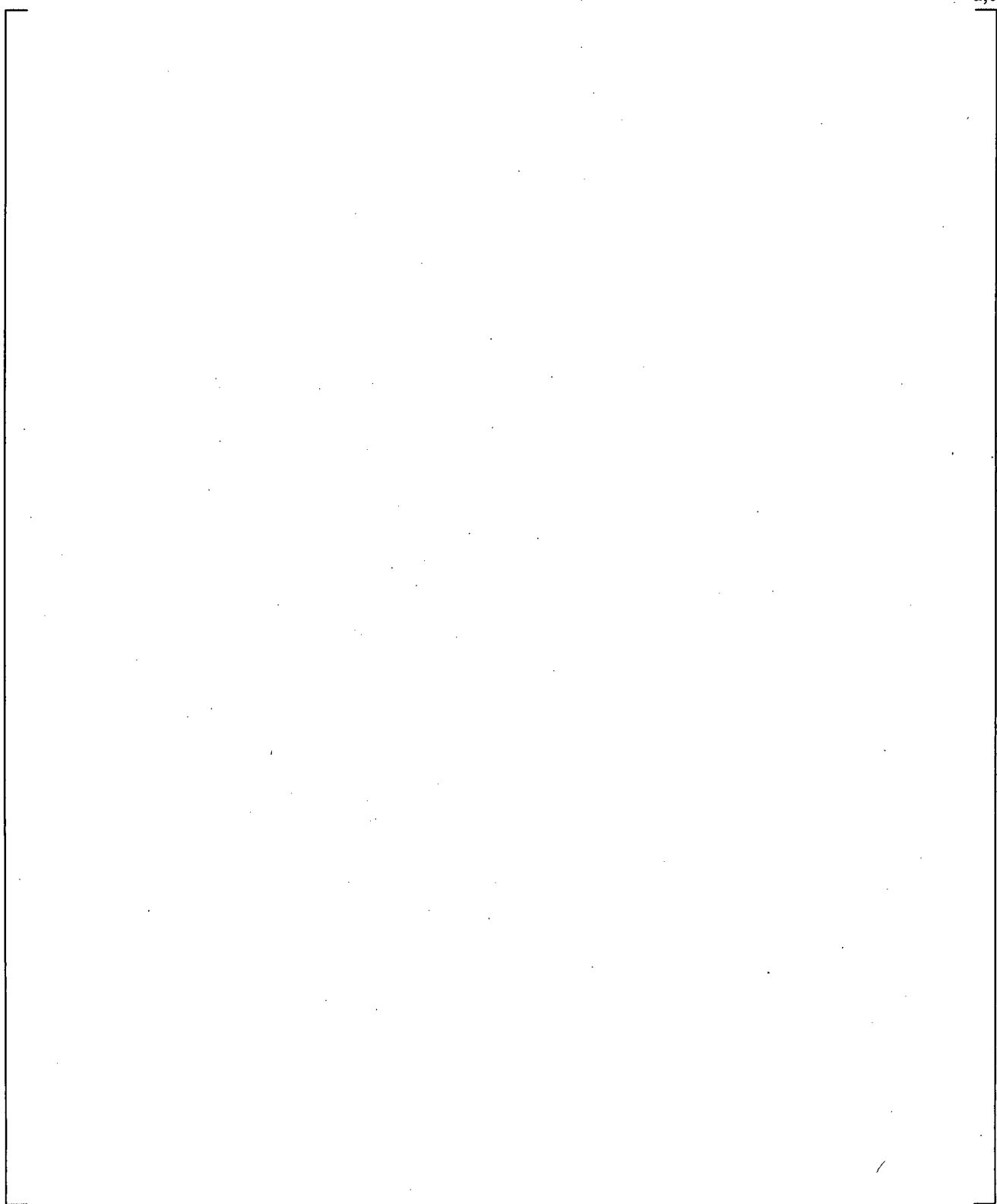
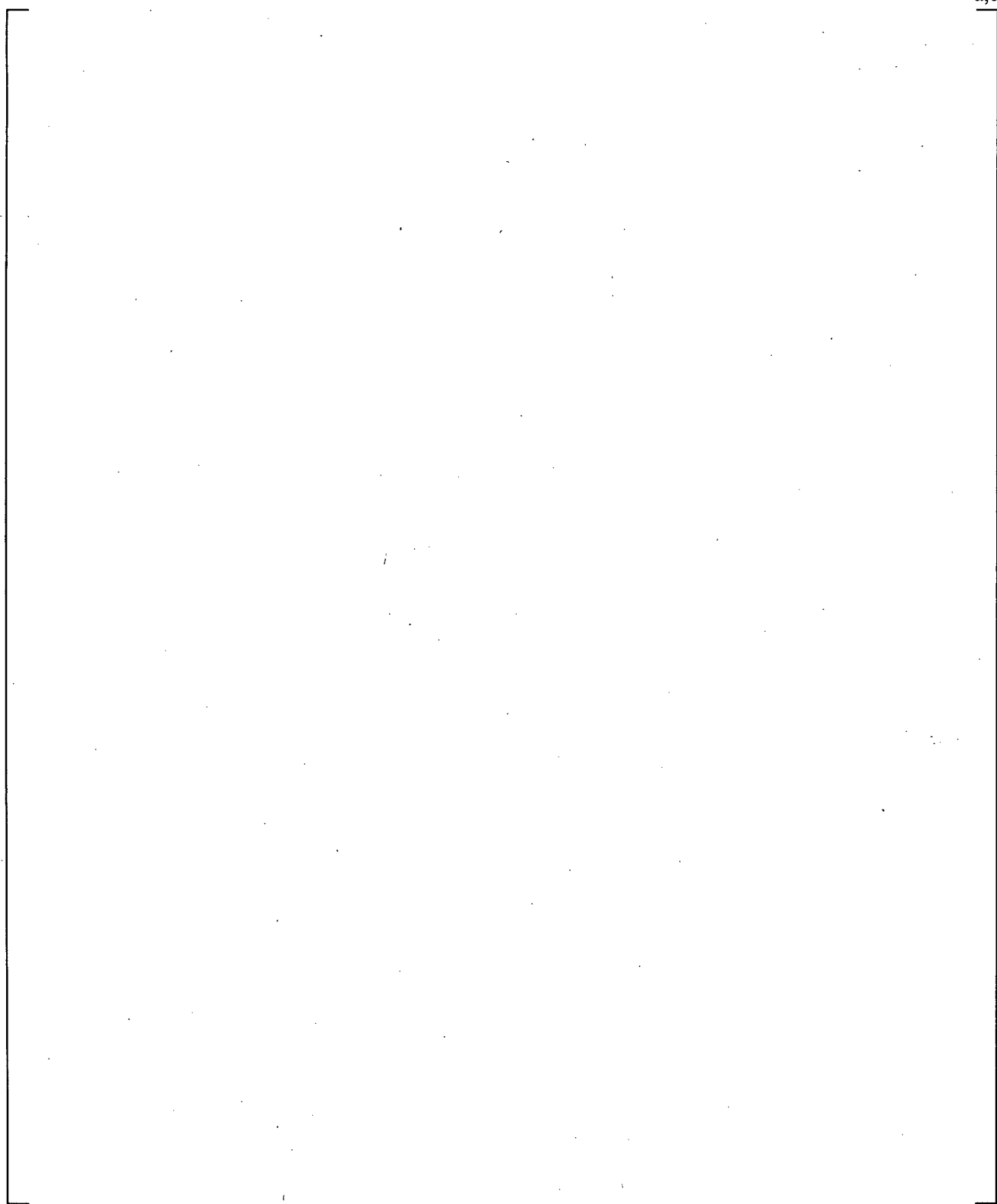


Figure 17-5 [

] a,c



**Figure 17-6 Comparison of Westinghouse Test Section and Framatome Test Section in Cross Section of Cold Leg**



**Figure 17-7**      **General Structure of Cold Leg from Crossover Leg to Downcomer in the ROSA Facility**

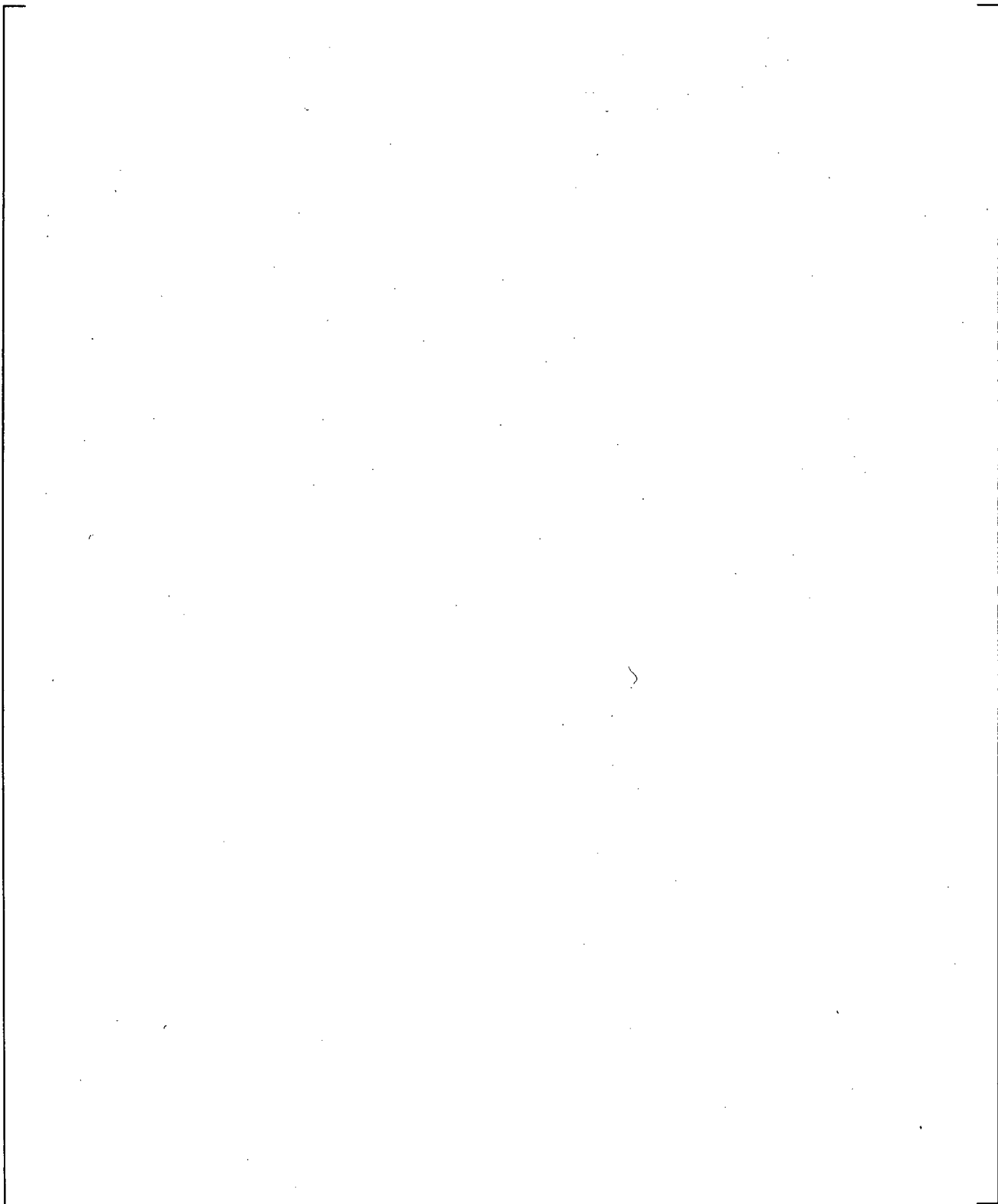


**Figure 17-8 Schematics of ECCS Configuration in ROSA IV SB-CL-05**

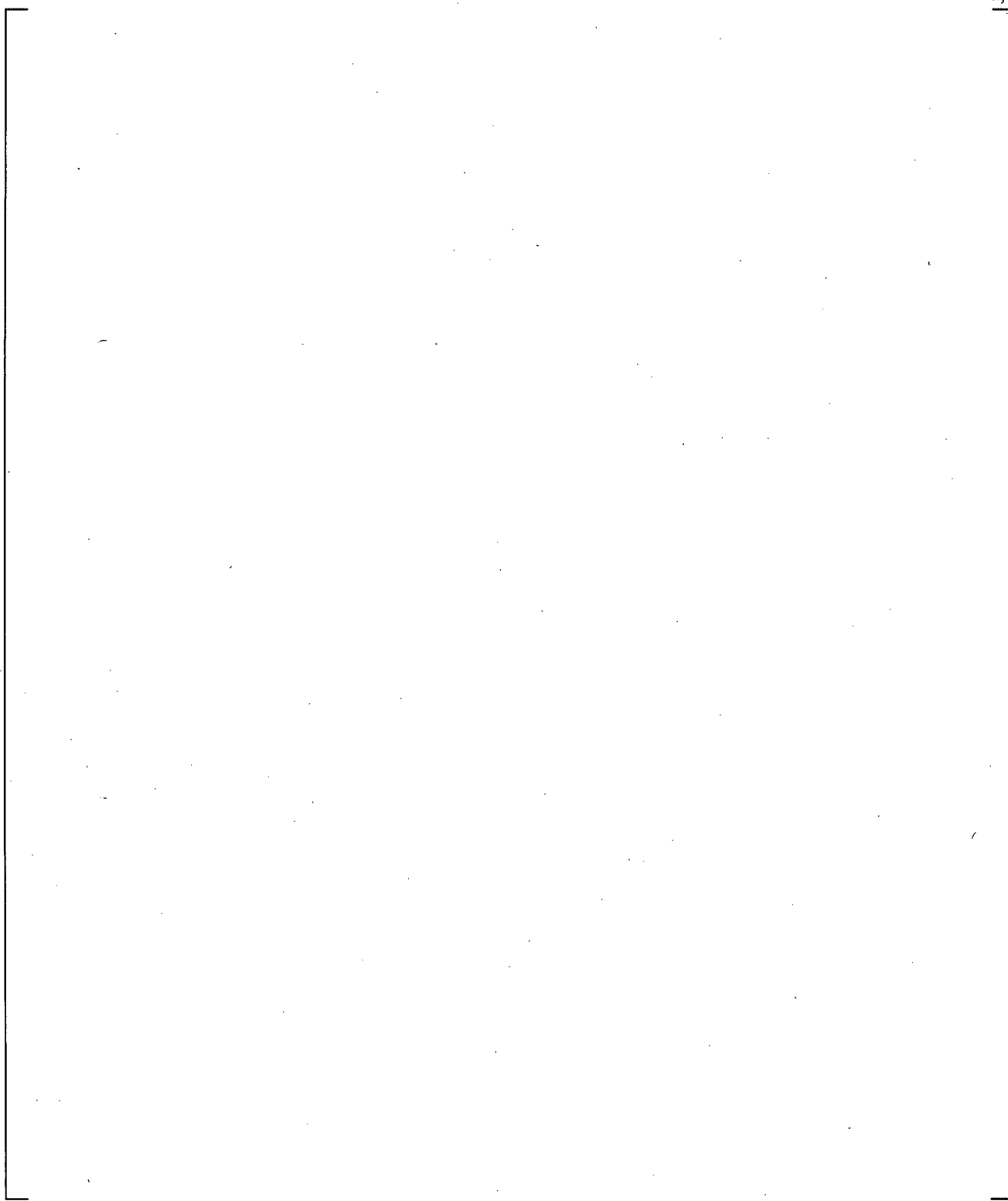


**Figure 17-9** WCOBRA/TRAC-TF2 Single TEE Noding Diagram for Westinghouse Vertical COSI, Framatome COSI, and ROSA IV SB-CL-05; for Westinghouse Vertical COSI, the Inclination angle of SI Line is 45°.

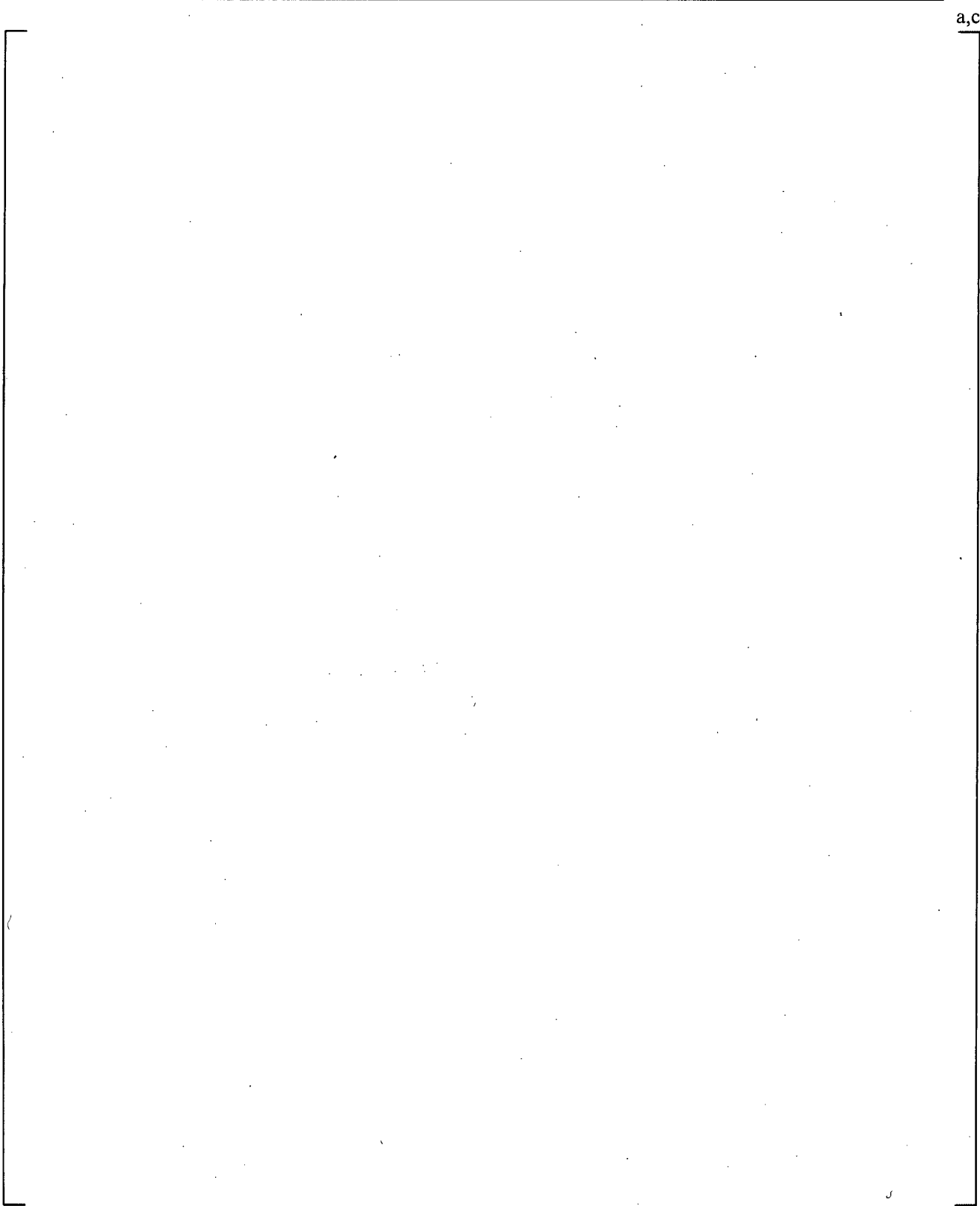


**Figure 17-10** WCOBRA/TRAC-TF2 Two-TEE Noding Diagram for Framatome Inverse COSI Tests

a,c

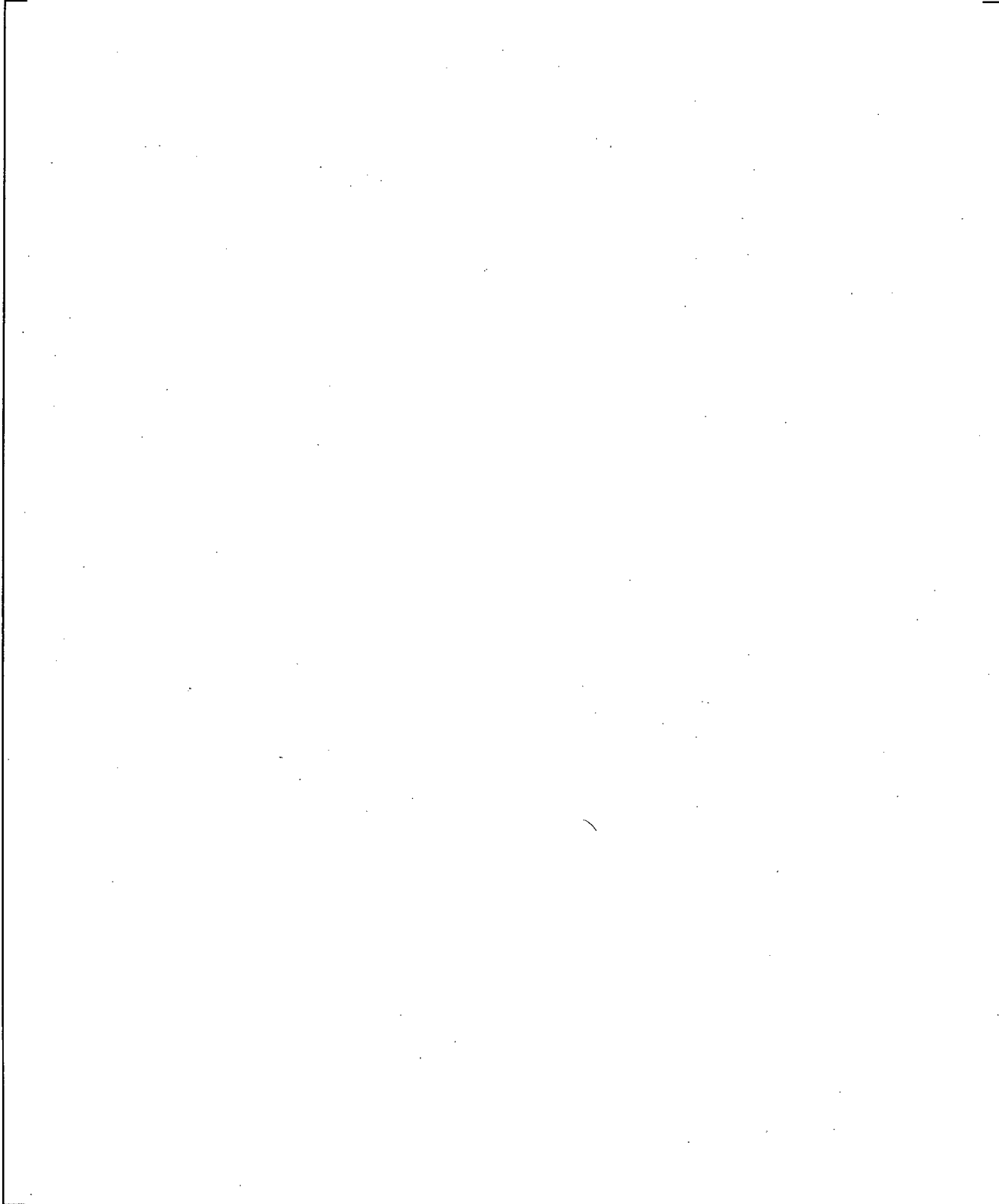


**Figure 17-11a Comparison between Measured Westinghouse COSI Condensation Heat Transfer Rate and WCOBRA/TRAC-TF2 Predicted Condensation Heat Transfer Rate**

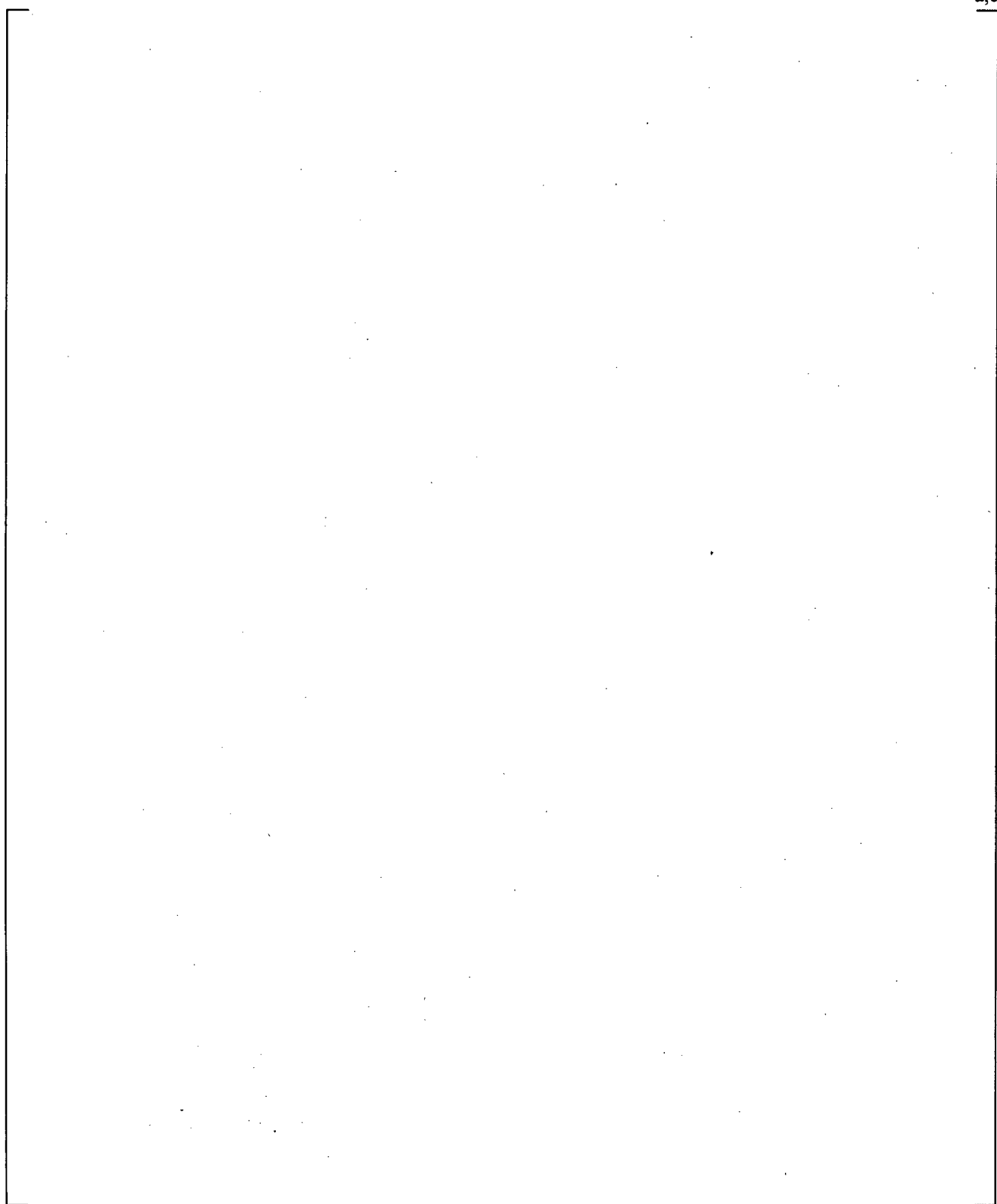


**Figure 17-11b Predicted Heat Transfer Rate for Westinghouse COSI (TEE junction cell is number 4)**

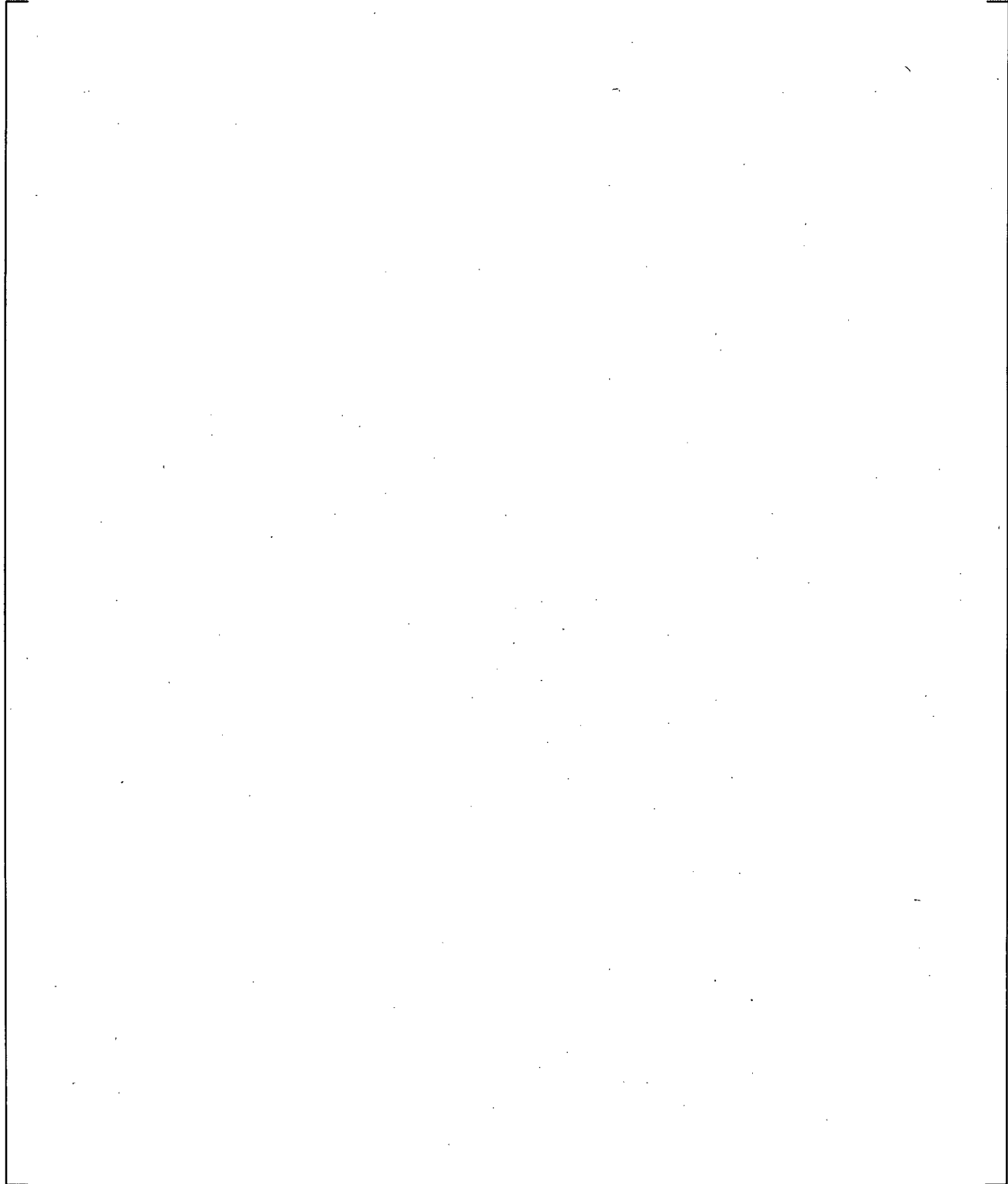


**Figure 17-12 Comparison between Measured Framatome COSI Condensation Heat Transfer Rate and WCOBRA/TRAC-TF2 Predicted Condensation Heat Transfer Rate. Data in Circles Are Tests with High SI Temperature (~80C)**

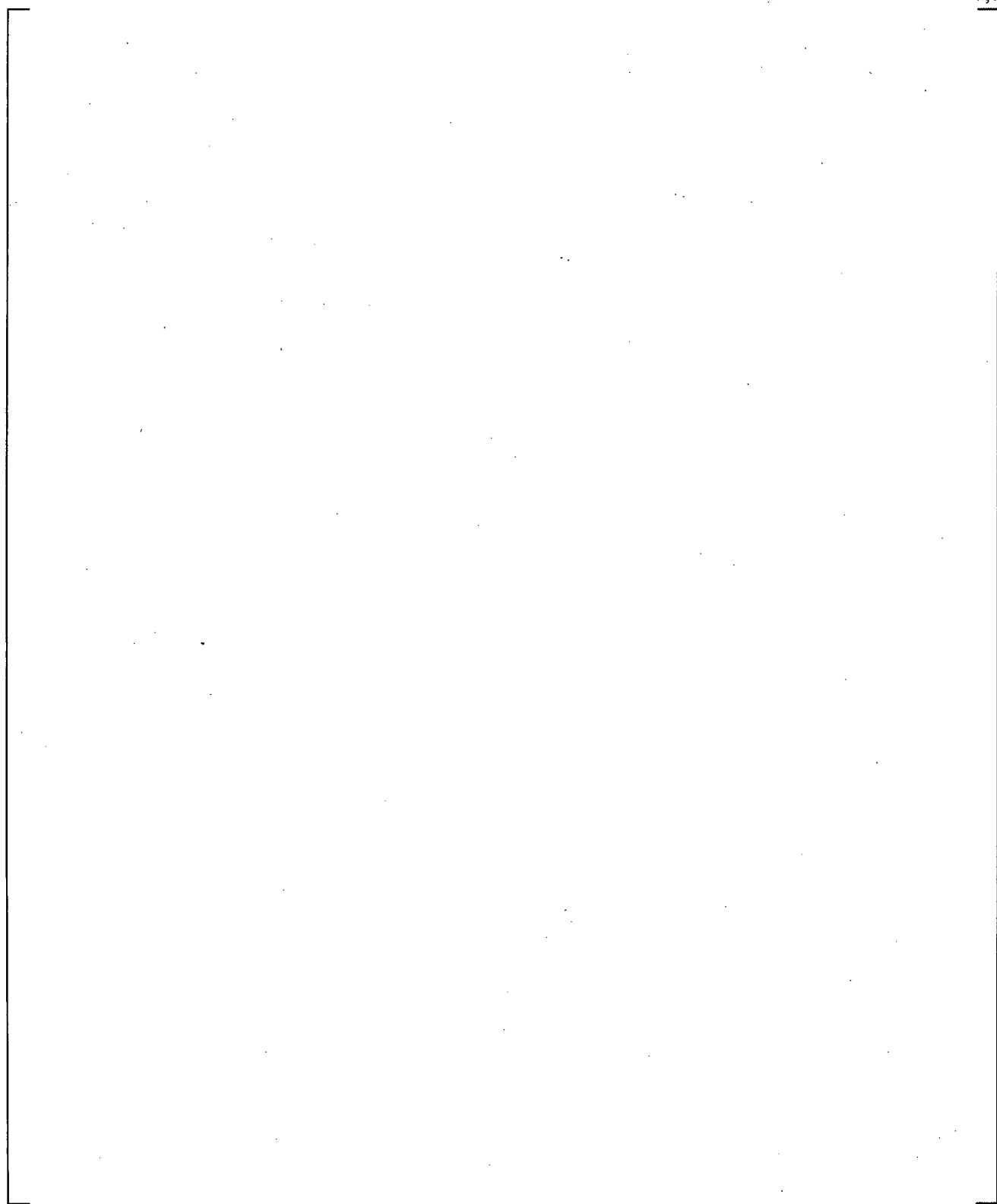


**Figure 17-13 Comparison between Measured ROSA SB-CL-05 SI Condensation Heat Transfer Rate and WCOBRA/TRAC-TF2 Predicted Condensation Heat Transfer Rate**

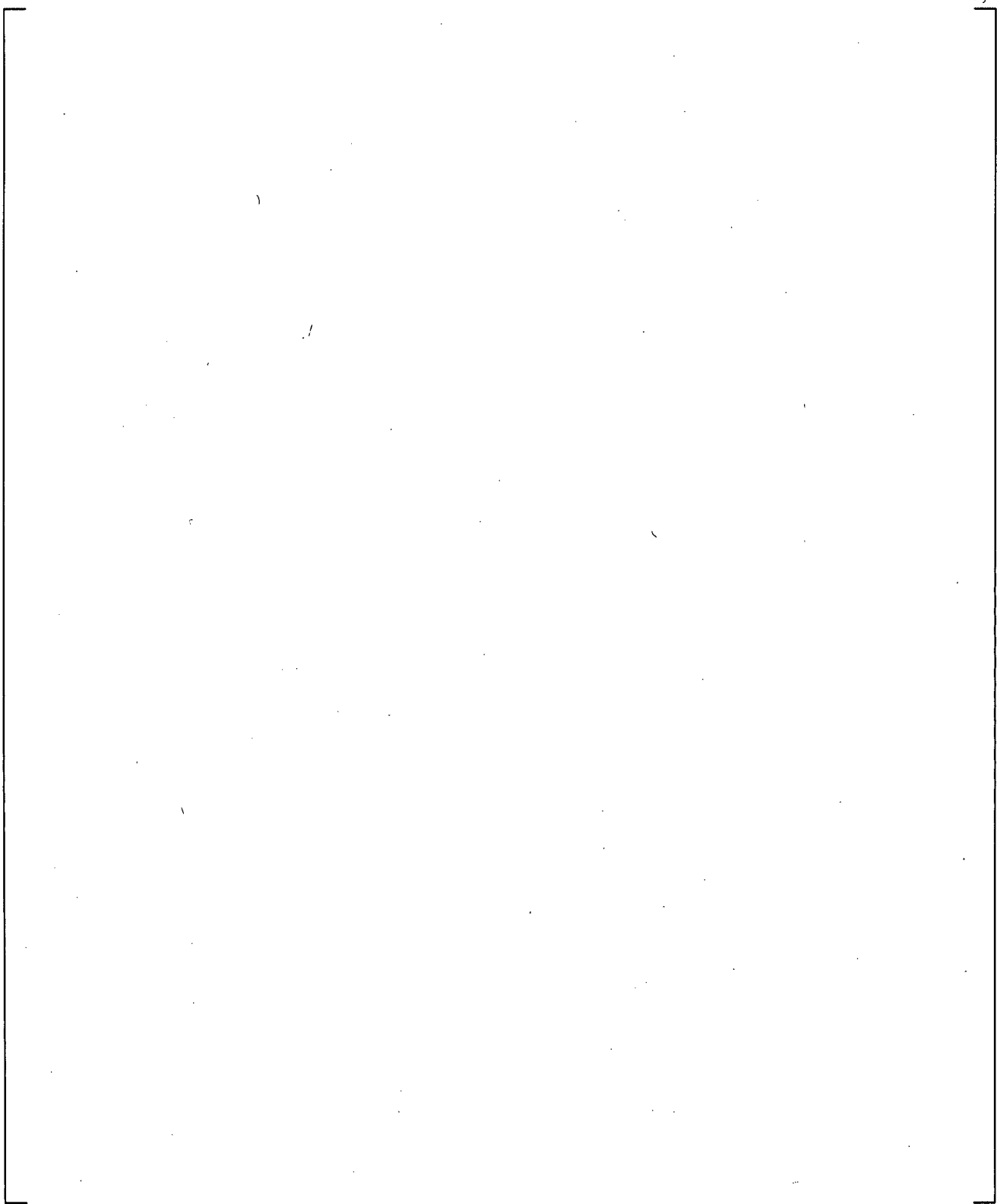


**Figure 17-14 Steam Temperature Profile in Cold Leg in ROSA Test No. 1**

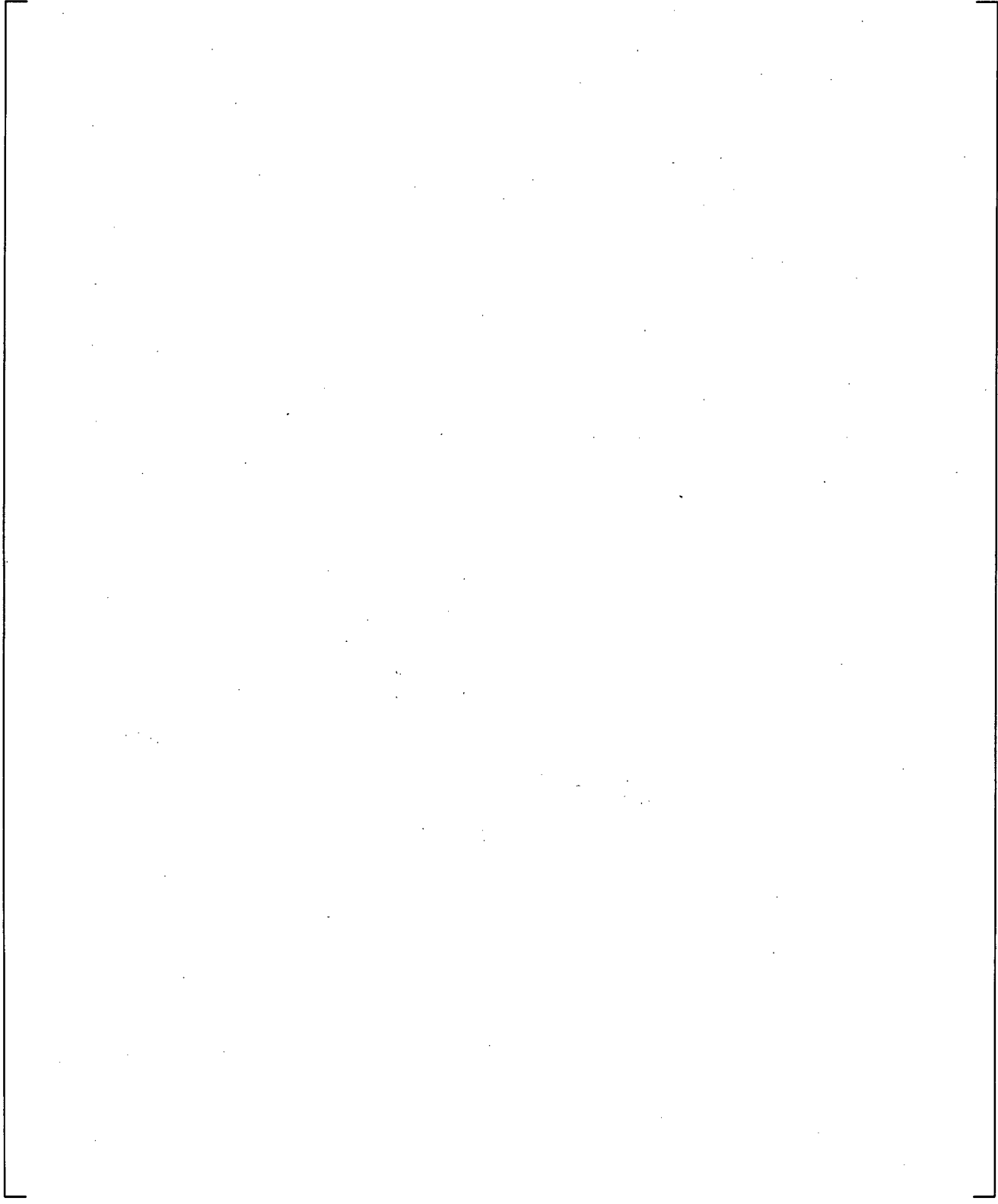


**Figure 17-15 Steam Temperature Profile in Cold Leg in ROSA Test No. 2**

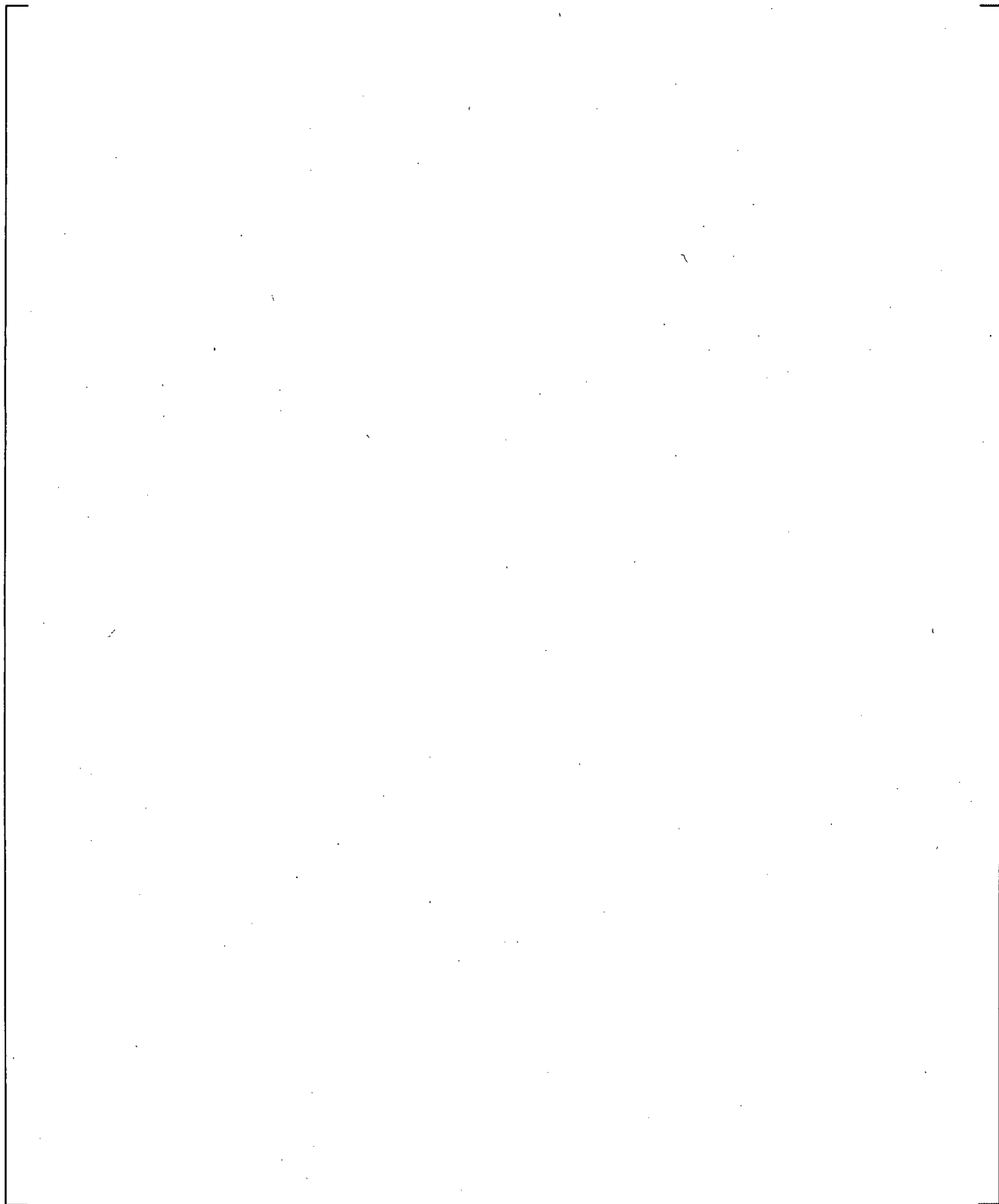


**Figure 17-16 Steam Temperature Profile in Cold Leg in ROSA Test No. 3**

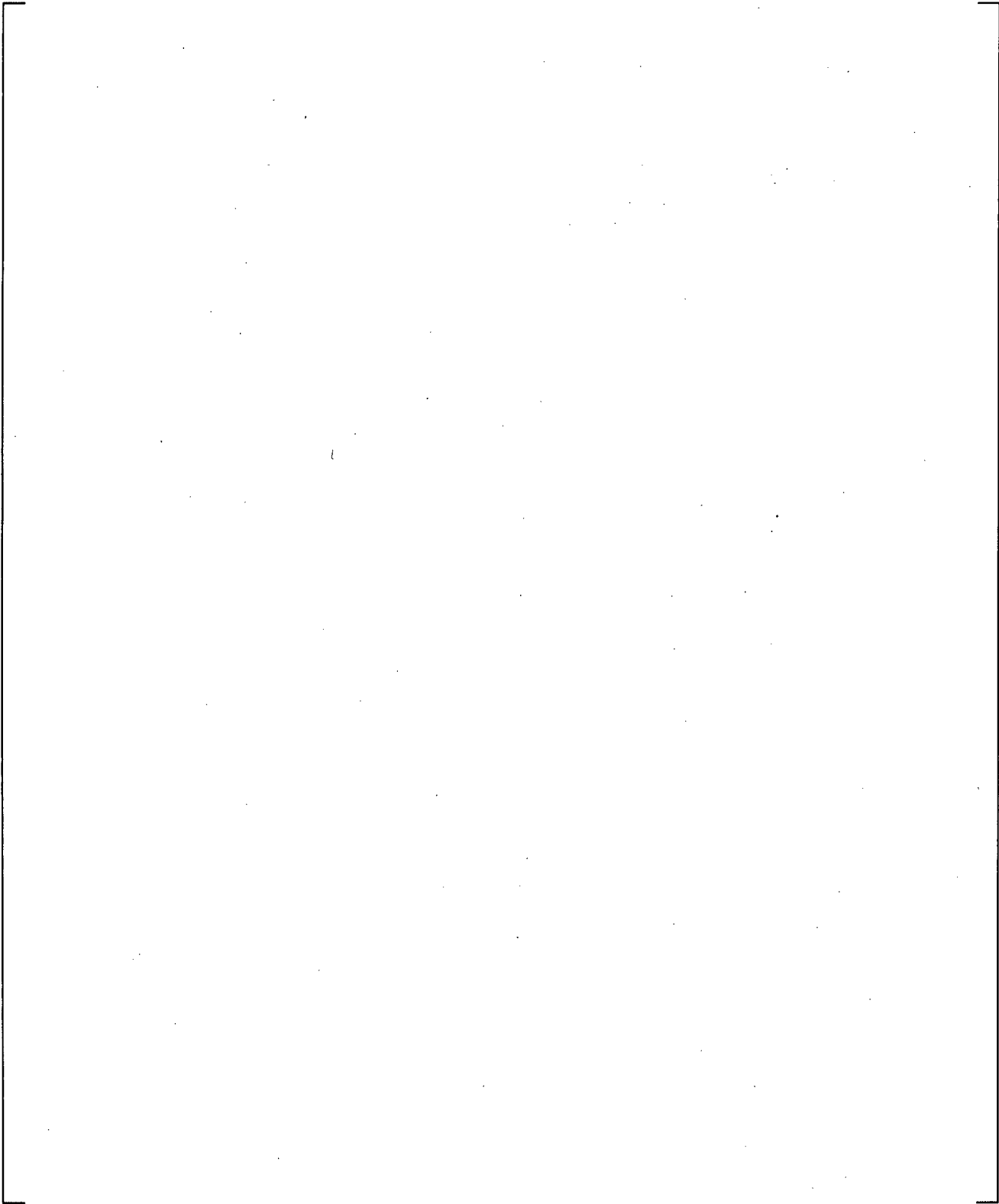


**Figure 17-17 Steam Temperature Profile in Cold Leg in ROSA Test No. 4**

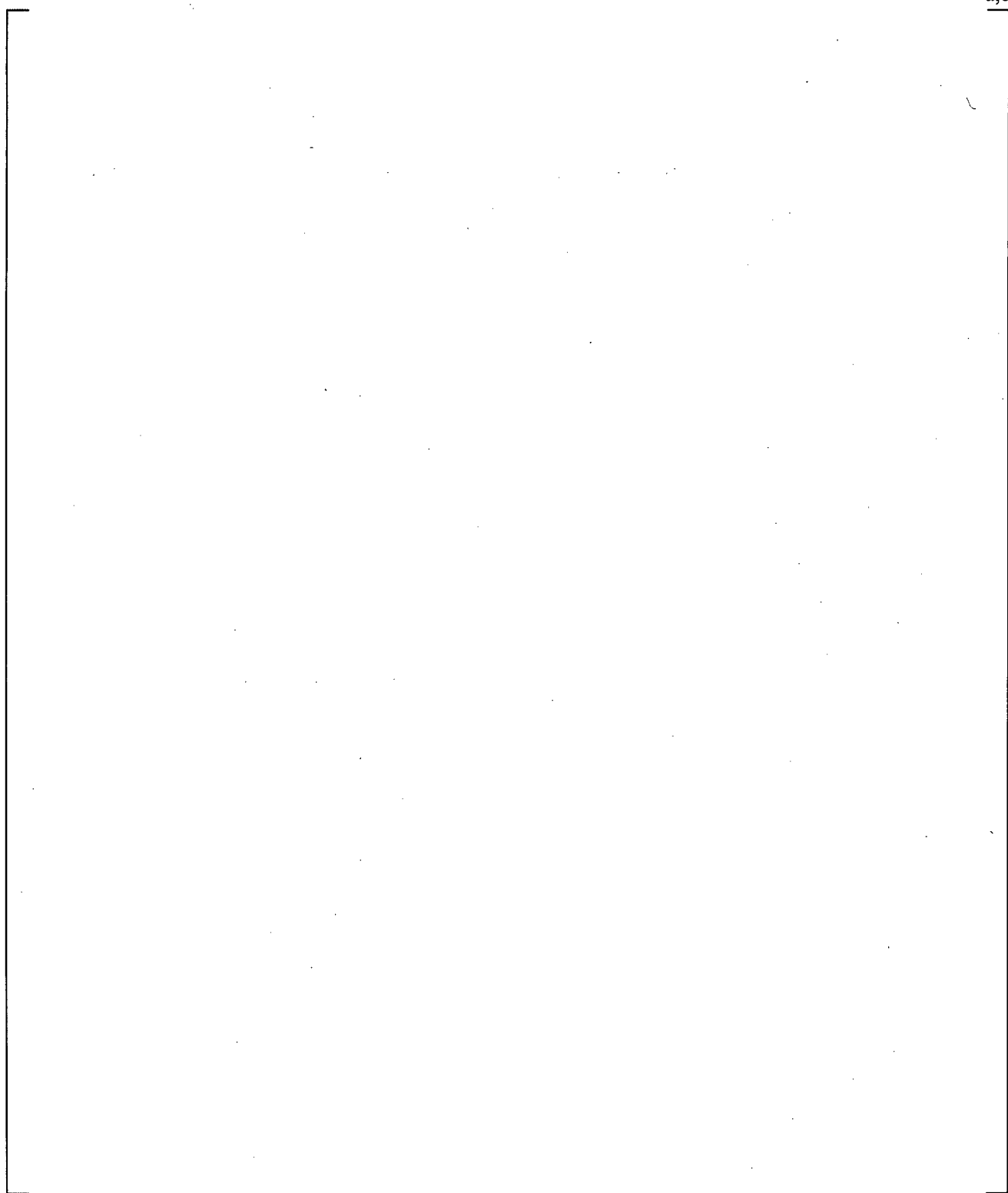


**Figure 17-18 Comparison between Measured Condensation Heat Transfer Rate and WCOBRA/TRAC-TF2 Predicted Condensation Heat Transfer Rate for All Validation Cases**

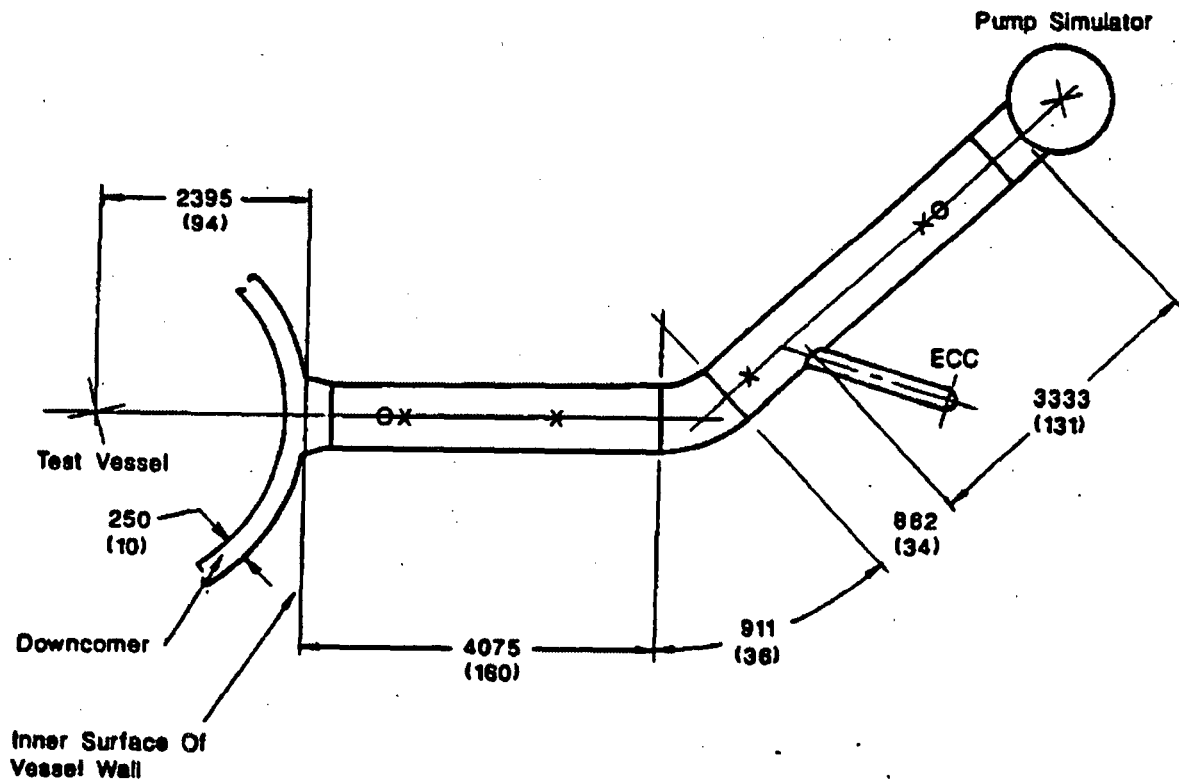
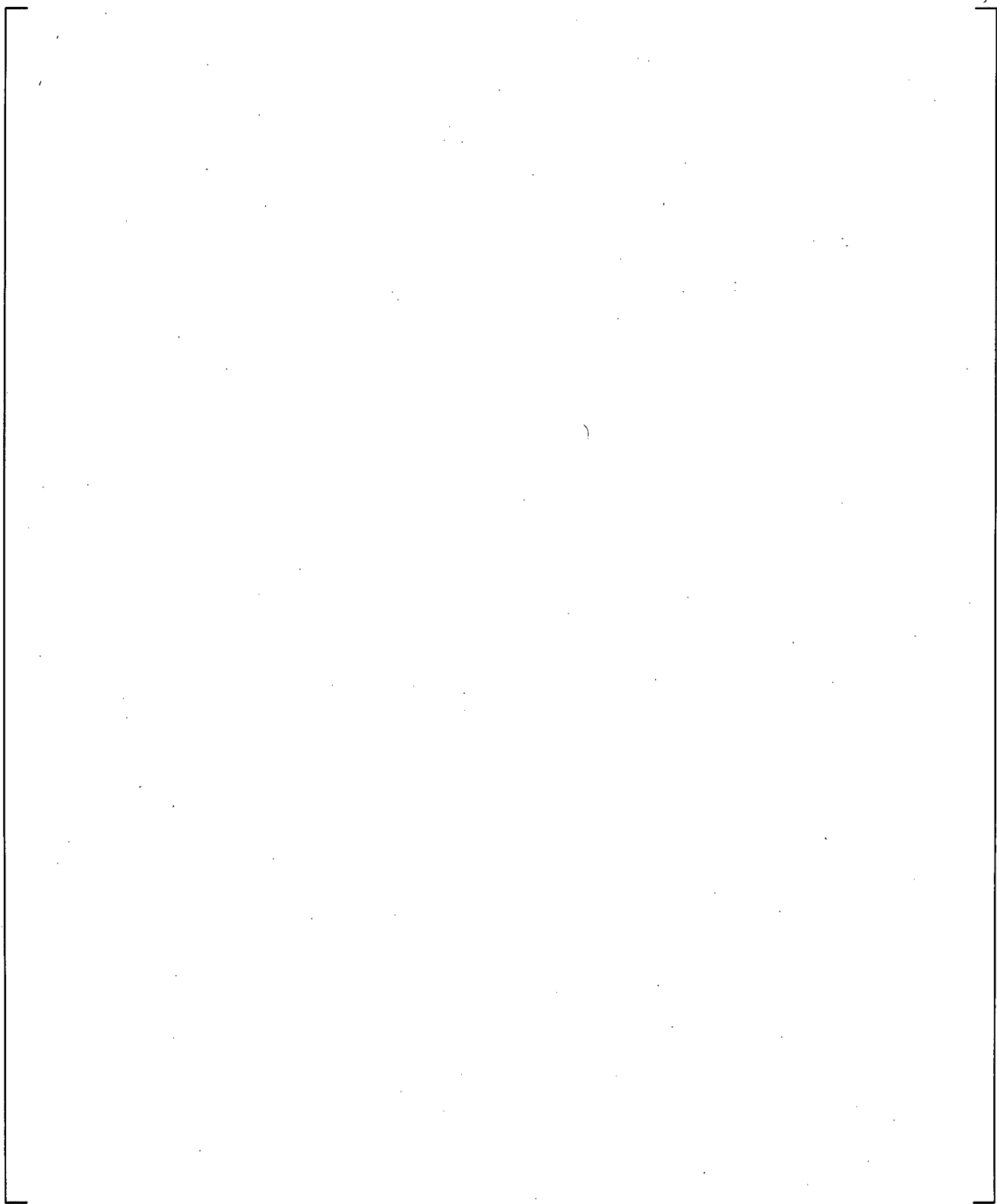
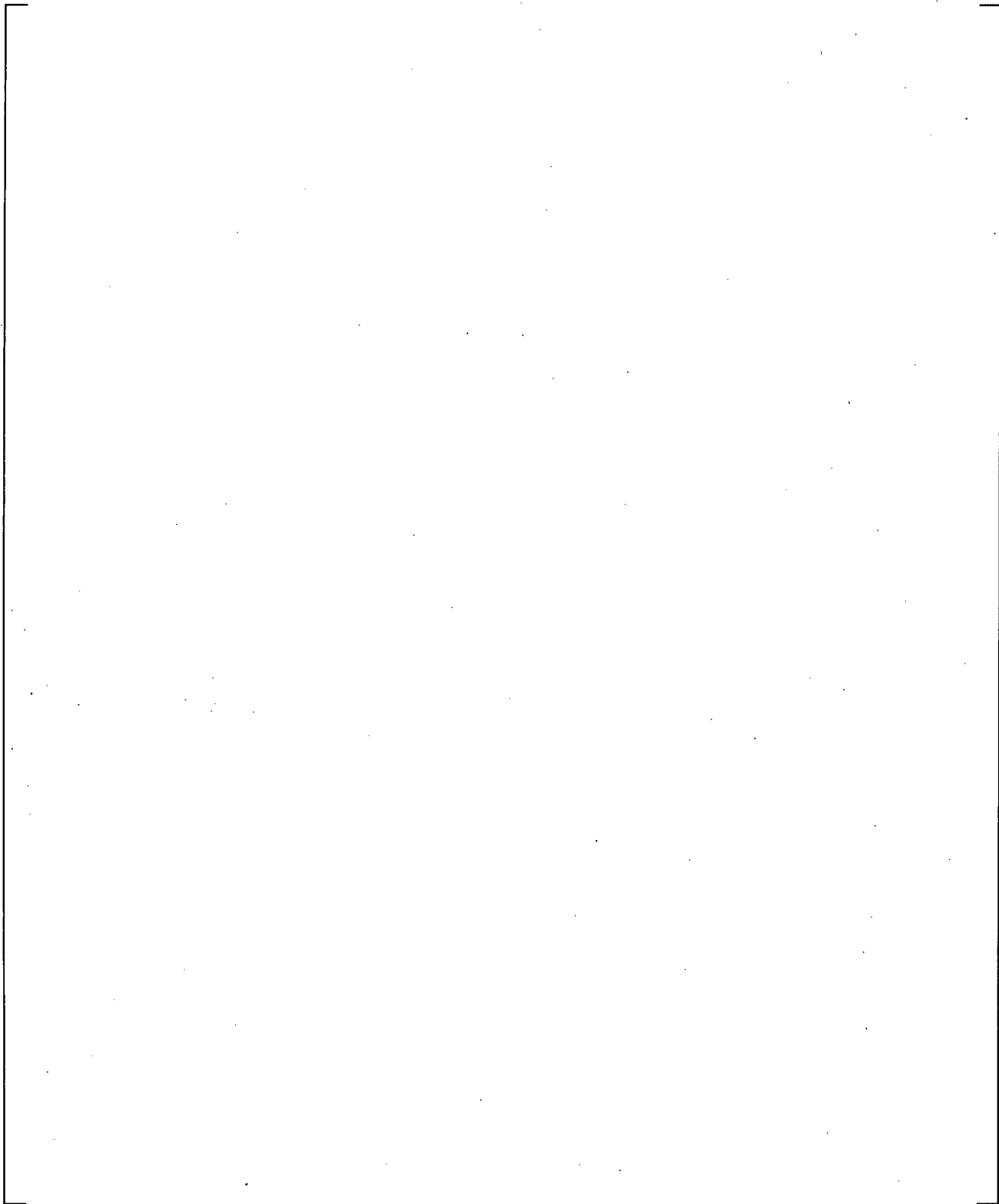


Figure 17-19 Cold Leg Piping Region of UPTF Test Facility



**Figure 17-20 WCOBRA/TRAC-TF2 Single TEE Model for UPTF-8 A**



**Figure 17-21 Comparison between Measured Fluid Temperature and WCOBRA/TRAC-TF2 Predicted Water Temperature at Pump Exit**

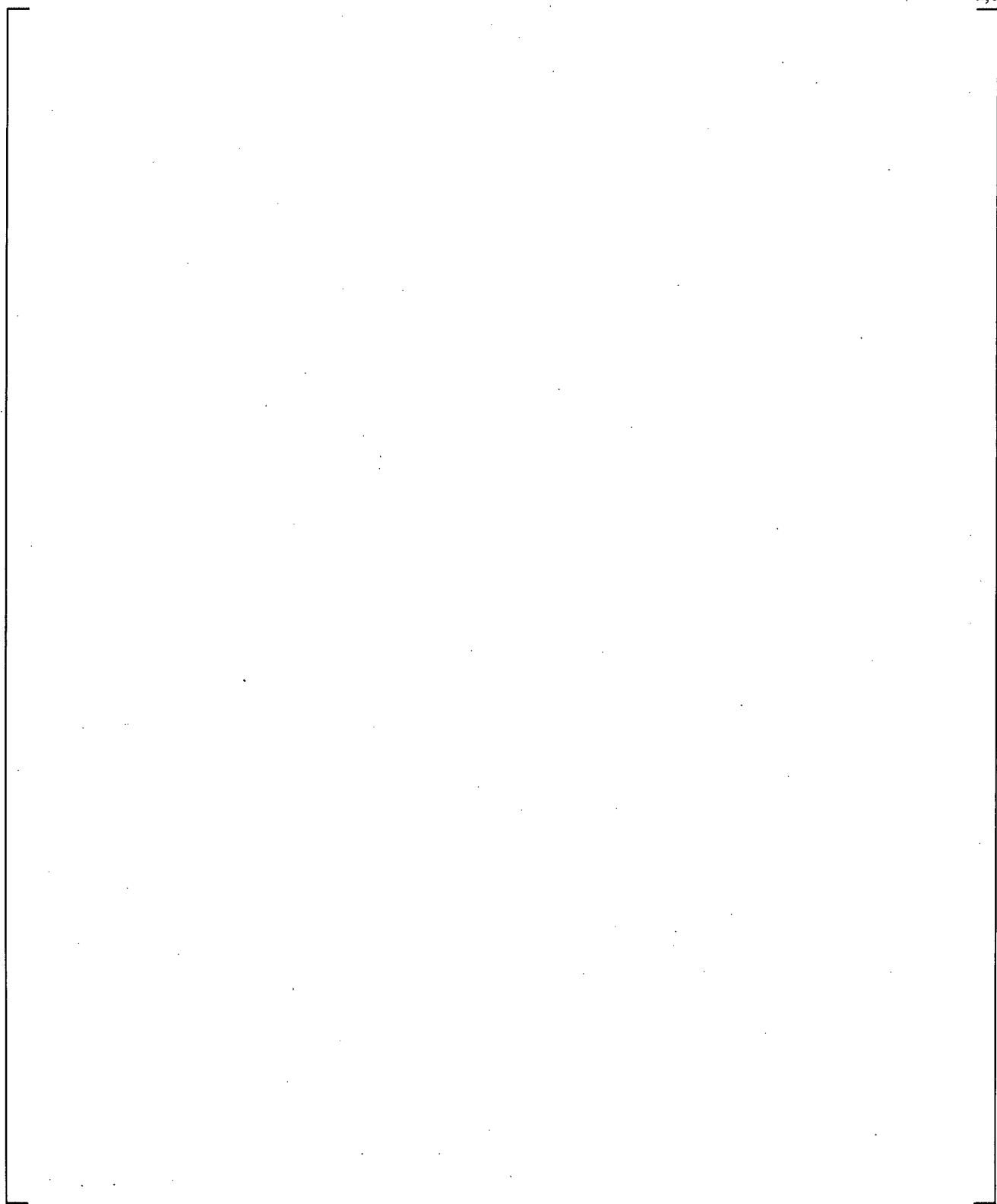


**Figure 17-22 Comparison between Measured Fluid Temperature and WCOBRA/TRAC-TF2 Predicted Water Temperature near Injection Point**

a,c

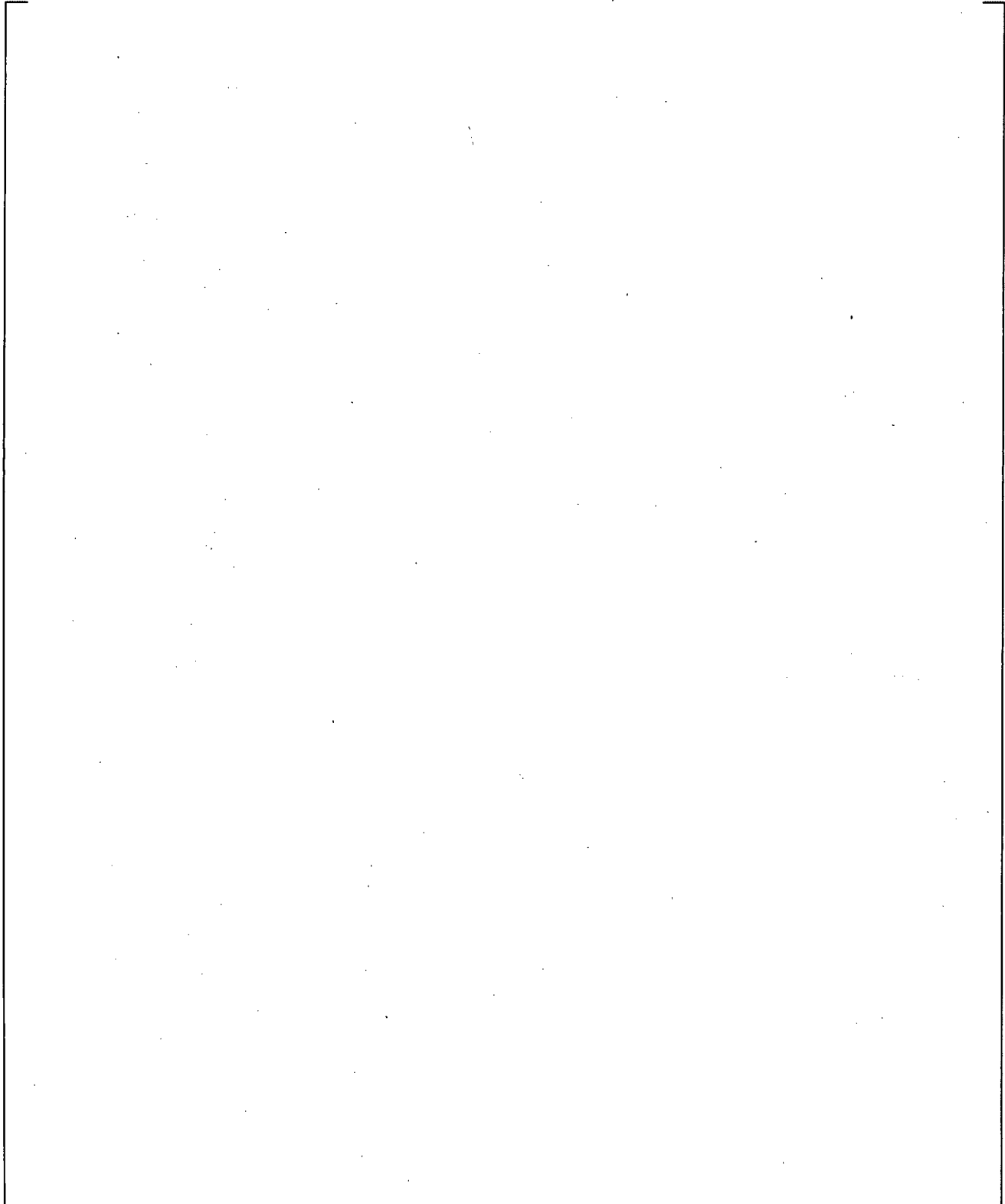


**Figure 17-23 Comparison between Measured Fluid Temperature and WCOBRA/TRAC-TF2 Predicted Water Temperature at Downstream of Injection Point**

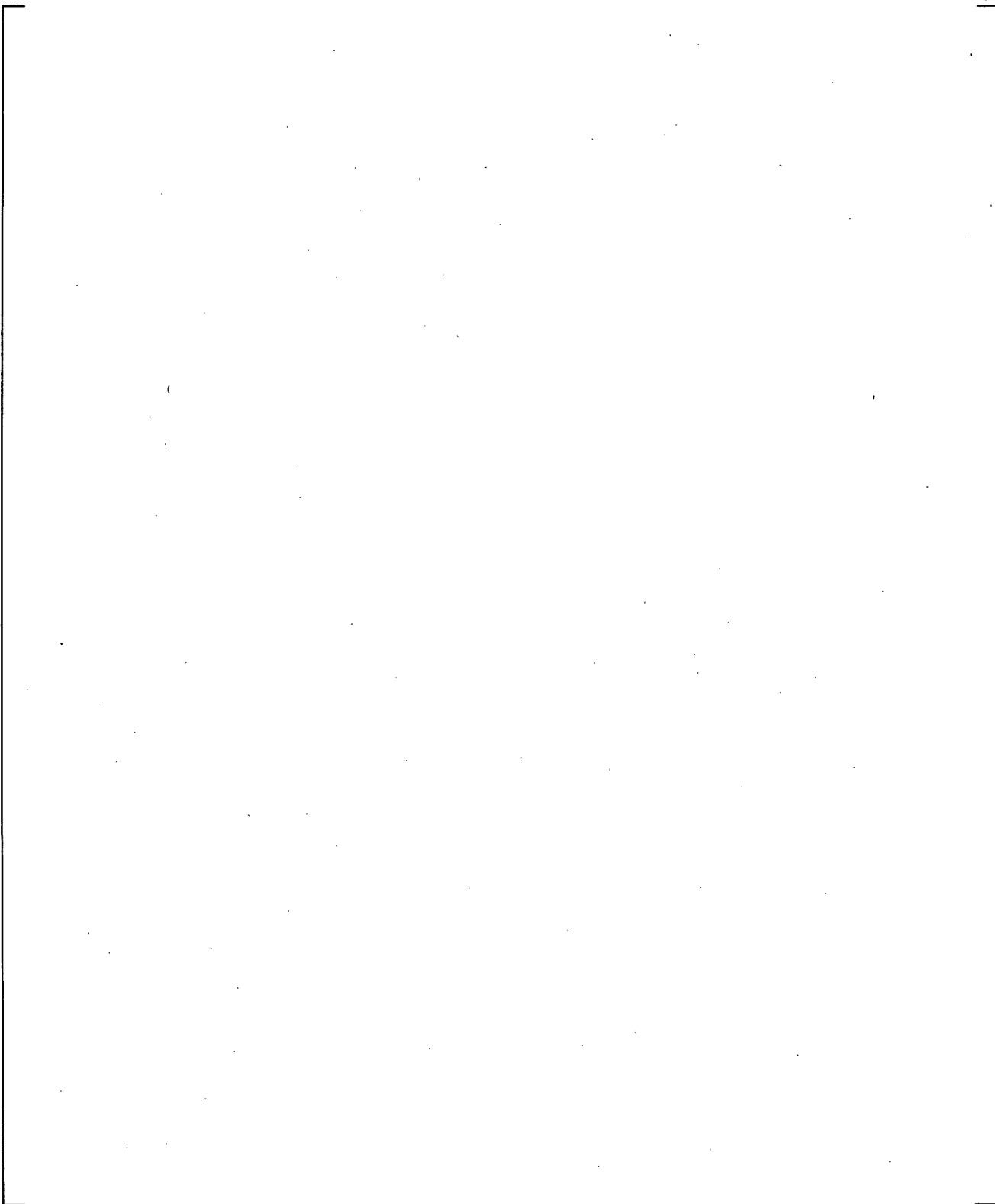


**Figure 17-24 Comparison between Measured Fluid Temperature and WCOBRA/TRAC-TF2 Predicted Water Temperature at Outlet of Cold Leg**

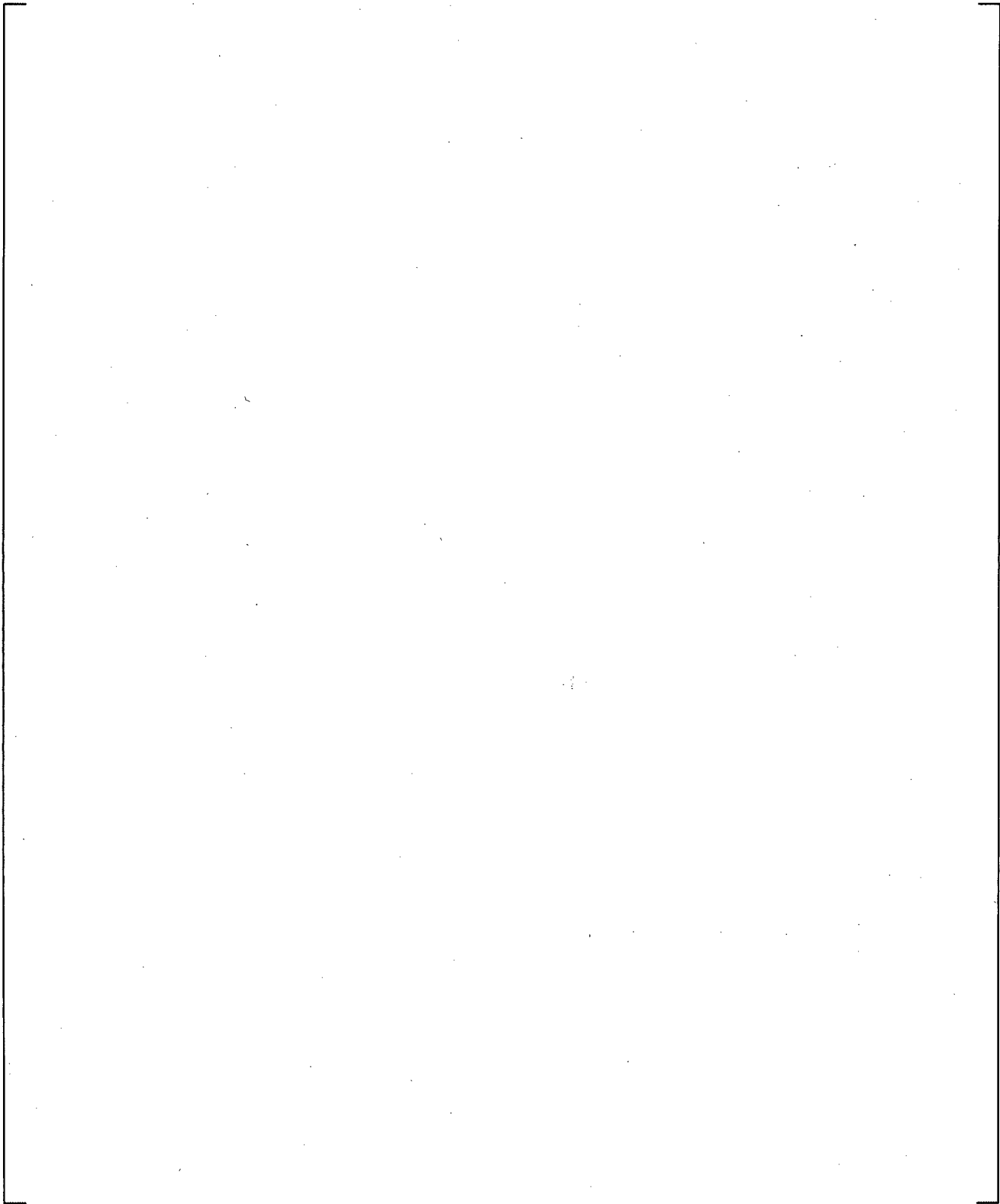


**Figure 17-25 Comparison between the Predicted Water Temperatures at Injection Cell of Cold Leg in ECC Injection Angel Sensitivity Study**

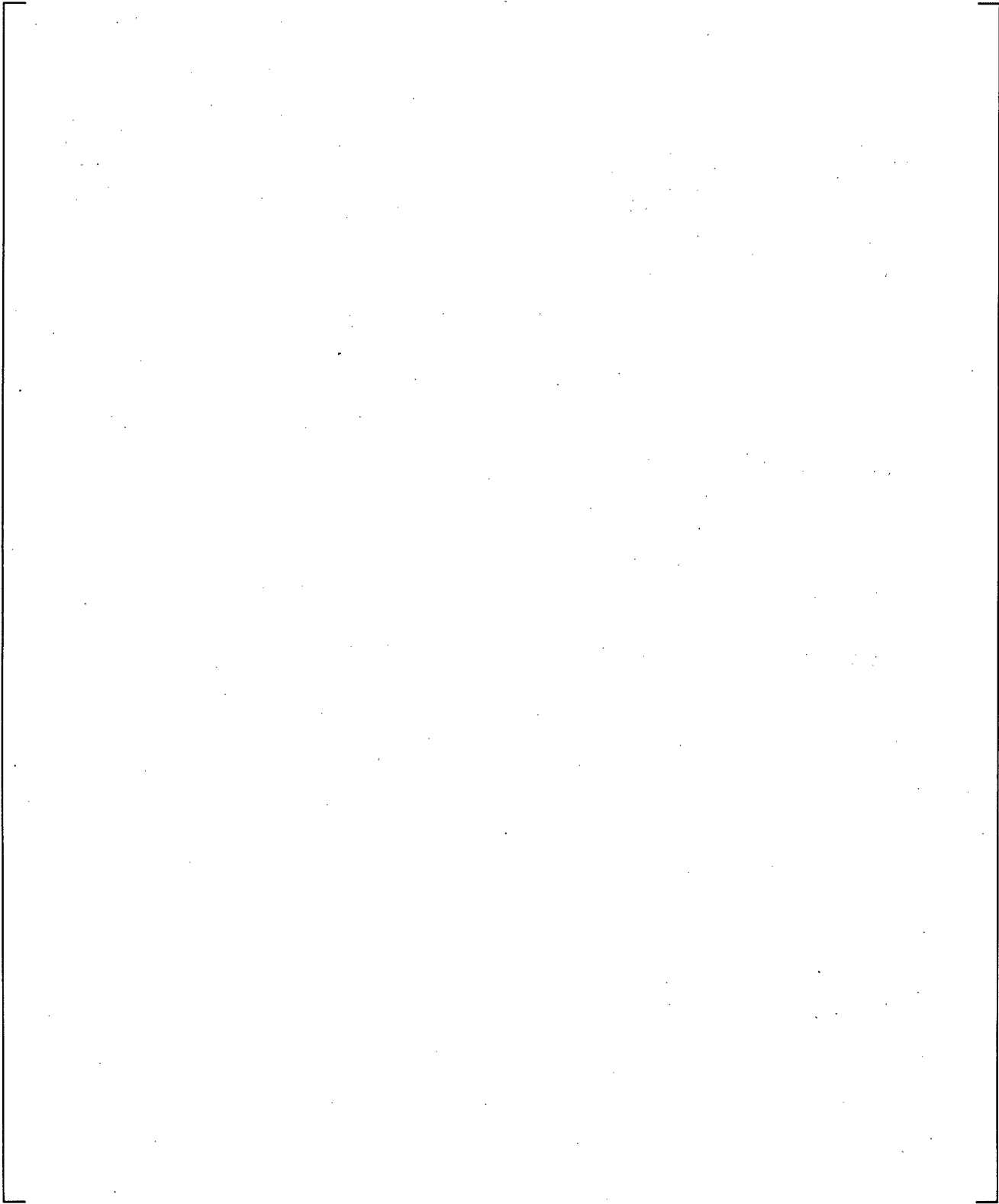


**Figure 17-26 Comparison between the Predicted Water Temperatures at Downstream Cell of Cold Leg in ECC Injection Angel Sensitivity Study**

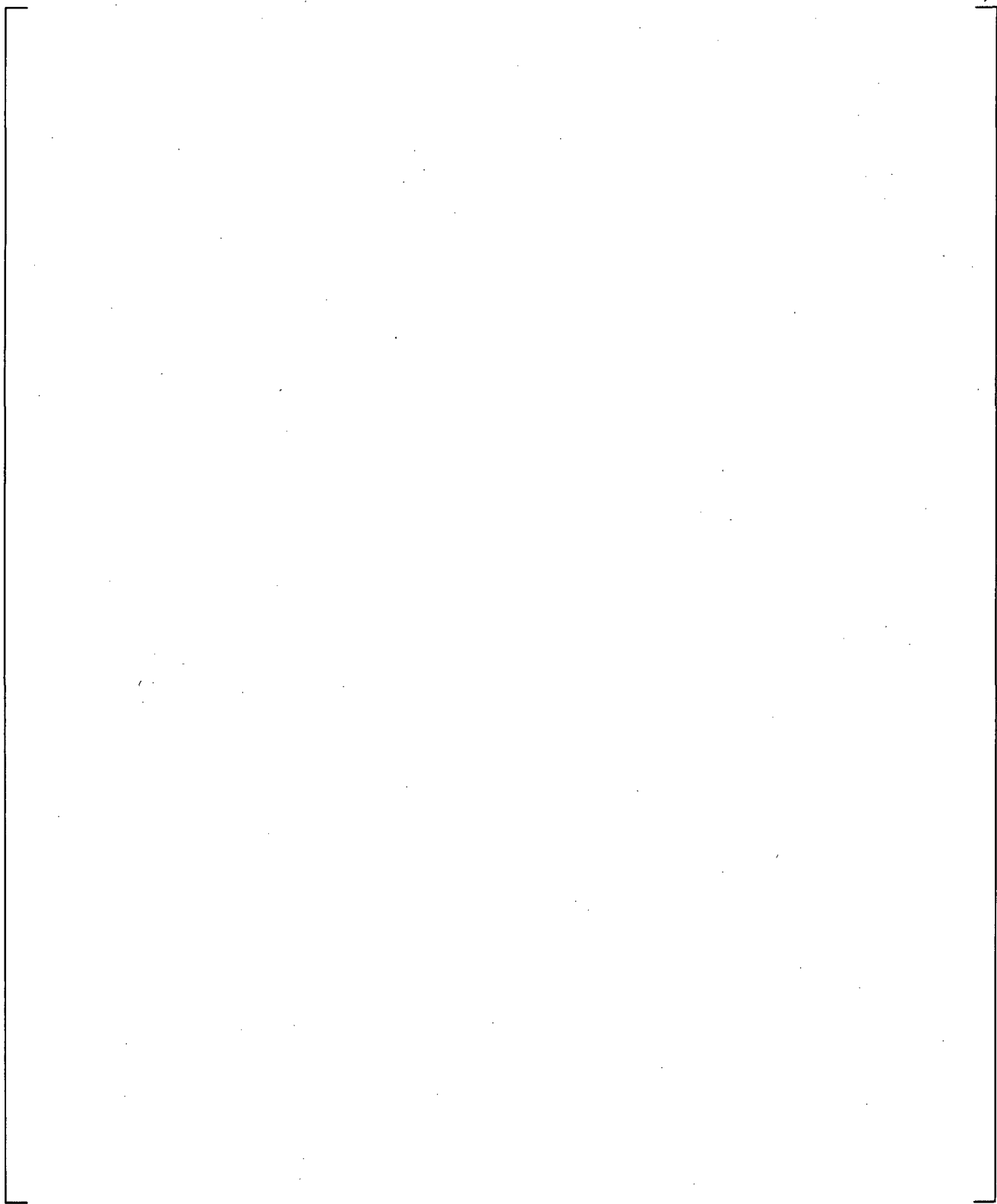


**Figure 17-27** Comparison between the Predicted Water Temperatures at Outlet of Cold Leg in ECC Injection Angel Sensitivity Study

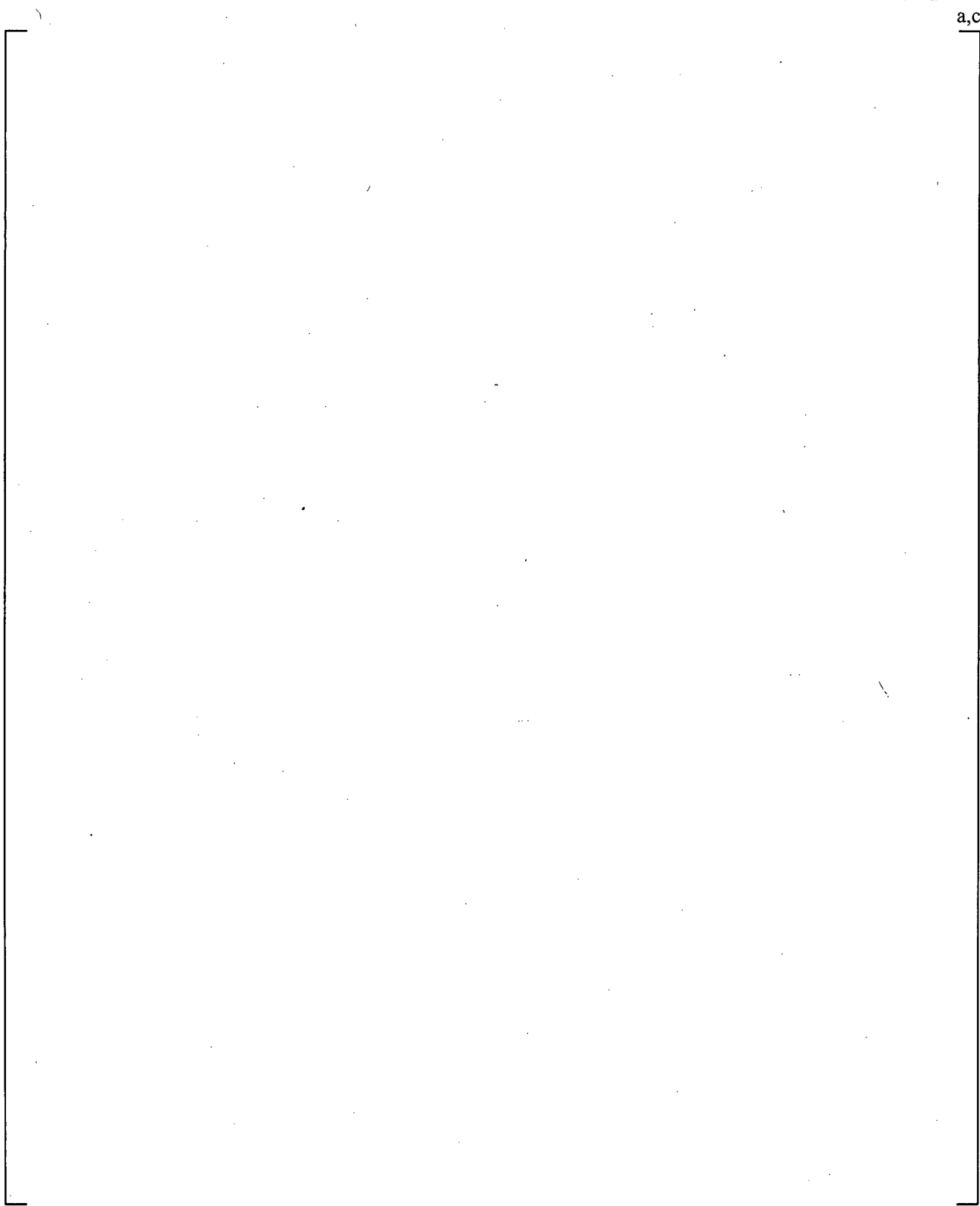


**Figure 17-28 Comparison between the Predicted Water Temperatures at Injection Cell of Cold Leg in Cold Leg Noding Sensitivity Study**

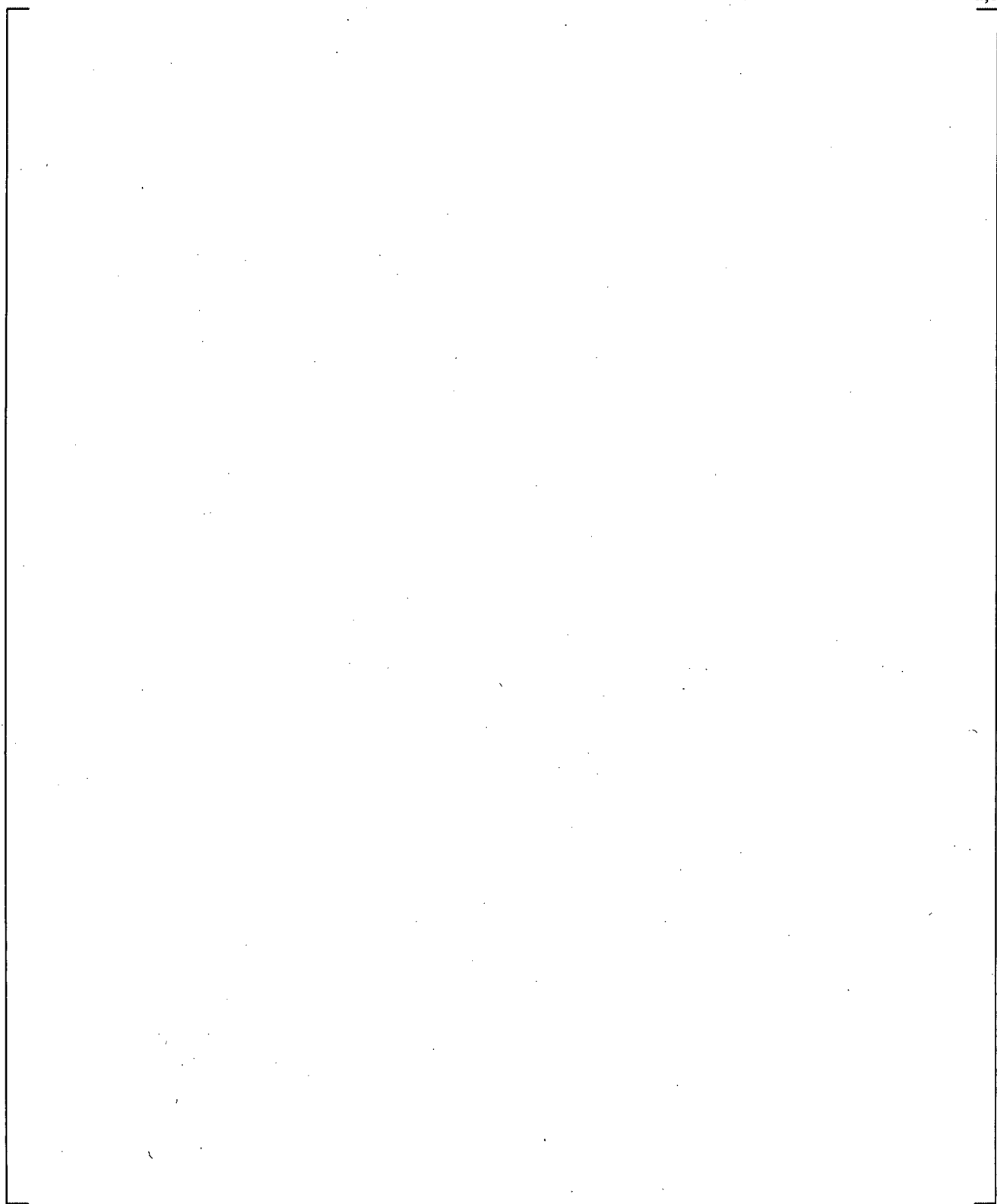


**Figure 17-29 Comparison between the Predicted Water Temperatures at Downstream of Injection Cell in Cold Leg in Cold Leg Noding Sensitivity Study**

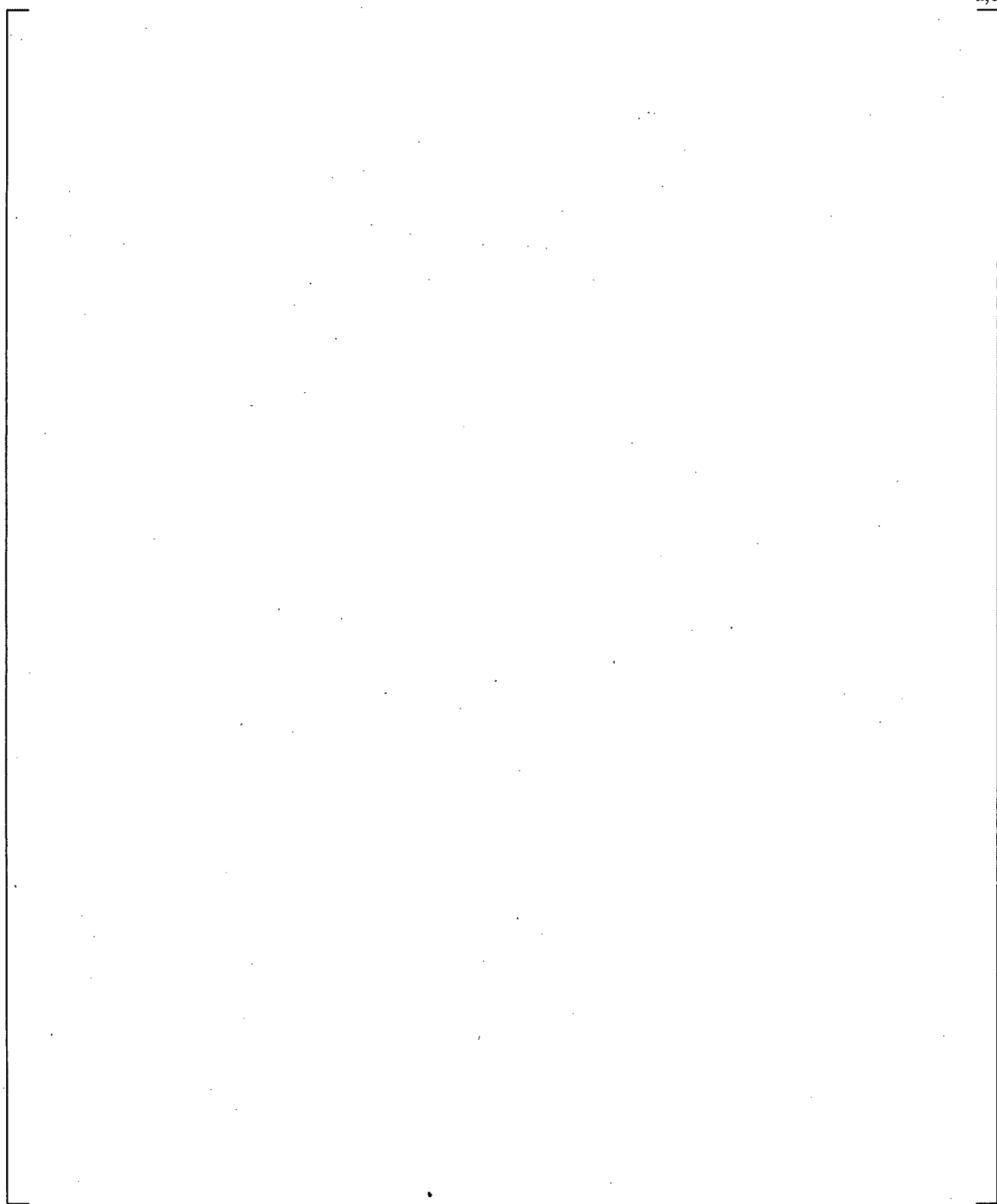


**Figure 17-30 Comparison between the Predicted Water Temperatures at Outlet of Cold leg in Cold Leg Noding Sensitivity Study**

a,c

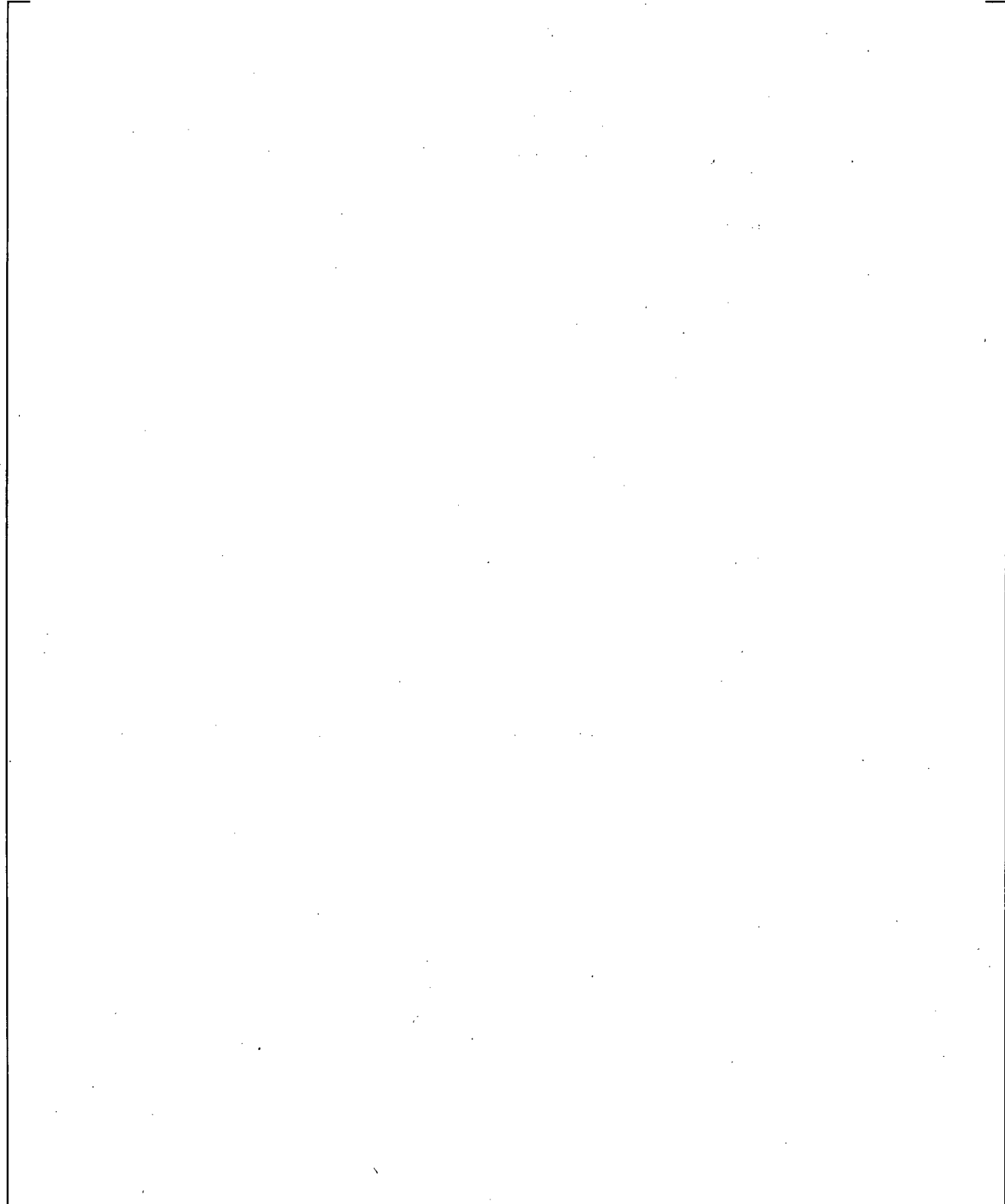


Figure 17-31 [

]a,c

a,c

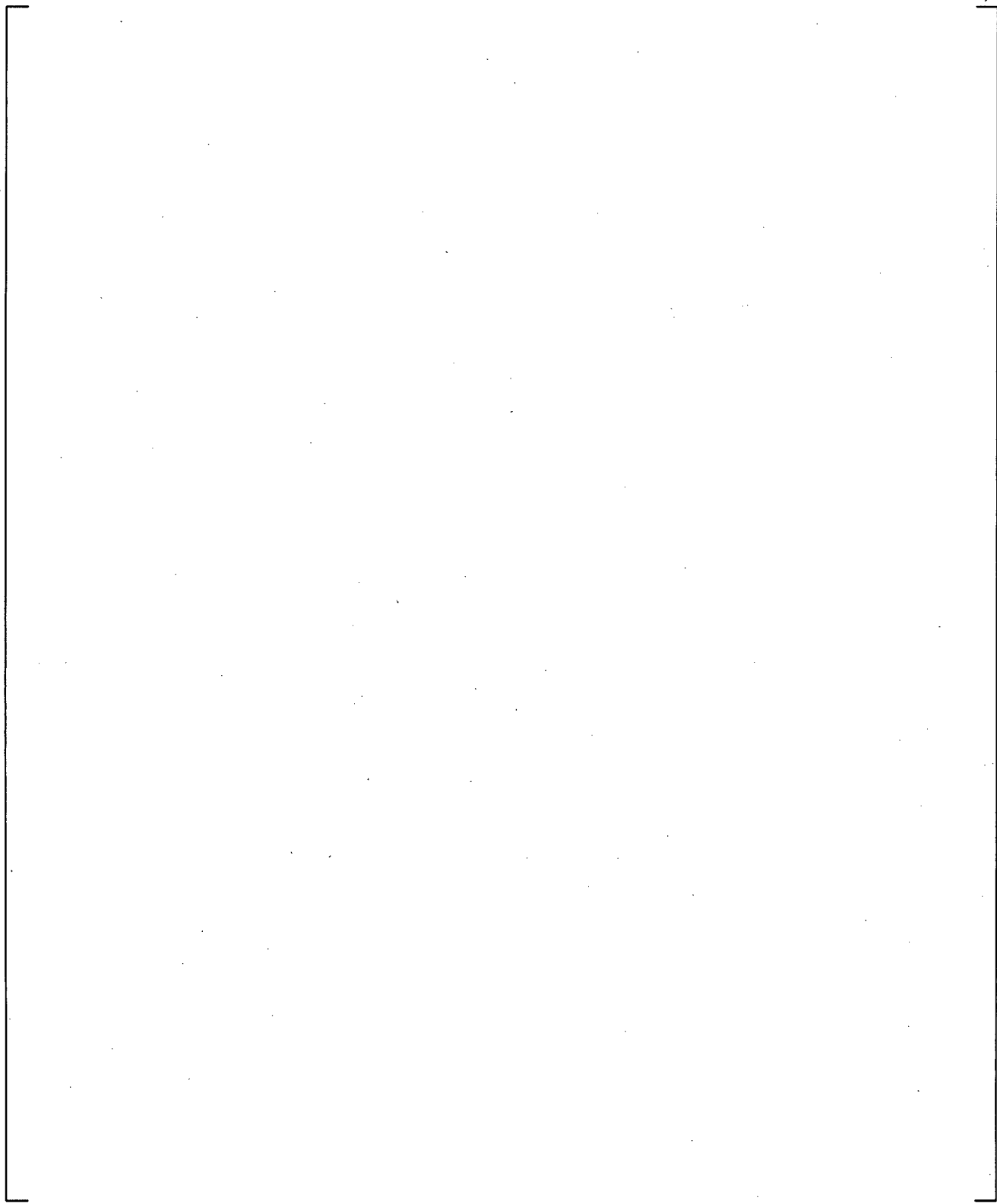


Figure 17-32 [

]a,c

a,c

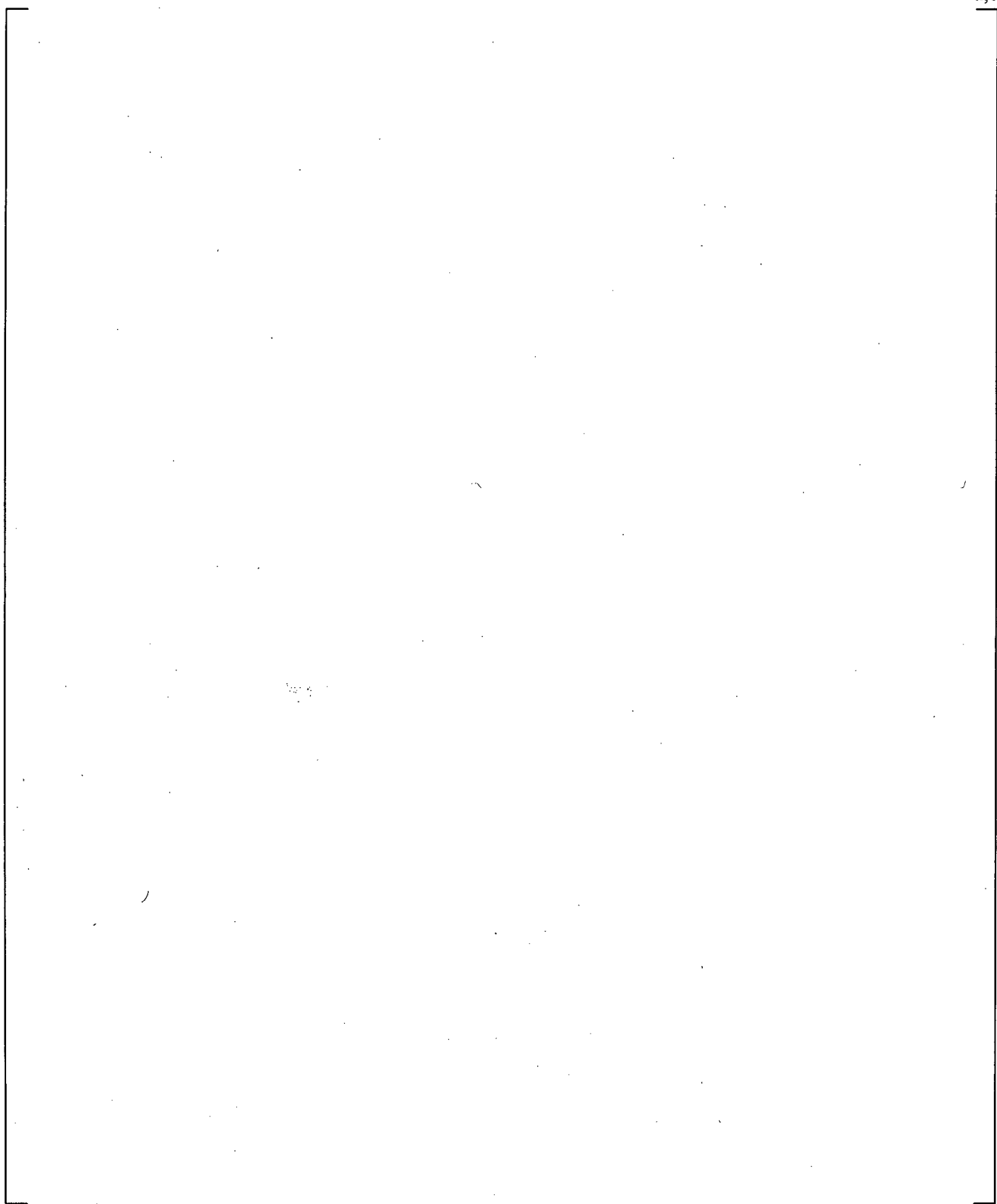


Figure 17-33 [

]a,c

a,c

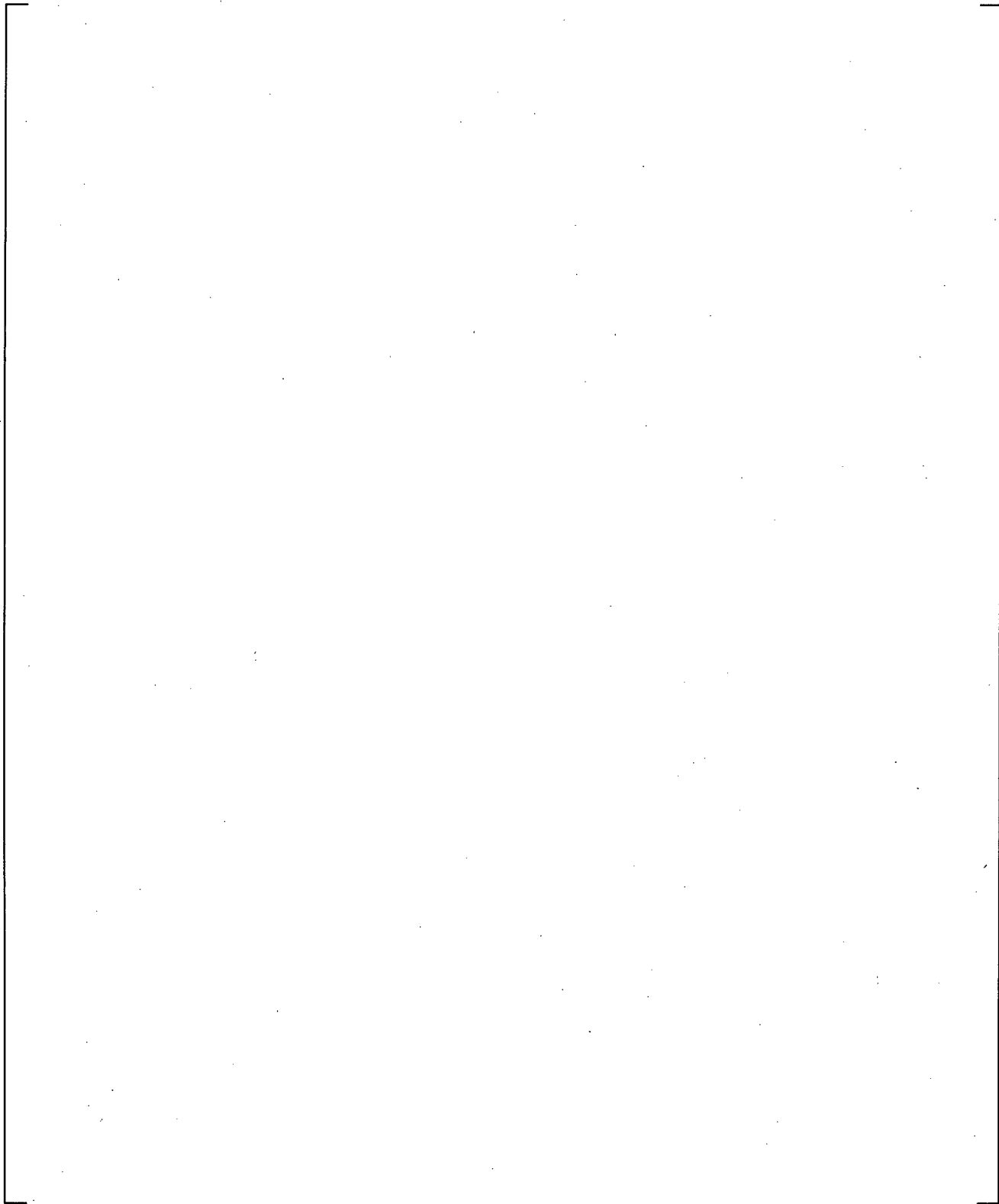
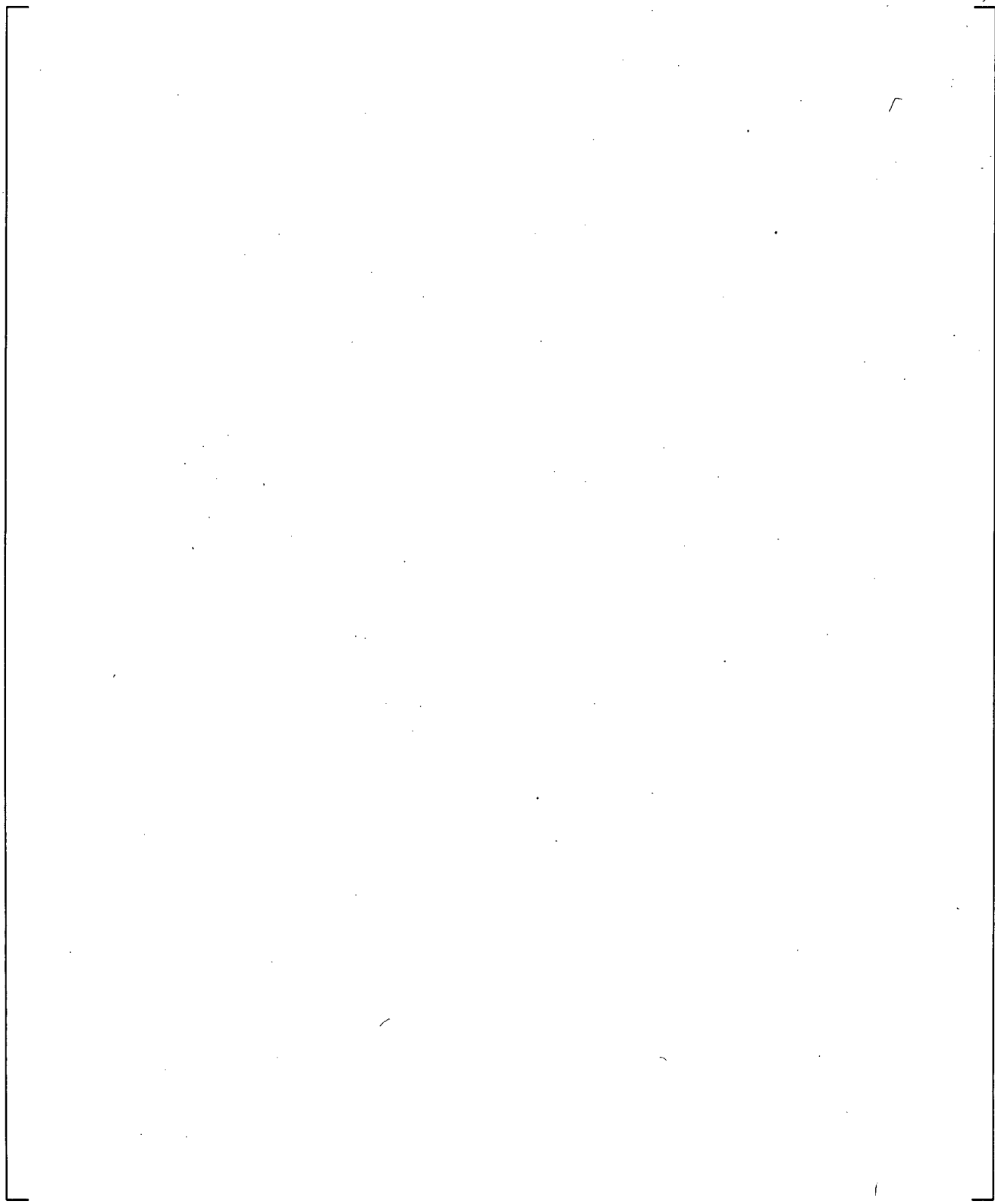


Figure 17-34 [

]a,c

a,c



**Figure 17-35** [

] a,c

a,c

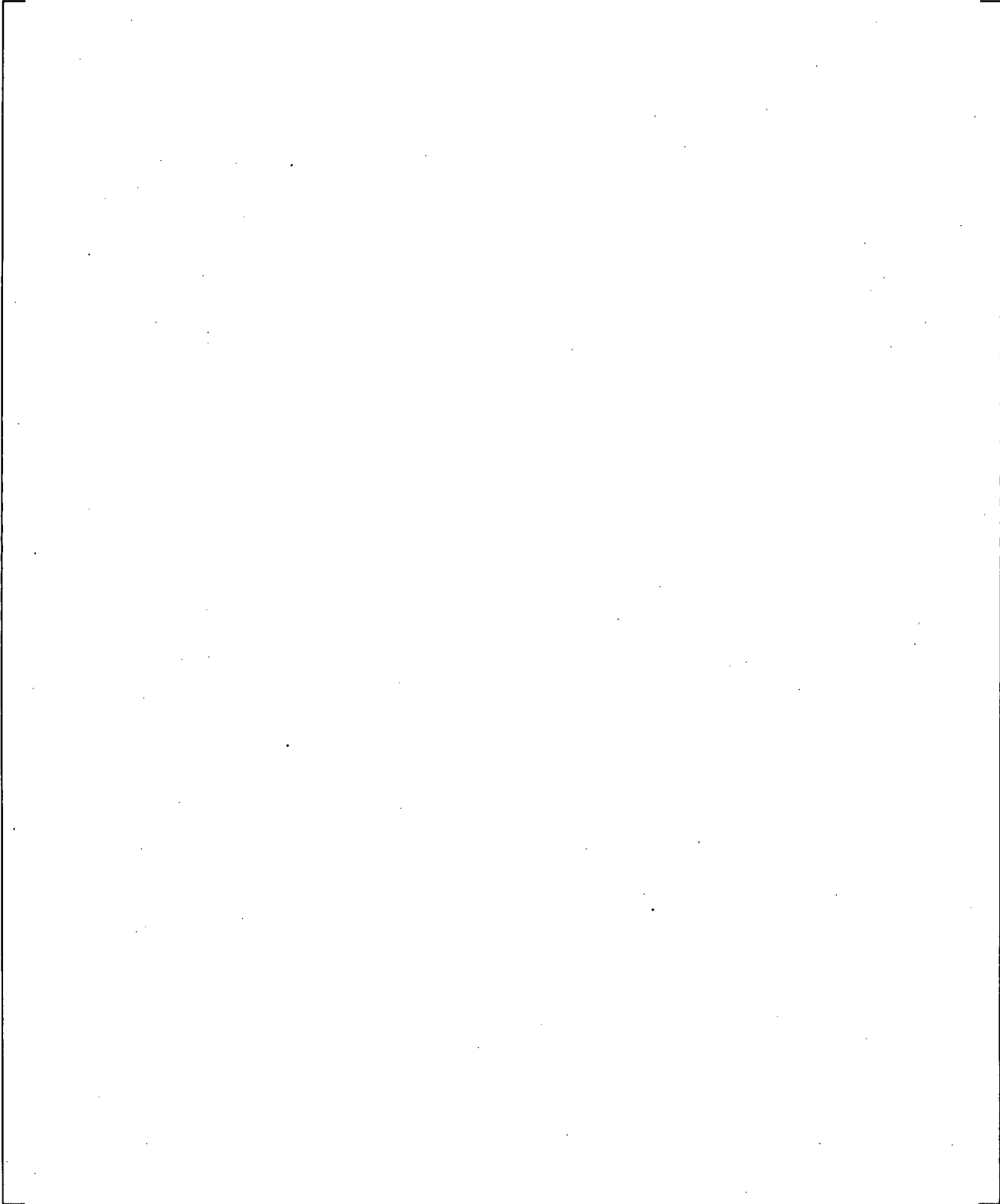


**Figure 17-36** [

] a,c

a,c

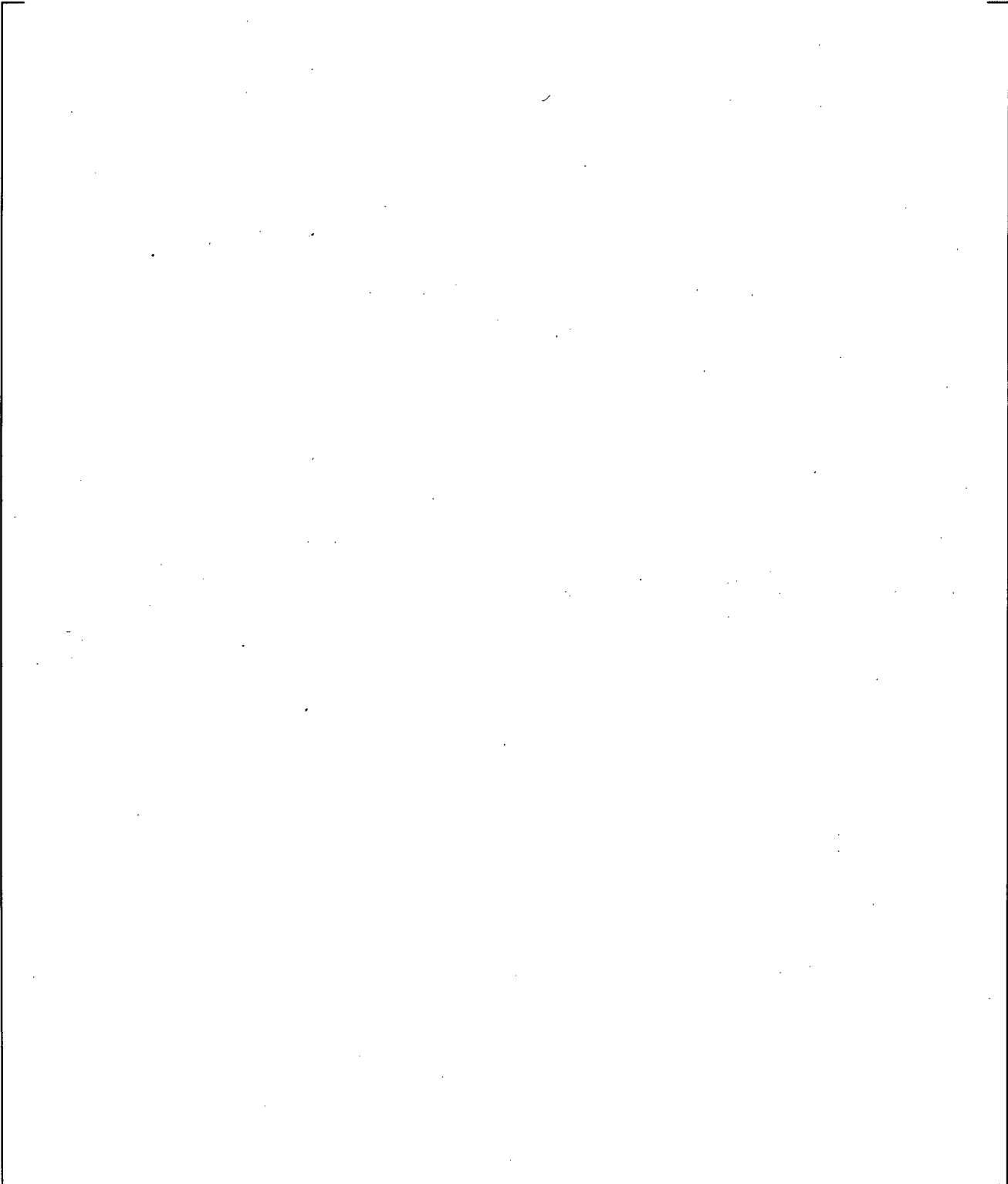
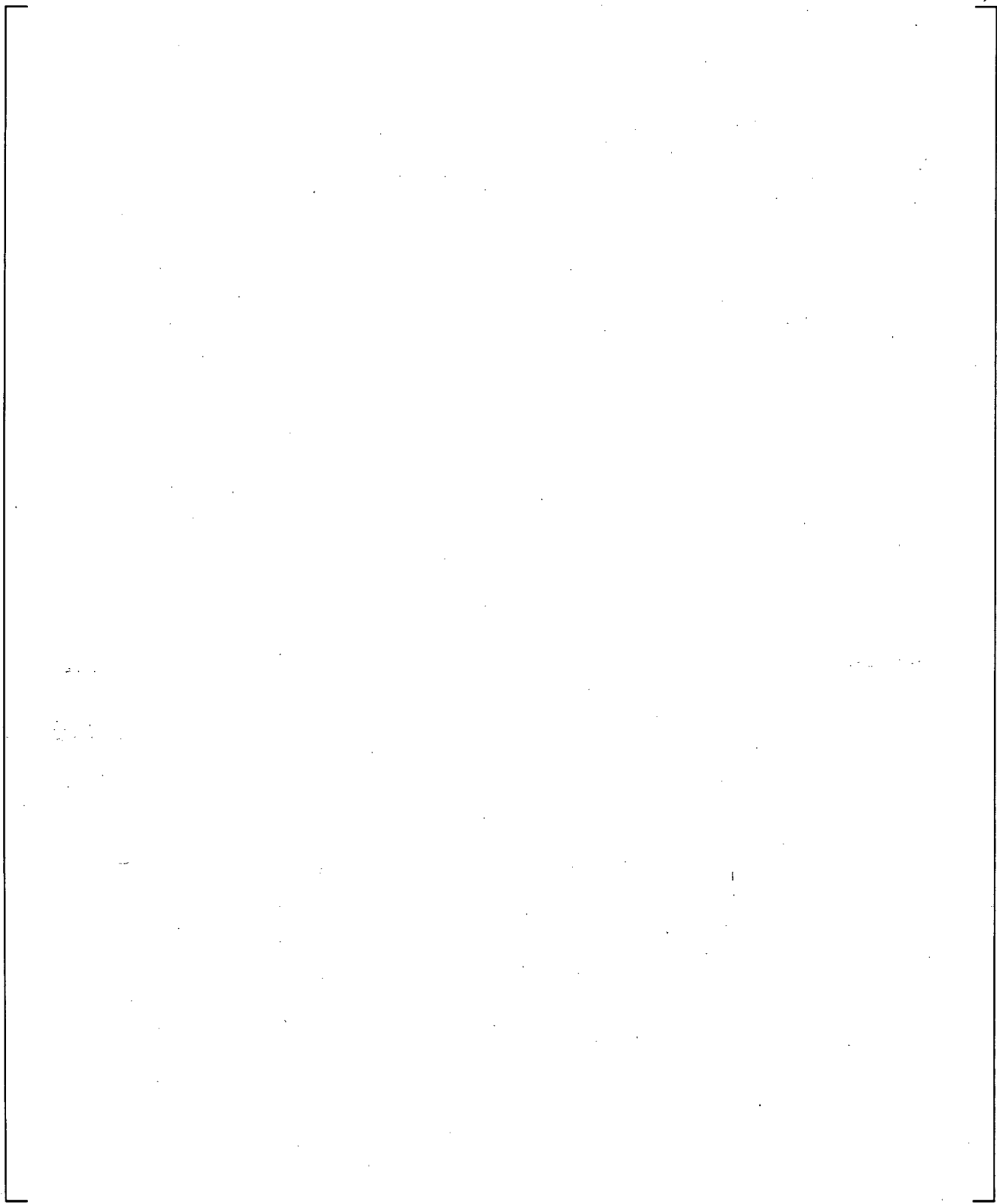


Figure 17-37 [

]a,c

a,c



**Figure 17-38** [

]a,c

## 18 LOOP SEAL CLEARANCE

### 18.1 INTRODUCTION

The FSLOCA PIRT in Section 2.3 of this document identifies the loop seal behavior as an important process affecting the evolution of a small break LOCA transient. This component and its effect on the transient are discussed in more detail below. The following sections identify the important phenomena occurring in the loop seal and the available experiments to assess the performance of WCOBRA/TRAC-TF2 in predicting such phenomena.

During a small break LOCA, mass is slowly depleted from the system. Early in the transient, the pumps continue to run and the flow through the pump suction piping remains single-phase. After generation of a reactor trip signal, the reactor trips and subsequently the pumps trip either due to loss of offsite power or operator action. The system then enters a natural circulation phase. Pressures have fallen sufficiently to cause boiling in the fluid entering the hot leg, but the steam generator acts as a heat sink, and the fluid entering the pump suction pipe is still nearly single-phase. Any bubbles that enter the pump suction pipe are carried through by natural circulation as illustrated in Figure 18.1-1a.

When the primary pressure approaches the secondary pressure, voids remain in the fluid as it enters the steam generator. As the loop mass flow rate decreases further, liquid begins to drain down both the uphill and downhill sides of the steam generator tubes. Natural circulation is terminated, and mixture levels form on both the uphill and downhill sides of the tubes. The levels then move downward as liquid drains and vapor rises as shown in Figure 18.1-1b.

Because there is no escape path for the steam generated in the core, except for some small bypass paths such as the upper head, the pressure in the region above the core (the upper plenum, the hot legs, and the steam generator tubes) rises and depresses the level in both the core and the downhill sides of the pump suction pipe. Eventually, the downhill side level reaches the top of the horizontal portion of the pump suction pipe, as shown in Figure 18.1-1c, and vapor begins to escape into the pump and flow toward the break.

At the onset of clearing, the fluid pressure in the downhill leg of the loop seal is higher than on the uphill side, due to the column of liquid from the horizontal leg to the pump outlet as shown in Figure 18.1-1c. Because the volume of steam at this pressure is significant in the steam generator tubes, hot legs, vessel upper plenum and upper head, the steam flowing through the pump suction becomes significantly greater than the core steam generation rate for a period of time (Kukita, 1990). This causes the loop seal to clear completely, not resealing until much later in the transient.

As the steam flows through the pump suction, the flow regime is first a slug regime with significant amounts of liquid being entrained from the pump suction pipe as seen in Figure 18.1-2 and described by (Tuomisto and Kajanto, 1988). Eventually, a residual level of liquid will remain in the pump suction pipe.

As the pressure in the system is relieved, the steam flow decreases to the core steam generation level. If this steam flow is low enough, liquid in the cold leg may begin to drain back through the pump and begin to fill the pump suction again as shown in Figure 18.1-1d. Another potential source of loop seal refilling is the draining of condensed steam from the downhill side of the steam generators. Because there is no

pressure driving force, the steam flow through the loop seal is quickly terminated when the liquid level reaches the top of the horizontal section and plugs the loop seal. The system pressure increases, and core and loop seal levels change once again as the loop seal plugging and clearing cycle is repeated (Kukita, 1990).

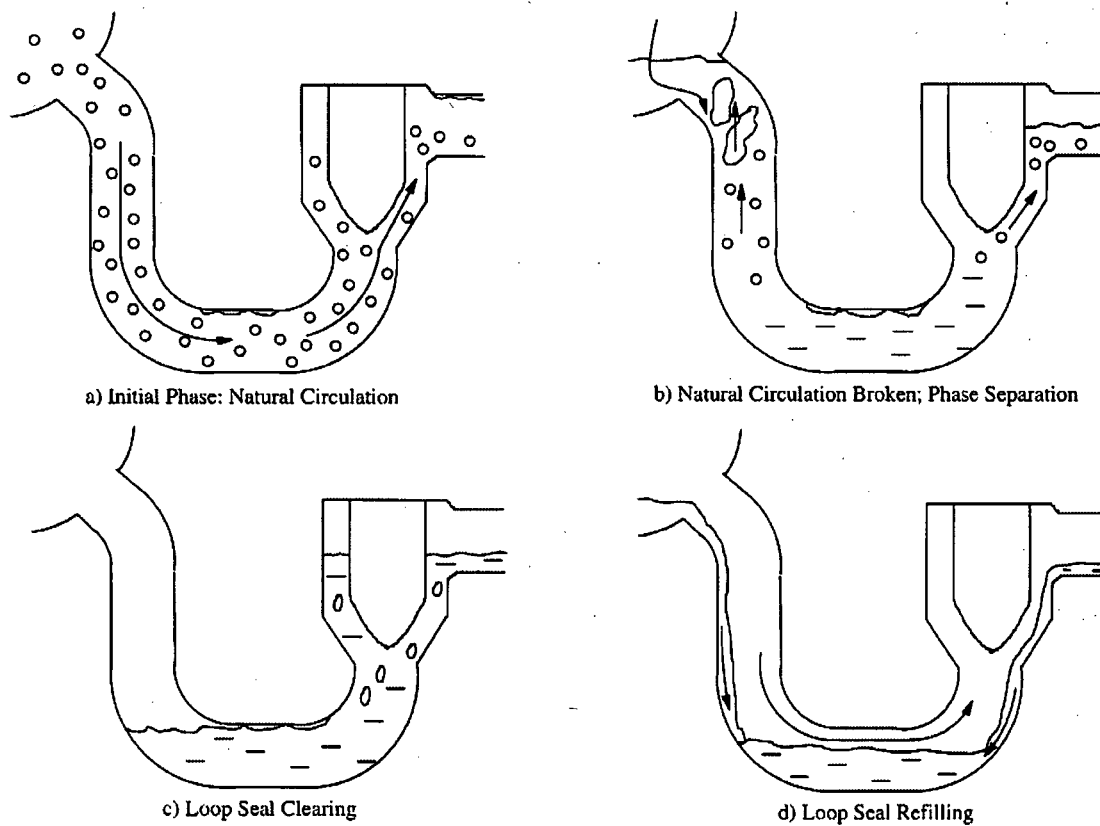


**Figure 18.1-1 Loop Seal Clearing and Refilling**

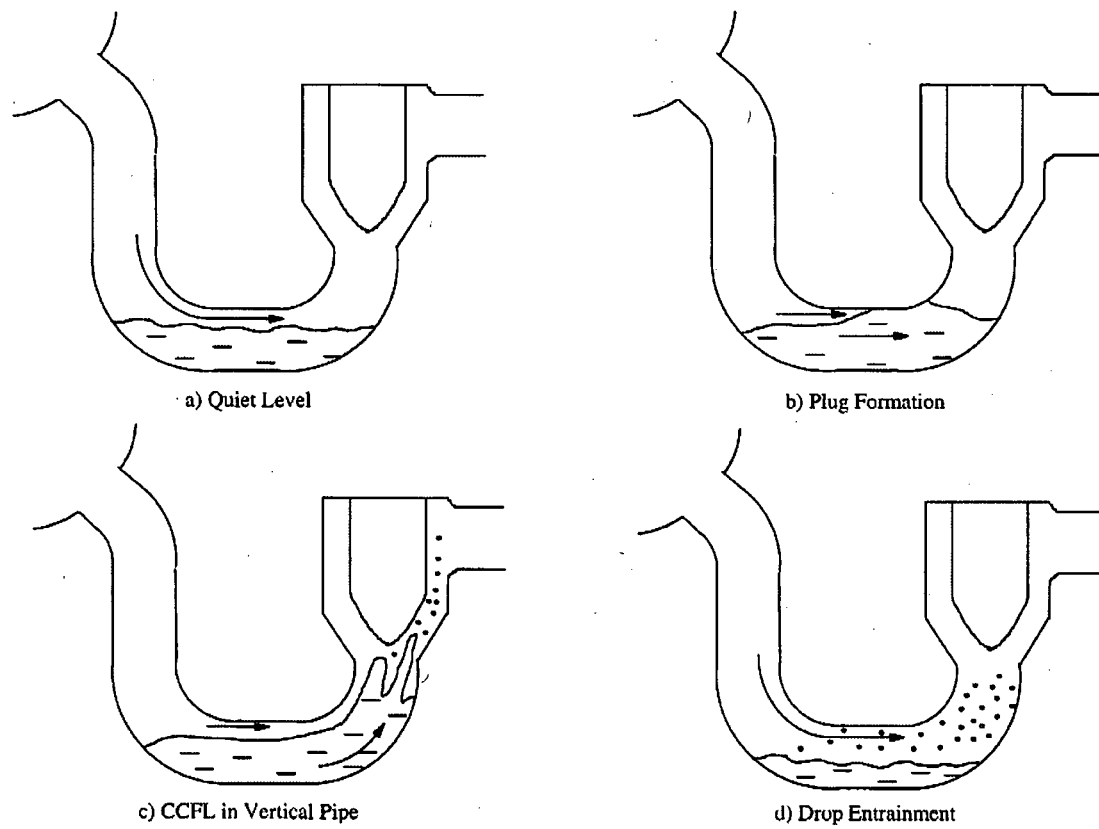


Figure 18.1-2 Loop Seal Clearing Process

## 18.2 IMPORTANT PHYSICAL PROCESSES AND SCALING LAWS

The onset of loop seal clearing is a function of the pressure difference across the loop seal, which depresses the level to the bottom of the loop seal and depends on the following factors:

- Core steam generation rate
- Bypass steam flow rate through vent paths
- Rate of accumulation of liquid in the pump suction pipe

These factors are the result of processes that occur elsewhere in the system and are accounted for in other components (for example, the core steam generation rate is accounted for by ranging core power and interfacial drag in core region).

The loop seal clearing and refilling process is a function of the interfacial drag between the vapor and the liquid. The initial steam flow surge and the interfacial drag determine the rate at which liquid is expelled. The steam flow rate, in turn, depends on the loop pressure drop, of which the loop seal is a part. This determines how quickly the venting process takes place and the final liquid level in the horizontal section. The residual liquid and degree to which liquid is held up by steam flowing out of the pump suction pipe determine the rate at which the pump suction refills and replugs. Based on these considerations, the following factors are considered to be important in the assessment of predictions of loop seal behavior:

- Overall loop seal pressure drop as a function of steam flow
- Liquid distribution in the loop seal as a function of steam flow

Various experiments have shown that the basic physical process is controlled by two factors: the extent to which a stratified flow regime can be maintained in the horizontal leg of the loop seal, and the degree to which liquid pushed into the downstream vertical leg can be entrained out of the loop seal. Figure 18-2 illustrates these processes.

First, the ROSA 5% and 10% break integral tests are examined for loop seal behavior. Then, scaled loop seal experiments are discussed in the following section to gain a better understanding of the loop seal behavior. These tests are used to highlight important physical and scaling features. The time period of interest is the steady-state, post clearing portion. Next, the scaled tests are compared with larger scale tests to confirm the indicated scaling trends. Finally, the larger scale tests are simulated using WCOBRA/TRAC-TF2 to assess the models and correlations in the code.

### 18.2.1 ROSA

Loop seal clearing behavior can be observed from the ROSA 5% and 10% break integral tests (Kumamaru, et al., 1989 and Koizumi and Tasaka, 1988; see Section 21 for test facility description). Figures 18.2.1-1a and 18.2.1-1b show the loop seal differential pressure behavior of the broken loop for the 5% and 10% breaks, respectively. As observed in the figures, [

] <sup>a,c</sup>.



**Figure 18.2.1-1a** Measured Pressure Drop in Broken Loop of ROSA 5% Break  
(Kumamaru, et al., 1989)



**Figure 18.2.1-1b** Measured Pressure Drop in Broken Loop of ROSA 10% Break  
(Koizumi and Tasaka, 1988 )

## 18.2.2 PWS 2.3 Loop Seal Tests

Scaled U-tube experiments designed to examine the hydraulic behavior of a U-tube under conditions similar to those encountered during a small break LOCA were performed as part of the ECTHOR Program (Boileau and Bourteele, 1985). The vapor flow required to clear the U-tube was a specific focus of the tests.

### 18.2.2.1 Test Facility Description

The tests were run in a plexiglass facility with air and water at atmospheric pressure. The facility, illustrated schematically in Figure 18.2.2-1, consists of a blower, a run of horizontal piping from the blower, a U-tube, and a catch tank.

The pipe diameter chosen for the facility was [ ]<sup>a,c</sup>. This corresponds to approximately [ ]<sup>a,c</sup> scale compared with a PWR, which has a pipe diameter of 2.58 feet. The air and water flow rates were scaled so that approximate similitude was maintained for the Froude number, shown to define the flow regime transition from stratified to intermittent and annular flow by (Taitel and Dukler, 1976). Figure 18.2.2-2 shows the predicted flow regime transition using the Taitel and Dukler flow regime map for atmospheric pressure, [ ]<sup>a,c</sup> scale, compared with the transition for steam at 1000 psia, full-scale geometry. This figure indicates that the transition from stratified to annular flow occurs at a higher vapor flux in the air-water tests. While better similitude could have been obtained with a smaller pipe, the chosen diameter also assures that the vertical pipes of the U-tube are sufficiently large so that any countercurrent flow limits (CCFL) that occur will not be affected by the pipe diameter. According to (Richter, 1981), the critical vapor flux for CCFL in pipes larger than approximately 2 inches in diameter depends only on pressure, not on pipe diameter.

Pressure drop across the U-tube was measured. In the horizontal and in the downstream vertical sections, several independent measurements of void fraction were made using pressure drops, optical probes, and gamma densitometers.

### 18.2.2.2 Test Procedures

Several test series were performed, as described below:

- Limit Line Tests

These tests were designed to obtain the liquid level in the horizontal portion of the U-tube, which produces significant liquid entrainment for a given air flow rate. This is equivalent in some ways to the CCFL limit and is termed the U-tube limit line. The tests were performed as follows:

[

]<sup>a,c</sup>

[

] <sup>a,c</sup>

- Within Limit Line Tests

These tests were performed at air and water flows inside the limit lines established in the first phase with little or no entrainment. The tests primarily examined the interaction, if any, between the gas and the liquid at non-limiting flows (i.e., no entrainment). The tests were run as follows:

[

] <sup>a,c</sup>

- Optical Probe Tests

These tests were performed similar to the Within Limit Line Tests. Optical probes were used to measure the liquid level. These tests confirmed the differential pressure measurements, later used to derive vapor fraction.

- Complementary Tests

In some of the tests with high initial liquid level, oscillatory flow was observed. These oscillations consisted of movements of water back and forth between the upstream and downstream elbows. Slugs of liquid momentarily filled the pipe, increasing the pressure drop across the U-tube. These slugs were then ejected from the U-tube. The tests were similar to the limit line tests except [

] <sup>a,c</sup>.

- Gamma Densitometer Tests

These tests used a gamma densitometer to measure the mixture density inside the horizontal portion of the U-tube. The tests confirmed void fraction measurements based on differential pressure.

### 18.2.2.3 Analysis of PWS 2.3 Test Results

Figure 18.2.2-3 plots the normalized residual liquid level in the loop seal ( $H/D$ ) as a function of the gas volumetric flux ( $j_g$ ). The loop seal was completely cleared when gas velocities exceeded about [ ]<sup>a,c</sup>. At low gas flows [

] <sup>a,c</sup>

The residual liquid level is an indication of the overall liquid mass contained in the loop seal as a function of gas flow, but does not represent the liquid distribution within the U-tube during the tests.

Figure 18.2.2-4 shows the average void fraction at the midpoint of the horizontal leg and in the downstream vertical leg during the test. At low gas flow rates, [

] <sup>a,c</sup>

Figure 18.2.2-6 shows the measured pressure difference between the upstream and downstream exits of the U-tube. As liquid collects in the downstream vertical leg for the low gas flows, the pressure difference increases.

The basic processes occurring during these tests can be explained in terms of several hydrodynamic limits applied to both the horizontal and vertical legs. Figure 18.2.2-7 shows the horizontal leg average void fraction as a function of  $j_g^*$ , defined as:

$$j_g^* = \frac{j_g}{\left[ \frac{(\rho_l - \rho_g)gD}{\rho_g} \right]^{0.5}} \quad (18-1)$$

where  $D$  is the pipe diameter.

Figure 18.2.2-8 shows the various flow regimes observed for the tests performed under the limit lines and that the liquid level in the horizontal leg was [

] <sup>a,c</sup>.

The loop seal behavior can be explained in terms of three regimes, bounded by the limit lines shown in Figure 18.2.2-7. The three regimes are described in the following paragraphs.

[

] <sup>a,c</sup>

I

J<sup>a,c</sup>

[

] <sup>a,c</sup>

#### 18.2.2.4 Effect of Scale

An important question which must be answered is what distortions the scaled geometry and low pressure used in these tests have introduced relative to the PWR. Having explained the data in terms of the limit lines above, we can examine the effect of scale by seeing how these limit lines change with scale (Figure 18.2.2-10). [

] <sup>a,c</sup>

a,c

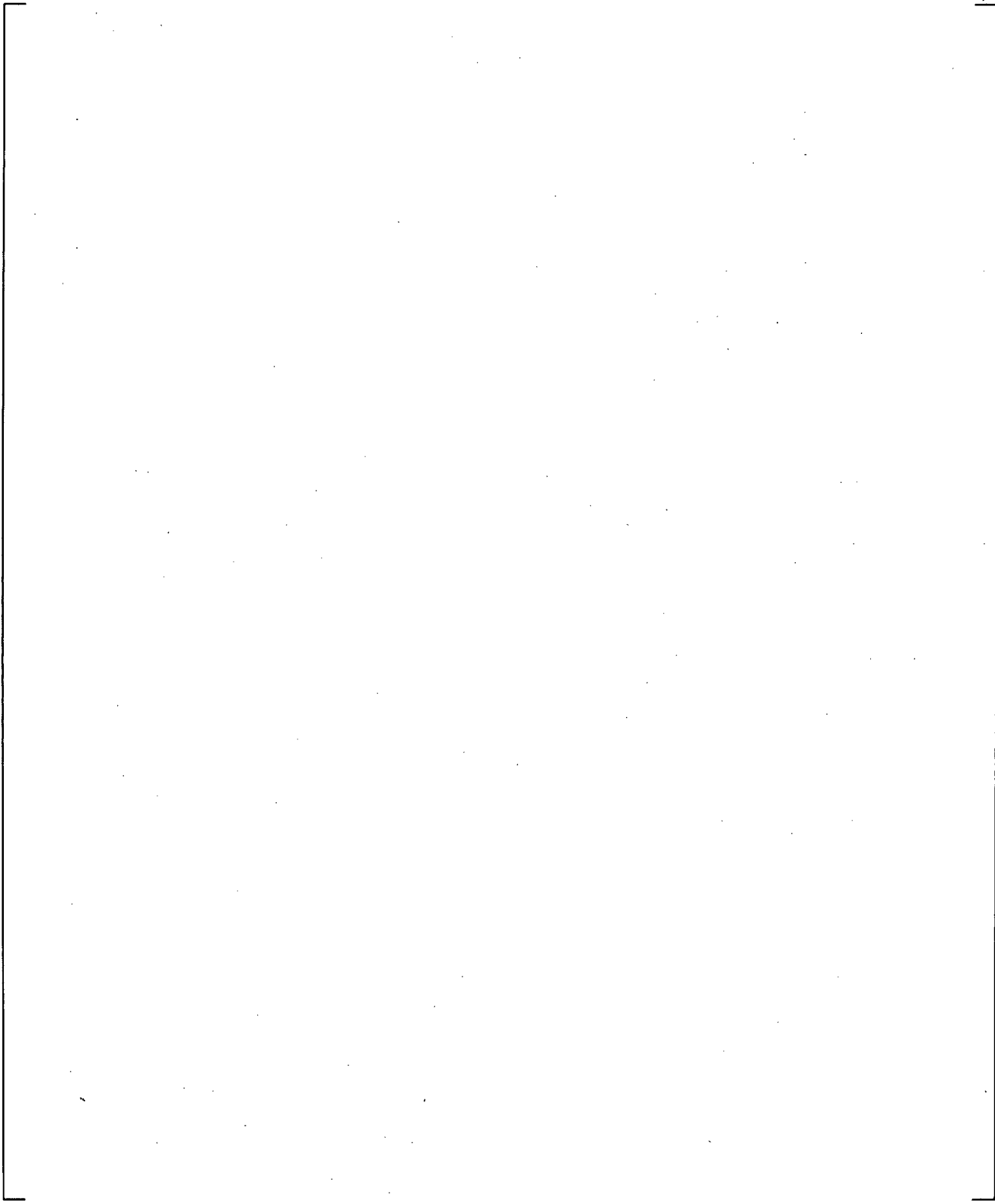


**Figure 18.2.2-1 PWS 2.3 U-Tube Test Facility**

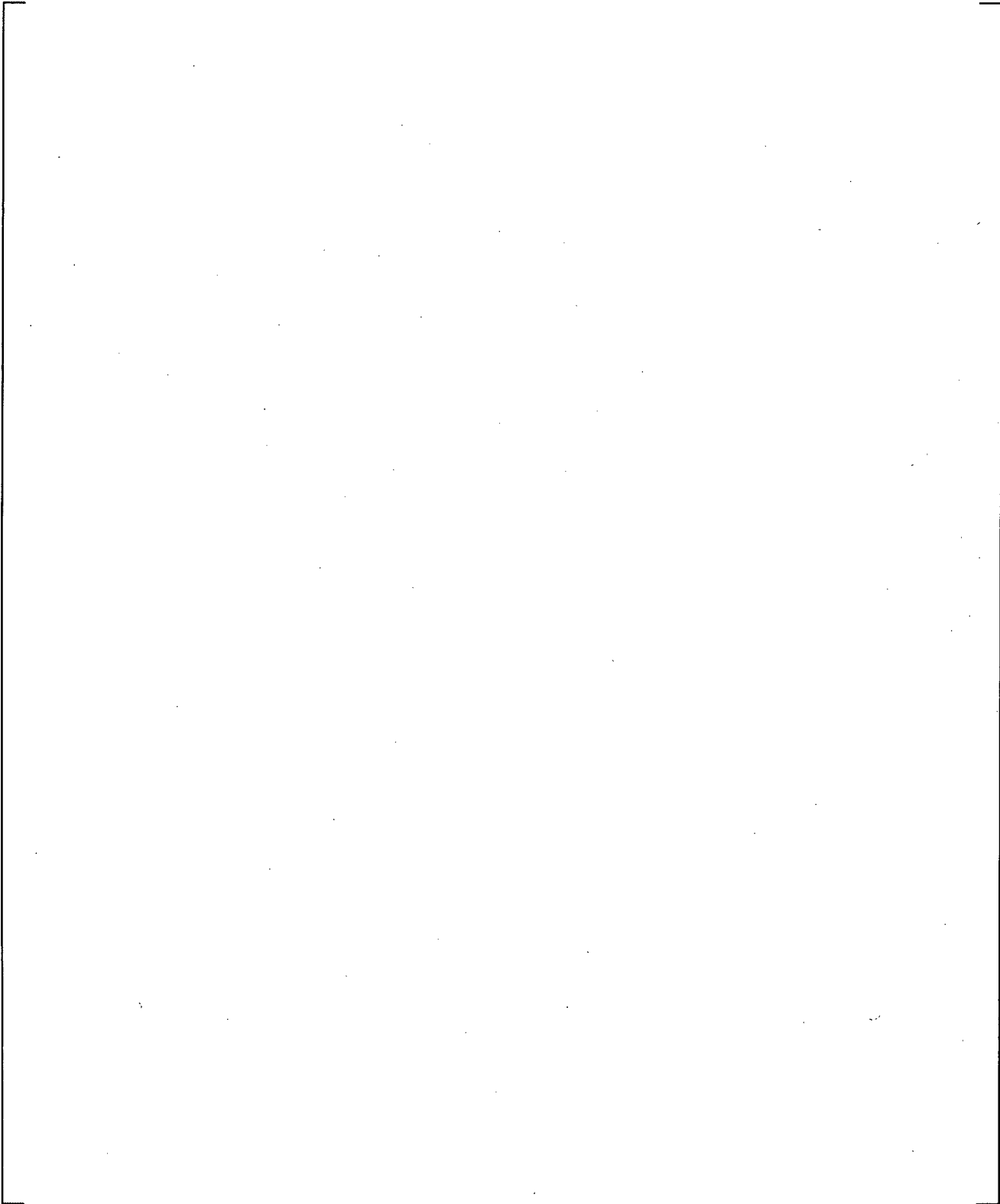


**Figure 18.2.2-2 Taitel-Dukler Flow Regime Map, Comparing 1/3-Scale Pipe at 14.7 psia and Full-Scale Pipe at 1000 psia**

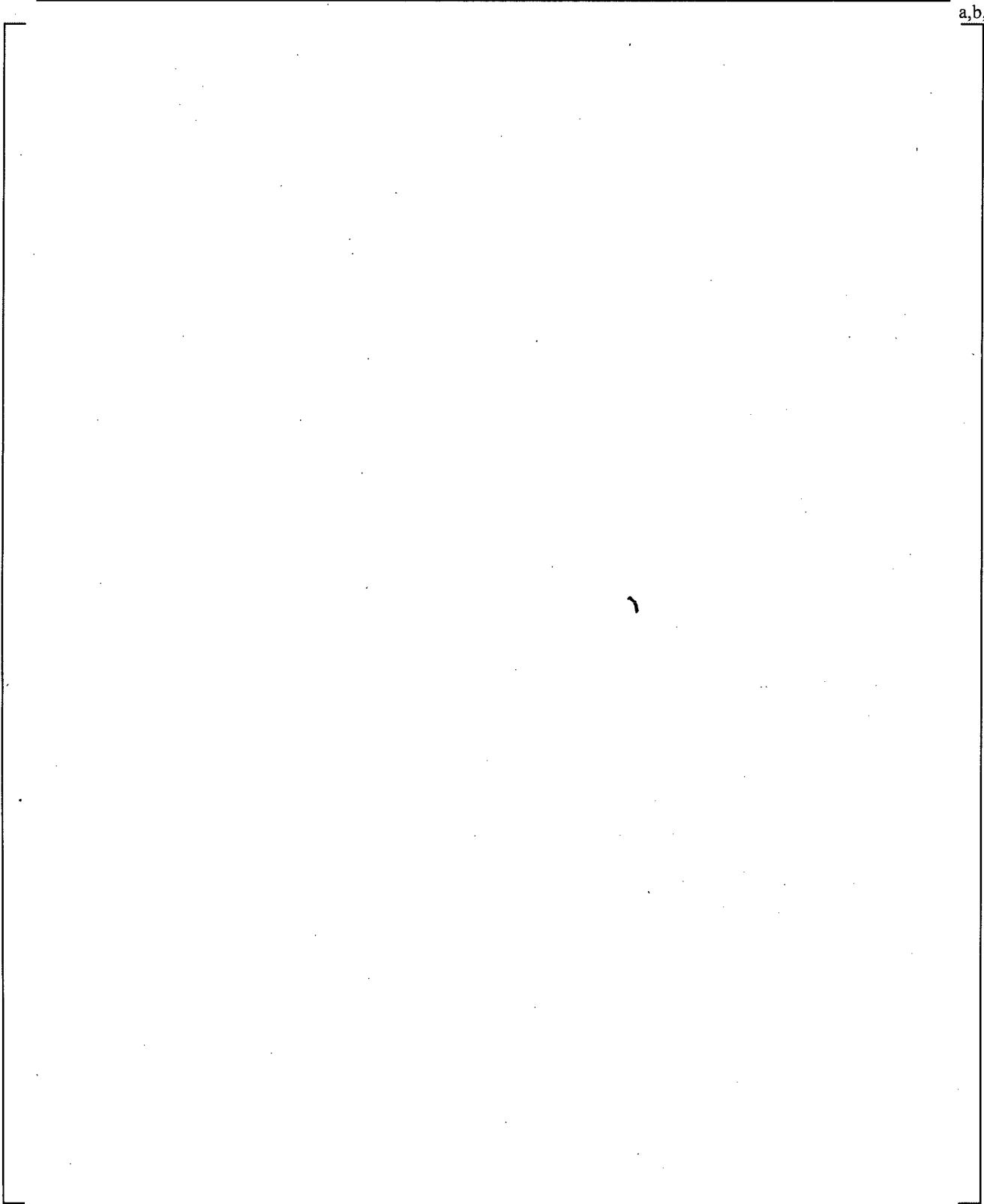


**Figure 18.2.2-3**

**PWS 2.3 U-Tube Residual Liquid Level Remaining After Test as a Function of Test Gas Flow rate**

a,b,c

**Figure 18.2.2-4 PWS 2.3 U-Tube Horizontal and Vertical Leg Average Void Fractions During Test**

a,b,c

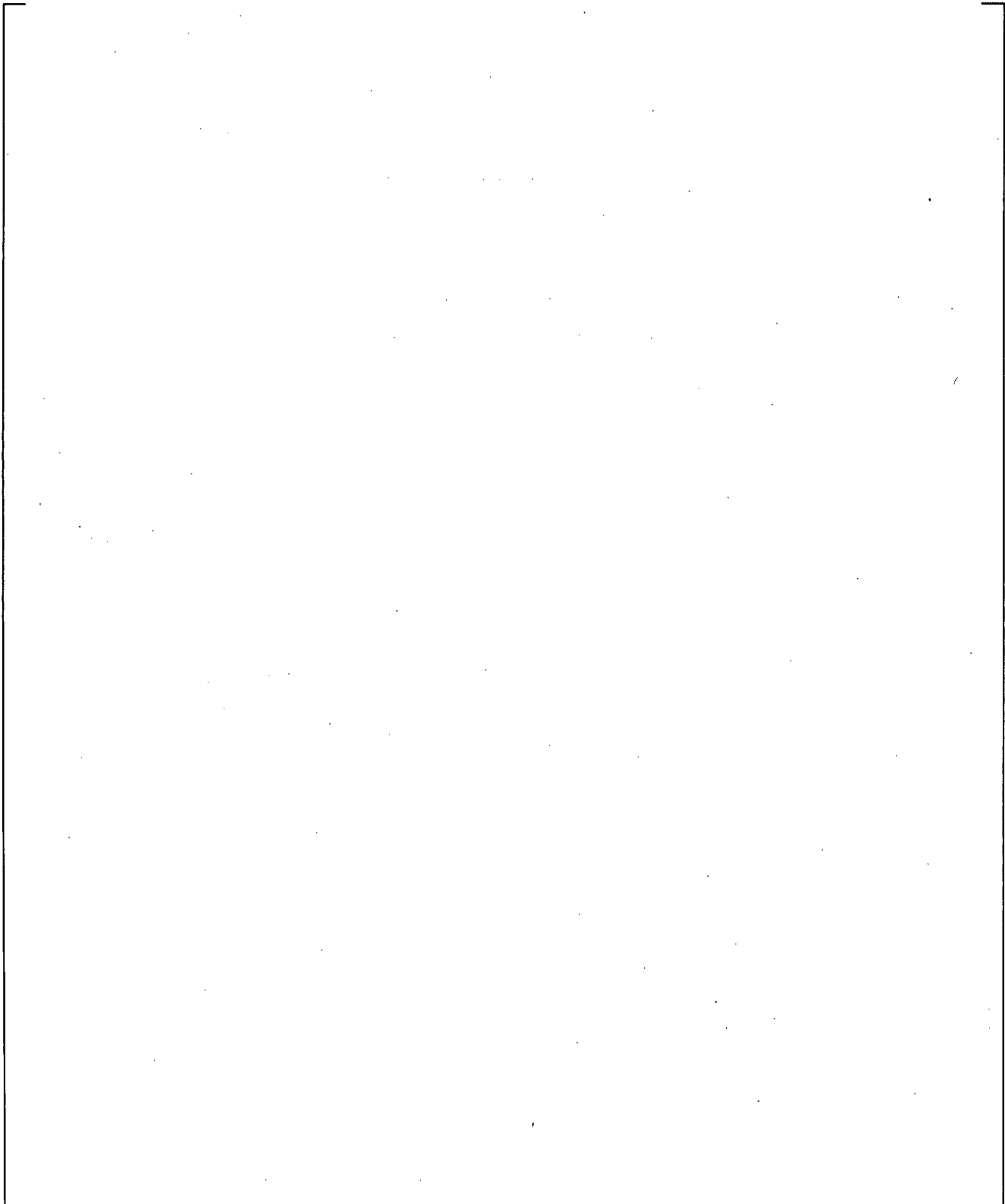


**Figure 18.2.2-5 PWS 2.3 U-Tube Horizontal Average Void Fraction During Test Compared with Average Void Fraction after Test**

a,b,c

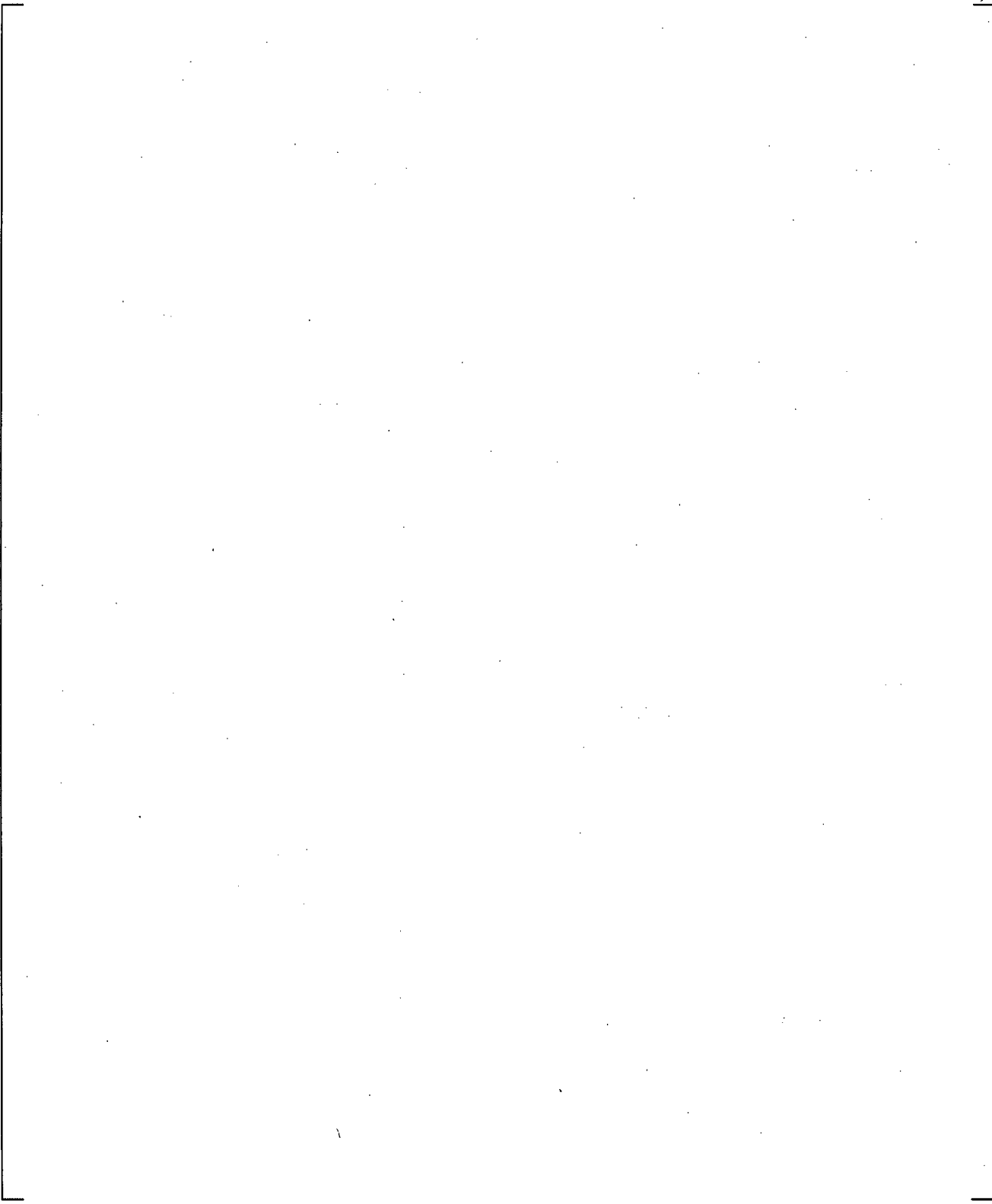


**Figure 18.2.2-6 Pressure Difference Across the PWS 2.3 U-Tube**

a,b,c

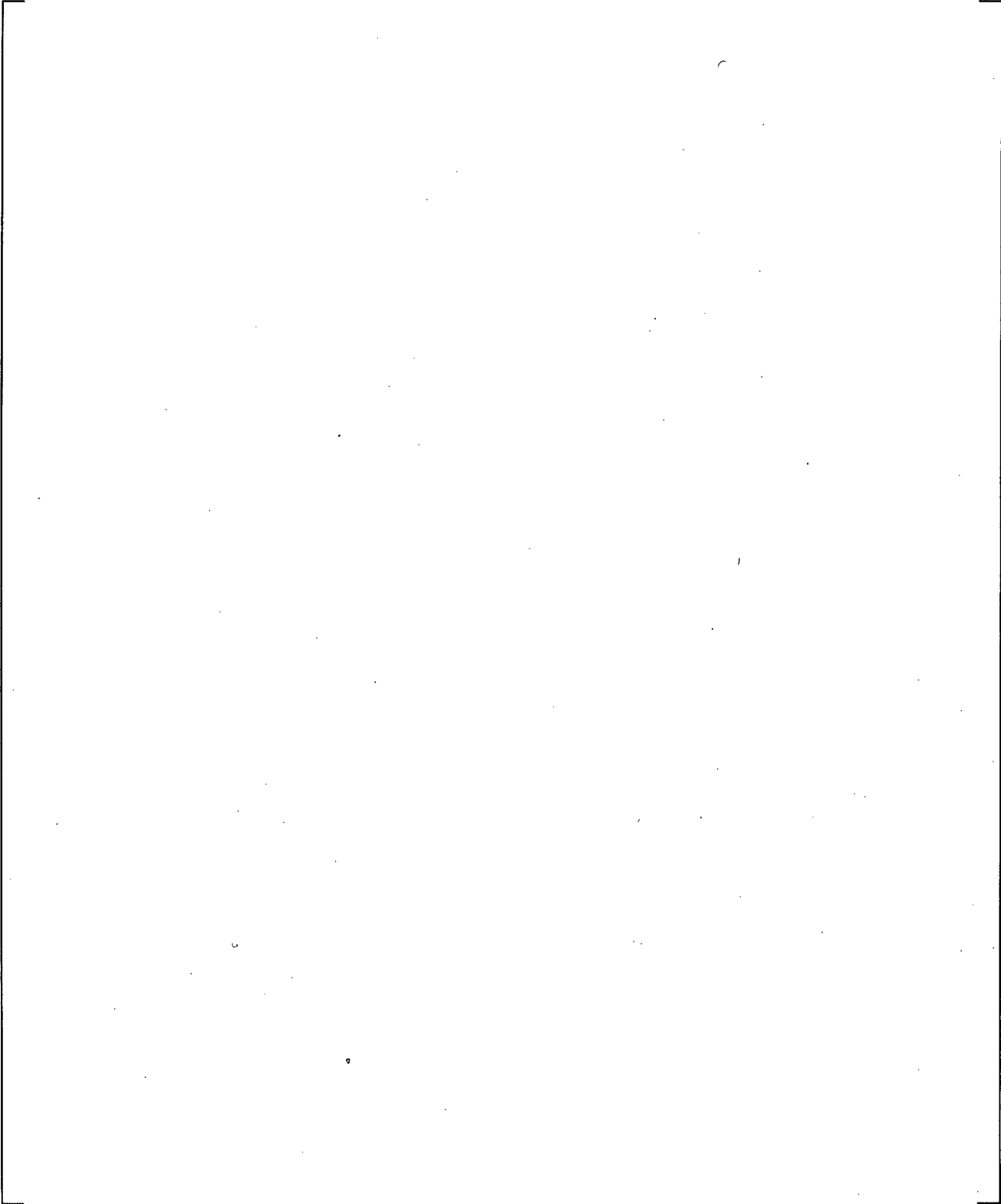


**Figure 18.2.2-7 PWS 2.3 U-Tube Normalized Level and Limit Lines**

a,b,c

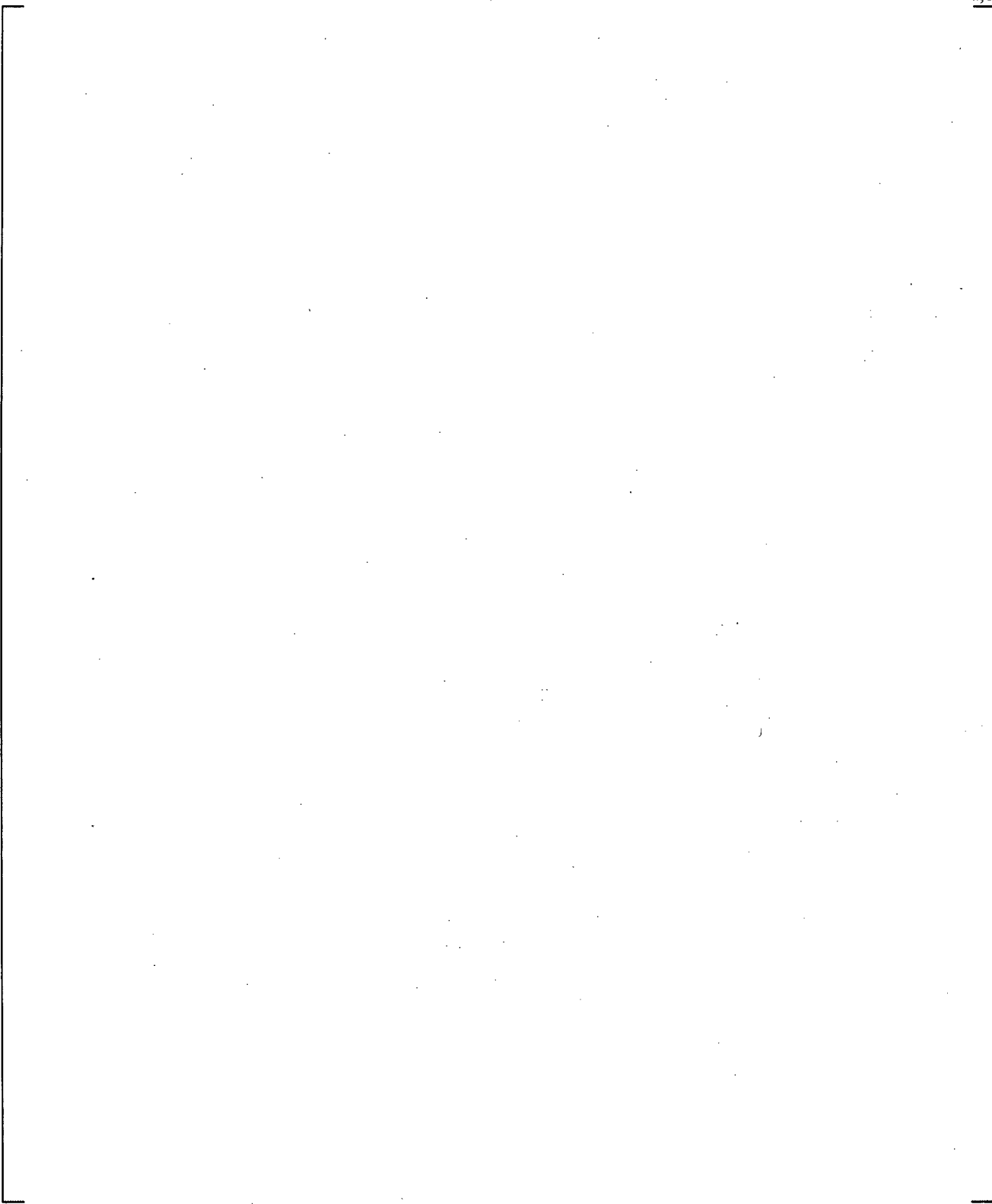


**Figure 18.2.2-8 PWS 2.3 U-Tube Flow Regimes Observed Under the Limit Line**

a,b,c

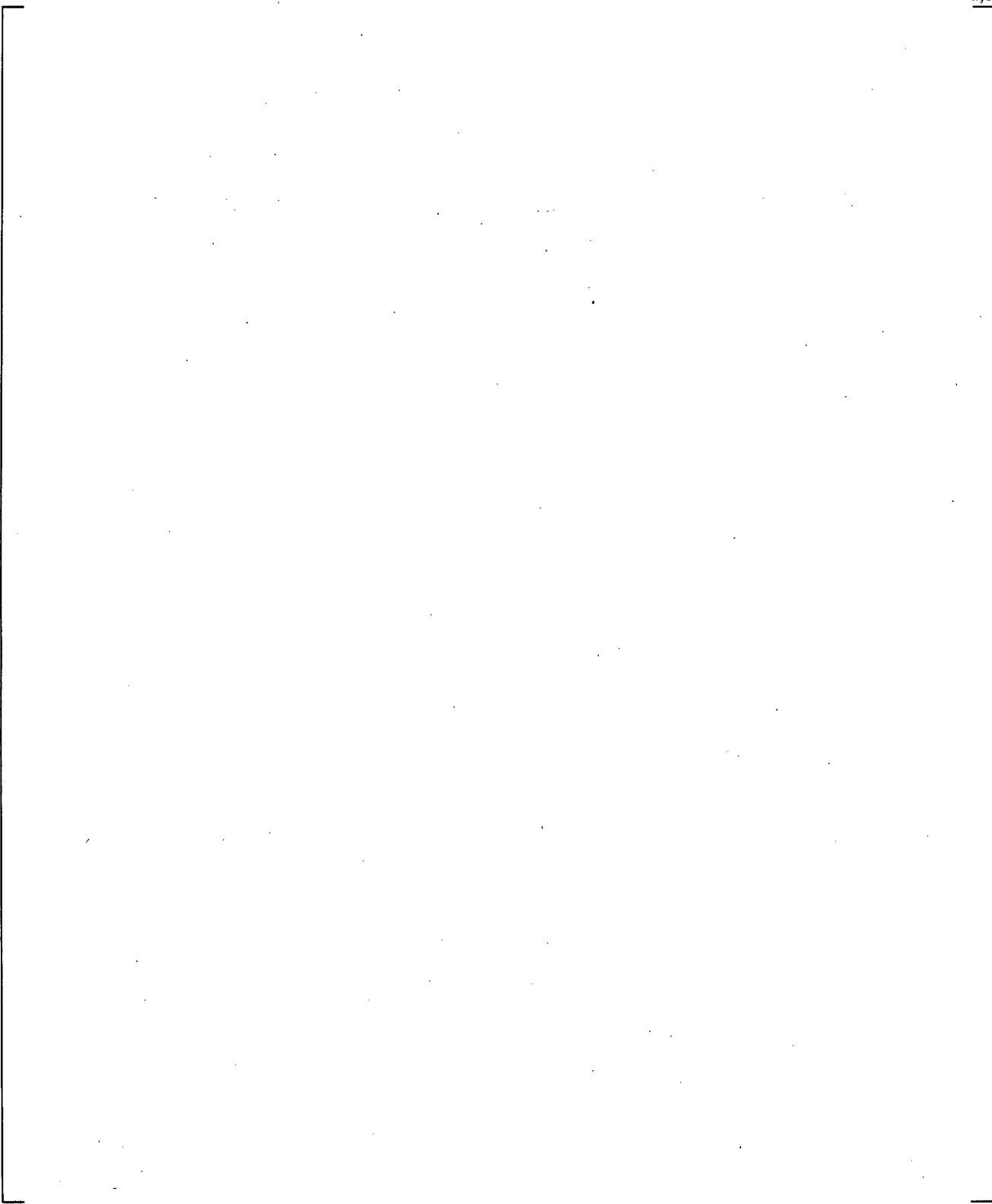


**Figure 18.2.2-9 Hysteresis in Loop Seal Limit Line**

a,c

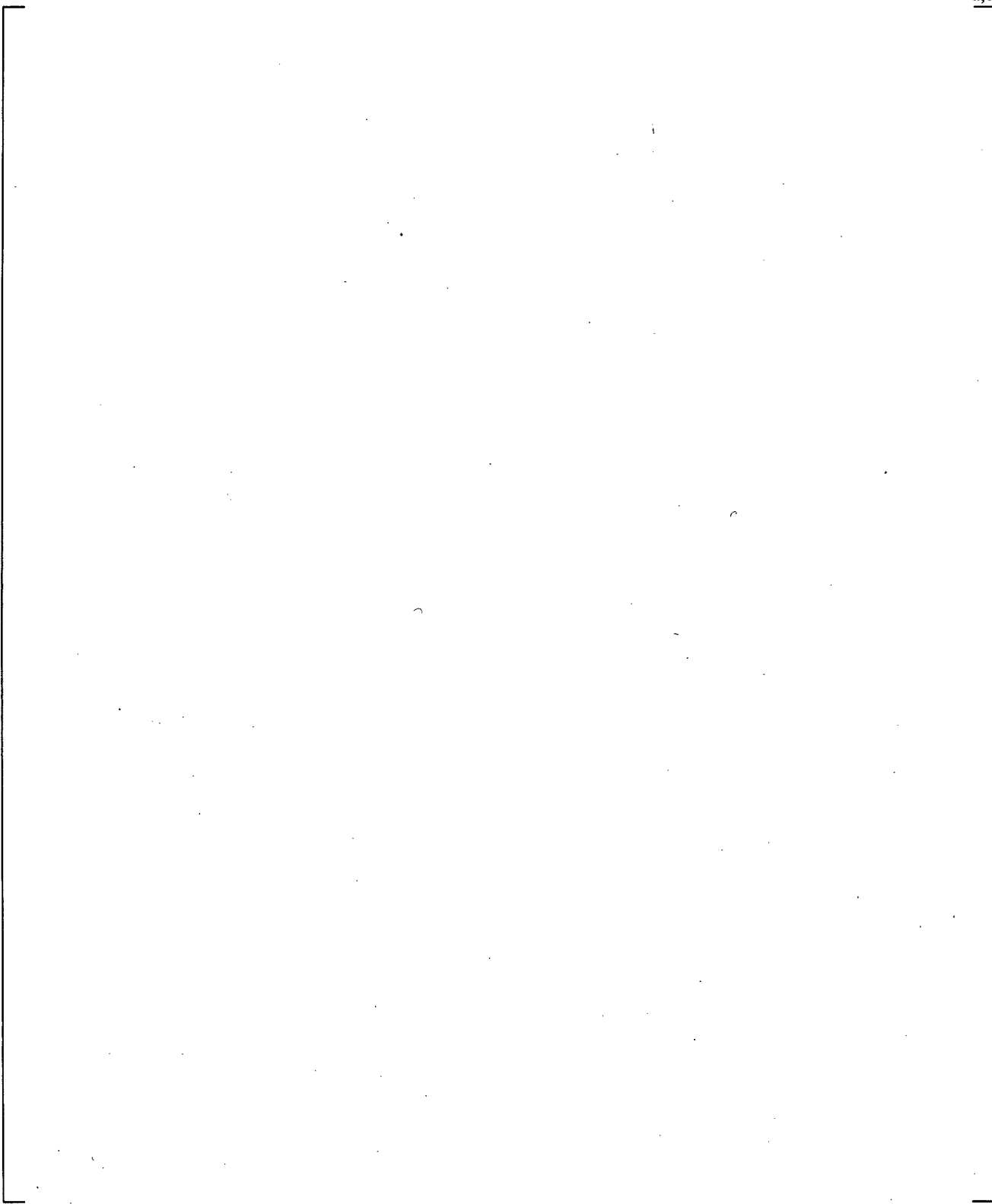


**Figure 18.2.2-10 Effect of Increased Geometric Scale on Limit Lines**

a,c

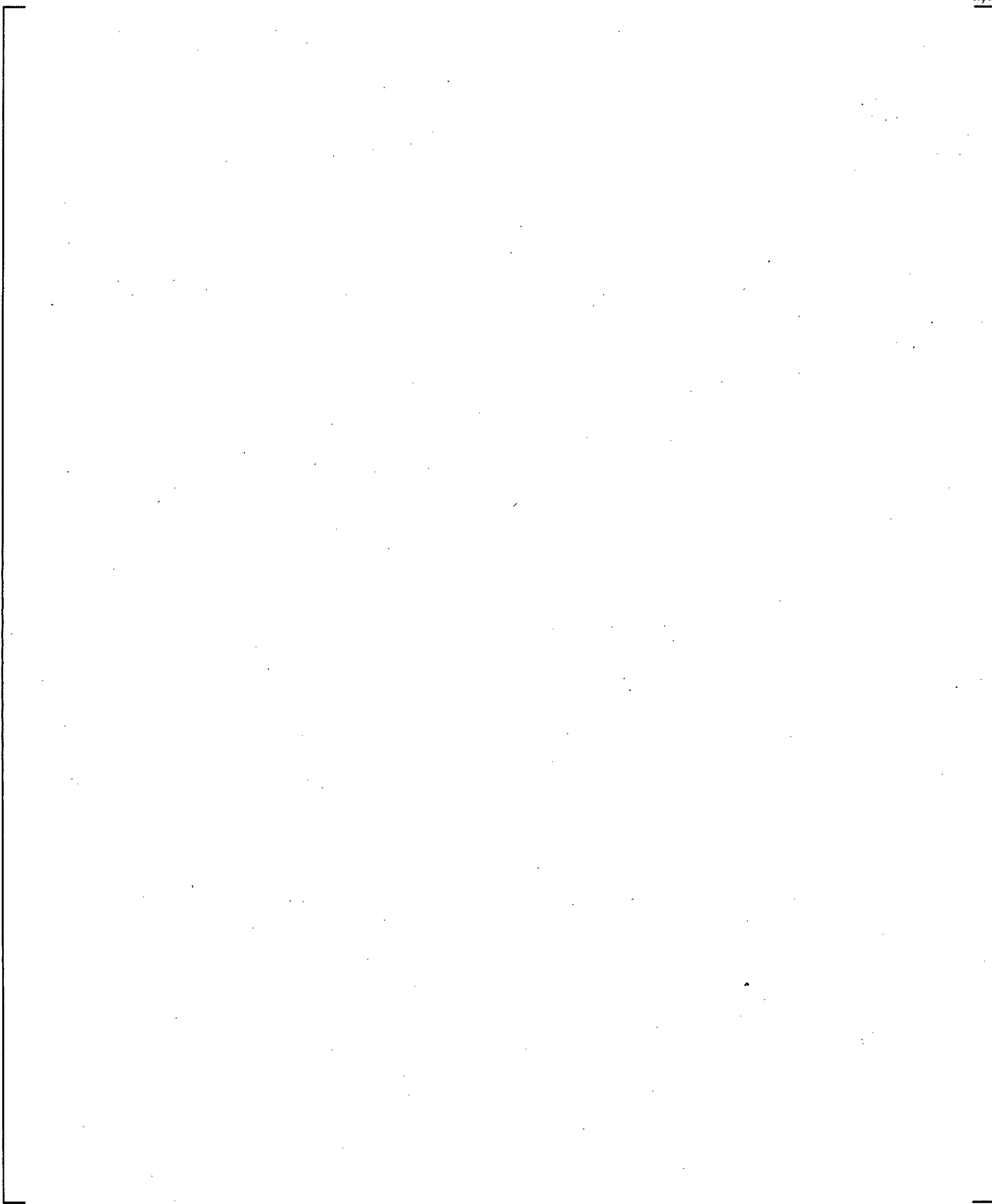


**Figure 18.2.2-11 Effect of Increased Pressure and Scale on Limit Lines**

a,c

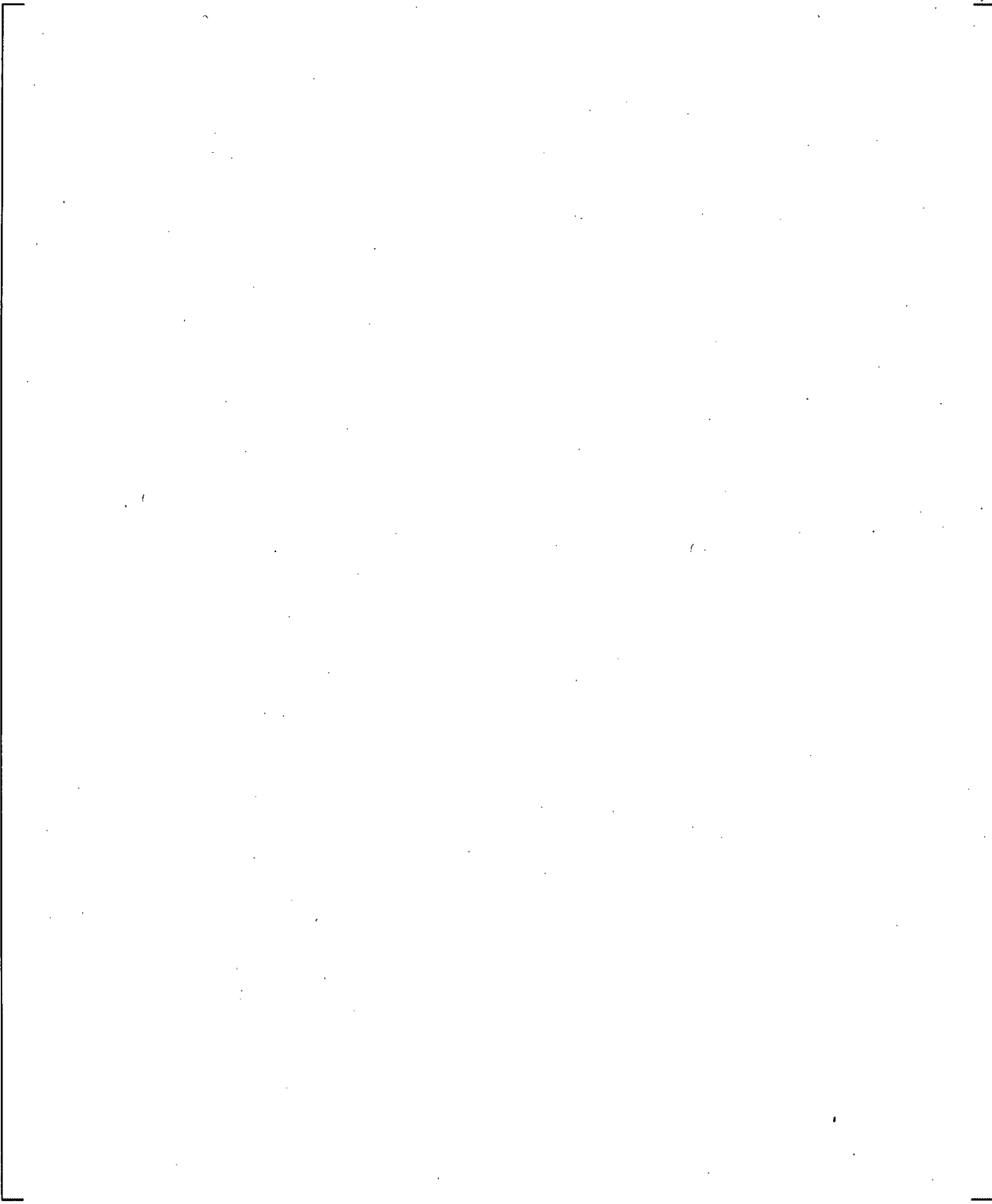


**Figure 18.2.2-12 IVO Full-Scale Final Void Fraction and Limit Lines**

### 18.2.3 Full-Scale Steam-Water Tests

Tests were performed at full-scale for a typical four-loop PWR in the Upper Plenum Test Facility (UPTF) at pressures of 3 bar (43.5 psia) and 15 bar (217.5 psia). The separate effects tests (Liebert and Emmerling, 1998) were conducted by blocking three of the four loops as seen in Figure 18.2.3-1, partially filling the loop seal in the open loop, injecting steam into the reactor vessel simulator, and measuring the residual level once entrainment had completed, but before the steam flow was terminated. The published data from the two test series are shown in Figure 18.2.3-2 (Liebert and Emmerling, 1998 and Ohvo, et al., 1998).

Lines are drawn through the data that represents a constant average gas velocity as seen in Figure 18.2.3-2. This velocity is the best-estimate of the minimum velocity at which entrainment from the liquid surface will take place within the horizontal section of the loop seal and is independent of the level in the horizontal run. Also shown is the Taitel-Dukler line for transition from slug to entrained flow. Liebert and Emmerling note that slugging was observed only at the lowest Froude number in each test series. Otherwise, the flow was observed to be stratified. The calculated critical gas velocities are 60 ft/s and 32 ft/s for the 3-bar and 15-bar test series, respectively.

Using the above critical velocities and calculated viscosity numbers and the critical velocity from the PWS 2.3 air-water tests (Figure 18.2.2-3), the results can be compared to Ishii's correlation as shown in Figure 18.2.3-3 (Ishii and Grolmes, 1975), where the Ishii parameter is calculated as:

$$Ish = \frac{w_g \mu_g}{\sigma} \left( \frac{\rho_g}{\rho_w} \right)^{0.5} \quad (18-7)$$

The UPTF and PWS 2.3 data (diamonds in the figure) lie [ ]<sup>a,c</sup> the database upon which Ishii's correlation was constructed (triangles in figure). While the UPTF data lie [ ]<sup>a,c</sup>. As shown in Figure 18.2.3-3, the UPTF data lie [ ]<sup>a,c</sup>

Using an Ishii number of 0.0033, a Reynolds number of approximately [ ]<sup>a,c</sup> is obtained from Equation 18-3. Recalling that this is the approximate Reynolds number for [ ]<sup>a,c</sup>



**Figure 18.2.3-2** Lines of Constant Gas Velocity Compared to UPTF Data for 3-Bar and 15-Bar Loop Seal Tests

a,c

**Figure 18.2.3-3 UPTF and PWS 2.3 Compared to the Ishii Correlation and Data Base**

### 18.3 WCOBRA/TRAC-TF2 MODELING OF LOOP SEAL CLEARING PROCESS

The objective of this assessment is to confirm that WCOBRA/TRAC-TF2 adequately predicts the loop seal clearing phenomena for a PWR, namely the residual liquid level in the loop seal and differential pressure across the loop seal post clearing. Discussions on the number of loop seals that clear and which loop seals clear are in Sections 28 and 31.

#### 18.3.1 WCOBRA/TRAC-TF2 Simulation of the UPTF 3-Bar and 15-Bar Tests

The two UPTF full-scale steam-water tests were simulated with WCOBRA/TRAC-TF2. The separate effects tests were conducted by blocking three of the four loops and injecting steam into the reactor vessel simulator as shown in Figure 18.2.3-1 (Liebert and Emmerling, 1998). The WCOBRA/TRAC-TF2 model for the simulations has three components, as depicted in Figure 18.3-1; a FILL is used to supply the vapor; a PIPE is used to simulate loop 2 of the facility; and, a BREAK is used to maintain the test pressure. The PIPE has a total of [ ]<sup>a,c</sup> making up the actual loop seal. [ ]<sup>a,c</sup> The noding in this model is judged sufficient for simulation of the UPTF tests, and similar modeling is expected to be used in the plant simulations.

The UPTF tests were run with a slightly superheated steam supply (Ohvo, et al., 1998). With the flow of superheated steam, liquid in the loop seal may be evaporated. However, it is expected that the amount of liquid evaporation is small compared to the amount of liquid lost due to slugs of liquid/entrained liquid being expelled out the loop seal. As such, the WCOBRA/TRAC-TF2 simulations were performed assuming [ ]<sup>a,c</sup>.

Although the initial liquid level was varied in the tests, the calculations are initialized [ ]<sup>a,c</sup>

[ ]<sup>a,c</sup> Liebert noted that varying the initial level and liquid flow did not significantly affect the test results. For the 3-bar tests, the residual levels are lower for the cases with liquid injection for approximately the same Froude number. Thus, a set of initial conditions consistent with a hypothetical small break LOCA are used for the simulations.

Each of the test simulations is run separately, starting from the same initial conditions. The steam flow rate is increased from zero to the specified flow rate [ ]<sup>a,c</sup>

[ ]<sup>a,c</sup>

The results of the 3-bar simulations are shown in Figure 18.3-2. WCOBRA/TRAC-TF2 generally [ ]<sup>a,c</sup>

[ ]<sup>a,c</sup> Figure 18.3-3 shows the total mass in the system for the 3-bar and 15-bar cases with  $j_g^* \approx 0.1$ .

The predicted behavior for the 15-bar tests compared to the data is shown in Figure 18.3-4. WCOBRA/TRAC-TF2 [ ]<sup>a,c</sup>

[ ]<sup>a,c</sup>

Figure 18.3-5 shows a comparison of the predicted versus measured residual liquid levels for both tests. As observed in the figure, the [ ]<sup>a,c</sup> for both pressures.

Although no data are known to exist for full geometric and pressure scale, WCOBRA/TRAC-TF2 calculations were performed using the UPTF model at 1000 psia. Based on the pressure-scaling discussion in Section 18.2.2.4, it is expected that [ ]<sup>a,c</sup>

Measured pressure drops across the UPTF loop seal are shown in Figure 18.3-7a. The highest pressure drops occur for  $j_g^* < 0.1$  and then become approximately constant with increasing steam velocity. Also the magnitude of the observed differential pressure oscillations is significantly greater for  $j_g^* < 0.1$ . The pressure drop calculated by WCOBRA/TRAC-TF2 is shown in Figure 18.3-7b. The calculated pressure drops shown in Figure 18.3-7b represent [ ]<sup>a,c</sup>

Figures 18.3-8a through 18.3-8c provide the pressure drop transient during the vapor injection period for three different 15-bar cases, which shows [ ]<sup>a,c</sup> in pressure drop amplitude and frequency observed in the tests (Figure 18.3-7a).

Figures 18.3-9a and 18.3-9b show smoothed pressure drop transients for the 3-bar and 15-bar  $j_g^* \approx 0.05$  cases, respectively, and Figures 18.3-9c and 18.3-9d show smoothed pressure drop transients for the 3-bar and 15-bar  $j_g^* \approx 0.22$  cases, respectively. For the 3-bar and 15-bar high vapor flow cases, [ ]<sup>a,c</sup>

[ ]<sup>a,c</sup>. For the 3-bar and 15-bar low vapor flow cases, [ ]<sup>a,c</sup>.

**Figure 18.3-1 WCOBRA/TRAC-TF2 Model of the UPTF Separate Effects Loop Seal Clearing Tests**



**Figure 18.3-2 Comparison of WCOBRA/TRAC-TF2 Calculations and UPTF Data for the 3-Bar Tests**



**Figure 18.3-3 Comparison of WCOBRA/TRAC-TF2 Calculations Total System Mass for UPTF 3-bar and 15-bar  $j_g^* \approx 0.1$  Cases**



**Figure 18.3-4 Comparison of WCOBRA/TRAC-TF2 Calculations and UPTF Data for the 15-Bar Tests**



**Figure 18.3-5 Comparison of Calculated vs. Measured Residual Liquid Levels**

a,c

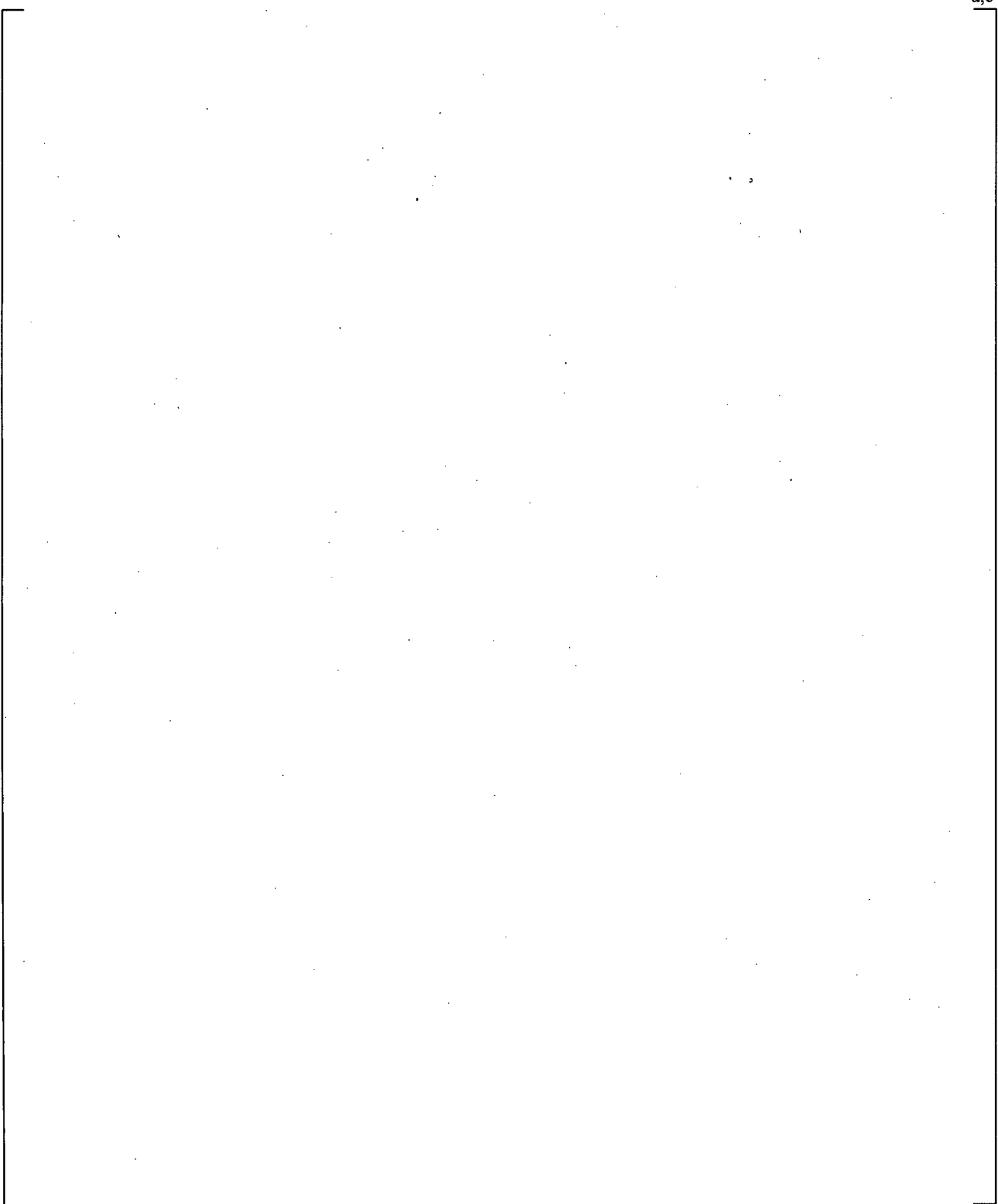


**Figure 18.3-6 Calculated Residual Liquid Levels and CCFL Limit ( $Ku = 3.2$ ) for 1000 psia**

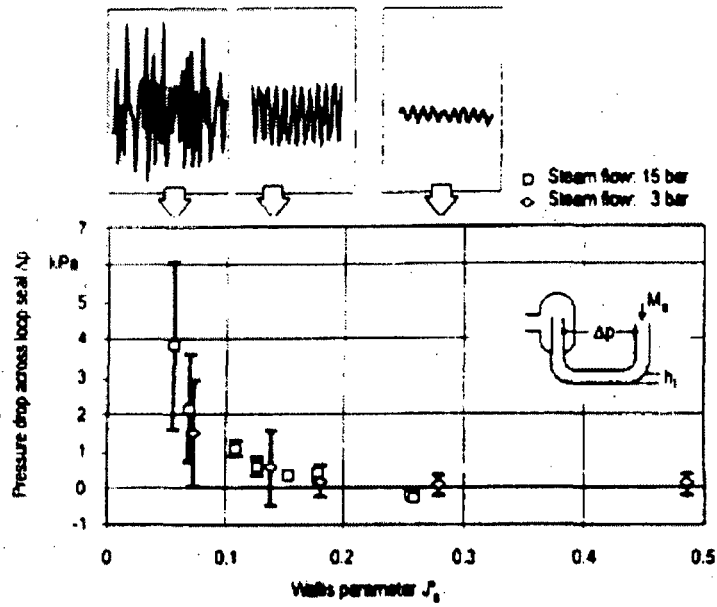


Figure 18.3-7a Measured Pressure Drop for UPTF 3-Bar and 15-Bar Loop Seal Tests (from Liebert and Emmerling, 1998)



Figure 18.3-7b Calculated Loop Seal Pressure Drop for 3-Bar, 15-Bar, and 1000 psia

a,c



**Figure 18.3-8a Calculated Pressure Drop for 15-Bar and  $j_g^* \approx 0.07$**

a,c



**Figure 18.3-8b Calculated Pressure Drop for 15-Bar and  $j_g^* \approx 0.18$**

a,c

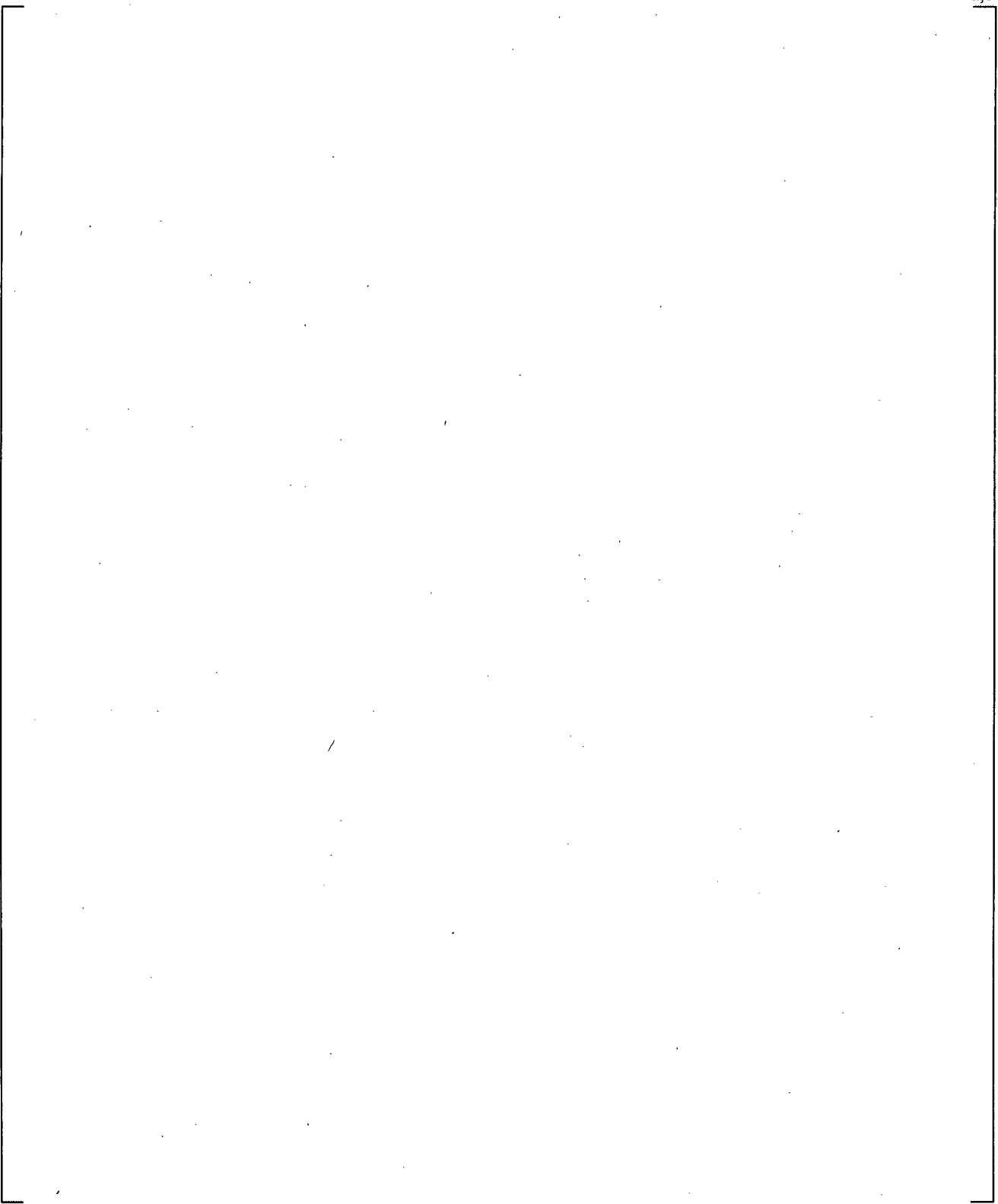
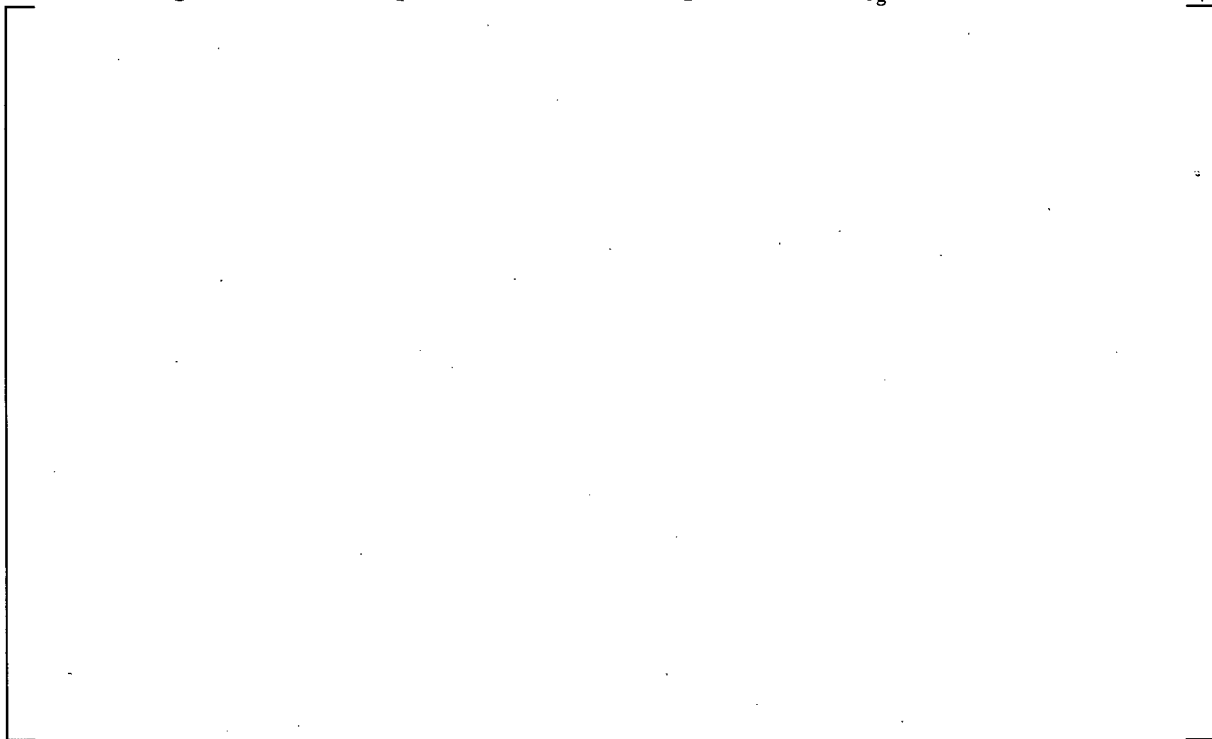


**Figure 18.3-8c Calculated Pressure Drop for 15-Bar and  $j_g^* \approx 0.32$**



a,c

**Figure 18.3-9a Comparison of Pressure Drop in Bends for  $j_g^* \approx 0.05$  3-bar Case**



a,c

**Figure 18.3-9b Comparison of Pressure Drop in Bends for  $j_g^* \approx 0.05$  15-bar Case**

a,c



**Figure 18.3-9c Comparison of Pressure Drop in Bends for  $j_g^* \approx 0.22$  3-bar Case**

a,c

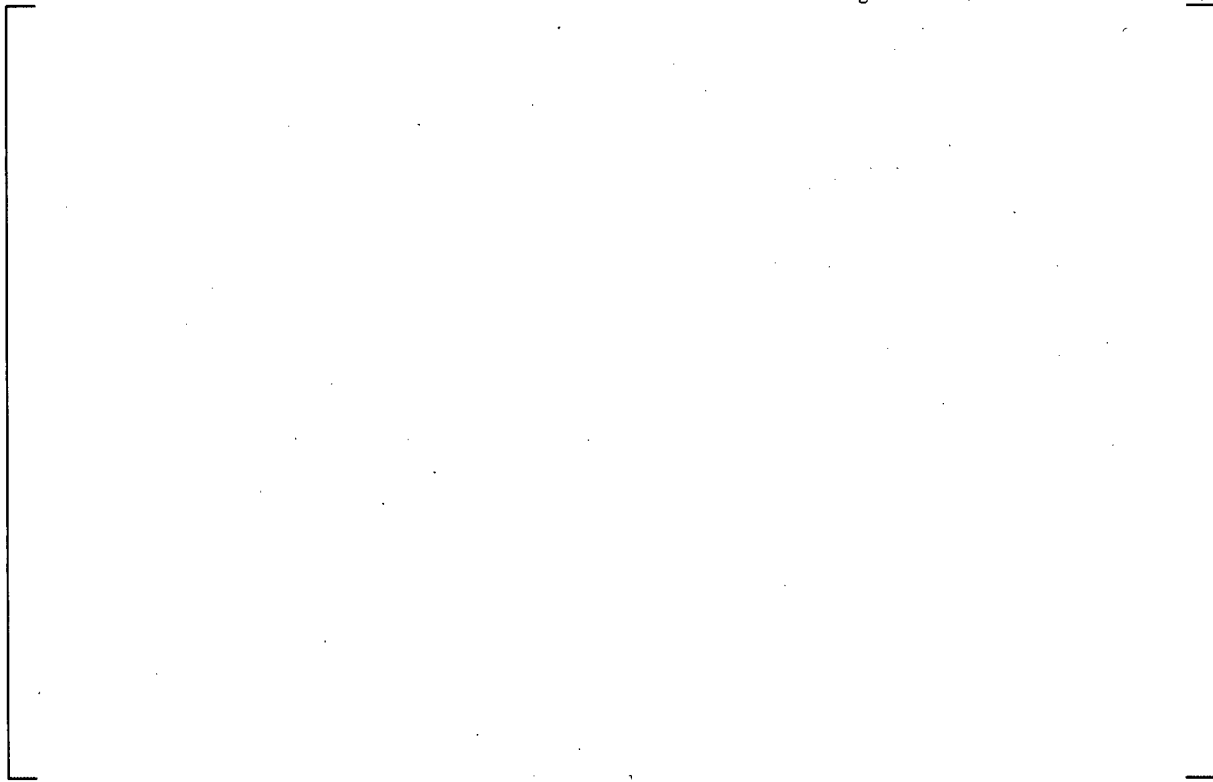


**Figure 18.3-9d Comparison of Pressure Drop in Bends for  $j_g^* \approx 0.22$  15-bar Case**

## 18.4 CONCLUSIONS

Assessment of the experimental data indicates the following:

[

] <sup>a,c</sup>

Assessment of WCOBRA/TRAC-TF2 relative to the experiments indicates the following:

[

] <sup>a,c</sup>

## 18.5 REFERENCES

1. Boileau, H., and Bourteele, J. P., 1985, "ECHTOR Program, PWS 2.3: Small Size Break, Final Report," EP/TA/DC 533.
2. Ishii, M. and Grolmes, M. A., 1975, "Inception Criteria for Droplet Entrainment in Two-Phase Concurrent Film Flow," AICHE J., Vol. 21, No 2.
3. Koizumi, and Tasaka, K., 1988, "Quick Look Report for ROSA-IV/LSTF 10% Cold Leg Break LOCA Test, SB-CL-14," JAERI-memo 63-262.
4. Kukita, Y. et al., 1990, "Loop Seal Clearing and Refilling During a PWR Small Break LOCA," Nuclear Eng. and Design, 121, 431-440.
5. Kumamaru, H. et al., 1989, "ROSA-IV/LSTF 5% Cold Leg Break LOCA Experiment Run SB-CL-18 Data Report," JAERI-memo 89-027.
6. Liebert, J. and Emmerling, R., 1998, "UPTF Experiment Flow Phenomena During Full-Scale Loop Seal Clearing of a PWR," Nuclear Engineering and Design, Vol. 179, pp. 51-64.
7. Ohvo, J., et al., 1998, "Simulation of Full-Scale UPTF Loop Seal Experiments with APROS, CATHARE and RELAP," 6th International Conference on Nuclear Engineering, ICONE6-6090.
8. Pushkina, O. L. and Sorokin, Y. L., 1969, "Breakdown of Liquid Film Motion in Vertical Tubes," Heat Transfer-Soviet Research, Vol. 1, No. 5.
9. Richter, H. J., 1981, "Flooding in Tubes and Annuli," Int. J. Multiphase Flow, Vol. 7, No. 6, pp. 647-658.
10. Taitel, Y. and Dukler, A. E., 1976, "A Model for Predicting Flow Regime Transitions in Horizontal and Near Horizontal Gas-Liquid Flow," AICHE J., Vol. 22, No 1.
11. Tuomisto, H. and Kajanto, P., 1988, "Two Phase Flow in a Full Scale Loop Seal Facility," Nuclear Eng. and Design, 107, 295-305.

## 19 ADDITIONAL LOCA HYDRODYNAMIC ASSESSMENT AGAINST LARGE SCALE EXPERIMENTS

### 19.1 INTRODUCTION

The phenomena identification and ranking table (PIRT) documented in Volume 1, Section 2 identified highly important hydrodynamic phenomena that occur during the LOCA sub-scenarios. The objective of this section is to complete the assessment of specific WCOBRA/TRAC-TF2 models that were not addressed with the Separate Effects Test (SET) or Integral Effects Test (IET) evaluation presented in the other sections. The phenomena considered here are associated in particular with the Large Break LOCA scenario.

For previous WCOBRA/TRAC evaluation models, an extensive assessment was performed, and has been documented in Sections 14 and 15 of the code qualification document, CQD (Bajorek, 1998). The most critical elements of this original assessment are repeated here to validate the performance of the new WCOBRA/TRAC-TF2 code, and confirm that the conclusions in term of biases remain consistent with the already validated versions. The rationale for the selection of the tests used in this assessment is discussed in Section 2.

The PIRT identified the following critical hydrodynamic models that can occur during a postulated LOCA transient.

#### Counter Current Flow Limiting (CCFL)

The Countercurrent Flow Limit (CCFL) is associated with the process of restricting liquid flow by counter-flowing vapor, due to interfacial drag forces. For example, liquid downflow in a pipe under the influence of gravity becomes unstable with increasing vapor upflow and eventually flows together with the vapor. Thus, stable countercurrent conditions can exist only within a certain range. The boundary of this range is recognized as the CCFL.

CCFL can occur in several locations in a PWR during a LOCA. Emergency Core Cooling (ECC) bypass during the blow-down phase of a large break LOCA is an example of exceeding CCFL conditions in the downcomer annulus. CCFL is possible in other locations in the vessel. Liquid in the upper plenum may be held up at the upper core plate or tie plate by an upflow of steam from the core. Note, tie plate is the most flow restrictive area between the core and upper plenum. For Westinghouse PWRs, tie plate corresponds to the fuel assembly top nozzle region. CCFL may also occur in the loops during some LOCA scenarios. CCFL may occur in the U-tubes of a steam generator during a small break LOCA, affecting the de-pressurization of the system, and therefore, the overall progression of the transient.

The predictive capability of WCOBRA/TRAC-TF2 for CCFL phenomena is assessed for different conditions, as follows:

1. CCFL in a Downcomer Annulus – [

] <sup>a,c</sup>

2. CCFL in a Perforated Plate – [

] <sup>a,c</sup>

3. CCFL in the Steam Generators – [

] <sup>a,c</sup>

### Entrainment and De-Entrainment

Entrainment from liquid films and de-entrainment on structures are important processes that determine the mass distribution in the Reactor Coolant System (RCS) during a LOCA. Droplets leaving the core can be de-entrained by the upper plenum structures, forming a pool above the upper core plate. The de-entrainment and liquid accumulation in the upper plenum has two competing effects on the core flooding rate. Liquid that de-entrains in the upper plenum does not carryover into the steam generators and forms a pool in the upper plenum. The pool in the upper plenum creates a static pressure head that could decrease the flooding rate by some amount. A beneficial effect of the upper plenum pooling is the potential for draining of water into the core in the low power regions, where the steam flow is insufficient to prevent counter-current flow conditions. Liquid draining from the upper plenum can contribute to cooling by replenishing the core liquid inventory and providing topdown cooling. The entrained droplets that leave the upper plenum can be brought to the steam generator and evaporate inside the steam generator U-tubes, if the secondary side temperature is higher than the primary side temperature. The steam acceleration and the high speed of steam result in a large pressure drop in the steam generators. This high pressure loss in the steam generator caused by the evaporation of droplets, which is called steam binding effect, further contributes to additional pressure increase in the upper plenum.

[

] <sup>a,c</sup>

Entrainment at the quench front has a strong effect on the net reflood rate and on the downstream heat transfer. Droplets entrained at the quench front readily evaporate, de-superheating the vapor, and can under certain conditions, impact on the fuel rods. Lower downstream vapor temperatures and direct contact heat transfer increases the rate of heat transfer far ahead of the quench front, decreasing the peak cladding temperatures. [

] <sup>a,c</sup>

Entrainment also occurs in the lower plenum during blowdown and the early part of refill. Droplets can be entrained from the liquid pool at the bottom of the vessel. During blowdown, these droplets are swept out of the vessel to the break through the voided downcomer. In refill period, some of the droplets may enter the core and contribute to cooling, while most de-entrain on the lower core plate and remain in the lower plenum. [ ]<sup>a,c</sup>

Finally, entrainment/de-entrainment occurs in the downcomer during reflood. As the water level in the downcomer approaches the loop level, high steam or non-condensable flow from the intact loops may cause some water entrainment out the break. [ ]

] <sup>a,c</sup>

Therefore, the predictive capability of WCOBRA/TRAC-TF2 for entrainment and de-entrainment phenomena needs to be assessed for different conditions, as follows:[ ]

] <sup>a,c</sup>

Entrainment/de-entrainment models are relevant in various regions of plant analyzed. The capability of the code to model these processes together with the interaction with other process (e.g., the heat transfer) is a potential source of compensating errors. Section 24 provides an in-depth analysis of such compensating errors and the assessment presented in this section is the basis of such analysis.

### **Condensation**

Condensation of steam by subcooled water will be initiated during a large break LOCA when accumulator water begins to flow into the cold leg piping. High head safety injection (HHSI) may begin earlier, but the flow rate is much lower than the accumulator (ACC) or low head safety injection (LHSI), and is therefore relevant only for the smaller breaks, where the time before accumulator or low head safety injection could

be significant. Condensation of steam is of critical importance for both small and larger breaks, but the physical conditions differ significantly, and the Westinghouse cold leg condensation models introduced in Section 6 must be robust and generic enough to adequately address these different conditions. It is noted that the high head safety injection and low head safety injection are named as SI and RHR in Section 26, respectively.

For large breaks, the subcooled Emergency Core Cooling System (ECCS) water will flow from the cold legs into the upper downcomer and, later in the transient, into the lower plenum and core. During late blowdown and refill, the flow of accumulator water is of sufficient magnitude to theoretically condense all the steam flowing into the cold leg. During the reflood phase, the low head safety injection flow, at its minimum levels, is typically insufficient to condense all the steam flowing into the cold leg.

Condensation of steam in the downcomer has been observed to strongly affect the countercurrent flow behavior in the downcomer as ECCS water penetrates into the lower plenum. As discussed above, ECCS bypass and Countercurrent Flow (CCFL) are basic processes, of which the accurate prediction is a fundamental requirement for a best-estimate LOCA code.

Also steam condensation affects steam velocity in the downcomer and as a result the sweep-out, entrainment of liquid toward the break. The higher steam flow rate, in turn, may entrain more water from the downcomer to the break, and may increase the pressure drop through the broken cold leg nozzle.

Condensation of steam by ECCS water was also observed to produce flow and pressure oscillations of sufficient magnitude to affect the flow through the intact loops during reflood. This led initially to a concern that condensation phenomena would induce resistance in the intact cold legs and impede the flow of steam from the core during reflood. Tests in which the injection of ECCS water into the cold leg was simulated indicated that, while the hydrodynamic behavior was highly oscillatory, the induced resistance was relatively small.

The degree to which condensation of steam occurs in the cold leg, usually indicated by the condensation efficiency, is also important in determining the steam flow rate and temperature of the water flowing into the vessel during reflood. If the condensation efficiency is high, the steam flow will be reduced, and the water temperature will be increased. The condensed water, if it is still subcooled, will reach saturation after it enters the vessel and begin to boil sooner in the downcomer and core. The lower steam flow may entrain less water from the downcomer out the break, and leads more vessel inventory. It also may result in a smaller pressure drop across the broken cold leg nozzle. If the condensation efficiency is low, the colder water will contribute to maintain the subcooling of the water in the downcomer.

Condensation is known to be strongly affected by the presence of non-condensable gases. As the accumulator empties, nitrogen is discharged in the system and results in pressurization of the downcomer as well as reduction in steam condensation rate. During reflood, a large volume of nitrogen is injected into the cold legs when the accumulator runs out of water. During refill, the Reactor Coolant System (RCS) pressure may momentarily drop below containment pressure because of condensation, allowing containment gases to flow into the RCS via the broken cold leg.

For larger breaks, the primary side system experiences a rapid depressurization so that most of the condensation phenomena take place at low pressure. For smaller breaks however, the system pressure transient is slower, as discussed in Section 2. In this case, condensation in the cold leg at the high head

safety injection is of significant importance, as condensation of the steam from the cold high head safety injection can significantly impact the transient pressure and vessel inventory. The assessment of the cold leg condensation for the small break LOCA is addressed in Section 17, while this section focuses on the large break LOCA.

Therefore, the predictive capability of WCOBRA/TRAC-TF2 for the condensation phenomenon needs to be assessed for different conditions, as follows: [

] <sup>a,c</sup>

The rest of this section discusses the performance of the models and correlations in WCOBRA/TRAC-TF2 used to simulate the processes discussed above.

The assessment roadmap is presented in Section 19.2. WCOBRA/TRAC-TF2 assessments are then documented in detail in Sections 19.3 through 19.6. Finally, Section 19.7 provides overall conclusions of the assessments documented in this Section.

## 19.2 HYDRODYNAMIC MODELS ASSESSMENT

### Counter Current Flow Limiting (CCFL)

Section 5.4 discusses the interfacial drag models that determine the existence of CCFL conditions in the vessel, and Section 5.7 describes the corresponding interfacial drag models used for 1D components. As discussed in the previous Section 19.1, the predictive capability of WCOBRA/TRAC-TF2 for CCFL phenomena needs to be assessed for the following conditions:

1. CCFL in a Downcomer Annulus – CCFL/ECC bypass in the downcomer annulus of the full-scale UPTF facility is evaluated in Section 19.3, where WCOBRA/TRAC-TF2 results are compared to experimental data for the UPTF 6 tests.
2. CCFL in a Perforated Plate – WCOBRA/TRAC-TF2 predictions of CCFL at a perforated plate are evaluated with saturated liquid and steam at 1000 psia and 35 psia, and results are compared with Northwestern test data in air-water at atmospheric conditions (Hsieh et al., 1980) in Section 19.4. The geometry of the plate (perforation ratio and thickness) simulates, at small scale,

the tie plate in a PWR. [

] <sup>a,c</sup>.

3. CCFL in the Steam Generators – The CCFL in steam generator U-tubes is evaluated based on simulations of the ROSA experiments in Section 21. [

] <sup>a,c</sup>.

### Entrainment and De-Entrainment

Section 5.6 of Volume 1 described the models and correlations in WCOBRA/TRAC-TF2 that are used to calculate the entrainment and de-entrainment processes. A summary of the applicable models in WCOBRA/TRAC-TF2 is provided for reader convenience in Section 19.2.1 herein.

As discussed in the previous Section 19.1, the predictive capability of WCOBRA/TRAC-TF2 for entrainment and de-entrainment phenomena needs to be assessed for the following conditions:

1. Upper Plenum Entrainment and Carryover – WCOBRA/TRAC-TF2 simulations were performed for tests that provided information on the net effects of entrainment/de-entrainment and carryover in the upper plenum. Applicable simulations include UPTF Test 29B, CCTF 62 and LOFT tests (LOFT analysis is presented in Section 22). UPTF Test 29B simulated the conditions in the upper plenum during reflood, and provided measurements of liquid level above the upper core plate. The UPTF upper plenum was full-scale in both height and cross section. The main purpose of Test 29B was to determine the amount of upper plenum de-entrainment and carryover. The WCOBRA/TRAC-TF2 simulation of this test is described in Section 19.3.
2. Downcomer Entrainment, during ECC Bypass Period and During Reflood – During the latter part of blowdown, ECC fluid injected into the cold legs begins to penetrate and fall into the downcomer. Partial penetration may occur, as liquid falls part way down the downcomer but is then swept back to the broken cold leg. As the steam flow rates in the downcomer decrease, liquid can eventually reach the lower plenum. Evaluations by Siemens of UPTF bypass tests showed that the ECC delivery to the lower plenum is multi-dimensional in nature. The fraction of ECC liquid reaching the lower plenum depended not only on the steam flow rate, but also on the relative location of the ECC downcomer entry point to the broken loop (Glaeser, 1992). In addition to determining the downcomer flooding limit, the five subphases of UPTF Test 6 are selected to evaluate the ability of WCOBRA/TRAC-TF2 to predict entrainment and de-entrainment phenomena that occur in a downcomer during the blowdown and early refill periods of a LOCA. These tests and the WCOBRA/TRAC-TF2 simulations of them are described in Section 19.3.

Downcomer entrainment is also an important process during the reflood phase. During reflood, the liquid level in the downcomer can oscillate and reach up to the level of the bottom of the cold legs. Liquid can be swept from the downcomer out of the break during these oscillations. While the liquid level is below the cold legs, drops can be entrained from the liquid pool and carried out the break if high steam flows occur around the downcomer. UPTF Test 25A was conducted in order to investigate entrainment and downcomer level behavior during the reflood phase of a

large break LOCA. The simulation of UPTF 25A using WCOBRA/TRAC-TF2 is described in Section 19.3.

3. Entrainment in the Core During Bottom Reflood – The correlation used to determine the entrainment rate at a quench front is described in Section 5.6 of Volume 1. The model is consistent with the work of Kataoka and Ishii (1983) and assumes the entrainment is due to vapor bubbling through a pool of liquid. The FLECHT reflood test simulations provide a means of examining the performance of the entrainment model for bottom reflood. Mass balances were calculated from the test data so that carryout fraction and mass retention in the test bundle could be estimated. Section 19.5 compares the WCOBRA/TRAC-TF2 predictions of carryout fraction, total bundle mass, steam exit flow, and liquid outflow to estimates derived from the FLECHT test data. The comparisons provide a means of assessing the bottom reflood entrainment model.

### Condensation

Section 6 of Volume 1 described the models and correlations in WCOBRA/TRAC-TF2 that are used to calculate the condensation processes (interfacial heat and mass transfer models). Section 6.2 describes the treatment of interfacial heat and mass transfer in the vessel component, while Section 6.3 addresses 1D components. The effect of non-condensable is described in Sections 6.2.11 and 6.3.7 for the respective vessel component and 1D components.

As discussed in the previous Section 19.1, the predictive capability of WCOBRA/TRAC-TF2 for condensation phenomena needs to be assessed for the following conditions:

1. Condensation in Downcomer Annulus – Condensation in the downcomer is an important contributor to the end of bypass/beginning of refill in a large break LOCA. Condensation in the downcomer of the full-scale UPTF facility is evaluated in Section 19.3, where WCOBRA/TRAC-TF2 results are compared to experimental data for the UPTF Test 6 series.
2. Condensation in Cold Legs, at both High and Low Pressure – Condensation in the cold legs was evaluated in Section 17. Condensation in the presence of safety injection at high pressures, representative of a small break LOCA, was assessed using data from the Westinghouse and Framatome COSI configurations, and the ROSA facility. Condensation at low pressures, representative of a large break LOCA, was assessed using data from UPTF Test 8A. The effect of condensation in both the cold legs and downcomer is also examined with respect to the sweep-out phenomena during reflood by examining UPTF test 25A. The assessment of code predictions against UPTF 8A and UPTF 25A is presented in Section 19.3
3. Effect of Non-Condensable Gases on Condensation – Accumulator nitrogen injection was part of the LOFT and ACHILLES experiments, and the WCOBRA/TRAC-TF2 assessment results are discussed in Section 20. Additional assessment of the effect of non-condensables is provided via numerical “thought problems” in Section 23.

## Integral Effects Assessment

CCTF is an integral effects test to evaluate the combined effect of CCFL in the tie plate, upper plenum de-entrainment, steam binding in steam generators, condensation in the cold leg and downcomer, entrainment/de-entrainment in the downcomer, and entrainment in the core, for the reflood phase of large break LOCA. The modeling, simulation and assessment of CCTF 62 are presented in Section 19.6.

### 19.2.1 WCOBRA/TRAC-TF2 Models for Entrainment

Section 5.6 of Volume 1 described the models and correlations in WCOBRA/TRAC-TF2 that are used to calculate the entrainment and de-entrainment processes. Entrainment is the result of interfacial shear between vapor and liquid film. In WCOBRA/TRAC-TF2, liquid is moved from the continuous liquid field to the entrained field when the interfacial shear forces acting on the liquid are sufficient. In de-entrainment, liquid is moved from the entrained field to the continuous liquid field. A summary of the applicable models in WCOBRA/TRAC-TF2 is as follows:

1. Entrainment in Film Flow – WCOBRA/TRAC-TF2 determines film entrainment rates by comparing the entrainment rate based on a stable film flow to an empirical entrainment rate based on the work of Walley et al. (1973).
2. Entrainment in Bottom Reflood – The model for entrainment in the core near the quench front is based on a model by Kataoka et al. (1983) assuming vapor bubbling through a liquid pool.
3. Entrainment in Top Down Reflood – Models describing the transfer of liquid from the continuous liquid to the entrained drop field is described in Section 5.6.4 of Volume 1. The models account for the entrainment of liquid draining from pools and the entrainment of films from the rods at a top down quench front.
4. De-Entrainment in Film Flow – The model to estimate the de-entrainment of entrained drops into the continuous liquid field uses an empirical model by Cousins et al. (1965).
5. Crossflow De-Entrainment – Entrained liquid in the upper plenum can de-entrain on structures there as the two-phase mixture flows from the vessel into the hot legs. WCOBRA/TRAC-TF2 uses a model based on experiments by Dallman and Kirchner (1980) to determine the amount of de-entrainment in the upper plenum and other regions of the reactor vessel.
6. De-Entrainment at Area Changes – De-entrainment occurs as a two-phase mixture encounters a flow restriction such as a tie plate. WCOBRA/TRAC-TF2 uses a simple area ratio to de-entrain a fraction of the droplet field where an area reduction occurs in the reactor vessel.
7. De-Entrainment at Solid Surfaces and Liquid Pools – Drops are assumed to de-entrain when the drops flow into a cell with a solid surface at the opposite face, or when the drops flow into a cell which is in a bubbly flow regime.

## 19.3 UPPER PLENUM TEST FACILITY TESTS

### 19.3.1 Introduction

The Upper Plenum Test Facility (UPTF) was designed to obtain experimental data relative to the multi-dimensional flows expected in a PWR during a Loss-of-Coolant Accident (LOCA). The UPTF was the German contribution to the 2D/3D program established by the United States (NRC), Japan (JAERI) and the Federal Republic of Germany (BMFT). Tests conducted in the UPTF gave special consideration to:

1. Entrainment and de-entrainment in the upper plenum,
2. Co-current and countercurrent two-phase flow in the upper core plate and tie plate region,
3. Co-current and countercurrent flow and bypass in the downcomer, and
4. Condensation and steam/water mixing processes caused by ECC injection in the cold legs.

This section describes the modeling and simulation of several of the UPTF experiments using WCOBRA/TRAC-TF2. The simulations used were Tests 6 (to evaluate the ability of the code to predict ECC bypass), Test 25A (to evaluate entrainment of liquid out of the downcomer due to steam flow during reflood and condensation in cold leg and downcomer), Test 8A (to evaluate the models and correlations for condensation in the cold leg), and Test 29B (to validate the models for calculating de-entrainment in the upper plenum).

An overall facility description is provided in Section 19.3.2. The ECC bypass, and entrainment/de-entrainment in downcomer and the simulations of UPTF 6 are described in Sections 19.3.3 to 19.3.5, while the upper plenum de-entrainment in UPTF 29B is described in Sections 19.3.12 to 19.3.14. The cold leg condensation and the simulation of UPTF 8A are described in Sections 19.3.6 to 19.3.8. The downcomer entrainment/de-entrainment and cold leg condensation in UPTF 25A is described and simulated in Sections 19.3.9 to 19.3.11.

### 19.3.2 UPTF Facility Description

The UPTF simulated a full-scale 3900 MWt German PWR. The facility had four loops, each with a steam/water separator to simulate a steam generator and a variable resistance to simulate a reactor coolant pump. The upper plenum contained full size internals in an arrangement typical of a KWU PWR. Figures 19.3-1 and 19.3-2 show an overall diagram of the UPTF.

The upper plenum test facility was designed to investigate:

1. Water entrainment and separation processes in the upper plenum,
2. Co-current and countercurrent steam/water flow phenomena in the upper core plate or tie plate region including water break-through into the core,
3. Co-current and countercurrent steam/water flow in the downcomer and possible bypass of the ECC water injected into the cold legs of the loops to the break nozzle,

4. Condensation and mixing processes in the hot and cold legs of the loops, in the upper plenum and in the downcomer as a result of the injection of cold ECC water and,
5. Loop behavior with regard to possible water plug formation and oscillations in the hot and cold legs of the loops with ECC injection.

This range of investigation was achieved by varying the configuration of the facility. Full details of the facility and its instrumentation are given in Emmerling et al. (1988).

There were three intact loops and one loop with a break in the cold leg. The loop break was represented by gate valves and orifice plates to control the flow and a containment simulator gave the desired back pressure. The broken loop cold leg contained a water separator to prevent water from entering the containment simulator. The steam generators were simulated by four steam/water separators and adjustable passive resistances were used to simulate the four reactor coolant pumps. The facility did not contain a heated core, but the internals at the top of the core and in the upper plenum were full-scale replicas. The core itself was simulated by a steam/water injection system to set up the appropriate flow conditions in the vessel. The tubes that deliver the fluid to the core came up through the lower plenum.

The reactor vessel is shown in Figure 19.3-3. The upper plenum contained sixty-one guide tubes, eight support columns above the simulated fuel assemblies and eight support columns outside the periphery of the core (Figure 19.3-4). The downcomer gap width was 0.25 meters (9.8 inches) and the vessel internal diameter was 4.87 meters (191.7 inches).

The UPTF facility simulated the upflow of steam and droplets through the core during reflood by injection of steam and water into dummy fuel rods. The dummy fuel rods represented the upper quarter of a core with 193 assemblies of 16x16 array of fuel rods. Sixty-one of the assemblies were below guide tubes and had control rod spider simulators (Figure 19.3-5). The remaining assemblies were below flow restrictors in the upper core plate. The water and steam injection nozzles are shown in Figure 19.3-6. There were seventeen independently controlled injectors which divided to provide a separate nozzle for each dummy fuel rod assembly.

The dummy control rods terminated at the bottom of the guide tubes which were sealed to prevent flow from the upper plenum to the upper head. The upper head was thereby isolated from the rest of the vessel and had no effect on the facility.

The UPTF cold legs had an inner diameter of 750 millimeters. The ECC injection was at an angle of 60° to the cold leg centerline in UPTF and was 5822 millimeters (19.1 feet) from the inside wall of the vessel.

The steam generator simulators for the intact and broken loops and the broken cold leg water separator are shown in Figure 19.3-7. Flow entered an inlet plenum, which had the same volume as a PWR steam generator, and rose through cyclone tubes. The cyclones separated the water from the steam and the water was removed from the loop. The steam flowed through the steam generator upper plenum and returned to the cold leg.

The water drainage system removed the large quantities of water that accumulated during a test. Generally these quantities were found in the test vessel, the steam generator simulators, the broken cold leg water separator, and in the drainage vessels of the broken loops.

The raw data produced from the instrumentation was continuously recorded throughout a test, some of which was post-processed to give computed parameters. An example of a computed parameter derived from raw data is liquid level, which is derived from the measurement of differential pressure.

The downcomer was instrumented with fluid distribution grids, turbine meters, differential and absolute pressure transducers, and fluid and wall thermocouples. The lower plenum and core regions were instrumented with optical liquid level detectors, differential pressure transducers, and fluid and wall thermocouples. The instrumentation in the upper plenum included:

1. Wall and fluid thermocouples,
2. Fluid thermocouples in end boxes and below tie plate,
3. Differential pressure transducers across the tie plate,
4. Differential pressure transducers and capacity liquid level detectors in upper plenum,
5. Optical liquid level detectors and fluid distribution grids,
6. Video probes in upper plenum,
7. Break-through detectors below tie plate,
8. Tie plate drag bodies in end boxes and,
9. Turbine meters in end boxes and in upper plenum.

#### **19.3.2.1 Scaling Consideration and Applicability to PWR**

The cold leg and the test vessel upper plenum, the lower plenum, and the downcomer of the UPTF facility are geometrically similar to a PWR. Table 19.3-1 compares the major dimensions of UPTF facility with a typical Westinghouse 4 loop PWR, which is referred as typical PWR in the following discussions. Comparisons of the primary system components are summarized below together.

##### **Downcomer**

The downcomer dimensions below the cold legs (e.g., gap, diameter, length, and flow area) are basically the same for UPTF and the typical PWR. The vessel wall of the UPTF facility is thinner than that of typical PWR.

##### **Cold Leg**

The cold leg piping diameters are fairly similar between UPTF and the typical PWR (0.75 m vs. 0.70 m). The UPTF cold leg flow area is only 15% larger than that for the typical PWR. The distance from the ECC nozzle to the downcomer at UPTF is 30% longer than that at the typical PWR. A longer mixing region in the cold leg may result in more condensation at UPTF than at a PWR. The ECC nozzle diameters are comparable between UPTF and typical PWR. For typical PWR, the ECC nozzles are typically located on top of the cold leg with injection angle of 90°. In UPTF facility, the nozzle lies in a horizontal plane at an angle of 60° from the cold leg piping.

## Reactor Core

UPTF did not have an active core, but there were 193 16x16 dummy fuel assemblies on top of the core, which is similar to the core of a typical PWR (193 15x15 fuel assemblies). As for flow area, UPTF has a core flow area of 1.05 times the core flow area of a typical PWR.

## Upper Plenum

The ratio of the UPTF upper plenum flow area to that of typical PWRs is around 1.2. It should be noted that the exact configuration and arrangement of the upper plenum structures are plant specific. The height of upper plenum in the UPTF facility is only about 0.67 of that in typical PWR because of the shorter distance from the hot leg nozzle to the upper support plate in UPTF. The height difference is not expected to be important for the assessment of the entrainment/de-entrainment in the upper plenum.

## Hot Leg

The hot leg diameter at UPTF is slightly larger than that at typical PWRs, while the flow area of an UPTF hot leg is less than the flow area of a typical PWR hot leg. This is because the flow area of the UPTF hot leg is reduced by an internal ECC injection pipe (called Hutze in UPTF). The difference of the hot leg between UPTF and typical PWR is judged inconsequential for the assessment.

UPTF 6, UPTF 8A, UPTF 25A, and UPTF 29B are utilized for the assessment in this section. The test conditions and the applicability of the test are analyzed below.

### UPTF 6

[

]<sup>a,c</sup>

### UPTF 25A

[

]<sup>a,c</sup>

[

] <sup>a,c</sup>

UPTF 8A

[

] <sup>a,c</sup>

UPTF 29B

[

] <sup>a,c</sup>

### 19.3.3 UPTF 6 ECC Bypass and Downcomer Countercurrent Flow Test Descriptions

During the blowdown phase of a large cold leg break LOCA, the reactor vessel rapidly depressurizes, causing most of the liquid inventory to flash into steam. This steam and entrained water flow up the downcomer and out the broken cold leg. After the system has partially depressurized, ECC is injected into the intact cold legs. The resulting counter-current steam/water flow in the downcomer is important since it affects how quickly the reactor vessel refills. As the pressure in the reactor vessel begins to reach an equilibrium state with the containment pressure, the steam flow is reduced and the ECC starts to fill the vessel and reflood the core. The objective of UPTF Test 6 was to investigate ECC penetration and counter-current flow phenomena in the downcomer of a PWR during the end of blowdown and refill portions of a LOCA. In addition to determining the downcomer flooding limit, simulation of these tests also evaluates the ability of WCOBRA/TRAC-TF2 to predict entrainment and de-entrainment phenomena in a downcomer during blowdown and early refill. The assessment of the condensation efficiency in the downcomer is also part of the objective of UPTF 6 simulations.

The system configuration of UPTF Test 6 is shown in Figure 19.3-8; the pump simulators were closed and only the cold leg break valve was opened. Steam was injected in the core simulator and steam generator simulator. Because flow paths to the intact cold leg and broken hot leg were blocked, the steam was forced to flow downward through the lower plenum, up the downcomer, and out the vessel through the broken cold leg. ECC water was injected to each intact cold leg.

A summary of test boundary conditions for UPTF-6 is given in Table 19.3-2. In UPTF Test 6, five steady-state runs were conducted with steam flows of 102, 203, 295, 396, and 439 kg/s to establish points on a flooding curve for UPTF. Steam injection was to both the core and steam generator simulators except for the low steam flow run during which injection was only to the core. ECC water was injected at approximately 500 kg/s to each of the three intact cold legs. The subcooling of ECC water varied from 28 to 65 K. The containment pressure was maintained around 2.5 bar except 135, where pressure was 3.4 bar.

### 19.3.4 WCOBRA/TRAC-TF2 Model for UPTF Test 6

The WCOBRA/TRAC-TF2 model VESSEL component for the calculations to compare to UPTF Test 6 simulations is shown in Figures 19.3-9 through 19.3-13. [

] <sup>a,c</sup>

The WCOBRA/TRAC-TF2 loop model used for the UPTF Test 6 transient calculations is shown in Figure 19.3-14. In the test facility, the broken loop is a piping system leading from the vessel to a steam water separator and then to the containment simulator (Figure 19.3-1). A simplified model was used to simulate UPTF Test 6. [

] <sup>a,c</sup>

The intact cold legs were represented by PIPE components, and the ECC was modeled as a boundary condition applied through the FILL components. The broken loop was represented by one PIPE component. The pressure at the broken loop flowmeter was specified by a BREAK component.

### 19.3.5 Simulation of UPTF Test 6

UPTF Test 6 was run in five separate sub-phases, each sub-phase with a different combination of liquid and steam injection rates. The intact loops were blocked at the pump simulators, forcing all steam down through the lower plenum and up the downcomer to the broken cold leg.

The results of the five tests UPTF 6-131, 132, 133, 135, and 136 are presented in the following sections. As discussed in Section 19.2, the UPTF 6 simulation with WCOBRA/TRAC-TF2 is used specifically to assess the code capability with regards to three specific processes: (1) ECC Bypass in the downcomer (CCFL); (2) entrainment and de-entrainment in the downcomer during ECC Bypass and (3) condensation in the downcomer. The discussion of CCFL during ECC bypass, entrainment and de-entrainment during ECC bypass, and condensation efficiency in the UPTF 6 tests is also given in this section.

#### 19.3.5.1 UPTF 6-131

The total core steam injection flow for Run 131 is shown in Figure 19.3-15, and the steam generator injection flows is shown in Figure 19.3-16. The ECC injection to each of the intact cold legs is shown in Figure 19.3-17. These as-measured injection flow rates were used as boundary conditions in the WCOBRA/TRAC-TF2 model for Run 131. The measured pressure at the pipe flow meter was applied to the BREAK component as the boundary condition.

The WCOBRA/TRAC-TF2 simulation was run for 100 seconds, which corresponds to the test time period of 30 to 130 seconds for Run 131. [

] <sup>a,c</sup>

[

] <sup>a,c</sup>

[

] <sup>a,c</sup>

### 19.3.5.2 UPTF 6-132

The total core steam injection flow for Run 132 is shown in Figure 19.3-33, and the steam generator injection flows in Figure 19.3-34. The ECC injection to each of the intact cold legs is shown in Figure 19.3-35. These as-measured injection flow rates were used as boundary conditions in the WCOBRA/TRAC-TF2 model for Run 132. The measured pressure at the pipe flow meter was applied to the BREAK component as the boundary condition.

The WCOBRA/TRAC-TF2 simulation was run for 100 seconds, which corresponds to the test time period of 31 to 131 seconds for Run 132. [

] <sup>a,c</sup>

[

] <sup>a,c</sup>

### 19.3.5.3 UPTF 6-133

The total core steam injection flow for Run 133 is shown in Figure 19.3-51, and the steam generator injection flows in Figure 19.3-52. The ECC injection to each of the intact cold legs is shown in Figure 19.3-53. These as-measured injection flow rates were used as boundary conditions in the WCOBRA/TRAC-TF2 model for Run 133. The measured pressure at the pipe flow meter was applied to the BREAK component as the boundary condition.

The WCOBRA/TRAC-TF2 simulation was run for 100 seconds, which corresponds to the test time period of 30 to 130 seconds for Run 133. [

] <sup>a,c</sup>

[

] <sup>a,c</sup>

#### 19.3.5.4 UPTF 6-135

The total core steam injection flow for Run 135 is shown in Figure 19.3-69, and the steam generator injection flows in Figure 19.3-70. The ECC injection to each of the intact cold legs is shown in Figure 19.3-71. These as-measured injection flow rates were used as boundary conditions in the WCOBRA/TRAC-TF2 model for Run 135. The measured pressure at the pipe flow meter was applied to the BREAK component as the boundary condition.

The WCOBRA/TRAC-TF2 simulation was run for 100 seconds, which corresponds to the test time period of 30 to 130 seconds for Run 135. [

] <sup>a,c</sup>

[

] <sup>a,c</sup>

### 19.3.5.5 UPTF 6-136

The total core steam injection flow for Run 136 is shown in Figure 19.3-87. The ECC injection to each of the intact cold legs is shown in Figure 19.3-88. No steam was injected through the steam generator simulators in this run. These as-measured injection flow rates were used as boundary conditions in the WCOBRA/TRAC-TF2 model for Run 136. The measured pressure at the pipe flow meter was applied to the BREAK component as the boundary condition.

The WCOBRA/TRAC-TF2 simulation was run for 100 seconds, which corresponds to the test time period of 30 to 130 seconds for Run 136. [

] <sup>a,c</sup>

### 19.3.5.6 ECC Bypass in UPTF 6: CCFL in Downcomer Annulus

The amount of ECC water which penetrated into the lower plenum during the UPTF 6 tests was obtained by converting a pressure difference to the lower plenum inventory (2D/3D, 1989) or performing a mass balance on the lower plenum (2D/3D, 1989) or the vessel (MPR-1163, 1990). Three different methods have been used to estimate the test ECC penetration flow rate:

Method 1: Lower plenum refill rate converted from measured pressure difference between the bottom of lower plenum and the top of lower plenum (direct way), as determined by Siemens (2D/3D, 1989).

Method 2: Lower plenum refill rate estimated from a mass balance (indirect way), as determined by Siemens (2D/3D, 1989).

Method 3: Vessel refill rates estimated from vessel liquid accumulation (direct way) and mass balance (indirect way), as determined by MPR (MPR-1163, 1990).

The ECC penetration rate was estimated for a certain period of time during the test, called the evaluation time period. The evaluation time period over which the pressure measurement or mass balance was taken extended from the point where full steam and water flow were established in the test, to the point where the lower plenum filled with liquid. The ECC penetration rate was then calculated as the average accumulation rate over this time period.

The evaluation period and refill rate of Method 1 are obtained from Table 4 in UPTF 6 test report (2D/3D, 1989), and lower plenum inventory of Runs 131, 132, 133, 135, and 136 are obtained from Tables 5, 6, 7, 8, 9, and 10 of the UPTF 6 test report (2D/3D, 1989), respectively. The evaluation period, lower plenum inventory, and refill rate of Method 1 are summarized in Table 19.3-3.

The evaluation period of Method 2 is the same as that of Method 1, and the refill rate of Method 2 is also obtained from Table 4 of the UPTF 6 test report (2D/3D, 1989). The evaluation period, lower plenum inventory, and refill rate of Method 2 are summarized in Table 19.3-4. It is noted that no refill rate of Method 2 is available for Run 135. There is no record of lower plenum inventory from Method 2. Instead, the lower plenum inventory at the beginning of evaluation period is assumed the same as that from Method 1. The lower plenum inventory at the end of evaluation period is evaluated from the inventory at the beginning, the length of the evaluation period, and the refill rate.

The difference between Method 1 and Method 2 is an indication that such estimates are affected by a large uncertainty.

The MPR report (MPR-1163, 1990) gives estimated vessel inventories from both measured pressure difference (direct way) and mass balance (indirect way) using Method 3. For estimation of the ECC penetration rate, the lower plenum inventory and the lower plenum refill rate are clearer indicators than the vessel inventory, which includes the downcomer inventory. Therefore, this report focuses on the comparison between the lower plenum refill rate from Method 1 and Method 2 and the WCOBRA/TRAC-TF2 prediction.

[

j<sup>a,c</sup>

The Countercurrent Flow Limitation (CCFL) behavior calculated by WCOBRA/TRAC-TF2 for UPTF Test 6 was evaluated by comparing the scaled Kutateladze number (UPTF scale) to the published data (Glaeser, 1992) and the following CCFL flooding curve suggested for UPTF (Glaeser, 1992):

$$\sqrt{K_g^*} + m\sqrt{K_l^*} = C \quad (19.3-1)$$

where  $K_g^*$  is the UTPF-scaled Kutateladze number  $K_g^* = \frac{K_g v_g^{2/3}}{g^{1/3} \left( \frac{l_2 + l_3}{2} \right)}$ ,  $m=0.011$  and  $C=0.0245$ .

The Kutateladze numbers are expressed as:

$$K_g = \frac{\dot{m}_s}{\sqrt{\rho_g} A_{DC} (g\sigma(\rho_l - \rho_g))^{1/4}} \quad (19.3-2)$$

$$K_l = \frac{\dot{m}_l}{\sqrt{\rho_l} A_{DC} (g\sigma(\rho_l - \rho_g))^{1/4}} \quad (19.3-3)$$

The symbols  $\dot{m}_s$  and  $\dot{m}_l$  are the steam mass flow rate and liquid mass flow rate, respectively, the phasic density is  $\rho$ , the surface tension is  $\sigma$ , and  $g$  is the gravitational acceleration. The value  $A_{DC}$ ,  $l_2$ , and  $l_3$  are geometry information of UPTF facility.

Table 19.3-7 presents the results of the calculation of Kutateladze numbers for both the experimental data and the WCOBRA/TRAC-TF2 prediction. The steam flow rates in Table 19.3-7 are the actual steam flow rates of the UPTF 6 tests in Table 19.3-5. The actual steam flow rate also served as the boundary condition for the prediction. Therefore, the Kutateladze number of the steam flow is the same for both the experiment and the prediction.

[

] <sup>a,c</sup>

### 19.3.5.7 Entrainment and De-Entrainment in the Downcomer During ECC Bypass

In the previous discussion, the lower plenum mass inventory was analyzed to assess the prediction of CCFL in a downcomer annulus during ECC bypass. In the following discussion, comparisons of the estimated and predicted mass distributions in the UPTF Test 6 series are used to assess the prediction of net entrainment/de-entrainment effects. The correctness of the prediction of net entrainment/de-entrainment requires the correct prediction of the vessel mass, and the correct prediction of the mass flow rate to the broken loop, with the condition of the same total ECC injection and steam injection.

In Run 131, steam was injected into the core simulators and the steam generator simulators at a combined initial rate of nearly 400 kg/sec. ECC was injected into each intact cold leg at a rate of 482 kg/sec. Figure 19.3-112 shows the estimated mass distribution for Run 131. Shortly after the start of ECC injection, fluid mass began to collect in the vessel. Later in time, after about 60 seconds, the rate of mass retention in the vessel increased. The vessel inventory leveled off, until after 65 seconds, when it began to increase more rapidly indicating that CCFL breakdown occurred. Figure 19.3-113 shows the WCOBRA/TRAC-TF2 prediction of the mass distribution during Run 131. For Run 131,

[

] <sup>a,c</sup>

In Run 132, the steam was injected into the core simulators and the steam generator simulators at a combined initial rate of nearly 300 kg/sec. The ECC was injected into each intact cold leg at a rate of 490 kg/sec. Figure 19.3-114 shows the estimated mass distribution for Run 132. Shortly after the start of ECC injection, the fluid mass began to slowly collect in the vessel. Later in time, between 60 and 67 seconds, the rate of mass retention in the vessel increased but then leveled off for the remainder of the test. Figure 19.3-115 shows the WCOBRA/TRAC-TF2 prediction of the mass distribution during Run 132. [

] <sup>a,c</sup>

Figures 19.3-116 and 19.3-117 compare the estimated and predicted mass distributions in Run 133. In this run, the steam was injected into the core simulators and the steam generator simulators at a combined initial rate of 203 kg/sec. ECC was injected into each intact cold leg at a rate of 491 kg/sec. [

] <sup>a,c</sup>

The estimated and predicted mass distributions for Run 135 are shown in Figures 19.3-118 and 19.3-119, respectively. Shortly after the start of ECC injection, the fluid mass began to collect rapidly in the vessel in the experiment. The estimated vessel mass became erratic for a brief period, actually decreasing near 55 seconds. [

] <sup>a,c</sup>

Figures 19.3-120 and 19.3-121 compare the estimated and predicted mass distributions in Run 136. In this subphase, steam was injected into the core simulator at an initial rate of 102 kg/sec. This was the lowest steam injection rate of the five runs. ECC was injected into each intact cold leg at a rate of 490 kg/sec. After 50 seconds, the vessel inventory was estimated to have increased steadily for the rest of the test.

[

] <sup>a,c</sup>

[ ]<sup>a,c</sup>

**19.3.5.8 Condensation Efficiency in UPTF 6**

The UPTF Test 6 series also gave consideration to the steam-water interaction in the downcomer. The steam-water interaction calculation with WCOBRA/TRAC-TF2 is reflected by the condensation efficiency calculation.

Condensation efficiencies were estimated by MPR (MPR-1163, 1990) for the UPTF flooding test series using two methods. The condensation efficiency was calculated in two ways. In Method 1, the efficiency is defined as [

$$\left[ \frac{\text{a,c}}{\text{a,c}} \right] \quad (19.3-4)$$

[

] <sup>a,c</sup>

The second method measured [

$$\left[ \frac{\text{a,c}}{\text{a,c}} \right] \quad (19.3-5)$$

[

] <sup>a,c</sup>

[

]<sup>a,c</sup>

The WCOBRA/TRAC-TF2 predicted condensation efficiencies for UPTF 6 Runs 131 to 136 were obtained from Equation 19.3-5, [

]<sup>a,c</sup>

### 19.3.5.9 DTMAX Sensitivity Study for UPTF 6

[

] <sup>a,c</sup>

### 19.3.5.10 Cold Leg Nozzle Loss Coefficient of UPTF 6

[

] <sup>a,c</sup>

A detailed analysis of the pressure drops in the broken cold leg from CCTF tests was performed, and a nozzle loss coefficient of 0.5 was estimated (Akimoto et al., 1984). UPTF ECC bypass (Test 6) data were examined here in more detail to determine whether they could be used to better define the value to be used in the PWR. There exists a short period of single-phase steam flow in UPTF before the ECC is injected into the cold legs. Using the measured steam flow, pressure, temperature, and measured differential pressure, a cold leg nozzle unrecoverable loss can be calculated from the extended Bernoulli Equation for a number of run points from UPTF Test 6.

#### 19.3.5.10.1 Data Reduction for the Cold Leg Nozzle Loss Coefficient

The calculation approach used in this analysis was to write the extended Bernoulli Equation between the pressure taps for pressure cell [ ] <sup>a,c</sup> which is shown on Figure 19.3-131. This cell spans the broken cold leg nozzle from the upper downcomer region to a point [ ] <sup>a,c</sup> down the broken cold leg.

The extended Bernoulli Equation (or Mechanical Energy Equation) is written as:

$$\frac{P_2 - P_1}{\rho} + \frac{U_2^2 - U_1^2}{2g_c} + \frac{fL}{D} \frac{U_2^2}{2g_c} + k_N \frac{U_2^2}{2g_c} + \frac{(Z_2 - Z_1)g}{g_c} = 0 \quad (19.3-6)$$

The first term is the static pressure change, the second term represents the kinetic energy change, the third term is the frictional drop in the cold leg, the fourth term represents the unrecoverable loss of the nozzle, both contraction and turning loss. The last term represents the potential energy change, and is set to zero since the flow is horizontal. Equation 19.3-6 assumes flow to be incompressible, which is a reasonable approximation for the purpose of this analysis.

The steam flow, pressure drop, steam temperature, and absolute pressure were taken directly from the data, and were averaged over the single-phase period. The friction factor was taken from the Moody chart for smooth pipes using the cold leg Reynolds number (Figure 19.3-132). The single-phase friction was used over the length of the cold leg up to the pressure tap.

Solving Equation 19.3-6 for the nozzle cold leg loss coefficient, where state 2 is the cold leg and state 1 is the downcomer annulus, results in:

$$K_N = - \frac{\left[ \left( \frac{P_{CL} - P_{DC}}{\rho} \right) + \frac{U_{CL}^2 - U_{DC}^2}{2g_c} + \frac{fL_{CL}}{D_{CL}} \frac{U_{CL}^2}{2g_c} \right]}{\frac{U_{CL}^2}{2g_c}} \quad (19.3-7)$$

The data for the steam mass flow rate, downcomer pressure, and steam temperature were taken from the UPTF data report (2D/3D, 1989). The selected values of the measured parameters are given in Tables 19.3-12 and 19.3-13. The data which was used to obtain these values are shown in Figures 19.3-133 to 19.3-142, and the selected values are indicated on the figures. [

] <sup>a,c</sup>

The steam mass flow values reflect the sum of the steam flow injected from the core simulator as well as the steam generator simulators. The measured broken cold leg steam flow was the measurement used to calculate the cold leg velocity in this analysis. The cold leg steam temperatures and the downcomer pressure minus one-half the pressure drop were used to calculate the effective density which was used in Equation 19.3-7.

Table 19.3-14 gives calculated thermal-hydraulic values for the different runs of Test 6. The broken cold leg velocity was calculated using the average density in Table 19.3-14 and the cold leg inside diameter  $D_{CL}=750$  mm (2.46 ft). That is:

$$U_{CL} = \frac{\dot{m}}{\rho A_{CL}} = \frac{\dot{m}}{\rho \left( \frac{\pi D_{CL}^2}{4} \right)} \quad (19.3-8)$$

where the cold leg area is:

$$A_{CL} = \frac{\pi D_{CL}^2}{4} \quad (19.3-9)$$

The cold leg Reynolds number was calculated from the cold leg velocity, cold leg diameter and the average steam density and viscosity as:

$$\text{Re}_{\text{CL}} = \frac{U_{\text{CL}} \bar{\rho} D_{\text{CL}}}{\mu_{\text{CL}}} \quad (19.3-10)$$

The cold leg Mach number was then calculated using the following value for the speed of sound,

$$C_{\text{CL}} = \sqrt{\gamma R (\bar{T}_{\text{CL}} + 460^{\circ}\text{R})} \quad (19.3-11)$$

where:

$$\gamma = 1.25 \text{ for steam}$$

$$R = 85.7 \frac{\text{ft} \cdot \text{lb}_f}{\text{lbm} \cdot ^{\circ}\text{R}} \text{ for steam}$$

the Mach number is then:

$$M_{\text{CL}} = \frac{V_{\text{CL}}}{C_{\text{CL}}} \quad (19.3-12)$$

The cold leg friction factor was taken from the Moody chart shown in Figure 19.3-132. A value of roughness for commercial pipe ( $\epsilon = 0.00015$  ft) was used. The  $\epsilon/D$  value for the UPTF cold leg is then:

$$\left[ \begin{array}{c} \text{a,c} \\ \phantom{\text{a,c}} \end{array} \right]$$

The steam density values calculated using the average pressure between the cold leg and the downcomer, and the cold leg temperature were found to agree with the cold leg density values estimated by MPR (1989).

The results of these calculations are summarized in Table 19.3-15. [

]<sup>a,c</sup> The average loss coefficient is recommended for the broken cold leg nozzle of IETs, SETs and plant models. The uncertainty of cold leg nozzle loss coefficient (KN) for plant models is discussed in Section 29.1.2.1.

#### 19.3.5.10.2 Nozzle Loss Assessment

The estimated average loss coefficient 0.54 has been applied to the broken cold leg nozzle in UPTF 6 input models in Section 19.3.4. Next, the predicted pressure loss across the broken cold leg nozzle is compared with the measured pressure loss. [ ]<sup>a,c</sup>

[

] <sup>a,c</sup>

In summary, an average broken cold leg nozzle loss coefficient of 0.54 is generated from UPTF 6 test data. The average loss coefficient 0.54 is applied to the broken cold leg nozzle in the UPTF 6 input models. [

] <sup>a,c</sup>

### 19.3.6 UPTF 8A Cold Leg Condensation Test Descriptions

The UPFT test facility is discussed in detail in Section 19.3.2. The components relevant to condensation in the cold leg are discussed in more detail below.

The cold leg flow regime tests focused on behavior in the cold legs in the region of ECC injection. This region is bounded by the reactor coolant pump simulator and the test vessel downcomer as shown in Figure 19.3-149. The cold leg piping has an internal diameter of 750 mm (29.5 inches) and each loop is 9181 mm (30.1 feet) long from the reactor coolant pump simulator outlet to the inner surface of the test vessel wall at the downcomer. The diameter of safety injection line is 222.5 mm.

The distance from the ECC nozzle to the downcomer is 30% longer at UPTF than at typical PWRs. The ECC nozzle diameters are comparable with the UPTF nozzle diameter slightly smaller (by no more than 16%). The most significant difference is that UPTF uses side injection whereas typical PWRs, generally use top injection.

#### Test Conditions

For UPTF Test 8 steam was injected only in the core simulator and flowed through the loops. ECC was injected into the cold leg of Loop 2. The steam injection rate was relatively constant while the ECC flow rate was decreased in steps. Each ECC flow rate was maintained for about 30 seconds to allow steady-state conditions to be established. The ECC flow rates covered the range of flows expected in a PWR during a large break LOCA. Test 8 had two phases with essentially the same conditions; the difference being that the pump simulator K-factor in Loop 2 was higher for Phase B than Phase A. This condition resulted in a slightly lower Loop 2 steam flow in Phase B compared to Phase A.

The steam flow in Loop 2 was held approximately constant due to Loop 3 being open to maintain a constant differential pressure across the reactor coolant loops. Loop 2 steam flow was maintained between 31 and 38 kg/sec throughout the test.

UPTF Test 8 was conducted in two major phases, each with two parts. In the first part of each phase ECC was injected to the Loop 2 cold leg, and in the second part the ECC injection went to the hot leg. Since there is not hot leg ECC injection to typical PWRs, and since the boundary conditions for Phase A (Run 112) and Phase B (Run 111) are similar, only the first part of Phase A was simulated with WCOBRA/TRAC-TF2. Figure 19.3-150 shows the system configuration for UPTF 8. The configurations of specific components are as follows:

- A water seal was maintained in the lower plenum of the test vessel to ensure the steam from the core simulator flows through the loops.
- Steam was injected through the test vessel core simulator.
- Loop 1 was blocked at the pump simulator.
- The Loop 2 pump simulator was set to provide a K factor of 10 based on a pipe diameter of 750 mm (29.5 inches).
- The Loop 3 pump simulator was set to provide a K factor of 18 based on a pipe diameter of 750 mm (29.5 inches).
- ECC was injected into the Loop 2 cold leg. No nitrogen was injected into the ECC water.
- The broken loop hot leg and broken loop cold leg were open to the containment simulator. The broken loop hot leg break valve was set to provide a K factor of 18.2 based on a pipe diameter of 750 mm (29.5 inches).

A summary of test boundary conditions for UPTF-8 is given in Table 19.3-16.

### Summary of Experimental Results

An observation on the temperature distribution in the cold leg in UPTF-8 is given in Figure 19.3-151. The flow regime and temperature stratification are clearly shown in Figure 19.3-151. The results of the UPTF cold leg flow regime separate effects tests indicate that plug flow only occurred when the condensation of the ECC exceeded the steam supply. At low steam flows, plug flow was unstable because the momentum of the steam flow was not sufficient to maintain the plug. The cyclic formation and decay of water plugs in unstable plug flow resulted in large pressure and flow oscillations. The test results also indicate that stratified flow always occurred when the steam supply exceeded the ECC condensation potential. In some cases, thermal stratification of the water layer in the bottom of the cold leg limited condensation to less than its maximum value and prevented total consumption of the steam.

The loop steam flow was completely condensed for plug conditions and only partially condensed for stratified flow conditions. The condensation efficiency (the ratio of condensation heat transfer rate to the condensation rate that would bring liquid to saturation temperature), during stratified flow conditions ranged from 80 to 100%. The efficiency was higher as ECC flow decreased or as steam flow increased.

### 19.3.7 WCOBRA/TRAC-TF2 Model for UPTF 8A

The validations against UPTF Test 8A serve as a separate effect test for the condensation in cold leg and downcomer during refill period and reflood period. The test is also part of validation for the cold leg condensation model discussed in Section 17. Two UPTF 8A models are developed. An integral UPTF 8A input model includes both vessel and loop structure of UPTF test facility. A simplified (separate effects) UPTF 8A TEE model documented in Section 17 only simulates the cold leg and the ECC line in UPTF 8A test. The UPTF 8A TEE model presented in Section 17 also serves as base model for the sensitivity studies on the ECC line injection angle, the cold leg nodding, the uncertainty of the cold leg condensation model and the uncertainty of the horizontal stratification model.

The integral UPTF 8A model presented here [

] <sup>a,c</sup>

### 19.3.8 Simulation of UPTF 8A

The WCOBRA/TRAC-TF2 simulation of UPTF Test 8 was run for the first 200 seconds of the test, which covered the period where flow was injected into loop 2 intact cold leg. The as-measured injection flow rates were used as boundary conditions in the WCOBRA/TRAC-TF2 model. The containment simulator was maintained at a constant pressure of 400 kPa (58 psia).

Since most of ECC injections were turned-off for Test 8, the condensation only exists in the intact loop 2. The WCOBRA/TRAC-TF2 simulation of Phase A (Run 112) modeled only the cold leg injection phase, so results after 200 seconds are not considered. The following comparison of WCOBRA/TRAC-TF2 results and UPTF Test 8A data considers the overall performance of the code and modeling of the facility. Note, the simulation of 200 seconds covers periods 1 through 6 in Table 19.3-16. The stage 7 is insignificant for the assessment because the ECC flow rate was too low related to the typical RHR flow.

[

J<sup>ac</sup>

[

] <sup>a,c</sup>

### 19.3.9 UPTF 25A Downcomer Entrainment/De-Entrainment and Cold Leg Condensation Test Descriptions

UPTF Test 25 was a quasi-steady state experiment to investigate entrainment/entrainment in downcomer and condensation in cold leg and downcomer during the reflood phase of a PWR LBLOCA. The UPTF test facility is discussed in detail in Section 19.3.2. Figure 19.3-164 shows the system configuration of UPTF Test 25.

The configurations of specific components are as follows:[

] <sup>a,c</sup>

UPTF Test 25 Phase A simulated conditions expected during the reflood phase of a large break LOCA. ECC was injected to the cold legs, while the steam flow through the UPTF was established by injecting steam in the steam generator simulators. UPTF 25 Phase B was similar to Phase A, but the vessel walls were not superheated and there was no waiting period between phases. Since UPTF 25A is more representative for the reflood period of a LBLOCA, only Phase A was simulated using WCOBRA/TRAC-TF2.

Table 19.3-17 lists the conditions for each Phase A sub-phase of Test 25.

### 19.3.10 WCOBRA/TRAC-TF2 Model for UPTF Test 25A

The vessel model for UPTF 25A is also similar to the vessel model for UPTF 6. [

] <sup>a,c</sup>

### 19.3.11 Simulation of UPTF Test 25A

The WCOBRA/TRAC-TF2 calculated transient corresponding to the UPTF Test 25A simulation is run for nearly the entire 900 seconds of the test. [

] <sup>a,c</sup>

The downcomer fluid temperatures at Level 28 are compared in Figures 19.3-170 and 19.3-171, while the downcomer fluid temperatures at Level 24 are compared in Figures 19.3-172 and 19.3-173. [

] <sup>a,c</sup>

[

] <sup>a,c</sup>

Figure 19.3-175 shows the measured and predicted axial differential pressure from the bottom of lower plenum to the middle of downcomer [ ] <sup>a,c</sup> and the axial differential pressure from the bottom of lower plenum to the top of downcomer [ ] <sup>a,c</sup> for UPTF 25-Phase A. The axial pressure difference is an indicator of the water level in the downcomer. [

] <sup>a,c</sup>

The measured and predicted axial differential pressures in the downcomer between the bottom of downcomer and the cold leg nozzle elevation are compared in Figure 19.3-176. In Figure 19.3-176, four WCOBRA/TRAC-TF2 curves are shown. Each curve represents the level in a different quadrant of the downcomer, each being adjacent to a loop connection. In the measured levels, the level was highest in the downcomer quadrant below the broken cold leg. [

] <sup>a,c</sup>

Figures 19.3-177 and 19.3-178 provide the steam and water flow rates to the broken loop. The vapor flow to the broken loop is shown in Figure 19.3-177. Figure 19.3-177 demonstrates that the vapor flow rate changes during each sub-phase with the change in steam injection rate. [

] <sup>a,c</sup>

One additional parameter of interest is the void height in the downcomer as a function of the steam flow rate. The void height is the distance from the average collapsed downcomer liquid level to the bottom of the cold leg nozzles. The distance from the bottom of the downcomer to the bottom of the cold leg nozzle is [ ] <sup>a,c</sup>. The WCOBRA/TRAC-TF2 calculated downcomer void height is determined for each of the four sub-phases, and then plotted against test data and estimates provided by MPR Associates (MPR-1346, 1993) in Figure 19.3-179.

[

] <sup>a,c</sup>

The measured and predicted fluid temperatures in the Loop 2 cold leg are compared in Figures 19.3-180 through 19.3-182. Figure 19.3-180 shows the comparison between the measured temperature and the TF2 predicted water temperature at the ECC injection point. The measured temperature profiles from the top of cold leg to the bottom of cold leg indicate a stratified flow pattern in all sub-phases, with superheated steam at the top and subcooled water at the bottom. The fluid temperature drops from sub-phase I to sub-phase IV as the steam flow rate reduces in a stepwise manner. [

] <sup>a,c</sup>

Figure 19.3-181 shows the comparison between the measured temperature and the TF2 predicted water temperature downstream of the injection point. Thermocouples were wetted by the liquid during the experiment and showed saturated or subcooled temperature. The measured liquid temperature at the bottom of cold leg increased substantially from measured temperature at the ECC injection point, which implies further condensation downstream of the ECC injection point. [

] <sup>a,c</sup>

Figure 19.3-182 shows the comparison between the measured temperature and the WCOBRA/TRAC-TF2 predicted water temperature at the cold leg near the vessel inlet. It is shown that the water temperature rose further for all four sub-phases. [

] <sup>a,c</sup>

Sensitivity Study with [ ] <sup>a,c</sup>

[

] <sup>a,c</sup>

[ ]<sup>a,c</sup>

Sensitivity Study with [ ]<sup>a,c</sup>

[

] <sup>a,c</sup>

### 19.3.12 UPTF 29B Upper Plenum Entrainment/De-Entrainment Test Descriptions

During the reflood phase of a LBLOCA, water rises through the core. The hot fuel rods cause the water to boil and the steam produced entrains droplets which are carried through the core into the upper plenum. The droplets either fall back into the core, de-entrain on the internals in the upper plenum, or pass through into the hot legs towards the steam generators. The entrained droplets which enter the hot steam generator tubes are vaporized, causing an increase in loop pressure, which inhibits core reflood. This phenomenon is known as steam binding.

UTPF Test 29B was a quasi-steady state experiment to investigate upper plenum entrainment and steam binding during reflood phase a PWR LBLOCA. The UPFT test facility is discussed in detail in Section 19.3.1. Figure 19.3-193 shows the system configuration of UPTF Test 29B. [

] <sup>a,c</sup>

[

] <sup>a,c</sup>

A summary of test boundary conditions for UPTF-29B (Run 212) is given in Table 19.3-19.

### 19.3.13 WCOBRA/TRAC-TF2 Model for UPTF Test 29B

The vessel model used in the simulation of the UPTF 29B is shown in Figure 19.3-195. Compared to the vessel models employed in the simulation of the UPTF 6, 8A, 25A tests, this model is more detailed above the tie plate and in the upper plenum region. The vessel model for the upper plenum tests used a coarser noding in the downcomer and the lower plenum regions because in these tests the flows into the downcomer were not significant. At the start of the tests, a liquid level was established in the bottom of the vessel to prevent the steam flow from the core to the downcomer through the lower plenum.

[

] <sup>a,c</sup>

[

] <sup>a,c</sup>

#### 19.3.14 Simulation of UPTF Test 29B

Test 29B was performed to determine the amount of upper plenum de-entrainment and carryover. This test consists of six sub-phases. Each sub-phase consists of a period of steady core simulator injection followed by a "rest" period. During the "rest" period, water suspended in the upper plenum was allowed to drain back into the vessel. Table 19.3-19 lists the core simulator injection rates for Test 29B.

Phase B of Test 29 is simulated using WCOBRA/TRAC-TF2 over the entire 900 seconds of the test. For each phase of UPTF Test 29B, a mass balance is performed based on test measurements by MPR Associates (MPR-1213, 1990b), and the mass distribution estimated.

Figure 19.3-199 compares the estimated and predicted upper plenum water mass in sub-phase 1 of UPTF Test 29B. [

] <sup>a,c</sup>

The estimated and predicted upper plenum mass for Sub-phase 2 of UPTF Test 29B is shown in Figure 19.3-200. [

] <sup>a,c</sup>

Figure 19.3-201 compares the estimated and predicted upper plenum mass for sub-phase 3.

[

] <sup>a,c</sup>

[

] <sup>a,c</sup>

The estimated and predicted upper plenum mass for sub-phase 5 of Test 29B are compared in Figure 19.3-203. [

] <sup>a,c</sup>

Finally, Figure 19.3-204 compares the estimated and predicted upper plenum mass for sub-phase 6. In this case, [

] <sup>a,c</sup>



Table 19.3-2 [ ] <sup>a,c</sup>						

a,c

Table 19.3-3 [ ] <sup>a,c</sup>							

a,c

Table 19.3-4 [ ] <sup>a,c</sup>							

a,c

Table 19.3-5 [ ] <sup>a,c</sup>					

a,c

Table 19.3-6 [ ] <sup>a,c</sup>					

a,c

Table 19.3-7 [ ] <sup>a,c</sup>							

a,c



Table 19.3-10 [

] <sup>a,c</sup>



a,c

Table 19.3-11 [

] <sup>a,c</sup>



a,c

**Table 19.3-12 Steam Mass Flows in UPTF Test 6 (all Values are in kg/sec)**

a,c


**Table 19.3-13 Selected Test Conditions from UPTF Test 6 (Single-Phase Steam Portion)**

a,c


**Table 19.3-14 Calculated Parameters for UPTF Test 6**

a,c


**Table 19.3-15 Calculated Cold Leg Nozzle K,  $U_{DC} = 0$**

a,c

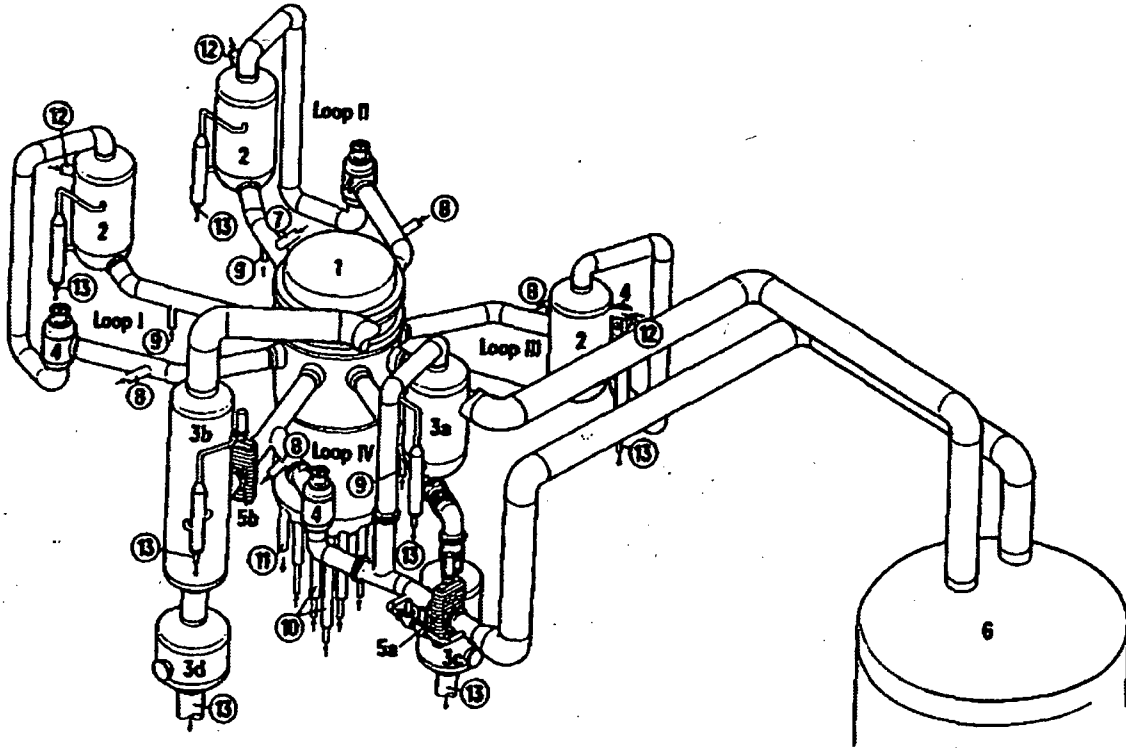

Table 19.3-16 UPTF Test 8 Phase A Conditions							
Conditions	Subphase						
	1	2	3	4	5	6	7
Pressure (kPa)	405						
Saturation Temperature (°C)	144						
Core Simulator Steam Flow (kg/s)	110						
Loop Steam Flow Rate (kg/s)	31~38 <sup>(1)</sup>						
Steam Temperature (°C)	145 <sup>(2)</sup>						
ECC Flow (Parts 1-7) (kg/s)	600	400	250	200	150	90	15
ECC Subcooling (°C)	110						
<b>Notes:</b>							
1. Estimated steam flow rate in loop 2.							
2. This steam temperature is cold leg inlet steam temperature. The nominal temperature of steam injection to core simulator is 201°C.							

Table 19.3-17 [ ] <sup>a,c</sup>							

a,c



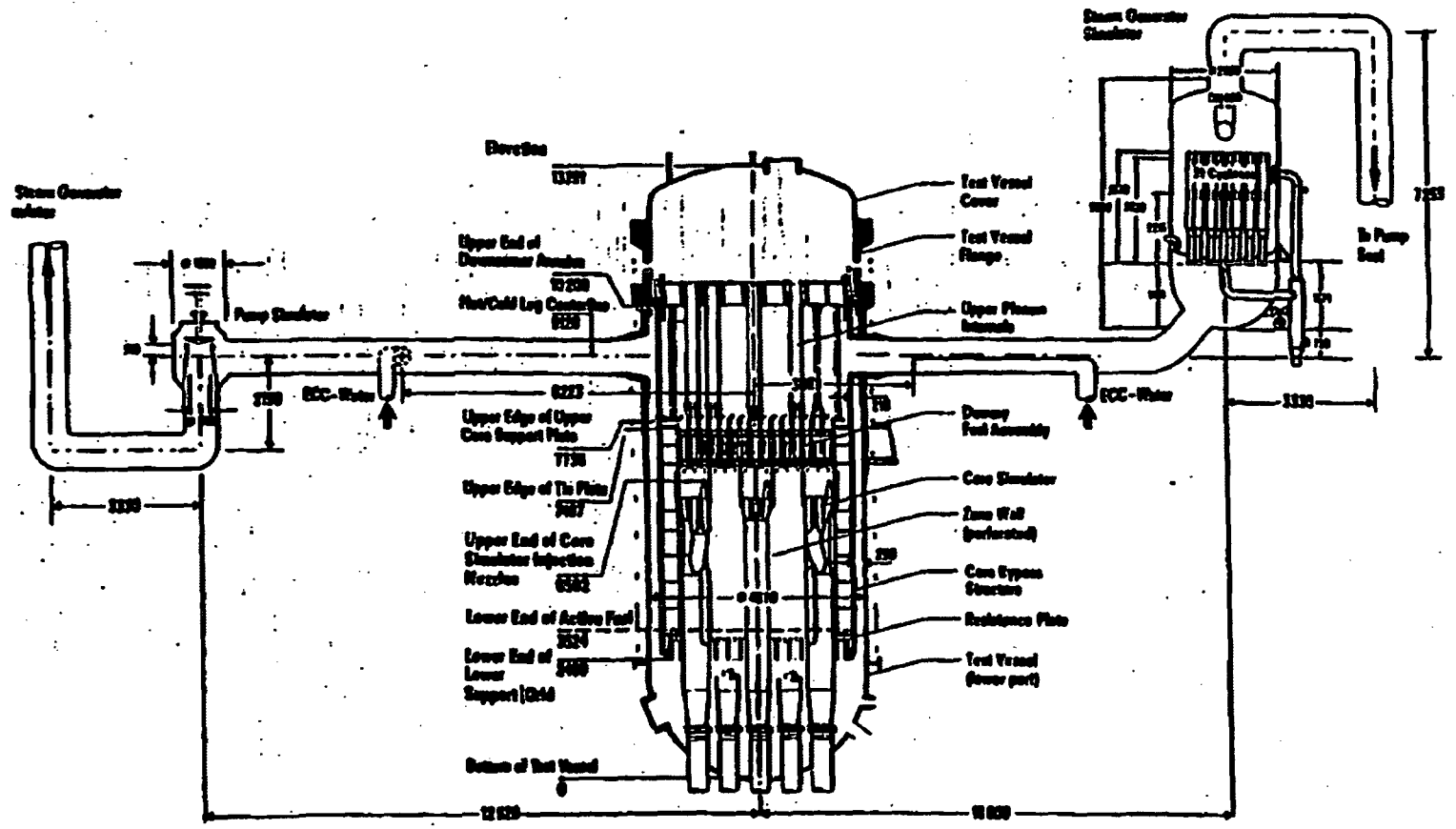
Figure 19.3-1 UPTF Plan View



- 2 Steam Generator Simulator (Intact Loop)
- 3a Steam Generator Simulator/ Water Separator (Broken Loop Hot Leg)
- 3b Water Separator (Broken Loop Cold Leg)
- 3c Drainage Vessel for Hot Leg
- 3d Drainage Vessel for Cold Leg
- 4 Pump Simulator
- 5a Break Valve (Hot Leg)
- 5b Break Valve (Cold Leg)
- 6 Containment Simulator

- 7 Surgefine-Nozzle
- 8 ECC-Injection Nozzles (Cold Leg)
- 9 ECC-Injection Nozzles (Hot Leg)
- 10 Core Simulator Injection Nozzle
- 11 TV-Drainage Nozzle
- 12 Steam Injection Nozzle
- 13 Drainage Nozzle

Figure 19.3-2 UPTF Test Vessel and Primary Loop



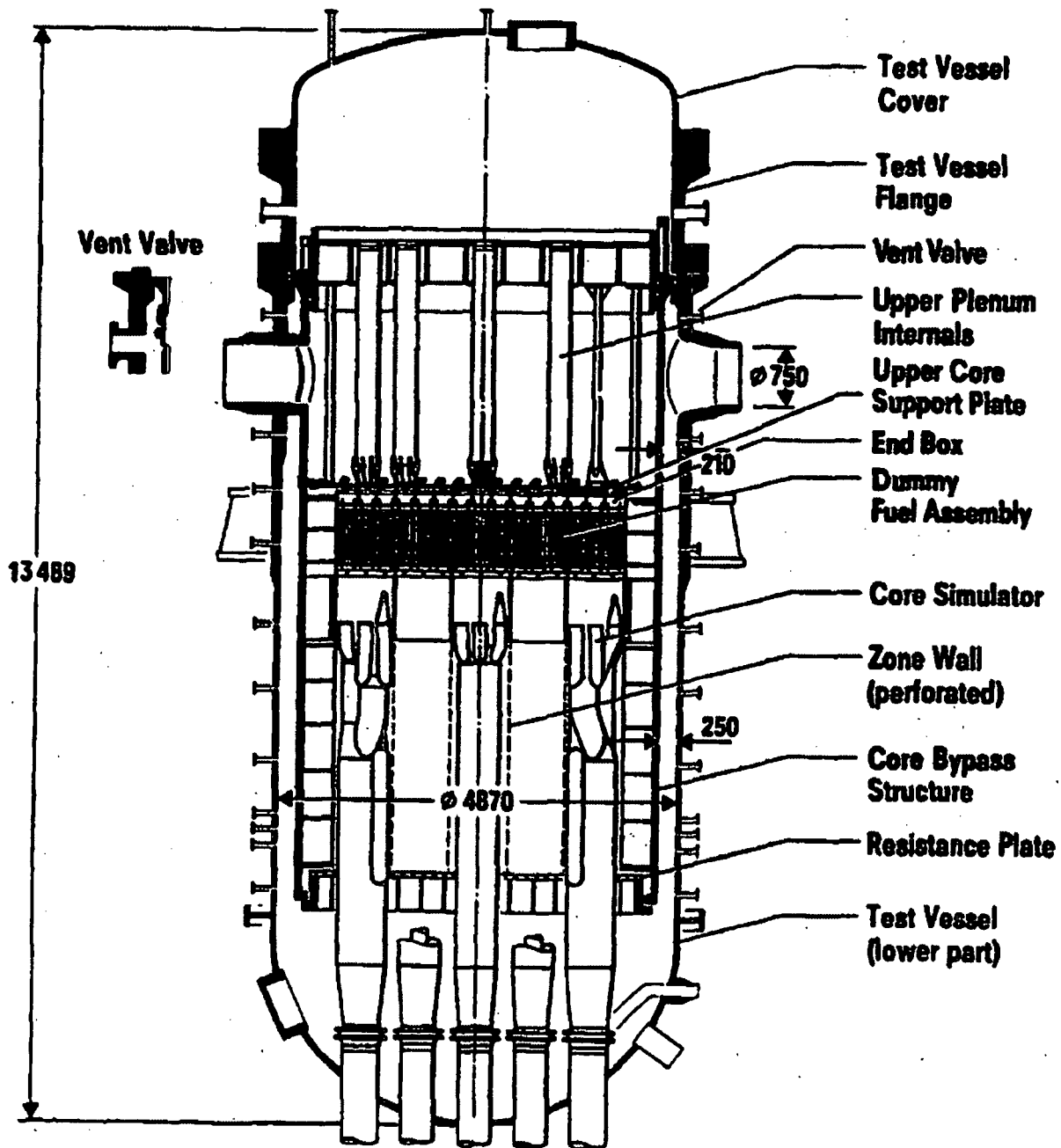


Figure 19.3-3 UPTF Reactor Vessel

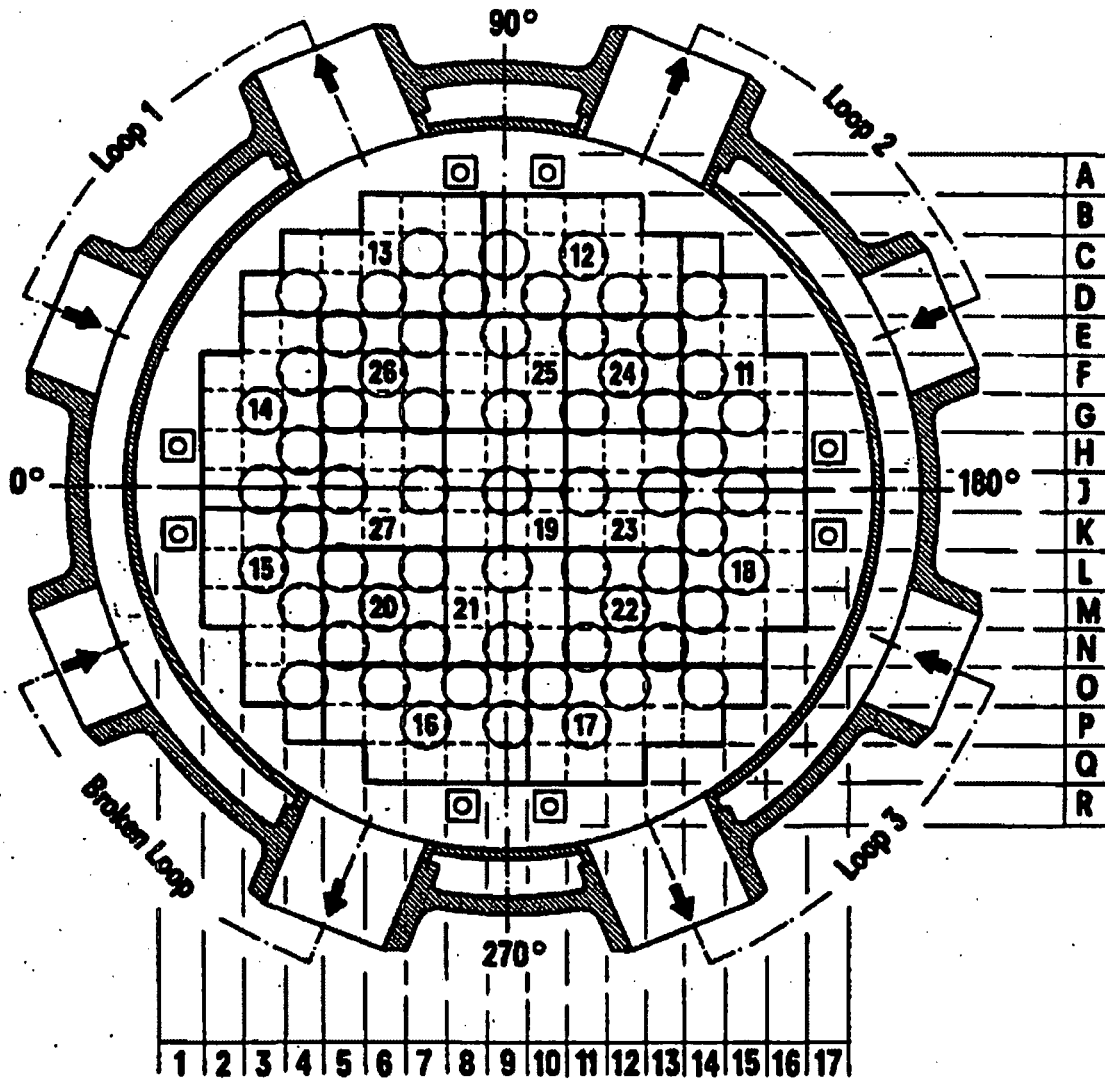


Figure 19.3-4 UPTF Upper Plenum Structures

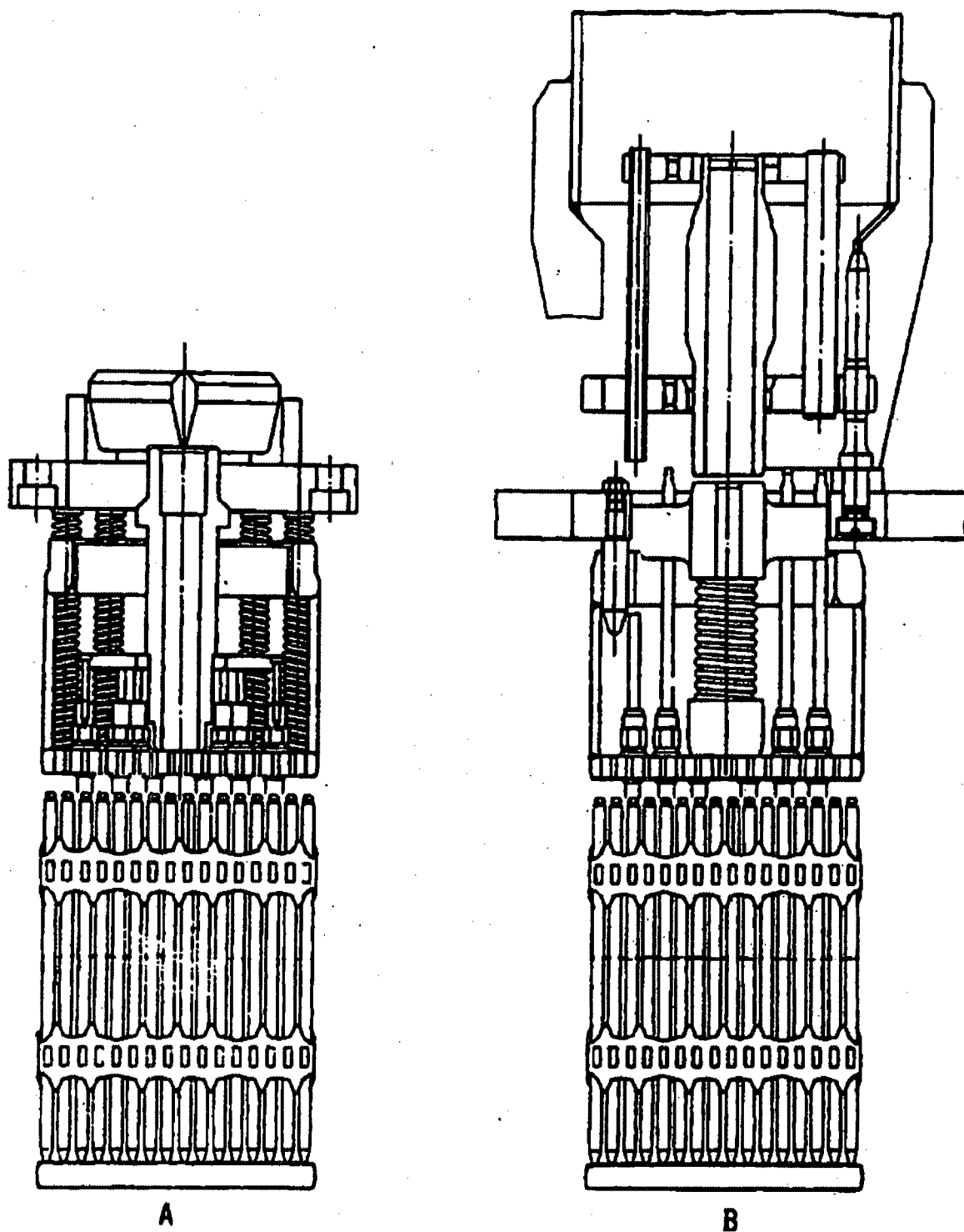


Figure 19.3-5 Dummy Fuel Assembly and End Box with Flow Restrictor (A) or Spider (B)

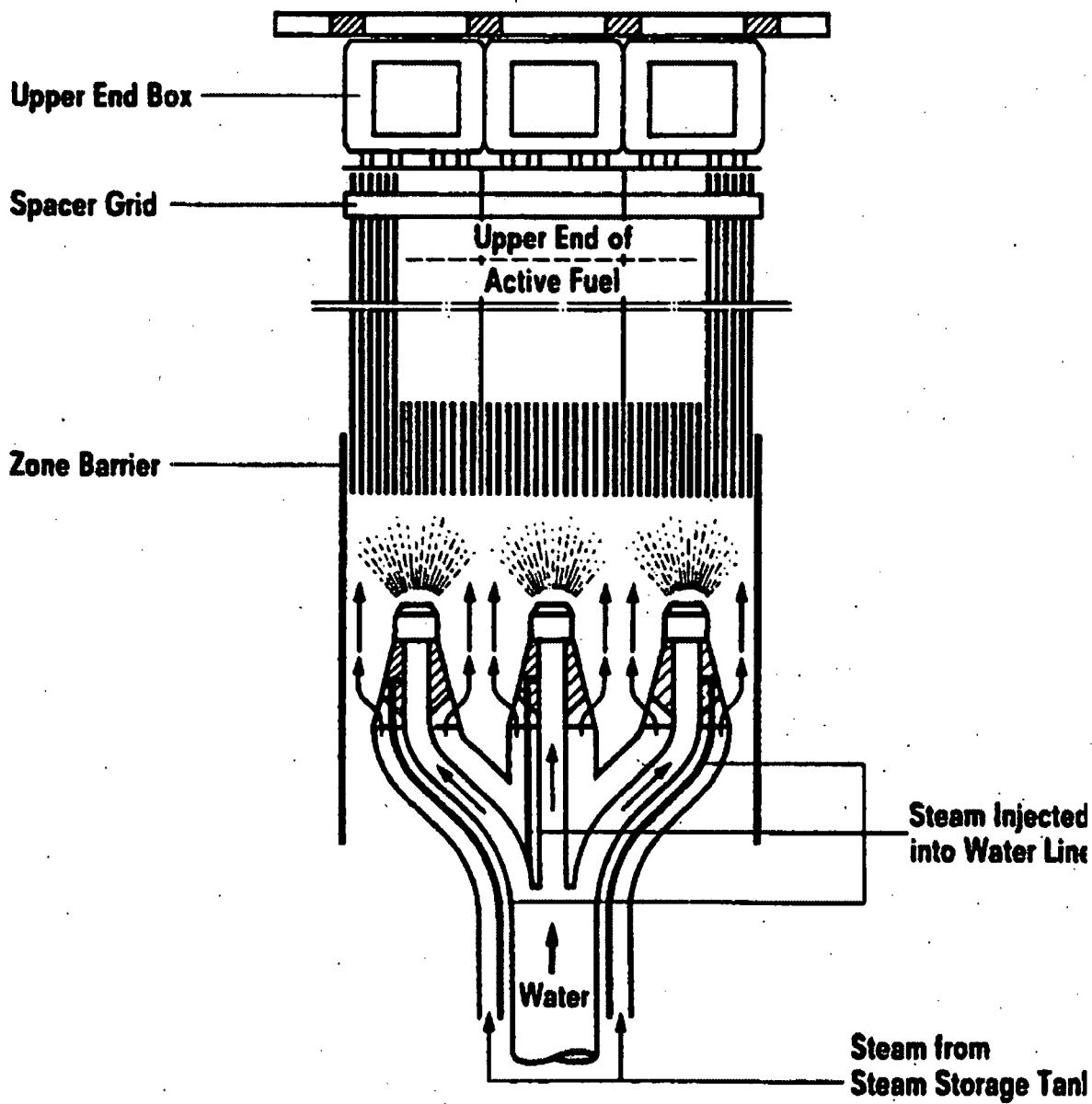
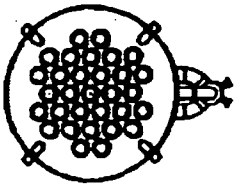
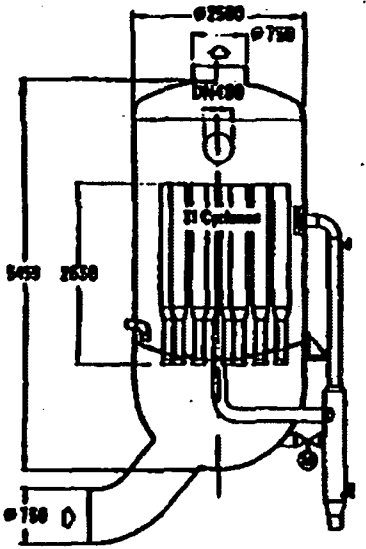
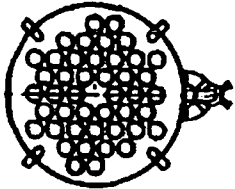
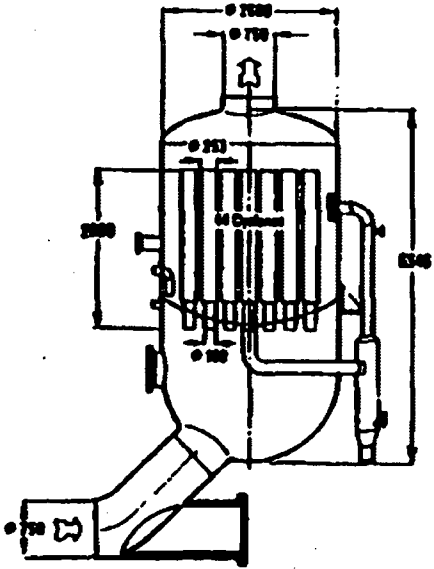


Figure 19.3-6 UPTF Core Simulator Injection Assembly

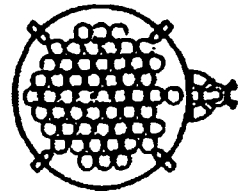
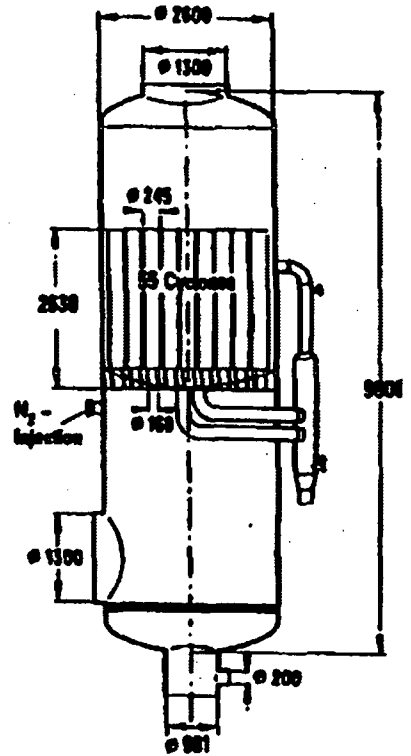
Figure 19.3-7 UPTF Steam Generator Simulators and Water Separators



**Steam Generator Simulator  
of Inlet Loops**



**Steam Generator Simulator  
(Water Separator) of  
Broken Loop Hot Leg**



**Water Separator of  
Broken Loop Cold Leg**

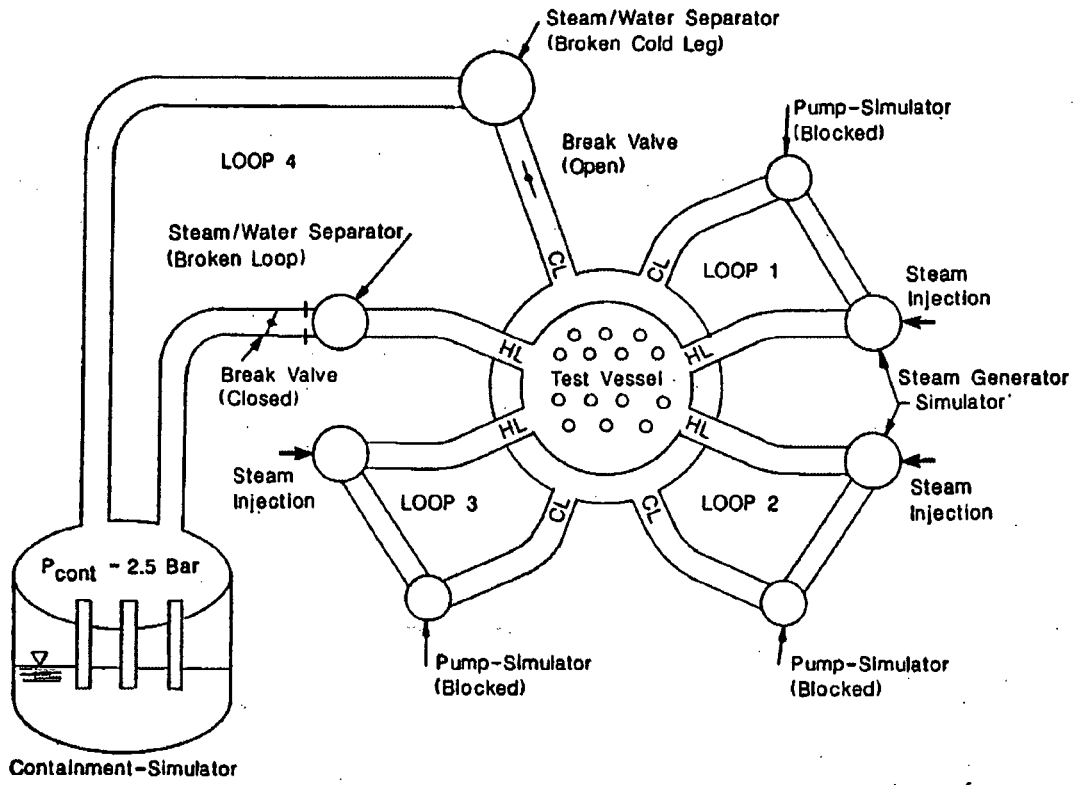


Figure 19.3-8 UPTF System Configuration for Test 6 (MPR-1163)

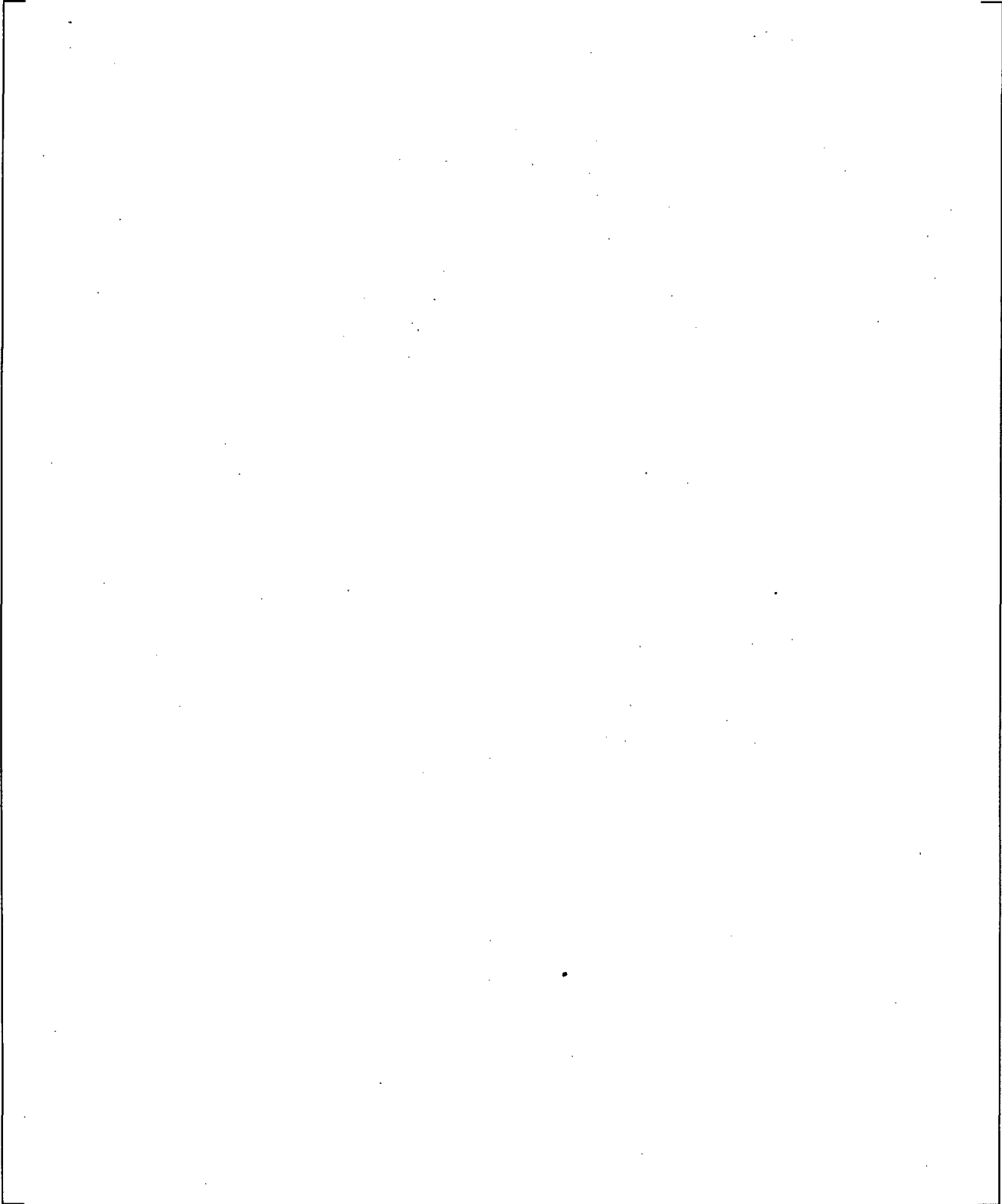
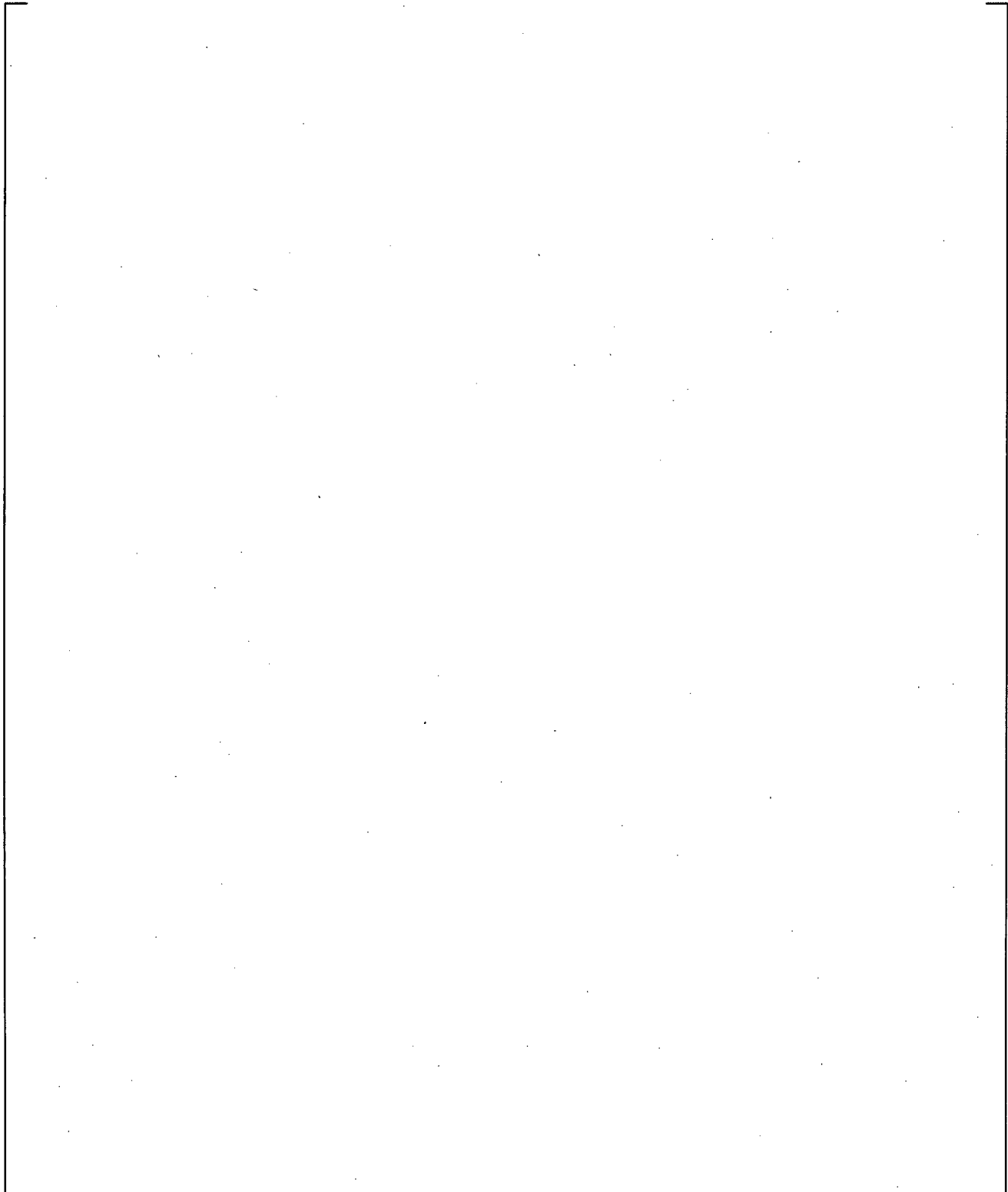
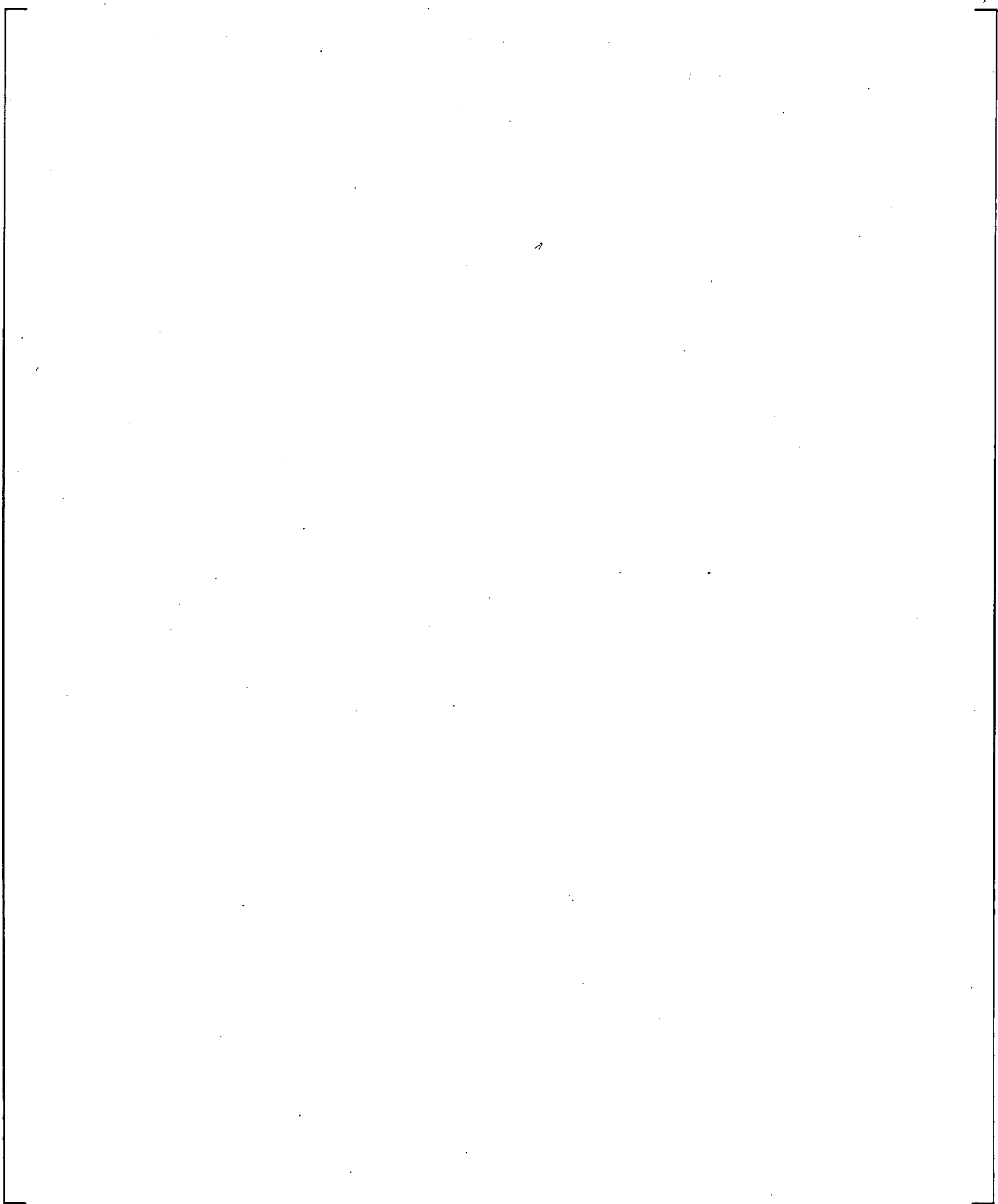


Figure 19.3-9 WCOBRA/TRAC-TF2 VESSEL Component Axial View for UPTF Bypass Tests

a,c



**Figure 19.3-10** WCOBRA/TRAC-TF2 VESSEL Component Sections 1 and 2 for UPTF Bypass Tests



**Figure 19.3-11** WCOBRA/TRAC-TF2 VESSEL Component Sections 3 and 4 for UPTF Bypass Tests

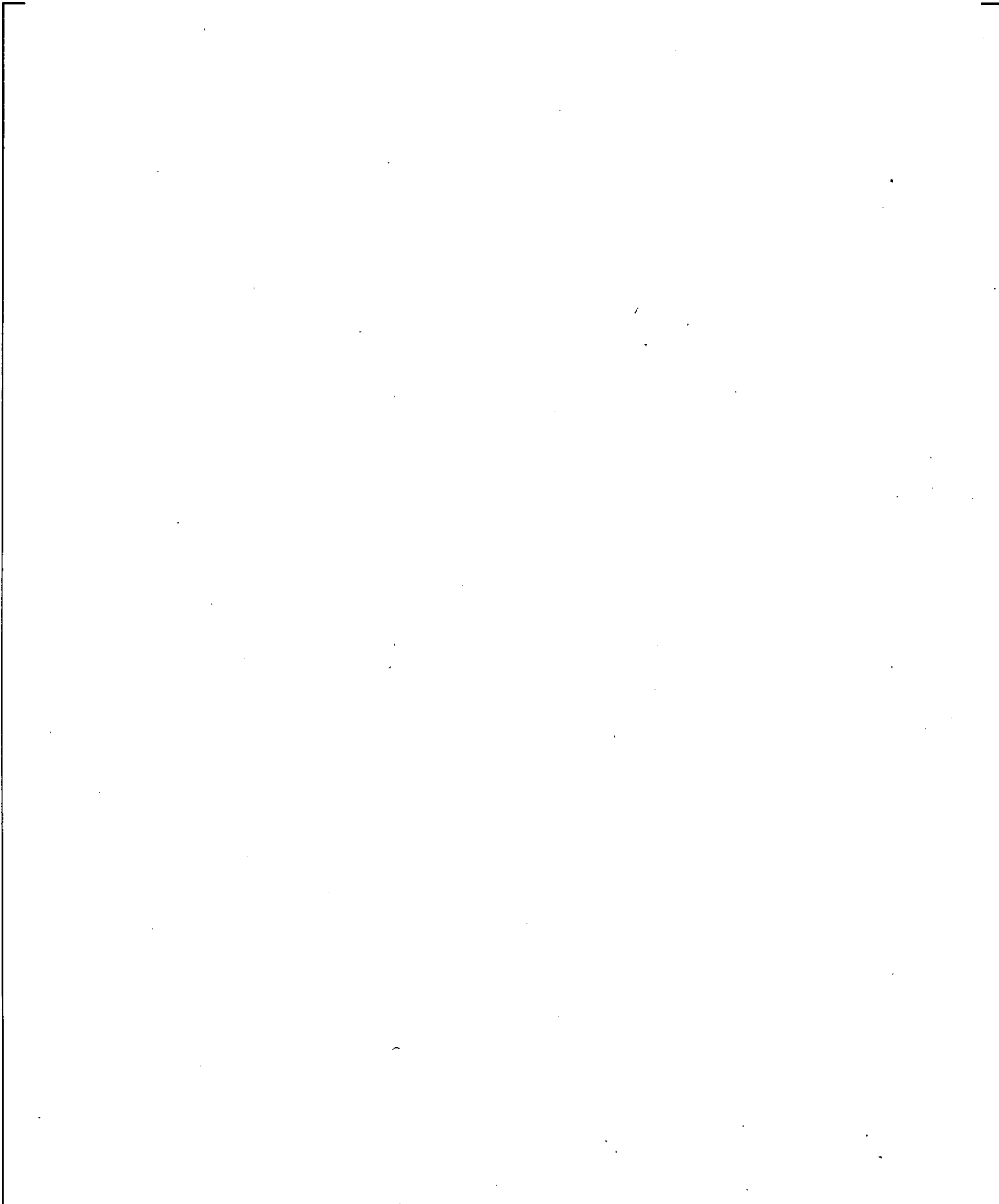


**Figure 19.3-12** WCOBRA/TRAC-TF2 VESSEL Component Sections 5 and 6 for UPTF Bypass Tests

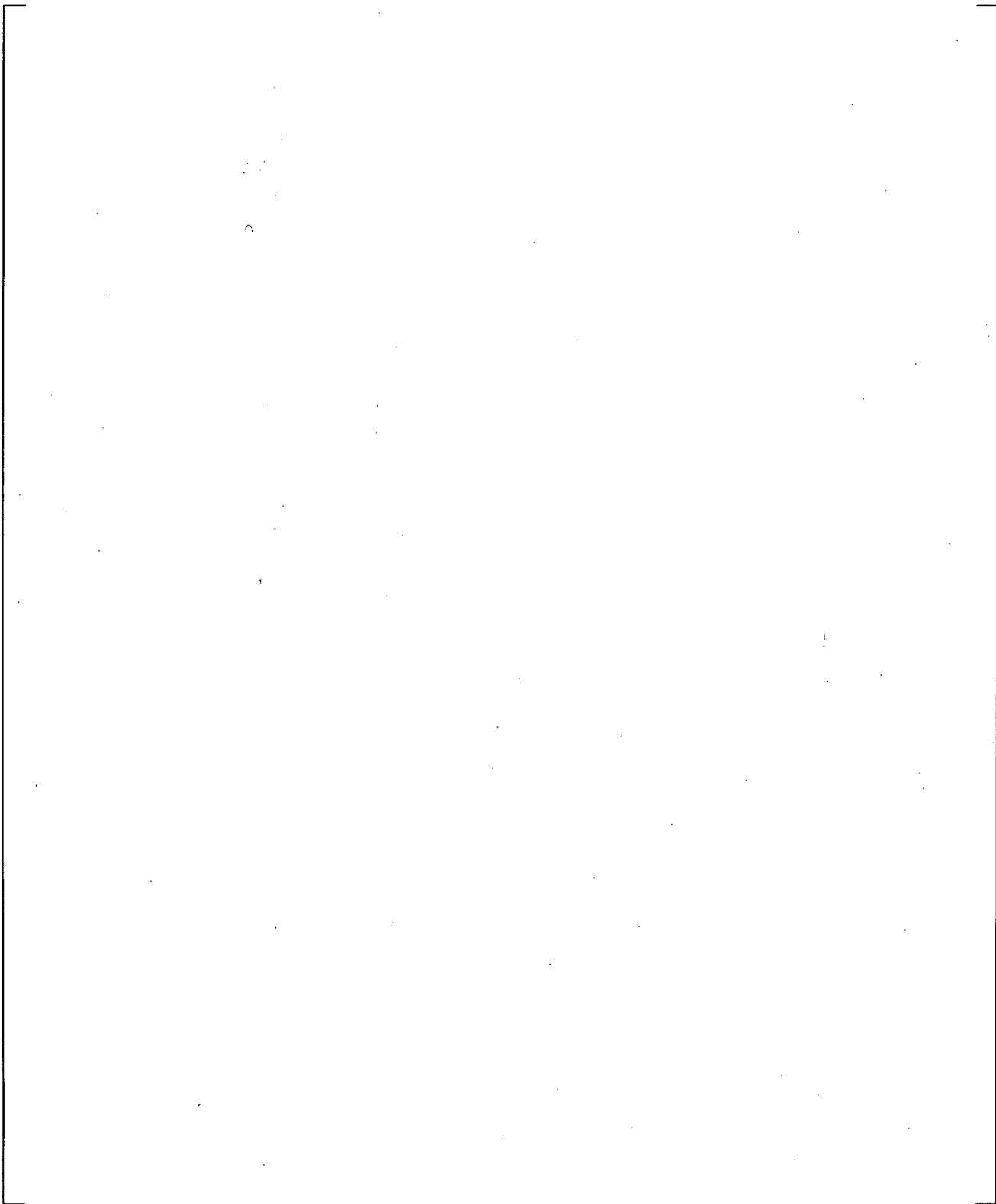


**Figure 19.3-13** WCOBRA/TRAC-TF2 VESSEL Component Sections 7 and 8 for UPTF Bypass Tests

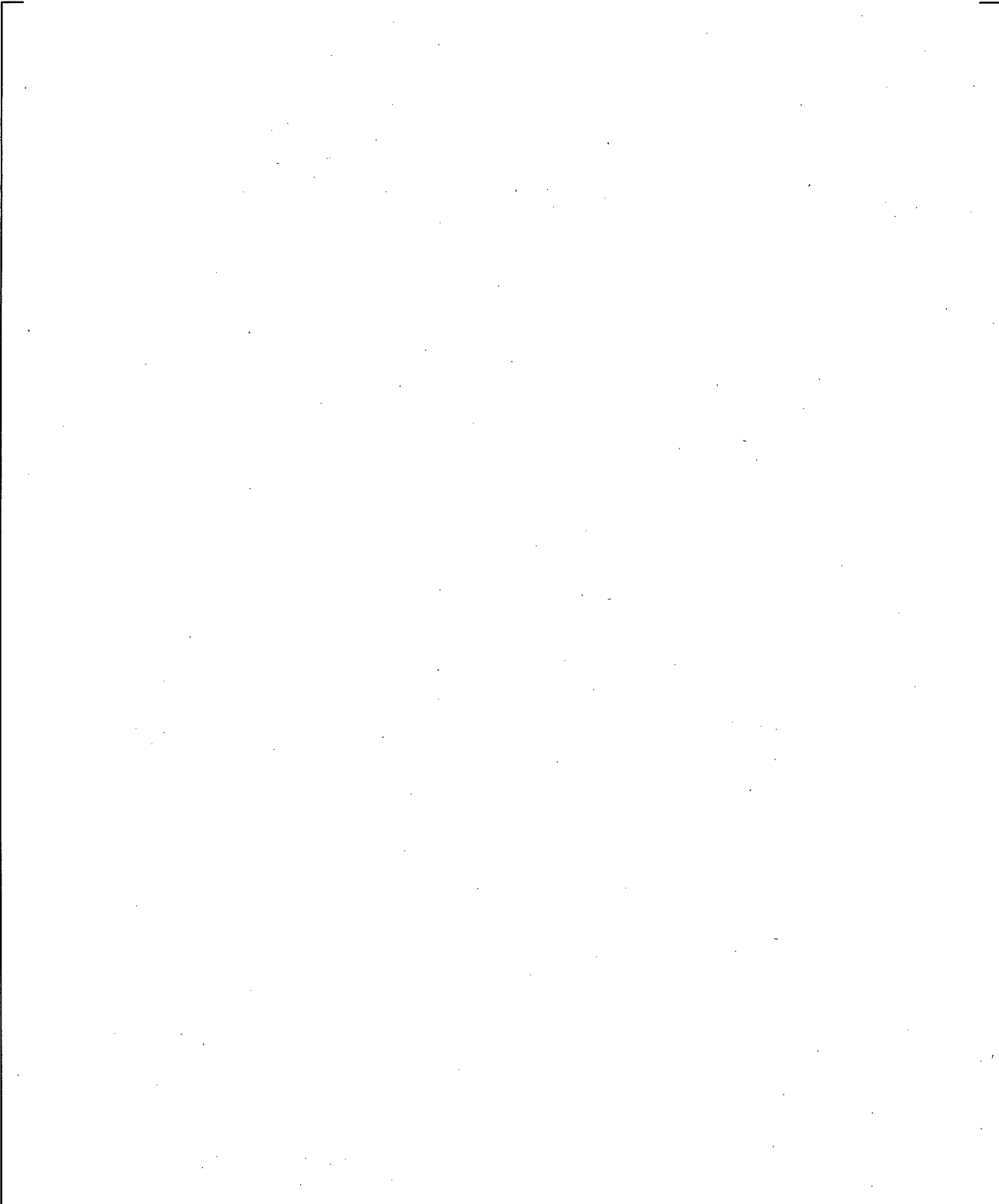


**Figure 19.3-14 WCOBRA/TRAC-TF2 One-Dimensional Component Model for UPTF Test 6**

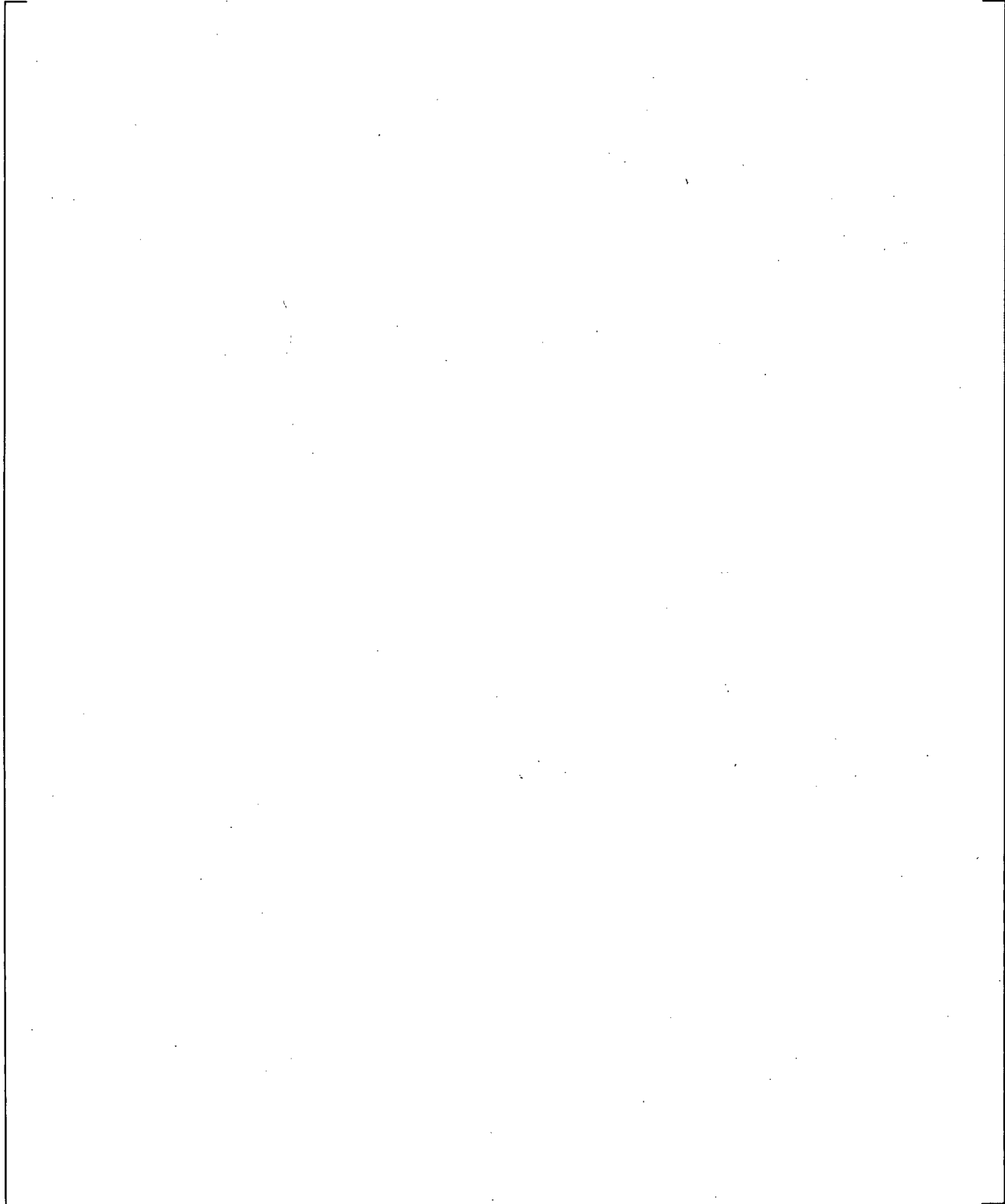


**Figure 19.3-15 Total Core Steam Injection, UPTF Test 6 – Run 131**

a,c

**Figure 19.3-16 Steam Generator Simulator Steam Injection, UPTF Test 6 – Run 131**

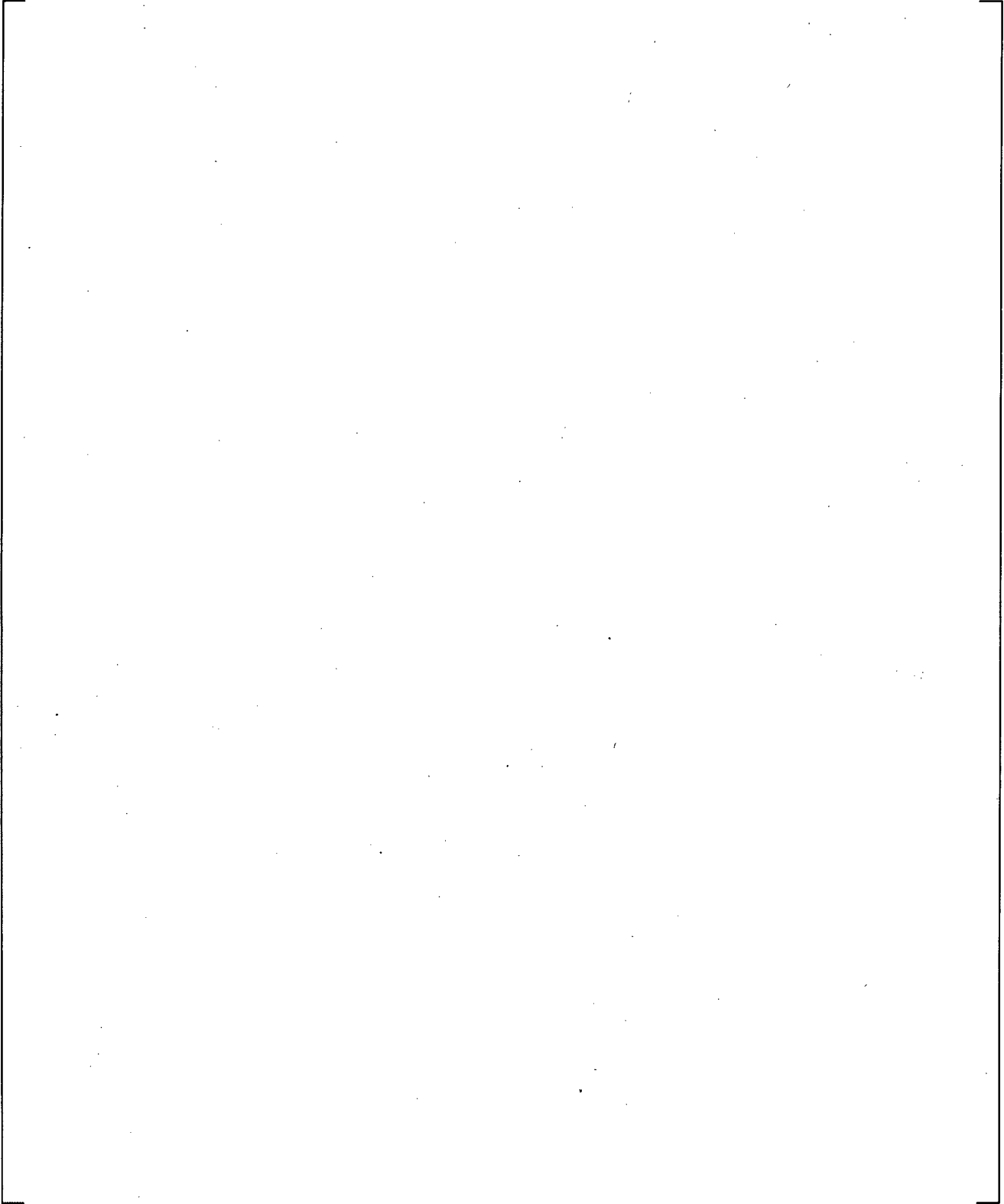


**Figure 19.3-17 Intact Loop ECC Injection, UPTF Test 6 – Run 131**

a,c

**Figure 19.3-18 Measured Absolute Pressures in the Upper Plenum and Downcomer, UPTF  
Test 6 – Run 131**

a,c

**Figure 19.3-19 Predicted Absolute Pressures in the Upper Plenum and Downcomer, UPTF  
Test 6 – Run 131**

a,c

**Figure 19.3-20 Measured Downcomer Fluid Temperature at Level 21, UPTF Test 6 – Run 131**

a,c

**Figure 19.3-21 Predicted Downcomer Fluid Temperature at Level 21, UPTF Test 6 – Run 131**

a,c

**Figure 19.3-22 Measured Downcomer Fluid Temperature at Level 01, UPTF Test 6 – Run 131**

a,c

**Figure 19.3-23 Predicted Downcomer Fluid Temperature at Level 01, UPTF Test 6 – Run 131**

a,c



**Figure 19.3-24 Predicted Liquid Flow at Bottom of the Downcomer in Intact Side, UPTF Test 6 - Run 131**

a,c



**Figure 19.3-25 Predicted Liquid Flow at Bottom of the Downcomer in Broken Side, UPTF Test 6 - Run 131**

a,c

**Figure 19.3-26 Measured Axial Differential Pressures in Downcomer, UPTF Test 6 – Run 131**

a,c

**Figure 19.3-27 Predicted Axial Differential Pressures in Downcomer, UPTF Test 6 – Run 131**

a,c



**Figure 19.3-28 Measured Azimuthal Differential Pressures in Downcomer at Level 06, UPTF Test 6 - Run 131**

a,c



**Figure 19.3-29 Predicted Azimuthal Differential Pressures in Downcomer at Level 06, UPTF Test 6 - Run 131**

a,c

**Figure 19.3-30 Measured Azimuthal Differential Pressures in Downcomer at Level 22, UPTF  
Test 6 – Run 131**

a,c

**Figure 19.3-31 Predicted Azimuthal Differential Pressures in Downcomer at Level 22, UPTF  
Test 6 – Run 131**

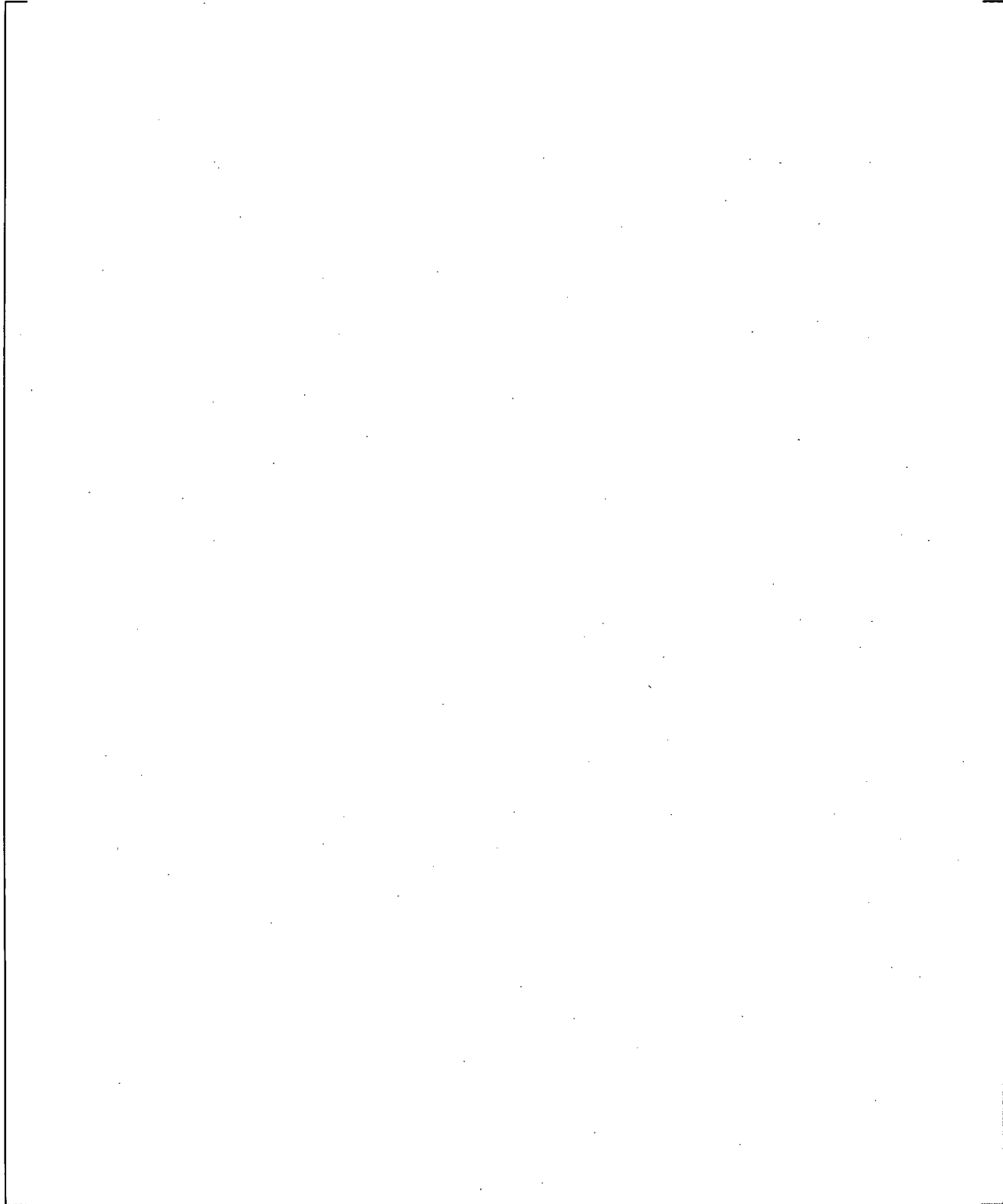


**Figure 19.3-32 Comparison on Differential Pressure in Lower Plenum, UPTF Test 6 – Run 131**

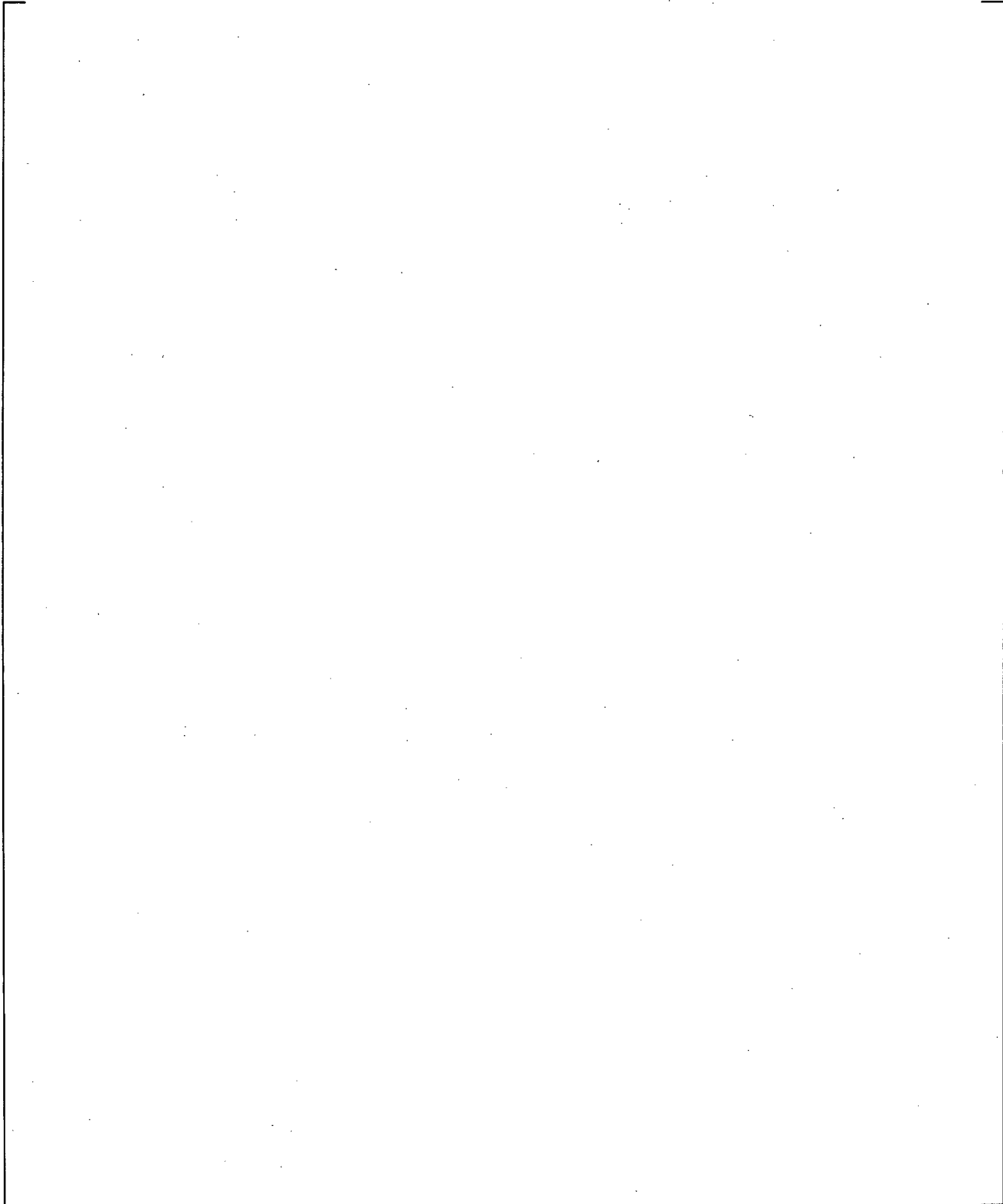


**Figure 19.3-33 Total Core Steam Injection, UPTF Test 6 – Run 132**

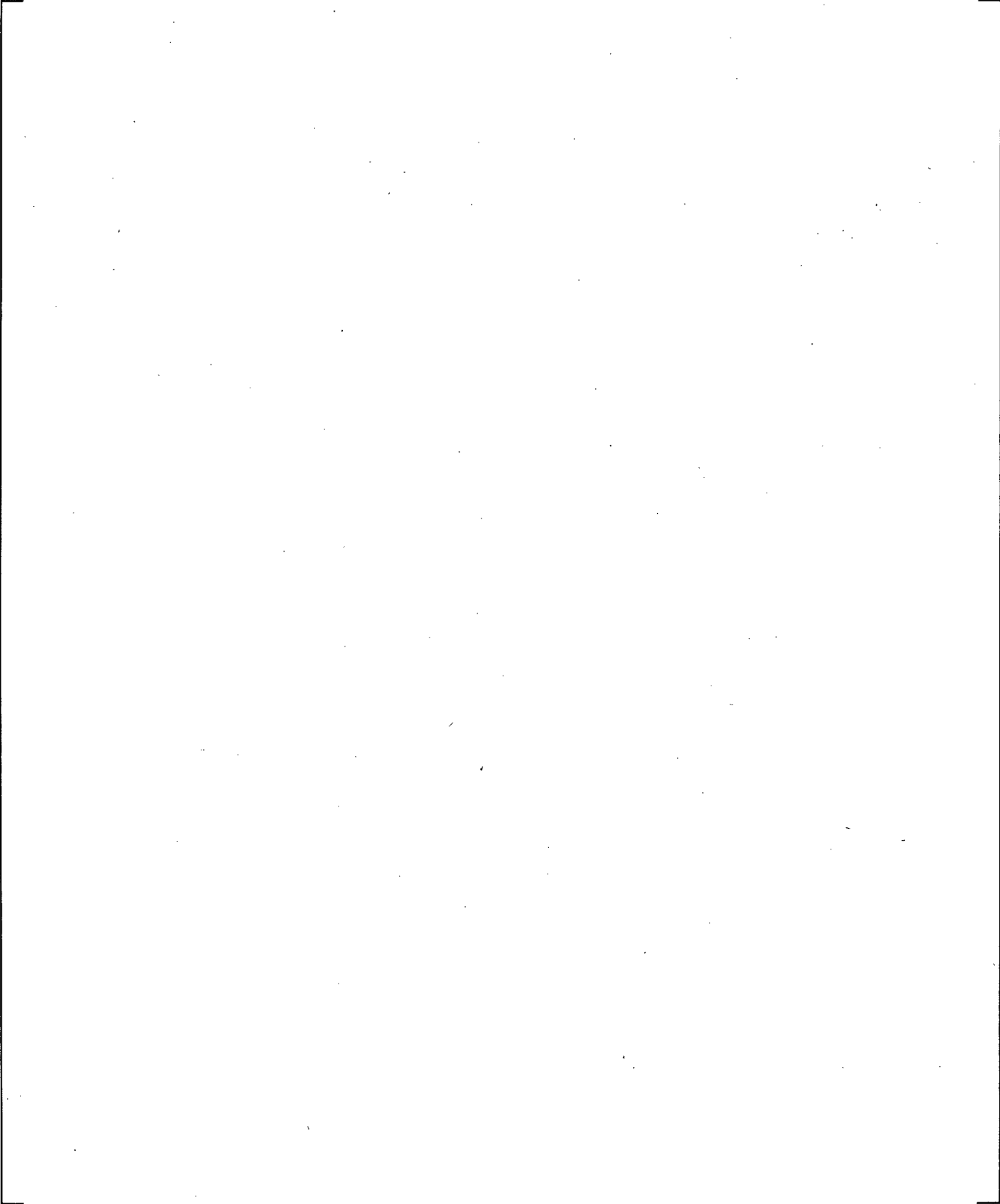


**Figure 19.3-34 Steam Generator Simulator Steam Injection, UPTF Test 6 – Run 132**

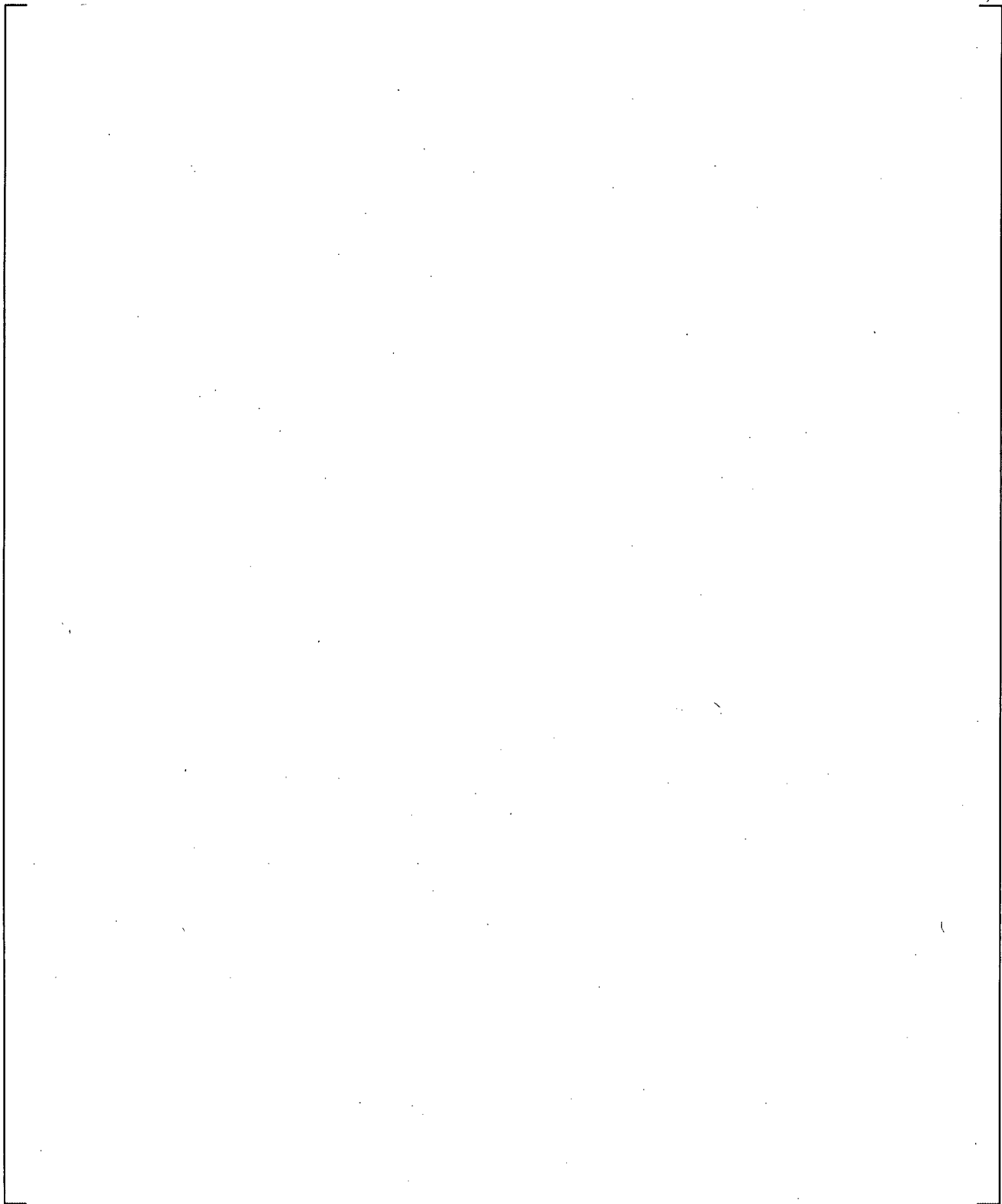


**Figure 19.3-35 Intact Loop ECC Injection, UPTF Test 6 – Run 132**

a,c



**Figure 19.3-36 Measured Absolute Pressures in the Upper Plenum and Downcomer, UPTF Test 6 - Run 132**

a,c



**Figure 19.3-37 Predicted Absolute Pressures in the Upper Plenum and Downcomer, UPTF Test 6 - Run 132**

a,c

**Figure 19.3-38 Measured Downcomer Fluid Temperature at Level 21, UPTF Test 6 – Run 132**

a,c

**Figure 19.3-39 Predicted Downcomer Fluid Temperature at Level 21, UPTF Test 6 – Run 132**

a,c

**Figure 19.3-40 Measured Downcomer Fluid Temperature at Level 01, UPTF Test 6 – Run 132**

a,c

**Figure 19.3-41 Predicted Downcomer Fluid Temperature at Level 01, UPTF Test 6 – Run 132**

a,c

**Figure 19.3-42 Predicted Liquid Flow at Bottom of the Downcomer in Intact Side, UPTF  
Test 6 – Run 132**

a,c

**Figure 19.3-43 Predicted Liquid Flow at Bottom of the Downcomer in Broken Side, UPTF  
Test 6 – Run 132**

a,c



**Figure 19.3-44 Measured Axial Differential Pressures in Downcomer, UPTF Test 6 – Run 132**

a,c



**Figure 19.3-45 Predicted Axial Differential Pressures in Downcomer, UPTF Test 6 – Run 132**

a,c



**Figure 19.3-46 Measured Azimuthal Differential Pressures in Downcomer at Level 06, UPTF Test 6 – Run 132**

a,c



**Figure 19.3-47 Predicted Azimuthal Differential Pressures in Downcomer at Level 06, UPTF Test 6 – Run 132**

a,c

**Figure 19.3-48 Measured Azimuthal Differential Pressures in Downcomer at Level 22, UPTF  
Test 6 – Run 132**

a,c

**Figure 19.3-49 Predicted Azimuthal Differential Pressures in Downcomer at Level 22, UPTF  
Test 6 – Run 132**

**Figure 19.3-50 Comparison on Differential Pressure in Lower Plenum, UPTF Test 6 – Run 132**

a,c

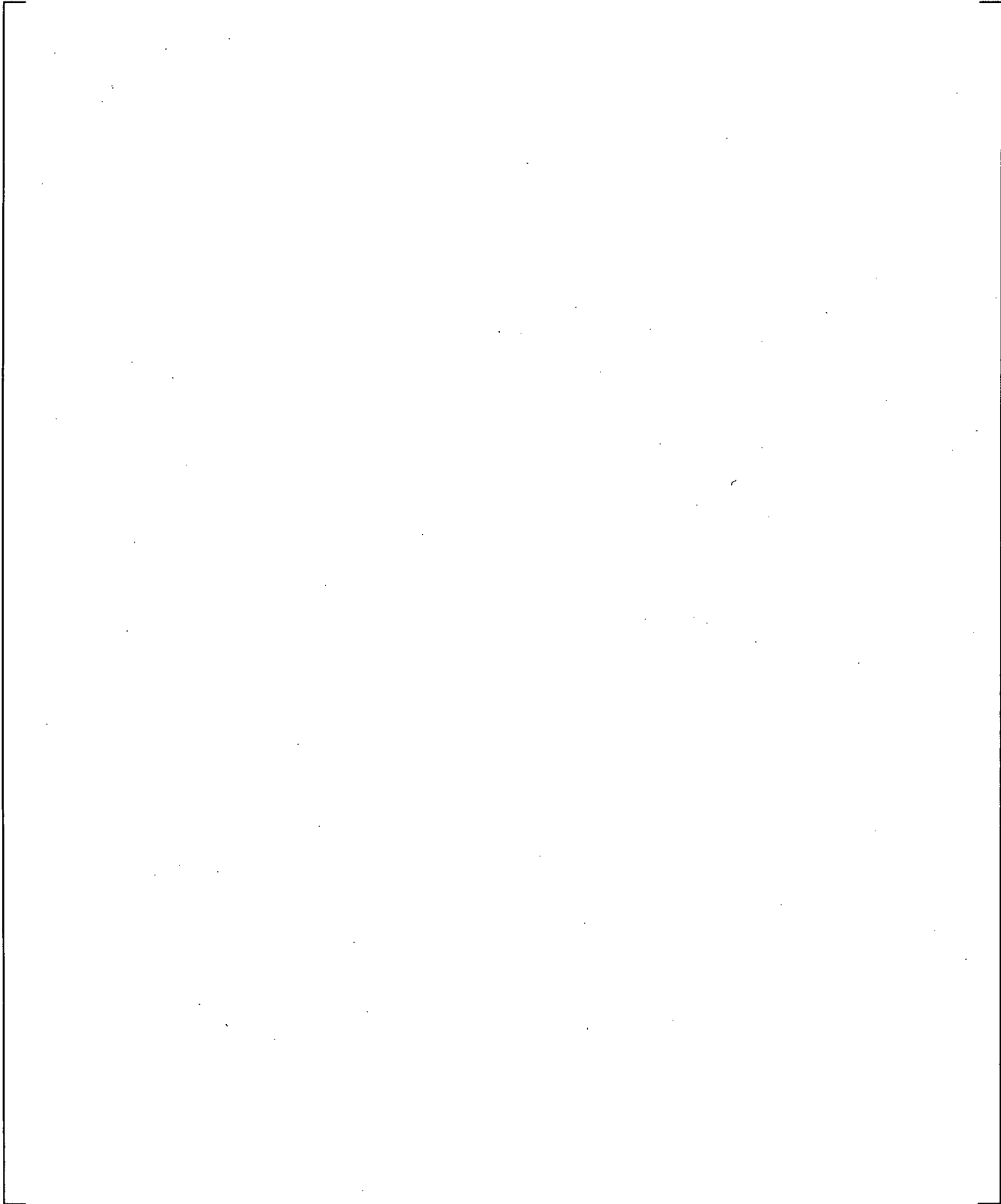


**Figure 19.3-51 Total Core Steam Injection, UPTF Test 6 – Run 133**

a,c

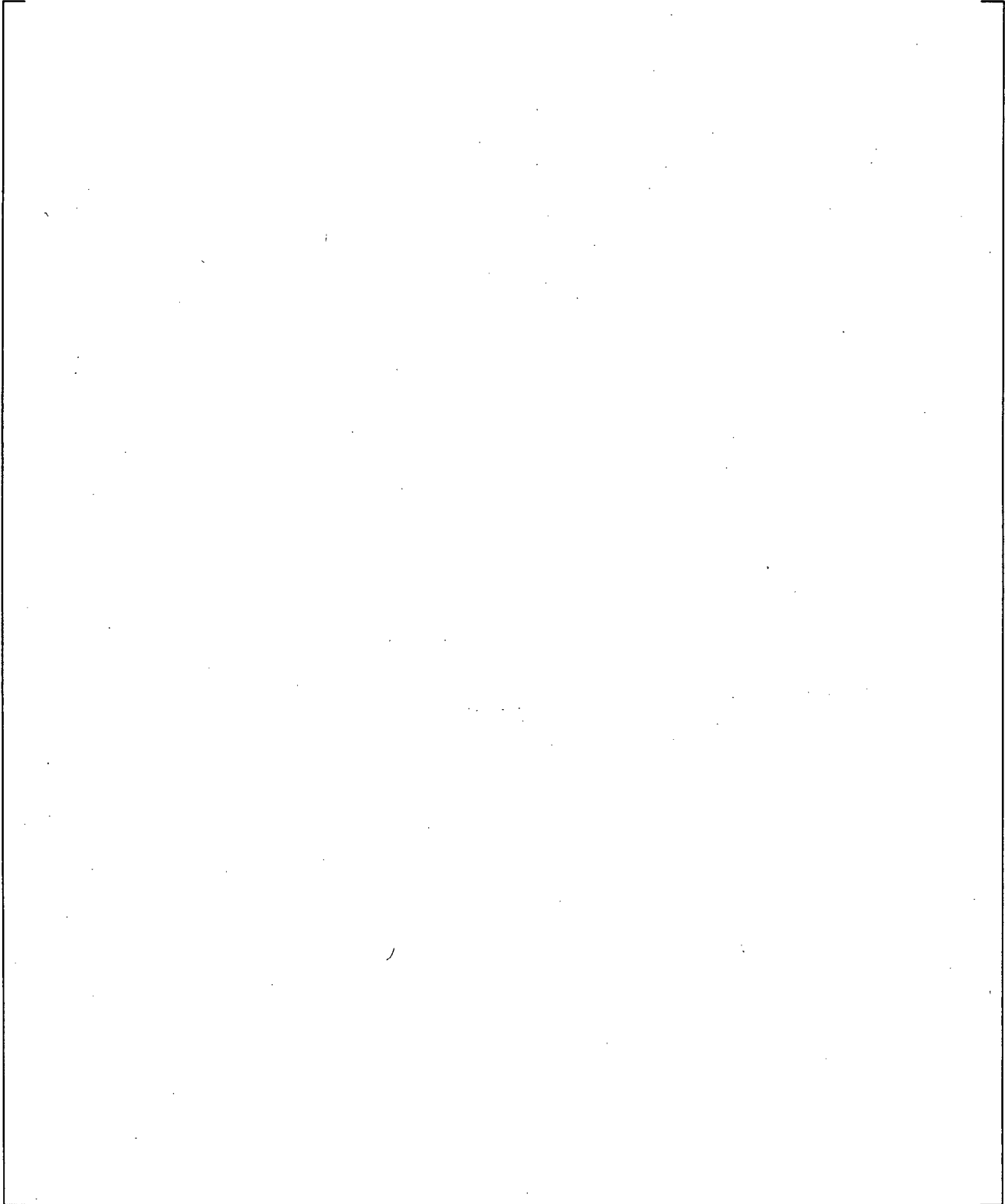


**Figure 19.3-52 Steam Generator Simulator Steam Injection, UPTF Test 6 – Run 133**

a,c

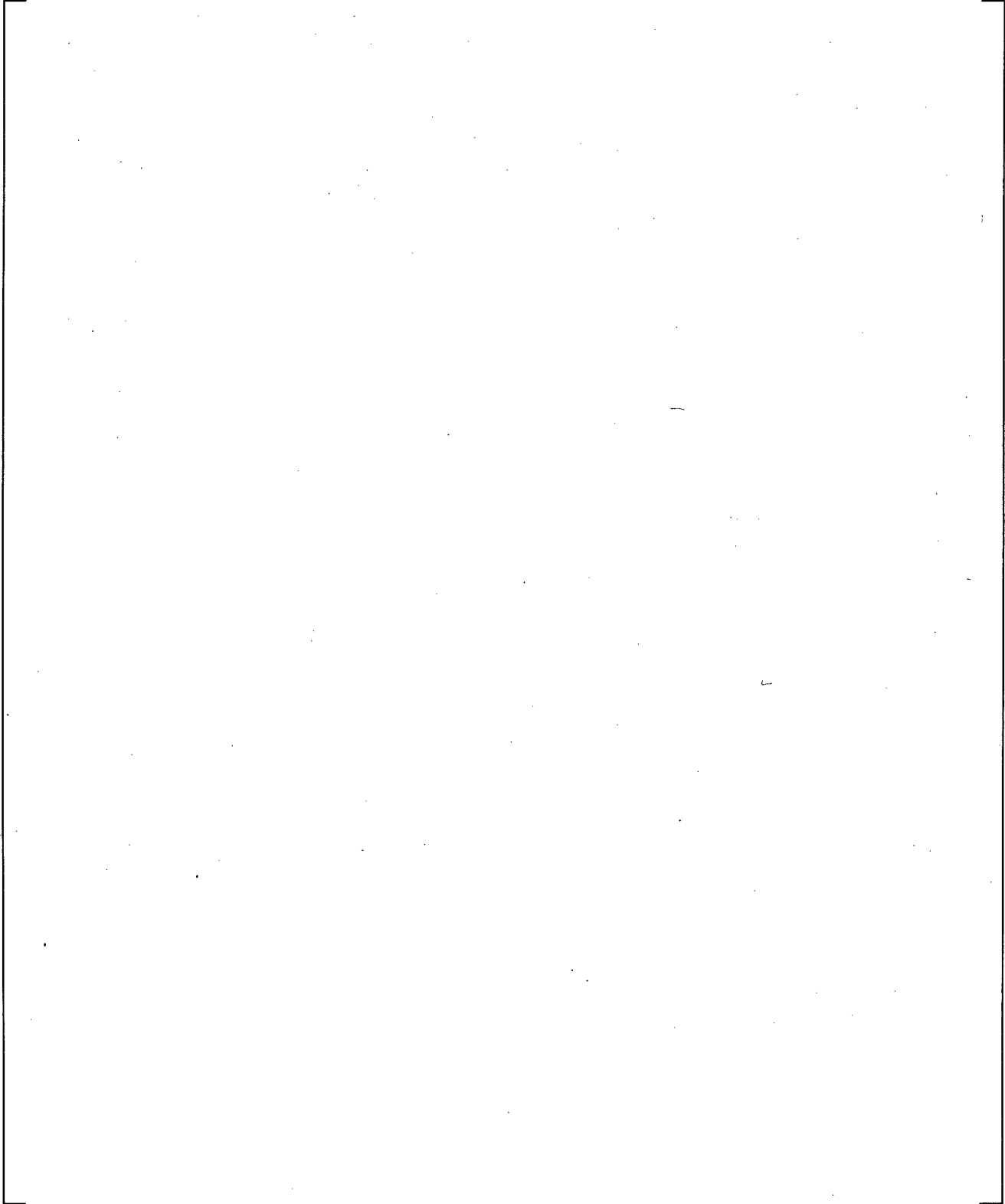


**Figure 19.3-53 Intact Loop ECC Injection, UPTF Test 6 – Run 133**

a,c

**Figure 19.3-54 Measured Absolute Pressures in the Upper Plenum and Downcomer, UPTF  
Test 6 – Run 133**

a,c

**Figure 19.3-55 Predicted Absolute Pressures in the Upper Plenum and Downcomer, UPTF  
Test 6 – Run 133**

a,c

**Figure 19.3-56 Measured Downcomer Fluid Temperature at Level 21, UPTF Test 6 – Run 133**

a,c

**Figure 19.3-57 Predicted Downcomer Fluid Temperature at Level 21, UPTF Test 6 – Run 133**

a,c

**Figure 19.3-58 Measured Downcomer Fluid Temperature at Level 01, UPTF Test 6 – Run 133**

a,c

**Figure 19.3-59 Predicted Downcomer Fluid Temperature at Level 01, UPTF Test 6 – Run 133**

a,c

**Figure 19.3-60. Predicted Liquid Flow at Bottom of the Downcomer in Intact Side, UPTF Test 6 – Run 133**

a,c

**Figure 19.3-61. Predicted Liquid Flow at Bottom of the Downcomer in Broken Side, UPTF Test 6 – Run 133**

a,c



**Figure 19.3-62 Measured Axial Differential Pressures in Downcomer, UPTF Test 6 – Run 133**

a,c



**Figure 19.3-63 Predicted Axial Differential Pressures in Downcomer, UPTF Test 6 – Run 133**

a,c



**Figure 19.3-64 Measured Azimuthal Differential Pressures in Downcomer at Level 06, UPTF Test 6 – Run 133**

a,c



**Figure 19.3-65 Predicted Azimuthal Differential Pressures in Downcomer at Level 06, UPTF Test 6 – Run 133**

a,c

**Figure 19.3-66 Measured Azimuthal Differential Pressures in Downcomer at Level 22, UPTF  
Test 6 – Run 133**

a,c

**Figure 19.3-67 Predicted Azimuthal Differential Pressures in Downcomer at Level 22, UPTF  
Test 6 – Run 133**

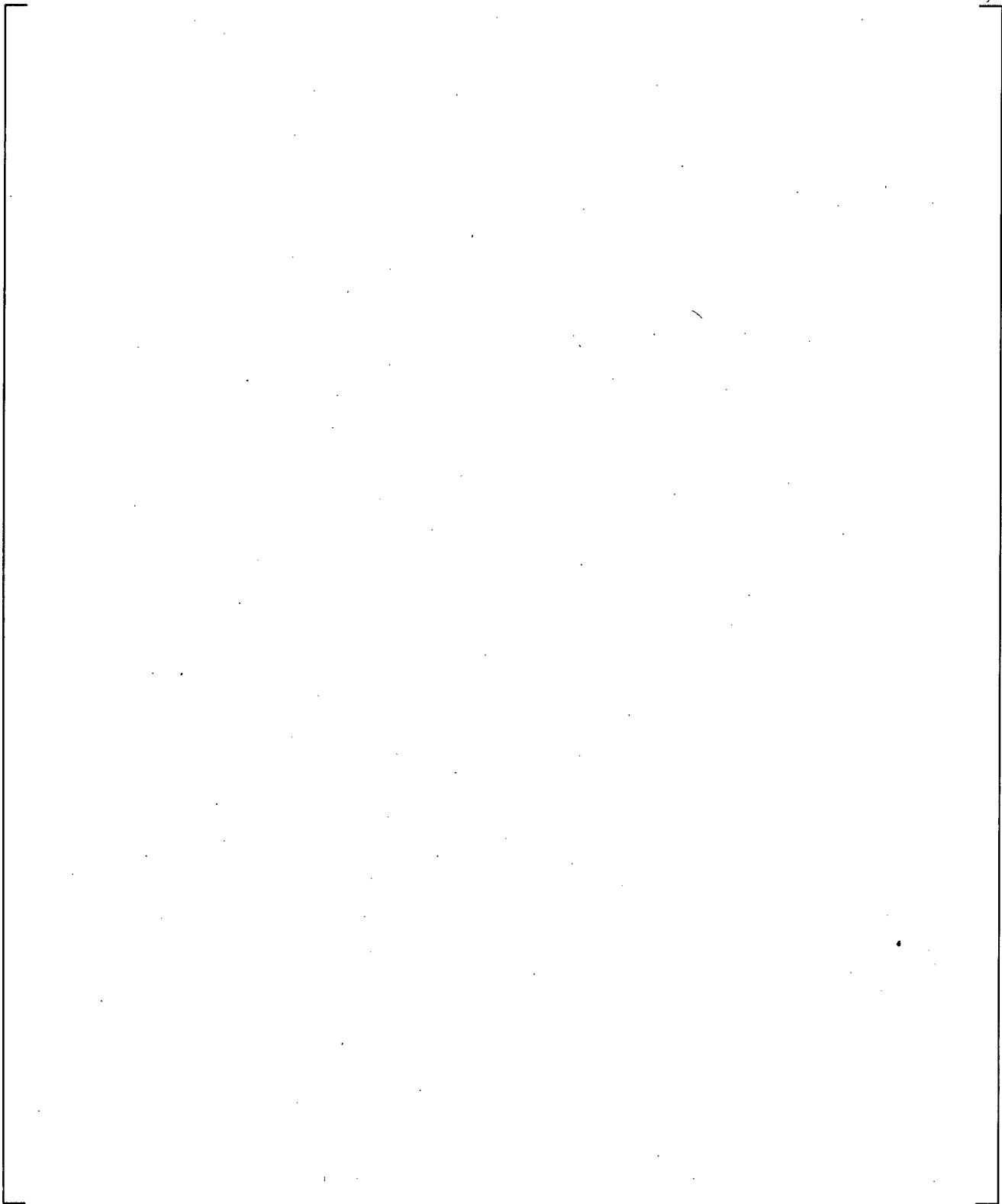


**Figure 19.3-68 Comparison on Differential Pressure in Lower Plenum, UPTF Test 6 – Run 133**

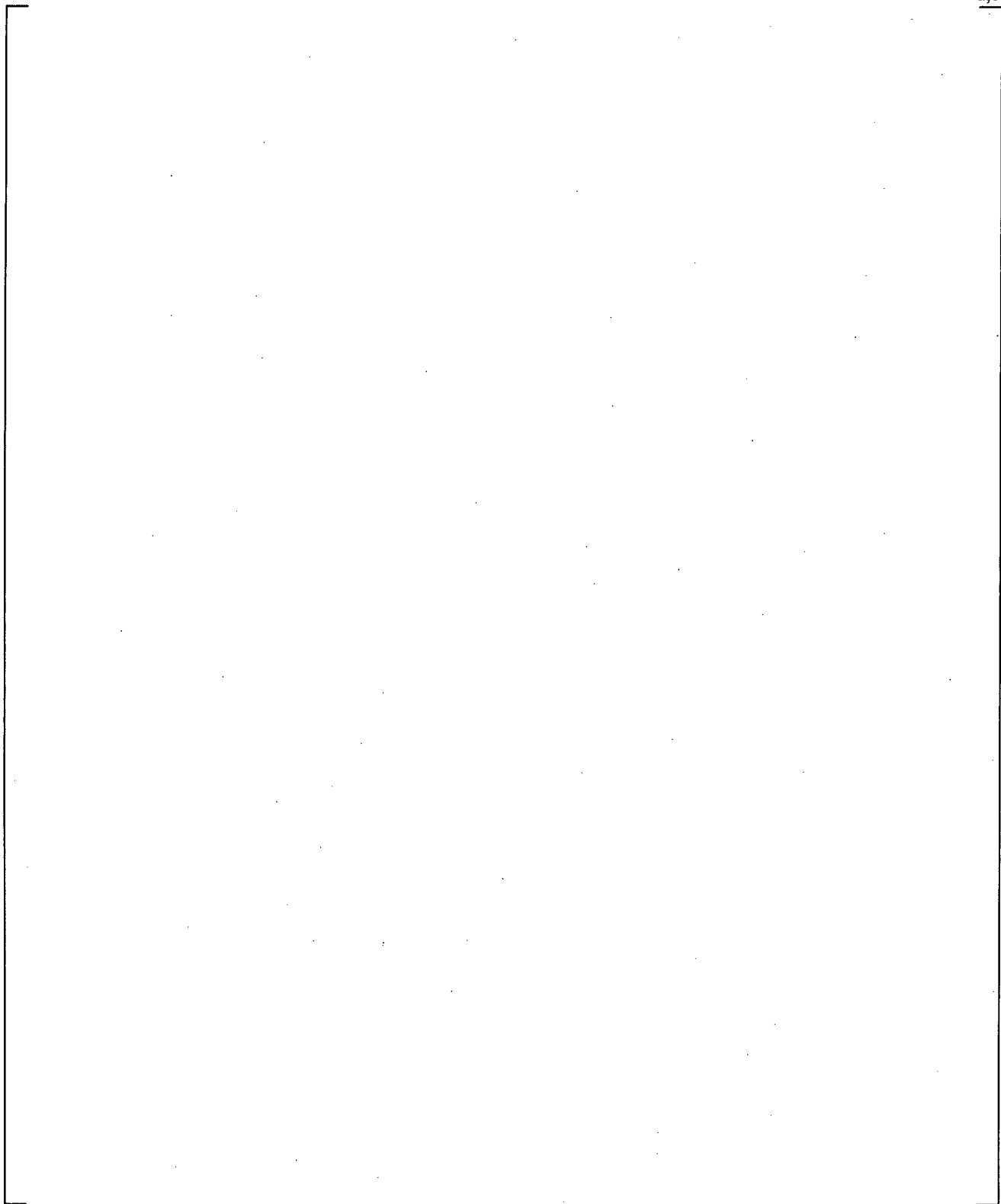


**Figure 19.3-69 Total Core Steam Injection, UPTF Test 6 – Run 135**

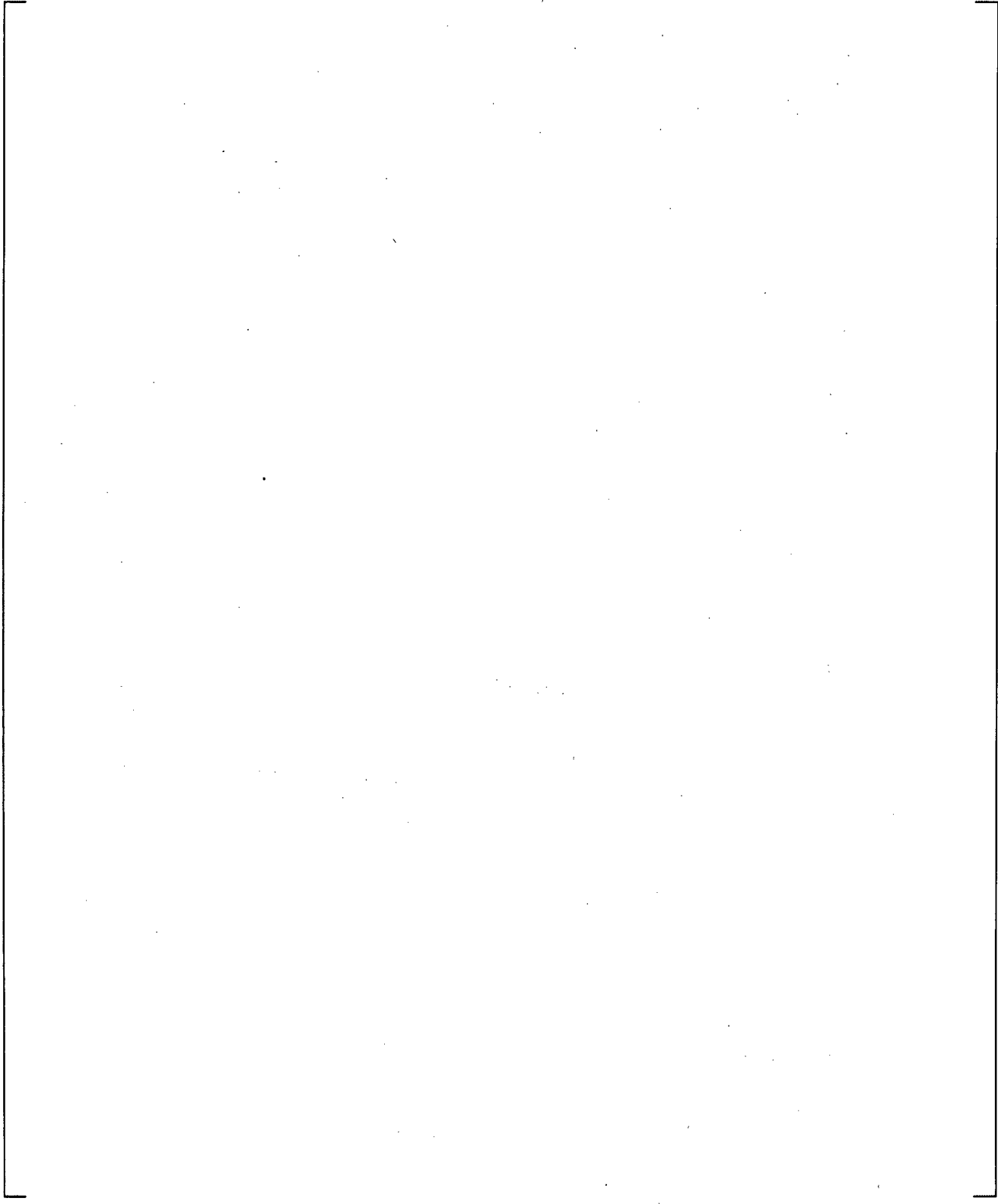


**Figure 19.3-70 Steam Generator Simulator Steam Injection, UPTF Test 6 – Run 135**

a,c

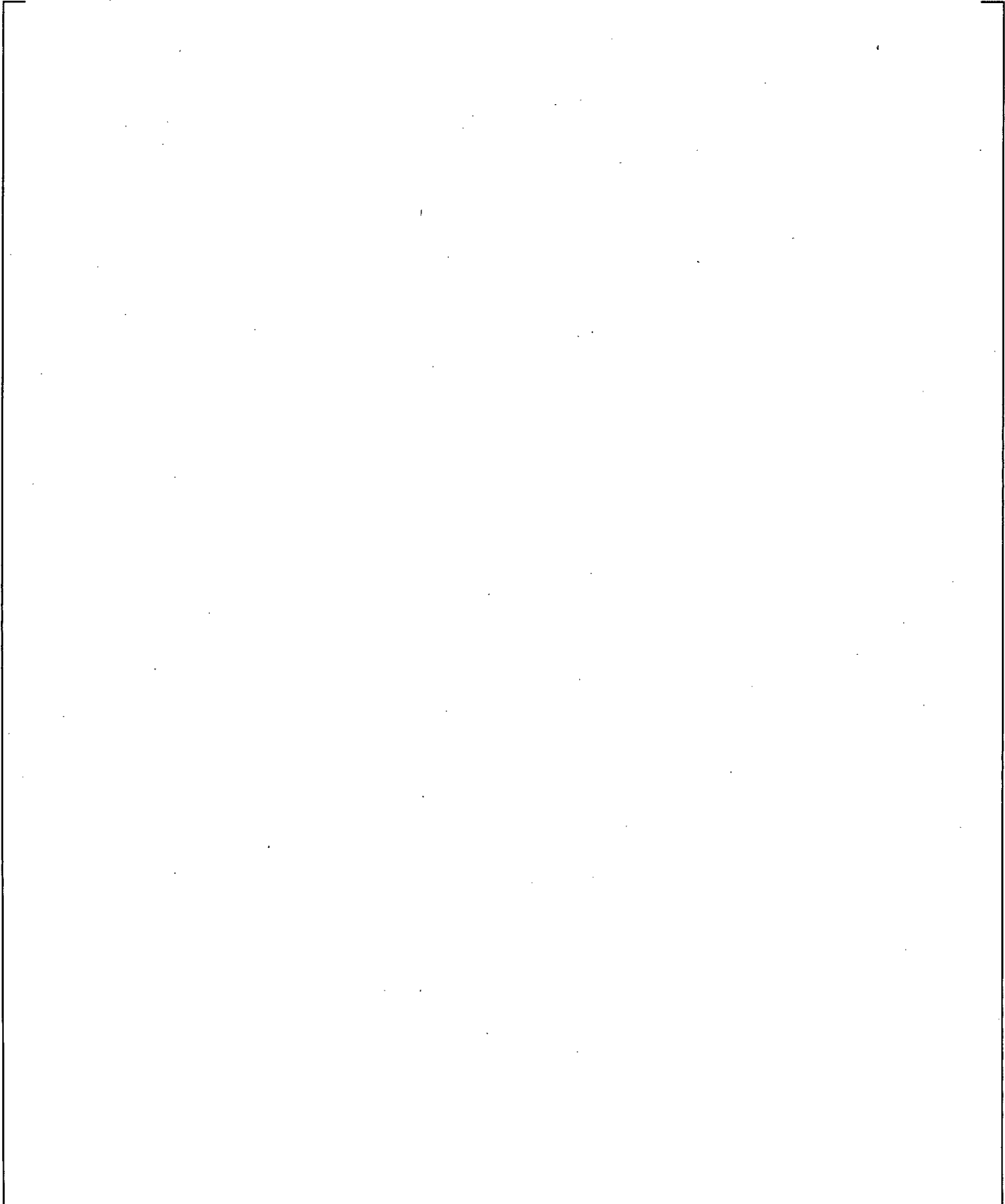


**Figure 19.3-71 Intact Loop ECC Injection, UPTF Test 6 – Run 135**

a,c



**Figure 19.3-72 Measured Absolute Pressures in the Upper Plenum and Downcomer, UPTF Test 6 – Run 135**

a,c



**Figure 19.3-73 Predicted Absolute Pressures in the Upper Plenum and Downcomer, UPTF Test 6 – Run 135**

a,c



**Figure 19.3-74 Measured Downcomer Fluid Temperature at Level 21, UPTF Test 6 – Run 135**

a,c



**Figure 19.3-75 Predicted Downcomer Fluid Temperature at Level 21, UPTF Test 6 – Run 135**

a,c

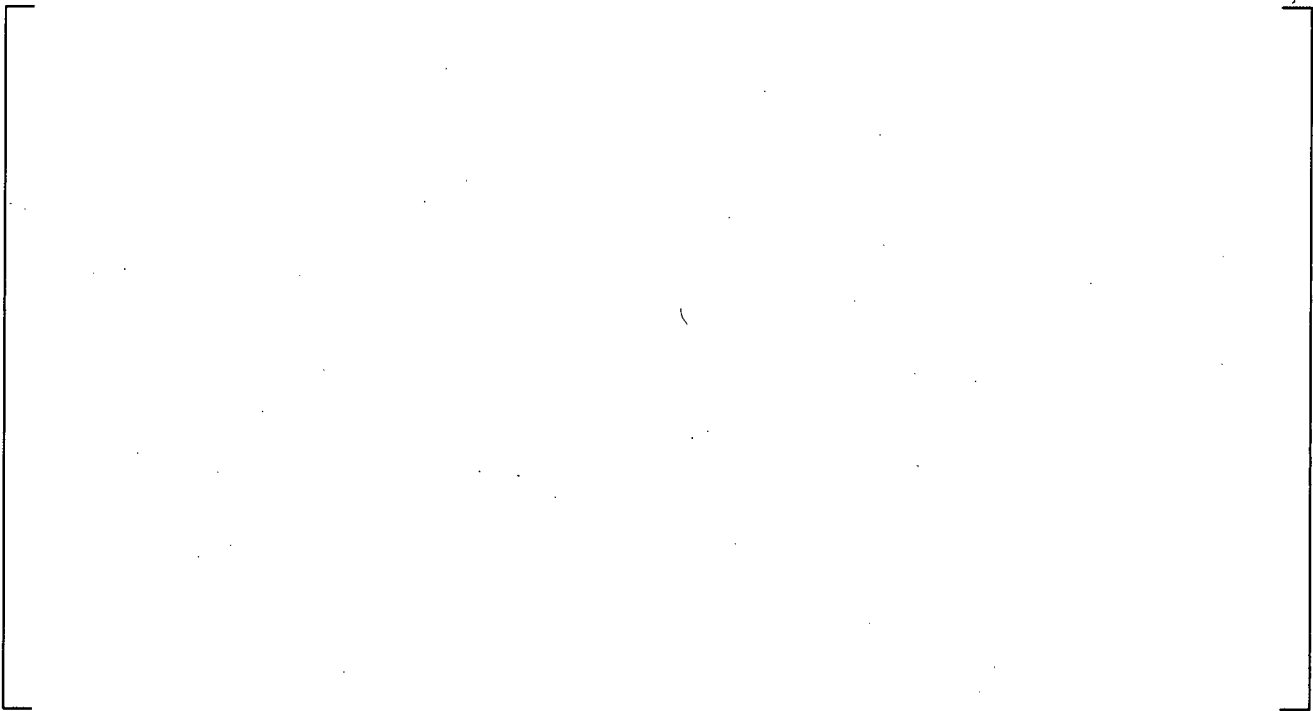


**Figure 19.3-76 Measured Downcomer Fluid Temperature at Level 01, UPTF Test 6 – Run 135**

a,c



**Figure 19.3-77 Predicted Downcomer Fluid Temperature at Level 01, UPTF Test 6 – Run 135**

a,c

**Figure 19.3-78 Predicted Liquid Flow at Bottom of the Downcomer in Intact Side, UPTF  
Test 6 – Run 135**

a,c

**Figure 19.3-79 Predicted Liquid Flow at Bottom of the Downcomer in Broken Side, UPTF  
Test 6 – Run 135**

a,c

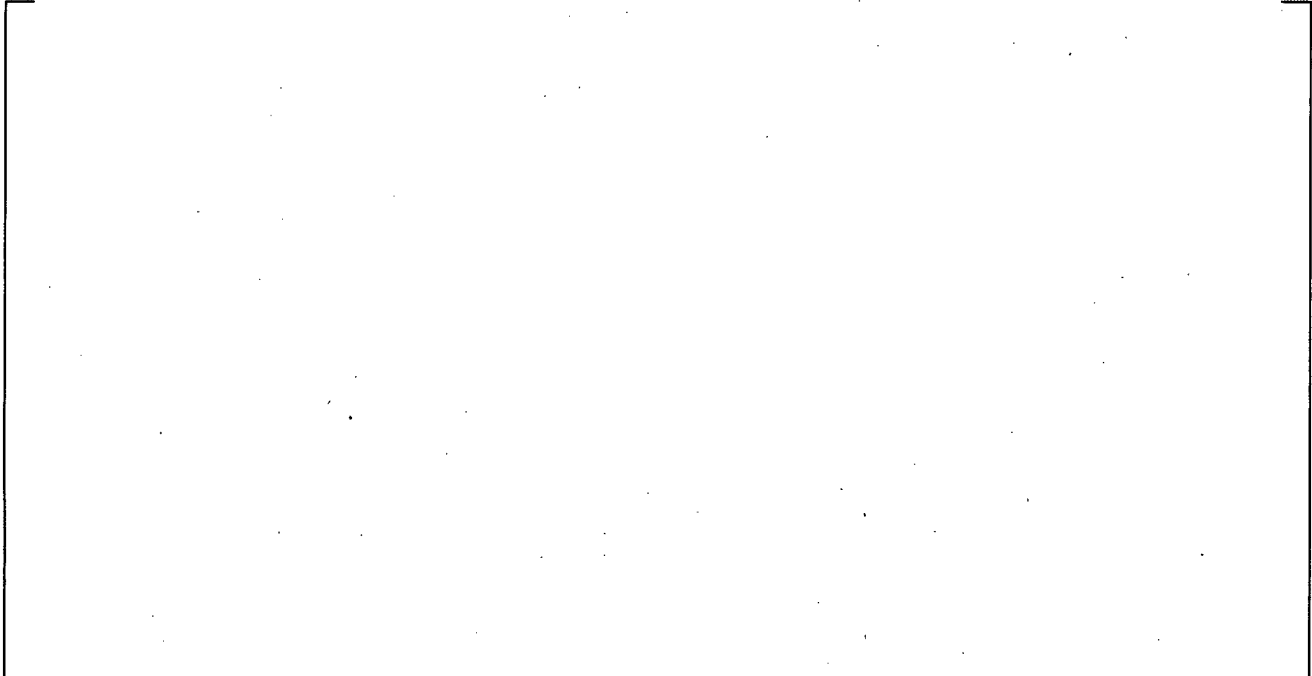


**Figure 19.3-80 Measured Axial Differential Pressures in Downcomer, UPTF Test 6 – Run 135**

a,c



**Figure 19.3-81 Predicted Axial Differential Pressures in Downcomer, UPTF Test 6 – Run 135**

a,c



**Figure 19.3-82 Measured Azimuthal Differential Pressures in Downcomer at Level 06, UPTF Test 6 - Run 135**

a,c



**Figure 19.3-83 Predicted Azimuthal Differential Pressures in Downcomer at Level 06, UPTF Test 6 - Run 135**

a,c

**Figure 19.3-84 Measured Azimuthal Differential Pressures in Downcomer at Level 22, UPTF Test 6 – Run 135**

a,c

**Figure 19.3-85 Predicted Azimuthal Differential Pressures in Downcomer at Level 22, UPTF Test 6 – Run 135**

**Figure 19.3-86 Comparison on Differential Pressure in Lower Plenum, UPTF Test 6 – Run 135**

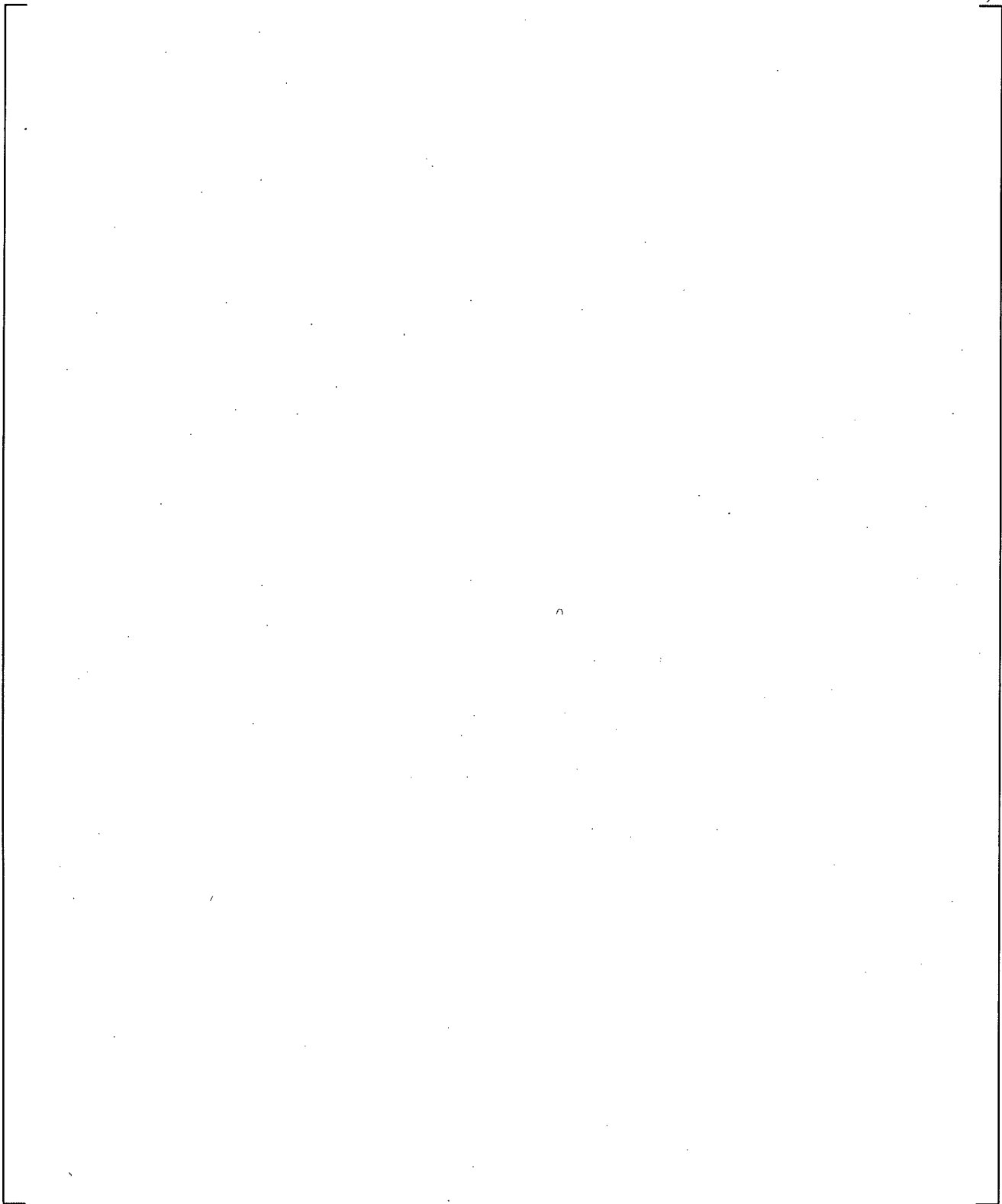
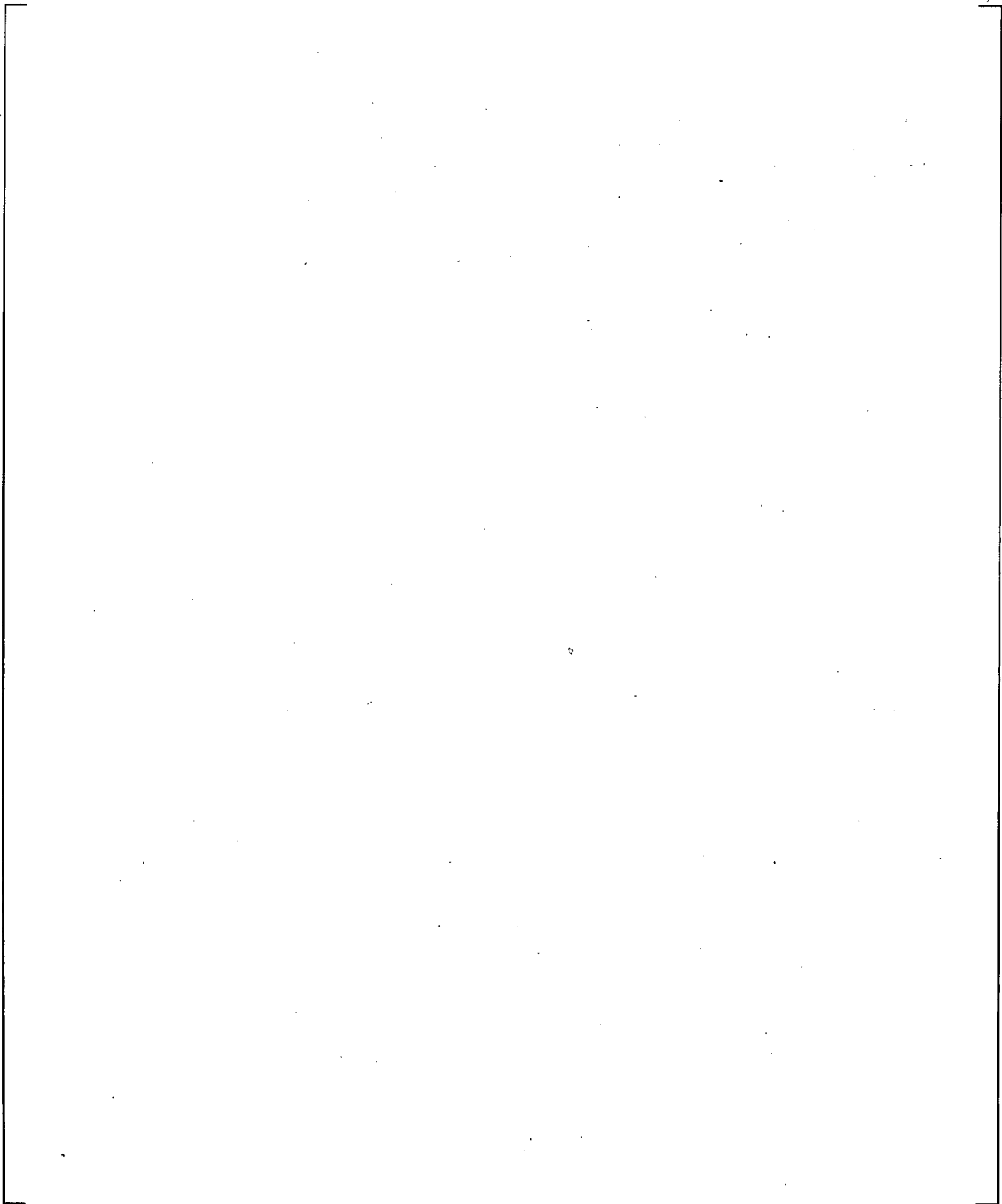


Figure 19.3-87 Total Core Steam Injection, UPTF Test 6 – Run 136



**Figure 19.3-88 Intact Loop ECC Injection, UPTF Test 6 – Run 136**

a,c

**Figure 19.3-89 Measured Absolute Pressures in the Upper Plenum and Downcomer, UPTF  
Test 6 – Run 136**

a,c

**Figure 19.3-90 Predicted Absolute Pressures in the Upper Plenum and Downcomer, UPTF  
Test 6 – Run 136**

a,c

**Figure 19.3-91 Measured Downcomer Fluid Temperature at Level 21, UPTF Test 6 – Run 136**

a,c

**Figure 19.3-92 Predicted Downcomer Fluid Temperature at Level 21, UPTF Test 6 – Run 136**

a,c



**Figure 19.3-93 Measured Downcomer Fluid Temperature at Level 01, UPTF Test 6 – Run 136**

a,c

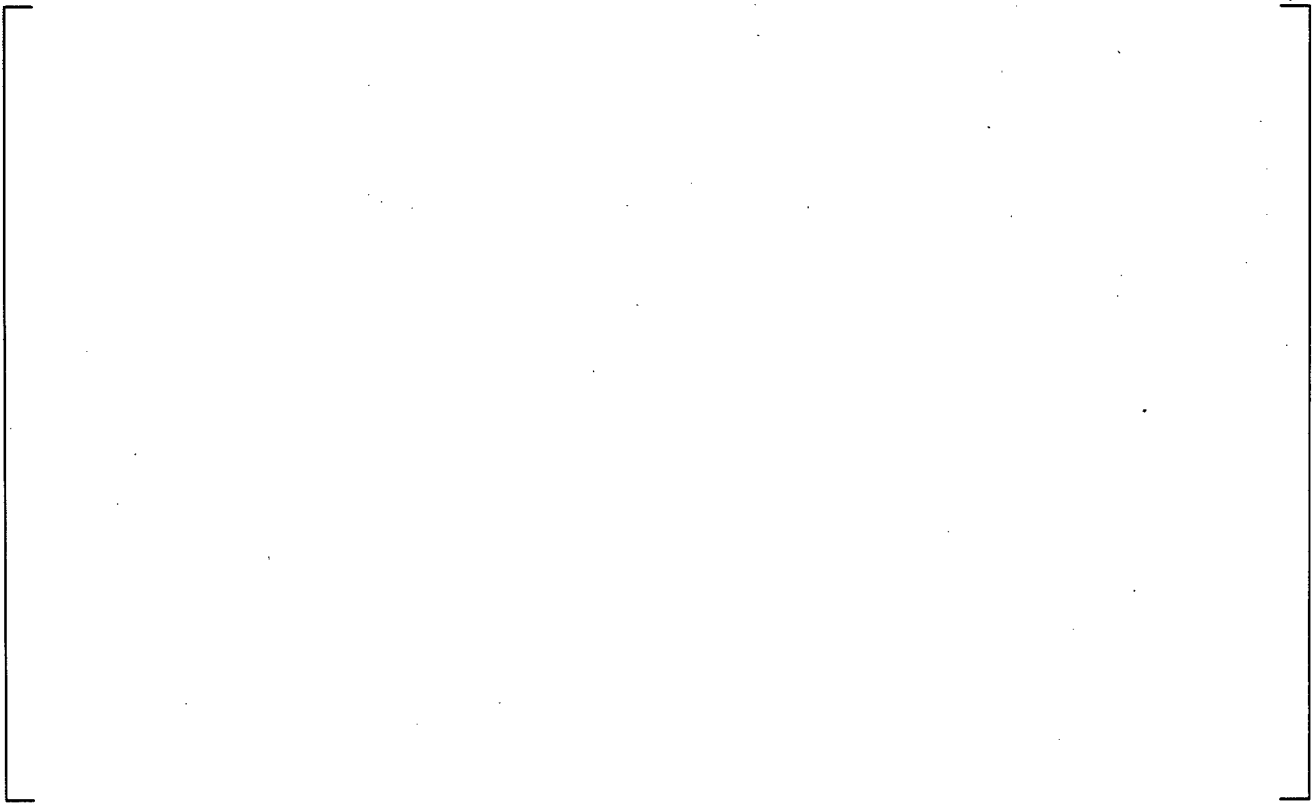


**Figure 19.3-94 Predicted Downcomer Fluid Temperature at Level 01, UPTF Test 6 – Run 136**

a,c

**Figure 19.3-95 Predicted Liquid Flow at Bottom of the Downcomer in Intact Side, UPTF  
Test 6 – Run 136**

a,c

**Figure 19.3-96 Predicted Liquid Flow at Bottom of the Downcomer in Broken Side, UPTF  
Test 6 – Run 136**

a,c



**Figure 19.3-97 Measured Axial Differential Pressures in Downcomer, UPTF Test 6 – Run 136**

a,c



**Figure 19.3-98 Predicted Axial Differential Pressures in Downcomer, UPTF Test 6 – Run 136**

a,c



**Figure 19.3-99 Measured Azimuthal Differential Pressures in Downcomer at Level 06, UPTF Test 6 – Run 136**

a,c



**Figure 19.3-100 Predicted Azimuthal Differential Pressures in Downcomer at Level 06, UPTF Test 6 – Run 136**

a,c



**Figure 19.3-101 Measured Azimuthal Differential Pressures in Downcomer at Level 22, UPTF Test 6 - Run 136**

a,c



**Figure 19.3-102 Predicted Azimuthal Differential Pressures in Downcomer at Level 22, UPTF Test 6 - Run 136**

a,c

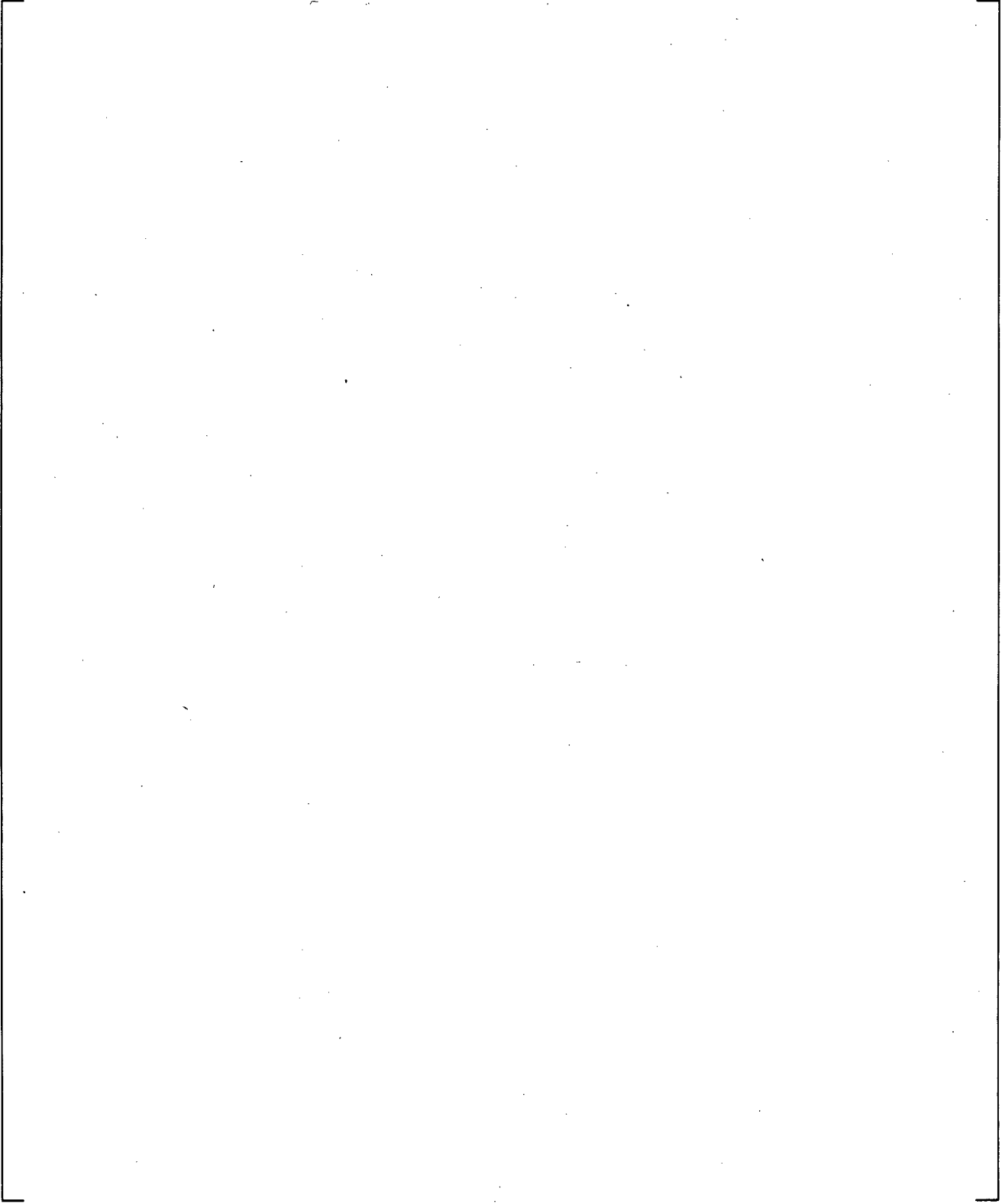


**Figure 19.3-103 Comparison on Differential Pressure in Lower Plenum, UPTF Test 6 – Run 136**

a,c

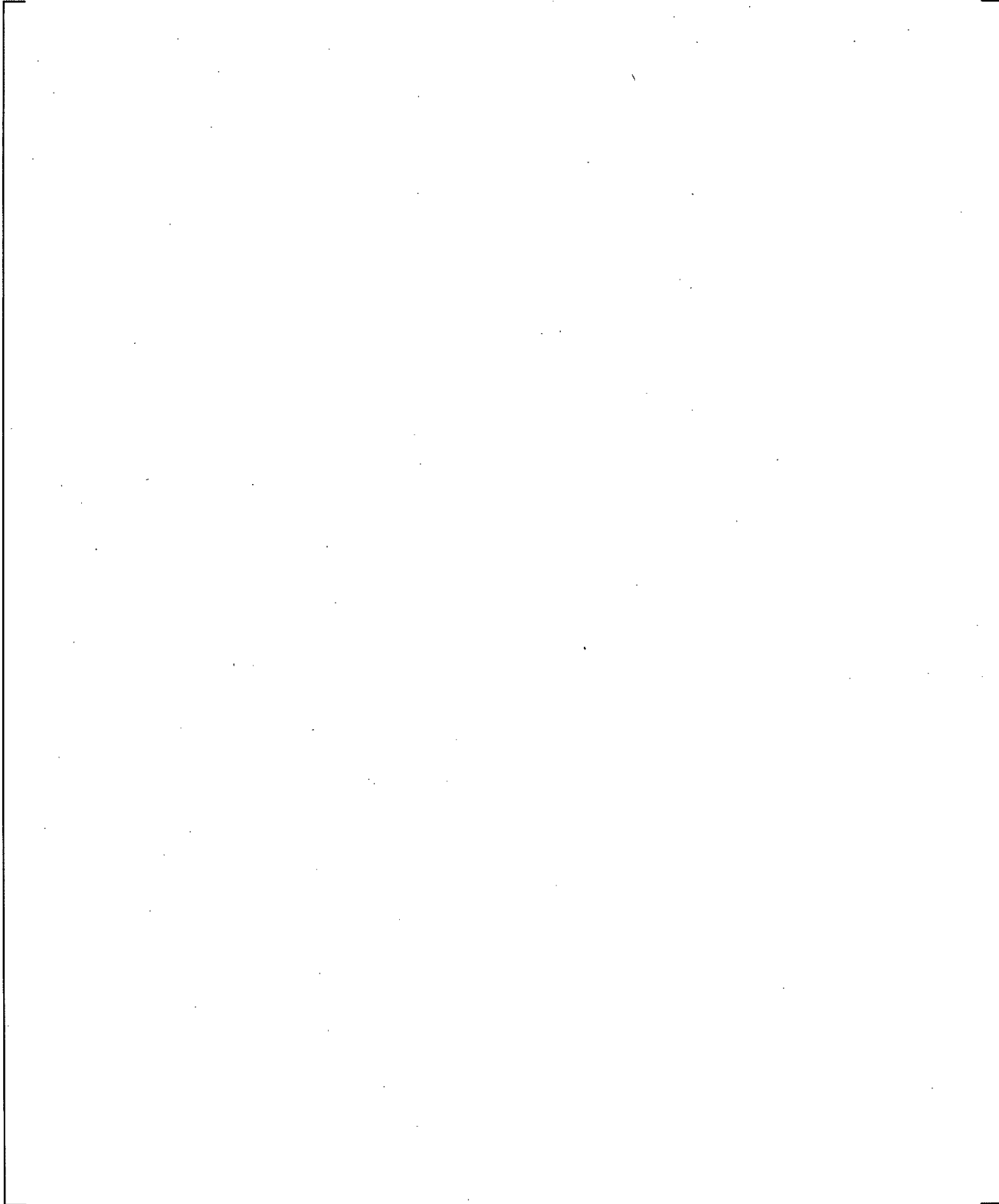


**Figure 19.3-104 Lower Plenum Fluid Inventory, UPTF Test 6 – Run 131**

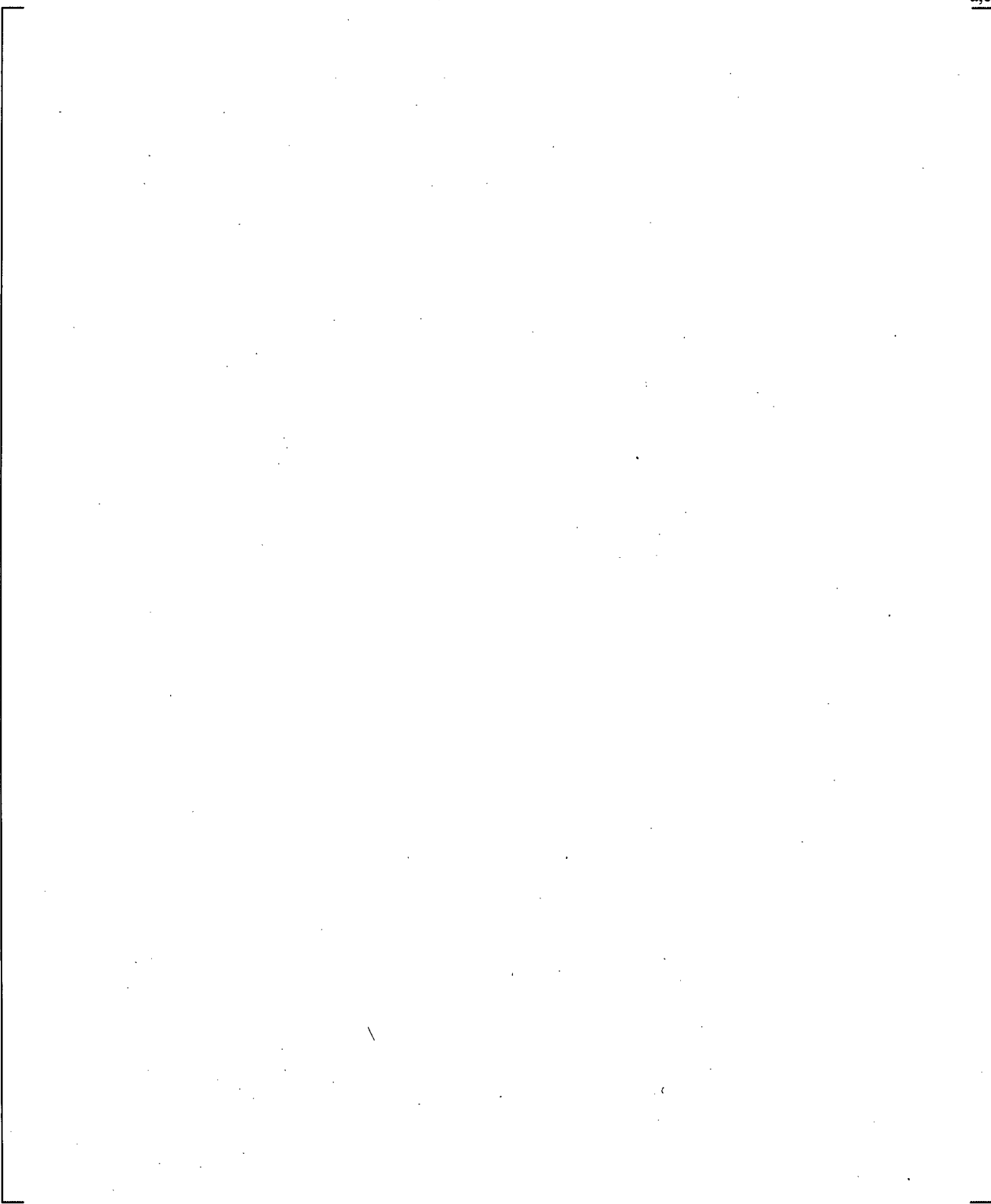


**Figure 19.3-105 Lower Plenum Fluid Inventory, UPTF Test 6 – Run 132**

a,c

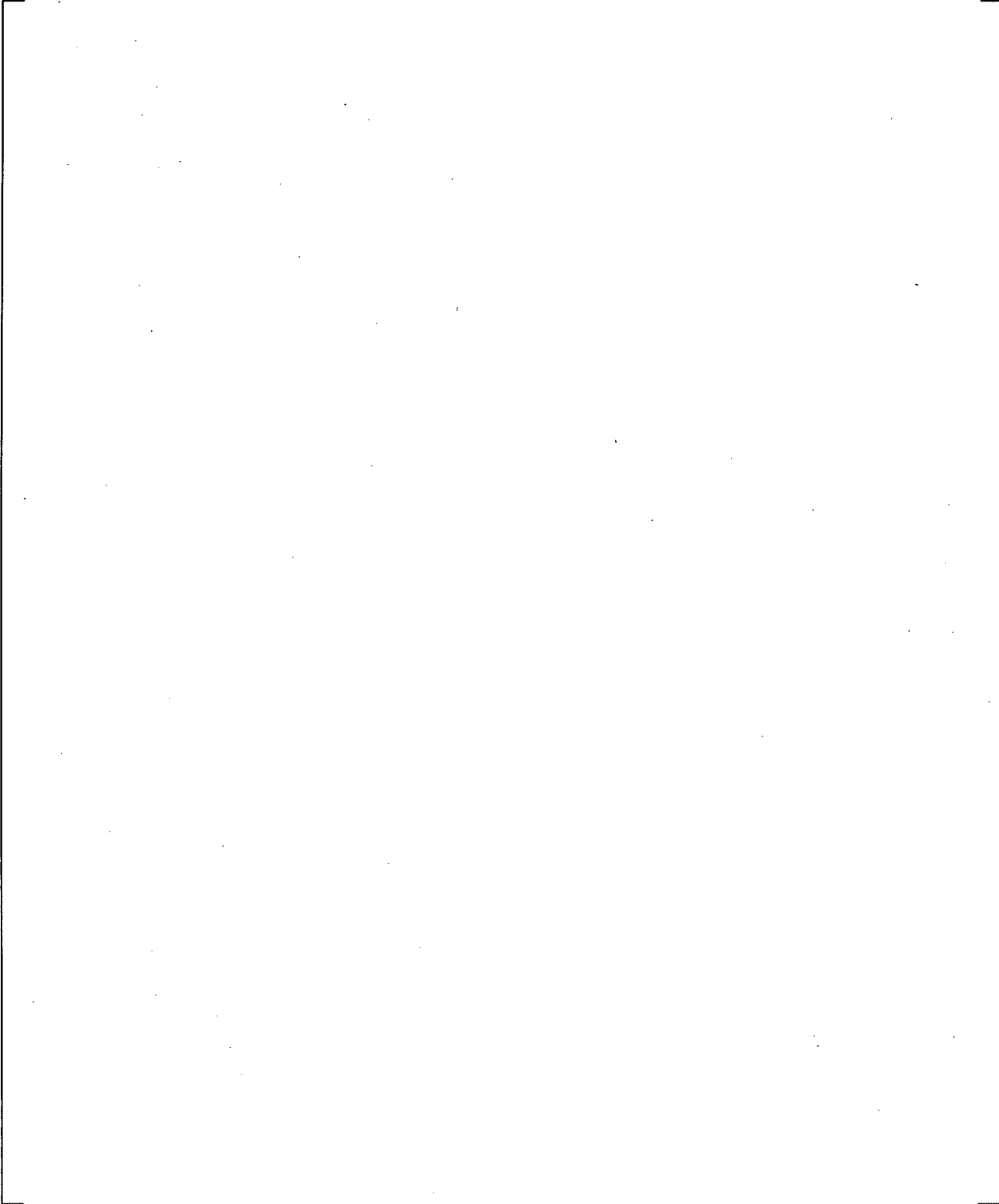


**Figure 19.3-106 Lower Plenum Fluid Inventory, UPTF Test 6 – Run 133**

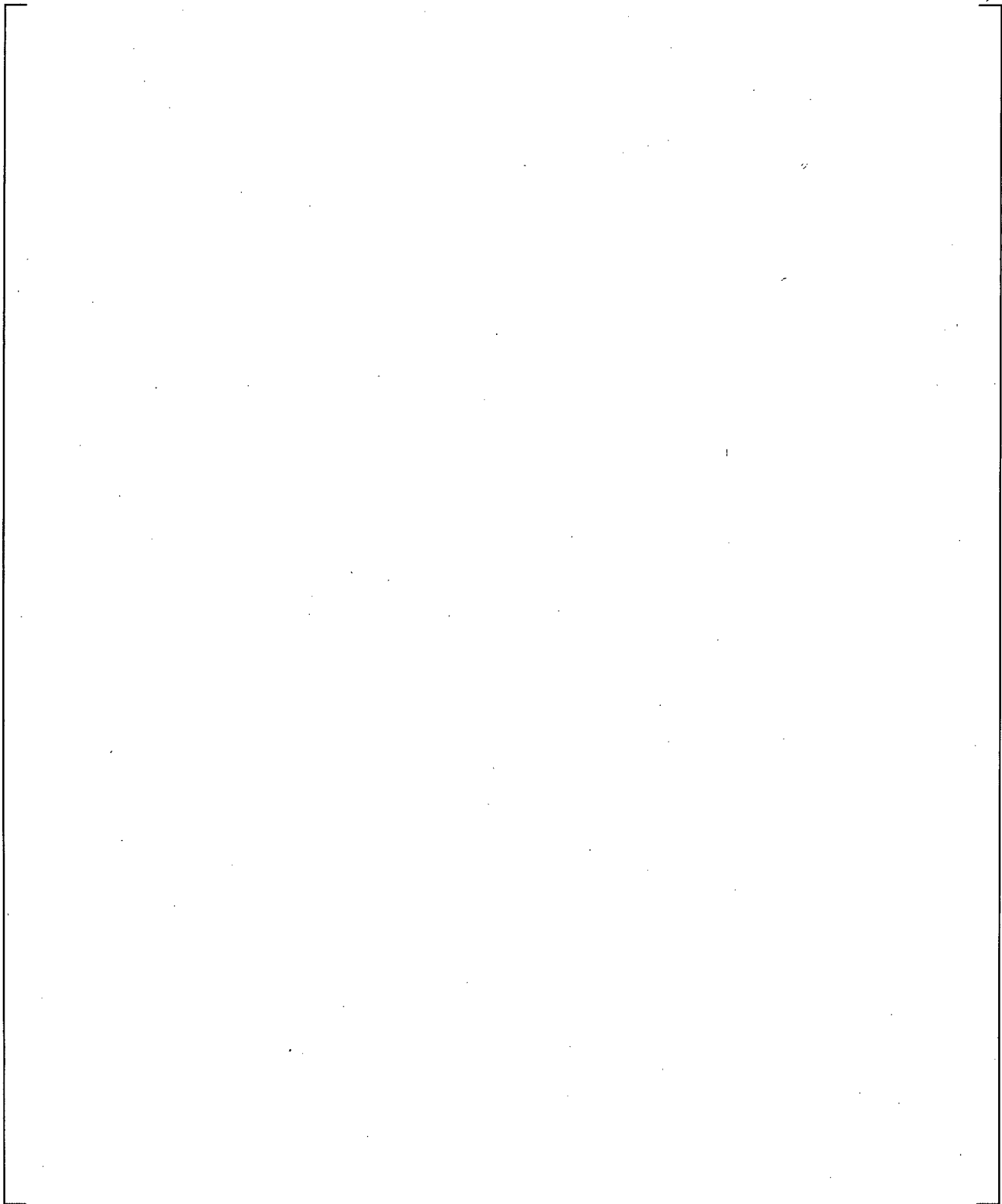


**Figure 19.3-107 Lower Plenum Fluid Inventory, UPTF Test 6 – Run 135**

a,c

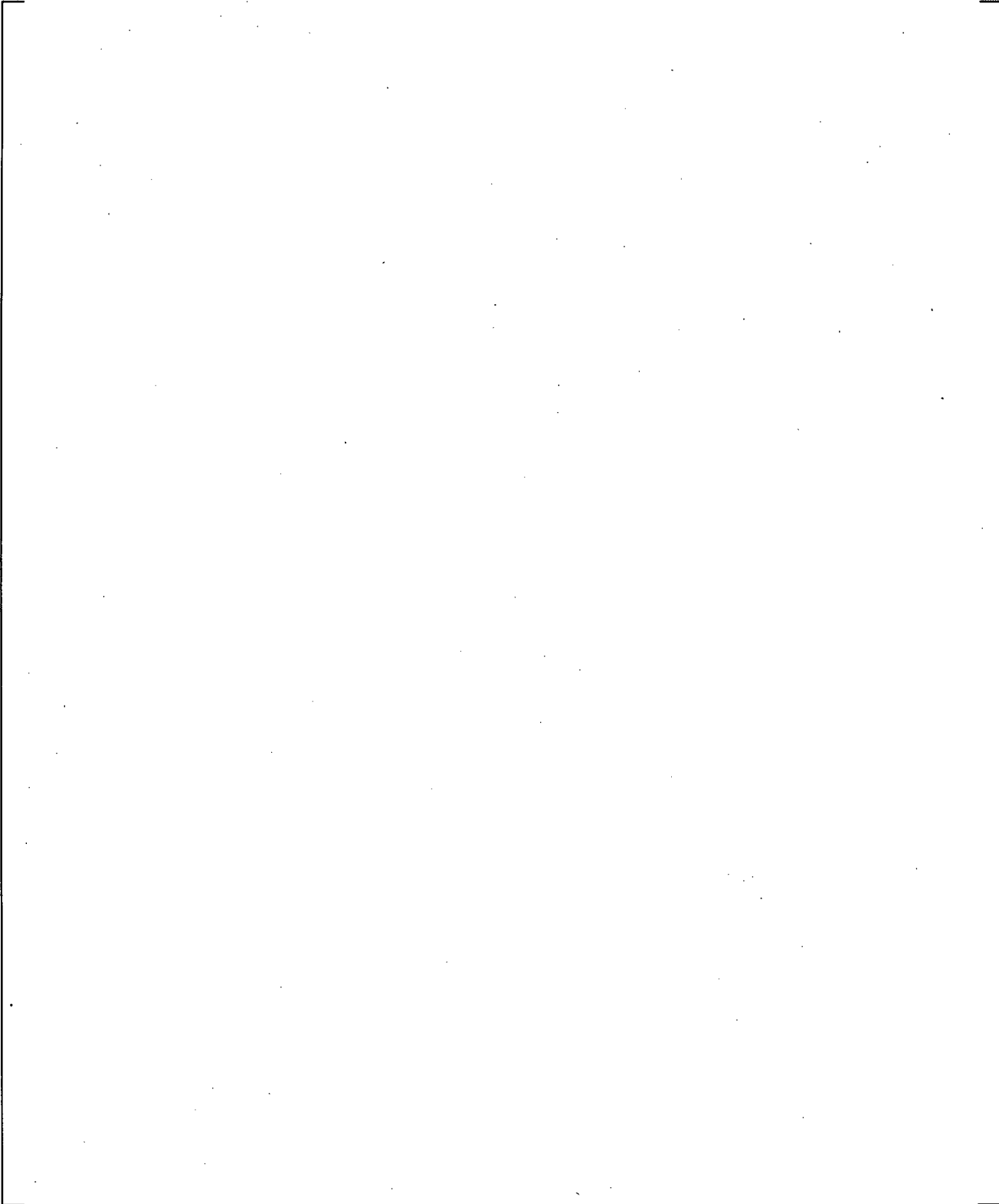


**Figure 19.3-108 Lower Plenum Fluid Inventory, UPTF Test 6 – Run 136**

**Figure 19.3-109 Comparison between Measured and Predicted Penetration Rates in UPTF Test 6**

**Figure 19.3-110 Comparison between Measured and Predicted Refill Periods versus Nominal Steam Flow Rate for Lower Plenum in UPTF Test 6**

b

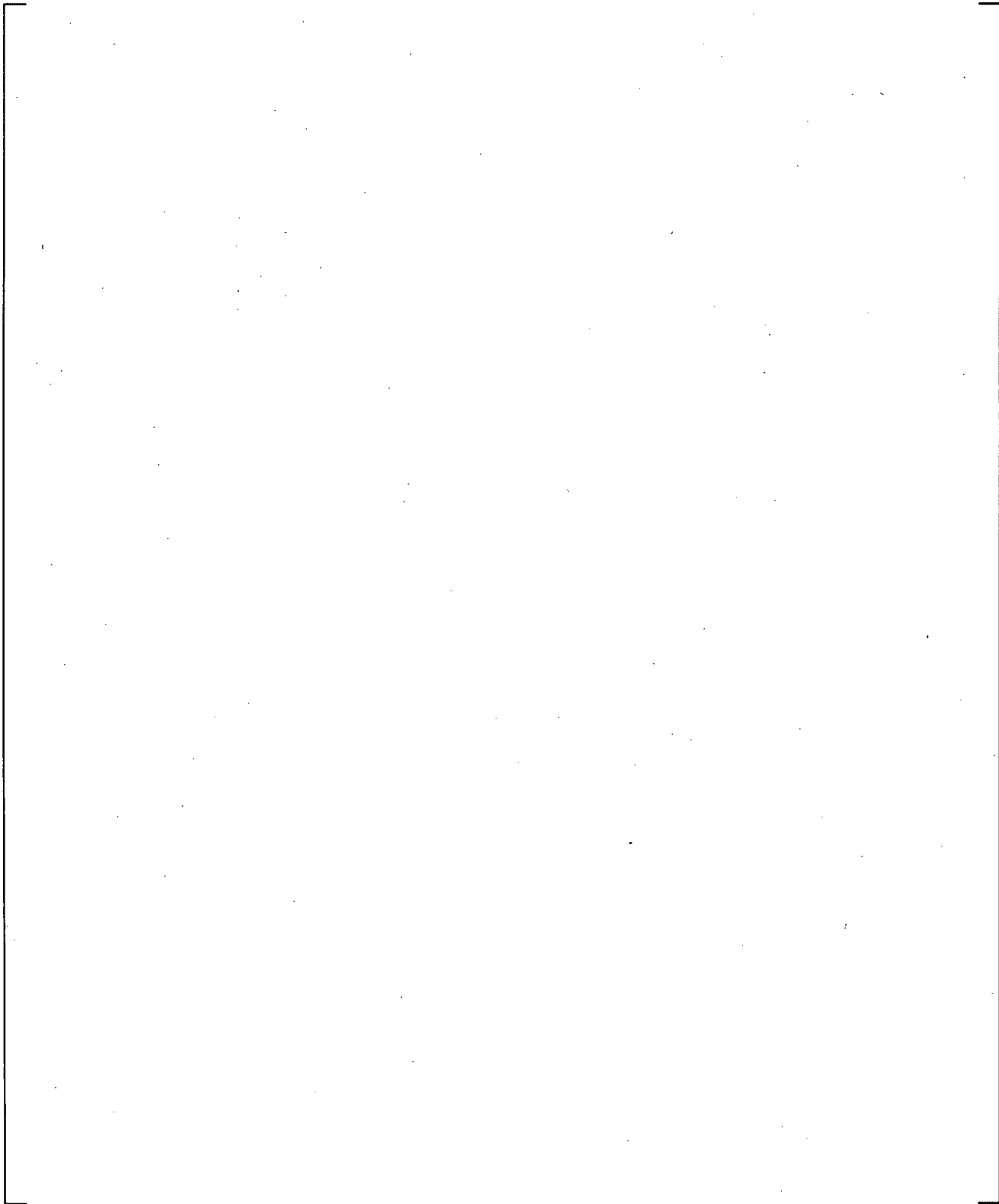


**Figure 19.3-111 Downcomer CCFL Behavior for UPTF Test 6**

a,c

**Figure 19.3-112 Estimated Mass Distribution, UPTF Test 6 – Run 131**

a,c

**Figure 19.3-113 Predicted Mass Distribution, UPTF Test 6 – Run 131**

a,c

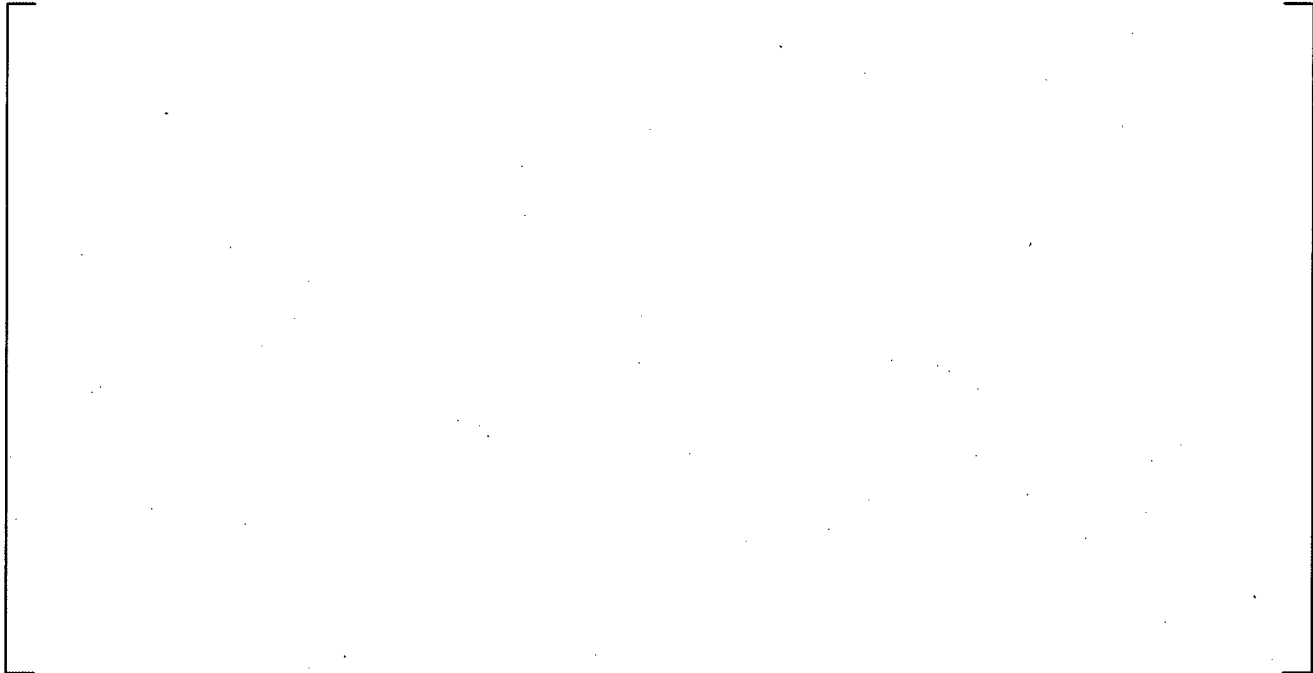


**Figure 19.3-114 Estimated Mass Distribution, UPTF Test 6 – Run 132**

a,c



**Figure 19.3-115 Predicted Mass Distribution, UPTF Test 6 – Run 132**

a,c



**Figure 19.3-116 Estimated Mass Distribution, UPTF Test 6 – Run 133**

a,c



**Figure 19.3-117 Predicted Mass Distribution, UPTF Test 6 – Run 133**

a,c

**Figure 19.3-118 Estimated Mass Distribution, UPTF Test 6 – Run 135**

a,c

**Figure 19.3-119 Predicted Mass Distribution, UPTF Test 6 – Run 135**

a,c

**Figure 19.3-120 Estimated Mass Distribution, UPTF Test 6 – Run 136**

a,c

**Figure 19.3-121 Predicted Mass Distribution, UPTF Test 6 – Run 136**

a,c

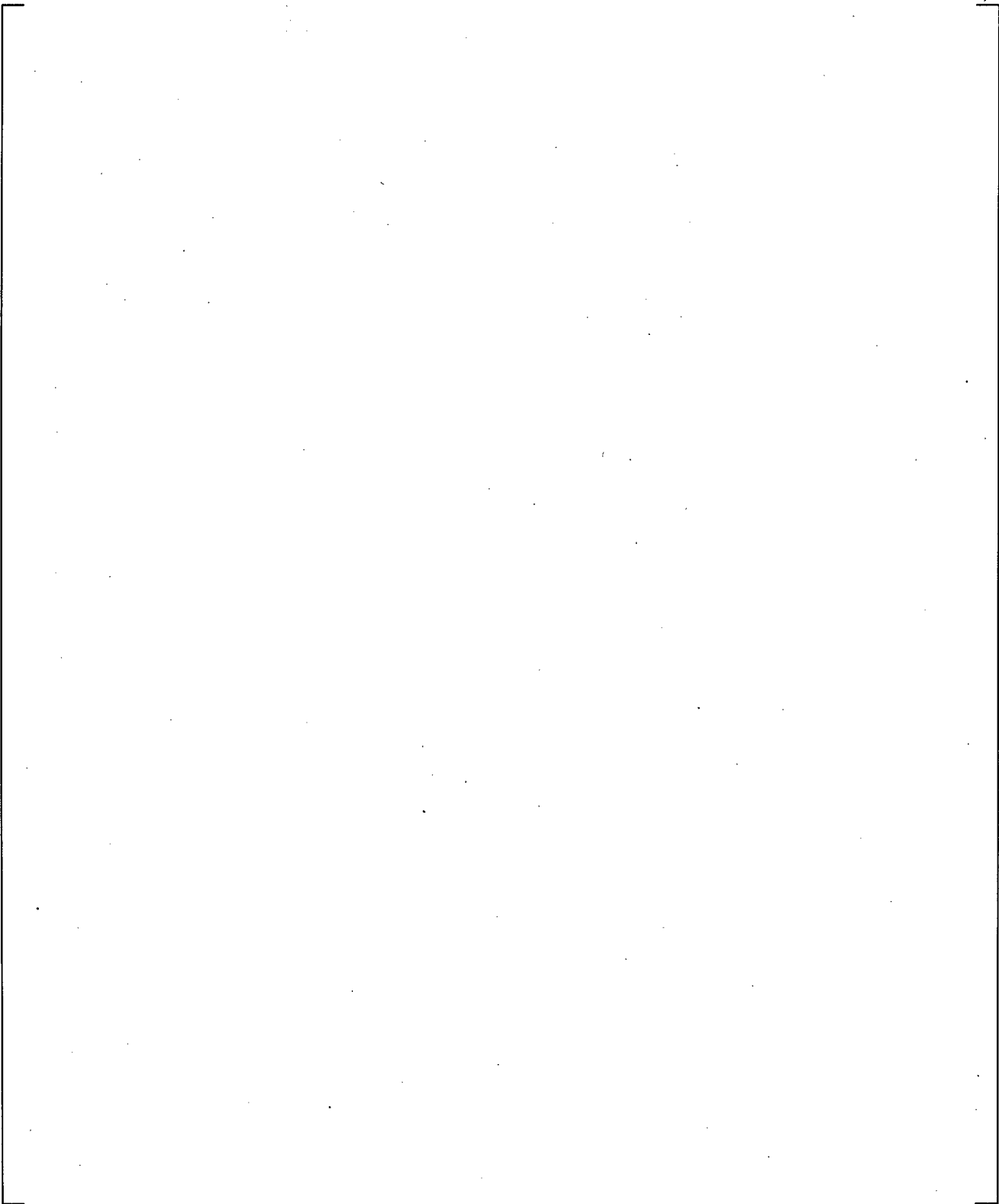


**Figure 19.3-122 Vessel Condensation Efficiency, UPTF Test 6 – Run 131**

a,c

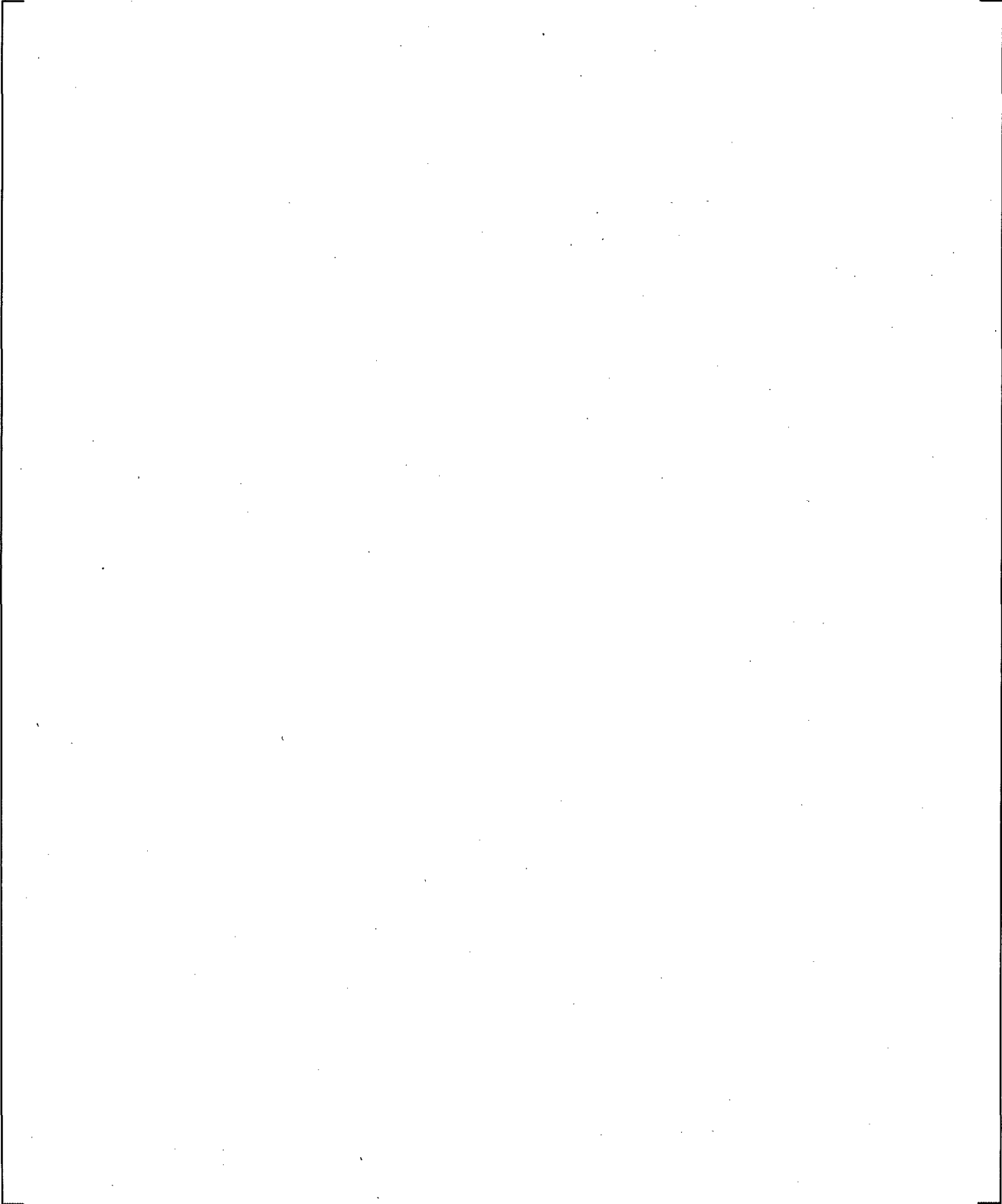


**Figure 19.3-123 Vessel Condensation Efficiency, UPTF Test 6 – Run 132**

a,c

**Figure 19.3-124 Vessel Condensation Efficiency, UPTF Test 6 – Run 133**

a,c

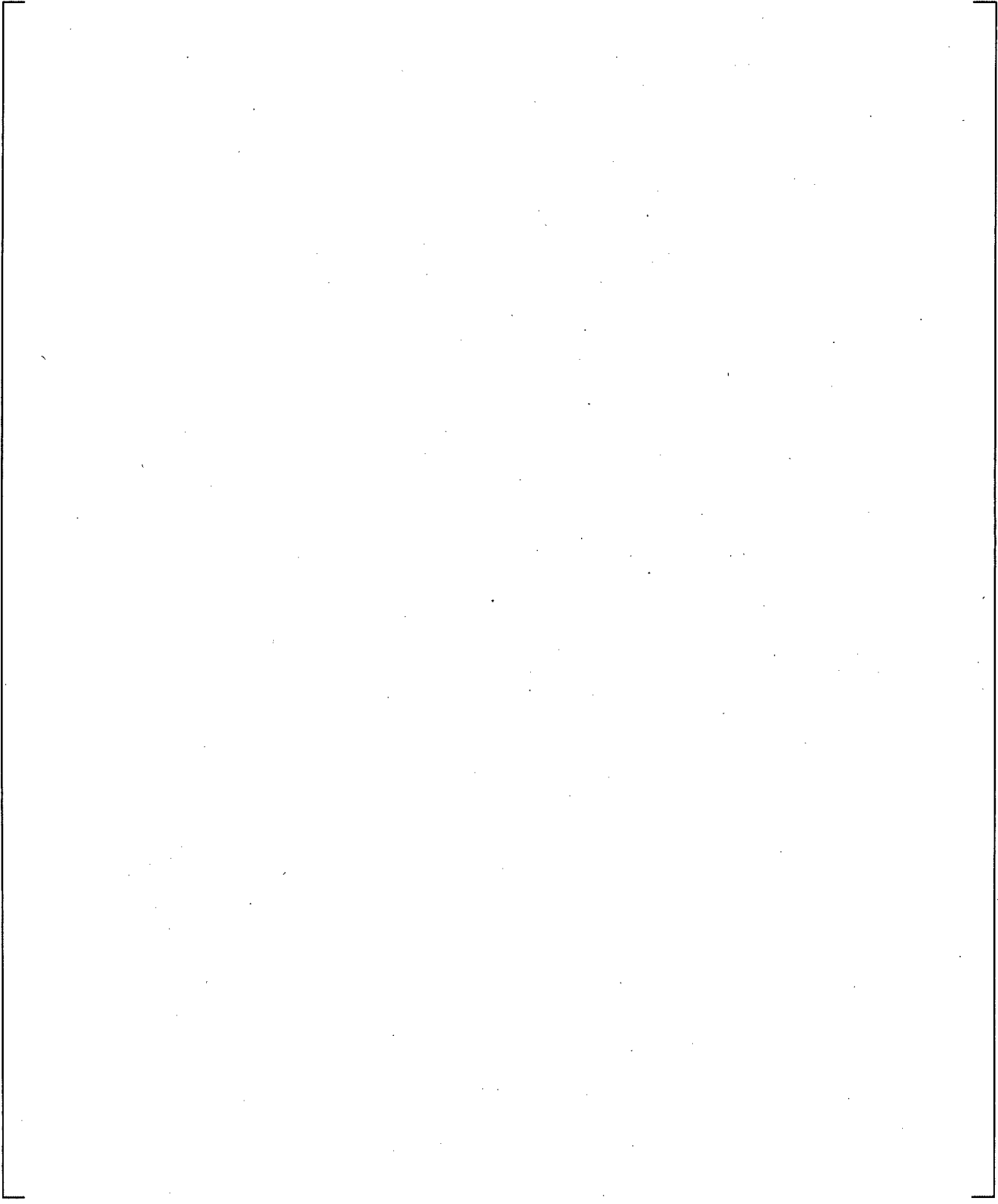


**Figure 19.3-125 Vessel Condensation Efficiency, UPTF Test 6 – Run 135**

a,c

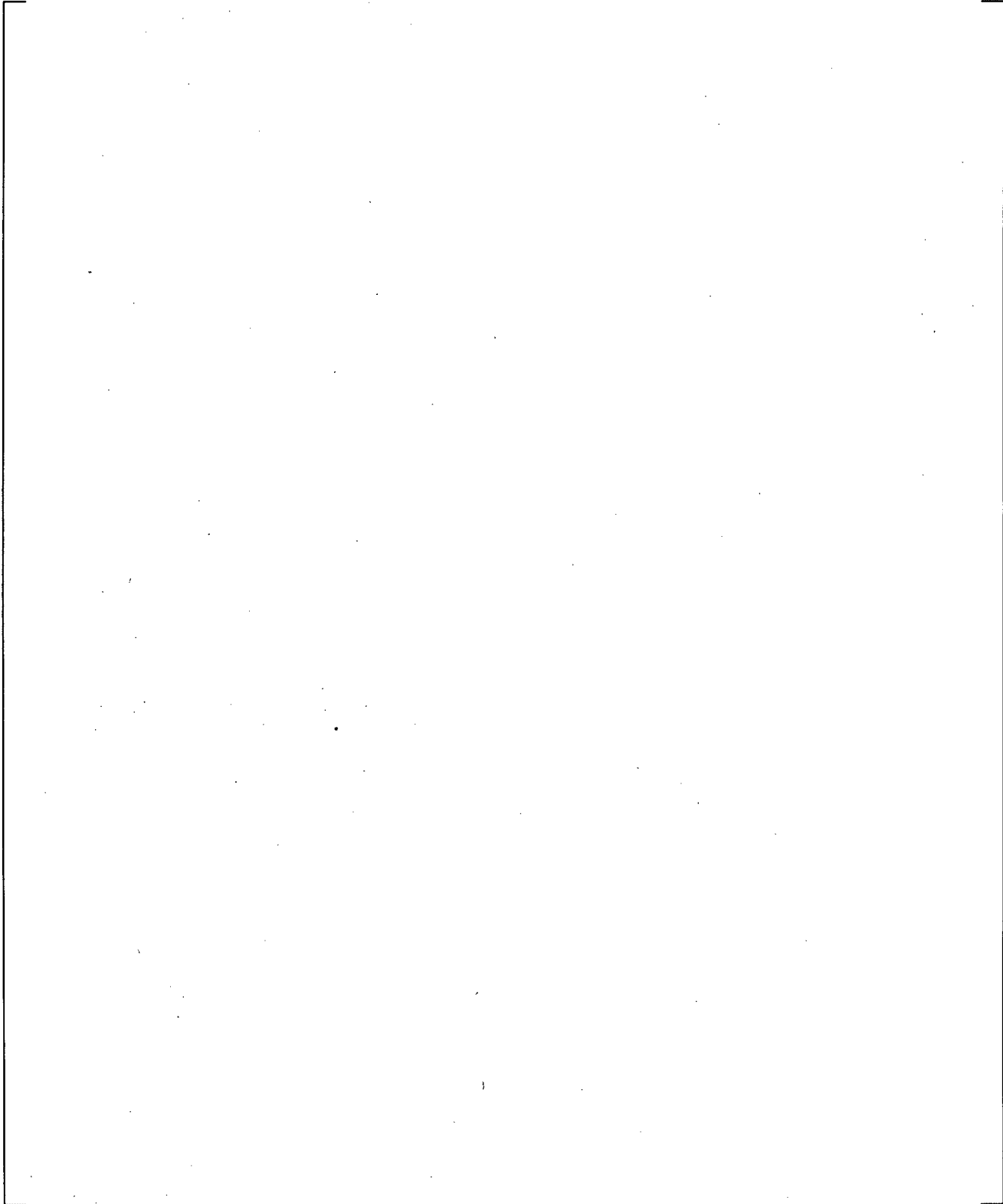


**Figure 19.3-126 Vessel Condensation Efficiency, UPTF Test 6 – Run 136**

**Figure 19.3-127 Comparison of Vessel Condensation Efficiency versus Nominal Steam Flow Rate, UPTF Test 6; Experimental Condensation Efficiency is Estimated by MPR (MPR-1163, 1990); Predicted Condensation Efficiency is Evaluated Using Steam Flow Rate at Break**

**Figure 19.3-128 Comparison of Vessel Condensation Efficiency versus Nominal Steam Flow Rate with Various DC Condensation Multipliers, UPTF Test 6; Predicted Condensation Efficiency is Evaluated Using Steam Flow Rate at Inlet of Broken Cold Leg**

**Figure 19.3-129 Comparison of Filling Period from Start of ECC Injection to End of Lower Plenum Filling with Various DC Condensation Multipliers versus Nominal Steam Flow Rate, UPTF Test 6. Note, Run 132 did not Fill the Lower Plenum at the End of the Calculation.**

**Figure 19.3-130 Comparison of Length of Refill Period from Start of ECC Injection to End of Lower Plenum Filling versus Nominal Steam Flow Rate with Various DTMAX, UPTF Test 6**

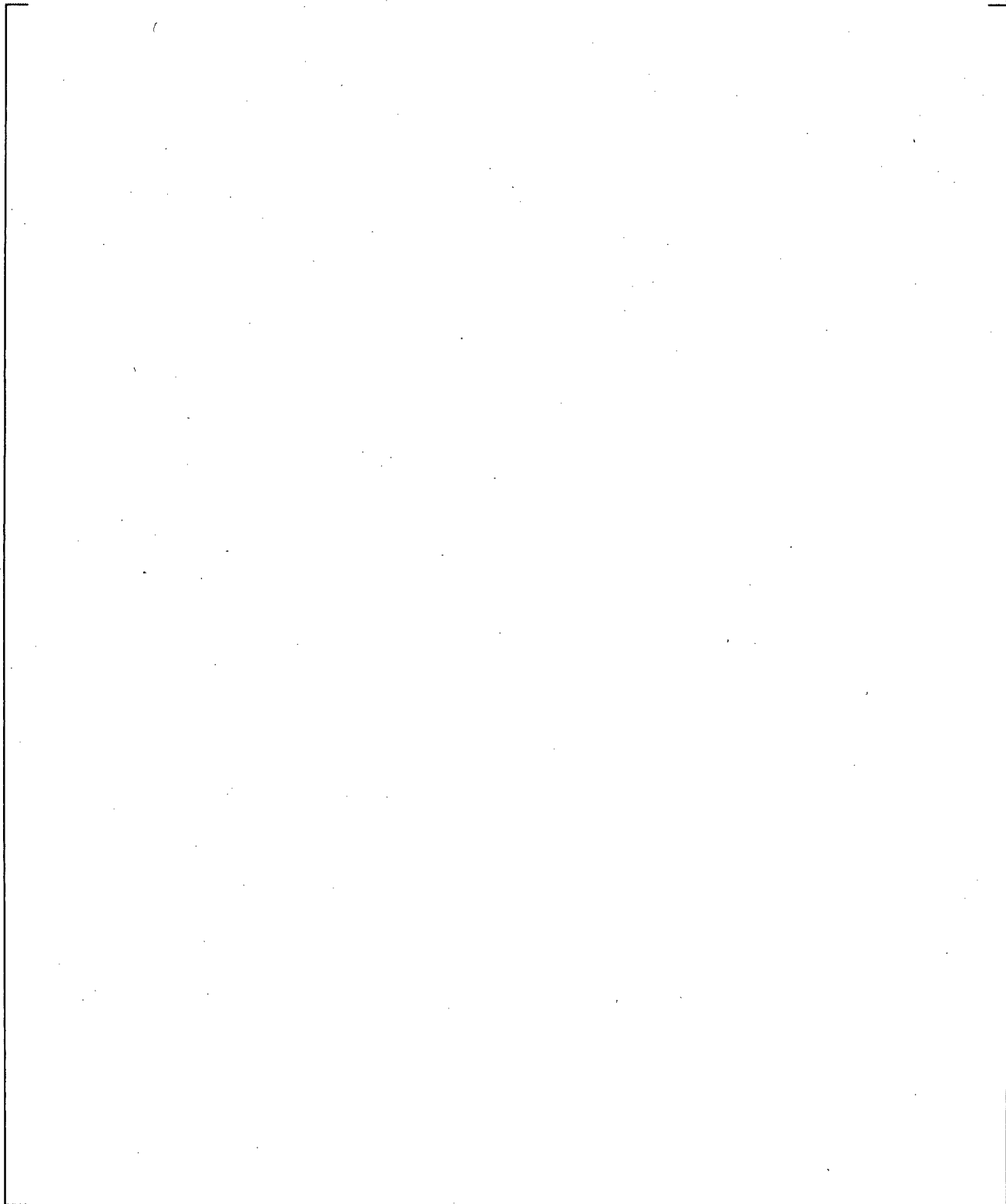


**Figure 19.3-131 Location of Fluid Thermocouples, Differential and Absolute Pressure Measurements in Broken Cold Leg of Loop 04**

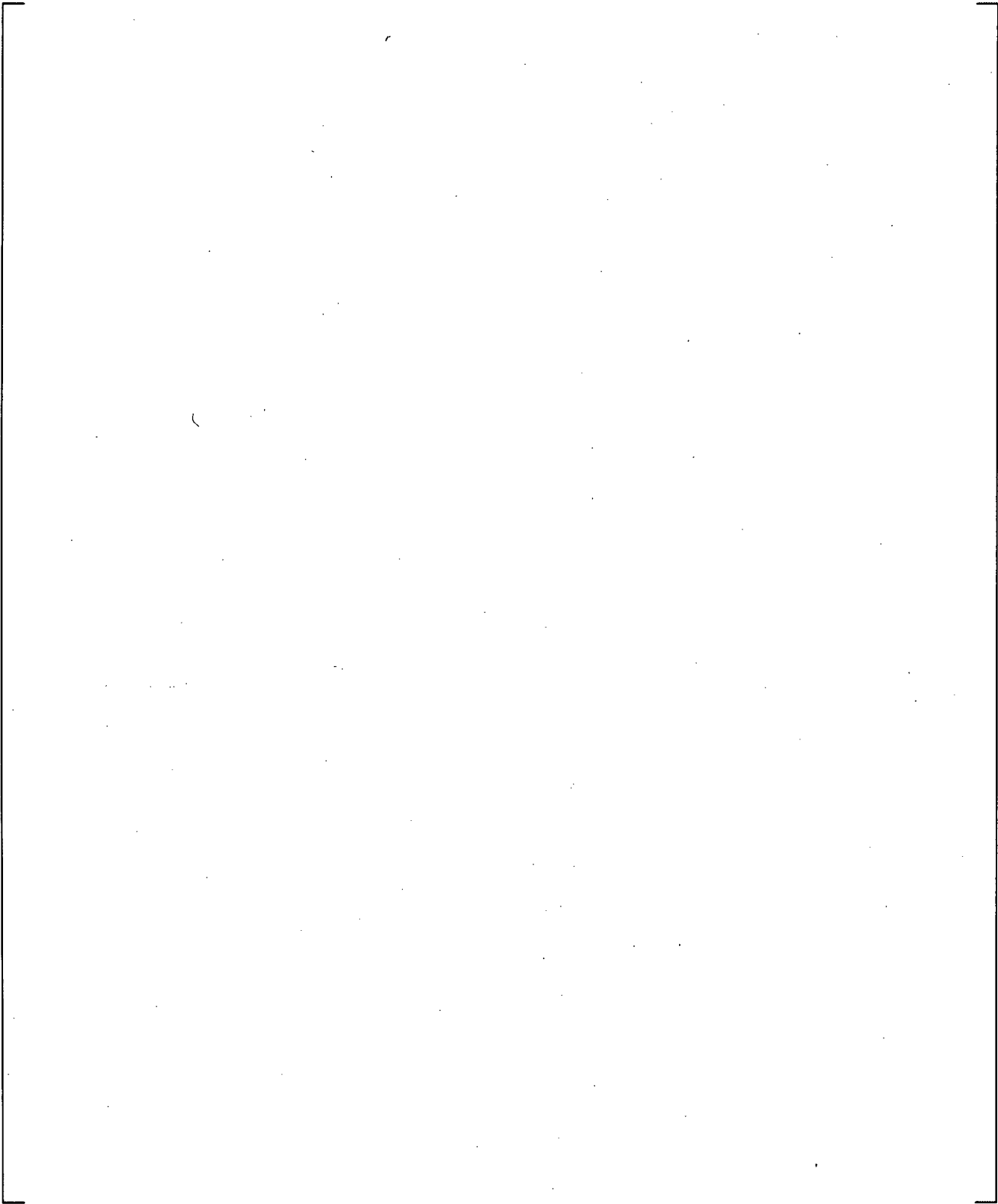


**Figure 19.3-132 Moody Diagram**

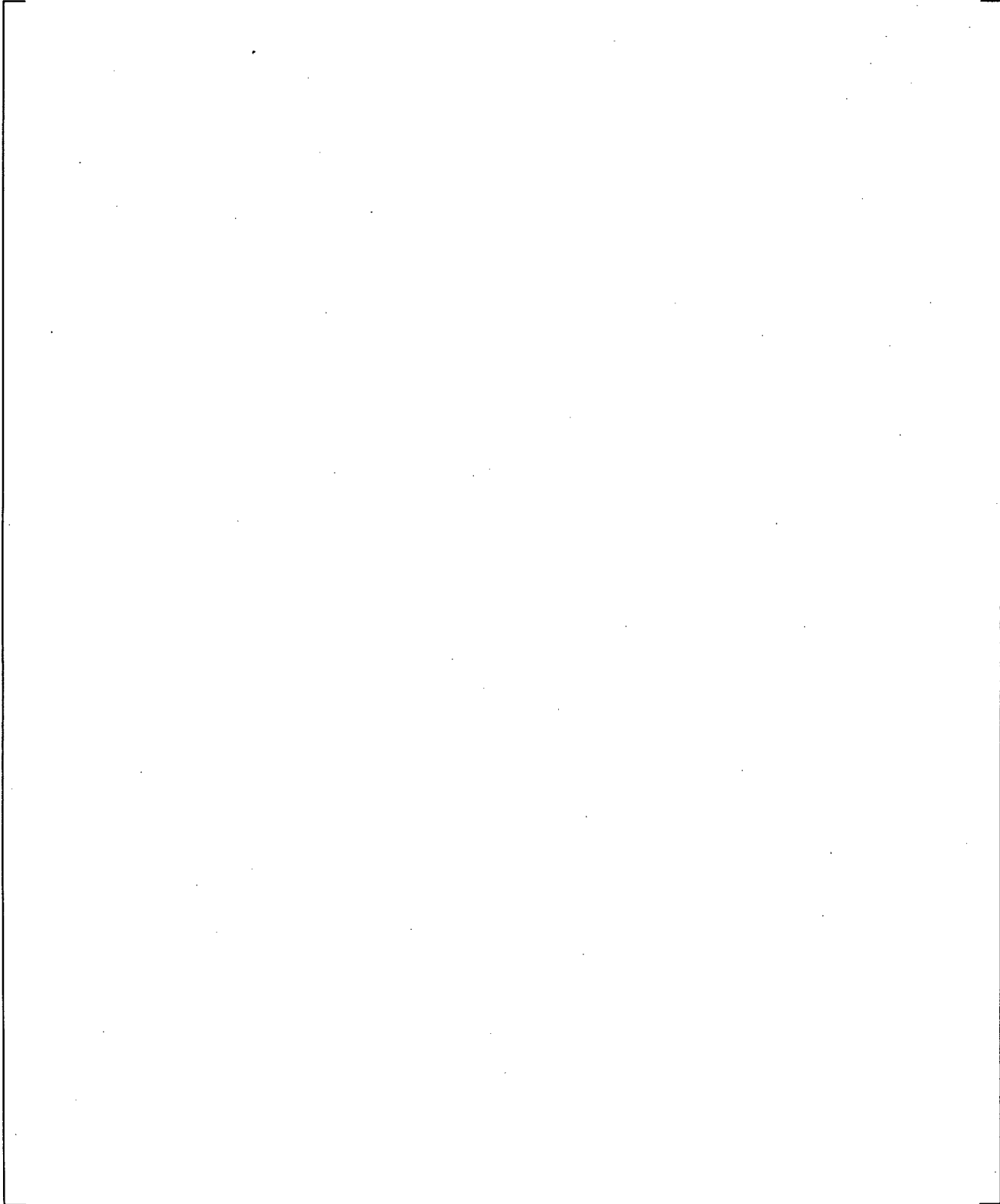


**Figure 19.3-133 Cold Leg Steam Flow Rate (Top) and Downcomer Pressure (Bottom) for Test Run 131**

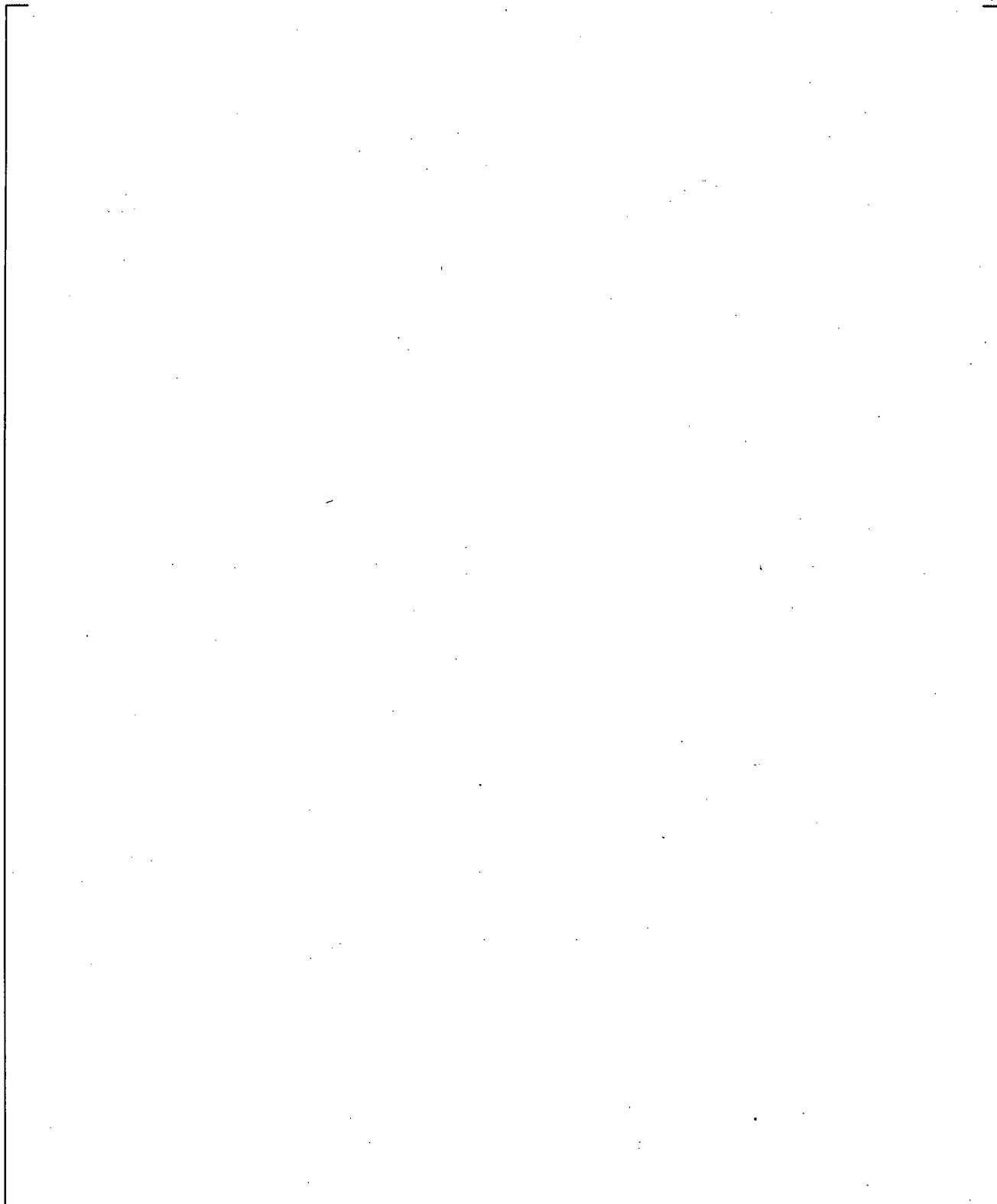


**Figure 19.3-134 Cold Leg Fluid Temperature (Top) and Cold Leg to Downcomer Pressure Drop (Bottom) for Test Run 131**

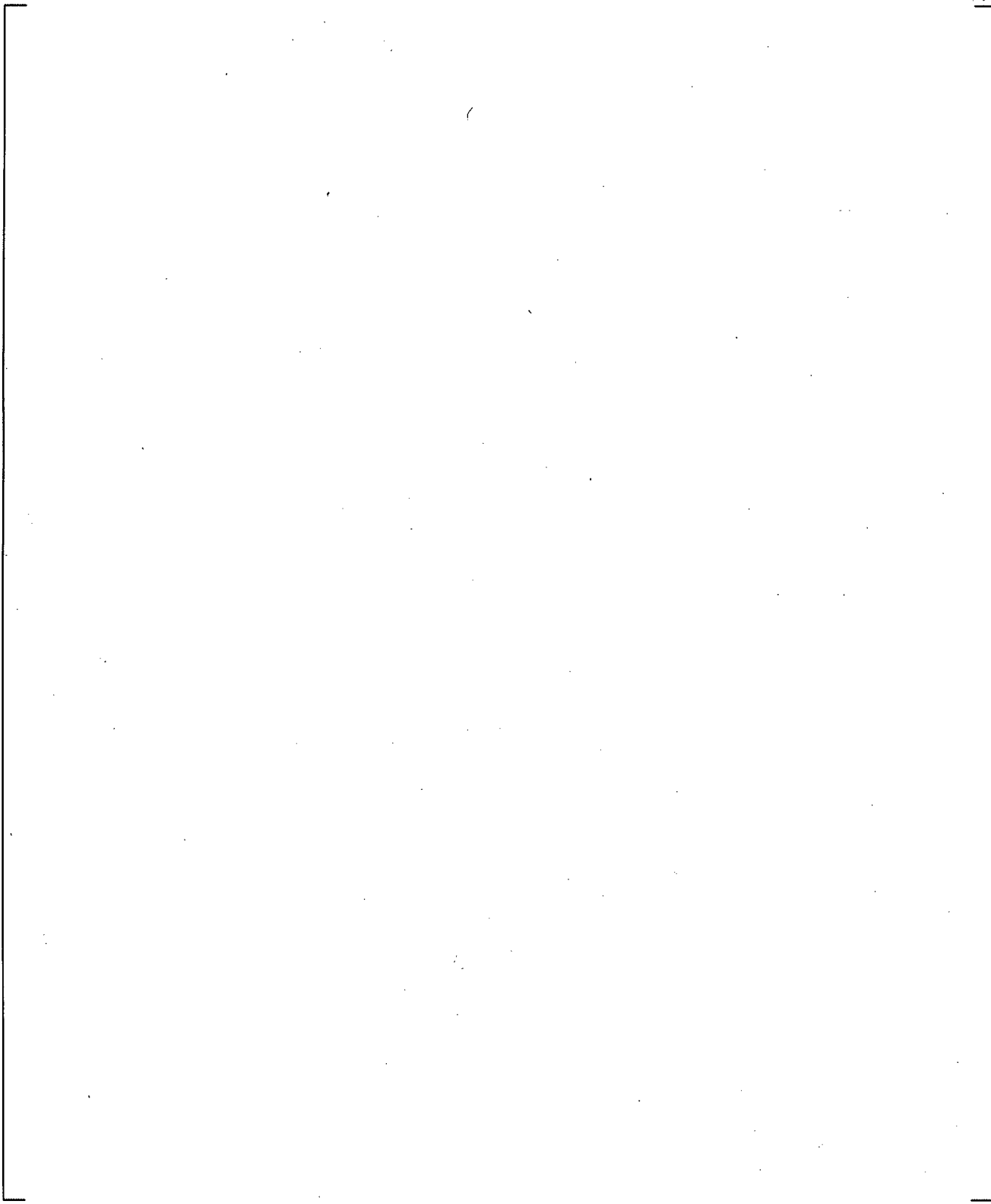


**Figure 19.3-135 Cold Leg Steam Flow Rate (Top) and Downcomer Pressure (Bottom) for Test Run 132**

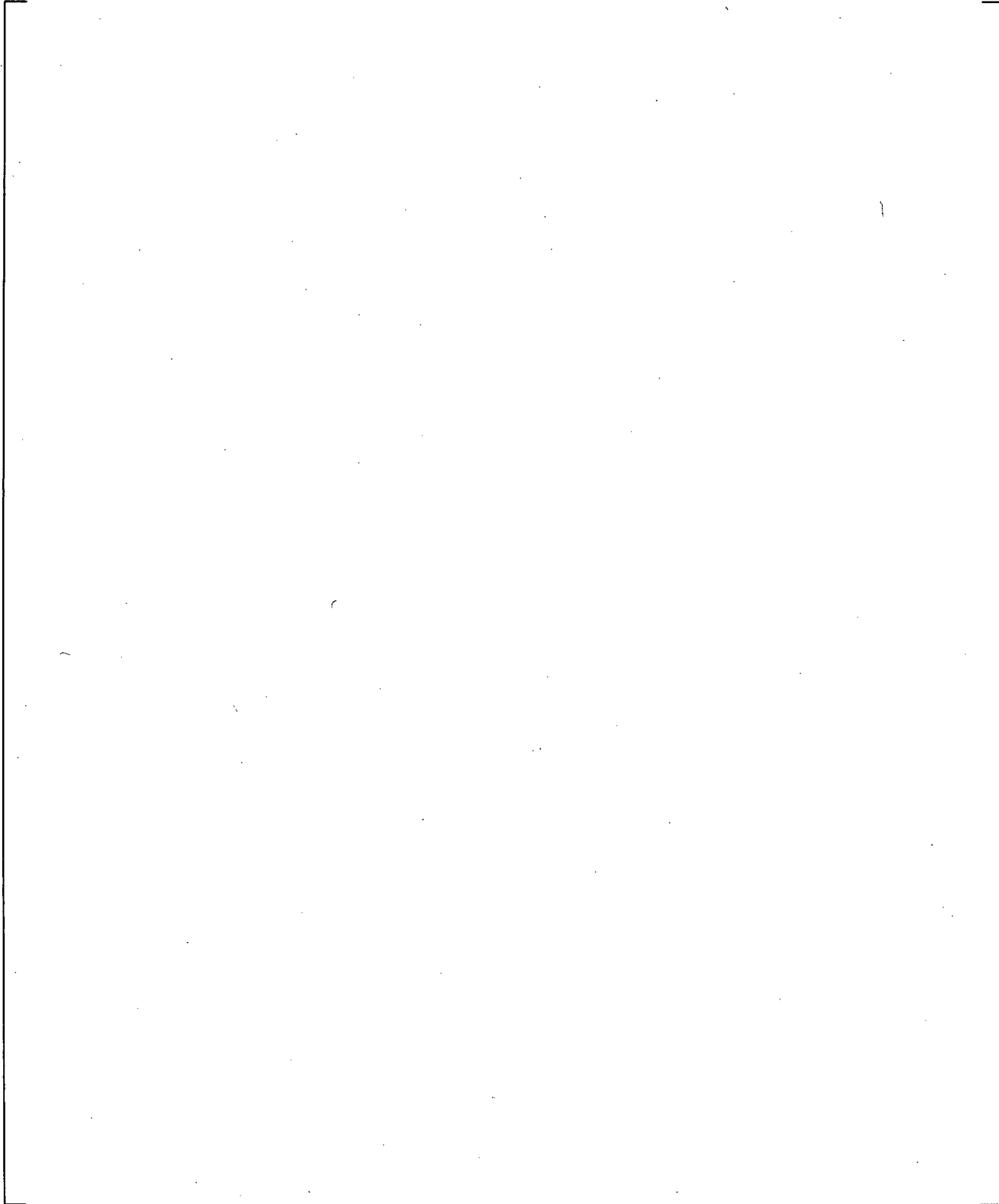


**Figure 19.3-136 Cold Leg Fluid Temperature (Top) and Cold Leg to Downcomer Pressure Drop (Bottom) for Test Run 132**

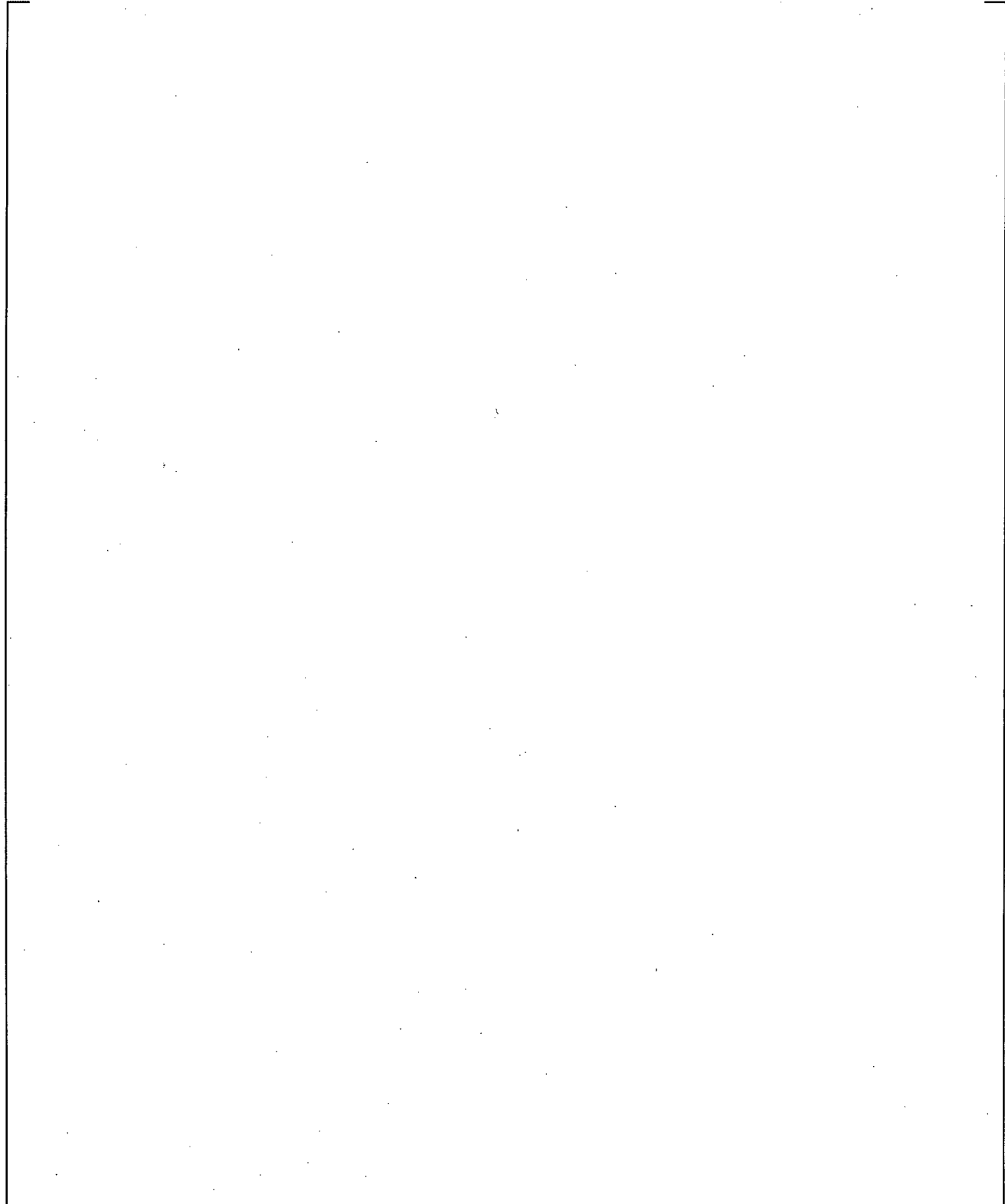


**Figure 19.3-137 Cold Leg Steam Flow rate (Top) and Downcomer Pressure (Bottom) for Test Run 133**

a,c

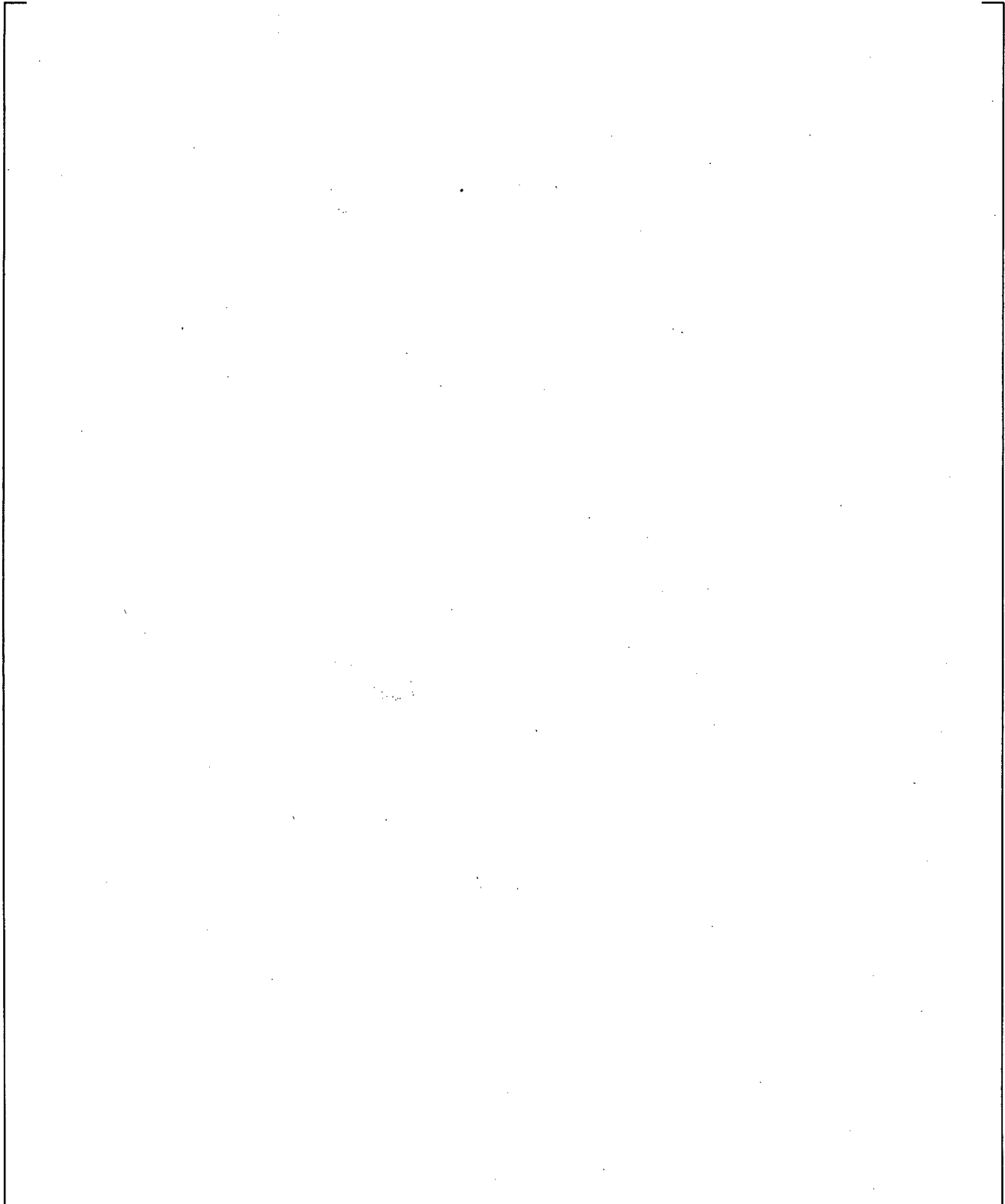


**Figure 19.3-138 Cold Leg Fluid Temperature (Top) and Cold Leg to Downcomer Pressure Drop (Bottom) for Test Run 133**

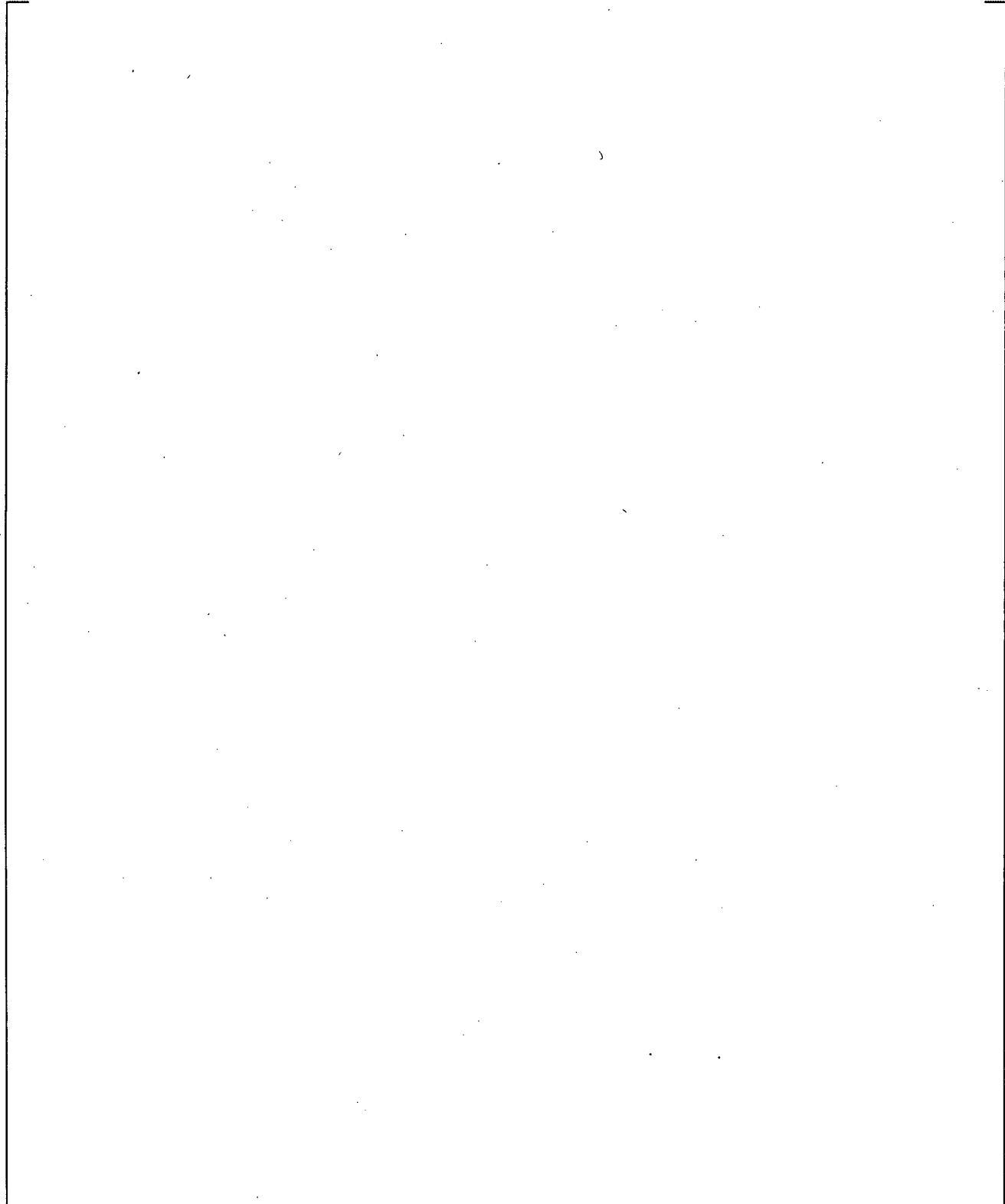


**Figure 19.3-139 Cold Leg Steam Flow rate (Top) and Downcomer Pressure (Bottom) for Test Run 135**

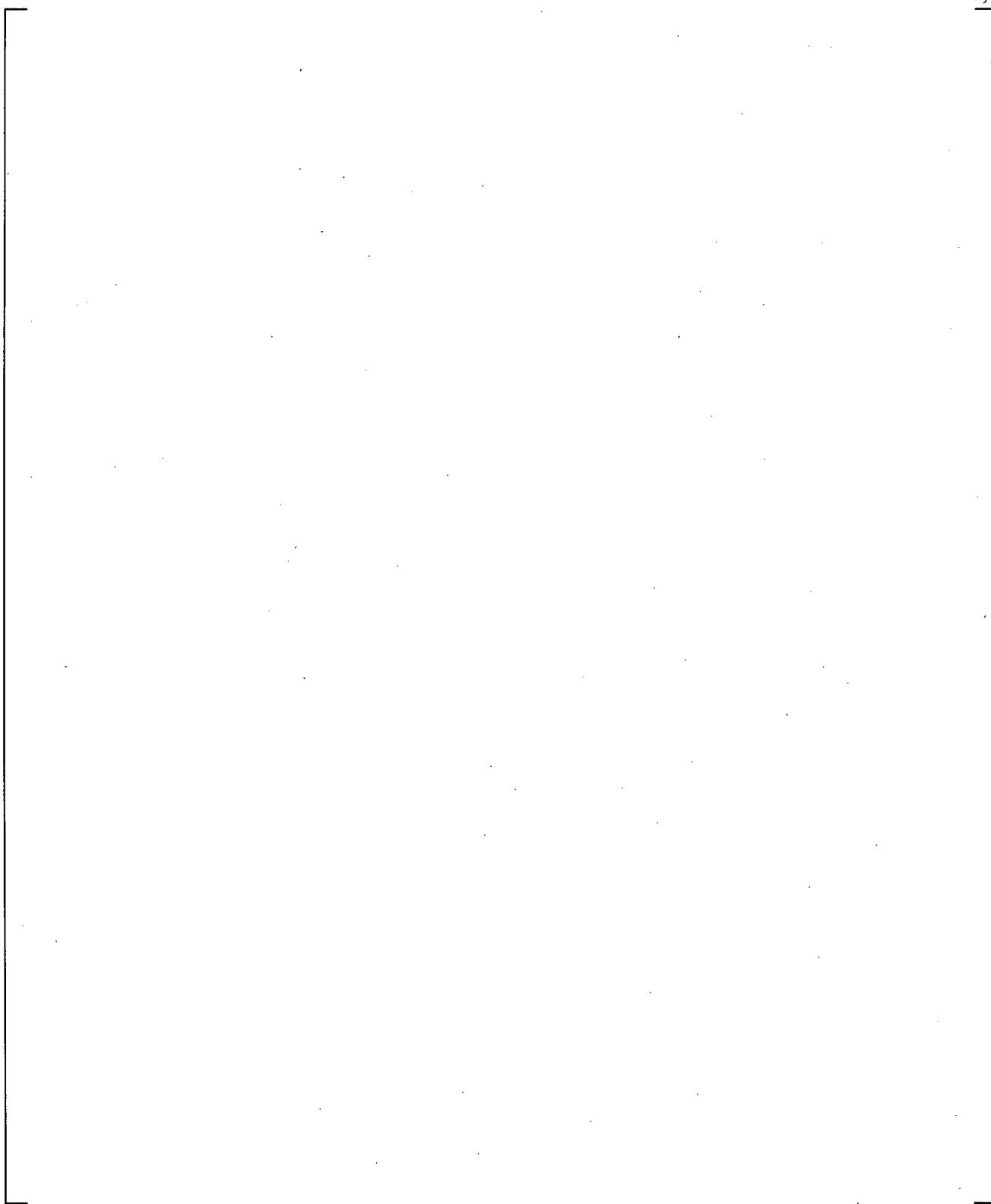


**Figure 19.3-140 Cold Leg Fluid Temperature (Top) and Cold Leg to Downcomer Pressure Drop (Bottom) for Test Run 135**

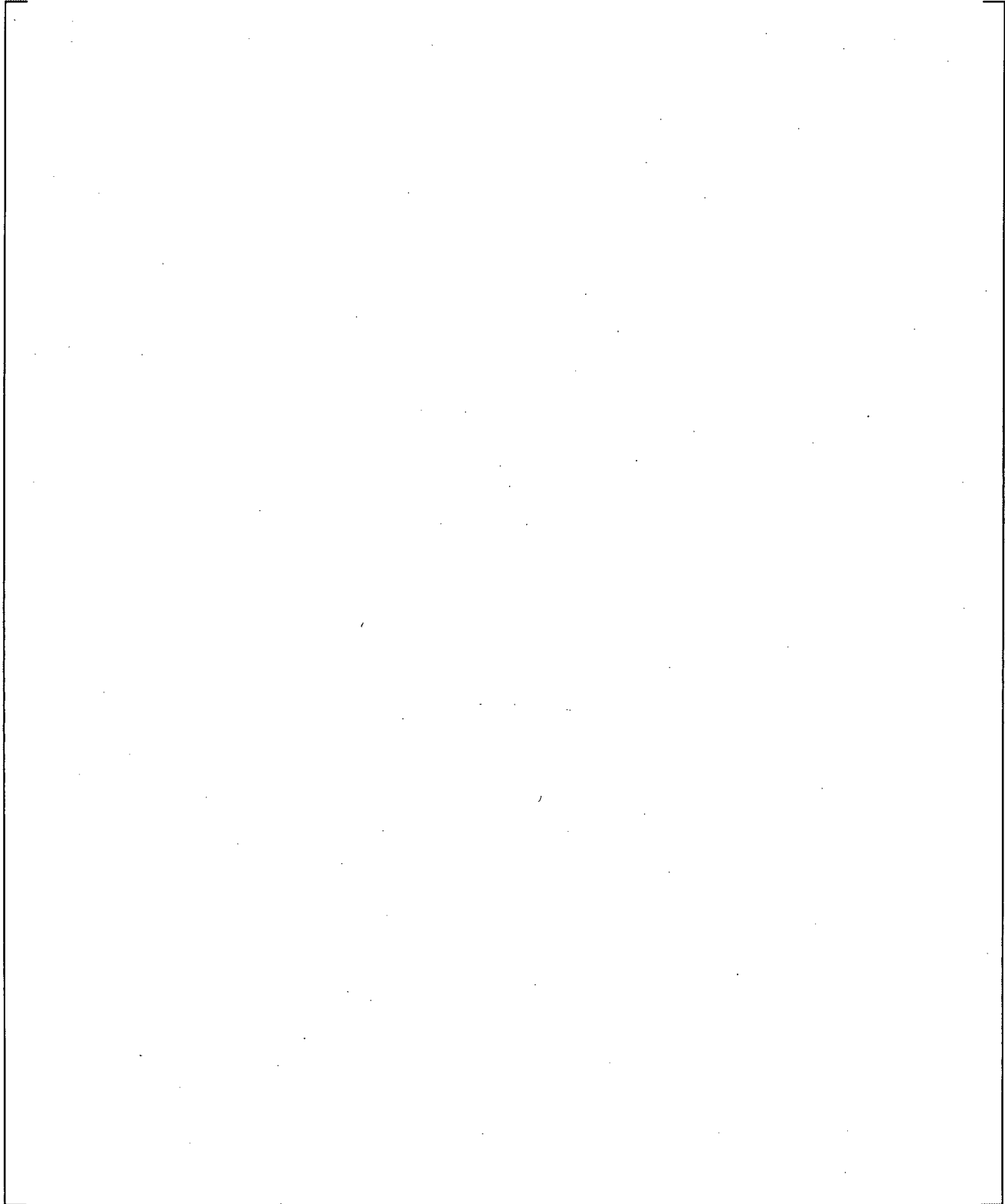


**Figure 19.3-141 Cold Leg Steam Flow Rate (Top) and Downcomer Pressure (Bottom) for Test Run 136**

a,c

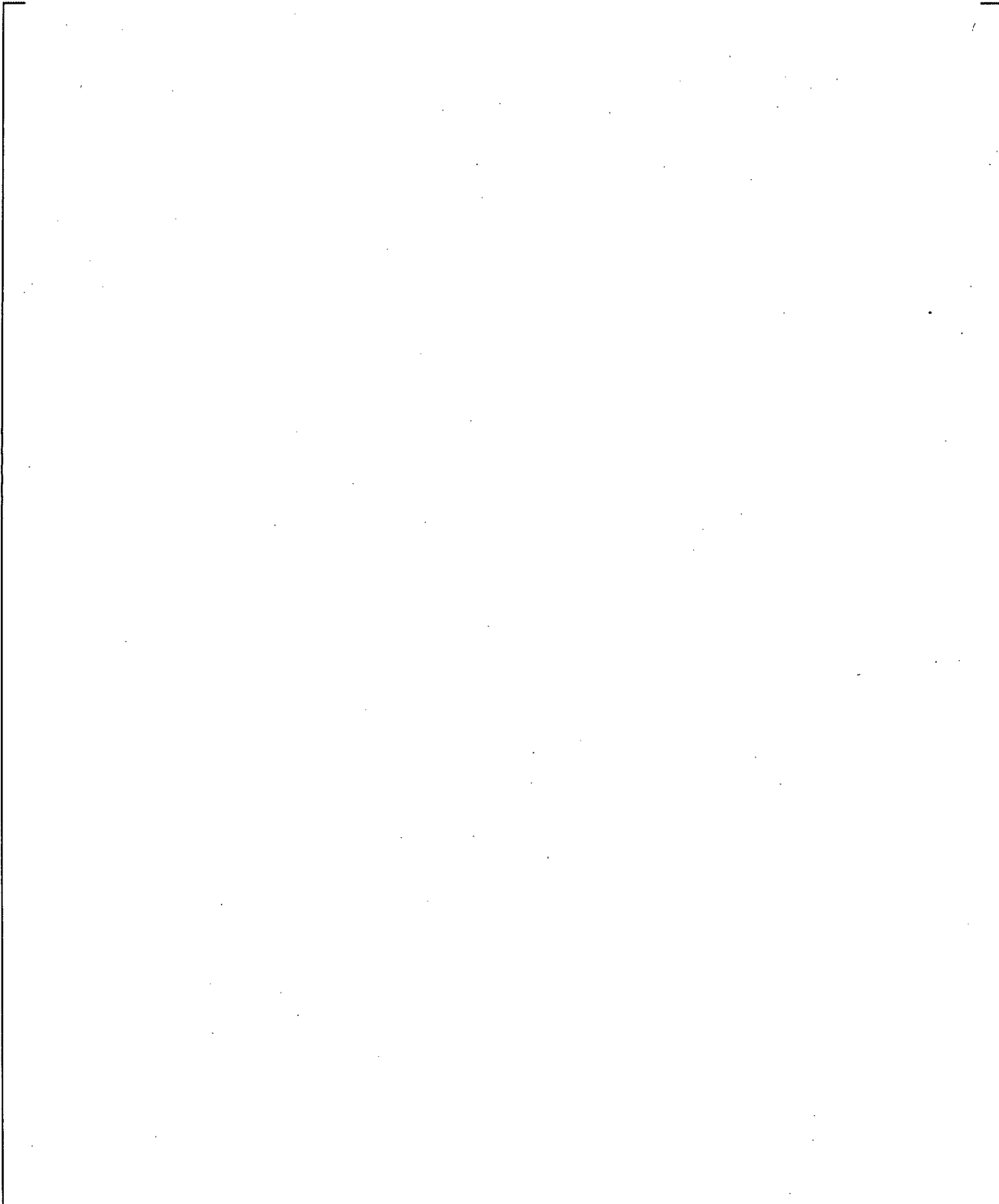


**Figure 19.3-142 Cold Leg Fluid Temperature (Top) and Cold Leg to Downcomer Pressure Drop (Bottom) for Test Run 136**

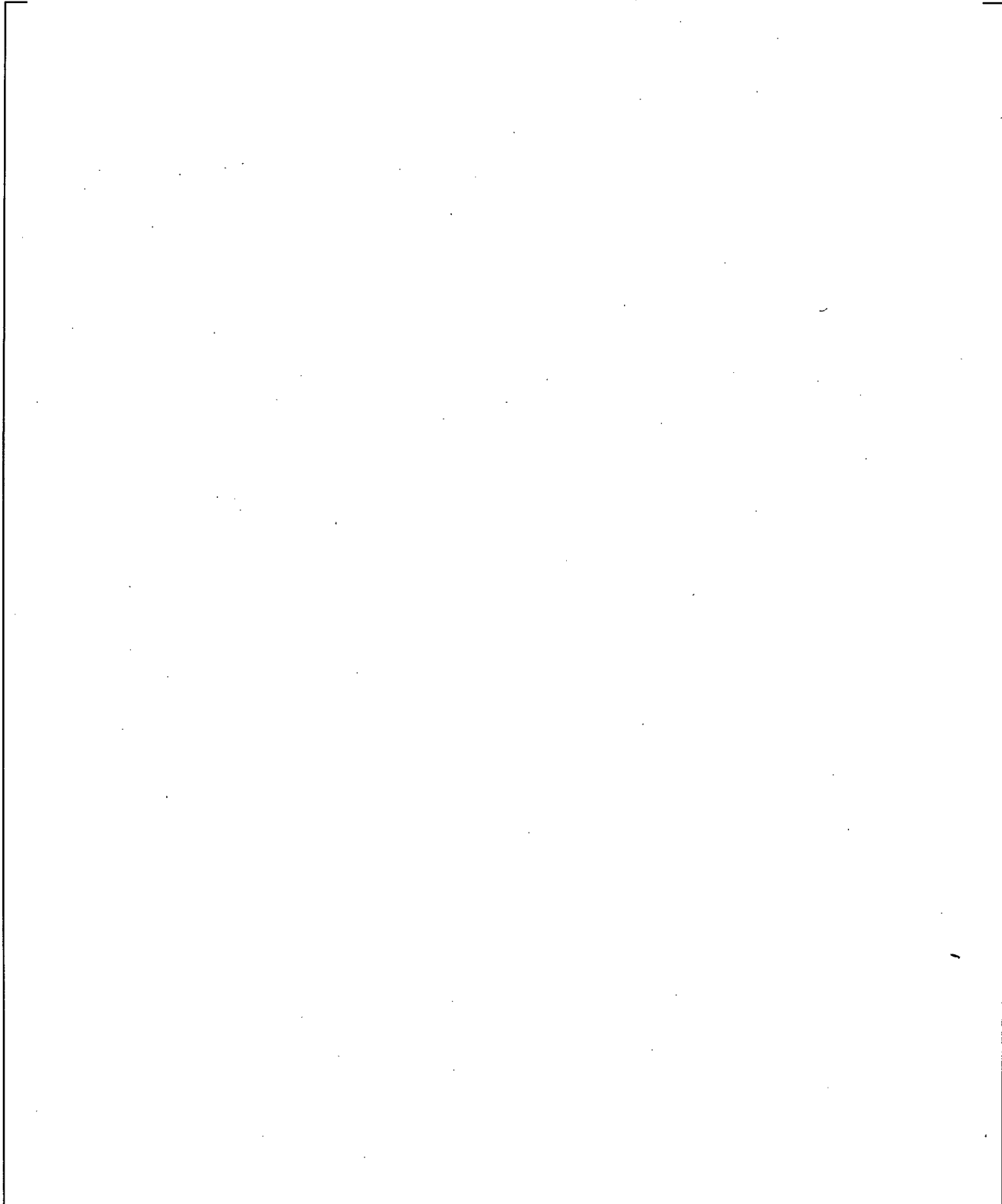


**Figure 19.3-143 An Illustration of Downcomer and Broken Cold Leg Nozzle Noding**

**Figure 19.3-144 Comparison between Measured Pressure Loss and Predicted Pressure Loss across Broken Cold Leg Nozzle for UPTF 6-131**

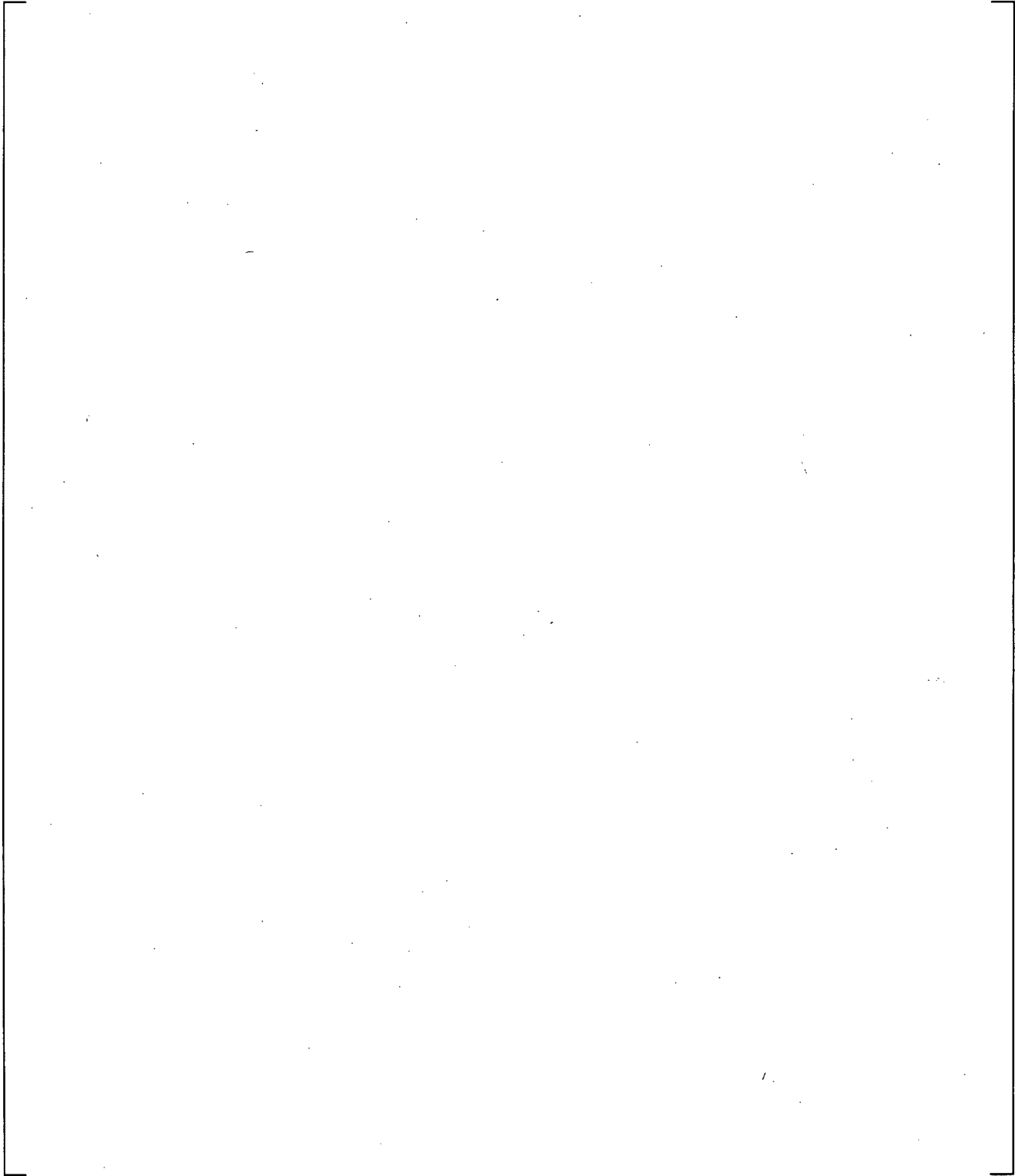


**Figure 19.3-145 Comparison between Measured Pressure Loss and Predicted Pressure Loss across Broken Cold Leg Nozzle for UPTF 6-132**

a,c

**Figure 19.3-146 Comparison between Measured Pressure Loss and Predicted Pressure Loss across Broken Cold Leg Nozzle for UPTF 6-133**

a,c

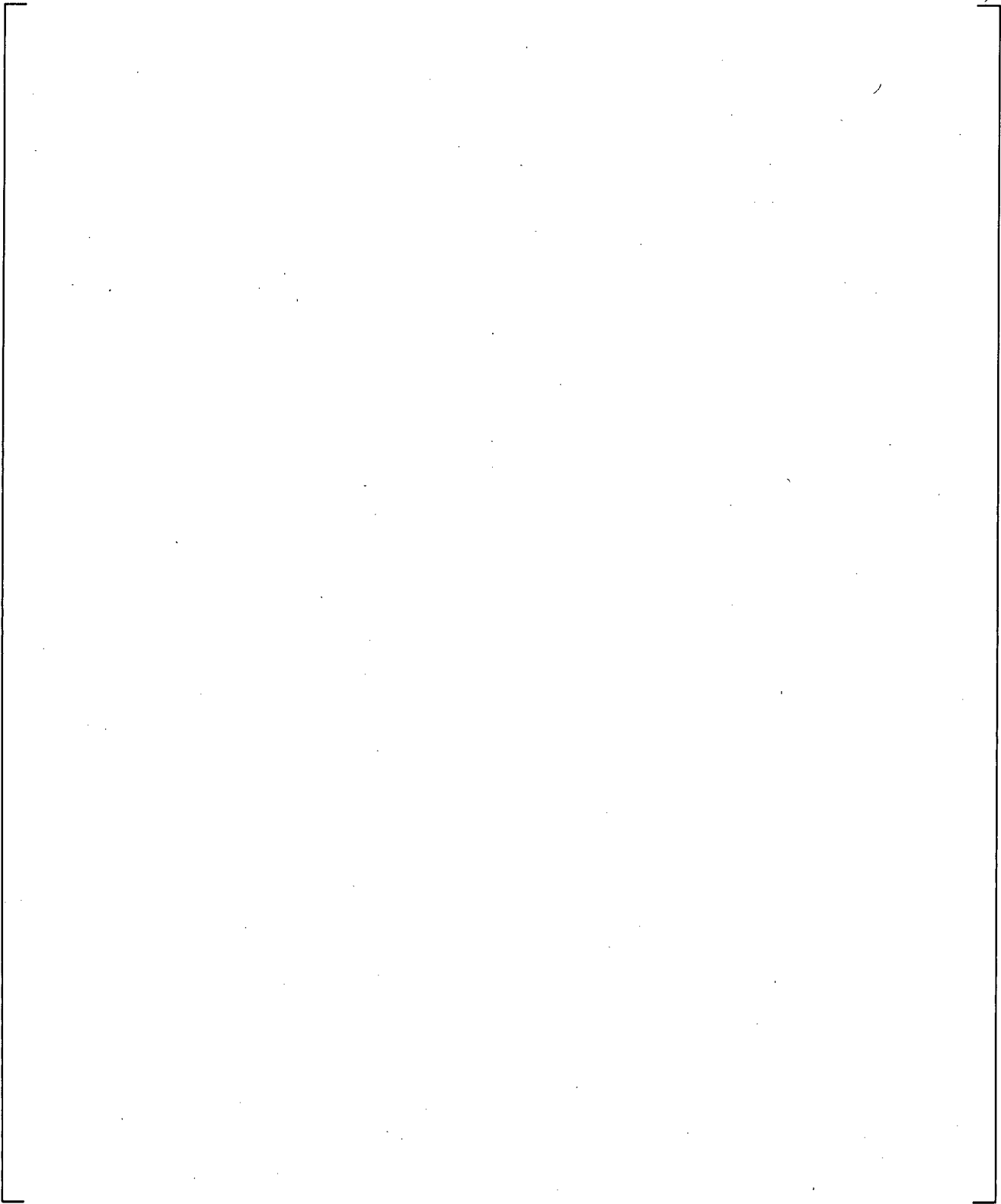


**Figure 19.3-147 Comparison between Measured Pressure Loss and Predicted Pressure Loss across Broken Cold Leg Nozzle for UPTF 6-135**

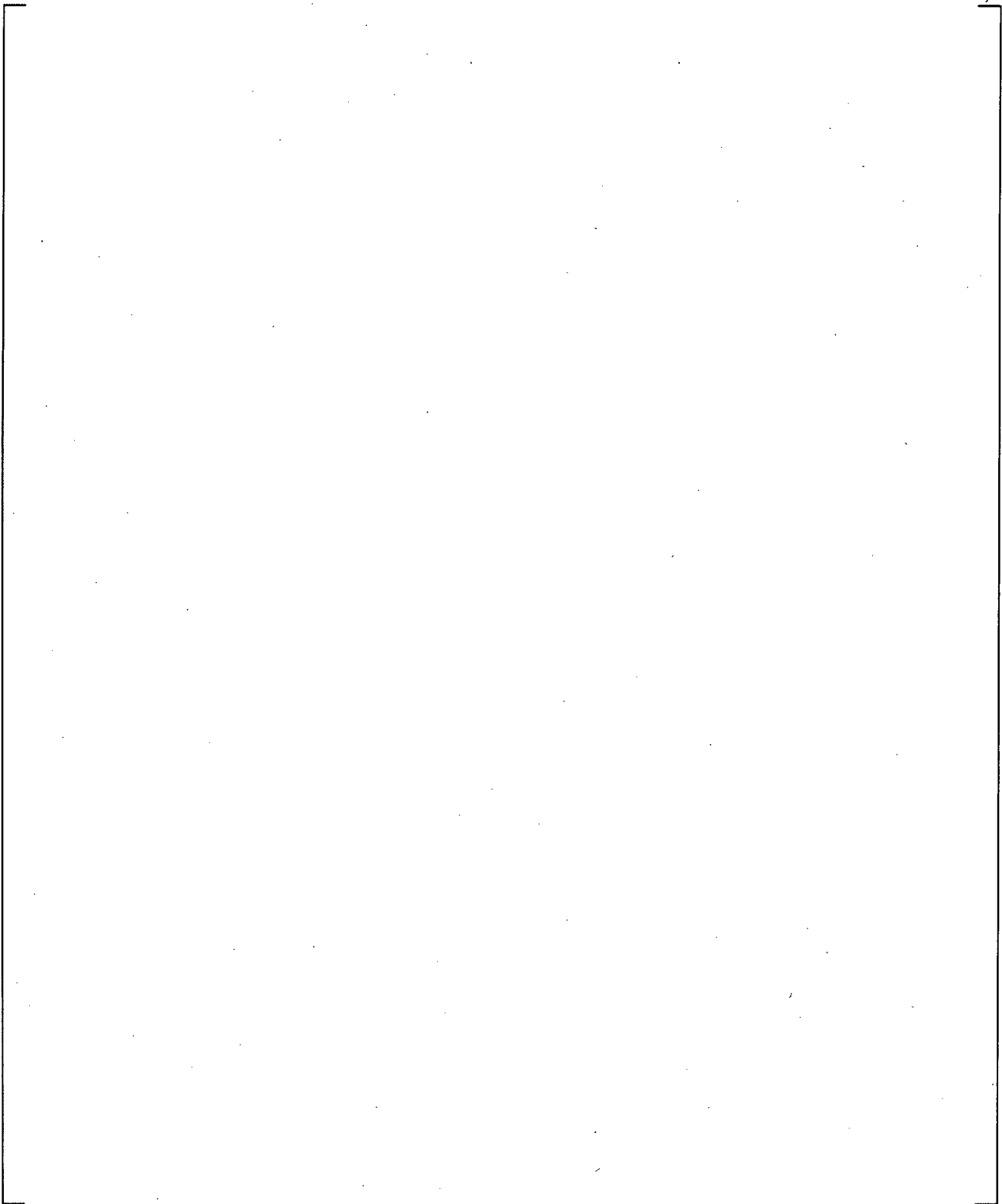


**Figure 19.3-148 Comparison between Measured Pressure Loss and Predicted Pressure Loss across Broken Cold Leg Nozzle for UPTF 6-136**

a,c

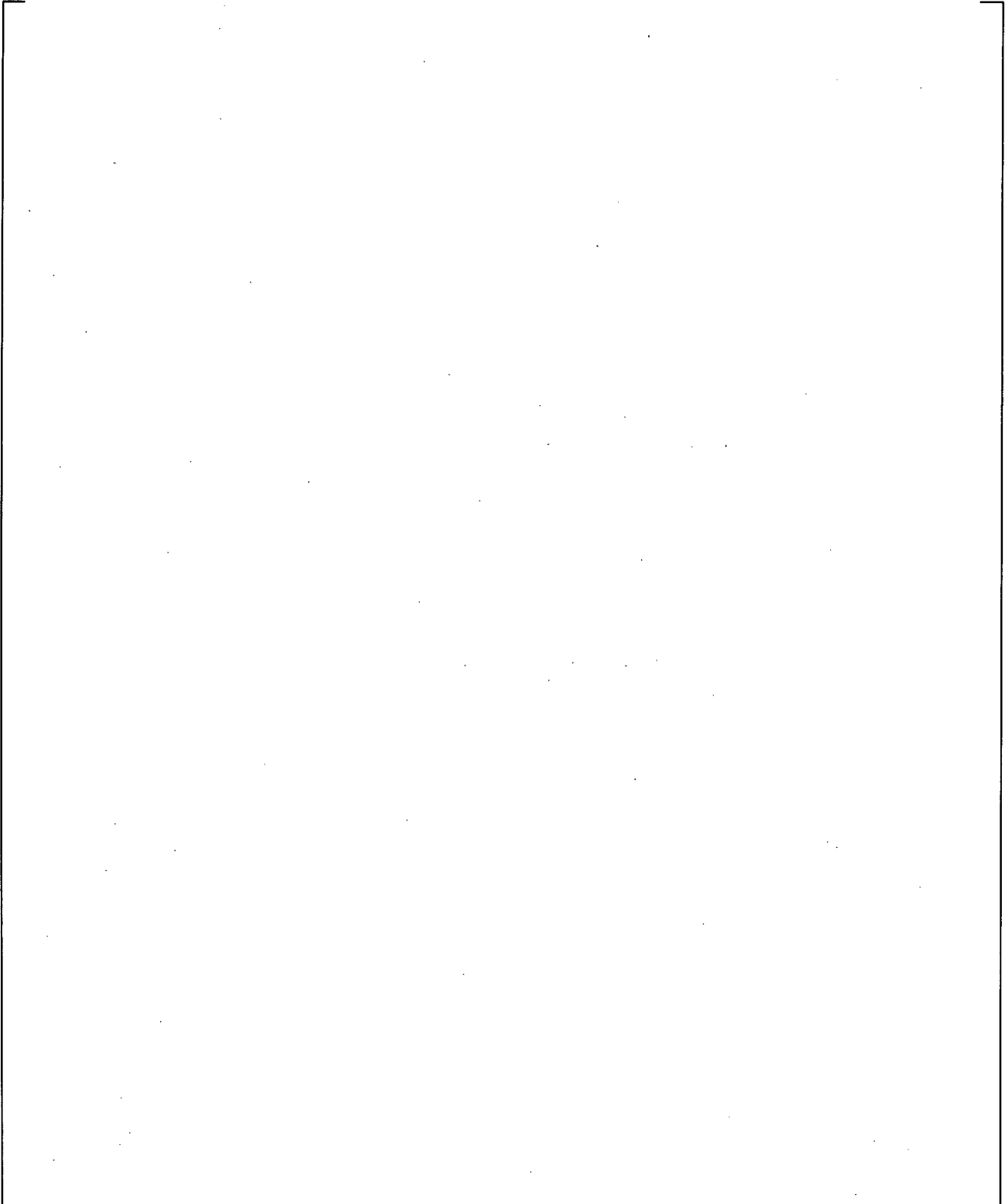


**Figure 19.3-149 Cold Leg Piping Region of UPTF Facility and Cold Leg Noding**

a,c

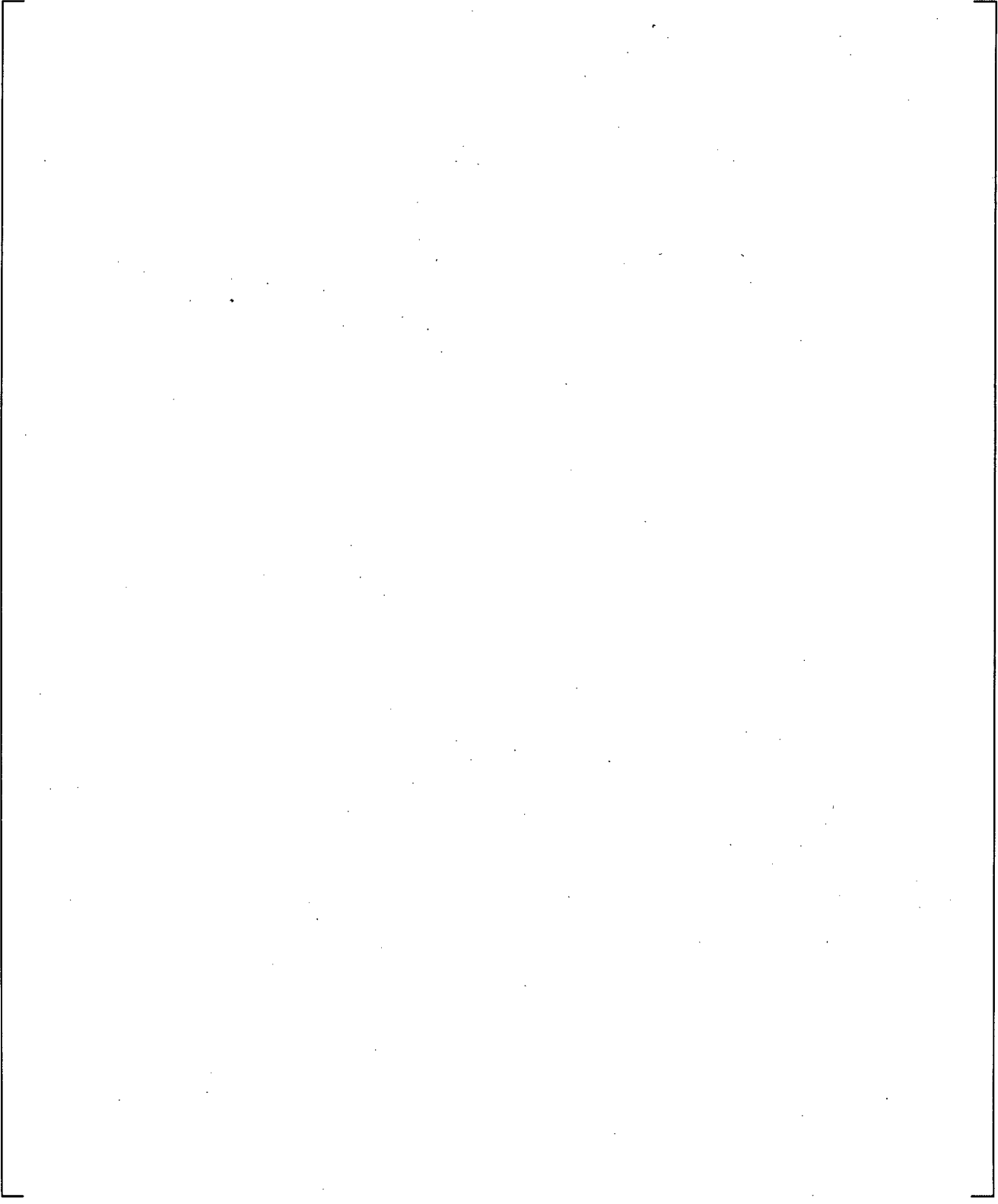


**Figure 19.3-150 System Configuration for UPTF-8A**

a,c

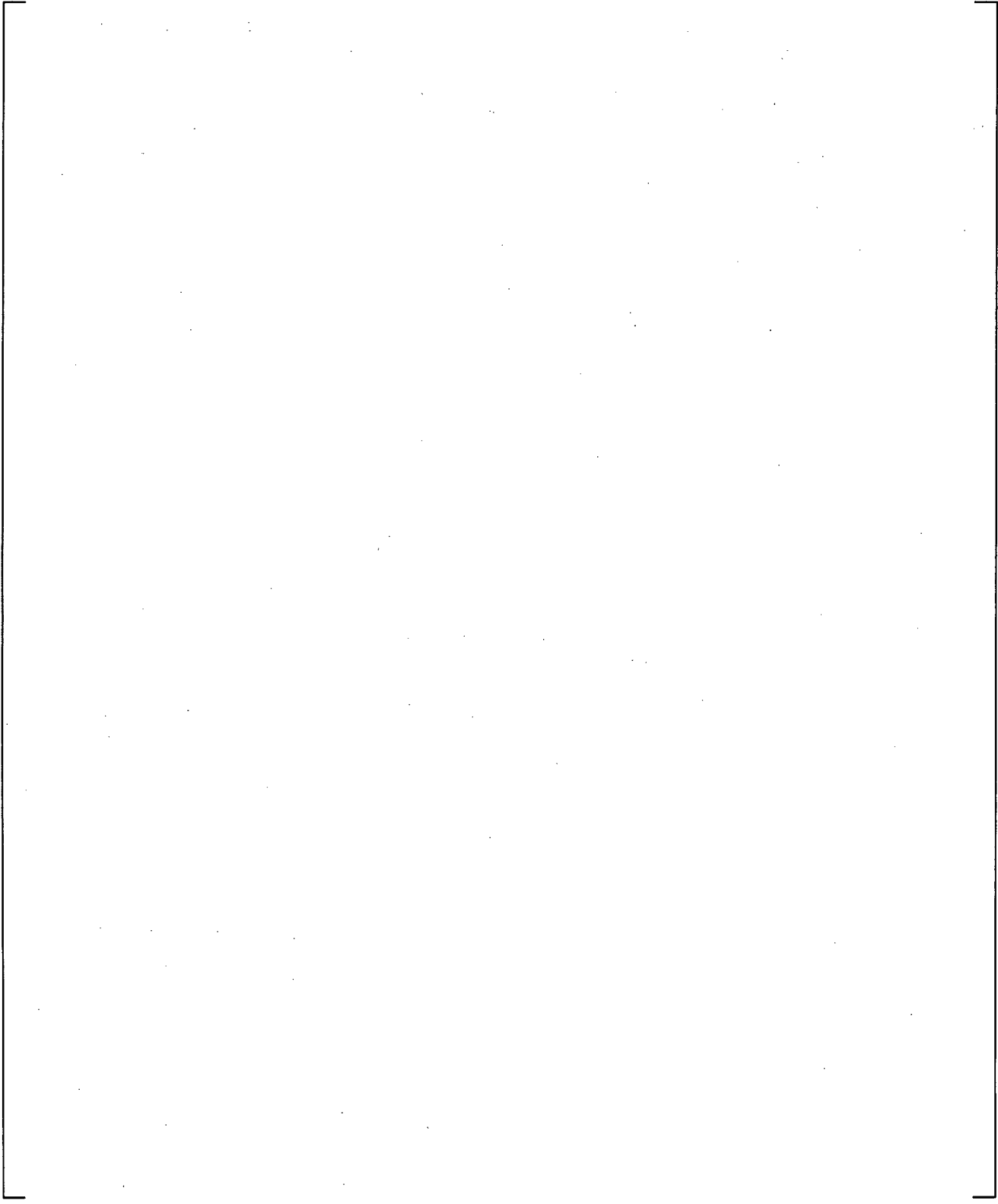


**Figure 19.3-151 Observation on Temperature Distribution in UPTF-8 Experiments (MPR Associates, 1992) and Comparison with Predictions from WCOBRA/TRAC-TF2**

a,c

**Figure 19.3-152 WCOBRA/TRAC-TF2 Vessel Model for UPTF Test 8A**

a,c

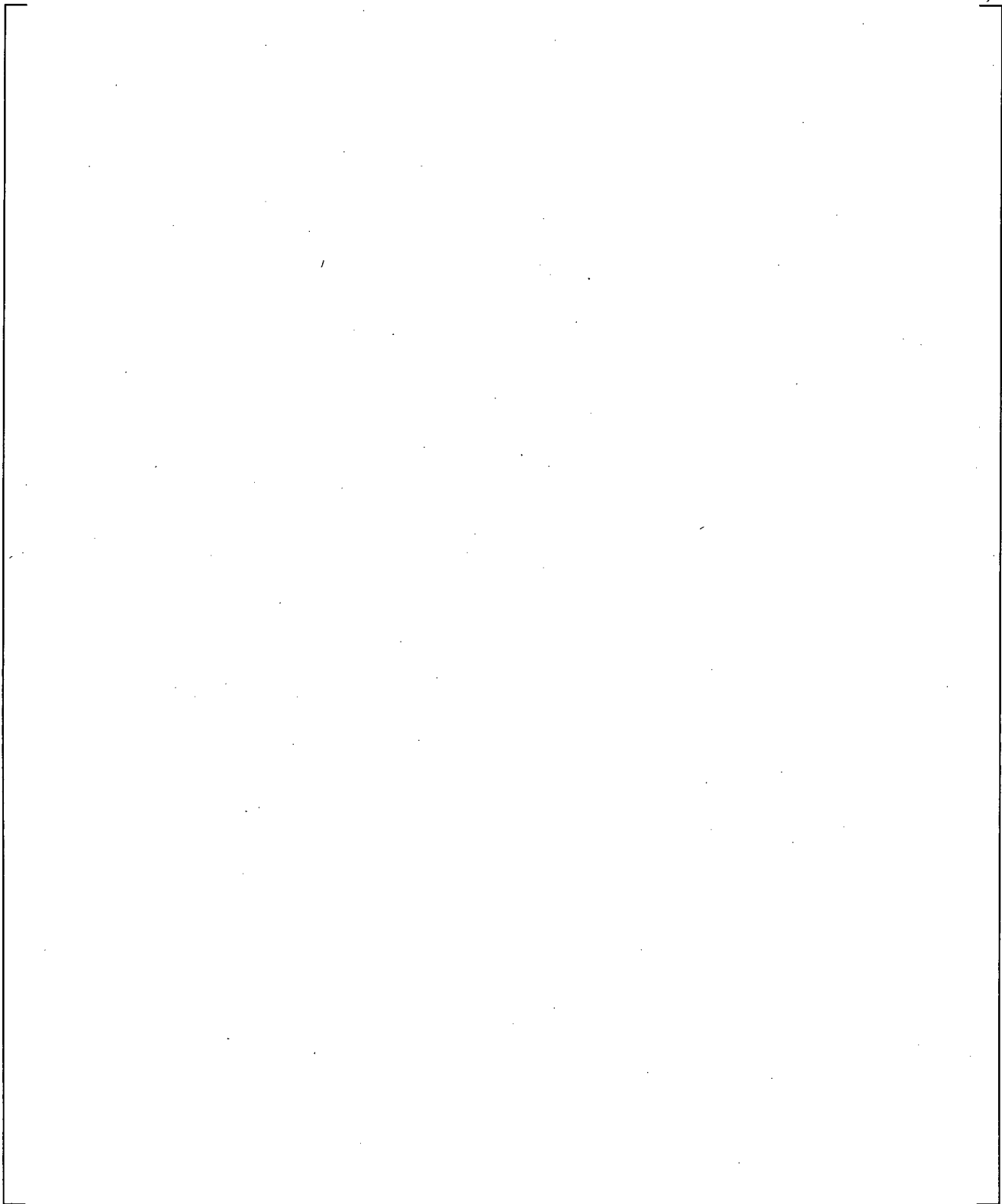


**Figure 19.3-153 WCOBRA/TRAC-TF2 Loop Model for UPTF-8 A**

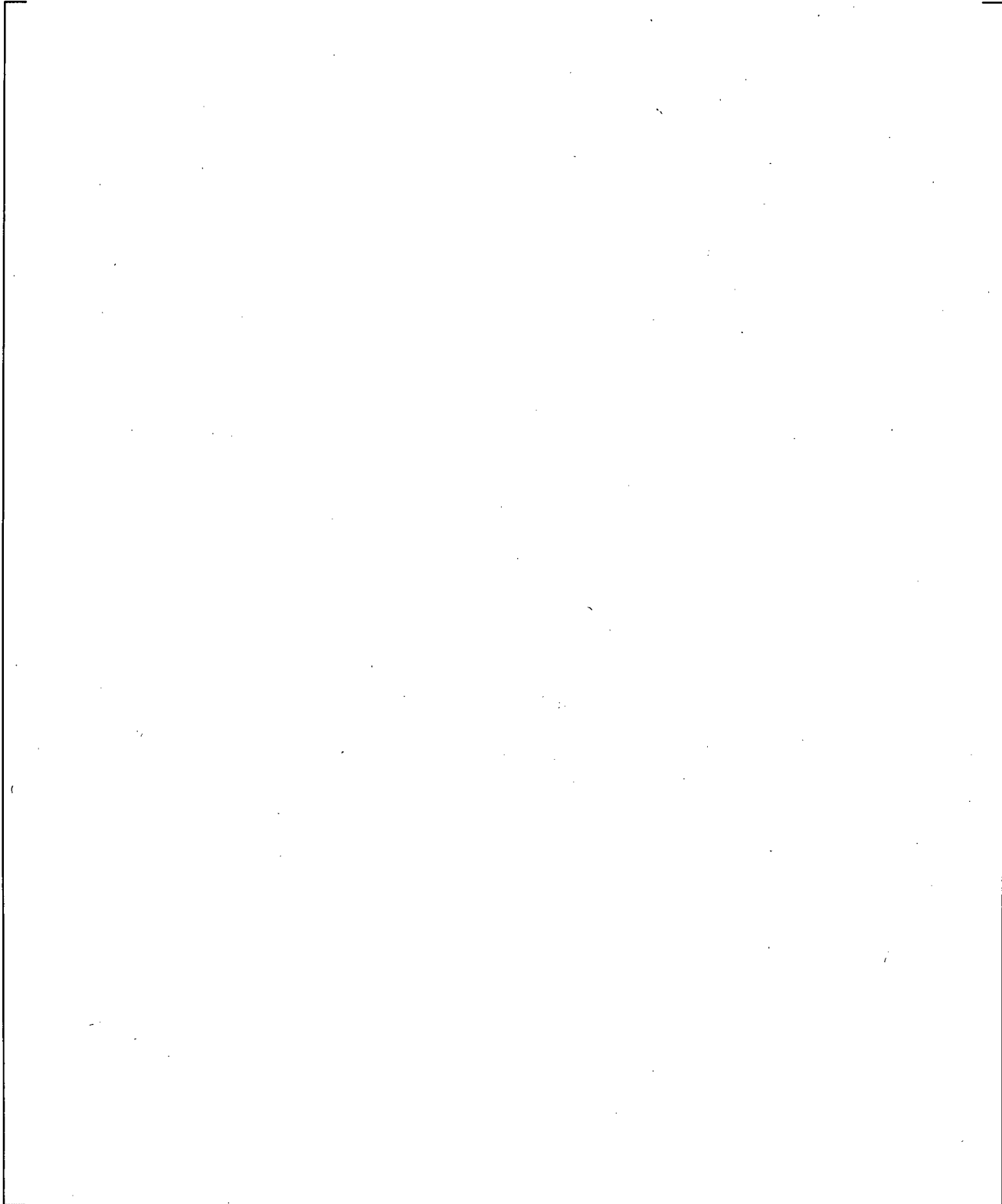


**Figure 19.3-154 Comparison between the Measured Steam Flow Rates and the WCOBRA/TRAC-TF2 Predicted Steam Flow Rates in the Cold Leg of the Loop 2**

a,c

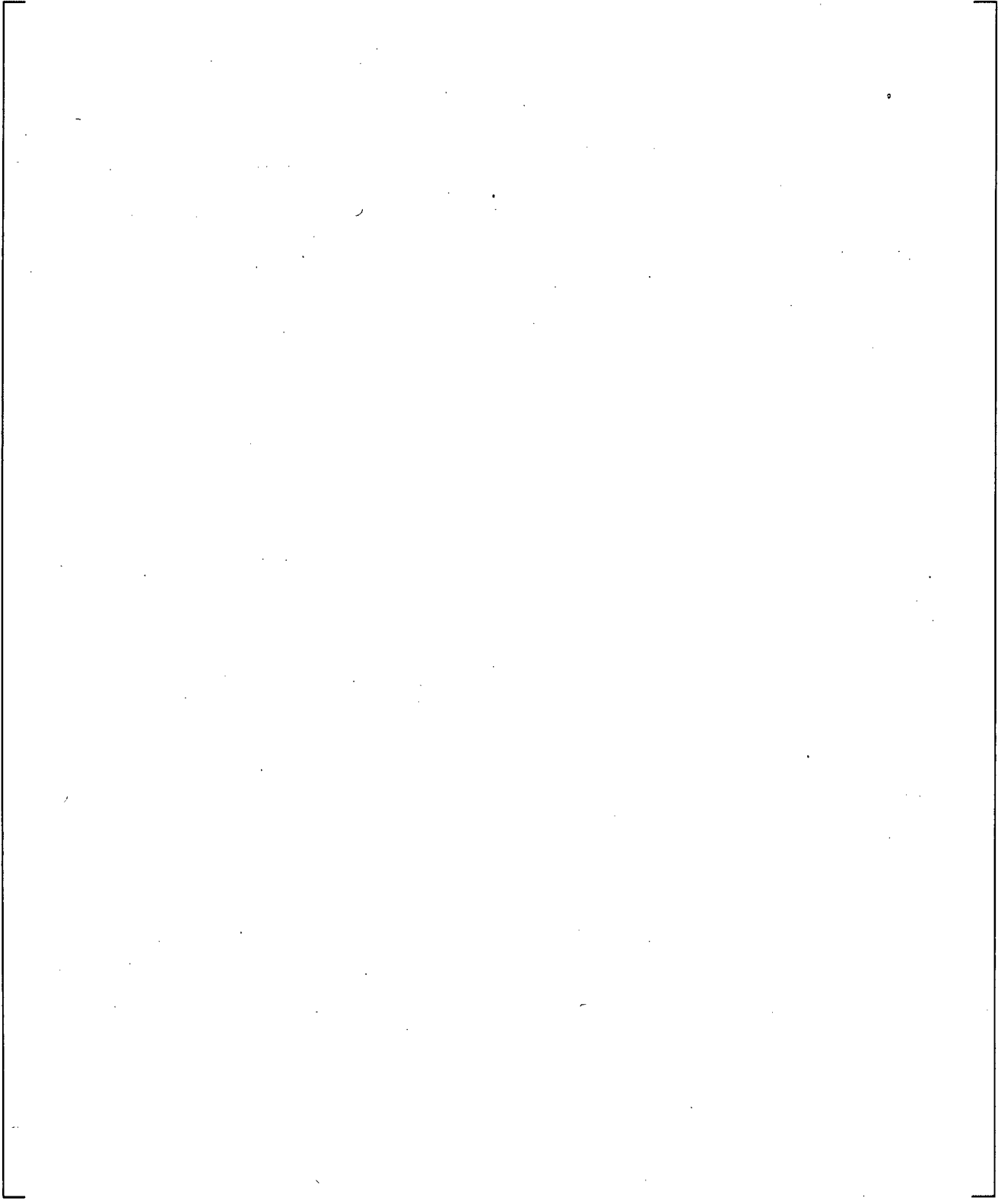


**Figure 19.3-155 ECC Injection Flow Rate to Cold Leg in Loop 2**

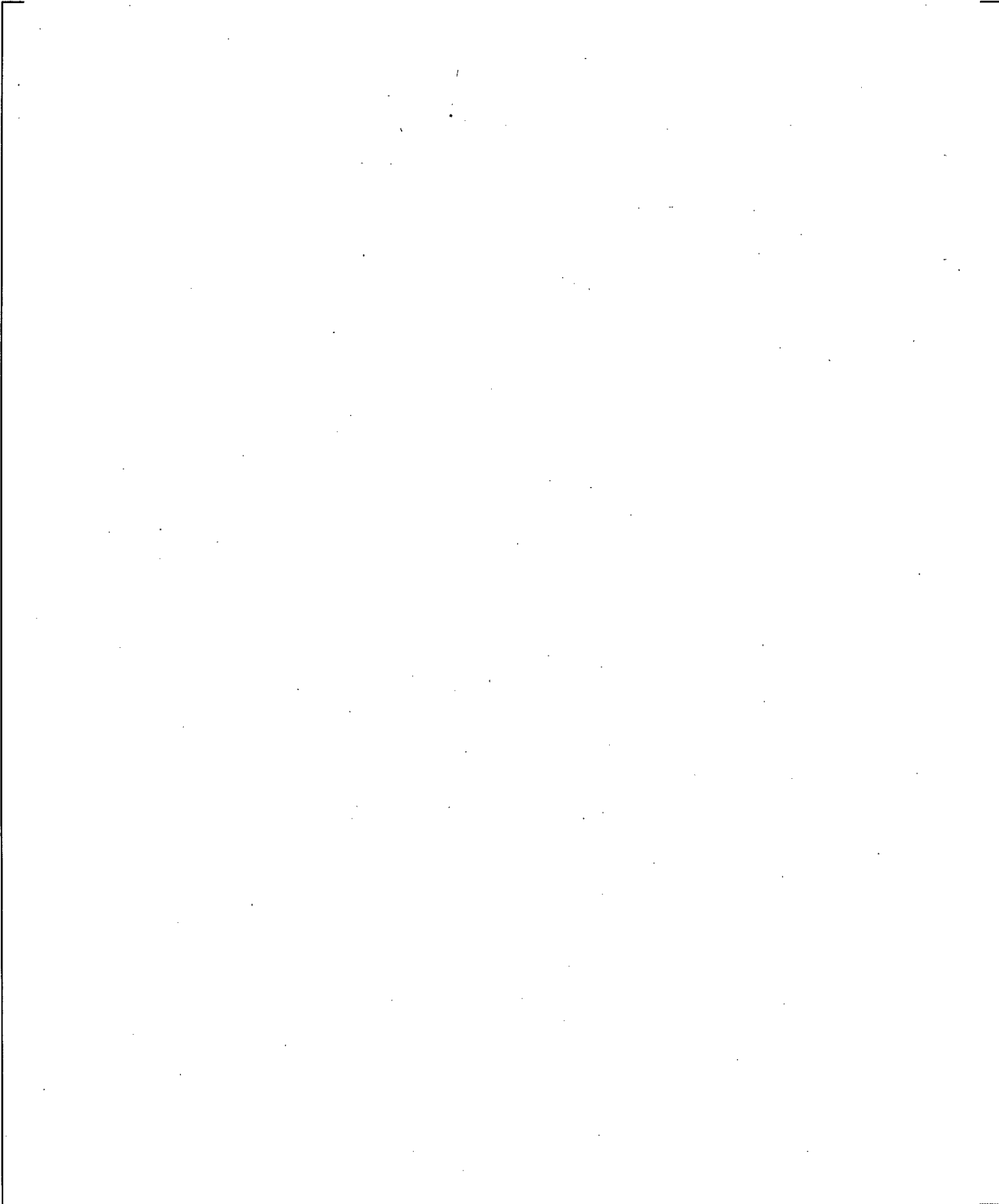


**Figure 19.3-156 Comparison between Measured Fluid Temperature and WCOBRA/TRAC-TF2 Predicted Water Temperature at Pump Exit**

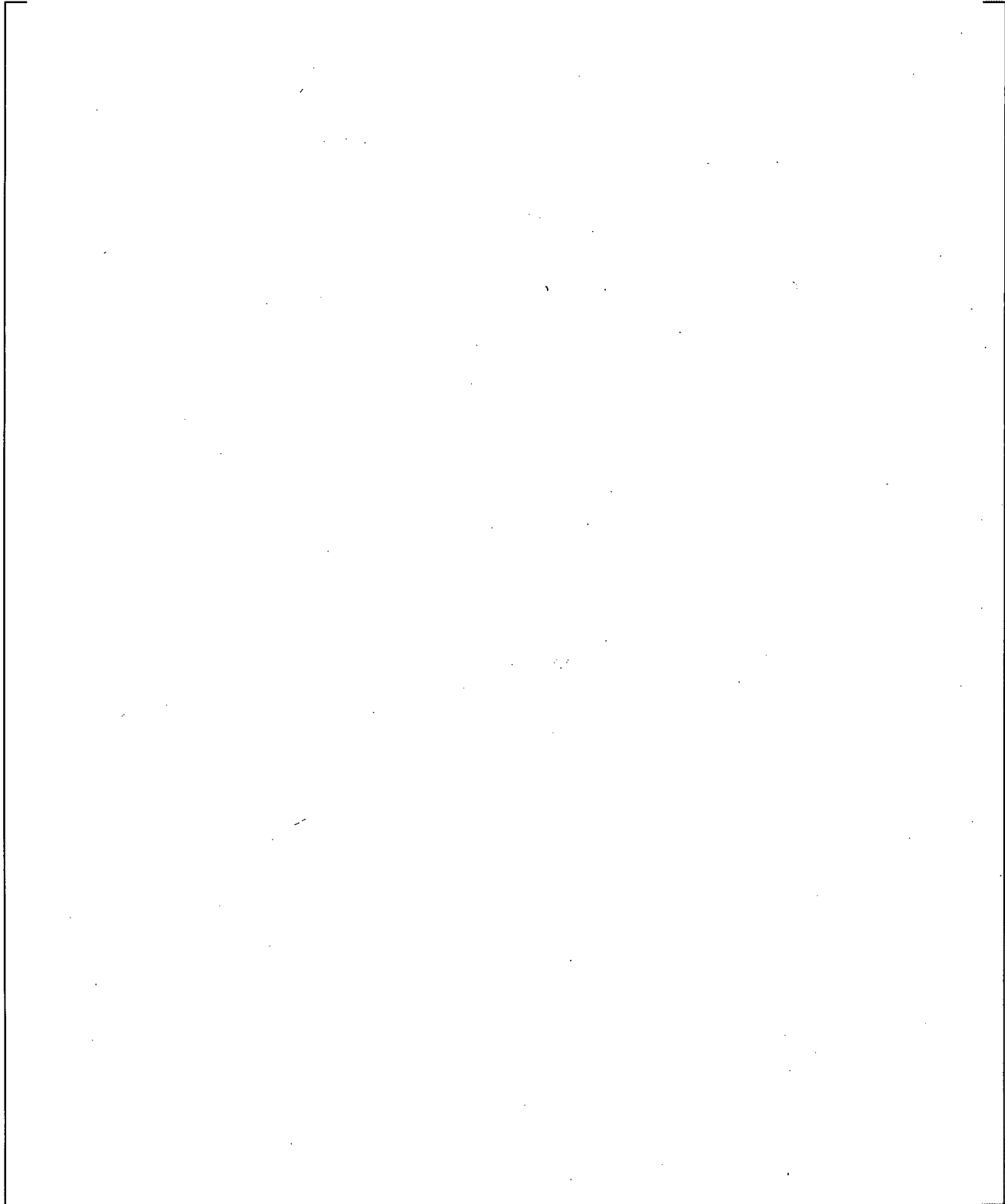


**Figure 19.3-157 Comparison between Measured Fluid Temperature and WCOBRA/TRAC-TF2 Predicted Water Temperature near Injection Point**

a,c

**Figure 19.3-158 Comparison between Measured Fluid Temperature and WCOBRA/TRAC-TF2 Predicted Water Temperature at Downstream of Injection Point**

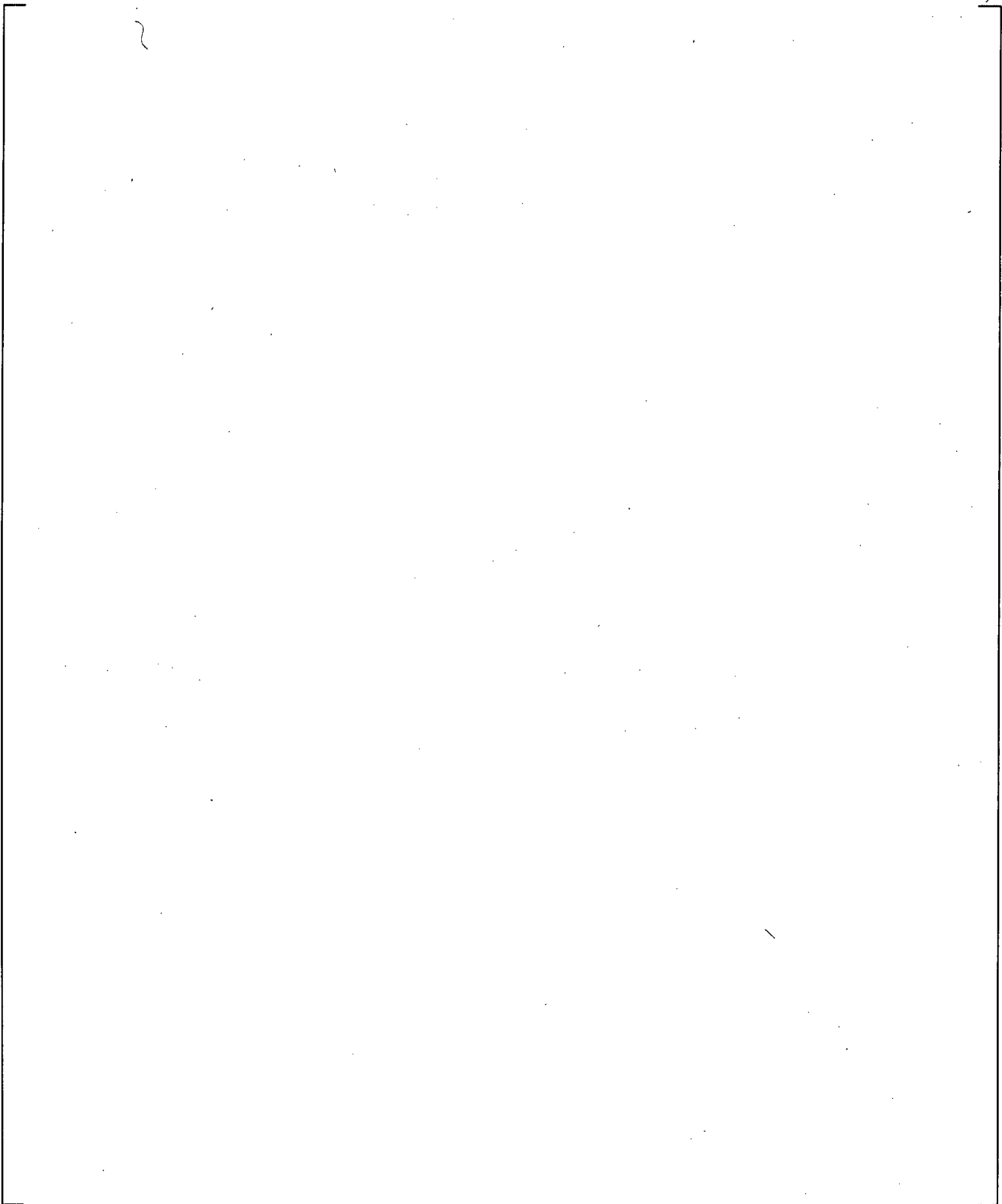


**Figure 19.3-159 Comparison between Measured Fluid Temperature and WCOBRA/TRAC-TF2 Predicted Water Temperature at Outlet of Cold Leg**

a,c

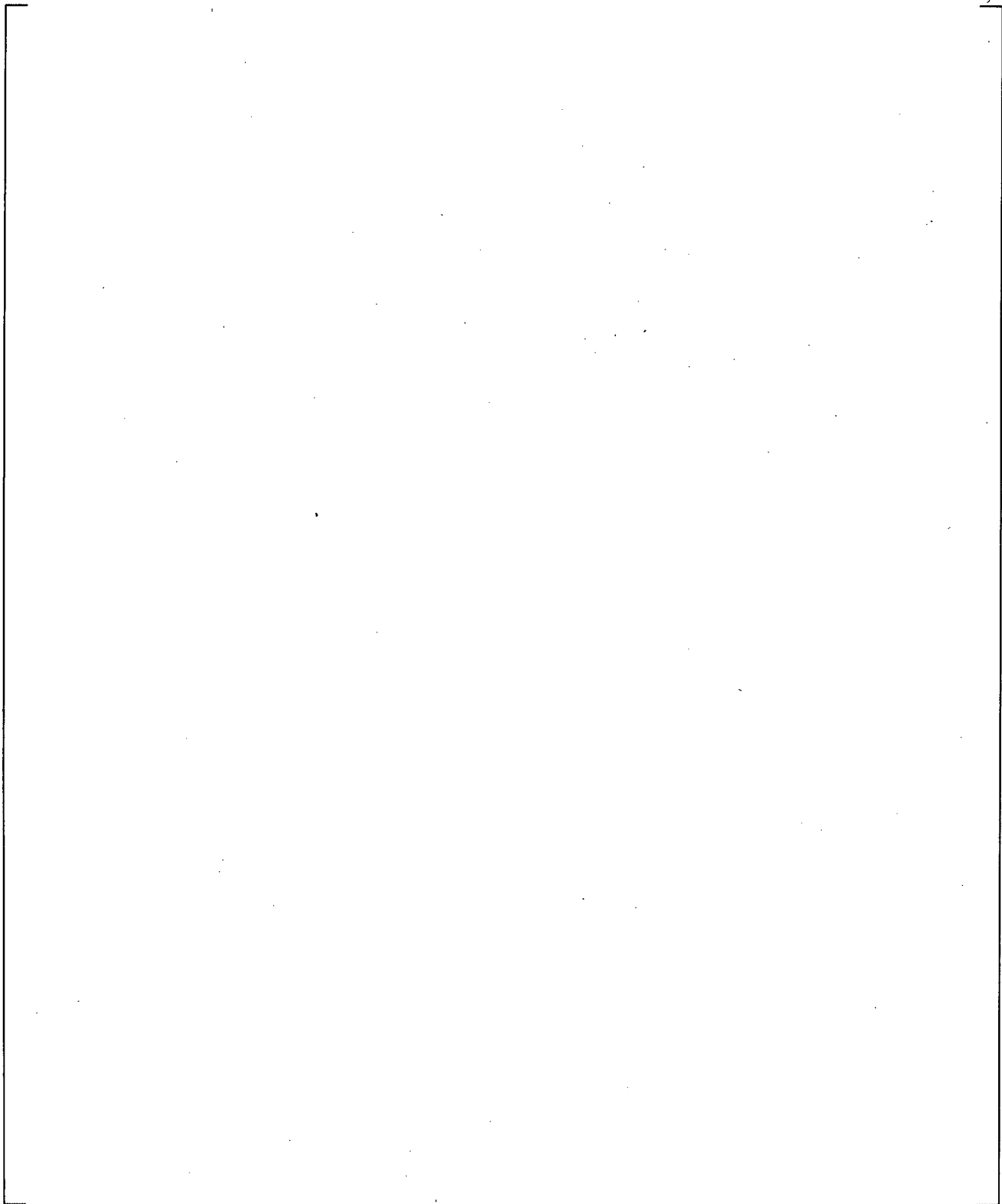


**Figure 19.3-160 Predicted Flow Regime Number of Cell Face 4 of Cold Leg**

a,c

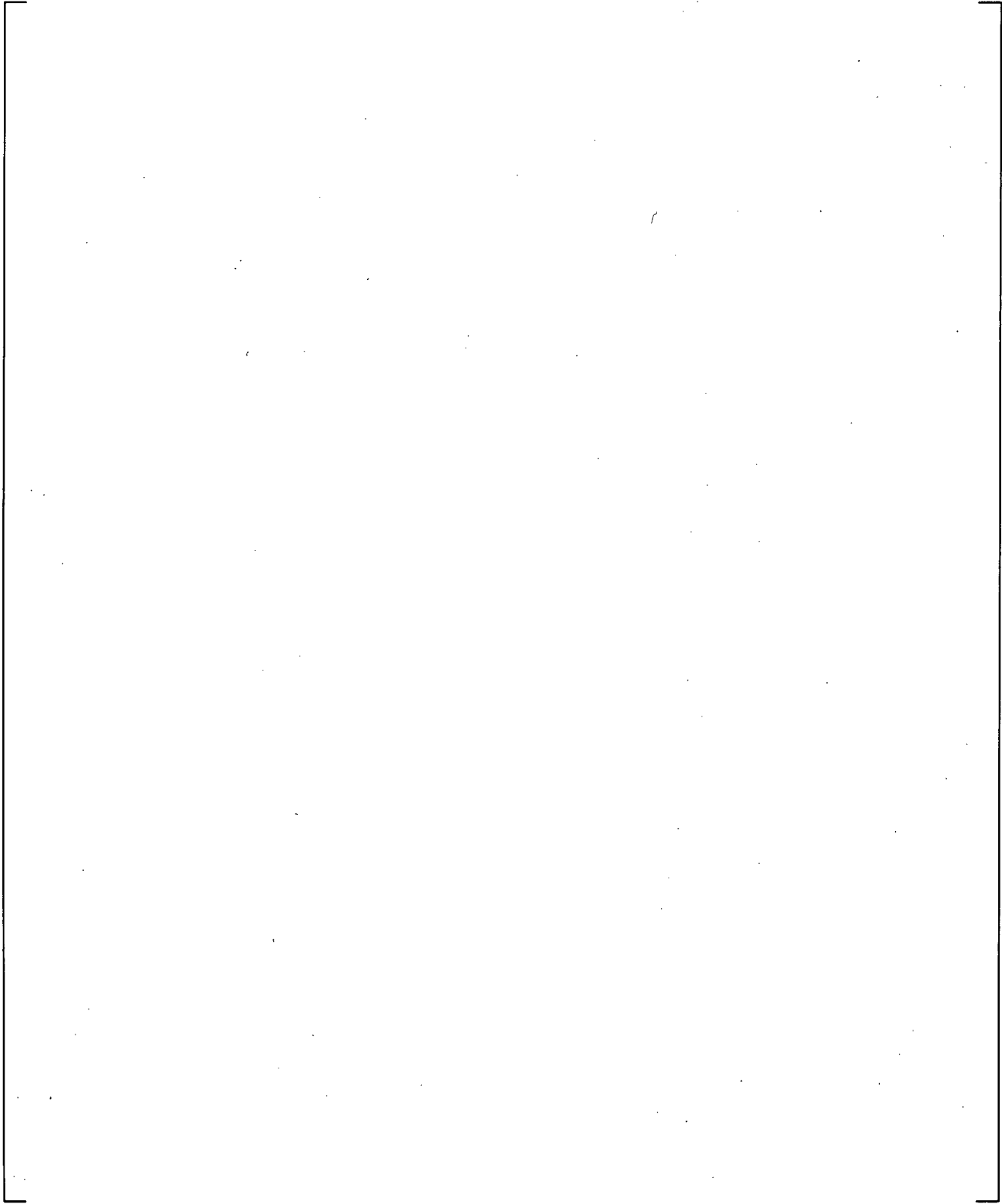


**Figure 19.3-161 Predicted Flow Regime Number of Cell Face 5 of Cold Leg**

a,c

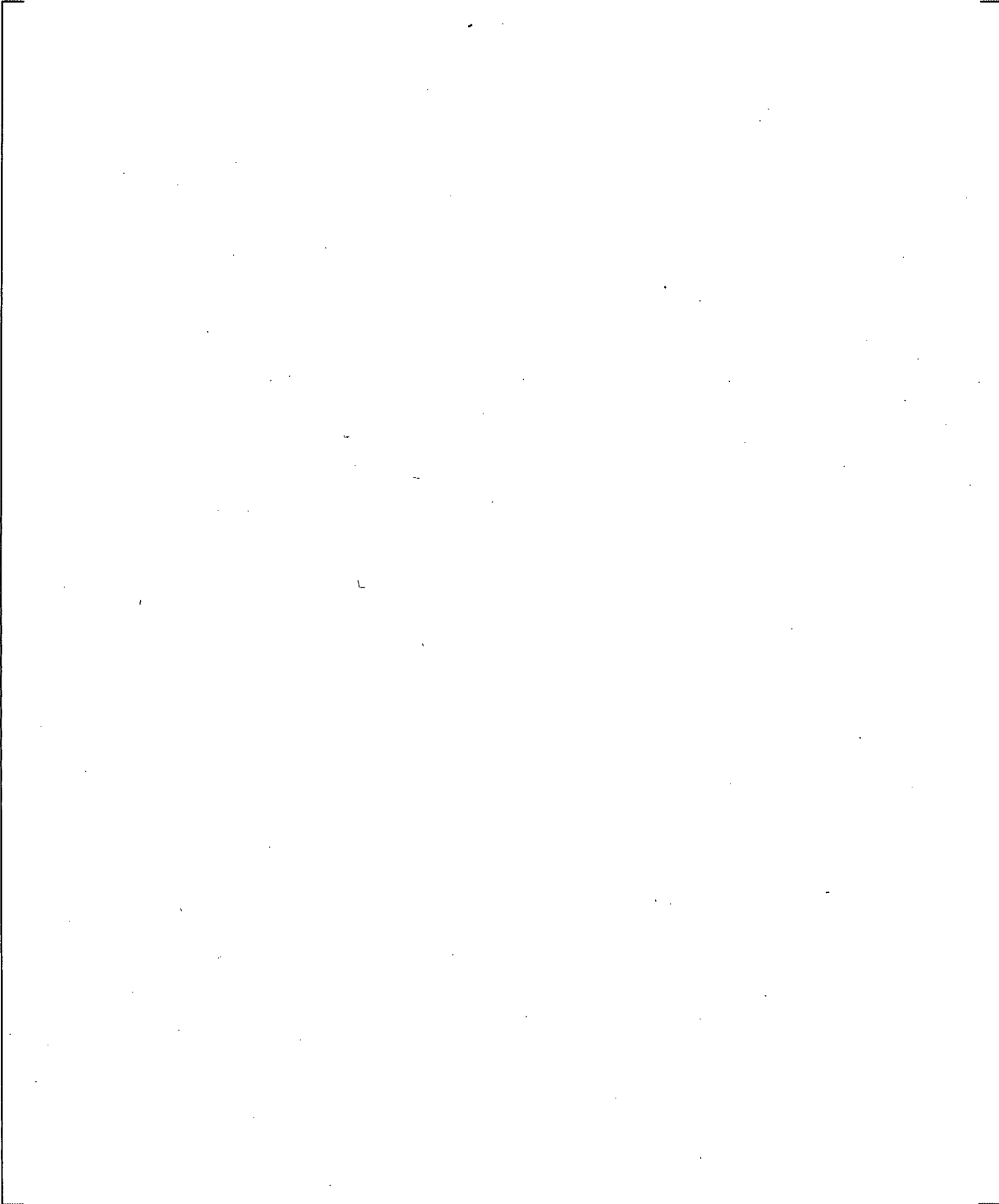


**Figure 19.3-162 Predicted Flow Regime Number of Cell Face 6 of Cold Leg**

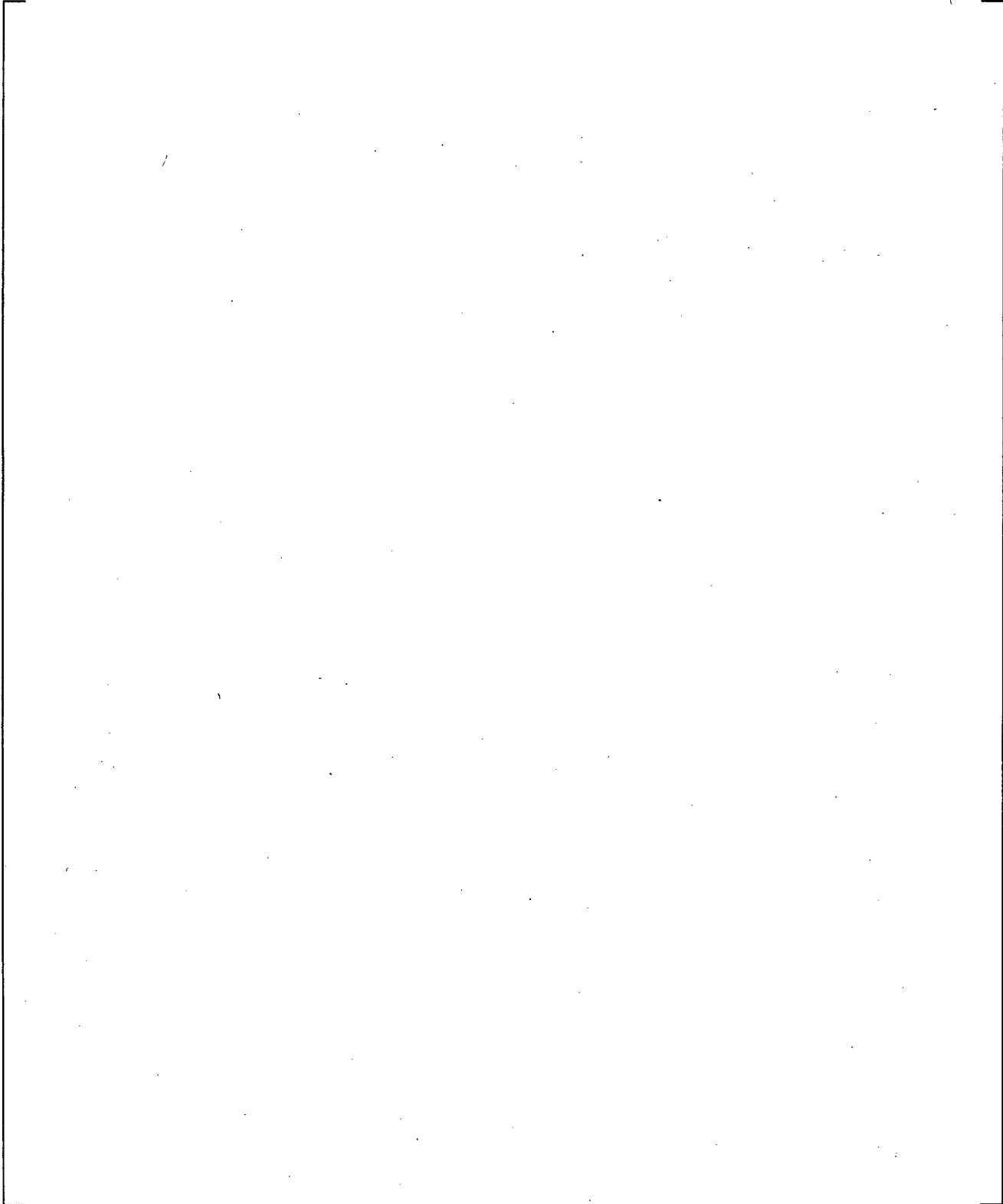


**Figure 19.3-163 Predicted Flow Regime Number of Cell Face 7 of Cold Leg**

**Figure 19.3-164 System Configuration for UPTF Test 25, Phase A (Run 242) and Phase B (Run 241)**

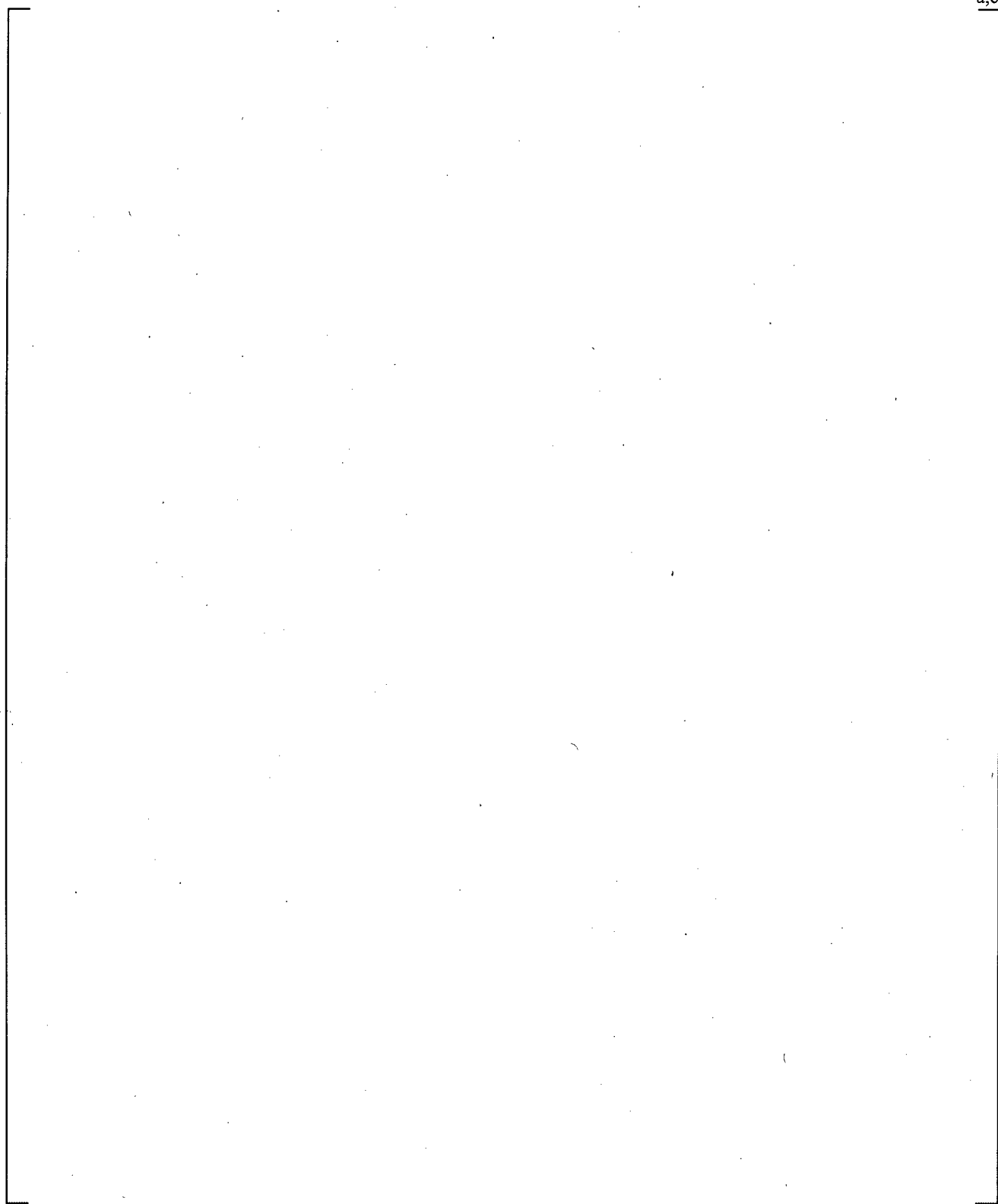


**Figure 19.3-165 Steam Flow Rate for UPTF Test 25, Phase A (Run 242)**

a,c

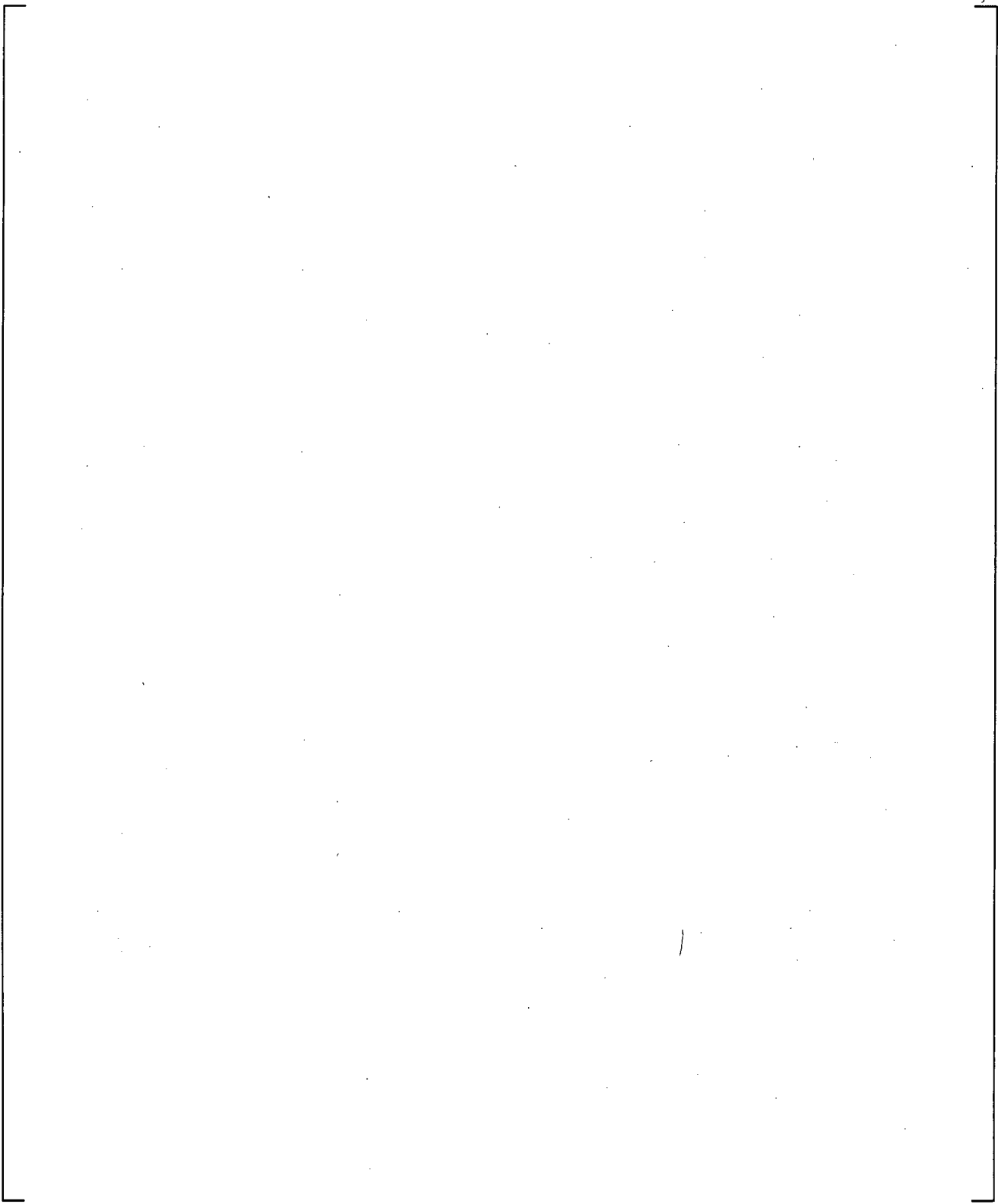


**Figure 19.3-166 ECC Flow Rate for UPTF Test 25, Phase A (Run 242)**

a,c

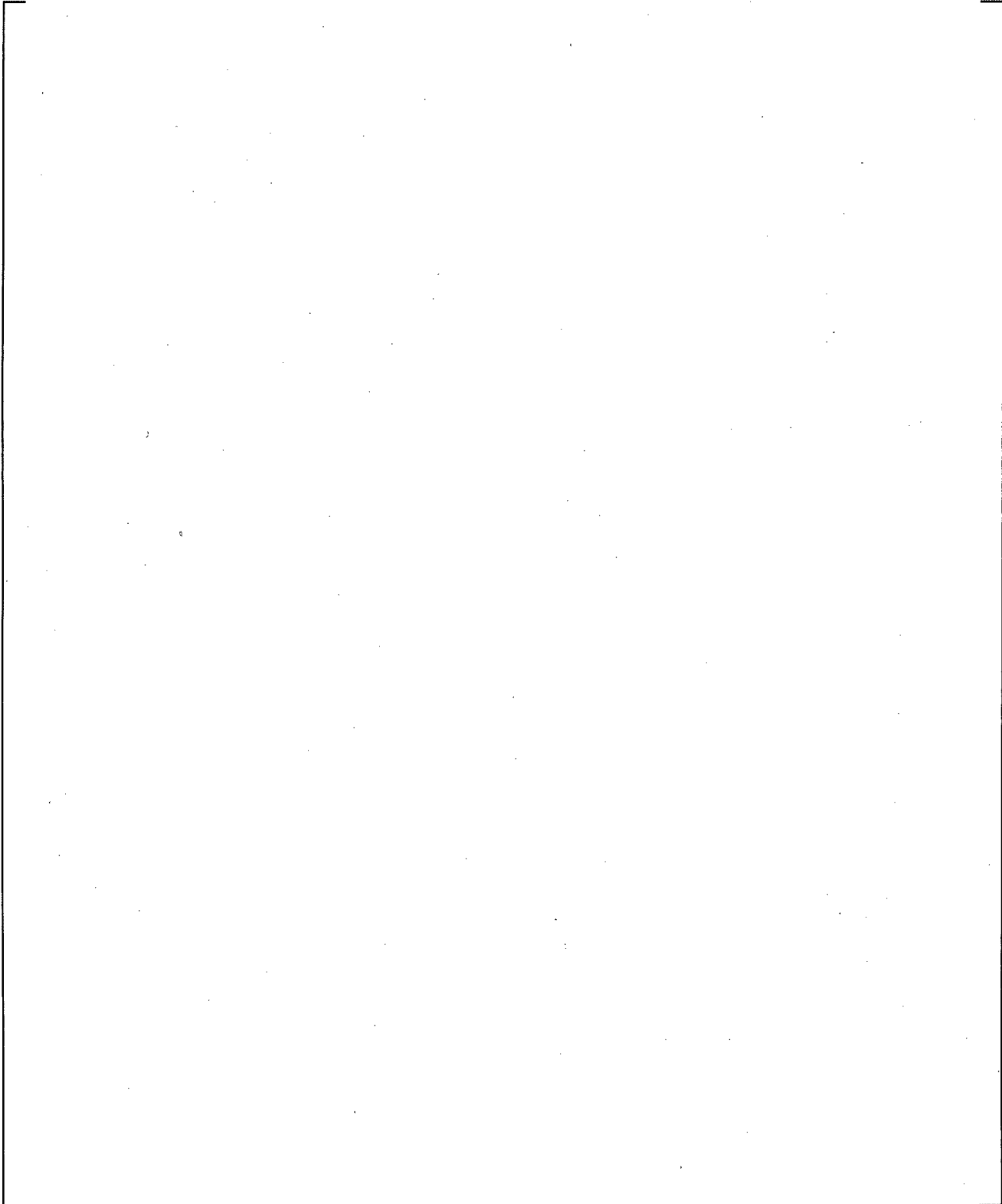


**Figure 19.3-167 Drainage Flow Rate for UPTF Test 25, Phase A (Run 242)**

a,c

Figure 19.3-168 WCOBRA/TRAC-TF2 Loop Model for UPTF Test 25A

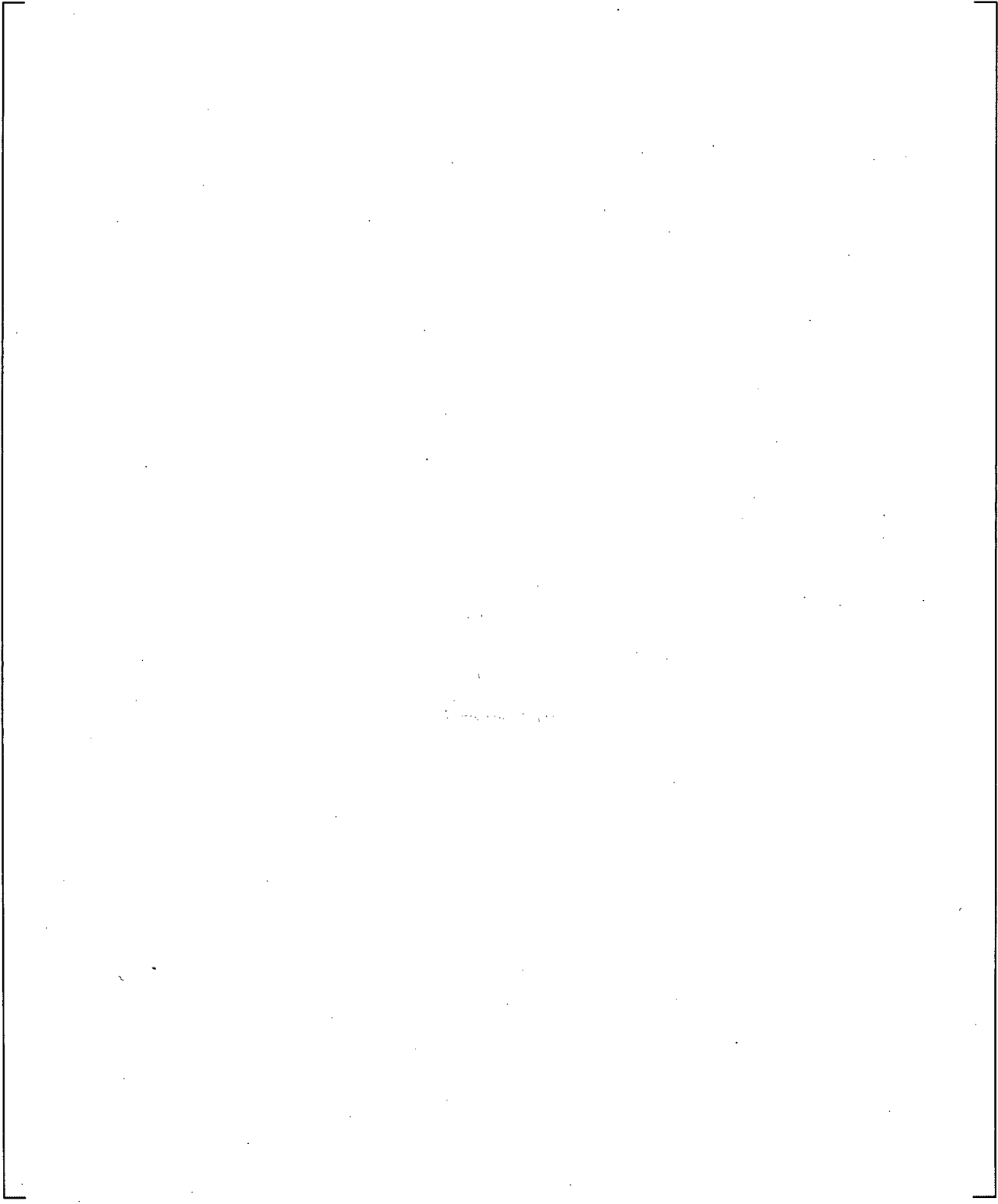


**Figure 19.3-169 Absolute Pressure in the Upper Plenum and Downcomer for UPTF Test 25A**

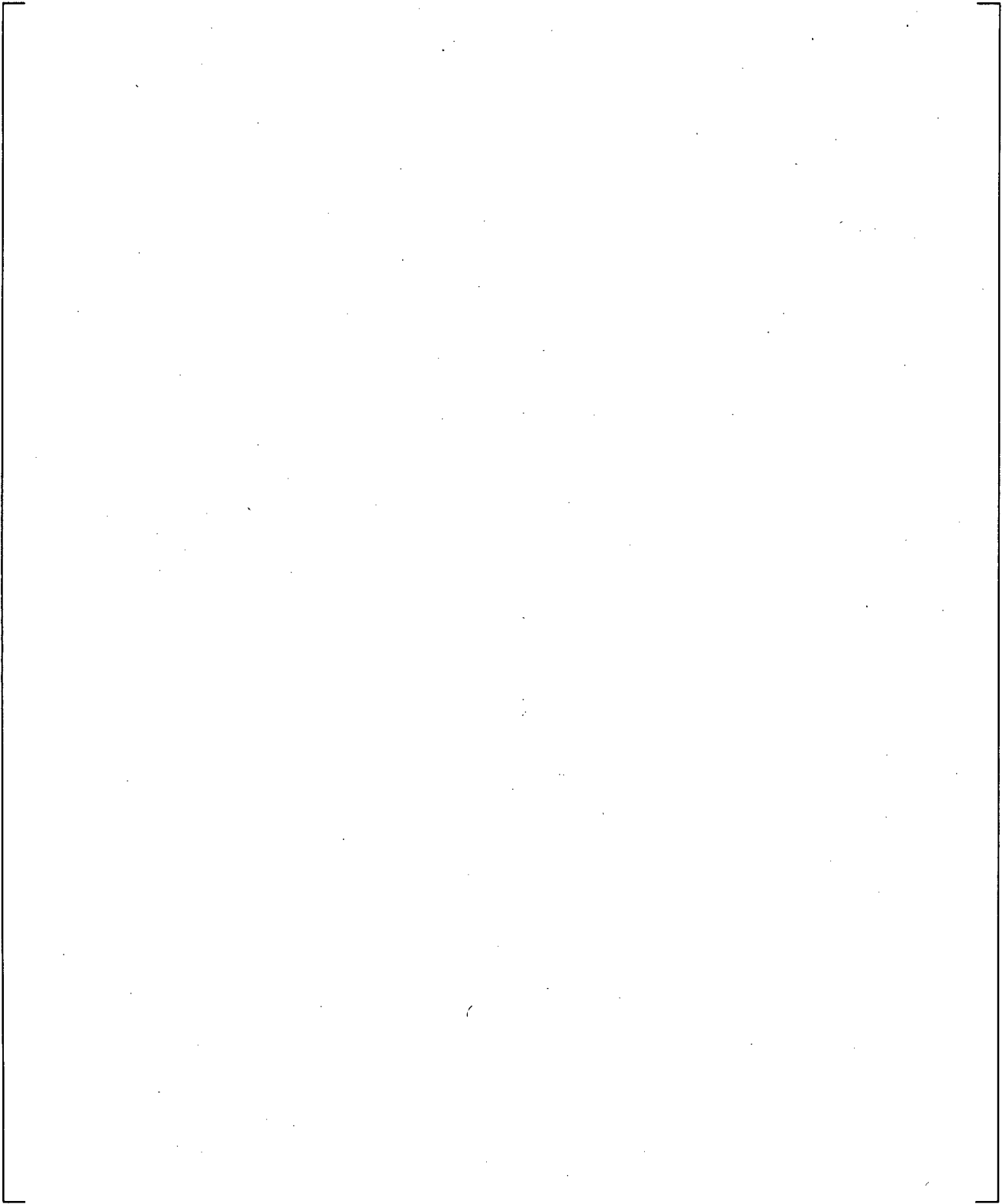


**Figure 19.3-170 Measured Downcomer Fluid Temperature at Level 28 for UPTF Test 25A**

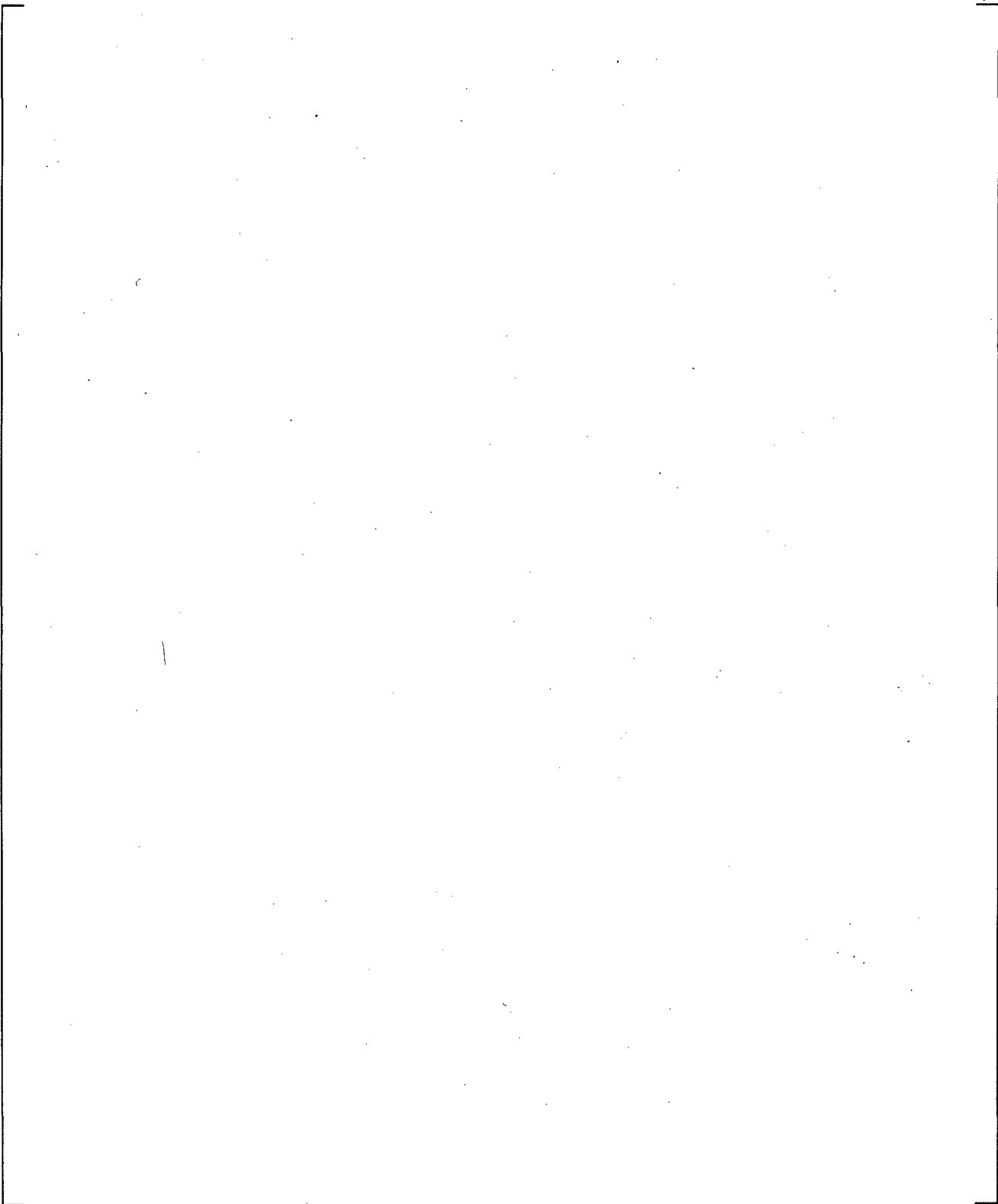


**Figure 19.3-171 Predicted Downcomer Fluid (Vapor) Temperature at Level 28 for UPTF Test 25A**

a,c

**Figure 19.3-172 Measured Downcomer Fluid Temperature at Level 24 for UPTF Test 25A**

a,c

**Figure 19.3-173 Predicted Downcomer Fluid (Liquid) Temperature at Level 24 for UPTF Test 25A**

a,c

**Figure 19.3-174 Differential Pressure between Upper Plenum and Downcomer for UPTF Test 25A**

a,c



**Figure 19.3-175 Axial Differential Pressure in Downcomer for UPTF Test 25A**

**Figure 19.3-176 Axial Differential Pressures in Downcomer for UPTF Test 25A; Curve 2 is in Broken Quadrant and Curves 1, 3 and 4 are in Intact Quadrants**

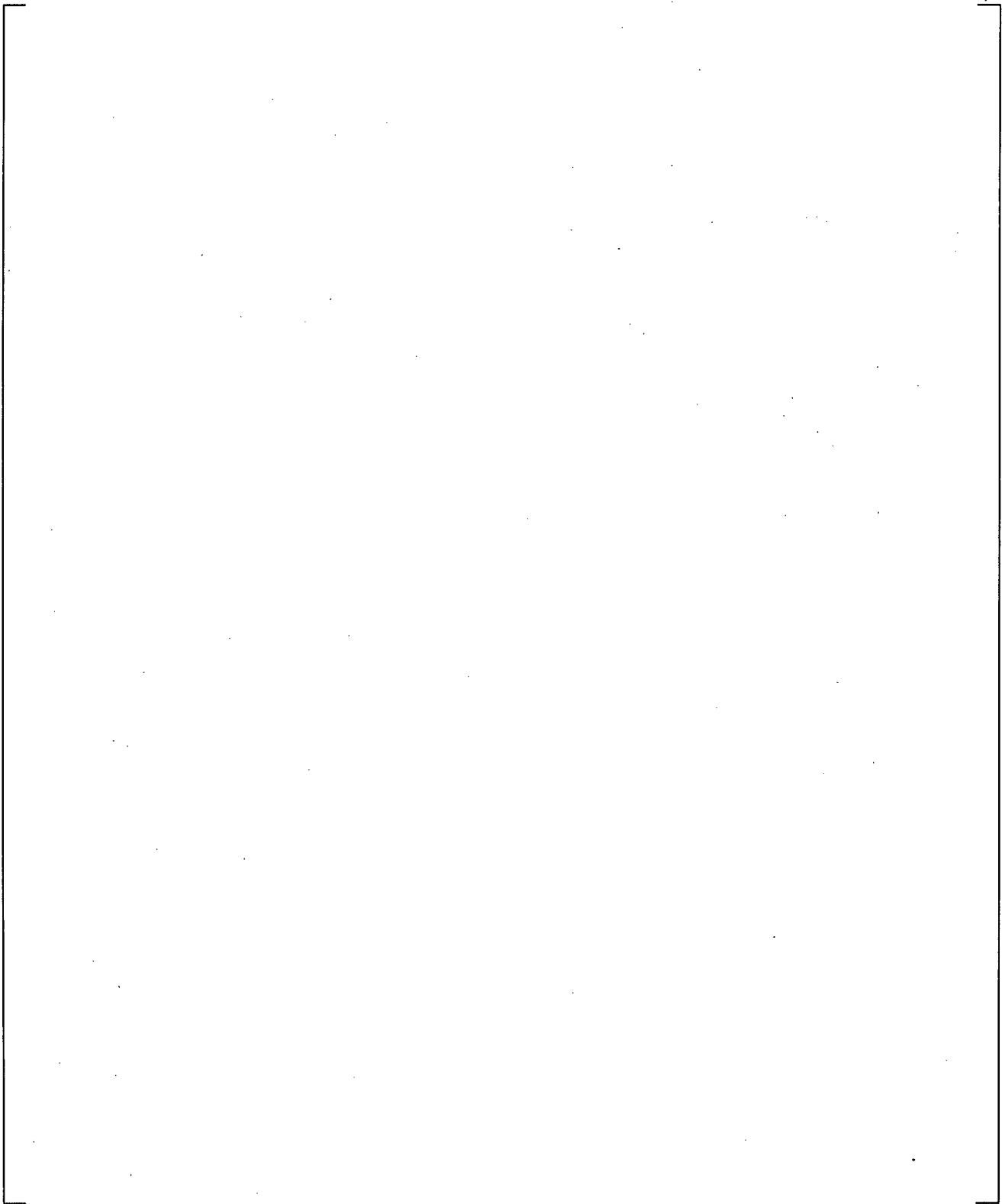


**Figure 19.3-177 Broken Loop Steam Flow Rate for UPTF Test 25A**

a,c

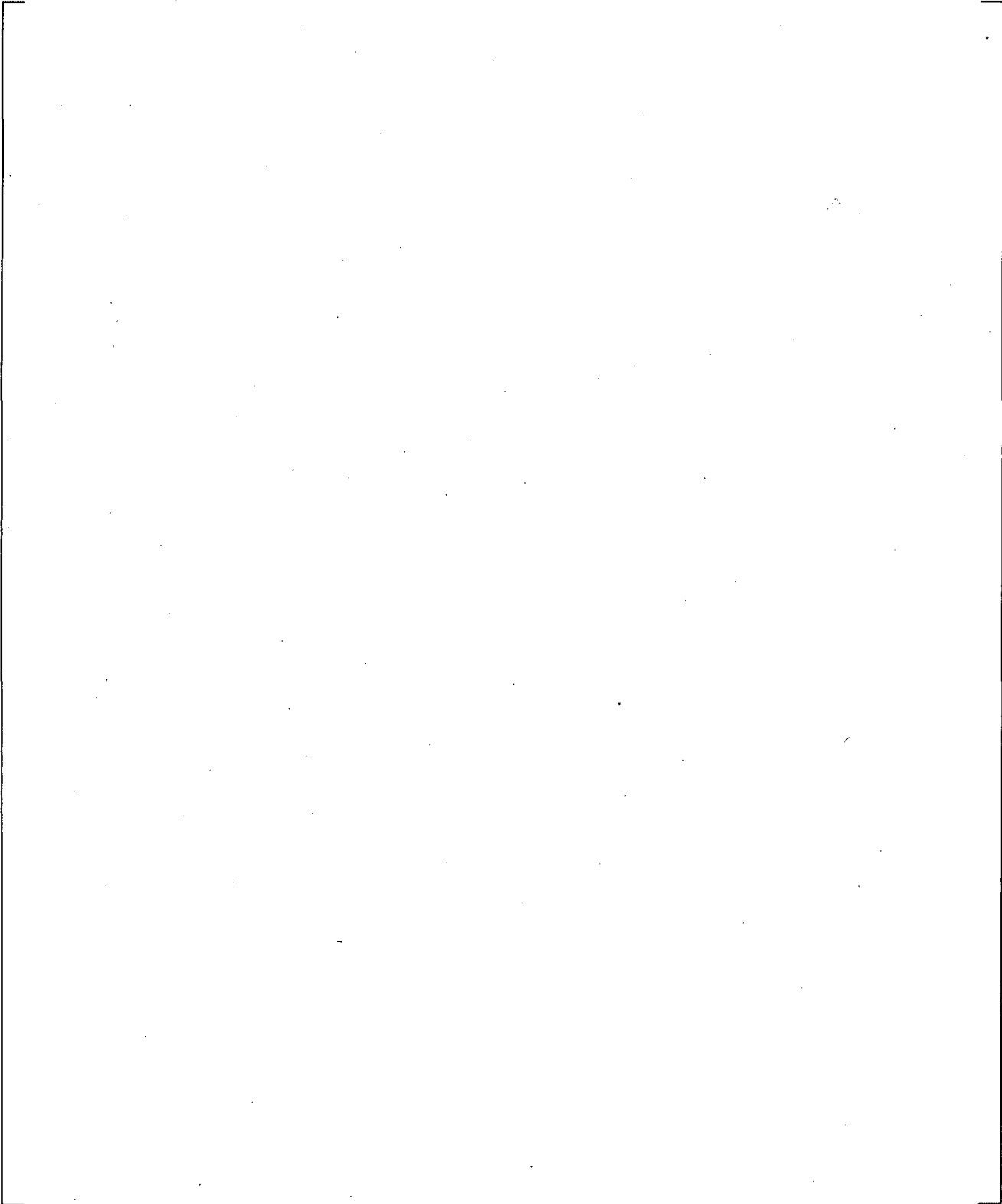


**Figure 19.3-178 Broken Loop Liquid Flow Rate for UPTF Test 25A**

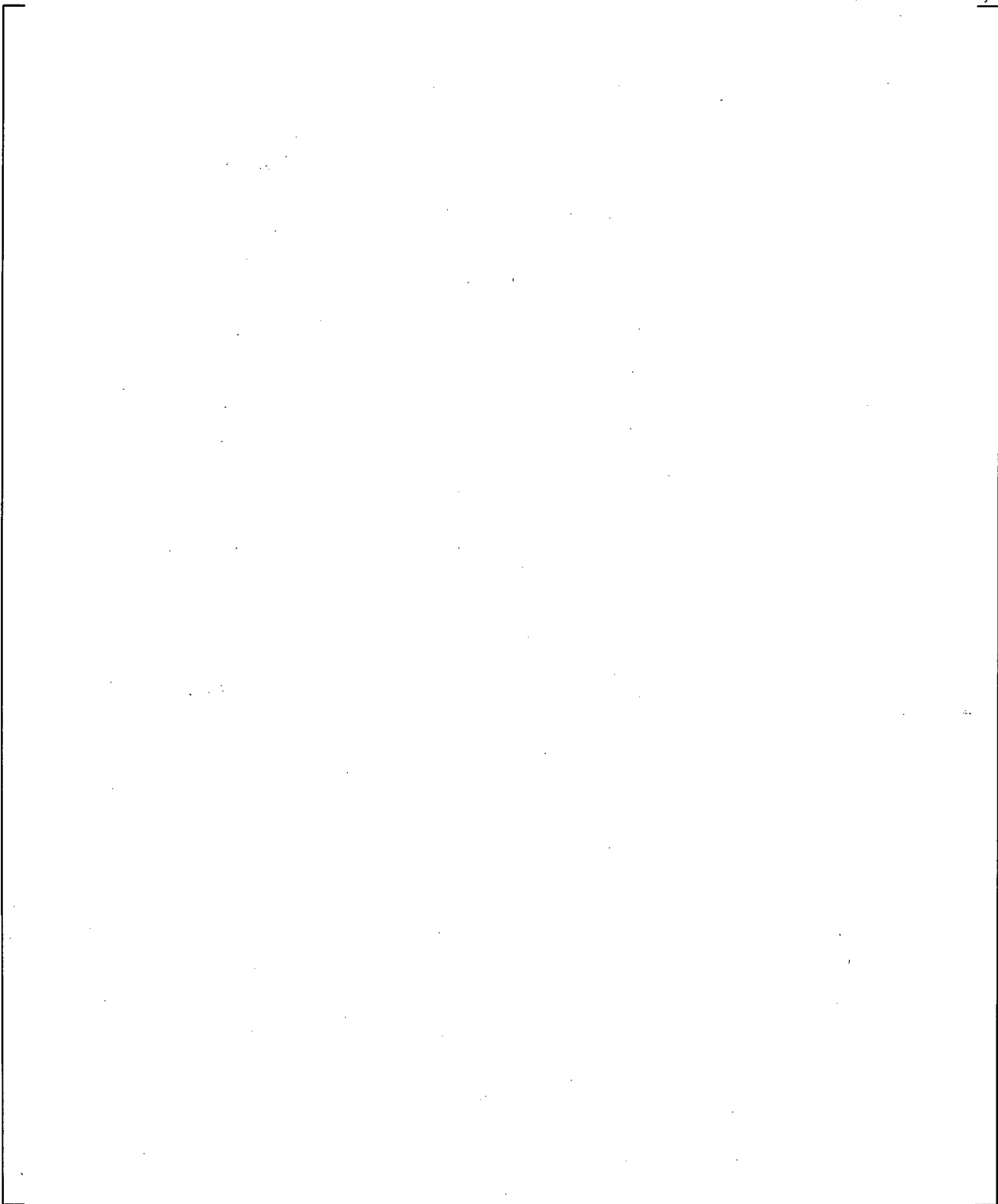


**Figure 19.3-179 Void Height versus Steam Flow Rate for UPTF Test 25A.**

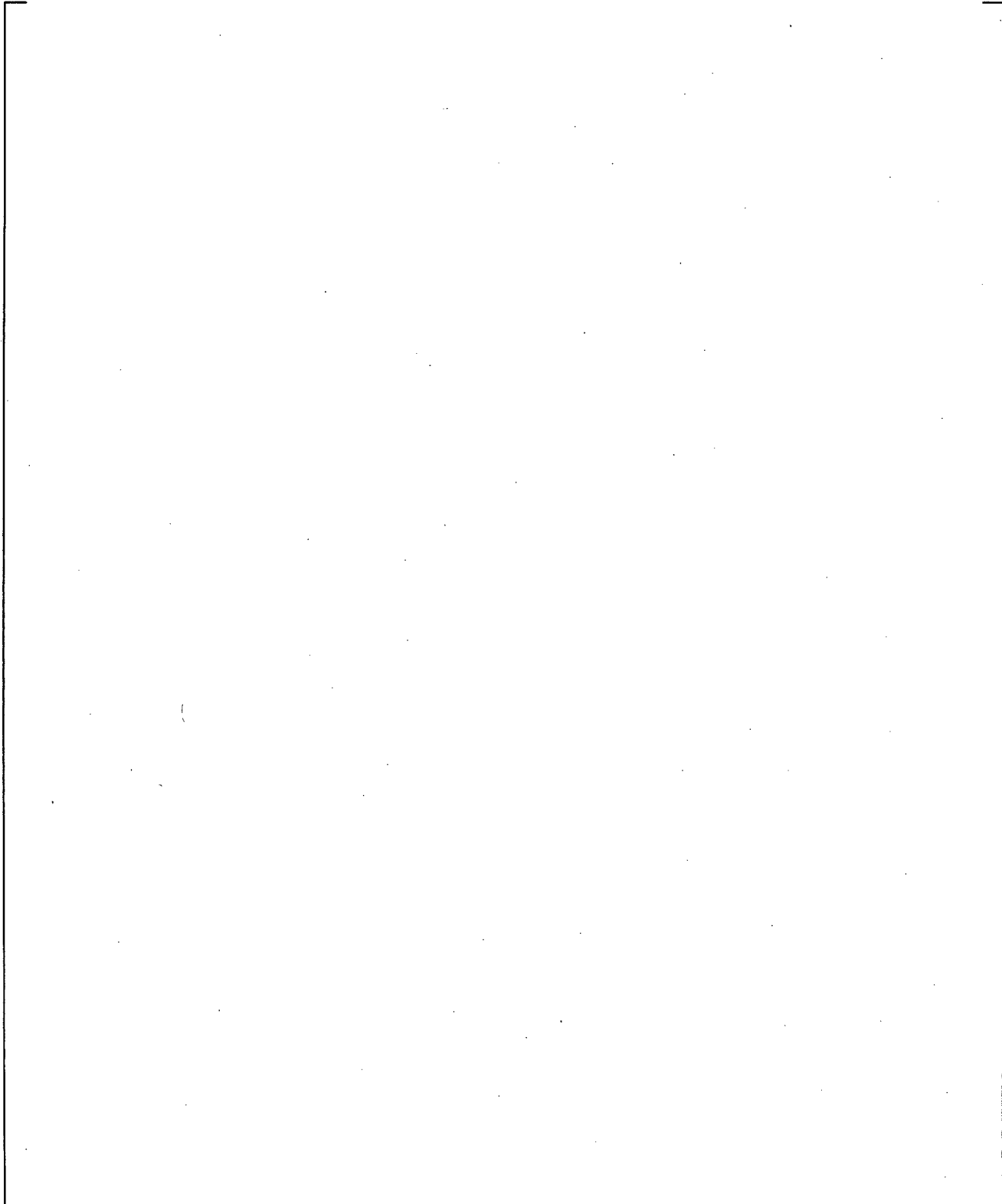


**Figure 19.3-180 Cold Leg Temperature near ECC Injection for UPTF Test 25A**

a,c

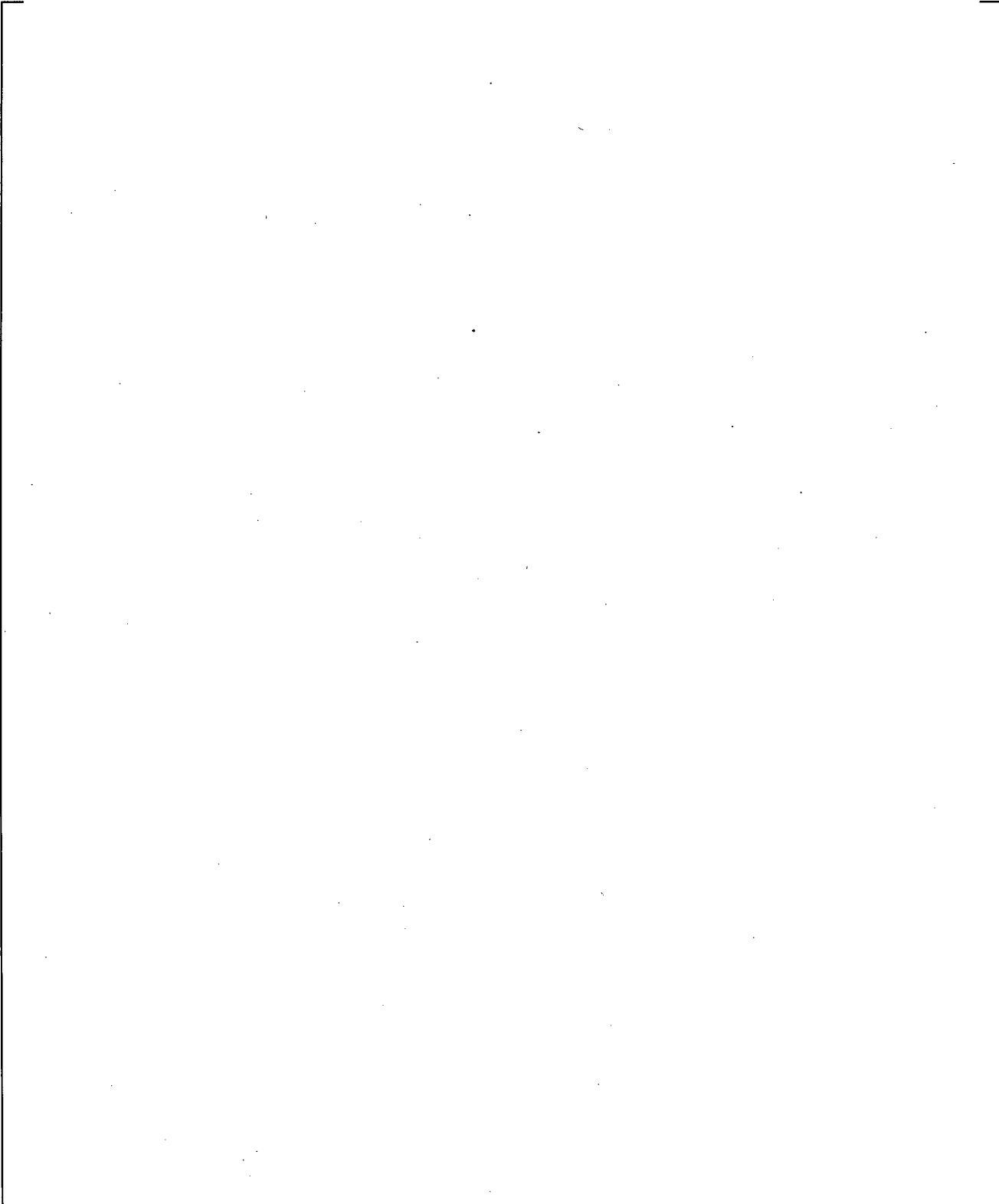


**Figure 19.3-181 Cold Leg Temperature Downstream of ECC Injection for UPTF Test 25A**

a,c

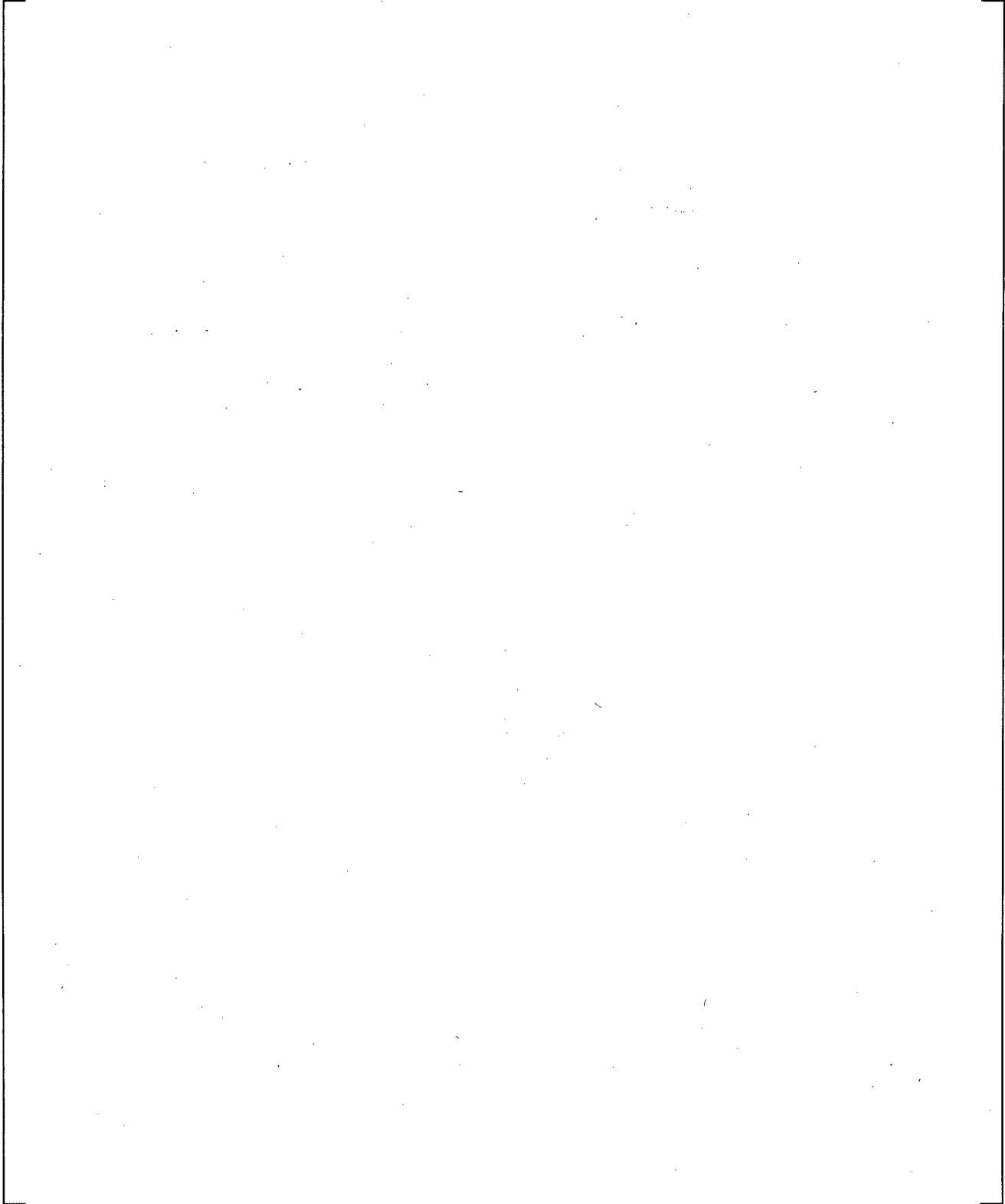


**Figure 19.3-182 Cold Leg Temperature at Exit of Cold Leg for UPTF Test 25A**

a,c

**Figure 19.3-183 Cold Leg Temperature near ECC Injection for UPTF Test 25A with KCOSI=0.4**

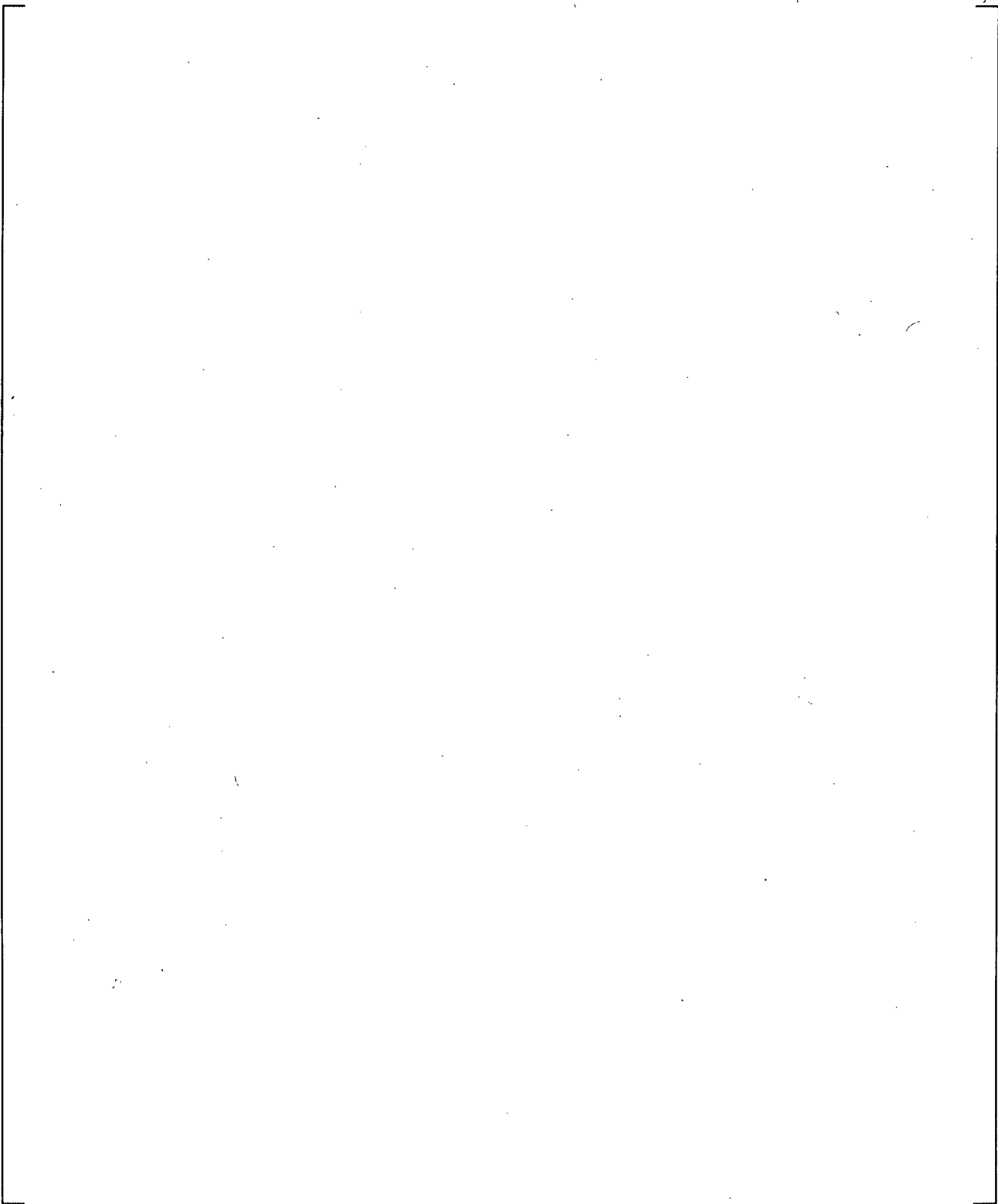


**Figure 19.3-184 Cold Leg Temperature Downstream of ECC Injection for UPTF Test 25A with KCOSI=0.4**

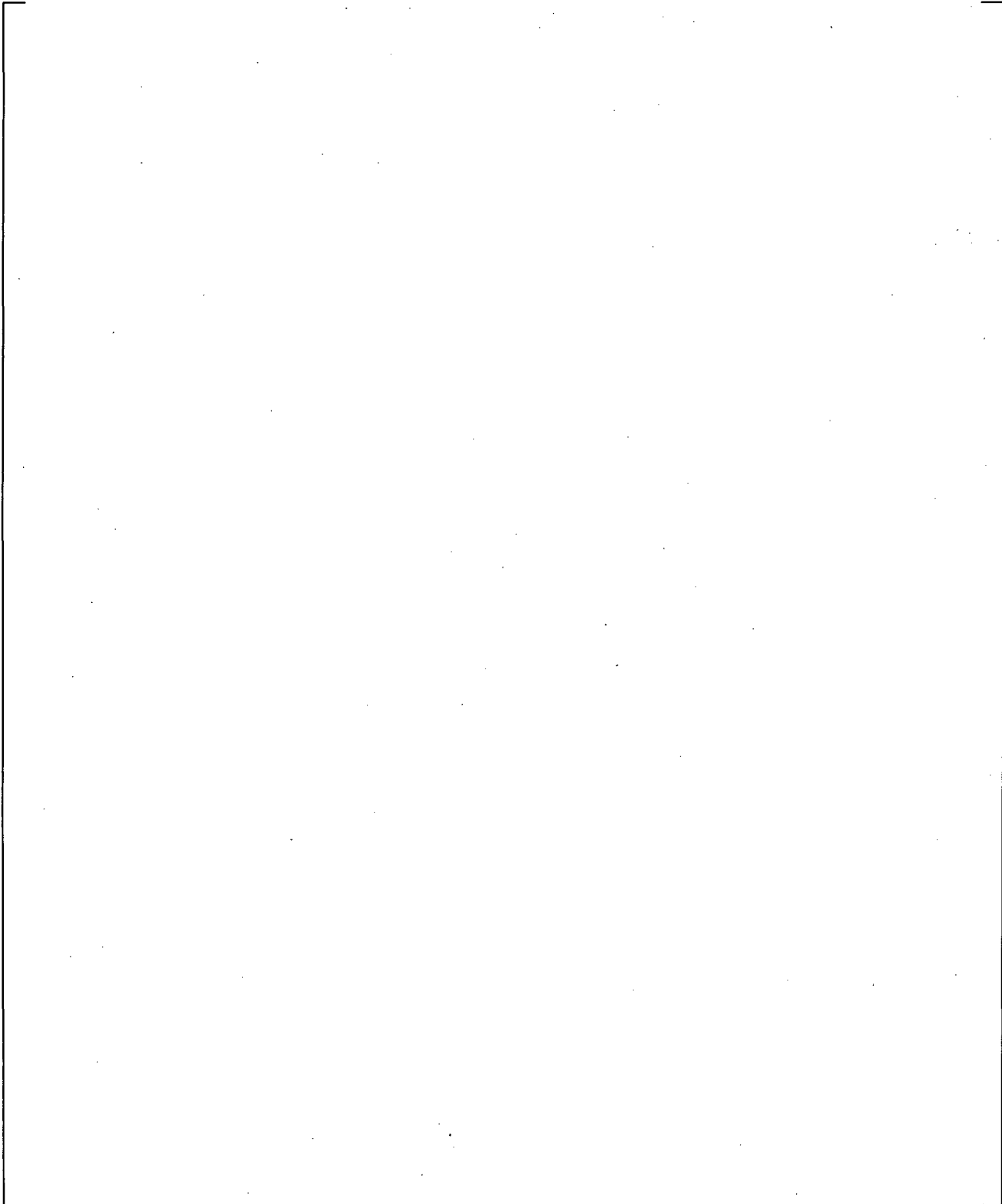


**Figure 19.3-185 Cold Leg Temperature at Exit of Cold Leg for UPTF Test 25A with KCOSI=0.4**

a,c

**Figure 19.3-186 Axial Differential Pressures in Downcomer for UPTF Test 25A with KCOSI=0.4**

a,c

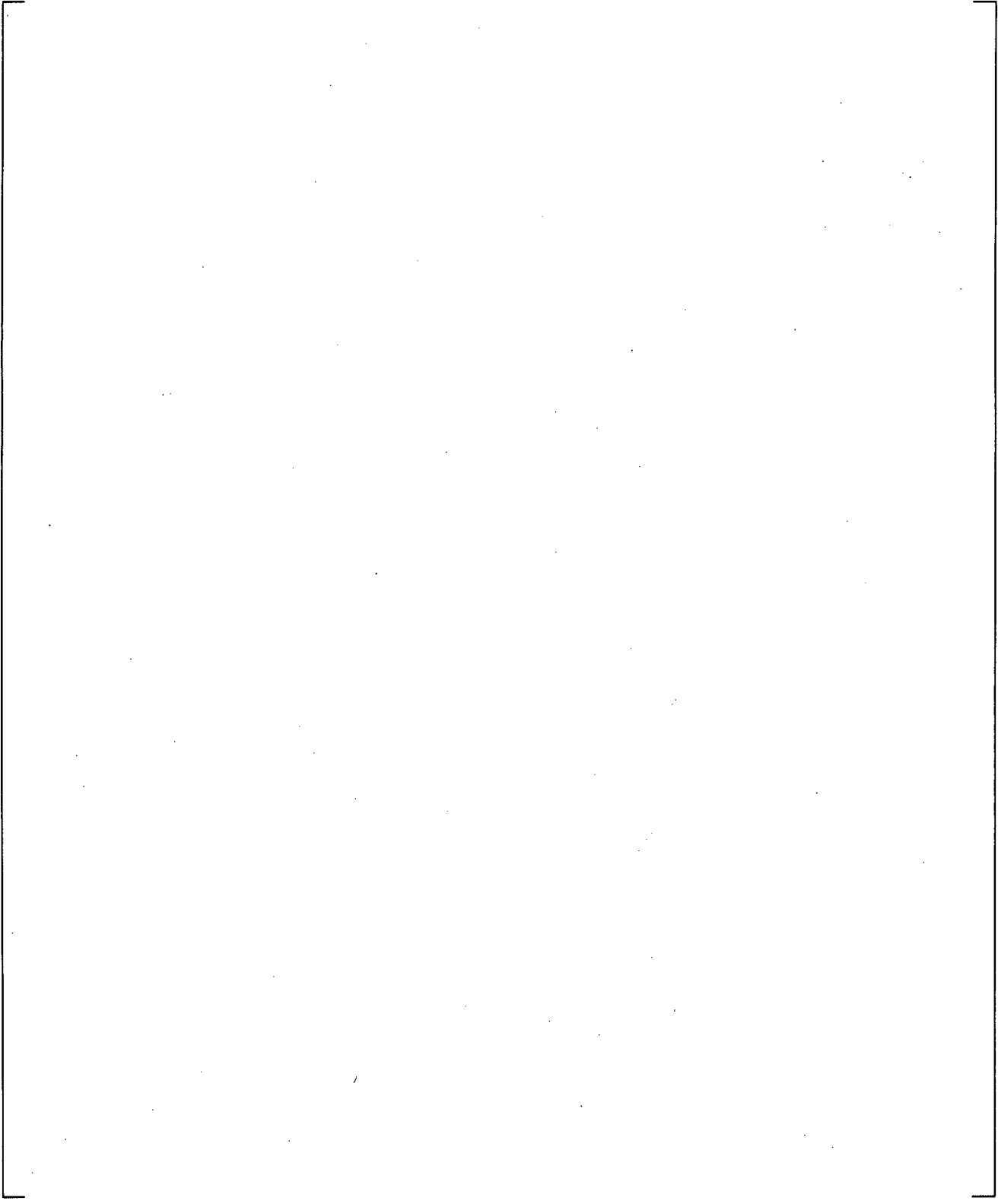


**Figure 19.3-187 Broken Loop Steam Flow Rate for UPTF Test 25A with KCOSI=0.4**

a,c

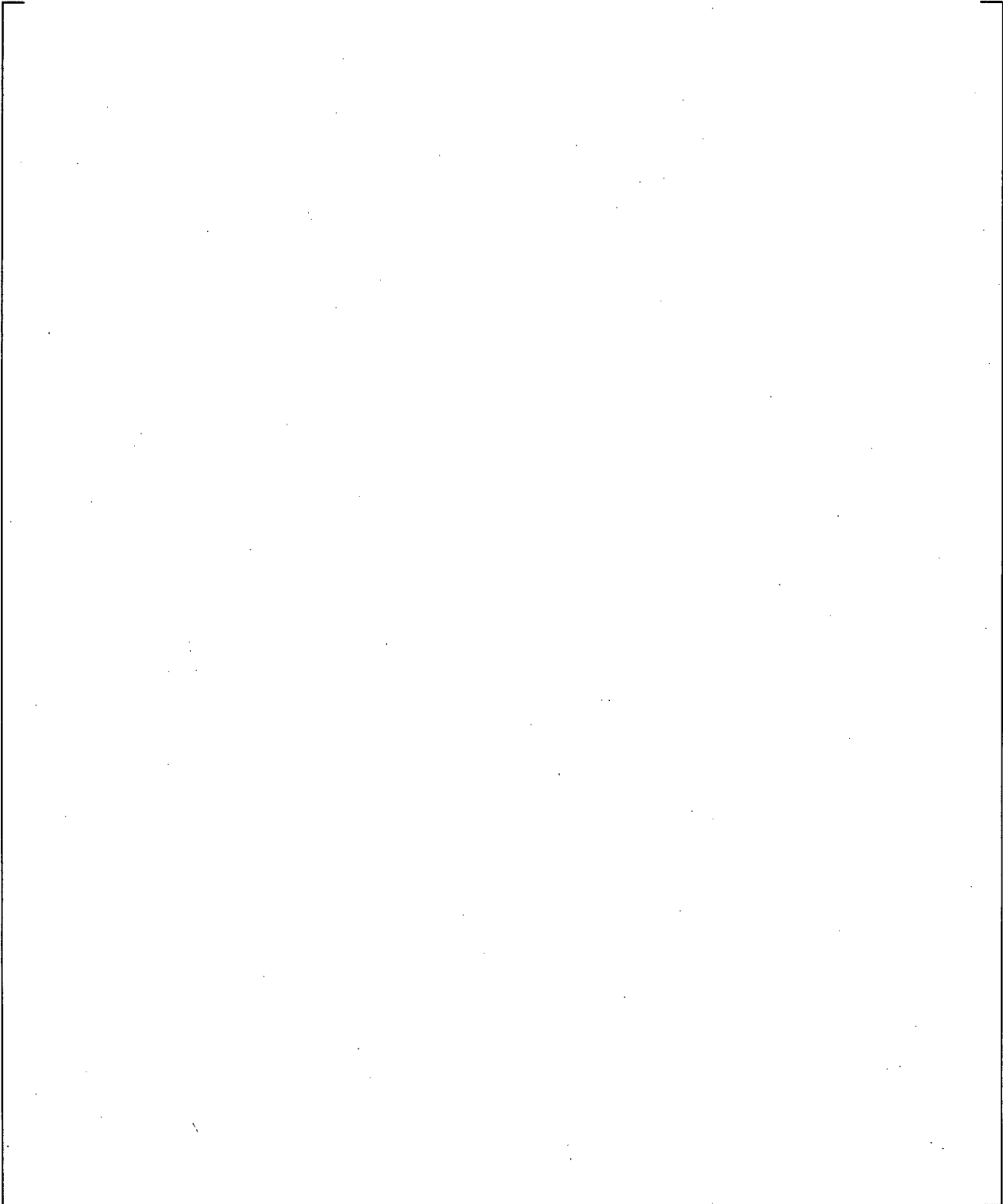


**Figure 19.3-188 Broken Loop Liquid Flow Rate for UPTF Test 25A with KCOSI=0.4**

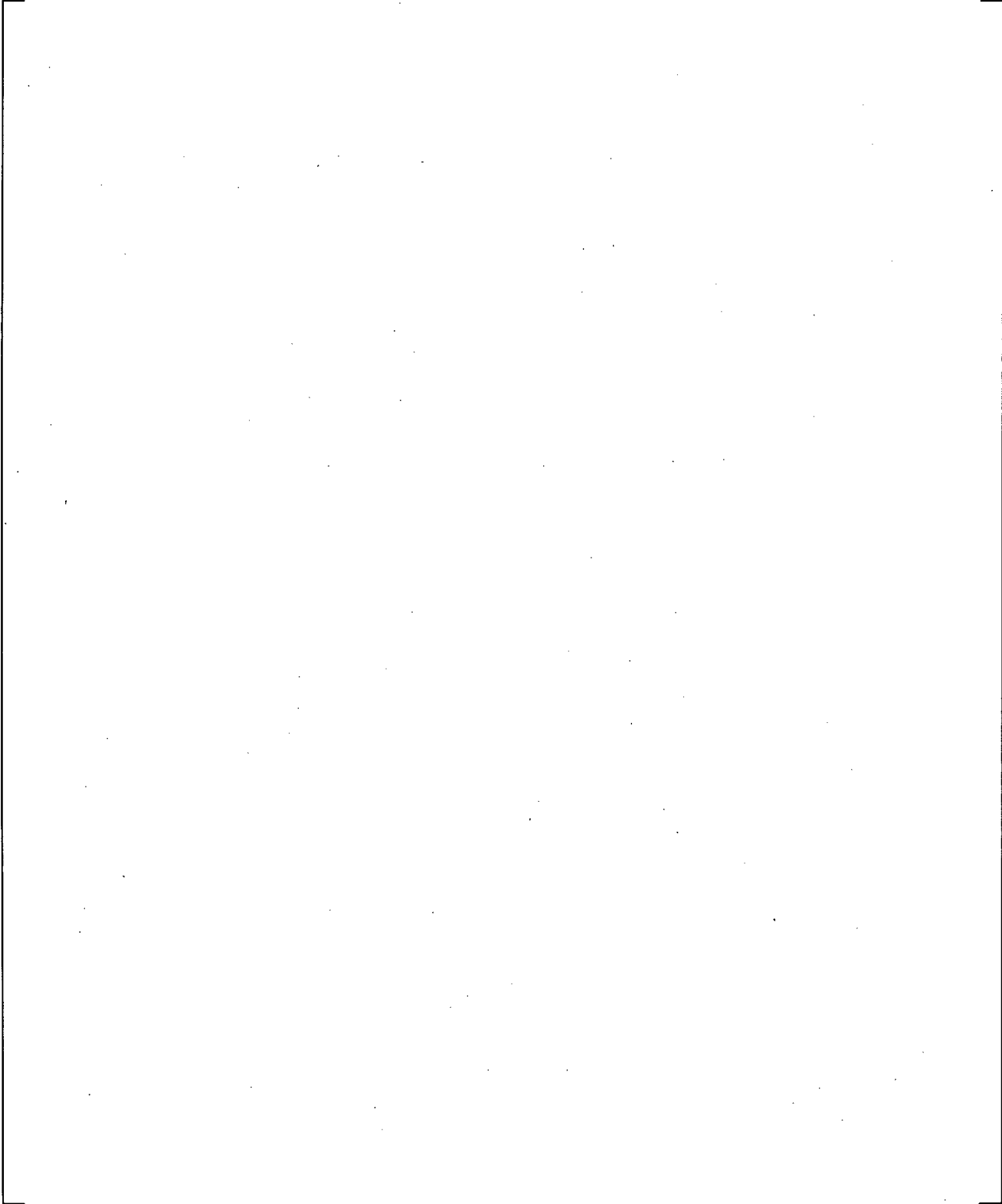


**Figure 19.3-189 Differential Pressure between Upper Plenum and Downcomer for UPTF Test 25A with XC=0.4**

**Figure 19.3-190 Axial Differential Pressure in Downcomer for UPTF Test 25A with XC=0.4**

a,c

**Figure 19.3-191 Axial Differential Pressures in Downcomer for UPTF Test 25A with XC=0.4**

a,c

**Figure 19.3-192 Void Height versus Steam Flow Rate for UPTF Test 25A with XC=0.4**

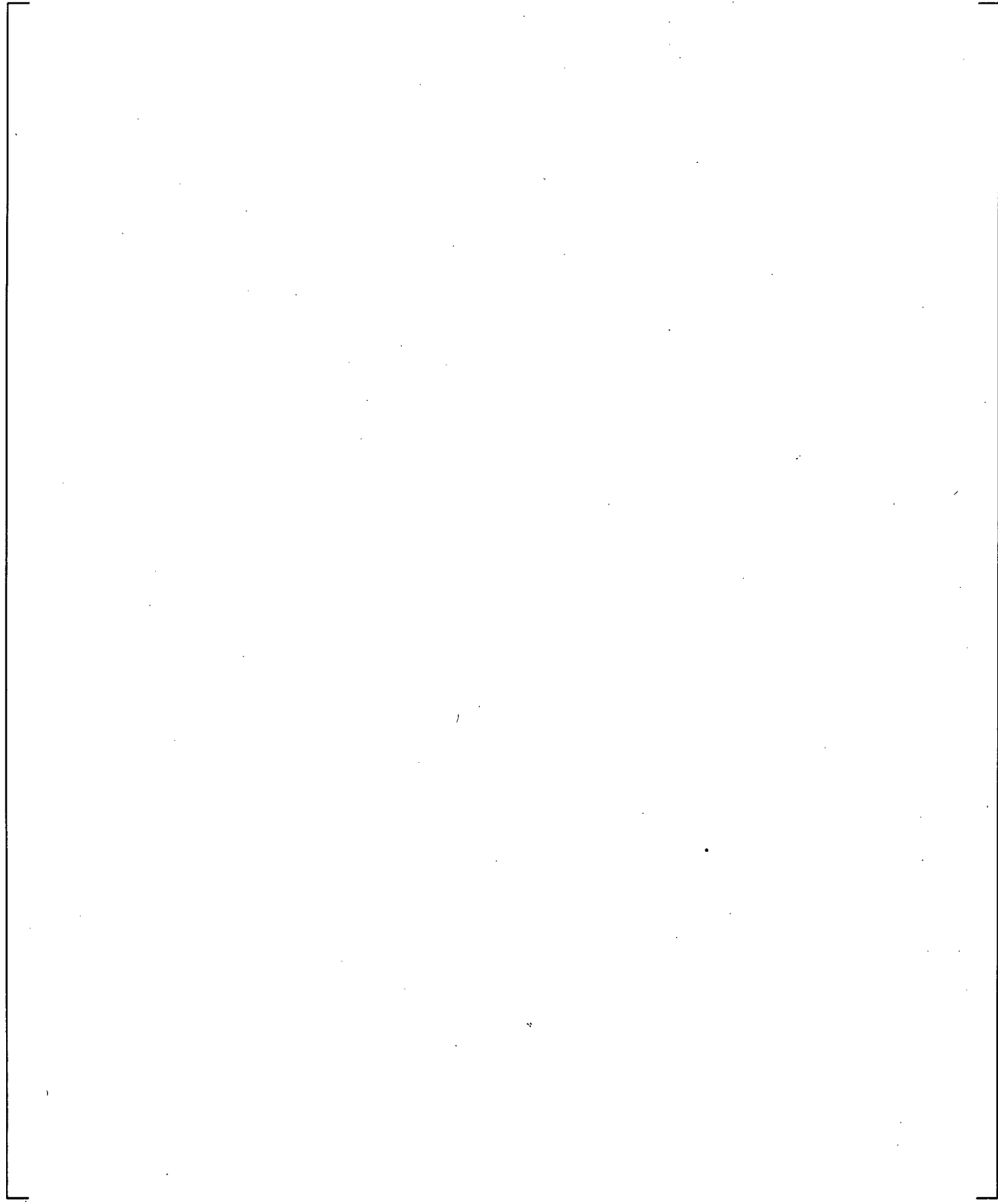


**Figure 19.3-193 System Configuration for UPTF, Test 29 Phase B (Run 212) (MPR-1213, 1990)**

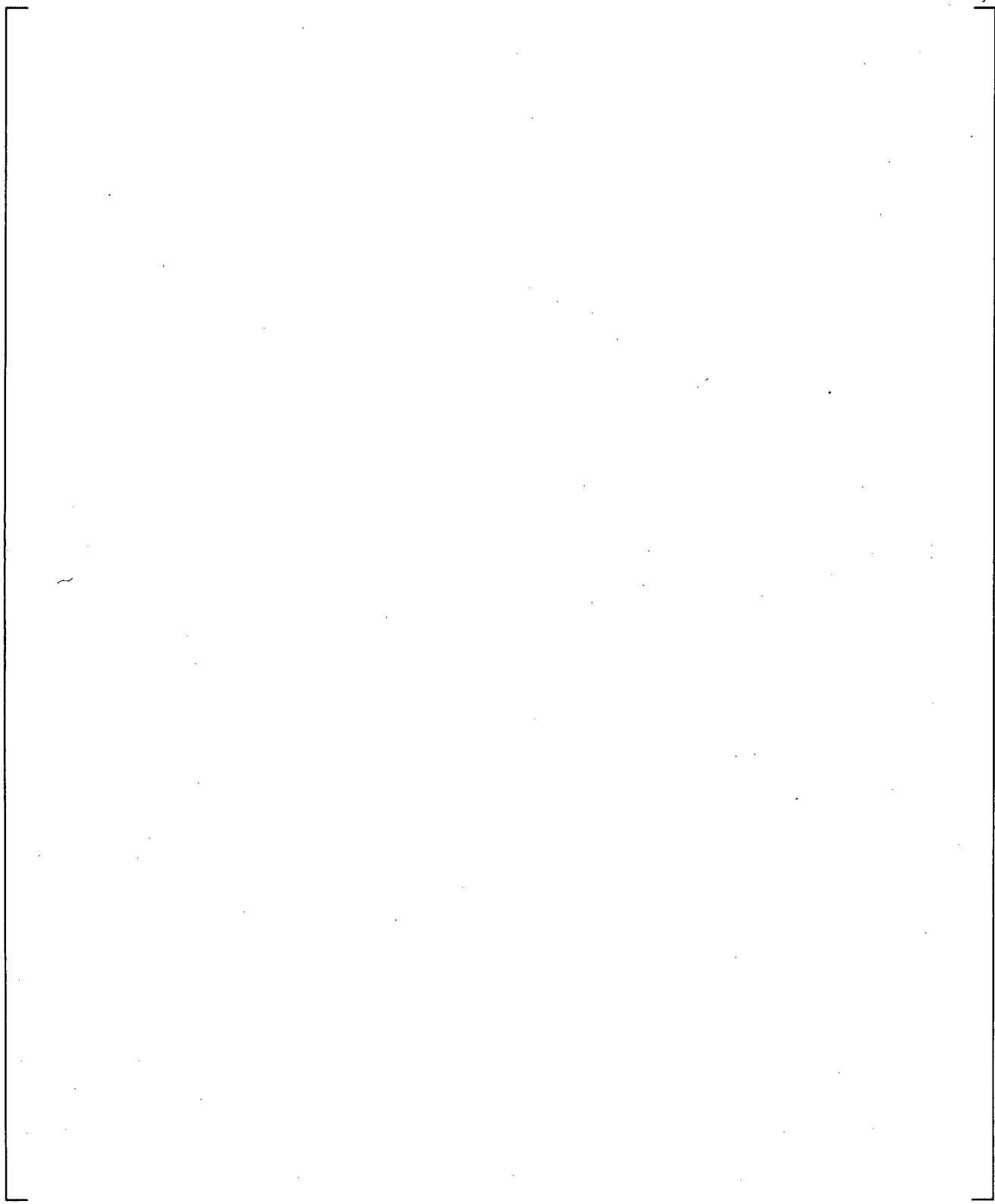


**Figure 19.3-194 Injection Rates into Core Simulator, UPTF 29B**

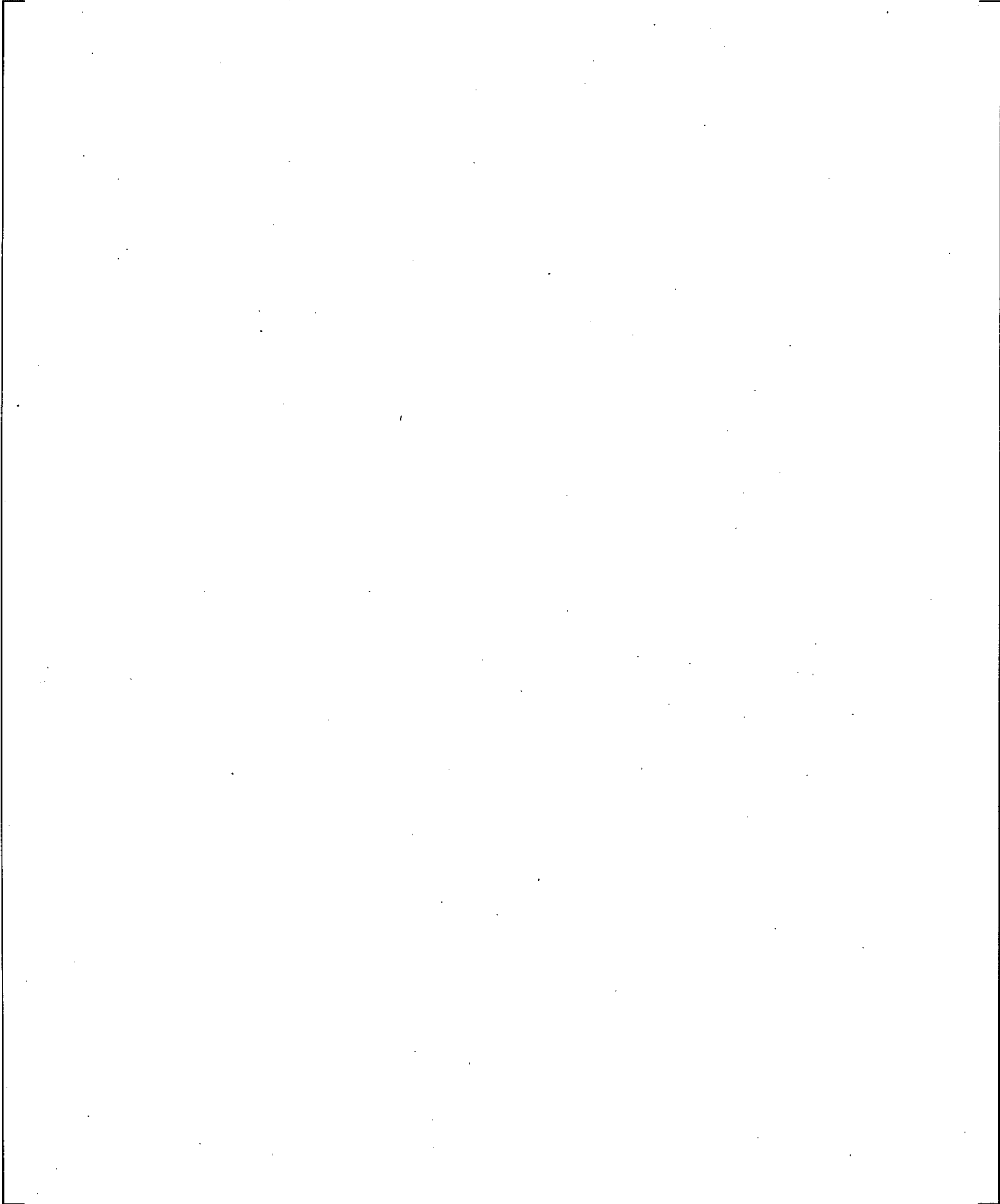


**Figure 19.3-195 WCOBRA/TRAC-TF2 Vessel Component for UPTF Test 29B**

a,c

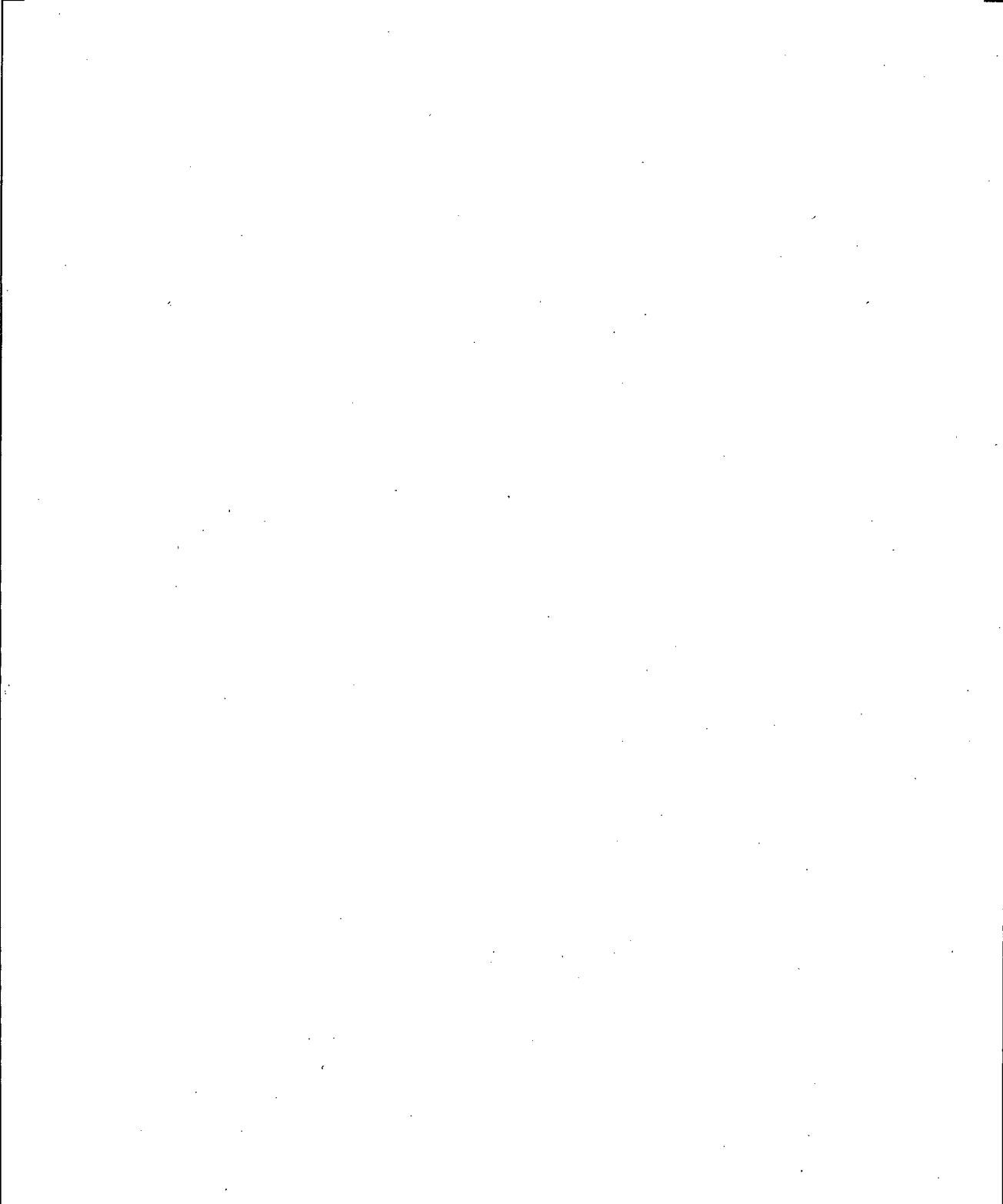


**Figure 19.3-196 Illustration of Jet Channel and Global Channel in Upper Plenum**

a,c

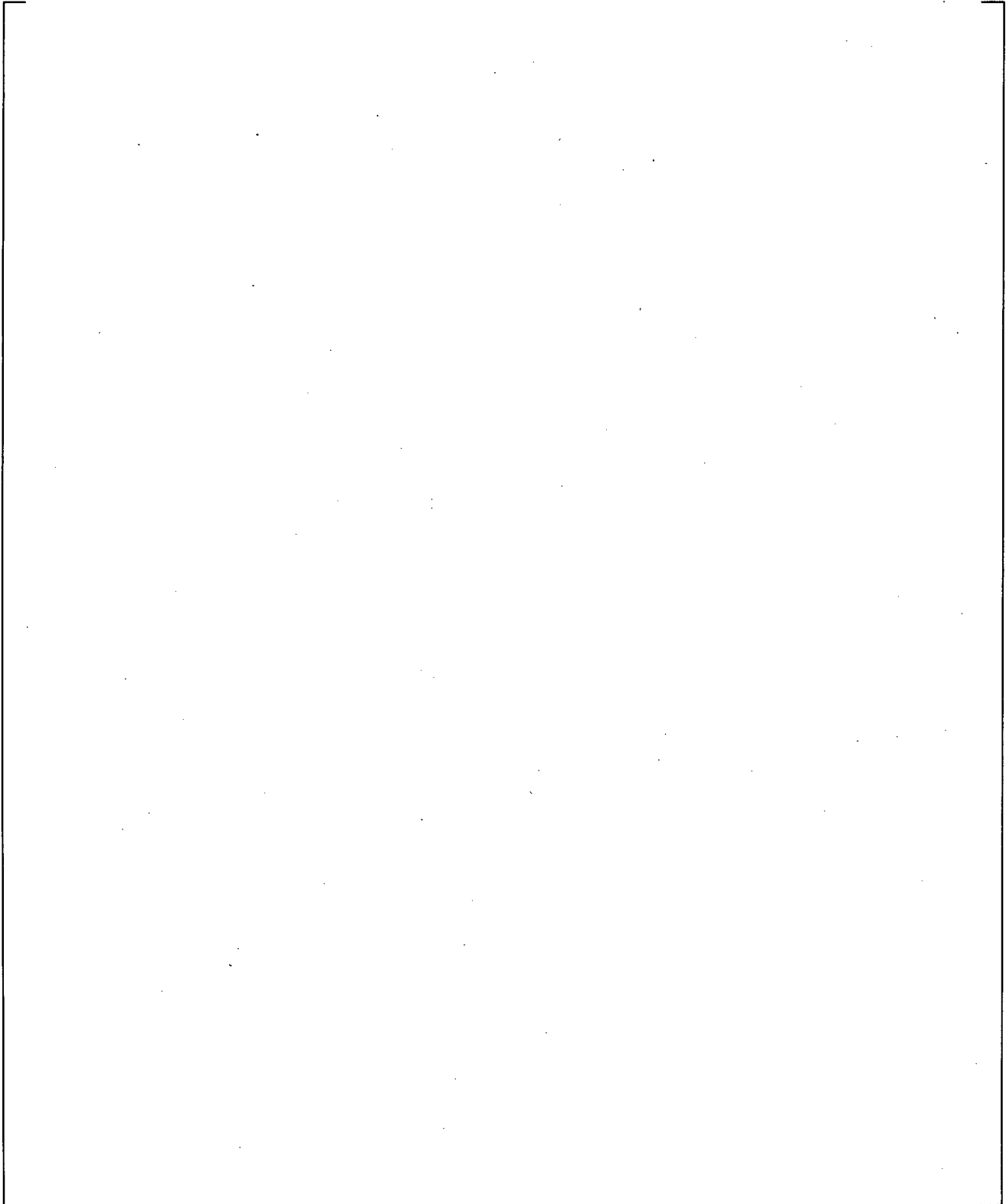


**Figure 19.3-197 Section 5 of Upper Plenum Noding Model for UPTF Test 29B**

a,c

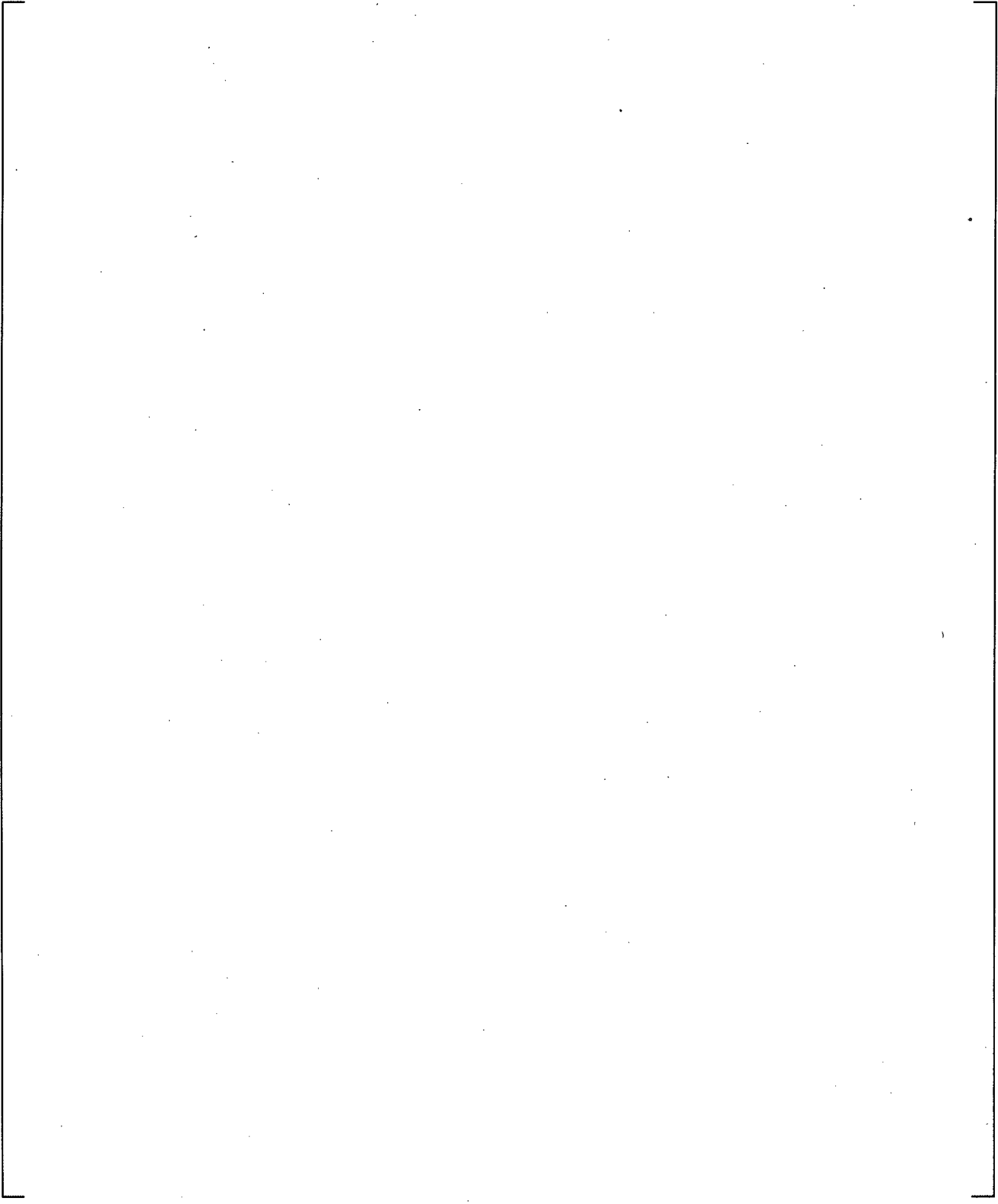


**Figure 19.3-198 WCOBRA/TRAC-TF2 Loop Model for UPTF Upper Plenum Test**

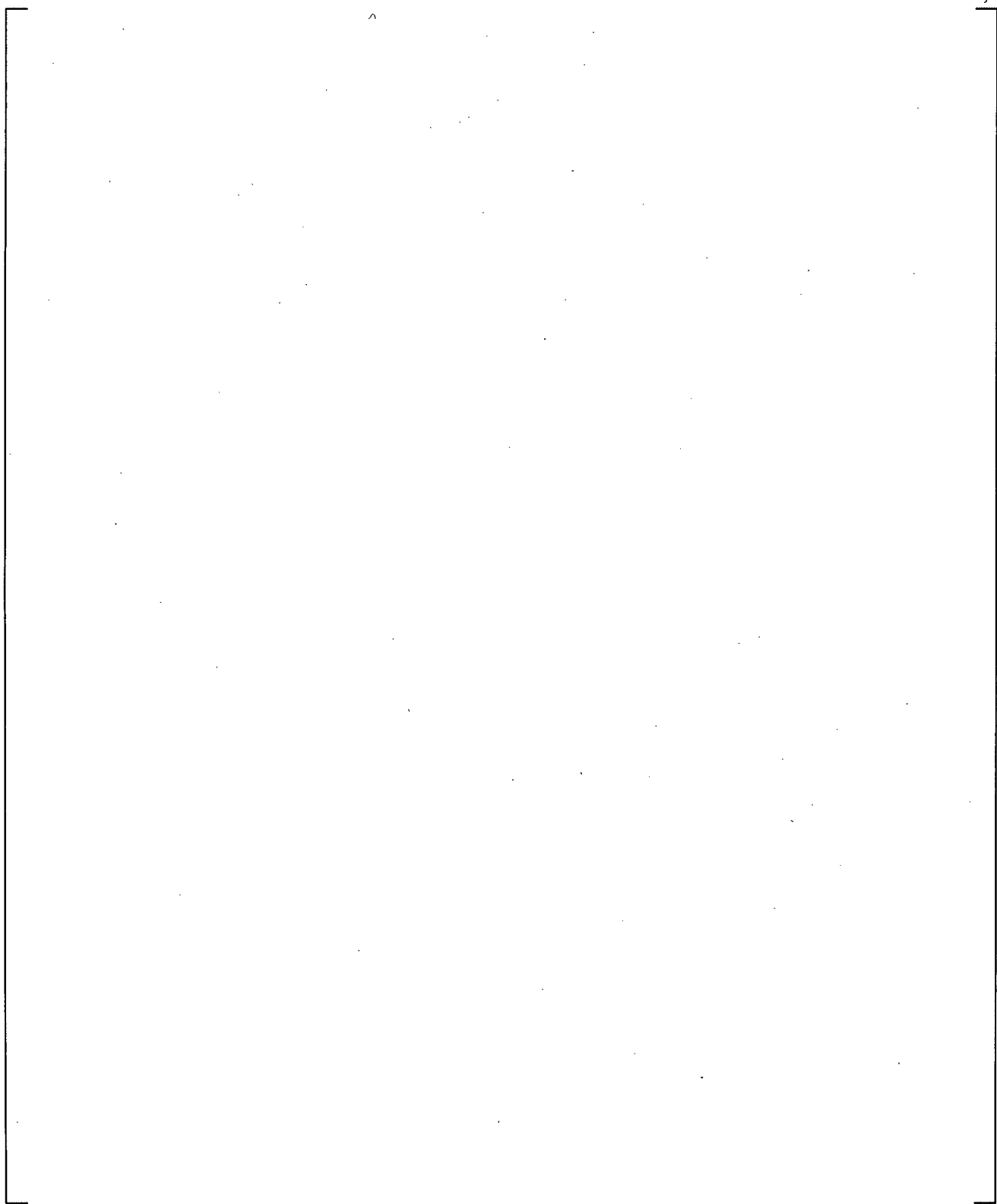


**Figure 19.3-199 Quasi-Steady State Upper Plenum Mass for Phase I of UPTF Test 29B**

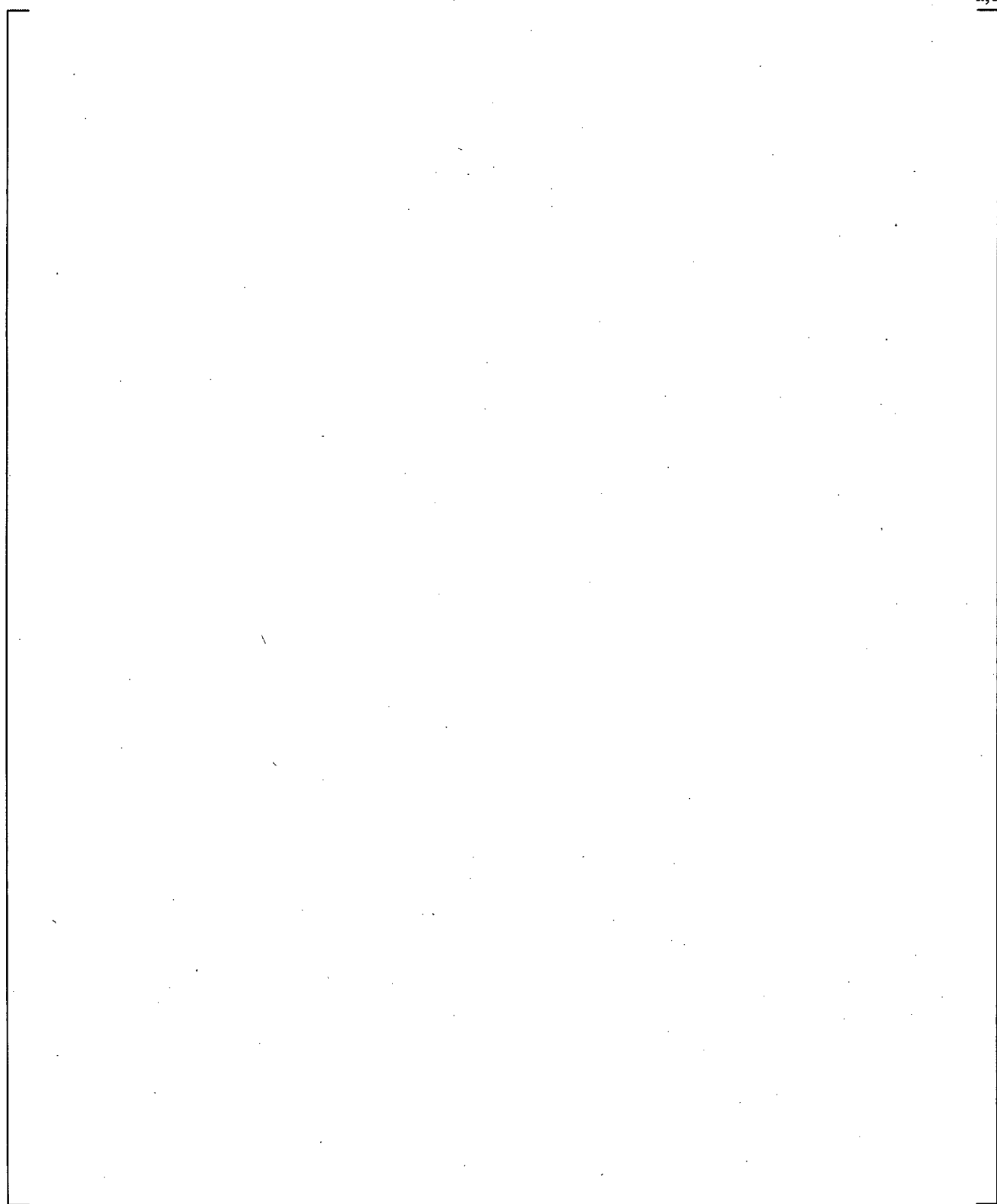


**Figure 19.3-200 Quasi-Steady State Upper Plenum Mass for Phase II of UPTF Test 29B**

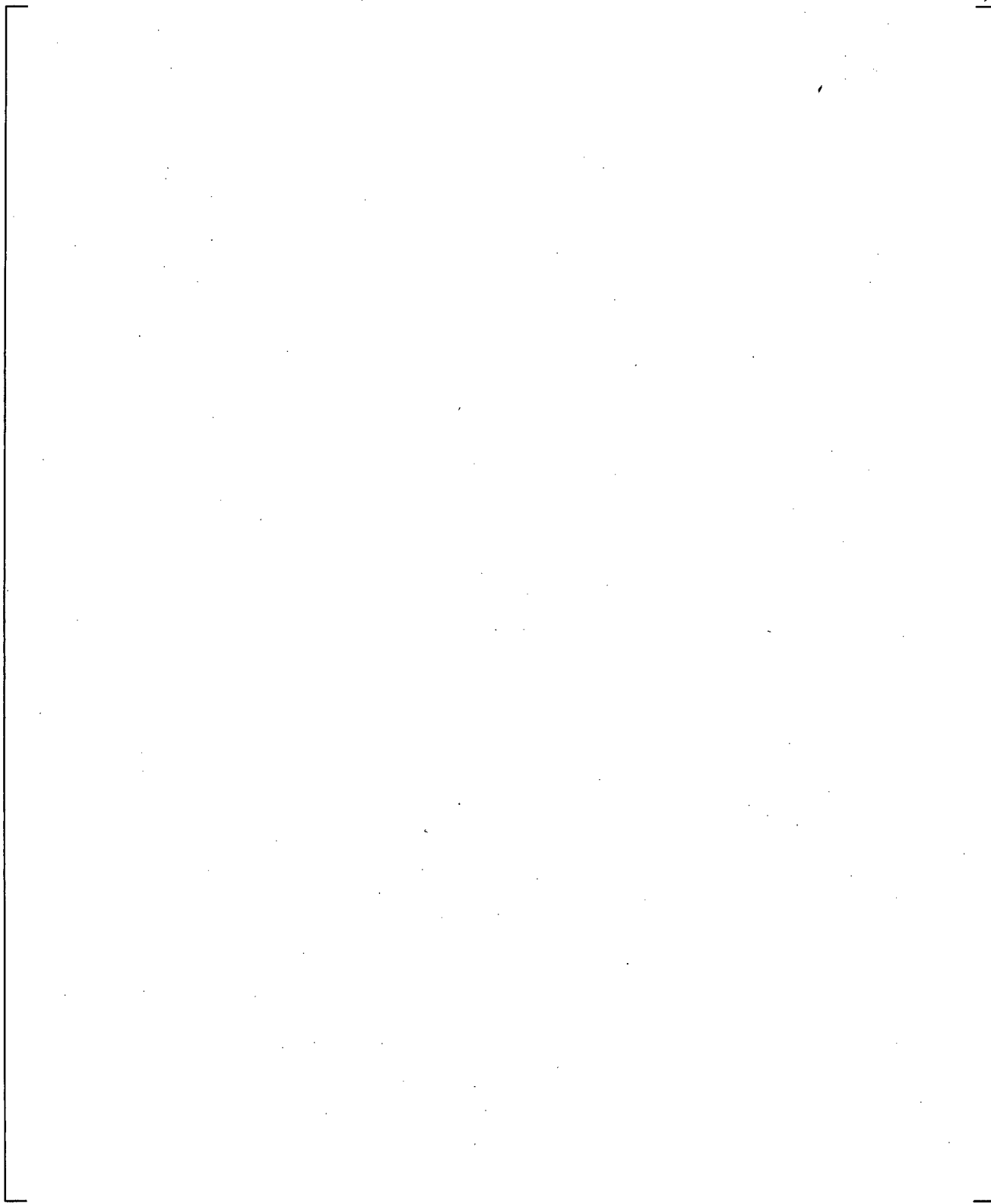


**Figure 19.3-201 Quasi-Steady State Upper Plenum Mass for Phase III of UPTF Test 29B**

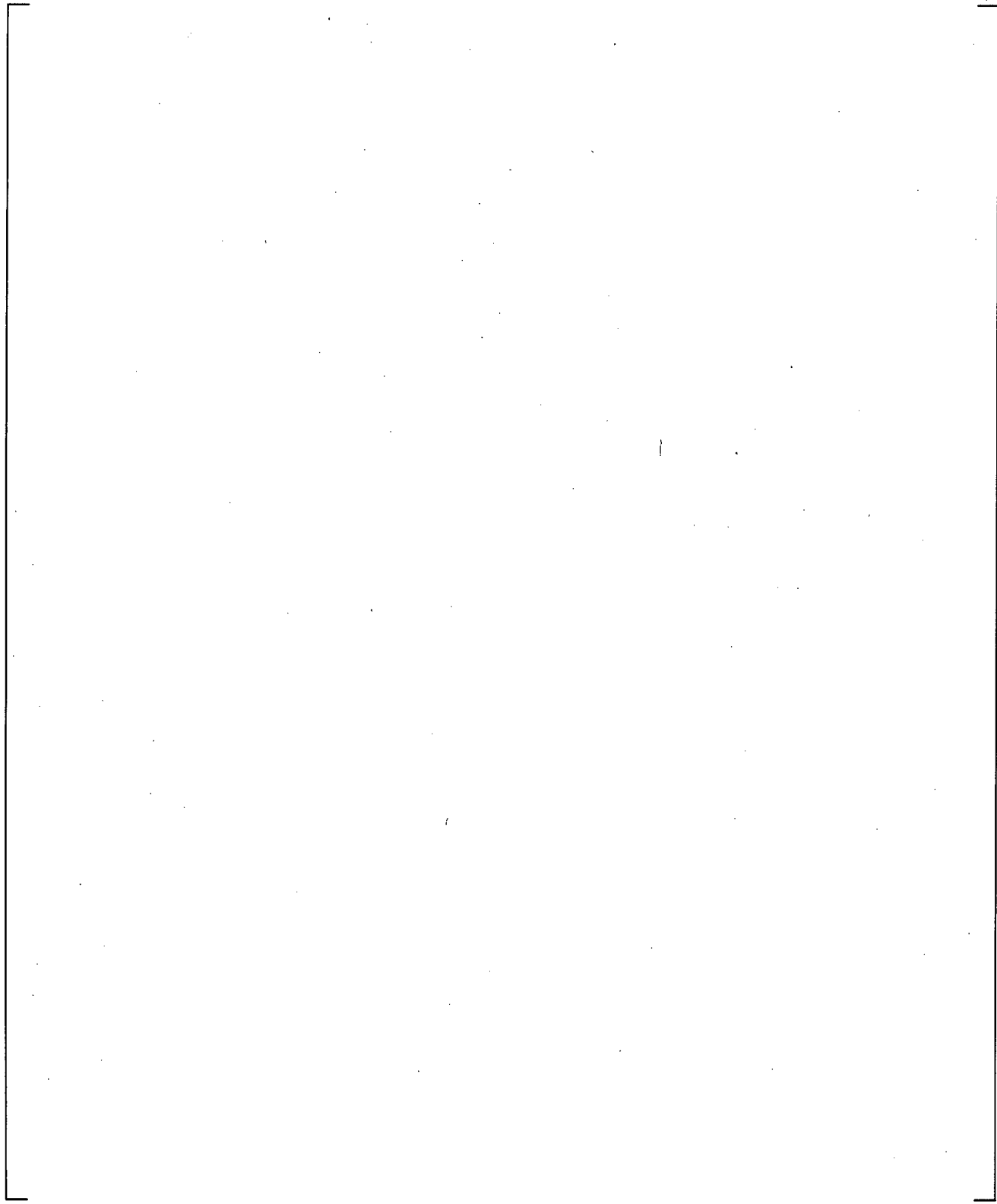


**Figure 19.3-202 Quasi-Steady State Upper Plenum Mass for Phase IV of UPTF Test 29B**

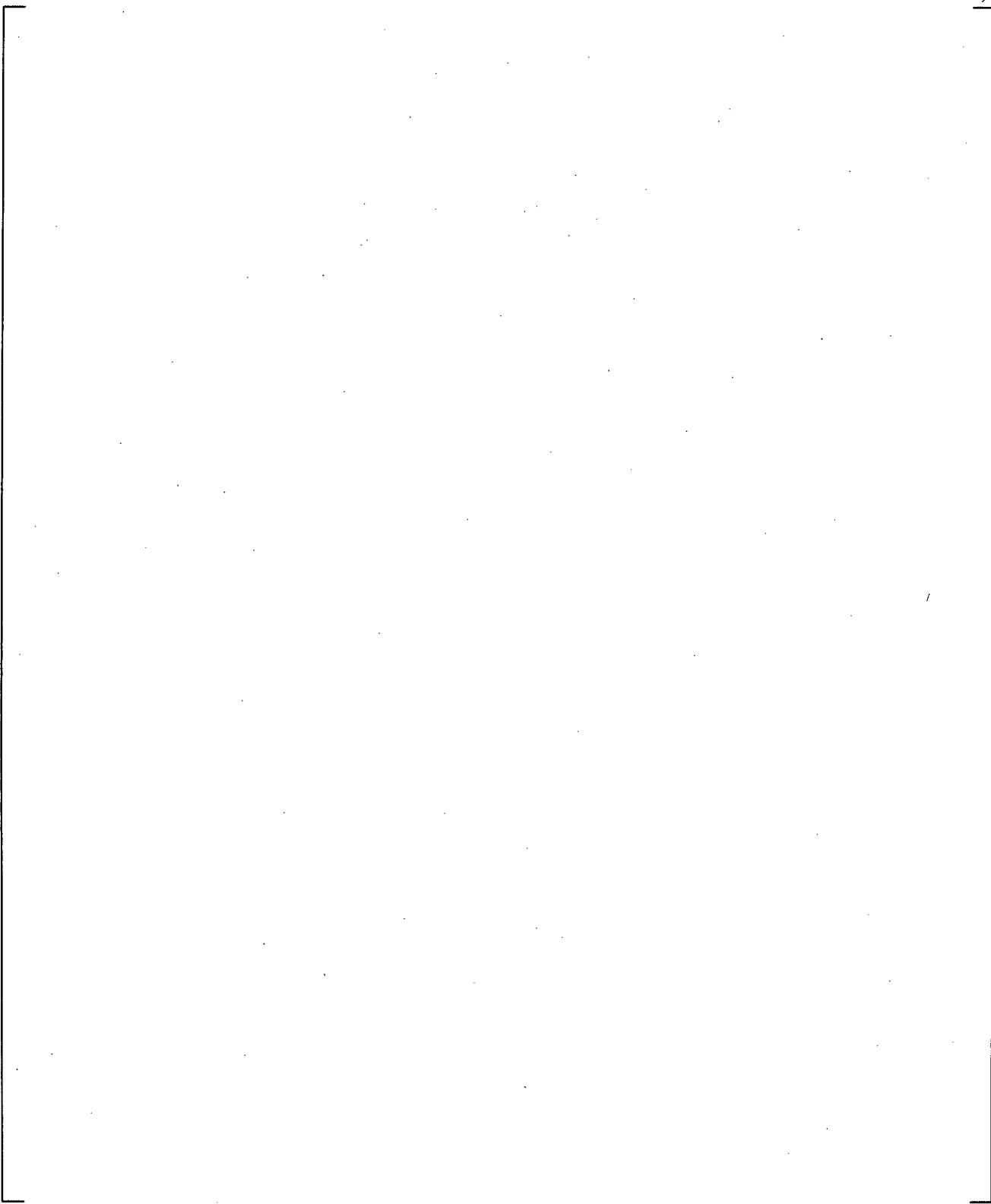


**Figure 19.3-203 Quasi-Steady State Upper Plenum Mass for Phase V of UPTF Test 29B**

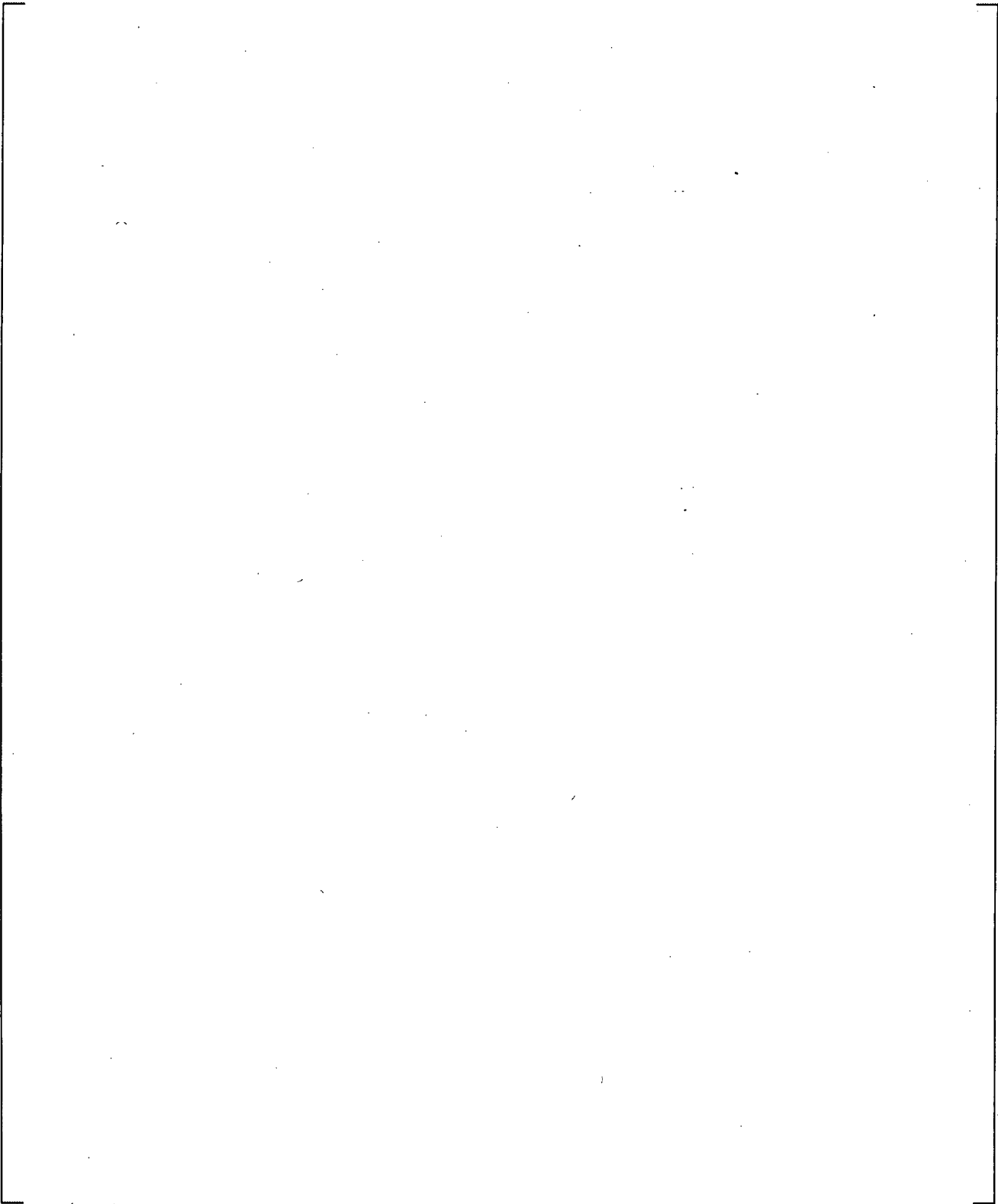


**Figure 19.3-204 Quasi-Steady State Upper Plenum Mass for Phase VI of UPTF Test 29B**

## 19.4 PERFORATED PLATE FLOODING ANALYSIS

CCFL in a perforated plate has been tested and analyzed by Hsieh et al. (1980). The tests were conducted with air/water and steam/water systems on perforated plates with different hole size and geometries. The air/water experiment was designed to investigate the effects of geometric factors on the rate of weeping. The steam/water tests investigated subcooling effects on the CCFL. To assess the capability of the WCOBRA/TRAC-TF2 on modeling the CCFL phenomenon, the air/water tests performed by Hsieh (1980) on their 15-hole perforated plate is simulated. The 15-hole plate tests were selected due to its similar geometry to a PWR fuel assembly top nozzle (or tie plate). As the steam/cold water CCFL on a perforated plate is not encountered in the LOCA transients of a typical PWR except for the UPI plant which is currently not included in the FSLOCA methodology, the steam/cold water CCFL tests reported by Hsieh (1980) was not used to assess the WCOBRA/TRAC-TF2. Furthermore, the test data on steam/water system are only limited to the boundaries of weeping and no-weeping and therefore insufficient to check the code on predicting the weeping liquid rate in the range between the 'no-weeping' and 'dumping' (all the inlet liquid falls down through the perforated plate). The obtained test data on the weeping rate in their air/water system are readily available to develop a test CCFL flooding limit which can then be checked against the applicable theoretical CCFL flooding limits based on the scaling factors developed, for example, by Hsieh (1980) among others.

Based on the available and applicable test data, first, the air/water test with a 15-hole perforated plate was simulated by WCOBRA/TRAC-TF2 using nitrogen/water to compare with the test and the CCFL curve based on the Northwestern scaling factor (Hsieh, 1980). The computed results of the nitrogen/water system are compared with the test data since the pertinent properties to CCFL of the air and nitrogen are within the appropriate range for the WCOBRA/TRAC-TF2 assessment.

[

] <sup>a,c</sup>

In Section 19.4.1, the different scaling factors used in the CCFL at a perforated plate are described. The WCOBRA/TRAC-TF2 input models for the perforated CCFL simulations are introduced in Section 19.4.2 for the nitrogen/water and high pressure and low pressure steam/water systems. The comparisons of the computed CCFL are presented and summarized in Section 19.4.3; [

] <sup>a,c</sup>.

### 19.4.1 Correlations and Scaling for CCFL in a Perforated Plate

#### Northwestern ( $H^*$ ) Scaling

Hsieh et al. (1980) developed a scaling parameter similar to the one employed by Wallis (1969) to define a non-dimensional volumetric flux, which is referred to here as Northwestern scaling,

$$H_k^* = j_k \left[ \frac{\rho_k}{g w (\rho_f - \rho_g)} \right]^{1/2} \quad (19.4-1)$$

$$w = d_h^{1-\alpha} L^\alpha \quad (19.4-2)$$

$$\alpha = \tanh(r \cdot k \cdot d_h) \quad (19.4-3)$$

where:

- $k$  = g, f for gas and liquid phase, respectively
- $d_h$  = the hole diameter
- $r$  =  $A_h/A_T$  (hole area divided by total plate area) and a wave number defined by:

$$k = \frac{2\pi}{t_p} \quad (19.4-4)$$

in which  $t_p$  is the thickness of the plate.

With these dimensionless volumetric fluxes, the test data for CCFL in the perforated plates was correlated by Hsieh et al. (1980) to yield:

$$H_g^{*1/2} + H_f^{*1/2} = C \quad (19.4-5a)$$

where:

$$C = \min \begin{cases} 1.07 + 4.32 \times 10^{-3} L^* \\ 2.0 \end{cases} \quad (19.4-5b)$$

$$L^* = n \pi d_h \left[ \frac{g(\rho_f - \rho_g)}{\sigma} \right]^{1/2} \quad (19.4-5c)$$

and  $n$  is the number of holes. One way to examine Northwestern scaling is to compare it to other scaling methods as discussed below.

**Wallis (J\*) Scaling**

$$j_k^* = j_k \left[ \frac{\rho_k}{g d_h (\rho_f - \rho_g)} \right]^{1/2} \quad (19.4-6)$$

**Kutateladze (K\*) Scaling**

$$K_k^* = j_k \left[ \frac{\rho_k}{g \left[ \frac{\sigma}{g(\rho_f - \rho_g)} \right]^{1/2} (\rho_f - \rho_g)} \right]^{1/2} = j_k \left[ \frac{\rho_k^2}{g\sigma(\rho_f - \rho_g)} \right]^{1/4} \quad (19.4-7)$$

or

$$K_k^* = j_k^* (D^*)^{1/2}$$

where use has been made of the dimensionless diameter,

$$D^* = d_h \left[ \frac{g(\rho_f - \rho_g)}{\sigma} \right]^{1/2} \quad (19.4-8)$$

**Westinghouse (L\*) Scaling**

Takeuchi and Young (1983) proposed a generalized scaling approach which combined  $j_k^*$  and  $K_k^*$  scaling as follows,

$$l_g^* \equiv j_g^* (D^*/K^2)^{1/2} \quad (19.4-9)$$

where  $K$  is the critical Kutateladze number which approaches  $K_0 \sqrt{D^*}$  at small diameters, and  $K_1$  at large diameters, respectively. That is,

$$l_g^* \rightarrow j_g^* / K_0 \text{ as } D^* \rightarrow 0 \quad (19.4-10)$$

$$l_g^* \rightarrow j_g^* / K_1 \text{ as } D^* \rightarrow \infty$$

where  $K_0 = 0.645$  and  $K_1 = 3.2$ . Similar relationships hold for the liquid phase.

For a given plate thickness ( $t$ ), the Northwestern scaling approaches the following limits:

For  $d_h \rightarrow 0$ , it approaches the Wallis number,

$$H_k^* \rightarrow J_k^*, \quad k = g, f \quad (19.4-11)$$

For  $d_h \rightarrow \infty$ , on the other hand,

$$H_k^* \rightarrow K_k^*, \quad k = g, f \quad (19.4-12)$$

#### 19.4.2 WCOBRA/TRAC-TF2 Model

For WCOBRA/TRAC-TF2 analyses of the test data, the test case with the 15-hole plate that approximates the typical dimensions in a PWR or LOFT fuel assembly top nozzle (tie plate) is selected. The 15-hole plate has the following dimensions:

$$\begin{aligned} d_h &= 0.413 \text{ in} \\ t_p &= 0.787 \text{ in} \\ A_T &= 4.754 \text{ in}^2 \\ A_h &= 2.013 \text{ in}^2 \\ r = A_h/A_T &= 0.4260 \end{aligned}$$

With these dimensions, the  $C$  in Equation (19.4-5) is calculated to be 1.9 and 2.0 using Equations (19.4-5b) and (19.4-5c) for the nitrogen/water and steam/water systems, respectively. The WCOBRA/TRAC-TF2 model used to predict the CCFL for the perforated plate is shown in Figure 19.4-1. [

] <sup>a,c</sup>

For steam/water or nitrogen/water system, the computational experiment is performed in the following manner. [ <sup>a,c</sup>

[

] <sup>a,c</sup>

[                      ] <sup>a,c</sup>

] <sup>a,c</sup>

### 19.4.3 WCOBRA/TRAC-TF2 Simulation

The predicted nitrogen/water system CCFL by WCOBRA/TRAC-TF2 is compared with the air/water test data in Figure 19.4-2, covering the range of liquid flow rate tested in the experiment. The nitrogen/water and air/water systems at the room temperature and pressure are considered to be comparable with regard to the concerns of the CCFL phenomena. The Northwestern flooding limit is also shown in the comparison in Figure 19.4-2 [

] <sup>a,c</sup>

Figures 19.4-3 and 19.4-4 show the predicted steam/water system flooding curve under the system [

] <sup>a,c</sup>

For a higher [   
 ] <sup>a,c</sup>

[

]a,c

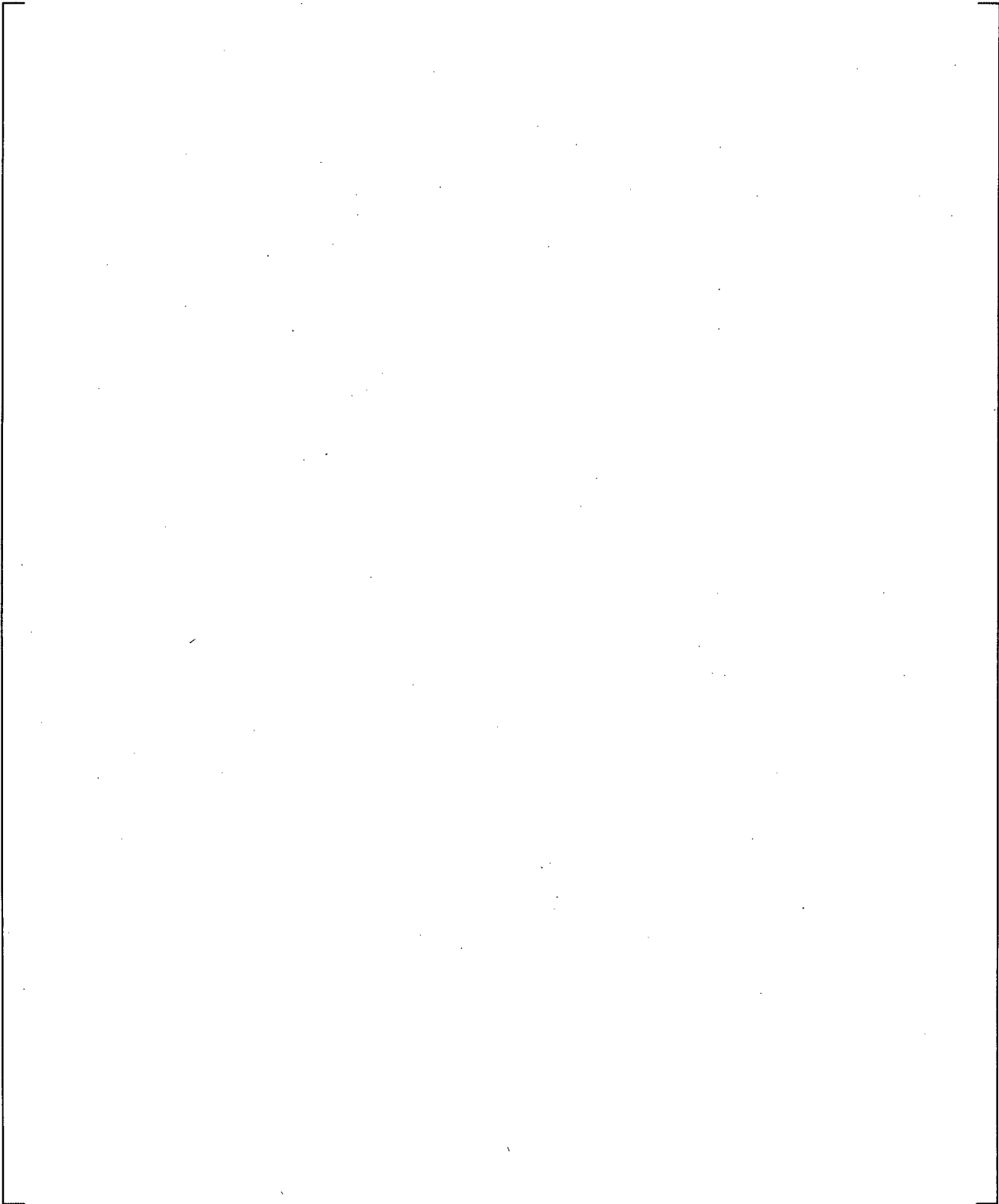


**Figure 19.4-1 Flooding Model for a Perforated Plate**

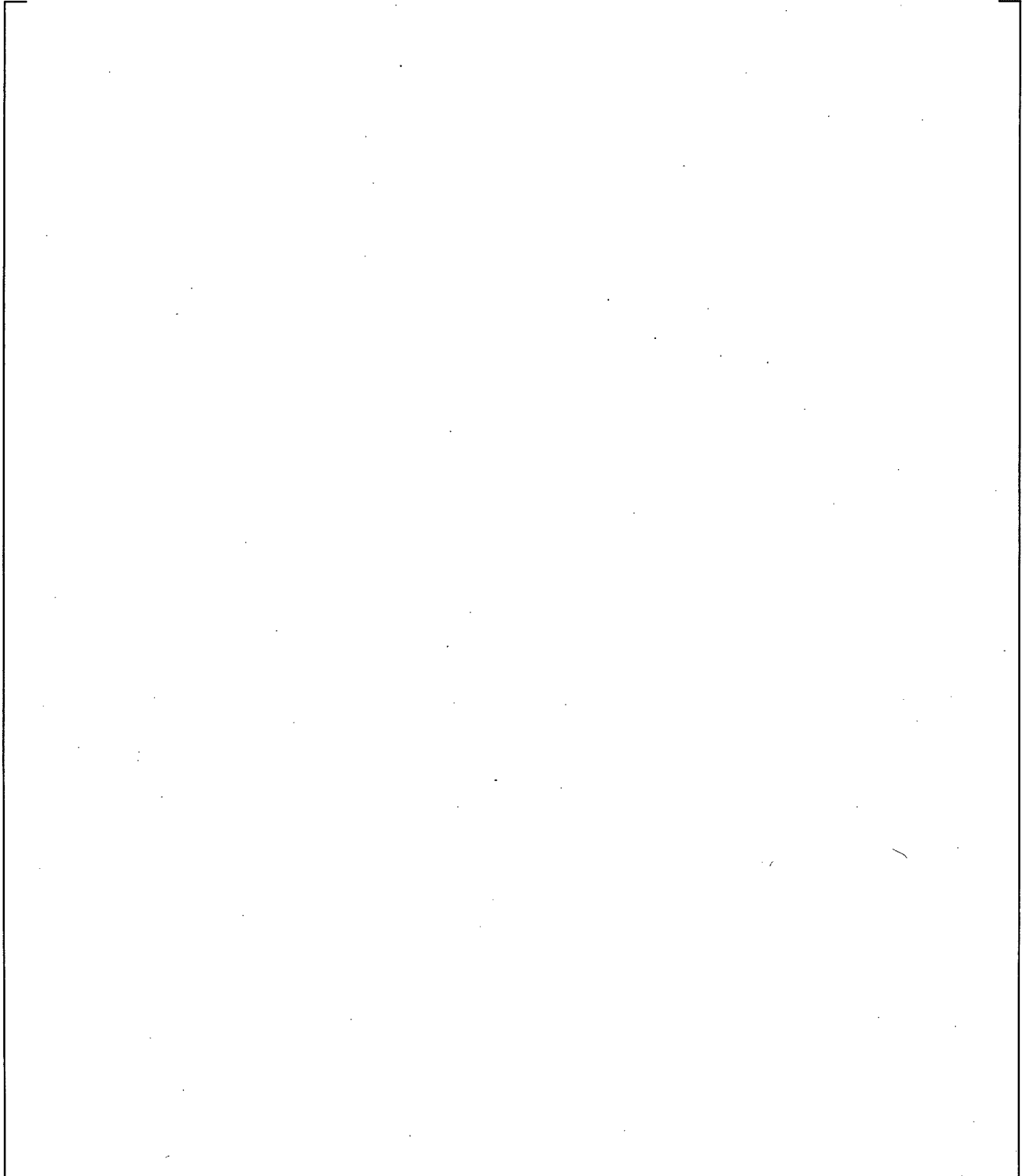


**Figure 19.4-2** Flooding Velocities for the Nitrogen/Water System at [ ]<sup>a,c</sup>  
Compared with the Air/Water Test (Hsieh, 1980) and Northwestern Flooding  
Limit

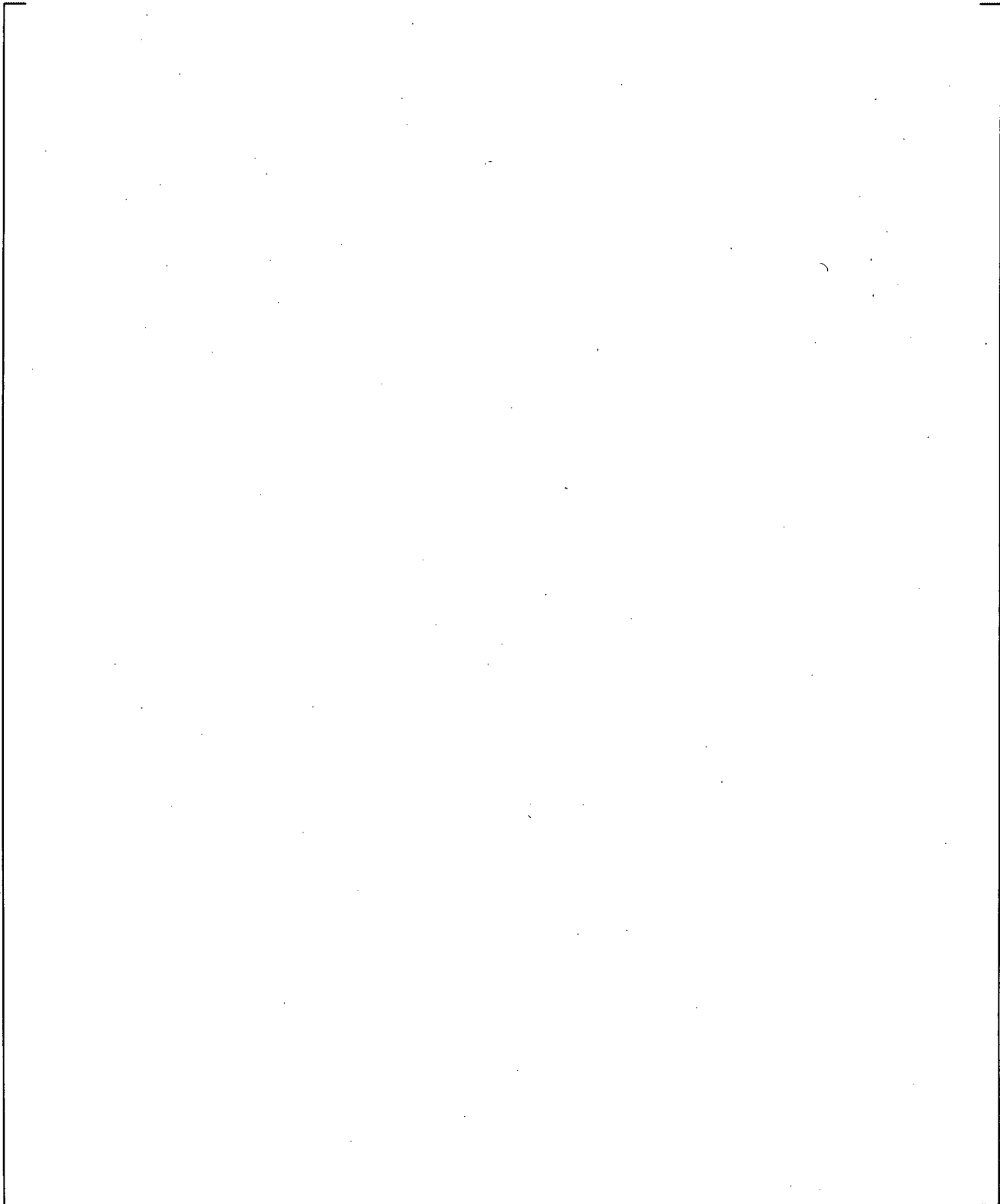


**Figure 19.4-3** Flooding Velocities for Saturated Liquid and Vapor at [ ]<sup>a,c</sup> Compared with Northwestern Flooding Limit (WCOBRA/TRAC-TF2)

a,c

**Figure 19.4-4** Flooding Velocities for Saturated Liquid and Vapor at [ ]<sup>a,c</sup> Compared with Northwestern Flooding Limit (WCOBRA/TRAC-TF2)

a,c

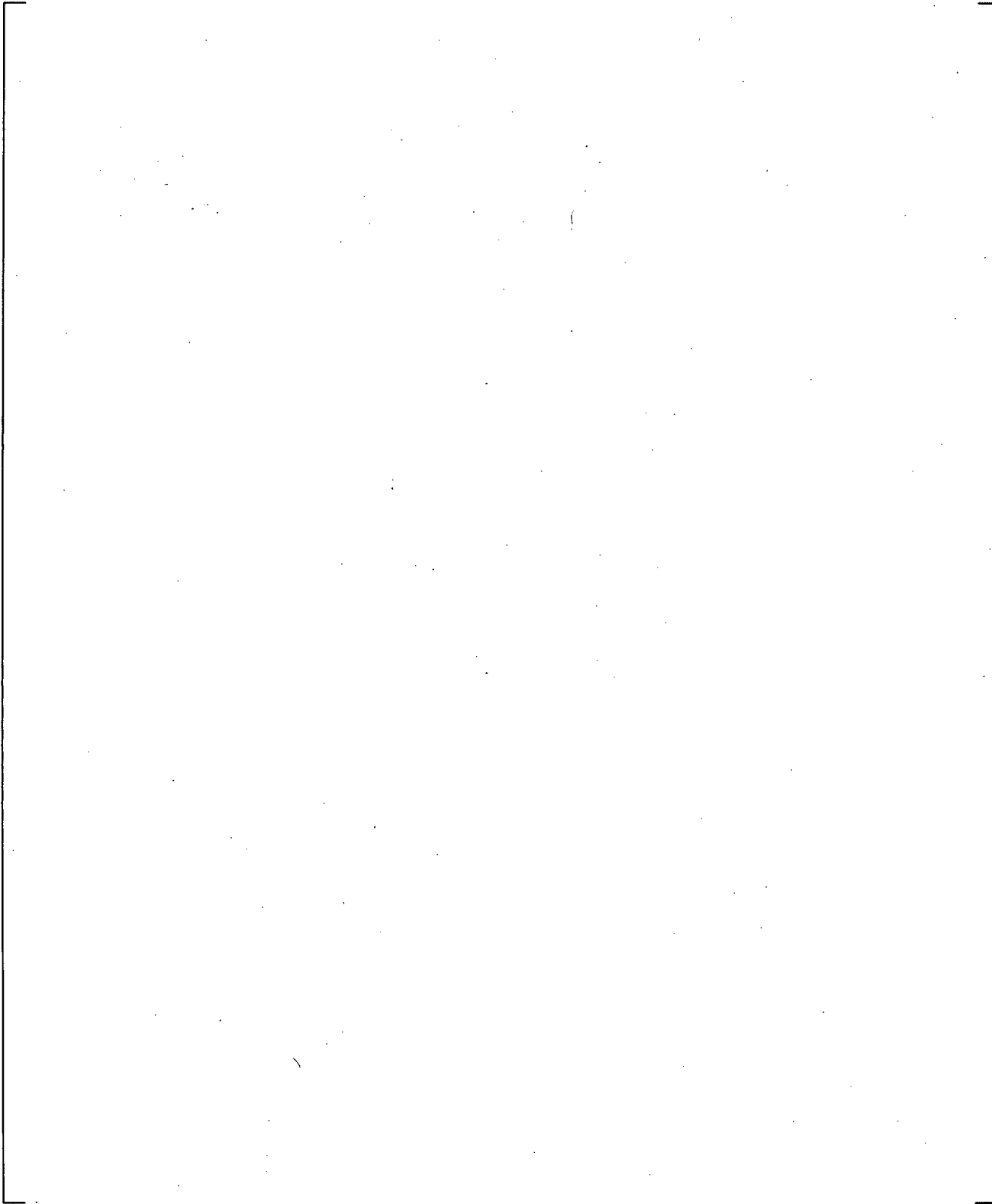
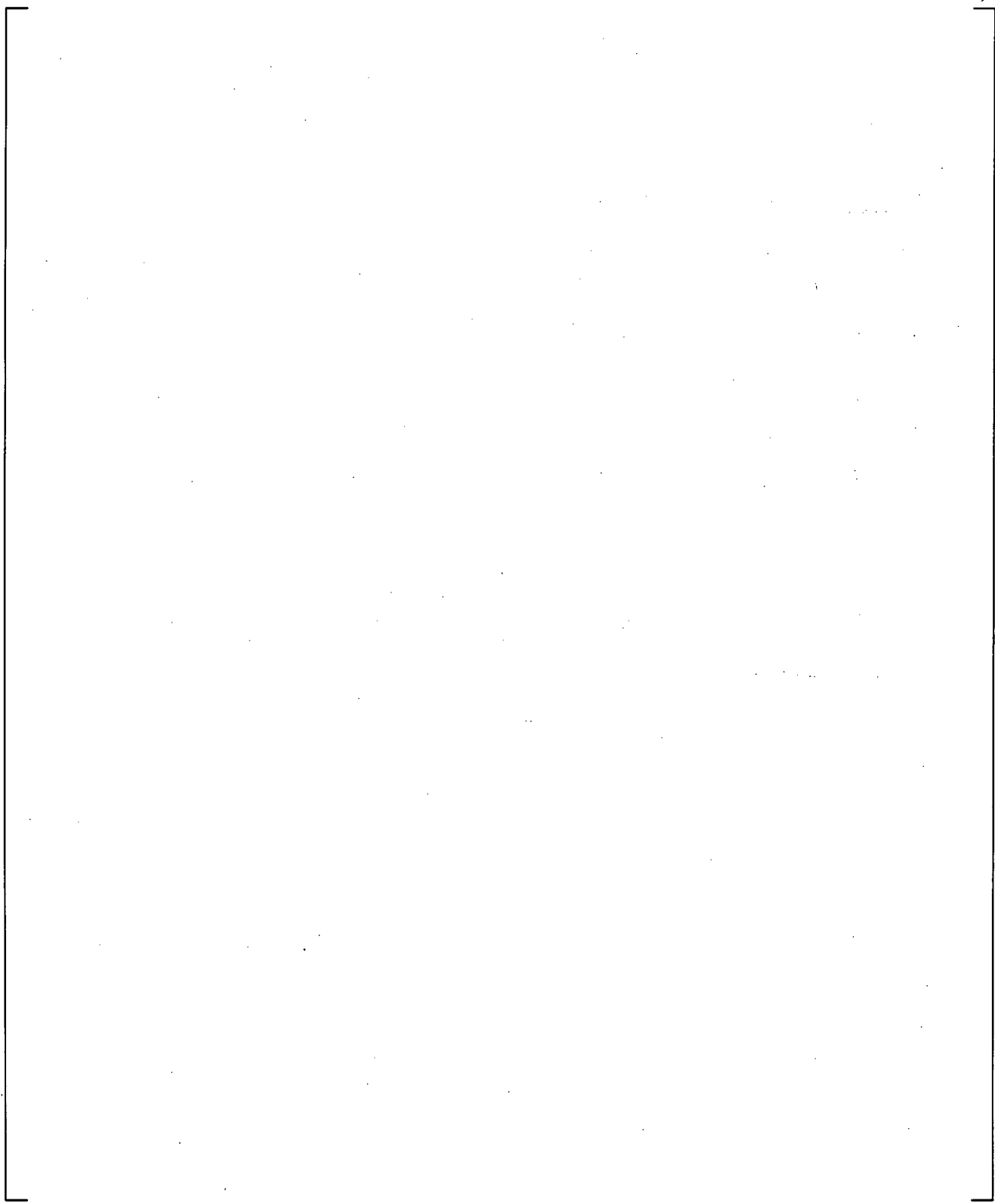
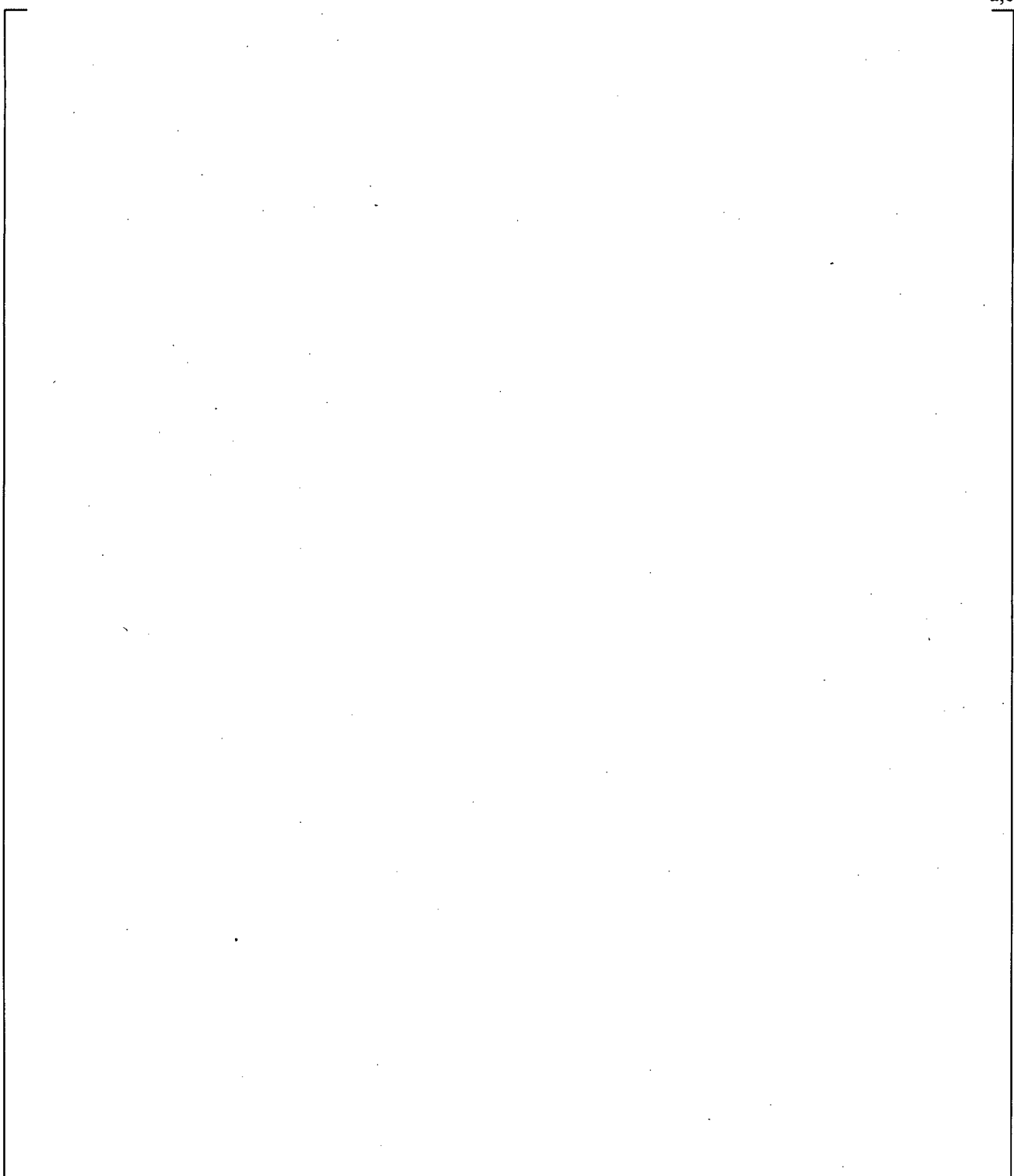


Figure 19.4-5 Liquid Mass Flow Rates through Perforated Plate at [  
(WCOBRA/TRAC-TF2)

]a,c



**Figure 19.4-6 Vapor/Liquid Mass Flow Rates through Perforated Plate at [ ]<sup>a,c</sup> (WCOBRA/TRAC-TF2)**



**Figure 19.4-7** Liquid Mass Flow rates through Perforated Plate at [  
WCOBRA/TRAC-TF2)

]a,c

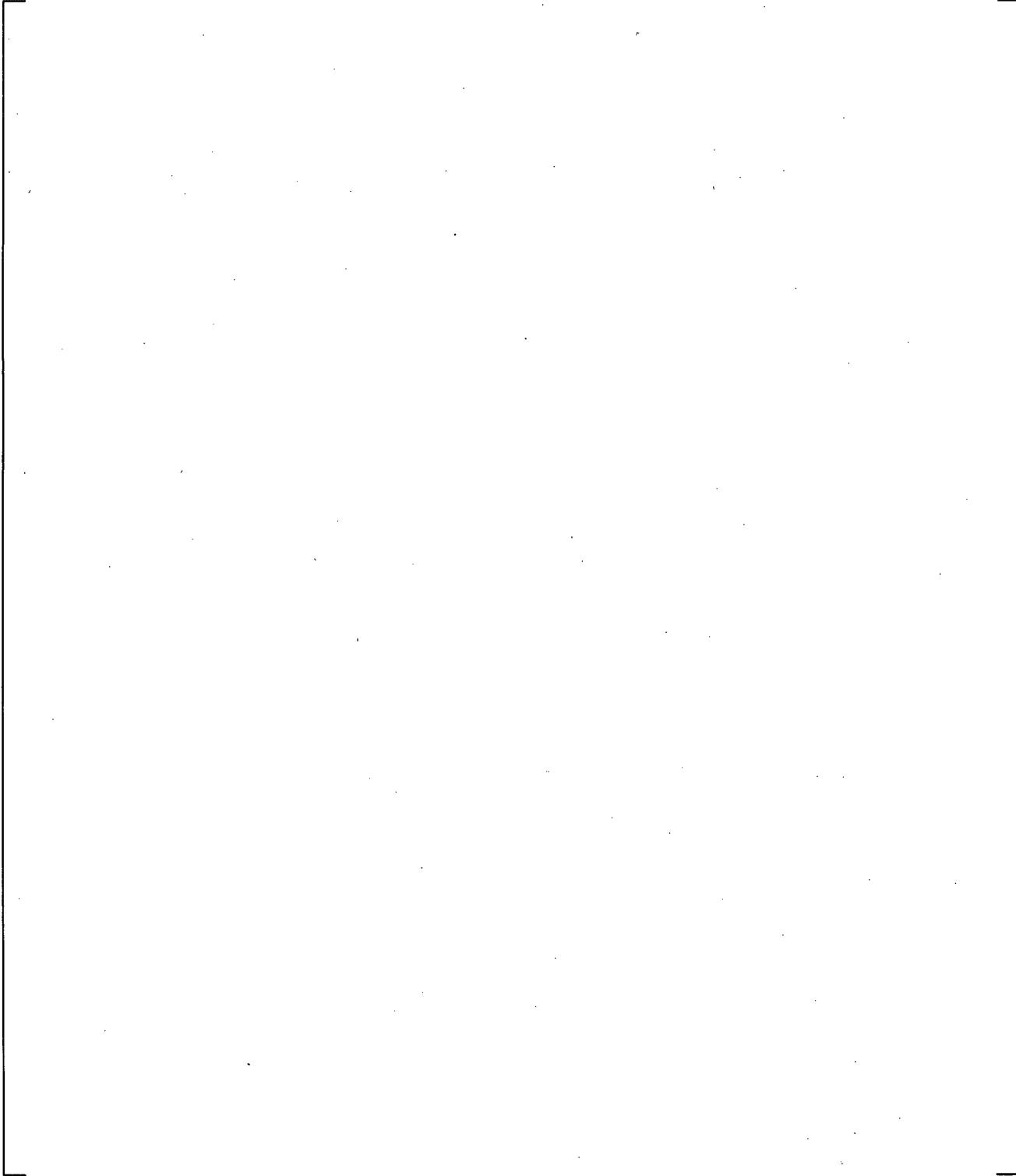


**Figure 19.4-8 Vapor/Liquid Mass Flow rates through Perforated Plate at [ ]<sup>a,c</sup> (WCOBRA/TRAC-TF2)**

## 19.5 FULL-LENGTH EMERGENCY COOLING/CORE HEAT TRANSFER

The correlation used to determine the entrainment rate at a quench front is described in Section 5.6. The model is consistent with the work of (Kataoka and Ishii, 1983) and assumes the entrainment is due to vapor bubbling through a pool of liquid.

The reflood test simulations provide a means of examining the performance of the entrainment model for bottom reflood. Mass balances were calculated from the test data so that carryover fraction and mass retention in the test bundle could be estimated. This section compares the WCOBRA/TRAC-TF2 predictions of carryover fraction, total bundle mass, steam exit flow, and liquid outflow to estimates derived from the test data. The comparisons provide a means of assessing the bottom reflood entrainment model.

### 19.5.1 FLECHT Test Facility

First, it is important to describe the data collection methods used to estimate carryover which are not discussed in Section 14 for the FLECHT facility. Figure 19.5-1 shows a schematic of the FLECHT facility, identifying mass collection and flow rate measurements. These measurements were used to determine the mass inventory in the bundle, and the carryover fraction. Each of the FLECHT facilities, FLECHT-SEASET, FLECHT Low Flooding Rate, and FLECHT Top Skewed Power, used the same type of collection system. The difference between the facilities was the design of the test bundle itself, and in the number of DP cells used in the test bundle.

Liquid was injected into the test bundle from an accumulator. The mass lost from this accumulator was reported in the test data and used as a check on the overall mass balance. Liquid leaving the accumulator was regulated, and the flow rate into the bundle was measured by a turbine meter. DP cells in the test bundle were used to estimate the bundle mass. The measurements were corrected for frictional effects.

The steam/droplet mixture leaving the heated bundle entered an upper plenum. In this plenum, the steam and most droplets were separated. The liquid went to a "Carryover Tank," where the total mass and its rate of change were determined from a DP cell.

After leaving the upper plenum, the steam went through another separator to remove any remaining droplets. The liquid removed at this second removal point went into a "Steam Separator Tank" and was measured. In general, this amount of liquid was small compared to the mass retained in the Carryover Tank.

Finally steam, now assumed to be "dry," was vented to the atmosphere through an exhaust orifice. The exhaust orifice provided the flow rate of steam from the facility. The data evaluation provided both the dry steam effluence rate, and the total mass of steam that exited the facility.

The instantaneous carryover fraction (CO) is defined as:

$$CO(t) = \frac{\dot{m}_{out}(t)}{\dot{m}_{inj}(t)} \quad (19.5-1)$$

where  $\dot{m}_{out}(t)$  and  $\dot{m}_{inj}(t)$  are the flow rate out of and into the bundle, respectively. Note that for forced injection reflood tests such as FLECHT SEASET, the flow rate into the bundle is essentially constant.

The instrumentation in the facility allowed the carryover fraction to be determined in two different ways; from mass stored in the bundle and from mass flows exiting the bundle. The following forms were calculated:

1. From mass stored in the test bundle,

$$CO_1 = 1 - \frac{m_{rs}(t)}{\int \dot{m}_{inj}(t) dt} \quad (19.5-2)$$

2. From the (instantaneous) rate of storage in the test bundle,

$$CO_2 = 1 - \frac{\dot{m}_{rs}(t)}{\dot{m}_{inj}(t)} \quad (19.5-3)$$

3. From the total mass that exited the test section and was stored in the separator tanks or exited as dry steam,

$$CO_3 = \frac{m_{CO}(t) + m_{ss}(t) + \int \dot{m}_{steam}(t) dt}{\int \dot{m}_{inj}(t) dt} \quad (19.5-4)$$

4. From the rate of change of mass in the separator tanks and the exhaust orifice flow rate,

$$CO_4 = \frac{\dot{m}_{CO}(t) + \dot{m}_{ss}(t) + \dot{m}_{steam}(t)}{\dot{m}_{inj}(t)} \quad (19.5-5)$$

(Nomenclature is indicated in Figure 19.5-1.)

The carryover fractions  $CO_1$  and  $CO_3$  are essentially the instantaneous carryover fraction integrated over time period "t" and then averaged over that same time period (this is true for the FLECHT tests, since the tests are at a constant flooding rate), while  $CO_2$  and  $CO_4$  are based entirely on instantaneous measurements. Both instantaneous and averaged forms show the amount of carryover. [

J<sup>a,c</sup>

The carryover fraction and bundle mass were calculated using WCOBRA/TRAC-TF2 predictions of several forced reflood tests. The carryover fraction for the WCOBRA/TRAC-TF2 results is based on the total integrated vapor mass flow (FGM), continuous liquid mass flow (FLM), and entrained liquid mass

flow (FEM) entering and leaving the bundle. (Recall from Figures 15.6.1-2, 15.6.2-2 and 15.6.3-2, the channels representing the bundle are Channels 2 and 3, and there are a total of [ ]<sup>a,c</sup> cells in the channels of the bundle region.) Since subcooled liquid was injected for all the tests, the inlet mass flow is taken to be only the liquid mass flow. So, the /TRAC-TF2 predictions are calculated as:

$$\left[ \int \dots \right]^{a,c} \quad (19.5-6)$$

The carryover fraction thus calculated by Equation 19.5-6 is of integral form. The carryover fraction for the prediction  $CO_{WCT}$ , is equivalent to the  $CO_1$  and  $CO_3$  definitions in the data evaluation, since in the calculation there is no "lost mass" as there can be in the experiment due to measurement inaccuracy. This form for  $CO_{WCT}$  was chosen, because it provides a more clear comparison with the data. Instantaneous values are too oscillatory to provide a clear indication of the trends.

### 19.5.2 WCOBRA/TRAC-TF2 Simulation

The tests presented here are FLECHT SEASET Tests 31805, 31701, and 31203; FLECHT Low Flooding Rate Tests 04641 and 05029; and, FLECHT Top Skewed Tests 15305, 13609, and 13812. Figures 19.5-2 through 19.5-9 show comparisons of predicted and measured carryover fraction. The most appropriate comparison to make in these figures is between the predicted carryover fraction and  $CO_1$ . [

] <sup>a,c</sup>

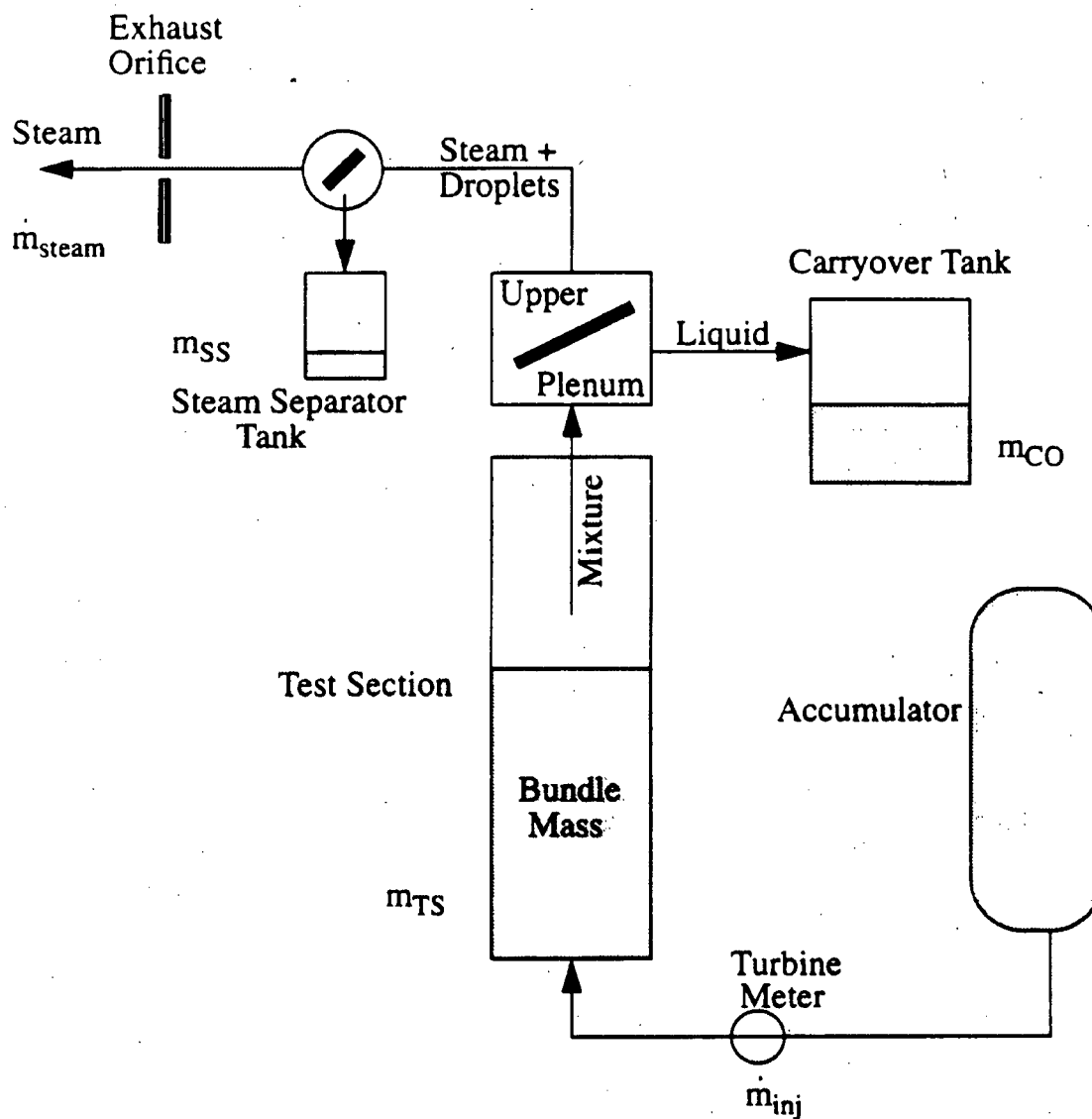
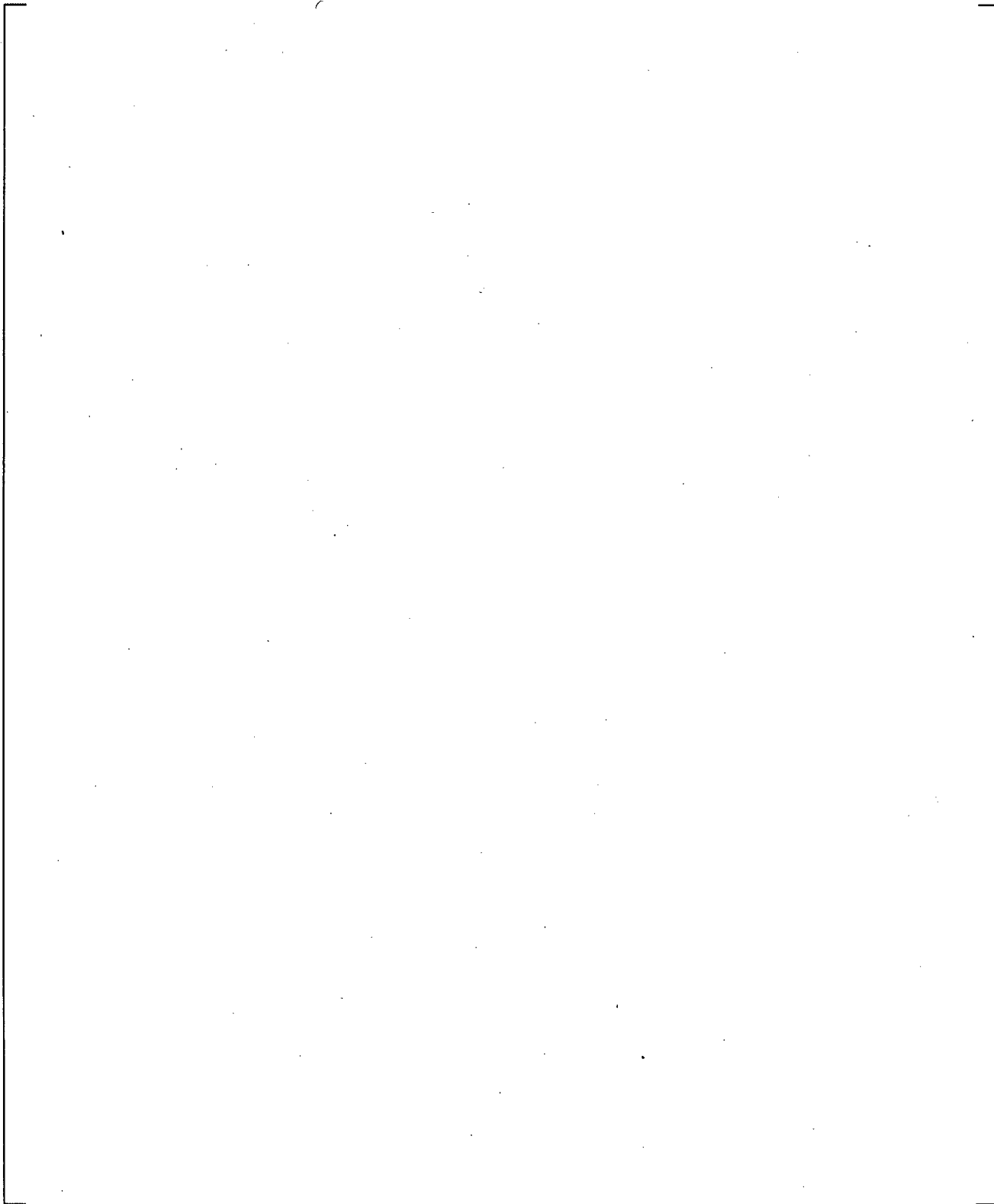
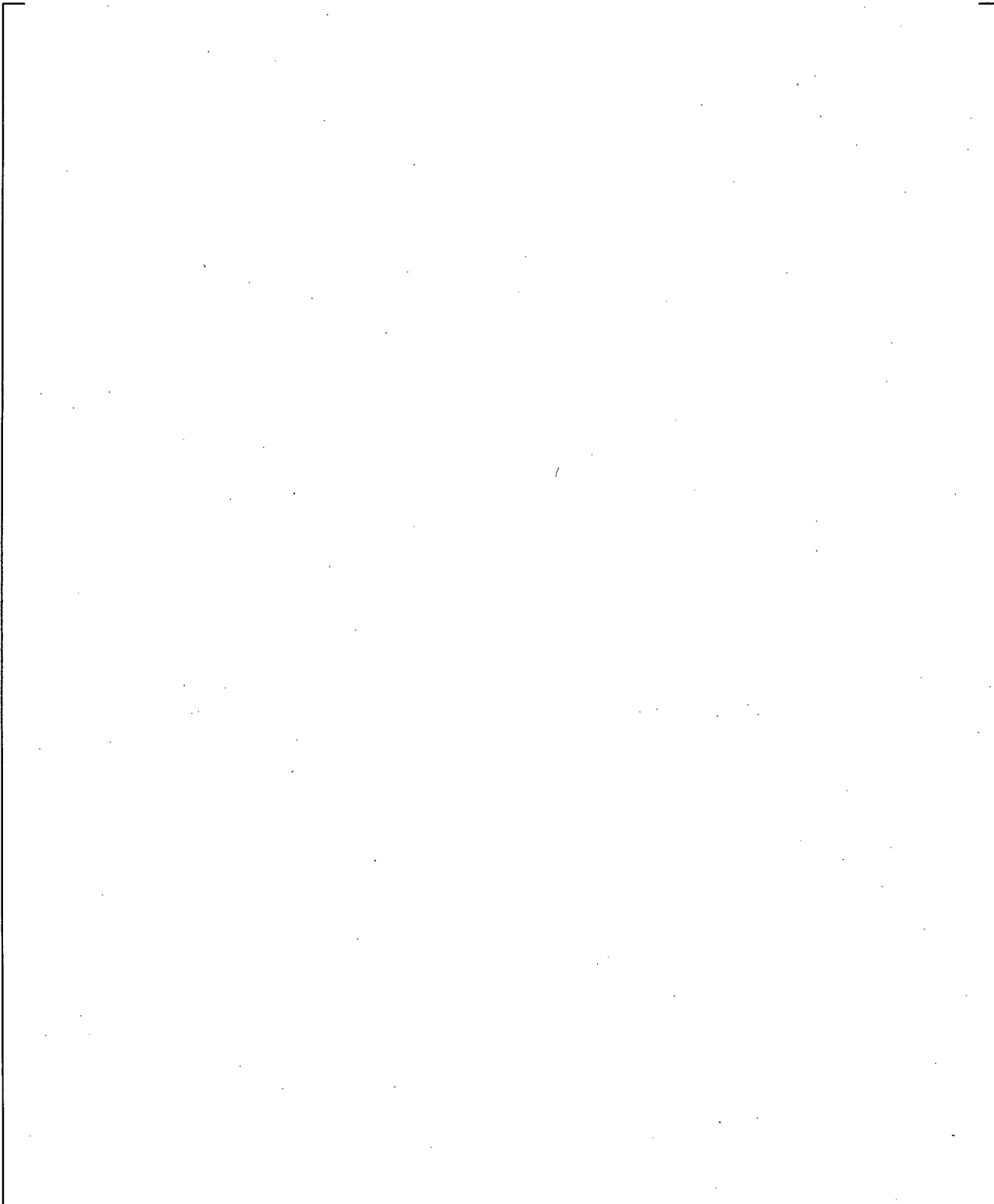


Figure 19.5-1 Mass Inventory Measurements in the FLECHT Facilities



**Figure 19.5-2 Predicted and Measured Carryover Fraction, FLECHT-SEASET Test 31805**



**Figure 19.5-3 Predicted and Measured Carryover Fraction, FLECHT-SEASET Test 31701**

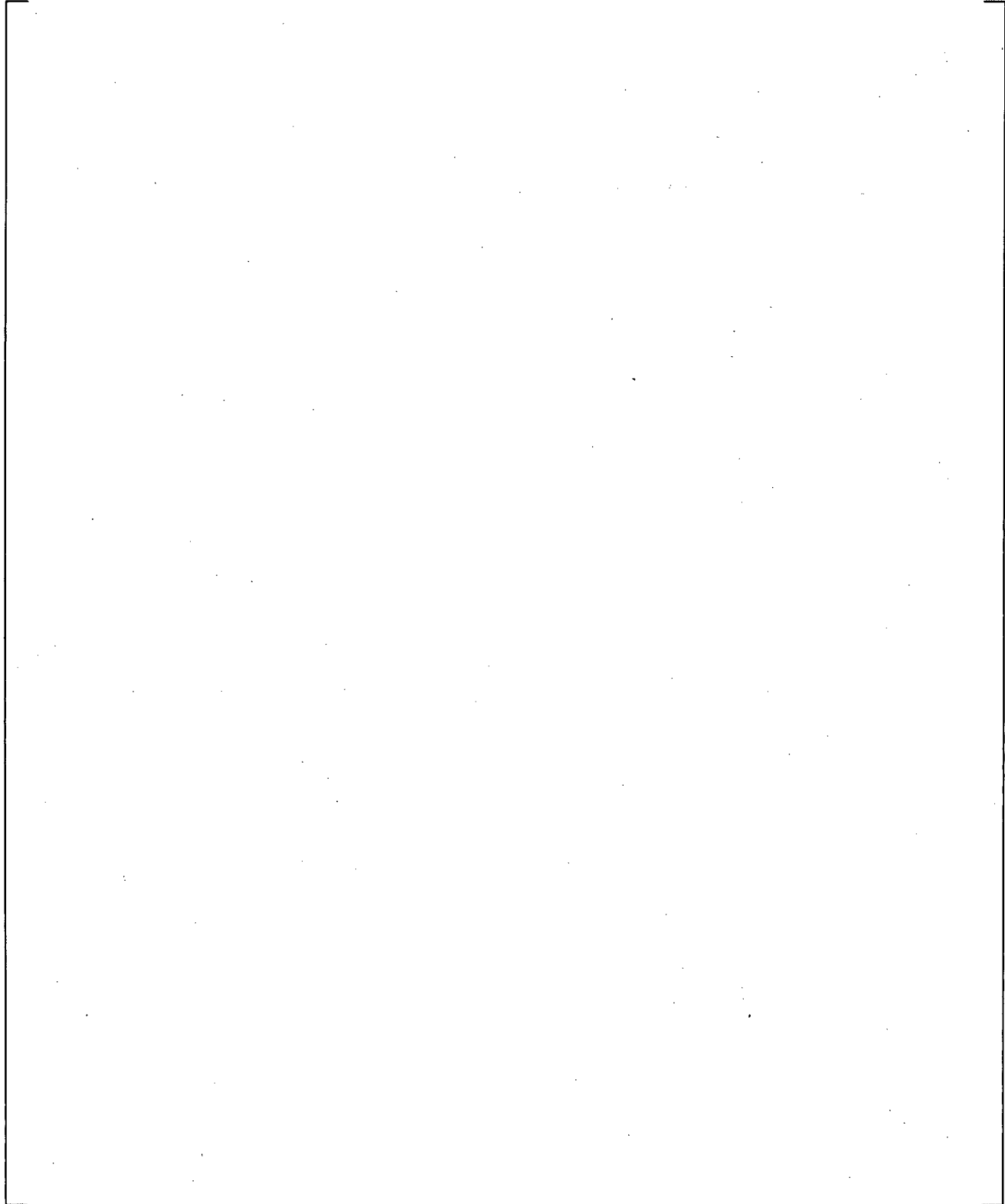


**Figure 19.5-4 Predicted and Measured Carryover Fraction, FLECHT-SEASET Test 31203**

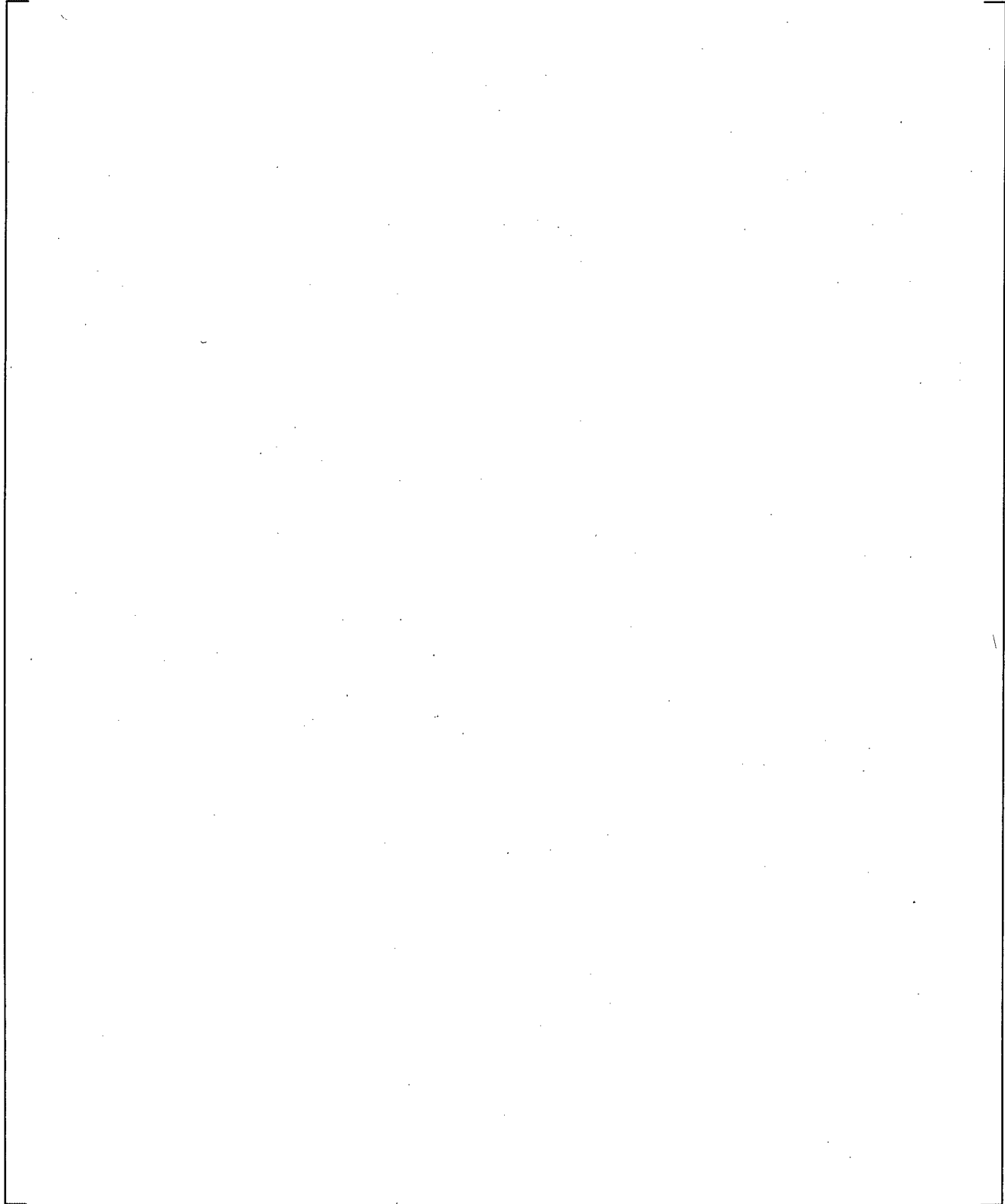


**Figure 19.5-5 Predicted and Measured Carryover Fraction, FLECHT Test 04641**

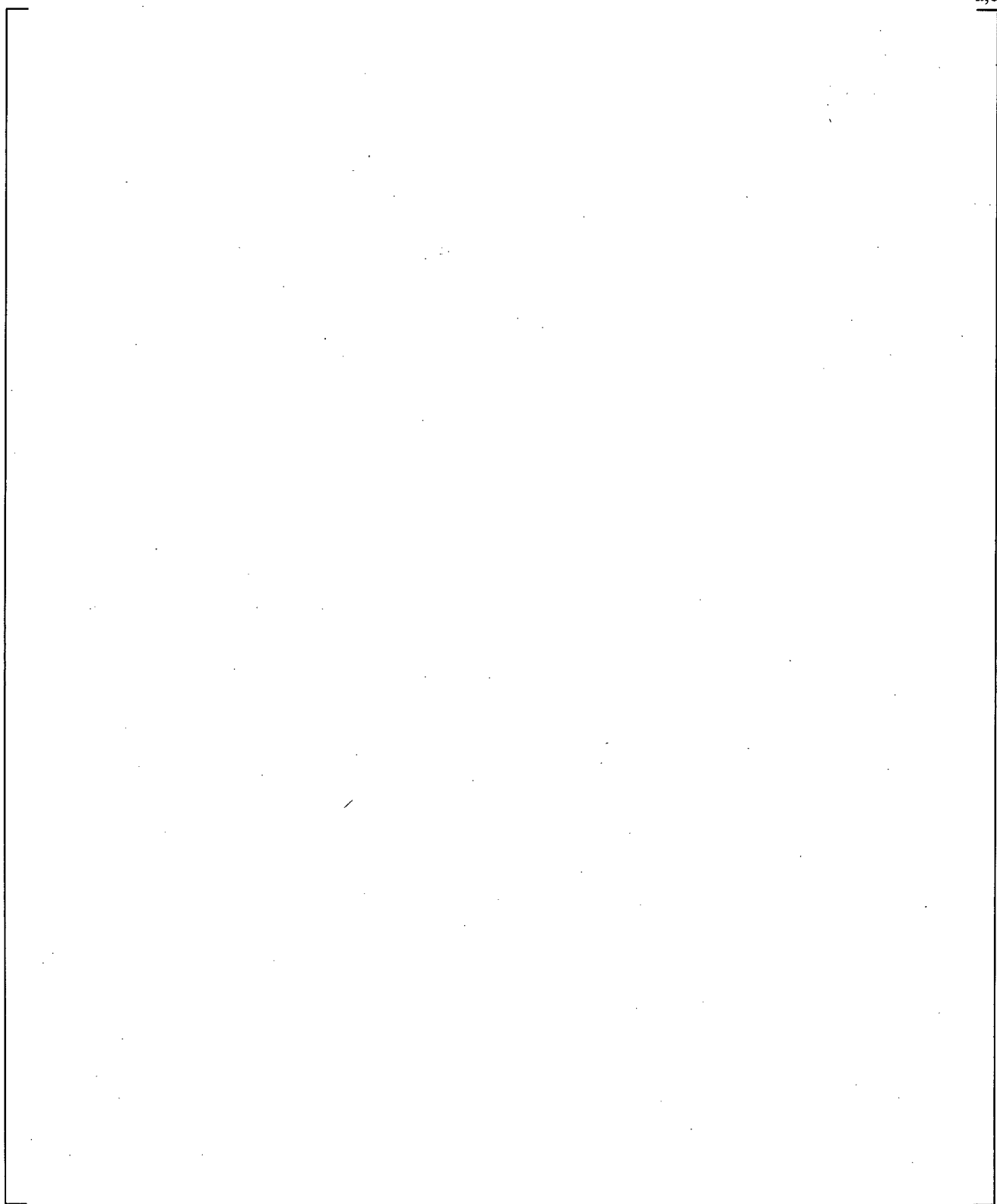


**Figure 19.5-6 Predicted and Measured Carryover Fraction, FLECHT Test 05029**

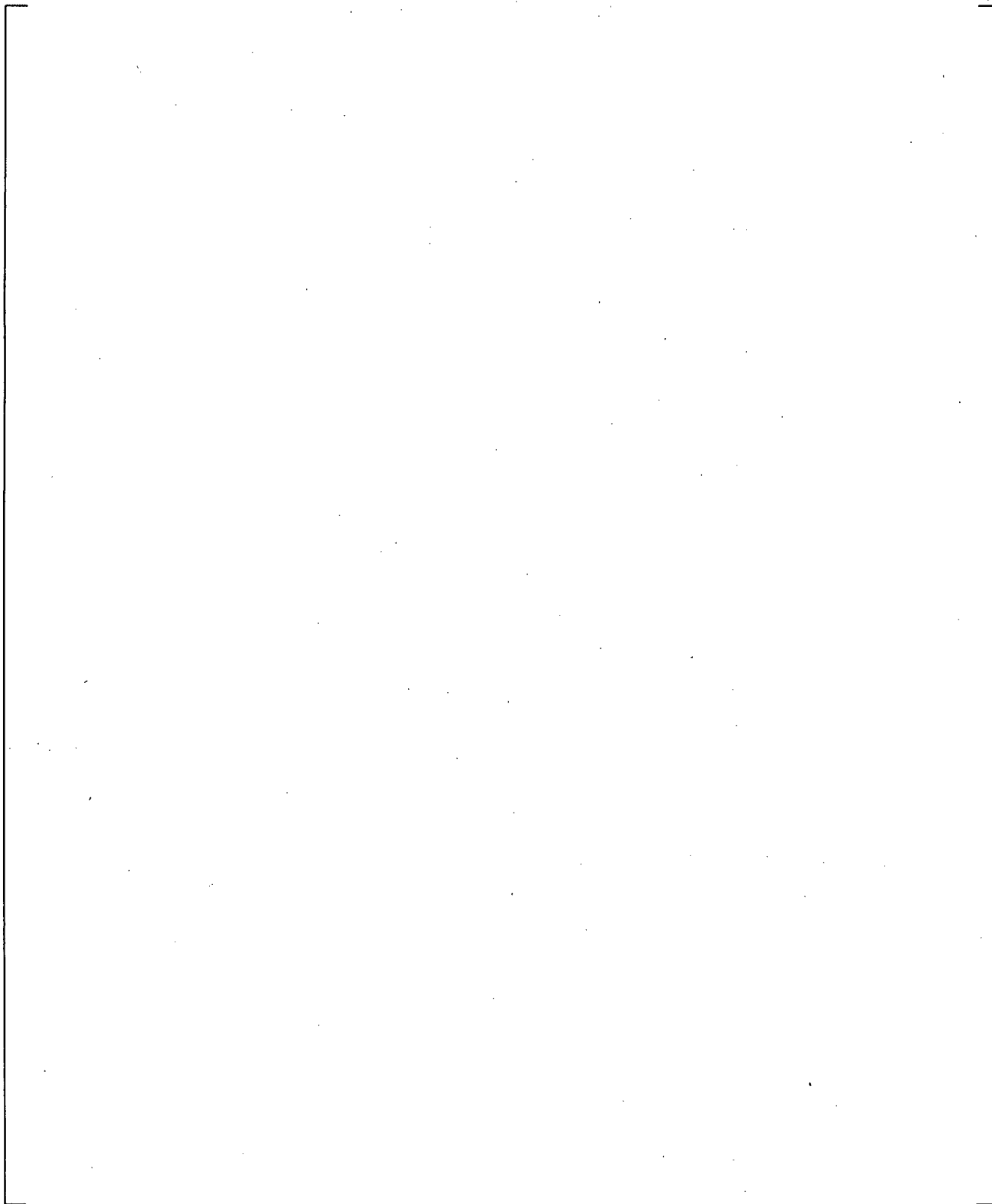


**Figure 19.5-7 Predicted and Measured Carryover Fraction, FLECHT Top Skewed Test 15305**

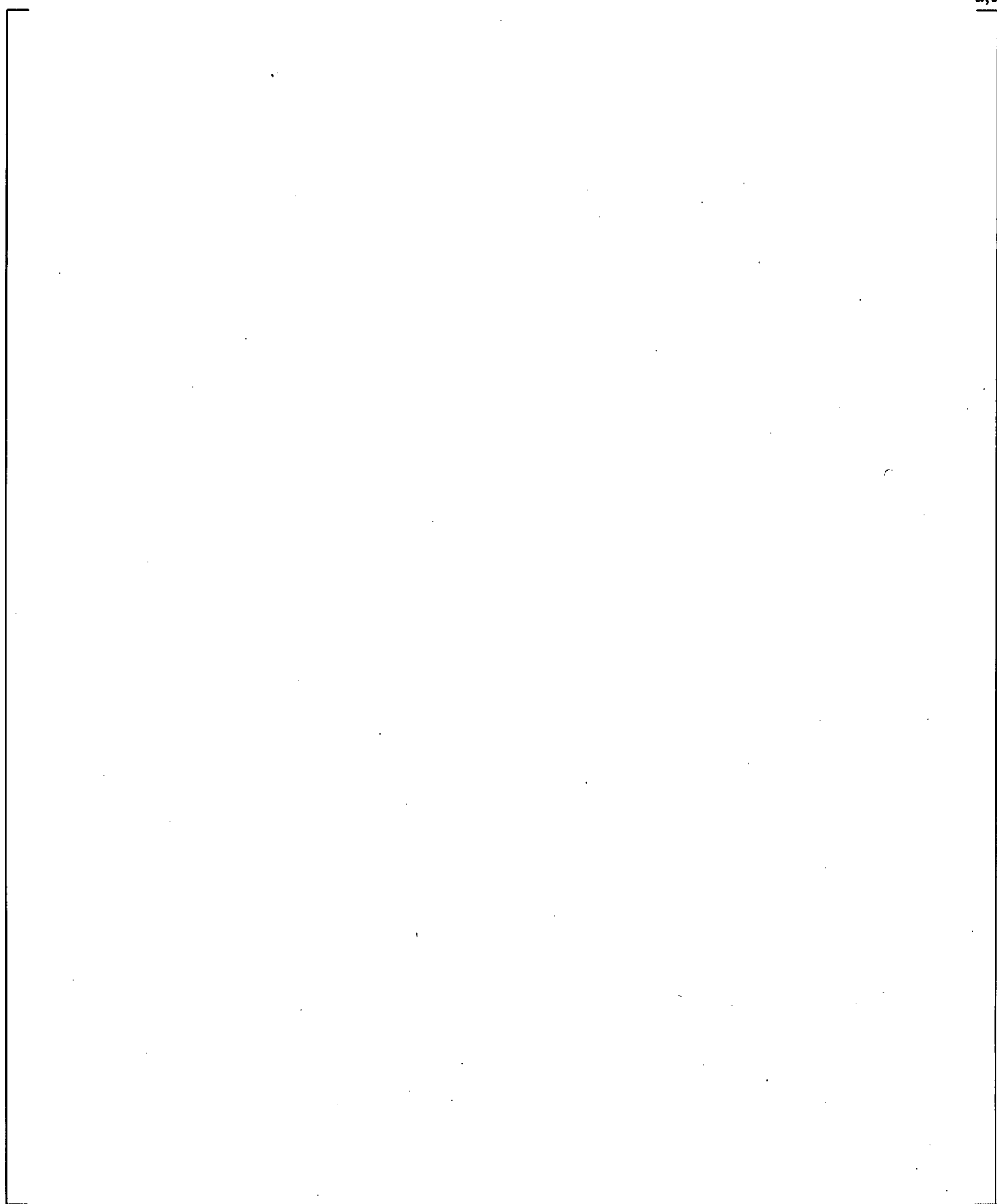


**Figure 19.5-8 Predicted and Measured Carryover Fraction, FLECHT Top Skewed Test 13609**

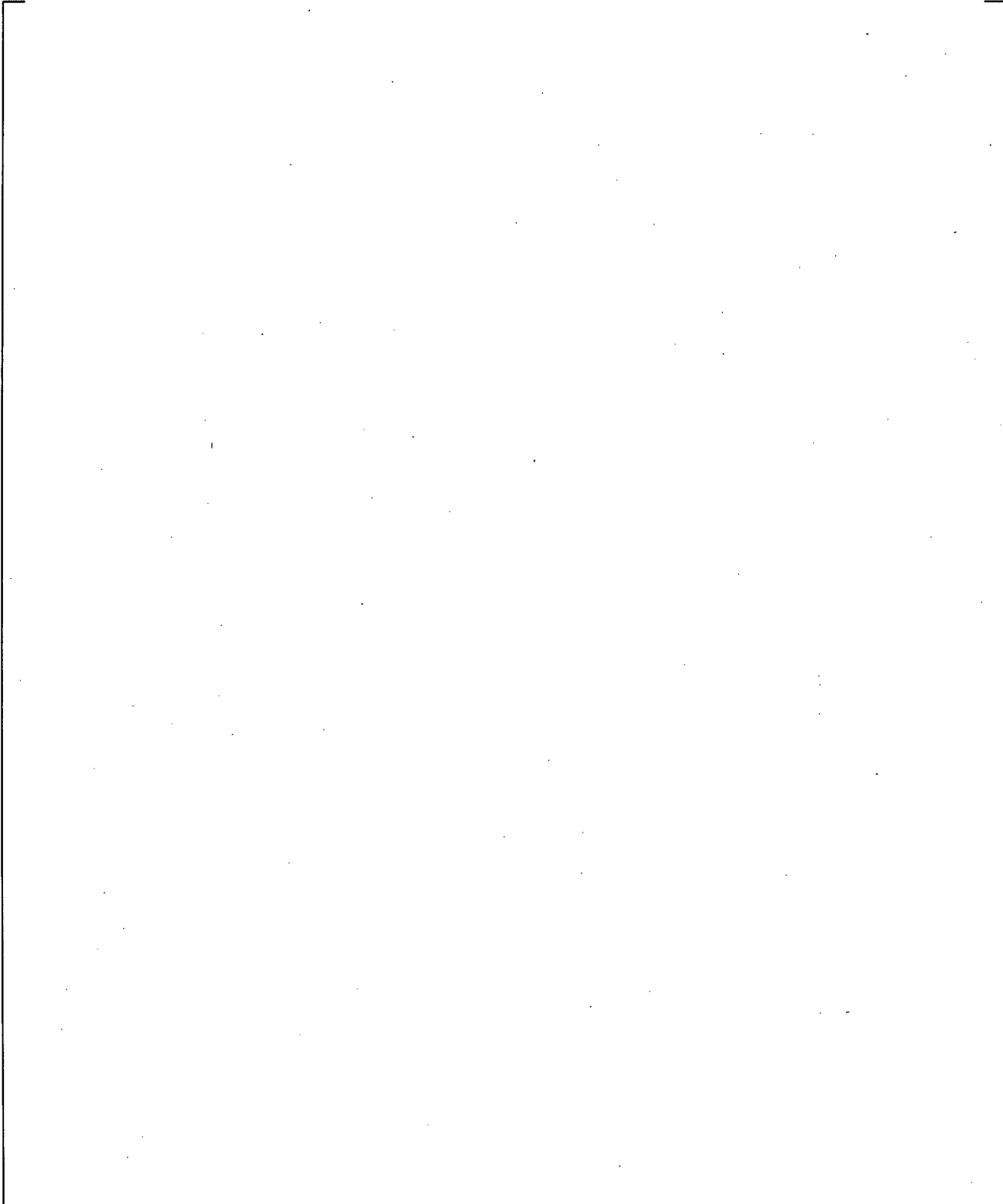


**Figure 19.5-9 Predicted and Measured Carryover Fraction, FLECHT Top Skewed Test 13812**

## 19.6 CYLINDRICAL CORE TEST FACILITY (CCTF)

To assess the capability of the WCOBRA/TRAC-TF2 computer code to predict the thermal-hydraulic core behavior in PWRs, specific code validation was performed using data from the Cylindrical Core Test Facility (CCTF, Core II). The CCTF test program was conducted by the Japan Atomic Energy Research Institute (JAERI) and was used to investigate the thermal-hydraulic response of the plant during the refill and reflood phases associated with a postulated Loss of Coolant Accident (LOCA).

The objective of this section is to assess the ability of WCOBRA/TRAC-TF2 to predict the cladding temperature response, mass flows, and liquid distribution in CCTF. The important phenomena to be addressed by CCTF 62 simulation are water accumulation in upper plenum, steam binding effect, and core quenching during gravity reflood. The facility and tests used for the prediction are summarized, the WCOBRA/TRAC-TF2 modeling is described in detail, and the predicted results are compared with data.

### 19.6.1 CCTF Tests

The CCTF tests are the largest scale integral tests available to investigate the phenomena important during the reflood phase of pressurized water reactor (PWR) during a large break loss of coolant accident (LBLOCA). CCTF has a flow area scaling of 1/21.4 of a four loop PWR. Their large scale makes them particularly suited as verification of the code's ability to handle the multi-dimensional thermal hydraulics in the core. In addition, the full-height scaling makes these tests important indicators on the extent to which core/downcomer oscillations affect the reflood transient.

The test chosen for simulation by WCOBRA/TRAC-TF2 is C2-4 (Run 62). Run 62 (Okubo et al., 1984) was taken as the reference test in the Code Qualification Document (Bajorek, 1998) CCTF Simulations; while other CCTF tests were examined in the CQD (63, 64, 67 and 75, as documented in Section 14-2-6-2 of the CQD), only this reference test is analyzed in detail herein.

The initial and boundary conditions for this test are given in Table 19.6-2. They are compared, where appropriate, with the range of conditions expected in a typical four-loop PWR at the beginning of reflood (scaled to CCTF).

### 19.6.2 CCTF Facility Description

The CCTF Core-II is a large scale experimental facility designed to study the system response of a typical four-loop PWR for loss-of-coolant transients (Figure 19.6-1). The facility is used to provide data on the thermal-hydraulic behavior in the primary system during the refill and reflood phases of a hypothetical LOCA in a PWR. Table 19.6-1 compares the scaled dimensions of the system components with those of a PWR.

The CCTF includes a full-height (12-foot heated length) core section with three intact loops, and a fourth loop simulating a full double-ended guillotine break. The test vessel includes a downcomer, lower plenum, core region, and upper plenum with associated internals (support columns and guide tubes). The dimensions for the vessel are shown in Figure 19.6-2. The configuration of the rods in the core and the upper plenum structure are shown in Figure 19.6-3. The core has 32 8x8 rod bundles each containing 57 electrically heated rods (0.421-inch OD) and 7 unheated/instrumented rods (0.543-inch OD). The rods

have a pitch spacing of 0.563 inches. The geometry of these rods is equivalent to a typical PWR 15x15 fuel assembly. Each heated rod has a nichrome heating element and is packed with magnesium oxide and boron nitride. The sheath is made of Inconel-600. The rods are held together by six grids spaced at 26.18-inch intervals up the bundle.

The core is divided into the three main power zones: low, intermediate, and high. The lower power zone consists of 16 assemblies on the periphery of the core, as shown in Figure 19.6-3. The intermediate power zone consists of 12 assemblies, while the high power zone consists of the 4 central assemblies. Under guide tubes, there are 4 low power assemblies and 6 medium power assemblies. Under support columns, there are 8 low power assemblies and 2 high power assemblies. Under open holes, there are 4 low power assemblies, 6 medium power assemblies, and 2 high power assemblies. The axial power profile, along with the locations at the grid spacers, is shown in Figure 19.6-4.

The three intact loops and the broken loop each contain a steam generator and pump simulator. Flow from the broken loop enters two interconnected containment tanks via two blowdown valves, connected to each break. ECC water can be injected either from two accumulator tanks or by an LPCI pump and its associated water storage tank. Water can be injected directly to injection ports positioned in the lower plenum or to the cold legs.

### 19.6.3 CCTF Test Procedure

The following is a general outline of the experimental test procedure. Figure 19.6-5 shows the sequence of events for CCTF 62 test. The initial and boundary conditions for this test are given in Table 19.6-2. They are compared, where appropriate, with the range of conditions expected in a typical four-loop PWR at the beginning of reflood (scaled to CCTF).

The primary system was heated with pre-heaters to its specified temperatures and pressurized to a specified pressure using steam. The water in the LPCI tanks and accumulator tanks was heated to its specified temperature. LPCI water was circulated to ensure that the injection lines were at the same temperature. The accumulator tanks were pressurized with nitrogen to give sufficient head for the required injection flow. The steam generator secondary fluid was then heated and pressurized. The heaters were then turned off and the lower plenum was filled to the specified level with saturated water. When the initial conditions had been established power was applied to the heater rods and data recording started (referred to as time zero.) The heater rods heated up under near adiabatic conditions until the cladding temperature reached a pre-specified value.

At this point accumulator injection to the lower plenum began. The containment tank pressure was maintained throughout the tests by controlling the outlet valve on the containment tanks. The heater rod power decay was initiated when the water reached the bottom of the heated length of the core (referred to as the BOCREC time). The water injection was changed from the lower plenum to the cold legs after a specified time. When the accumulator flow was coming to an end, LPCI flow was introduced to the cold legs and was maintained until the end of the test.

The generated steam and the entrained water flowed via broken and intact loops to the containment tanks. The steam was then vented to the atmosphere to maintain a constant pressure in the containment tanks. After all thermocouples on the surface of the heater rods indicated quench, the power supply to the heater

rods and the ECC water injection were turned off. The recording system was then stopped, terminating the test.

#### **19.6.4 WCOBRA/TRAC-TF2 CCTF Model**

The WCOBRA/TRAC-TF2 model used for the CCTF simulations uses one-dimensional components for the intact loops (which models three CCTF loops) and for the broken loop, and employs a sub channel formulated mesh for the vessel. First, the vessel component model is described. This is followed by a description of the loop model.

[

] <sup>a,c</sup>

##### **19.6.4.1 Vessel Component Model**

The vessel component model is developed following the noding strategy in Section 26.1.1. A comparison between the CCTF and the PWR noding as presented in the FSLOCA application is summarized in Table 19.6-3.

[

] <sup>a,c</sup>

[

] <sup>a,c</sup>

[

] <sup>a,c</sup>

#### 19.6.4.2 Loop Component Model

[

] <sup>a,c</sup>

[

] <sup>a,c</sup>

### 19.6.5 CCTF Run 62 Transient Calculation

In the following sections, the WCOBRA/TRAC-TF2 predictions are examined. Predicted cladding temperatures are compared with data averages of all instrumented rods within the channel (excluding obviously bad data channels). Predicted vapor fractions are compared with vapor fractions estimated from differential pressure (delta-p) measurements. In the core, the delta-p between several one-foot spans is available. Collapsed water levels and masses in various components are also estimated from the delta-p measurements. In CCTF, the liquid and vapor mass flows in the loops were measured at instrument spool pieces containing turbine meters and drag discs. The locations of these measurements in the system are shown in Figure 19.6-1.

The discussion provided here is intended to assess key variables and identify important differences between the predictions and the data. This run has the nominal test conditions which are summarized in Table 19.6-2. It is noted the simulation of CCTF 62 starts from BOCREC (bottom of core recovery) which is 94s after the test initialized, and the comparisons in this section are based on time of BOCREC.

In general, PCTs and quench times in the CCTF tests tend to be [ ] <sup>a,c</sup> (Figures 19.6-20 to 19.6-22). [

] <sup>a,c</sup>

There are two thermal couples at 6 ft. [

] <sup>a,c</sup>

The core collapsed liquid level is shown in Figure 19.6-24. [

] <sup>a,c</sup>

Figures 19.6-31 to 19.6-33 compare the predicted steam temperature rise and the measured temperature rise across the steam generators in 3 intact loops. [

] <sup>a,c</sup>

Figures 19.6-34 and 19.6-35 compare the predicted and the measured total flow rates in the intact and broken hot legs. [

] <sup>a,c</sup>

The integrated core inlet mass flow rates are shown in Figure 19.6-36. [

] <sup>a,c</sup>

[

] <sup>a,c</sup>

For the CCTF Test C2-4 Run 62 simulation, the WCOBRA/TRAC-TF2 calculated clad temperature is [

] <sup>a,c</sup>

### 19.6.6 DTMAX Sensitivity Study for CCTF 62

To support time step sensitivity study in Section 28.1.3, the sensitivity studies for DTMAX are carried out for the CCTF 62 test. [

] <sup>a,c</sup> Those time step sizes are consistent with those used in plant model in Section 26. In this sensitivity study, the relative [ ] <sup>a,c</sup> time step sizes are chosen to show the effect of time step sensitivity. For the initial surge stage, the time step size is increased from [ ] <sup>a,c</sup>, while [ ] <sup>a,c</sup> are used for the remaining reflood period.

Figures 19.6.37 to 19.6.39 compare the prediction cladding temperatures at elevations of 6.0 ft, 8.0 ft, and 10.0 ft, respectively. [

] <sup>a,c</sup>

In general, the time step sensitivity study shows the time step size effect is [ ] <sup>a,c</sup> for CCTF 62 simulation, which covers the initial surge of reflood period of LBLOCA.



Table 19.6-2 [ ]<sup>a,c</sup>



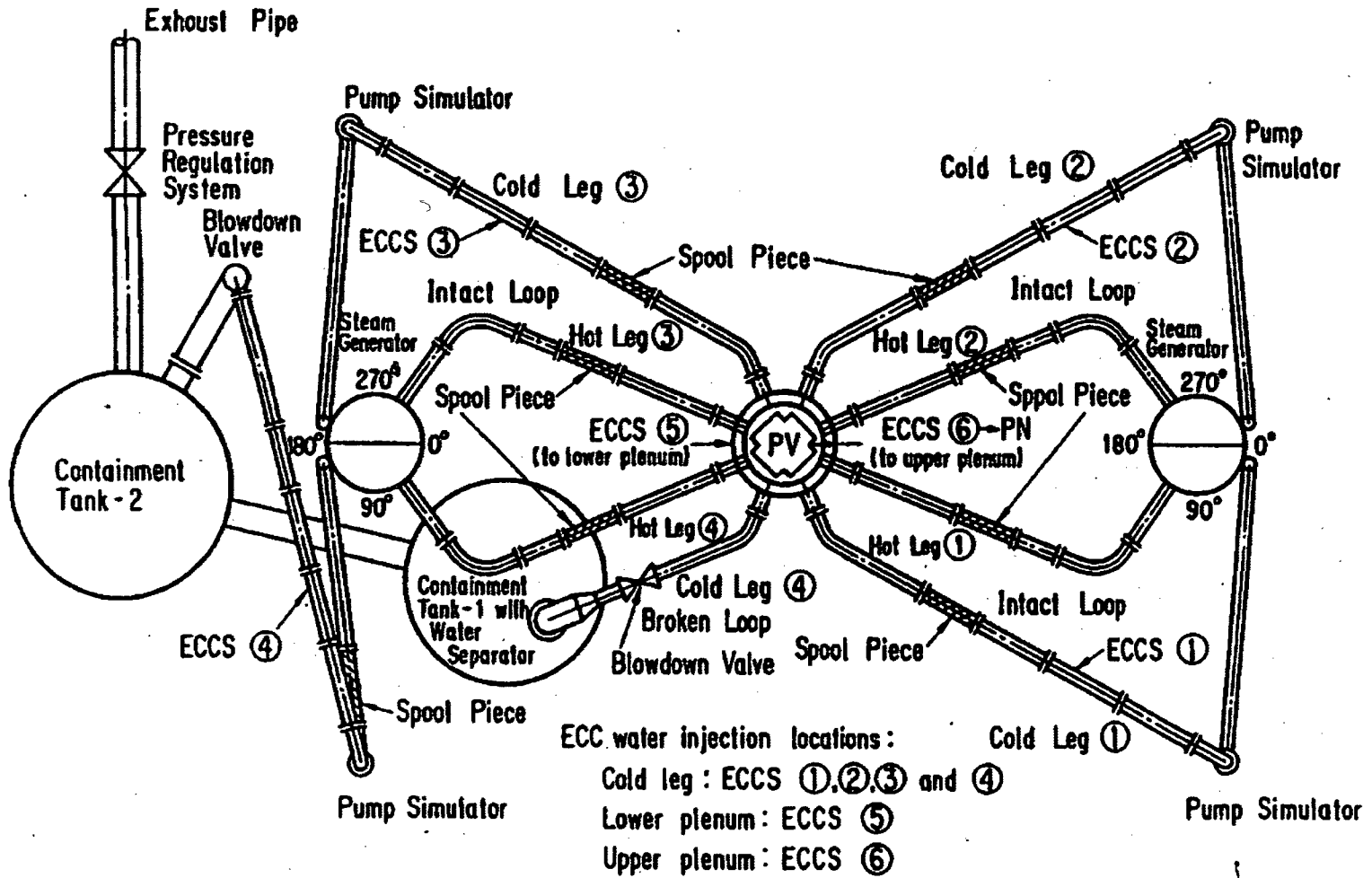

Table 19.6-4 [ ]<sup>a,c</sup>


a,c

Table 19.6-5 [ ]<sup>a,c</sup>


a,c

Figure 19.6-1 Top View of Primary Loop Piping



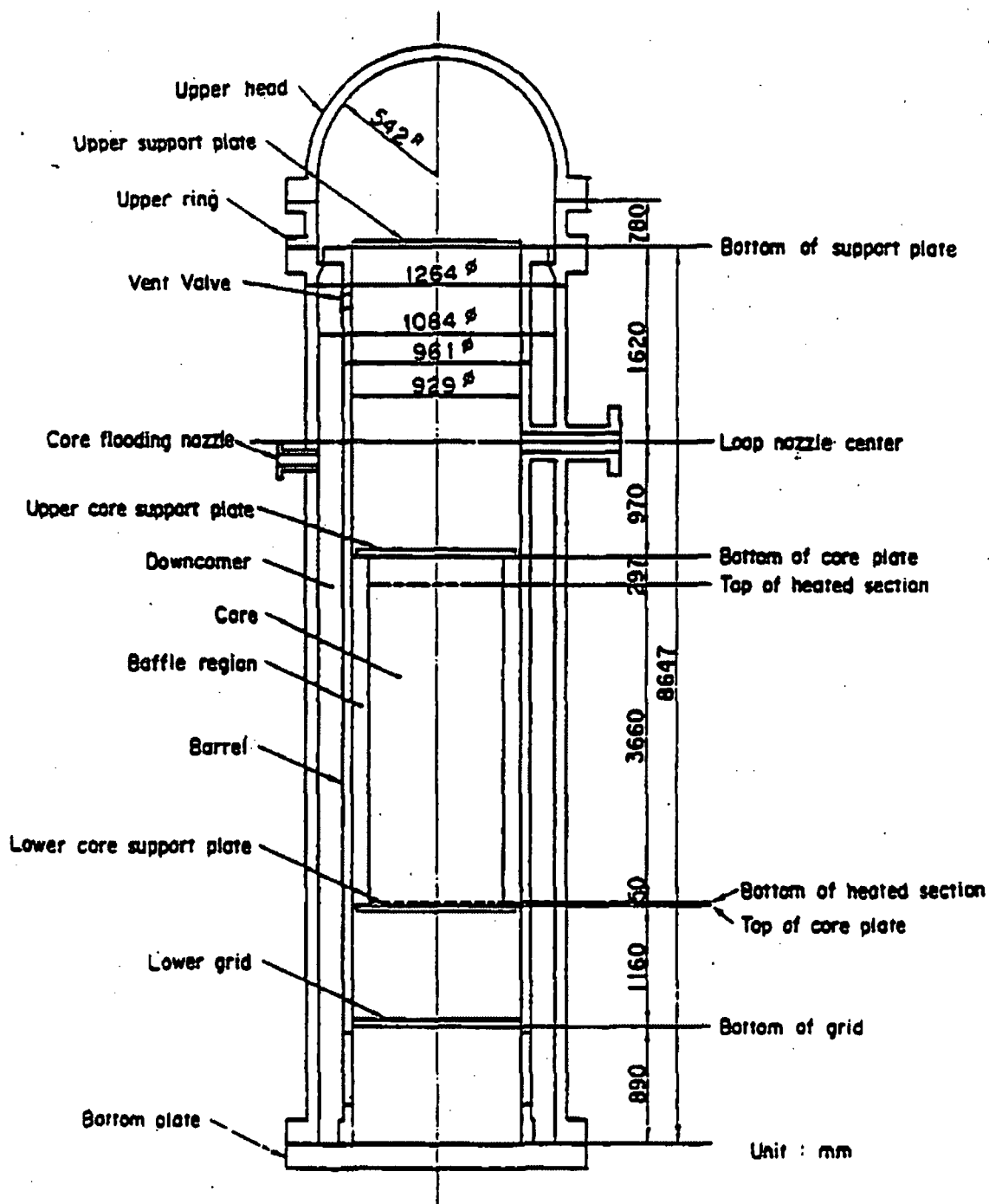


Figure 19.6-2 Diagram of CCTF Pressure Vessel

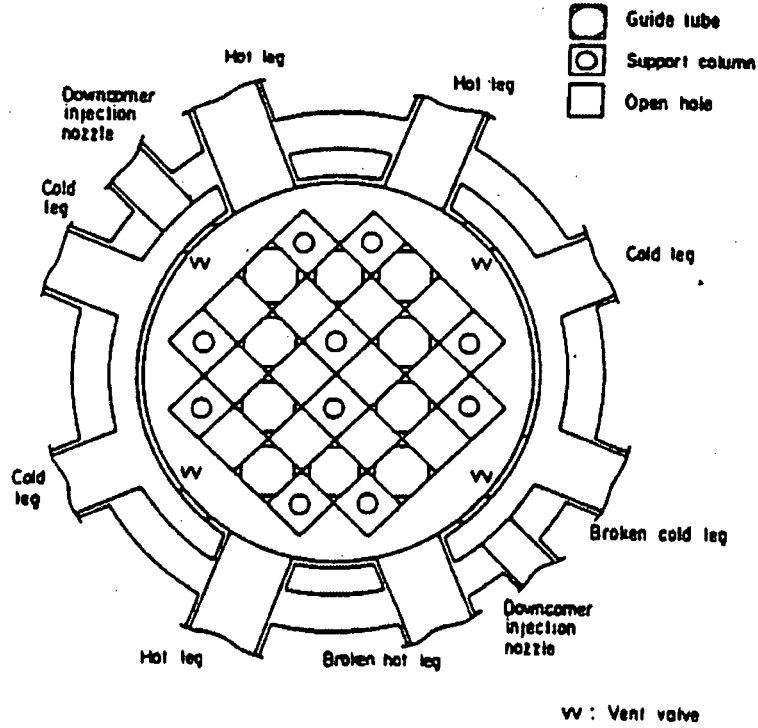
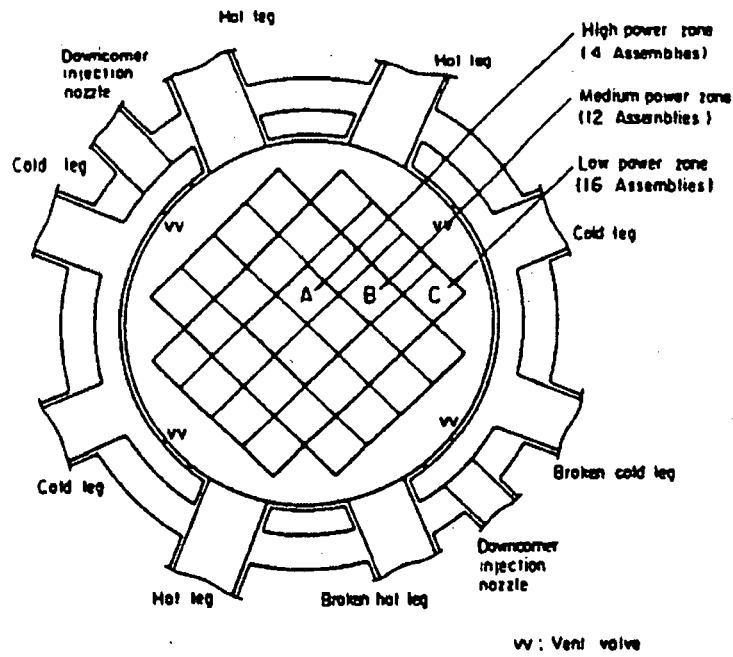
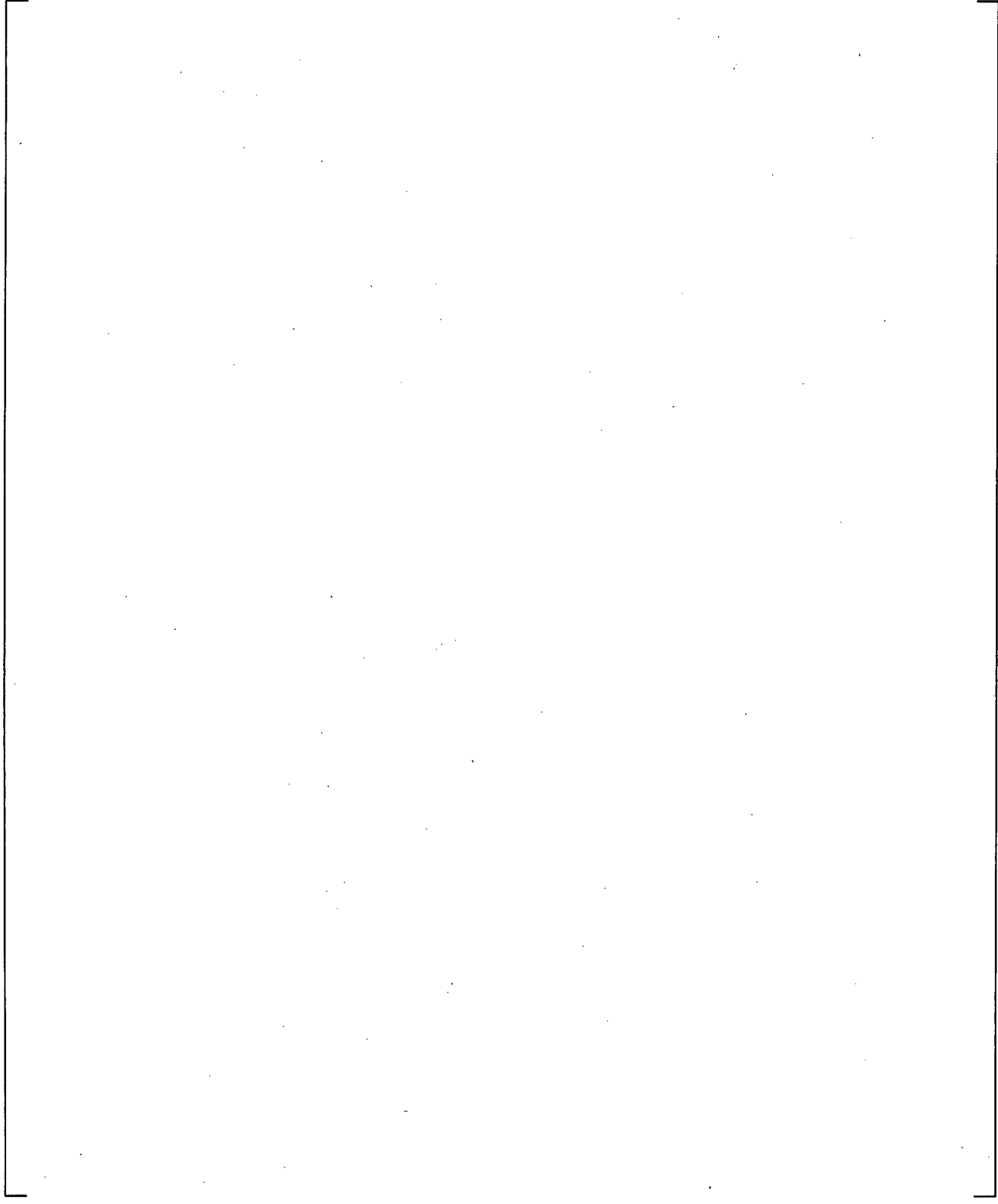
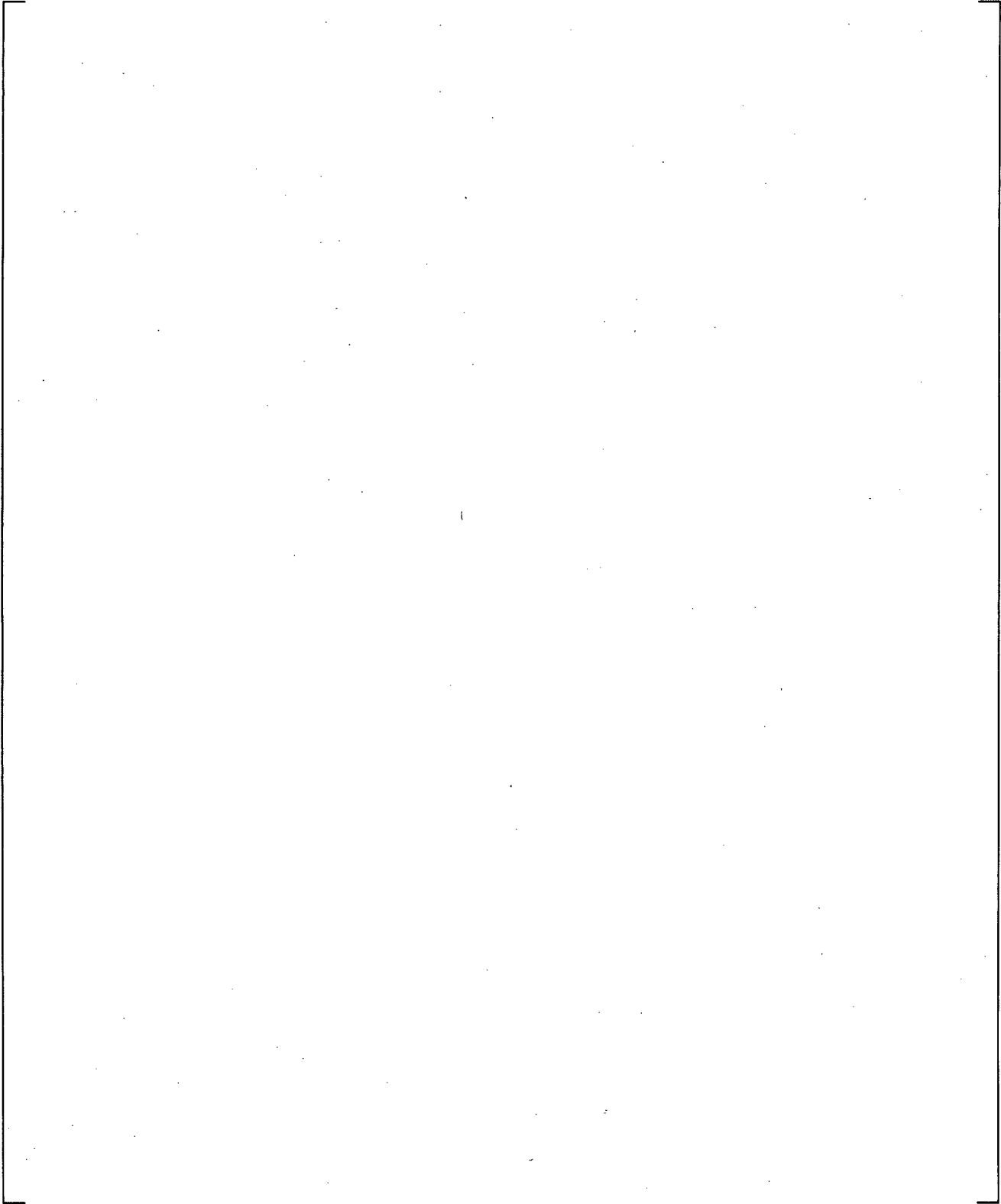


Figure 19.6-3 CCTF Cross Sections (a) Pressure Vessel (b) Upper Plenum Internals



**Figure 19.6-4 Axial Power Profile of Heated Rods in CCTF**



**Figure 19.6-5 CCTF Test Sequence for Run 62**

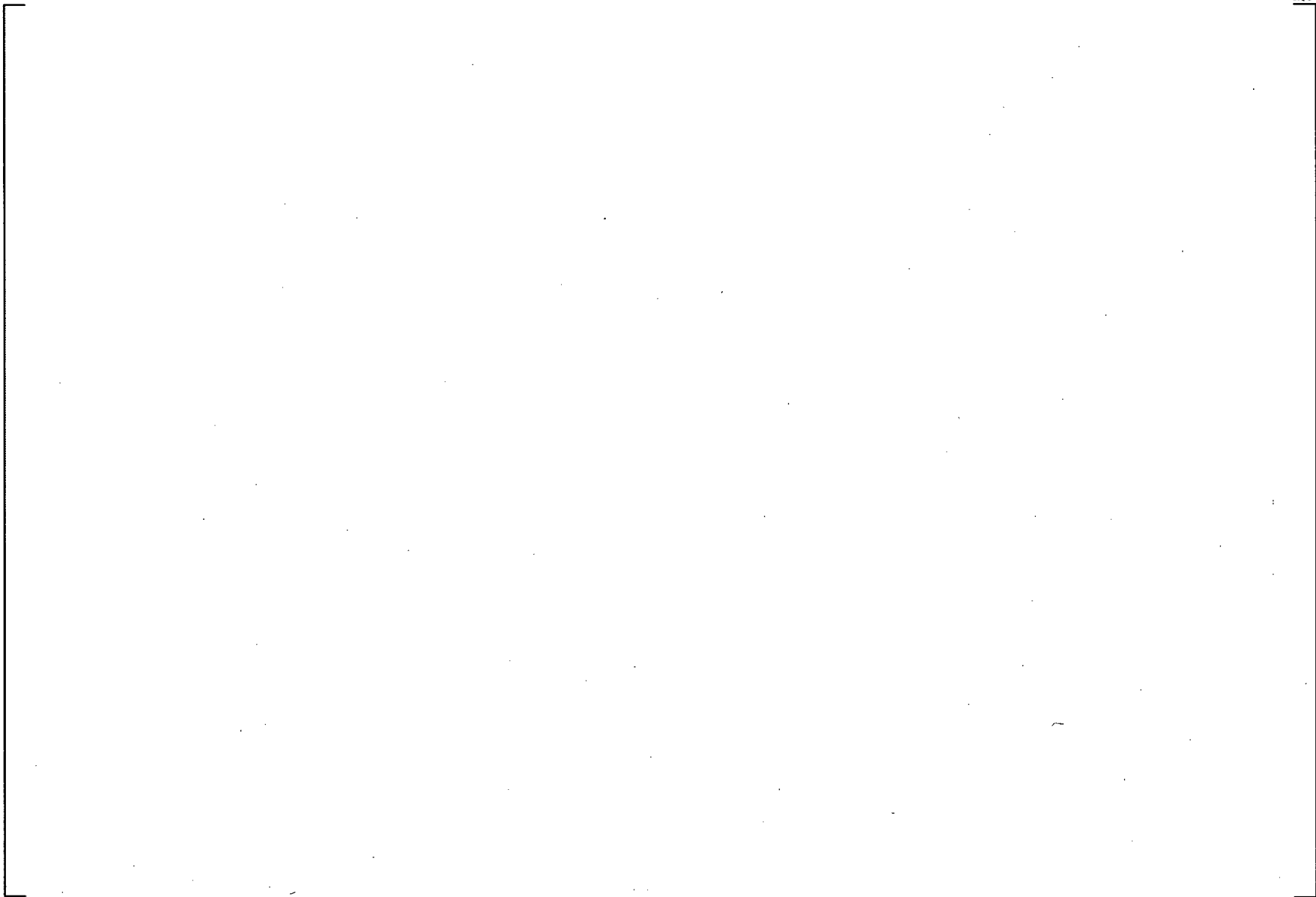


**Figure 19.6-6 CCTF Vessel Noding Diagram**

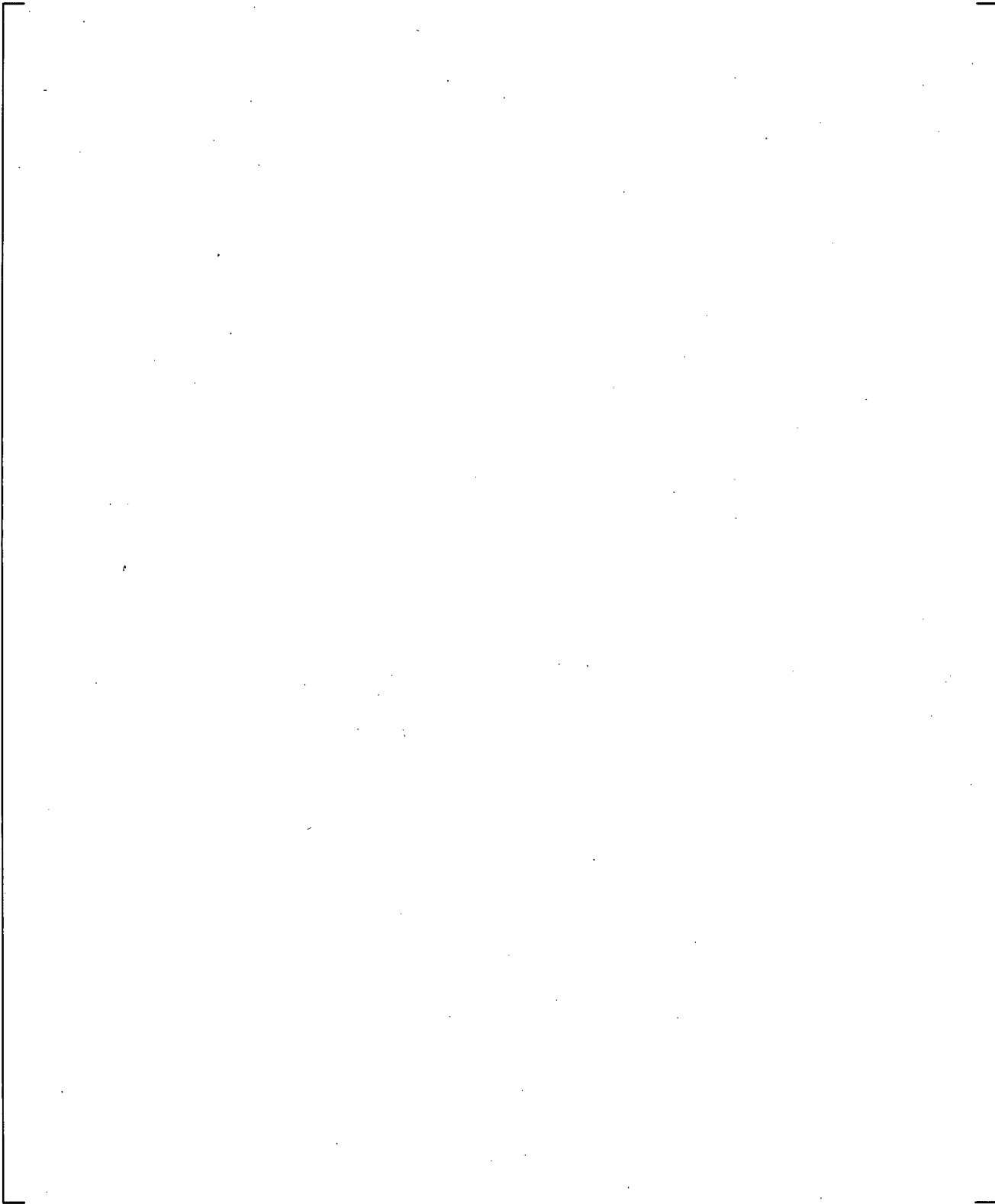


**Figure 19.6-7 CCTF Section 1 Noding**

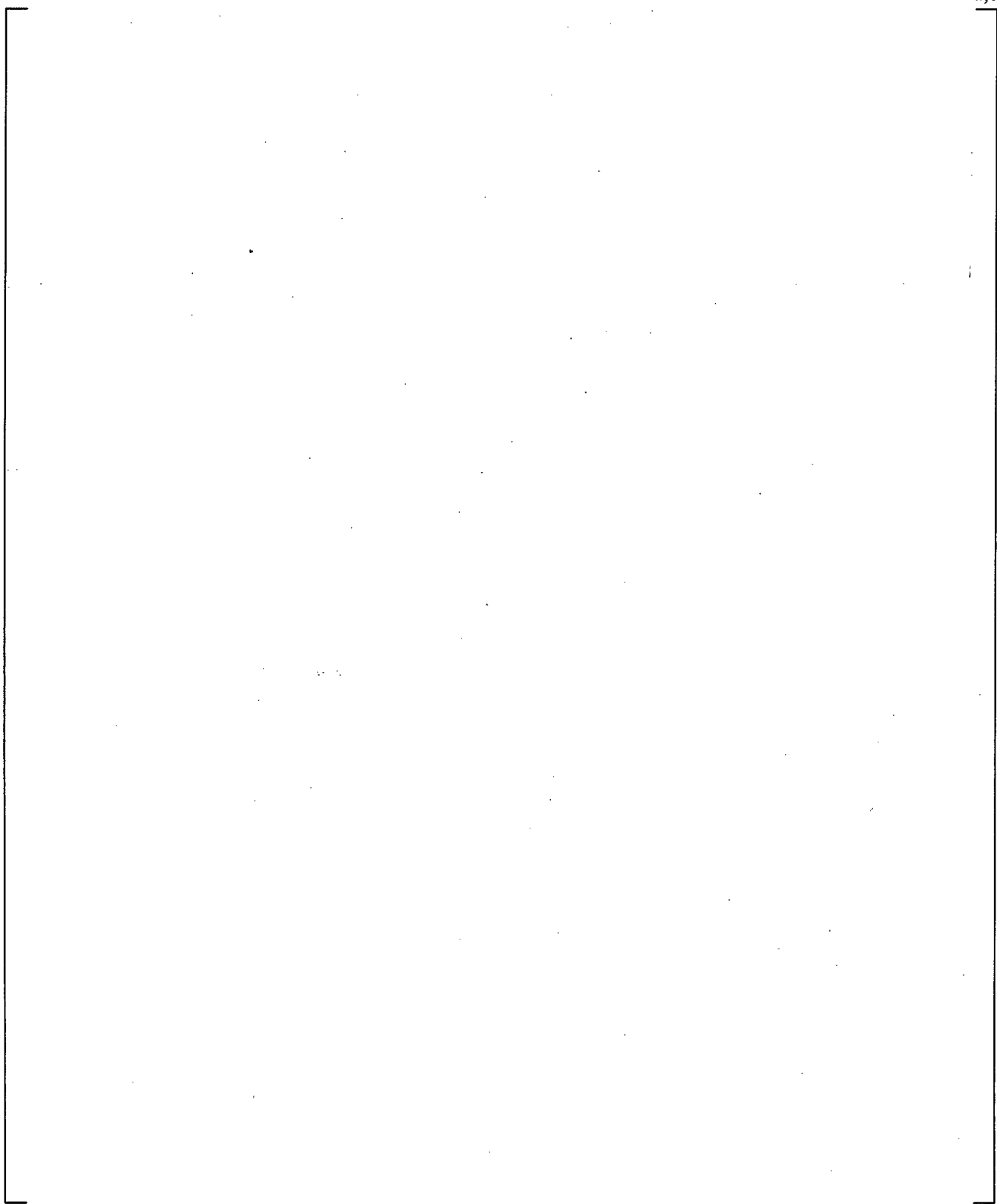


**Figure 19.6-8 CCTF Section 2 Noding**

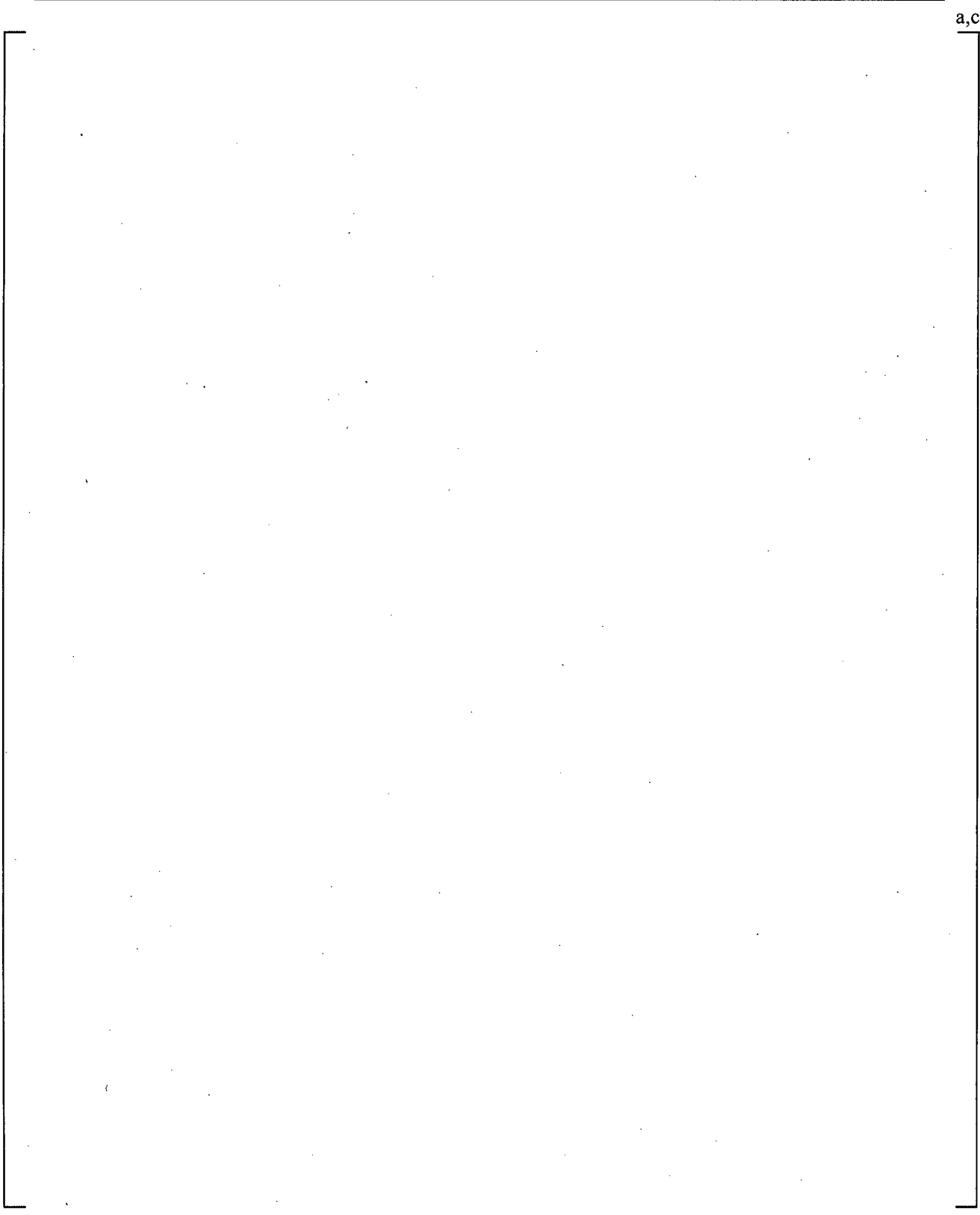


**Figure 19.6-9 CCTF Section 3 Noding**

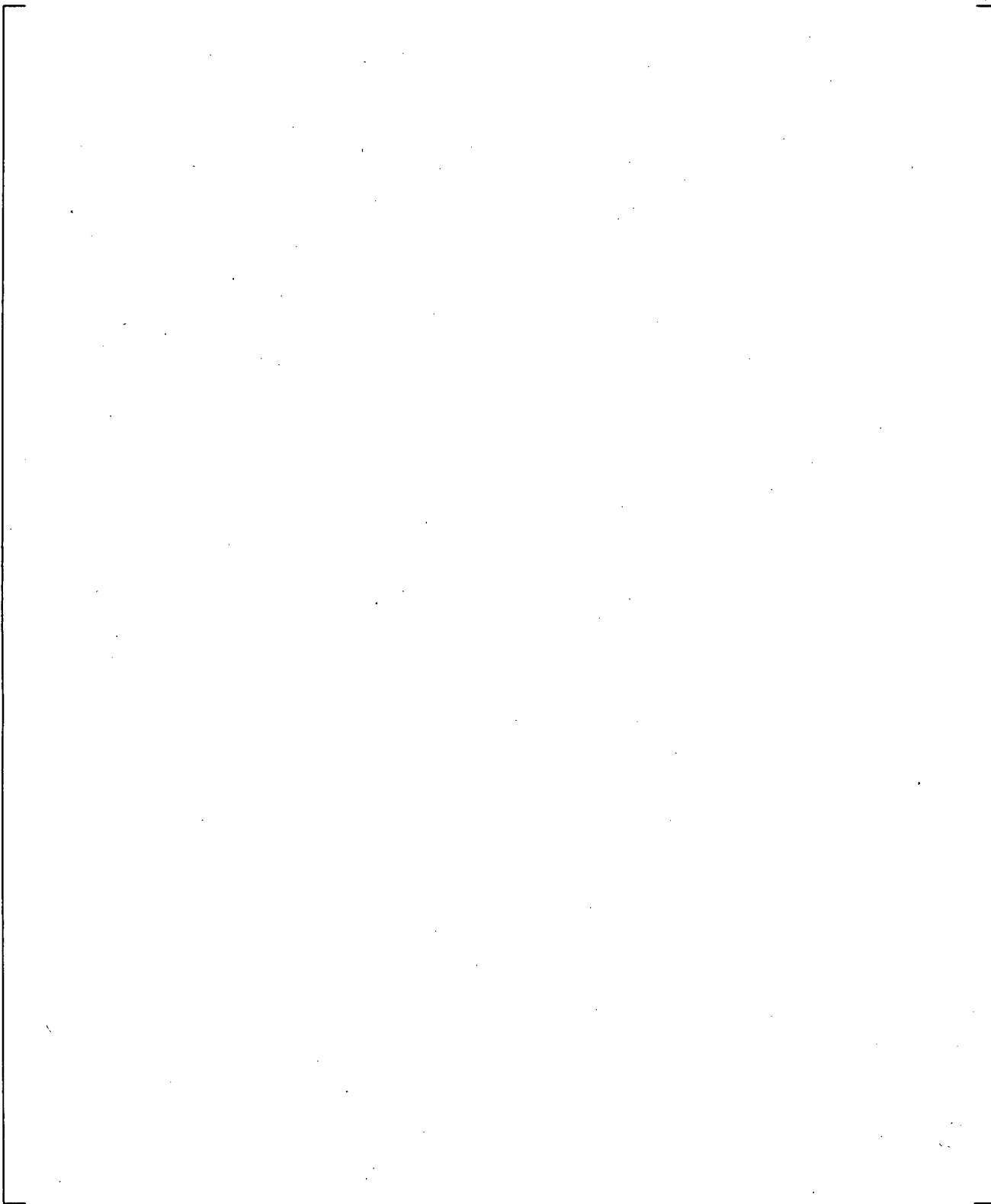


**Figure 19.6-10 CCTF Section 4 Noding**

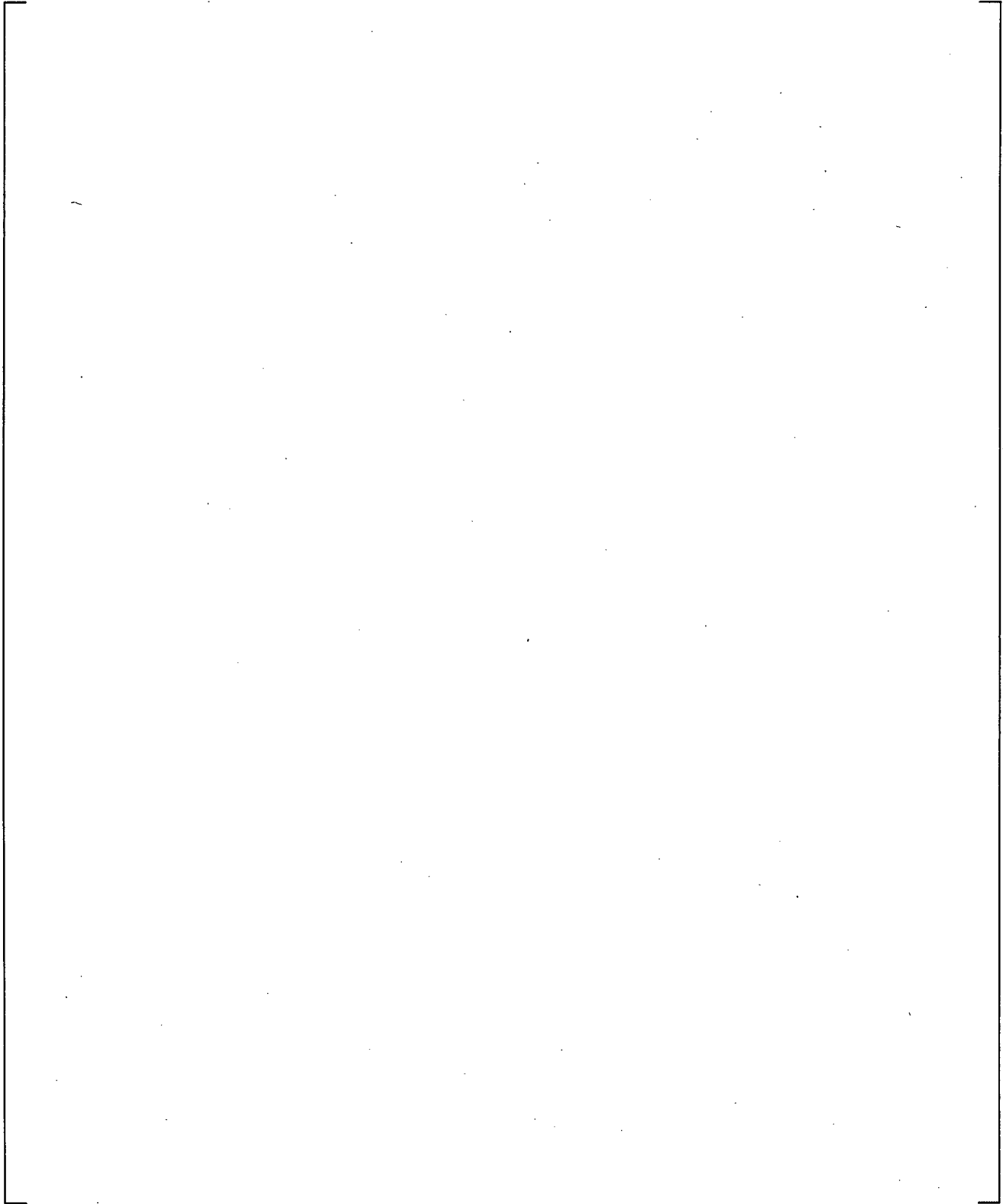


**Figure 19.6-11 CCTF Section 5 Noding**

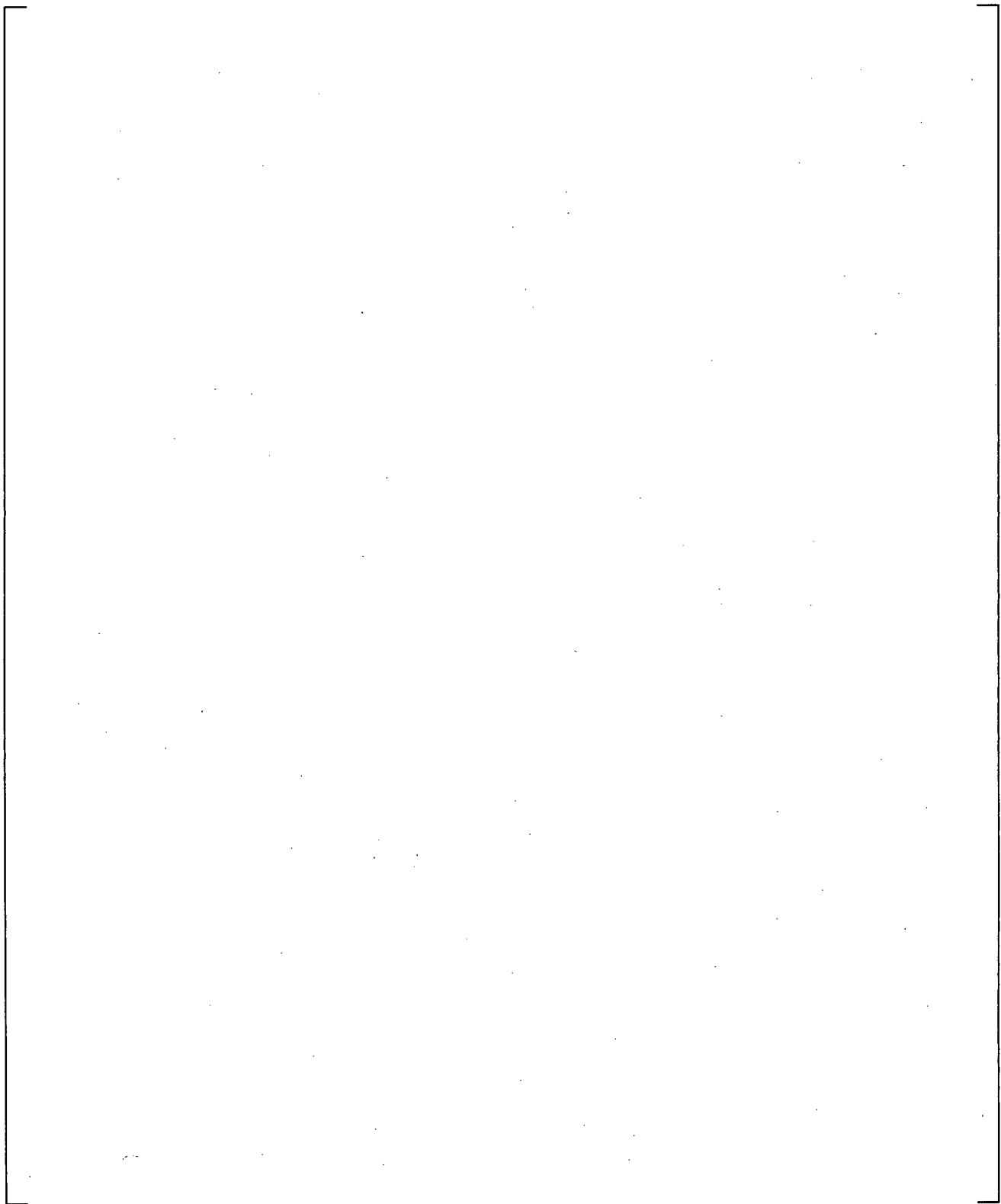


**Figure 19.6-12 CCTF Section 6 Noding**

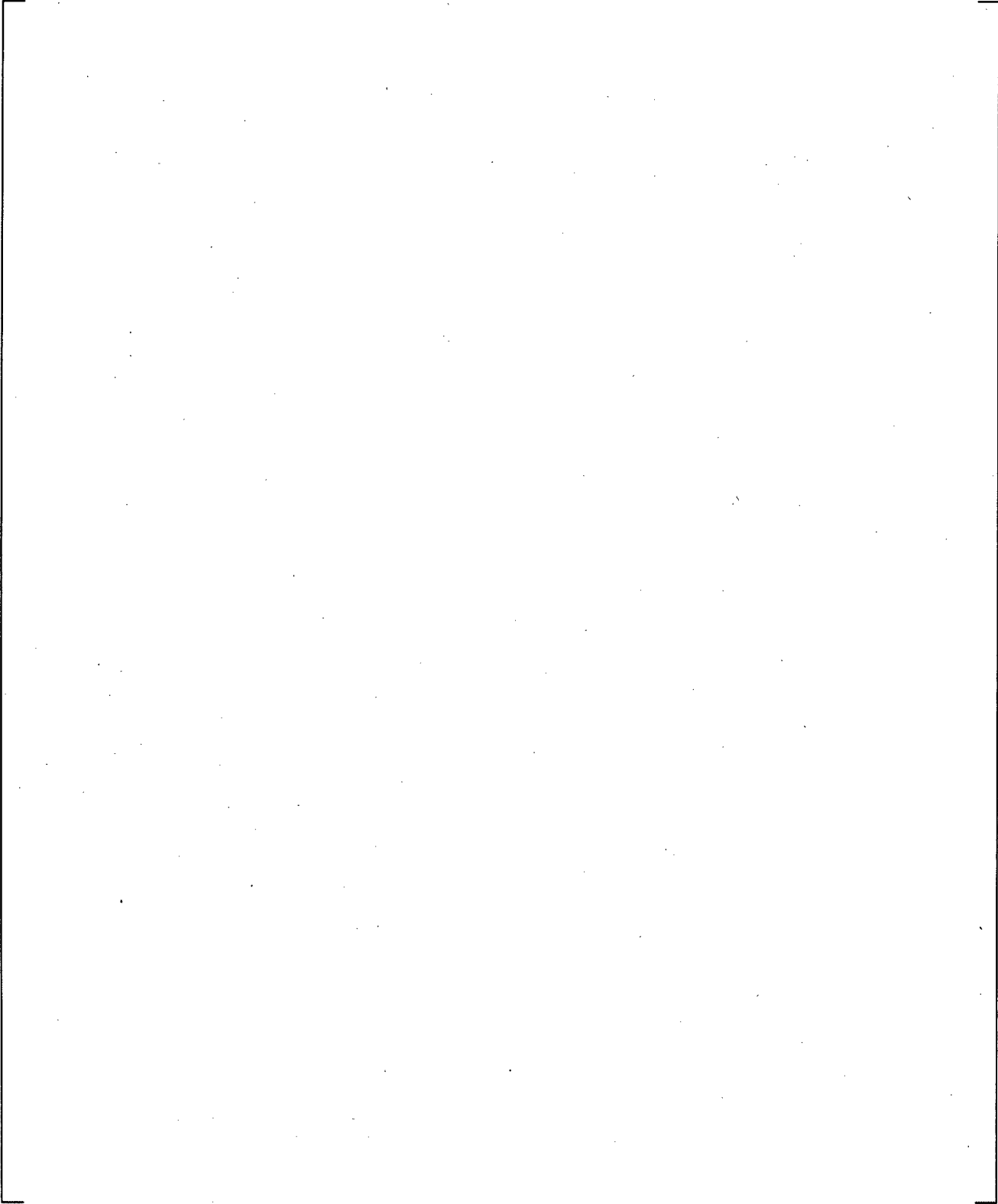


**Figure 19.6-13 CCTF Section 7 Noding**

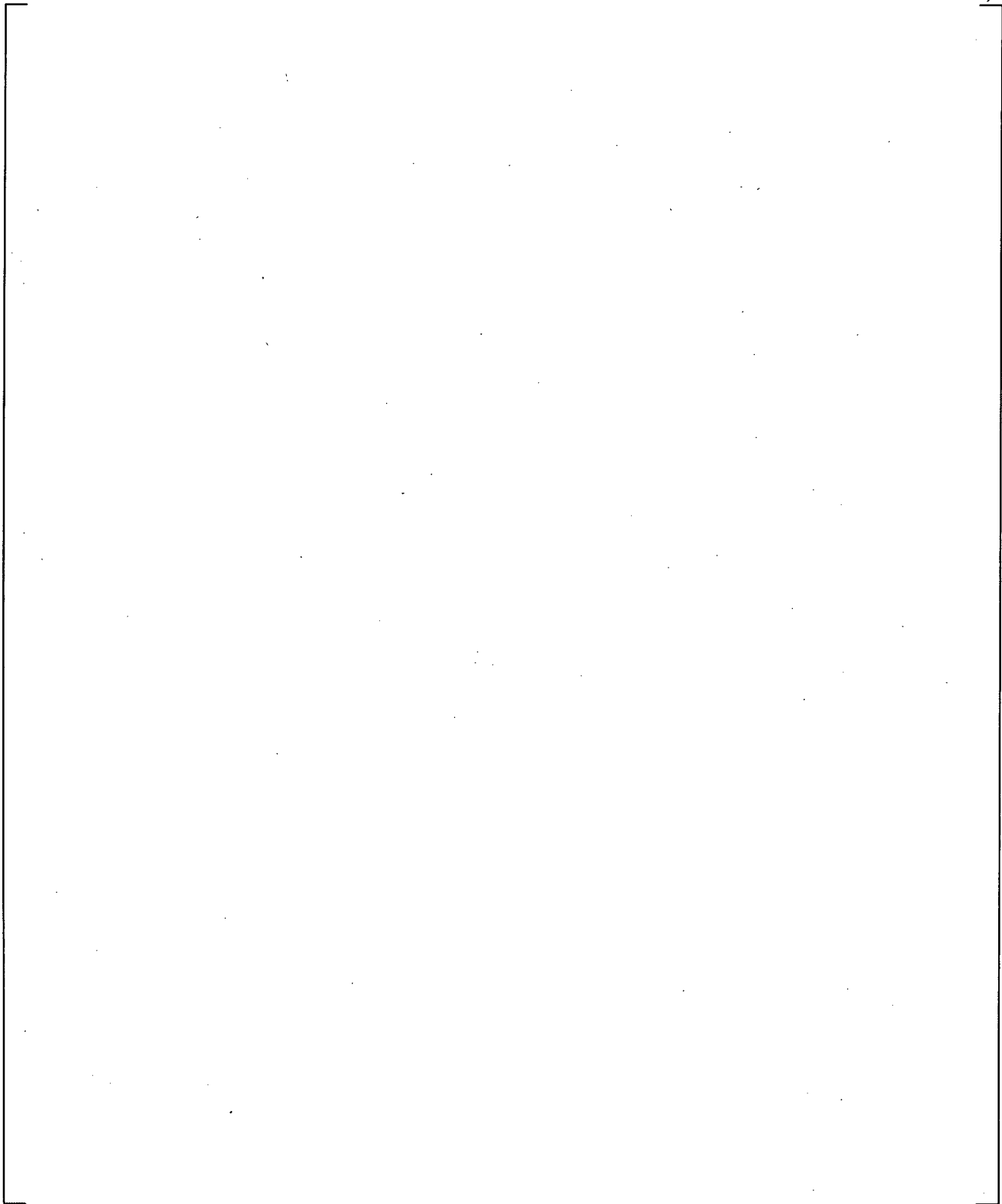


**Figure 19.6-14 CCTF Loop Component Diagram**



**Figure 19.6-15 Dimensions of Hot Leg in CCTF Facility**



**Figure 19.6-16 Noding Diagram of Hot Leg**



**Figure 19.6-17 Dimension of Crossover Leg, Pump Simulator, Cold Leg, and ECC Port in CCTF Facility**



**Figure 19.6-18 Noding Diagram of Crossover Leg, Pump Simulator, Cold Leg, and ECC Port in Loop 1; Other Intact Loops are Identical to Loop 1**

a,c

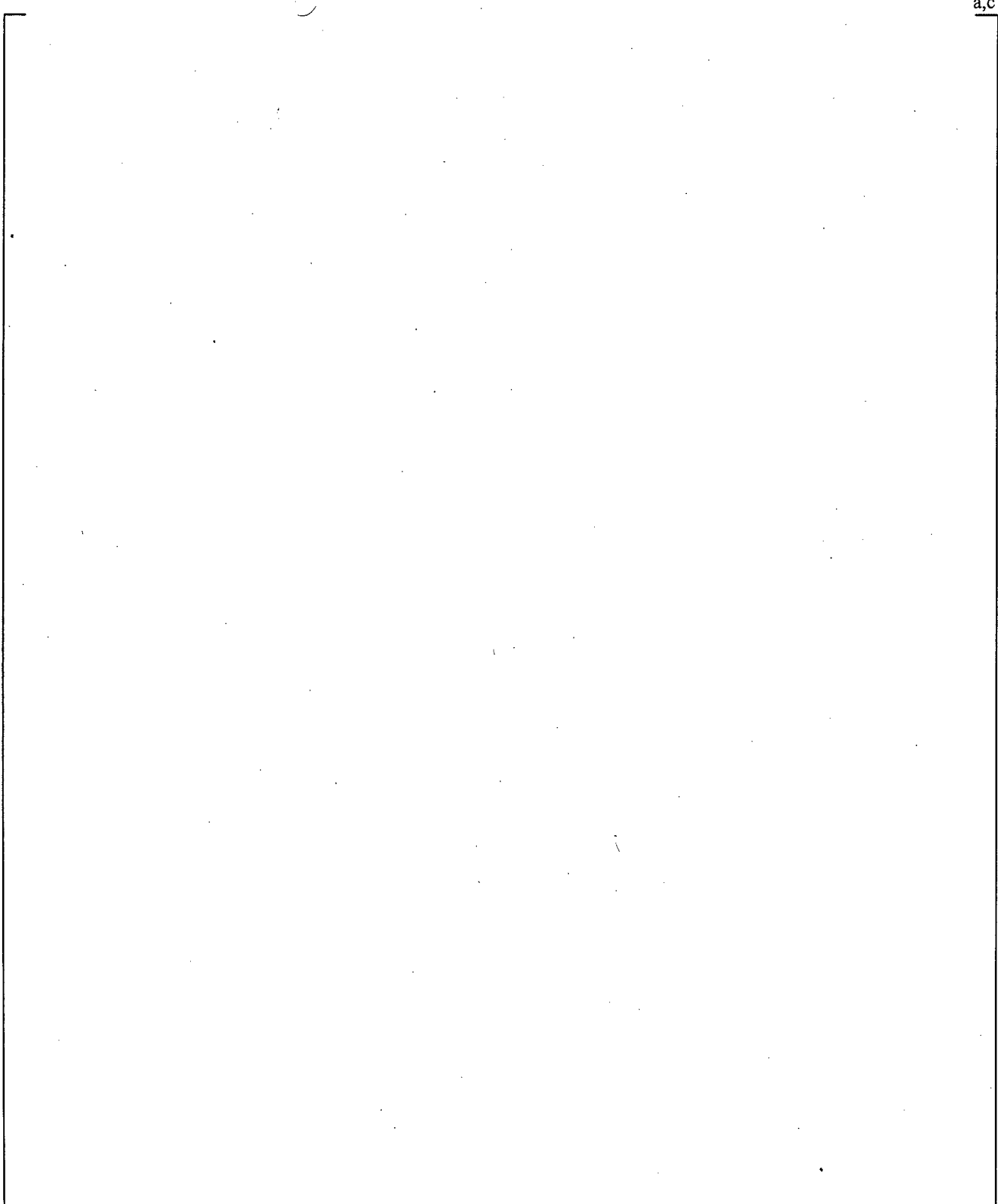


**Figure 19.6-19 Steam Generator Component Diagram**

a,c

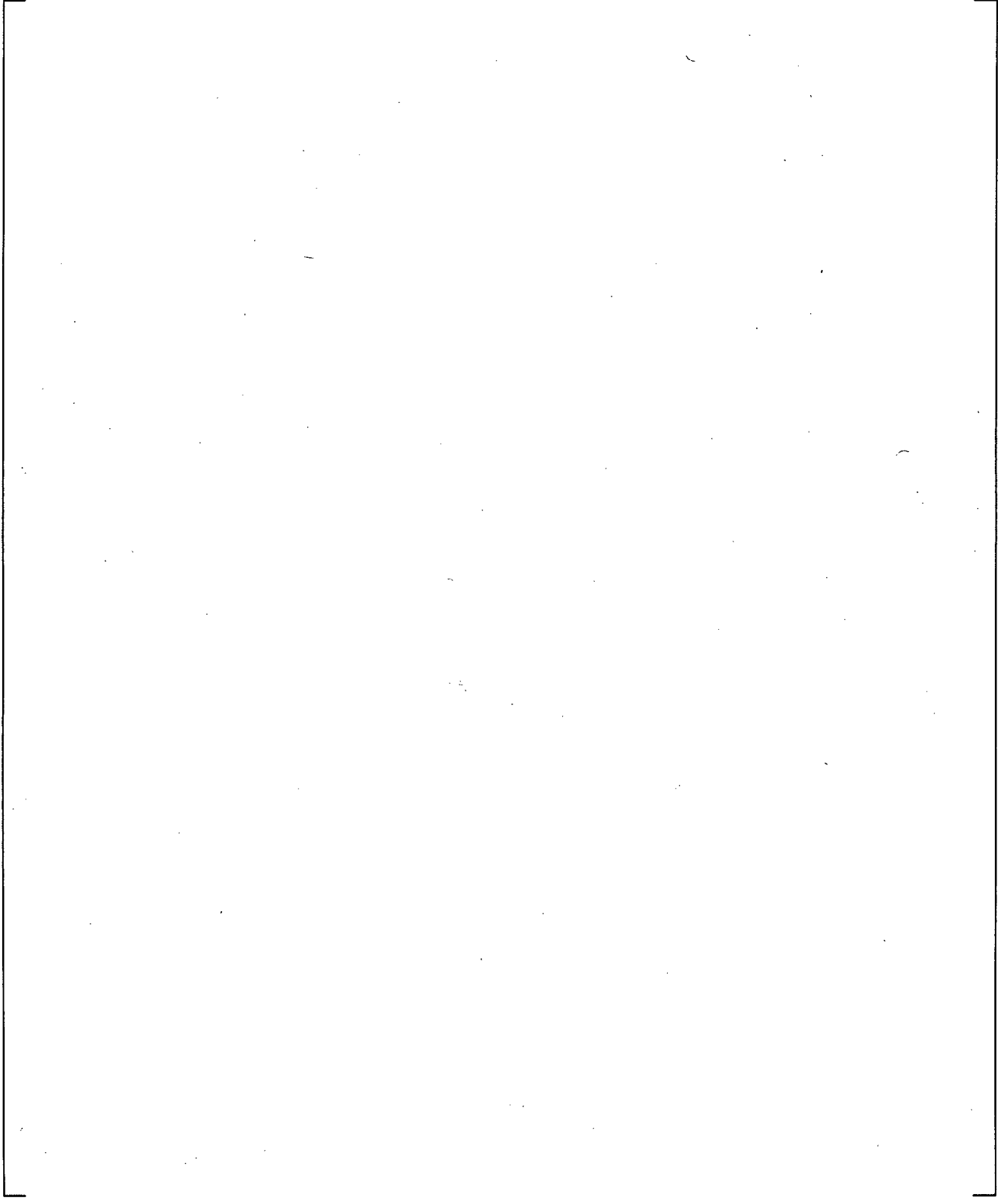


**Figure 19.6-20 CCTF Run 62 Cladding Temperature at 6.0 ft for Channel 9 (Rod 6)**

**Figure 19.6-21 CCTF Run 62 Cladding Temperature at 8.0 ft for Channel 9 (Rod 6)**

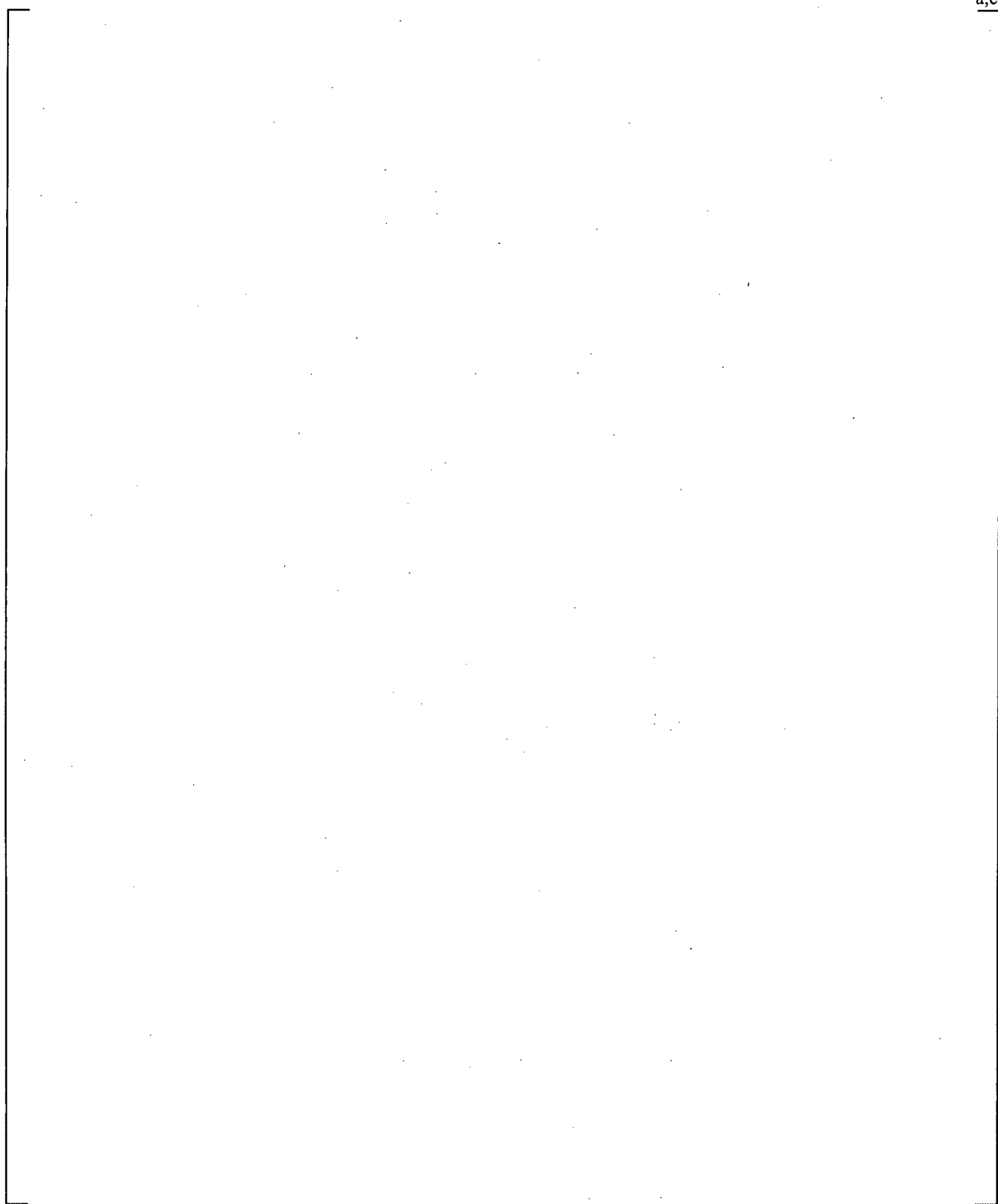


**Figure 19.6-22 CCTF Run 62 Cladding Temperature at 10.0 ft for Channel 9 (Rod 6)**

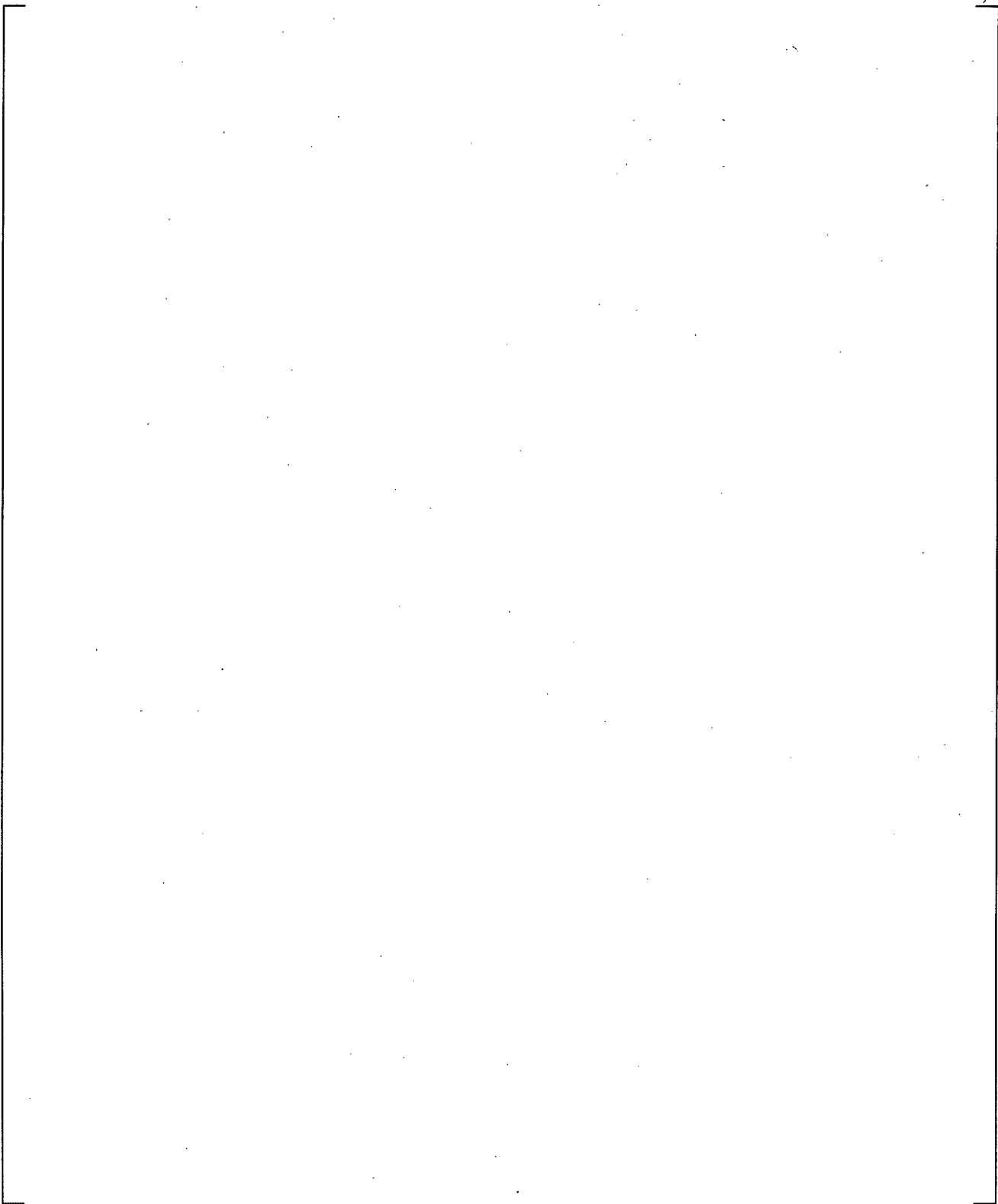


**Figure 19.6-23 CCTF Run 62 Vapor Temperature at 6.0 ft for Channel 9**

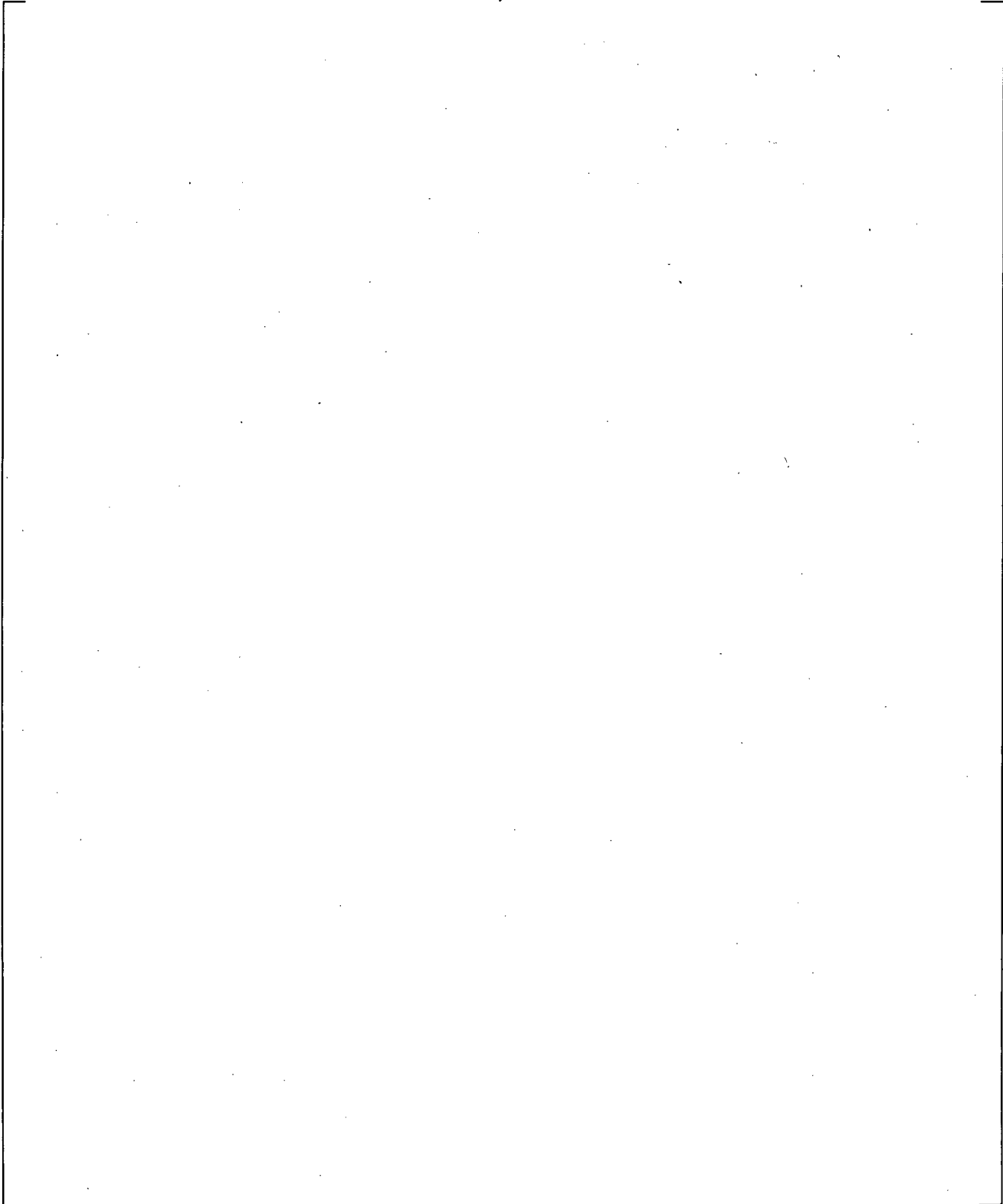


**Figure 19.6-24 CCTF Run 62 Liquid Level in Core**

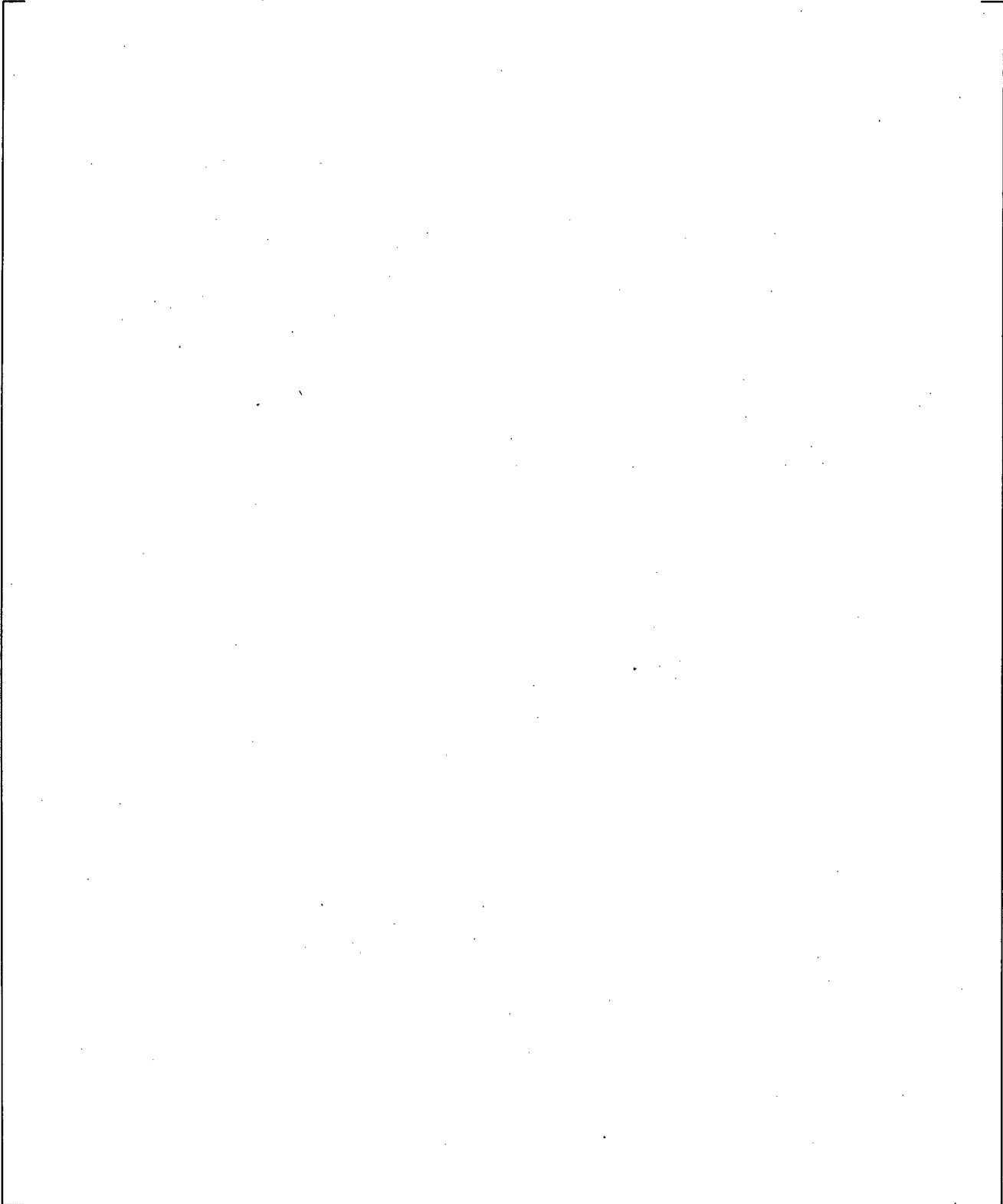


**Figure 19.6-25 CCTF Run 62 Liquid Level in Upper Plenum**

a,c

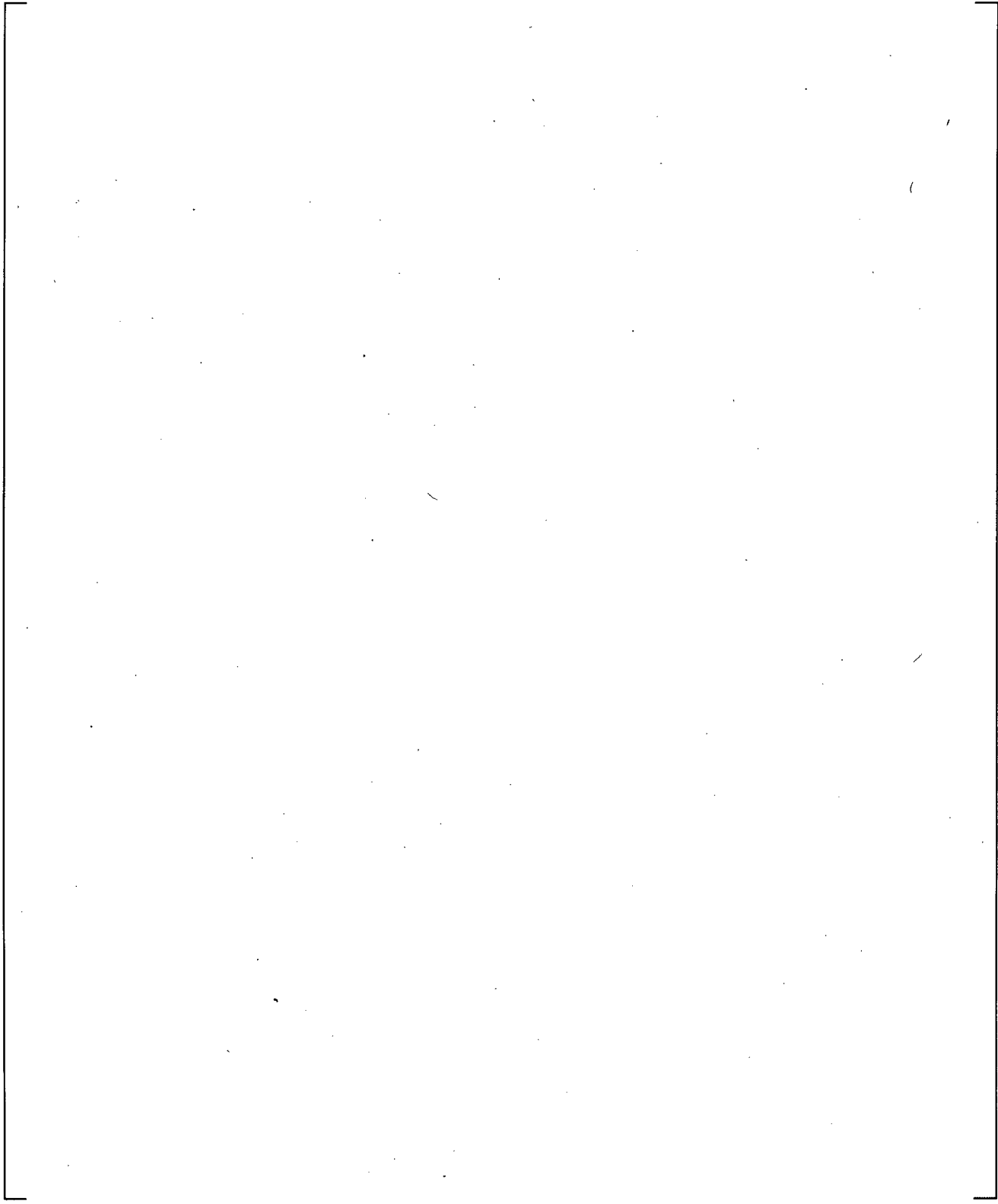


**Figure 19.6-26 CCTF Run 62 Pressure Difference from Lower Plenum to Upper Plenum**

a,c

**Figure 19.6-27 CCTF Run 62 Pressure Difference from Lower Plenum to Top of Downcomer**

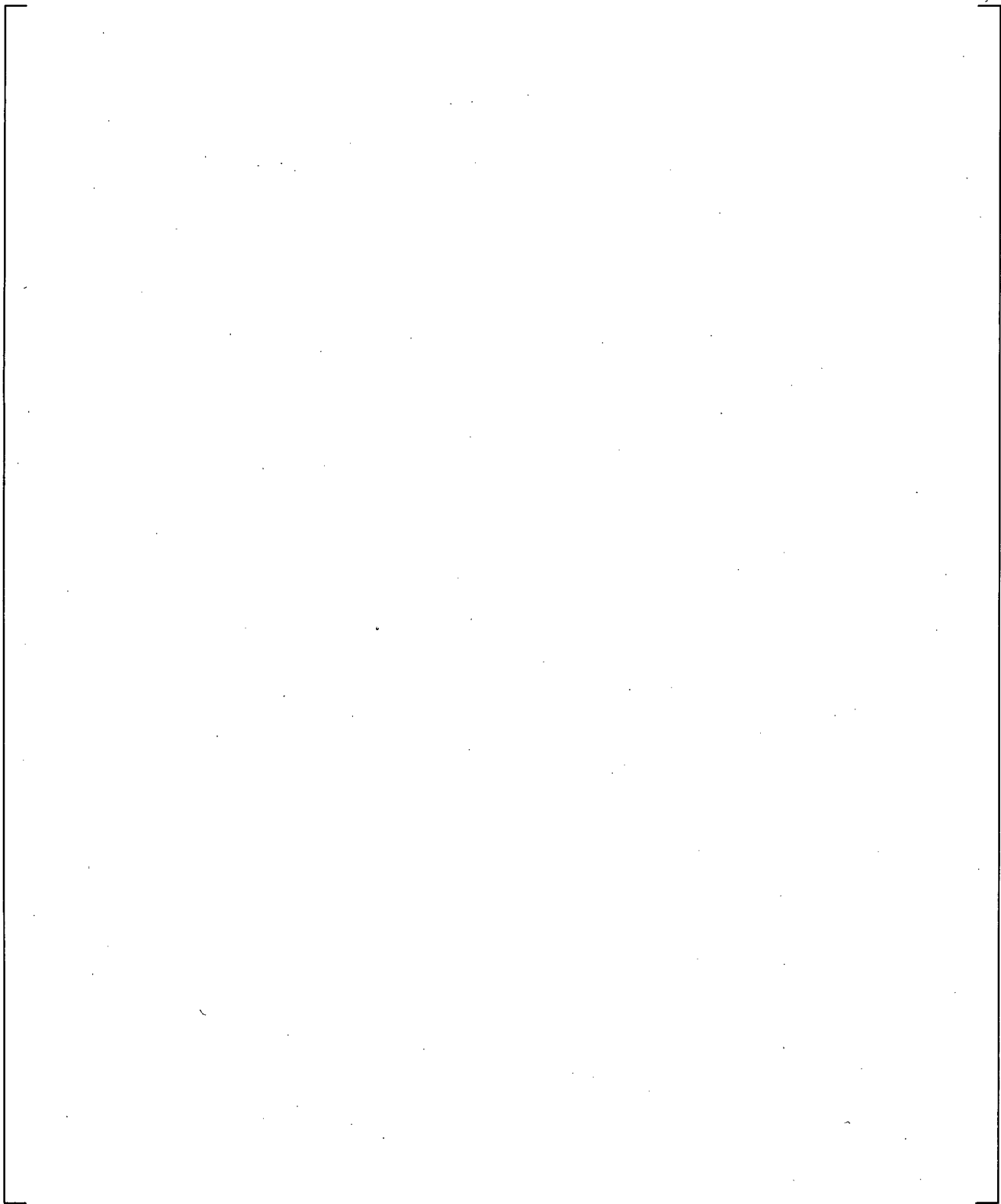


**Figure 19.6-28 CCTF Run 62 Pressure Difference across Intact Loop**

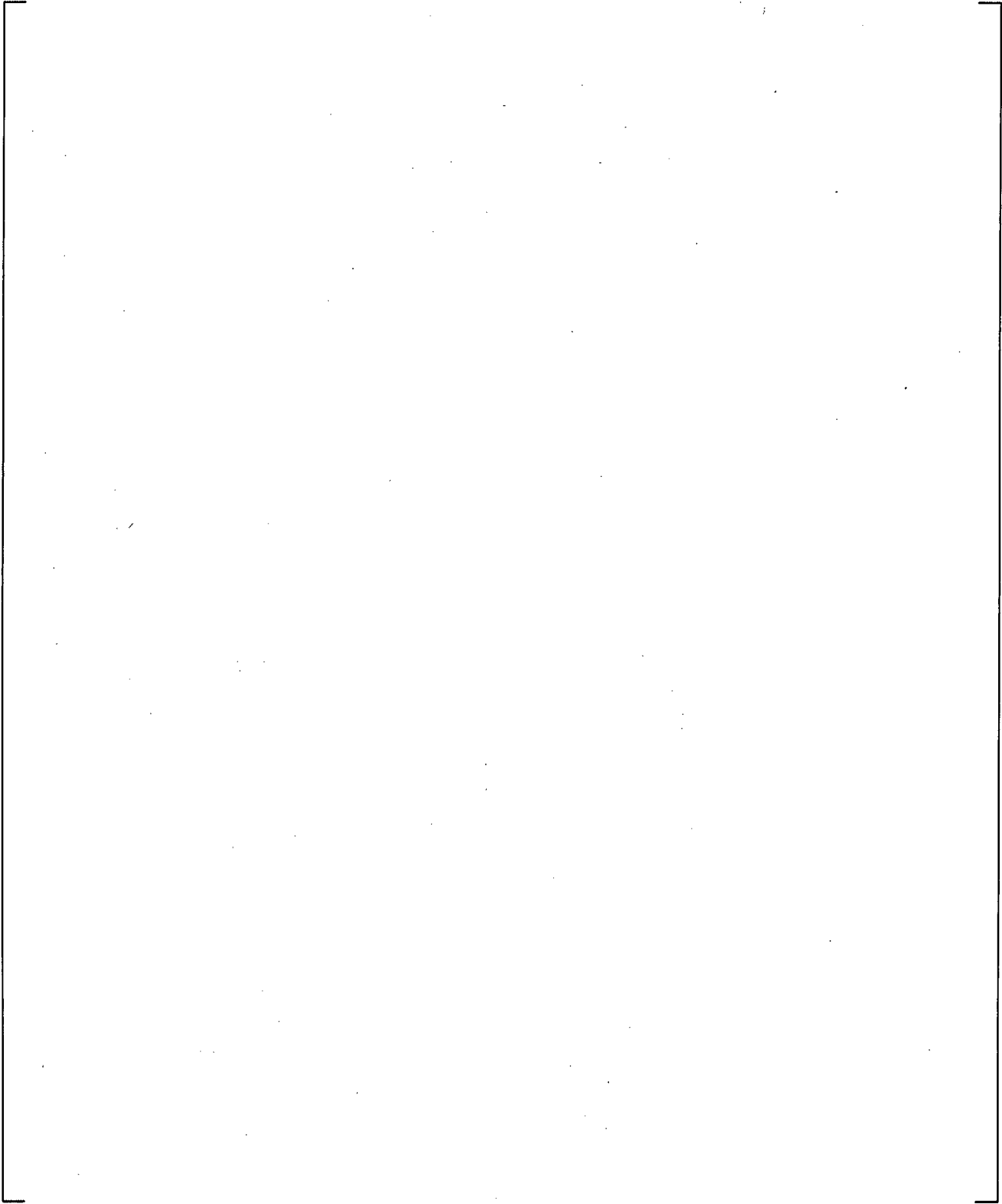


**Figure 19.6-29 CCTF Run 62 Pressure Difference across Broken Loop**

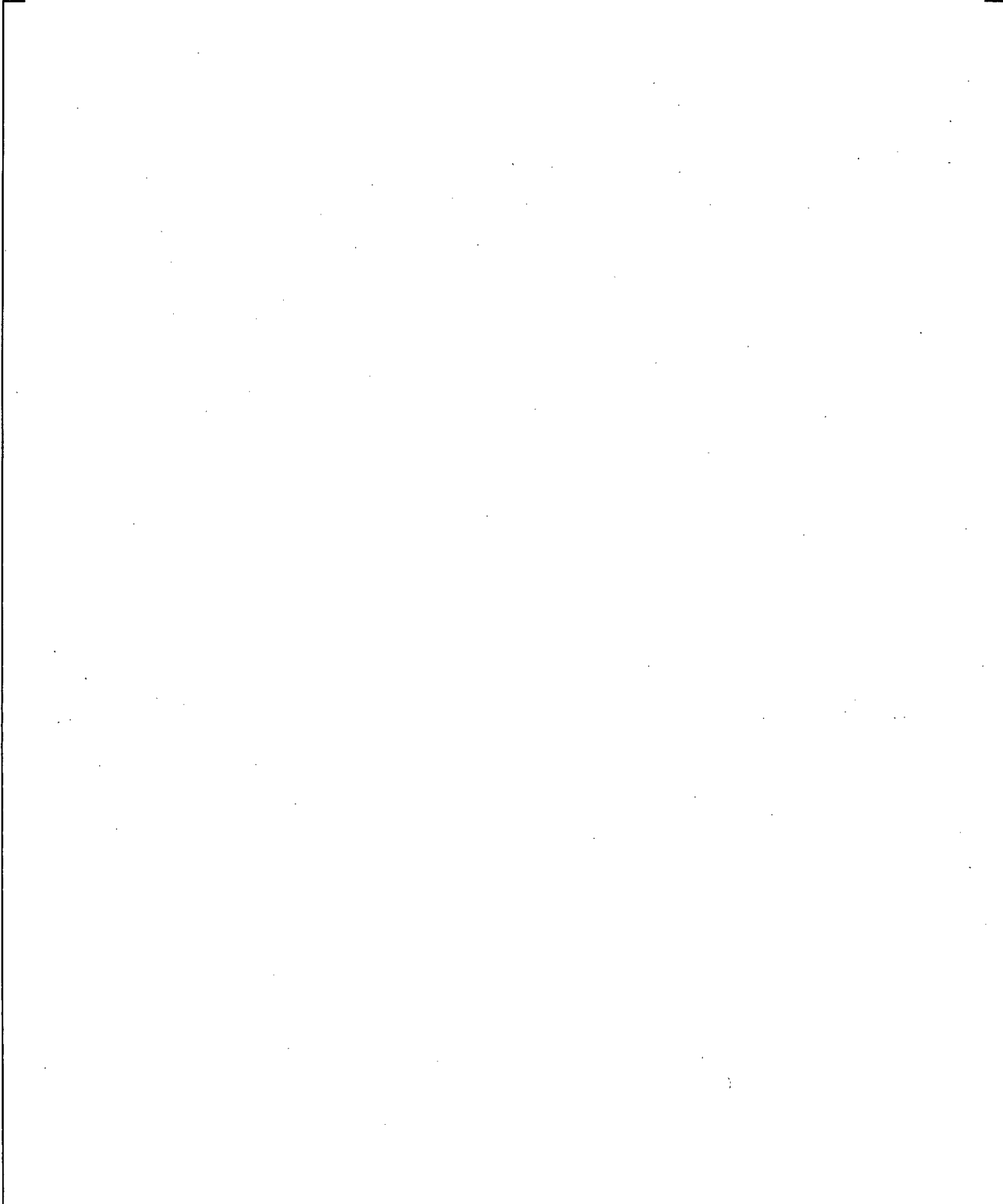


**Figure 19.6-30 CCTF Run 62 Pressure Difference across Steam Generators; Averaged for 3 Intact Loops**

**Figure 19.6-31 CCTF Run 62 Temperature Rise across Steam Generator of Loop 1**

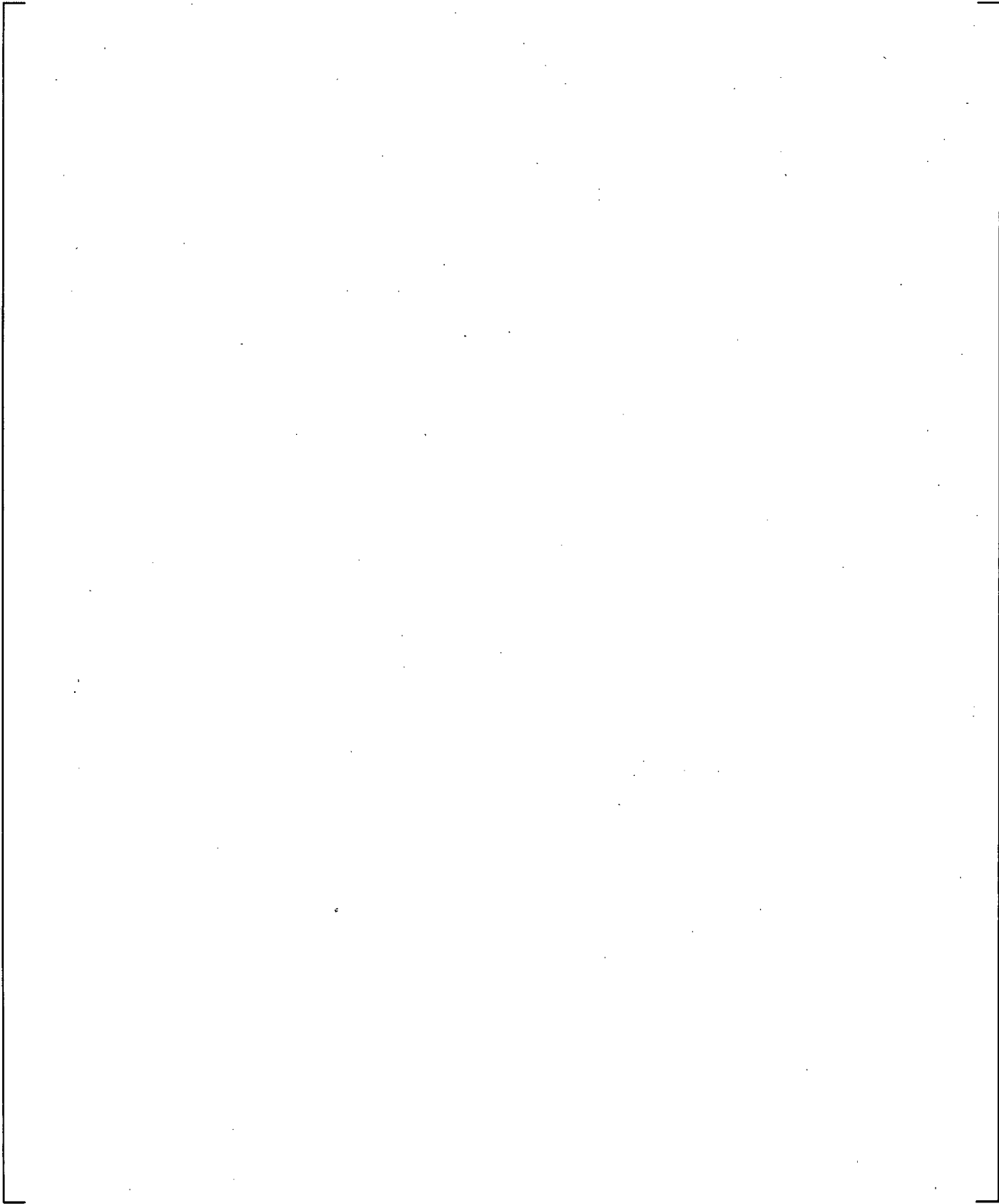


**Figure 19.6-32 CCTF Run 62 Temperature Rise across Steam Generator of Loop 2**

**Figure 19.6-33 CCTF Run 62 Temperature Rise across Steam Generator of Loop 3**

a,c

**Figure 19.6-34 CCTF Run 62 Total (Liquid and Vapor) Mass Flow Rate in Intact Loop Hot Leg**

a,c

**Figure 19.6-35 CCTF Run 62 Total (Liquid and Vapor) Mass Flow Rate in Broken Loop Hot Leg**

a,c

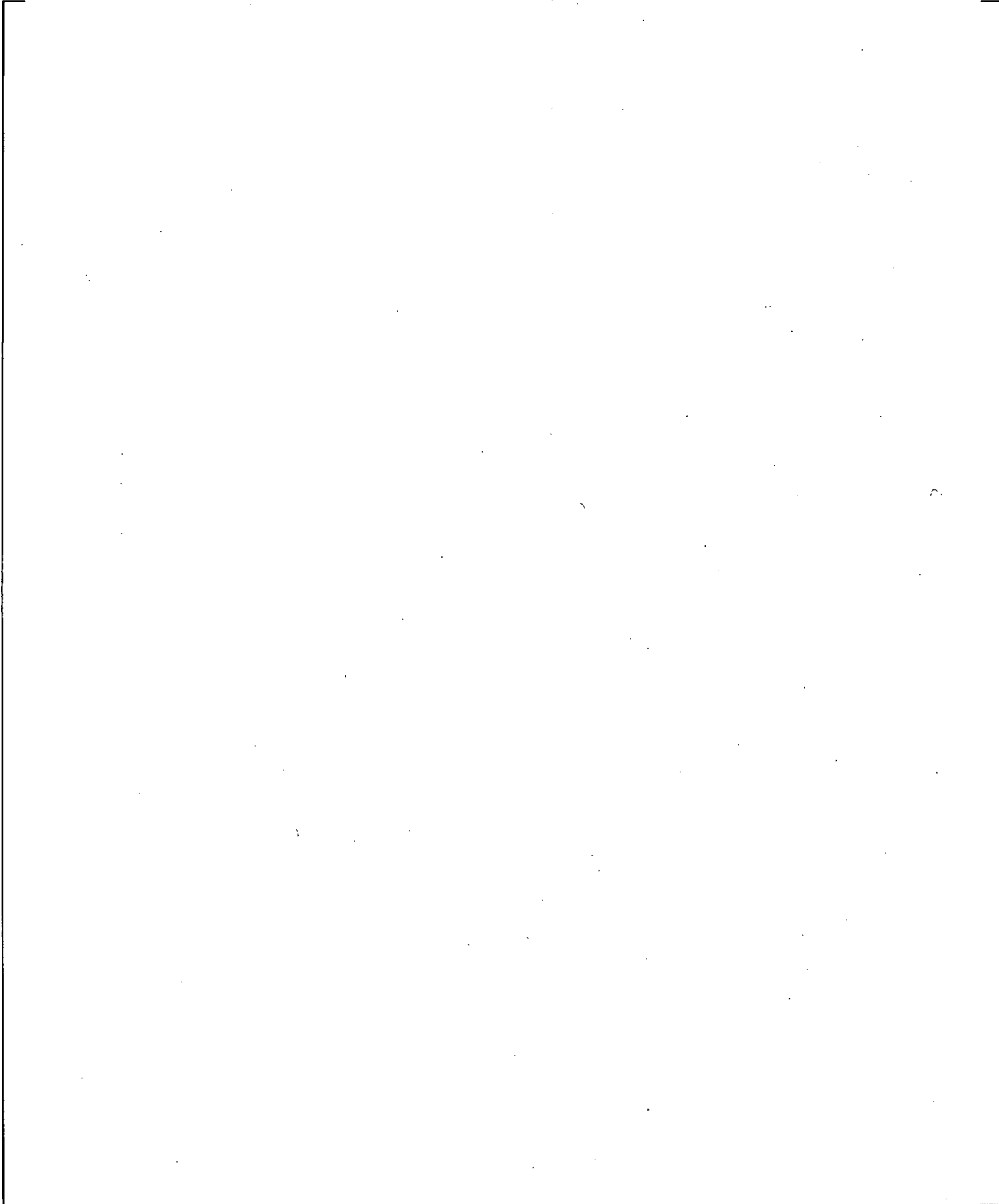


**Figure 19.6-36 CCTF Run 62 Core Inlet Mass Flow Rate**

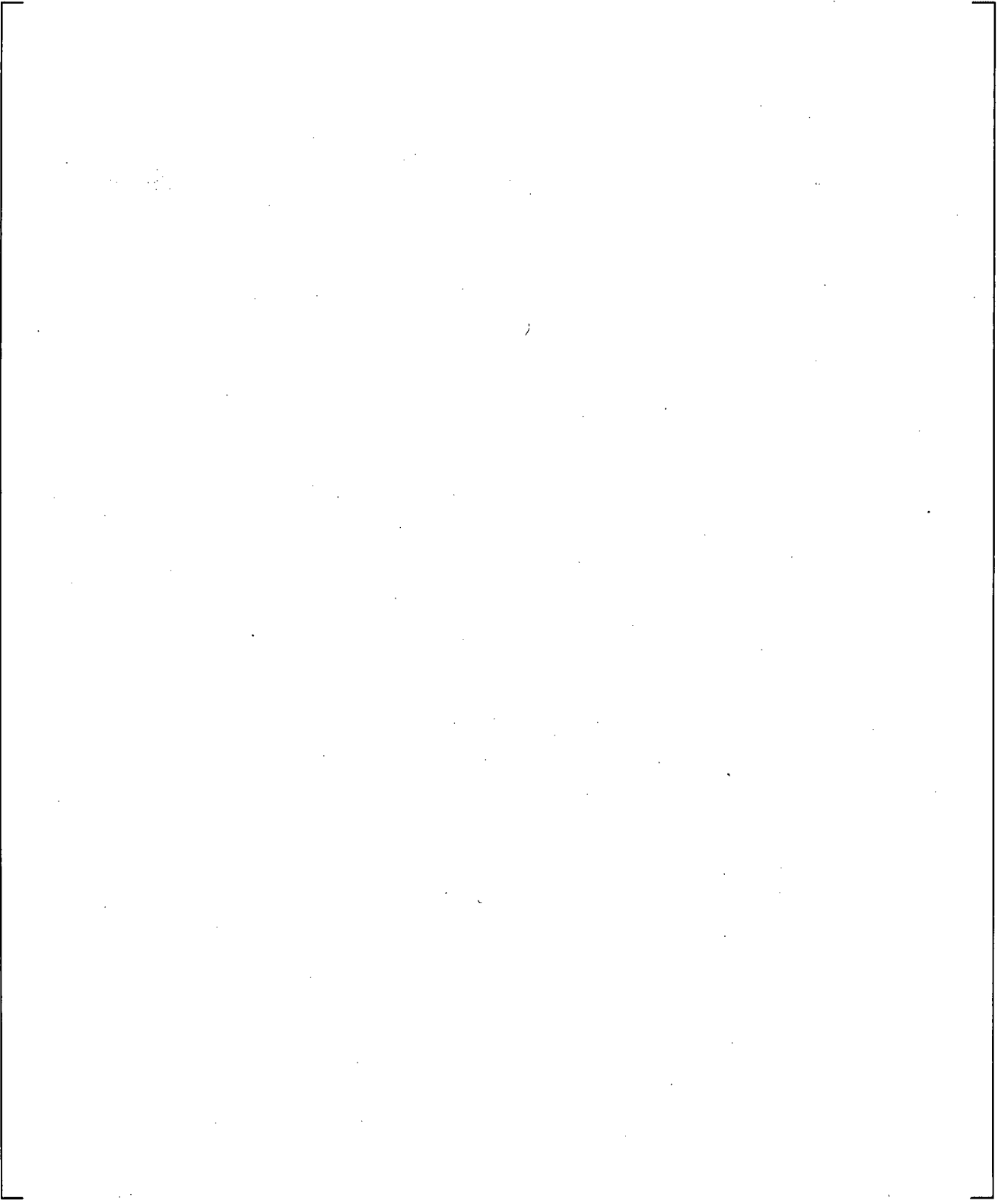


**Figure 19.6-37 CCTF Run 62 Time Step Sensitivity Study: Cladding Temperature at 6.0 ft.**

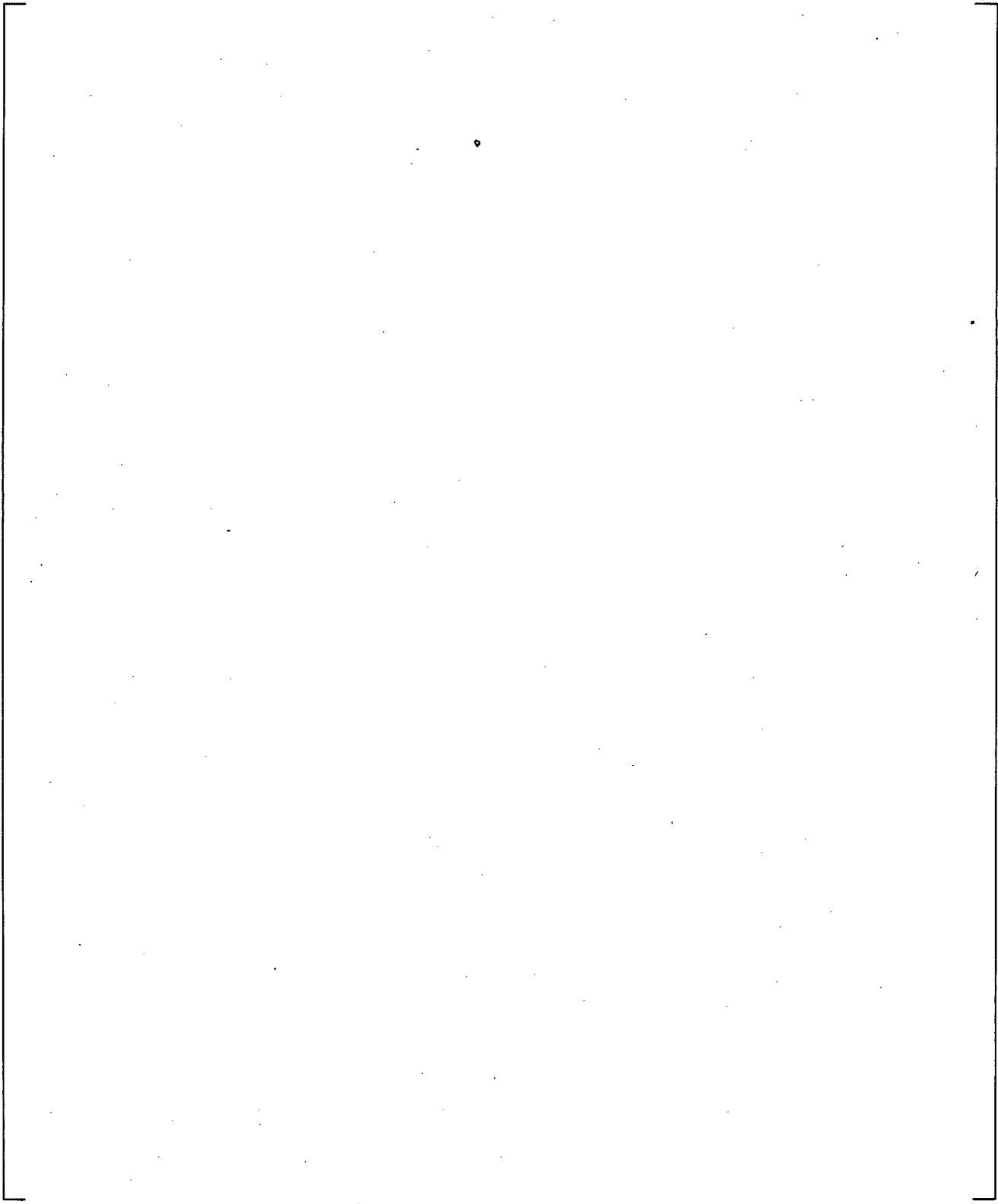


**Figure 19.6-38 CCTF Run 62 Time Step Sensitivity Study: Cladding Temperature at 8.0 ft.**

**Figure 19.6-39 CCTF Run 62 Time Step Sensitivity Study: Cladding Temperature at 10.0 ft.**

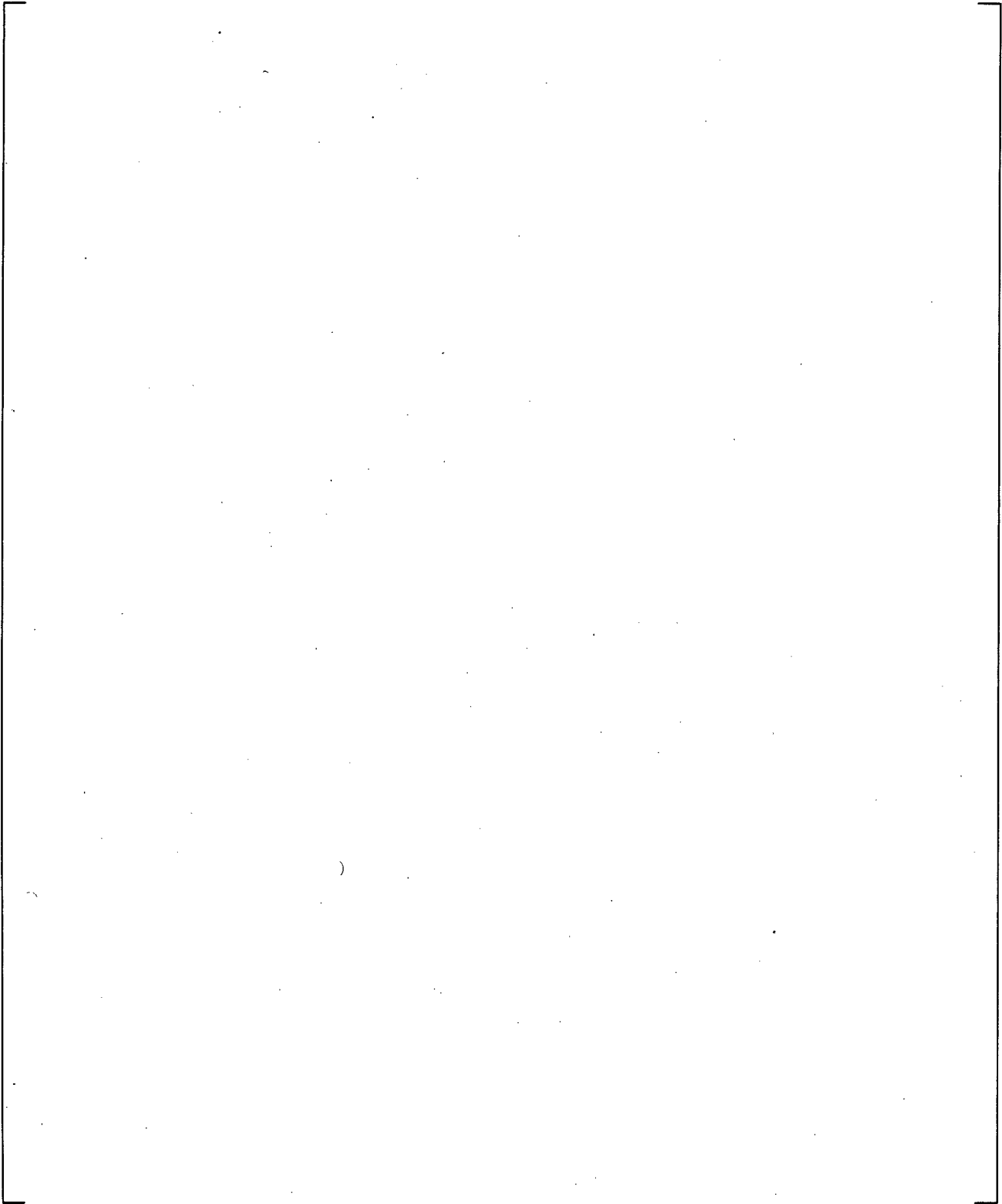


**Figure 19.6-40 CCTF Run 62 Time Step Sensitivity Study: Collapsed Liquid Level in Core**

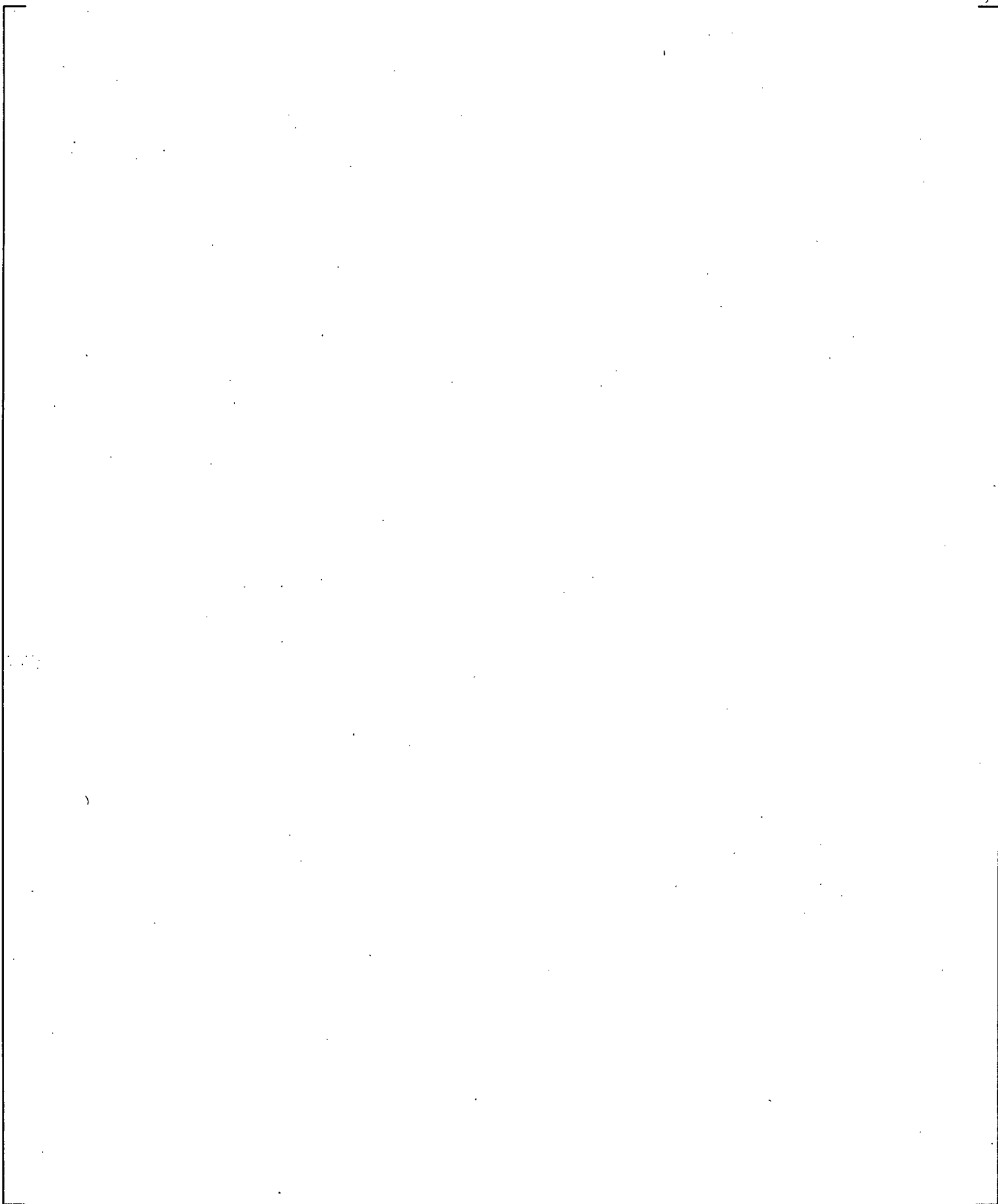


**Figure 19.6-41 CCTF Run 62 Time Step Sensitivity Study: Collapsed Liquid Level in Upper Plenum**

**Figure 19.6-42 CCTF Run 62 Time Step Sensitivity Study: Pressure Difference from Lower Plenum to Upper Plenum**

a,c

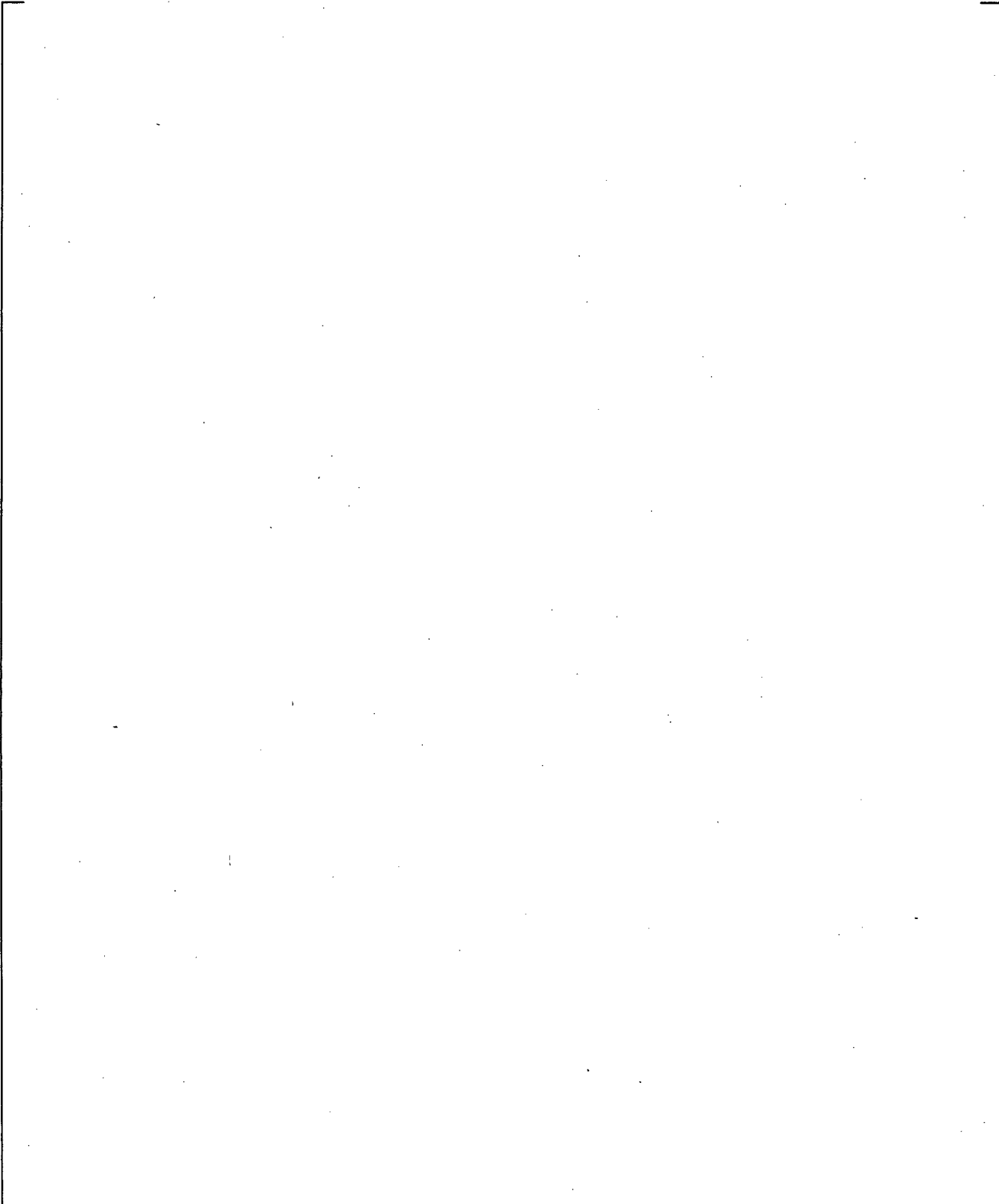


**Figure 19.6-43 CCTF Run 62 Time Step Sensitivity Study: Pressure Difference from Cold Leg Nozzle to Upper Plenum**

## 19.7 CONCLUSIONS

The results of the assessment of CCFL, entrainment and de-entrainment, and condensation documented in these sections are summarized as follows. The assessment includes Separate Effects Tests of UPTF 6, UPTF 8A, UPTF 25A, UPTF 29B, FLECHT, and perforated plate, and CCTF-62 Integral Effects Tests.

### Counter Current Flow Limiting (CCFL)

1. CCFL in a Downcomer Annulus – CCFL/ECC bypass in the downcomer annulus of the full-scale UPTF facility was evaluated in Section 19.3, where WCOBRA/TRAC-TF2 results were compared to experimental data for the UPTF 6 tests. [

] <sup>a,c</sup>

2. CCFL in a Perforated Plate – The perforated plate analysis documented in Section 19.4 shows that that the WCOBRA/TRAC-TF2 predictions [

] <sup>a,c</sup>

3. CCFL in the Steam Generators – This is addressed in Section 21. [

] <sup>a,c</sup>

### Entrainment and De-Entrainment

As discussed in the previous Section 19.1, the predictive capability of WCOBRA/TRAC-TF2 for entrainment and de-entrainment phenomena needs to be assessed for the following conditions:

1. Upper Plenum Entrainment and Carryover – UPTF Test 29B has been simulated and the predicted upper plenum inventories were compared to test data in Section 19.3.14. [

] <sup>a,c</sup>

2. Downcomer Entrainment, During ECC Bypass Period and During Reflood – UPTF Tests 6 and 25A were simulated and the results were used to examine the ability to model the entrainment process in the downcomer in Sections 19.3.5 and 19.3.9, respectively. [

] <sup>a,c</sup>

3. [

] <sup>a,c</sup>

4. Entrainment During Bottom Reflood – The ability of WCOBRA/TRAC-TF2 to calculate the entrainment rate at a quench front was evaluated by comparing the predicted bundle mass, carryout fraction and exit flows to experimental data from the FLECHT forced reflood facilities in Section 19.5. [

] <sup>a,c</sup>

### Condensation

1. Condensation in Downcomer Annulus – Condensation, CCFL, and entrainment/de-entrainment in the downcomer are inter-related physical processes that affect the ability to predict end-of-bypass and beginning of reflood. [

] <sup>a,c</sup>

2. Condensation in Cold Legs, at Low Pressure – [

] <sup>a,c</sup>

3. Effect of Non-Condensable Gases on Condensation – Non-condensable effects on interfacial heat transfer in the 1D and 3D components were assessed in Section 20.

### Integral Effects Assessment

The results from the CCTF 62 test show the code giving [

] <sup>a,c</sup>. The comparisons between the prediction and the measurements show that WCOBRA/TRAC-TF2 predicts the overall thermal-hydraulics of a reflood transient properly. In particular, [

] <sup>a,c</sup>

## 19.8 REFERENCES

1. 2D/3D Program Upper Plenum Test Facility Quick Look Report, 1989, "Test No. 6; Downcomer Countercurrent Flow Test," Siemens/KWU U9 316/89/2.
2. 2D/3D Program Upper Plenum Test Facility Experimental Data Report, 1990, "Test No. 25, Downcomer/Cold Leg Steam/Water Interaction Test," E314/90/11, KWU.
3. 2D/3D Program Upper Plenum Test Facility Experimental Data Report, 1988, "Test No. 8, Cold/Hot Leg Flow Pattern Test," U9 316/88/12, KWU.
4. 2D/3D Program Upper Plenum Test Facility Experimental Data Report, 1988, "Test No. 10, Tie-Plate Countercurrent Flow Test," U9 316/88/1, KWU.
5. 2D/3D Program Upper Plenum Test Facility Quick Look Report, 1990, "Test No. 21; Downcomer Injection Test," Siemens/KWU E314/90/16.
6. 2D/3D Program Upper Plenum Test Facility Experimental Data Report, 1990, "Test No. 29, Entrainment/De-entrainment Test," E314/90/05, KWU.
7. Akimoto, H., et al., 1984a, "Data Report on Large Scale Reflood Test – 84 – CCTF CORE-II TEST C2-6 (RUN 064) –," Department of Nuclear Safety Research, Tokai Research Establishment, JAERI-memo – 59-452.
8. Akimoto, H., et al., 1984b, "Data Report on Large Scale Reflood Test – 86 – CCTF CORE-II TEST C2-8 (RUN 067) –," Department of Nuclear Safety Research, Tokai Research Establishment, JAERI-memo – 59-453.
9. Akimoto, H., et al., 1984c, "Pressure Drop through Broken Cold Leg During Reflood Phase of Loss-of-Coolant Accident of PWR," Journal of Nuclear Science and Technology, 21 [6].
10. Bajorek, S. M., et al., 1998, "Code Qualification Document for Best-estimate LOCA Analysis," WCAP-12945-P-A, Volume 1, Revision 2, and Volumes 2 through 5, Revision 1, and WCAP-14747 (Non-Proprietary)
11. Cousins, L. B., et al., 1965, "Liquid Mass Transfer in Annular Two-Phase Flow," Paper C4, Symposium on Two-Phase Flow, Volume 2, Exeter, England.
12. Dallman, J. C., and Kirchner, W. L., 1980, "De-Entrainment Phenomena on Vertical Tubes in Droplet Cross Flow," NUREG/CR-1421.
13. Glaeser, H., 1992, "Downcomer and Tie Plate Countercurrent Flow in the Upper Plenum Test Facility (UPTF)," Nucl. Eng. Des., 133.
14. Hochreiter, L. E., et al., 1988, "Westinghouse Large Break LOCA Methodology, Volume 1: Model Description and Validation," WCAP-10924-P-A.

15. Hsieh, C., et al., 1980, "Countercurrent Air/Water and Steam/Water Flow above a Perforated Plate," NUREG/CR-1808.
16. Kataoka, I. and Ishii, M., 1983, "Mechanistic Modeling and Correlations for Pool Entrainment
17. Iguchi, T., et al., 1984, "Data Report on Large Scale Reflood Test – 83 – CCTF CORE-II TEST C2-5 (RUN 063) –," Department of Nuclear Safety Research, Tokai Research Establishment, JAERI-memo – 59-451.
18. MPR Associates, 1990a, "Summary of Results from the UPTF Downcomer Separate Effects Tests, Comparison to Previous Scaled Tests, and Application to U.S. PWRs," MPR-1163.
19. MPR Associates, 1990b, "Summary of Results from the UPTF Carryover/Steam Binding Separate Effects Tests, Comparison to Previous Scaled Tests, and Application to U.S. Pressurized Water Reactors," MPR-1213.
20. MPR Associates, 1992, "Summary of Results from the UPTF Cold Leg Flow Regime Separate Effects Tests, Comparison to Previous Scaled Tests, and Application to U.S. Pressurized Water Reactors," MPR-1208.
21. MPR Associates, 1993, "Reactor Safety Issues Resolved by the 2D/3D Program," MPR-1346.
22. Okubo, T., et al., 1984, "Data Report on Large Scale Reflood Test – 82 – CCTF CORE-II TEST C2-4 (RUN 062) –," Department of Nuclear Safety Research, Tokai Research Establishment, JAERI-memo – 59-450.
23. Okubo, T., Iguchi, T., Okabe, K., Sugimoto, J., Akimoto, H., and Murao, Y., 1985, "Evaluation Report on CCTF Core-II Reflood Test C2-4 (Run 62)," JAERI-M 85-026.
24. USNRC Regulatory Guide 1.157, 1989, "Best-Estimate Calculations of Emergency Core Cooling System Performance."
25. Walley, P. B., et al., 1973, "Experimental Wave and Entrainment Measurements in Vertical Annular Two-Phase Flow," AERE-R7521, Atomic Energy Research Establishment, Harwell, England.
26. Wallis, G. B., 1969, "One-Dimensional Two-Phase Flow," McGraw-Hill Inc., NY.
27. Waring, J. P., et al., 1975, "PWR FLECHT-SET Phase B Evaluation Report," WCAP-8583.

## 20 ADDITIONAL COMPONENT MODEL ASSESSMENTS

This section provides additional validation of components not individually addressed in previous sections. Section 20.1 examines the accumulator component, Section 20.2 examines the pump, and Section 20.3 presents a control-volume verification of mass and energy conservation at the 1D/3D junction. The momentum coupling treatment and assessment is discussed in Section 19.3.5.10 regarding the cold leg nozzle loss coefficient.

### 20.1 ACCUMULATOR COMPONENT

#### 20.1.1 Introduction

The accumulator component model was described in Volume I, Section 10.8. That section also described the phases of accumulator water injection, emptying, and accumulator nitrogen discharge.

The Phenomena Identification and Ranking Table (PIRT) identifies 3 highly ranked phenomena associated with the accumulator behavior during a LOCA transient:

1. **Injection Flow Rate/Flow Resistance.** The delivery flow rate of the accumulator is of high or medium importance for the whole spectrum of postulated LOCAs: for the smaller breaks, injection from the accumulator is responsible for terminating the transient and limiting the duration of clad heatup (medium rank). For intermediate and large breaks, injection from the accumulator is responsible for re-filling the downcomer and initiating reflood, and the flow rate/flow resistance is ranked high. The IPP and Callaway Blowdown Tests, as described in Sections 20.1.2 and 20.1.3, document the capability of a simplified accumulator model in adequately predicting accumulator injection flow rate both under rapid discharge conditions (i.e., larger break scenarios) and gradual discharge conditions (i.e., smaller break scenarios). In addition to these separate effect tests, the accumulator discharge is analyzed in the ROSA and LOFT integral effect tests, as documented in Sections 21 and 22. Finally, the accumulator discharge for the LOFT 2-5 and ACHILLES tests are documented in Section 20.1.4.
2. **Nitrogen Discharge (Non-condensable effects).** The accumulator nitrogen provides the main source of non-condensable gas in the system during the LOCA transient. While the potential effects of non-condensables are discussed elsewhere as applicable, it is recognized that the accumulator cover gas provides the main source of non-condensable gas in the system, and thus the discharge process and impact on the transient is discussed herein. In general, large amounts of non-condensable gas will be released from the accumulator only during the larger breaks (for the period of interest in the analysis), and thus the assessment is focused on these break sizes. The LOFT 2-5 and ACHILLES tests documented in Section 20.1.4 are used to assess the discharge of nitrogen from the accumulator and the effect on the PWR reflood transient.
3. **Broken Loop Accumulator Treatment.** The approach and justification for the treatment of the accumulator in the broken loop for different break sizes is discussed in Section 26.2.1.3 and with plant scoping studies in Section 28.2.6.

This overall assessment demonstrates the adequacy of the accumulator model documented in Volume I, Section 10.8.

### 20.1.2 IPP Accumulator Test

An accumulator blowdown test was performed at Indian Point Unit 2 (IPP) in 1971 during startup testing. The initial gas pressure in the accumulator was about 100 psig, the gas volume was about 400 cubic feet and the water volume was 700 cubic feet. Test runs were performed at ambient temperature (80°F), with RCS back pressure of 0 psig. The cold legs were empty and water level in the vessel was well below the cold leg nozzle elevation. The control valves used to initiate the test runs were set to open from 0 to 100 percent in 10 seconds. Test runs were performed for the four accumulators which had various accumulator line lengths. The test runs would terminate when the pressure in the accumulator reached approximately 20 psig while the accumulator line was still in single-phase liquid flow. The measured pressure responses of the four accumulators were all similar. Pressure response for one of the accumulators was selected for WCOBRA/TRAC-TF2 model verification. Figure 20.1-1 is a sketch showing the layout of the accumulator piping.

#### 20.1.2.1 WCOBRA/TRAC-TF2 Model

A WCOBRA/TRAC-TF2 model was constructed to simulate the accumulator test. A typical PWR model of the accumulator and its piping consists of [

] <sup>a,c</sup> as shown in Figure 20.1-2. [

] <sup>a,c</sup> In this model, the RCS was simulated by a BREAK component, supplying a constant back pressure. The volume, length, and hydraulic diameter for the accumulator and the accumulator line were all preserved. [

] <sup>a,c</sup> Section 28.1.5 presents a large break LOCA sensitivity study with an accumulator elevation varying [

] <sup>a,c</sup>

The resistance in the accumulator line was simulated [

] <sup>a,c</sup>. The initial and boundary conditions were the same as those used in the 1971 IPP test. Both the water and nitrogen cover gas were initially at 80°F. A steady-state run of 20 seconds was first performed, followed by a blowdown run initiated by opening a control valve in the accumulator line. The valve reached 100 percent opening within the first 10 seconds of the blowdown run.

#### 20.1.2.2 WCOBRA/TRAC-TF2 Simulation Results

The accumulator pressure predicted by WCOBRA/TRAC-TF2 is compared to measured test data (the only data available) in Figure 20.1-3. It can be seen that WCOBRA/TRAC-TF2 prediction and test data are in good agreement [

] <sup>a,c</sup>

[

] <sup>a,c</sup>

### 20.1.3 Callaway Accumulator Test

In order to evaluate the small break LOCA ECCS model, Westinghouse, with the cooperation of the personnel of the Callaway Nuclear Plant, conducted a slow accumulator blowdown test at the plant in December 1982.

In order to simulate the accumulator discharge during a small break LOCA within constraints of the plant, the accumulators would discharge into an empty reactor vessel from normal pressure. The discharge was extended by using an orifice to restrict the flow so that the tank would empty at a prescribed time. An orifice plate was installed in the outlet nozzle of the accumulator. The [

] <sup>a,c</sup> was calculated to result in a discharge time of approximately 15 minutes.

The test was conducted by opening the motor operated gate valve which would allow the tank to drain and the data to be recorded. The test was performed from an initial pressure of 600 psig and with initial water volume of 850 cubic feet.

The opening time of the accumulator isolation valve was 11 seconds. The time required for the water to discharge from the accumulator was 954 seconds.

#### 20.1.3.1 WCOBRA/TRAC-TF2 Model

The Callaway small break accumulator blowdown was simulated [

] <sup>a,c</sup>. Water and gas volumes, as well as the accumulator discharge nozzle diameter were preserved to accurately represent the test conditions. [

] <sup>a,c</sup> Liquid and gas temperatures were set to 87°F, consistent with test data.

#### 20.1.3.2 WCOBRA/TRAC-TF2 Simulation Results

Figure 20.1-6 shows a comparison of the accumulator pressure and the test data. [

] <sup>a,c</sup>

[

] <sup>a,c</sup>

#### 20.1.4 Effect of Accumulator Nitrogen on PWR Reflood Transients

In Appendix K-based evaluation models, simple models were incorporated to simulate the effect of the nitrogen injecting from the accumulator into the cold legs and out the break for approximately 30 seconds during reflood. The effect of the nitrogen is to pressurize the downcomer and force water into the core, while promoting core cooling. Typically, the effect of nitrogen was ignored in these earlier evaluation models.

The previous Westinghouse Best-Estimate LOCA methodologies (CQD and ASTRUM) used experimental evidence to support the conclusion that the effect of accumulator nitrogen realistically improves reflood rates and heat transfer. A simplified method was developed for WCOBRA/TRAC MOD7A to treat the effects of accumulator discharge on the reflood transient, without considering an explicit transport of the non-condensable gases.

WCOBRA/TRAC-TF2 explicitly provides the capability of treating non-condensable gases, which allows more mechanistic treatment of the effects of the nitrogen discharge on the reflood transient, without the need of a simplified model. The experimental evidence that assesses the WCOBRA/TRAC-TF2 on modeling the effects of the nitrogen discharge on the reflood transient is discussed below.

#### 20.1.4.1 LOFT Test L2-5

The description of the LOFT facility and tests are provided in Sections 22.2 and 22.3, and the WCOBRA/TRAC-TF2 input models and simulation results of the six simulated LOFT tests, including L2-5, are presented in Section 22.4.

The sequence of events for the LOFT large break Test L2-5 (Bayless et al., 1982) during the period of accumulator flow is similar to that calculated for a typical plant transient. The accumulator liquid flows down into the downcomer directly below the intact loop cold leg nozzle while steam and dispersed liquid flows up the opposite side and out of the cold leg break during the blowdown. Toward the end of the period of accumulator flow, the downcomer is partially full of subcooled liquid.

As the LOFT accumulator empties of liquid, the nitrogen contained in the accumulator begins to flow down the accumulator line and into the cold leg. Figures 20.1-10 and 20.1-11 show the accumulator liquid level and pressure for Test L2-5. From the density measurement in the intact loop cold leg, as shown in Figure 20.1-12, the nitrogen in the accumulator entered the RCS after the accumulator emptied at about 50 seconds (Figure 20.1-10).

It can be seen from the core bubble plot (Figure 20.1-13a) that there is an increase in core level beginning at about 43 seconds. By 60 seconds the core is completely covered. Figure 20.1-13b shows the cladding temperature in one of the central bundles at different elevations in the test, and indicates a progressive quenching at two lower elevations, 8 inches and 26 inches from the bottom of the core, from approximately 48 to 60 seconds, respectively. Therefore, the appearance of the nitrogen in the downcomer does not cause a simultaneous sudden quench at these two different elevations.

A more recent analysis of the LOFT Self-Power Neutron Detectors (SPNDs) (Mackley and Birchley, 1985) provides further qualitative evidence of the density of the fluid in the LOFT core. Figure 20.1-14 shows the fluid densities in the central fuel bundle for LOFT Test L2-5 at elevations of 27 and 44 inches above the bottom of the core, and the fuel clad temperature transients at the same elevations were also co-plotted with the fluid densities respectively. In this experiment, the peripheral low power regions of the core were quenched either during blowdown or by the liquid entering the core prior to 60 seconds, and the high power regions were quenched by 60 seconds.

Evidence of the effect of nitrogen on the downcomer pressure is shown in Figure 20.1-15. A sudden increase in pressure is observed in the suppression tank at 60 seconds, coincident with the time that nitrogen enters the cold leg from the accumulator.

#### 20.1.4.2 WCOBRA/TRAC Prediction of LOFT Reflood Transient

In the simulation of the LOFT tests (Section 22.3), the accumulators were modeled as in a PWR, [

] <sup>a,c</sup> The

simulation results show that the accumulator water is predicted to flow down into the downcomer after the check valve in its discharging line is opened by low RCS pressure and makes its way into the cold leg and vessel. [ ] <sup>a,c</sup>

[

] <sup>a,c</sup>

#### 20.1.4.3 ACHILLES Experiments

A series of reflood heat transfer experiments were conducted in the ACHILLES test facility, using boundary conditions based on best-estimate computer code calculations (Dore and Denham, 1990). Two types of tests were conducted; “forced” reflood experiments, in which the downcomer water was forced into the core by applying a high nitrogen overpressure, and “natural” reflood experiments, in which the nitrogen overpressure was created by nitrogen discharged from a scaled accumulator. In both

types of tests, the initial surge of water resulted in significant cooling, and entrainment of water out of the top of the test bundle. This was followed by a period of poor cooling, until the downcomer driving head could be re-established by the continuation of pumped safety injection. However, the net result was a significant reduction in the maximum cladding temperatures attained, relative to comparable tests with no initial surge into the bundle.

#### 20.1.4.4 WCOBRA/TRAC Prediction of ACHILLES International Standard Problem 25

Westinghouse has used WCOBRA/TRAC-TF2 to simulate International Standard Problem (ISP) number 25 (Holmes, 1991), an experiment which simulated the end of the accumulator discharge period in a postulated large break loss of coolant accident. The test was performed in the ACHILLES test facility at AEA Technology Winfrith. The test facility was described by Denham et al. (1989), and ISP 25 results were reported by Holmes (1991). The facility layout is shown in Figure 20.1-24.

The WCOBRA/TRAC-TF2 model of the ACHILLES test facility is shown in Figure 20.1-25. [

] <sup>a,c</sup>

The test section was modeled [

] <sup>a,c</sup>

[

] <sup>a,c</sup>

Comparisons of the WCOBRA/TRAC-TF2 simulation with the experimental data are shown in Figures 20.1-27 through 20.1-36. Figures 20.1-27 and 20.1-28 show the accumulator depressurization and mass flow rate through the injection line during the early part of the transient. [

] <sup>a,c</sup>

[ ]<sup>a,c</sup>

The predicted pressure loss from the top of the downcomer to the break is compared with the measured pressure loss in Figure 20.1-30. [

] <sup>a,c</sup> The predicted gas mass flow rates to the break are compared with the measured data in Figure 20.1-31. [

] <sup>a,c</sup>

Downcomer and core collapsed liquid levels are shown in Figures 20.1-32 and 20.1-33. [

] <sup>a,c</sup>

Figures 20.1-34 through 20.1-36 show the cladding temperature transients at 1.08m, 2.01m, and 2.65m. [

] <sup>a,c</sup>

### **Broken Pipe Pressure Loss Sensitivity Study**

[

] <sup>a,c</sup>

[

] <sup>a,c</sup>

In general, the ACHILLES test simulation shows that [

] <sup>a,c</sup>

[

] <sup>a,c</sup> However, they do show that the effect of the initial surge on core cooling is reasonably predicted.

### 20.1.5 Conclusion

The accumulator model as used in the PWR, was assessed against both SETs and IETs. The prediction of discharge of subcooled water into the RCS in both LBLOCA and SBLOCA conditions is [

] <sup>a,c</sup>

[  
] <sup>a,c</sup> Therefore, based on the assessment it is concluded that the WCOBRA/TRAC-TF2 accumulator model [  
] <sup>a,c</sup>.

### 20.1.6 References

1. Andreychek, T. A., et al., 1988, "Loss of RHRS Cooling While the RCS is Partially Filled," WCAP-11916.
2. Bayless, P. D., et al., 1982, "Experimental Data Report for LOFT Large-Break Loss-of-Coolant Experiment L2-5," NUREG/CR-2826, EGG-2210.
3. Denham, M. K., et al., 1989, "ACHILLES Unballooned Cluster Experiments Part 1: Description of the ACHILLES Rig, Test Section, and Experimental Procedures," AEEW-R2336.
4. Dore, P. and Denham, M. K., 1990, "ACHILLES Unballooned Cluster Experiments Part 5: Best Estimate Experiments," AEEW-R2412.
5. Holmes, B. J., 1991, "ISP 25 Comparison Report," AEA-TRS-1043.
6. Mackley, A. D. and Birchley, J. C., 1985, "Estimated Post-Scram Reactor Coolant Densities from Prompt Response Self Powered Neutron Detectors in Loss-of-Coolant Experiments," Instrumentation Society of America, 31st International Instrumentation Symposium, San Diego, California.

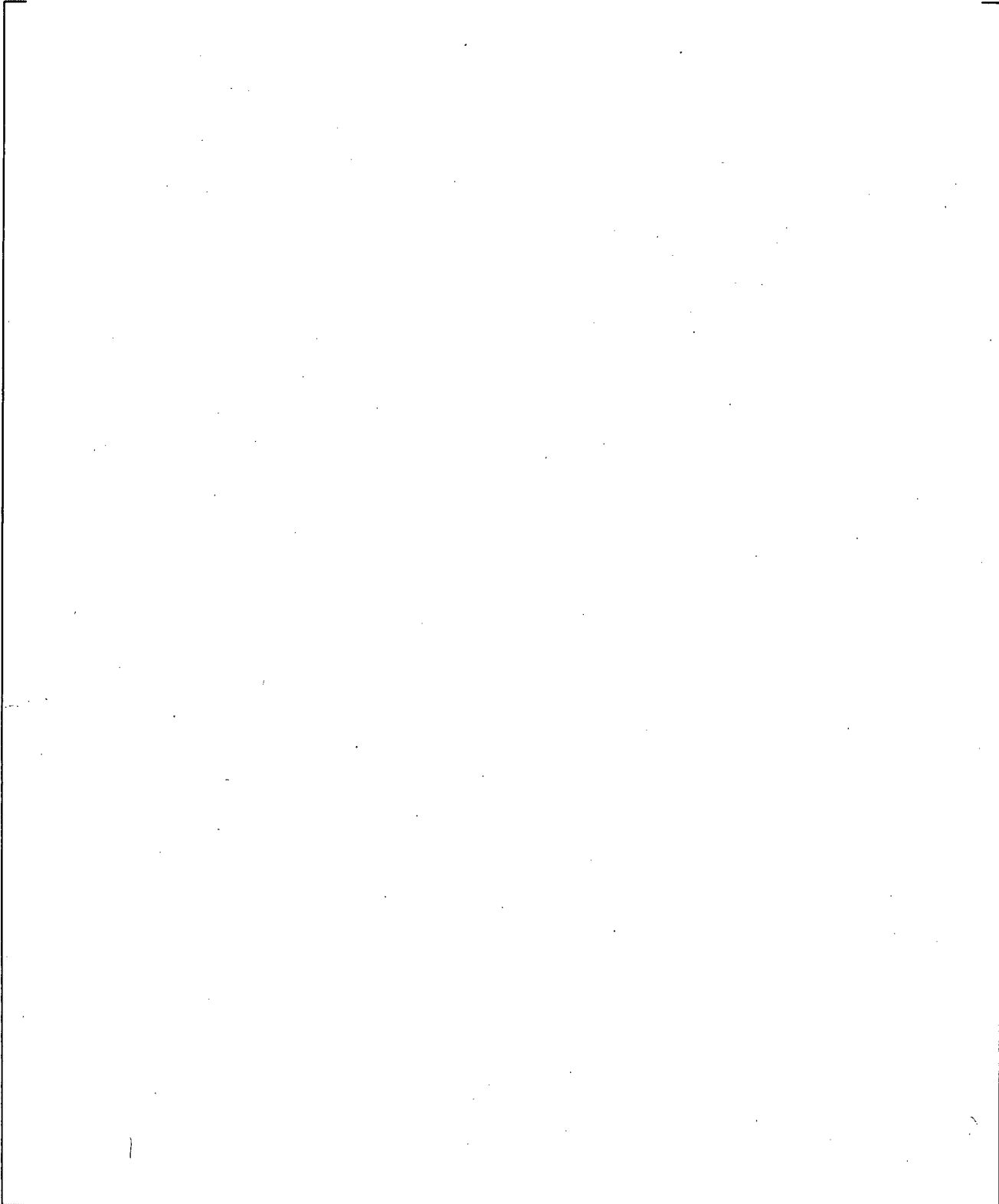


**Figure 20.1-1 IPP Loop #2 Accumulator Line Schematic**

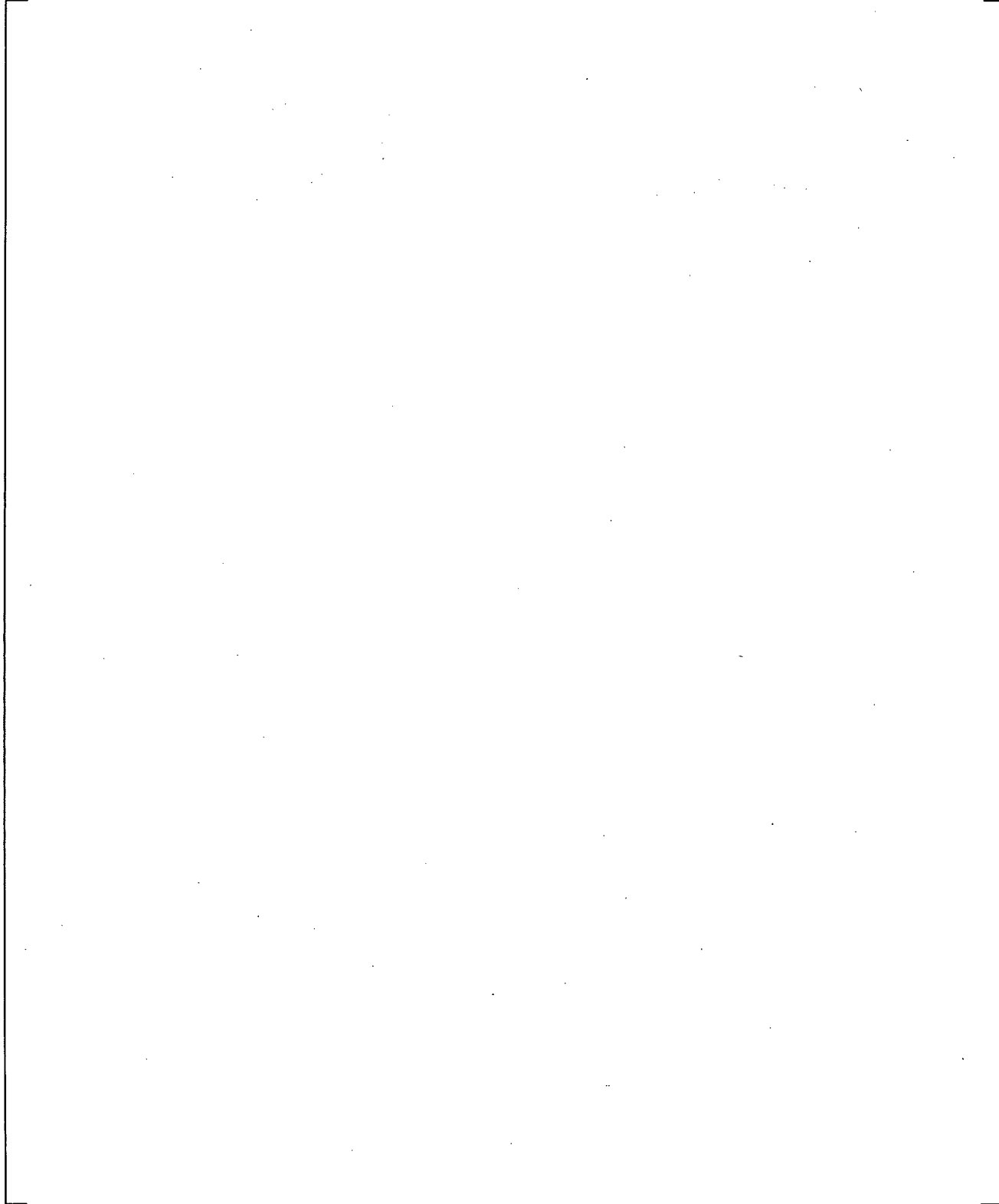


**Figure 20.1-2** WCOBRA/TRAC-TF2 Model of Accumulator and SI Line in IPP and Callaway  
**Test Models**

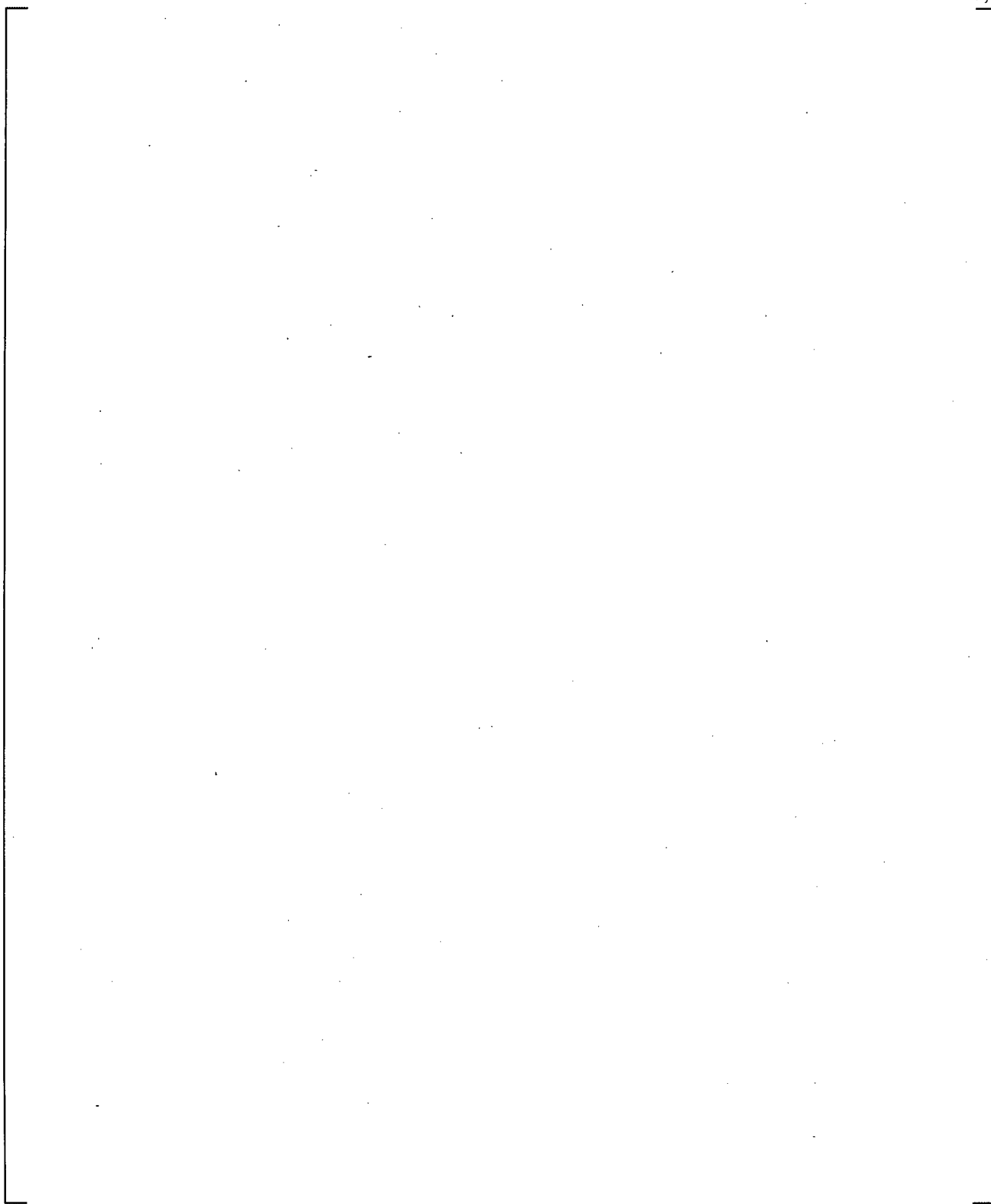


**Figure 20.1-3 Predicted Accumulator Pressure (Solid Line) Compared with Measured Test Data (Dashed Line)**

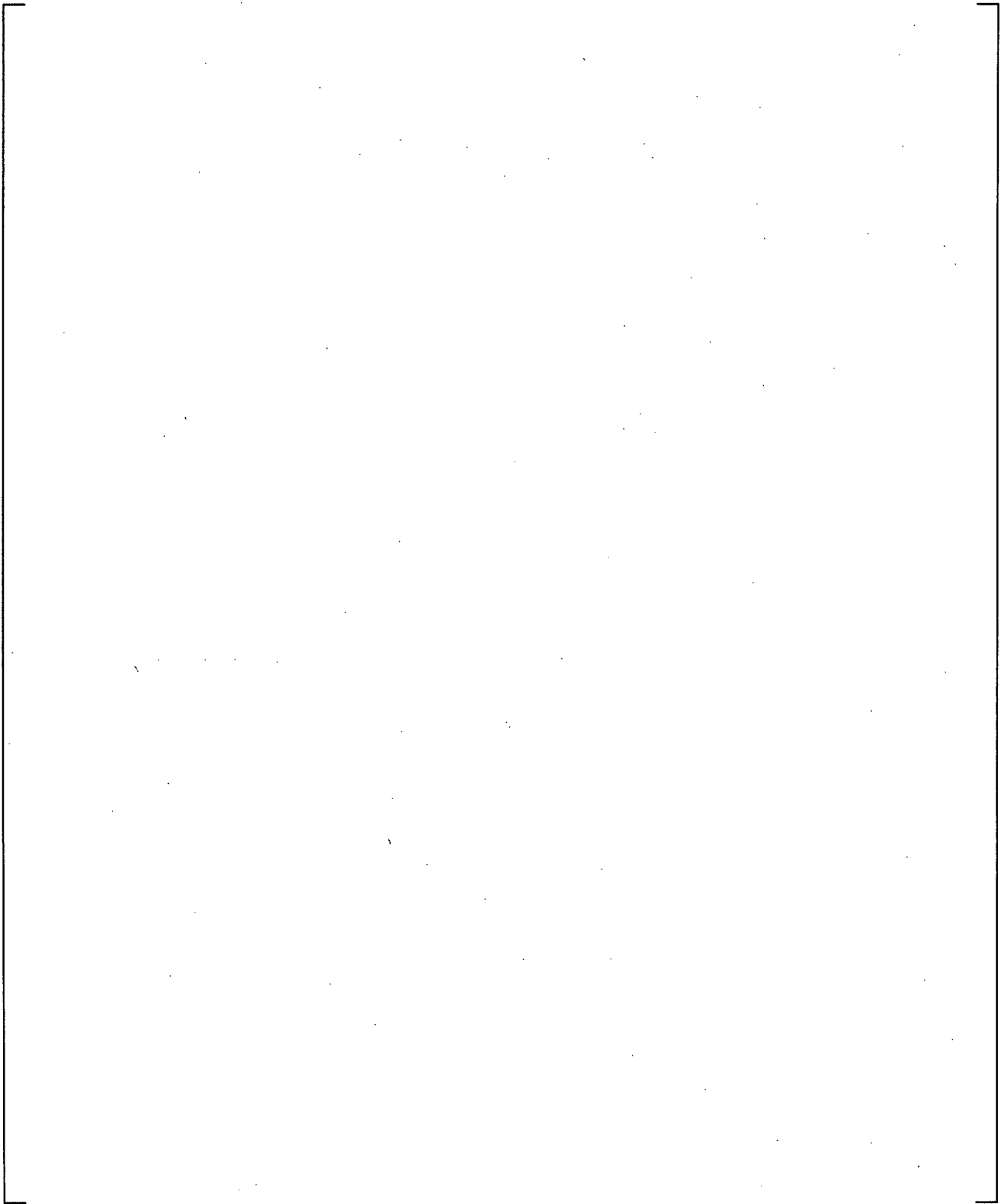


**Figure 20.1-4 Predicted Accumulator Flow Rate**

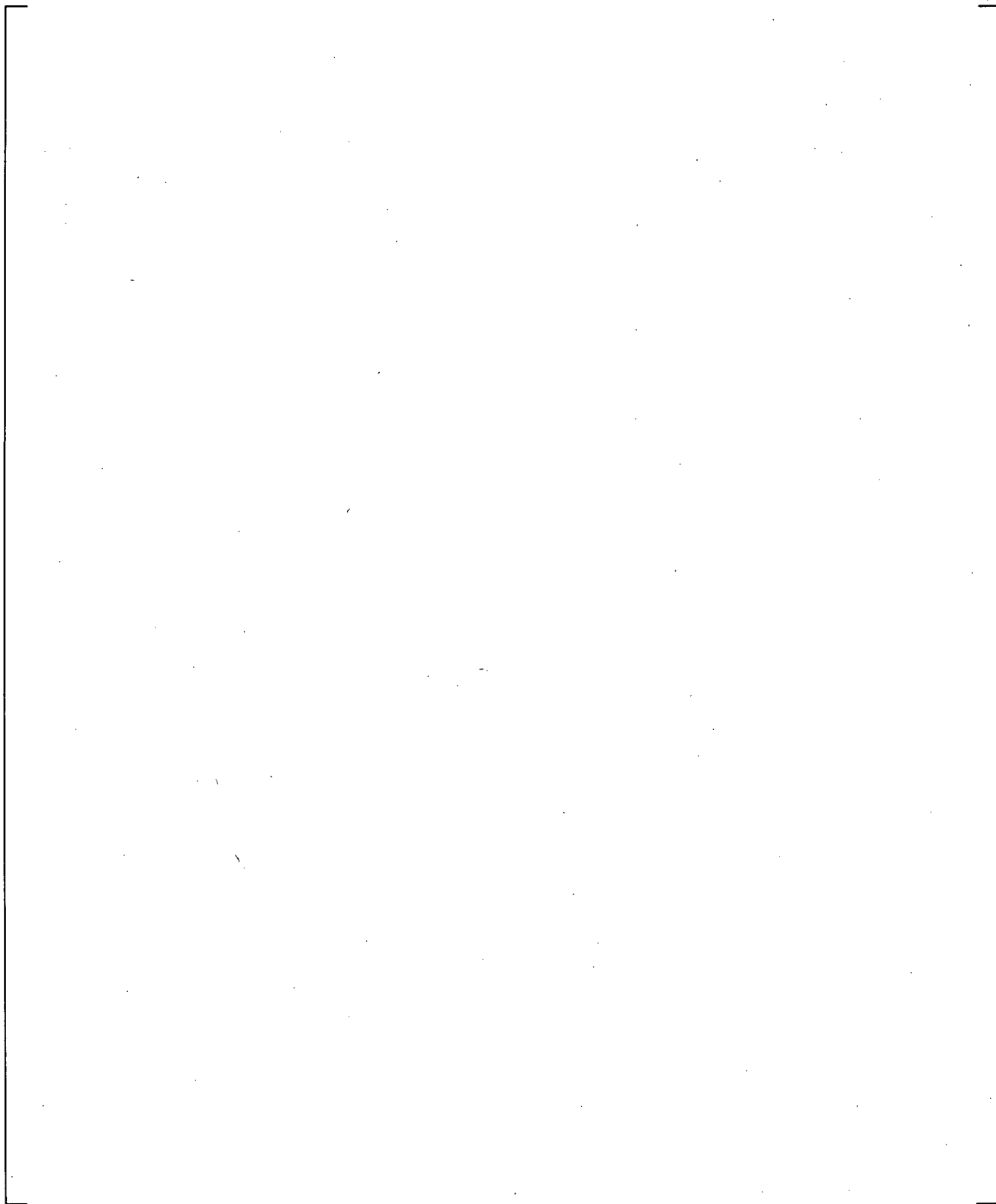


**Figure 20.1-5 Predicted Gas Temperature at Top of Accumulator**

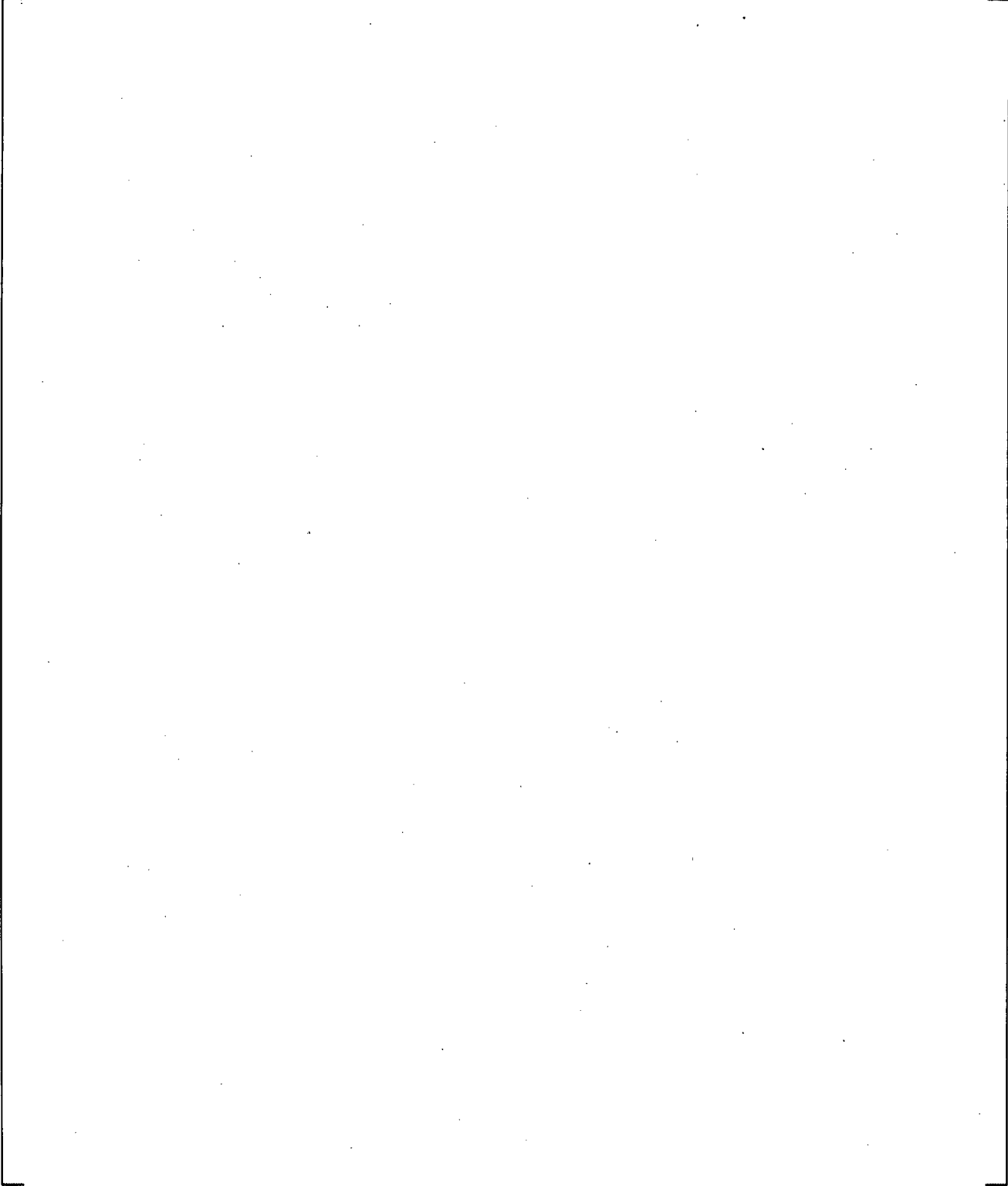


**Figure 20.1-6 Comparison of CALLAWAY Accumulator Blowdown Test Data and WCOBRA/TRAC-TF2 Prediction of Accumulator Pressure**

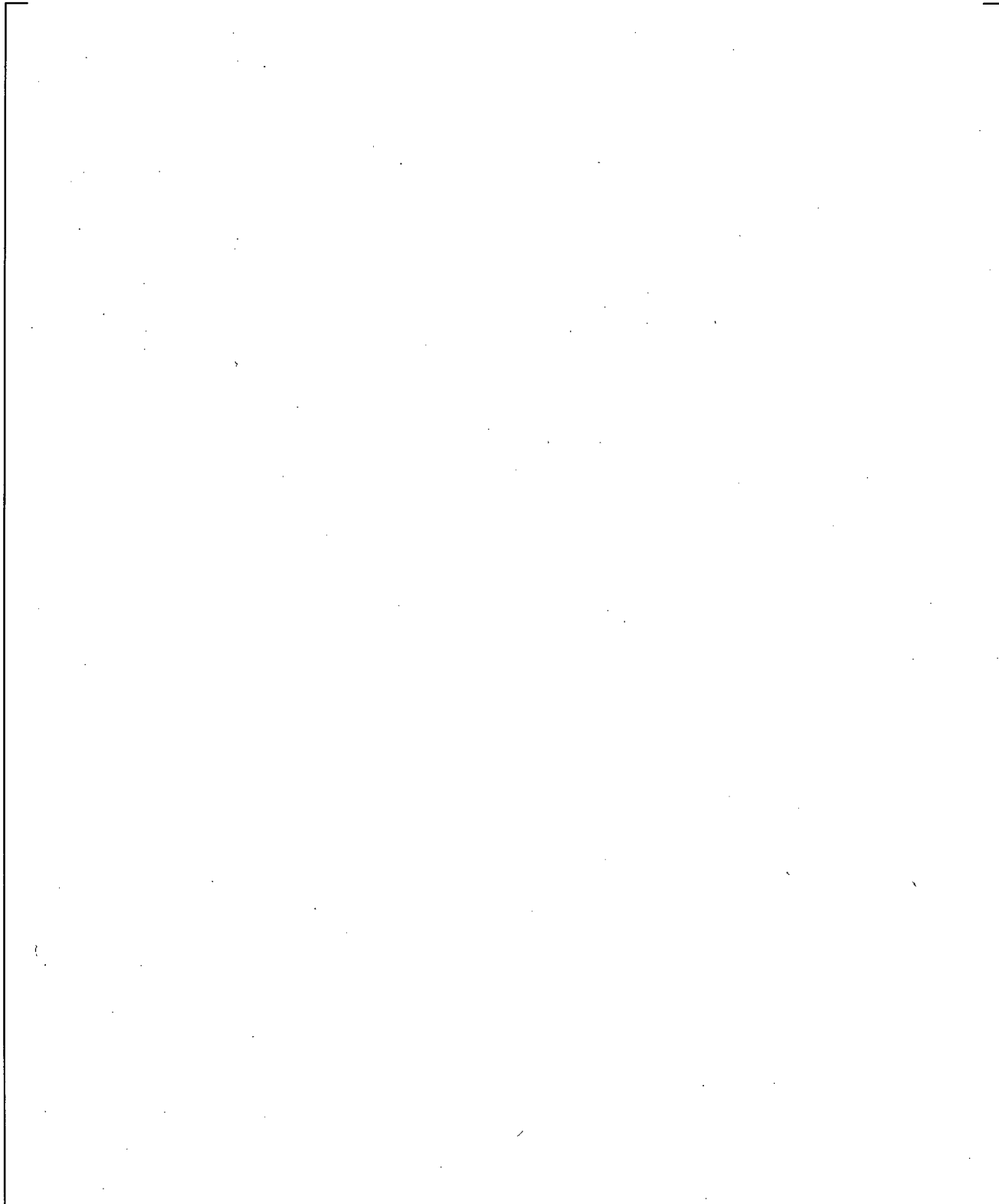


**Figure 20.1-7 Comparison of CALLAWAY Accumulator Blowdown Test Data and WCOBRA/TRAC-TF2 Prediction of Accumulator Gas Volume**

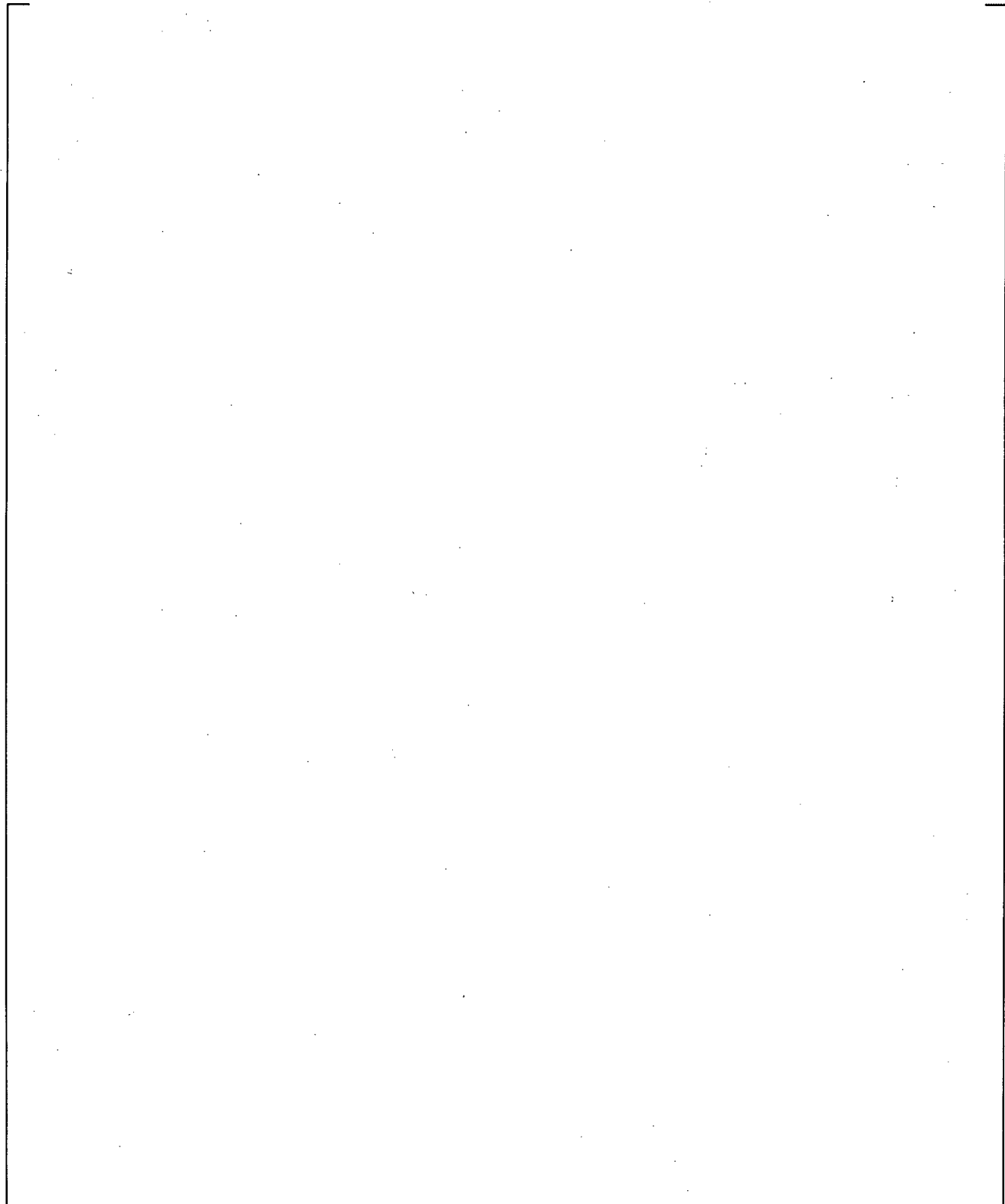


**Figure 20.1-8 Comparison of CALLAWAY Accumulator Blowdown Test Data and WCOBRA/TRAC-TF2 Prediction of Accumulator Gas Temperature**

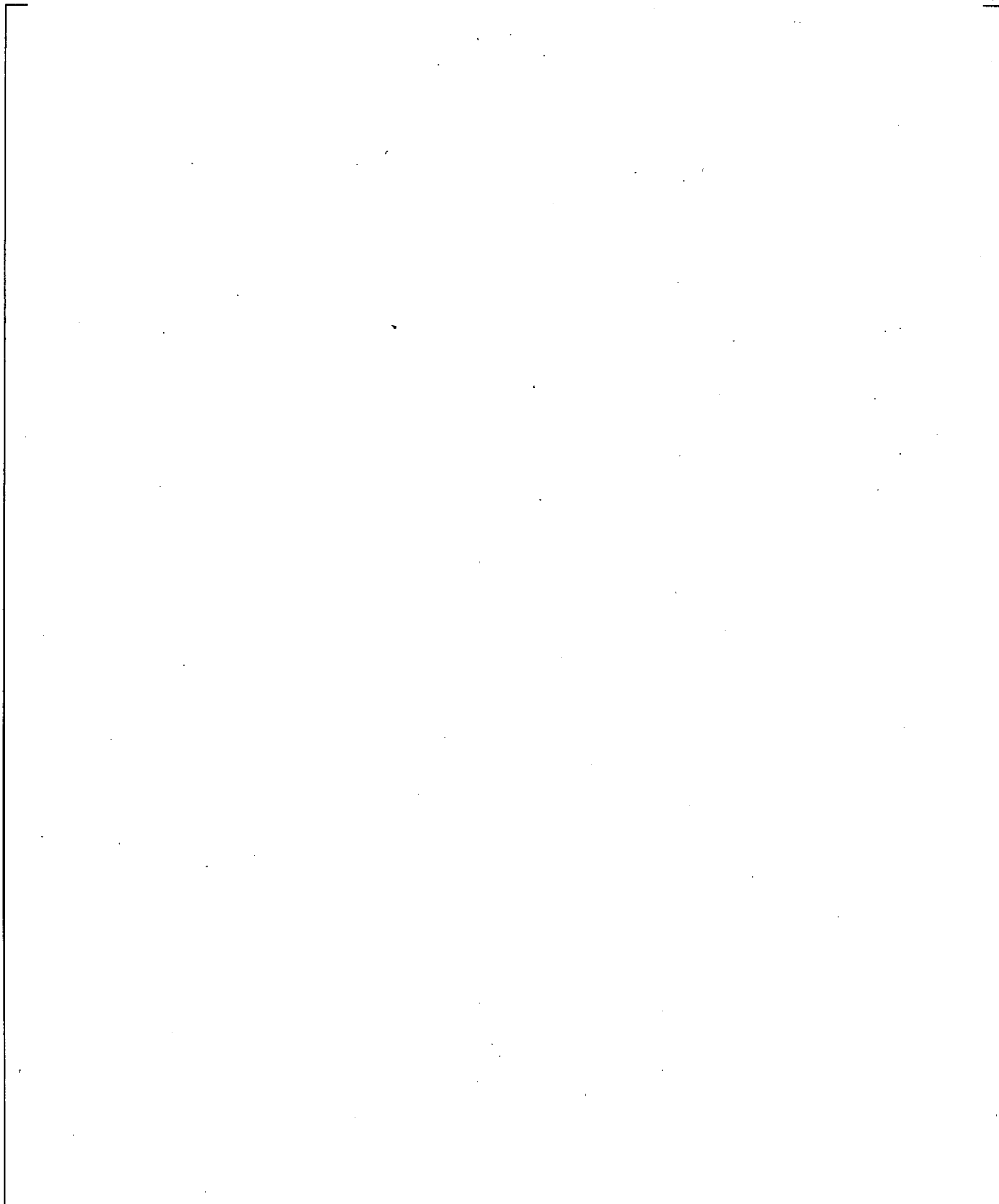


**Figure 20.1-9 Best-fit Calculation of Polytropic Exponent from CALLAWAY Accumulator Blowdown WCOBRA/TRAC-TF2 Prediction**

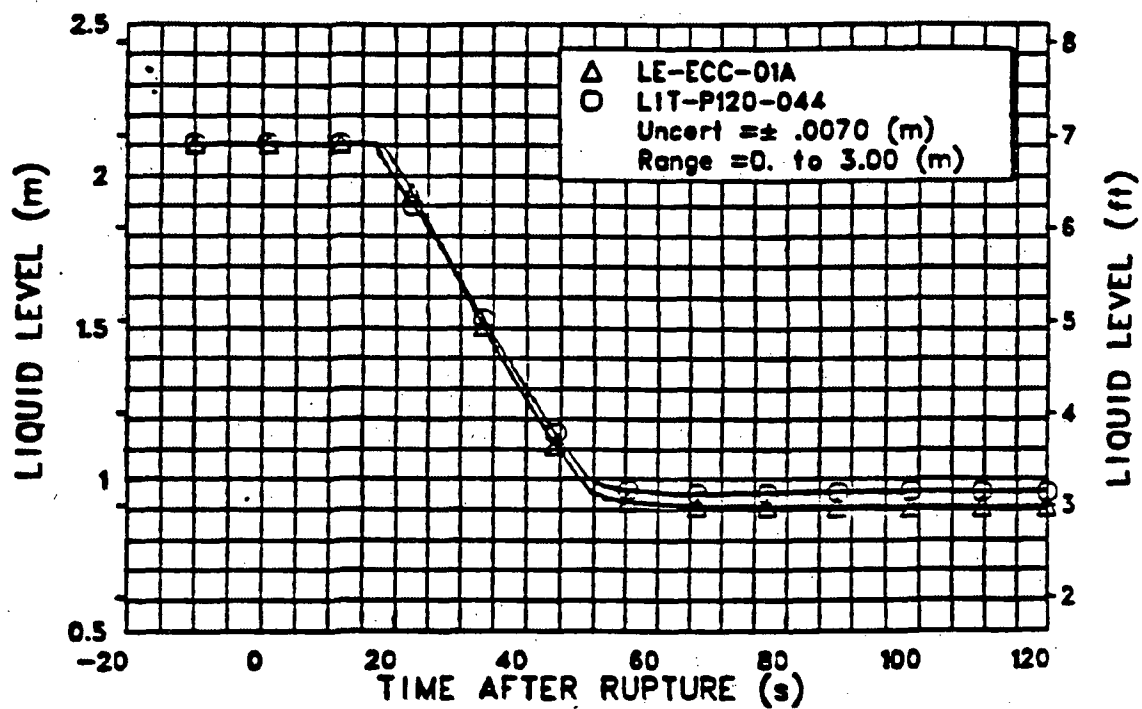


Figure 20.1-10 Accumulator Liquid Level for LOFT Test L2-5 (Bayless et al., 1982)

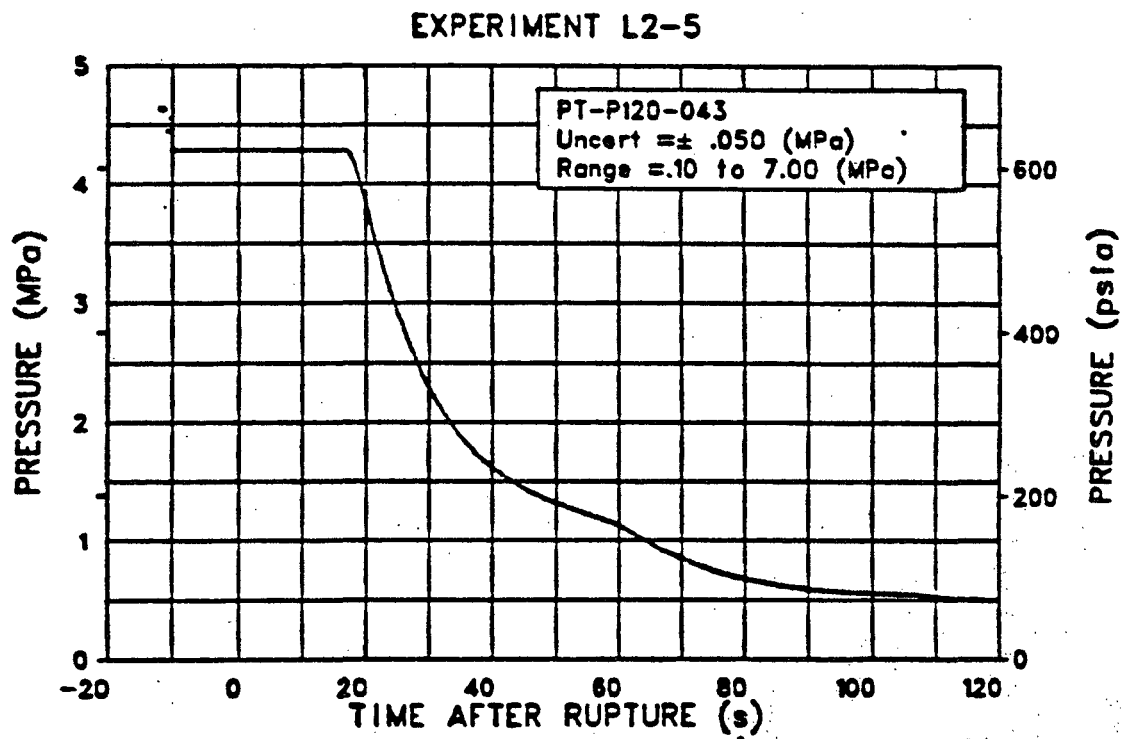


Figure 20.1-11 Accumulator Pressure for LOFT Test L2-5 (Bayless et al., 1982)

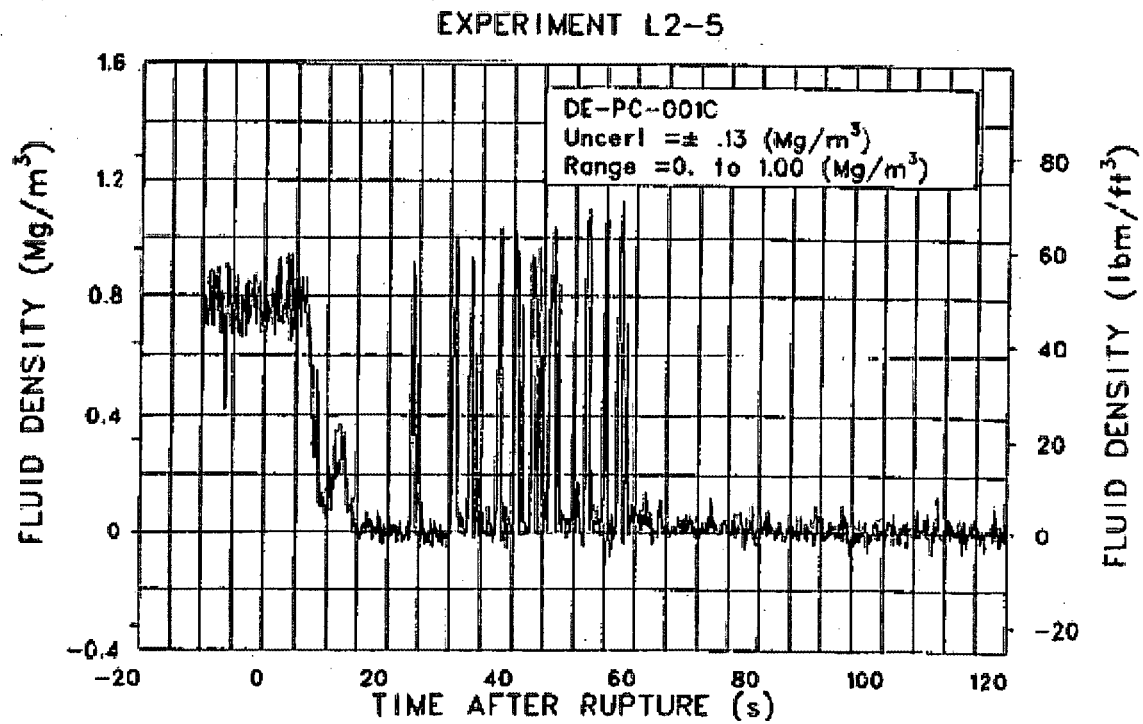
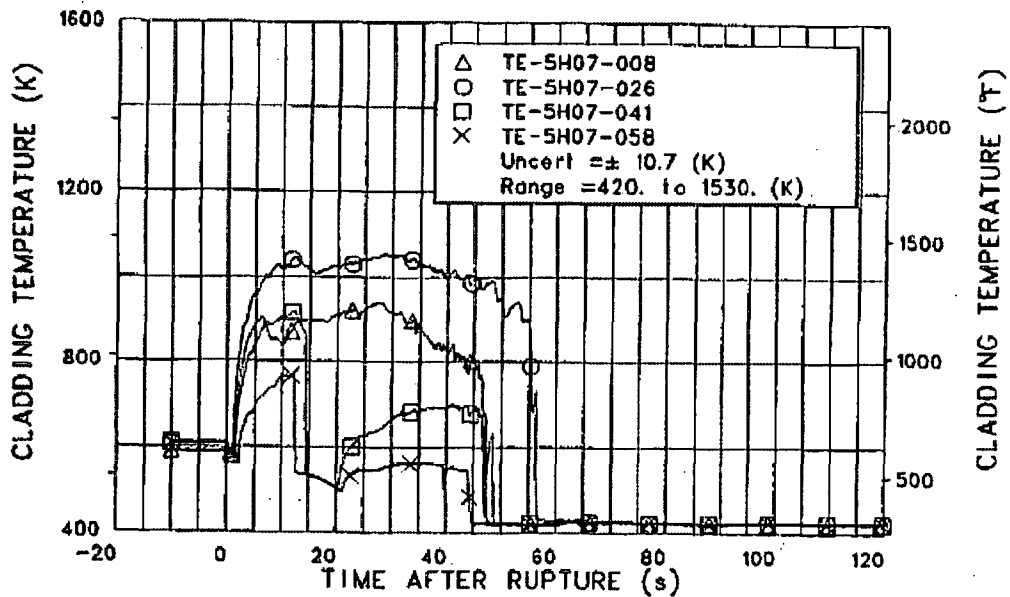
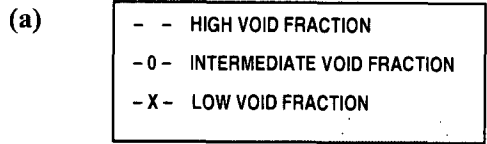
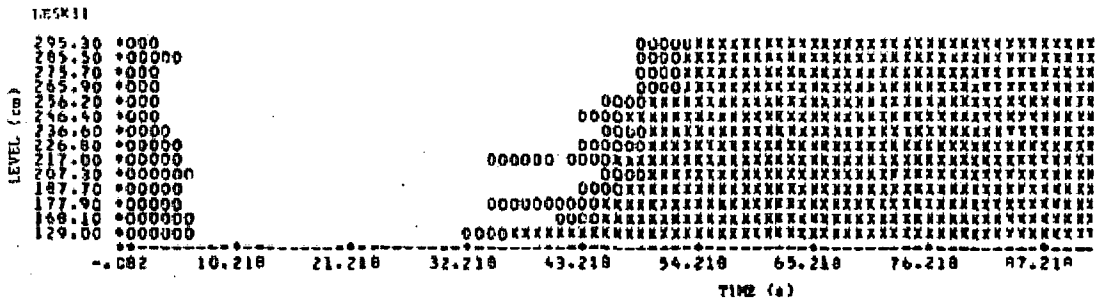


Figure 20.1-12 Intact Loop Cold Leg Density for LOFT Test L2-5 (Bayless et al., 1982)



(b)

Figure 20.1-13 (a) Core Liquid Level Plots for LOFT Test L2-5 (Bayless et al., 1982)  
 (b) Fuel Rod Clad Temperatures (Bayless et al., 1982)

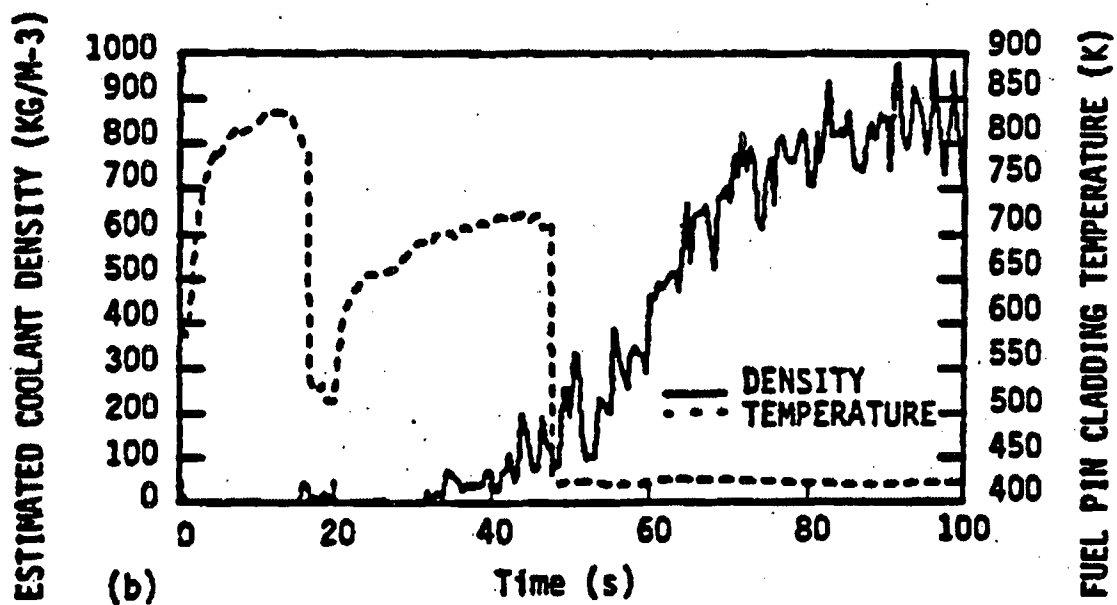
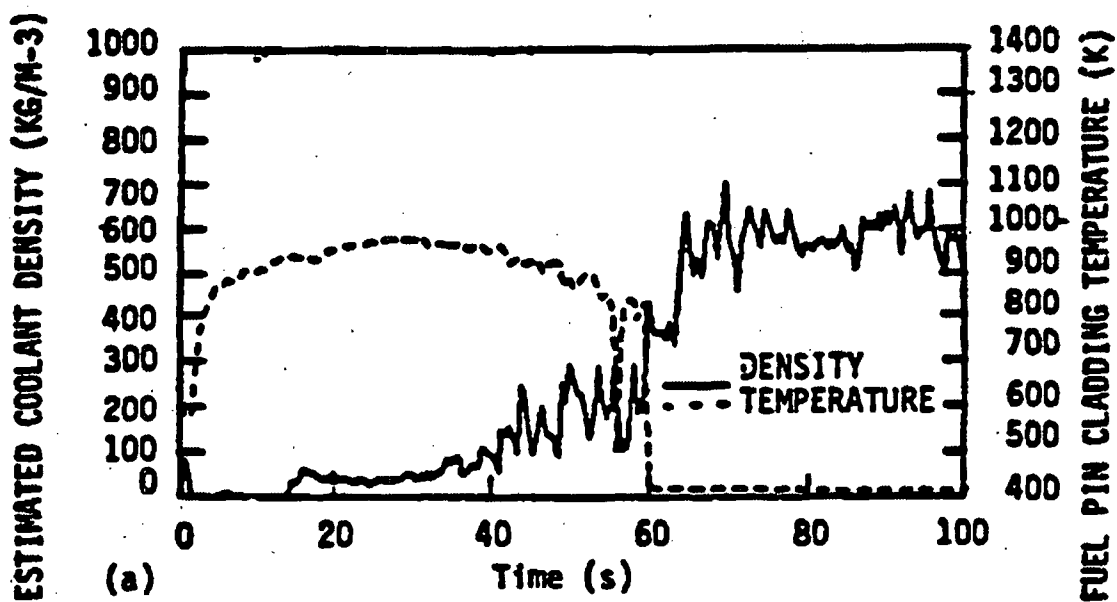


Figure 20.1-14 Fluid Density and Clad Temperature in Core at  
 a) 27 inches,  
 b) 44 inches Above Bottom of Core (Mackley and Birchley, 1985)

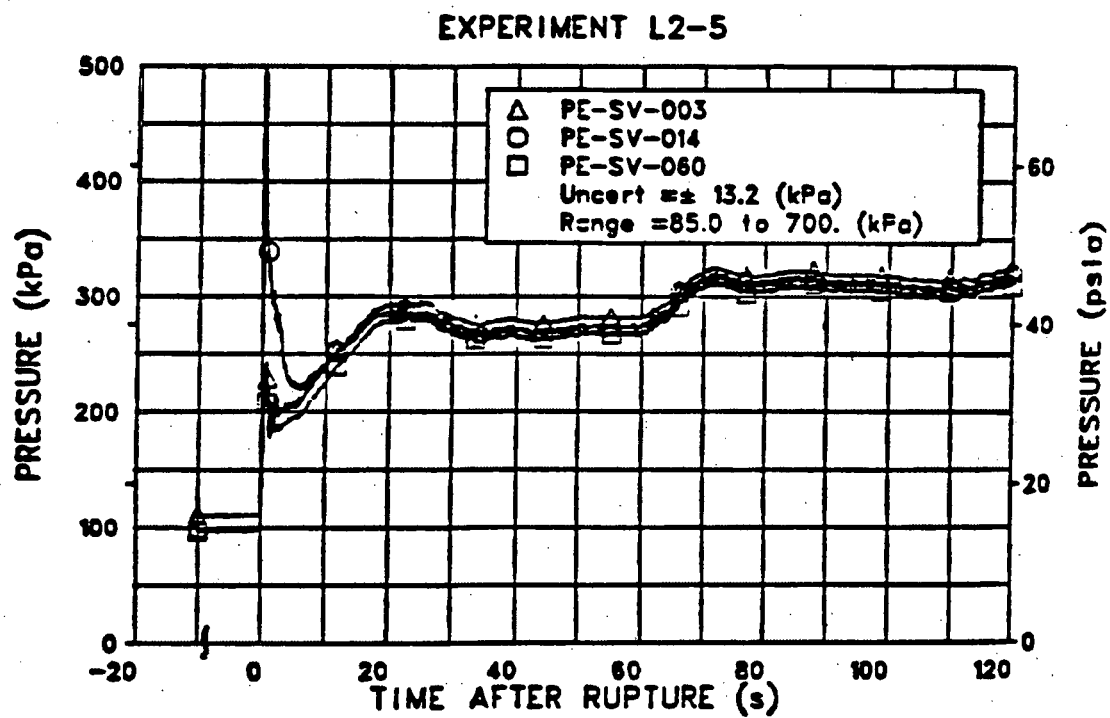


Figure 20.1-15 Suppression Tank Pressure for LOFT Test L2-5 (Bayless et al., 1982)

a,c

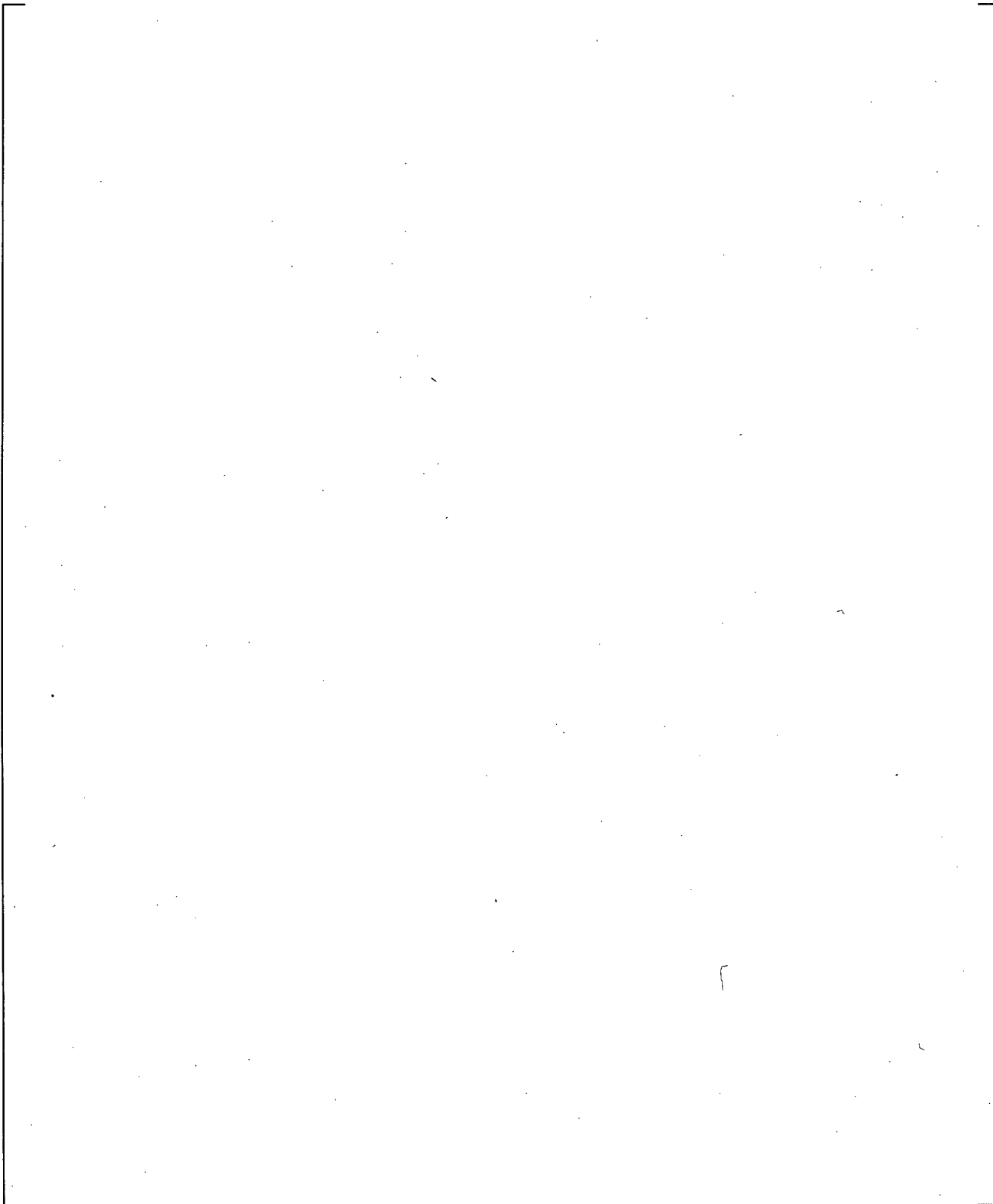


Figure 20.1-16 [

] a,c

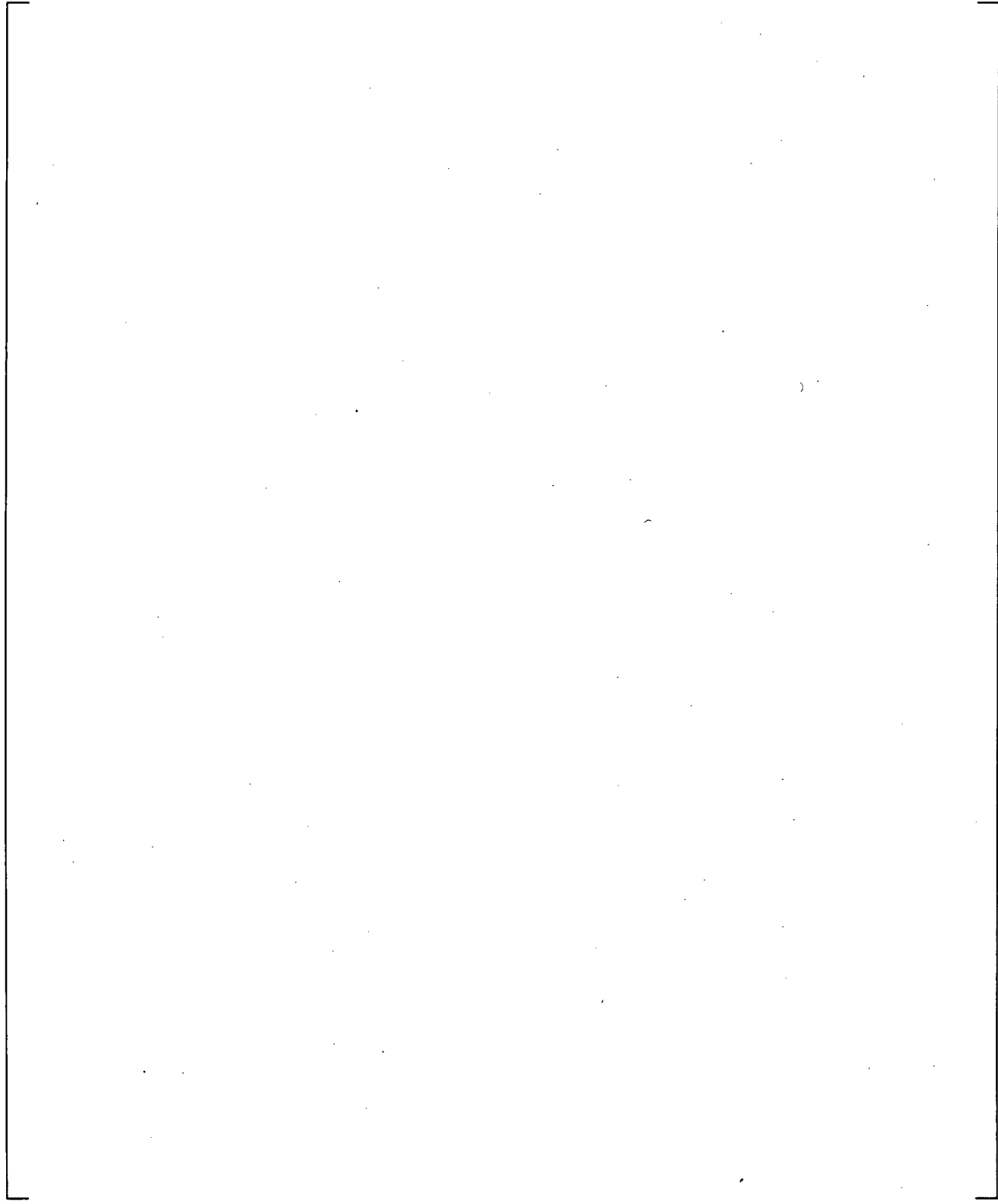


Figure 20.1-17 [

]a,c

a,c

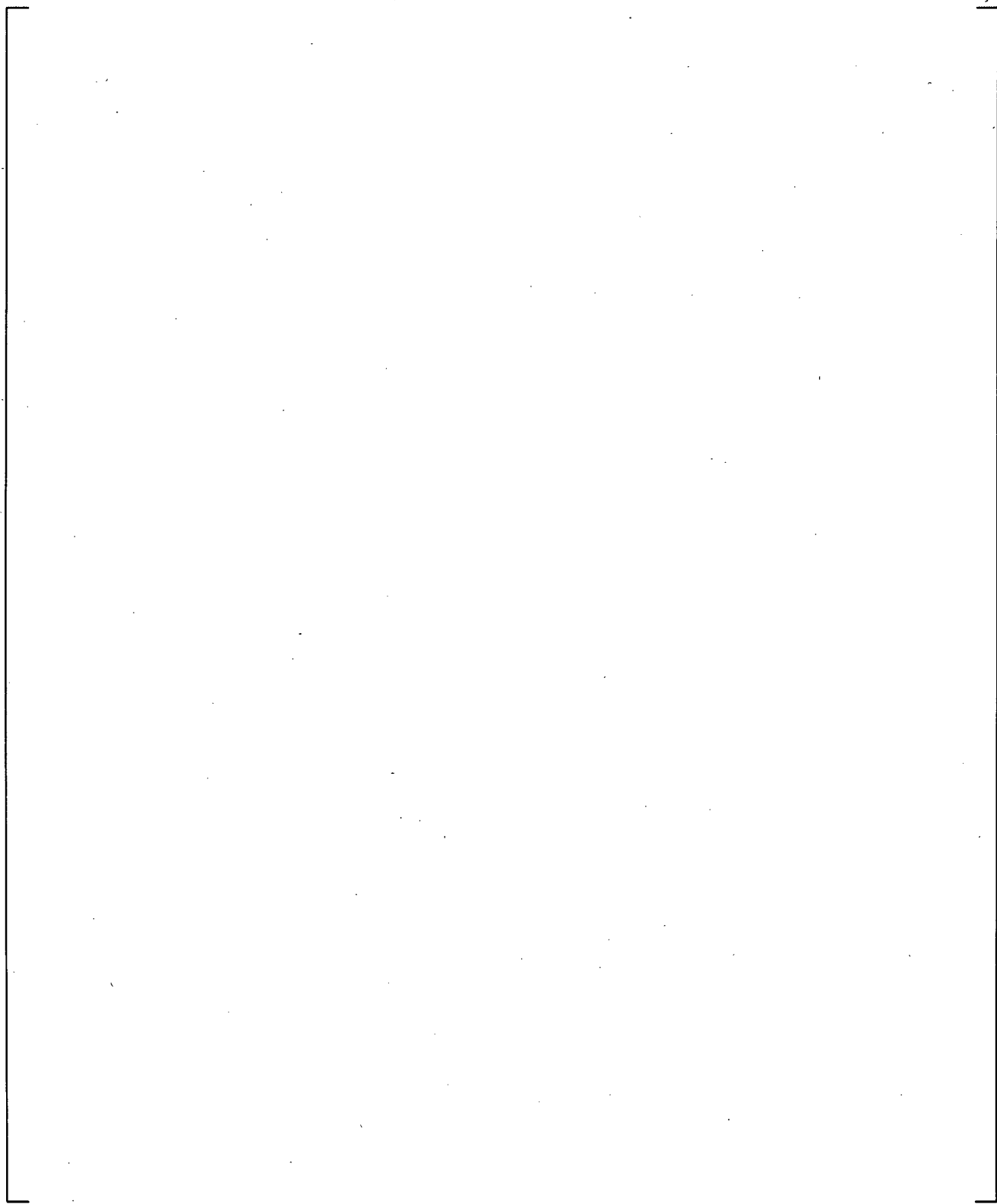
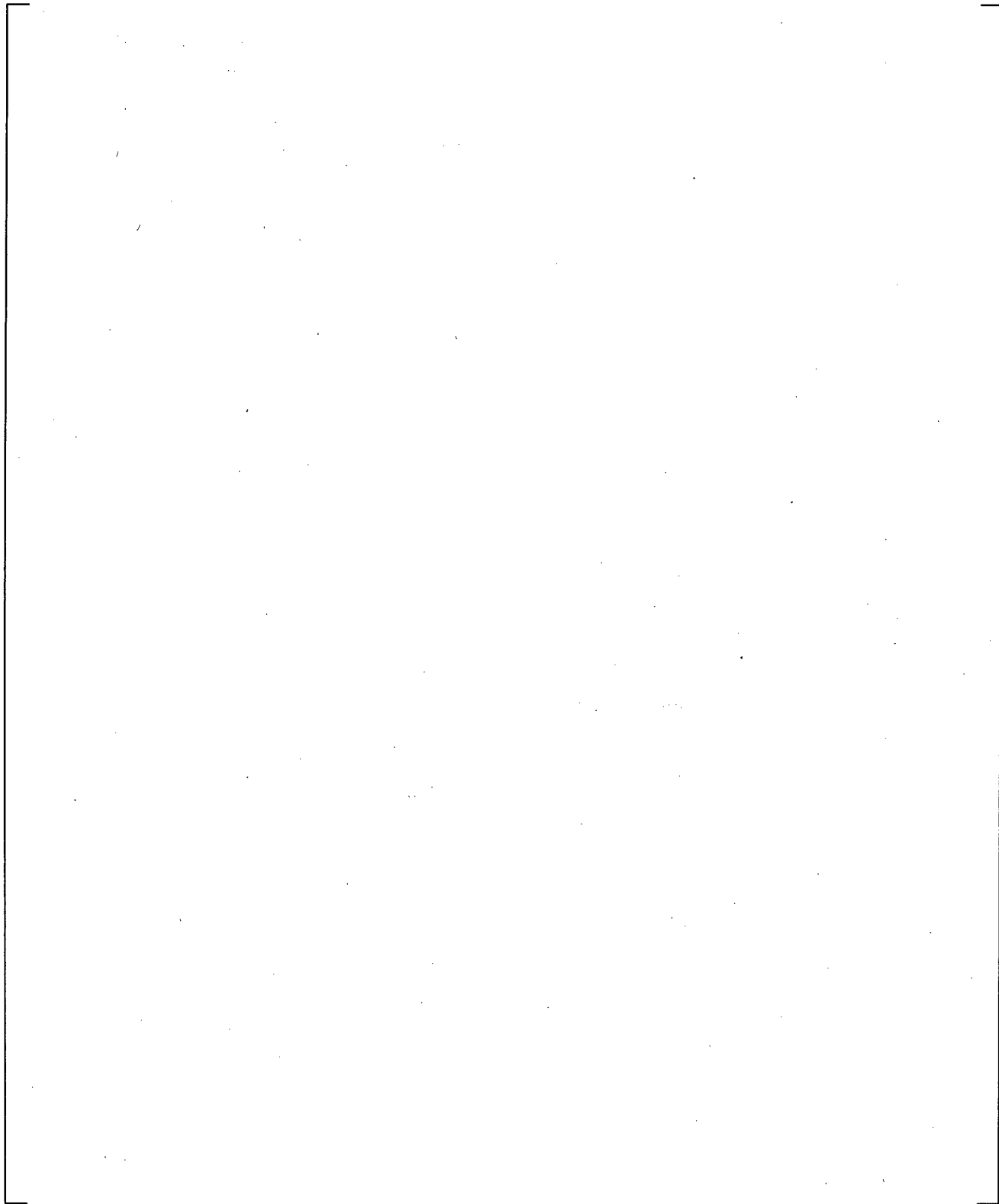


Figure 20.1-18 [

] a,c

a,c



**Figure 20.1-19** [

] <sup>a,c</sup>

a,c

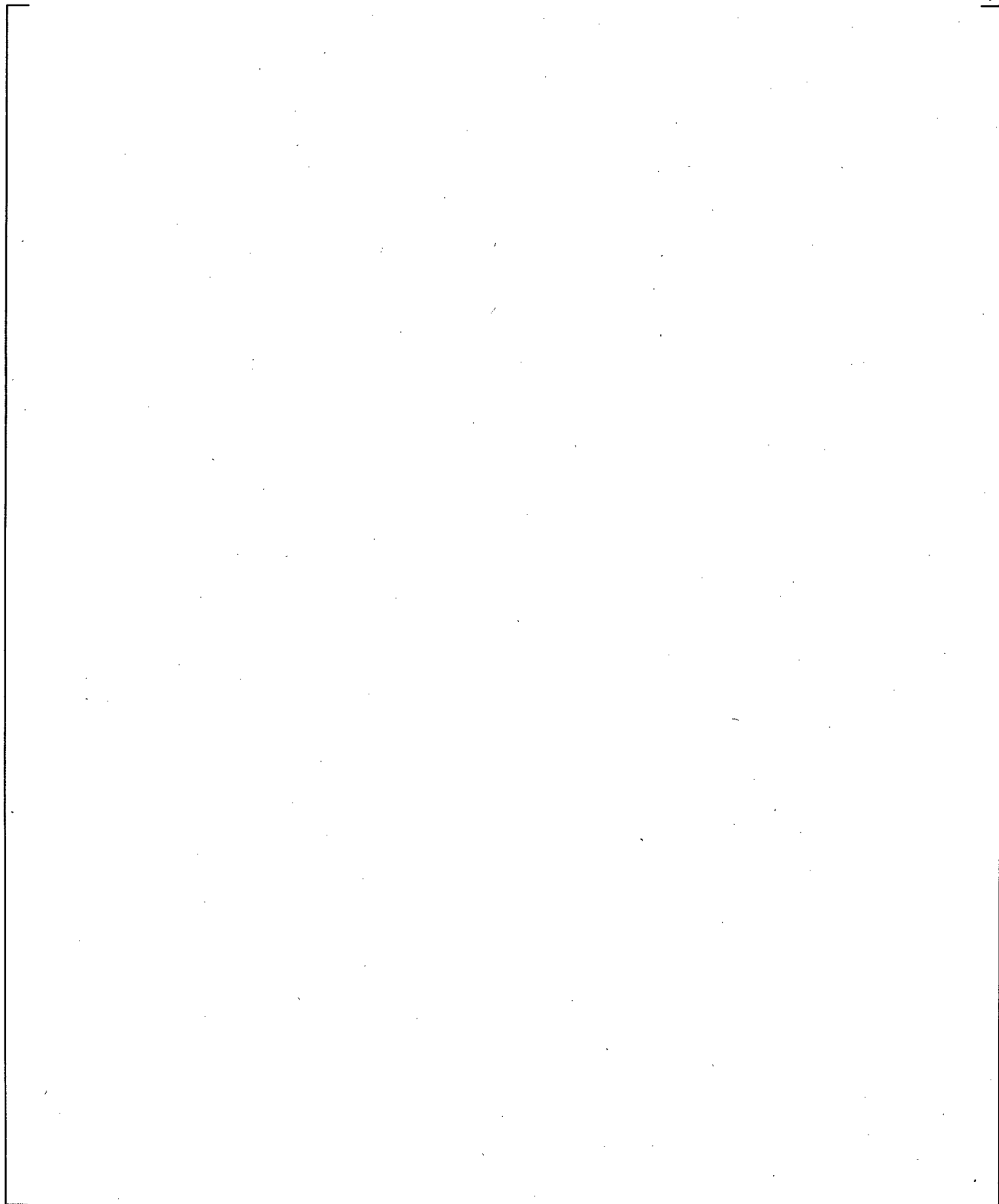


Figure 20.1-20 [

] a,c

a,c

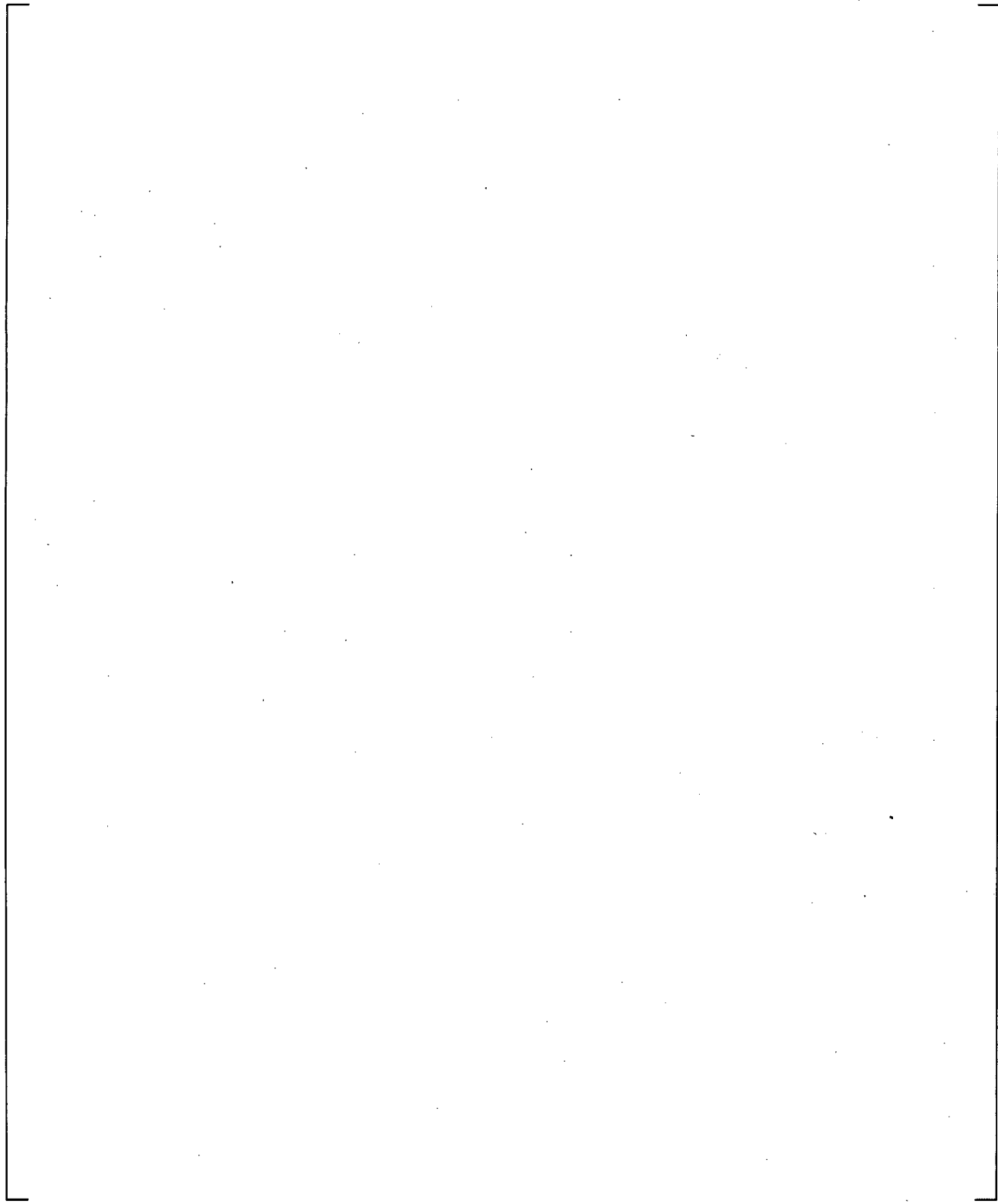


Figure 20.1-21 [

]a,c

a,c

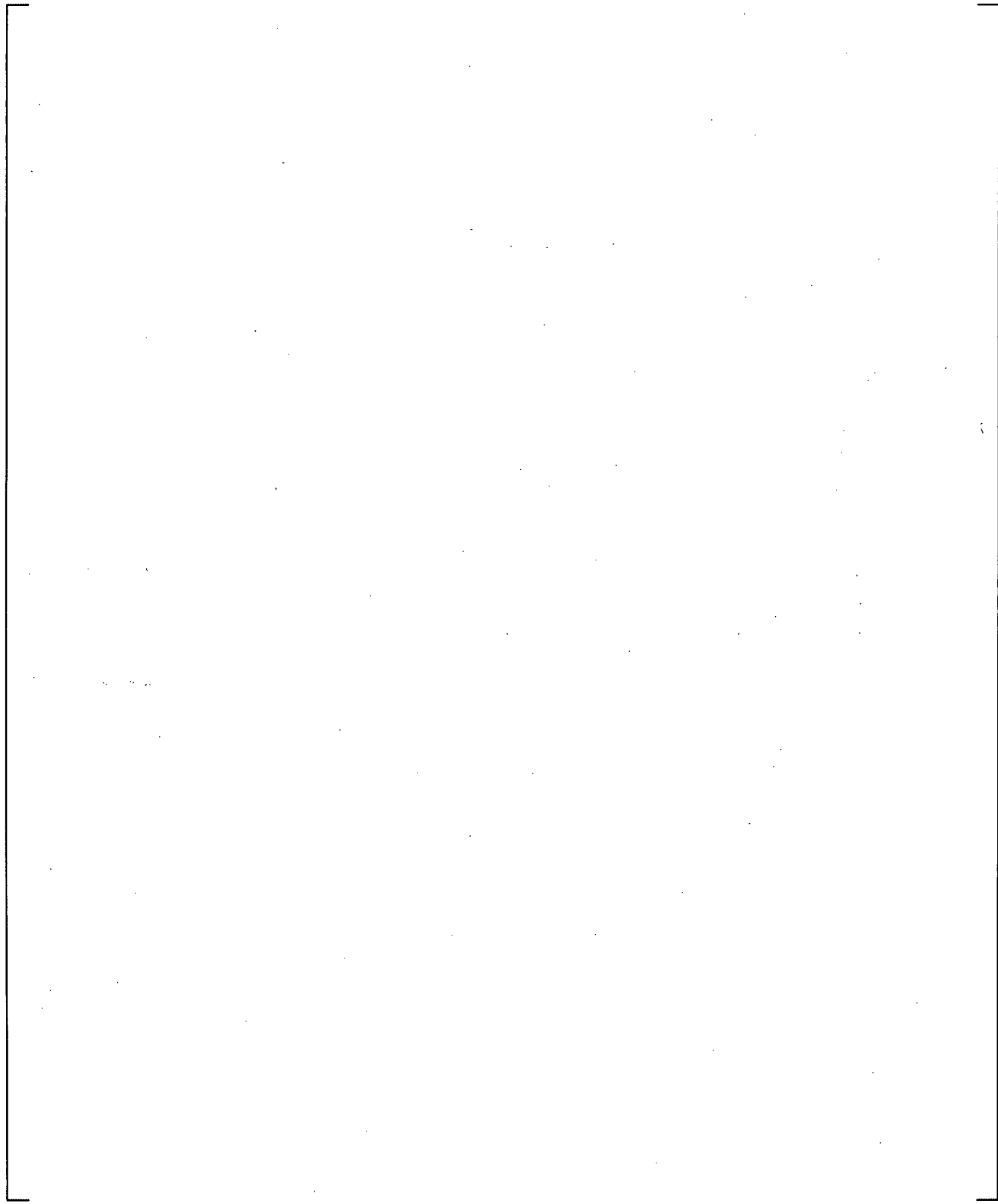


Figure 20.1-22 [

]a,c

a,c

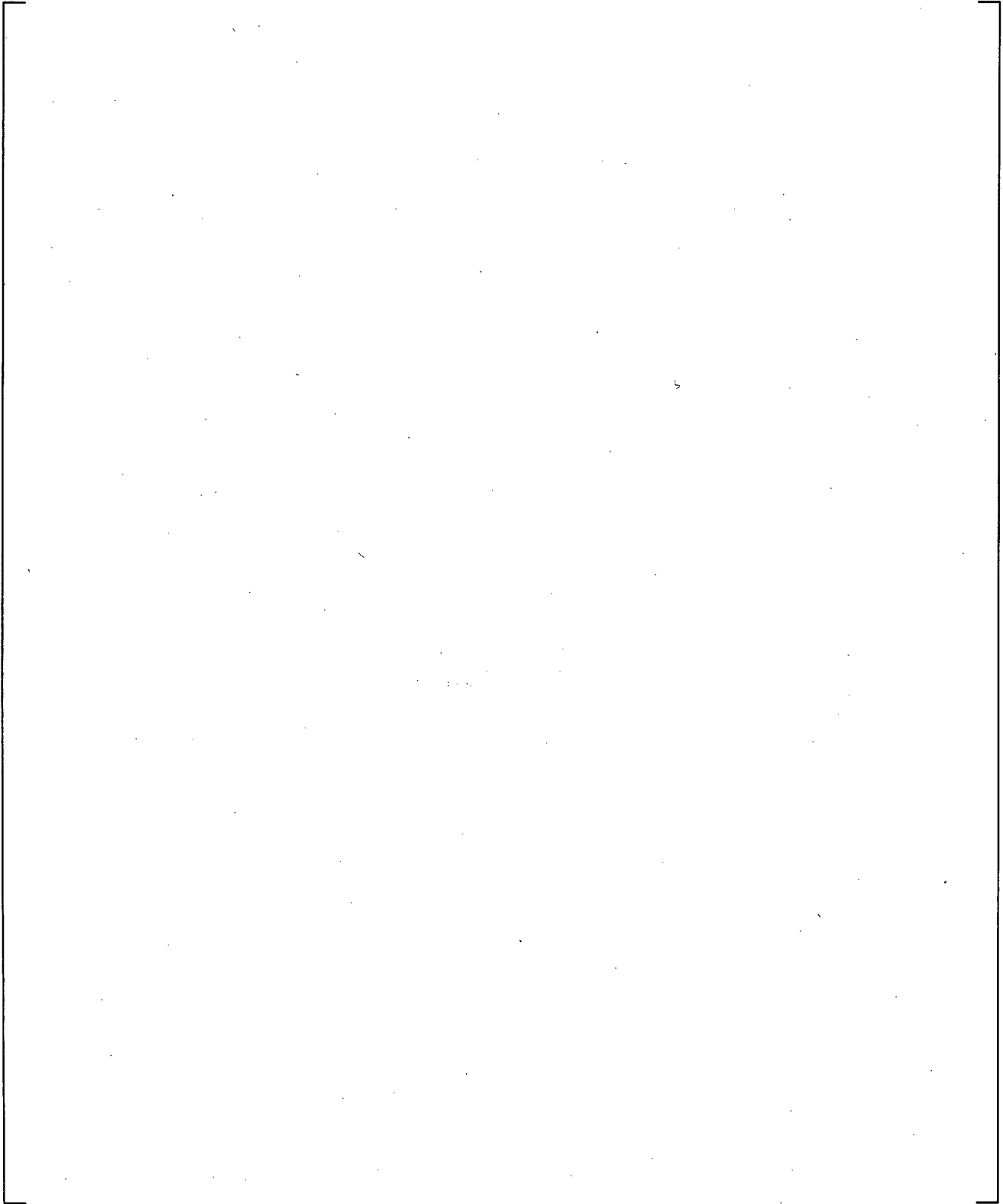


Figure 20.1-23 [

] a,c

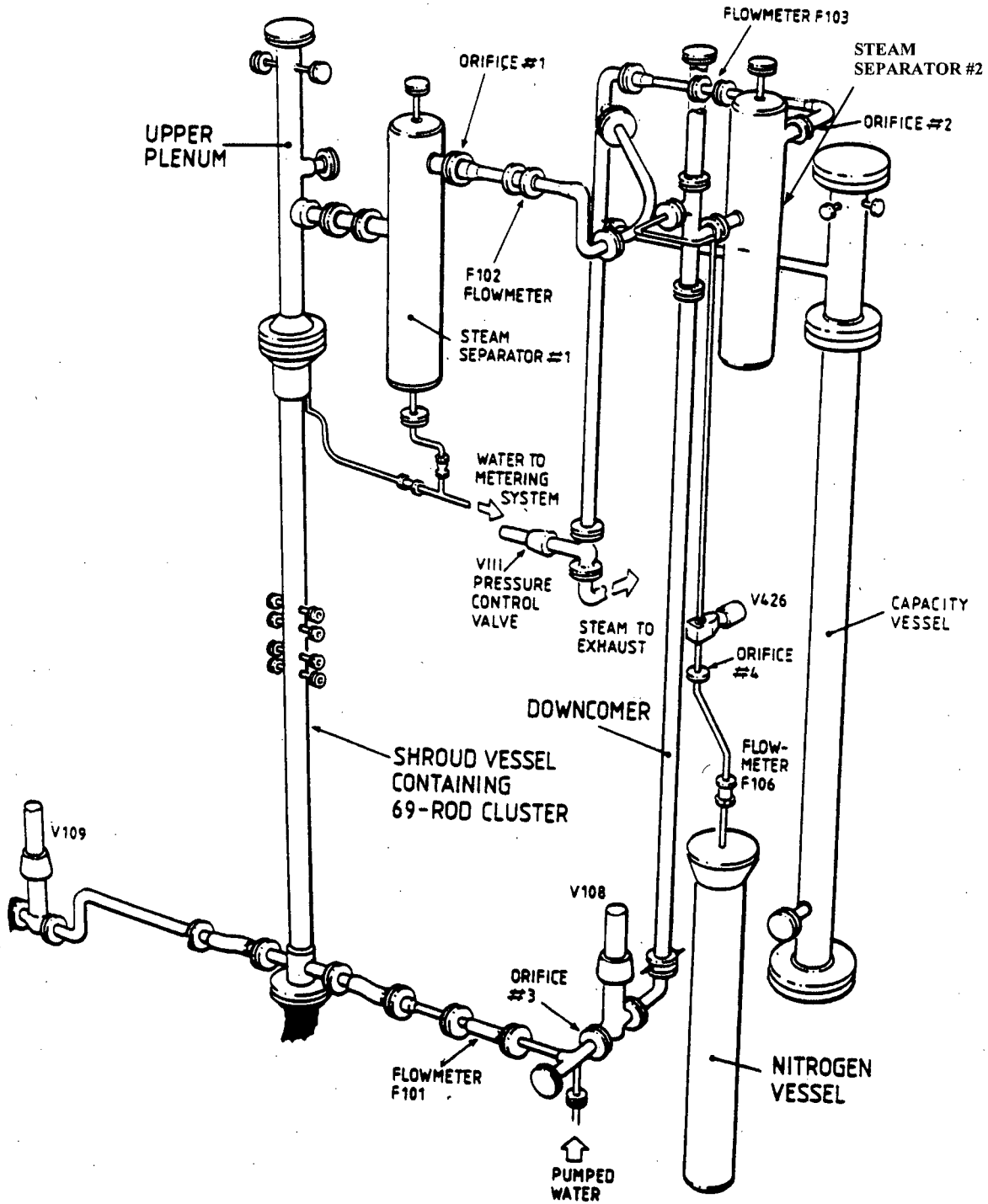
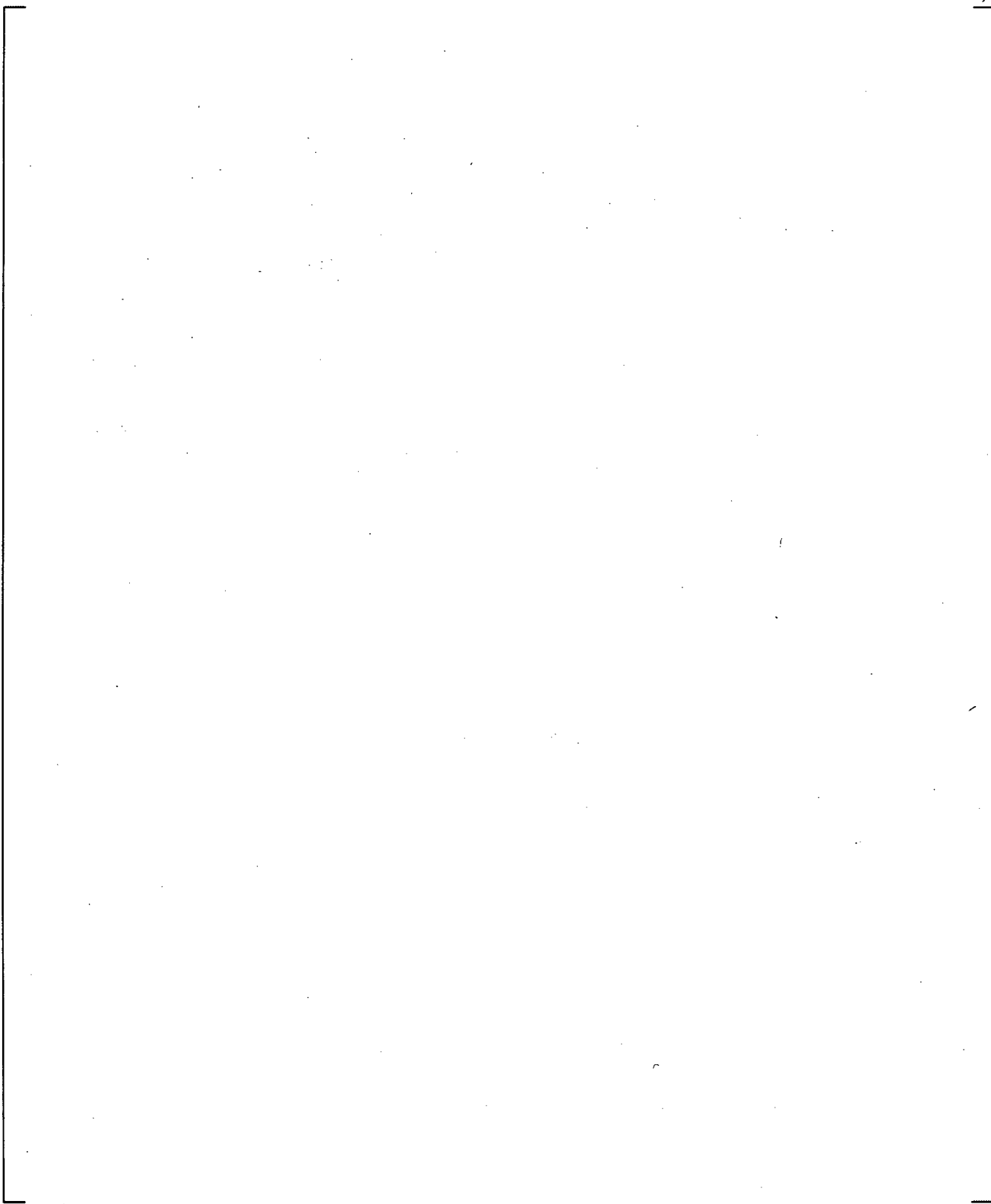
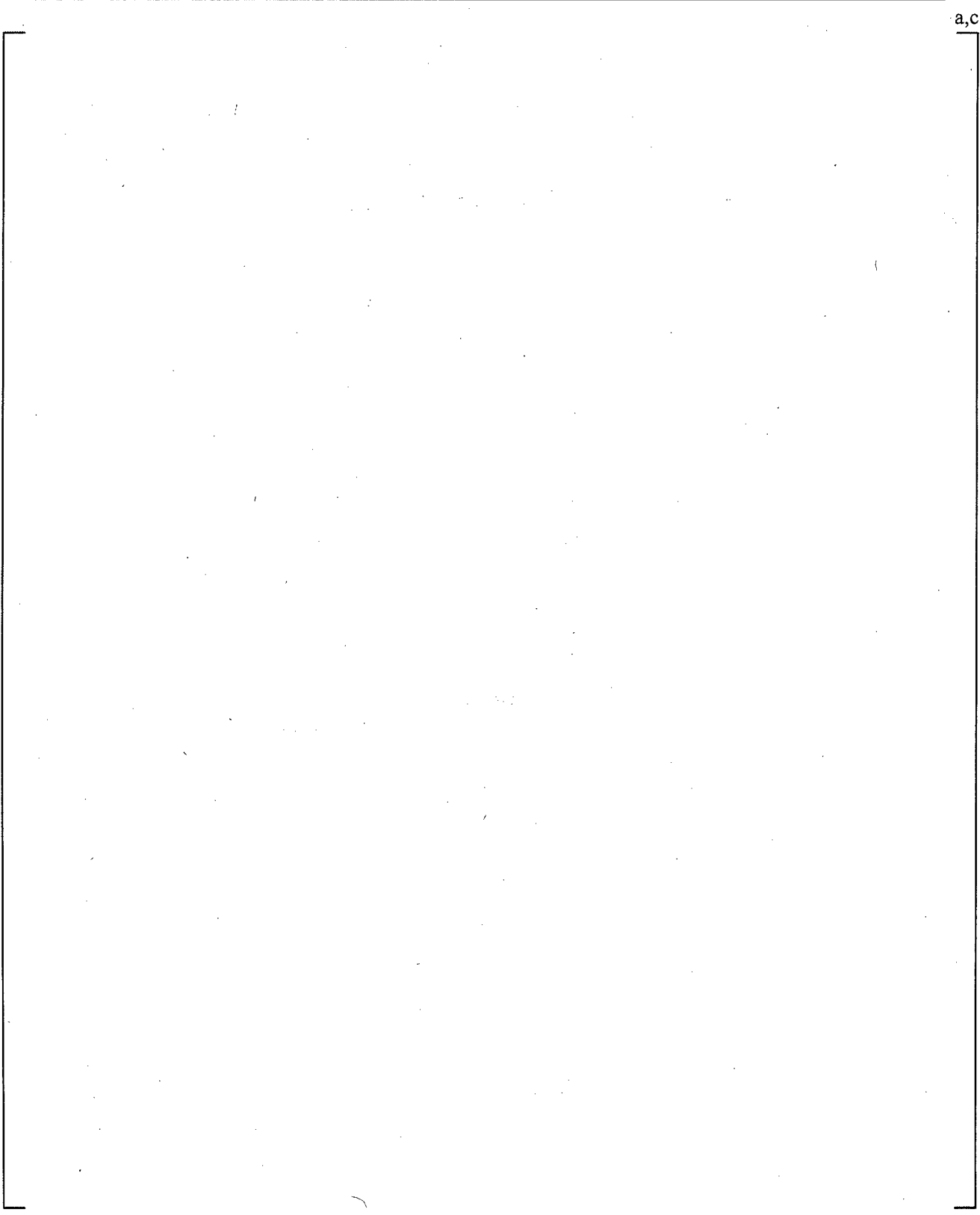


Figure 20.1-24 ACHILLES Rig Configured for Best-Estimate Transients



**Figure 20.1-25 WCOBRA/TRAC-TF2 Model of ACHILLES Test**

a,c



**Figure 20.1-26 Cross Section of ACHILLES Cluster**

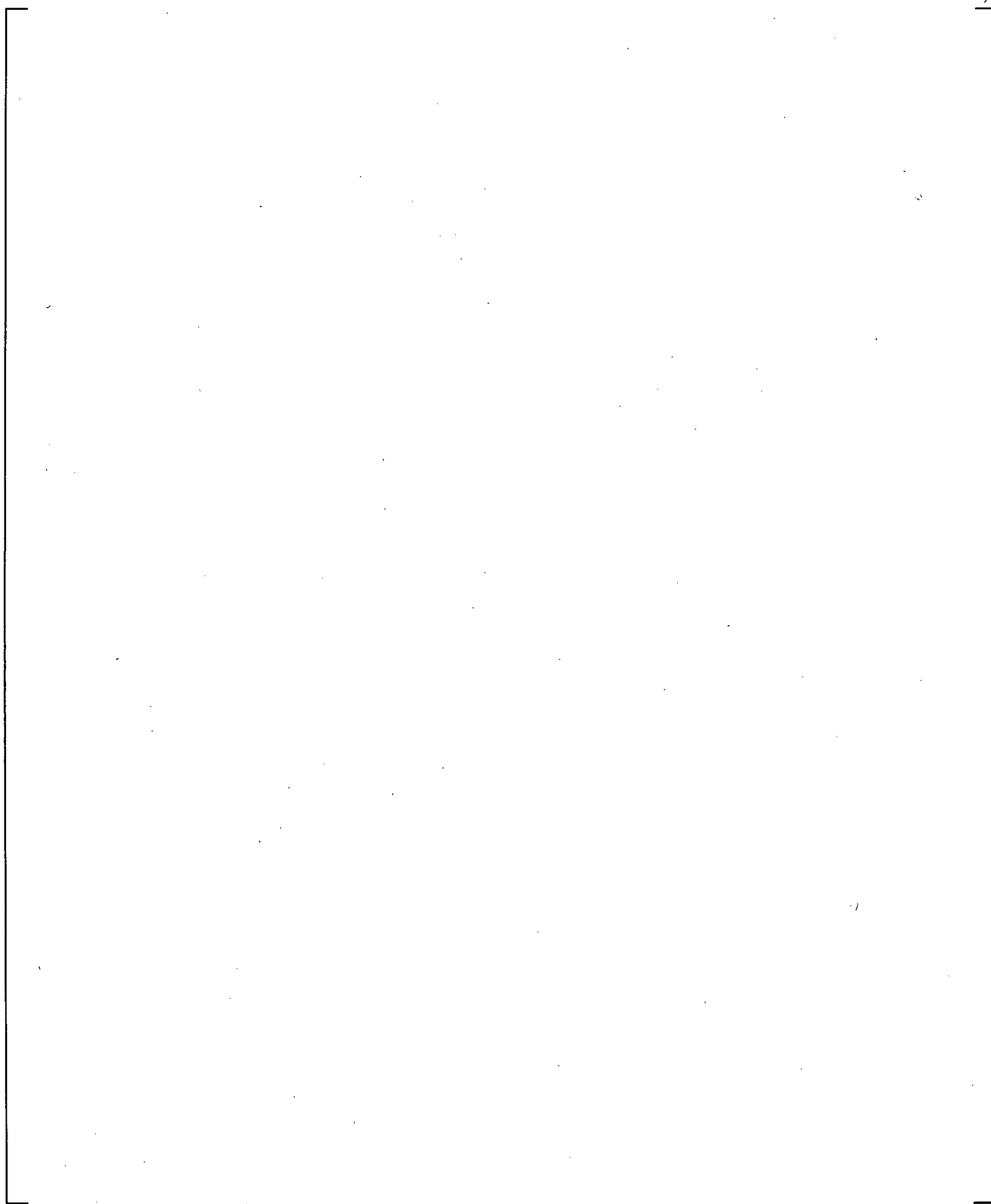


**Figure 20.1-27 Measured and Predicted Accumulator Pressure**

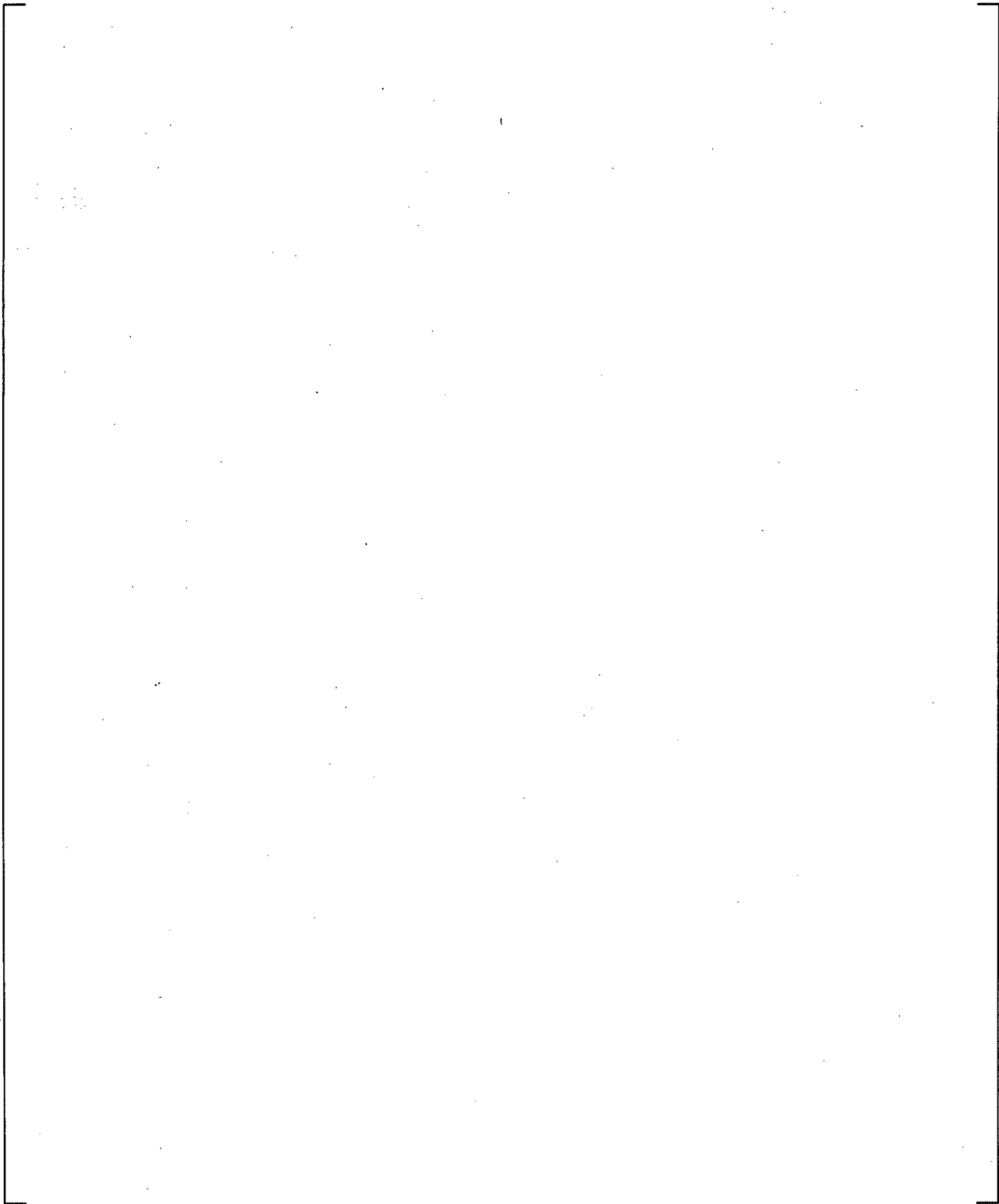


**Figure 20.1-28 Measured and Predicted Accumulator Discharge Line Mass Flow Rate**

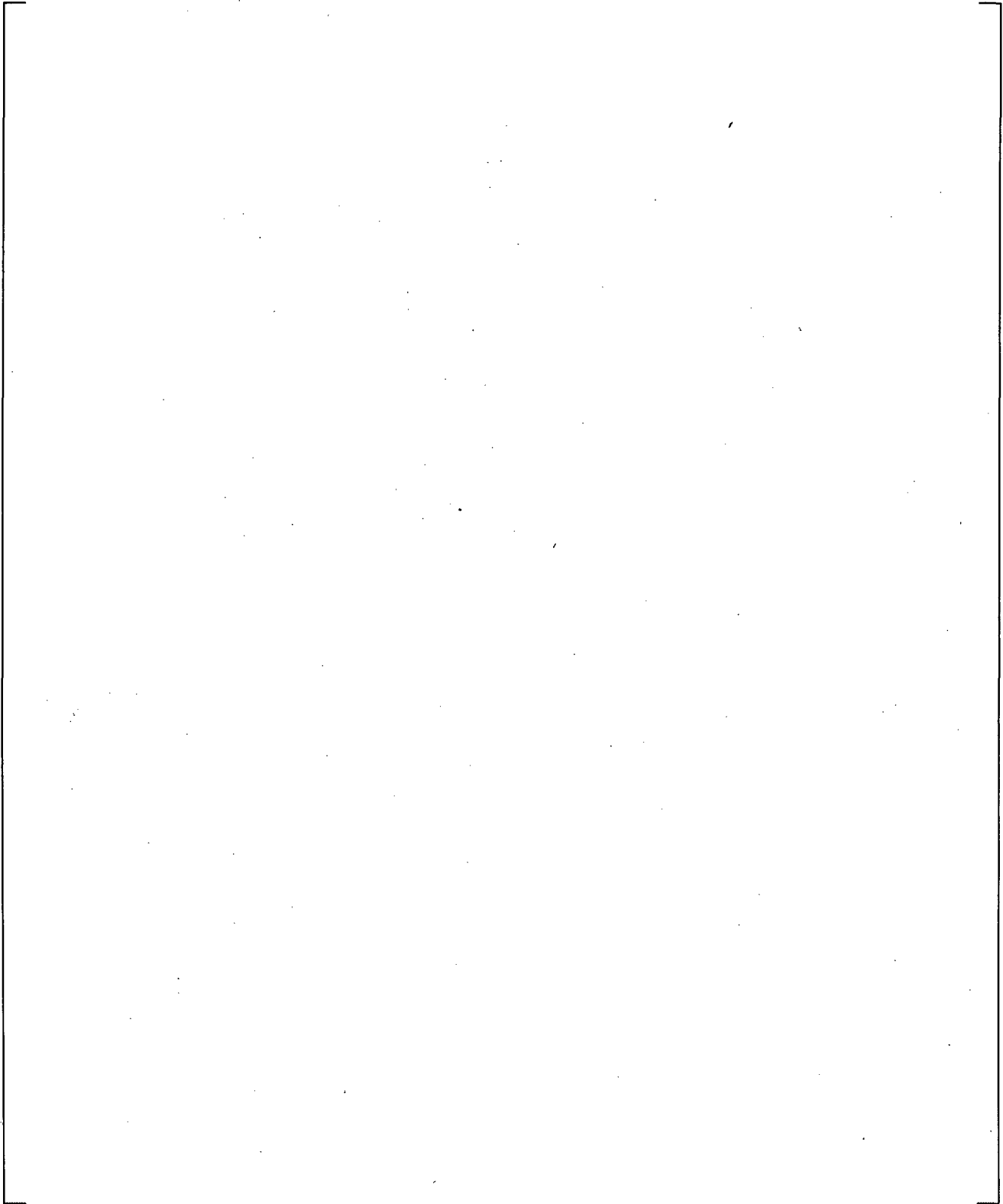


**Figure 20.1-29 Measured and Predicted Pressure at Top of Downcomer**

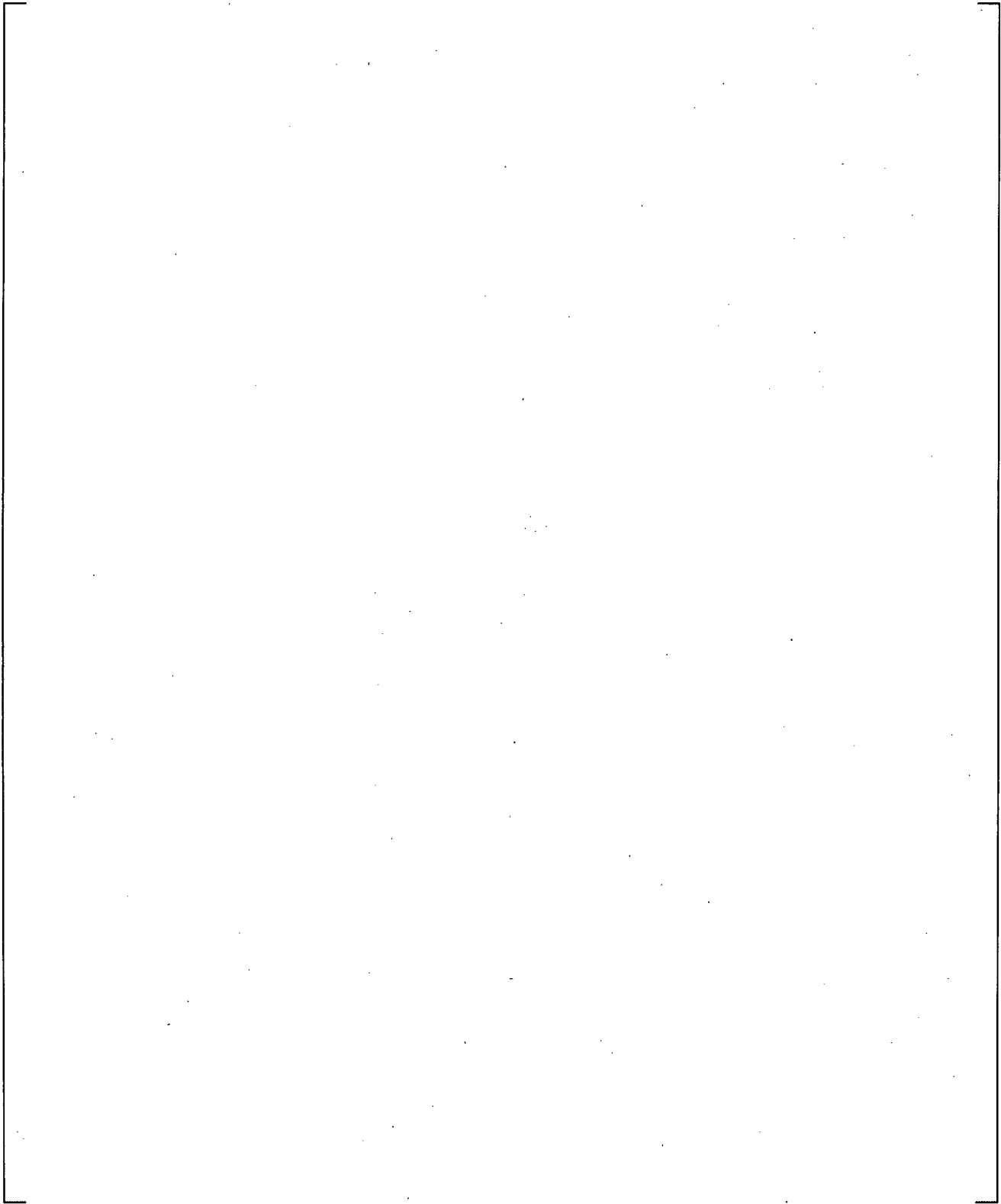


**Figure 20.1-30 Measured and Predicted Pressure Loss from Top of Downcomer to Break**

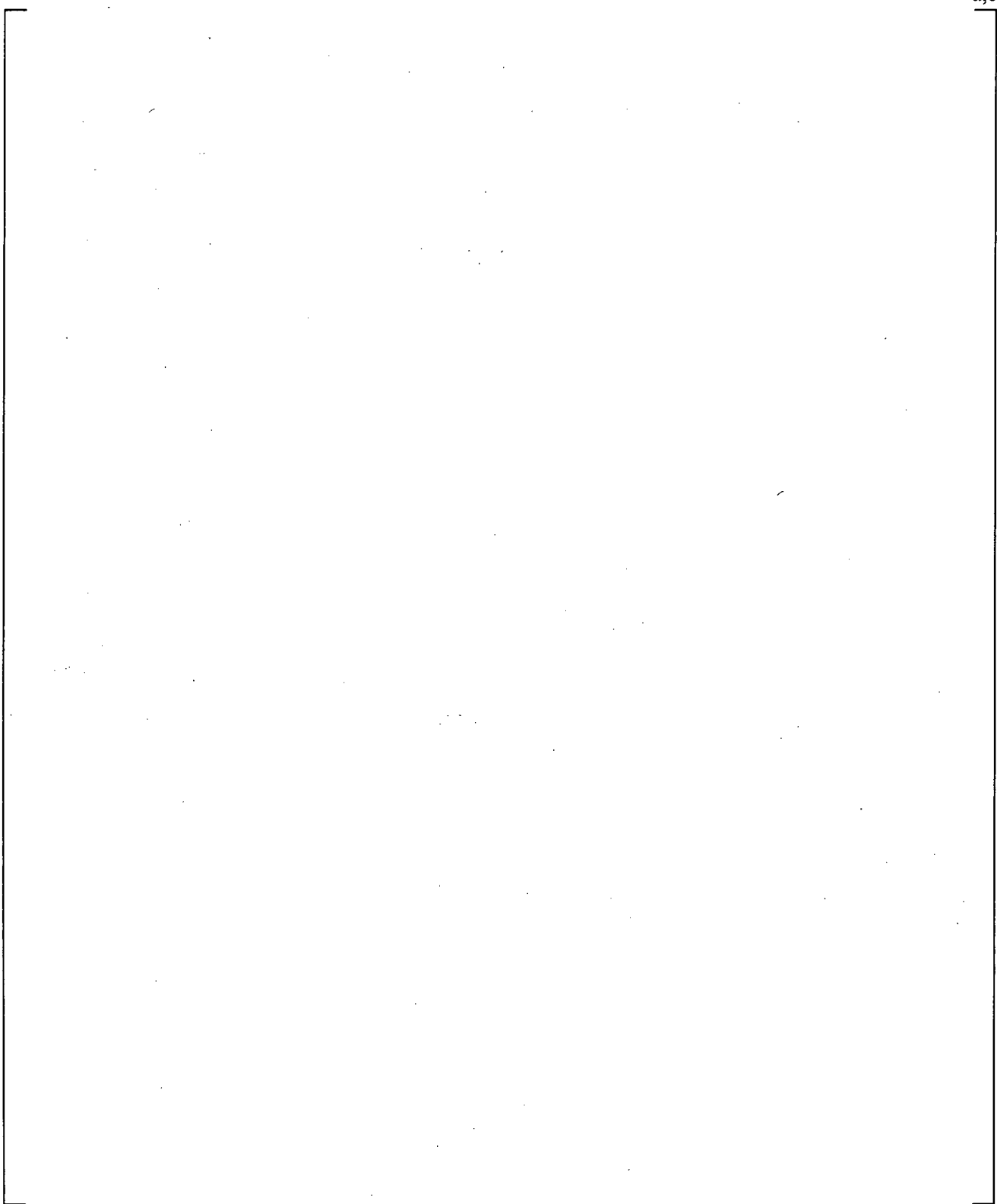


**Figure 20.1-31 Measured and Predicted Gas Flow Rate from Top of Downcomer to Break**

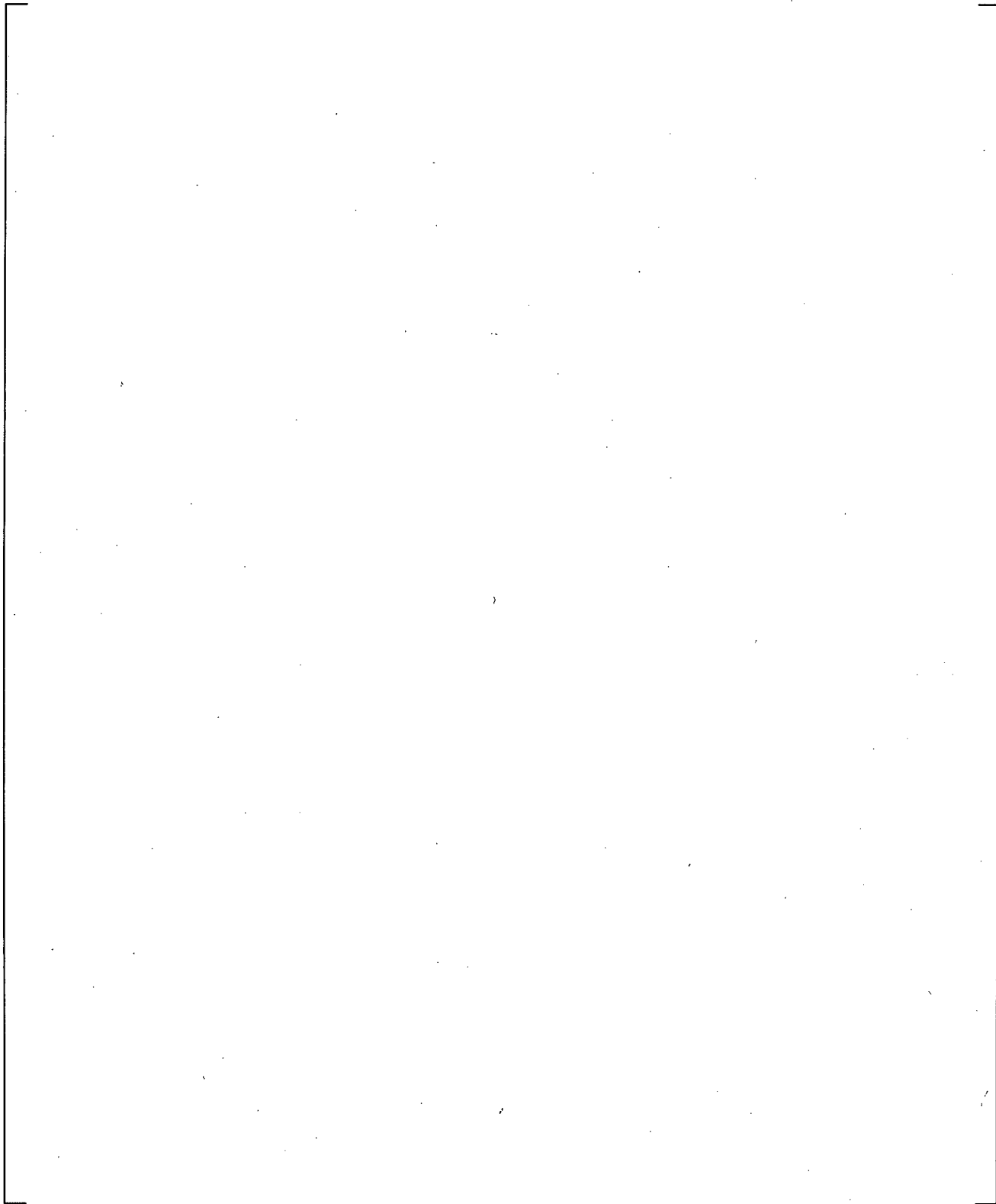


**Figure 20.1-32 Measured and Predicted Downcomer Liquid Level**

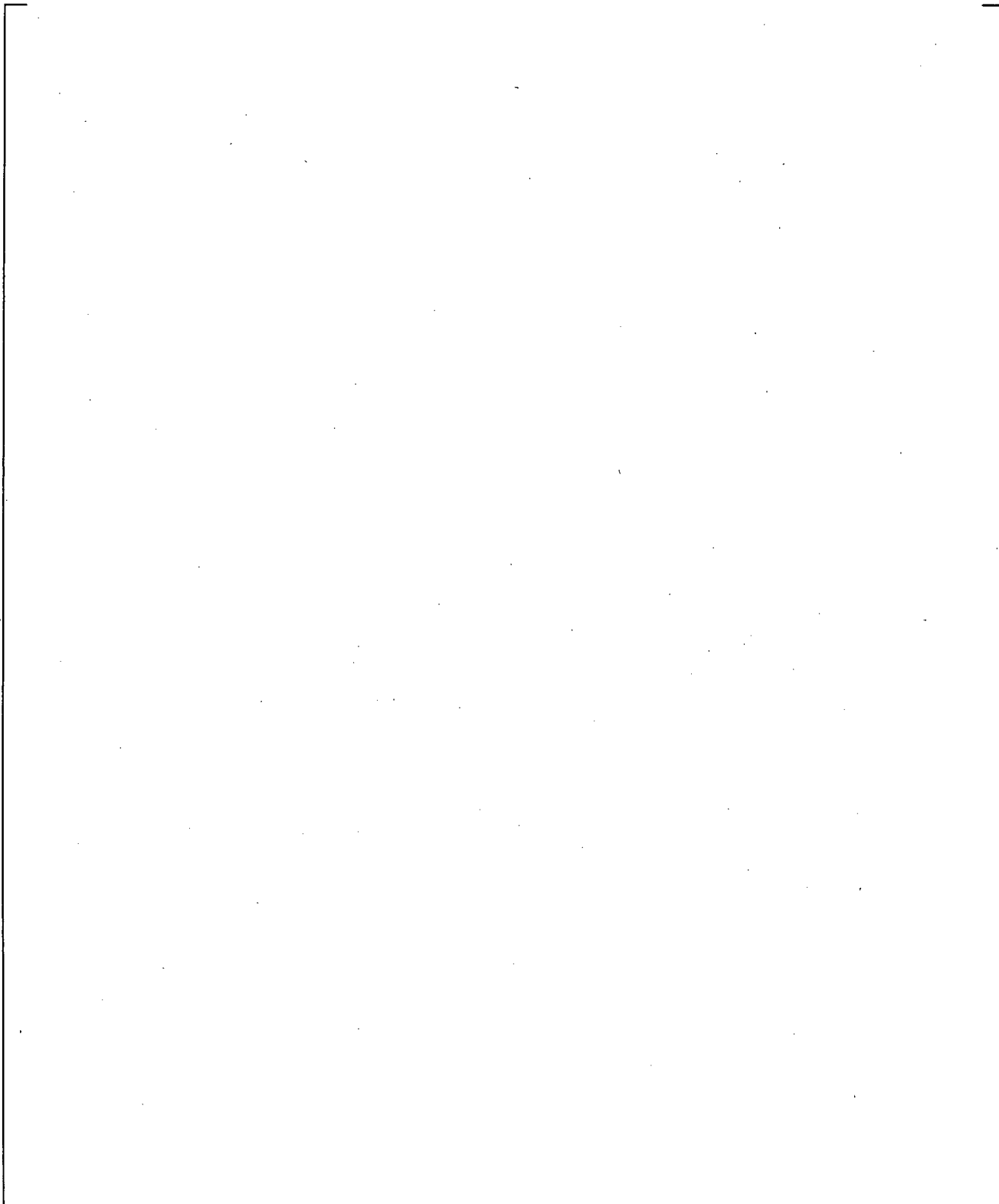


**Figure 20.1-33 Measured and Predicted Test Section Liquid Level**

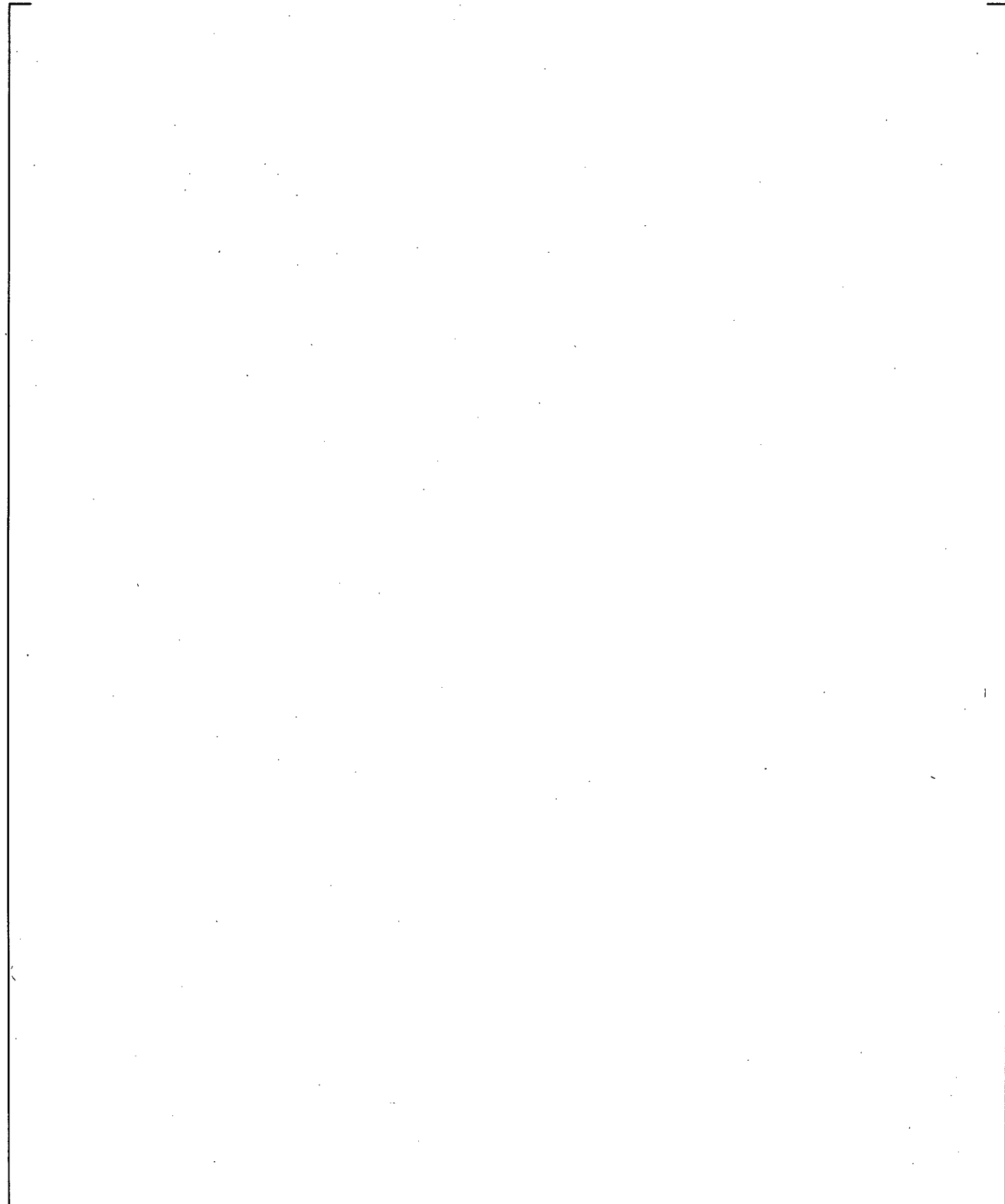


**Figure 20.1-34 Measured and Predicted Cladding Temperature at 1.08m (3.54 ft)**

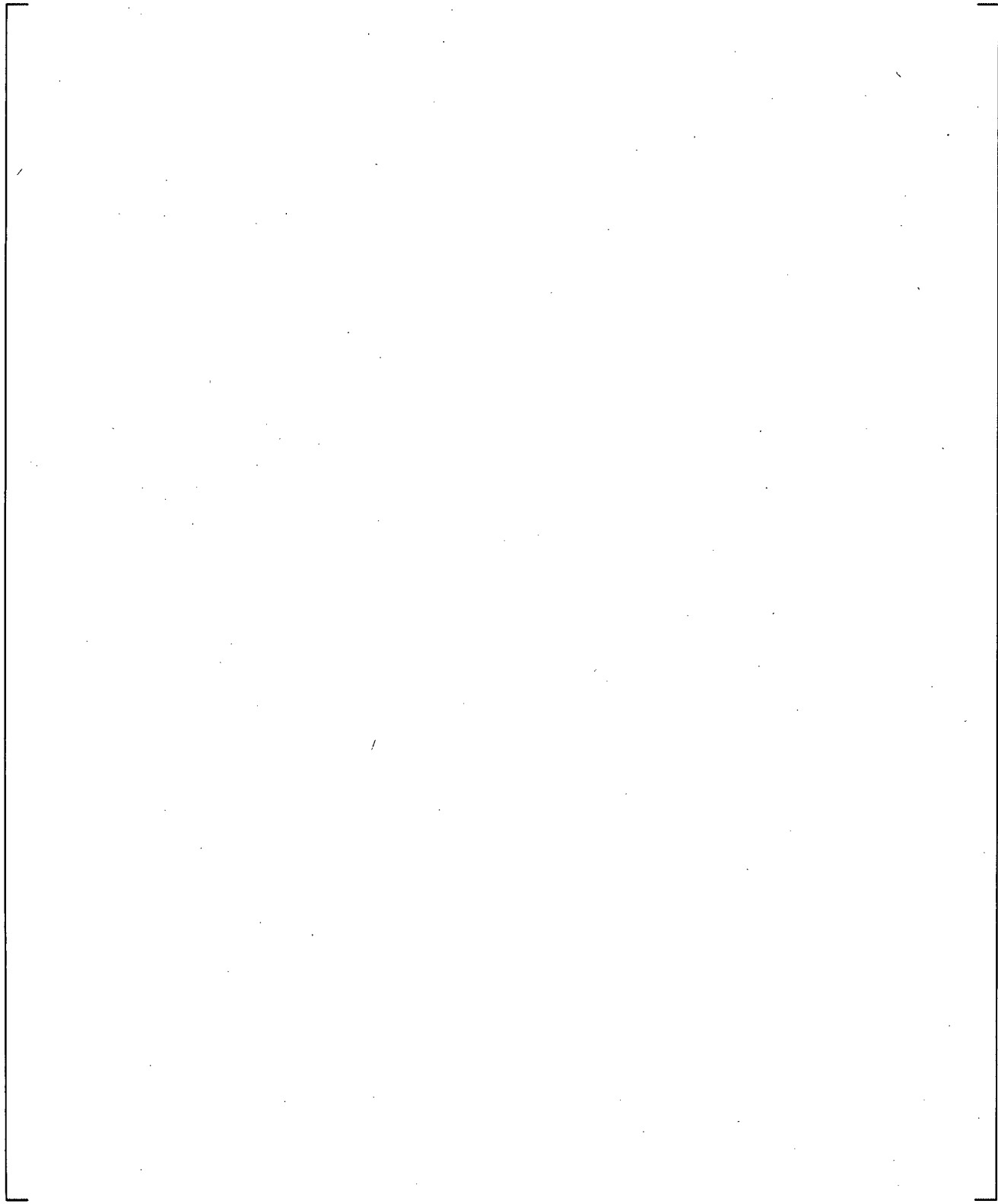


**Figure 20.1-35 Measured and Predicted Cladding Temperature at 2.01m (6.59 ft)**

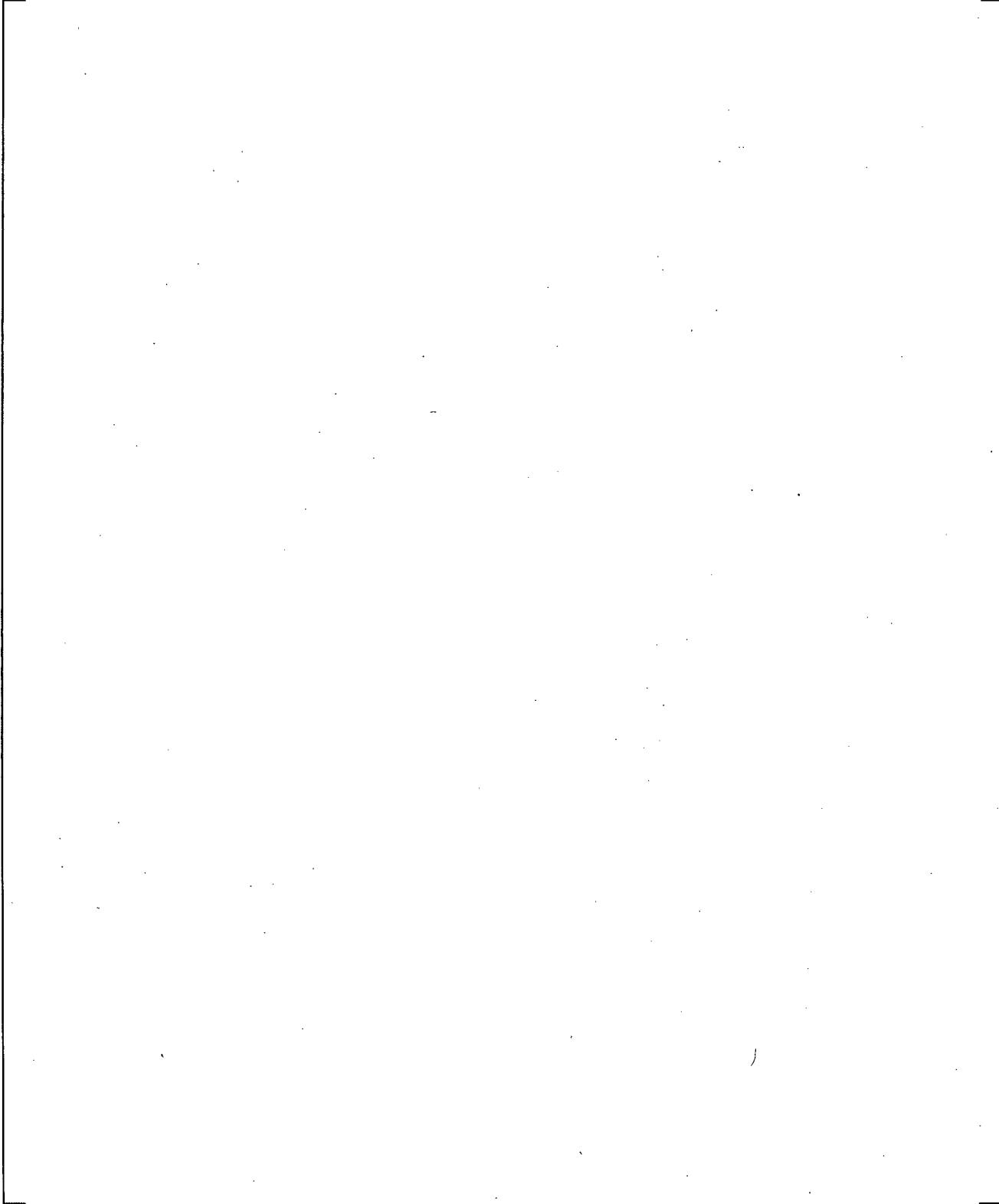


**Figure 20.1-36 Measured and Predicted Cladding Temperature at 2.65m (8.69 ft)**

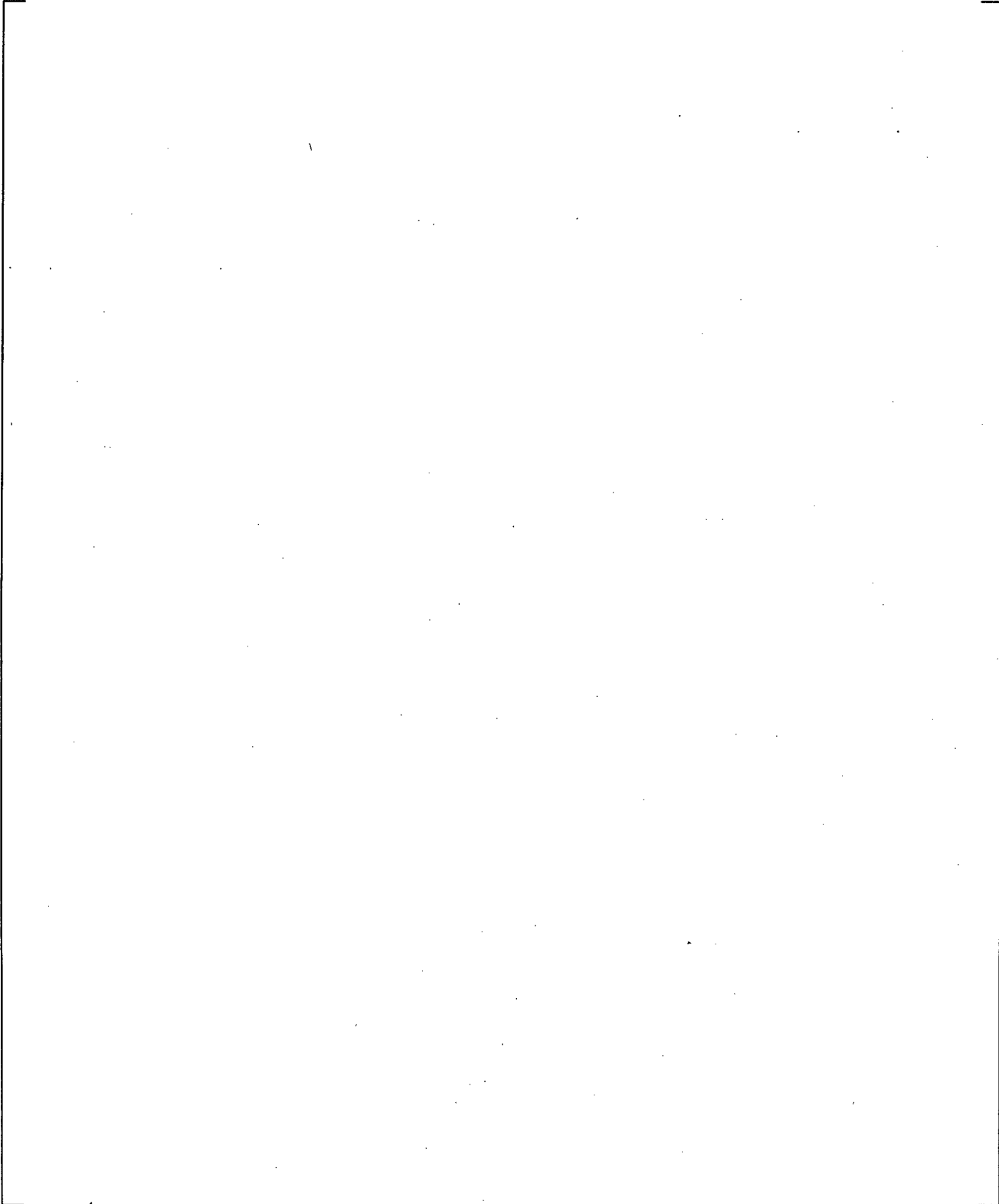


**Figure 20.1-37 Measured and Predicted Accumulator Pressure (Broken Pipe Pressure Loss Sensitivity Study)**

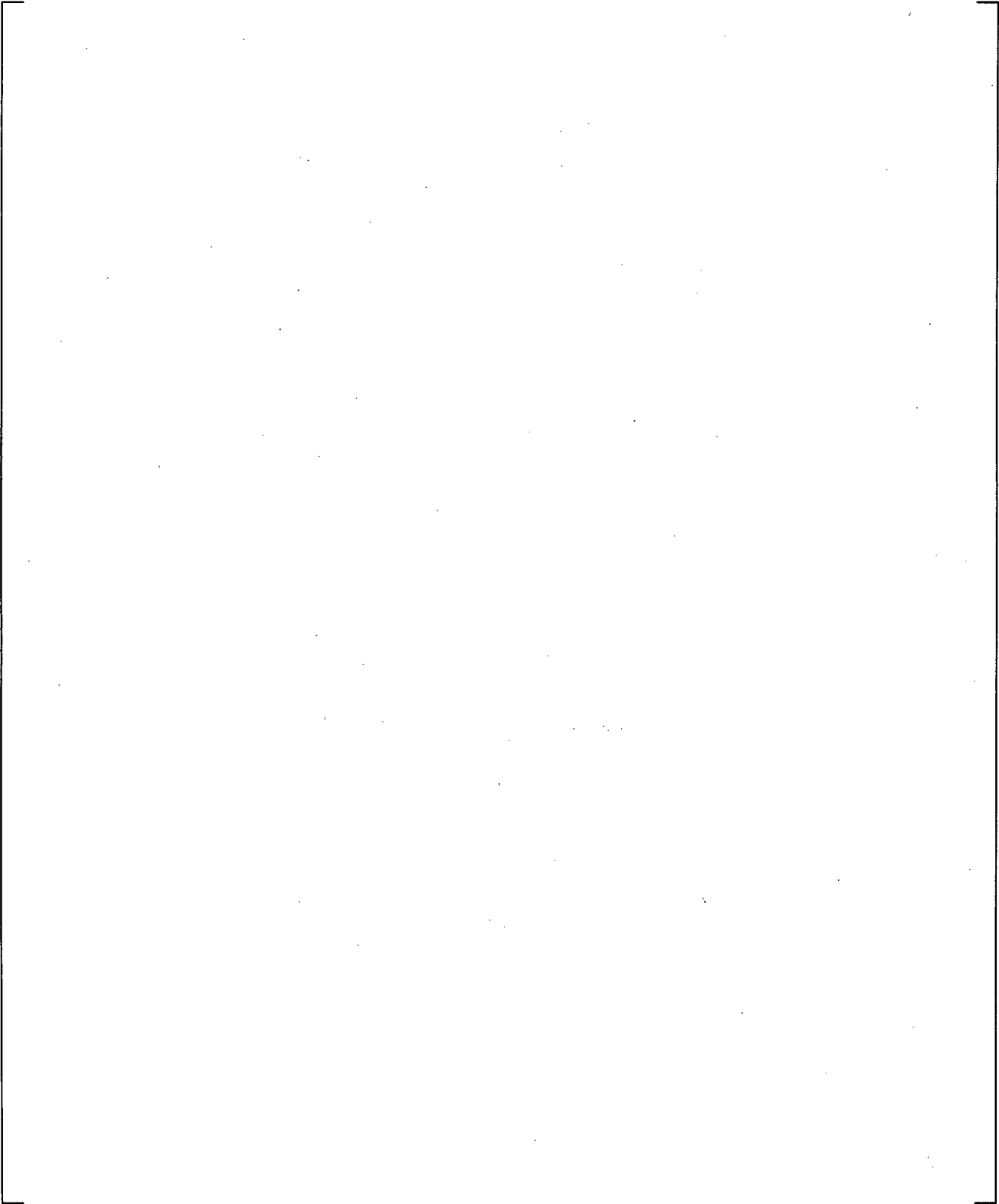


**Figure 20.1-38 Measured and Predicted Accumulator Discharge Line Mass Flow Rate (Broken Pipe Pressure Loss Sensitivity Study)**

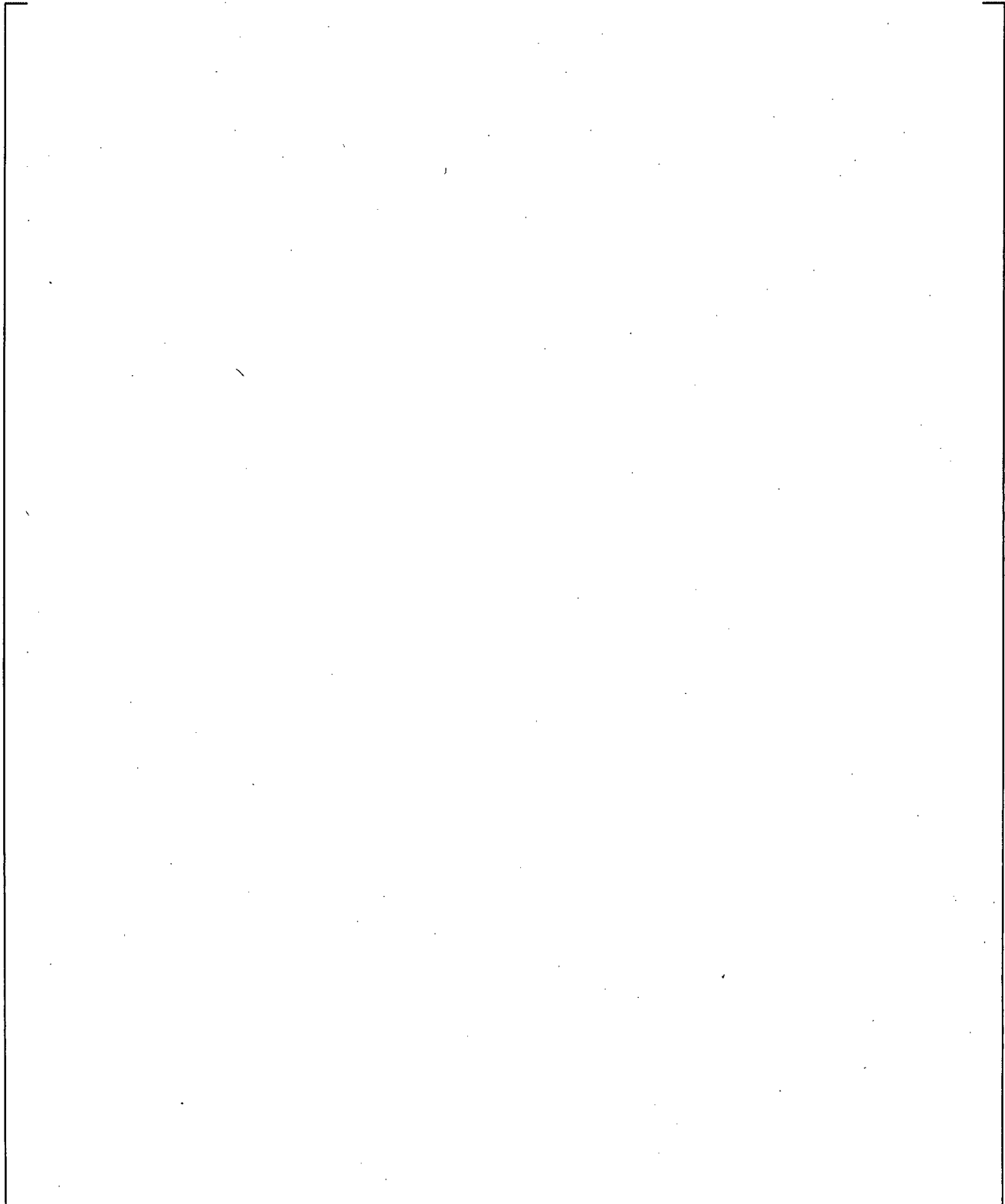


**Figure 20.1-39 Measured and Predicted Pressure at Top of Downcomer (Broken Pipe Pressure Loss Sensitivity Study)**

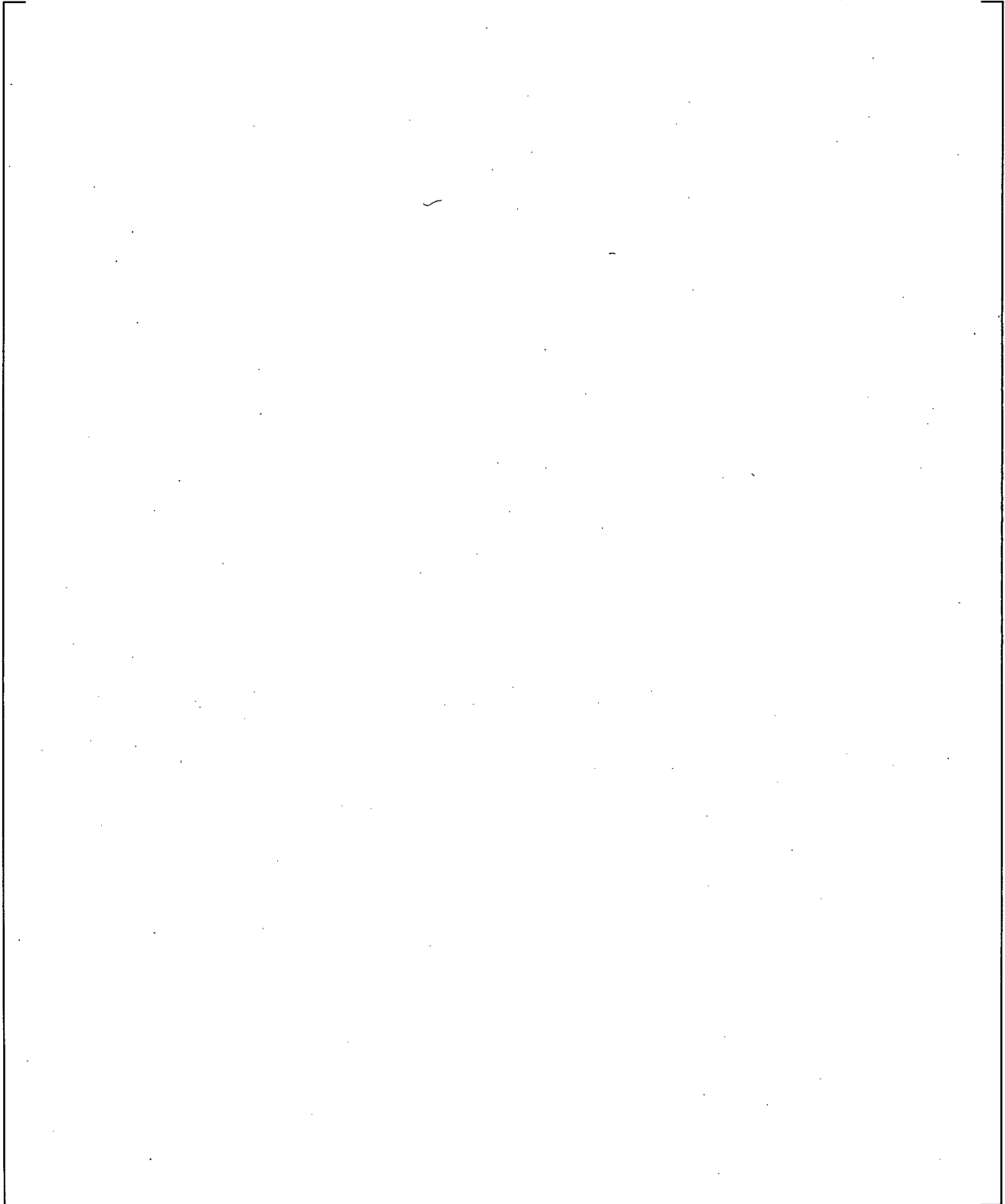


**Figure 20.1-40 Measured and Predicted Downcomer Liquid Level (Broken Pipe Pressure Loss Sensitivity Study)**

a,c

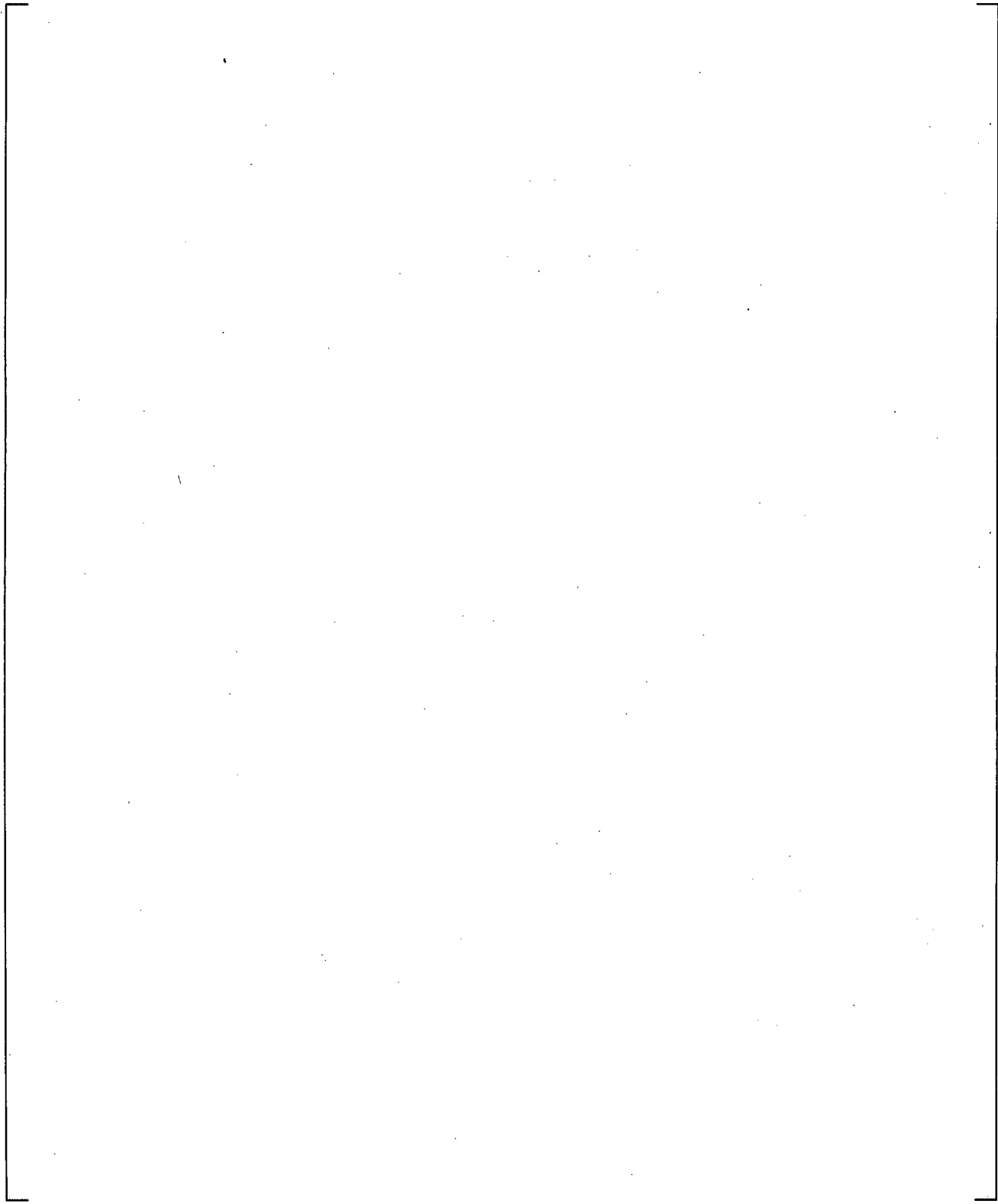


**Figure 20.1-41 Measured and Predicted Test Section Liquid Level (Broken Pipe Pressure Loss Sensitivity Study)**

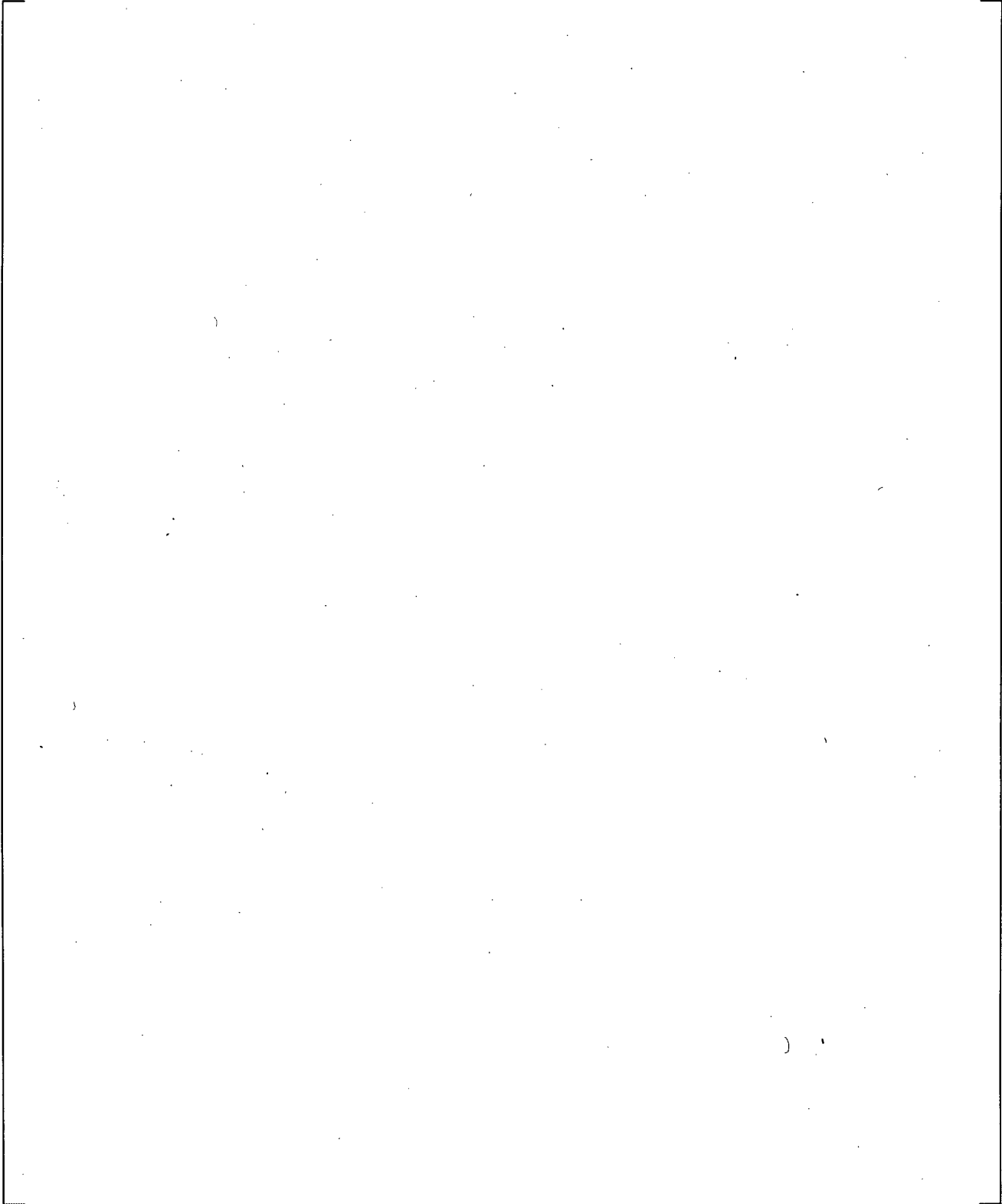


**Figure 20.1-42 Measured and Predicted Cladding Temperature at 1.08m (3.54 ft) (Broken Pipe Pressure Loss Sensitivity Study)**

a,c

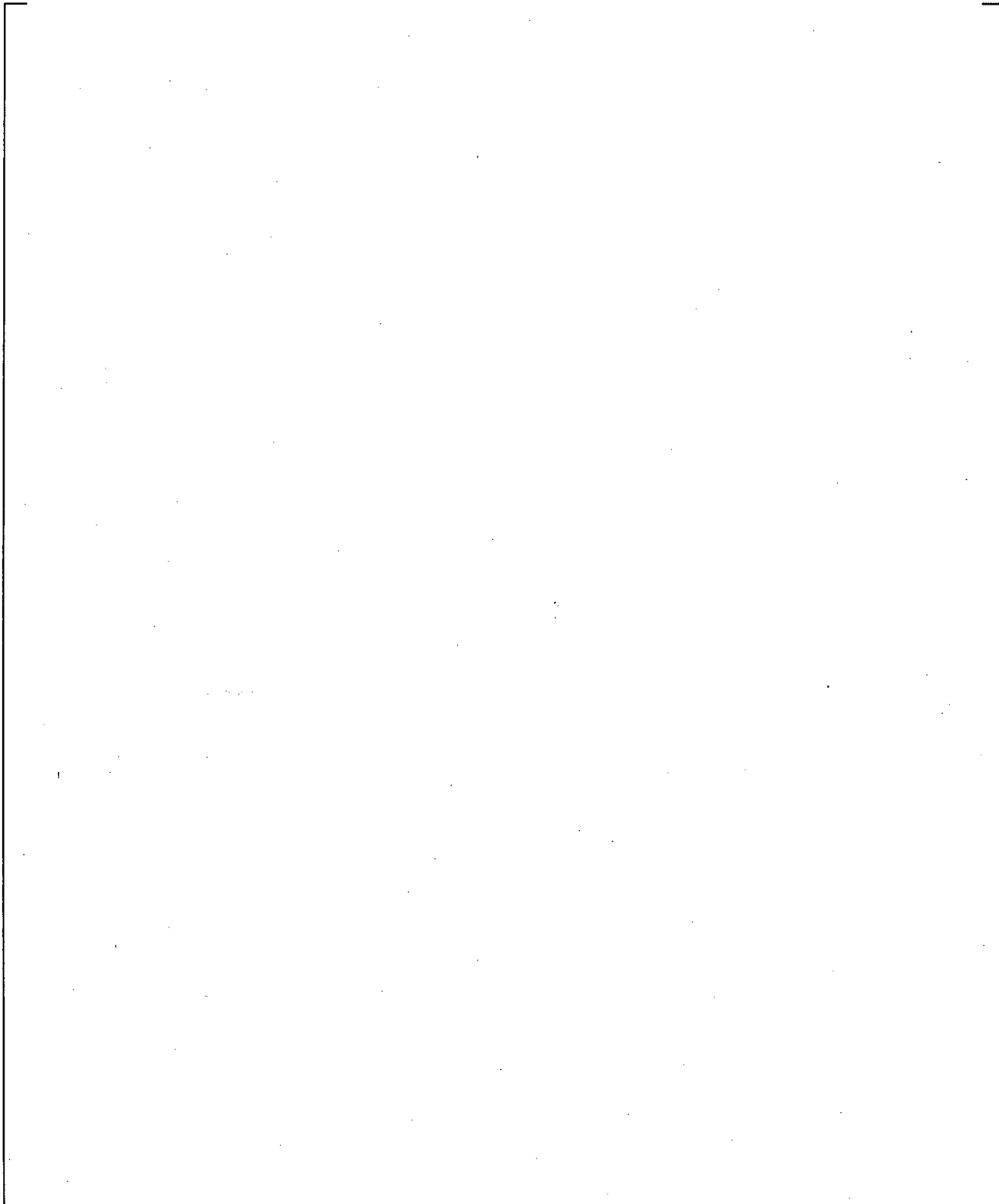


**Figure 20.1-43 Measured and Predicted Cladding Temperature at 2.01m (6.59 ft) (Broken Pipe Pressure Loss Sensitivity Study)**

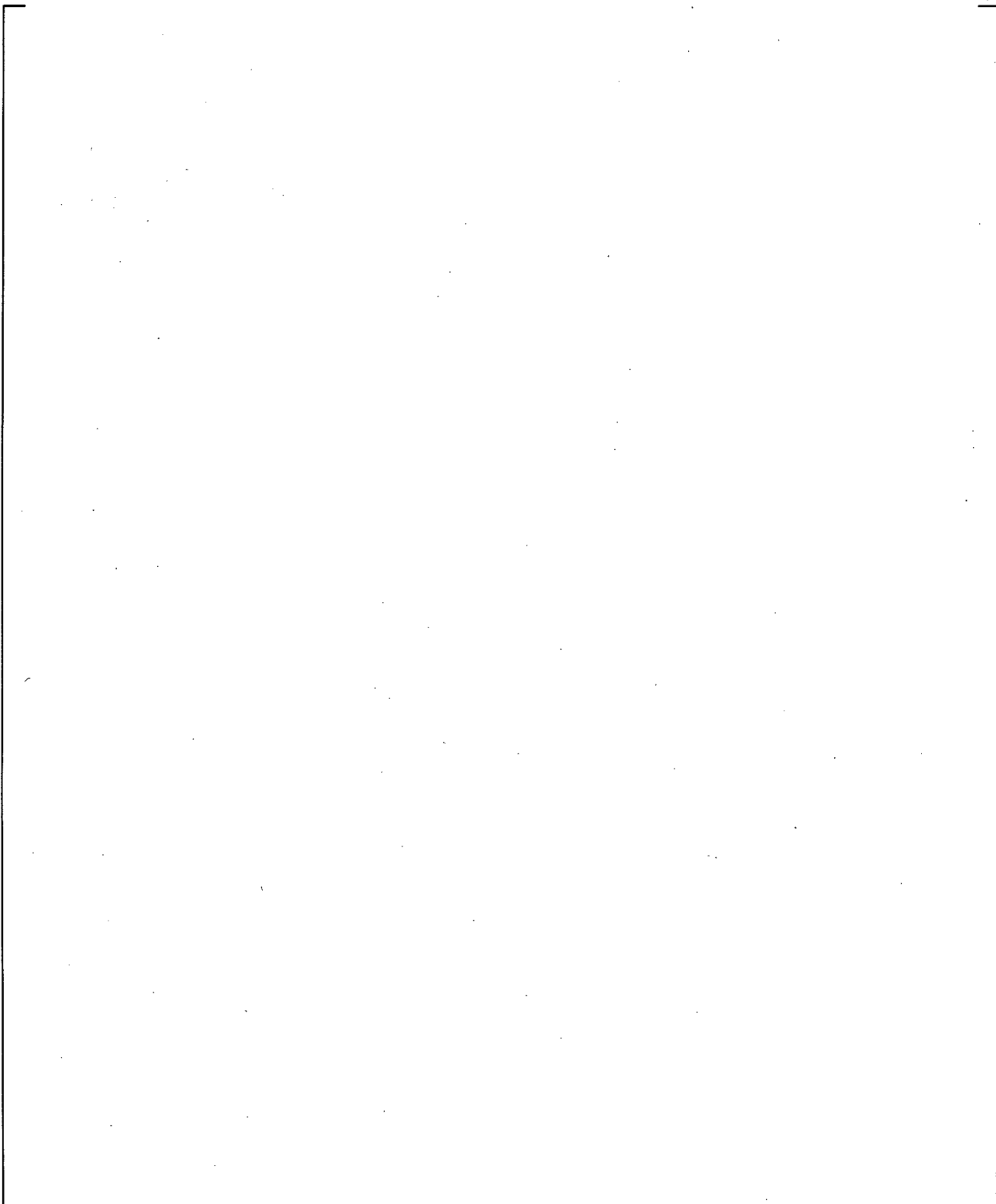


**Figure 20.1-44 Measured and Predicted Cladding Temperature at 2.65m (8.69 ft) (Broken Pipe Pressure Loss Sensitivity Study)**

## 20.2 PUMP COMPONENT MODEL

The pump component model was described in Section 10.4 of Volume 1. It is an empirical model in which the pressure differential generated by the pump, and the corresponding torque applied to the pump during single- and two-phase flow, is derived from single- and two-phase flow data in scaled pumps. In particular, the pump head and torque during two-phase flow is assumed to vary as a function of void fraction from the single-phase value to a "fully degraded," or minimum value which occurs at intermediate void fractions. For the pump head,

$$H = H_1 - M(\alpha) * (H_1 - H_2) \quad (20.2-1)$$

where:

H	=	pump head
H <sub>1</sub>	=	single-phase pump head
H <sub>2</sub>	=	fully degraded pump head
M(α)	=	two-phase multiplier

A similar equation is used for the pump torque (Equation 10-9) with the multiplier defined as N(α).

This is clearly an approximate description of the actual variation of the pump head. As described by Rohatgi et al. (1989), the uncertainty associated with such a model is relatively large and needs to be considered in the code uncertainty. In Section 2.3.2.9, the performance of the reactor coolant pump was included as part of the PIRT. For one- and two-phase performance, a medium (M) ranking was assigned during blowdown. Pump coastdown was ranked medium (M) during blowdown for intermediate breaks as well, and was ranked high (H) for large breaks. Flow resistance was ranked medium (M) for intermediate breaks and high (H) for large breaks during blowdown. The purpose of this section is to describe the basis for the empirical model used in the LOCA analysis of the PWR, establish the basis for its uncertainty, and relate it to the pump model used in LOFT. Comparisons with LOFT data of the predicted pump head then serve as validation that the empirical model adequately predicts pump head for both LOFT and a PWR.

### 20.2.1 Westinghouse Pump Data

The Westinghouse pump model is based on air/water data obtained from a scale model of a 93A model pump, designed to operate at a pump head of 92.6 feet, a flow of 7420 gpm, and an impeller speed of 1799 rpm. The scale model used to obtain single- and two-phase data is shown in Figure 20.2-1. It was designed to be geometrically similar to a full-scale Westinghouse model 93A pump, with an equivalent specific speed. The specific speed N<sub>s</sub> of a centrifugal pump is defined as:

$$N_s = N Q^{1/2} / H^{3/4} \quad (20.2-2)$$

where:

N	is in rpm
Q	is in gpm
H	is in feet of water

Specific speed has been found to be a convenient parameter distinguishing the performance characteristics of different pumps. The specific speeds of Westinghouse pumps range from approximately 5000 to 7000 rpm. In contrast, the specific speed of the LOFT pumps is 3300 rpm.

### Single-Phase Data

Figures 20.2-2 and 20.2-3 show some of the test data used to determine the single-phase homologous curves for forward and reverse flow through the pump. The data consists of water data from the scale model of the 93A pump, as well as air data from the same scale model and test facility where two-phase data was obtained (Howland and Lamers, 1973). It can be seen that the air and water data agree well, indicating that the change in test fluid and test facility had little effect on the test results.

The uncertainty of the single-phase data was determined by evaluating two data sources. The first source was from the Westinghouse single-phase data cited above. A band can be drawn to bound the data in Figure 20.2-3 (the normalized head ratio  $h/v^2$  data is plotted against the inverse of the normalized flow ratio  $v/\alpha$  in this figure). [

] <sup>a,c</sup>

The second source examined was from data developed by Cudlin (1977), where the normalized head ratio in the forward flow, dissipative quadrant for a 1/3-scale model pump is shown in Figure 20.2-4. [

] <sup>a,c</sup>

### Two-Phase Data

The two-phase data were obtained by running air/water mixtures through the pump (Howland and Muench, 1975). The test facility is illustrated in Figure 20.2-5. Water was drawn from a large basin using a diesel powered pump, mixed with air in a mixing chamber, and pushed through the scale model pump. Inlet line venturi meters and orifices were used to measure inlet flow rates. Pump pressure differential, impeller speed, and impeller torque were also measured. The inlet void fraction was not measured but was inferred from the flow rates. A correlation was used to estimate the void fraction from the flow rates. In addition, a homogeneous void fraction was used. It was found that the basic nature of the data was not affected by the choice of void fraction. In the following discussion, the homogeneous (zero slip) void fraction is used.

Typically, homologous head data is plotted using two x-axes, normalized flow divided by normalized speed ( $v/\alpha$  as in Figure 20.2-2), and normalized speed divided by normalized flow ( $\alpha/v$  as in Figure 20.2-3). An alternative way to plot the head data is to show normalized head divided by normalized speed squared ( $h/\alpha^2$ ), versus normalized flow divided by normalized speed ( $v/\alpha$ ), for all forward flow conditions. This results in Figure 20.2-6, which more clearly shows the transition, as flow increases, from a positive head or pumping mode, to a negative head or energy dissipation mode. The intact loop pumps are operating in the pumping mode during the initial stages of a cold leg break LOCA, while the broken loop pump is operating in an energy dissipation mode during the entire transient. The two-phase data is also shown on this figure, and indicates that the pumping mode data shows relatively little scatter, while the dissipation mode data shows more scatter. The increased scatter may be due to the fact that, when the downstream pressure is lower, the upstream conditions are no longer as accurate a

representation of conditions within the pump. Also plotted on this figure are the single-phase head curve and a fully degraded head curve drawn through the lower bound data.

The method for determining the two-phase multiplier  $M(\alpha)$  and  $N(\alpha)$  in Equations 10-8 and 10-9 from the pump data is as follows:

1. Determine single-phase homologous head and torque. The pressure difference across the pump, and the torque applied to the pump impeller, are measured under a variety of flow conditions. Homologous head and torque curves are derived by dividing these data by the appropriate quantities (rated flow, rated speed, etc.). Each pump model (designated 93, 93A, 100, etc.) designed by Westinghouse has a set of homologous curves derived from scale model single-phase tests using both air and water.
2. Measure the pump pressure difference and torque under two-phase conditions over a range of void fractions. The lower boundary of the data, when converted to homologous form, is defined as the "fully degraded" homologous head and torque. These data were obtained from a 1/3-scale model pump with the same specific speed as the model 93A pump. The pump head data are shown in Figure 20.2-7, and the pump torque data in Figure 20.2-8. The single-phase and "fully degraded" curves constructed from these data are also shown (they are also shown in Figures 10-4 to 10-7). In Figure 20.2-7, HSP1 and HTP1 are the single- and fully degraded two-phase head ( $h/\alpha^2$ ) curves presented as a function of  $v/\alpha$ , while HSP2 and HTP2 present the head ( $h/v^2$ ) as a function of  $\alpha/v$ . Note that the fully degraded curves are always drawn below the single-phase curves, and bound nearly all the data.

The two-phase data indicate that the amount of full degradation in head or torque is approximately a constant. That is, the fully degraded curve is offset from the single-phase curve by a constant. This is more easily seen in Figure 20.2-6. This observation allows the fully degraded curve to be extended into areas where data is sparse or lacking.

3. Assume that the homologous head and torque go from single-phase to fully degraded back to single-phase values as the pump inlet void fraction ranges from 0 to 1.0. Use Equation 20.2-1 in the following form to calculate  $M(\alpha_i)$  for each pump head data point  $H(\alpha_i)$ :

$$M(\alpha_i) = \frac{H(\alpha_i) - H_1}{H_2 - H_1}$$

Use the  $M(\alpha_i)$  data to define the appropriate shape of the  $M(\alpha)$  function, as in Figures 20.2-9 and 20.2-10. Figure 20.2-9 includes only the pumping mode data, while Figure 20.2-10 includes all the data. Perform a similar exercise for the pump torque (Figure 20.2-11).

Data are lacking for void fractions greater than approximately 65 percent. [

] <sup>b,c</sup> This assumption is supported by test data from other design pumps, for example, Figure 2.1 on page L-9 of the CSAU report (Boyack et al., 1989).

The simple form of the  $M(\alpha)$  function results in considerable scatter in the data in the dissipative, or turbine mode of pump operation. The effect of this uncertainty was examined by defining a new multiplier which was drawn below the lower bound of the data and was found to result in a relatively small effect for large breaks, due to the relatively short time that the pump is in the fully degraded low void fraction two-phase regime. This result is consistent with results obtained in the CSAU report (Boyack et al., 1989). For small breaks, the use of a multiplier representing the lower bound of the data has only a small effect when offsite power is available. In that case, because the pumps continue to rotate at fixed speed into the early portion of the natural circulation phase, differential pressure across the pumps is predicted differently when the flow is two-phase using the lower bound degradation curve. This effect subsides before loop seal clearance, however, so the effect on the transient is negligible. With a loss of offsite power, the effect on the small break transient is negligible due to the early coastdown of the pumps and the presence of primarily single phase flow in the loops.

[

] <sup>a,c</sup>

### 20.2.2 Pump Model Comparison to Data

The only large break test which contains a powered pump is the LOFT test. Although the pumps in LOFT are of a different design than PWR pumps, they exhibit similar overall performance as can be seen from Figure 20.2-12. The pump model used in the LOFT simulations, described in Section 22 of this report, is the same as that used in the PWR, except that the homologous curves and the two-phase multiplier used were the LOFT specific curves, obtained from tests on the Semiscale pump (Reeder, 1978). Another difference was that the pump speed was input from the LOFT data, rather than calculated. This was done to examine specifically the pump head prediction, which will be shown later to be the more important parameter in the PWR calculation. The resulting prediction for LOFT Test L2-5 is shown in Figure 22-43.

These comparisons show that the predicted pressure difference across the pumps in the intact loops compares well with the measured pressure difference during blowdown.

The ROSA-IV test facility provides a means for comparison in the context of small breaks. Figure 21.5-2 shows that WCOBRA/TRAC-TF2 adequately predicts the pump speed throughout the SB-CL-05 test. Figure 21.6-1 shows the same for SB-CL-14. This, in conjunction with the reasonable prediction of pressures throughout the primary loops suggests that the pump model in WCOBRA/TRAC-TF2 is adequate.

These comparisons indicate that the relatively simple pump model in WCOBRA/TRAC adequately predicts pump behavior during LOCA. In addition, for the Westinghouse pump, the uncertainty in the data is most significant for a broken loop pump operating in the dissipative mode. Section 29.1.2.2 describes how this uncertainty will be treated in plant analyses.

### 20.2.3 References

1. Boyack, et al., 1989, "Quantifying Reactor Safety Margins," NUREG/CR-5249.
2. Cudlin, J. J., 1977, "1/3 Scale Air-Water Pump Program, Analytical Pump Performance Model," EPRI NP-160.
3. Howland, G. R. and Lamers, R. P., 1973, "Air Test Program to Establish the Complete Pump Characteristics of WEMD 93A Model Reactor Coolant Pump," Westinghouse Research Report 73-7E9-TAPSC-R1.
4. Howland, G. R. and Muench, R. A., 1975, "Air/Water Mixed Flow Testing of the WEMD 93A Model Reactor Coolant Pump," Westinghouse Research Report 75-7E9-CORCL-R1.
5. Reeder, D. L., 1978, "LOFT System and Test Description," NUREG/CR-0247.
6. Rohatgi, et al., 1989, "Quantifying Reactor Safety Margins," NUREG/CR-5249.

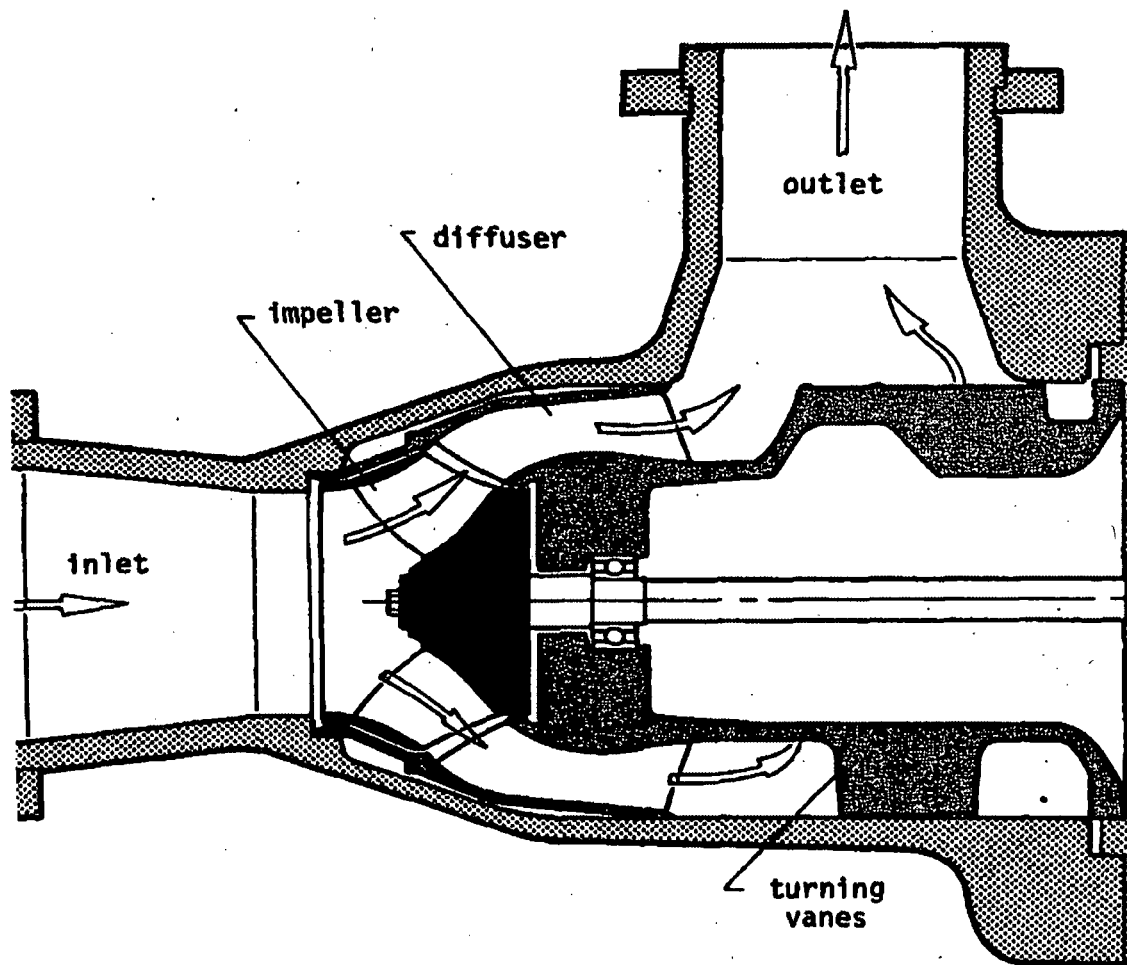
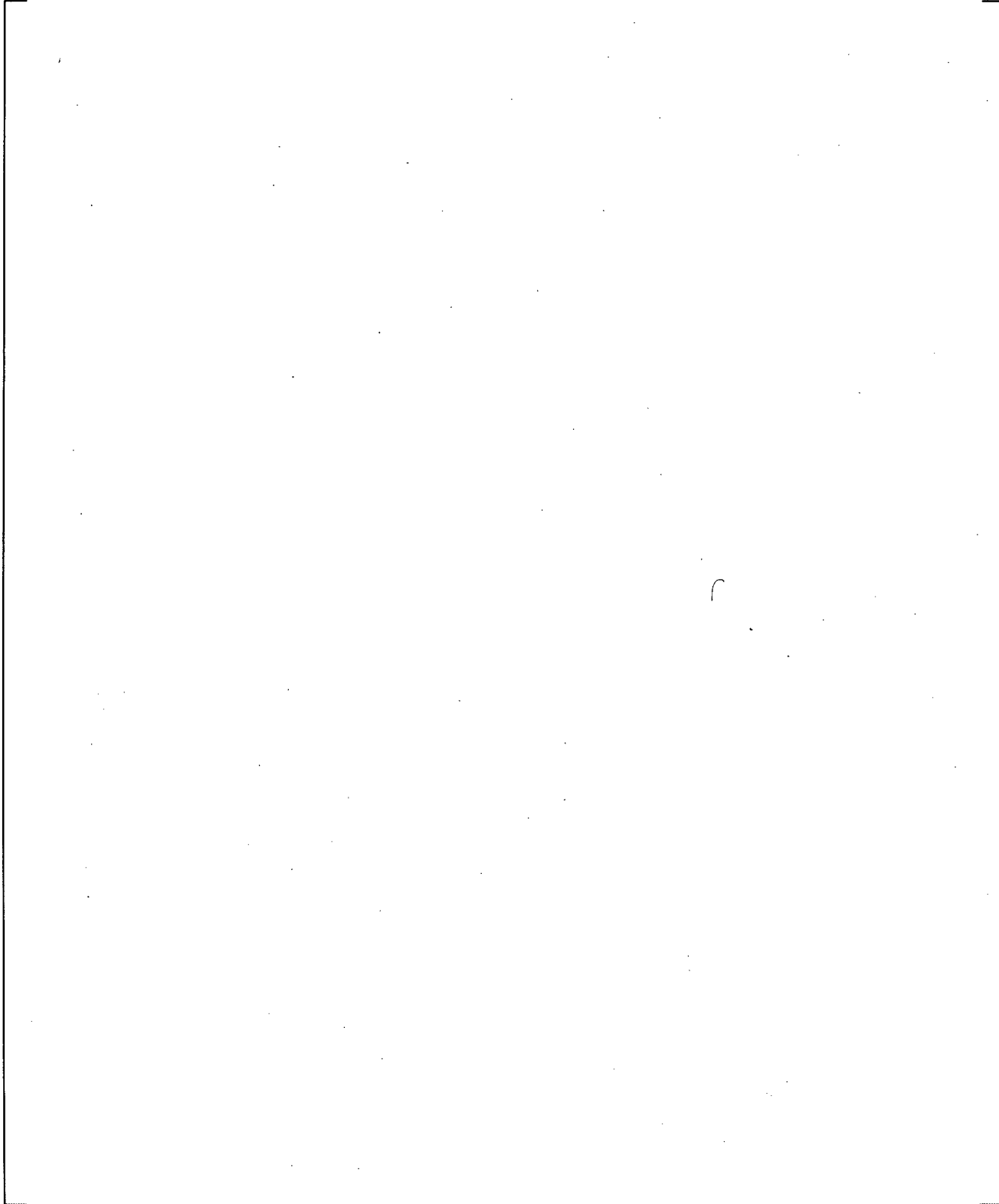
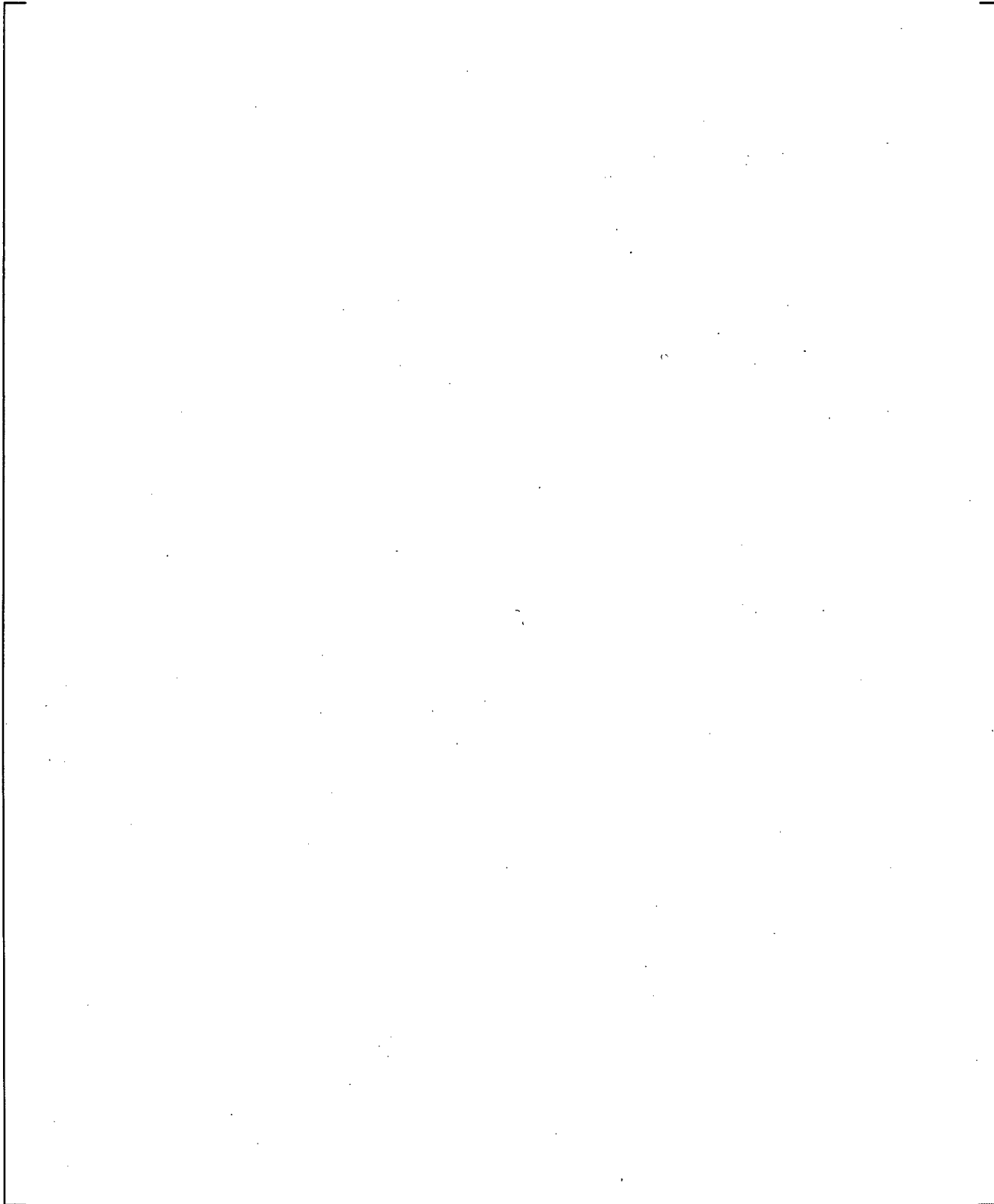


Figure 20.2-1 Cross-Sectional View of the Westinghouse Scale Model Pump



**Figure 20.2-2 Scale Model Homologous Head Single-Phase Data in the Pumping Mode, Forward and Reverse Flow**



**Figure 20.2-3 Scale Model Homologous Head Single-Phase Data in the Dissipation Mode, Forward Flow**

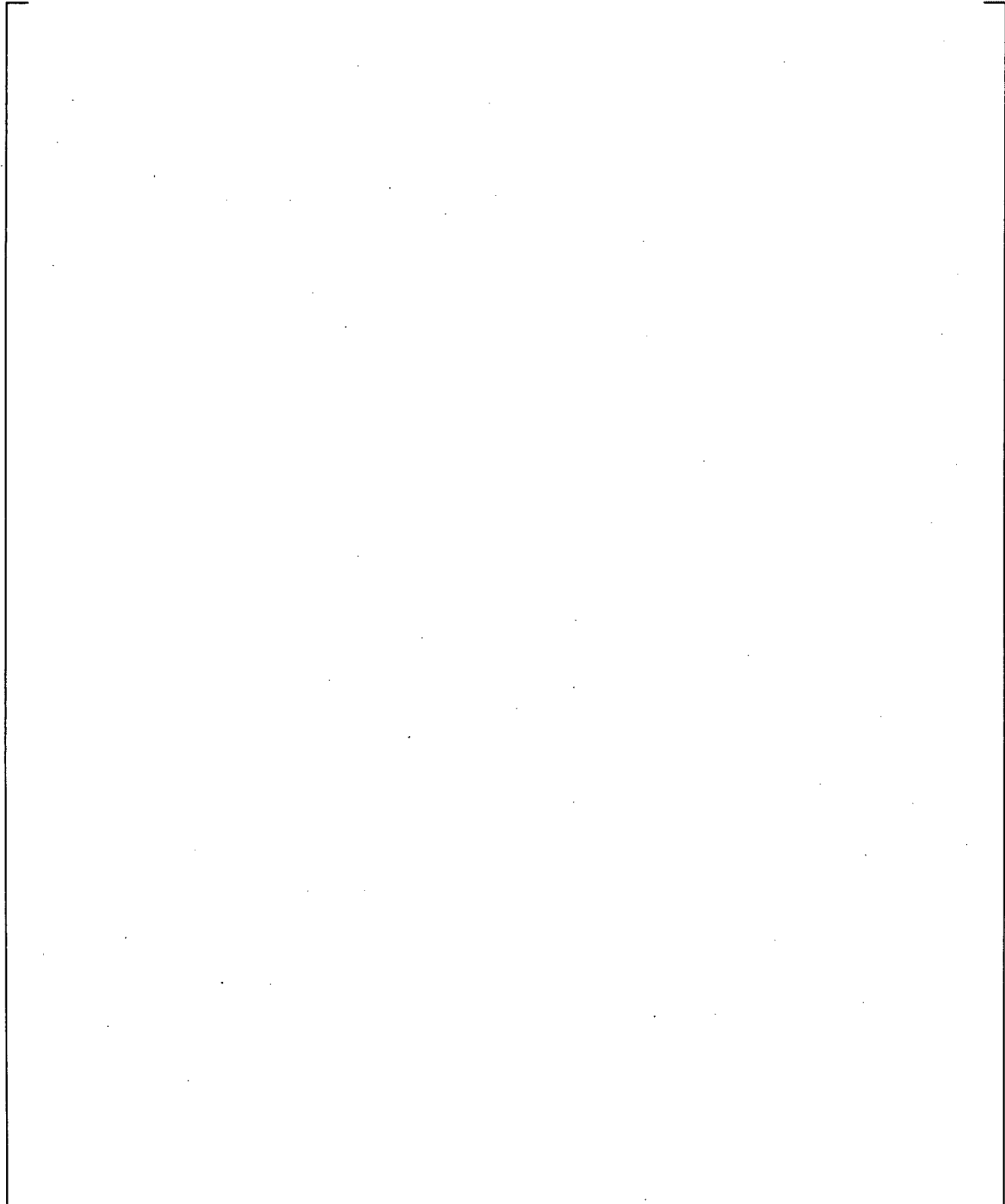


**Figure 20.2-4 Data Scatter for Dissipative Mode 1/3-Scale Pump Data (Cudlin, 1977)**

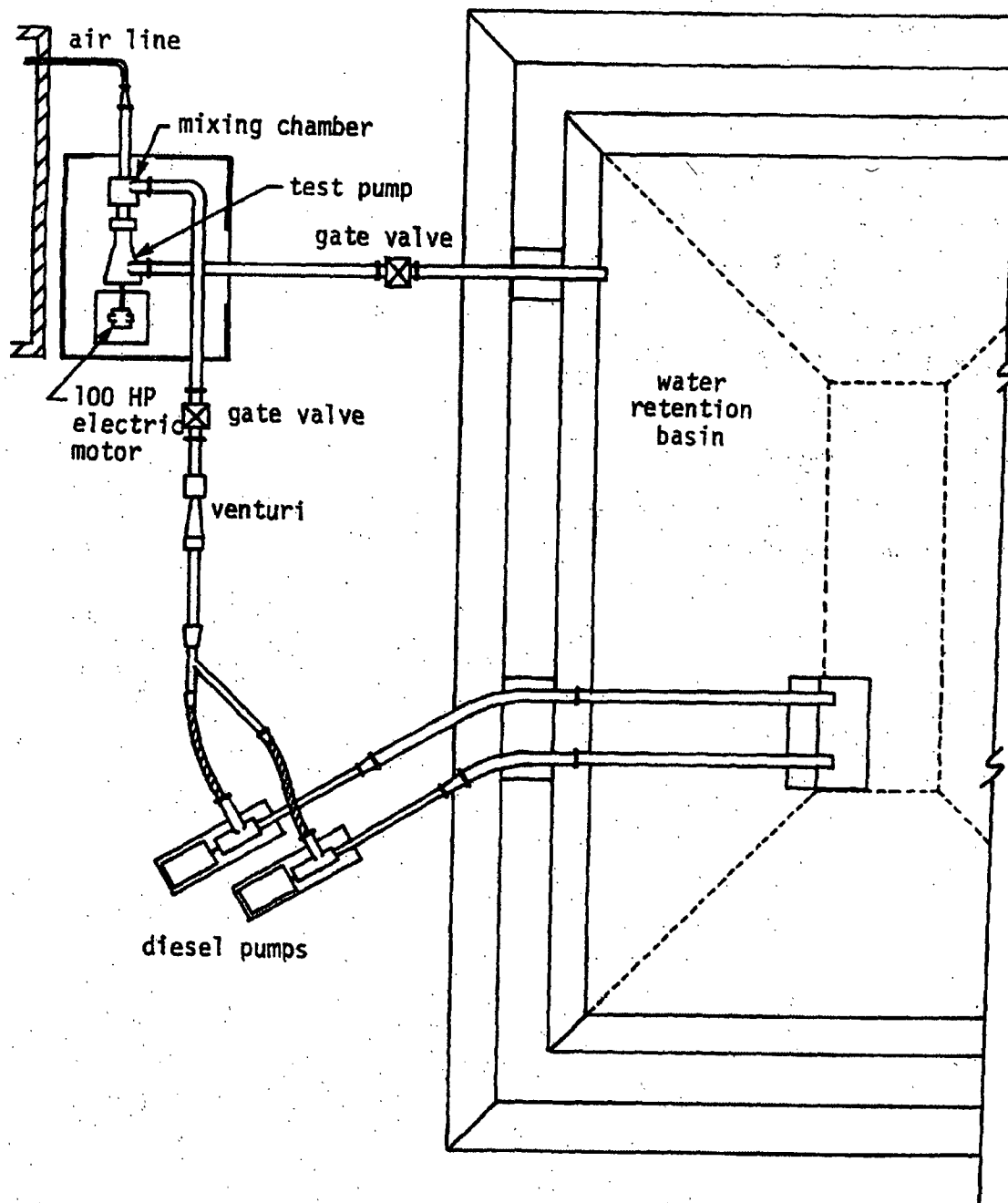
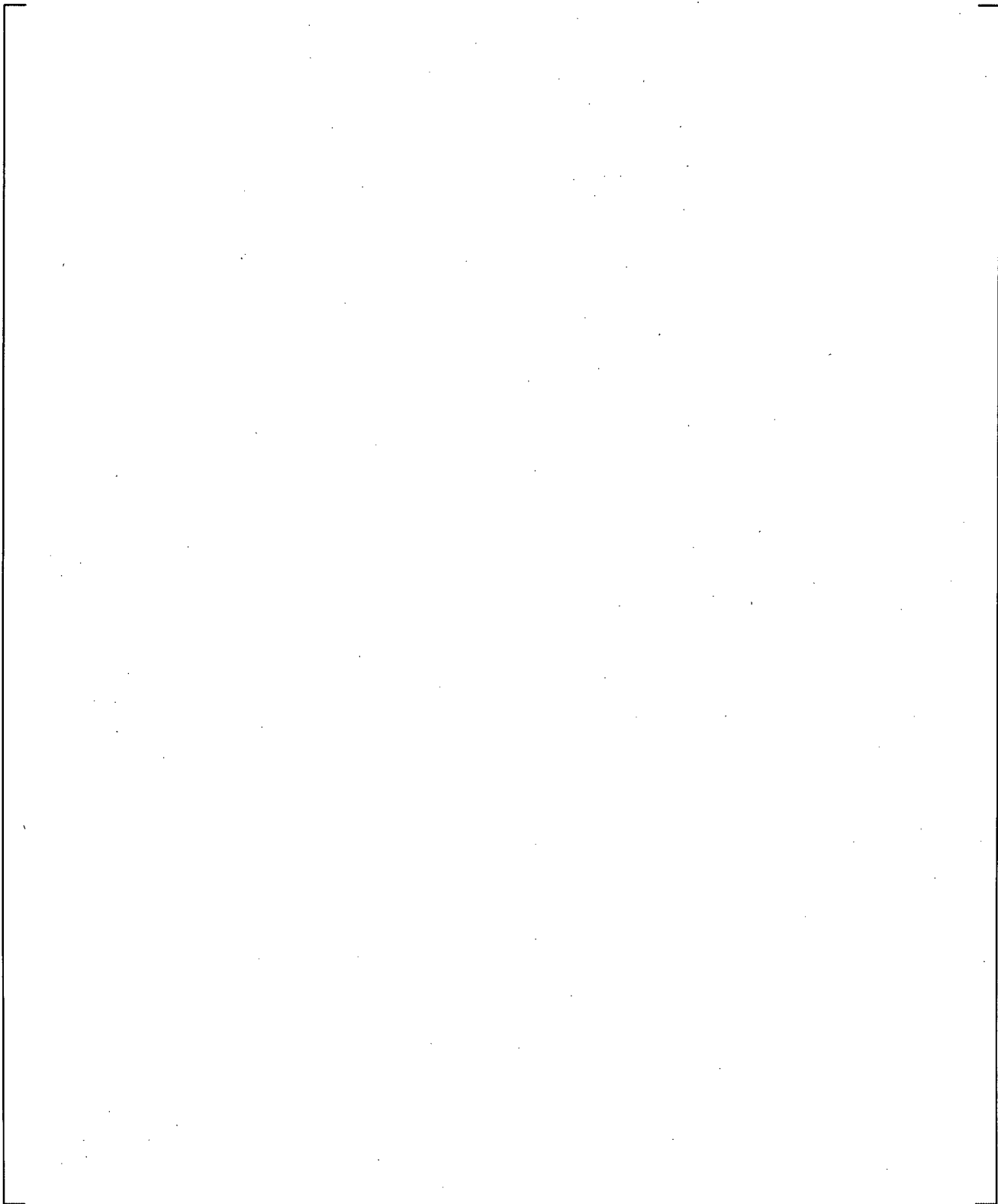
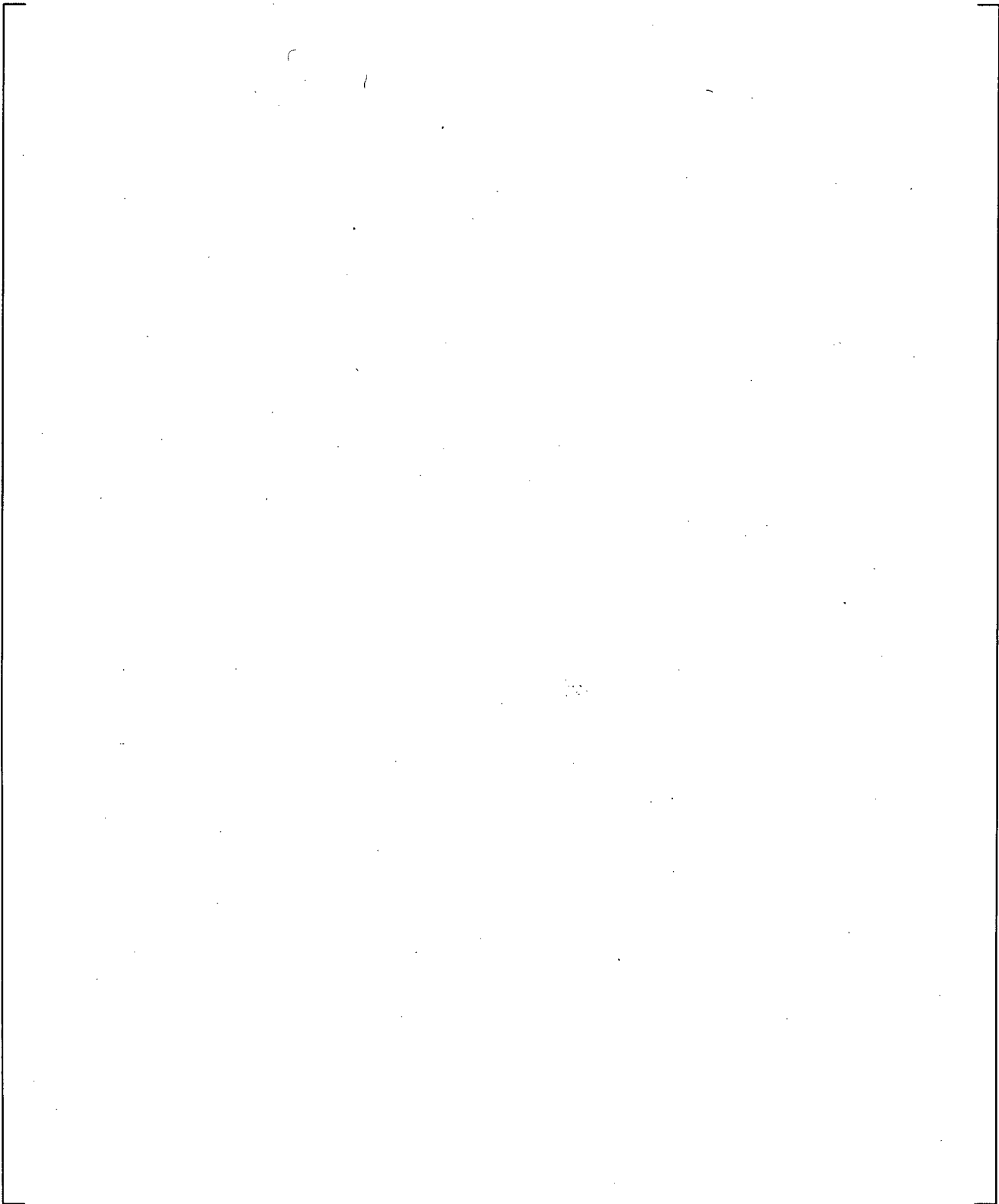


Figure 20.2-5 Schematic of the Air/Water Test Facility



**Figure 20.2-6 Homologous Head Curves and Westinghouse Air/Water Data**



**Figure 20.2-7 Single-Phase and Fully Degraded Pump Head Curves Compared With Two-Phase Data**

a,c

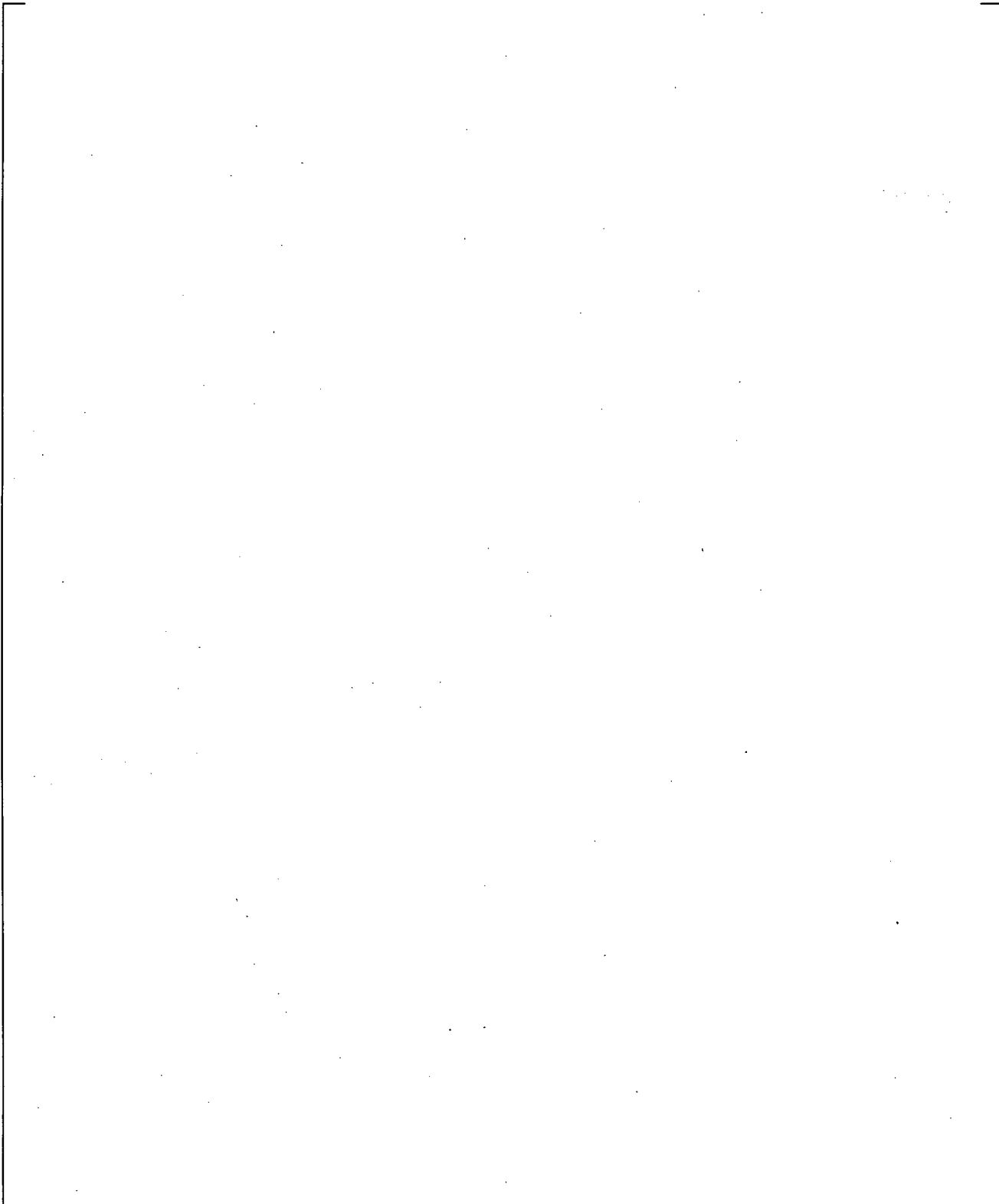


**Figure 20.2-8 Pump Single-Phase and Fully Degraded Torque Curves, Compared With Two-Phase Data**

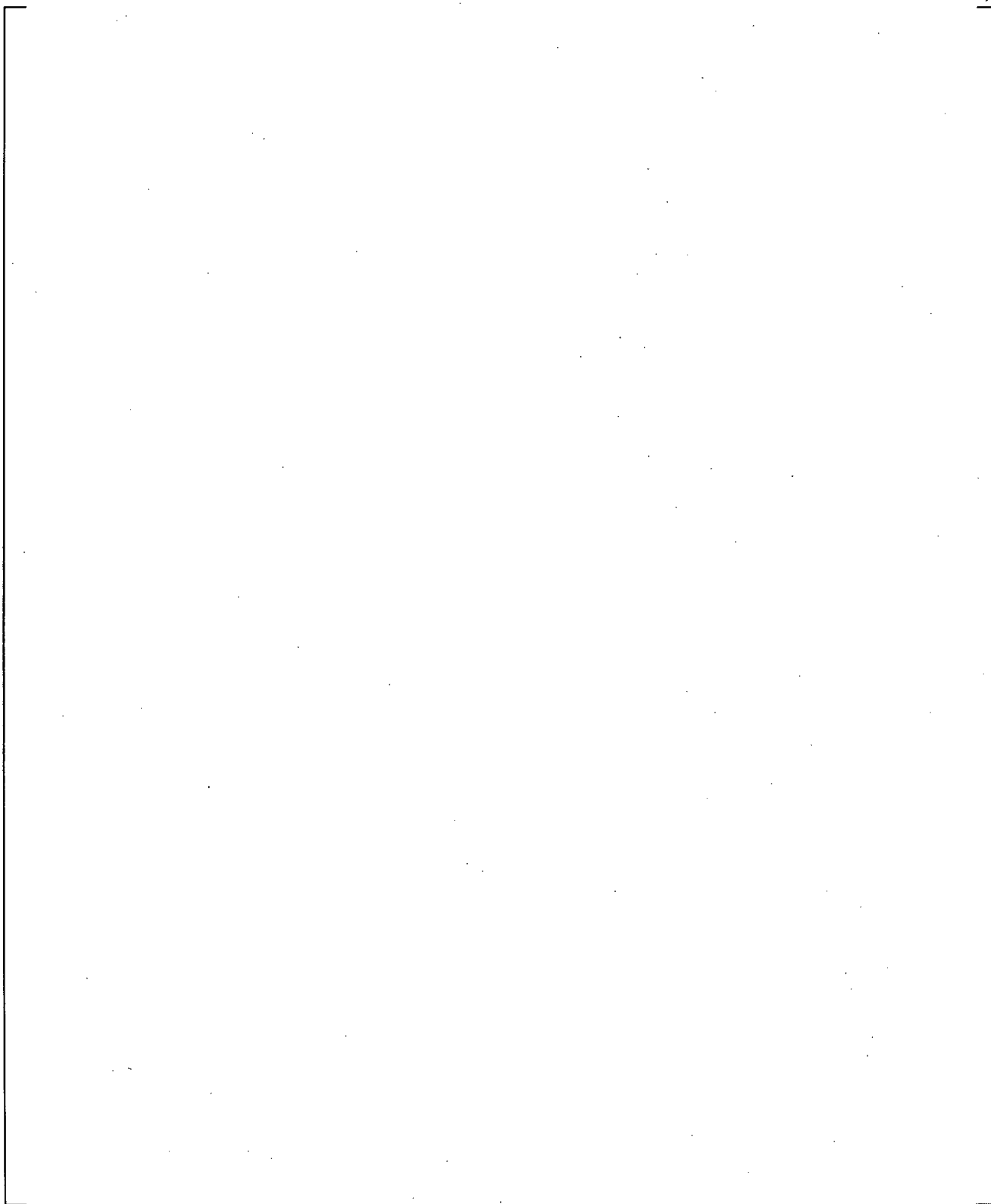


**Figure 20.2-9 Two-Phase Multiplier and Pumping Mode Data**

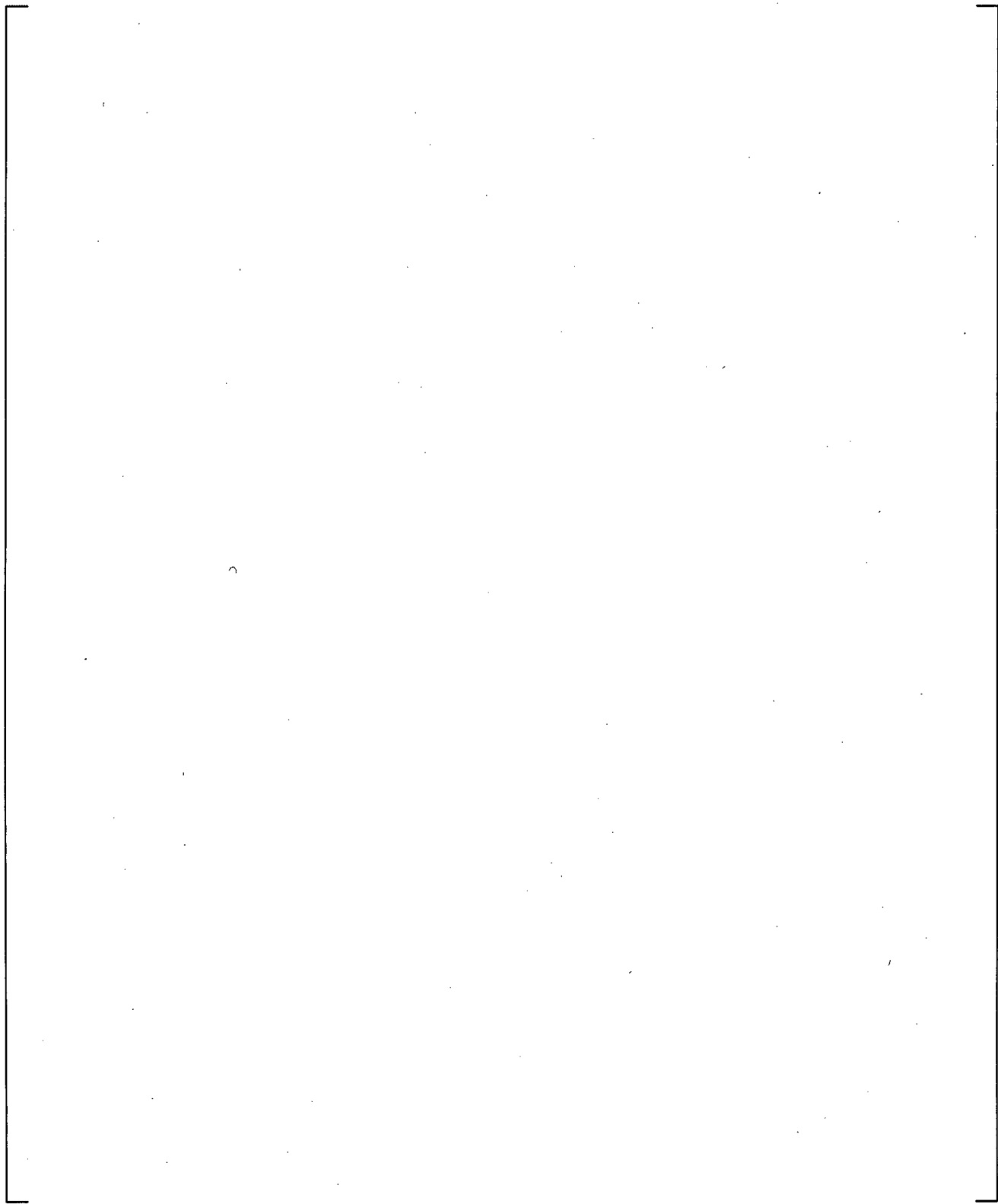


**Figure 20.2-10 Two-Phase Multiplier and All Two-Phase Data**

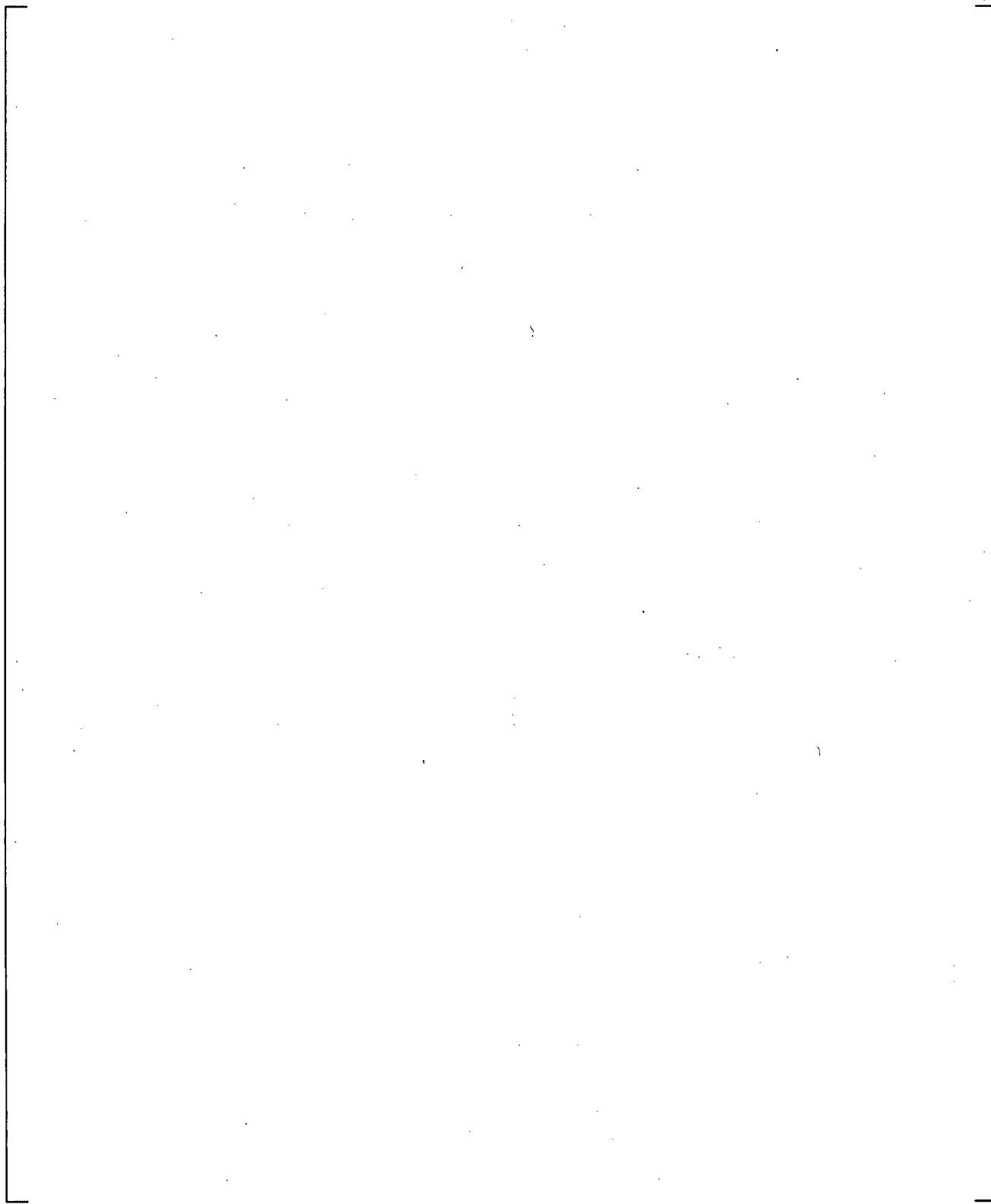


**Figure 20.2-11  $M(\alpha)$  for Pump Torque (Referred to as  $N(\alpha)$  in Equation 10-9)**

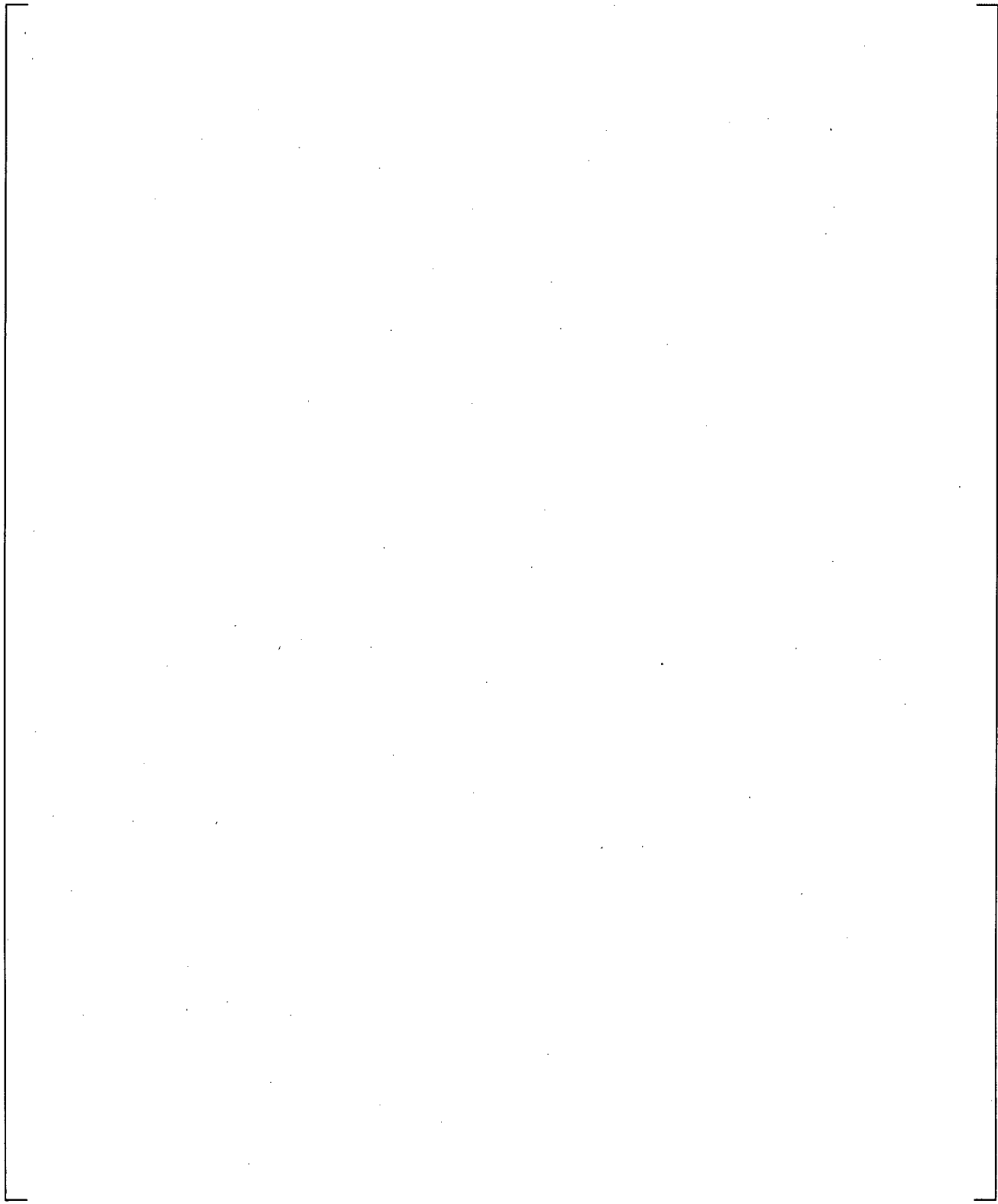


**Figure 20.2-12 Westinghouse Pump Head Curves Compared With LOFT Pump Head Curves**

## 20.3 MASS AND ENERGY CONSERVATION ACROSS 1D/3D JUNCTION

WCOBRA/TRAC-TF2, as described in Section 3, is comprised of a two-fluid, three field representation of the vessel component (3D) and a two-phase, two-fluid representation for the one-dimensional components (1D). At the interfaces, such as cold and hot leg nozzles, are junctions coupling the numerical solution. This section serves to demonstrate the conservation of mass and energy across such a junction with the use of a simple numerical test problem. The momentum coupling treatment and assessment is discussed in Section 19.3.5.10 regarding the cold leg nozzle loss coefficient.

### 20.3.1 Scenario Description and WCOBRA/TRAC-TF2 Model Description

A single channel, 10 node vessel (node height = 1.0 ft, node diameter = 2 in.) is connected to PIPE components at junctions at the bottom and top nodes (Figure 20.3-1). A third pipe is connected to node 5. Each PIPE has a diameter of 0.2 ft. A liquid velocity ramping up to 5 ft/s in the first 10s of the transient and to 10 ft/s within the first 50s is supplied with FILL components connected through junctions at the top and middle node. Zero axial flow boundary conditions are prescribed at the top and bottom of the vessel such that both inlet flows must exit the vessel at the 1D junction at the bottom node, where a 100 psia pressure boundary condition is prescribed with a BREAK component. The assumed temperature is 60°F.

The solution requires mass and energy to be conserved for the control volume. Given that the problem considers single phase, quasi-steady flow, and there is no net mass or energy accumulation in the vessel component, the following equations must be satisfied at the junctions:

$$\begin{aligned}\dot{m}_{in} &= \dot{m}_{out} \\ h_{in}\dot{m}_{in} &= h_{out}\dot{m}_{out}\end{aligned}$$

where  $h$  is the enthalpy of the mixture per unit mass and  $\dot{m}$  is the mixture mass flow rate.

### 20.3.2 Results and Conclusions

Figure 20.3-2 shows that throughout the transient as the velocity of each of the FILL components ramps to 10 ft/s, the mass flow entering the vessel equals the mass flow exiting the vessel. After 100 seconds, the mass flow rate error is [ ]<sup>a,c</sup>. Figure 20.3-3 shows that the energy (enthalpy) flow rate into the vessel equals the energy flow out of the vessel throughout the transient. After 100 seconds, the error is [ ]<sup>a,c</sup>.

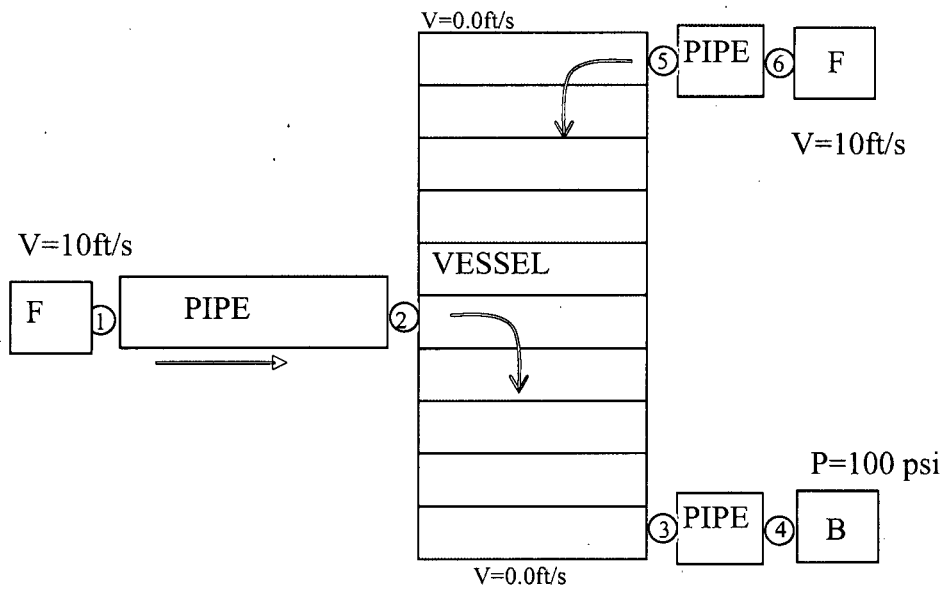
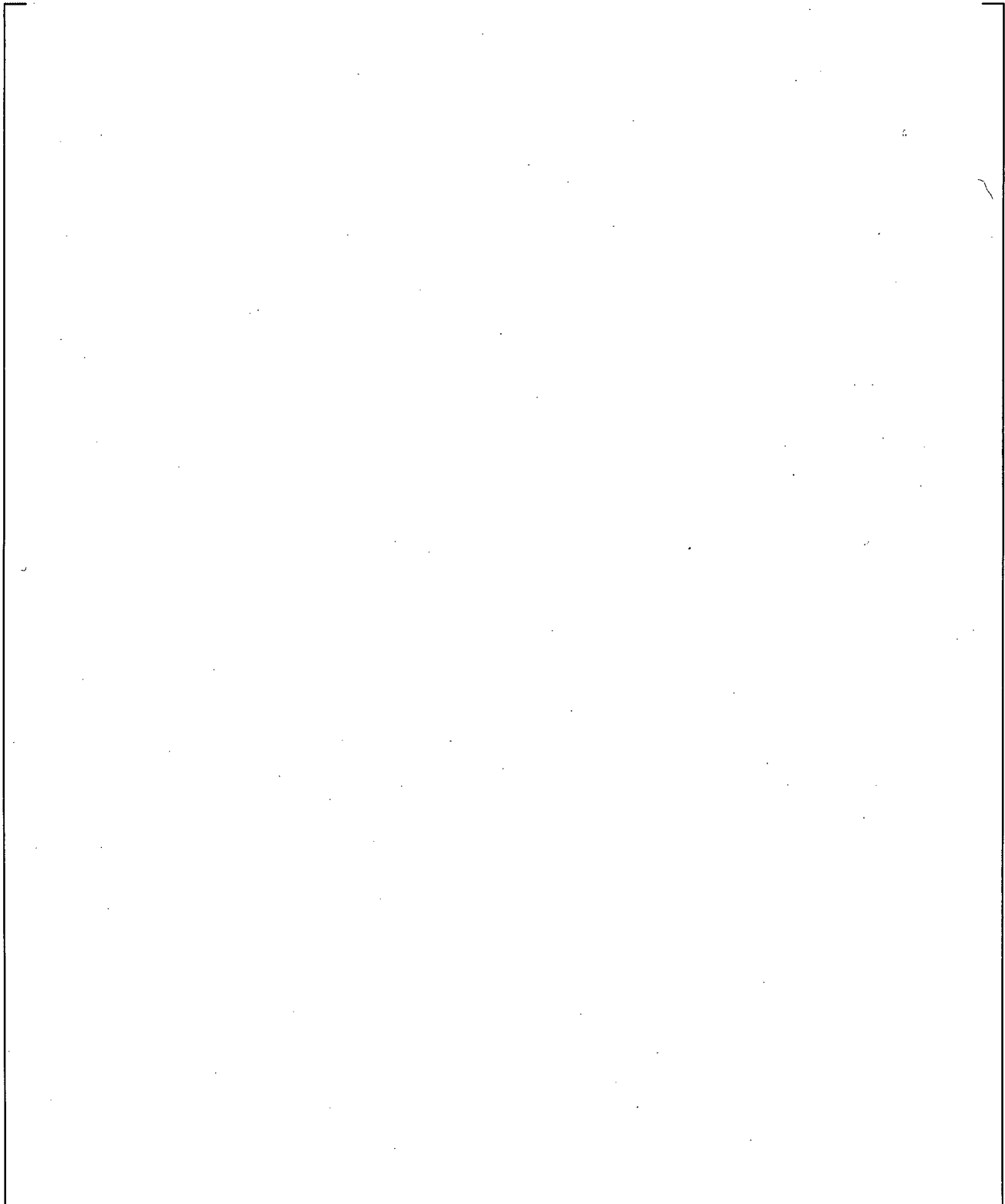
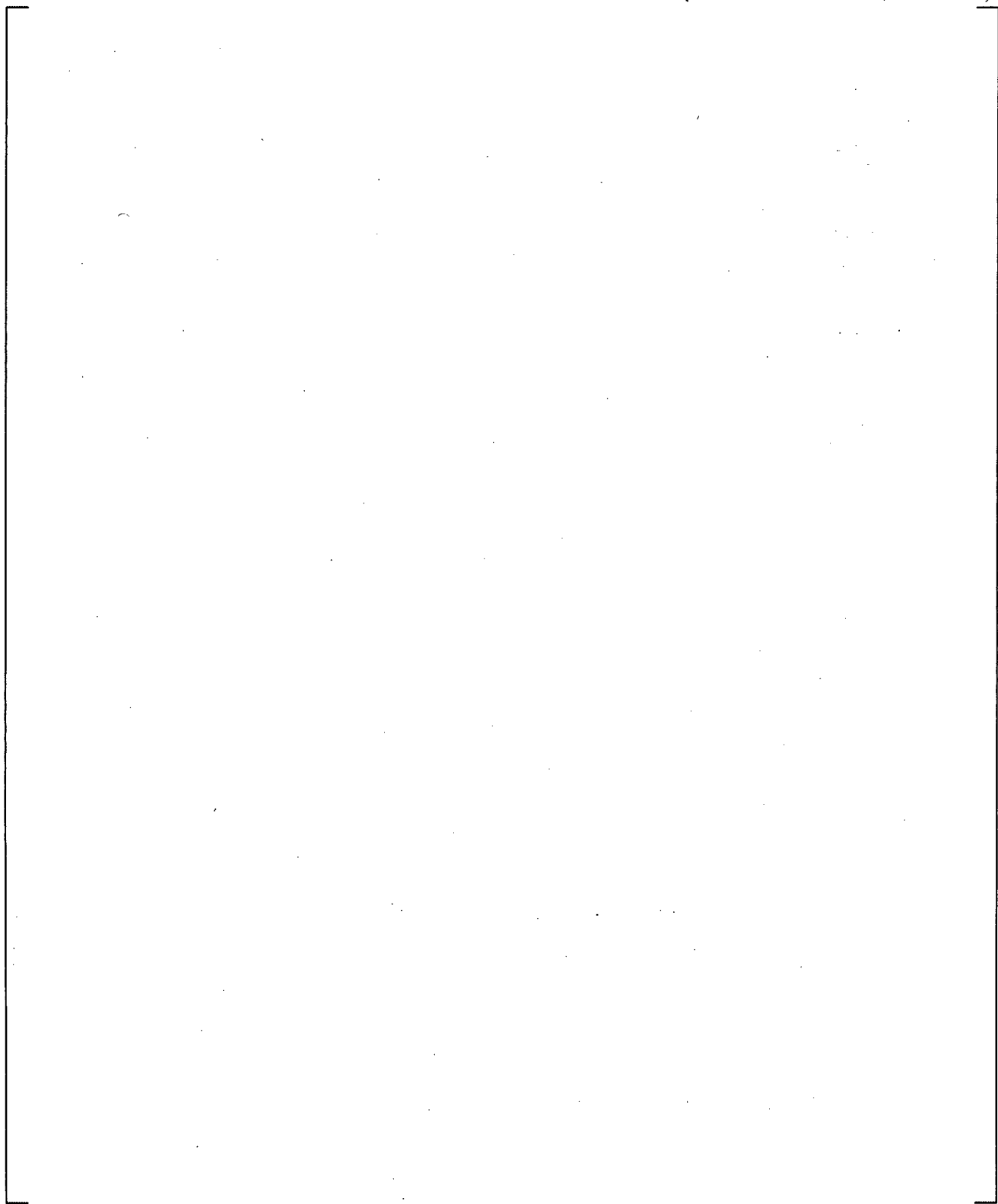


Figure 20.3-1 Scenario and Noding Diagram for 1D/3D Mass and Energy Test



**Figure 20.3-2 Mass Conservation for 1D/3D Mass and Energy Test**



**Figure 20.3-3 Energy Conservation for 1D/3D Mass and Energy Test**

## 20.4 SUMMARY AND CONCLUSIONS

This section considered the WCOBRA/TRAC-TF2 component models that have special importance during the simulation of a LOCA in a PWR, and that have not been discussed in previous sections.

Section 20.1 documented the validation performed for the accumulator model. Accumulator blowdown tests performed at Indian Point Unit 2 and Callaway were modeled and simulated with WCOBRA/TRAC-TF2, and [

] <sup>a,c</sup> Simulations of the LOFT experiments were made with accumulator modeling similar to that used in a PWR. The LOFT simulations showed that WCOBRA/TRAC-TF2 predicted [

] <sup>a,c</sup>

The WCOBRA/TRAC-TF2 pump model was discussed in Section 20.2. The model was used in the simulation of the LOFT and ROSA tests, and the comparison of the predicted versus measured pressure difference across the pump was [

] <sup>a,c</sup>

Finally, Section 20.3 provided [

] <sup>a,c</sup>.